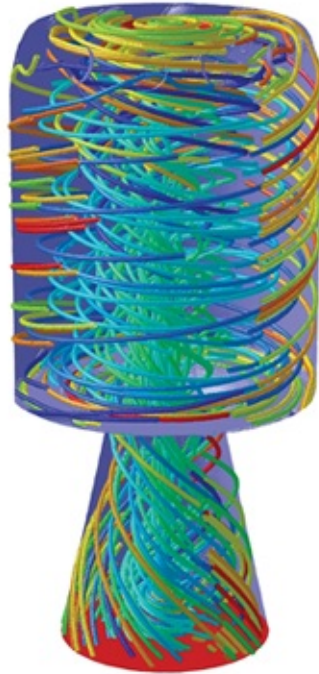


This International Student Edition is for use outside of the U.S.

Frank M. White

Joseph Majdalani

VISCOUS FLUID FLOW



Mc
Graw
Hill

Fourth
Edition

VISCOUS FLUID FLOW

VISCOUS FLUID FLOW

Fourth Edition

Frank M. White

University of Rhode Island

Joseph Majdalani

Auburn University





VISCOUS FLUID FLOW

Published by McGraw Hill LLC, 1325 Avenue of the Americas, New York, NY 10121. Copyright ©2022 by McGraw Hill LLC. All rights reserved. Printed in the United States of America. No part of this publication may be reproduced or distributed in any form or by any means, or stored in a database or retrieval system, without the prior written consent of McGraw Hill LLC, including, but not limited to, in any network or other electronic storage or transmission, or broadcast for distance learning.

Some ancillaries, including electronic and print components, may not be available to customers outside the United States.

This book is printed on acid-free paper.

1 2 3 4 5 6 7 8 9 LWI 26 25 24 23 22 21

ISBN 978-1-260-59780-6

MHID 1-260-59780-6

Cover Image: *Joseph C. Majdalani*

All credits appearing on page or at the end of the book are considered to be an extension of the copyright page.

The Internet addresses listed in the text were accurate at the time of publication. The inclusion of a website does not indicate an endorsement by the authors or McGraw Hill LLC, and McGraw Hill LLC does not guarantee the accuracy of the information presented at these sites.

mheducation.com/highered

ABOUT THE AUTHORS



Frank M. White is Professor Emeritus of Mechanical and Ocean Engineering at the University of Rhode Island. He is a native of Augusta, Georgia, and went to undergraduate school at Georgia Tech, receiving a B.M.E. degree in 1954. Then he attended the Massachusetts Institute of Technology for an S.M. degree in 1956, returning to Georgia Tech to earn a Ph.D. degree in mechanical engineering in 1959. He began teaching aerospace engineering at Georgia Tech in 1957 and moved to the University of Rhode Island in 1964. He retired in January 1998.

At the University of Rhode Island, Frank became interested in oceanographic and coastal flow problems and in 1966 helped found the first Department of Ocean Engineering in the United States. His research interests have mainly been in viscous flow and convection heat transfer. Known primarily as a teacher and writer, he received the ASEE Westinghouse Teaching Excellence Award in addition to seven University of Rhode Island teaching awards. His modest research accomplishments include some 80 technical papers and reports, the ASME Lewis F. Moody Research Award in 1973, and the ASME Fluids Engineering Award in 1991. He is a Fellow of the ASME and for 12 years served as editor-in-chief of the ASME *Journal of Fluids Engineering*. He received a Distinguished Alumnus award from Georgia Tech in 1990 and was elected to the Academy of Distinguished Georgia Tech Alumni in 1994.

In addition to the present text, he has written three undergraduate textbooks: *Fluid Mechanics*, *Heat Transfer*, and *Heat and Mass Transfer*. He has served as a consulting editor of the McGraw-Hill Encyclopedia of Science and Technology from 1992 until 2006, and on the ASME Publications Committee until 2009. He continues to be inspired by his late wife, Jeanne, and lives in Narragansett, Rhode Island, with his dog Jack and his cat Kerry. [Photo Credit: Ellen Emerson White]



Joseph (“Joe”) Majdalani is the Hugh and Loeda Francis Chair of Excellence and Professor of Aerospace Engineering at Auburn University. A native of Beirut, Lebanon, he pursued his undergraduate studies in mechanical engineering at the American University of Beirut, where he received a B.E. degree in 1989. He then attended the University of Utah, completing additional M.S. and Ph.D. degrees in 1991 and 1995. He began teaching mechanical engineering at Marquette University in 1997 and moved to the University of Tennessee in 2003, serving consecutively as Jack D. Whitfield Professor of High Speed Flows and Arnold Chair of Excellence in Advanced Propulsion within the Department of Mechanical, Aerospace, and Biomedical Engineering. In 2013, he joined Auburn University as the Auburn Alumni Engineering Council Endowed Professor and Department Chair of Aerospace Engineering.

Joe is mostly known for his work on oscillating and rotating flows that are driven by either wall-normal or wall-tangential injection. These motions arise in a variety of physical settings such as porous enclosures and simulated rocket motors. His present research devotes itself to the study of unsteady flow phenomena in the context of solid, liquid, hybrid, and nuclear rocket systems, especially those driven by swirl or cyclonic motion. His interests span rocket internal flow fields, vorticity dynamics, computational mathematics, and singular perturbation theory. His research activities since 1997 have materialized in around 300 publications. Throughout his research investigations, he has identified a total of eighteen dimensionless parameters. These parameters have played a key role in guiding experimental procedures and shaping several research investigations in the areas of boundary-layer characterization, wave propagation, and swirl.

Throughout his career, Joe has received several professional recognitions. These include the ASEE/AIAA J. Leland Atwood Educator Award in 2018, the Abe M. Zarem Educator Award in 2013 and, again, in 2018, the Solid Rocket viRockets Best Paper Award (thrice recipient), the AIAA Sustained Service Award in 2016, the Aerospace Engineering Outstanding Faculty Member in 2015, the Konrad Dannenberg Educator of the Year in 2014, the Ralph R. Teetor Educational Award in 2007, the General “Hap” Arnold Award in 2007, the NSF CAREER Award in 2002, Marquette’s Outstanding Teaching Award in 1998–2000 (twice recipient), and Marquette’s College of Engineering Research Award in 1997–1998.

Joe is presently a Fellow of ASME, Associate Fellow of AIAA, past Chair of the AIAA Solid Rockets Technical Committee (2017-2019), past Chair of the AIAA Hybrid Rockets Technical Committee (2015-2017), and past Director of Honors and Awards within the Greater Huntsville Section (2016-2020). He lives with his wife, Inna, and their children, George, Laura, and Maya, in Auburn, Alabama.

At the time of this writing, a group photo of Joe's research students is provided below.



DEDICATION

To two remarkable women in our lives,
Jeanne Faucher White,
and Laure Wakim Majdalani,
to whom we reserve a very special place in our hearts.

CONTENTS

[Preface xiii](#)

[List of Symbols xvii](#)

[1 Preliminary Concepts 1](#)

[1-1 Historical Outline 1](#)

[1-2 Some Examples of Viscous-Flow Phenomena 2](#)

[1-3 Properties of a Fluid 8](#)

[1-4 Boundary Conditions for Viscous-Flow Problems 27](#)

[Summary 31](#)

[Problems 31](#)

[2 Fundamental Equations of Compressible Viscous Flow 38](#)

[2-1 Introduction 38](#)

[2-2 Classification of The Fundamental Equations 38](#)

[2-3 Conservation of Mass: The Equation of Continuity 39](#)

[2-4 Conservation of Momentum: The Navier–Stokes Equations 40](#)

[2-5 The Energy Equation \(First Law of Thermodynamics\) 46](#)

[2-6 Boundary Conditions for Viscous Heat-Conducting Flow 49](#)

[2-7 Orthogonal Coordinate Systems 50](#)

[2-8 Mathematical Character of the Equations of Motion 52](#)

[2-9 Dimensionless Parameters in Viscous Flow 56](#)

[2-10 Vorticity Considerations in Incompressible Viscous Flow 59](#)

[2-11 Two-Dimensional Considerations: The Stream Function 60](#)

[2-12 Non-Inertial Coordinate Systems 63](#)

2-13 [Control-Volume Formulations 63](#)

[Summary 65](#)

[Problems 66](#)

3 [Solutions of the Newtonian Viscous-Flow Equations 76](#)

3-1 [Introduction And Classification of Solutions 76](#)

3-2 [Couette Flows Due to Moving Surfaces 77](#)

3-3 [Poiseuille Flow Through Ducts 82](#)

3-4 [Unsteady Duct Flows 95](#)

3-5 [Unsteady Flows with Moving Boundaries 103](#)

3-6 [Asymptotic Suction Flows 108](#)

3-7 [Wind-Driven Flows: The Ekman Drift 117](#)

3-8 [Similarity Solutions 119](#)

3-9 [Low Reynolds Number: Linearized Creeping Motion 133](#)

[Summary 144](#)

[Problems 145](#)

Page x

4 [Laminar Boundary Layers 153](#)

4-1 [Introduction 153](#)

4-2 [Laminar-Boundary-Layer Equations 164](#)

4-3 [Similarity Solutions for Steady Two-Dimensional Flow 167](#)

4-4 [Free-Shear Flows 185](#)

4-5 [Other Analytic Two-Dimensional Solutions 190](#)

4-6 [Approximate Integral Methods 192](#)

4-7 [Numerical Solutions 199](#)

4-8 [Thermal-Boundary-Layer Calculations 204](#)

4-9 [Developing Inlet Flow in Ducts 210](#)

4-10 [Rotationally Symmetric Boundary Layers 212](#)

- [4-11 Three-Dimensional Laminar Boundary Layers 219](#)
- [4-12 Unsteady Boundary Layers: Separation Anxiety 226](#)
- [4-13 Free-Convection Boundary Layers 227](#)
- [Summary 232](#)
- [Problems 232](#)

5 [The Stability of Laminar Flows 249](#)

- [5-1 Introduction: The Concept of Small-Disturbance Stability 249](#)
- [5-2 Linearized Stability of Parallel Viscous Flows 253](#)
- [5-3 Parametric Effects in the Linear Stability Theory 261](#)
- [5-4 Transition to Turbulence 271](#)
- [5-5 Engineering Prediction of Transition 276](#)
- [5-6 Biglobal Stability of Incompressible Viscous Flow 287](#)
- [5-7 Biglobal Stability of Compressible Viscous Flow 295](#)
- [Summary 310](#)
- [Problems 311](#)

6 [Incompressible Turbulent Mean Flow 323](#)

- [6-1 Physical and Mathematical Description of Turbulence 323](#)
- [6-2 The Reynolds Equations of Turbulent Motion 328](#)
- [6-3 The Two-Dimensional Turbulent-Boundary-Layer Equations 332](#)
- [6-4 Velocity Profiles: The Inner, Outer, and Overlap Layers 334](#)
- [6-5 Turbulent Flow in Pipes and Channels 341](#)
- [6-6 The Turbulent Boundary Layer on a Flat Plate 347](#)
- [6-7 Turbulence Modeling 353](#)
- [6-8 Analysis of Turbulent Boundary Layers with a Pressure Gradient 362](#)
- [6-9 Free Turbulence: Jets, Wakes, and Mixing Layers 375](#)
- [6-10 Turbulent Convective Heat Transfer 383](#)
- [Summary 392](#)
- [Problems 393](#)

7 Compressible Boundary-Layer Flow 400

- 7-1 Introduction: The Compressible-Boundary-Layer Equations 400
- 7-2 Similarity Solutions for Compressible Laminar Flow 405
- 7-3 Solutions for Laminar Flat-Plate and Stagnation-Point Flow 407
- 7-4 Compressible Laminar Boundary Layers Under Arbitrary Conditions 415
- 7-5 Special Topics in Compressible Laminar Flow 424
- 7-6 The Compressible-Turbulent-Boundary-Layer Equations 430
- 7-7 Wall and Wake Laws for Turbulent Compressible Flow 432
- 7.8 Compressible Turbulent Flow Past a Flat Plate 436
- 7-9 Compressible-Turbulent-Boundary-Layer Calculation with a Pressure Gradient 441
- 7-10 Compressible-Flow Approximations for Quasi-Viscous Flows 444
 - Summary 451
 - Problems 451

Page xi

Appendices 457

- A Vector Identities 457
- B1 3d Kinematic Expressions in Cartesian Coordinates 458
- B2 Reduced Kinematic Expressions in Steady 2D Cartesian Coordinates 459
- B3 3D Kinematic Expressions in Cylindrical Coordinates 460
- B4 Reduced Kinematic Expressions in Steady 2D Cylindrical Coordinates 462
- C Transport Properties of Various Newtonian Fluids 463
- D Einstein's Indicial Notation 472
- E1 Advanced Energy Loss Evaluation 474
- E2 Traditional/Iterative Energy Loss Evaluation 476
- F Bragg-Hawthorne Equation for Axisymmetric Flow in Spherical Coordinates 478
- G Equations of Motion of Incompressible Newtonian Fluids in Cylindrical

[and Spherical Polar Coordinates 480](#)

H1 [Determination of Dimensionless Parameters 483](#)

H2 [List of Dimensionless Parameters 485](#)

I [Trigonometric Identities 490](#)

[Bibliography 492](#)

[Index 517](#)

Page xii



PREFACE

OVERVIEW

This book is known for its academic rigor and effectiveness at serving as a convenient “one-stop shop” for a large constituency of seniors, graduate students, researchers, and scholars who are genuinely interested in expanding their knowledge of the rich and evolving field of fluid mechanics.

The fourth edition maintains the tradition of fulfilling the role of a senior or first-year graduate textbook on viscous motion with an eclectic mix of engineering applications. Students are expected to understand the basic foundations of fluid mechanics, vector calculus, partial differential equations, and rudimentary numerical analysis. The material can be selectively presented in a one-semester course or, with more extensive coverage, in two (or even three) semesters.

The evolution of viscous-flow prediction continues its journey toward more highly resolved, sophisticated, stable, and high-order simulations. This book, however, retains its focus on presenting viscous-flow *concepts*, not software. As such, we place a strong emphasis on the physical insight and mathematical depth that we gain while exploring, systematically, a rich variety of flow problems. Our objective is to make the book readable, descriptive, and introductory to the field.

New to this edition:

- We have increased the number of problems by 50 percent, thus adding a total of 128 new problems to an original set of 255. Only 6 problems have been replaced, to avoid pedagogical disruptions. Taking student feedback into account, most new problems are example-like or life-like, and either have “answers” or are “self-guided,” i.e., with step-by-step instructions to obtain a specified outcome. The chapter breakdown in the table below identifies the actual number of problems added to each chapter. Note that 58 “levelling” problems have been added to Chaps. 1 and 2, which can be used as “refreshers” in the areas of kinematic analysis, scaling analysis, dimensional analysis, streamline analysis, and integral analysis. These techniques, we feel, are essential to grasp before progressing to the more advanced concepts that unfold in Chaps. 3–7. We have also provided complementary examples on the use of the vorticity-streamfunction approach as well as the Bragg–Hawthorne formulation in the context of two- and quasi three-dimensional flow configurations. An additional 30 problems are featured in Chaps. 3 and 4 to further explore the benefits of differential analysis, the momentum-integral

approach, and the celebrated Blasius solution.

Chapter	Original Probs.	New Probs.	Total	Increase
1	23	20	43	87%
2	21	38	59	181%
3	53	6	59	11%
4	53	24	77	45%
5	31	26	57	84%
6	47	9	56	19%
7	27	5	32	19%
All chaps.	255	128	383	50%

- New material has been incorporated into Chaps. 2–7. More specifically, we have introduced the highly effective Bragg–Hawthorne approach for solving steady axisymmetric flow problems ([Chap. 2](#)); some pulsatory flow extensions and solutions discovered in the context of injection or suction-driven porous ducts ([Chap. 3](#)); newly found solutions to the Blasius equation for flow over flat plates that overcome the Pohlhausen paradox ([Chap. 4](#)); a generalization of Kármán’s momentum-integral approach for both laminar and turbulent boundary layers (Chaps. 4 Page xiv and 6); a two-dimensional biglobal stability approach for both incompressible and compressible flow configurations ([Chap. 5](#)); closed-form analytical expressions for the fundamental compressible, isentropic flow equations, the weakly compressible water hammer problem, and several two-dimensional and axisymmetric flow profiles, such as the compressible Hart–McClure, Taylor, and Taylor–Culick profiles ([Chap. 7](#)).
- To overcome noted deficiencies reported by incoming students, and to assist in problem solving, we have removed one appendix and added seven more to the original set of three, for a total assortment of nine appendices, A–I. These contain review material on (A) vector identities; (B) reduced forms of the incompressible Navier–Stokes equations, which can be readily applied to either two-dimensional or three-dimensional planar or axisymmetric flow configurations; (D) Einstein’s indicial notation; (E) energy loss evaluation; (F) Bragg–Hawthorne’s equations in spherical polar coordinates; (H) Edgar Buckingham’s Pi procedure with a list of 88 non-dimensional parameters; and, lastly, (I) various trigonometric identities. We have eliminated the appendix detailing the Runge–Kutta code, and relabeled the “Transport Properties of Various Newtonian Fluids” and “Equations of Motion” as Apps. C and G.
- To avoid mixing vector and indicial notations in key equations throughout the text, we have presented their entirely vector and entirely indicial forms side by side, to help those unfamiliar with the indicial notation, without requiring it. We have also supplied a short appendix to introduce Einstein’s indicial notation (App. D). We have deliberately eliminated cases where the indicial and vector notations are collocated in the same expression.
- We have tried to unify the nomenclature seamlessly, by implementing minimal amendments and avoiding disruptions to any particular segment of the book. So while the

Blasius similarity variable is kept as $\eta = y\sqrt{U/(2\nu x)}$, the normalized coordinate across the boundary layer is renamed as $\xi = y/\delta = \eta/\eta_\delta$. This is done to avoid confusion between the two transformations, especially that the Blasius similarity variable extends out to infinity in the far field above the boundary layer, whereas the normalized y -coordinate remains bracketed within the interval $0 \leq \xi \leq 1$. Not only do we provide the conversion factors between η and ξ , we also reexamine their dependent variables. In this vein, we maintain the characteristic Blasius stream function as $f(\eta)$, but relabel the normalized velocity in the boundary layer as $F(\xi) = u/U = df/d\eta$. In previous editions, f is used to denote both the stream function and its derivative, while η is used to represent the Blasius similarity variable as well as the normalized boundary layer coordinate, despite their dissimilar definitions. This distinction, we hope, will help.

- We have introduced in [Chap. 4](#) simplified analytic expressions that follow from Kármán's momentum-integral equation absent a pressure gradient: these compact formulas enable us to reproduce, rather straightforwardly, all boundary layer characteristics, such as the disturbance, displacement, and momentum thicknesses, for any assumed velocity profile. As a result, skin friction coefficients and other boundary layer properties, which are typically tabulated in most fluid textbooks, can be readily reproduced and verified, for any mean flow function $f(\xi)$, using these simple relations.
- On its centennial anniversary, we now offer a compelling rational explanation for the 1921 Pohlhausen paradox, namely, the reason why the use of a fourth-order, quartic polynomial approximation of the velocity profile in the viscous region leads to less accurate predictions of the skin friction coefficient and disturbance, displacement, and momentum thicknesses, than using, for example, quadratic or cubic Pohlhausen polynomials (Table 4-1). Not only do we clarify the Pohlhausen paradox, we provide an alternative quartic polynomial in [Chap. 4](#) that does not suffer from the principal deficiency undermining Pohlhausen's. This new formulation, $F(\xi) = (5\xi - 3\xi^3 + \xi^4)/3$, enables us to achieve an appreciable order-of-magnitude improvement in accuracy between our analytical predictions and the robustly computed Blasius values in both viscous and thermal analyses, particularly, those that are traditionally carried out using Pohlhausen's quartic polynomial, $F(\xi) = 2\xi - 2\xi^3 + \xi^4$. Instead of accruing a 10–20 percent error in each boundary layer estimate, the new formulation leads to relative errors that do not exceed 1.7 percent.
- Since no coverage of viscous flow theory is complete without a detailed discussion of the Blasius similarity equation, we expand the corresponding material by providing in Sec. 4-3.1 a summary of advances made in the past 100 years while trying to solve it. These advancements include elegant numerical schemes as well as persistent analytical efforts that give rise to series solutions, intuitive approximations, and other uniformly valid expansions that are based on a variety of theoretical techniques. After reviewing the pertinent literature and describing a set of continuous functions that approximate the Blasius profile over its semi-infinite range of $0 \leq \eta < \infty$, we present the reader with a real treat: a compact, quasi-exact exponential function that entails a maximum $L_2 = 6 \times 10^{-4}$

error (Table 4-4), thus placing it within the same margin of error associated with the Blasius equation itself! The reader may enjoy verifying that this one-term closed-form expression, $F(\xi) = 1 - \exp[-s\xi(1 + \frac{1}{2}s\xi + \xi^2)]$, with $s = 1.6304$, matches the Blasius solution virtually identically, not only from the wall to the edge of the boundary layer, but all the way to infinity (Fig. 4-13).

Page xv

- Two foundational sections have been added to [Chap. 5](#), thus extending the essentially one-dimensional hydrodynamic stability coverage to the fast-growing biglobal approach in the context of both incompressible and compressible motions.
- An extension of Kármán’s momentum-integral formulation to a turbulent, power law profile with an arbitrary exponent is presented in [Chap. 6](#).
- Analytically inverted forms of the isentropic equations for compressible gases are provided in [Chap. 7](#) along with new coverage of the weakly compressible water hammer problem, which has remained unresolved for nearly 120 years. Compressible forms of several classical profiles are also introduced.
- Over 200 new references have been cited or updated.
- An Instructor Manual and Student Resource Web Site have been developed. We have added PowerPoint slides to accompany the Instructor Manual, which should prove useful to those adopting this text.

ORGANIZATION

We have retained the effective seven-chapter format of the Viscous Fluid Flow textbook.

Chapter 1 introduces viscous-flow concepts and boundary conditions while overviewing the basic transport properties of Newtonian and non-Newtonian fluids and their constitutive relations. New material has been added on mass diffusivity and Fick’s law. Based on popular demand, [Chap. 1](#) has been shortened while being augmented by several practical appendices: these begin with vector identities in App. A, and are followed by abridged kinematic expressions in App. B, and transport properties in App. C.

Chapter 2 overviews the basic equations of motion. We have expanded the section describing the hyperbolic, parabolic, and elliptic nature of the elusive Navier–Stokes equations. We have provided, as much as practical, both vector and indicial forms for key equations. Material has been added on the Bragg–Hawthorne formulation for the effective analysis of axisymmetric flow configurations. We have unified recurring symbols by adopting, for example, the traditional σ for the total stress component—which can absorb the normal pressure—and by reserving τ for the shear stress. We have also embraced the spherical polar coordinate system preferred by mathematicians, wherein θ refers to the azimuthal angle, and φ stands for the polar inclination, or zenith angle. Within this setup, θ remains invariant in both cylindrical and spherical coordinates. Before leaping into Chaps. 3

and 4, however, 38 refresher problems are furnished, which emphasize force scaling, proper normalization, and dimensional analysis, as well as streamline analysis, kinematic analysis, and integral analysis; these can be beneficial to practice or review before engaging more advanced content. Among the newly formulated problems, some involve attractive models of cyclones and tornadoes, as well as the internal mean flow of an idealized rocket motor.

Chapter 3 continues to unravel a variety of laminar-flow solutions of the Navier–Stokes equations. As usual, several collections of new exact and asymptotic solutions are described, and the Stokes paradox is clarified. More detail is provided while presenting oscillatory and pulsatory flow solutions for porous channels and tubes. Along similar lines, the connectivity of the Stokes number to the kinetic Reynolds number and the Womersley number is illuminated. The section describing various computational fluid dynamics (CFD) models is extracted and converted into an online supplement, to avoid producing an excessively long chapter.

Chapter 4 and its references have been updated by incorporating several new breakthrough developments that simplify the use of Kármán’s momentum-integral approach for laminar boundary layers with no pressure gradients. Not only is Pohlhausen’s paradox illuminated, its quartic flow approximation is superseded by a compact polynomial approximation that enables us to achieve much greater accuracy while retaining the flexibility and simplicity of a polynomial representation. Newly devised Blasius flow formulations that remain valid beyond the boundary layer edge are also compared and discussed.

Chapter 5 has been expanded from its one-dimensional coverage to a fully two-dimensional, biglobal stability treatment of both incompressible and compressible flow fields. Illustrations are taken from the class of Taylor and Taylor–Culick profiles, which are injection-driven Berman solutions in porous channels and tubes at high crossflow Reynolds numbers.

Chapter 6 preserves the basic outline for turbulent mean-flow characterization. As usual, the power-law overlap layer controversy is explained, DNS predictions are included, and Sec. 6-6.1 on the momentum-integral analysis, which leads to reasonable predictions of turbulent boundary layer properties by Prandtl’s and Coles’ wall-wake laws, is generalized using a power-law profile of arbitrary exponent. New problems focus on foundational issues such as the use of wall coordinates to reproduce the fundamental linear and log-law relations in the viscous and inertial sublayers, and the effectiveness of turbulent-flow models at providing channel and pipe flow estimates of the wall friction factor.

Page xvi

Chapter 7 has been supplemented by several essential sections. For example, having added in the 3rd edition the isentropic flow equations, the 4th edition provides analytically inverted expressions of these compressible-flow relations that eliminate the need to use iteration or gas dynamics tables. At the outset, predicting properties such as the subsonic or supersonic flow Mach numbers for a given area expansion ratio can be carried out

straightforwardly, with no need for root finding, iteration, or interpolation. A systematic methodology for deriving a compressible correction to a two-dimensional or axisymmetric flow profile using a Rayleigh–Janzen expansion is presented. Examples provided include the quasi-viscous Taylor and Taylor–Culick flows in porous channels and tubes as well as the academic Hart–McClure motion in a porous tube. Lastly, a solution to the weakly compressible water hammer problem, which has eluded researchers for over 120 years, is outlined.

Of the three original appendices, we have dropped the third, on Runge–Kutta integration, and added seven more, for a total set of nine. These begin with fundamental vector identities and end with trigonometric identities; they also journey through abbreviated equations of motion, Einstein’s notation, energy loss evaluation tools, and a comprehensive list of non-dimensional parameters.

ACKNOWLEDGMENTS

There are many individuals that we wish to thank. We are especially grateful for the support and encouragement received from Dr. Li-Jun Xuan, postdoctoral scholar at Auburn University, as well as several amazing doctoral candidates, for assisting in this major effort. These include, in no particular order, Gaurav Sharma, Timothy A. Marquardt, Orie M. Cecil, Tharikaa Ramesh–Kumar, Langston L. Williams, Paul Kovacic, Cody M. Shelton, Hemanth Kumar Mandya Nagaiah, Yokeswaran Subramanian, Cory M. Thomas, Jack N. Finnegan, and Rudy Al-Ahmar. We also thank the National Science Foundation and the Hugh and Loeda Francis Chair of Excellence for supporting Professor Majdalani during the execution of this project.

Much appreciated comments, suggestions, photos, charts, corrections, and encouragement were received from Leon van Dommelen of Florida State University; Gary Settles of Penn State University; Steven Schneider of Purdue University; Kyle Squires of Arizona State University; Chihyung Wen of Da-Yeh University, Taiwan; Brooks Martner of the NOAA Environmental Technology Laboratory; Jay Khodadadi of Auburn University; Philipp Epple of Friedrich-Alexander-Universitaät; Juergen Thoenes of the University of Alabama at Huntsville; Luca d’Agostino of Università Degli Studi di Pisa; Raul Machado of the Royal Institute of Technology (KTH), Sweden; Gordon Holloway of the University of New Brunswick; Abdulaziz Almukbel of George Washington University; Dale Hart of Louisiana Tech University; Debendra K. Das of the University of Alaska Fairbanks; Alexander Smits of Princeton University; Hans Fernholz of Technische Universitaet Berlin; Peter Bernard of the University of Maryland; John Borg of Marquette University; Philip Drazin of the University of Bristol, UK; Ashok Rao of Rancho Santa Margarita, CA; Deborah Pence of Oregon State University; Joseph Katz of Johns Hopkins University; Pierre Dogan of the Colorado School of Mines; Philip Burgers of San Diego, CA; Beth Darchi of the American Society of Mechanical Engineers; and Norma Brennan of the American Institute of Aeronautics and Astronautics.

We have tried to incorporate almost all of the reviewer comments, criticisms, corrections,

and improvements. The fourth edition has greatly benefited from the reviewers of the second and third editions, as well as the reviewers of the fourth edition manuscript:

Malcolm J. Andrews, *Texas A&M University*
Mehdi Asheghi, *Carnegie Mellon University*
Robert Breidenthal, *University of Washington*
Trevor S. Elliott, *University of Tennessee*
Roy J. Hartfield, Jr, *Auburn University*
H. A. Hassan, *North Carolina State University*
Herman Krier, *University of Illinois, Urbana-Champaign*
Brian A. Maicke, *Pennsylvania State University*
Daniel Maynes, *Brigham Young University*
Suresh Menon, *Georgia Institute of Technology*
Meredith Metzger, *University of Utah*
Kamran Mohseni, *University of Colorado*
Ugo Piomelli, *University of Maryland*
Steven P. Schneider, *Purdue University*

Page xvii

Kendra Sharp, *Pennsylvania State University*
Marc K. Smith, *Georgia Institute of Technology*
Leon van Dommelen, *FAMU-FSU*
Steve Wereley, *Purdue University*

Last, but certainly not least, we often thank all of those around us and forget those closest to us. The editors and staff at McGraw Hill Higher Education, Heather Ervolino, Jeni Mcatee, and Beth Bettcher were constantly helpful, professional, and responsive to our needs. We owe them a tremendous deal of gratitude. The book was typeset by Aptara using Adobe InDesign and InMath. Special thanks are owed to Sadika Rehman and Vibhor Singh.

We want to close by stressing that we are particularly indebted to Ellen Emerson White, who went beyond her ways to help us, and who often traveled back and forth during the execution of this project. Ellen has been absolutely amazing. Without her involvement and daily interactions, this effort would not have been possible. Thank you Ellen!

A Final Word

No book is perfect, and this one is no exception. We invite you, our most valued reader, to send us your comments and suggested contributions, to joe.majdalani@gmail.com, so they may be incorporated into our supplemental material, real-time addons, companion slides, and future revisions. Given the rapid pace at which science is expanding, it is essential that new generations of users join us and become part of our “knowledge-generation” team. In this revision, you may be pleased to see that we have incorporated much of the feedback received

from students and instructors who have been using this textbook for several decades, some since 1974. Several sections that needed more clarity have been further detailed, and some lengthy sections have been carefully abbreviated. An effort to unify the nomenclature has been made, and seven practical appendices have been provided. We remain student-centered and, as such, we strive to listen. As you may expect, the book is rather comprehensive, so you may want to hold on to it after class is over, as it will very likely serve as an excellent reference, even if you later part ways with the subject of fluids.

Frank M. White
Joseph C. Majdalani

LIST OF SYMBOLS

English Symbols

a	speed of sound; acceleration (Chap. 2); body radius (Chap. 4)
A	area; amplitude, Eq. (5-48); damping parameter, Eq. (6-90)
b	jet or wake width, Fig. 6-35
B	stagnation-point velocity gradient (Sec. 3-8.1); turbulent wall-law intercept constant, Eq. (6-38a)
ΔB	wall-law shift due to roughness, Eq. (6-49)
c, c_i, c_r	wave phase speeds (Chap. 5)
c_p, c_v	specific heats, Eq. (1-60)
C	Chapman–Rubesin parameter, Eq. (7-35)
C_i	species concentrations (Chap. 1)
D	diameter; drag force (Chap. 4); diffusion coefficient (Chap. 1)
D_h	duct hydraulic diameter, $4A/P$
D_{ij}	turbulent transport or diffusion, Eq. (6-111)
e	, E internal energy
e_t	sum of internal, kinetic and potential energies, Eq. (2-113)
\mathbf{f}, \mathbf{F}	force
f, F, g	similarity variables; dimensionless velocity, u/U
g	gravitational acceleration vector
G	(Pr) heat-transfer parameter, Eqs. (3-227) and (4-100)
h	enthalpy; duct width; heat-transfer coefficient
h_i	scaling factors, Eqs. (2-58) and (4-233)
h	h_0 stagnation enthalpy, $h + V^2/2$
H	shape factor, δ^*/θ ; stagnation enthalpy, Eq. (7-3)
H_1	alternate shape factor, $(\delta - \delta^*)/\theta$
J	jet momentum, Eqs. (4-125) , (4-227) , and (6-144)
k	thermal conductivity; roughness height (Chaps. 5 and 6)
K	bulk modulus, Eq. (1-74) ; duct pressure-drop parameter, Eq. (4-197) ; turbulence

	kinetic energy, Eq. (6-16) ; stagnation-point velocity gradient, Fig. 7-6
ℓ	mean-free path (Chap. 1); mixing length, Eq. (6-88)
L	characteristic length
L_{slip}	slip length, $u_w/(\partial u/\partial n)_w$
m	mass; wedge-velocity exponent, Eq. (4-91)
\dot{m}	mass flow rate
M	molecular weight, Eq. (1-65); moment, Eq. (3-245)
n	normal to the wall; power-law exponent, Eq. (1-33)
p	pressure
\hat{p}	effective pressure (with gravity), $p + \rho gz$
P	pressure gradient parameter, $(-d\hat{p}/dx)h^2/(2\mu U)$ (Chap. 3); $(\delta/\tau_w)(dp_e/dx)$ (Chap. 6); duct perimeter
q	heat-transfer rate per unit area; turbulence level, Eq. (5-51)
Q	heat; volume flow rate, Eq. (3-35)
r	radial coordinate; recovery factor, Eq. (7-31)
r, θ, z	cylindrical polar coordinates, Eq. (2-63)

Page xx

r, φ, θ	spherical polar coordinates preferred by mathematicians, Eq. (2-65) ; permeability parameter (φ in Chap. 6)
r_0	cylinder surface radius, Fig. 4-39
R	gas constant; body radius
s	entropy; velocity slope or Blasius slope s at the wall, $\sigma a/\sqrt{2} = dF(0)/d\xi \approx 1.6304$ (Chap. 4)
S	Sutherland constant, Eq. (1-34) ; laminar shear parameter, Eq. (4-155) ; van Driest parameter, Eq. (7-145)
t	time
T	temperature; percent turbulence, Eq. (5-51)
T^*	wall heat-flux temperature, $q_w/(\rho c_p v^*)$; compressible-flow reference temperature, Eq. (7-57)
\mathfrak{J}	surface tension coefficient
u, v, w	Cartesian velocity components
u_r, u_θ, u_z	cylindrical polar velocity components
u', v', w'	turbulent velocity fluctuations
Δu	wake velocity defect, Fig. 6-35c and Eq. (6-155)

U, W	freestream velocity components
u^*	wall-friction velocity, $(\tau_w/\rho_w)^{1/2}$
u, β	wake velocity, Eq. (6-137)
V	velocity; also U_e/U_0 , Eq. (6-133)
ϑ	volume (Chap. 2)
w	rate of work done on an element, Eq. (2-36)
x, y, z	Cartesian coordinates
Z	gas compressibility factor, $p/(\rho RT)$

Greek Symbols

α	thermal diffusivity, $k/(\rho c_p)$; wedge angle (Fig. 3-39); wave number, Eq. (5-12) ; angle of attack
α, β	finite-difference mesh-size parameters, Eq. (4-167) ; also compressible wall-law parameters, Eqs. (7-141)
α^*, β, ζ	compressible finite-difference mesh-size parameters, Eq. (7-85)
β	thermal expansion coefficient, Eq. (1-76) ; Falkner–Skan parameter, Eq. (4-93) ; Clauser parameter, Eq. (6-42) , $(\delta^*/\tau_w) dp_e/dx = P\eta^*$
γ	specific-heat ratio, c_p/c_v ; finite-difference parameter Eq. (4-184) ; intermittency, Fig. 6-5; compressibility parameter, Eq. (7-141)
δ, δ_u	velocity or viscous boundary-layer thickness
δ^*	displacement thickness, Eq. (4-4)
δ_c	conduction thickness, Eq. (4-177)
δ_h	enthalpy thickness, Eq. (4-29)
δ_T	temperature or thermal boundary-layer thickness
δ_3	dissipation thickness, Eq. (4-149)
δ_{ij}	Kronecker delta
Δ	defect thickness, Eq. (6-43)
ϵ	small perturbation parameter; turbulent dissipation [Eq. (6-26)]
ϵ_{ij}	strain-rate tensor; Reynolds stress dissipation, Eq. (6-111)
κ	Kármán constant, approximately 0.41
λ	second coefficient of viscosity (Chap. 2); Thwaites' parameter $(\theta^2/\nu)dU/dx$, Eq. (4-132) ; $(2/C_f)^{1/2}$ (Chap. 6)
Λ	Kármán–Pohlhausen parameter, $-\delta^2(dp/dx)/(\mu U) = (\delta^2/\nu)dU/dx$; Darcy friction factor, Eq. (3-38) ; pipe-friction factor, Eq. (6-54)
λ_n	Graetz function eigenvalues, Table 3-1

η	similarity variable; Blasius similarity variable (Chap. 4), $y\sqrt{U/(2\nu x)}$; free-surface elevation (Chap. 5)
η^*	dimensionless displacement thickness (Chap. 4), δ^*/δ
μ	dynamic viscosity
ν	kinematic viscosity, μ/ρ
π	a circle's perimeter divided by its diameter, 3.14159265 . . .

Page xxi

Π	Coles' wake parameter, Eq. (6-47)
ϕ	velocity potential (Chap. 2); latitude (Chap. 3); wave angle, Eq. (5-12) ; dimensionless disturbance, Eq. (5-29)
φ	polar or zenith angle in spherical coordinates, Chap. 2
Φ	dissipation function, Eq. (2-46)
ψ	stream function
θ	azimuthal coordinate angle; momentum thickness, Eq. (4-6)
θ^*	dimensionless momentum thickness (Chap. 4), θ/δ
Θ	reduced temperature (dimensionless temperature ratio), Eq. (3-222) or Eq. (4-78)
ρ	density
σ	stress; turbulent jet growth parameter, Eq. (6-149) ; eigenmode (Chap. 5); Blasius constant, $f''(0) \approx 0.4696$ for $\eta = y\sqrt{U/(2\nu x)}$ (Chap. 4)
τ	boundary-layer shear stress
τ_{ij}	stress tensor
χ	hypersonic interaction parameter, Eq. (7-104)
ξ	similarity variable, y/δ
ω	vorticity; angular velocity; frequency
Ω	angular velocity
ζ	heat-transfer coefficient, Eq. (3-14) ; ratio δ_T/δ , Eq. (4-31)

Dimensionless Groups[†]

Re_a	Acoustic Reynolds number, $aL/\nu = Re/Ma$
Br	Brinkman number, $\mu U^2/(k\Delta T) = PrEc$
β	Clauser's equilibrium parameter, $(\delta^*/\tau_w)dp_e/dx$
Ca	cavitation number, $(p_\infty - p_{sat})/(\rho U^2)$
C_D	drag coefficient, $2F_D/(\rho U^2 A)$
C_f	Fanning's skin-friction coefficient, $2\tau_w/(\rho U^2)$

C_h	Stanton number, $q_w/(\rho U c_p \Delta T) = Nu/(Re Pr)$
C_L	lift coefficient, $2 F_L/(\rho U^2 A)$
C_p	pressure coefficient, $2(p - p_\infty)/(\rho U^2)$
Ec	Eckert number, $U^2/(c_p \Delta T) = Br/Pr$
Ek	Ekman number, $\nu/(\Omega L^2)$
Eu	Euler number, $2\Delta p/(\rho U^2)$
Fr	Froude number, $U^2/(gL)$
Fo	Fourier number, $\alpha\tau/L^2$
f or Λ	Darcy's friction factor, $2\Delta p/(\rho U^2 L/D)$
Gr	Grashof number, $g\beta L^3 \Delta T/\nu^2$
Gr^*	modified Grashof number, $GrNu = g\beta q_w L^4/(k\nu^2)$
Re_k or ω^*	Kinetic Reynolds number, $Re_\omega = \omega L^2/\nu = StRe = MjSt^3$
K	Knudsen number, ℓ/L
L	* Graetz number (Sec. 3-3.8), $L/(d_0 Re_D Pr)$
Le	Lewis number, $D/\alpha = Sc/Pr$
Λ	Kármán–Pohlhausen parameter, $-\delta^2(dp/dx)/(\mu U) = (\delta^2/\nu) dU/dx$
Ma	Mach number, U/a
Mj	Majdalani number, $U^3/(\omega^2 \nu L) = Re_k/St^3$
Nu	Nusselt number, $q_w L/(k\Delta T) = C_h Re Pr$
Pe	Péclet number, $Re Pr$
Po	Poiseuille number, $2\tau L/(\mu U)$
Pr	Prandtl number, $\mu c_p/k$
Page xxii	
Pr_t	Turbulent Prandtl number, $\mu_t c_p/k_t$
Ra	Rayleigh number, $Gr Pr = g\beta L^3 \Delta T/(\nu\alpha)$
Re	Reynolds number, UL/ν
Ro	Rossby number, $U/(\Omega L)$
Ri	Richardson number, $g\beta L \Delta T/U^2 = Gr/Re^2$
Sc	Schmidt number, ν/D
λ_S	Stokes parameter, $L\sqrt{\omega/(2\nu)} = \sqrt{Re_k/2}$ or fL/U
St	Strouhal number, $\omega L/U$ or fL/U
Ta	Taylor number, $4\Omega^2 R^4/\nu^2$ or Eq. (5-42)

Re_w	Wave Reynolds number, $U^2/(\omega\nu) = StMj$
We	Weber number, $\rho U^2 L/\mathfrak{J}$
Wo	Womersley number, $\dot{L}\sqrt{\omega/\nu} = \sqrt{Re_k} = \sqrt{2}\lambda_s$

Subscripts

a	w adiabatic wall
∞	far field
e	freestream, boundary-layer edge
$e\ q$	equivalent or van Driest's effective velocity (Chap. 7)
0	initial or reference value
c, crit	critical, at the point of instability
comp	compressible
incomp	incompressible
lam	laminar
liq	liquid
m	mean
max	maximum
n	normal
r	recovery or adiabatic wall
rms	root mean square
sep	separation point
sol	solid
t	turbulent, tangential
T	thermal property
turb	turbulent
tr	transition
θ	azimuthal, swirl, or tangential component
φ	polar, zenith, or tangential component
V	viscous property
vap	vapor property
w	wall property
x	at position x

Superscripts

–	time-averaged properties
---	--------------------------

- ' primes denote differentiation; turbulent fluctuations
- * asterisks usually denote dimensionless variables (Chaps. 2, 3, and 4)
- + law-of-the-wall variables
- ^ circumflexes (carets) denote small-disturbance variables ([Chap. 5](#))
- ~ tildes denote total or instantaneous variables ([Chap. 5](#))

†A more detailed list is provided in Appendix H2.

CHAPTER 1

PRELIMINARY CONCEPTS

. . . the progress of human knowledge will be rapid and discoveries made of which we have present no conception. I begin to be almost sorry I was born so soon, since I cannot have the happiness of knowing what will be known a hundred years hence.

Benjamin Franklin (1706–1790)

1-1 HISTORICAL OUTLINE

THE STUDY of viscous fluid flow phenomena may be viewed as one of the most exhilarating and yet daunting areas of engineering as it brings into perspective decades of research as well as a multitude of tools, models, and methods of analysis. These include, but are not limited to, the tools of dimensional analysis, similitude, kinematics, streamline analysis, head loss and energy analysis, integral or control volume analysis, differential or infinitesimal analysis, point-by-point analysis, von Kármán's momentum-integral analysis, boundary-layer analysis, hydrodynamic stability analysis, turbulence, and numerical analysis.

Although it is not necessary to review the history of the discipline one wishes to pursue, it can be useful to highlight the individual contributions and notable efforts that have been invested in its development. This brief section outlines some of the major contributions to the subject of fluid mechanics. In fact, several excellent books on fluid mechanics history exist that the reader may be referred to, namely, Rouse and Ince (1957), G. A. Tokaty (1994), J. D. Anderson (1997), M. Eckert (2006), and J. S. Calero (2008).

According to G. Garbrecht (1987), fluid mechanics has a rich history that can be traced back to prehistoric times. Archeological records suggest that early communities possessed sufficient intellect to develop streamlined spears, fin-stabilized arrows, boats, and hydraulic channels. Later, Roman engineers designed and built gravity-driven stone-arch aqueducts to

transport water from distant sources to Rome and its surrounding areas. The first such aqueduct was constructed in 312 BC, and eventually hundreds more were built throughout the Roman Empire.

The first analysis of a viscous fluid at rest may be attributed to the Greek mathematician Archimedes (287–212 BC), i.e., when he postulated the two principles of buoyancy now bearing his name. Other Greek inventors developed pumps, valves, and siphons. Outside of Europe, the Arabian world witnessed an era of unparalleled scientific growth that led to the development of reliable measurements of density and volume, controller valves, and reciprocating pumps. During the same period, the study of fluid mechanics in the West slipped into the “dark ages” of inactivity, which lasted for more than 1,500 years.

Incidentally, in the year 1500, the multitalented Italian prodigy, Leonardo da Vinci, deduced the formula for mass conservation of an incompressible one-dimensional flow. This painter, sculptor, musician, philosopher, anatomist, botanist, geologist, architect, engineer, and scientist also designed an anemometer, a flying machine, a parachute, a submarine, scuba gear, and other military contraptions. His notes conveyed surprisingly accurate sketches of waves, hydraulic jumps, jets, eddies, vortices, and wakes.

Despite sporadic developments during the Renaissance period, the 17th century may be viewed as the dawn of fluid mechanics research. It started when Evangelista Torricelli (1608–1647) published the velocity of efflux from an orifice and Edme Mariotte (1620–1684) built a wind tunnel with a drag balance. It then accelerated when Sir Isaac Newton (1643–1727) published his *Principia* and proposed in 1687 that resistance to flow was “proportional to the Page 2velocity by which the parts of the fluid are being separated from each other.” Most common liquids and gases that follow this rule are now called *Newtonian*.

Ironically, Newton indirectly discouraged viscous-flow research by introducing and promoting interest in differential calculus. This enabled some of the greatest mathematicians of the 18th century—Leonhard Euler (1707–1783), Jean le Rond d’Alembert (1717–1783), Joseph-Louis Lagrange (1736–1813), Pierre-Simon Laplace (1749–1827), and Franz Josef von Gerstner (1756–1832)—to produce brilliant, but highly idealistic, solutions to inviscid fluid motions that were called *perfect* or *ideal*. Euler, for example, proved Bernoulli’s postulate that pressure and velocity were related. Nonetheless, practical engineers realized that these solutions were quite limited; for example, d’Alembert proved that frictionless fluid motion past a body predicted zero drag, which contradicted viscous-flow behavior. The disagreement between theory and practice led some engineers to focus on producing and interpreting experimental results with little or no reliance on theory.

Later, Navier in 1827, Cauchy in 1828, Poisson in 1829, St. Venant in 1843, and Stokes in 1845 added viscosity to the equations of motions and made them applicable to *real* fluids. The corresponding Navier–Stokes equations were nonlinear and difficult to solve except for simple geometries and low to moderate speeds. A breakthrough occurred in 1904 when Ludwig Prandtl (1875–1953) proved the existence of a thin *boundary layer* in fluids with small viscosity. This concept greatly improved our understanding of viscous flows and the manner by which they can be mathematically subdivided and synthesized. Prandtl’s

breakthrough was quickly followed by groundbreaking contributions by three of his students: Heinrich Blasius's spatially reductive similarity solution for the boundary-layer equations in 1908, Theodore von Kármán's ever so useful momentum-integral formulation in 1921, and, concurrently, Pohlhausen's polynomial approximations of the boundary-layer velocity. Pohlhausen's approximations, however, deteriorated most paradoxically in their effectiveness at predicting boundary-layer characteristics as their polynomial orders increased. This paradox lingered until the time of this writing.

The second most important breakthrough, which also took place in the early 20th century, was the development of tools necessary to correlate various experiments using *dimensional analysis*. Leaders in this field were Osborne Reynolds (1842–1919), Lord Rayleigh (1842–1919), and Prandtl himself. All new results could now be expressed in a compact, universal, highly portable, dimensionless form.

The latter part of the 20th century saw the invention of digital computing and both qualitative flow visualization techniques that use Schlieren, shadowgraph, laser-induced fluorescence, tufts, yarns, smoke, dye, bubbles, oils, etc., and quantitative measurement techniques, such as hot-wire and hot-film anemometry, laser-doppler velocimetry, holography, particle image and particle tracking velocimetry, as well as pressure, temperature, and shear-sensitive paints. Presently, advancements in ultrasound, X-ray, computerized tomography, and magnetic resonance velocimetry continue to be made. When combined with modern turbulence models and supercomputers, researchers are now able to simulate almost every prototypical viscous fluid motion.

1-2 SOME EXAMPLES OF VISCOUS-FLOW PHENOMENA

Before embarking upon the inevitable detailed studies of theoretical and experimental viscous flows, let us discuss three examples, chosen to illustrate both the strength and the limitations of the subject: (1) airfoil flow, (2) a cylinder in crossflow, and (3) pipe-entry flow. These examples remind us that a textbook tends to emphasize analytical power while deemphasizing practical difficulties. Viscous-flow theory does have limitations, especially in the high-Reynolds-number *turbulent-flow* regime, where the flow undergoes random fluctuations and is only modeled on a semiempirical time-mean or statistical basis.

Although geometry, fluid buoyancy, and compressibility will be important in all viscous flows, the primary controlling parameter is the dimensionless *Reynolds number*:

$$Re_L = \frac{\rho UL}{\mu} \quad (1-1)$$

where U is a velocity scale, L is a characteristic geometric size, and ρ and μ refer to the fluid density and viscosity, respectively. Fluid properties alone can cause dramatic differences in the Reynolds number and, consequently, the flow pattern. For example, if $U = 1$ m/s and $L =$

1 m at 20°C, one gets $Re_L = 9 \times 10^3$, 7×10^4 , and 1×10^6 for SAE-10 oil, air, and water, respectively. By allowing for possible changes in size and speed, the Reynolds number can vary from a small fraction (falling dust particles) to 5×10^9 (a cruising supertanker). For a given geometry, as Re_L increases, the flow pattern changes from smooth or *laminar* through a transitional region into a fluctuating or *turbulent* regime. Page 3

Example 1 Flow past a thin airfoil. Consider flow past a thin airfoil at small angle of incidence, $\alpha < 5^\circ$ as sketched in [Fig. 1-1a](#). In practical applications, the *Reynolds number*, Re_L , is large. For example, if $L = 1$ m, $U = 100$ m/s, and $\nu = \mu/\rho \approx 1.5 \times 10^{-5}$ m²/s (air at 20°C and 1 atm), $Re_L = 6.7 \times 10^4$. Under these circumstances, the flow creates a thin boundary layer near the airfoil surface and a thin wake downstream. The measured surface-pressure distribution on the foil can be predicted by inviscid-flow theory [e.g., White (2016), Sec. 8.7], and the wall shear stress can be computed with the boundary-layer theory of Chaps. 4 to 6. The sharp trailing edge establishes the flow pattern, because a viscous fluid cannot go around such a sharp edge but instead must leave smoothly and tangentially, as shown in [Fig. 1-1a](#).

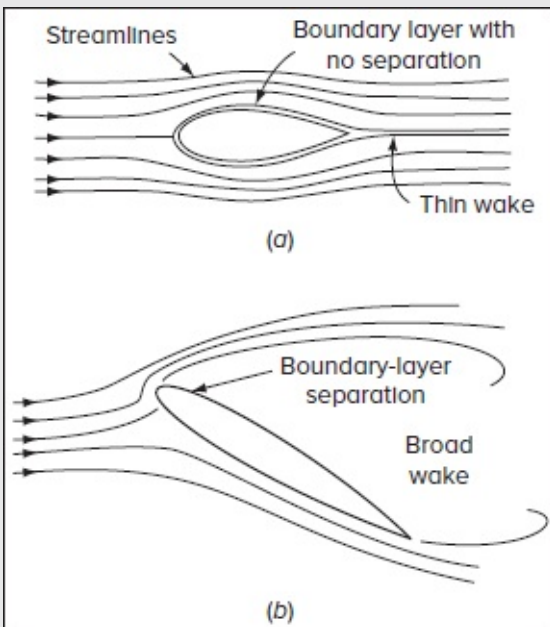


FIGURE 1-1

Flow past a thin airfoil: (a) low incidence angle, smooth flow, no separation; (b) high incidence angle, upper surface separates or “stalls,” lift decreases.

According to inviscid theory, if F is the lift force per unit depth on a symmetric (two-dimensional) airfoil, the dimensionless lift coefficient C_L is given by

$$C_L = \frac{F}{\frac{1}{2} \rho U^2 L} \approx 2\pi \sin(\alpha) \quad (1-2)$$

where L is the chord length of the airfoil.

At larger incidence angles (10–15°), boundary-layer separation, or *stall*, will occur on the upper or *suction* (low-pressure) surface, as shown in [Fig. 1-1b](#). For thicker airfoils, separation generally occurs at the trailing edge. Thin airfoils may form a partial separation, or *bubble*, near the leading edge. In stalled flow, the upper surface-pressure distribution - deviates considerably from inviscid theory, resulting in a loss of lift and an increase in drag force.

When an airfoil flow separates, its lift coefficient levels off to a maximum and then decreases, sometimes gradually, sometimes quickly as a short leading-edge bubble is suddenly elongated. [Figure 1-2](#) compares typical theoretical and experimental lift curves for a symmetric airfoil.

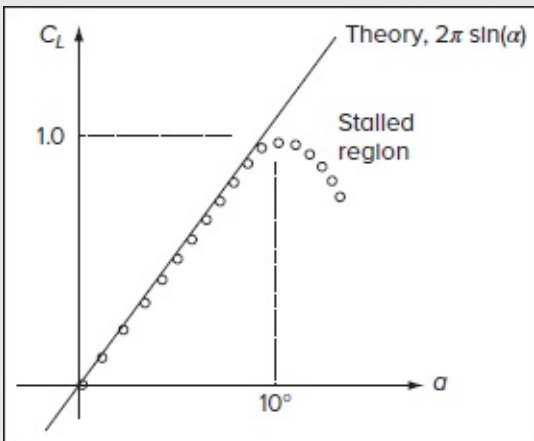


FIGURE 1-2

Typical comparison of theory and experiment for lift coefficient on a symmetric airfoil.

As long as the angle of attack is below stall, the lift can be predicted by inviscid theory and the friction by boundary-layer theory. The onset of stall can be predicted. In the stalled region, however, boundary-layer theory is no longer valid, and one must resort to either experimentation or numerical simulation on a digital computer.

[Figures 1-1](#) and [1-2](#) are for two-dimensional airfoils—of infinite span into the paper. Practical wings, of course, have tips and can have leading edges *swept* or nonorthogonal to the oncoming stream. The flow over them is three-dimensional and the lift coefficient is

reduced, due to decreased lift on the tips [White (2016), p. 558].

Example 2 Flow past a circular cylinder. A very common geometry in fluids engineering is crossflow of a stream at velocity U_∞ past a circular cylinder of radius R . For plane inviscid flow, the solution superimposes a uniform stream with a line doublet and is given in polar coordinates by [White (2016), p. 539]

$$v_r = U_\infty \left(1 - \frac{R^2}{r^2} \right) \cos \theta \quad \text{and} \quad v_\theta = -U_\infty \left(1 + \frac{R^2}{r^2} \right) \sin \theta \quad (1-3)$$

The streamlines of this flow can then be plotted as in [Fig. 1-3](#). At the surface of the cylinder, $r = R$, we have $v_r = 0$ and $v_\theta = -2U_\infty \sin \theta$; the latter remains finite and thus violative of the no-slip condition imposed by intermolecular forces between the fluid and the solid.

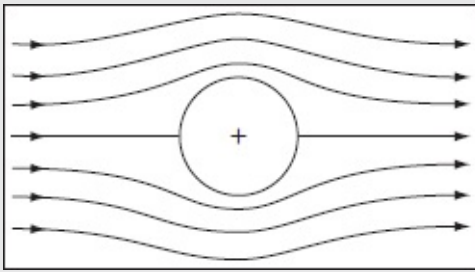


FIGURE 1-3

Perfect-fluid flow past a circular cylinder.

The pressure distribution at the cylinder surface can be found from Bernoulli's equation, $p + \frac{1}{2} \rho V^2 = \text{const}$, where ρ is the fluid density. The result is

$$p_s = p_\infty + \frac{1}{2} \rho U_\infty^2 (1 - 4 \sin^2 \theta) \quad \text{or} \quad C_p = \frac{p_s - p_\infty}{\frac{1}{2} \rho U_\infty^2} = 1 - 4 \sin^2 \theta$$

This distribution is shown as the dash-dot line in [Fig. 1-4](#). Equations (1-3) illustrate a characteristic of inviscid flow without a free surface or “deadwater” region: There are no parameters such as the Reynolds number and no dependence upon physical properties. Also, the symmetry of $C_p(\theta)$ in [Fig. 1-4](#) indicates that the integrated surface-pressure force in the streamwise direction—the cylinder *drag*—is zero. This is an example of the unrealistic d’Alembert paradox for inviscid flow past immersed bodies.

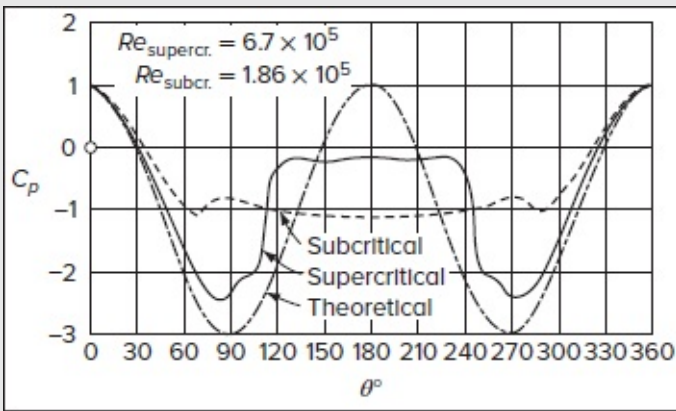
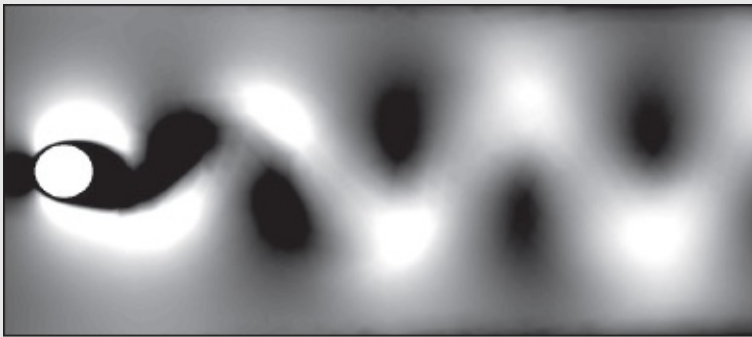


FIGURE 1-4

Comparison of perfect-fluid theory and an experiment for the pressure distribution on a cylinder. [After Flachsbart (1932).]

The experimental facts differ considerably from this inviscid symmetrical picture and depend strongly upon the Reynolds number. [Figure 1-4](#) shows measured C_p by Flachsbart (1932) for two Reynolds numbers. The pressure on the rear or lee side of the cylinder is lower everywhere than the freestream pressure. Consequently, unlike the d'Alembert paradox, the real fluid causes a large pressure-drag force on the body. Page 5

Moreover, the real streamlines are far from symmetrical behind the cylinder. [Figure 1-5](#) displays the numerically simulated flow pattern in water moving past a cylinder at $Re_D = 170$. The flow breaks away or “separates” from the rear surface, forming a broad, pulsating wake. The same pattern has been visualized by releasing hydrogen bubbles at the tube’s entrance in *streaklines* parallel to the stream and *timelines* normal to the flow [Nakayama (1988)]. Note that the wake consists of pairs of vortices that shed alternately from the upper and lower parts of the rear surface. These are called Kármán vortex streets, after a paper by Kármán (1911) explaining this alternation to be a stable configuration for vortex pairs. Beginning for $Re_D > 35$, the vortex streets occur in almost any bluff-body flow and persist over a wide range of Reynolds numbers, as shown in [Fig. 1-6](#). As the Reynolds number increases, the wake becomes more complex—and turbulent—but the alternating shedding can still be detected at $Re_D = 10^7$.



(a) Velocity contours



(b) Streamlines

FIGURE 1-5

Velocity contours and streamlines for flow past a cylinder at $Re_D = 170$ that illustrate the development of alternating Kármán vortex streets [Produced by T. Ramesh-Kumar and J. Majdalani using a finite volume solver.]

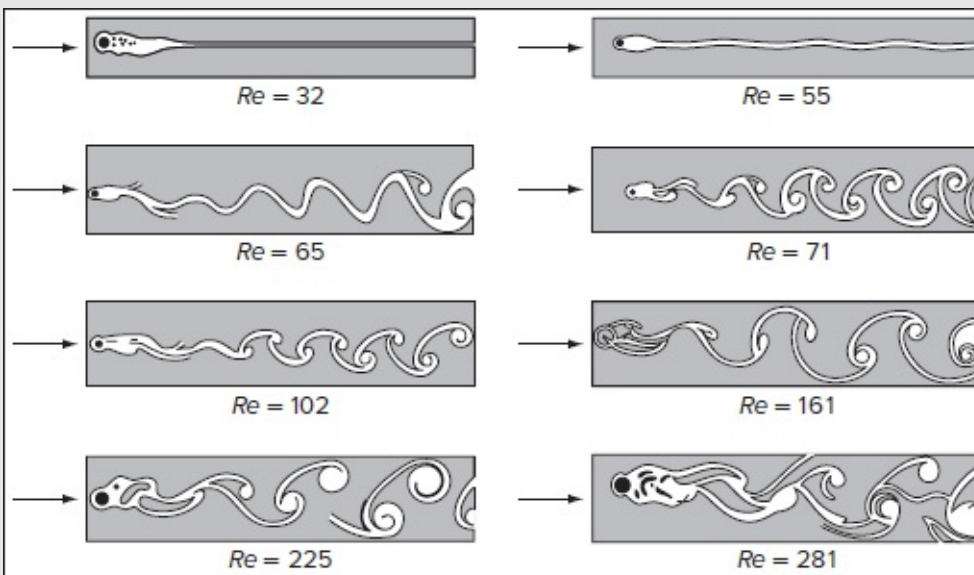


FIGURE 1-6

Effect of the Reynolds number on the flow past a cylinder. [After Homann (1936).]

Page 6

As shown in [Fig. 1-7](#), the dimensionless cylinder shedding frequency or *Strouhal number* falls around $St = fD/U \approx 0.2$ for Reynolds numbers ranging from 100 to 10^5 . Thus, the shedding cycle takes place during the time that the freestream moves approximately five cylinder diameters. Vortex shedding is a characteristic of many viscous flows which, though posed with fixed and steady boundary conditions, evolve into unsteady motions because of flow instability. The pressure distributions in [Fig. 1-4](#) are time averaged for this reason.

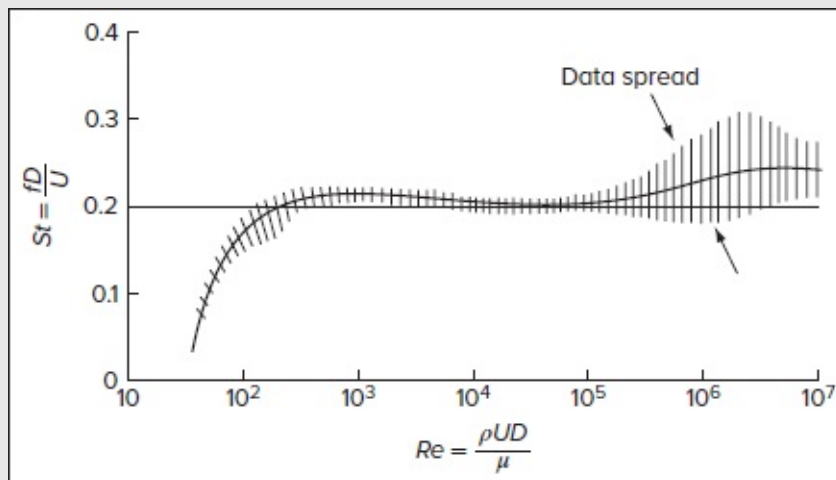


FIGURE 1-7

Measured Strouhal number for vortex shedding frequency behind a circular cylinder.

The drag coefficient on a cylinder, defined as $C_D = F/(\rho U^2 RL)$, is plotted in [Fig. 1-8](#) over a wide range of Reynolds numbers. The solid curve, for a smooth wall, shows a sharp drop, called the *drag crisis*, at $Re_D \approx 2 \times 10^5$, which occurs when the boundary layer on the front surface becomes turbulent. If the surface is rough, the drag crisis occurs earlier, a fact exploited in sports by the deliberate dimpling of golf balls. As shown in [Fig. 1-8](#), freestream turbulence also causes an early drag crisis.

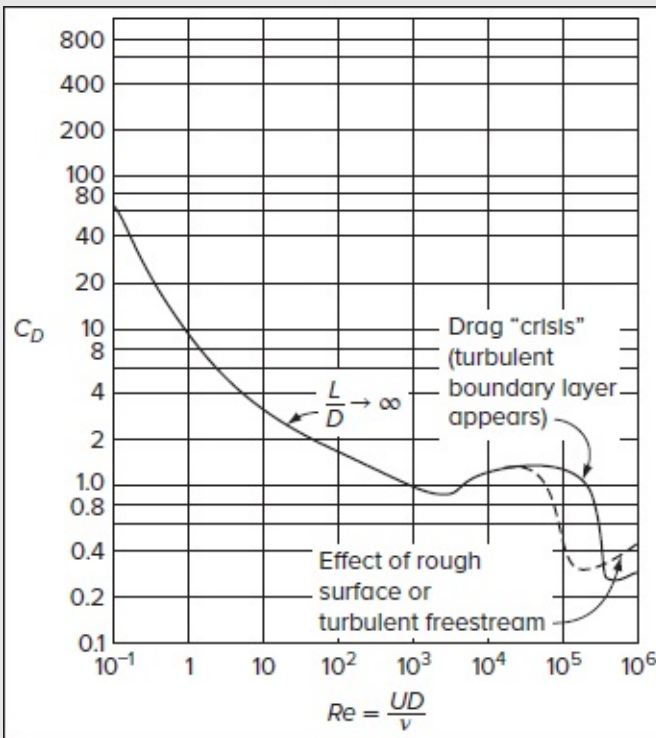


FIGURE 1-8

Drag coefficient of a circular cylinder.

To summarize, real fluid flow past a bluff body such as a circular cylinder can differ markedly from the inviscid-flow prediction. Viscous forces which are extremely small (only a few percent of the total drag), actually control the flow by inducing separation and wake formation at the rear of the body. Boundary-layer theory can predict the onset of separation, but the surface-pressure distribution changes so markedly from inviscid theory (Fig. 1-4) that Prandtl's matching scheme of Chap. 4 fails to be quantitative. For $Re \ll 1$, Stokes' creeping-flow theory can be used effectively (Sec. 3-9). For higher Reynolds numbers, numerical modeling of both laminar and turbulent flows is possible [Sidebottom, Ooi, and Jones (2015)]. Some perturbation solutions are also possible [Van Dyke (1964); Nayfeh (2000)].

Example 3 Flow in a circular pipe. Consider now the flow illustrated in Fig. 1-9, where a steady viscous flow enters a tube from a reservoir. Wall friction causes a viscous layer, probably laminar, to begin at the inlet and grow in thickness downstream, possibly becoming turbulent further inside the tube. Unlike the *external* flows of Examples 1 and 2, this *internal* flow is constrained by the solid walls, and inevitably the viscous layers must

coalesce at some distance x_L , so that the tube is then completely filled with boundary layer. Slightly further downstream of the coalescence, the flow profile ceases to change with axial position and is said to be fully developed.

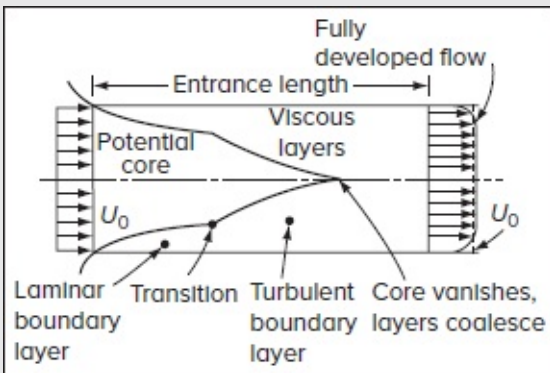


FIGURE 1-9

Flow in the entry region of a tube.

The developed flow in [Fig. 1-9](#) ends up turbulent, which typically occurs for a Reynolds number $U_0 D/\nu > 2000$. At lower Re , both the developing and developed regions remain laminar. [Figure 1-10](#) illustrates the evolution of a uniform flow entering a circular tube. Note that the fluid near the wall slows down and the central core accelerates. The numerically simulated profiles change from near-slug flow at the inlet to near-parabolic downstream.

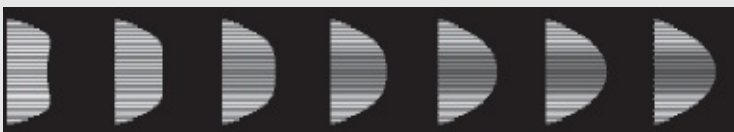


FIGURE 1-10

Development of laminar flow in the entrance of a tube at $Re = 1600$. [*Produced by T. Ramesh-Kumar and J. Majdalani using a finite-volume solver.*]

Pipe flow is common in engineering. The theory of constant-area duct flow, for both developing and developed laminar and turbulent conditions, is well formulated and satisfying. Analytical difficulties arise if the duct diameter is tapered. Tapered flow does not become fully developed and, if the area increases in the flow direction (subsonic diffuser), separation, backflow, and unsteadiness complicate the flow pattern. A sketch of flow in a “stalled” diffuser is shown in [Fig. 1-11](#), after Kline et al. (1959). Diffusers can now be

analyzed by numerical methods, using either boundary-layer theory [Johnston (1998)], or computational fluid dynamics [Muggli (1997)]. If the duct area *decreases* in the flow direction (subsonic nozzle), there is no flow separation or unsteadiness, and the nozzle can be readily analyzed by elementary boundary-layer theory.

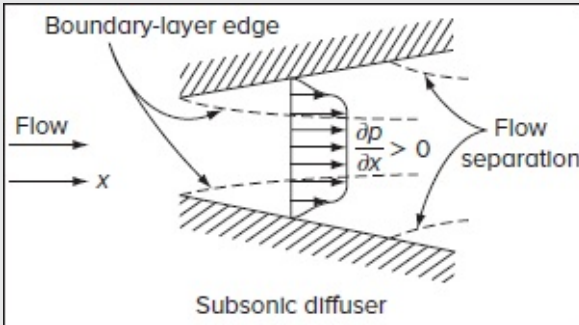


FIGURE 1-11

Flow separation in a diffuser.

1-3 PROPERTIES OF A FLUID

It is common in introductory physics to divide materials into the three classes of solids, liquids, and gases, noting their different characteristics when placed in a container. This is a handy classification in thermodynamics, for example, because of the strong differences in state relations among the three. In fluid mechanics, however, there are only two classes of matter: fluids and nonfluids (solids). A solid can resist an applied shear force and remain at rest, while a fluid cannot. This distinction is not completely clear-cut. Consider a barrel full of pitch (tar or asphalt) at room temperature. The pitch looks hard as a rock and will easily support a brick placed on its surface. But if the brick is left there for several days, one will have trouble retrieving the brick from the bottom of the barrel. Pitch, then, is usually classed as a fluid. Consider the metal aluminum. At room temperature, aluminum is solid to all appearances and will resist any applied shear stress below its strength limit. However, at 400°F, well below its 1200°F melting point, aluminum flows gently and continuously under applied stress and has a measurable viscosity. Nor is high temperature the criterion for fluid behavior in metals, since lead exhibits this gentle viscous creep at room temperature. Note also that mercury is a fluid and has the lowest viscosity relative to its own density (kinematic viscosity) of any common substance.

This text is primarily concerned, then, with easily recognizable fluids that flow readily

under applied shear, although some slight attention will be paid to the borderline substances, which partly flow and partly deform when sheared. All gases are true fluids, as are the common liquids, such as water, oil, gasoline, and alcohol. Some liquid substances, which may not be true fluids, are emulsions, colloids, high-polymer solutions, and slurries. The general study of flow and deformation of materials constitutes the subject of *rheology*, of which viscous flow is a special case [see, for example, the texts by Owens and Phillips (2002), Irgens (2013), and Spagnolie (2014)].

Restricting ourselves to true fluids, we now return and illustrate their properties. These properties are of at least four classes:

1. *Kinematic* properties (linear velocity, angular velocity, vorticity, acceleration, and strain rate). Strictly speaking, these are properties of the flow field itself rather than of the fluid.
2. *Transport* properties (viscosity, thermal conductivity, and mass diffusivity).
3. *Thermodynamic* properties (pressure, density, temperature, enthalpy, entropy, specific heat, Prandtl number, bulk modulus, and coefficient of thermal expansion).
4. Other miscellaneous properties (surface tension, vapor pressure, eddy-diffusion coefficients, and surface-accommodation coefficients).

Some items in class 4 are not true properties but depend upon flow conditions, surface conditions, and contaminants in the fluid.

The use of class 3 properties requires hedging. It is a matter of some concern that classical thermodynamics, strictly speaking, does *not* apply to this subject, since a viscous fluid in motion is technically not in equilibrium. Fortunately, deviations from local thermodynamic equilibrium are usually not significant except when flow residence times are short and the number of molecular particles is small, e.g., hypersonic flow of a rarefied gas. The reason is that gases at normal pressures are quite dense in the statistical sense: A cube of sea-level air $1\ \mu\text{m}$ on a side contains approximately 10^8 molecules. Such a gas, when subjected to a change of state—even a shock change—will rapidly smooth itself into local equilibrium because of the enormous number of molecular collisions occurring in a short distance. A liquid is even more dense, and thus we accept thermodynamic equilibrium as a good approximation in this text.[†]

1-3.1 The Kinematic Properties

In fluid mechanics, one's first concern is normally with the fluid velocity. In solid mechanics, on the other hand, one might instead follow particle displacements, since particles in a solid are bonded together in a relatively rigid manner.

Consider the rigid-body dynamics problem of a rocket trajectory. After solving for the paths of any three noncollinear particles on the rocket, one is finished, since all other particle

paths can be inferred from these three. The scheme of following the trajectories of individual particles is called the *Lagrangian description* of motion, which proves to be very useful in solid mechanics. However, it is not as practical in fluid mechanics unless a discrete number of particles is to be tracked. Page 9

Now consider the fluid flow out of the nozzle of that rocket. Surely, we cannot follow the millions of separate paths. Fluids are composed of countless particles whose individual paths can be very challenging and often unmanageable to describe separately. Even the point of view is important, since an observer on the ground would perceive a complicated unsteady flow, while an observer fixed to the rocket would see a nearly steady flow of quite regular pattern. Thus, it is generally useful in fluid mechanics (1) to choose the most convenient origin of coordinates that can make the flow appear steady, and (2) to study only the velocity *field* as a function of position and time, by focusing on the properties of interest at one specific location in space, instead of trying to follow innumerable particle paths. This scheme of describing the flow at every fixed point as a function of time is called the *Eulerian formulation* of motion. As such, the field or Eulerian method of description seeks to describe the properties of a flow at a given point in space as a function of time. Consequently, all field properties become functions of both space and time. For example, the Eulerian velocity vector field can be defined in the following Cartesian form:

$$\mathbf{V}(x, y, z, t) = u(x, y, z, t) \mathbf{i} + v(x, y, z, t) \mathbf{j} + w(x, y, z, t) \mathbf{k} \quad (1-4)$$

Complete knowledge of the scalar variables u , v , and w as functions of (x, y, z, t) is often the solution to a problem in fluid mechanics. Note that we have used the notation (u, v, w) to represent the velocity components, not the spatial displacements, as we would in solid mechanics. Actual displacements are of so little use in fluid problems that they are seldom discussed.

The Eulerian, or velocity-field system, is certainly the proper choice in fluid mechanics, but it comes with an added mathematical complication. The three fundamental laws of mechanics—conservation of mass, momentum, and energy—are formulated for particles (systems) of fixed identity, i.e., they are Lagrangian in nature. All three of these laws relate to the time rate of change of some property for a fixed particle. Let Q represent any property of the fluid. If (dx, dy, dz, dt) represent arbitrary changes in the four independent variables, the total differential change in Q is given by

$$dQ = \frac{\partial Q}{\partial x} dx + \frac{\partial Q}{\partial y} dy + \frac{\partial Q}{\partial z} dz + \frac{\partial Q}{\partial t} dt \quad (1-5)$$

Since we are deliberately following an infinitesimal particle of fixed identity, the spatial increments must be such that

$$dx = udt \quad dy = vdt \quad dz = wdt \quad (1-6)$$

Substituting in [Eq. \(1-5\)](#), we find the proper expression for the time derivative of Q for a particular elemental particle:

$$\frac{dQ}{dt} = \frac{\partial Q}{\partial t} + u \frac{\partial Q}{\partial x} + v \frac{\partial Q}{\partial y} + w \frac{\partial Q}{\partial z} \quad (1-7)$$

The quantity dQ/dt is variously termed the *substantial derivative*, *particle derivative*, *total derivative*, or *material derivative*—all names which try to invoke the feeling that we are following a fixed fluid particle. To strengthen this feeling, it is traditional to give this derivative the special symbol DQ/Dt , which is a purely a mnemonic device, not intended to frighten readers. In [Eq. \(1-7\)](#), the last three terms represent the *spatial transport* or *convective derivative*, since they vanish if the velocity is zero or if Q has no spatial change. The term $\partial Q/\partial t$ is called the *local derivative*. Also note the neat vector form

$$\frac{DQ}{Dt} = \frac{\partial Q}{\partial t} + (\mathbf{V} \cdot \nabla)Q \quad (1-8)$$

where ∇ denotes the gradient operator which, in Cartesian coordinates, is given by

$$\nabla \equiv \mathbf{i} \frac{\partial}{\partial x} + \mathbf{j} \frac{\partial}{\partial y} + \mathbf{k} \frac{\partial}{\partial z}$$

1-3.2 Acceleration of a Fixed-Identity Particle

If Q is \mathbf{V} itself, we obtain our first kinematic property, the particle-acceleration vector:

$$\frac{D\mathbf{V}}{Dt} = \frac{\partial \mathbf{V}}{\partial t} + (\mathbf{V} \cdot \nabla) \mathbf{V} = \frac{Du}{Dt} \mathbf{i} + \frac{Dv}{Dt} \mathbf{j} + \frac{Dw}{Dt} \mathbf{k}; \quad \mathbf{V}(\mathbf{r}, t) = \mathbf{V}(x, y, z, t) \quad (1-9)$$

Note that the acceleration is concerned with u , v , w , and 12 scalar derivatives, i.e., the local changes $\partial u/\partial t$, $\partial v/\partial t$, and $\partial w/\partial t$ as well as the nine spatial derivatives of the form $\partial u_i/\partial x_j$, where i and j can be made to loop over the three coordinate directions. In what follows, we will avoid using i , j , and k to denote unit vectors but instead use them as Cartesian indexes. Page 10

The convective terms in D/Dt present unfortunate mathematical difficulty because they are nonlinear products of variable terms. For this reason, viscous flows with finite convective accelerations are nonlinear in character and give rise to vexing analytical problems that cannot be solved using the superposition principle; nonunique solutions, even in steady laminar flow; and coupled oscillatory motion in a continuous frequency spectrum, which is the chief feature of a high Reynolds number, or turbulent, flow. Note that these nonlinear terms are accelerations, not viscous stresses. It is ironic that the main obstacle in viscous-flow analysis stems from an inviscid term; the viscous stresses themselves remain linear when the viscosity and density are assumed constant.

In frictionless flow, nonlinear convective accelerations still exist but do not misbehave, as it can be seen with reference to the valuable vector identity,

$$(\mathbf{V} \cdot \nabla) \mathbf{V} \equiv \frac{1}{2} \nabla (\mathbf{V}^2) - \mathbf{V} \times (\nabla \times \mathbf{V}) \quad (1-10)$$

For the reader's convenience, several other vector identities that are relevant to fluid mechanics are provided in App. A. As we shall see, the term $\nabla \times \mathbf{V}$ often vanishes when the viscosity is zero (although rotational inviscid flows also exist), leaving the convective acceleration equal only to the familiar kinetic-energy term of Bernoulli's equation. Inviscid flow, then, is nonlinear also, but the nonlinearity is confined to the calculation of static pressure, not to the determination of the velocity field, which is linear.

If we agree from this brief discussion that viscous motion is mathematically formidable, we deduce that a very important problem consists of modeling a viscous-flow experiment. The corresponding question becomes at this point: When can a velocity distribution \mathbf{V}_1 measured in a flow about or through a model shape B_1 be scaled by (say) a simple multiplier to yield the velocity distribution \mathbf{V}_2 about or through a geometrically similar but larger (say) model shape B_2 ? This desirable condition is called *similarity*, and the conditions for achieving it are discussed in [Chap. 2](#).

1-3.3 Other Kinematic Properties

In fluid mechanics, as in solid mechanics, we are interested in the general motion, deformation, and rate of deformation of particles. Like its solid counterpart, a fluid element can undergo four different types of motion or deformation: (1) translation, (2) rotation, (3) extensional strain or dilatation, and (4) shear strain. The four types are easy to separate geometrically, which is of course the reason they are so defined. The reader who is familiar with, say, the theory of elasticity for solids will find the following analysis of fluid kinematic properties almost identical to that in solid mechanics. Consider an initially square fluid element at time t and then again later at time $t + dt$, as illustrated in [Fig. 1-12](#) for motion in the xy plane. We can see by inspection the four types of motion that have acted on the element. There has been translation of the reference corner B to its new position B' . There has been a counterclockwise rotation of the diagonal BD to the new position $B'D'$. There has been dilatation; the element looks slightly larger. There has been shear strain, i.e., the square has become rhombic.

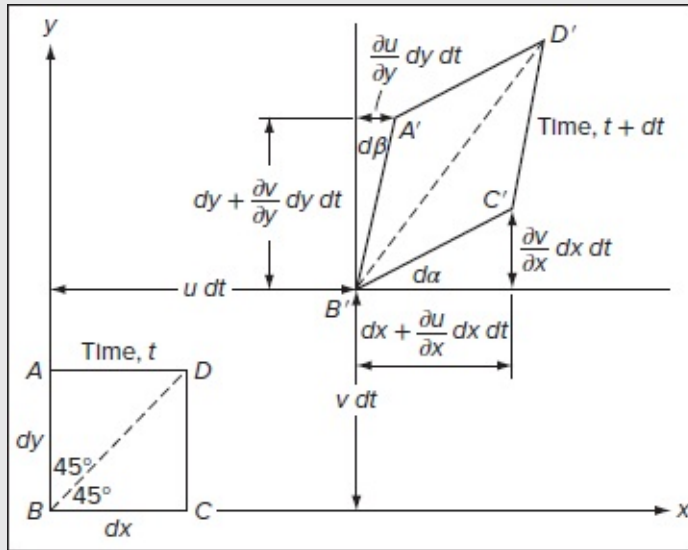


FIGURE 1-12

Distortion of a moving fluid element.

Now let us shift this discussion to a quantitative basis. Note in each case that the final result will be a *rate*, i.e., a time derivative.

The translation is defined by the displacements $u dt$ and $v dt$ of the point B . The *rate* of translation is (u, v) ; in three-dimensional motion, the rate of translation is the velocity (u, v, w) .

The angular rotation of the element about the z axis is defined as the *average* counterclockwise rotation of the two sides BC and BA . As shown in [Fig. 1-12](#), BC has rotated an amount $d\alpha$. Meanwhile, BA has rotated clockwise; thus, its counterclockwise turn is $(-d\beta)$. The average rotation is therefore

$$d\Omega_z = \frac{1}{2} (d\alpha - d\beta) \quad (1-11)$$

where the subscript z denotes rotation about an axis parallel to the z axis. We actually perceive the counterclockwise rotation in [Fig. 1-12](#) because $d\alpha$ is drawn deliberately larger than $d\beta$. Referring to [Fig. 1-12](#), we find that both $d\alpha$ and $d\beta$ are directly related to velocity derivatives through the calculus limit:

$$d\alpha = \lim_{dt \rightarrow 0} \left(\tan^{-1} \frac{\frac{\partial v}{\partial x} dx dt}{dx + \frac{\partial u}{\partial x} dx dt} \right) = \frac{\partial v}{\partial x} dt \quad \text{and} \quad d\beta = \lim_{dt \rightarrow 0} \left(\tan^{-1} \frac{\frac{\partial u}{\partial y} dy dt}{dy + \frac{\partial v}{\partial y} dy dt} \right) = \frac{\partial u}{\partial y} dt \quad (1-12)$$

Substituting [Eq. \(1-12\)](#) into [\(1-11\)](#), we find that the *rate* of rotation (angular velocity) about the z axis is given by

$$\frac{d\Omega_z}{dt} = \frac{1}{2} \left(\frac{\partial v}{\partial x} - \frac{\partial u}{\partial y} \right) \quad (1-13)$$

In an exactly similar fashion, the *rates* of rotation about the x and y axes can be determined from

$$\frac{d\Omega_x}{dt} = \frac{1}{2} \left(\frac{\partial w}{\partial y} - \frac{\partial v}{\partial z} \right) \quad \frac{d\Omega_y}{dt} = \frac{1}{2} \left(\frac{\partial u}{\partial z} - \frac{\partial w}{\partial x} \right) \quad (1-14)$$

These are clearly the three components of the angular velocity vector $d\mathbf{\Omega}/dt$. The three factors of one-half are irritating, and it is customary to work instead with a quantity $\mathbf{\omega}$ equal to twice the angular velocity:

$$\mathbf{\omega} = 2 \frac{d\mathbf{\Omega}}{dt} \quad (1-15)$$

The new quantity $\mathbf{\omega}$, which proves to be of vital interest in fluid mechanics, is called the *vorticity* of the fluid. By inspecting [Eqs. \(1-13\)](#) to [\(1-15\)](#), we see that vorticity and velocity are related by basic vector calculus:

$$\mathbf{\omega} = \text{curl } \mathbf{V} = \nabla \times \mathbf{V} \quad (1-16)$$

and hence the divergence of vorticity vanishes identically:

$$\text{div } \mathbf{\omega} = \nabla \cdot \mathbf{\omega} = 0 \quad (1-17)$$

Mathematically speaking, we say the vorticity vector is *solenoidal*. Moreover, the vorticity is intimately connected to the convective acceleration through [Eq. \(1-10\)](#). If $\mathbf{\omega} = 0$, the flow is termed *irrotational*.

Now consider the two-dimensional shear strain, which is commonly defined as the average *decrease* of the angle between two lines which are initially perpendicular in the unstrained state. The strain rate represents the rate at which a fluid element is being strained or deformed at a given point in space. Taking AB and BC in [Fig. 1-12](#) as our initial lines, the shear-strain increment may be estimated from $\frac{1}{2}(d\alpha - d\beta)$. In the (x, y) plane, the shear-strain *rate* is

$$\epsilon_{xy} = \frac{1}{2} \left(\frac{d\alpha}{dt} + \frac{d\beta}{dt} \right) = \frac{1}{2} \left(\frac{\partial v}{\partial x} + \frac{\partial u}{\partial y} \right) \quad (1-18)$$

Similarly, the other two components of the shear-strain *rate* are

$$\epsilon_{yz} = \frac{1}{2} \left(\frac{\partial w}{\partial y} + \frac{\partial v}{\partial z} \right) \quad \epsilon_{zx} = \frac{1}{2} \left(\frac{\partial u}{\partial z} + \frac{\partial w}{\partial x} \right) \quad (1-19)$$

By analogy with solid mechanics, the shear-strain rates are symmetric, that is, $\epsilon_{ij} = \epsilon_{ji}$.
Page 12

The fourth and final particle motion is dilatation, or extensional strain. Again with reference to [Fig. 1-12](#), the extensional strain in the x direction is defined as the fractional increase in length of the horizontal side of the element. This is given by

$$\epsilon_{xx} dt = \frac{[dx + (\partial u / \partial x) dx dt] - dx}{dx} = \frac{\partial u}{\partial x} dt \quad (1-20)$$

with precisely similar expressions for the other two strains. The three extensional strain *rates* become

$$\epsilon_{xx} = \frac{\partial u}{\partial x} \quad \epsilon_{yy} = \frac{\partial v}{\partial y} \quad \epsilon_{zz} = \frac{\partial w}{\partial z} \quad (1-21)$$

Taken as a whole, the strain rates, both extensional and shear, constitute a symmetric second-order tensor, which may be visualized as the array

$$\{\epsilon_{ij}\} = \begin{pmatrix} \epsilon_{xx} & \epsilon_{xy} & \epsilon_{xz} \\ \epsilon_{yx} & \epsilon_{yy} & \epsilon_{yz} \\ \epsilon_{zx} & \epsilon_{zy} & \epsilon_{zz} \end{pmatrix} \quad (1-22)$$

Although the component magnitudes vary with a change of axes x , y , and z , the strain-rate tensor, like the stress tensor [Eq. (2-14)] and the strain tensor of elasticity, follows the transformation laws of symmetric tensors [see, for example, Aris (1990), Spiegel et al. (2009), and Haskell (2015)]. In particular, there are three invariants that are independent of direction or choice of axes:

$$\begin{cases} I_1 = \epsilon_{xx} + \epsilon_{yy} + \epsilon_{zz} \\ I_2 = \epsilon_{xx} \epsilon_{yy} + \epsilon_{yy} \epsilon_{zz} + \epsilon_{zz} \epsilon_{xx} - \epsilon_{xy}^2 - \epsilon_{yz}^2 - \epsilon_{zx}^2 \\ I_3 = \begin{vmatrix} \epsilon_{xx} & \epsilon_{xy} & \epsilon_{xz} \\ \epsilon_{yx} & \epsilon_{yy} & \epsilon_{yz} \\ \epsilon_{zx} & \epsilon_{zy} & \epsilon_{zz} \end{vmatrix} \end{cases} \quad (1-23)$$

A further property of symmetric tensors is that there exists one and only one set of axes for which the off-diagonal terms (the shear-strain rates in this case) vanish. These are known as the *principal axes* for which the strain-rate tensor becomes

$$\begin{pmatrix} \epsilon_1 & 0 & 0 \\ 0 & \epsilon_2 & 0 \\ 0 & 0 & \epsilon_3 \end{pmatrix} \quad (1-24)$$

The quantities $(\epsilon_1, \epsilon_2, \epsilon_3)$ are called the *principal strain rates*. For this special case, the three tensor invariants become

$$\begin{aligned} I_1 &= \epsilon_1 + \epsilon_2 + \epsilon_3 \\ I_2 &= \epsilon_1 \epsilon_2 + \epsilon_2 \epsilon_3 + \epsilon_3 \epsilon_1 \\ I_3 &= \epsilon_1 \epsilon_2 \epsilon_3 \end{aligned} \quad (1-25)$$

If the invariants are known, the system in [Eq. \(1-25\)](#) is necessary and sufficient to solve for

the principal strain rates, although there are actually much simpler ways to achieve this [Timoshenko and Goodier (1970)].

Finally, if we adopt the short notation $u_{i,j} = \partial u_i / \partial x_j$, where i and j are any two coordinate directions, any velocity derivative of this type can be split into two parts, one symmetric and one antisymmetric:

$$u_{i,j} = \frac{1}{2} (u_{i,j} + u_{j,i}) + \frac{1}{2} (u_{i,j} - u_{j,i}) \quad (1-26)$$

By comparing [Eq. \(1-26\)](#) with [Eqs. \(1-13\)](#), [\(1-14\)](#), [\(1-18\)](#), [\(1-19\)](#), and [\(1-21\)](#), we see that [Eq. \(1-26\)](#) can also be written as

$$\frac{\partial u_i}{\partial x_j} = \epsilon_{ij} + \frac{d\Omega_{ij}}{dt} \quad (1-27)$$

That is, each velocity derivative can be resolved into a strain rate plus an angular velocity. The angular velocity does not distort the element, so that only the strain rate will cause a viscous stress, a fact which is exploited in [Chap. 2](#).

To summarize, we have shown that all the kinematic properties of fluid flow—acceleration, translation, angular velocity, rate of dilatation, and shear—strain rate—are directly related to the fluid velocity vector $\mathbf{V} = (u, v, w)$. These Page 13relations are identical to the equivalent expressions from infinitesimal solid mechanics, if (u, v, w) are instead taken to be components of the *displacement* vector. This analogy between fluid and solid continuum mechanics is sometimes used to produce the equations of motion of a viscous linear fluid as a direct carryover from the equations of linear (Hookean) elasticity, with which students are often more familiar. For the reader's convenience, a summary of kinematic expressions is provided in App. B using both Cartesian and cylindrical coordinates.

1-3.4 The Transport Properties of a Fluid

The three so-called transport properties are the coefficients of viscosity, thermal conductivity, and diffusion, so named because of the relation that they bear to movement, or transport, of momentum, heat, and mass, respectively. Each of the three coefficients relates a flux or transport of a specific property to its gradient. Viscosity relates the momentum flux to its velocity gradient, thermal conductivity relates the heat flux to its temperature gradient, and the diffusion coefficient relates the mass transport to its concentration gradient. Further, the mathematical properties of momentum, heat, and mass-flux problems are often similar and expressible using analogous equations.

1-3.5 The Coefficient of Viscosity

The layperson knows from experience what *viscosity* means and associates it with the ability of a fluid to flow freely. Heavy oil takes a long time to flow out of a can. Light oil flows out

quickly. The disastrous Boston molasses-tank explosion of 1919 [Shank (1954)] caused one of the slowest floods in history. Viscosity also affects the behavior of molten lava venting out of the mouths of volcanoes. The higher the viscosity of the magma, the more explosive the eruption, the thicker the lava, and the steeper the volcano can be. The idea of viscosity being proportional to time to flow has become accepted practice in the petroleum industry. Thus, the motorist purchases oil with a viscosity labeled SAE 30. This means that 60 ml of this oil at a specified temperature takes 30 s to run out of a 1.76-cm hole in the bottom of a cup. This experiment is convenient and reproducible for very viscous liquids such as oil, but the time to flow is *not* viscosity, any more than the speed of sound is the time it takes an echo to return from a mountainside. It is an intriguing fact that the flow of a viscous liquid out of the bottom of a cup is a difficult problem for which no analytic solution exists at present.

A more fundamental approach to viscosity is to view it as the property of a fluid connecting any applied stress to the resulting strain rate. The corresponding relations are considered in Sec. 2-4. In fact, the main distinction between fluids and solids is that a fluid deforms continuously under the application of a shearing stress, no matter how small this stress may be. In fluids, the stress is proportional to the strain rate or rate of deformation, whereas in solids the stress is proportional to the deformation angle, and the proportionality constant is simply the shear modulus or modulus of rigidity, which is often denoted by G . Here we consider a simple and widely used example of a fluid sheared between two plates, as in [Fig. 1-13](#). This geometry is such that the shear stress τ_{xy} must be constant throughout the fluid. The motion $u = u(y)$ is in the x direction and varies with y only. Thus, there is only a single finite strain rate in this flow:

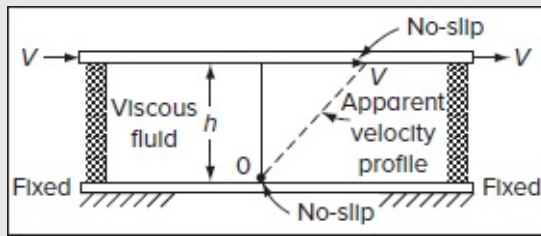
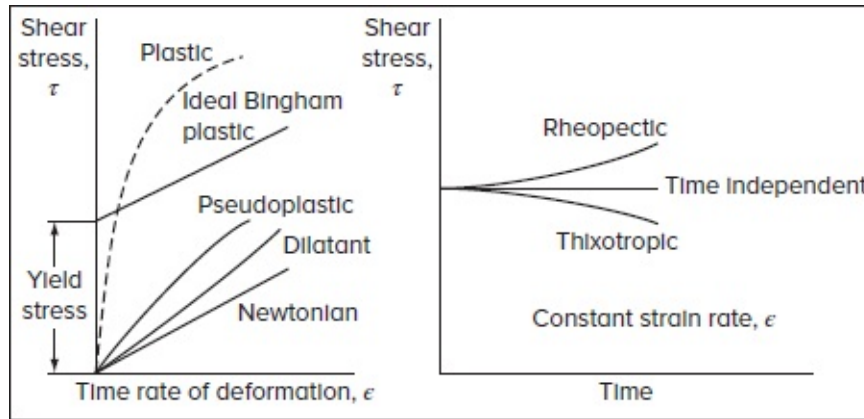


FIGURE 1-13

A fluid sheared between two plates.

$$\epsilon_{xy} = \frac{1}{2} \left(\frac{\partial u}{\partial y} + \frac{\partial v}{\partial x} \right) = \frac{1}{2} \frac{\partial u}{\partial y} = \frac{1}{2} \frac{du}{dy} \quad (1-28)$$

If one performs this experiment, one finds that, for all the common fluids, the applied shear is a unique function of the strain rate:



Since, for a given motion V of the upper plate, τ_{xy} is a constant, it follows that in these fluids ϵ_{xy} , and hence du/dy , is a constant, so that the resulting velocity profile is linear across the plate, as illustrated in [Fig. 1-13](#). This is true regardless of the actual form of the functional relationship in [Eq. \(1-29\)](#). If the no-slip condition holds, the velocity profile varies from zero at the lower wall to V at the upper wall (Prob. 1-16 considers the case of a slip boundary Page 14condition). Repeated experiments with various values of τ_{xy} have helped to establish the functional relationship in [Eq. \(1-29\)](#). For simple fluids such as water, oils, or gases, the relationship is linear or *Newtonian*:

$$\tau_{xy} \sim \epsilon_{xy} \quad \text{or} \quad \tau_{xy} = \mu \frac{V}{h} = 2\mu \epsilon_{xy} = \mu \frac{du}{dy} \quad (1-30)$$

The quantity μ , called the *coefficient of viscosity of a Newtonian fluid*, is what handbooks commonly quote when listing the viscosity of a fluid (see App. C). Actually, there is also a second coefficient, λ , related to bulk fluid expansions, but it is rarely encountered in practice (see Sec. 2-4). Equation (1-30) shows that the dimensions of μ are stress–time: $\text{N} \cdot \text{s}/\text{m}^2$ [or $\text{kg}/(\text{m} \cdot \text{s})$] in metric units and $\text{lbf} \cdot \text{s}/\text{ft}^2$ [or $\text{slugs}/(\text{ft} \cdot \text{s})$] in English units. The conversion factor is $1 \text{ N} \cdot \text{s}/\text{m}^2 = 0.020886 \text{ lbf} \cdot \text{s}/\text{ft}^2$. The coefficient μ is a thermodynamic property that varies with temperature and pressure. Data for common fluids are given in App. C. Note that, for gases, μ increases with T because an increase in the rate of collisions leads to more resistance to motion. For liquids, however, μ decreases with T because the added spacing between molecules at higher temperatures allows liquid layers to slide more easily. The kinematic viscosity, $\nu = \mu/\rho$, which has units of m^2/s (or ft^2/s), tends to be larger for gases because of their generally lower densities. Conversely, it is the smallest for mercury because of its relatively high density.

If the functional relationship in [Eq. \(1-29\)](#) is nonlinear, the fluid is said to be *non-Newtonian*. Some examples of non-Newtonian behavior are sketched in [Fig. 1-14](#). Curves for true fluids, which cannot resist shear, must pass through the origin on a plot of τ vs. ϵ . Other substances, called *yielding fluids*, show a finite stress at zero strain rate and are really part fluid and part solid.

$$\tau_{xy} = f(\epsilon_{xy})$$

FIGURE 1-14

Viscous behavior of various materials.

The curve labeled *pseudoplastic* in [Fig. 1-14](#) is said to be shear thinning, since its slope (local viscosity) decreases with increasing stress. If the thinning effect is very strong, the fluid may be termed *plastic*, as shown with the dashed line. The opposite case of a shear-thickening fluid is usually called a *dilatant* fluid.

Also illustrated in [Fig. 1-14](#) is a material with a finite yield stress, followed by a linear curve at finite strain rate. This idealized material, part solid and part fluid, is called a *Bingham plastic* and is commonly used in analytic investigations of yielding materials under flow conditions. Yielding substances need not be linear but may show either dilatant or pseudoplastic behavior. More specifically, if a fluid behaves as a solid until a minimum shear stress is exceeded and then exhibits a strictly linear relation between stress and strain, it is called an ideal Bingham plastic (e.g., clay suspensions, putty, toothpaste, drilling muds, and cement slurries).

Still another complication of some non-Newtonian fluids is that their behavior may be time dependent. If the strain rate is held constant, the shear stress may vary, and vice versa. If the shear stress decreases, the material is called *thixotropic*, while the opposite effect is termed *rheopectic*. Such curves are also sketched in [Fig. 1-14](#). Viscoelastic fluids partially return to their original shape after releasing stress.

A simple but often effective analytic approach to non-Newtonian behavior is the power-law approximation of Ostwald and de Waele:

$$\tau_{xy} \approx 2K\epsilon_{xy}^n \quad (1.31a)$$

where K and n are material parameters which, in general, vary with pressure, temperature, and composition in the case of mixtures. The exponent n delineates three cases on the left-hand side of [Fig. 1-14](#):

$$\begin{cases} n < 1 & \text{pseudoplastic} \\ n = 1 & \text{Newtonian } (K = \mu) \\ n > 1 & \text{dilatant} \end{cases} \quad (1.31b)$$

Note that Eq. (1-31a) is unrealistic near the origin, where it would incorrectly predict the pseudoplastic to have an infinite slope and the dilatant a zero slope. Hence, many other formulas have been proposed for non-Newtonian fluids; see, for example, Hutton et al. (1989) or Bird et al. (2007). The readers are encouraged to familiarize themselves with such

flows, although the present text is mainly focused on the study of Newtonian fluids.

1-3.6 Viscosity as a Function of Temperature and Pressure

The coefficient of viscosity of a Newtonian fluid is directly related to molecular interactions and thus may be considered a thermodynamic property in the macroscopic sense, varying with temperature and pressure. The theory of the transport properties of gases and liquids is still being developed, and a comprehensive review is given by Hirschfelder et al. (1954). Extensive data on properties of fluids are given by Reid et al. (1987).

No single functional relation $\mu(T, p)$ really describes any large class of fluids, but reasonable accuracy (± 20 percent) can be achieved by nondimensionalizing the data with respect to the critical point (T_c, p_c) . This procedure is the so-called principle of corresponding states [Keenan (1941)]; accordingly, a given property, here μ/μ_c , can be written as a function of T/T_c and p/p_c , the reduced temperature and pressure. This principle is *not* justified on thermodynamic grounds but arises simply from dimensional analysis and experimental observation. Since changes occur very rapidly near the critical point, T_c and P_c are known only approximately, and it is essentially impossible to measure μ_c accurately. Appendix C contains a table of critical constants (T_c, p_c, μ_c, k_c) for common fluids, which should be regarded as best-fit values.

[Figure 1-15](#) shows a recommended correlation of reduced viscosity μ/μ_c vs. reduced temperature T/T_c and reduced pressure p/p_c . As stated, the accuracy for any given fluid is about ± 20 percent. By examining this figure, one can make the following general statements:

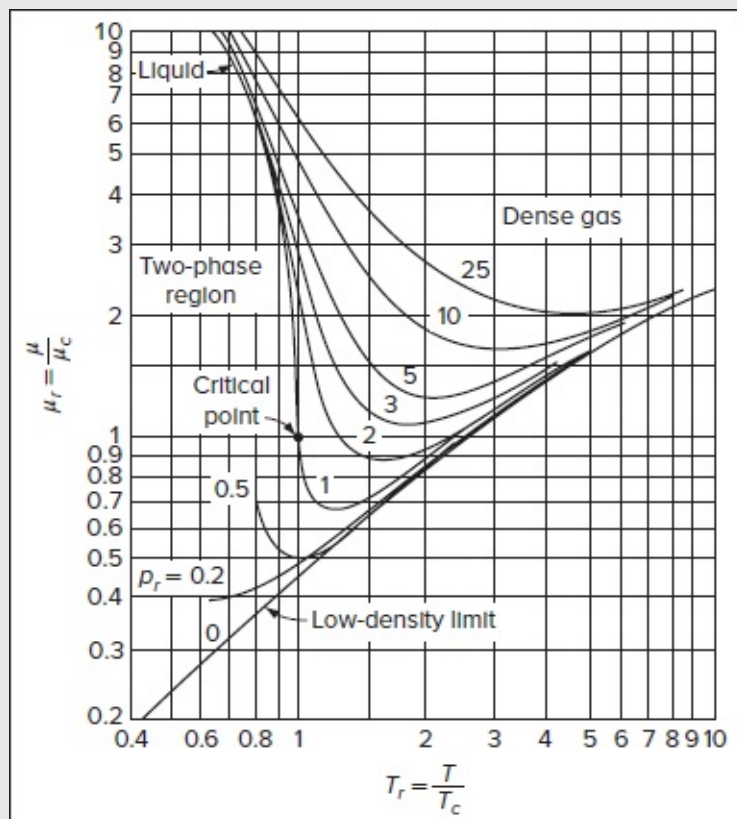


FIGURE 1-15

Reduced viscosity vs. reduced temperature for several values of reduced pressure $p_r = p/p_c$. [After Uyehara and Watson (1944).]

1. The viscosity of liquids decreases rapidly with temperature.
2. The viscosity of low-pressure (dilute) gases increases with temperature.
3. The viscosity always increases with pressure.
4. Very poor accuracy is obtained near the critical point.

Page 16 Since p_c for most fluids is greater than 10 atm (App. C), typical gas flow problems correspond to low reduced pressure and approximately the low-density-limit curve of [Fig. 1-15](#). Thus, it is common in aerodynamics, for example, to ignore the pressure dependence of gas viscosity and consider only temperature variations.

1-3.7 The Low-Density Limit

The kinetic theory of dilute gases is now highly refined and has been the subject of several excellent texts, e.g., Hirschfelder et al. (1954), Present (1958), and Brush (1972). According to some theories, which date back to Maxwell, the macroscopic concept of viscosity is

related to a statistical average of the momentum exchange occurring between molecules of the fluid. For dilute gases, the viscosity is found to be proportional to the density ρ , the mean free path ℓ , and the speed of sound a in the gas. The accepted approximation for nonpolar gases is a slight adjustment of Maxwell's original expression:

$$\mu = 0.67 \rho \ell a \quad (1-32)$$

The product $\rho \ell$ is approximately constant for dilute gases, but more refined calculations by Chapman and Cowling (1970) show that it varies slightly with temperature.

For routine calculations, a common approximation for the viscosity of dilute gases is the power law

$$\frac{\mu}{\mu_0} \approx \left(\frac{T}{T_0} \right)^n \quad (1-33)$$

where n is of the order of 0.7, and T_0 and μ_0 are reference values. This formula was also suggested by Maxwell and later deduced on purely dimensional grounds by Rayleigh. [Table 1-1](#) lists empirical values of n for various gases and the accuracy obtainable for a given temperature range.

TABLE 1-1

Power-law and Sutherland-law viscosity parameters for gases[\[Eqs. \(1-33\) and \(1-34\)\]](#)[†]

Gas	T_0 [K]	μ_0 [N·s/m ²]	n	Error %, temperature range [K]	S [K]	Temperature range for 2% error
Air	273	1.716×10^{-5}	0.666	±4 210–1900	111	170–1900
Argon	273	2.125×10^{-5}	0.72	±3 200–1500	144	120–1500
CO ₂	273	1.370×10^{-5}	0.79	±5 209–1700	222	190–1700
CO	273	1.657×10^{-5}	0.71	±2 230–1500	136	130–1500
N ₂	273	1.663×10^{-5}	0.67	±3 220–1500	107	100–1500
O ₂	273	1.919×10^{-5}	0.69	±2 230–2000	139	190–2000
H ₂	273	8.411×10^{-6}	0.68	±2 80–1100	97	220–1100
Steam	350	1.120×10^{-5}	1.15	±3 280–1500	1064	360–1500

Source: Data from Hirschfelder et al. (1954).

[†]No data given above maximum temperature listed. Formulas inaccurate below minimum temperature listed.

A second widely used kinetic theory approximation was derived by Sutherland (1893) using an idealized intermolecular-force potential. The final formula is

$$\frac{\mu}{\mu_0} \approx \left(\frac{T}{T_0} \right)^{3/2} \frac{T_0 + S}{T + S}; \quad \mu_{\text{air}} [\text{Pa} \cdot \text{s}] = \frac{0.006584}{T [\text{K}] + 110.6} \left(\frac{T [\text{K}]}{273.1} \right)^{1.5} \quad (1-34)$$

where S is an effective temperature, called the *Sutherland constant*, which is characteristic of

the gas. The accuracy is slightly better than that of [Eq. \(1-33\)](#) for the same temperature range. Values of S for common gases are also given in [Table 1-1](#). Less common gases are tabulated in App. C.

These dilute-gas formulas are strictly valid only for a single-component substance; air qualifies because its two principal components, oxygen and nitrogen, consist of nearly identical diatomic molecules. For mixtures of gases with markedly different species, the mixture viscosity varies strongly with species concentration. A good discussion of transport properties of gas mixtures is given in Bird et al. (2007).

Page 17

1-3.8 The Coefficient of Thermal Conductivity

It is well established in thermodynamics that heat flow is the result of temperature variation, i.e., a temperature gradient. This can be formally expressed as a proportionality between the heat flux and the driving temperature gradient, i.e., Fourier's law:

$$\mathbf{q} = \frac{\dot{\mathbf{Q}}}{A} = -k\nabla T \quad (1-35)$$

where \mathbf{q} stands for the vector rate of heat transfer per unit area and the quantity k represents our second transport coefficient, the thermal conductivity. Note that in one-dimensional space, \mathbf{q} reduces to

$$q = -k \frac{\partial T}{\partial x} \approx -k \frac{T(x + \Delta x) - T(x)}{\Delta x} = k \frac{T(x) - T(x + \Delta x)}{\Delta x} \quad (1-36)$$

which shows that heat will have a positive sign when $T(x) - T(x + \Delta x) > 0$, thus confirming that heat flows in the direction of decreasing temperature. Solid substances often show anisotropy, or directional sensitivity, when their thermal conductivities differ with spatial orientation,

$$\mathbf{q}_{\text{sol}} = -\left(k_x \frac{\partial T}{\partial x}, k_y \frac{\partial T}{\partial y}, k_z \frac{\partial T}{\partial z}\right) \quad (1-37)$$

Fortunately, a fluid is isotropic, i.e., has no directional characteristics, and thus k may be viewed as a thermodynamic property which, like viscosity, varies with temperature and pressure. Moreover, much like viscosity, the common fluids will correlate with their critical properties, as shown in [Fig. 1-16](#). Note that the general remarks for [Fig. 1-15](#) also apply to [Fig. 1-16](#), although the actual numerical values are quite different. The low-density limit for k is quite practical for the problems in this text, and the kinetic theory of dilute gases applies once more.

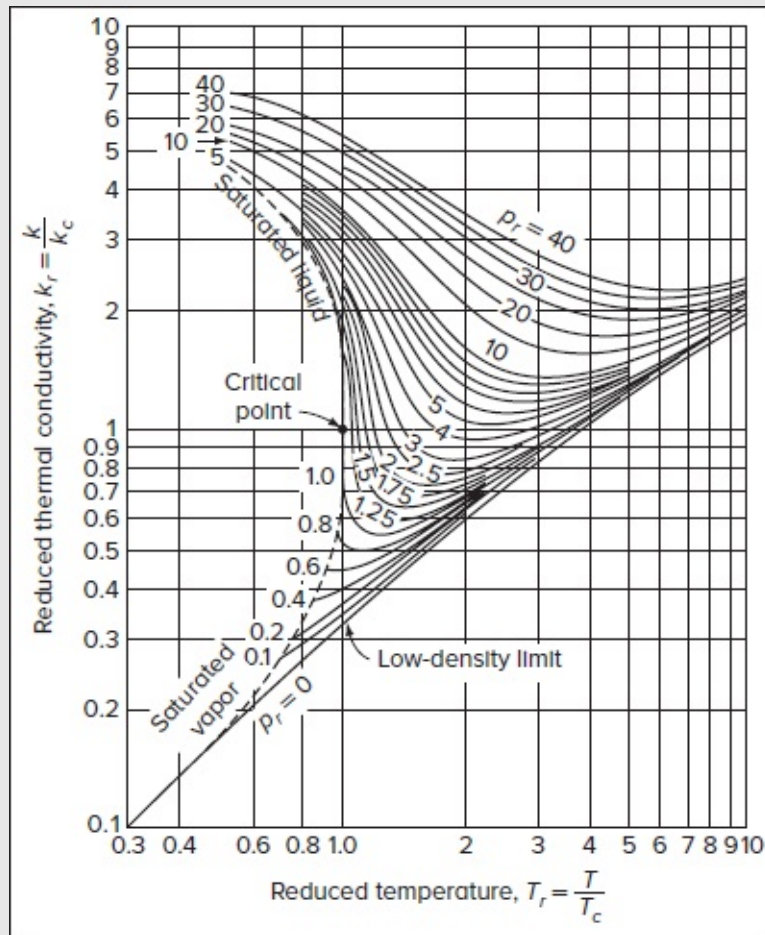


FIGURE 1-16

Reduced thermal conductivity vs. reduced temperature. [After Owens and Thodos (1957).]

Page 18 By inspection of [Eq. \(1-35\)](#), we see that thermal conductivity k should have dimensions of energy per time per length per degree, the common engineering unit being $\text{W}/(\text{m} \cdot \text{K})$ or $\text{Btu}/(\text{h} \cdot \text{ft} \cdot ^\circ\text{R})$. The metric to English unit conversion factor is

$$1 \text{ W}/(\text{m} \cdot \text{K}) = 0.5778 \text{ Btu}/(\text{h} \cdot \text{ft} \cdot ^\circ\text{R}) \quad (1-38)$$

Also, k has the dimensions of viscosity times specific heat, so that the ratio of these forms a fundamental parameter called the *Prandtl number*:

$$Pr = \frac{\mu c_p}{k} \quad (1-39)$$

This parameter involves fluid properties only, rather than length and velocity scales. As we shall see, the Prandtl number is important in heat transfer calculations but does not enter into friction computations.

The kinetic theory for conductivity of dilute gases is very similar to the viscosity analysis and enables us to write

$$Pr \approx \frac{\mu c_p}{k} = \frac{(\mu/\rho)}{k/(\rho c_p)} = \frac{\nu}{\alpha} = \frac{4\gamma}{15\gamma - 15} \quad \gamma = \frac{c_p}{c_v} \quad (1-40)$$

where $\nu = \mu/\rho$ and $\alpha = k/(\rho c_p)$ represent the kinematic viscosity and thermal diffusivity, respectively. This expression relates the Prandtl number to γ , the specific-heat ratio of the gas. In fact, it is seen to be a fair approximation to the Prandtl numbers of the gases plotted in [Fig. 1-17](#).

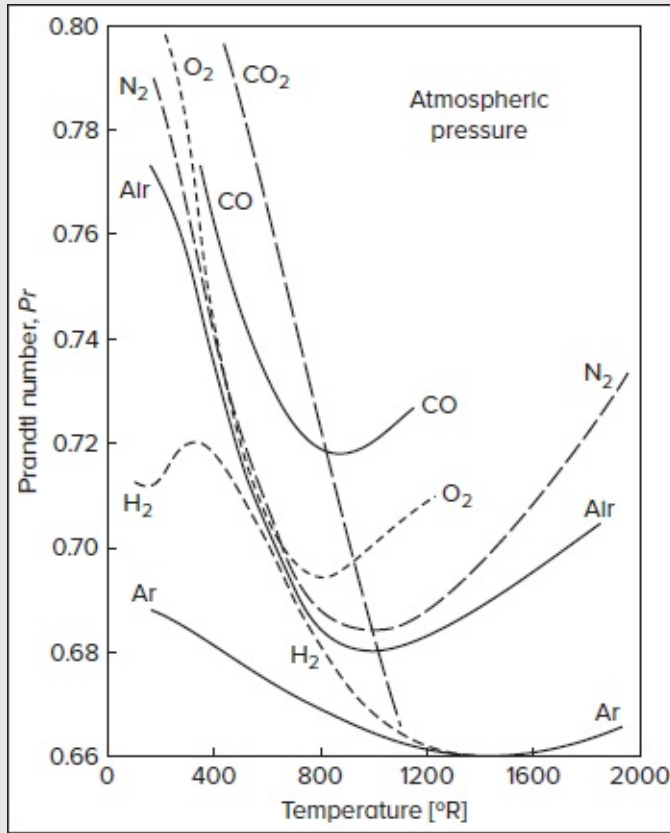


FIGURE 1-17

Prandtl number vs. temperature for seven gases. [Data from Hilsenrath et al. (1955).]

For routine calculations with dilute gases, the power law and Sutherland formula, which correlate viscosity data, can also be used for thermal conductivity:

$$\frac{k}{k_0} \approx \left(\frac{T}{T_0} \right)^n \quad (1.41a)$$

$$\frac{k}{k_0} \approx \left(\frac{T}{T_0}\right)^{3/2} \frac{T_0 + S}{T + S} \quad (1.41b)$$

The accuracy is from 2 to 4 percent, depending upon the gas. Values of n , S , k_0 , and T_0 are given for the common gases in [Table 1-2](#), along with their accuracy when compared with the data compiled by White (2016).Page 19

TABLE 1-2

Power-law and Sutherland-law thermal-conductivity parameters for gases[Eqs. (1-41a) and (1-41b)]

Gas	T_0 [K]	k_0 [W/(m·K)]	n	Error %, temperature range [K]	S [K]	Temperature range for $\pm 2\%$ error [K]
Air	273	0.0241	0.81	± 3 210–2000	194	160–2000
Argon	273	0.0163	0.73	± 4 210–1800	170	150–1800
CO ₂	273	0.0146	1.30	± 2 180–700	1800	180–700
CO	273	0.0232	0.82	± 2 210–800	180	200–800
N ₂	273	0.0242	0.74	± 3 210–1200	150	200–1200
O ₂	273	0.0244	0.84	± 2 220–1200	240	200–1200
H ₂	273	0.168	0.72	± 2 200–1000	120	200–1000
Steam	300	0.0181	1.35	± 2 300–900	2200	300–700

Source: Data from White (1988).

1-3.9 The Coefficient of Mass Diffusivity

The third and final transport coefficient is associated with the movement of mass due to molecular exchange. This process, called *mass* or *species diffusion*, constantly occurs in a fluid because of random molecular motion; the air in a given portion of a room continually loses some particles and gains others, so that the specific content of a given volume is always changing. Diffusion becomes macroscopically evident when a variable mixture of two or more species is involved. If we stand on one side of a room while an amount of hydrogen sulfide gas is released at the other side, we soon sense the odor as the hydrogen sulfide diffuses to our side, replacing some of our air, which diffuses to the other side. The transfer of mass is equal and opposite; i.e., diffusion is an equal exchange of species, and the final state in this case would be a uniform mixture of air and hydrogen sulfide throughout the room. It is well to note that the rate of diffusion is *not* equal to the mean molecular speed \bar{c} but is far slower. Many molecular collisions occur in a short distance, the mean free path; hence, the hydrogen sulfide “front” advances slowly, a mean free path at a time, so to speak.

Mass diffusion occurs, then, whenever there is a gradient in the proportions of a mixture, i.e., a *concentration gradient*. There are two different definitions of concentration in frequent use: (1) the volume concentration $\rho_i = m_i / \vartheta$ = mass of component i per unit volume and (2) the mass concentration $C_i = \rho_i / \rho$ = mass of species i per unit mass of the mixture. The second

definition or mass concentration will be more useful in this text if for no other reason than that it is a dimensionless fraction less than or equal to unity. By analogy with viscosity and thermal conductivity, we postulate that mass diffusion per unit area is proportional to the local concentration gradient. In vector form, we have

$$\frac{\dot{\mathbf{m}}_i}{A} = -D\nabla(\rho_i) \quad (1-42)$$

where $\dot{\mathbf{m}}_i$ denotes the mass flux of species i in the direction of decreasing concentration (which accounts for the minus sign). The quantity D is called the *coefficient of mass diffusivity* and has dimensions of (length)²/time usually either square feet per second or square centimeters per second. Equation (1-42) is referred to as *Fick's law of diffusion*.

In terms of the mass concentration, $C_i = \rho_i / \rho$, [Eq. \(1-42\)](#) may be manipulated to write

$$\frac{\dot{\mathbf{m}}_i}{A} = -D\nabla(\rho C_i) = -(\rho C_i) D \frac{\nabla C_i}{C_i} = -\rho_i D \nabla(\ln C_i) \quad (1-43)$$

where “ln” denotes the natural logarithm. Since mass flux per unit area equals density times velocity, we can write, by definition,

$$\frac{\dot{\mathbf{m}}_i}{A} = \rho_i \mathbf{V}_i \quad (1-44)$$

where \mathbf{V}_i represents the *diffusion velocity* of species i . In this simpler form, then, Fick's law can be written as

$$\mathbf{V}_i = -D\nabla(\ln C_i) \quad (1-45)$$

which, in one-dimensional space, shows that the diffusion speed is proportional to the relative difference in species concentration per unit distance, namely,

$$V_i = -D \frac{d \ln(C_i)}{dx} = -\frac{D}{C_i} \frac{dC_i}{dx}$$

The diffusion coefficient D has the same dimensions as the kinematic viscosity ν or the thermal diffusivity $\alpha = k / (\rho c_p)$. Thus, their ratios, like the Prandtl number, give rise to important dimensionless parameters in a fluid-diffusion problem. These are:

$$\text{Schmidt number: } Sc = \frac{\mu}{\rho D} = \frac{\nu}{D} \quad \text{and} \quad \text{Lewis number: } Le = \frac{\rho c_p D}{k} = \frac{\nu}{\alpha} \quad (1-46)$$

The Schmidt number relates viscous diffusion to mass diffusion, and the Lewis number compares mass diffusion to thermal diffusion.

1-3.10 Transport Properties of Liquids

The theoretical analysis of liquid transport properties is not nearly as well developed as that for gases. The difficulty is that liquid molecules are very closely packed compared to gases and thus dominated by large intermolecular forces. Momentum transfer by collisions—so dominant in gases—is secondary in liquids. The kinetic theory of liquids is summarized in the texts by Bird et al. (2007) and Reid et al. (1987). However, the theory is not yet quantitative, in the sense that a given liquid's properties cannot be predicted from other thermodynamic data.

If no data are available, we recommend the reduced temperature and pressure plots, given by [Figs. 1-15](#) and [1-16](#), with ± 20 percent accuracy. If data measurements are available for calibration, however, they may be fit accurately to the empirical formula:

$$\ln\left(\frac{\mu}{\mu_0}\right) \approx a + b\left(\frac{T_0}{T}\right) + c\left(\frac{T_0}{T}\right)^2 \quad \text{or} \quad \mu \approx \mu_0 e^{a+b\left(\frac{T_0}{T}\right) + c\left(\frac{T_0}{T}\right)^2} \quad (1-47)$$

where (μ_0, T_0) are reference values and (a, b, c) are dimensionless curve-fit constants. For nonpolar liquids, $c \approx 0$, i.e., the plot is linear.

For example, App. C tabulates the viscosity of water at atmospheric pressure. If these data sets are plotted in the manner suggested by [Eq. \(1-47\)](#), the results are shown in [Fig. 1-18](#). The plot is nearly linear, and the curve-fit values are

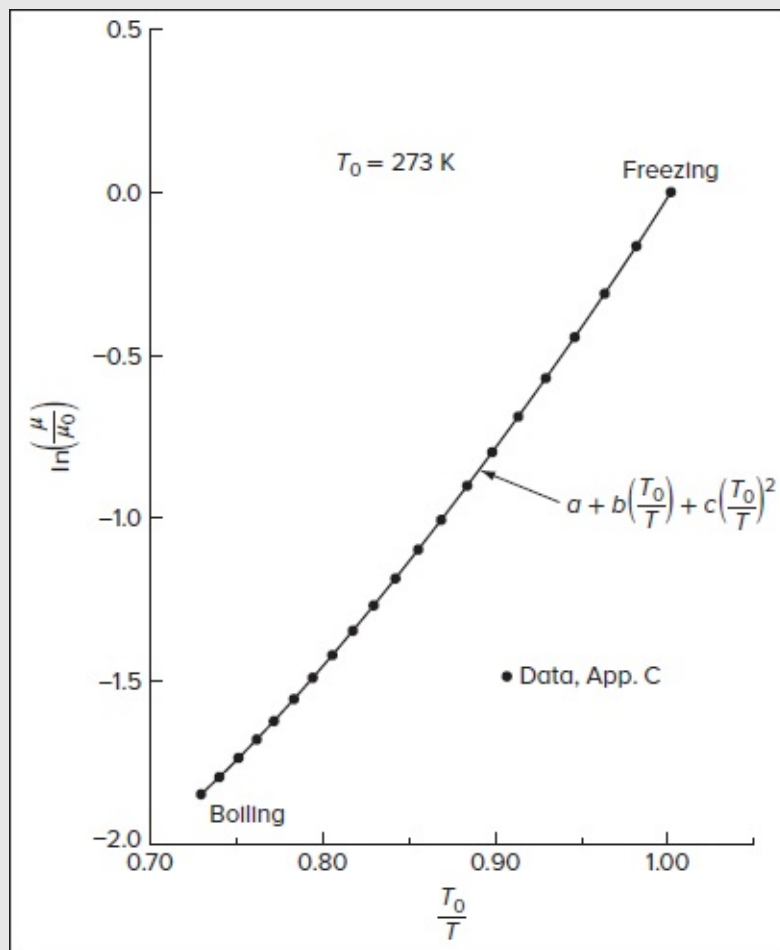


FIGURE 1-18

Empirical plot of the viscosity of water in the manner suggested by [Eq. \(1-47\)](#).

$$a = -2.10 \quad b = -4.45 \quad c = 6.65 \quad (1-48)$$

corresponding to $T_0 = 273 \text{ K}$ and $\mu_0 = 0.00179 \text{ kg/(m} \cdot \text{s)}$. The accuracy of the curve fit is ± 1 percent when compared to the data of App. Table C.1.

For thermal conductivity of liquids, [Eq. \(1-47\)](#) may not be a good fit—e.g., data for water in App. Fig. C-5. Reid et al. (1987) recommend the simple linear fit

$$k_{\text{liq}} \quad \text{or} \quad D_{\text{liq}} \approx a + bT \quad (1-49)$$

which will be accurate at least over a limited temperature range.

1-3.11 The Thermodynamic Properties

As stated before, by their very nature, viscous flows are technically not in equilibrium, but at normal densities the deviations from equilibrium are negligible. Two exceptions to this are

chemically reacting flows and very sudden state changes, as in a strong shock wave. Generally, though, it is quite reasonable to assume that a moving viscous fluid is a pure substance whose properties are related by ordinary equilibrium thermodynamics. The properties most important to this subject are pressure, density, temperature, entropy, enthalpy, and internal energy. Of these six, two may be regarded as the independent variables from which all others follow through experimental (or theoretical) equations of state. In [Chap. 2](#), it will be convenient to consider p and T as primary variables, but technically this is not a perfect choice.

The first law of thermodynamics can be written as

$$dE = dQ + dW \quad \text{where} \quad \begin{aligned} dE &= \text{change in system internal energy} \\ dQ &= \text{heat added to system} \\ dW &= \text{work done on system} \end{aligned} \quad (1-50)$$

dW = work done on system

For a substance at rest with infinitesimal changes, we have

$$dQ = TdS \quad dW = -pd\vartheta \quad (1-51)$$

where ϑ represents the volume and $d(\vartheta / m) = d(\rho^{-1}) = -\rho^{-2}d\rho$. Substituting these terms into [Eq. \(1-50\)](#) and expressing the result on a unit mass basis using $e = E / m$, $s = S / m$, and $\rho = m / \vartheta$, we get

$$de = Tds + \frac{p}{\rho^2} d\rho \quad (1-52)$$

which is one form of the first and second laws combined for infinitesimal processes. Equation (1-52) implies that the single state relation

$$e = e(s, \rho) \quad (1-53)$$

is entirely sufficient to define a fluid thermodynamically. For, in terms of the calculus of two variables,

$$de = \frac{\partial e}{\partial s} ds + \frac{\partial e}{\partial \rho} d\rho \quad (1-54)$$

from which, by comparison with [Eq. \(1-52\)](#), the temperature and pressure can be extracted using

$$T = \left. \frac{\partial e}{\partial s} \right|_{\rho} \quad p = \rho^2 \left. \frac{\partial e}{\partial \rho} \right|_s \quad (1-55)$$

Page 22 after which the enthalpy can be deduced from its definition:

$$h = e + \frac{p}{\rho} \quad (1-56)$$

Thus, a single chart of e vs. s for lines of constant p is sufficient to determine all thermodynamic properties. Equation (1-53) is therefore called a *canonical* equation of state.

A second and more popular canonical equation of state is obtained by using [Eq. \(1-56\)](#) to eliminate de in [Eq. \(1-52\)](#), with the result

$$dh = Tds + \frac{1}{\rho} dp \quad (1-57)$$

Again, using calculus, we find that from the canonical relation

$$h = h(s, p) \quad (1-58)$$

all other properties can be retrieved, i.e.,

$$T = \left. \frac{\partial h}{\partial s} \right|_p, \quad \frac{1}{\rho} = \left. \frac{\partial h}{\partial p} \right|_s \quad \text{and} \quad e = h - \frac{p}{\rho} \quad (1-59)$$

In this case, a chart of h vs. s for lines of constant p will define the substance completely. Such a plot is very popular and is called a *Mollier chart*, after Richard Mollier (1863–1935), a German engineering professor who first proposed it.

[Figure 1-19](#) is a sketch of the Mollier chart for air as given by Little (1963). Tabular properties for eight common gases are given by Hilsenrath et al. (1955). [Figure 1-19](#) shows only the constant-pressure lines, which are quite sufficient thermodynamically, as discussed previously. However, in preparing such a Mollier chart for publication, it is usual to include other lines (constant density, temperature, and speed of sound). Data for water and steam are given by Harvey et al. (2014).

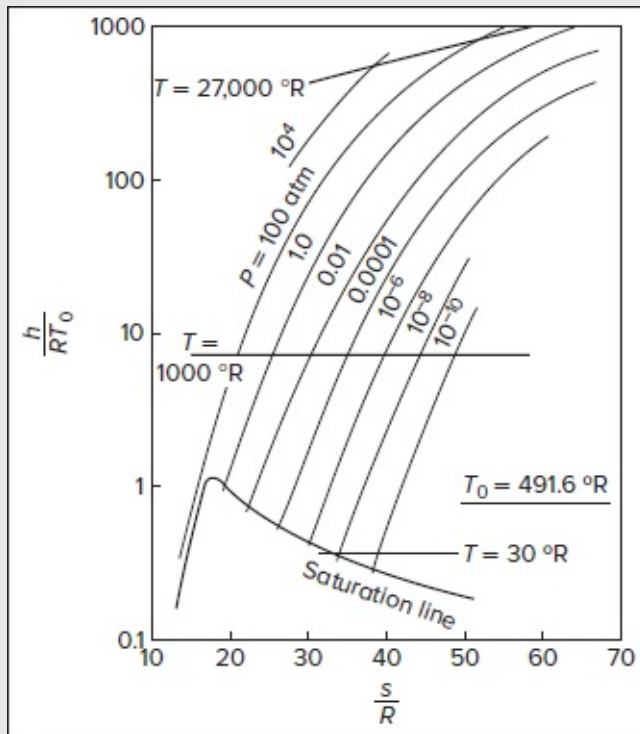


FIGURE 1-19

Mollier chart for equilibrium air. [After Little (1963).]

1-3.12 Secondary Thermodynamic Properties

Still other properties are often used in flow analyses, particularly with idealized equations of state such as the perfect-gas law. Two of these are the specific heats (so-called) at constant pressure and constant volume:

$$c_p = \left. \frac{\partial h}{\partial T} \right|_p \quad \text{and} \quad c_v = \left. \frac{\partial e}{\partial T} \right|_v \quad (1-60)$$

which of course are not heats at all but expressions of energy change. The ratio of specific heats

$$\gamma = \frac{c_p}{c_v} \quad (1-61)$$

represents an important dimensionless parameter in high-speed (compressible) flow problems. This ratio lies between 1.0 and 1.7 for all fluids. For a liquid, which is nearly incompressible, $c_p \approx c_v$ and $\gamma \approx 1.0$. [Figure 1-20](#) shows values of γ at atmospheric pressure for various gases as a function of absolute temperature. The pressure dependence of γ is very weak, and the figure shows that the approximation ($\gamma = \text{const.}$) is accurate over fairly wide temperature variations.

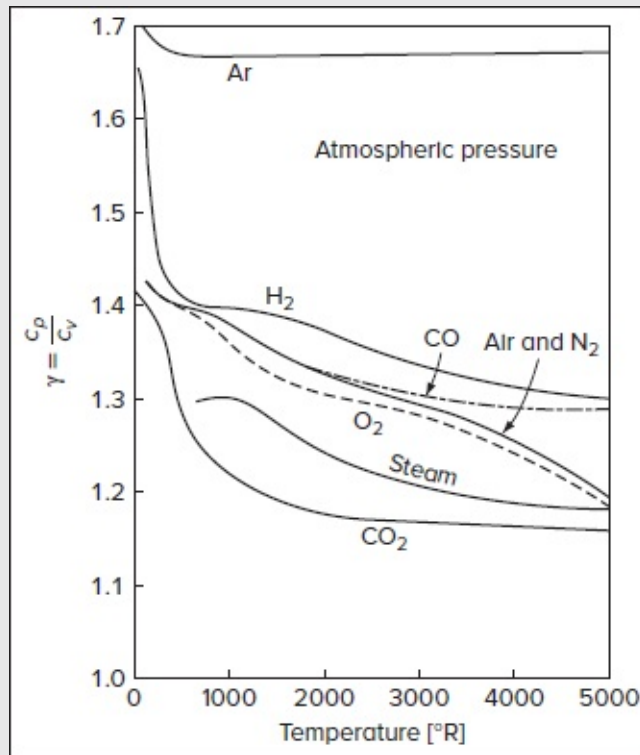


FIGURE 1-20

Specific-heat ratio for eight common gases. [Data from Hilsenrath et al. (1955).]

Another minor but important thermodynamic property is the *speed of sound* a , defined as the rate of propagation of infinitesimal pressure pulses [White (2016), Sec. 9.2]:

$$a^2 = \left. \frac{\partial p}{\partial \rho} \right|_s \quad (1-62)$$

Since the partial derivative in [Eq. \(1-62\)](#) is rather inconvenient to handle, an alternative relation can be used, specifically,

$$a^2 = \gamma \left(\frac{\partial p}{\partial \rho} \right)_T \quad (1-63)$$

The reader may prove as an exercise that [Eqs. \(1-62\)](#) and [\(1-63\)](#) are thermodynamically identical. Since viscous flows are definitely *not* isentropic in general, the speed of sound is not a natural ingredient of viscous analyses but enters instead through the assumption of perfect-gas relations, as does the Mach number.

1-3.13 The Perfect Gas

All the common gases follow with reasonable accuracy, at least in some finite region, the so-called ideal or perfect-gas law:

$$p = \rho RT \quad (1-64)$$

Page 24 where R is called the gas constant. Equation (1-64) has a solid theoretical basis in the kinetic theory of dilute gases, e.g., Kauzmann (2012), and should not be regarded as an empirical formula. The gas constant R may be written in terms of the molecular weight M of the gas:

$$R_{\text{gas}} = \frac{R_0}{M_{\text{gas}}} \quad (1-65)$$

where R_0 is a universal constant similar to Boltzmann's constant. The value of R_0 is

$$R_0 = 8,314 \text{ J}/(\text{kmol} \cdot \text{K}) \quad (1-66)$$

which has too many significant figures, since no gas really fits the law that well. Equations (1-64) and (1-65) are also suitable for mixtures of gases if the equivalent molecular weight is properly defined in terms of the mass fractions, $C_i = \rho_i/\rho$:

$$M_{\text{mix}} = \frac{1}{\sum (C_i/M_i)} \quad (1-67)$$

In terms of the mole fractions x_i (the number of moles of species i per mole of mixture), we have

$$M_{\text{mix}} = \sum x_i M_i \quad (1-68)$$

As a classic example, air at ordinary temperatures has mole fractions of approximately 78 percent nitrogen, 21 percent oxygen, and 1 percent argon. Then, from [Eq. \(1-68\)](#), we have

$$M_{\text{air}} = 0.78(28.016) + 0.21(32.000) + 0.01(39.944) = 28.97$$

from which

$$R_{\text{air}} = \frac{8314}{28.97} = 287 \text{ J}/(\text{kg} \cdot \text{K}) = 1716 \text{ ft} \cdot \text{lbf}/(\text{slug} \cdot ^\circ\text{R})$$

These are the accepted values for room-temperature dry air.

According to [Eq. \(1-64\)](#), the so-called compressibility factor

$$Z = \frac{p}{\rho RT} \quad (1-69)$$

should be unity for gases. Actually, Z varies from zero to 4.0 or greater, depending on the temperature and pressure. To good accuracy, Z is a function only of the reduced variables, $p_r = p/p_c$ and $T_r = T/T_c$, which are normalized by their critical values and referred to as the reduced temperature and pressure. This is illustrated in [Figs. 1-21](#) and [1-22](#), which are

representative of all gases. Examining these figures, we see that the perfect-gas law ($Z = 1$) is accurate to $\pm 10\%$ in the range $1.8 \leq T_r \leq 15$ and $0 \leq p_r \leq 10$, which is the range of interest for the majority of viscous-flow problems. The higher temperatures should be viewed with suspicion for multiatomic molecules, which may dissociate into smaller particles and raise the value of Z markedly. In air, for example, dissociation happens twice: at 2000 K, where $\text{O}_2 \rightarrow 2\text{O}$ and at 4000 K, where $\text{N}_2 \rightarrow 2\text{N}$. [Figure 1-23](#) shows the compressibility factor of air as calculated by Hansen (1958). Note the first and second plateaus corresponding to O_2 and then N_2 dissociation. The effect is particularly strong at low pressure.

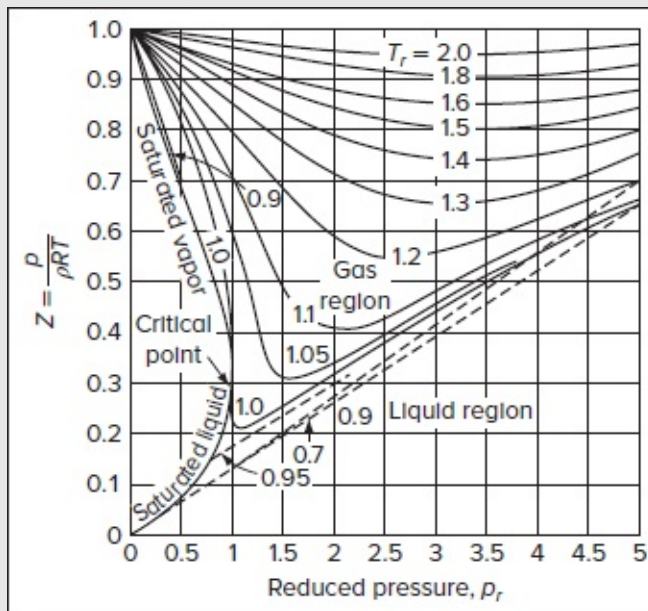


FIGURE 1-21

Compressibility factors for gases. [After Weber (1939).]

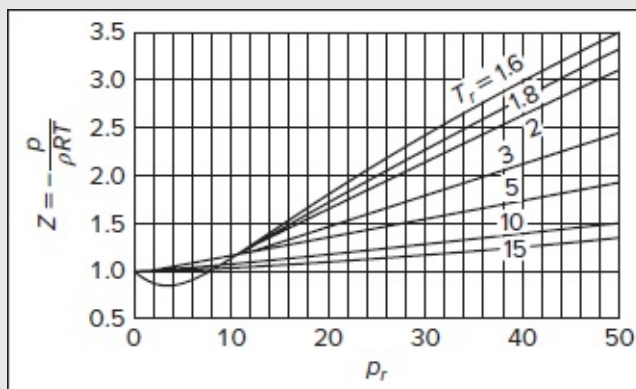


FIGURE 1-22

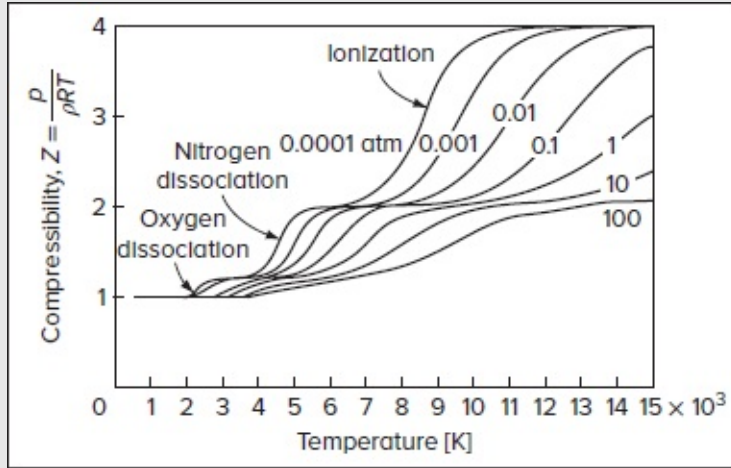


FIGURE 1-23

Calculated compressibility of air. [After Hansen (1958).]

1-3.14 Other Properties of the Perfect Gas

As a direct consequence of the perfect-gas law [Eq. (1-64)], many useful and simple relations arise. The specific heats are constrained to be functions of temperature only:

$$c_p = c_p(T) \text{ only} \quad \text{and} \quad c_v = c_v(T) \text{ only} \quad (1-70)$$

Hence, from [Eqs. \(1-60\)](#), we have

$$de = c_v dT \quad \text{and} \quad dh = c_p dT \quad (1-71)$$

Further, it follows that

$$\gamma = \gamma(T) \text{ only} \quad c_p(T) = c_v(T) + R = \frac{\gamma(T)R}{\gamma(T) - 1} \quad \text{and} \quad c_v(T) = \frac{R}{\gamma(T) - 1} \quad (1-72)$$

Finally, from [Eq. \(1-63\)](#), the speed of sound takes the simple form

$$a_{\text{perfect gas}}^2 = \gamma RT \quad (1-73)$$

Because of their reasonable accuracy and delightful simplicity, the perfect-gas relations are understandably popular in viscous-flow analysis. We make liberal use of the perfect-gas law in [Chap. 7](#).

As shown in [Fig. 1-20](#), the specific-heat ratio γ tends to decrease with temperature. Because all of these gases are reasonably perfect, it follows from [Eqs. \(1-72\)](#) that c_p and c_v must increase with temperature. Moreover, since R is known from [Eq. \(1-65\)](#), [Fig. 1-20](#) may be used to calculate c_p and c_v to good accuracy.

Page 26Finally, [Fig. 1-17](#) discussed earlier displays the Prandtl number $Pr = \mu c_p / k$ versus temperature for various common gases.

1-3.15 Bulk Modulus

In flow problems that involve sound-wave propagation, it is useful to introduce a thermodynamic property that expresses the change of density with increasing pressure. This property is the *bulk modulus* K :

$$K = \rho \left(\frac{\partial p}{\partial \rho} \right)_T \quad (1-74)$$

From [Eq. \(1-63\)](#), then, we see that the speed of sound can be written in terms of K :

$$a^2 = \gamma K / \rho \quad (1-75)$$

where γ may be taken as 1.0 for liquids and solids.[‡] For liquids, K is fairly constant, varying slightly with pressure and temperature. For water, a good average value is $K = 2.2 \times 10^9$ Pa. Taking $\gamma = 1.0$ and an average water density of 998 kg/m³, we calculate the speed of sound in water to be approximately 1480 m/s. For a perfect gas, one may readily verify that $K = p$ by simply equating [Eqs. \(1-73\)](#) and [\(1-75\)](#) as both are equal to the speed of sound squared, $\gamma K / \rho = \gamma RT$, or $K = \rho RT = p$.

1-3.16 Coefficient of Thermal Expansion

There is a subset of flow problems, called *natural convection*, where the flow pattern is due to buoyant forces caused by temperature differences. Such buoyant forces are proportional to the coefficient of thermal expansion β , defined as

$$\beta = -\frac{1}{\rho} \left(\frac{\partial \rho}{\partial T} \right)_p \quad (1-76)$$

For a perfect gas [[Eq. \(1-64\)](#)], one can show that $\beta = 1/T$. This can be seen by taking the derivative with regard to T at a constant pressure

$$\left. \frac{\partial \rho}{\partial T} \right|_p = \frac{\partial}{\partial T} \left(\frac{p}{RT} \right) \Big|_p = \frac{p}{R} \frac{\partial}{\partial T} \left(\frac{1}{T} \right) = -\frac{p}{RT^2}$$

Substituting this expression back into [Eq. \(1-76\)](#), and reapplying the state relation $\rho = p / (RT)$, one arrives at

$$\beta = -\frac{1}{\rho} \left(-\frac{p}{RT^2} \right) = \frac{1}{T}$$

For a liquid, β is usually smaller than $1/T$ and may even be negative (the celebrated inversion of water near the freezing point). For imperfect gases, β can be considerably larger than $1/T$ near the saturation line, particularly at high pressures. This is illustrated in [Fig. 1-24](#) for steam. We see that steam is well approximated by the perfect-gas result $\beta = 1/T$ at low pressures and high temperatures.

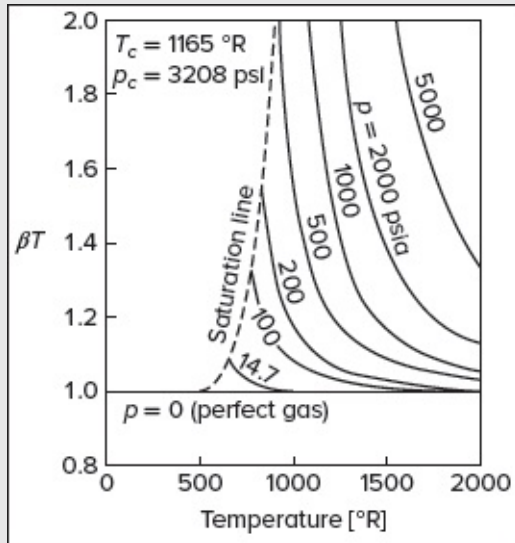


FIGURE 1-24

Thermal-expansion coefficient for steam.

The quantity β is also useful in estimating the dependence of enthalpy on pressure based on the thermodynamic relation

$$dh = c_p dT + (1 - \beta T) \frac{dp}{\rho} \quad (1-77)$$

where we remark that, of course, T must be absolute temperature. For a perfect gas, the second term vanishes, so that $h = h(T)$ only. [Figure 1-24](#) shows that imperfect gases such as steam often fit this approximation, $dh \approx c_p dT$. Page 27

[Table 1-3](#) provides measured values of the bulk modulus K and the thermal-expansion coefficient β for water at saturation pressures.

TABLE 1-3

Bulk modulus K and expansion coefficient β for water at saturation conditions

T [K]	p_{sat} [kPa]	βT	K [MPa]
273	0.61	-0.019	2,062
293	2.34	0.057	2,230
313	7.38	0.119	2,304
333	19.92	0.176	2,301
353	47.35	0.230	2,235
373	101.3	0.281	2,120
423	461	0.447	1,692
473	1,580	0.637	1,190
523	3,970	0.985	716
573	8,560	1.80	342
623	16,500	4.8	82
647 [†]	22,090 [†]	∞	0

[†]Critical point.

1-4 BOUNDARY CONDITIONS FOR VISCOUS-FLOW PROBLEMS

The equations of motion to be discussed in [Chap. 2](#) will require mathematically tenable and physically realistic boundary conditions. It is of interest here to study the underlying physical mechanisms of the boundary approximations commonly used. For fluid flow, there are five types of boundaries considered:

1. A solid surface (which may be porous).
2. A free liquid surface.
3. A liquid–vapor interface.
4. A liquid–liquid interface.
5. An inlet or exit section.

Cases 2 and 3 are related in the sense that a free liquid surface is a special case of the liquid–vapor interface where the vapor causes a negligible interaction. Let us take up these cases in order.

1-4.1 Conditions at a Solid Surface

Wall boundary conditions depend upon whether the fluid is a liquid or a gas. For *macroflows*, system dimensions are large compared to molecular spacing, so that both liquid and gas particles contacting the wall must essentially be in equilibrium with the solid. At a solid surface, the fluid will assume the velocity of the wall (the *no-slip* condition) and the temperature of the wall (the *no-temperature-jump* condition):

$$\mathbf{V}_{\text{fluid}} = \mathbf{V}_{\text{sol}} \quad T_{\text{fluid}} = T_{\text{sol}} \quad (1-78)$$

Equation (1-78) will be used throughout this text for Newtonian liquids.

1-4.2 Kinetic Theory for Slip Velocity in Gases

If the fluid is a gas, [Eqs. \(1-78\)](#) will fail when the mean free path ℓ is comparable to the length-scale L of the flow. The ratio of these two lengths is called the Knudsen number, Kn :

$$Kn = \frac{\ell}{L} \quad (1-79)$$

Thus, if $Kn \ll 1$ there is negligible slip. If $Kn = O(10^{-1})$, there is slip. If $Kn = O(1)$ or greater, the flow is molecular and slip is an inadequate concept. There are two ways for the Knudsen number to dominate: (1) if ℓ is very large, that is, a very rarefied gas [Sharipov (2016)]; and (2) if L is very small, as in the case of microflows and nanoflows [Karniadakis and Beskok (2001)].

Consider gas molecules as they strike and reflect from a solid wall, as in [Fig. 1-25](#). If the wall is perfectly smooth, a molecule would impinge and reflect at the same angle θ similar to the reflection of a light ray from a mirror. This behavior is referred to as *specular reflection*, where molecules conserve their tangential momentum and exert no wall shear. In this case, there is perfect slip flow at the wall.

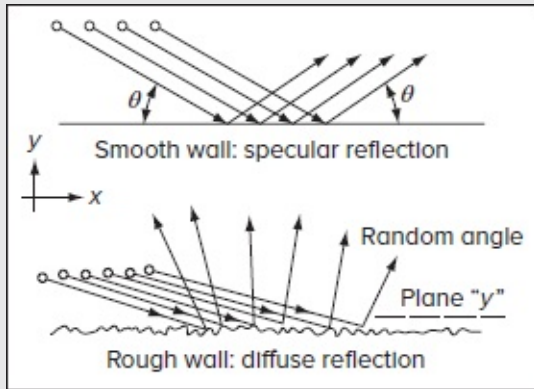


FIGURE 1-25

Specular and diffuse reflection of particles.

On a molecular scale, however, even the most highly polished wall appears rough. It is more likely that the impinging molecules view the wall as rough and reflect at random angles uncorrelated with their entry angle. This is termed *diffuse reflection* and is shown in the lower half of [Fig. 1-25](#). Equilibrium across a plane y near the wall requires that the loss of tangential momentum be balanced by a finite slip velocity u_w to transmit shear to the wall. As postulated by Navier in 1827, the slip velocity is proportional to the wall shear:

$$u_w \approx \alpha \tau_w$$

where α is a constant. Later, Maxwell in 1879 showed with kinetic theory that $\alpha \approx \ell / \mu$ or

$$u_w \approx \ell \left(\frac{\partial u}{\partial y} \right)_w \quad (1-80)$$

where ℓ is the mean free path of the gas. See, for example, Kauzmann (2012). One can approximate the fluid away from the wall as a Newtonian continuum. If we assume that a fraction f of the molecules is reflected diffusely, the slip velocity becomes

$$u_w \approx \left(\frac{2-f}{f} \right) \ell \left(\frac{\partial u}{\partial y} \right)_w \quad (1-81)$$

Page 29However, this correction seems superfluous, as a review by Sharipov and Seleznev (1998) suggests that the simpler [Eq. \(1-80\)](#) is quite accurate for single-component gases. That is, $f \approx 1$.

Is slip important in boundary-layer flows? Many researchers have concluded that, for boundary layers,

Turbulent gas flow:	no slip	
Laminar gas flow:	possible slip at low Re_L and high Ma	(1-82)

where $Ma = U / a$ denotes the Mach number of the freestream. For further study of microflows, nanoflows, and rarefied gases, see the monographs by Sharipov (2016) and Kandlicar and Garimella (2016). For most gas flow analyses in this text, we will use the standard no-slip condition [Eq. (1-78)].

1-4.3 Kinetic Theory for Wall-Temperature Jump

The temperature condition in [Eq. \(1-78\)](#) will also fail for a gaseous motion if the mean free path is large compared to flow dimensions. This effect is called *temperature jump* and is analogous to velocity slip. The kinetic-theory expression for the jump $T_{\text{gas}} - T_w$ in a gas is given by Smoluchowski (1898):

$$T_{\text{gas}} - T_w \approx \left(\frac{2}{\alpha} - 1 \right) \frac{2\gamma}{\gamma + 1} \frac{\ell k}{\mu c_p} \left(\frac{dT}{dy} \right)_w \quad (1-83)$$

where α is the so-called thermal-accommodation coefficient, defined as the fraction of impinging molecules, which is equated to the temperature of the wall. Clearly α is analogous to the diffuse-reflection coefficient f in [Eq. \(1-81\)](#). Experiments have shown that α is also fairly close to unity. Thus, the same remarks as before apply here. The temperature jump in turbulent flow is entirely negligible, and the jump in laminar flow is also extremely small except at low Reynolds number and high Mach number. It is customary, then, to adopt the no-slip and no-temperature-jump conditions in routine analysis of viscous gas-flow problems:

$$\mathbf{V}_{\text{gas}} \approx \mathbf{V}_w \quad T_{\text{gas}} \approx T_w \quad (1-84)$$

In many cases, of course, the coordinate system is such that the wall is stationary, so that the velocity condition is simply $\mathbf{V}_{\text{fluid}} = 0$.

1-4.4 Conditions at a Free Liquid Surface

There are many flow problems where the liquid fluid ends, not at a solid wall, but at an open or free surface exposed to an atmosphere of either gas or vapor. We distinguish between two cases: (1) the ideal or classic free surface that exerts only a known pressure on the liquid boundary and (2) a more complicated case where the atmosphere exerts not only pressure but also shear, heat flux, and mass flux at the surface. This latter, more involved surface is more properly termed a liquid–vapor interface, the ocean surface being a splendid example.

The classic free surface is sketched in [Fig. 1-26](#). Let us assume that the xy plane is more or less parallel to the free surface, so that the actual deflected shape of the surface can be denoted by $z = \eta(x, y)$.

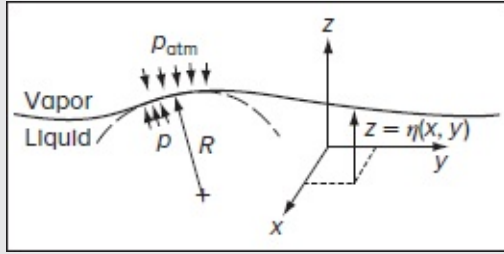


FIGURE 1-26

Conditions at an ideal free surface.

The two required conditions for this surface are: (1) the fluid particles at the surface must remain attached (kinematic condition) and (2) the liquid and the atmospheric pressure must balance except for surface-tension effects. The kinematic condition is specified mathematically by requiring the particle's upward velocity to equal the motion of the free surface, namely,

$$w(x, y, \eta) = \frac{D\eta}{Dt} = \frac{\partial \eta}{\partial t} + u \frac{\partial \eta}{\partial x} + v \frac{\partial \eta}{\partial y} \quad (1-85)$$

The pressure equilibrium is expressed by

$$p(x, y, \eta) = p_a - \mathfrak{J} \left(\frac{1}{R_x} + \frac{1}{R_y} \right) \quad (1-86)$$

where R_x and R_y represent the radii of curvature of the surface and \mathfrak{J} denotes the coefficient

of surface tension of the interface. For a two-dimensional surface deflection with $\eta = \eta(x)$ only, [Eq. \(1-86\)](#) becomes

$$p(x, \eta) = p_a - \frac{\mathfrak{S} d^2\eta/dx^2}{[1 + (d\eta/dx)^2]^{3/2}} \quad (1-87)$$

We see from this relation that, when the interface smiles (concave upward, positive curvature), $p > p_a$, while a frowning interface (concave downward) results in $p < p_a$. Equations (1-85) and (1-86) represent complex nonlinear conditions, but they can be evaluated numerically.

In the range 0 to 100°C, a clean air–water interface has a nearly linear variation of surface tension with temperature:

$$\mathfrak{S} \text{ [N/m]} \approx 0.076 - 0.00017 T \text{ [°C]} \quad (1-88)$$

with accuracy of ± 1 percent. Measured values of air–water surface tension are given in [Table 1-4](#) for temperatures up to the critical point. These are ideal for a very clean interface. Under field conditions, \mathfrak{S} can vary greatly due to the presence of surface contaminants or slicks.

TABLE 1-4

Surface-tension coefficient for an air–water interface

$T \text{ [°C]}$	$\mathfrak{S} \text{ [N/m]}$	$T \text{ [°C]}$	$\mathfrak{S} \text{ [N/m]}$
0	0.0757	200	0.0377
20	0.0727	220	0.0331
40	0.0696	240	0.0284
60	0.0662	260	0.0237
80	0.0627	280	0.0190
100	0.0589	300	0.0144
120	0.0550	320	0.0099
140	0.0509	340	0.0056
160	0.0466	360	0.0019
180	0.0422	374 [†]	0.0 [†]

[†]Critical point.

In large-scale problems, such as open-channel or river flow, the free surface deforms only slightly and surface-tension effects become negligible. Equations (1-85) and (1-86) then simplify into

$$w \approx \frac{\partial \eta}{\partial t} \quad p \approx p_a \quad (1-89)$$

These are obviously very attractive linearized conditions.

Note: The present discussion concerns the deformation of an interface by *uniform* surface

tension. If the surface tension varies along the interface due, for example, to a temperature gradient, a flow called *Marangoni convection* will be induced from the hot surface toward the cold surface. This mechanism is beyond the scope of the present text. For an example of Marangoni flow analysis, see the paper by Sasmal and Hochstein (1994) or the reviews by Ostrach (1982) and Davis (1987).

1-4.5 Conditions at a Deformable Fluid–Solid Interface

In most of the problems of this text, a solid boundary will be taken to be a rigid interface that merely imposes no-slip and no-temperature-jump conditions on the fluid. The dynamics and thermodynamics of the solid are neglected. However, there is a growing field of research in which the solid is coupled to the fluid through deformable and dynamic interactions. In this case, we must match the velocity, stress, temperature, and heat transfer across the interface, and the equations of motion for both the fluid and the solid must be solved simultaneously. Material–behavior Page 31relations can be used when the fluid is Newtonian and the solid satisfies Hooke’s law. For details, see the texts by Blevins (2001) and Au-Yang (2001).

SUMMARY

This chapter overviews the introductory concepts of fluid motion with which the reader should already be conversant. A brief history and some sample viscous-flow problems are outlined, followed by an extensive discussion of the different quantities that distinguish a fluid: (1) the kinematic properties, (2) the transport properties, and (3) the thermodynamic properties. The chapter closes with a cursory look at various boundary conditions relevant to viscous-fluid flow.

PROBLEMS

- 1-1. A sphere 1.4 cm in diameter is placed in a freestream of 18 m/s at 20°C and 1 atm. Compute the diameter Reynolds number of the sphere if the fluid is (a) air, (b) water, and (c) hydrogen.
- 1-2. A telephone wire 8 mm in diameter is subjected to a crossflow wind and begins to shed vortices. From [Fig. 1-7](#), what wind velocity (in m/s) will cause the wire to “sing” at middle C (256 Hz)?
- 1-3. If the wire in Prob. 1-2 is subjected to a crossflow wind of 12 m/s, use [Fig. 1-8](#) to estimate its drag force (in N/m).
- 1-4. For oil flow in a pipe far downstream of the entrance ([Figs. 1-9](#) and [1-10](#)), the axial velocity profile is a function of r only and is given by $u = (C/\mu)(R^2 - r^2)$, where C is a constant and R is the pipe radius. Suppose the pipe is 1 cm in diameter and $u_{\max} =$

30 m/s. Compute the wall shear stress (in Pa) if $\mu = 0.3 \text{ kg}/(\text{m} \cdot \text{s})$.

- 1-5.** Glycerin at 20°C is confined between two large parallel plates. One plate is fixed and the other moves parallel at 17 mm/s. The distance between plates is 3 mm. Assuming no-slip, estimate the shear stress in the glycerin, in Pa.

- 1-6.** A plane unsteady viscous flow is given in polar coordinates by

$$v_r = 0 \quad v_\theta = \frac{C}{r} \left[1 - \exp\left(-\frac{r^2}{4\nu t}\right) \right]$$

where C is a constant and ν is the kinematic viscosity. Compute the vorticity $\omega_z(r, t)$ and sketch an array of representative velocity and vorticity profiles for various times.

- 1-7.** A two-dimensional unsteady flow has the velocity components:

$$u = \frac{x}{1+t} \quad v = \frac{y}{1+2t}$$

Find the equation of the streamlines of this flow which pass through the point (x_0, y_0) at time $t = 0$.

- 1-8.** Using [Eq. \(1-3\)](#) for inviscid flow past a cylinder, consider the flow along the streamline approaching the forward stagnation point $(r, \theta) = (R, \pi)$. Compute (a) the distribution of strain rates ϵ_{rr} and $\epsilon_{r\theta}$ along this streamline and (b) the time required for a particle to move from the point $(2R, \pi)$ to the stagnation point.

- 1-9.** A commonly used equation of state for water is approximately independent of temperature:

$$\frac{p}{p_0} \approx (A + 1) \left(\frac{\rho}{\rho_0} \right)^n - A$$

where $A \approx 3000$, $n \approx 7$, $p_0 = 1 \text{ atm}$, and $\rho_0 = 998 \text{ kg}/\text{m}^3$. From this formula, compute (a) the pressure (in atm) required to double the density of water, (b) the bulk modulus of water at 1 atm, and (c) the speed of sound in water at 1 atm.

- 1-10.** As shown in [Fig. P1-10](#), a 3×3 -ft plate slides down a long 30° incline on which there is a film of oil 0.005 in. thick with viscosity $\mu = 0.0005 \text{ slug}/(\text{ft} \cdot \text{s})$. Assuming that the plate does not deform the oil film, estimate (a) the terminal sliding velocity (in ft/s) and (b) the time required for the plate to accelerate from rest to 99 percent of the terminal velocity.

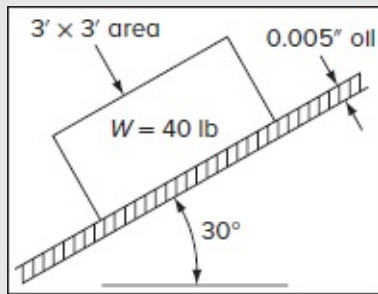


FIGURE P1.10

Page 32

- 1-11.** Estimate the viscosity of nitrogen at 36 MPa and 49°C , and then compare with the measured value of $45 \mu\text{Pa} \cdot \text{s}$.
- 1-12.** Estimate the thermal conductivity of helium at 420°C , 1 atm, and compare with the measured value of $0.28 \text{ W}(\text{m} \cdot \text{K})$.
- 1-13.** According to Table C-5 and [Fig. 1-15](#), at what pressure is the viscosity of CO_2 equal to approximately $30 \times 10^{-5} \text{ Pa} \cdot \text{s}$ when the temperature is 800°R ?
- 1-14.** Some measured values for the viscosity of ammonia gas are as follows:

T, K	300	400	500	600	700	800
$\mu, \text{Pa} \cdot \text{s}$	1.03×10^{-5}	1.39×10^{-5}	1.76×10^{-5}	2.14×10^{-5}	2.51×10^{-5}	2.88×10^{-5}

Fit these data measurements, in the least-square-error sense, to the power law, [Eq. \(1-33\)](#), and the Sutherland law, [Eq. \(1-34\)](#).

- 1-15.** Experimental data for the viscosity of helium at low pressure are as follows:

$T, ^\circ\text{C}$	0	100	200	300	400	500
$\mu, \text{Pa} \cdot \text{s}$	1.87×10^{-5}	2.32×10^{-5}	2.73×10^{-5}	3.12×10^{-5}	3.48×10^{-5}	3.48×10^{-5}

Fit these values to a suitable formula.

- 1-16.** Repeat the analysis of the velocity profile between two plates ([Fig. 1-13](#)) for a Newtonian fluid but allow for a slip velocity $\delta u \approx \ell(du/dy)$ at both walls. Compute the shear stress at both walls. [$\tau_w = \mu V/(h + 2\ell)$ at both walls.]
- 1-17.** By considering the equilibrium of forces on the element shown in [Fig. P1-17](#),

derive [Eq. \(1-86\)](#), which expresses the pressure jump across a curved surface due to surface tension.

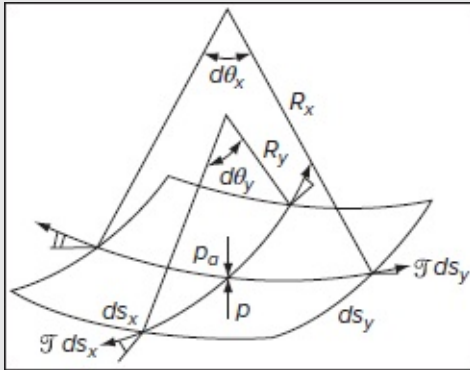


FIGURE P1.17

- 1-18.** Two spherical bubbles of radii R_1 and R_2 , which contain air, coalesce into a single bubble of radius R_3 . If the ambient air pressure is p_0 and the merging process is isothermal, derive a formula that relates R_3 to $(p_0, R_1, R_2, \mathfrak{T})$.
- 1-19.** In Prob. 1-1, if the temperature, sphere size, and velocity remain the same for airflow, at what air pressure will the Reynolds number Re_D be equal to 10,000?
- 1-20.** A solid cylinder of mass m , radius R , and length L falls concentrically through a vertical tube of radius $R + \Delta R$, where $\Delta R \ll R$. The tube is filled with gas of viscosity μ and mean free path ℓ . Neglect fluid forces on the front and back faces of the cylinder and consider only shear stress in the annular region, assuming a linear velocity profile. Find an analytic expression for the terminal velocity of fall, V , of the cylinder (a) for no slip and (b) with slip [Eq. (1-80)].
- 1-21.** Solve P1-20 for the terminal fall velocity for no slip if the cylinder is aluminum, with diameter 4 cm and length 10 cm. The tube has a diameter of 4.02 cm and is filled with argon gas at 20°C.
- 1-22.** In [Fig. P1-22](#) a disk rotates steadily inside a disk-shaped container filled with oil of viscosity μ . Assume linear velocity profiles with no slip and neglect stress on the outer edges of the disk. Find a formula for the torque M required to drive the disk.

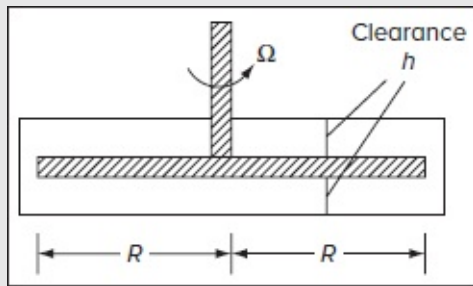


FIGURE P1.22

Page 33

- 1-23. Based on [Eq. \(1-76\)](#), it can be shown that the coefficient of thermal expansion of a perfect gas is given by $\beta = 1/T$. Use this approximation to estimate β of ammonia gas (NH_3) at 20°C and 1 atm and then compare with the accepted value from a data reference.
- 1-24. The *rotating-cylinder viscometer* in [Fig. P1-24](#) shears the fluid in a narrow clearance Δr , as shown. Assuming a linear velocity distribution in the gaps, if the driving torque M is measured, find an expression for μ by (a) neglecting and (b) including the bottom friction.

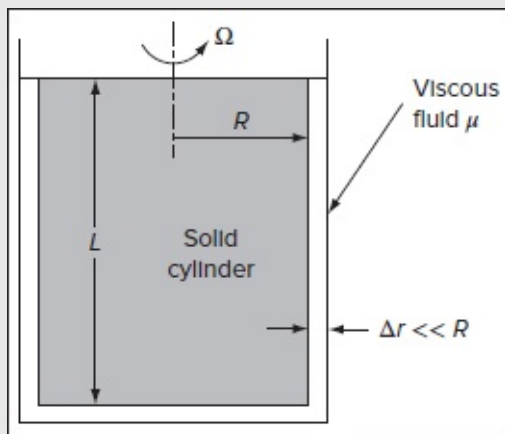


FIGURE P1.24

- 1-25. Consider 1 m^3 of a fluid at 20°C and 1 atm. For an isothermal process, calculate the final density and the energy, in joules, required to compress the fluid until the pressure is 10 atm for (a) air and (b) water. Discuss the difference in results.

- 1-26. Equal layers of two immiscible fluids are being sheared between a moving and a fixed plate, as in Fig. P1-26. Assuming linear velocity profiles, find an expression for the interface velocity U as a function of V , μ_1 , and μ_2 .

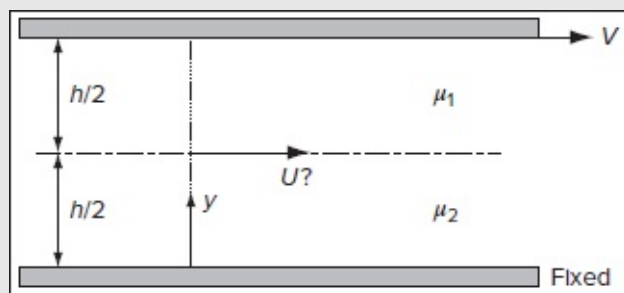


FIGURE P1.26

- 1-27. Use the inviscid-flow solution of flow past a cylinder, Eq. (1-3), to (a) find the location and value of the maximum fluid acceleration along the cylinder surface. Is your result valid for gases and liquids? (b) Apply your formula for a_{\max} to airflow at 10 m/s past a cylinder of diameter 1 cm and express your result as a ratio compared to the acceleration of gravity. Discuss what your result implies about the ability of fluids to withstand acceleration.

- 1-28. The coefficient of thermal expansion is defined as

$$\beta = -\frac{1}{\rho} \left. \frac{\partial \rho}{\partial T} \right|_p$$

Determine β for an ideal gas with $p = \rho RT$. Show your work in detail.

- 1-29. Starting with Maxwell's low-density approximation of the viscosity, namely, $\mu \approx \frac{2}{3} \rho \ell a$, and Newton's expression of the wall shear stress as a function of the velocity gradient, $\tau_w = \mu(\partial u / \partial y)_w$, express Maxwell's slip velocity, $u_w = (\partial u / \partial y)_w$,
 (a) as a function of the shear stress, density, and speed of sound a ;
 (b) as a function of the Mach number, the mean-flow velocity U , and the skin friction coefficient, $C_f = 2 \tau_w / (\rho U^2)$. Page 34

- 1-30. Consider a hydraulic lift with a 50 cm diameter shaft sliding inside a housing with an inside diameter of 50.02 cm. If the shaft travels at 0.25 m/s, calculate the shaft resistance to motion per unit length. You may use water as the working fluid.

- 1-31. Consider a thin air gap of 1 mm that is formed between two parallel surfaces that are maintained at 20°C and 40°C, respectively. In the case of a quiescent medium (say

still air), calculate the heat transfer rate across the gap per unit area.

- 1-32.** In the presence of viscosity, the pressure drop associated with a fully developed laminar motion in a horizontal tube of length L and diameter D may be evaluated analytically. One finds:

$$\Delta p = p_1 - p_2 = \frac{128\mu L Q}{\pi D^4}$$

where μ stands for the dynamic viscosity and $Q = \frac{1}{4} \pi D^2 V$ denotes the volumetric flow rate. Show that the corresponding head loss may be written as

$$h_L \equiv \frac{p_1 - p_2}{\rho g} = f_{\text{lam}} \frac{L}{D} \frac{V^2}{2g}$$

What value of f_{lam} do you obtain?

- 1-33.** A time-dependent, two-dimensional motion has three velocity components that are given by

$$u = \frac{x}{1 + at} \quad v = \frac{y}{1 + bt} \quad w = 0$$

where a and b are pure constants. The objective of this problem is to compare and contrast the streamlines in this flow with the pathlines of the fluid particles.

- (a) Find the equations governing the streamline that passes through the point $(1, 1)$ at time t .
- (b) Calculate the path of a particle that starts at $\mathbf{r}_0 = (x_0, y_0) = (1, 1)$ at $t = 0$. Determine the location of a particle at $t = 1$, denoted as \mathbf{r}_1 .
- (c) Use the results of part (a) to determine the condition under which the streamlines and pathlines coincide.

- 1-34.** A tornado may be simulated as a two-part circulating flow in cylindrical coordinates, with $v_r = v_z = 0$,

$$v_\theta = \omega r \quad \text{if } r \leq R \quad \text{and} \quad v_\theta = \omega R^2 / r \quad \text{if } r \geq R$$

- (a) Calculate the divergence of the velocity. Is the flow compressible or incompressible?
- (b) Determine the vorticity. Is the flow rotational or irrotational?
- (c) Determine the strain rates in each segment of the flow. What is the sum of the three normal strain rates?

- 1-35.** In modeling the motion of an 8-meter diameter tornado rotating at an angular speed ω at the point of maximum swirl, it is possible to use the Maicke–Majdalani profile (Maicke and Majdalani 2009) as a piecewise approximation for which $v_r = v_z = 0$ and the tangential velocity is given by

$$v_\theta(r) = \begin{cases} 16\omega r[1 - \ln(r^2)]; & 0 < r \leq 1 \quad (\text{inner, forced vortex segment}) \\ \frac{16\omega}{r}; & r > 1 \quad (\text{outer, free vortex segment}) \end{cases}$$

- State whether the flow is 1D, 2D, or 3D, steady or unsteady, and specify $v_\theta(r)$ as $r \rightarrow \infty$.
- Calculate the divergence of the velocity. Is the flow compressible or incompressible?
- Determine the vorticity. Is the flow rotational or irrotational?
- Determine the strain rates and the shear stresses in the inner and outer flow segments.
- What is the limit of $v_\theta(r)$ as $r \rightarrow 0$? Hint: In taking the limit, it is helpful to remember that $(\ln u)' = u'/u$ and that, in the inner segment, the tangential velocity can be rewritten as

$$v_\theta = 16\omega \frac{[1 - \ln(r^2)]}{r^{-1}}$$

- 1-36.** The Taylor profile, which has been used to describe the bulk gaseous motion in planar, slab rocket chambers (Maicke and Majdalani 2008), corresponds to a self-similar profile in porous channels that bears symmetry with respect to the chamber's midsection plane. Using normalized Cartesian coordinates, the streamfunction may be written as $\psi = x \sin(\frac{1}{2}\pi y); 0 \leq y \leq 1, \quad 0 \leq x \leq l$, where l represents the aspect ratio of the chamber (i.e., the length of the porous surface normalized by the chamber half height). In this problem, the velocity vector, normalized by the wall injection speed, may be expressed as $\mathbf{V}(x, y) = u \mathbf{i} + v \mathbf{j}$.

- Determine the axial and normal velocity profiles using:

$$u = \frac{\partial \psi}{\partial y} \quad \text{and} \quad v = -\frac{\partial \psi}{\partial x}$$

- Evaluate the velocity divergence and determine whether the motion is compressible or incompressible.
- Evaluate the vorticity and determine whether the motion is rotational or irrotational.

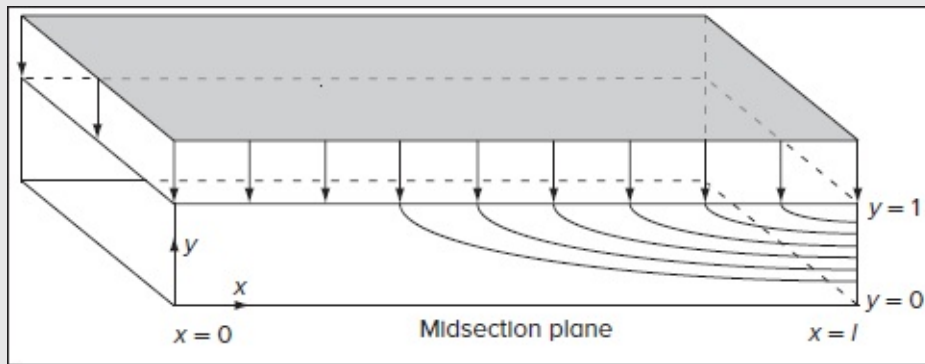


FIGURE P1.36

1-37. In the Taylor flow problem described above, determine the following:

- (a) The strain rates.
- (b) The Lagrangian time-dependent coordinates $x_j(t)$ and $y_j(t)$ for a particle j that enters the porous chamber at the sidewall where $y_j = 1$ and $x_j = X_j$ at $t = 0$. Recall that

$$\frac{dx_j}{dt} = u \quad \text{and} \quad \frac{dy_j}{dt} = v$$

- (c) The pathlines of a particle j entering the chamber at $X_j = 1, 2, 3, 4, 5$. Display your results in the (x, y) plane.

1-38. The Taylor–Culick profile, which describes the bulk gaseous motion in solid rocket motors (Culick 1966), corresponds to an axisymmetric, self-similar profile in porous tubes. Using normalized cylindrical coordinates, the streamfunction may be written as $\psi = z \sin(\frac{1}{2}\pi r^2)$; $0 \leq r \leq 1$, $0 \leq z \leq l$, where l represents the aspect ratio of the motor (i.e., the length of the porous surface normalized by the chamber radius). In this problem, the velocity vector, normalized by the wall injection speed, may be expressed as $\mathbf{V}(r, z) = v_r \mathbf{e}_r + v_z \mathbf{e}_z$.

- (a) Determine the axial and radial velocity profiles using Stokes' definition:

$$v_z = \frac{1}{r} \frac{\partial \psi}{\partial r} \quad \text{and} \quad v_r = -\frac{1}{r} \frac{\partial \psi}{\partial z}$$

- (b) Evaluate the velocity divergence and determine whether the motion is compressible or incompressible.
- (c) Evaluate the vorticity and determine whether the motion is

rotational or irrotational.

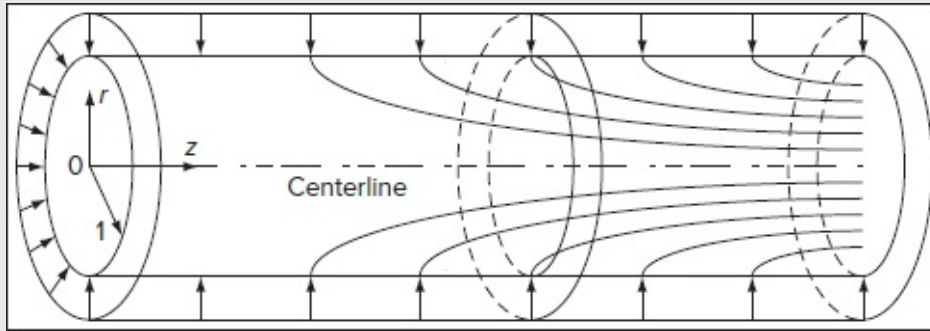


FIGURE P1.38

- 1-39.** In the Taylor–Culick flow problem described above, determine the following:
- The strain rates.
 - The Lagrangian time-dependent coordinates $r_j(t)$ and $z_j(t)$ for a particle j that enters the cylindrical rocket chamber at the sidewall where $r_j = 1$ and $z_j = Z_j$ at $t = 0$. Recall that

$$\frac{dr_j}{dt} = v_r \quad \text{and} \quad \frac{dz_j}{dt} = v_z$$

- The pathlines of a particle j entering the chamber at $Z_j = 1, 2, 3, 4, 5$. Display your results in the (r, z) plane.

- 1-40.** The Vyas–Majdalani profile, which describes the helical motion of a cyclonic chamber (Vyas and Majdalani 2006), consists of a three-component velocity profile, $\mathbf{V}(r, z) = v_r \mathbf{e}_r + v_\theta \mathbf{e}_\theta + v_z \mathbf{e}_z$, where

$$v_r = -\kappa U \frac{a}{r} \sin\left(\pi \frac{r^2}{a^2}\right) \quad v_\theta = \frac{a}{r} U \quad v_z = 2\pi\kappa U \frac{z}{a} \cos\left(\pi \frac{r^2}{a^2}\right); \quad \begin{cases} 0 \leq r \leq a \\ 0 \leq z \leq L \end{cases}$$

Here a denotes the radius of the cyclonic chamber, U stands for the average tangential velocity at $r = a$, and κ represents a dimensionless offset swirl parameter that gauges the relative importance of axial and tangential speeds.

- Is the flow one-dimensional, two-dimensional, or three-dimensional?
- Is the flow steady or unsteady?
- Calculate the divergence of the velocity. Is the flow compressible or

incompressible?

- (d) Determine the vorticity. Is the flow rotational or irrotational?
- (e) Determine the strain rates. What is the sum of the three normal strain rates?
- (f) Assuming a circular opening of radius $r = b = a/\sqrt{2}$ at $z = L$, calculate the volumetric flow rate by integrating the axial velocity from $r = 0$ to $r = a/\sqrt{2}$.

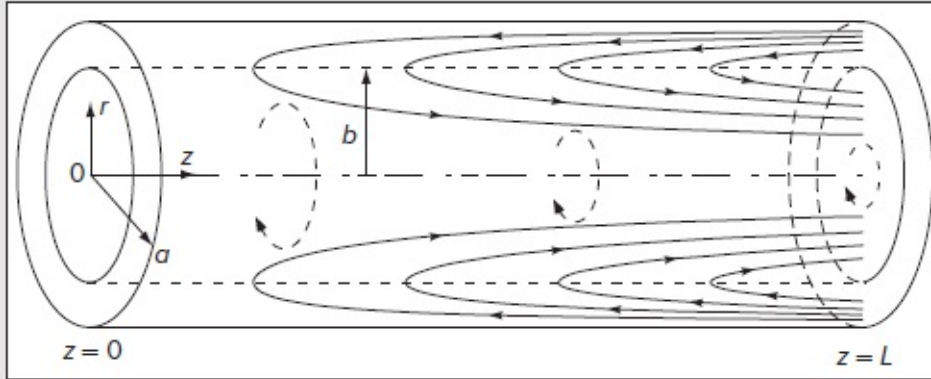


FIGURE P1.40

- 1-41.** The Maicke–Majdalani profile, which may be used to describe the motion of an unbounded tornado (Maicke and Majdalani 2009), can be expressed as a simple piecewise approximation for which $v_r = v_z = 0$ and

$$v_{\theta}(r) = \begin{cases} \frac{\omega r}{X^2} \left[1 - \ln \left(\frac{r^2}{X^2 R^2} \right) \right]; & r \leq XR \\ \frac{R^2 \omega}{r}; & r > XR \end{cases}$$

where R denotes the radius at which the wind's angular speed ω may be measured and X represents the fraction of the radius R where the free vortex behavior ceases.

- (a) Is this flow one-dimensional, two-dimensional, or three-dimensional?
- (b) Is this flow steady or unsteady?
- (c) Calculate the divergence of the velocity. Is the flow compressible or incompressible?
- (d) Determine the vorticity. Is the flow rotational or irrotational?
- (e) Determine the strain rates and the shear stresses in each segment of

the flow.

(f) What is the limiting value of $v_\theta(r)$ as $r \rightarrow 0$?

1-42. Assuming ϕ to be a scalar and \mathbf{V} a vector, evaluate the following quantities:

- (a) $\nabla \times \nabla \phi$
- (b) $(\nabla \phi) \times (\nabla \phi)$
- (c) $(\nabla \phi) \cdot (\nabla \phi)$
- (d) $\nabla \cdot (\nabla \phi)$
- (e) $\nabla \cdot (\nabla \times \mathbf{V})$

Page 37

1-43. Assuming \mathbf{U} , \mathbf{V} , and \mathbf{W} to be Cartesian vectors, prove the following identities:

- (a) $(\mathbf{V} \cdot \nabla)\mathbf{V} = \frac{1}{2}\nabla(\mathbf{V} \cdot \mathbf{V}) - \mathbf{V} \times (\nabla \times \mathbf{V})$ (Lamb's vector identity)
- (b) $\nabla \times (\nabla \times \mathbf{V}) = \nabla(\nabla \cdot \mathbf{V}) - \nabla^2 \mathbf{V}$
- (c) $\nabla \cdot (\mathbf{U} \times \mathbf{V}) = \mathbf{V} \cdot (\nabla \times \mathbf{U}) - \mathbf{U} \cdot (\nabla \times \mathbf{V})$
- (d) $(\mathbf{U} \times \mathbf{V}) \cdot \mathbf{W} = \mathbf{U} \cdot (\mathbf{V} \times \mathbf{W})$ (mixed vector scalar product)
- (e) $\mathbf{U} \times (\mathbf{V} \times \mathbf{W}) = (\mathbf{U} \cdot \mathbf{W})\mathbf{V} - (\mathbf{U} \cdot \mathbf{V})\mathbf{W}$ (vector triple product)
- (f) $(\mathbf{U} \times \mathbf{V}) \cdot (\mathbf{U} \times \mathbf{V}) = (\mathbf{U} \cdot \mathbf{U})(\mathbf{V} \cdot \mathbf{V}) - (\mathbf{U} \cdot \mathbf{V})(\mathbf{U} \cdot \mathbf{V})$ (Lagrange's identity)
- (g) $(\mathbf{U} - \mathbf{V}) \times (\mathbf{U} + \mathbf{V}) = 2\mathbf{U} \times \mathbf{V}$
- (h) $\nabla \cdot (\phi \mathbf{V}) = \phi \nabla \cdot \mathbf{V} + \mathbf{V} \cdot \nabla \phi$
- (i) $\nabla \times (\phi \mathbf{V}) = \phi \nabla \times \mathbf{V} + (\nabla \phi) \times \mathbf{V}$
- (j) $\nabla \cdot (\mathbf{U}\mathbf{V}) = (\nabla \cdot \mathbf{U})\mathbf{V} + \mathbf{U} \cdot (\nabla \mathbf{V})$

[†]Note, however, that flows involving chemical or nuclear reactions require an extended concept of equilibrium. Such flows typically involve knowledge of reaction rates and are not treated here.

[‡]A solid has *two* sound speeds: $(K/\rho)^{1/2}$ is the dilatation or longitudinal-wave speed, and $(G/\rho)^{1/2}$ is the rotational or shear-wave speed. Fluids have only one sound speed.

CHAPTER 2

FUNDAMENTAL EQUATIONS OF COMPRESSIBLE VISCOUS FLOW

The more we learn of science, the more we see that its wonderful mysteries are all explained by a few simple laws so connected together and so dependent upon each other, that we see the same mind animating them all.

Olympia Brown (1835–1906)

2-1 INTRODUCTION

THE EQUATIONS of viscous flow have been known for more than 100 years. In their complete form, these equations are difficult to solve, even on modern digital computers. In fact, at high Reynolds numbers (under turbulent-flow conditions), the equations are, in effect, *impossible* to solve with present mathematical techniques because the boundary conditions become randomly time dependent. Nevertheless, it is very instructive to derive and discuss these fundamental equations because they provide many insights, yield several particular solutions, and can be reduced according to several modeling laws. Moreover, these exact equations can be simplified, using Prandtl's boundary-layer approximations, as it will be later shown. The resulting simpler system is very practical and yields many fruitful engineering solutions.

2-2 CLASSIFICATION OF THE FUNDAMENTAL EQUATIONS

The basic equations considered here represent the three conservation principles for physical systems:

1. Conservation of mass (continuity).
2. Conservation of momentum (Newton's second law).
3. Conservation of energy (first law of thermodynamics).

The three unknowns that must be obtained simultaneously from these three basic equations are the velocity \mathbf{V} , the thermodynamic pressure p , and the absolute temperature T . We consider p and T to be the two required independent thermodynamic variables. However, the final forms of the conservation equations also contain four other thermodynamic variables: the density ρ , the enthalpy h (or the internal energy e), and the two transport properties μ and k . Using our tacit assumption of local thermodynamic equilibrium, the latter four properties are uniquely determined by the values of p and T . Thus, the system is completed by specifying four state relations

$$\rho = \rho(p, T) \quad h = h(p, T) \quad \mu = \mu(p, T) \quad k = k(p, T) \quad (2-1)$$

which can be provided in the form of tables, charts, or semi-theoretical formulas based on kinetic theory. Many useful analyses simply assume that ρ , μ , and k are constants and that h is proportional to T through $h = c_p T$.

Finally, to specify a particular problem completely, we must impose conditions on \mathbf{V} , p , and T at every point of the boundary of the flow regime.

The preceding considerations apply to a fluid of assumed uniform, homogeneous composition, i.e., where diffusion and chemical reactions are not considered. Multicomponent reacting fluids must consider at least two more relations:

4. Conservation of species.
5. Chemical reaction laws.

Additional relations that must be considered consist of the diffusion coefficient $D = D(p, T)$, chemical-equilibrium constants, reaction rates, and heats of formation. This text does not consider reacting boundary-layer flows [see Kee et al. (2003)].

Finally, even more relations are necessary if one considers the flow to be influenced by electromagnetic effects. This is the subject of the field of *magnetohydrodynamics*. Such effects are not considered in the present text either.

Instead, let us proceed to derive the three basic equations of a single-component fluid, bearing in mind that the results will also apply to uniform nonreacting mixtures, such as air or liquid solutions.[†]

2-3 CONSERVATION OF MASS: THE EQUATION OF CONTINUITY

As mentioned in the discussion of [Eq. \(1-5\)](#), all three conservation laws are Lagrangian in nature; i.e., they apply to a fixed system of particles. Thus, in the Eulerian system appropriate to fluid flow, our three laws rely on the particle derivative

$$\frac{D}{Dt} \equiv \frac{\partial}{\partial t} + (\mathbf{V} \cdot \nabla) \quad (1-8)$$

which is a formidable expression. In Lagrangian terms, the law of conservation of mass is surpassingly simple:

$$m = \rho \vartheta = \text{const} \quad (2-2)$$

where ϑ is the volume of a particle. In Eulerian terms, this is equivalent to

$$\frac{Dm}{Dt} = \frac{D}{Dt}(\rho \vartheta) = \rho \frac{D\vartheta}{Dt} + \vartheta \frac{D\rho}{Dt} = 0 \quad (2-3)$$

We can relate $D\vartheta/Dt$ to the fluid velocity by noting that the total dilatation or normal-strain rate is equal to the relative time rate of change of the volume of a particle:

$$\epsilon_{xx} + \epsilon_{yy} + \epsilon_{zz} = \frac{1}{\vartheta} \frac{D\vartheta}{Dt} \quad (2-4)$$

Further, we can substitute for the strain rates from our kinematic relations in [Eqs. \(1-21\)](#) to retrieve:

$$\epsilon_{xx} + \epsilon_{yy} + \epsilon_{zz} = \frac{\partial u}{\partial x} + \frac{\partial v}{\partial y} + \frac{\partial w}{\partial z} = \text{div } \mathbf{V} \equiv \nabla \cdot \mathbf{V} \quad (2-5)$$

Combining [Eqs. \(2-3\)](#) through [\(2-5\)](#) to eliminate ϑ , we obtain the equation for continuity in its most general form,

$$\frac{D\rho}{Dt} + \rho \nabla \cdot \mathbf{V} = 0 \quad \text{or} \quad \frac{\partial \rho}{\partial t} + \nabla \cdot (\rho \mathbf{V}) = 0 \quad (2-6)$$

If the fluid is incompressible, [Eq. \(2-6\)](#) reduces to the simpler condition for a solenoidal velocity, namely,

$$\nabla \cdot \mathbf{V} = 0 \quad (2-7)$$

which is equivalent to requiring that particles retain a constant volume.[‡] It may be instructive to note that although all constant density fluids are incompressible, the converse is not true. It is possible to have incompressible fluids with varying densities. A clear example is salt water which maintains a constant volume although its density varies with depth.

2-3.1 A Useful Strategy: The Stream Function

If the continuity [Eq. \(2-6\)](#) reduces to only two nonzero terms, it can be satisfied identically, and therefore replaced, by the so-called *stream function* ψ . The idea dates back to the French

mathematician Joseph-Louis Lagrange in 1755. The Cartesian incompressible-flow stream function is treated in detail in Sec. 2-11. Here, we illustrate its properties using a steady, two-dimensional compressible flow in the xy plane, for which the continuity equation reduces to

$$\frac{\partial}{\partial x}(\rho u) + \frac{\partial}{\partial y}(\rho v) = 0 \quad (2-8)$$

Page 40

If we now define the stream function ψ such that

$$\rho u = \frac{\partial \psi}{\partial y} \quad \text{and} \quad \rho v = -\frac{\partial \psi}{\partial x} \quad (2-9)$$

we see by direct substitution that [Eq. \(2-8\)](#) is satisfied identically, assuming of course that ψ is continuous to the second-order derivative. Thus, the continuity equation can be discarded and the number of dependent variables reduced by one. The penalty, however, is that the remaining velocity derivatives are increased by one order.

The stream function is not only useful but has physical significance:

$$d\psi = \frac{\partial \psi}{\partial x} dx + \frac{\partial \psi}{\partial y} dy = -\rho v dx + \rho u dy = \rho \mathbf{V} \cdot d\mathbf{A} \quad (2-10)$$

which means that a change in the stream function represents a change in the mass flow rate. Moreover, lines of constant ψ , along which $d\psi = 0$, represent lines across which there is no mass flow ($dm = 0$); that is, they are streamlines of the flow. Also, the difference between the values of ψ of any two streamlines is numerically equal to the mass flow between those streamlines.

2-4 CONSERVATION OF MOMENTUM: THE NAVIER-STOKES EQUATIONS

This relation, commonly known as Newton's second law, expresses a proportionality between an applied force and the resulting acceleration of a particle of mass m :

$$\mathbf{F} = m\mathbf{a} \quad (2-11)$$

where $\mathbf{a} = \mathbf{F}/m$ reminds us that the acceleration represents a force per unit mass. If the system is a fluid particle, it is convenient to divide [Eq. \(2-11\)](#) by the volume of the particle, so that the analysis is carried out in terms of the fluid density instead of the particle mass. It is also traditional to reverse the terms and place the acceleration on the left-hand side such that

$$\rho \frac{D\mathbf{V}}{Dt} = \mathbf{f} = \mathbf{f}_{\text{body}} + \mathbf{f}_{\text{surface}} \quad (2-12)$$

where \mathbf{f} is the applied force per unit volume on the fluid particle. Note that in our chosen

Eulerian system, the acceleration is the rather complicated particle derivative from [Eq. \(1-9\)](#) and \mathbf{f} is divided into two types: surface forces and body forces.

The so-called body forces are those that apply from a distance to the entire mass of the fluid element. Such forces are usually due to external fields such as gravity or an applied electromagnetic potential. We ignore magnetohydrodynamic effects here and consider only the gravitational body force per unit volume,

$$\mathbf{f}_{\text{body}} = \rho \mathbf{g} \quad (2-13)$$

where \mathbf{g} is the gravitational acceleration vector.

The surface forces are those applied by external stresses on the sides of the element. The quantity stress σ_{ij} is a tensor, just as the strain rate ϵ_{ij} in Sec. 1-3. The sign convention for stress components on a Cartesian element is shown in [Fig. 2-1](#), where all stresses are positive. The stress tensor, which comprises both viscous and surface pressure effects, can be written as

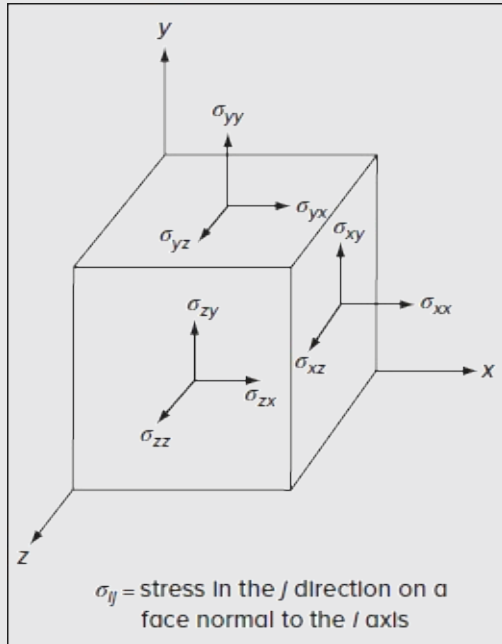


FIGURE 2-1

Notation for stresses.

$$\boldsymbol{\sigma} = \{\sigma_{ij}\} = \begin{pmatrix} \sigma_{xx} & \sigma_{xy} & \sigma_{xz} \\ \sigma_{yx} & \sigma_{yy} & \sigma_{yz} \\ \sigma_{zx} & \sigma_{zy} & \sigma_{zz} \end{pmatrix} = \begin{pmatrix} \tau_{xx} - p & \tau_{xy} & \tau_{xz} \\ \tau_{yx} & \tau_{yy} - p & \tau_{yz} \\ \tau_{zx} & \tau_{zy} & \tau_{zz} - p \end{pmatrix} = \{\tau_{ij}\} - p\{\delta_{ij}\} \quad (2-14)$$

where the viscous stress tensor may be represented by the nine components

$$\boldsymbol{\tau} = \{\tau_{ij}\} = \begin{pmatrix} \tau_{xx} & \tau_{xy} & \tau_{xz} \\ \tau_{yx} & \tau_{yy} & \tau_{yz} \\ \tau_{zx} & \tau_{zy} & \tau_{zz} \end{pmatrix}$$

and δ_{ij} stands for the Kronecker delta function ($\delta_{ij} = 1$ if $i = j$ and $\delta_{ij} = 0$ if $i \neq j$ as described in App. D). Note that, unlike the viscous stresses, the pressure can be exerted only normally to the surface of the fluid element. Following the strain rate ϵ_{ij} , σ_{ij} , and τ_{ij} form symmetric tensors such that $\sigma_{ij} = \sigma_{ji}$ and $\tau_{ij} = \tau_{ji}$; $i \neq j$. This symmetry is required to maintain the equilibrium of moments about the three axes of the element.⁸Page 41

The positions of the stresses in the array of [Eq. \(2-14\)](#) are not arbitrary; the rows correspond to applied forces in each coordinate direction. Considering the front faces of the element in [Fig. 2-1](#), the total force in each direction due to stress is

$$dF_x = \sigma_{xx} dy dz + \sigma_{yx} dx dz + \sigma_{zx} dx dy \quad (2-15)$$

$$dF_y = \sigma_{xy} dy dz + \sigma_{yy} dx dz + \sigma_{zy} dx dy$$

$$dF_z = \sigma_{xz} dy dz + \sigma_{yz} dx dz + \sigma_{zz} dx dy$$

For an element in equilibrium, these forces would be balanced by equal and opposite forces on the back faces of the element. If the element is accelerating, however, the front- and back-face stresses will be different by differential amounts. For example,

$$\sigma_{xx, \text{front}} = \sigma_{xx, \text{back}} + \frac{\partial \sigma_{xx}}{\partial x} dx \quad (2-16)$$

Hence, the *net* force on the element in the x direction, for example, will be due to three derivative terms:

$$dF_{x, \text{net}} = \left(\frac{\partial \sigma_{xx}}{\partial x} dx \right) dy dz + \left(\frac{\partial \sigma_{yx}}{\partial y} dy \right) dx dz + \left(\frac{\partial \sigma_{zx}}{\partial z} dz \right) dx dy$$

or, on a unit volume basis, dividing by $dx dy dz$, since $\sigma_{ij} = \sigma_{ji}$, we get

$$f_x = \frac{\partial \sigma_{xx}}{\partial x} + \frac{\partial \sigma_{xy}}{\partial y} + \frac{\partial \sigma_{xz}}{\partial z} \quad (2-17)$$

which we note is equivalent to taking the divergence of the vector $(\sigma_{xx}, \sigma_{xy}, \sigma_{xz})$. Similarly, f_y and f_z are the divergences of the second and third rows of σ_{ij} . Recalling that

$$\nabla \equiv \mathbf{i} \frac{\partial}{\partial x} + \mathbf{j} \frac{\partial}{\partial y} + \mathbf{k} \frac{\partial}{\partial z}$$

it may be seen that [Eq. \(2-17\)](#) is simply $ff_x = \nabla \cdot (\sigma_{xx} \mathbf{i} + \sigma_{xy} \mathbf{j} + \sigma_{xz} \mathbf{k})$. Along similar lines, the total vector surface force may be expressed as

$$\begin{cases} \mathbf{f}_{\text{sur}} = \nabla \cdot \boldsymbol{\sigma} & \text{(vector form)} \\ (\mathbf{f}_{\text{sur}})_i = \nabla_j \sigma_{ij} = \frac{\partial \sigma_{ij}}{\partial x_j} & \text{(indicial form)} \end{cases} \quad (2-18)$$

Page 42 where the divergence of σ_{ij} is to be interpreted in the tensor sense, so that the result is a vector.

Newton's law, [Eq. \(2-12\)](#), now becomes:

$$\begin{cases} \rho \frac{D\mathbf{V}}{Dt} = \rho \mathbf{g} + \nabla \cdot \boldsymbol{\sigma} = \rho \mathbf{g} + \nabla \cdot \boldsymbol{\tau} - \nabla p & \text{(vector form)} \\ \rho \frac{Du_i}{Dt} = \rho g_i + \nabla_j \sigma_{ij} = \rho g_i + \nabla_j (\tau_{ij} - \delta_{ij} p) = \rho g_i + \nabla_j \tau_{ij} - \nabla_i p & \text{(indicial form)} \end{cases} \quad (2-19)$$

and it remains only to express σ_{ij} in terms of the velocity \mathbf{V} . This is done by relating τ_{ij} to ϵ_{ij} through the assumption of some viscous deformation-rate law, e.g, for a Newtonian fluid.**

2-4.1 The Fluid at Rest: Hydrostatics

From the definition of a fluid (Sec. 1-3), viscous stresses vanish if the fluid is at rest. The velocity and shear stresses are zero, and the normal stresses become limited to the hydrostatic pressure contribution. Equation (2-19) reduces to the hydrostatic relation if $\mathbf{V} = 0$:

$$\begin{cases} \sigma_{xx} = \sigma_{yy} = \sigma_{zz} = -p & \text{or} & \sigma_{ij} = -p & \text{for} & i = j \\ \sigma_{xy} = \sigma_{xz} = \sigma_{yz} = 0 & \text{or} & \sigma_{ij} = 0 & \text{for} & i \neq j \end{cases} \quad \text{and so} \quad \begin{cases} \nabla p = \rho \mathbf{g} & \text{(vector form)} \\ \nabla_i p = \rho g_i & \text{(indicial form)} \end{cases} \quad (2-20)$$

If we take the z coordinate as up and assume ρ and g are constants, the pressure will vary linearly with z , according to $\delta p = -\rho g \delta z$. As such, pressure will increase downwardly and proportionately to the specific weight of the fluid, as covered in the *hydrostatics* subdiscipline, e.g., White (2016). Here, we must ensure that our dynamic momentum equation reduces to [Eq. \(2-20\)](#) when $\mathbf{V} = 0$.

2-4.2 Deformation Law for a Newtonian Fluid

By analogy with Hookean elasticity, the simplest assumption for the variation of viscous stress with strain rate is a linear law. These considerations were first made by Stokes (1845) and, as far as we know, the resulting deformation law is satisfied by all gases and most common fluids. Stokes' three postulates are

1. The fluid is continuous, and its stress tensor σ_{ij} is at most a linear function of the strain rates ϵ_{ij} .
2. The fluid is isotropic, i.e., its properties are independent of direction, and therefore the deformation law is independent of the coordinate axes in which it is expressed.
3. When the strain rates are zero, the deformation law must reduce to the hydrostatic

pressure condition, $\sigma_{ij} = -p\delta_{ij}$.

Note that the isotropic condition 2 requires that the principal stress axes be identical to the principal strain-rate axes. This makes the principal axes a convenient place to begin the deformation-law derivation. Let x_1, y_1 , and z_1 be the principal axes, where the shear stresses and shear strain rates vanish [see [Eq. \(1-24\)](#)]. With these axes, the deformation law could involve at most three linear coefficients, C_1, C_2 , and C_3 . For example,

$$\sigma_{11} = -p + C_1 \epsilon_{11} + C_2 \epsilon_{22} + C_3 \epsilon_{33} \quad (2-21)$$

The term $-p$ is added to satisfy the hydrostatic condition 3 above. But the isotropic condition 2 requires that the crossflow effect of ϵ_{22} and ϵ_{33} be identical, i.e., that $C_2 = C_3$. Therefore, there are really only *two* independent linear coefficients in an anisotropic Newtonian fluid. We can rewrite [Eq. \(2-21\)](#) in the simpler form

$$\sigma_{11} = -p + K\epsilon_{11} + C_2(\epsilon_{11} + \epsilon_{22} + \epsilon_{33}) \quad (2-22)$$

where $K = C_1 - C_2$, for convenience. Note also that $\epsilon_{11} + \epsilon_{22} + \epsilon_{33} = \nabla \cdot \mathbf{V}$ from [Eq. \(2-5\)](#).

Now let us transform [Eq. \(2-22\)](#) to some arbitrary axes x, y, z , where shear stresses are *not* zero, and thereby find an expression for the general deformation law. With respect to the principal axes x_1, y_1, z_1 , let the x axis have direction cosines l_1, m_1, n_1 , let the y axis have l_2, m_2, n_2 , and let the z axis have l_3, m_3, n_3 . Recall that $l_1^2 + m_1^2 + n_1^2 = 1$ for any set of direction cosines. Then, the transformation rule between a normal stress or strain rate in the new system and the principal stresses or strain rates is given by, for example,

$$\begin{aligned} \sigma_{xx} &= \sigma_{11}l_1^2 + \sigma_{22}m_1^2 + \sigma_{33}n_1^2 \\ \epsilon_{xx} &= \epsilon_{11}l_1^2 + \epsilon_{22}m_1^2 + \epsilon_{33}n_1^2 \end{aligned} \quad (2-23)$$

Similarly, the shear stresses (strain rates) may be related to the principal stresses (strain rates) by the following transformation law:

$$\begin{aligned} \sigma_{xy} &= \tau_{xy} = \sigma_{11}l_1l_2 + \sigma_{22}m_1m_2 + \sigma_{33}n_1n_2 \\ \epsilon_{xy} &= \epsilon_{11}l_1l_2 + \epsilon_{22}m_1m_2 + \epsilon_{33}n_1n_2 \end{aligned} \quad (2-24)$$

We can now eliminate $\sigma_{11}, \epsilon_{11}, \sigma_{22}$, etc., from [Eq. \(2-23\)](#) by using the principal-axis deformation law, [Eq. \(2-22\)](#), and the fact that $l_2 + m_2 + n_2 = 1$. The result is

$$\sigma_{xx} = -p + K\epsilon_{xx} + C_2\nabla \cdot \mathbf{V} \quad (2-25)$$

with exactly similar expressions for σ_{yy} and σ_{zz} . Similarly, we can eliminate $\sigma_{11}, \epsilon_{11}$, etc., from [Eq. \(2-24\)](#) to retrieve

$$\sigma_{xy} = \tau_{xy} = K\epsilon_{xy} \quad (2-26)$$

and precisely analogous expressions for σ_{xz} and σ_{yz} . Note that the direction cosines have all vanished systematically. Equations (2-25) and (2-26) are, in effect, the desired general deformation law. By comparing [Eq. \(2-26\)](#) and [Eq. \(1-30\)](#) for shear flow between parallel plates, we see that the linear coefficient K is equal to twice the ordinary coefficient of viscosity, $K = 2\mu$. The coefficient C_2 is new and independent of μ and may be called the *second coefficient of viscosity*. In linear elasticity, C_2 is called Lamé's constant and is given the symbol λ , which is also adopted here. Since λ is associated *only* with volume expansion, it is customary to call it the *coefficient of bulk viscosity*, λ .

Equations (2-25) and (2-26) can be combined and rewritten as a single general deformation law for a viscous Newtonian fluid. We get

$$\begin{cases} \boldsymbol{\sigma} = -p\boldsymbol{\delta} + \boldsymbol{\tau} = -p\boldsymbol{\delta} + \mu[\nabla\mathbf{V} + (\nabla\mathbf{V})^T] + \lambda\boldsymbol{\delta}\nabla\cdot\mathbf{V} & \text{(vector form)} \\ \sigma_{ij} = -p\delta_{ij} + \tau_{ij} = -p\delta_{ij} + \mu(\nabla_j u_i + \nabla_i u_j) + \lambda\delta_{ij}\nabla_k u_k = -p\delta_{ij} + \mu\left(\frac{\partial u_i}{\partial x_j} + \frac{\partial u_j}{\partial x_i}\right) + \lambda\delta_{ij}\frac{\partial u_k}{\partial x_k} & \text{(indicial form)} \end{cases} \quad (2-27)$$

where we have written ϵ_{ij} in terms of the velocity gradients from [Eq. \(1-27\)](#). This deformation law was first given by Stokes (1845) and assumes knowledge of the geometric rules for coordinate transformation of stresses and strain rates. The interested reader may refer to the textbooks on continuum mechanics by Lai et al. (1995), Malvern (1997), or Talpaert (2003). The scalar forms of τ_{ij} are provided in App. B for incompressible flow using both Cartesian and cylindrical coordinates.

2-4.3 Thermodynamic Pressure versus Mechanical Pressure

Stokes (1845) pointed out an interesting consequence of [Eq. \(2-27\)](#). By analogy with the strain relation [[Eqs. \(1-25\)](#)], the sum of the three normal stresses $\sigma_{xx} + \sigma_{yy} + \sigma_{zz}$ leads to an invariant tensor. In this context, the *mechanical pressure* \bar{p} is defined as the negative one-third of this sum, i.e., the average compression stress on the element. Then, by summing [Eq. \(2-27\)](#), we obtain

$$\bar{p} = -\frac{1}{3}(\sigma_{xx} + \sigma_{yy} + \sigma_{zz}) = p - \left(\lambda + \frac{1}{2}\mu\right)\nabla\cdot\mathbf{V} \quad (2-28)$$

where p represents the thermodynamic pressure. Thus, the mean pressure in a deforming viscous fluid is *not* equal to the thermodynamic property called pressure. This distinction is rarely important, since $\text{div } \mathbf{V}$ is usually very small in typical flow problems, but the precise meaning of [Eq. \(2-28\)](#) has been a controversial subject for more than a century. Stokes himself simply resolves the issue using an assumption that is as good as any other, namely, by setting

Stokes' hypothesis (1845): $\lambda + \frac{2}{3}\mu = 0$

Taking the second coefficient of viscosity to be $\lambda = -\frac{2}{3}\mu$ simply eliminates the discrepancy

between the mechanical and thermodynamic pressures. However, the available experimental evidence from the measurement of sound-wave attenuation, as reviewed by Karim and Rosenhead (1952), suggests that λ for most liquids is actually positive, rather than $-2\mu/3$, and is often much larger than μ . However, the experiments themselves have been a matter of some controversy [Truesdell (1954)].

A second type of flow condition will also make \bar{p} equal to p regardless of the value of λ , specifically

$$\text{Incompressible flow: } \nabla \cdot \mathbf{V} = 0 \quad \text{or} \quad \frac{\partial u_i}{\partial x_i} = 0$$

As such, the bulk viscosity cannot affect a truly incompressible fluid, but in fact, it *does* affect certain phenomena occurring in *nearly* incompressible fluids, e.g., sound absorption in liquids. Meanwhile, if $\nabla \cdot \mathbf{V} \neq 0$ (e.g., compressible flow), we may still avoid the problem if viscous normal stresses are negligible. This is the case in *boundary-layer flows* of compressible fluids, for which only the *first* coefficient of viscosity μ proves to be important. However, the normal shock wave problem represents a case where the coefficient λ cannot be neglected. The second such case is the previously mentioned problem of sound-wave absorption and attenuation.

It appears, then, that the second viscosity coefficient is still a controversial quantity. In fact, λ may not even be a thermodynamic property since it is apparently frequency dependent. Fortunately, the disputed term, $\lambda \nabla \cdot \mathbf{V}$, is typically so very small that the effect of λ may be ignored altogether. An interesting discussion of the second coefficient of viscosity may be found in Landau and Lifshitz (1959, Sec. 78) and Panton (1996).

2-4.4 The Navier–Stokes Equations

The desired momentum equation for a general linear (Newtonian) viscous fluid is obtained by substituting the stress relations, [Eq. \(2-27\)](#), into Newton's law [Eq. (2-19)]. The result is the famous equation of motion that bears the names of Navier and Stokes. In fact, this equation brackets the works of four scientists: Navier (1827), Poisson (1831), Saint Venant (1843), and Stokes (1845). In scalar form, we obtain

$$\rho \frac{Du}{Dt} = \rho g_x - \frac{\partial p}{\partial x} + \frac{\partial}{\partial x} \left(2\mu \frac{\partial u}{\partial x} + \lambda \nabla \cdot \mathbf{V} \right) + \frac{\partial}{\partial y} \left[\mu \left(\frac{\partial u}{\partial y} + \frac{\partial v}{\partial x} \right) \right] + \frac{\partial}{\partial z} \left[\mu \left(\frac{\partial w}{\partial x} + \frac{\partial u}{\partial z} \right) \right] \quad (2-28a)$$

$$\rho \frac{Dv}{Dt} = \rho g_y - \frac{\partial p}{\partial y} + \frac{\partial}{\partial x} \left[\mu \left(\frac{\partial v}{\partial x} + \frac{\partial u}{\partial y} \right) \right] + \frac{\partial}{\partial y} \left(2\mu \frac{\partial v}{\partial y} + \lambda \nabla \cdot \mathbf{V} \right) + \frac{\partial}{\partial z} \left[\mu \left(\frac{\partial v}{\partial z} + \frac{\partial w}{\partial y} \right) \right]$$

$$\rho \frac{Dw}{Dt} = \rho g_z - \frac{\partial p}{\partial z} + \frac{\partial}{\partial x} \left[\mu \left(\frac{\partial w}{\partial x} + \frac{\partial u}{\partial z} \right) \right] + \frac{\partial}{\partial y} \left[\mu \left(\frac{\partial v}{\partial z} + \frac{\partial w}{\partial y} \right) \right] + \frac{\partial}{\partial z} \left(2\mu \frac{\partial w}{\partial z} + \lambda \nabla \cdot \mathbf{V} \right)$$

These are the Navier–Stokes equations, fundamental to the subject of viscous fluid flow. Considerable economy is achieved by rewriting them as a single-vector equation, with and

without the indicial notation (App. D):

$$\begin{cases} \rho \frac{D\mathbf{V}}{Dt} = \rho \mathbf{g} - \nabla p + \nabla \cdot \{ \mu [\nabla \mathbf{V} + (\nabla \mathbf{V})^T] + \lambda \delta \nabla \cdot \mathbf{V} \} \\ \rho \frac{Du_i}{Dt} = \rho g_i - \nabla_i p + \nabla_j [\mu (\nabla_j u_i + \nabla_i u_j) + \lambda \delta_{ij} \nabla_k u_k] \end{cases} \quad (2-29b)$$

As usual, the indicial form may be further compacted into

$$\rho \frac{Du_i}{Dt} = \rho g_i - \frac{\partial p}{\partial x_i} + \frac{\partial}{\partial x_j} \left[\mu \left(\frac{\partial u_i}{\partial x_j} + \frac{\partial u_j}{\partial x_i} \right) + \lambda \delta_{ij} \frac{\partial u_k}{\partial x_k} \right]$$

2-4.5 Incompressible Flow: Thermal Decoupling

If the fluid is assumed to be of constant density, $\text{div } \mathbf{V}$ vanishes due to continuity [Eq. (2-7)], and the vexing bulk coefficient λ disappears from Newton's law. Equations (2-29a) and (2-29b) are not greatly simplified, though, if the first viscosity μ is still permitted to vary with temperature and pressure (and hence with position). If, however, we assume that μ is *spatially uniform*, many terms vanish, leaving us with a much simpler Navier–Stokes equation for *an incompressible fluid with constant viscosity*:

$$\rho \frac{D\mathbf{V}}{Dt} = \rho \mathbf{g} - \nabla p + \mu \nabla^2 \mathbf{V} \quad (2-30)$$

Most of the problems in this text correspond to incompressible flows that can be solved using Eqs. (2-7) and (2-30). Note that it is sufficient for ρ and μ to be constant for these equations to become independent of the temperature. One may then solve the continuity and momentum equations for the velocity and pressure, and later solve for the temperature from the thermally decoupled *energy equation* described in Sec. 2-5. This approximation often divides textbooks into those devoted to the discipline of “fluid mechanics” and those of “heat transfer.” Despite the main focus of the present text on fluid dynamical concepts, it will maintain a limited heat-transfer coverage throughout.

2-4.6 Steady Inviscid Flow: The Euler and Bernoulli Equations

If we further assume that viscous terms are negligible, Eq. (2-30) reduces to

$$\rho \frac{D\mathbf{V}}{Dt} \approx \rho \mathbf{g} - \nabla p \quad (2.30a)$$

This is called *Euler's equation* (derived by Leonhard Euler in 1755) for inviscid flow. It is first order in \mathbf{V} and p and thereby simpler than the second-order Navier–Stokes Eq. (2-30). In the absence of viscosity, the no-slip condition must be *relaxed* at a fixed wall, and the tangential velocity can be allowed to slip. Much research has been reported for Euler's equation: analytical (Currie 1993), numerical (Tannehill et al. 1997), and mathematical theorems (Kreiss and Lorenz 1989). As shown in several undergraduate texts (e.g., White

2016), Euler's equation for steady, incompressible, frictionless motion may be integrated along a streamline between any two points 1 and 2 to yield

$$\left(p + \frac{1}{2}\rho V^2 + \rho g z\right)_1 \approx \left(p + \frac{1}{2}\rho V^2 + \rho g z\right)_2 = \text{const} \quad (2.30b)$$

where z is vertical upward. This is *Bernoulli's equation* for steady frictionless flow. Though approximate, since all fluids are viscous, it has many applications in aeronautics and hydrodynamics and serves as an outer boundary matching condition in boundary-layer theory ([Chap. 4](#)). The unsteady form of Bernoulli's equation will be given in Sec. 2-10.

Bernoulli's equation stands at the basis of streamline analysis and can be rewritten in units of length, which is a more convenient form to use when analyzing problems with irreversible losses. The latter are often lumped into an energy head loss term, h_L , which reduces the total amount of energy left in the stream at the downstream location. Thus, going from point 1 to 2, one can write

$$\left(\frac{p}{\rho g} + \frac{1}{2g} V^2 + z\right)_1 \approx \left(\frac{p}{\rho g} + \frac{1}{2g} V^2 + z\right)_2 + h_L \quad (2.30c)$$

where the head loss may be determined using the procedures described in White (2016) and summarized in App. E on head loss calculations.

2-4.7 Steady Inviscid Axisymmetric Flow: The Bragg–Hawthorne Equation

In the treatment of steady, inviscid, and incompressible flow where the motion is axisymmetric, Euler's equation reduces to a compact, scalar, second-order partial differential equation in the stream function. Known as the Bragg–Hawthorne equation (Bragg and Hawthorne 1950), this relation represents the projection of Euler's steady-state equation along the axis of rotation.

$$\begin{cases} \nabla H \cdot d\mathbf{z} = \frac{\partial H}{\partial z} dz = \frac{dH}{d\psi} \frac{\partial \psi}{\partial z} dz & \text{and so} & \frac{dH}{d\psi} \frac{\partial \psi}{\partial z} = v_r \left(\frac{\partial v_r}{\partial z} - \frac{\partial v_z}{\partial r} \right) + v_\theta \frac{\partial v_\theta}{\partial z} \\ (\mathbf{V} \times \boldsymbol{\omega}) \cdot d\mathbf{z} = (v_r \omega_\theta - v_\theta \omega_r) dz \end{cases} \quad (2.30d)$$

At this stage, the incompressible Stokes stream function may be invoked to replace the radial and axial velocities, namely, by letting $rv_r \equiv -\partial\psi/\partial z$ and $rv_z \equiv \partial\psi/\partial r$. As for the tangential velocity v_θ , it may be expressed in terms of the angular momentum by recognizing that the tangential momentum equation for this axisymmetric case reduces to

$$v_r \frac{\partial(rv_\theta)}{\partial r} + v_z \frac{\partial(rv_\theta)}{\partial z} = 0 \quad \text{or} \quad \frac{D(rv_\theta)}{Dt} = 0$$

The requirement for a vanishing material derivative of the angular momentum enables us to write $rv_\theta = B(\psi)$, which must be conserved along a streamline. In fact, $2\pi B$, which represents the flow circulation, as well as the total head H , cannot change along a streamline. Forthwith,

backward substitution into Eq. (2-30d) leads to

$$\frac{dH}{d\psi} \frac{\partial \psi}{\partial z} = -\frac{1}{r} \frac{\partial \psi}{\partial z} \left[-\frac{1}{r} \frac{\partial^2 \psi}{\partial z^2} - \frac{\partial}{\partial r} \left(\frac{1}{r} \frac{\partial \psi}{\partial r} \right) \right] + \frac{B}{r} \frac{\partial}{\partial z} \left(\frac{B}{r} \right)$$

which may be readily rearranged and simplified into

$$\frac{\partial^2 \psi}{\partial r^2} - \frac{1}{r} \frac{\partial \psi}{\partial r} + \frac{\partial^2 \psi}{\partial z^2} = r^2 \frac{dH(\psi)}{d\psi} - B \frac{dB(\psi)}{d\psi}$$

This second-order partial differential equation in $\psi(r, z)$, also referred to as the Hicks equation (Hicks 1898) or the Long–Squire equation (Long 1953; Squire 1956), proves to be extraordinarily important in the treatment of axisymmetric and swirl-dominated flows, particularly, those arising in cyclone separators and wall-bounded vortex rocket engines (Bloor and Ingham 1987; Vyas and Majdalani 2006; Majdalani 2012; Maicke, Cecil, and Majdalani 2017). Although an equivalent form does not conveniently exist in Cartesian coordinates, a spherical analog with several important applications is available, as shown in App. F (e.g., Majdalani and Rienstra 2007; Barber and Majdalani 2017).

2-5 THE ENERGY EQUATION (FIRST LAW OF THERMODYNAMICS)

The first law of thermodynamics for a system states that the change in system energy is simply the sum of the work and heat added to the system:

$$dE_t = dQ + dW, \text{ where } Q = \text{heat added, and } W = \text{work done on the system} \quad (2-31)$$

The quantity E_t denotes the total energy of the system; hence, in a moving system, such as a flowing fluid particle, E_t will include not only the internal energy but also the kinetic and potential energies. Thus, for a fluid particle, the energy per unit volume is

$$E_t = \rho \left(e + \frac{1}{2} V^2 - \mathbf{g} \cdot \mathbf{r} \right) \quad (2-32)$$

where e = internal energy per unit mass

\mathbf{r} = particle displacement or position vector

\mathbf{g} = gravitational acceleration vector

Just as in conservation of mass and momentum, the energy equation for a fluid may be conveniently written as a time rate of change, following the particle. Thus, [Eq. \(2-31\)](#) becomes

$$\frac{DE_t}{Dt} = \frac{DQ}{Dt} + \frac{DW}{Dt} \quad \text{where} \quad \frac{D(\phi)}{Dt} \equiv \left[\frac{\partial}{\partial t} + (\mathbf{V} \cdot \nabla) \right] \phi = \frac{\partial \phi}{\partial t} + (\mathbf{V} \cdot \nabla) \phi \quad (2-33)$$

From [Eq. \(2-32\)](#), we then have

$$\frac{DE_t}{Dt} = \rho \left(\frac{De}{Dt} + \frac{1}{2} \frac{DV^2}{Dt} - \mathbf{g} \cdot \frac{D\mathbf{r}}{Dt} \right) = \rho \left(\frac{De}{Dt} + V \frac{DV}{Dt} - \mathbf{g} \cdot \mathbf{V} \right) \quad (2-34)$$

It remains to express Q and W in terms of fluid properties.

It is assumed that the heat transfer Q to the element is given by Fourier's law. From [Eq. \(1-35\)](#), the heat flow per unit area is given by the vector

$$\mathbf{q} = -k\nabla T \quad (1-35)$$

Referring to [Fig. 2-2](#), the heat flow into the left face of the element is $q_x dy dz$, while the heat flow out of the right face is

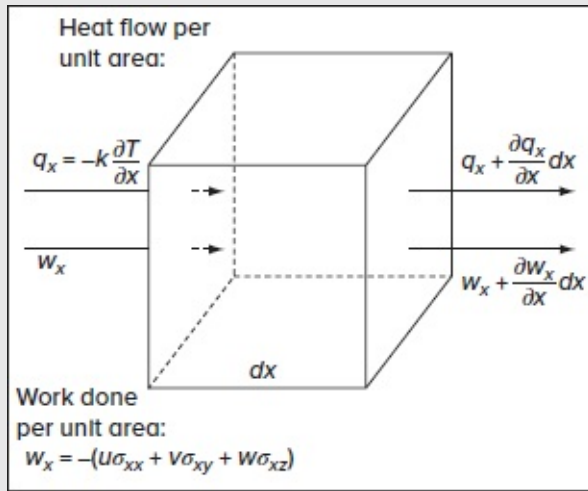


FIGURE 2-2

Heat and work exchange on the left and right sides of an element.

$$\left(q_x + \frac{\partial q_x}{\partial x} dx \right) dy dz$$

Page 47A similar situation holds for the upper and lower faces involving q_y , and the front and rear faces involving q_z . In each case, the net heat flow is out of the element. Hence, the net heat transferred to the element is

$$-\left(\frac{\partial q_x}{\partial x} + \frac{\partial q_y}{\partial y} + \frac{\partial q_z}{\partial z} \right) dx dy dz$$

Dividing by the element volume $dx dy dz$, we have the desired expression for the heat-transfer term neglecting internal heat generation:

$$\frac{DQ}{Dt} = -\nabla \cdot \mathbf{q} = \nabla \cdot (k\nabla T) \quad (2-35)$$

Referring again to [Fig. 2-2](#), the rate of work done to the element per unit area on the left face is $w_x = -(u\sigma_{xx} + v\sigma_{xy} + w\sigma_{xz})$, and the rate of work done by the right-face stresses is

$$-w_x - \frac{\partial w_x}{\partial x} dx \quad \text{per unit area}$$

Again, the other faces are similar. In just the same fashion as the heat transfer, then, the net rate of work done on the element may be determined from

$$\frac{DW}{Dt} = -\nabla \cdot \mathbf{w} = \frac{\partial}{\partial x} (u\sigma_{xx} + v\sigma_{xy} + w\sigma_{xz}) + \frac{\partial}{\partial y} (u\sigma_{yx} + v\sigma_{yy} + w\sigma_{yz}) + \frac{\partial}{\partial z} (u\sigma_{zx} + v\sigma_{zy} + w\sigma_{zz}) \quad (2-36)$$

Using the indicial notation (App. E), this becomes, very simply,

$$\frac{DW}{Dt} = \nabla \cdot (\mathbf{V} \cdot \boldsymbol{\sigma}) = \nabla_j (u_i \sigma_{ij}) \quad (2-37)$$

The ensuing expression can be further decomposed in a very convenient fashion into

$$\begin{cases} \nabla \cdot (\mathbf{V} \cdot \boldsymbol{\sigma}) = \mathbf{V} \cdot (\nabla \cdot \boldsymbol{\sigma}) + \boldsymbol{\sigma} : \nabla \mathbf{V} \\ \nabla_j (u_i \sigma_{ij}) = u_i (\nabla_j \sigma_{ij}) + \sigma_{ij} \nabla_j u_i \end{cases} \quad \text{and so} \quad \frac{\partial (u_i \sigma_{ij})}{\partial x_j} = u_i \frac{\partial \sigma_{ij}}{\partial x_j} + \sigma_{ij} \frac{\partial u_i}{\partial x_j} \quad (2-38)$$

where the “:” symbol is termed *double contraction* or *double-dot product* and has the property $\mathbf{A} : \mathbf{B} = \{a_{ij}b_{ji}\}$. At this point, the divergence of the stress tensor may be directly related to the momentum equation via

$$\nabla \cdot \boldsymbol{\sigma} = \rho \left(\frac{D\mathbf{V}}{Dt} - \mathbf{g} \right) \quad (2-19)$$

Hence, after some vector algebra,^{††} we get

$$\mathbf{V} \cdot (\nabla \cdot \boldsymbol{\sigma}) = \rho \left(\mathbf{V} \cdot \frac{D\mathbf{V}}{Dt} - \mathbf{V} \cdot \mathbf{g} \right) = \rho \left\{ \mathbf{V} \cdot \frac{\partial \mathbf{V}}{\partial t} + \mathbf{V} \cdot [(\mathbf{V} \cdot \nabla) \mathbf{V}] - \mathbf{g} \cdot \mathbf{V} \right\} = \rho \left(\mathbf{V} \cdot \frac{D\mathbf{V}}{Dt} - \mathbf{g} \cdot \mathbf{V} \right) \quad (2-39)$$

$$\begin{aligned} \overline{\dagger\dagger \rho \left\{ \mathbf{V} \cdot \frac{\partial \mathbf{V}}{\partial t} + \mathbf{V} \cdot [(\mathbf{V} \cdot \nabla) \mathbf{V}] - \mathbf{g} \cdot \mathbf{V} \right\}} &= \rho \left\{ \mathbf{V} \cdot \frac{\partial \mathbf{V}}{\partial t} + \mathbf{V} \cdot \left[\frac{1}{2} \nabla (\mathbf{V} \cdot \mathbf{V}) + (\mathbf{V} \times \mathbf{V}) \times \mathbf{V} \right] - \mathbf{g} \cdot \mathbf{V} \right\} \\ &= \rho \left[\frac{1}{2} \left(\mathbf{V} \cdot \frac{\partial \mathbf{V}}{\partial t} + \frac{\partial \mathbf{V}}{\partial t} \cdot \mathbf{V} \right) + \frac{1}{2} \mathbf{V} \cdot \nabla (\mathbf{V} \cdot \mathbf{V}) - \mathbf{g} \cdot \mathbf{V} \right] = \rho \left[\frac{1}{2} \frac{\partial (\mathbf{V} \cdot \mathbf{V})}{\partial t} + \frac{1}{2} \mathbf{V} \cdot \nabla V^2 - \mathbf{g} \cdot \mathbf{V} \right] = \rho \left(\frac{1}{2} \frac{DV^2}{Dt} - \mathbf{g} \cdot \mathbf{V} \right) \end{aligned}$$

Page 48 which are exactly the kinetic- and potential-energy terms in [Eq. \(2-34\)](#). Thus, the kinetic and potential energies vanish when we substitute for E_t , Q , and W in [Eq. \(2-33\)](#) from [Eqs. \(2-34\)](#), [\(2-35\)](#), and [\(2-38\)](#):

$$\rho \frac{De}{Dt} = \nabla \cdot (k\nabla T) + \boldsymbol{\sigma} : \nabla \mathbf{V} \quad \text{or} \quad \rho \frac{De}{Dt} = \frac{\partial}{\partial x_j} \left(k \frac{\partial T}{\partial x_j} \right) + \sigma_{ij} \frac{\partial u_i}{\partial x_j} \quad (2-40)$$

This is a widely used form of the first law of thermodynamics for fluid motion. If we split the stress tensor into pressure and viscous terms, using [Eq. \(2-27\)](#), we have

$$\boldsymbol{\sigma} : \nabla \mathbf{V} = \boldsymbol{\tau} : \nabla \mathbf{V} - p \nabla \cdot \mathbf{V} \quad \text{or} \quad \sigma_{ij} \frac{\partial u_i}{\partial x_j} = \tau_{ij} \frac{\partial u_i}{\partial x_j} - p \frac{\partial u_k}{\partial x_k} \quad (2-41)$$

From the equation of continuity [Eq. (2-6)], we have

$$p \nabla \cdot \mathbf{V} = -\frac{p}{\rho} \frac{D\rho}{Dt} = \rho \frac{D}{Dt} \left(\frac{p}{\rho} \right) - \frac{Dp}{Dt} \quad (2-42)$$

Combining Eqs. (2-40) to (2-42) gives

$$\begin{cases} \rho \frac{D}{Dt} \left(e + \frac{p}{\rho} \right) = \frac{Dp}{Dt} + \nabla \cdot (k \nabla T) + \boldsymbol{\tau} : \nabla \mathbf{V} \\ \rho \frac{D}{Dt} \left(e + \frac{p}{\rho} \right) = \frac{Dp}{Dt} + \frac{\partial}{\partial x_j} \left(k \frac{\partial T}{\partial x_j} \right) + \tau_{ij} \frac{\partial u_i}{\partial x_j} \end{cases} \quad \text{or} \quad \begin{cases} \rho \frac{Dh}{Dt} = \frac{Dp}{Dt} + \nabla \cdot (k \nabla T) + \boldsymbol{\tau} : \nabla \mathbf{V} \\ \rho \frac{Dh}{Dt} = \frac{Dp}{Dt} + \frac{\partial}{\partial x_j} \left(k \frac{\partial T}{\partial x_j} \right) + \tau_{ij} \frac{\partial u_i}{\partial x_j} \end{cases} \quad (2-43)$$

The final expression consolidates the internal and pressure energies into the fluid enthalpy,

$$h = e + p/\rho \quad (2-44)$$

Generally, enthalpy will prove to be a more useful function than internal energy, particularly in boundary-layer flows. Furthermore, the pressure term Dp/Dt may often be neglected in Eq. (2-43), while the related term $p \nabla \cdot \mathbf{V}$ in Eq. (2-40) will be nonnegligible for the same flow.

The last term in Eq. (2-43), involving viscous stresses, is customarily called the *dissipation function* Φ :

$$\Phi = \tau_{ij} \frac{\partial u_i}{\partial x_j} \quad (2-45)$$

The term Φ is always positive definite, in accordance with the second law of thermodynamics, since viscosity cannot add energy to the system. For a Newtonian fluid, using τ from Eq. (2-27), we obtain

$$\Phi = \mu \left[2 \left(\frac{\partial u}{\partial x} \right)^2 + 2 \left(\frac{\partial v}{\partial y} \right)^2 + 2 \left(\frac{\partial w}{\partial z} \right)^2 + \left(\frac{\partial v}{\partial x} + \frac{\partial u}{\partial y} \right)^2 + \left(\frac{\partial w}{\partial y} + \frac{\partial v}{\partial z} \right)^2 + \left(\frac{\partial u}{\partial z} + \frac{\partial w}{\partial x} \right)^2 \right] + \lambda \left(\frac{\partial u}{\partial x} + \frac{\partial v}{\partial y} + \frac{\partial w}{\partial z} \right)^2 \quad (2-46)$$

which is always positive since all the terms are quadratic. On the other hand, λ may actually be negative, e.g., Stokes' hypothesis with $\lambda = -\frac{2}{3}\mu$. It is an interesting exercise, using Eq. (2-46), to prove that the correct conditions in which Φ may not be negative are

$$\mu \geq 0 \quad \text{and} \quad 3\lambda + 2\mu \geq 0 \quad (2-47)$$

Using this short notation, the energy relation (2-43) takes the final form

$$\rho \frac{Dh}{Dt} = \frac{Dp}{Dt} + \nabla \cdot (k \nabla T) + \Phi \quad (2-48)$$

where Φ is given by Eq. (2-46).

2-5.1 The Incompressible-Flow Approximation

From the thermodynamic identity (1-77), we can rewrite [Eq. \(2-48\)](#) as

$$\rho c_p \frac{DT}{Dt} = \beta T \frac{Dp}{Dt} + \nabla \cdot (k \nabla T) + \Phi \quad (2-49)$$

Now, if the flow velocity scale U becomes smaller, while heat transfer remains important, the fluid kinetic energy U^2 will eventually become much smaller than the enthalpy change $c_p \Delta T$. Since both Dp/Dt and Φ are of order U^2 , the limit of low-velocity or *incompressible* flow will be

$$\rho c_p \frac{DT}{Dt} \approx \nabla \cdot (k \nabla T) \quad (2-50)$$

If we further assume uniform thermal conductivity, we obtain the more familiar incompressible heat-convection equation:

$$\rho c_p \frac{DT}{Dt} \approx k \nabla^2 T \quad (2-51)$$

Note that the correct specific heat is c_p , not c_v , even in the incompressible-flow limit of near-zero Mach number. A very good discussion of this point is given in Panton (1996, Sec. 10.9).

2-5.2 Summary of the Basic Equations

To summarize, the three basic laws of conservation of mass, momentum, and energy have been adapted for use in fluid motion. They are, respectively,

$$\frac{\partial \rho}{\partial t} + \nabla \cdot (\rho \mathbf{V}) = 0 \quad (2-6)$$

$$\rho \frac{D\mathbf{V}}{Dt} = \rho \mathbf{g} - \nabla p + \nabla \cdot \boldsymbol{\tau} \quad (2-19)$$

$$\rho \frac{Dh}{Dt} = \frac{Dp}{Dt} + \nabla \cdot (k \nabla T) + \boldsymbol{\tau} : \nabla \mathbf{V} \quad (2-48)$$

where $\boldsymbol{\tau} : \nabla \mathbf{V} = \nabla \cdot (\mathbf{V} \cdot \boldsymbol{\tau}) - \mathbf{V} \cdot (\nabla \cdot \boldsymbol{\tau})$ and, for a linear (Newtonian) fluid, the viscous stresses are

$$\begin{cases} \boldsymbol{\tau} = \mu [\nabla \mathbf{V} + (\nabla \mathbf{V})^T] + \lambda \delta \nabla \cdot \mathbf{V} \\ \tau_{ij} = \mu (\nabla_j u_i + \nabla_i u_j) + \lambda \delta_{ij} \nabla_k u_k = \mu \left(\frac{\partial u_i}{\partial x_j} + \frac{\partial u_j}{\partial x_i} \right) + \lambda \delta_{ij} \frac{\partial u_k}{\partial x_k} \end{cases} \quad (2-27)$$

As mentioned in the beginning of this chapter, [Eqs. \(2-6\)](#), [\(2-19\)](#), and [\(2-48\)](#) involve seven variables, of which three are assumed to be primary: p , \mathbf{V} , and T (say). The remaining four variables are assumed known from auxiliary relations and data of the form

$$\rho = \rho(p, T) \quad \mu = \mu(p, T) \quad h = h(p, T) \quad k = k(p, T)$$

Finally, we note that these relations are fairly general and involve only a few restrictive assumptions: (1) the fluid forms a (mathematical) continuum, (2) the particles are essentially in thermodynamic equilibrium, (3) the only effective body forces are due to gravity, (4) the heat conduction follows Fourier's law, and (5) there are no internal heat sources.

2-6 BOUNDARY CONDITIONS FOR VISCOUS HEAT-CONDUCTING FLOW

The various types of boundary conditions have been discussed in detail in Sec. 1-4 for the three different basic boundaries: (1) a fluid–solid interface, (2) a fluid–fluid interface, and (3) an inlet or exit section. These various types of conditions are sketched in [Fig. 2-3](#). The general results are that, for the majority of viscous-flow analyses, the following conditions must be imposed:

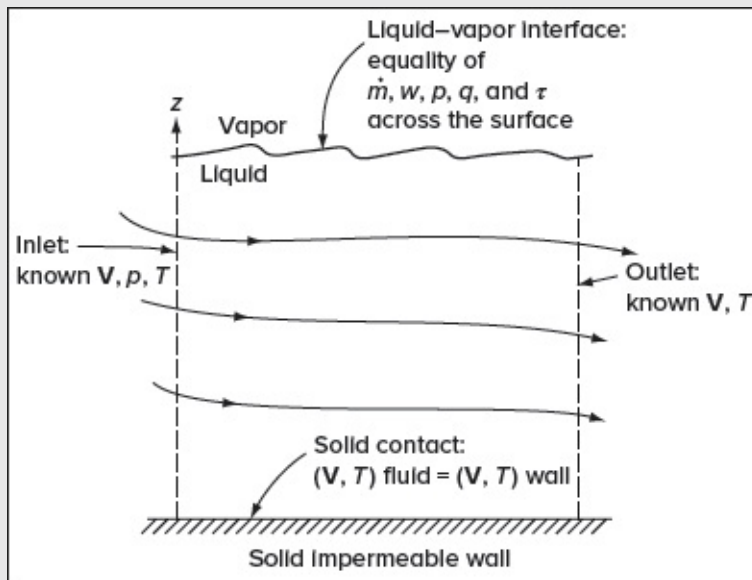


FIGURE 2-3

Various boundary conditions in fluid flow.

1. At a fluid–solid interface, there must be no slip

$$\mathbf{V}_{\text{fluid}} = \mathbf{V}_{\text{sol}} \quad (2-52)$$

and either no temperature jump (when the wall temperature is known)

$$T_{\text{fluid}} = T_{\text{sol}} \quad (2-53)$$

or equality of heat flux in the normal direction n to the surface (when the solid heat flux

is known)

$$\left(k \frac{\partial T}{\partial n}\right)_{\text{fluid}} = q \text{ (from solid to fluid)} \quad (2-54)$$

2. At the interface between a liquid and a gaseous substance, such as the standard atmosphere, there must be kinematic equivalence in the normal direction to the interface

$$V_{n, \text{liq}} \approx \dot{\eta} \quad (2-55)$$

Page 50

where η is the surface coordinate, and there must be equality of normal momentum flux

$$p_{\text{liq}} \approx p_{\text{gas}} \quad (2-56)$$

We must also have equality of tangential shear stress and normal heat flux at the interface, which translate into

$$\left.\frac{\partial V_t}{\partial n}\right|_{\text{liq}} = \frac{\mu_{\text{gas}}}{\mu_{\text{liq}}} \left.\frac{\partial V_t}{\partial n}\right|_{\text{gas}} \approx 0 \quad \text{and} \quad \left.\frac{\partial T}{\partial n}\right|_{\text{liq}} = \frac{k_{\text{gas}}}{k_{\text{liq}}} \left.\frac{\partial T}{\partial n}\right|_{\text{gas}} \approx 0 \quad (2-57)$$

where V_t is the tangential velocity component parallel to the direction of shear. These simplifications occur when the gaseous substance has negligibly small transport coefficients relative to those of the liquid. Also, in some problems, such as the analysis of confused, stormy seas, we need to know the moisture evaporation rate m' at the interface.

3. At any inlet section of the flow, we need the three quantities \mathbf{V} , p , and T at every point on the boundary. At the exit section, we generally need to know \mathbf{V} and T , but not the pressure p . Exit conditions are difficult because of the formation of wakes and other a priori unknown outflow behavior. One approximation is to let the streamwise flow gradients vanish far downstream of the flow field of interest.

Note: If the pressure can be eliminated, as, for example, with the vorticity/stream-function approach to be discussed in Sec. 2-11, then there is no need to impose a pressure boundary condition. The computer-oriented *vortex methods*, explained in the monograph by Cottet and Koumoutsakos (1999), do not compute the pressure at all.

2-7 ORTHOGONAL COORDINATE SYSTEMS

Most of the previous discussion has been illustrated by Cartesian coordinates, and only lip service has been paid to other important orthogonal systems. The basic equations of motion, [Eqs. \(2-6\)](#), [\(2-19\)](#), and [\(2-48\)](#) are, of course, valid for any coordinate system when written in tensor form; the problem for non-Cartesian systems is to derive the correct formula for the gradient vector ∇ plus the related expressions for divergence and curl. A straightforward

procedure is to use the metric *stretching factors* h_i to relate the new curvilinear coordinates to a Cartesian system, as discussed in standard mathematical references, e.g., Pipes (1958). Let the general curvilinear system (x_1, x_2, x_3) be related to a Cartesian system (x, y, z) so that the element of arc length ds is given by

$$(ds)^2 = (dx)^2 + (dy)^2 + (dz)^2 = (h_1 dx_1)^2 + (h_2 dx_2)^2 + (h_3 dx_3)^2 \quad (2-58)$$

which defines the factors h_i . Note that the h_i stretching factors in general will be functions of the new coordinates x_i . Then, in the new system, the components of the gradient of a scalar ϕ are

$$\frac{1}{h_1} \frac{\partial \phi}{\partial x_1} \quad \frac{1}{h_2} \frac{\partial \phi}{\partial x_2} \quad \frac{1}{h_3} \frac{\partial \phi}{\partial x_3} \quad (2-59)$$

The divergence of any vector $\mathbf{A} = (A_1, A_2, A_3)$ may be reconstructed from

$$\nabla \cdot \mathbf{A} = \frac{1}{h_1 h_2 h_3} \left[\frac{\partial}{\partial x_1} (h_2 h_3 A_1) + \frac{\partial}{\partial x_2} (h_3 h_1 A_2) + \frac{\partial}{\partial x_3} (h_1 h_2 A_3) \right] \quad (2-60)$$

Page 51

and the spatial components of the vector $\mathbf{B} = \nabla \times \mathbf{A}$ may be obtained from

$$B_1 = \frac{1}{h_2 h_3} \left[\frac{\partial}{\partial x_2} (h_3 A_3) - \frac{\partial}{\partial x_3} (h_2 A_2) \right] \quad (2-61)$$

with exactly similar expressions for B_2 and B_3 . Equations (2-59) to (2-61) are sufficient to derive the equations of motion in the new coordinate system x_i . We illustrate with the two classic (and probably most important) systems, cylindrical and spherical.

2-7.1 Cartesian Coordinates

Just to review our previous results, let $x_i = (x, y, z)$, from which $h_i = (1, 1, 1)$. If $\mathbf{V} = (u, v, w)$, the vector operations are

$$\begin{aligned}
\nabla \phi &= \left(\frac{\partial \phi}{\partial x}, \frac{\partial \phi}{\partial y}, \frac{\partial \phi}{\partial z} \right) \\
\nabla^2 \phi &= \frac{\partial^2 \phi}{\partial x^2} + \frac{\partial^2 \phi}{\partial y^2} + \frac{\partial^2 \phi}{\partial z^2} \\
\nabla \cdot \mathbf{V} &= \frac{\partial u}{\partial x} + \frac{\partial v}{\partial y} + \frac{\partial w}{\partial z} \\
\mathbf{V} \cdot \nabla &= u \frac{\partial}{\partial x} + v \frac{\partial}{\partial y} + w \frac{\partial}{\partial z} \\
\nabla \times \mathbf{V} &= \left(\frac{\partial w}{\partial y} - \frac{\partial v}{\partial z}, \frac{\partial u}{\partial z} - \frac{\partial w}{\partial x}, \frac{\partial v}{\partial x} - \frac{\partial u}{\partial y} \right) \\
\boldsymbol{\tau} : \nabla \mathbf{V} &= \tau_{xx} \frac{\partial u}{\partial x} + \tau_{xy} \frac{\partial u}{\partial y} + \tau_{xz} \frac{\partial u}{\partial z} + \tau_{yx} \frac{\partial v}{\partial x} + \tau_{yy} \frac{\partial v}{\partial y} + \tau_{yz} \frac{\partial v}{\partial z} + \tau_{zx} \frac{\partial w}{\partial x} + \tau_{zy} \frac{\partial w}{\partial y} + \tau_{zz} \frac{\partial w}{\partial z}
\end{aligned} \tag{2-62}$$

2-7.2 Cylindrical Polar Coordinates

These radial, azimuthal, and axial (or vertical) coordinates (r, θ, z) are related to the Cartesian system (x, y, z) by

$$x = r \cos \theta \quad y = r \sin \theta \quad z = z \tag{2-63}$$

Page 52

from which we find that $h_1 = 1$, $h_2 = r$, and $h_3 = 1$. Let the cylindrical polar velocity components be (v_r, v_θ, v_z) . Then, the new vector relations are

$$\begin{aligned}
\nabla \phi &= \left(\frac{\partial \phi}{\partial r}, \frac{1}{r} \frac{\partial \phi}{\partial \theta}, \frac{\partial \phi}{\partial z} \right) \\
\nabla^2 \phi &= \frac{1}{r} \frac{\partial}{\partial r} \left(r \frac{\partial \phi}{\partial r} \right) + \frac{1}{r^2} \frac{\partial^2 \phi}{\partial \theta^2} + \frac{\partial^2 \phi}{\partial z^2} \\
\nabla \cdot \mathbf{V} &= \frac{1}{r} \frac{\partial}{\partial r} (r v_r) + \frac{1}{r} \frac{\partial v_\theta}{\partial \theta} + \frac{\partial v_z}{\partial z} \\
\mathbf{V} \cdot \nabla &= v_r \frac{\partial}{\partial r} + \frac{v_\theta}{r} \frac{\partial}{\partial \theta} + v_z \frac{\partial}{\partial z} \\
\nabla \times \mathbf{V} &= \left(\frac{1}{r} \frac{\partial v_z}{\partial \theta} - \frac{\partial v_\theta}{\partial z}, \frac{\partial v_r}{\partial z} - \frac{\partial v_z}{\partial r}, \frac{1}{r} \left[\frac{\partial (r v_\theta)}{\partial r} - \frac{\partial v_r}{\partial \theta} \right] \right) \\
\boldsymbol{\tau} : \nabla \mathbf{V} &= \tau_{rr} \frac{\partial v_r}{\partial r} + \tau_{r\theta} \left(\frac{1}{r} \frac{\partial v_r}{\partial \theta} - \frac{v_\theta}{r} \right) + \tau_{rz} \frac{\partial v_r}{\partial z} + \tau_{\theta r} \frac{\partial v_\theta}{\partial r} + \tau_{\theta\theta} \left(\frac{1}{r} \frac{\partial v_\theta}{\partial \theta} + \frac{v_r}{r} \right) + \tau_{\theta z} \frac{\partial v_\theta}{\partial z} + \tau_{zr} \frac{\partial v_z}{\partial r} + \tau_{z\theta} \frac{1}{r} \frac{\partial v_z}{\partial \theta} + \tau_{zz} \frac{\partial v_z}{\partial z}
\end{aligned} \tag{2-64}$$

2-7.3 Spherical Polar Coordinates

As clarified in [Fig. 2-4](#), the spherical polar coordinates (r, φ, θ) , which stand for radial, polar, and azimuthal variables, respectively, are defined by the relations

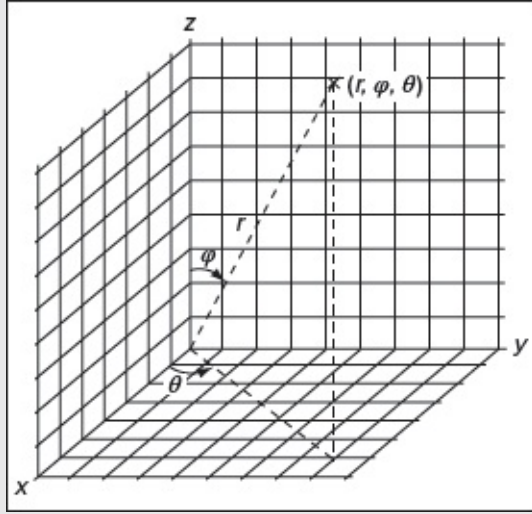


FIGURE 2-4

Spherical coordinate system with the same azimuthal angle as in cylindrical coordinates

$$x = r \sin \varphi \cos \theta \quad y = r \sin \varphi \sin \theta \quad z = r \cos \varphi \quad (2-65)$$

from which we find that $h_1 = 1$, $h_2 = r$, and $h_3 = r \sin \varphi$. Let the velocity components be $\mathbf{V} = (v_r, v_\varphi, v_\theta)$. Then, the desired new vector relations are

$$\begin{aligned} \nabla \phi &= \left(\frac{\partial \phi}{\partial r}, \frac{1}{r} \frac{\partial \phi}{\partial \varphi}, \frac{1}{r \sin \varphi} \frac{\partial \phi}{\partial \theta} \right) \\ \nabla^2 \phi &= \frac{1}{r^2} \frac{\partial}{\partial r} \left(r^2 \frac{\partial \phi}{\partial r} \right) + \frac{1}{r^2 \sin \varphi} \frac{\partial}{\partial \varphi} \left(\sin \varphi \frac{\partial \phi}{\partial \varphi} \right) + \frac{1}{r^2 \sin^2 \varphi} \frac{\partial^2 \phi}{\partial \theta^2} \\ \nabla \cdot \mathbf{V} &= \frac{1}{r^2} \frac{\partial}{\partial r} (r^2 v_r) + \frac{1}{r \sin \varphi} \frac{\partial}{\partial \varphi} (v_\varphi \sin \varphi) + \frac{1}{r \sin \varphi} \frac{\partial v_\theta}{\partial \theta} \\ \mathbf{V} \cdot \nabla &= v_r \frac{\partial}{\partial r} + \frac{v_\varphi}{r} \frac{\partial}{\partial \varphi} + \frac{v_\theta}{r \sin \varphi} \frac{\partial}{\partial \theta} \\ \nabla \times \mathbf{V} &= \left(\frac{1}{r \sin \varphi} \left[\frac{\partial(v_\theta \sin \varphi)}{\partial \varphi} - \frac{\partial v_\varphi}{\partial \theta} \right], \frac{1}{r \sin \varphi} \frac{\partial v_r}{\partial \theta} - \frac{1}{r} \frac{\partial(r v_\theta)}{\partial r}, \frac{1}{r} \left[\frac{\partial(r v_\varphi)}{\partial r} - \frac{\partial v_r}{\partial \varphi} \right] \right) \\ \boldsymbol{\tau} : \nabla \mathbf{V} &= \tau_{rr} \frac{\partial v_r}{\partial r} + \tau_{r\varphi} \left(\frac{1}{r} \frac{\partial v_r}{\partial \varphi} - \frac{v_\varphi}{r} \right) + \tau_{r\theta} \left(\frac{1}{r \sin \varphi} \frac{\partial v_r}{\partial \theta} - \frac{v_\theta}{r} \right) + \tau_{\varphi r} \frac{\partial v_\varphi}{\partial r} + \tau_{\varphi\varphi} \left(\frac{1}{r} \frac{\partial v_\varphi}{\partial \varphi} + \frac{v_r}{r} \right) + \tau_{\varphi\theta} \left(\frac{1}{r \sin \varphi} \frac{\partial v_\varphi}{\partial \theta} - \frac{v_\theta}{r} \cot \varphi \right) \\ &\quad + \tau_{\theta r} \frac{\partial v_\theta}{\partial r} + \tau_{\theta\varphi} \frac{1}{r} \frac{\partial v_\theta}{\partial \varphi} + \tau_{\theta\theta} \left(\frac{1}{r \sin \varphi} \frac{\partial v_\theta}{\partial \theta} + \frac{v_r}{r} + \frac{v_\varphi}{r} \cot \varphi \right) \end{aligned} \quad (2-66)$$

It is seen that the terms in non-Cartesian systems are somewhat more complicated in form but relatively straightforward. The complete equations of motion in cylindrical and spherical coordinates [i.e., the special-case forms of [Eqs. \(2-6\)](#), [\(2-19\)](#), and [\(2-48\)](#)] are given in App. G.

2-8 MATHEMATICAL CHARACTER OF THE EQUATIONS OF MOTION

The character of the basic relations, [Eqs. \(2-6\)](#), [\(2-19\)](#), and [\(2-48\)](#), is extremely complex. There are at least two factors that hinder our analysis: (1) the equations are coupled in the three variables \mathbf{V} , p , and T , and (2) each equation contains one or more nonlinearities. Are these equations of the boundary-value type, initial-value type, or are they wavelike in nature? The answer is that they contain mixtures of boundary-value, initial-value, and wavelike characteristics.

The general theory concerning the character of partial differential equations has developed from the study of the interesting but rather specialized quasi-linear second-order equation, which remains linear in its highest derivatives:

$$A(x_1, x_2) \frac{\partial^2 \phi}{\partial x_1^2} + B(x_1, x_2) \frac{\partial^2 \phi}{\partial x_1 \partial x_2} + C(x_1, x_2) \frac{\partial^2 \phi}{\partial x_2^2} = D\left(x_1, x_2, \phi, \frac{\partial \phi}{\partial x_1}, \frac{\partial \phi}{\partial x_2}\right) \quad (2-67)$$

Page 53where the coefficients A , B , and C may be constants or functions of (x_1, x_2) , and where D may be a nonlinear function of x_1 , x_2 , ϕ , $\partial \phi / \partial x_1$, and $\partial \phi / \partial x_2$. By developing an analytic continuation of the second derivatives, it is found that the character of [Eq. \(2-67\)](#) changes radically, depending on the sign of the *discriminant* $B^2 - 4AC$. In particular,

$$B^2 - 4AC \quad \begin{cases} < 0 \text{ the equation is } \textit{elliptic} & (\text{no real characteristic solutions}) \\ = 0 \text{ the equation is } \textit{parabolic} & (\text{one real characteristic solution}) \\ > 0 \text{ the equation is } \textit{hyperbolic} & (\text{two real characteristic solutions}) \end{cases} \quad (2-68)$$

The names elliptic, parabolic, and hyperbolic are related to the conic sections of analytic geometry. Like the conic sections, these names denote a vastly different character for [Eq. \(2-67\)](#):

1. If the equation is *elliptic*, it can be solved by specifying the boundary conditions on a *complete contour enclosing the region*; it is a boundary-value problem.
2. If the equation is *parabolic*, boundary conditions must be *closed in one direction* but remain *open at one end* of the other direction; it becomes a mixed initial- and boundary-value problem.
3. If the equation is *hyperbolic*, it can be solved in a given region by specifying conditions at only *one portion* of the boundary, the other boundaries remaining *open*; it proves to be an initial-value problem.

Many of the partial differential equations of mathematical physics may be classified with reference to [Eq. \(2-67\)](#), albeit expressed in terms of two variables only. For example, the most popular forms may be expanded in Cartesian coordinates and written as

$$\left\{ \begin{array}{l} \text{elliptic} \\ \nabla^2 \phi = f \end{array} \right. \left\{ \begin{array}{l} \text{Two-dimensional Laplace equation:} \\ \text{Three-dimensional Laplace equation:} \\ \text{Two-dimensional Poisson equation:} \\ \text{Three-dimensional Poisson equation:} \end{array} \right. \begin{array}{l} \frac{\partial^2 \phi}{\partial x^2} + \frac{\partial^2 \phi}{\partial y^2} = 0 \\ \frac{\partial^2 \phi}{\partial x^2} + \frac{\partial^2 \phi}{\partial y^2} + \frac{\partial^2 \phi}{\partial z^2} = 0 \\ \frac{\partial^2 \phi}{\partial x^2} + \frac{\partial^2 \phi}{\partial y^2} = f(x, y) \\ \frac{\partial^2 \phi}{\partial x^2} + \frac{\partial^2 \phi}{\partial y^2} + \frac{\partial^2 \phi}{\partial z^2} = f(x, y, z) \end{array} \quad (2.69a)$$

$$\left\{ \begin{array}{l} \text{parabolic} \\ \nabla^2 \phi = \frac{1}{c^2} \frac{\partial \phi}{\partial t} \end{array} \right. \left\{ \begin{array}{l} \text{One-dimensional heat-conduction equation:} \\ \text{Two-dimensional heat-conduction equation:} \\ \text{Three-dimensional heat-conduction equation:} \end{array} \right. \begin{array}{l} \frac{\partial \phi}{\partial t} - c^2 \frac{\partial^2 \phi}{\partial x^2} = 0 \\ \frac{\partial \phi}{\partial t} - c^2 \left(\frac{\partial^2 \phi}{\partial x^2} + \frac{\partial^2 \phi}{\partial y^2} \right) = 0 \\ \frac{\partial \phi}{\partial t} - c^2 \left(\frac{\partial^2 \phi}{\partial x^2} + \frac{\partial^2 \phi}{\partial y^2} + \frac{\partial^2 \phi}{\partial z^2} \right) = 0 \end{array} \quad (2.69b)$$

$$\left\{ \begin{array}{l} \text{hyperbolic} \\ \nabla^2 \phi = \frac{1}{c^2} \frac{\partial^2 \phi}{\partial t^2} \end{array} \right. \left\{ \begin{array}{l} \text{One-dimensional wave equation:} \\ \text{Two-dimensional wave equation:} \\ \text{Three-dimensional wave equation:} \end{array} \right. \begin{array}{l} \frac{\partial^2 \phi}{\partial t^2} - c^2 \frac{\partial^2 \phi}{\partial x^2} = 0 \\ \frac{\partial^2 \phi}{\partial t^2} - c^2 \left(\frac{\partial^2 \phi}{\partial x^2} + \frac{\partial^2 \phi}{\partial y^2} \right) = 0 \\ \frac{\partial^2 \phi}{\partial t^2} - c^2 \left(\frac{\partial^2 \phi}{\partial x^2} + \frac{\partial^2 \phi}{\partial y^2} + \frac{\partial^2 \phi}{\partial z^2} \right) = 0 \end{array} \quad (2.69c)$$

In applying the two-variable canonical form of [Eq. \(2-67\)](#) to [Eq. \(2-69\)](#), one may use $x_1 = x$ and $x_2 = y$ or else $x_1 = t$ and $x_2 = x$ (when both spatial and temporal variables are present), while ignoring the remaining spatial variables, to classify the corresponding two-variable problem. In general, multidimensional equations written in two- or three-dimensional space exhibit the same character as their reduced one- or two-dimensional spatial forms. Some equations may even exhibit a mixed character that depends on the value of their discriminant. The Euler–Tricomi equation, $\partial^2 \phi / \partial x^2 + x \partial^2 \phi / \partial y^2 = 0$, represents a linear partial differential equation with a variable coefficient, which proves to be elliptic for $x > 0$, parabolic for $x = 0$, and hyperbolic for $x < 0$.

From a physical standpoint, it may be worth mentioning that in parabolic and elliptic equations, any perturbation of the initial or boundary-distributed values is felt at once everywhere in the domain. Conversely, solutions of hyperbolic equations exhibit a wavelike character. Hyperbolic equations tend to be the most challenging to solve because when their initial values are disturbed, the disturbances cannot be immediately sensed at all spatial locations. In a hyperbolic problem, the disturbances travel at a finite propagation speed along the so-called characteristics of the equation. For further examples and discussion of these partial-differential-equation classifications, see Chap. 21 of the text by Kreyszig (2011).

Most importantly, the viscous-flow equations, [\(2-6\)](#), [\(2-19\)](#), and [\(2-48\)](#), display a mixture of elliptic, parabolic, and hyperbolic behavior depending on whether they are steady or

unsteady, viscous or inviscid, and compressible or incompressible. While parabolic behavior may be associated with time dependence and strongly directional motions, elliptic and hyperbolic characters prove to be dependent on the relative dominance of viscous diffusion and spatial convection terms. For example, the Navier–Stokes equations, which are parabolic in the presence of viscosity and unsteadiness, become elliptic under steady flow conditions. Conversely, Euler’s inviscid equations, which prove to be hyperbolic for unsteady (compressible) supersonic conditions, become elliptic for steady subsonic conditions (both compressible and incompressible), and parabolic for unsteady incompressible-flow conditions. As for the energy equation, it follows the Navier–Stokes equation in its display of a parabolic or elliptic character depending on its time dependence. Finally, in the treatment of thin shear layers and boundary-layer flows, velocity gradients in the streamwise direction become significantly smaller than velocity gradients in the cross-streamwise direction. The corresponding equations are left with only one second-order spatial derivative of the velocity and hence become parabolic under both steady and unsteady flow conditions. The monograph by Kreiss and Lorenz (1989) develops a variety of mathematical properties and theorems for the Navier–Stokes equations.

It is instructive now to consider the special case of *diffusion*.

2-8.1 Low-Speed Diffusion: The Prandtl Number

Consider an incompressible Newtonian fluid at low speed with constant ρ , μ , and k . Let the streamwise changes be small, that is, neglect the convective derivatives compared to local changes. Then, the momentum and energy equations reduce to

$$\text{Momentum:} \quad \rho \frac{\partial \mathbf{V}}{\partial t} \approx \rho \mathbf{g} - \nabla p + \mu \nabla^2 \mathbf{V} \quad (2-70)$$

$$\text{Energy:} \quad \rho c_p \frac{\partial T}{\partial t} \approx k \nabla^2 T \quad (2-71)$$

We recognize [Eq. \(2-71\)](#) as a multidimensional form of Fourier’s heat-conduction equation (2-69b). The temperature has elliptic boundary-value behavior in space (x, y, z) and parabolic “marching” behavior in time. We only need an initial condition $T(x, y, z, 0)$ to get started and can “march” forward in time indefinitely if we know boundary values on T at all times.

The behavior of [Eq. \(2-70\)](#) is not so obvious. But we can eliminate \mathbf{V} by taking the divergence of the entire equation, noting that $\nabla \cdot \mathbf{V} = 0$ for incompressible motion. The result is

$$\nabla^2 p = 0 \quad (2-72)$$

which is elliptic based on [Eq. \(2-69a\)](#). Recalling that $\boldsymbol{\omega} = \nabla \times \mathbf{V}$ represents the fluid vorticity, the pressure can be entirely eliminated by taking the curl of [Eq. \(2-70\)](#); one gets

$$\frac{\partial \boldsymbol{\omega}}{\partial t} = \frac{\mu}{\rho} \nabla^2 \boldsymbol{\omega} \quad (2-73)$$

This relation, like [Eq. \(2-71\)](#), is also a heat-conduction equation in the vorticity, with diffusivity coefficients that are purely fluid properties:

$$\nu = \frac{\mu}{\rho} = \text{viscous diffusivity} \quad \text{and} \quad \alpha = \frac{k}{\rho c_p} = \text{thermal diffusivity} \tag{2-74}$$

Note that the *kinematic viscosity* ν and thermal diffusivity α have no mass units. The units of both coefficients are m²/s, identical to the *mass diffusivity* D from [Eq. \(1-42\)](#). As we saw in [Chap. 1](#), their ratios constitute fundamental dimensionless fluid-property groups that provide a measure of relative rates of diffusion:

Prandtl number:
$$Pr = \frac{\nu}{\alpha} = \frac{\text{viscous diffusion rate}}{\text{thermal diffusion rate}}$$

Schmidt number:
$$Sc = \frac{\nu}{D} = \frac{\text{viscous diffusion rate}}{\text{mass diffusion rate}}$$

Lewis number:
$$Le = \frac{D}{\alpha} = \frac{\text{mass diffusion rate}}{\text{thermal diffusion rate}}$$

(2-75)

Page 55Note that $Pr = Sc \, Le$. Since mass diffusion is not emphasized here, we limit our attention to viscous and thermal effects. [Table 2-1](#) catalogs values of the Prandtl number for various fluids at 20°C. It is clear that the Prandtl number is small for liquid metals, slightly less than unity for gases, somewhat higher than unity for light liquids, and very large for oils because of their relatively large viscosities. In short, there are significant differences among fluids in their abilities to spread viscous and thermal effects.

TABLE 2-1

Prandtl number of various fluids at 20°C

Fluid	Prandtl number, Pr	Fluid	Prandtl number, Pr
Mercury	0.024	Benzene	7.4
Helium	0.70	Carbon tetrachloride	7.9
Air	0.72	Ethyl alcohol	16
Liquid ammonia	2.0	SAE 30 oil	3500
Freon-12	3.7	Castor oil	10,000
Methyl alcohol	6.8	Glycerin	12,000
Water	7.0		

[Figure 2-5](#) shows low-speed viscous flow past a hot wall as an example. The sketches illustrate low Reynolds number or laminar-flow effects. High Reynolds number or turbulent flows agree qualitatively with [Fig. 2-5](#), but the profile differences are not so broadly obvious.

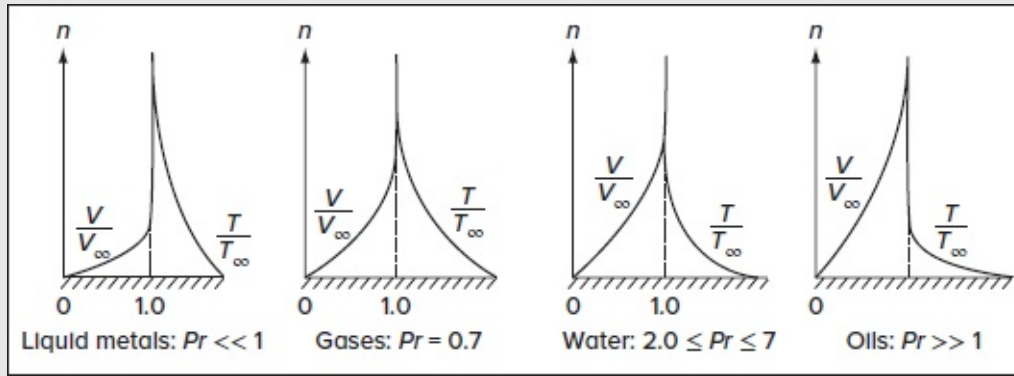


FIGURE 2-5

Prandtl number effects on viscous and thermal diffusion. (Hot wall shown for - convenience.)

A quantitative formula for the relative spreading of viscous and thermal effects may be deduced from the two diffusion equations

$$\frac{\partial T}{\partial t} = \alpha \nabla^2 T \quad (2-76)$$

$$\frac{\partial \omega}{\partial t} = \nu \nabla^2 \omega \quad (2-77)$$

This may be accomplished by defining new spatial variables: $x_i/\sqrt{\alpha}$ for the heat-conduction equation and $x_i/\sqrt{\nu}$ for the vorticity transport equation. The transformed equations will have identical unit diffusion constants and hence spreading rates. For a given unit time, the thermal spreading distance $L_T/\sqrt{\alpha}$ will then be identical to the viscous spreading length $L_V/\sqrt{\nu}$:

$$\frac{L_T}{\sqrt{\alpha}} = \frac{L_V}{\sqrt{\nu}} \quad \text{or} \quad \frac{L_V}{L_T} = \sqrt{Pr} \quad (2-78)$$

Equation (2-78) proves to be a good approximation for all laminar boundary-layer flows, even at high speeds.

2-9 DIMENSIONLESS PARAMETERS IN VISCOUS FLOW

Since our basic equations of motion are challenging to say the least, it is essential to recast them in their most efficient form, thereby increasing the usefulness, portability, and parametric independence of whatever solutions we find. This is accomplished by nondimensionalizing the governing equations and their boundary conditions.

For simplicity, we may assume constant c_p and c_v , approximately true for all gases, and neglect the second coefficient of viscosity, λ , which is seldom needed, unless compressibility effects are significant. Then, our four variables, p , ρ , \mathbf{V} , and T , will depend upon space, time, and eight parameters that occur in the basic equations and boundary conditions:

$$\mathbf{V}, p, \rho, \text{ or } T = f(x_i, t, \mu, k, g, c_p, T_w, q_w, \ell, \mathfrak{J}) \quad (2-79)$$

The eight parameters, μ through \mathfrak{J} , are assumed to be known from data or thermodynamic state relations. Note that \mathfrak{J} represents the coefficient of surface tension defined in [Chap. 1](#). Given a constant $\mathbf{g} = -g\mathbf{k}$, several reference properties appropriate to the flow may be used, specifically:

1. Reference velocity U (usually taken as the freestream or boundary-driven velocity for external flows and the mean or suction, injection, or boundary-driven velocity for internal flows). (2-80)
2. Reference length scale L (usually taken to be the body length for external flows and the duct hydraulic diameter for internal flows).
3. Freestream, mean, or reference properties p_0 , ρ_0 , T_0 , μ_0 , and k_0 .

Steady viscous flows have no characteristic time scale of their own, so a particle residence time of L/U may be chosen as a reference time scale. In seeking more generality, however, a reference time scale of ω^{-1} may be associated with an unsteady flow with a characteristic frequency ω . The corresponding dimensionless variables may be denoted by an asterisk and written as

$$\begin{aligned} x_i^* &= \frac{x_i}{L} & t^* &= \omega t & \mathbf{V}^* &= \frac{\mathbf{V}}{U} & p^* &= \frac{p - p_0}{\rho U^2} & \Phi^* &= \frac{L^2}{\mu_0 U^2} \Phi \\ \rho^* &= \frac{\rho}{\rho_0} & T^* &= \frac{T - T_0}{T_w - T_0} & \mu^* &= \frac{\mu}{\mu_0} & k^* &= \frac{k}{k_0} & \nabla^* &= L \nabla \end{aligned} \quad (2-81)$$

2-9.1 Nondimensionalizing the Basic Equations

After substituting the above variables into our basic [equations \(2-6\)](#), [\(2-19\)](#), and [\(2-48\)](#), we may collect terms and divide out dimensional constants so that all remaining terms are made dimensionless. We thus arrive at our nondimensional equations of motion:

$$\begin{aligned} \text{Continuity:} \quad & St \frac{\partial \rho^*}{\partial t^*} + \nabla^* \cdot (\rho^* \mathbf{V}^*) = 0 \\ \text{Navier-Stokes:} \quad & \rho^* \left[St \frac{\partial \mathbf{V}^*}{\partial t^*} + (\mathbf{V}^* \cdot \nabla^*) \mathbf{V}^* \right] = -\frac{1}{Fr} \rho^* \mathbf{k} - \nabla^* p^* + \frac{1}{Re} \nabla^* \cdot \{ \mu^* [\nabla^* \mathbf{V}^* + (\nabla^* \mathbf{V}^*)^T] \} \\ \text{Energy:} \quad & \rho^* \left[St \frac{\partial T^*}{\partial t^*} + (\mathbf{V}^* \cdot \nabla^*) T^* \right] = Ec \left[St \frac{\partial p^*}{\partial t^*} + (\mathbf{V}^* \cdot \nabla^*) p^* \right] + \frac{1}{RePr} \nabla^* \cdot (k^* \nabla^* T^*) + \frac{Ec}{Re} \Phi^* \end{aligned} \quad (2-82)$$

It can be immediately seen that the Navier-Stokes equation contains three dimensionless groupings:

$$\text{Reynolds number: } Re = \frac{\rho_0 U L}{\mu_0} \quad \text{Froude number: } Fr = \frac{U^2}{g L} \quad \text{Strouhal number: } St = \frac{\omega L}{U} \quad (2-83)$$

The Reynolds number is the most important dimensionless group in fluid mechanics. Almost all viscous-flow phenomena depend on it. The Froude number is important only if there is a free surface in the flow. Moreover, the degree of unsteadiness is concisely captured by the dimensionless frequency, or the Strouhal number, $St = \omega L/U$, which represents the ratio of unsteady and steady inertial forces. Since St appears as the coefficient of the unsteady terms in [Eq. \(2-82\)](#), all time-dependent terms are dropped altogether in steady or quasi-steady flows where the Strouhal number is negligible. Conversely, in the field of linear acoustics, all terms are ignored except for the unsteady inertial and pressure gradient terms in the momentum equation.

As we move to the dimensionless energy equation, we recover two additional parameters:

$$\text{Prandtl number: } Pr = \frac{\mu_0 c_p}{k_0} \quad \text{Eckert number: } Ec = \frac{U^2}{c_p T_0} \quad (2-84)$$

For a perfect gas, the more familiar *Mach* number, $Ma = U/a_0$, can replace the Eckert number through the transformation:

$$Ec = \frac{U^2}{c_p T_0} = \frac{U^2}{[\gamma R/(\gamma - 1)] T_0} = (\gamma - 1) \frac{U^2}{\gamma R T_0} = (\gamma - 1) \frac{U^2}{a_0^2} = (\gamma - 1) Ma^2 \quad (2-85)$$

The Prandtl number is always important in convective heat-transfer problems. In high-speed flows, Re , Pr , γ , and Ma are all important ([Chap. 7](#)), but at low speeds ($Ma < 0.3$), the Eckert/Mach number terms are often negligible and the energy equation reduces to $\rho^* [St \partial T^* / \partial t^* + (\mathbf{V}^* \cdot \nabla^*) T^*] = \nabla^* \cdot (k^* \nabla^* T^*) / (Re Pr)$, which is the non-dimensional form of [Eq. \(2.51\)](#). The product $Re Pr$ in the conduction term is called the *Peclet* number, Pe .

An important point, sometimes neglected in elementary approaches, is that the variables ρ , μ , and k must be specified as thermodynamic functions for the particular fluid studied: $\rho^*, \mu^*, k^* = f(p^*, T^*)$. Thus, if different fluids are being compared, Re , Pr , and Ec might not be sufficient if there are large temperature variations. As we have seen in [Chap. 1](#), gases and liquids have markedly dissimilar temperature-dependent ρ , μ , and k to the extent that temperature corrections might be needed. We recall that when a set of parameters is known to affect a problem, the Buckingham Pi theorem may be used to identify the corresponding dimensionless groupings, as summarized in App. H1.

2-9.2 Momentum with Free Convection

In free or “natural” convection, there is no freestream U . The flow is driven by gravity acting on slight density changes. Pressure is nearly constant, and the density can be modeled as $\rho \approx \rho_0 [1 - \beta(T - T_0)]$ with the coefficient of thermal expansion,

$$\beta = -\frac{1}{\rho} \left(\frac{\partial \rho}{\partial T} \right)_p \quad (2-86)$$

The parameter U is replaced by the velocity grouping $\mu/(\rho_0 L)$. The reader is invited (as a problem exercise) to nondimensionalize the Navier–Stokes equation again and find a new parameter characteristic of free convection:

$$\text{Grashof number: } Gr = \frac{g\beta\rho_0^2 L^3 (T_w - T_0)}{\mu_0^2} \quad (2-87)$$

As we shall see in Sec. 4-13, Gr and Pr correlate heat-transfer results in free convection.

2-9.3 Nondimensionalizing the Boundary Conditions

Just analyzing the basic equations is not enough. The boundary conditions also contain important dimensionless parameters. In the freestream, where $V = U$ and $T = T_0$, the conditions simply become $V^* = 1$ and $T^* = 0$. Subsequently, if we substitute the same variables from [Eqs. \(2-81\)](#) into the boundary conditions of Sec. 2-6 at a fixed wall, we obtain

$$\mathbf{V}_w^* = 0 \quad T_w^* = 1 \quad \text{or} \quad \left(k^* \frac{\partial T^*}{\partial n^*}\right)_w = \frac{q_w L}{k_0 (T_w - T_0)} = Nu \quad (2-88)$$

So the temperature conditions specify either a unit temperature ratio or a dimensionless wall heat transfer parameter that is called the *Nusselt number*, Nu . The computed results at the wall will then be the opposite: either a Nusselt number or a (nonunit) temperature ratio.

If there is slip or temperature jump at the wall, [Eqs. \(1-80\)](#) and [\(1-83\)](#) become

$$u_w^* = Kn \left(\frac{\partial u^*}{\partial n^*}\right)_w \quad \text{and} \quad T_w^* = 1 + \frac{2\gamma}{Pr(\gamma + 1)} Kn \left(\frac{\partial T^*}{\partial n^*}\right)_w \quad (2-89)$$

Slip conditions introduce the Knudsen number, $Kn = \ell/L$, and the specific-heat ratio, $\gamma = c_p/c_v$.

Finally, at an interface where surface tension is important, [Eq. \(1-86\)](#) for interfacial pressure becomes

$$p_{\text{interface}}^* = Ca + \frac{1}{Fr} \eta^* - \frac{1}{We} \left(\frac{1}{R_x^*} + \frac{1}{R_y^*} \right) \quad (2-90)$$

This equation introduces two additional dimensionless groups:

$$\text{Cavitation number: } Ca = \frac{P_a - P_0}{\rho U^2} \quad \text{Weber number: } We = \frac{\rho_0 U^2 L}{\mathfrak{F}} \quad (2-91)$$

As seen earlier in [Eq. \(2-83\)](#), the Froude number is fundamental to all free-surface flows and can never be neglected. The Weber number is important only if it is small, of $O(10)$ or less, which is usually due to a small length scale L . The cavitation number is

appropriate if the pressure p_0 is interpreted as the *vapor pressure* of the liquid, p_v . If $Ca \ll 1$, the liquid might vaporize (cavitate) when the local pressure drops below p_v . For further details, see the text by Brennen (1995).

To summarize, the following parameters are important for any particular flow:

1. All viscous flows, especially those with surface boundaries (to guide the motion): Reynolds number.
2. Variable-temperature problems: Prandtl and Eckert (or Mach) numbers.
3. Flow with free convection: Grashof and Prandtl numbers.
4. Wall heat transfer: temperature ratio or Nusselt number.
5. Slip flow: Knudsen number and specific-heat ratio.
6. Free-surface conditions: Froude number (always); Weber number (sometimes), and cavitation number (sometimes).

It is interesting to note that, in spite of our care, we have missed two parameters which become important at higher Reynolds numbers, where the flow becomes turbulent (a mean flow plus a superimposed random unsteadiness). These two parameters, which occur in Chaps. 5–7, are the degree of surface roughness (a departure from geometric similarity) and the amount of turbulence (percentage of random fluctuation) in the reference velocity U (called freestream turbulence). Reference to these two effects was made in the discussion of the drag of a cylinder in [Fig. 1-8](#). To the novice, these parameters express unexpected effects—timely reminders that fluid mechanics is a daunting subject, containing many hidden surprises to confound or delight the would-be analyst.

As the subject of fluid dynamics continues to evolve, new dimensionless parameters are still being found, thereby adding to our repertoire of scaling tools. In the interest of clarity, an extensive list of dimensionless parameters is provided in App. H2. For example, let us consider y_p to be the penetration depth of a rotational wave in a right-cylindrical porous tube; y_p defines the fraction of the radius (measured from the porous wall) where rotationality prevails. Pursuant to an asymptotic study of the penetration depth in a rocket chamber, which can be modeled as a porous tube with uniformly distributed sidewall injection, a similarity parameter, Mj , coined *penetration number*, was first reported by Majdalani to W. K. Van Moorhem in 1993:

$$Mj = \frac{U^3}{\nu \omega^2 L} = \frac{U^3 \tau^2}{\nu L} = \frac{Re}{St^2}$$

where $Re = UL / \nu$ and $St = \omega L / U$ denote the wall injection (crossflow) Reynolds number and the Strouhal number associated with the dimensionless oscillation frequency in a chamber of radius L . Majdalani's penetration number gauges the relative importance of unsteady inertial and viscous forces and has been shown to control the thickness of the oscillatory Stokes layer over a porous surface with hard blowing (Majdalani and Van Moorhem 1995; Majdalani

1999; Majdalani and Roh 2000). As illustrated in Fig. 2-6, by fixing Mj at 0.1, the frequency (or Strouhal number) Page 59 can be varied from one end of the spectrum to the other without affecting the penetration depth. Such a parameter does not appear in the governing equations of motion and is, therefore, difficult to guess because it depends on a nonlinear combination of the Reynolds and Strouhal numbers. Nonetheless, its usage enables us to collapse large families of curves characterizing the depth of penetration, and taken at different spatial locations, Re and St , into single curves taken at specific axial locations within a porous chamber (see Fig. 2-7).

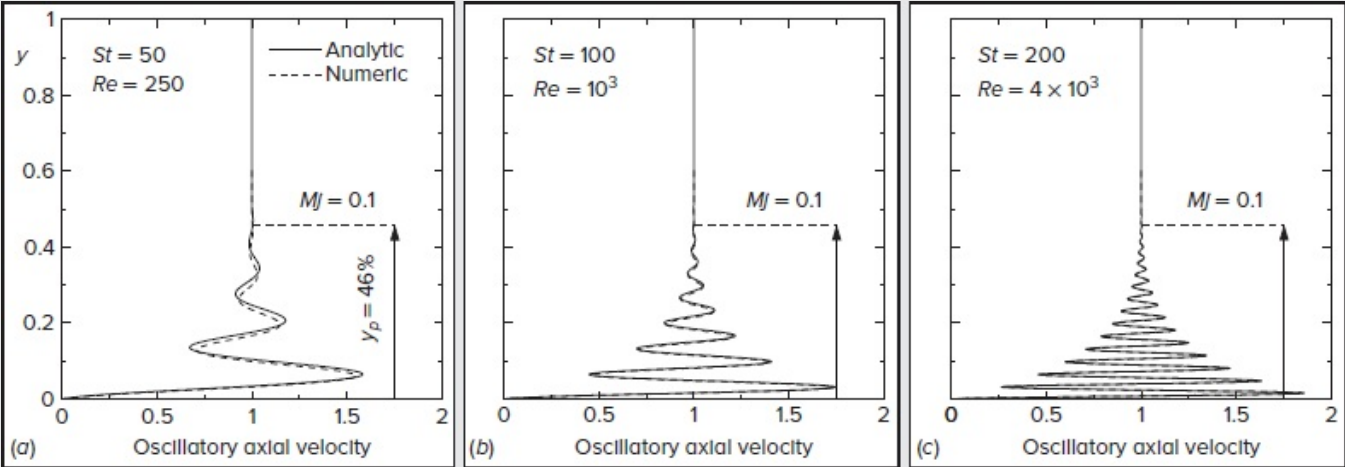


FIGURE 2-6
Analytical and numerical solutions for the axial wave in a simulated porous tube driven by sidewall mass injection (Majdalani 1995; Majdalani and Roh 2002). Oscillations are shown for the first fundamental mode and three specific values of the Strouhal (St) and Reynolds numbers (Re) based on the sidewall injection speed. By fixing the penetration number Mj , the depth of penetration remains constant despite the increase in the Strouhal number.

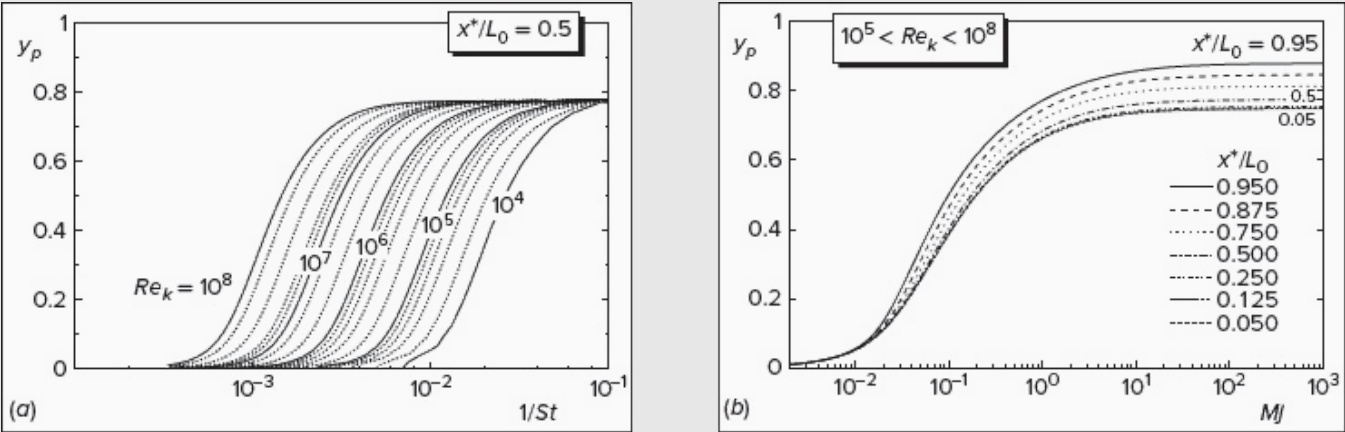


FIGURE 2-7

Depth of penetration of the oscillatory rotational velocity in a porous tube driven by sidewall mass injection (Majdalani 1995): (a) in the form of multiple curves computed at one axial station and different Strouhal and kinetic Reynolds numbers, St and $Re_k = ReSt$; (b) in the form of curves that converge into single lines at multiple axial stations when plotted versus Mj . Note that the entire family of curves in (a) collapses into a single curve in (b) corresponding to $x^*/L_0 = 0.5$.

Another important parameter that arises in the context of wall-bounded cyclonic motions is the vortex Reynolds number, namely,

$$\text{Vortex Reynolds number: } Re_v = \frac{Q_i}{\nu L} = \frac{Re R}{\sigma L}$$

where R and L represent the radius and length of the cyclonic chamber, while $Re = UR / \nu$ and $\sigma = R^2/A_i$ refer to the Reynolds and modified swirl number, respectively. This parameter combines the effects of the Reynolds number, modified swirl number, and chamber aspect ratio, thereby taking into account variations in the finite body length in a wall-bounded cyclonic chamber, which can have a significant bearing on the corresponding helical structure (Majdalani 2014). Moreover, the vortex Reynolds number is shown to control the value of the maximum tangential (swirl) velocity as well as the thickness of the forced vortex core, which develops around the axis of rotation in a cyclonic flow.

2-10 VORTICITY CONSIDERATIONS IN INCOMPRESSIBLE VISCOUS FLOW

As discussed in [Chap. 1](#), the vorticity vector $\boldsymbol{\omega} = \text{curl } \mathbf{V}$ is a measure of rotational effects, being equal to twice the local angular velocity of a fluid element. While vorticity is not a primary variable in flow analysis, the velocity itself being far more useful and significant, it is still instructive to examine the impact of the vorticity vector on the Navier–Stokes equation. To keep the lesson from being lost in a maze of algebra, we assume constant ρ and μ , so that [Eq. \(2-30\)](#) applies. We also take $\mathbf{g} = -g\mathbf{k}$ to the extent of reducing the Navier–Stokes equation into

$$\rho \frac{D\mathbf{V}}{Dt} = -\nabla p - \rho g\mathbf{k} + \mu \nabla^2 \mathbf{V} \quad (2-92)$$

As per App. A, vorticity can be introduced into both the acceleration and the viscous terms using the two vector identities,

$$(\mathbf{V} \cdot \nabla)\mathbf{V} = \frac{1}{2} \nabla V^2 - \mathbf{V} \times \boldsymbol{\omega} \quad (1-10)$$

$$\nabla^2 \mathbf{V} = \nabla(\nabla \cdot \mathbf{V}) - \nabla \times \boldsymbol{\omega} \quad (2-93)$$

Page 60 Then remembering that $\nabla z \equiv \mathbf{k}$ and $\nabla(\nabla \cdot \mathbf{V}) = 0$ when ρ is constant, [Eq. \(2-92\)](#) becomes

$$\rho \frac{\partial \mathbf{V}}{\partial t} + \nabla \left(p + \frac{1}{2} \rho V^2 + \rho g z \right) = \rho \mathbf{V} \times \boldsymbol{\omega} - \mu \nabla \times \boldsymbol{\omega} \quad (2-94)$$

Equation (2-94) is most illuminating. The left-hand side is the sum of the classic Euler terms for inviscid flow. The right-hand side vanishes if the vorticity is zero, regardless of the value of the viscosity. Thus, if $\boldsymbol{\omega} = 0$ identically, which is the classic assumption of irrotational flow, the velocity vector must by definition be a potential function, $\mathbf{V} = \nabla \phi$, where ϕ is the velocity potential, and [Eq. \(2-94\)](#) becomes the celebrated Bernoulli equation for unsteady incompressible flow:

$$\rho \partial \phi / \partial t + p + \frac{1}{2} \rho V^2 + \rho g z = \text{const} \quad (2-95)$$

It follows that Bernoulli's equation is valid even for *viscous* fluids if the flow is irrotational. Put another way, [Eq. \(2-94\)](#) shows that every potential-flow solution of classical hydrodynamics is in fact an exact solution of the full Navier–Stokes equations. The difficulty is, of course, that potential flows do not and cannot satisfy the no-slip condition at a solid wall, which requires both the normal and tangential velocities to vanish. This is because the assumption of irrotationality eliminates the second-order velocity derivatives from [Eq. \(2-92\)](#), leaving only first-order derivatives, so that only *one* velocity condition can be satisfied at a solid wall. In potential flow, then, we require only the normal velocity to vanish at a hard wall and place no restrictions on the tangential velocity, which is allowed to slip. It would appear at this point that potential solutions are no aid in viscous analysis, but in fact at high Reynolds numbers, viscous flow past a solid body is primarily potential flow everywhere except close to the body, where the velocity drops off sharply through a thin viscous boundary layer to satisfy the no-slip condition. In many cases, the boundary layer is so thin that it does not really disturb the outer potential flow, which can be determined by the methods of classical hydrodynamics described, for example, in the texts by Milne-Thomson (1968) or Robertson (1965). This was the case in [Fig. 1-1a](#). It benefits the reader, therefore, to master potential-flow analysis as a natural introduction to the study of viscous flow.

We can ascertain when irrotational flow occurs by deriving an expression for the rate of change of vorticity. One form is obtained by taking the curl of [Eq. \(2-94\)](#), with the result

$$\frac{D\boldsymbol{\omega}}{Dt} = (\boldsymbol{\omega} \cdot \nabla) \mathbf{V} + \nu \nabla^2 \boldsymbol{\omega} \quad (2-96)$$

which is the *vorticity transport equation* for an incompressible fluid with a uniform and constant viscosity. By dropping the second term involving the kinematic viscosity, one recovers the famous Helmholtz equation of hydrodynamics. The first term on the right arises from the convective derivative and is called the *vortex-stretching term*; this term was zero in the special case of [Eq. \(2-77\)](#). The second term is obviously a viscous-diffusion term; if it is

neglected (for an ideal fluid), [Eq. \(2-96\)](#) leads to Helmholtz' theorem that the strength of a vortex remains constant and also to Lagrange's theorem that $\omega = 0$ for all time if it vanishes everywhere at $t = 0$. Still a third result of neglecting the viscous term is Kelvin's theorem that the circulation about any closed path moving with the fluid is a constant. All three theorems are valid and useful in the inviscid approximation, but all three fail when the viscosity is finite because the second term in [Eq. \(2-96\)](#) is constrained by the no-slip condition not to vanish near solid walls. Thus, in all viscous flows, vorticity is generally present, being generated by relative motion near solid walls. However, vorticity can also be present in inviscid flows. If the Reynolds number is large, the vorticity is swept downstream and remains close to the wall. A boundary layer is formed, outside of which the vorticity may be taken as zero. If the flow is between two walls, as in duct flow, the two boundary layers will meet and fill the duct with vorticity, as in [Fig. 1-10](#), so that the potential-flow model is rarely applied to internal duct flow.

2-11 TWO-DIMENSIONAL CONSIDERATIONS: THE STREAM FUNCTION

In [Eq. \(2-9\)](#) we noted that the stream function is an exact solution of the continuity equation when only two independent spatial variables appear in the flow. For maximum benefit, let us examine the simple case of constant μ and ρ and two-dimensional flow in the xy plane, i.e., a flow with only the two velocity components $u(x, y, t)$ and $v(x, y, t)$. The equations of motion here are the continuity and the two components of the Navier–Stokes equations:

$$\frac{\partial u}{\partial x} + \frac{\partial v}{\partial y} = 0 \quad (2-97)$$

$$\frac{\partial u}{\partial t} + u \frac{\partial u}{\partial x} + v \frac{\partial u}{\partial y} = g_x - \frac{1}{\rho} \frac{\partial p}{\partial x} + \nu \left(\frac{\partial^2 u}{\partial x^2} + \frac{\partial^2 u}{\partial y^2} \right) \quad (2-98)$$

$$\frac{\partial v}{\partial t} + u \frac{\partial v}{\partial x} + v \frac{\partial v}{\partial y} = g_y - \frac{1}{\rho} \frac{\partial p}{\partial y} + \nu \left(\frac{\partial^2 v}{\partial x^2} + \frac{\partial^2 v}{\partial y^2} \right) \quad (2-99)$$

Page 61These are to be solved for the three dependent variables u , v , and p . Note that the momentum equation has been uncoupled from the energy equation by the assumption of constant μ and ρ , so that $T(x, y, t)$ can be solved later from [Eq. \(2-50\)](#) if needed. By analogy with [Eq. \(2-9\)](#), [Eq. \(2-97\)](#) can be immediately satisfied by a stream function $\psi(x, y, t)$ of the type

$$u = \frac{\partial \psi}{\partial y} \quad v = - \frac{\partial \psi}{\partial x} \quad (2-100)$$

where ψ takes on the meaning of volume flow rather than mass flow, since the density does not appear in its definition. Meanwhile, the pressure and gravity can be eliminated from [Eqs. \(2-98\)](#) and [\(2-99\)](#) by cross-differentiation, i.e., by taking the curl of the two-dimensional vectorial momentum equation. The result is

$$\frac{\partial \omega_z}{\partial t} + u \frac{\partial \omega_z}{\partial x} + v \frac{\partial \omega_z}{\partial y} = \nu \left(\frac{\partial^2 \omega_z}{\partial x^2} + \frac{\partial^2 \omega_z}{\partial y^2} \right) \quad \text{where} \quad \omega_z = \left(\frac{\partial v}{\partial x} - \frac{\partial u}{\partial y} \right) \quad (2-101)$$

Since $\mathbf{V} = \mathbf{V}(x, y, t)$ only, the vorticity reduces to a single nonvanishing component ω_z . At the same time, the gradient operator becomes independent on z . By comparison with the more general vorticity transport relation, [Eq. \(2-96\)](#), we see that the vortex-stretching term $(\boldsymbol{\omega} \cdot \nabla)\mathbf{V}$ vanishes identically because, for this special case of flow in the xy plane, the vorticity vector $\boldsymbol{\omega}$ is perpendicular to the gradient of \mathbf{V} . Combining [Eqs. \(2-100\)](#) and the definition of ω_z , we have the intriguing relation

$$\omega_z = -\nabla^2 \psi \quad (2-102)$$

so that [Eq. \(2-101\)](#) can be rewritten as a fourth-order partial differential equation with the stream function as the only variable:

$$\frac{\partial}{\partial t}(\nabla^2 \psi) + \frac{\partial \psi}{\partial y} \frac{\partial}{\partial x}(\nabla^2 \psi) - \frac{\partial \psi}{\partial x} \frac{\partial}{\partial y}(\nabla^2 \psi) = \nu \nabla^4 \psi \quad (2-103)$$

At this stage, the boundary conditions can be expressed in terms of the first derivatives of ψ , from [Eq. \(2-100\)](#). For example, in the flow of a uniform stream in the x direction past a solid body, the auxiliary conditions can be written as

$$\frac{\partial \psi}{\partial x} = 0 \quad \frac{\partial \psi}{\partial y} = U_\infty \quad (\text{at infinity}) \quad \frac{\partial \psi}{\partial x} = \frac{\partial \psi}{\partial y} = 0 \quad (\text{no slip at the body}) \quad (2-104)$$

This *stream-function vorticity* approach is an alternative to the direct or “primitive” variable approach of solving for (u, v, p) in [Eqs. \(2-97\)](#) to [\(2-99\)](#). Equations (2-103) and (2-104) are convenient for numerical analysis as exemplified in the first (hand-calculated) CFD solution by Thom (1933).

2-11.1 Creeping Flow: $Re \ll 1$

If the viscosity is very large, the Reynolds number UL/ν is very small, $Re \ll 1$, and the right-hand side of [Eq. \(2-103\)](#) dominates. We are left with a linear fourth-order equation,

$$Re \ll 1: \quad \nabla^4 \psi = 0 \quad (2-105)$$

which is the two-dimensional *biharmonic* equation for “creeping flow.” Many solutions are known from elasticity [Timoshenko and Goodier (1970)], which can be adapted to creeping flow. A wide variety of low Reynolds number flows are treated in the monographs by Langlois (1964) and by Happel and Brenner (1983). We shall briefly treat this subject in Sec. 3-9.

2-11.2 High Reynolds Number, Quasi-Viscous Flow: $Re \gg 1$

At the opposite side of the spectrum, if the Reynolds number is sufficiently large, the right-

hand side of [Eq. \(2-103\)](#) becomes so small that it can be either dropped or used at the basis of a matched-asymptotic expansion. In such series expansions, the far field is generally represented by the outer inviscid solution, and a small viscous correction is added, if needed, using a stretching transformation of the inner region. Moreover, if the motion is steady or quasi steady, the far field can be captured by solving a lower-order equation, namely,

$$Re \gg 1 \quad \frac{\partial \psi}{\partial y} \frac{\partial}{\partial x} (\nabla^2 \psi) - \frac{\partial \psi}{\partial x} \frac{\partial}{\partial y} (\nabla^2 \psi) = 0 \quad \text{or} \quad \frac{\partial \psi}{\partial y} \frac{\partial \omega_z}{\partial x} = \frac{\partial \psi}{\partial x} \frac{\partial \omega_z}{\partial y} \quad (2-106)$$

Due to its symmetry, it can be easily shown that the resulting vorticity transport equation is fully satisfied by any rotational flow so long as its vorticity can be expressed as $\omega_z = f(\psi)$, including the linear relation $\omega_z = C_2 \psi$. The latter can be used to derive several interesting solutions, such as the Taylor profile for a porous channel with uniform sidewall injection [e.g., Taylor (1956), Griffond and Casalis (2000, 2001), and Féraille and Casalis (2003)]. Many such profiles are termed “quasi-viscous” as they can be made to satisfy the no-slip requirement at some of the walls despite their inviscid character. A modest collection of these is reviewed by Majdalani and Saad (2012).

2-11.3 Axisymmetric Flow: The Stokes Operator

Besides its convenient two-dimensional planar form, the vorticity transport equation can be equally simplified for axisymmetric flows. As we have seen in Sec. 2.4-7, the radial and axial velocities can be related to the incompressible Stokes stream function using

$$v_r = -\frac{1}{r} \frac{\partial \psi}{\partial z} \quad \text{and} \quad v_z = \frac{1}{r} \frac{\partial \psi}{\partial r} \quad (2-107)$$

Since the motion is confined to the rz plane, the vorticity reduces to a single component in the θ direction, namely,

$$\boldsymbol{\omega} = \omega_\theta \mathbf{e}_\theta = \left(\frac{\partial v_r}{\partial z} - \frac{\partial v_z}{\partial r} \right) \mathbf{e}_\theta = -\frac{1}{r} \left(\frac{\partial^2 \psi}{\partial r^2} - \frac{1}{r} \frac{\partial \psi}{\partial r} + \frac{\partial^2 \psi}{\partial z^2} \right) \mathbf{e}_\theta \quad (2-108)$$

Instead of recovering the Laplacian of the stream function, as we have seen in [Eq. \(2-102\)](#), we now stumble upon the Stokes operator D^2 , which is a minor variant of the Laplacian in cylindrical coordinates. Specifically, we get,

$$\omega_\theta = -\frac{1}{r} D^2 \psi \quad \text{with} \quad D^2 \equiv \frac{\partial^2}{\partial r^2} - \frac{1}{r} \frac{\partial}{\partial r} + \frac{\partial^2}{\partial z^2} \quad (2-109)$$

As for the vorticity transport equation, since $(\boldsymbol{\omega} \cdot \nabla) = 0$ for all axisymmetric flows bearing only one vorticity component, [Eq. \(2-96\)](#) can be rearranged into

$$\frac{\partial \omega_\theta}{\partial t} - \frac{\partial \psi}{\partial z} \frac{\partial}{\partial r} \left(\frac{\omega_\theta}{r} \right) + \frac{\partial \psi}{\partial r} \frac{\partial}{\partial z} \left(\frac{\omega_\theta}{r} \right) = \nu \left(\nabla^2 - \frac{1}{r^2} \right) \omega_\theta = -\nu \left(\nabla^2 - \frac{1}{r^2} \right) \left(\frac{D^2 \psi}{r} \right); \quad \nabla^2 = \frac{\partial^2}{\partial r^2} + \frac{1}{r} \frac{\partial}{\partial r} + \frac{\partial^2}{\partial z^2} \quad (2-110)$$

Note that the Laplacian and Stokes operators only differ by the sign of the curvature term. Nonetheless, compared to [Eq. \(2-101\)](#), the expression we obtain is less compact, especially when expanded. In this vein, the axisymmetric counterpart of [Eq. \(2-103\)](#) can be written as

$$\frac{\partial}{\partial t} \left(\frac{D^2 \psi}{r} \right) + \frac{\partial \psi}{\partial r} \frac{\partial}{\partial z} \left(\frac{D^2 \psi}{r^2} \right) - \frac{\partial \psi}{\partial z} \frac{\partial}{\partial r} \left(\frac{D^2 \psi}{r^2} \right) = \nu \left[\frac{1}{r} \left(\frac{\partial^4 \psi}{\partial r^4} + \frac{\partial^4 \psi}{\partial z^4} + 2 \frac{\partial^4 \psi}{\partial r^2 \partial z^2} \right) - \frac{2}{r^2} \left(\frac{\partial^3 \psi}{\partial r^3} + \frac{\partial^3 \psi}{\partial r \partial z^2} \right) + \frac{3}{r^3} \frac{\partial^2 \psi}{\partial r^2} - \frac{3}{r^4} \frac{\partial \psi}{\partial r} \right] \quad (2-111)$$

Although the resulting right-hand side is slightly longer than the biharmonic creeping flow relation for $Re \ll 1$, the large Reynolds number case leads to an appreciable simplification. Thus, by limiting our attention to a steady flow with $Re \gg 1$, we are left with

$$Re \gg 1 \quad \frac{\partial \psi}{\partial r} \frac{\partial}{\partial z} \left(\frac{D^2 \psi}{r^2} \right) - \frac{\partial \psi}{\partial z} \frac{\partial}{\partial r} \left(\frac{D^2 \psi}{r^2} \right) = 0 \quad \text{or} \quad \frac{\partial \psi}{\partial z} \frac{\partial}{\partial z} \left(\frac{\omega_\theta}{r} \right) = \frac{\partial \psi}{\partial z} \frac{\partial}{\partial r} \left(\frac{\omega_\theta}{r} \right) \quad (2-112)$$

Here too, any rotational motion with $\omega_\theta = r f(\psi)$ can be shown to satisfy the vorticity transport equation identically. In fact, by using $\omega_\theta = C^2 r \psi$, several solutions have been advanced and shown to remain viable for Reynolds numbers as low as 200. Two simple examples that will be later discussed correspond to the Taylor-Culick and Vyas-Majdalani profiles for which $C = \pi$ and 2π , respectively [Culick (1966); Vyas and Majdalani (2006)]. These have been used extensively as bulk flow idealizations in both cylindrically-shaped rocket motors and cyclonically-driven rocket engines. As for the case of a swirling rocket motor, it is considered separately in Sec. 3-6.4, namely, in the treatment of rotating porous tubes. Page 63

2-12 NON-INERTIAL COORDINATE SYSTEMS

By far the majority of flow problems are treated in a fixed, or inertial, coordinate system. Cases do arise, though, such as the flow over rotating turbine blades or the geophysical boundary layer on a rotating earth, where we may wish to use non-inertial coordinates that move with the accelerating system. Then we must modify Newton's law, [Eq. \(2-11\)](#), which is valid only if \mathbf{a} is the absolute acceleration of the particle relative to inertial coordinates.

Suppose that (X, Y, Z) belong to an inertial frame and that our chosen coordinates (x, y, z) are translating and rotating relative to that frame. Let \mathbf{R} and $\mathbf{\Omega}$ be the displacement and angular velocity vector of the (x, y, z) system relative to (X, Y, Z) . Then, by straightforward vector calculus [see [Eq. \(2-106\)](#) in Greenwood (1987, pp. 49–51.)], we can relate the absolute acceleration \mathbf{a} of a particle to its displacement \mathbf{r} and velocity \mathbf{V} relative to the moving system:

$$\mathbf{a} = \frac{d^2 \mathbf{R}}{dt^2} + \frac{d\mathbf{\Omega}}{dt} \times \mathbf{r} + \mathbf{\Omega} \times (\mathbf{\Omega} \times \mathbf{r}) + \frac{d\mathbf{V}}{dt} + 2\mathbf{\Omega} \times \mathbf{V} \quad (2-113)$$

Thus, if \mathbf{V} is a non-inertial velocity vector, the entire formidable right-hand side of [Eq. \(2-113\)](#) must replace the derivative $D\mathbf{V}/Dt$ in [Eq. \(2-12\)](#) or (2-19). However, we would be

expected to know the functions $\mathbf{R}(t)$ and $\mathbf{\Omega}(t)$, which relate the two systems, so that in a sense we are merely adding known inhomogeneities to the problem.

Geophysical Flows: The Rossby Number

A classic example of a non-inertial system is the use of earth-fixed coordinates to calculate large-scale (geophysical) motions, where the earth's rotation cannot be neglected. In this case, the first three terms of [Eq. \(2-113\)](#) can be neglected, for three different reasons: (1) the first term is the earth's acceleration relative to the fixed stars and is surely almost zero; (2) the second term vanishes because $d\mathbf{\Omega} / dt$ is nearly zero for the earth; and (3) the third term is nothing more than the earth's centripetal acceleration, which essentially accounts for the variation of the gravity vector \mathbf{g} with latitude. Thus, for geophysical flows,

$$\mathbf{a} \approx \frac{d\mathbf{V}}{dt} + 2\mathbf{\Omega} \times \mathbf{V} \quad (2-114)$$

the second term of which is called the *Coriolis acceleration*, named after the French mathematician G. Coriolis, who was the first, in 1835, to study this phenomenon. If, as before, we use U and L to nondimensionalize this expression, we obtain

$$\mathbf{a}^* \approx \frac{d\mathbf{V}^*}{dt^*} + \frac{1}{Ro} (2\mathbf{\Omega}^* \times \mathbf{V}^*) \quad (2-115)$$

where $Ro = U/(\Omega L)$ is the dimensionless Rossby number (App. H2). It follows that the Coriolis term can be neglected if Ro is large, which will be true if the motion scale L is small compared to the earth's radius. We shall study a geophysical viscous flow (Ekman flow) in [Chap. 3](#).

2-13 CONTROL-VOLUME FORMULATIONS

The expressions that we have seen so far have all been differential relations: fluid flow in the small, so to speak. We also need to use integral relations to calculate the gross fluxes of mass, momentum, and energy passing through a finite region of the flow. This is the so-called *integral*, control-volume approach now widely used in fluid mechanics [see White (2016), [Chap. 3](#)]. We limit ourselves here to a fixed control volume; the text by Hansen (1967) treats moving and deformable control volumes.

Let the closed solid curve in [Fig. 2-4](#) represent a finite region (control volume) through which a fluid flow passes. At any instant t , the region is filled by an aggregate of fluid particles that define the *system*, i.e., a quantity of known identity. Our goal here is to calculate the rate of change dB / dt of any *extensive* gross property B (mass, kinetic energy, enthalpy, etc.) of the system that depends on its mass at that instant t . We do so by considering a limiting process: At time $t + \Delta t$, the system has passed on slightly to the right, as indicated by the dotted lines in [Fig. 2-8](#) and suggested by the streamline arrows. Page 64

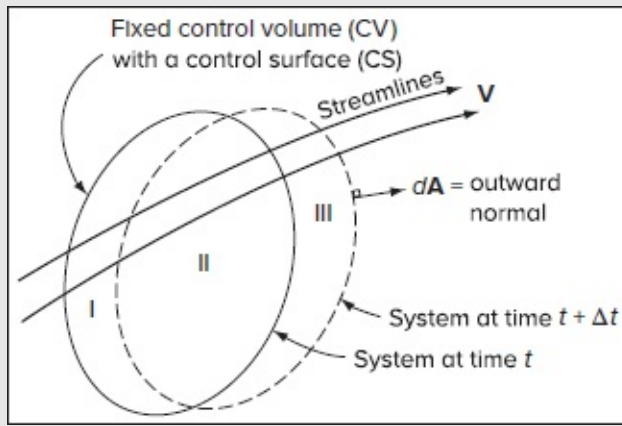


FIGURE 2-8

Sketch of a control volume.

The slight motion outlines three regions, I, II, and III, as marked on the figure. The limit we are looking for is

$$\left. \frac{dB_{\text{sys}}}{dt} \right|_t = \lim_{\Delta t \rightarrow 0} \frac{(B_{\text{III}} + \Delta B_{\text{III}})_{t+\Delta t} - (\Delta B_{\text{I}} + B_{\text{II}})_t}{\Delta t} = \lim_{\Delta t \rightarrow 0} \left[\frac{(B_{\text{II}})_{t+\Delta t} - (B_{\text{II}})_t}{\Delta t} + \frac{\Delta B_{\text{III}}}{\Delta t} - \frac{\Delta B_{\text{I}}}{\Delta t} \right] \quad (2-116)$$

As shown in undergraduate texts, such as White (2016), Sec. 3.2, the region II terms in the brackets become the rate of change of B within the control volume. The region III term is the outflow of B , and the region I term is the inflow of B into the control volume. By defining the area vector $d\mathbf{A} = \mathbf{n} dA$ as having the direction of the *outward* normal unit vector to the control surface (see [Fig. 2-8](#)), we can account for outflow and inflow with a single relation known as the *Reynolds transport theorem*, specifically

$$\frac{dB_{\text{sys}}}{dt} = \frac{d}{dt} \int_{\text{CV}} \beta \rho d\vartheta + \int_{\text{CS}} \beta \rho \mathbf{V} \cdot d\mathbf{A}; \quad B_{\text{CV}} = \int_{\text{CV}} \beta \rho d\vartheta; \quad \rho = dm/d\vartheta \quad (2-117)$$

where $\beta = dB/dm$ represents the mass-independent intensive property associated with the quantity B that happens to be enclosed within the control volume. Accordingly, the time rate of change of an extensive property associated with a fixed system crossing a control volume must equal the rate of accumulation of that property within the control volume plus the net flux of that property out of the control surface. In what follows, we apply this formulation to three extensive properties, namely, the mass, momentum, and energy.

2-13.1 Conservation of Mass

The relevant property is the mass $B = m$ for which $\beta = dm/dm = 1$. Equation (2-117) becomes

$$\frac{dm_{\text{sys}}}{dt} = \frac{d}{dt} \int_{\text{CV}} \rho d\vartheta + \int_{\text{CS}} \rho \mathbf{V} \cdot d\mathbf{A} = 0 \quad (2-118)$$

This relation is true for any fixed control volume and will be very useful in boundary-layer theory, [Chap. 4](#). As an exercise, one can show, using Gauss' theorem, that [Eq. \(2-118\)](#) is identical to the differential continuity equation given by [Eq. \(2-6\)](#).

2-13.2 Conservation of Linear Momentum

The intensive property corresponding to the linear momentum $B = m\mathbf{V}$ is the velocity itself, $\beta = d(m\mathbf{V})/dm = \mathbf{V}$. Equation (2-117) becomes equal to the total force $\Sigma\mathbf{F}$ acting on the system passing through the control volume:

$$\frac{d}{dt}(m\mathbf{V})_{\text{sys}} = \frac{d}{dt} \int_{CV} \rho \mathbf{V} d\vartheta + \int_{CS} \mathbf{V}(\rho \mathbf{V} \cdot d\mathbf{A}) = \Sigma\mathbf{F} \quad (2-119)$$

It must be emphasized that this relation holds only for an inertial control volume and that the force $\Sigma\mathbf{F}$ incorporates both surface forces acting on the control volume and body forces acting from a distance on the mass within. Equation (2-119) was first applied to viscous boundary layers by Kármán (1921).Page 65

2-13.3 Conservation of Energy

When the extensive property is taken to be the total, mass-dependent energy $B = E$, the corresponding intensive quantity becomes the specific energy $\beta = e_t = dE/dm$. Recalling the first law of thermodynamics $dE = dQ + dW$, [Eq. \(2-117\)](#) becomes

$$\frac{dE}{dt} = \frac{dQ}{dt} + \frac{dW}{dt} = \frac{d}{dt} \int_{CV} \rho e_t d\vartheta + \int_{CS} e_t(\rho \mathbf{V} \cdot d\mathbf{A}) \quad (2-120)$$

where $e_t = e + \frac{1}{2}V^2 - \mathbf{g} \cdot \mathbf{r} = e + \frac{1}{2}V^2 + g\mathbf{k} \cdot (x\mathbf{i} + y\mathbf{j} + z\mathbf{k}) = e + \frac{1}{2}V^2 + gz$

The work term dW includes work on the boundaries of normal and shear stresses plus any shaft work added to the system:

$$W = W_{\text{normal stress}} + W_{\text{shear stress}} + W_{\text{shaft}} \quad (2-121)$$

Equation (2-120) may be applied to boundary layers to determine the heat transfer.

2-13.4 The Steady-Flow Energy Equation

An important special case of [Eq. \(2-120\)](#) occurs in steady flow when the control volume consists of fixed solid walls plus a simple one-dimensional inlet and outlet, as shown in [Fig. 2-9](#). The work of boundary forces is zero at the fixed walls because of the no-slip condition. Further, if the inlet and outlet flows are approximately uniform and parallel, we may reasonably neglect viscous normal stresses locally, so that the only important boundary work is due to pressure forces at the inlet and outlet. The term d/dt vanishes for steady flow, and [Eq. \(2-120\)](#) reduces to

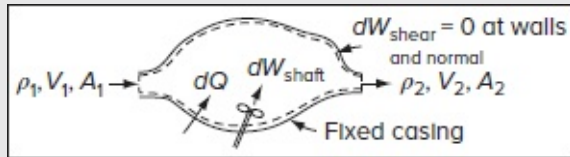


FIGURE 2-9

Sketch for the one-dimensional steady-flow energy equation.

$$\frac{dQ}{dt} + \frac{dW_{\text{shaft}}}{dt} - \int_{CS} p \mathbf{V} \cdot d\mathbf{A} = \int_{CS} e_t (\rho \mathbf{V} \cdot d\mathbf{A}) \quad (2-122)$$

But the only contributions to $\mathbf{V} \cdot d\mathbf{A}$ are $-V_1 A_1$ and $+V_2 A_2$ at the inlet and outlet, respectively. Thus, we can carry out the integration to yield two terms

$$\frac{dQ}{dt} + \frac{dW_s}{dt} = \left(\frac{p}{\rho} + e + \frac{1}{2} V^2 + gz \right)_2 \rho_2 A_2 V_2 - \left(\frac{p}{\rho} + e + \frac{1}{2} V^2 + gz \right)_1 \rho_1 A_1 V_1 \quad (2-123)$$

where the subscript s denotes shaft work. For steady flow, $\rho_1 A_1 V_1 = \rho_2 A_2 V_2$ equals the mass flow rate dm/dt through the control volume. Also, the quantity $p/\rho + e$ is the fluid enthalpy h . We may now divide through by dm/dt to achieve the familiar form

$$\frac{dQ}{dt} + \frac{dW_s}{dm} = \left(h + \frac{1}{2} V^2 + gz \right)_2 - \left(h + \frac{1}{2} V^2 + gz \right)_1 \quad (2-124)$$

which we recognize as the so-called steady-flow energy equation, stating that the change in total enthalpy $h + \frac{1}{2} V^2 + gz$ equals the sum of the heat and shaft-work addition per unit mass. The formula does not hold in boundary-layer theory unless we are careful to define our control volume to match [Fig. 2-9](#) conditions.

SUMMARY

The role of this chapter is to derive and discuss the basic equations of viscous fluid flow: conservations of mass, momentum, and energy plus the auxiliary state relations. The various boundary conditions and coordinate systems are discussed, and dimensionless parameters are derived and related to particular classes of flow. Stream-function and vorticity approaches are discussed, and the basic relations are also derived in integral form for finite control volumes. It is the purpose of the remainder of this text to tackle these equations as best as we can for particular classes of viscous flow.

PROBLEMS

2-1. By consideration of the cylindrical elemental control volume shown in [Fig. P2-1](#),

use the conservation of mass to derive the continuity equation in cylindrical coordinates [App. G, Eq. (G-3)].

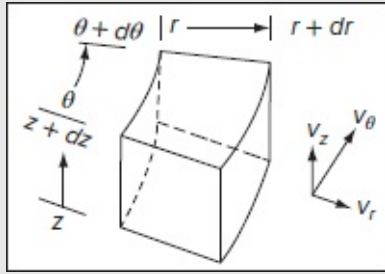


Figure P2.1

- 2-2. Simplify the equation of continuity in cylindrical coordinates (r, θ, z) to the case of steady compressible flow in polar coordinates $\partial/\partial z = 0$ and derive a stream function for this case.
- 2-3. Simplify the equation of continuity in cylindrical coordinates to the case of steady compressible flow in axisymmetric coordinates $\partial/\partial \theta = 0$ and derive a stream function for this case.

$$\text{Answer: } \frac{\partial \psi}{\partial r} = \rho v_z; \quad \frac{\partial \psi}{\partial z} = -\rho v_r$$

- 2-4. For steady incompressible flow with negligible viscosity, show that the Navier–Stokes relation [Eq. (2-30)] reduces to the condition that $p/\rho + \frac{1}{2}V^2 + gh = \text{const}$ along a streamline of the flow, where h denotes the height of the fluid particle above a horizontal datum. This is the weaker form of the so-called Bernoulli’s relation.
- 2-5. Show that for incompressible steady flow with negligible viscosity and thermal conductivity, the energy [Eq. \(2-40\)](#) reduces to the condition that $e + p/\rho + \frac{1}{2}V^2 + gh = \text{const}$ along a streamline of the flow. This is the stronger form of Bernoulli’s relation.
- 2-6. Consider the proposed incompressible axisymmetric flow field $v_z = C(R_2 - r_2)$ in the region $0 \leq z \leq L$, $0 \leq r \leq R$, where C is a constant. (a) Determine if this is an exact solution of the Navier–Stokes equation. (b) What might it represent? (c) If an axisymmetric stream function $\psi(r, z) = 0$ exists for this flow, find its form.
- 2-7. Investigate the two-dimensional stream function $\psi = Cxy$, with C a constant, to determine whether it can represent (a) a realistic incompressible frictionless flow and (b) a realistic incompressible viscous flow. Sketch some streamlines of the flow.

2-8. Investigate a proposed plane stream function for isothermal incompressible flow $\psi = C(x^2y - \frac{1}{3}y^3)$, where C is a constant. Determine whether this flow is an exact solution for constant μ and, if so, find the pressure distribution $p(x, y)$ and plot a few representative streamlines.

2-9. Consider the incompressible plane unsteady flow by Lamb-Oseen (1932):

$$v_r = 0 \quad v_\theta = \frac{C}{r} \left[1 - \exp\left(-\frac{r^2}{4\nu t}\right) \right]$$

where C and ν are constants, and gravity is neglected. Is this an exact solution of the continuity and Navier–Stokes equations? If so, plot some velocity profiles for representative times. Is there any vorticity in the flow? If so, plot some vorticity profiles.

2-10. Using the expression for dissipation Φ from [Eq. \(2-46\)](#), prove the inequalities about μ and λ given by [Eq. \(2-47\)](#).

2-11. The differential equation for irrotational plane compressible gas flow [Shapiro (1954), Chap. 9] is

$$\frac{\partial^2 \phi}{\partial t^2} + \frac{\partial}{\partial t}(u^2 + v^2) + (u^2 - a^2) \frac{\partial^2 \phi}{\partial x^2} + (v^2 - a^2) \frac{\partial^2 \phi}{\partial y^2} + 2uv \frac{\partial^2 \phi}{\partial x \partial y} = 0$$

where ϕ is the velocity potential and a the (variable) speed of sound in the gas. In the spirit of Sec. 2-9.1, nondimensionalize this equation and define any parameters which appear.

2-12. . In flow at moderate to high Reynolds numbers, pressure changes scale with $(\rho_0 U_0^2)$ as in [Eq. \(2-83\)](#). In very viscous (low Reynolds number) flow, pressure scales $\mu U_0/L$. Make this change in [Eqs. \(2-83\)](#) and repeat the nondimensionalization of the Navier–Stokes equation. Define any parameters which arise and show what happens if the Reynolds number is very small.

2-13. The equations of motion for free convection near a hot vertical plate for incompressible flow with constant properties are

$$\frac{\partial u}{\partial x} + \frac{\partial v}{\partial y} = 0 \quad u \frac{\partial u}{\partial x} + v \frac{\partial u}{\partial y} = g\beta(T - T_1) + \nu \left(\frac{\partial^2 u}{\partial x^2} + \frac{\partial^2 u}{\partial y^2} \right) \quad \rho c_p \left(u \frac{\partial T}{\partial x} + v \frac{\partial T}{\partial y} \right) = k \left(\frac{\partial^2 T}{\partial x^2} + \frac{\partial^2 T}{\partial y^2} \right)$$

Introduce the dimensionless variables

$$u^* = \frac{uL}{\nu} \quad v^* = \frac{vL}{\nu} \quad x^* = \frac{x}{L} \quad y^* = \frac{y}{L} \quad T^* = \frac{T - T_1}{T_0 - T_1}$$

where L is the length of the plate. Use these variables to nondimensionalize the free convection equations and define any parameters that arise.

- 2-14.** For laminar flow in the entrance to a pipe, as shown in [Fig. P2-14](#), the entrance flow is uniform, $u = U_0$. Using the integral relations of Sec. 2-13, show that the viscous drag exerted on the pipe walls between 0 and x is given by $\text{Drag} = \pi r_0^2 (p_0 - p_x - \frac{1}{3} \rho U_0^2)$.

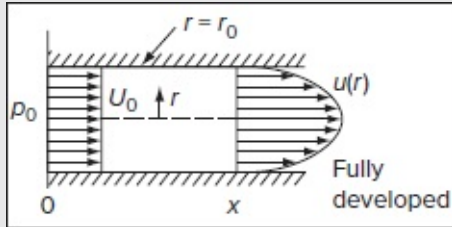


Figure P2.14

- 2-15.** To illustrate “boundary-layer” behavior, i.e., the effect of the no-slip condition for large Reynolds numbers, Prandtl in a 1932 lecture proposed the following model (linear) differential equation:

$$\epsilon \frac{d^2 u}{dy^2} + \frac{du}{dy} + u = 0 \quad \epsilon \ll 1$$

where ϵ mimics the effects of small fluid viscosity. The boundary conditions are (1) $u(0) = 2$, and (2) u remains bounded as y becomes large. Solve this equation for these conditions and plot the profile $u(y)$ in the range $0 < y < 2$ for $\epsilon = 0$, 0.01, and 0.1. Comment on the results. Is the plot for $\epsilon = 0$ the same as that obtained by setting $\epsilon = 0$ in the original differential equation and then solving?

- 2-16.** Consider the plane, incompressible, Cartesian stream function in the region $0 \leq y \leq \infty$:

$$\psi = ax + by + \frac{b}{c} e^{-cy}$$

where (a, b, c) are positive constants. (a) Determine if this is an exact solution to the continuity and Navier–Stokes equations if gravity and the pressure gradient are neglected. (b) What are the dimensions of (a, b, c) ? (c) If $y = 0$ represents a wall, does the no-slip condition hold there? (d) Is there any vorticity in the flow field? If so, what is its form?

- 2-17.** Use [Eq. \(2-86\)](#) for density in the gravity term of the Navier–Stokes equation (2-29b), let $\rho \approx \rho_0$ in the acceleration term, and let $\mu = \text{constant}$. For free convection, with U replaced by $\mu / (\rho_0 L)$, nondimensionalize the Navier–Stokes equations and

show that the Grashof number appears.

- 2-18.** Flow through a well-designed contraction or nozzle is nearly frictionless, as shown, for example, in White (2016), Sec. 6-12. Suppose that water at 20°C flows through a horizontal nozzle at a weight flow of 50 N/s. If entrance and exit diameters are 8 cm and 3 cm, respectively, and the exit pressure is 1 atm, estimate the entrance pressure from Bernoulli's equation.
- 2-19.** Show, using Gauss' theorem [Kreyszig (2011), Sec. 9.8] that the control-volume mass relation, [Eq. \(2-118\)](#), leads directly to the partial differential equation of continuity, [Eq. \(2-6\)](#).
- 2-20.** In discussing incompressible flow with constant μ , [Eq. \(2-30\)](#), we cavalierly said, "many terms vanish" from Eq. (2-29a). Be less cavalier and show that the many viscous terms in Eqs. (2-29a) do indeed reduce to the single vector term $\mu \nabla^2 \mathbf{V}$ in three dimensions.
- 2-21.** In deriving the basic equations of motion in this chapter, we skipped over the partial differential equation of *angular momentum*. Did we forget? Do some reading, perhaps in Lai et al. (1995) or Malvern (1997), and explain the significance of the angular momentum equation.
- 2-22.** Normalize the Navier–Stokes equation with constant properties, specifically,

$$\frac{\partial \mathbf{V}}{\partial t} + (\mathbf{V} \cdot \nabla) \mathbf{V} = -\frac{\nabla p}{\rho}$$

(a) by setting:

$$\begin{aligned} x^* &= \frac{x}{L} & y^* &= \frac{y}{L} & z^* &= \frac{z}{L} & \nabla^* &= L \nabla \\ t^* &= \omega t & \mathbf{V}^* &= \frac{\mathbf{V}}{U} & p^* &= \frac{p}{P} & \mathbf{g} &= -g \mathbf{k} \end{aligned}$$

(b) Define the dimensionless parameters that appear in the following nondimensional form:

$$St \frac{\partial \mathbf{V}^*}{\partial t^*} + (\mathbf{V}^* \cdot \nabla^*) \mathbf{V}^* = -Eu \nabla^* p^* + \frac{1}{Re} \nabla^{*2} \mathbf{V}^* - \frac{1}{Fr} \mathbf{k}$$

Page 68

- 2-23.** In order to better analyze the boundary-layer structure over a flat plate with a characteristic length L , the traditional variables are rescaled using

$$x^* = \frac{x}{L}, y^* = \frac{y}{\epsilon L}, u^* = \frac{u}{U}, v^* = \frac{v}{\epsilon U}, p^* = \frac{p}{\rho U^2}$$

where $\varepsilon \approx \delta / L \ll 1$ and δ denotes the boundary layer thickness. Show that $\partial^2 u / \partial x^2 \ll \partial^2 u / \partial y^2$ in the axial momentum equation written for the boundary-layer region. For steady-state motion with constant fluid properties, you may start with the axial momentum equation given by:

$$\rho u \frac{\partial u}{\partial x} + \rho v \frac{\partial u}{\partial y} = -\frac{\partial p}{\partial x} + \mu \left(\frac{\partial^2 u}{\partial x^2} + \frac{\partial^2 u}{\partial y^2} \right)$$

2-24. Given the dimensionally scaled expressions of the basic fluid dynamical forces:

$$\begin{aligned} \text{Gravitational force: } F_g &= mg \approx \rho L^3 g \\ \text{Viscous force: } F_\mu &= \tau A = (\mu dV/dy)A \approx \mu UL \\ \text{Steady inertial force: } F_i &= mVdV/dx \approx \rho U^2 L^2 \\ \text{Unsteady inertial force: } F_u &= m dV/dt \approx \rho L^3 U \omega \\ \text{Pressure force: } F_p &= \Delta p A \approx \Delta p L^2 \\ \text{Compressibility force: } F_c &= \rho(dp/d\rho)A \approx \rho c^2 L^2 \\ \text{Surface tension force: } F_\sigma &= \mathfrak{S} D \approx \mathfrak{S} L \end{aligned}$$

where the velocity gradient is approximated using $dV/dy \approx U/L$, verify the following characteristic ratios:

$$\begin{aligned} \text{Inertia and viscosity: } \frac{F_i}{F_\mu} &= \frac{\rho UL}{\mu}: \text{Osborne Reynolds (British)} \\ \text{Inertia and compressibility: } \frac{F_i}{F_c} &= \frac{U^2}{c^2} = Ma^2: \text{Ernst Mach (German)} \\ \text{Inertia and gravity: } \frac{F_i}{F_g} &= \frac{U^2}{gL} = Fr: \text{William Froude (British)} \\ \text{Inertia and surface tension: } \frac{F_i}{F_\sigma} &= \frac{\rho U^2 L}{\mathfrak{S}} = We: \text{Moritz Gustav Weber (German)} \\ \text{Pressure and inertia: } \frac{F_p}{F_i} &\approx \frac{\Delta p}{\frac{1}{2}\rho U^2} = Eu: \text{Leonhard Euler (Swiss)} \\ \text{Unsteadiness and inertia: } \frac{F_u}{F_i} &= \frac{\omega L}{U} = St: \text{Vincenc Strouhal (Czech physicist)} \\ \text{Unsteadiness and viscosity: } \frac{F_u}{F_\mu} &= \frac{L^2 \omega}{\nu} = Sk^2: \text{Sir George Gabriel Stokes (Irish)} \\ \text{Viscosity and surface tension: } \frac{F_\mu}{F_\sigma} &= \frac{\mu U}{\mathfrak{S}} = Ca: \text{Capillary Number} \end{aligned}$$

2-25. In 1851, Stokes introduced an expression for the drag force, $F_D = 3\pi\mu VD$, in the context of laminar flow over a smooth sphere of diameter D . Express the drag coefficient $C_D = F_D / (\frac{1}{2}\rho V^2 A)$ as a function of the Reynolds number. Recall that

A should be the projected area of the sphere. *Answer:* $C_D = 24/Re$.

2-26. In normalizing the basic equations of motion in Sec. 2-9.1, we have assumed a characteristic time constant that scales with the unsteady period, i.e., the reciprocal of

the frequency, $\tau = 1/\omega$, when we set $t^* = \omega t$. Show that by taking a different $t^* = tU/L$, for which $\tau = L/U$ represents the time for a fluid particle to travel a distance L at the characteristic mean-flow velocity, (a) the continuity and momentum equations reduce to

$$\text{Continuity:} \quad \frac{\partial \rho^*}{\partial t^*} + \nabla^* \cdot (\rho^* \mathbf{V}^*) = 0$$

$$\text{Navier-Stokes:} \quad \rho^* \frac{D\mathbf{V}^*}{Dt^*} = -\frac{1}{Fr} \rho^* \mathbf{k} - \nabla^* p^* + \frac{1}{Re} \nabla^* \cdot \{ \mu^* [\nabla^* \mathbf{V}^* + (\nabla^* \mathbf{V}^*)^T] \}$$

(b) the energy equation reduces to

$$\text{Energy:} \quad \rho^* \frac{DT^*}{Dt^*} = Ec \frac{Dp^*}{Dt^*} + \frac{1}{RePr} \nabla^* \cdot (k^* \nabla^* T^*) + \frac{Ec}{Re} \Phi^*$$

2-27. Renormalize the basic equations of motion in Sec. 2-9.1 assuming an incompressible fluid with negligible dissipation function Φ as well as constant viscosity and thermal conductivity, $\mu = \mu_0$ and $k = k_0$. The normalization will correspond to

$$\begin{aligned} x_i^* &= \frac{x_i}{L} & t^* &= \omega t & \mathbf{V}^* &= \frac{\mathbf{V}}{U} & p^* &= \frac{p}{p_0} & \Phi &= 0 & \nabla \cdot \mathbf{V} &= 0 \\ \rho^* &= \frac{\rho}{\rho_0} & T^* &= \frac{T - T_0}{T_w - T_0} & \gamma &= \frac{c_p}{c_v} & \nabla^* &= L \nabla \end{aligned}$$

(a) Show that the continuity and momentum equations can be simplified into

$$\text{Continuity:} \quad St \frac{\partial \rho^*}{\partial t^*} + \nabla^* \cdot (\rho^* \mathbf{V}^*) = 0$$

$$\text{Navier-Stokes equation:} \quad \rho^* \left(St \frac{\partial \mathbf{V}^*}{\partial t^*} + \mathbf{V}^* \cdot \nabla^* \mathbf{V}^* \right) = -\frac{1}{Fr} \rho^* \mathbf{k} - Eu \nabla^* p^* + \frac{1}{Re} \nabla^{*2} \mathbf{V}^*$$

(b) Show that the energy equation reduces to

$$\text{Energy:} \quad \rho^* \left[St \frac{\partial T^*}{\partial t^*} + (\mathbf{V}^* \cdot \nabla^*) T^* \right] = \frac{\gamma - 1}{\gamma} \left[St \frac{\partial p^*}{\partial t^*} + (\mathbf{V}^* \cdot \nabla^*) p^* \right] + \frac{1}{RePr} \nabla^{*2} T^*$$

(c) Under what circumstances does the Euler number become important?

(d) What happens to this set of equations if the density $\rho = \rho_0$ is assumed to be constant?

2-28. In deep water, the average speed V of a free-surface wave can be expressed as a function of the density, ρ , gravity, g , depth, D , and spatial wavelength, λ . Obtain a dimensionless representation of the free-surface wave speed as a function of these controlling parameters.

- 2-29.** A model sphere of diameter D is to be immersed in a water tunnel running at a speed of V in order to obtain data that can be used to predict the drag force on a weather balloon that is traveling in air at 1.5 m/s. For a model diameter of 50 mm, the measurement of the drag force on the small sphere yields 3.78 N. Assuming similarity conditions have been established between the spherical lab-scale model and the air balloon, what should be the water tunnel speed if the diameter of the balloon is 3 m? Estimate the drag force on the full-scale balloon.
- 2-30.** Surface tension is responsible for causing capillary waves to develop on a liquid-free surface with an average speed, V , that is dependent on the fluid density, ρ , surface tension, \mathfrak{J} , and spatial wavelength, λ . Obtain the nondimensional relations linking the speed of the capillary waves to these three independent quantities.
- 2-31.** The lifting force F on an air-launched rocket depends on its length L , velocity V , diameter D , angle of attack α , density ρ , dynamic viscosity μ , and speed of sound c . Using the Buckingham Pi theorem, determine the dimensionless groups or Pi parameters needed to characterize the functional relation between the lifting force and the quantities that affect it.
- 2-32.** A solid propellant rocket chamber is often modeled as a porous tube with sidewall injection (Majdalani 1999). The oscillatory Stokes boundary layer that develops inside a porous tube with sidewall injection (due to pressure oscillations) is affected by variations in several parameters. These include the injection velocity U , the frequency of oscillations ω , the kinematic viscosity ν , the hydraulic radius of the chamber R , the chamber length L , and the axial location within the chamber X . The dependence of the Stokes boundary-layer thickness Δ on these parameters may be expressed as $\Delta = f(U, \omega, \nu, R, L, X)$. Using scaling principles, show that the penetration depth of the unsteady rotational wave, $y_p = \Delta/R$, may be related to the following dimensionless parameters

$$y_p = \frac{\Delta}{R} = F\left(Mj, St, \frac{R}{L}, \frac{X}{L}\right) \text{ where } Mj = \frac{U^3}{\omega^2 \nu R} \text{ and } St = \frac{\omega L}{U}$$

Note that the square, square-root, or reciprocal of a dimensionless parameter as well as the product of two dimensionless parameters, such as X/R and R/L , can also produce a nondimensional group.

- 2-33.** The fluid hammer or hydraulic shock can occur when a valve is closed rapidly in a fluid supply line. Given a circular tube, the pressure impulse $\Delta p = p_1 - p_2$, also known as the strength of the fluid hammer, depends on the fluid density, ρ , the speed of sound in the fluid, c , the diameter of the tube, D , the dynamic viscosity, μ , and the mean-flow velocity, V . Using the Buckingham Pi Theorem, identify the dimensionless groups that will minimize the number of test cases needed to fully characterize the pressure impulse sensitivity to these five independent parameters. Note that the

dimensionless pressure impulse is traditionally referenced to the speed of sound and that the Reynolds number based on the speed of sound is known as the acoustic Reynolds number.

- 2-34. The drag force acting on a submarine can be taken to be a function of the water density, ρ , speed, V , viscosity, μ , and displaced volume, ϑ . Using a 1:50 scaled-down model of the submarine in a laboratory-size water tunnel, start by specifying the dimensionless parameters needed to guide your drag force measurements. Assuming a leveling of the drag force Page 70coefficient at increasing speeds, provide a best guess of the drag force on a full-scale prototype traveling at 27 knots if a value of 13 N is obtained in a water tunnel running at 10 knots.
- 2-35. Experimental measurements of the pressure drop across a sudden contraction in a circular tube suggest that $\Delta p = p_1 - p_2$ can be a function of the density, ρ , dynamic viscosity, μ , mean-flow velocity, V , and both large and small diameters, D_1 and D_2 . Identify the dimensionless groups that will minimize the number of test cases needed to fully characterize the pressure dependence on these five independent parameters.

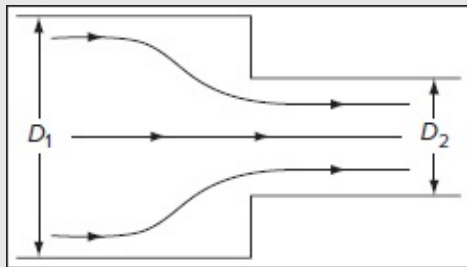


Figure P2.35

- 2-36. Water at 15°C flows through a 0.1 m internal diameter galvanized iron pipe ($\epsilon = 0.00015$ m) at a mass flow rate, \dot{m} , of 15 kg/s. We are told that:
- The total pipe length, which is $L = 150$ m, runs in a horizontal plane.
- The pipe contains one check valve ($L_e/D = 55$), and four 90° elbows ($L_e/D = 30$ each).
- The properties of water are: $\rho = 1000$ kg/m³, $\mu = 0.00114$ N·s/m², and $g = 9.81$ m/s².
- Find the Reynolds number. Is the flow turbulent?
 - Find the Darcy friction factor f .
 - Find the major head loss, h_M .
 - Find the minor head loss, h_m .

(e) What percentage of the total head loss is due to minor losses?

(f) Find the pressure drop across this pipe.

2-37. Consider a water pipe of length 100 m, diameter of 0.1541 m (6 inches), roughness of 4.6×10^{-5} m (DN 150 Schedule 40 Steel), viscosity of 1.08×10^{-5} m²/s, specific weight of 8630 N/m³, and an inlet pressure of 120 kPa at Point 1. In the presence of minor losses, determine:

- (a) The maximum permissible volumetric flow rate (in m³/s) and average velocity at Point 2 that will ensure that the pressure drop in the pipe does not exceed 60 kPa.
- (b) The total head loss in meters.
- (c) The percentage of the total head loss that corresponds to minor losses.

We are told that the pipe runs in a horizontal plane and that it contains an open butterfly valve ($L_e/D = 45$), and two standard 90° elbows ($L_e/D = 30$ each).

2-38. A 200 m long cast iron pipe has a roughness of $\varepsilon = 0.00025$ m and a diameter of 0.05 m. It carries water with a density of 1000 kg/m³ and a kinematic viscosity of 10^{-6} m²/s. The gage pressure in the water main is 1500 kPa. The supply line will require the installation of eight elbows ($L_e/D = 30$ each), two standard tees ($L_e/D = 60$ each), and one square-edged entrance ($K = 0.5$), in the total length of 200 m. The gage pressure required at the discharge point is 500 kPa. Find the discharge flow rate Q .

2-39. Water at 15°C flows through a galvanized iron pipe with a roughness of $\varepsilon = 0.00015$ m, at a mass flow rate, \dot{m} , of 20 kg/s. We are told that:

The total pipe length, which is $L = 200$ m, runs in a horizontal plane.

The pipe contains one check valve ($L_e/D = 55$), and four 90° elbows ($L_e/D = 30$ each).

The properties of water are: $\rho = 1000$ kg/m³, $\mu = 0.00114$ N · s/m², and $g = 9.81$ m/s².

The total pressure drop across the pipe is 169 kPa. What is the diameter of the pipe?

2-40. Water with a density of $\rho = 1000$ kg/m³ negotiates a 180° turn through an elbow as shown below. As the water enters the elbow, its gage pressure is 200 kPa. The pressure at the outlet section is atmospheric. Assuming uniform properties everywhere, we have $A_1 = 0.002$ m², $A_2 = 0.0006$ m², and $U_1 = 2$ m/s. Determine the

horizontal force that is needed to prevent the elbow from separating. Are the bolts in tension or compression?Page 71

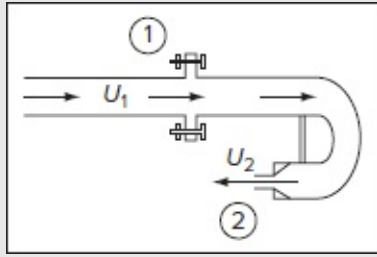


Figure P2.40

- 2-41.** Consider a two-dimensional planar channel with one inlet and two outlets that include a reducing bend. The velocity distribution at the inlet varies linearly from zero to U_1 . The velocity at the two outlets is uniform and the motion may be taken to be incompressible and steady. Determine (a) the maximum velocity at Section 1 using the integral, control-volume approach and (b) the reaction forces needed to support the channel.

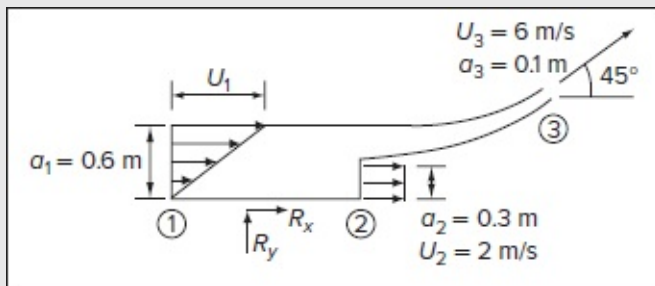


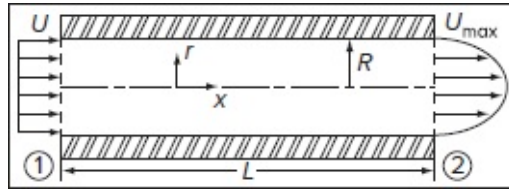
Figure P2.41

- 2-42.** Consider the steady incompressible motion of a fluid across an axisymmetric tube of length L and radius $R = 3$ cm.
- (a) Determine the uniform velocity at the inlet, U , if the velocity profile at the outlet can be approximated using

$$u(r) = U_{\max} \cos\left(\frac{\pi r^2}{2R^2}\right)$$

- (b) Evaluate your result for $U_{\max} = 10$ m/s and water with a density of $\rho = 1000$ kgm³.

(c) Determine the difference in the fluid momentum flux between the inlet and outlet sections of the tube.



- 2-43.** Consider a contraction between two pipes in a hydraulic system, which is known as a reducer. With the pressure and velocity measurements available across the reducer, and given the empty volume and mass of the reducer (ϑ_r , m_r), determine the reaction forces that must be supplied by the surrounding system to hold the reducer. You may assume that gravity is downward.

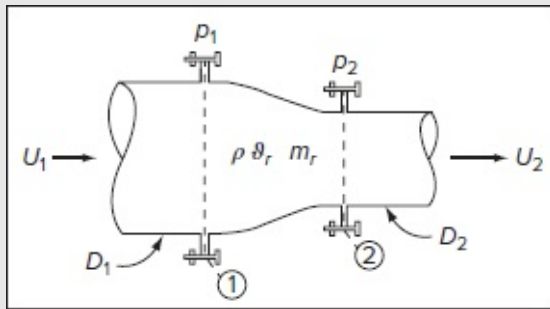


Figure P2.43

Page 72

- 2-44.** A two-dimensional velocity field is given by

$$u = -\frac{Ay}{x^2 + y^2}, \quad v = \frac{Ax}{x^2 + y^2}$$

where A is a constant. Does the field satisfy continuity?

- 2-45.** For a certain incompressible, three-dimensional flow field, the velocity components in the x and y directions are given by

$$\begin{cases} u = x^2 + y^2 + z^2 \\ v = xy + yz + z \end{cases}$$

- (a) Determine the simplest velocity component w in the z direction so that the volume dilatation rate is zero.
- (b) Determine the components of the vorticity vector. Is this an

irrotational flow field?

2-46. For a two-dimensional flow field, the velocity is defined by $\mathbf{v} = (x^2 - y^2)\mathbf{i} - 2xy\mathbf{j}$. Determine whether this motion is compressible or not.

2-47. For an incompressible, two-dimensional flow field, the velocity component in the y direction is given by

$$v = 3xy + x^2y$$

Determine the velocity component u in the x direction so that the volume dilatation rate is zero.

2-48. The three components of the velocity in a flow field are given by

$$\begin{cases} u = x^2 + y^2 + z^2 \\ v = xy + yz + z^2 \\ w = -3xz - \frac{1}{2}z^2 + 4 \end{cases}$$

Determine the divergence (volumetric dilatation rate) and interpret the results. Determine an expression for the vorticity vector. Is this an irrotational flow field?

2-49. The velocity vector in a certain flow field is prescribed by

$$\mathbf{V}(x, y, t) = 2xt \mathbf{i} - 2yt \mathbf{j}$$

where (x, y) have units of feet and t has units of seconds. Determine expressions for the local (unsteady) and convective (spatial) acceleration terms. Evaluate the magnitude and direction of the velocity and acceleration at the point $x = y = 2$ ft at time $t = 0$ s.

2-50. For steady flow, show that the curl of the inviscid momentum equation reduces to $\nabla \times (\mathbf{V} \times \boldsymbol{\omega}) = 0$, where $\boldsymbol{\omega} = \nabla \times \mathbf{V}$. Start with the steady expression of Euler's equation, namely,

$$(\mathbf{V} \cdot \nabla)\mathbf{V} = \frac{1}{2}\nabla(\mathbf{V} \cdot \mathbf{V}) - \mathbf{V} \times (\nabla \times \mathbf{V}) = -\nabla p / \rho + \mathbf{g}$$

2-51. For planar flow in the xy plane, show that the vorticity has only one nonvanishing component in the z direction, specifically, $\boldsymbol{\omega} = \omega_z \mathbf{k}$. Show that the vorticity, when written in terms of the incompressible stream function, becomes

$$\omega_z = -\left(\frac{\partial^2 \psi}{\partial x^2} + \frac{\partial^2 \psi}{\partial y^2}\right) \quad \text{where} \quad u = \frac{\partial \psi}{\partial y} \quad v = -\frac{\partial \psi}{\partial x}$$

2-52. For steady, inviscid, planar flow in the xy plane, (a) show that $\nabla \times (\mathbf{V} \times \boldsymbol{\omega}) = 0$

reduces to

$$\left(\frac{\partial \omega_z}{\partial x} \frac{\partial \psi}{\partial y} - \frac{\partial \omega_z}{\partial y} \frac{\partial \psi}{\partial x} \right) = 0 \quad \text{where} \quad u = \frac{\partial \psi}{\partial y} \quad v = -\frac{\partial \psi}{\partial x}$$

- (b) Show that any solution of the form $\omega_z = f(\psi)$ will satisfy this condition, including the linear relation $\omega_z = C_2\psi$, where C is a constant.

2-53. For planar flow in the xy plane, any solution of the form $\omega_z = C_2\psi$ can be shown to satisfy the steady, inviscid vorticity transport equation. When this relation is inserted into the vorticity expression, one gets

$$\frac{\partial^2 \psi}{\partial x^2} + \frac{\partial^2 \psi}{\partial y^2} + C^2 \psi = 0 \quad \text{where} \quad u = \frac{\partial \psi}{\partial y} \quad v = -\frac{\partial \psi}{\partial x}$$

- (a) Apply the classification test given by [Eq. \(2-68\)](#) to determine the character of the equation.
- (b) How many boundary conditions will be needed in order to solve this equation?

2-54. The Taylor profile, which has been used to describe the bulk gaseous motion in two-dimensional rocket chambers, corresponds to a planar profile in porous channels that bears symmetry with respect to the chamber's midsection plane at $y = 0$. Page 73 Assuming unit wall injection and unit chamber half height, the domain may be defined over $0 \leq x \leq 1$ and $0 \leq y \leq 1$, as shown in [Fig. P2-54](#). Using the stream-function vorticity approach, one may take $\omega_z = C_2\psi$ to secure the vorticity transport equation and then eliminate Page 74 the velocities in favor of the stream function everywhere. The resulting vorticity equation in terms of the stream function becomes

$$\frac{\partial^2 \psi}{\partial x^2} + \frac{\partial^2 \psi}{\partial y^2} + C^2 \psi = 0 \quad \text{where} \quad u = \frac{\partial \psi}{\partial y} \quad v = -\frac{\partial \psi}{\partial x}$$

- (a) Using the method of separation of variables with $\psi(x, y) = X(x)Y(y)$, find the general form of the solution.
- (b) Express the problem's four fundamental boundary conditions in terms of the stream function knowing that:

$u(x, 1) = 0$	no axial speed at the wall as the fluid enters only normally
$v(x, 1) = -1$	normal speed matches the unit injection value at the wall
$v(x, 0) = 0$	symmetry about the midsection plane prevents flow crossing
$u(0, y) = 0$	no axial inflow at the chamber headwall

(c) Find the solution that satisfies these boundary conditions.

(d) Determine the velocities associated with this solution and verify that they satisfy the four boundary conditions stated in Part (b).

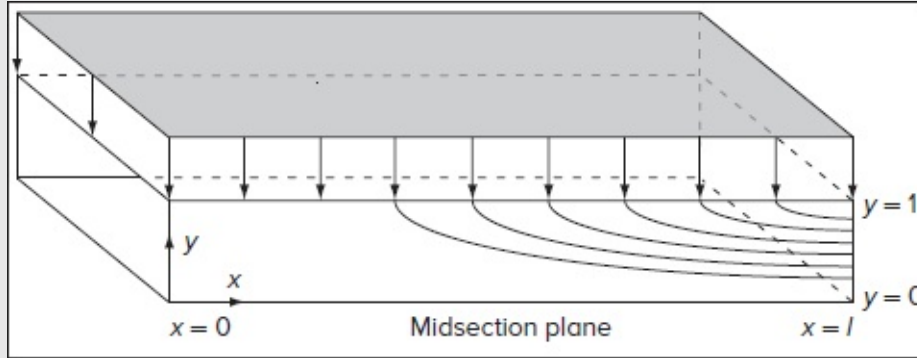


Figure P2.54

2-55. For axisymmetric flow in the rz plane, show that the vorticity has only one nonvanishing component in the θ direction, specifically, $\boldsymbol{\omega} = \omega_\theta \mathbf{e}_\theta$. Show that the vorticity, when written in terms of the incompressible stream function, becomes

$$\omega_\theta = -\frac{1}{r} \frac{\partial^2 \psi}{\partial z^2} + \frac{1}{r^2} \frac{\partial \psi}{\partial r} - \frac{1}{r} \frac{\partial^2 \psi}{\partial r^2} \quad \text{where} \quad v_r = -\frac{1}{r} \frac{\partial \psi}{\partial z} \quad v_z = \frac{1}{r} \frac{\partial \psi}{\partial r}$$

2-56. For steady, inviscid, axisymmetric flow in the rz plane, (a) show that the vorticity transport equation $\nabla \times (\mathbf{V} \times \boldsymbol{\omega}) = 0$ reduces to

$$\frac{\partial(\omega_\theta/r)}{\partial r} \frac{\partial \psi}{\partial z} - \frac{\partial(\omega_\theta/r)}{\partial z} \frac{\partial \psi}{\partial r} = 0 \quad \text{where} \quad v_r = -\frac{1}{r} \frac{\partial \psi}{\partial z} \quad v_z = \frac{1}{r} \frac{\partial \psi}{\partial r}$$

(b) Show that any solution of the form $\omega_\theta = rg(\psi)$ satisfies this condition, including the linear relation $\omega_\theta = C \, 2r\psi$, where C is a constant.

2-57. For axisymmetric flow in the rz plane, any solution of the form $\omega_\theta = C^2 r \psi$ can be shown to satisfy the steady, inviscid vorticity transport equation. When this relation is inserted into the vorticity expression, one gets

$$\frac{\partial^2 \psi}{\partial r^2} - \frac{1}{r} \frac{\partial \psi}{\partial r} + \frac{\partial^2 \psi}{\partial z^2} + C^2 r^2 \psi = 0 \quad \text{where} \quad v_r = -\frac{1}{r} \frac{\partial \psi}{\partial z} \quad v_z = \frac{1}{r} \frac{\partial \psi}{\partial r}$$

(a) Apply the classification test given by [Eq. \(2-68\)](#) to determine the

character of the equation.

- (b) How many boundary conditions will be needed to solve this equation?
- (c) How should you define $B(\psi)$ and $H(\psi)$ in the Bragg–Hawthorne Eq. (2-30e) to reproduce the same partial differential equation considered here?

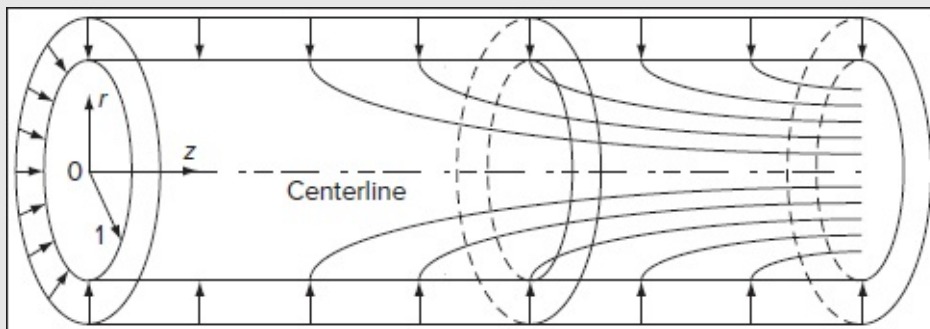
2-58. The Taylor–Culick profile, which has been extensively used to describe the bulk gaseous motion in axisymmetric rocket chambers (Culick 1966), corresponds to a self-similar axisymmetric profile in porous tubes. Assuming a unit wall injection and a unit chamber radius, the domain may be defined over $0 \leq r \leq 1$ and $0 \leq z \leq 1$, as shown in [Fig. P2-58](#). Using the stream-function vorticity approach, one may take $\omega_\theta = r C^2 \psi$ to secure the vorticity transport equation and then eliminate the velocities in favor of the Stokes stream function everywhere. The resulting vorticity equation in terms of the Stokes stream function becomes

$$\frac{\partial^2 \psi}{\partial r^2} - \frac{1}{r} \frac{\partial \psi}{\partial r} + \frac{\partial^2 \psi}{\partial z^2} + C^2 r^2 \psi = 0 \quad \text{where} \quad v_r = -\frac{1}{r} \frac{\partial \psi}{\partial z} \quad v_z = \frac{1}{r} \frac{\partial \psi}{\partial r}$$

- (a) Using the method of separation of variables with $\psi(r, z) = R(r)Z(z)$, find the general form of the solution.
- (b) Express the problem's four fundamental boundary conditions in terms of the stream function knowing that:

$v_z(1, z) = 0$	no axial speed at the wall as the fluid enters only radially
$v_r(1, z) = -1$	radial speed matches the unit injection value at the wall
$v_r(0, z) = 0$	symmetry about the centerline prevents flow crossing
$v_z(r, 0) = 0$	no axial inflow at the chamber headwall

- (c) Find the solution that satisfies these boundary conditions.
- (d) Determine the velocities associated with this solution and verify that they satisfy the four boundary conditions stated in Part (b).



2-59. In order to derive an exact solution for the velocity field in a wall-bounded cyclonic flow evolving in a cylindrical chamber ([Fig. P2-59](#)), Vyas and Majdalani (2006) assumed that the flow is steady, incompressible, inviscid, and axisymmetric with respect to the centerline. Because of the presence of swirl, a three-component velocity profile is used, namely, $\mathbf{V}(r, z) = v_r \mathbf{e}_r + v_\theta \mathbf{e}_\theta + v_z \mathbf{e}_z$. In this problem, a and $b(= a/\sqrt{2})$ denote the outer and outlet radii of the cyclonic chamber, U stands for the circumferential tangential velocity at $r = a$, $A_i = Q_i/U$ denotes the injection area for a volume flow rate of Q_i , and $\kappa = A_i/(2\pi aL)$ represents a dimensionless offset swirl parameter that gauges the relative importance of the axial-to-tangential speed ratio. The boundary conditions for this problem can be chosen to be

$$\begin{cases} v_\theta(r=a) = U & \text{tangential speed matches imposed injection value} \\ v_z(z=0) = 0 & \text{no axial flow penetration at chamber headwall} \\ v_r(r=0) = 0 & \text{no flow crossing at centerline} \\ v_r(r=a) = 0 & \text{no radial flow penetration at chamber sidewall} \\ Q_i = 2\pi \int_0^b v_z(r, L) r dr & \text{conservation of volume flowrate, } Q_i = UA_i \text{ at } z = L \end{cases}$$

(a) Guided by experimental data and numerical simulations, we may assume $v_\theta = v_\theta(r)$ to be an axially invariant function. Under this assumption, the azimuthal momentum equation in cylindrical coordinates, namely,

$$v_r \frac{\partial v_\theta}{\partial r} + \frac{v_\theta}{r} \frac{\partial v_\theta}{\partial \theta} + v_z \frac{\partial v_\theta}{\partial z} + \frac{v_\theta v_r}{r} = -\frac{1}{\rho r} \frac{\partial p}{\partial \theta}$$

decouples from its axial and radial counterparts. Recalling that the motion is axisymmetric (i.e., there are no variations in θ), show that the solution to the azimuthal momentum equation given above reduces to

$$v_r \left(\frac{\partial v_\theta}{\partial r} + \frac{v_\theta}{r} \right) = 0 \quad \text{or} \quad \frac{1}{r} \frac{\partial (rv_\theta)}{\partial r} = 0$$

(b) Realizing that the solution to Part (a) constitutes a statement of conservation of angular momentum, $rv_\theta = B = \text{const}$, solve for B and $v_\theta(r)$ using the first boundary condition, $v_\theta(a) = U$.

(c) Express the remaining four boundary conditions as functions of the Stokes stream function using

$$v_r = -\frac{1}{r} \frac{\partial \psi}{\partial z} \quad \text{and} \quad v_z = \frac{1}{r} \frac{\partial \psi}{\partial r}$$

(d) Because the vorticity transport equation $\nabla \times (\mathbf{V} \times \boldsymbol{\omega}) = 0$ reduces to

$$\frac{\partial(\omega_\theta/r)}{\partial r} \frac{\partial \psi}{\partial z} - \frac{\partial(\omega_\theta/r)}{\partial z} \frac{\partial \psi}{\partial r} = 0$$

use partial differentiation to prove that any solution of the form $\omega_\theta = rg(\psi)$ satisfies this condition, including the linear relation $\omega_\theta = C_2 r \psi$, where C is a constant.

(e) Substitute the Stokes stream function into the tangential vorticity to show that

$$\omega_\theta = \frac{\partial v_r}{\partial z} - \frac{\partial v_z}{\partial r} = \frac{1}{r^2} \frac{\partial \psi}{\partial r} - \frac{1}{r} \frac{\partial^2 \psi}{\partial r^2} - \frac{1}{r} \frac{\partial^2 \psi}{\partial z^2}$$

(f) Substitute $\omega_\theta = C_2 r \psi$, which satisfies the vorticity transport equation, into the vorticity equation to obtain

$$\frac{\partial^2 \psi}{\partial r^2} - \frac{1}{r} \frac{\partial \psi}{\partial r} + \frac{\partial^2 \psi}{\partial z^2} + C^2 r^2 \psi = 0$$

(g) Using the method of separation of variables with $\psi(r, z) = R(r) Z(z)$, find the general form of the solution to the resulting partial differential equation.

(h) Find the particular solution that satisfies the four boundary conditions formulated in Part (c).

(i) Show that the velocities associated with this profile are:

$$v_r = -\kappa U \left(\frac{a}{r} \right) \sin \left(\pi \frac{r^2}{a^2} \right); \quad v_\theta = \left(\frac{a}{r} \right) U; \quad v_z = 2\pi \kappa U \left(\frac{z}{a} \right) \cos \left(\pi \frac{r^2}{a^2} \right); \quad \begin{cases} 0 \leq r \leq a \\ 0 \leq z \leq L \end{cases}$$

(j) Verify that the velocities satisfy the problem's boundary conditions.

(k) Show that the same governing equation may be restored from the Bragg–Hawthorne Eq. (2-30e), where $B = \text{const}$ and $H(\psi) = H_0 - \frac{1}{2} C^2 \psi^2$ may be readily substituted. The form of the latter may be easily deduced from a pressure analysis along a streamline.

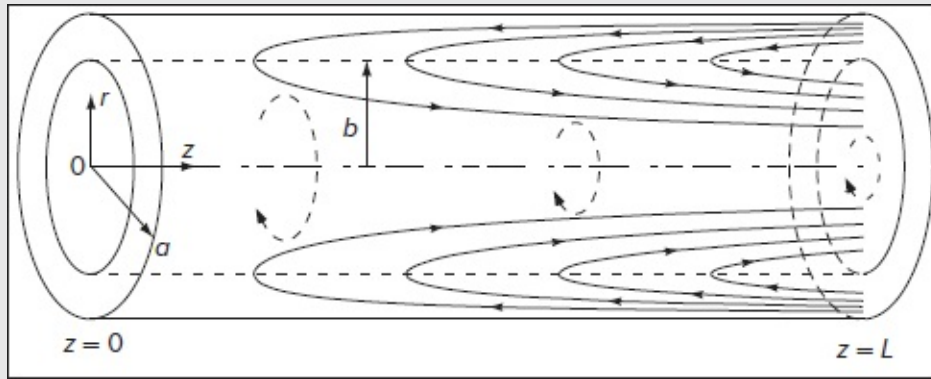


Figure P2.59

[†]Note, however, that air flowing at very high temperatures will undergo spontaneous diffusion and chemical reactions, as will many other mixtures. Even single-component fluids, such as oxygen, will dissociate into atomic oxygen at high temperatures.

[‡]But not necessarily a constant shape, i.e., the element may undergo normal strains of opposite sign plus shear strains of any sign.

[§]Here, we assume the absence of concentrated coupled stresses.

****Realizing that $\nabla_j (\delta_{ij} p) = \nabla_i p = \partial p / \partial x_i$, an equivalent indicial form of [Eq. \(2-19\)](#) is**

$$\rho \frac{Du_i}{Dt} = \rho g_i + \frac{\partial \sigma_{ij}}{\partial x_j} = \rho g_i + \frac{\partial \tau_{ij}}{\partial x_j} - \frac{\partial p}{\partial x_i}$$

CHAPTER 3

SOLUTIONS OF THE NEWTONIAN VISCOUS-FLOW EQUATIONS

Science simply means the aggregate of all of the recipes that are always successful. All the rest is literature.

Paul Valéry (1898–195

3-1 INTRODUCTION AND CLASSIFICATION OF SOLUTIONS

THE EQUATIONS of continuity, momentum, and energy, derived in [Chap. 2](#), form a formidable system of nonlinear partial differential equations. No general analytical method exists, and no general existence or uniqueness theorems exist. For example, no exact solution is known for the thin airfoil problem of [Fig. 1-1a](#), and certainly not for the stalled airfoil of [Fig. 1-1b](#). However, the boundary-layer techniques of [Chaps. 4](#) and [6](#) will provide simple approximate tools for many problems. Meanwhile, for *laminar* flows, where no fine-scale turbulent fluctuations occur, computational fluid dynamics (CFD) simulations are fairly accurate, if rather specific, for a variety of flows and geometries. See, for example, Orszag et al. (1991), Chung (2002), Lomax et al. (2001), or Tannehill et al. (1997). For turbulent flow ([Chap. 6](#)), except for *direct numerical simulation* (DNS) at low Reynolds numbers, we must either resort to empirical correlations or use approximate CFD models that are reliable only for a limited subset of flow patterns.

In our efforts to uncover exact solutions, then, we are poor but not destitute. Over the past 170 years, a considerable number [†] of exact solutions have been found, which satisfy the complete equations for some specialized geometries. This chapter will outline some of these particular solutions, many of which are very illuminating about viscous-flow phenomena.

As we might expect, most of the known particular solutions are for incompressible Newtonian flow with constant transport properties, for which the basic equations [(2-6), (2-19), and (2-48)] reduce to

$$\text{Continuity:} \quad \nabla \cdot \mathbf{V} = 0 \quad (3-1)$$

$$\text{Momentum:} \quad \rho \frac{D\mathbf{V}}{Dt} = -\nabla \hat{p} + \mu \nabla^2 \mathbf{V} \quad (3-2)$$

$$\text{Energy:} \quad \rho c_p \frac{DT}{Dt} = k \nabla^2 T + \Phi \quad (3-3)$$

where Φ denotes the mechanical dissipation function from Eq. (2-46) and \hat{p} is the total hydrostatic pressure, which includes the gravity term according to

$$\nabla \hat{p} = \nabla p - \rho \mathbf{g} \quad \text{or} \quad \hat{p} = p + \rho g z \quad (3.2a)$$

where z is the vertical coordinate. The three unknowns in Eqs. (3-1) to (3-2) are \mathbf{V} , \hat{p} , and T . Note an important fact, mentioned earlier: Since we assume that μ is constant, Eqs. (3-1) and (3-2) are uncoupled from the temperature and thus can be solved for \mathbf{V} and \hat{p} independently of T , after which T can be deduced from Eq. (3-3). Note also that T itself is dependent on \hat{p} and \mathbf{V} , since the velocity, which may be pressure dependent, enters Eq. (3-3) through the terms Φ and $DT/Dt = \partial T / \partial t + \mathbf{V} \cdot \nabla T$. Because of this uncoupling of temperature in incompressible flows, many texts simply ignore the energy equation, albeit very important, both practically and pedagogically.

Basically, there are two types of exact solutions of Eq. (3-2):

1. Linear solutions, where the convective acceleration term $\mathbf{V} \cdot \nabla$ vanishes.
2. Nonlinear solutions, where $\mathbf{V} \cdot \nabla$ does not vanish.

It is also possible to classify solutions by the type or flow configuration geometry in question:

1. Couette (wall-driven) steady flows.
2. Poiseuille (pressure-driven) steady (internal) duct flows.
3. Unsteady duct flows.
4. Unsteady flows with moving boundaries.
5. Duct flows with suction and injection.
6. Wind-driven (Ekman) flows.
7. Similarity solutions (rotating disk, stagnation flows, etc.).

These are the topics of the next several sections of this chapter.

Although a general solution is unattainable, particular exact solutions of the Navier–Stokes equations are still being found. Here are some recent examples: a porous channel with

moving walls, Dauenhauer and Majdalani (2003); oscillating flow in a rectangular duct, Tsangaris and Vlachakis (2003); pulsatory flow in a channel with an arbitrary pressure gradient, Majdalani (2008); chaotic flow in cylindrical tubes, Blyth et al. (2003); generalized Beltrami flows, Wang (1990); an unsteady stretching surface, Smith (1994); free shear layers, Varley and Seymour (1994); and two interacting vortices, Agullo and Verga (1997). For further study of laminar viscous flows, see the monographs by Constantinescu (1995), Ockendon and Ockendon (1995), and Papanastasiou et al. (1999).

3-2 COUETTE FLOWS DUE TO MOVING SURFACES

These flows are named in honor of M. Couette (1890), who performed experiments on the flow between a fixed and moving concentric cylinder. We consider several examples.

3-2.1 Steady Flow Between a Fixed and a Moving Plate

In [Fig. 3-1](#), two infinite plates are $2h$ apart, and the upper plate moves at speed U relative to the lower. The pressure \hat{p} is assumed constant. The upper plate is held at temperature T_1 and the lower plate at T_0 . These boundary conditions are independent of x or z (“infinite plates”); hence, it follows that $u = u(y)$ and $T = T(y)$. Equations (3-1) to (3-3) reduce to

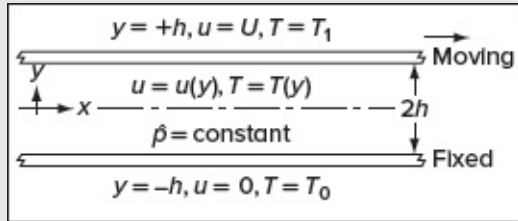


FIGURE 3-1

Couette flow between parallel plates.

Continuity:

$$\frac{\partial u}{\partial x} = 0 \quad (3-4)$$

Momentum:

$$\mu \frac{d^2 u}{dy^2} = 0$$

Energy:

$$k \frac{d^2 T}{dy^2} + \mu \left(\frac{du}{dy} \right)^2 = 0 \quad (3-5)$$

where continuity merely verifies our assumption that $u = u(y)$ only. Equation (3-4) can be integrated twice to obtain

$$u = C_1 y + C_2$$

Page 78The boundary conditions are no slip, $u(-h) = 0$ and $u(+h) = U$, whence $C_1 = U/(2h)$ and $C_2 = U/2$. Then the velocity distribution is

$$u = \frac{U}{2} \left(1 + \frac{y}{h} \right) \quad (3-6)$$

This expression is plotted in [Fig. 3-2a](#), where it appears as a straight line connecting the no-slip condition at each plate. We term this plot a *velocity profile* and commonly sketch in line segments with arrows, as shown, to indicate motion. Since $\mu = \text{const}$ and we have neglected buoyancy, this profile is independent of the temperature distribution.

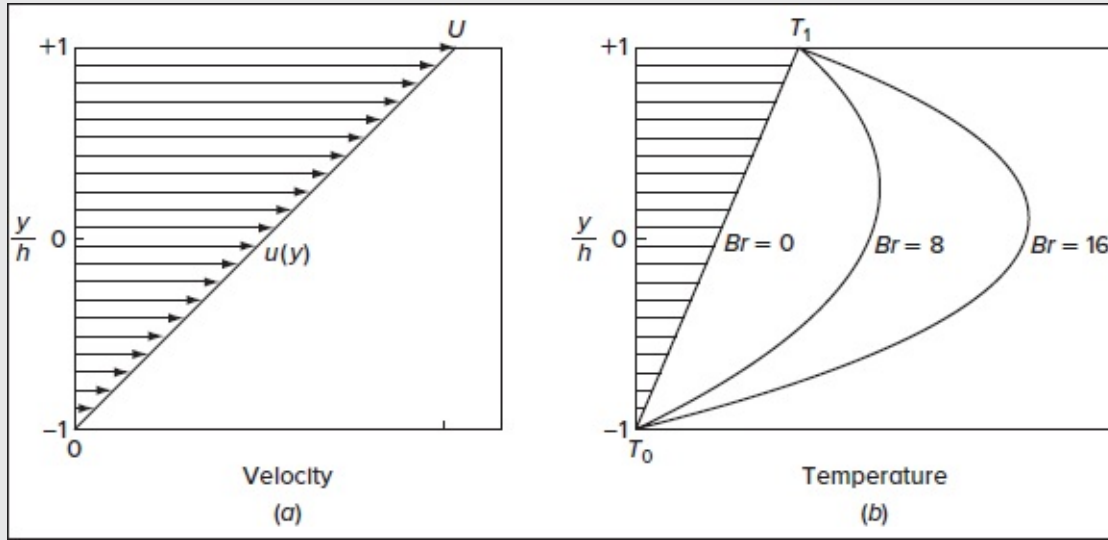


FIGURE 3-2

Couette flow between a fixed and a moving plate: (a) the velocity profile; (b) temperature profiles for various Brinkman numbers, where $Br = \mu U^2/[k(T_1 - T_0)]$.

The shear stress at any point in the flow follows from Newton's law for viscosity:

$$\tau = \mu \left(\frac{\partial u}{\partial y} + \frac{\partial v}{\partial x} \right) = \mu \frac{du}{dy} = \frac{\mu U}{2h} = \text{const} \quad (3-7)$$

Thus, for this simple flow, the shear stress is constant throughout the fluid, as is the strain rate—even a non-Newtonian fluid would maintain a linear velocity profile.

The dimensionless shear stress is usually defined in engineering flows as the *friction coefficient*,

$$C_f = \frac{\tau}{\frac{1}{2} \rho U^2} = \frac{\mu}{\rho U h} = \frac{1}{Re_h} \quad (3-8)$$

Thus, the Reynolds number $Re_h = \rho U h / \mu$ arises naturally when the shear stress is nondimensionalized. Or perhaps *unnaturally* is more appropriate: Churchill (1988) points out that the Reynolds number is unsuitable for this nonaccelerating flow, since density does not play a part. He suggests that one should instead use the *Poiseuille number*, which happens to be a unit value for this problem:

$$Po = C_f Re_h = \frac{2h\tau}{\mu U} = 1 \quad (3-9)$$

Clearly, a unit Poiseuille number is more convenient than a varying friction coefficient.

With $du/dy = U/(2h)$ known from [Eq. \(3-6\)](#), we may substitute into [Eq. \(3-5\)](#) and integrate twice to obtain the temperature distribution:

$$T = -\frac{\mu U^2}{4kh^2} \frac{y^2}{2} + C_3 y + C_4 \quad (3-10)$$

The no-temperature-jump conditions require $T(-h) = T_0$ and $T(+h) = T_1$, whence C_3 and C_4 can be evaluated. The final solution is

$$T = \left(\frac{T_1 + T_0}{2} + \frac{T_1 - T_0}{2} \frac{y}{h} \right) + \frac{\mu U^2}{8k} \left(1 - \frac{y^2}{h^2} \right) \quad (3-11)$$

The first term in parentheses represents the straight-line distribution that would arise due to pure conduction in the fluid. The second (parabolic) term is the temperature rise due to *viscous dissipation* in the fluid. The temperatures $T(y)$ from [Eq. \(3-11\)](#) are plotted in [Fig. 3-2b](#). If T is nondimensionalized by $(T_1 - T_0)$, a dimensionless dissipation parameter emerges, namely, the *Brinkman number*:

$$Br = \frac{\mu U^2}{k(T_1 - T_0)} = \frac{\mu c_p}{k} \frac{U^2}{c_p(T_1 - T_0)} = PrEc \quad (3-12)$$

From [Fig. 3-2b](#), a Brinkman number of order unity or greater means that the temperature rise due to dissipation is significant. Qualitatively, it represents the ratio of dissipation effects to fluid conduction effects.

For low-speed flows, only the most viscous fluids (oils) have significant Brinkman numbers. For example, take $U = 10$ ms, $(T_1 - T_0) = 10^\circ\text{C}$ and compare the following numerical values for four fluids:

Fluid	μ [kg/(m·s)]	k [W/(m·°C)]	Brinkman number
Air	1.8×10^{-5}	0.26	0.0007
Water	1.0×10^{-3}	0.60	0.017
Mercury	1.54×10^{-3}	8.7	0.0018
SAE 30 oil	0.29	0.145	20.0

Thus, except for heavy oils, we commonly neglect dissipation effects in low-speed flow temperature analyses.

To complete this lengthy initial-case discussion, we compute the rate of heat transfer at the walls:

$$q_w = \left| k \frac{\partial T}{\partial y} \right|_{\pm h} = \frac{k}{2h} (T_1 - T_0) \pm \frac{\mu U^2}{4h} \quad (3-13)$$

where the (\pm) refers to the lower and upper surfaces, respectively. The first term on the right represents pure conduction through the fluid.

Since many convection analyses result in q_w being proportional to ΔT , it is customary to refer to their ratio as the *heat-transfer coefficient*:

$$\zeta = \frac{q_w}{T_1 - T_0} \quad (3-14)$$

One then nondimensionalizes ζ either as the Stanton or the *Nusselt number*:

$$Nu_L = \zeta L / k = C_h Re_L Pr \quad (3-15)$$

where L is the characteristic length of the flow geometry. Here we select L as the plate separation distance ($2h$) and compute, from [Eq. \(3-13\)](#),

$$Nu_{2h} = 2h\zeta / k = 1 \pm \frac{1}{2} Br \quad (3-16)$$

where again the $(+)$ means the lower surface. If $Br > 2$, both the upper and lower surfaces must be cooled to maintain their temperatures. Note that, since $Nu \approx 1$ for pure conduction, the numerical value of Nu represents the ratio of convective and conductive heat transfer for the same value of ΔT .

3-2.2 Axially Moving Concentric Cylinders

Let us now consider two long concentric cylinders with a viscous fluid filling the annular gap between them, as in [Fig. 3-3](#). Let either the inner ($r = r_0$) cylinder move axially at $u = U_0$ or the outer ($r = r_1$) cylinder move at $u = U_1$, as shown. Let the pressure and temperature be constant for this example. The no-slip condition will set the fluid into steady motion $u(r)$, and both u_θ and u_r will be zero. The equations of motion in cylindrical coordinates are given in App. G. Continuity is satisfied identically if $u = u(r)$, and the axial momentum equation reduces to

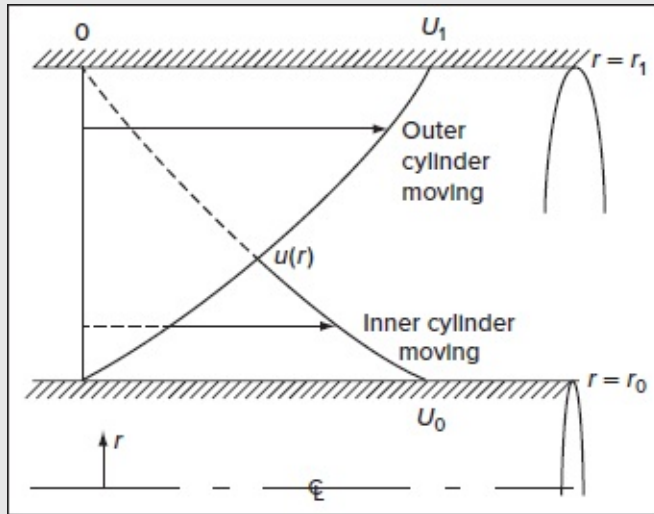


FIGURE 3-3

Axial annular Couette flow between concentric moving cylinders. The velocity distributions are plotted from [Eqs. \(3-18\)](#) and [\(3-19\)](#).

$$\nabla^2 u = \frac{\partial^2 u}{\partial r^2} + \frac{1}{r} \frac{\partial u}{\partial r} = \frac{1}{r} \frac{\partial}{\partial r} \left(r \frac{\partial u}{\partial r} \right) = 0 \quad (3-17)$$

Integrating twice and rearranging, we get

$$u = C_1 \ln(r) + C_2$$

Page 80 If the inner cylinder moves, the no-slip conditions become $u(r_0) = U_0$ and $u(r_1) = 0$, whence $C_1 = U_0 / \ln(r_0/r_1)$ and $C_2 = -C_1 \ln(r_1)$. We deduce

$$u = U_0 \frac{\ln(r_1/r)}{\ln(r_1/r_0)} \quad \text{and} \quad \tau = -\frac{\mu U_0}{r \ln(r_1/r_0)} \quad (3-18)$$

If, instead, the outer cylinder moves, the boundary conditions switch to $u(r_0) = 0$ and $u(r_1) = U_1$, which then lead to

$$u = U_1 \frac{\ln(r/r_0)}{\ln(r_1/r_0)} \quad \text{and} \quad \tau = \frac{\mu U_1}{r \ln(r_1/r_0)} \quad (3-19)$$

These two velocity distributions are sketched in [Fig. 3-3](#), where they are seen to mirror the temperature distribution $T(r)$ for pure conduction through a fluid. Note the difference in curvature for the two cases: If the inner cylinder moves, $u(r)$ is concave, whereas it is convex if the outer cylinder moves. The temperature distribution is given as a problem exercise, as is the question of what happens if both cylinders move simultaneously.

3-2.3 Flow Between Rotating Concentric Cylinders

Let us now consider the steady flow maintained between two concentric cylinders by steady angular velocity of one or both cylinders. In this configuration, the inner cylinder has radius r_0 , angular velocity ω_0 , and temperature T_0 , and the outer cylinder has r_1 , ω_1 , and T_1 , respectively. The geometry is such that the only nonzero velocity component is u_θ and the variables u_θ , T , and p are sole functions of the radius r . The equations of motion in polar coordinates [Eq. (2-64)] reduce to

$$\begin{aligned}
 \text{Continuity:} & \quad \frac{\partial u}{\partial \theta} = 0 \\
 r - \text{momentum:} & \quad \frac{dp}{dr} = \rho \frac{u_\theta^2}{r} \\
 \theta - \text{momentum:} & \quad \frac{d^2 u_\theta}{dr^2} + \frac{d}{dr} \left(\frac{u_\theta}{r} \right) = 0 \\
 \text{Energy:} & \quad \frac{k}{r} \frac{d}{dr} \left(r \frac{dT}{dr} \right) + \mu \left(\frac{du_\theta}{dr} - \frac{u_\theta}{r} \right)^2 = 0
 \end{aligned} \tag{3-20}$$

with boundary conditions at each cylindrical surface that are given by

$$\begin{aligned}
 \text{At } r = r_0: & \quad u_\theta = r_0 \omega_0 & T = T_0 & p = p_0 \\
 \text{At } r = r_1: & \quad u_\theta = r_1 \omega_1 & T = T_1 &
 \end{aligned} \tag{3-21}$$

Forthwith, the solution to the θ -momentum equation takes the form

$$u_\theta = C_1 r + \frac{C_2}{r}$$

Page 81 This two-term expression represents the superposition of a “forced” vortex undergoing solid-body rotation and an irrotational “potential” vortex. We may find C_1 and C_2 from the boundary conditions in [Eq. \(3-21\)](#) and write the solution as the sum of inner and outer driven motions:

$$u_\theta = r_0 \omega_0 \frac{r_1/r - r/r_1}{r_1/r_0 - r_0/r_1} + r_1 \omega_1 \frac{r/r_0 - r_0/r}{r_1/r_0 - r_0/r_1} \tag{3-22}$$

If this velocity distribution is substituted into the energy equation in [Eq. \(3-20\)](#), the temperature distribution may be deduced as follows:

$$\frac{T - T_0}{T_1 - T_0} = PrEc \frac{r_1^4}{(r_1^2 - r_0^2)^2} \left[\left(1 - \frac{r_0^2}{r^2} \right) - \left(1 - \frac{r_0^2}{r_1^2} \right) \frac{\ln(r/r_0)}{\ln(r_1/r_0)} \right] + \frac{\ln(r/r_0)}{\ln(r_1/r_0)} \tag{3-23}$$

where $PrEc = \mu r_0^2 \omega_0^2 / [k(T_1 - T_0)]$ is the Brinkman number expressing the temperature rise due to dissipation. If $PrEc = 0$, T reduces to the simple heat-conduction solution. The evaluation of the pressure $p(r)$ follows straightforwardly and is left as an exercise.

Some special cases are of interest here. On the one hand, in the limit as the inner cylinder vanishes ($r_0 = \omega_0 = 0$), we obtain from [Eq. \(3-22\)](#):

$$u_\theta = \omega_1 r = \text{const} \quad (3-24)$$

This implies that the steady outer rotation of a tube filled with fluid leads to a case of solid-body rotation.

On the other hand, in the limit as the stationary outer cylinder becomes very large ($r_1 \rightarrow \infty, \omega_1 = 0$), we obtain

$$u_\theta = r_0^2 \omega_0 r^{-1} \quad (3-25)$$

This expression represents a *potential vortex*, driven by the rotating cylinder by virtue of the no-slip condition. As anyone who paddles a canoe knows, a vortex, if not maintained by a driving moment, will decay. Two examples of decaying vortex distributions are given as end-of-chapter Probs. 3-14 and 3-22.

At this point, [Fig. 3-4a](#) is used to illustrate the velocity distributions for various relative ratios (r_1/r_0), when only the inner cylinder is rotating. [Figure 3-4b](#) displays the temperature distributions for the $r_1/r_0 = 5$ configuration in [Fig. 3-4a](#).

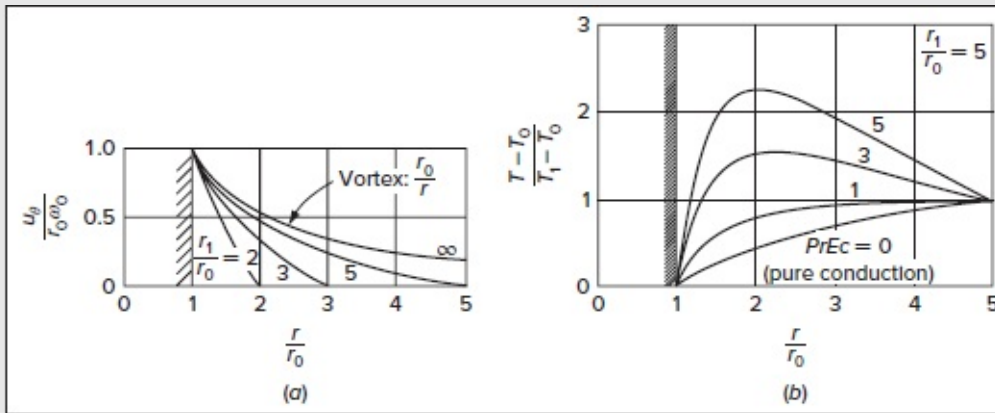


FIGURE 3-4

Velocity and temperature distributions between a stationary outer and a rotating inner cylinder, [Eqs. \(3-22\)](#) and [\(3-23\)](#): (a) velocity distribution; (b) temperature distribution for $r_1/r_0 = 5$.

Another interesting special case is that of very small clearance between the cylinders, $r_1 - r_0 \ll r_0$. Again, by keeping the outer cylinder stationary, [Eq. \(3-22\)](#) becomes, in the limit,

Small clearance:

$$\frac{u_\theta}{r_0 \omega_0} \approx 1 - \frac{r - r_0}{r_1 - r_0} \quad (3-26)$$

which is a linear Couette flow between essentially parallel plates, as in [Fig. 3-1](#). Note that, in [Fig. 3-4a](#), the approach to linearity is already being hinted at for $r_1/r_0 = 2$. With the velocity gradient being high, a wide variety of shear stresses can be generated in a small-clearance apparatus.

Of interest in viscometry is the moment or torque exerted by the cylinders upon each other. This moment is independent of r and has the value (per unit depth of cylinder) of

$$M = 4\pi\mu \frac{r_1^2 r_0^2}{r_1^2 - r_0^2} (\omega_1 - \omega_0) \quad (3-27)$$

Page 82By knowing the geometry and measuring M at either cylinder, one can calculate the viscosity of the fluid, as first suggested by Couette (1890). This is still a popular method in viscometry.

3-2.4 Stability of Couette Flows

All solutions in this section are exact steady-flow solutions of the Navier–Stokes equations. They are called *laminar* flows and have a smooth-streamline character. It is known that all laminar flows become *unstable* at a finite value of some critical parameter, usually the Reynolds number. A different type of flow then ensues, sometimes still laminar or, more often, an entirely new fluctuating flow regime called *turbulent*.

In this context, the laminar straight-line profile of flow between plates, [Fig. 3-2a](#), turns out to be valid only up to $Re_h = Uh/\nu \approx 1500$. Above this value, the pattern changes into a randomly fluctuating field whose time-mean S-shaped profile is shown in [Fig. 3-5](#). This shape, sketched from data given by Reichardt (1956), varies slightly with the Reynolds number and increases the wall shear (and heat-transfer rate) by two orders of magnitude. We will discuss these effects in detail in Chaps. 5 and 6.

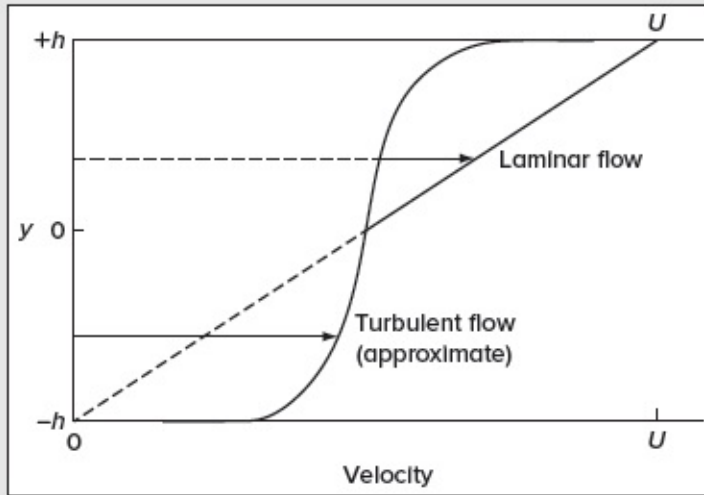


FIGURE 3-5

Instability of Couette flow between parallel plates: The straight-line laminar profile of [Eq. \(3-6\)](#) is valid only up to $Re_h = Uh/\nu \approx 1500$. [*Reichardt (1956)*.]

The axial annular flows of [Fig. 3-3](#) are also unstable. Experiments by Polderman et al. (1986), with the inner cylinder moving, predict fully turbulent flow at a clearance Reynolds number $Re_c = U_0(r_1 - r_0)/\nu \geq 7000$. The probable point of “transition” from laminar to turbulent flow, not reported, is around $Re_c \approx 2000$.

Although early work [Rayleigh (1916)] suggests that the rotating inner cylinder motions in [Fig. 3-4a](#) are unstable for all rotation rates, a classic paper by Taylor (1923) shows that the laminar profiles remain valid until a critical rotation rate. For small clearance, $(r_1 - r_0) \ll r_0$, the critical value for instability is given by the *Taylor number*:

$$Ta = r_0(r_1 - r_0)^3 \frac{\omega_0^2}{\nu^2} \approx 1700$$

Above this value, the pattern changes into strikingly different three-dimensional laminar flows consisting of counterrotating pairs of toroidal vortices—see [Fig. 5-22a](#).

We close this section by reminding the reader that since all laminar flows are subject to instability, all exact solutions described in this chapter are, in principle, valid only over a finite range of their governing parameters, such as the Reynolds or Taylor numbers.

3-3 POISEUILLE FLOW THROUGH DUCTS

Whereas Couette flows are driven by moving walls, Poiseuille flows are generated by pressure gradients, with application primarily to ducts. They are named after Jean Léonard

Marie Poiseuille (1840), a French physicist who experimented with low-speed flow in tubes.

The Poiseuille motion arises in the context of a straight duct of arbitrary but constant shape, as illustrated in [Fig. 3-6](#). There will be an *entrance effect*, i.e., a thin initial shear layer and core acceleration as depicted in [Fig. 1-10](#). The shear layers grow and meet, and the core disappears within a fairly short entrance length L_e . Page 83 Shah and London (1978) show that, regardless of duct shape, the entrance length can be correlated for laminar motions according to

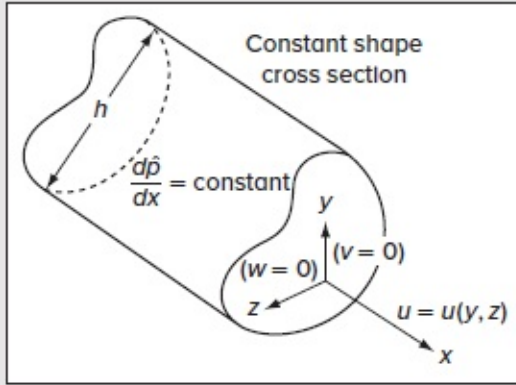


FIGURE 3-6

Fully developed duct flow.

$$\frac{L_e}{D_h} \approx C_1 + C_2 Re_{D_h} \quad (3-28)$$

where $C_1 \approx 0.5$, $C_2 \approx 0.05$, and D_h is a suitable “diameter” scale for the duct. Since transition to turbulence occurs at about $Re \approx 2000$, L_e is thus limited to, at most, 100 diameters.

For $x > L_e$, the velocity becomes purely axial and no longer varies with the streamwise coordinate x . In this case, $v = w = 0$ and $u = u(y, z)$. The flow is then called *fully developed*, as depicted in [Fig. 3-6](#). For fully developed flow, the continuity and momentum equations for incompressible fluids, [Eqs. \(3-1\)](#) and [\(3-2\)](#), reduce to

$$\begin{aligned} \text{Continuity:} \quad & \frac{\partial u}{\partial x} = 0 \quad \text{or} \quad u \neq u(x) \\ \text{Momentum equations:} \quad & \frac{\partial \hat{p}}{\partial x} = \mu \left(\frac{\partial^2 u}{\partial y^2} + \frac{\partial^2 u}{\partial z^2} \right) \quad \text{and} \quad \frac{\partial \hat{p}}{\partial y} = \frac{\partial \hat{p}}{\partial z} = 0 \quad \text{or} \quad \hat{p} \neq \hat{p}(y, z) \end{aligned} \quad (3-29)$$

These relations indicate that the total pressure \hat{p} can only be a function of x for this fully developed flow. Further, since u does not vary with x , it follows from the x -momentum equation that the gradient $\partial \hat{p} / \partial x = d\hat{p} / dx = \text{const.}$ Then the basic equation of fully developed

duct flow becomes

$$\frac{\partial^2 u}{\partial y^2} + \frac{\partial^2 u}{\partial z^2} = \frac{1}{\mu} \frac{d\hat{p}}{dx} = \text{const} \quad (3-30)$$

which is subject to the no-slip condition $u_w = 0$ everywhere along the duct surface. This is the classic Poisson equation and is equivalent to the torsional stress problem in elasticity [Timoshenko and Goodier (1970)] for a simply connected cross section.[‡] Thus, there are many known solutions for different duct shapes, especially well summarized by Berker (1963). Shah and London (1978) tabulate and chart both the laminar friction and heat-transfer characteristics of many different shapes. If new shapes arise, [Eq. \(3-30\)](#) can be solved using complex-variable or numerical techniques.

Note that, as in the Couette flow problems, the acceleration terms vanish here, taking the density with them. These motions are of the creeping flow type in the sense that they remain density independent, even though the Reynolds number need not be small, as required in Sec. 2-11.1. There is no characteristic velocity U and no axial length scale L either, since we are supposedly far from the entrance or exit. The proper scaling of [Eq. \(3-30\)](#) involves μ , $d\hat{p}/dx$, and some characteristic duct width h , as suggested in [Fig. 3-6](#). The corresponding dimensionless variables may be written as

$$y^* = \frac{y}{h}, \quad z^* = \frac{z}{h}, \quad \text{and} \quad u^* = \frac{\mu u}{h^2 (-d\hat{p}/dx)} \quad (3-31)$$

where the negative pressure gradient is needed to make u^* a positive quantity. In terms of these variables, [Eq. \(3-30\)](#) becomes

$$\nabla^{*2}(u^*) = -1 \quad (3-32)$$

which is subject to $u^* = 0$ at all points on the boundary of the duct cross section.

Page 84

3-3.1 The Circular Pipe: Hagen–Poiseuille Flow

The circular pipe problem leads to our most celebrated viscous-flow profile, first studied by Hagen (1839) and Poiseuille (1840). Because the flow is fully developed, the single spatial variable we have is $r^* = r/r_0$, where r_0 denotes the pipe radius. The Laplacian operator reduces to

$$\nabla^2 = \frac{1}{r} \frac{d}{dr} \left(r \frac{d}{dr} \right)$$

and the solution of [Eq. \(3-32\)](#) is simply

$$u^* = -\frac{1}{4} r^{*2} + C_1 \ln r^* + C_2 \quad (3-33)$$

Since the velocity must remain finite (i.e., physically bounded) at the centerline, we reject the logarithmic term and set $C_1 = 0$. Moreover, the no-slip condition will be satisfied by setting $C_2 = +\frac{1}{4}$. The pipe-flow solution turns into

$$u = u_{\max} \left(1 - \frac{r^2}{r_0^2} \right); \quad u_{\max} = \left(-\frac{d\hat{p}}{dx} \right) \frac{r_0^2}{4\mu} \quad (3-34)$$

Thus, the velocity distribution in fully developed laminar pipe flow is a paraboloid of revolution about the centerline (i.e., the *Poiseuille paraboloid*). With the velocity profile in hand, it is helpful to evaluate the total volume flow rate Q , which is defined as

$$Q = \int_{\text{section}} u dA$$

where the circular element of area $dA = 2\pi r dr$ is suitable for this cross section because along any such circular strip the integrand remains constant. For this reason, straightforward integration of Poiseuille's paraboloid yields

$$Q_{\text{pipe}} = -\frac{\pi r_0^4}{8\mu} \frac{d\hat{p}}{dx} \quad (3-35)$$

The average speed or mean-flow velocity may be immediately deduced using $\bar{u} = Q/A$ or

$$\bar{u} = -\frac{r_0^2}{8\mu} \frac{d\hat{p}}{dx} = \frac{1}{2} u_{\max} \quad (3-36)$$

The maximum centerline speed is, therefore, twice the average speed. Finally, the constant wall shear stress may be determined to be

$$\tau_w = \mu \left(-\frac{du}{dr} \right)_w = \frac{1}{2} r_0 \left(-\frac{d\hat{p}}{dx} \right) = \frac{4\mu \bar{u}}{r_0} \quad (3-37)$$

Even though τ_w is proportional to the mean-flow velocity (laminar flow), it is customary, anticipating turbulent flow, to nondimensionalize wall shear with the pipe *dynamic pressure*, $\frac{1}{2} \rho \bar{u}^2$ by analogy with the skin-friction coefficient in [Eq. \(3-8\)](#). In fact, two different friction factor definitions are commonly used in the literature:

$$\Lambda = \frac{8\tau_w}{\rho \bar{u}^2} = \text{Darcy friction factor} \quad (3-38)$$

$$C_f = \frac{2\tau_w}{\rho \bar{u}^2} = \frac{1}{4} \Lambda = \text{Fanning friction factor, or skin friction coefficient}$$

By substituting [Eq. \(3-37\)](#) into [Eqs. \(3-38\)](#), we recover the classic relations

$$\Lambda = \frac{64}{Re_D} \quad \text{and} \quad C_f = \frac{16}{Re_D} \quad (\text{laminar pipe flow}) \quad (3-39)$$

As with Couette flow's [Eq. \(3-9\)](#), the Poiseuille number turns into a pure constant in laminar tube flow, namely,

$$Po = C_f Re_D = \frac{2\tau_w D}{\mu \bar{u}} = 16$$

This classic laminar-flow solution proves to be in good agreement with experimental measurements, as shown in [Fig. 3-7](#). The flow undergoes transition to turbulence at approximately $Re_D \approx 2000$, a value that can be raised somewhat by reducing flow disturbances. Above $Re_D \approx 3000$, the flow becomes fully turbulent. The curve labeled “Blasius” is a curve fit to turbulent-flow data, $C_f \approx 0.0791/Re_D^{1/4}$, by Prandtl's celebrated student Heinrich Blasius (1913)—one of the first demonstrations of the power of dimensional analysis.

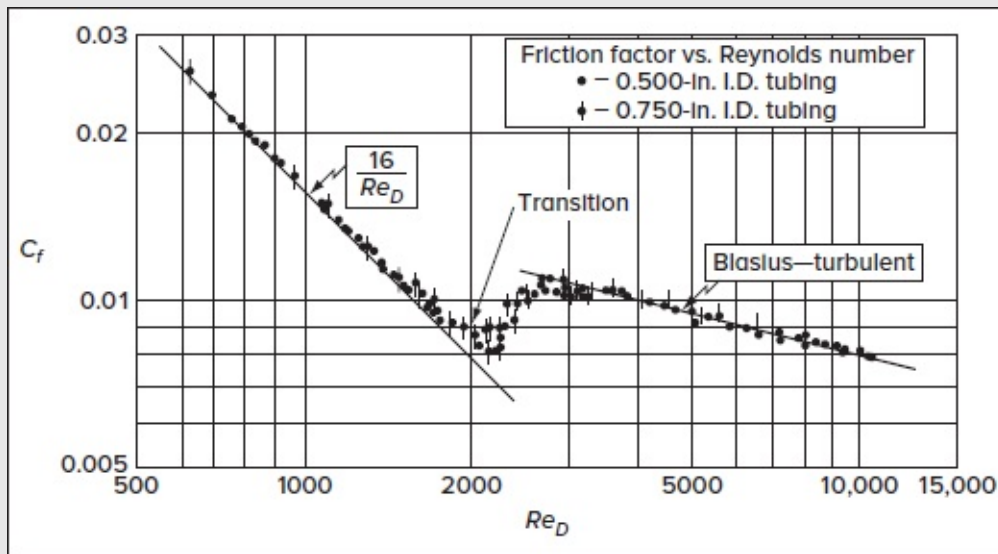


FIGURE 3-7

Comparison of theory and experiment for the friction factor of air flowing in small-bore tubes. [After Senecal and Rothfus (1953).]

3-3.1.1 MICROFLOWS: TUBE FLOW OF GASES WITH SLIP. The classical Poiseuille flow, [Eq. \(3-34\)](#), assumes no-slip conditions at the walls. If the Knudsen number, $Kn = \ell/D$, is sufficiently large, due to either large ℓ or small D , slip can occur at the walls, and the flow rate and velocity will increase for a given pressure gradient. In [Eq. \(3-33\)](#), C_1 will still be zero, but C_2 will have to satisfy the slip condition of [Eq. \(1-80\)](#): $u_w = \ell(\partial u/\partial r)$ at $r = r_0$. When the new value of C_2 is found, the velocity and flow rate become

$$u = -\frac{1}{4\mu} \frac{d\hat{p}}{dx} (r_0^2 - r^2 + 2\ell r_0) \quad \text{and} \quad Q = \frac{\pi r_0^4}{8\mu} \left(-\frac{d\hat{p}}{dx} \right) \left(1 + 8 \frac{\ell}{D} \right) \quad (3-40)$$

The flow rate is thus increased over the no-slip case by the fraction $8\ell/D = 8Kn$. If we require, for example, that the slip flow-rate effect be less than 2 percent, then Kn must be less than 0.0025. This is why we stated in Sec. 1-4.2 that if $Kn = O(0.1)$ is not small enough, slip can occur. The complete derivation of [Eqs. \(3-40\)](#) is given as an end-of-chapter problem.

Equations (3-40) are applicable to gases. For *liquid* slip flows, one can, as a first approximation, replace the mean free path ℓ by the slip length $L_{\text{slip}} = u_w/(\partial u/\partial n)_w$. For further reading on microchannel flows, see the monograph by Karniadakis and Bestok (2001).

3-3.2 Combined Couette–Poiseuille Flow Between Plates

Let us now return to our first Couette flow example, illustrated in [Fig. 3-1](#), and impose a constant pressure gradient $(d\hat{p}/dx)$ on the flow in addition to the moving upper wall. The differential equation to be solved becomes

$$\mu \frac{d^2 u}{dy^2} = \frac{d\hat{p}}{dx} = \text{const} \quad (3-41)$$

subject to the no-slip condition $u(-h) = 0$. The solution is

$$\frac{u}{U} = \frac{1}{2} \left(1 + \frac{y}{h} \right) + P \left(1 - \frac{y^2}{h^2} \right) \quad P = \left(-\frac{d\hat{p}}{dx} \right) \frac{h^2}{2\mu U} \quad (3-42)$$

The outcome may be seen to be a linear superposition, made possible by the absence of the nonlinear convective acceleration, of Couette wall-driven motion (first term) and Poiseuille pressure-driven motion (second term). The joint expression is plotted in [Fig. 3-8](#) for various values of the dimensionless pressure gradient P . Of particular interest is the dashed line at $P = -\frac{1}{4}$, for which the shear stress $\mu(\partial u/\partial y)$ at the lower wall vanishes. For $P < -\frac{1}{4}$ there is *backflow* or *reverse* flow at the lower wall, which is an indication of “flow separation” in unbounded shear layers Page 86([Chap. 4](#)). In terms of the “thickness” ($2h$) of the shear layer, we may write the separation criterion $P = -\frac{1}{4}$ in the form

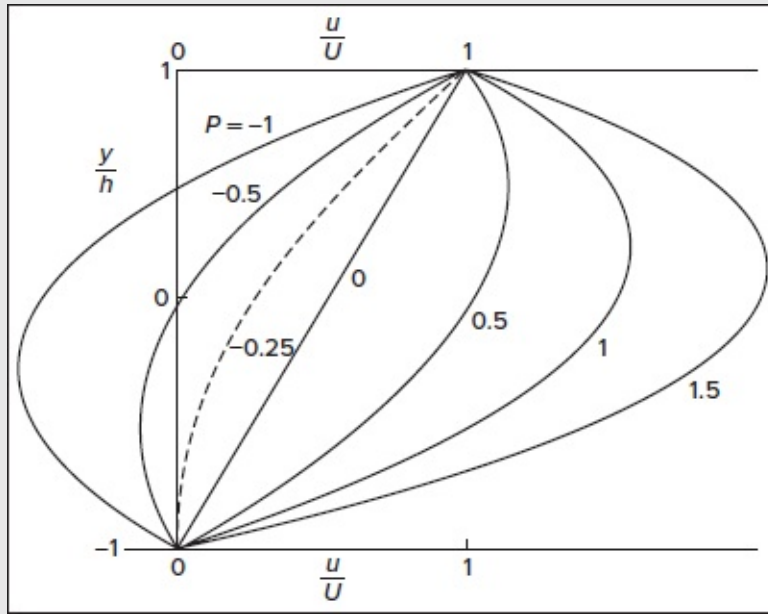


FIGURE 3-8

Combined Couette–Poiseuille flow between parallel plates, from [Eq. \(3-42\)](#). Backflow or “flow separation” occurs if $P < 1/4$.

$$\frac{d\hat{p}}{dx} \frac{(2h)^2}{\mu U} = 2 \quad (3-43)$$

This is identical in form to the laminar-boundary-layer separation estimates to be discussed in [Chap. 4](#), except that the constant “2” is too small.

If $U = 0$ (fixed walls), [Eq. \(3-42\)](#) reduces to pure Poiseuille flow between parallel plates:

$$u = u_{\max} \left(1 - \frac{y^2}{h^2} \right); \quad u_{\max} = \left(-\frac{d\hat{p}}{dx} \right) \frac{h^2}{2\mu} \quad (3-44)$$

This expression is reminiscent of the laminar pipe flow [Eq. \(3-34\)](#). As usual, the flow rate per unit depth can be readily determined to be

$$Q = \int_{-h}^{+h} u dy = \frac{4}{3} h u_{\max} \quad \text{or} \quad \bar{u} = \frac{Q}{2h} = \frac{2}{3} u_{\max} \quad (3-45)$$

The average speed, therefore, increases to two-thirds of the maximum centerline speed relative to the pipe flow result in [Eq. \(3-36\)](#). The wall shear stress is $\tau_w = 3\mu\bar{u}/h$ or, in dimensionless form,

$$\Lambda = \frac{8\tau_w}{\rho\bar{u}^2} = \frac{24\mu}{\rho h\bar{u}} = \frac{24}{Re_h} \quad C_f = \frac{2\tau_w}{\rho\bar{u}^2} = \frac{6\mu}{\rho\bar{u}h} \quad \text{or} \quad Po = C_f Re_h = 6 \quad (3-46)$$

It can hence be seen that the characteristics of Poiseuille flow between plates are analogous to their laminar pipe-flow counterparts.

3-3.3 Noncircular Ducts

Since [Eq. \(3-32\)](#) for fully developed duct flow is equivalent to a classic Dirichlet problem, it is not surprising that an enormous number of exact solutions are known for noncircular shapes, as reviewed by Berker (1963). Some of these shapes are shown in [Fig. 3-9](#). Each solution is fascinating, but our mathematical ardor should be dampened somewhat by the practical fact that limacon-shaped ducts, for example, are not commercially available at present. Nevertheless, we list a few of these solutions because they lead to a valuable approximate principle, namely, the *hydraulic radius*.

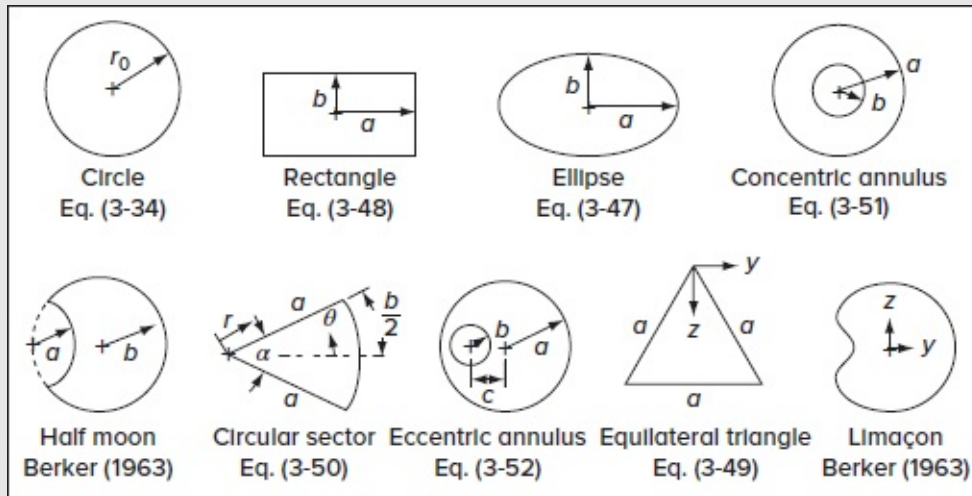


FIGURE 3-9

Some cross sections for which fully developed flow solutions are known; for additional configurations, consult Berker (1963) or Shah and London (1978).

Elliptical section: $y^2/a^2 + z^2/b^2 \leq 1$:

$$u(y, z) = \frac{1}{2\mu} \left(-\frac{d\hat{p}}{dx} \right) \frac{a^2 b^2}{a^2 + b^2} \left(1 - \frac{y^2}{a^2} - \frac{z^2}{b^2} \right) \quad Q = \frac{\pi}{4\mu} \left(-\frac{d\hat{p}}{dx} \right) \frac{a^3 b^3}{a^2 + b^2} \quad (3-47)$$

Page 87Rectangular section: $-a \leq y \leq a, -b \leq z \leq b$:

$$u(y, z) = \frac{16a^2}{\mu\pi^3} \left(-\frac{d\hat{p}}{dx} \right) \sum_{i=1,3,5,\dots}^{\infty} (-1)^{(i-1)/2} \left[1 - \frac{\cosh(\frac{1}{2}i\pi z/a)}{\cosh(\frac{1}{2}i\pi b/a)} \right] \frac{\cos(\frac{1}{2}i\pi y/a)}{i^3} \quad (3-48)$$

$$Q = \frac{4ba^3}{3\mu} \left(-\frac{d\hat{p}}{dx} \right) \left[1 - \frac{192a}{\pi^5 b} \sum_{i=1,3,5,\dots}^{\infty} \frac{\tanh(\frac{1}{2}i\pi b/a)}{i^5} \right]$$

Equilateral triangle of side a : coordinates in [Fig. 3-9](#):

$$u(y, z) = \frac{1}{2\sqrt{3}a\mu} \left(-\frac{d\hat{p}}{dx} \right) \left(z - \frac{1}{2}a\sqrt{3} \right) (3y^2 - z^2) \quad Q = \frac{a^4\sqrt{3}}{320\mu} \left(-\frac{d\hat{p}}{dx} \right) \quad (3-49)$$

Circular sector: $-\frac{1}{2}\alpha \leq \theta \leq +\frac{1}{2}\alpha$, $0 \leq r \leq a$:

$$u(r, \theta) = \frac{d\hat{p}/dx}{4\mu} \left[r^2 \left(1 - \frac{\cos 2\theta}{\cos \alpha} \right) - \frac{16a^2\alpha^2}{\pi^3} \sum_{i=1,3,5,\dots}^{\infty} (-1)^{(i+1)/2} \left(\frac{r}{a} \right)^i \frac{\cos(i\pi\theta/\alpha)}{i(i+2\alpha/\pi)(i-2\alpha/\pi)} \right] \quad (3-50)$$

$$Q = \frac{a^4}{4\mu} \left(-\frac{d\hat{p}}{dx} \right) \left[\frac{\tan \alpha - \alpha}{4} - \frac{32\alpha^4}{\pi^5} \sum_{i=1,3,5,\dots}^{\infty} \frac{1}{i^2(i+2\alpha/\pi)^2(i-2\alpha/\pi)} \right]$$

Concentric circular annulus: $b \leq r \leq a$:

$$u(r) = -\frac{d\hat{p}/dx}{4\mu} \left[a^2 - r^2 + (a^2 - b^2) \frac{\ln(a/r)}{\ln(b/a)} \right] \quad Q = \frac{\pi}{8\mu} \left(-\frac{d\hat{p}}{dx} \right) \left[a^4 - b^4 - \frac{(a^2 - b^2)^2}{\ln(a/b)} \right] \quad (3-51)$$

This assortment is but a sample of the wealth of solutions available. The formula for a concentric annulus is important in viscometry, with a measured Q being used to calculate μ . To increase the pressure drop, the clearance $(a - b)$ is held small, in which case [Eq. \(3-51\)](#) for Q becomes the difference between two nearly equal numbers. However, if we expand the bracketed term in a series, the result is

$$(a^4 - b^4) - \frac{(a^2 - b^2)^2}{\ln(a/b)} = \frac{4}{3}b(a - b)^3 + \frac{2}{3}(a - b)^4 + \dots + O(a - b)^5$$

so that Q for small clearances is seen to be cubic in $(a - b)$, namely, $\mu Q \approx -\frac{1}{6}\pi b(a - b)^3 d\hat{p}/dx$.

The eccentric annulus in [Fig. 3-9](#) has practical applications, for example, when a needle valve becomes misaligned. The solution was given by Piercy et al. (1933), using an elegant complex-variable method which transformed the geometry to a concentric annulus, for which the solution was already given by [Eq. \(3-51\)](#). We reproduce here only their expression for the volume rate of flow:

$$Q = \frac{\pi}{8\mu} \left(-\frac{d\hat{p}}{dx} \right) \left[a^4 - b^4 - \frac{4c^2 M^2}{\beta - \alpha} - 8c^2 M^2 \sum_{n=1}^{\infty} \frac{ne^{-n(\beta+\alpha)}}{\sinh(n\beta - n\alpha)} \right] \quad (3-52)$$

Page 88

$$\text{where } M = (F^2 - a^2)^{1/2} \quad F = \frac{a^2 - b^2 + c^2}{2c} \quad \alpha = \frac{1}{2} \ln \frac{F+M}{F-M} \quad \beta = \frac{1}{2} \ln \frac{F-c+M}{F-c-M}$$

Flow rates computed from this formula are compared in [Fig. 3-10](#) to the concentric result $Q_{c=0}$ from [Eq. \(3-51\)](#). It is seen that eccentricity substantially increases the flow rate, the maximum ratio of $Q/Q_{c=0}$ being 2.5 for a narrow annulus of maximum eccentricity. The curve for $b/a = 1$ can be derived from lubrication theory:

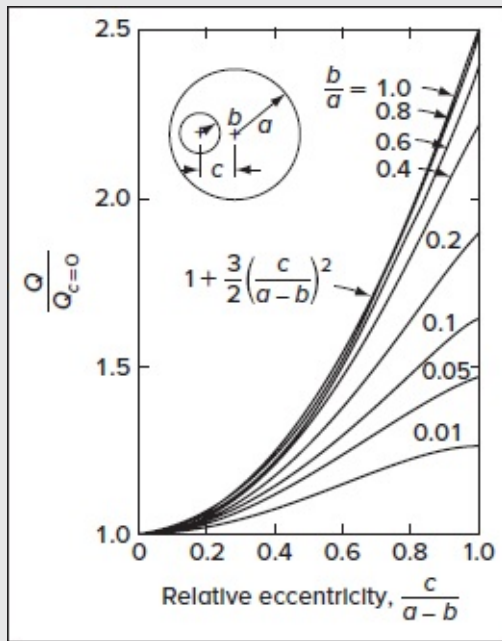


FIGURE 3-10

Volume flow through an eccentric annulus as a function of eccentricity, [Eq. \(3-52\)](#).

Narrow annulus:

$$\frac{Q}{Q_{c=0}} = 1 + \frac{3}{2} \left(\frac{c}{a-b} \right)^2 \quad (3-53)$$

The reason for the increase in Q is that the fluid tends to bulge through the wider side. This is illustrated for one case in [Fig. 3-11](#), where the wide side develops a set of closed high-velocity streamlines. This effect is well known to piping engineers, who have long noted the drastic leakage that occurs when a nearly closed valve binds to one side.

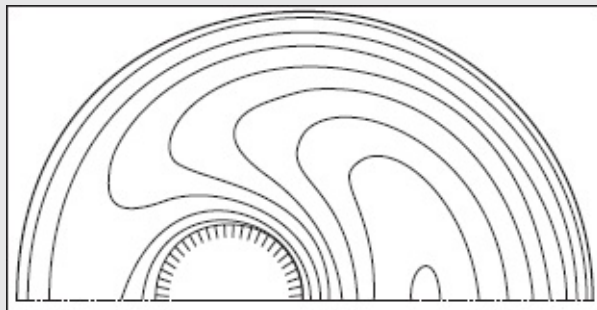


FIGURE 3-11

Constant-velocity lines for an eccentric annulus, $\frac{Q}{Q_{c=0}} = 1 + \frac{3}{2} \left(\frac{c}{a-b} \right)^2$ [After Piercy *et al.* (1933).]

3-3.4 The Hydraulic Diameter Concept

The definition of Λ proposed in [Eq. \(3-39\)](#) fails for a noncircular duct since τ_w varies around the perimeter. For example, in the equilateral-triangle duct, [Eq. \(3-49\)](#), τ_w vanishes in the corners and peaks at the midpoints of the sides. The remedy, at least partially, is to define a mean wall shear stress

$$\bar{\tau}_w = \frac{1}{P} \int_0^P \tau_w ds$$

where ds = element of arc length

P = section perimeter

Page 89 If we isolate a slug of fluid passing through the duct as in [Fig. 3-12](#) and note that there is no net momentum flux due to the fully developed flow, we can equate the net pressure and wall shear force on the fluid as follows:

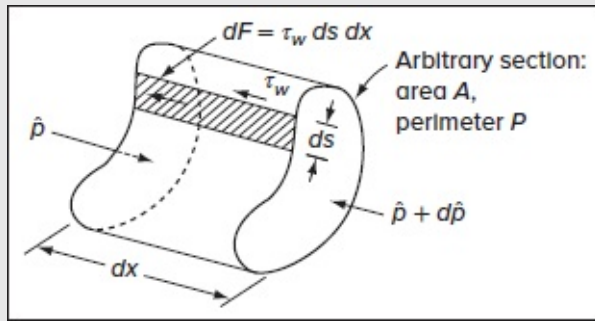


FIGURE 3-12

Force equilibrium in fully developed arbitrary duct flow.

$$dx \int_0^P \tau_w ds = -A d\hat{p}$$

or, from the definition of mean shear, we have

$$\bar{\tau}_w = \frac{A}{P} \left(-\frac{d\hat{p}}{dx} \right) \quad (3-54)$$

which is identical to [Eq. \(3-37\)](#) for a circular duct. The quantity A/P is a length that equals $\pi r_0^2 / (2\pi r_0) = r_0/2$ if the duct is circular. For a noncircular duct, then, we set $A/P = D_h/4$, where D_h denotes the *hydraulic diameter* of the cross section:

$$D_h = \frac{4A}{P} = \frac{4 \times \text{flow area}}{\text{wetted perimeter}} \quad (3-55)$$

For a cross section with multiple surfaces, P must include all wetted walls. For example, for the concentric annulus in [Fig. 3-9](#), we have

$$D_h(\text{annulus}) = \frac{4\pi(a^2 - b^2)}{2\pi a + 2\pi b} = 2(a - b) \quad (3-56)$$

or twice the clearance. By dimensional reasoning for laminar fully developed flow, we are guaranteed that the friction factor of a noncircular duct will vary inversely with a Reynolds number based on a hydraulic diameter:

$$C_f = \frac{\Lambda}{4} = \frac{\text{const}}{Re_{D_h}} \quad Re_{D_h} = \frac{\rho \bar{u} D_h}{\mu} \quad (3-57)$$

In other words, the Poiseuille number $Po = C_f Re$ remains constant for a noncircular duct. However—and this is the critical flaw—the constant usually does *not* equal 16 as it did for a circular pipe.

Using our many exact solutions from [Eqs. \(3-47\) to \(3-51\)](#), we may compute the value of $Po = C_f Re_{D_h}$ and plot them versus the section slenderness ratio b/a in [Fig. 3-13](#). We see that some are higher, and some are lower than the nominal circle value of 16, and that the error can be as high as 50 percent. For laminar flow, then, one should use the exact values of Po from [Fig. 3-13](#) or the exact formulas given here or by Shah and London (1978).

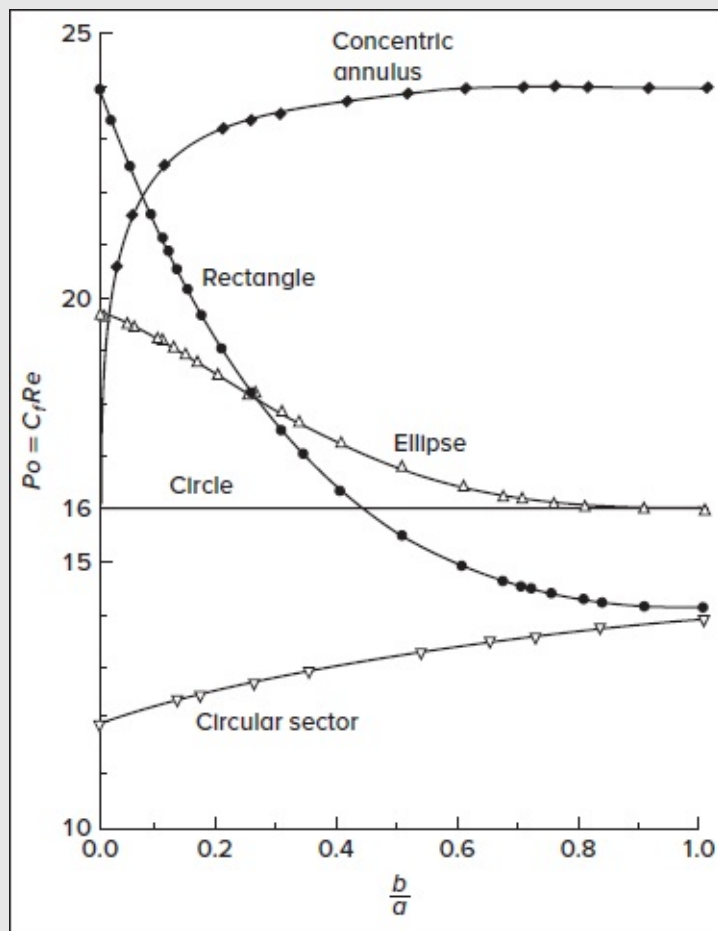


FIGURE 3-13

Comparison of Poiseuille numbers for various duct cross sections when the Reynolds number is scaled by the hydraulic diameter. [Numerical data taken from Shah and London (1978).]

We note for completeness that the equilateral triangle associated with [Eq. \(3-49\)](#) has a hydraulic diameter of $D_h = a/\sqrt{3}$ and $C_f Re = 13.33$, which is 17 percent lower than 16.

Especially vexing is the fact that the hydraulic diameter concept is insensitive to core eccentricity. The eccentric annulus in [Fig. 3-10](#) has the same value $D_h = 2(a - b)$ regardless of the value of c , yet its flow rate may vary by over 100 percent depending upon c . Analytical solutions are definitely needed. In fact, [Fig. 3-13](#) has a surprising—and very relevant—use in determining the friction factor for *turbulent* flow in noncircular ducts for which the laminar solution is known ([Chap. 6](#)).

3-3.5 Temperature Distribution in Fully Developed Duct Flow

The assumption of constant viscosity uncouples the energy and momentum equations if natural convection is neglected, and this enables us to solve for the velocity distribution in

several ducts. With $u(y, z)$ known, [Eq. \(3-3\)](#) can be solved for T , which may be a function of (x, y, z) if the boundary conditions change with x . Equation (3-3) is linear in T , making it possible to examine some separate effects and add them together later, if desired. To start, we look at the effect of viscous dissipation, assuming constant T_w . For the pipe case, $T = T(r)$ only, and [Eq. \(3-3\)](#) becomes

$$\frac{k}{r} \frac{d}{dr} \left(r \frac{dT}{dr} \right) = -\mu \left(\frac{du}{dr} \right)^2 = -\frac{16\mu \bar{u}^2 r^2}{r_0^4} \quad (3-58)$$

where we have introduced $u(r)$ from [Eq. \(3-34\)](#). Double integration leads to a logarithmic term which we discard to avoid a singularity at $r = 0$. Finally, imposing $T = T_w$ at $r = r_0$ leads to

$$T = T_w + \frac{\mu \bar{u}^2}{k} \left(1 - \frac{r^4}{r_0^4} \right) \quad (3-59)$$

which is similar to [Eq. \(3-11\)](#) for flow between parallel plates. In practice, however, the maximum temperature rise $\mu \bar{u}^2/k$ amounts to about 1°F for air and 3°F for water, assuming $\bar{u} = 100$ ft/s. This modest increase justifies ignoring dissipation except for oils, where the viscosity is large, or in gas dynamics, where velocities are high ([Chap. 7](#)). Note that the wall heat flux, which is $q_w = k dT/dr$ at $r = r_0$, gives $q_w = 4k (T_w - T_0)/r_0$, showing that the wall must be cooled in the process of maintaining constant T_w . The Nusselt number at the wall can also be determined using [Eq. \(3-15\)](#), with L taken as the pipe diameter:

$$Nu = \frac{(2r_0) q_w}{k(T_w - T_0)} = 8 \quad \text{for viscous dissipation} \quad (3-60)$$

Despite this relatively large Nu , the heat flux remains small because of the negligible temperature difference $T_w - T_0$.

3-3.6 Asymptotic Uniform Heat-Flux Approximation

Before examining the thermal-entrance problem of a sudden change in wall temperature, let us consider the conditions far downstream of such an entrance. Although the temperature varies with x , the deviation $T_w - T$ remains nearly independent of x , with a nearly constant q_w . Here we have

$$\frac{\partial}{\partial x} (T_w - T) = 0 \quad \frac{q_w}{k} = \frac{\partial T}{\partial r} = \text{const} \quad (3-61)$$

Page 91 Taken together, these conditions require that the axial gradient be independent of r :

$$\frac{\partial T}{\partial x} = \frac{\partial T_w}{\partial x} = \text{const independent of } r \quad (3-62)$$

When we neglect (or separate out) dissipation, [Eq. \(3-3\)](#) becomes

$$\rho c_p u \frac{\partial T}{\partial r} = (\text{const}) u = \frac{k}{r} \frac{\partial}{\partial r} \left(r \frac{\partial T}{\partial r} \right) \quad (3-63)$$

which can be integrated twice; again, we discard the logarithmic term that becomes unbounded at $r = 0$. With $T = T_w$ at $r = r_0$, we obtain

$$T_w - T = \frac{c_p \bar{u} r_0^2}{8k} \frac{\partial T_w}{\partial x} \left(3 - \frac{4r^2}{r_0^2} + \frac{r^4}{r_0^4} \right) \quad (3-64)$$

from which we can calculate the *Nusselt* number. However, from a practical standpoint, Nu should not be based upon $T_w - T_0$ but upon a mean difference $T_w - T_m$, where T_m is the *cup-mixing temperature* of the fluid, computed by averaging T over the mass distribution of fluid in the pipe. This parameter is defined as

$$T_m = \frac{\int T dm}{\int dm} = \frac{\int_0^{r_0} T \rho u dA}{\int_0^{r_0} \rho u dA} \quad (3-65)$$

where $dA = 2\pi r dr$ for this geometry. For incompressible flow, the density cancels out, and using u from [Eq. \(3-34\)](#) for Poiseuille flow and T from [Eq. \(3-64\)](#), we obtain

$$T_w - T_m = \frac{11}{18} \left(\frac{3\rho c_p \bar{u} r_0^2}{8k} \frac{\partial T_w}{\partial x} \right) = \frac{11}{18} (T_w - T_0) \quad (3-66)$$

It is this temperature difference upon which engineers base the dimensionless wall heat-transfer, or Nusselt, number,

$$Nu_m = \frac{2r_0 q_w}{k(T_w - T_m)} = \frac{48}{11} = 4.36 \quad \text{asymptotic uniform heat flux} \quad (3-67)$$

A similar but algebraically more complicated solution for the asymptotic constant wall temperature yields

$$Nu_m = 3.66 \quad (3-68)$$

as will be shown in the next section. These asymptotic values are more sensitive to duct cross section than to wall conditions. Calculations for other duct shapes (rectangular, triangular, etc.) are given by Shah and London (1978).

3-3.7 Thermal Entrance: The Graetz Problem

Let us move to the problem of developing temperature profiles $T(x, r)$ in a pipe, due to a sudden change in wall temperature ([Fig. 3-14](#)). By neglecting dissipation and axial heat conduction, [Eq. \(3-3\)](#) reduces to

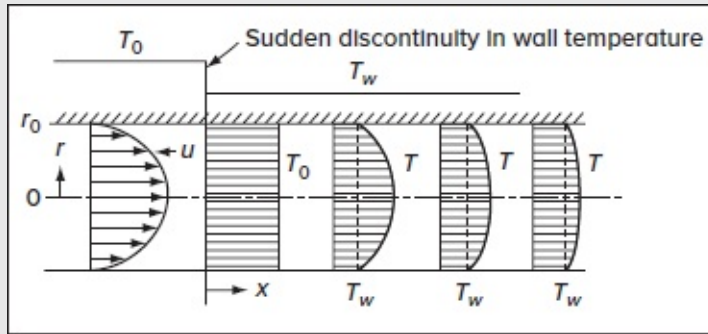


FIGURE 3-14

A thermal-entrance problem.

$$u \frac{\partial T}{\partial x} \approx \frac{\alpha}{r} \frac{\partial}{\partial r} \left(r \frac{\partial T}{\partial r} \right) \quad (3-69)$$

Page 92 where $\alpha = k/(\rho c_p)$ is the thermal diffusivity of the fluid. The velocity distribution $u(x, r)$ is assumed known in this expression and may be one of three types:

1. $u = \bar{u} = \text{const}$, or slug flow: appropriate for low Prandtl number fluids (such as liquid metals), where T develops much faster than u .
2. $u = 2\bar{u}(1 - r^2/r_0^2)$, or Poiseuille flow: appropriate for high Prandtl number fluids (oils), or when the thermal entrance is far downstream of the duct entrance.
3. Developing u profiles (Sec. 4-9): suitable for any Prandtl number when the velocity and temperature entrance values are taken at the same position.

The thermal-entrance problem with a sudden change in wall temperature is illustrated in [Fig. 3-14](#). The solution was given as an infinite series by Graetz (1883) for slug flow and another series in 1885 for Poiseuille flow. Further details and other geometries are given in the texts by Shah and London (1978) or by Kays and Crawford (1993).

With reference to [Fig. 3-14](#), the proper boundary conditions on $T(x, r)$ for [Eq. \(3-69\)](#) are

$$T(0, r) = T_0 \quad \text{and} \quad T(r_0, x) = T_w \quad (3-70)$$

Let us now outline Graetz' solution for the Poiseuille motion. A suitable assortment of dimensionless variables includes

$$T^* = \frac{T_w - T}{T_w - T_0} \quad r^* = \frac{r}{r_0} \quad x^* = \frac{x}{d_0 Re Pr} \quad (3-71)$$

where $Re = \bar{u}d_0/\nu$ stands for the diameter Reynolds number, Pr denotes the Prandtl number, and so $RePr = \rho c_p \bar{u}d_0/k$ represents the Peclet number, named after the French physicist Jean Claude Eugène Péclet. The variables in [Eq. \(3-71\)](#) transform [Eqs. \(3-69\)](#) and [\(3-70\)](#) into

$$\frac{\partial T^*}{\partial x^*} = \frac{2}{r^*(1-r^{*2})} \frac{\partial}{\partial r^*} \left(r^* \frac{\partial T^*}{\partial r^*} \right) \quad \text{with} \quad T^*(r^*, 0) = 1 \quad \text{and} \quad T^*(1, x^*) = 0 \quad (3-72)$$

Note that [Eqs. \(3-72\)](#) are parameter free because of our judicious choice of variables (T^* , r^* , x^*). It is clear that the variables are separable, so that a product solution is viable. Using

$$T^*(r^*, x^*) = f(r^*) g(x^*) \quad (3-73)$$

we may substitute into [Eq. \(3-72\)](#) and retrieve

$$\frac{g'}{2g} = \frac{r^* f'' + f'}{r^* (1 - r^{*2}) f} = -\lambda^2 = \text{const} \quad (3-74)$$

Although $g(x^*)$ exhibits the exponential form $g = C \exp(-2\lambda^2 x^*)$, the equation for $f(r^*)$ is somewhat less familiar. To make the product solution $T = f(r^*) g(x^*)$ satisfy the condition $T^*(r^*, 0) = 1$ for all r^* , we take advantage of linearity and superimpose all possible solutions, so that the proper formulation is, finally,

$$T^*(r^*, x^*) = \sum_{n=0}^{\infty} C_n f_n(r^*) \exp(-2\lambda_n^2 x^*) \quad (3-75)$$

where the functions f_n are characteristics of [Eq. \(3-74\)](#), namely,

$$r^* f_n'' + f_n' + \lambda_n^2 r^* (1 - r^{*2}) f_n = 0 \quad (3-76)$$

To make further headway, we take $f_n(0) = 1$ for simplicity and force $f_n(1) = 0$ to satisfy the wall-temperature condition $T^*(1, x^*) = 0$ in [Eq. \(3-72\)](#). Then the solution is complete if the other (initial) condition from [Eq. \(3-72\)](#) is satisfied:

$$T^*(r^*, 0) = 1 = \sum_{n=0}^{\infty} C_n f_n(r^*) \quad (3-77)$$

Graetz proves that the eigenfunctions f_n are orthogonal over the interval 0 to 1 with respect to the weighting function $r^*(1 - r^{*2})$. Thus, if one multiplies [Eq. \(3-77\)](#) by $r^*(1 - r^{*2}) f_m$ and integrates from 0 to 1, the constants may be found as follows:

$$C_n = \frac{\int_0^1 r^* (1 - r^{*2}) f_n dr^*}{\int_0^1 r^* (1 - r^{*2}) f_n^2 dr^*} \quad (3-78)$$

We remark that [Eq. \(3-76\)](#), with its two conditions $f_n(0) = 1$ and $f_n(1) = 0$, constitute an eigenvalue problem that can be satisfied only for certain discrete values of λ_n , namely, the *eigenvalues* of the Graetz function f_n . [Table 3-1](#) gives Page 93 the first 10 eigenvalues and their associated constants. These are sufficient to calculate Nusselt numbers for almost any given wall condition, even an arbitrary distribution of T_w^* .

TABLE 3-1**Important constants in the Graetz problem**

n	λ_n	C_n	$-C_n f'_n(1)$
0	2.7043644	+1.46622	1.49758
1	6.679032	-0.802476	1.08848
2	1.67338	+0.587094	0.92576
3	14.67108	-0.474897	0.83036
4	18.66987	-0.404402	0.76474
5	22.67	-0.35535	0.71571
6	26.67	+0.31886	0.67798
7	30.67	-0.29049	0.64711
8	34.67	+0.26769	0.62119
9	38.67	-0.24890	0.59900

For large n , Sellars et al. (1956) provide the following approximations:

$$\lambda_n \approx 4n + \frac{8}{3} \quad C_n \approx (-1)^n \frac{2\Gamma\left(\frac{2}{3}\right)6^{2/3}}{\pi\lambda_n^{2/3}} = \frac{(-1)^n(2.8461)}{\lambda_n^{2/3}} \quad \text{and} \quad -C_n f'_n(1) \approx \frac{4\left(\frac{4}{3}\right)^{1/6}\Gamma\left(\frac{2}{3}\right)}{\pi\lambda_n^{1/3}\Gamma\left(\frac{4}{3}\right)} = \frac{2.0256}{\lambda_n^{1/3}} \quad (3-79)$$

These formulas have been used to compute the last five rows of [Table 3-1](#) with an error of less than 0.15 percent.

To calculate the Nusselt number at the wall, the cup-mixing temperature is needed, which can be obtained by combining [Eqs. \(3-65\)](#) and [\(3-77\)](#):

$$T_m^* = 4 \int_0^1 T^* (1 - r^{*2}) r^* dr^* \quad (3-80)$$

By inserting T^* from [Eq. \(3-75\)](#), we arrive at

$$Nu_x = \frac{2r_0 q_w}{k(T_w - T_m)} = \frac{\sum C_n f'_n(1) \exp(-2\lambda_n^2 x^*)}{2 \sum C_n \lambda_n^{-2} f'_n(1) \exp(-2\lambda_n^2 x^*)} \quad (3-81)$$

which converges well except at very small x^* . For large $x^*(> 0.05)$, the first term of the series is dominant, giving the asymptotic result

$$Nu_x(x^* > 0.05) \approx \frac{1}{2} \lambda_0^2 = 3.66 \quad (3-82)$$

which is the thermally fully developed result already mentioned in [Eq. \(3-68\)](#). For small x^* , the results fit the approximation

$$Nu_x \approx 1.076x^{*-1/3} - 1.064 \quad (3-83)$$

which carries a smaller than 1 percent error for $x^* < 0.0004$.

3-3.8 Mean Nusselt Number

The total heat transferred to (or from) the wall is a useful quantity, since it equals the heat lost (or gained) by the fluid over the total length L of the tube. In this vein, we define a mean wall heat flux per unit area

$$\bar{q}_w = \frac{1}{A_w} \int q_w dA_w = \frac{1}{L} \int_0^L q_w dx \quad (3-84)$$

This mean heat flux must exactly balance the enthalpy change of the fluid between $x = 0$ and $x = L$:

$$\bar{q}_w A_w = \rho \bar{u} c_p (\pi r_0^2) [T_m(L) - T_0] \quad (3-85)$$

so that $T_m(L)$ at the exit can be calculated from the mass flow rate in the tube. The dimensionless form \bar{q}_w is called the mean Nusselt number and is given by

$$Nu_m = \frac{2r_0 \bar{q}_w}{k \Delta T} \quad (3-86)$$

Page 94 If T_w varies, the choice of a suitable temperature difference ΔT becomes somewhat arbitrary. The reader may verify as an exercise that if one chooses the logarithmic mean-temperature difference,

$$\Delta T_{\ln} = \frac{[T_w(0) - T_m(0)] - [T_w(L) - T_m(L)]}{\ln \{ [T_w(0) - T_m(0)] / [T_w(L) - T_m(L)] \}} \quad (3-87)$$

then Nu_m is simply the average value of Nu_x in the tube between 0 and L :

$$Nu_m (\log \text{ mean}) = \frac{2r_0 \bar{q}_w}{k \Delta T_{\ln}} = \frac{1}{L} \int_0^L Nu_x dx \quad (3-88)$$

For the present Graetz problem (with a large Prandtl number), we can evaluate Nu_m by using the differential form of [Eq. \(3-85\)](#), namely,

$$q_w 2\pi r_0 dx = \rho \bar{u} \pi r_0^2 c_p dT_m \quad \text{or} \quad 4Nu_x dx^* = -dT_m^* / T_m^* \quad (3-89)$$

We can integrate this from $x^* = 0, T_m^* = 1$ to $x^* = L^*, T_m^* = T_m^*(L)$ with a starkly simple result:

$$Nu_m = -\frac{1}{4L^*} \ln T_m^*(L) \quad (3-90)$$

This is a general result for constant wall temperature. By carrying out the integration of [Eq. \(3-80\)](#), we find

$$\text{Poiseuille flow:} \quad T_m^*(x^*) = \sum_{n=0}^{\infty} 4C_n f'_n(1) \lambda_n^{-2} \exp(-2\lambda_n^2 x^*) \quad (3-91)$$

Figure 3-15 shows the computations of Goldberg (1958) for a mean Nusselt number with velocity and temperature effects which are assumed to start at the same point, $x = 0$. The upper curve corresponds to slug flow (type 1), valid for $Pr \ll 1$ (liquid metals). The lowest curve is for Poiseuille flow (type 2) for $Pr \gg 1$ (oils) and is computed from Eqs. (3-90) and (3-91). The intermediate curves are for type 3, where velocity and temperature develop simultaneously. Note that the abscissa is the Graetz number, $L^* = x^* (L)$, which is based on the diameter $2r_0$. The slug-flow curve ($Pr = 0$) is unique in that the parabolic velocity never develops and the limiting value of Nu_m is 5.78 at large L^* [Graetz (1883)].

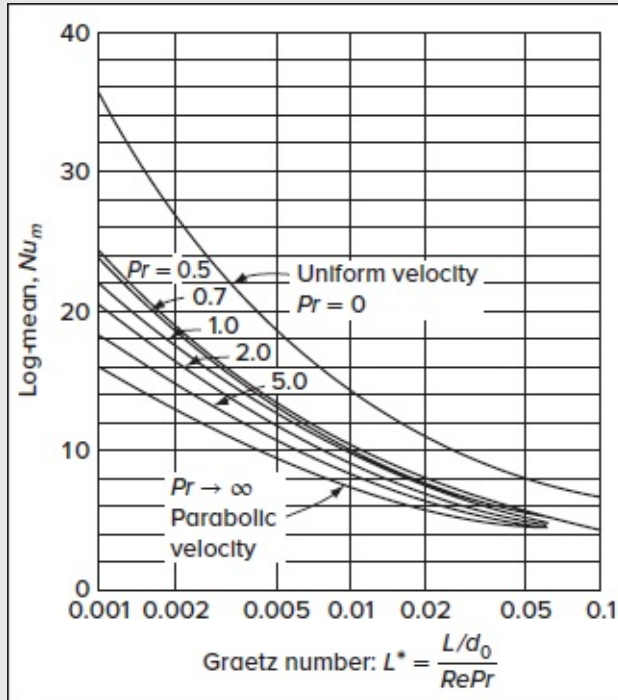


FIGURE 3-15

Finite-difference calculations for the log-mean Nusselt number in laminar pipe flow with developing velocity profiles. [After Goldberg (1958).]

All of the curves for finite Pr in Fig. 3-15 approach $Nu_m = 3.66$ at large L^* . We are reasonably close to this limit when $L^* \approx 0.05$. Thus, we may define the *thermal-entrance length* in pipe flow as

$$L_{e,\text{thermal}} \approx 0.05 d_0 Re_D Pr \quad (3-92)$$

The resulting expression resembles the velocity-entrance-length correlation of Eq. (3-28) with the addition of the Prandtl number multiplier.

The Graetz problem, especially for oils ($Pr \gg 1$), has many practical applications. For computation, one may reproduce the lower curve in Fig. 3-15 using a formula proposed by

Hausen (1943),

$$Nu_m(Pr \gg 1) \approx 3.66 + \frac{0.075/L^*}{1 + 0.05/L^{*2/3}} \quad (3-93)$$

where $L^* = (L/d_0)/(Re_d Pr)$. The error of this approximation is ± 5 percent.

Finally, we remark that the present analysis assumes constant fluid transport properties, whereas both liquids and gases have significant variations in μ and k with temperature. A first-order correction for this effect would be to evaluate fluid properties at the “film” temperature $(T_w + T_m)/2$. If the wall and fluid temperatures differ by more than 20°C, one should further correct the previous formulas for variable properties. Chapter 15 of the text by Kays and Crawford (1993) offers a detailed discussion of these correction factors.

3-4 UNSTEADY DUCT FLOWS

Some interesting problems of unsteady duct flow can be solved by retaining the fully developed flow assumption, and we give two examples here for circular pipe flow, with the same principle being applicable to other shapes. If we assume that the pipe axial velocity $u = u(r, t)$ only, with $v = w = 0$, then the continuity equation becomes identically satisfied and the momentum equation reduces to

$$\rho \frac{\partial u}{\partial t} = -\frac{d\hat{p}}{dx} + \mu \left(\frac{\partial^2 u}{\partial r^2} + \frac{1}{r} \frac{\partial u}{\partial r} \right) \quad (3-94)$$

which is analogous to the linear heat-conduction equation with a source term. The pressure gradient can vary only with time and hence represents a uniformly distributed heat source. In what follows, let us consider two cases.

3-4.1 Starting Flow in a Circular Pipe

Let us suddenly apply a constant pressure gradient $d\hat{p}/dx$ to a fluid occupying a long circular pipe, which is otherwise at rest at $t = 0$. An axial motion is induced, which gradually approaches the steady Poiseuille profile

$$u = u_{\max}(1 - r^{*2})$$

where $r^* = rr_0$. This important problem was solved by Szymanski (1932). Two boundary conditions may be applied here:

$$u(r, 0) = 0 \quad (\text{initial condition}) \quad \text{and} \quad u(r_0, t) = 0 \quad (\text{no-slip condition}) \quad (3-95)$$

Taking advantage of linearity, the variables in [Eq. \(3-94\)](#) can be separated by subtracting the steady Poiseuille flow and working with the *deviation* of u from the Poiseuille paraboloid.

This removes the inhomogeneity $d\hat{p}/dx$ and converts the solution of [Eq. \(3-94\)](#) to the form $u = J_0(\lambda r^*) e^{-\lambda^2 t^*}$, where J_0 denotes the Bessel function of the first kind. The no-slip condition requires $J_0(\lambda_n)$ to vanish for each value of the separation constant, thus making λ_n the zeroes of the Bessel function, which are tabulated in [Table 3-2](#). Since J_0 is not a paraboloid, we must sum over the functions $J_0(\lambda_n r^*)$ to obtain a negative paraboloid and thus satisfy the initial condition of the fluid at rest. The coefficients can be readily determined using orthogonality, and the final solution for this pipe starting-flow problem reduces to

TABLE 3-2

First ten roots of the Bessel function J_0^\dagger

n	λ_n	$J_1(\lambda_n)$
1	2.4048	0.5191
2	5.5201	-0.3403
3	8.6537	0.2715
4	11.7915	-0.2325
5	14.9309	0.2065
6	18.0711	-0.1877
7	21.2116	0.1733
8	24.3525	-0.1617
9	27.4935	0.1522
10	30.6346	-0.1442

[†] For $n > 10$: $\lambda_n \approx \frac{(4n-1)\pi}{4}$ $J_1(\lambda_n) \approx (-1)^{n+1} \left(\frac{2}{\pi \lambda_n}\right)^{1/2}$

$$\frac{u}{u_{\max}} = (1 - r^{*2}) - \sum_{n=1}^{\infty} \frac{8J_0(\lambda_n r^*)}{\lambda_n^3 J_1(\lambda_n)} \exp\left(-\lambda_n^2 \frac{vt}{r_0^2}\right) \tag{3-96}$$

where $u_{\max} = (-\frac{1}{4}d\hat{p}/dx)r_0^2/\mu$ from [Eq. \(3-36\)](#). Numerical results are plotted in [Fig. 3-16](#) for various values of the dimensionless time $t^* = vt/r_0^2$. Two points are of particular interest: (1) initially a boundary-layer effect occurs near the wall, where the fluid’s central core accelerates uniformly (potential flow) while the wall region is slowed down by friction; and (2) the flow approaches the Poiseuille paraboloid very closely even at $t^* \approx 0.75$, thus providing an estimate of how rapidly laminar tube flow responds to sudden changes. In fact, based on t^* , flows with small diameters and large viscosities develop very rapidly. For example, in a 1 cm diameter tube, the value $t^* = 0.75$ for air ($\nu = 1.5 \times 10^{-5} \text{ m}^2/\text{s}$) translates into $t = 1.25 \text{ s}$. For SAE 30 oil under the same conditions, Poiseuille flow develops in 0.06 s. Thus, in laminar small-bore pipe flows under varying pressure gradients, it is common to use a quasi-steady Poiseuille flow approximation.

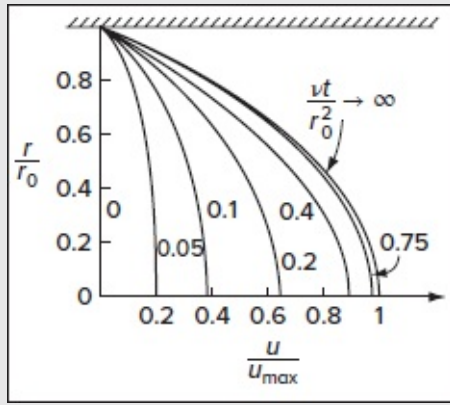


FIGURE 3-16

Instantaneous velocity profiles for starting flow in a pipe, Eq. (3.96). [After Szymanski (1932).]

3-4.2 Pipe Flow Due to an Oscillatory Pressure Gradient

As a second example, let us reconsider the solution of [Eq. \(3-94\)](#) when the pressure gradient varies sinusoidally with time, specifically

$$-\frac{1}{\rho} \frac{d\hat{p}}{dx} = K e^{i\omega t} \quad \text{where} \quad e^{i\omega t} = \cos \omega t + i \sin \omega t \quad \text{and} \quad i = \sqrt{-1} \quad (3-97)$$

We may then apply the no-slip condition and look for a long-term steady oscillation, neglecting the transient, or start-up, of the flow. This is a classic problem in mathematical physics that leads to a Bessel function with imaginary arguments:

$$\text{Oscillatory pipe flow:} \quad u(r, t) = \frac{K}{i\omega} \left[1 - \frac{J_0(ir\sqrt{i\omega/\nu})}{J_0(ir_0\sqrt{i\omega/\nu})} \right] e^{i\omega t} = \frac{K}{i\omega} \left[1 - \frac{I_0(r\sqrt{i\omega/\nu})}{I_0(r_0\sqrt{i\omega/\nu})} \right] e^{i\omega t} \quad (3-98)$$

where the identity $J_0(iz) = I_0(z)$ has been used. Equation (3-98) was first discovered by Sexl (1930), and further numerical calculations were given by Uchida (1956). Without delving into exact calculations, we can explore the general behavior of this solution using two overlapping series approximations

$$J_0(z) \approx \begin{cases} 1 - \frac{z^2}{4} + \frac{z^4}{64} - \dots & \text{for } z \ll 1 \\ \sqrt{\frac{2}{\pi z}} \cos\left(z - \frac{\pi}{4}\right) & \text{for } z \gg 1 \end{cases} \quad (3-99)$$

A closer look at [Eq. \(3-98\)](#) shows that the proper dimensionless variables are

$$r^* = \frac{r}{r_0} \quad \omega^* = \frac{\omega r_0^2}{\nu} \quad u^* = \frac{u}{u_{\max}} \quad (3-100)$$

where $u_{\max} = Kr_0^2/(4\nu)$ is the centerline velocity for steady Poiseuille flow with a pressure gradient $-\rho K$. The quantity ω^* (or Re_k) represents the *kinetic Reynolds number*, which is a measure of viscous effects in oscillating flow. It is also related to the Stokes number, $\lambda_s = \frac{1}{2}\sqrt{\omega^*}$, and the Womersley number, $\alpha = \sqrt{\omega^*}$. Similar to the static Reynolds number, oscillating flows may become turbulent when ω^* exceeds approximately 2000.

By combining [Eqs. \(3-98\)](#) and [\(3-99\)](#), two asymptotic approximations can be obtained for the velocity, which is the real part of the solution:

Small $\omega^* \ll 1$:

$$\frac{u(r^*, t)}{u_{\max}} = (1 - r^{*2}) \cos \omega t + \frac{\omega^*}{16}(r^{*4} + 4r^{*2} - 5) \sin \omega t + O(\omega^{*2}) \quad (3-101)$$

Large $\omega^* \gg 1$ (and $r^* \approx 1$):

$$\frac{u(r^*, t)}{u_{\max}} = \frac{4}{\omega^*} \left[\sin \omega t - \frac{e^{-B}}{\sqrt{r^*}} \sin(\omega t - B) \right] + O(\omega^{*-2}); \quad B \equiv (1 - r^*) \sqrt{\omega^*/2} \quad (3-102)$$

Remembering that $d\hat{p}/dx$ is proportional to $\cos \omega t$, we see that for very small ω^* , the velocity is nearly a quasi-static Poiseuille flow in phase with the slowly varying pressure gradient; the second term in [Eq. \(3-101\)](#) adds a lagging component that reduces the velocity at the centerline. At large ω^* , from [Eq. \(3-102\)](#), the flow approximately lags the pressure gradient by 90° , and again the centerline velocity is less than u_{\max} . However, near the wall, there is a region of high axial velocity, as can be seen by averaging [Eq. \(3-102\)](#) over one cycle to obtain the mean square velocity $\overline{u^2}(r^*)$. We obtain

$$\frac{\overline{u^2}}{K^2/(2\omega^2)} = 1 - \frac{2}{\sqrt{r^*}} e^{-B} \cos B + \frac{e^{-2B}}{r^*} \quad (3-103)$$

This relation is plotted in [Fig. 3-17](#) for two values of ω^* . There is an overshoot in mean velocity near the wall, which occurs when $\cos B + \sin B \approx e^{-B}$, or $B \approx 2.2841$ and $r^* \approx 1 - 3.23021/\sqrt{\omega^*}$. The corresponding speed overshoot ratio may be deduced from [Eq. \(3-103\)](#) to be

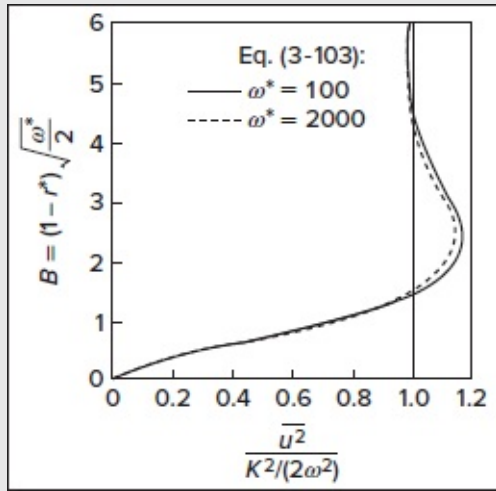


FIGURE 3-17

The near-wall velocity overshoot (Richardson's annular effect) due to an oscillatory pressure gradient.

$$\frac{\bar{u}^2}{K^2/(2\omega^2)} = \frac{\bar{u}^2}{8u_{\max}^2/\omega^{*2}} = 1.143685 + \frac{0.248826}{\sqrt{\omega^*}} + O(\omega^{*-1}) \quad (3-104)$$

The weak dependence on ω^* explains why the overshoot in [Fig. 3-17](#) diminishes slightly when the kinetic Reynolds number is increased from 100 to 2000. This effect is characteristic of oscillating duct flows and was first noted by Richardson and Tyler (1929) in a tube-flow experiment. The overshoot, now called *Richardson's annular effect*, was then verified theoretically through [Eq. \(3-102\)](#) by Sexl (1930). For a further discussion of these problems, the reader is referred to Uchida (1956) and the general review article by Rott (1964). A solution for oscillating flow in a rectangular duct is given by Tsangaris and Vlachakis (2003). The solutions for a pulsatory motion in tubes and channels with a nonzero mean pressure gradient are provided by Uchida (1956) and Majdalani (2012). They are briefly outlined in the next section.

3-4.3 Duct Flow Due to a Pulsatory Pressure Gradient

A generalization of Sexl's model can be achieved by allowing the pressure gradient to contain a steady part, which promotes unidirectional axial motion, plus an oscillatory part, which enables us to capture the effects of an arbitrary periodic motion. Such an extension can be useful in modeling arterial flows and other biological motions. To account for this pulsatory gradient, [Eq. \(3-97\)](#) can be modified using a Fourier series representation of the form

$$-\frac{1}{\rho} \frac{\partial \hat{p}}{\partial x} = K_0 + \sum_{n=1}^{\infty} K_n e^{i\omega n t} \quad \text{and} \quad u = u_0 + \sum_{n=1}^{\infty} u_n e^{i\omega n t} \quad (3-105)$$

where both the pressure gradient and corresponding velocity profile, with yet to be determined coefficients, are defined. To make further headway in specifying our geometric configuration, we consider the incompressible periodic flow in a channel of height $2h$ and width $b \gg h$. We assume that the channel is sufficiently long and wide to justify the use of a two-dimensional planar model, as depicted in [Fig. 3-1](#). With x denoting the axial direction, we take, as usual, the y coordinate to be measured from the midsection plane up, thus setting the top and bottom channel walls at $y = \pm h$. Further substitution of the expanded series of $u(y, t)$ into the Cartesian analog of [Eq. \(3-94\)](#) yields two sets of equations, namely,

$$\frac{d^2 u_0}{dy^2} + \frac{K_0}{\nu} = 0 \quad \text{and} \quad \frac{d^2 u_n}{dy^2} - \frac{i\omega n}{\nu} u_n + \frac{K_n}{\nu} = 0 \quad \text{with} \quad u_n(h, t) = \frac{\partial u_n}{\partial y}(0, t) = 0; \quad n = 0, 1, 2, \dots \quad (3-106)$$

The solution to this set is straightforward, as detailed by Majdalani (2012). One obtains

$$\text{Pulsatory channel flow:} \quad u(y, t) = \frac{K_0 h^2}{2\nu} \left(1 - \frac{y^2}{h^2}\right) + \sum_{n=1}^{\infty} \frac{K_n}{i\omega n} \left[1 - \frac{\cosh(y \sqrt{i\omega n / \nu})}{\cosh(h \sqrt{i\omega n / \nu})}\right] e^{i\omega t} \quad (3-107)$$

Unsurprisingly, the motion consists of a linear superposition of the steady Poiseuille and the oscillatory channel flow solutions. Note that for $K_0 = 0$, $n = 1$, and $K_1 = K$, we reclaim the oscillatory channel flow expression,

$$\text{Oscillatory channel flow:} \quad u(y, t) = \frac{K}{i\omega} \left[1 - \frac{\cosh(y \sqrt{i\omega / \nu})}{\cosh(h \sqrt{i\omega / \nu})}\right] e^{i\omega t} \quad (3-108)$$

Here again, two overlapping approximations may be explored depending on the asymptotic behavior of the cosine hyperbolic function

$$\cosh(z) \approx \begin{cases} 1 + \frac{1}{2}z^2 + \frac{1}{24}z^4 + \dots & \text{for } z \ll 1 \\ \frac{1}{2}e^z + \dots & \text{for } z \gg 1 \end{cases} \quad (3-109)$$

These may be substituted into [Eq. \(3-108\)](#) to obtain

Small $\omega^* \ll 1$

$$\frac{u(y^*, t)}{u_{\max}} = \left[(1 - y^{*2}) \cos(\omega t) + \frac{\omega^*}{12} (y^{*4} - 6y^{*2} + 5) \sin(\omega t) \right] + O(\omega^{*2}) \quad (3-110)$$

Large $\omega^* \gg 1$ and $1 - y^* \ll 1$:

$$\frac{u(y^*, t)}{u_{\max}} = \frac{2}{\omega^*} [\sin(\omega t) - e^{-B} \sin(\omega t - B)] + O(\omega^{*-1} e^{-\sqrt{\omega^*}}) \quad (3-111)$$

where $u_{\max} = K h^2 / (2\nu)$, $B = (1 - y^*) \sqrt{\omega^* / 2}$, $\omega^* = \omega h^2 / \nu$, and $y^* = y / h$. Equations (3-110) and (3-111) mirror their axisymmetric counterparts given by [Eqs. \(3-101\)](#) and [\(3-102\)](#). For example,

we can readily see that [Eq. \(3-110\)](#) reproduces the two-dimensional Poiseuille profile under quasi-steady conditions as $\omega^* \rightarrow 0$. Moreover, for the case of $\omega^* \gg 1$ and $1 - y^* \ll 1$, one can retrieve the complex amplitude by noting that

$$\frac{K}{i\omega} \left[1 - \frac{\cosh(y\sqrt{i\omega/\nu})}{\cosh(h\sqrt{i\omega/\nu})} \right] = \frac{2iu_{\max}}{\omega^*} \left[e^{-B(1+i)} - 1 \right] + O(\omega^{*-1} e^{-\sqrt{\omega^*}}) \quad (3-112)$$

As before, the amplitude reaches its maximum at $B \approx 2.2841$, which enables us to calculate the location of the maximum velocity overshoot at $y^* \approx 1 - 3.2302/\sqrt{\omega^*}$. The corresponding speed overshoot can be determined to be

$$\text{Overshoot: } \frac{\overline{u^2}}{4u_{\max}^2/\omega^{*2}} = 1.143685 + O(\omega^{*-2} e^{-2\sqrt{\omega^*}}) \quad \text{or} \quad \frac{u_{\text{rms}}}{2u_{\max}/\omega^*} = 1.069432 + O(\omega^{*-1} e^{-\sqrt{\omega^*}}) \quad (3-113)$$

For a pipe of radius r_0 , the same procedure can be repeated to extract,

$$\text{Pulsatory pipe flow: } u(r, t) = \frac{K_0 r_0^2}{4\nu} \left(1 - \frac{r^2}{r_0^2} \right) + \sum_{n=1}^{\infty} \frac{K_n}{i\omega n} \left[1 - \frac{I_0(r\sqrt{i\omega n/\nu})}{I_0(r_0\sqrt{i\omega n/\nu})} \right] e^{i\omega n t} \quad [\text{Uchida (1956)}] \quad (3-114)$$

Here too, if the mean pressure gradient vanishes, and the oscillations are driven at a single frequency, one can set $K_0 = 0$, $n = 1$, and $K_1 = K$ to recover [Eq. \(3-98\)](#) identically.

3-4.4 Porous Duct Flow with an Oscillatory Pressure Gradient

Let us now consider the oscillatory motion in a porous tube with uniform wall injection. This problem has been studied extensively by Majdalani (1995) in both planar and axisymmetric settings. In the interest of brevity, we shall focus on the axisymmetric formulation. As shown in [Fig. 3-18](#), a fluid may be injected radially inwardly at a constant speed of v_w into a tube of length L_0 and radius r_0 . The tube is closed at the fore end and either choked or unchoked at the aft end. From the perspective of an oscillatory pressure wave, we refer to these conditions as either closed–closed or closed–open. We further permit pressure oscillations of the type, $A_0 \cos(l\pi x^*/L_0) \cos(l\pi a_s t^*/L_0)$, namely, of a small amplitude A_0 relative to the mean pressure, to occur at a frequency ω , where $\omega = l\pi a_s/L_0$ or $(l - \frac{1}{2})\pi a_s/L_0$ for the closed–closed or closed–open tubes, respectively. Here a_s represents the speed of sound at a reference pressure p_s , and l denotes the longitudinal oscillatory mode number. To simplify the asymptotic analysis, it is customary to define $Ma_w = v_w/a_s$ as a wall injection Mach number.

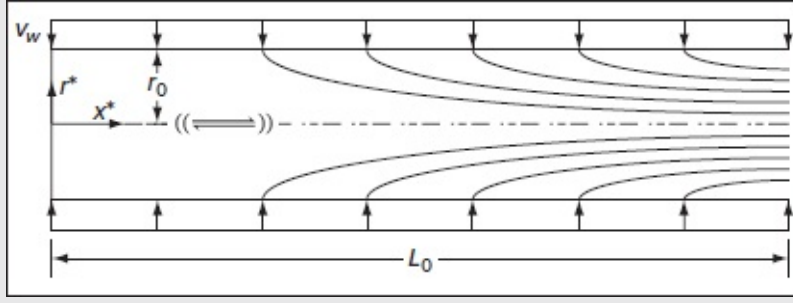


FIGURE 3-18

Porous tube with uniform wall injection depicting the dimensional coordinate system used along with both mean-flow streamlines and a superimposed axial pressure oscillation.

In view of this assortment of parameters, the axial and radial coordinates x^* and r^* can be made dimensionless using $r = r^*/r_0 \in [0, 1]$ and $x = x^*/r_0 \in [0, L]$, where $L = L_0/r_0$ denotes the tube's aspect ratio. The dimensionless velocity, pressure, density, and time follow suit using $p = p^*/(\gamma p_s)$, $\mathbf{u} = \mathbf{u}^*/a_s$, $\rho = \rho^*/\rho_s$, and $t = a_s t^*/r_0$, where γ stands for the ratio of specific heats. In this section, asterisks are used to label dimensional rather than dimensionless variables, and the wall injection (crossflow) Reynolds number, $Re = v_w r_0/\nu$, is taken to be positive for injection.

The mean flow can be described by a stream function that takes the form of $\psi = x f(r)$, where $f(r)$ depends on the configuration at hand. For the porous tube, several researchers such as Berman (1953), Yuan and Finkelstein (1956), Taylor (1956), and Culick (1966) have provided useful approximations that become exact in the limit of large or small injection Reynolds numbers. Some of these will be revisited in more depth in Sec. 3-6. To make further headway, we consider only two possible mean-flow profiles

$$f(r) \approx \begin{cases} \sin(\frac{1}{2}\pi r^2); & Re > 100 \quad [\text{Taylor-Culick (1956)}] \\ r^2(2 - r^2); & Re < 100 \quad [\text{Berman- (1953)}] \end{cases} \quad (3-115)$$

where, we reiterate, $Re = v_w r_0/\nu > 0$ for injection. The corresponding axial and radial velocities as well as the vorticity can be obtained by simple differentiation

$$u_0 = \frac{1}{r} \frac{\partial \psi}{\partial r} = \frac{x f'(r)}{r}, \quad v_0 = -\frac{1}{r} \frac{\partial \psi}{\partial x} = -\frac{f(r)}{r}, \quad \text{and} \quad \Omega_0 = \frac{\partial v_0}{\partial x} - \frac{\partial u_0}{\partial r} \quad (3-116)$$

Hence,

$$\begin{cases} u_0 = 4x(1 - r^2); & v_0 = r^3 - 2r; & \Omega_0 = 8rx; & 10 < Re < 100 \\ u_0 = \pi x \cos(\frac{1}{2}\pi r^2); & v_0 = -\frac{1}{r} \sin(\frac{1}{2}\pi r^2)/r; & \Omega_0 = \pi^2 r x \sin(\frac{1}{2}\pi r^2); & Re > 100 \end{cases} \quad (3-117)$$

The corresponding pressure is found to be

$$p_0 = 1/\gamma - \frac{1}{2}r^{-2}Ma_w^2\{f^2 + x^2[f'^2 + (r^{-1}f' - f'')(f - \varepsilon) - \varepsilon r f'''] + \varepsilon r f'\} = 1/\gamma + O(Ma_w^2 x^2) \quad (3-118)$$

Page 100 Assuming small amplitude oscillations, the instantaneous variables may be decomposed into mean and oscillatory components

$$p = \gamma^{-1} + \bar{\varepsilon}p_1; \quad \rho = 1 + \bar{\varepsilon}\rho_1; \quad \mathbf{u} = Ma_w \mathbf{u}_0 + \bar{\varepsilon}\mathbf{u}_1; \quad \boldsymbol{\Omega}_0 = Ma_w \boldsymbol{\Omega}_0 + \bar{\varepsilon}\boldsymbol{\Omega}_1 \quad (3-119)$$

where $\bar{\varepsilon} = A_0/(\gamma p_s) < 1$ is the pressure wave parameter. The small pressure amplitude enables us to linearize the Navier–Stokes equations, thus leading to the so-called interaction equations that prescribe the behavior of the oscillatory motion. These are

$$\frac{\partial \rho_1}{\partial t} + \nabla \cdot (\mathbf{u}_1) = -Ma_w \nabla \cdot (\rho_1 \mathbf{u}_0) + O(\bar{\varepsilon}) \quad (3-120)$$

$$\frac{\partial \mathbf{u}_1}{\partial t} = -Ma_w [\nabla(\mathbf{u}_0 \cdot \mathbf{u}_1) - \mathbf{u}_1 \times \boldsymbol{\Omega}_0 - \mathbf{u}_0 \times \boldsymbol{\Omega}_1] - \nabla p_1 + \varepsilon Ma_w \left[\frac{4}{3} \nabla(\nabla \cdot \mathbf{u}_1) - \nabla \times \boldsymbol{\Omega}_1 \right] + O(\bar{\varepsilon}) \quad (3-121)$$

Using Helmholtz–Hodge decomposition, the oscillatory components can be further decomposed into irrotational compressible and divergence-free vortical fluctuations. This can be accomplished by splitting each oscillatory component into

$$\mathbf{u}_1 = \hat{\mathbf{u}} + \tilde{\mathbf{u}}, \quad \boldsymbol{\Omega}_1 = \tilde{\boldsymbol{\Omega}}, \quad p_1 = \hat{p}, \quad \text{and} \quad \rho_1 = \hat{\rho} \quad (3-122)$$

where the circumflex and tildes denote irrotational “compressible” and divergence-free “vortical” oscillations that are characterized by $\nabla \times \hat{\mathbf{u}} = \mathbf{0}$ and $\nabla \cdot \tilde{\mathbf{u}} = 0$, respectively. The substitution of the decomposed variables into the interaction equations leads to the individual relations for the irrotational and vortical oscillations. First, for the irrotational pressure oscillation, we obtain,

$$\frac{\partial^2 \hat{p}}{\partial t^2} - \nabla^2 \hat{p} = -Ma_w \left[\nabla \cdot \left(\mathbf{u}_0 \frac{\partial \hat{p}}{\partial t} \right) - \nabla^2 (\hat{\mathbf{u}} \cdot \mathbf{u}_0) + \nabla \cdot (\hat{\mathbf{u}} \times \boldsymbol{\Omega}_0) \right] - \frac{4}{3} \varepsilon Ma_w \nabla^2 (\nabla \cdot \hat{\mathbf{u}}) \quad (3-123)$$

With a closer look, we may recognize the wave equation on the left-hand side, which enables us to recover the longitudinal pressure oscillation and its companion velocity at $O(Ma_w)$:

$$\hat{p}(x, t) = \cos(\omega_l x) \exp(-i\omega_l t) \quad \text{and} \quad \hat{u}(x, t) = i \sin(\omega_l x) \exp(-i\omega_l t) \quad (3-124)$$

where the dimensionless frequency depends on whether the aft end of the tube is “acoustically” closed or open, i.e., $\omega_l = \omega r_0 / a_s = l\pi / L$ (closed–closed) or $(l - \frac{1}{2})\pi / L$ (closed–open), with $l \in \mathbb{N}^*$. Second, for the oscillatory vortical response at $O(\bar{\varepsilon})$, we collect

$$\frac{\partial \tilde{\mathbf{u}}}{\partial t} = -Ma_w [\nabla(\tilde{\mathbf{u}} \cdot \mathbf{u}_0) - \tilde{\mathbf{u}} \times \boldsymbol{\Omega}_0 - \mathbf{u}_0 \times \tilde{\boldsymbol{\Omega}}] - \varepsilon Ma_w \nabla \times \tilde{\boldsymbol{\Omega}} \quad (3-125)$$

By further expressing $\tilde{\mathbf{u}}(x, r, t) = \hat{\mathbf{u}}(x, r) \exp(-i\omega_l t)$ with $\hat{\mathbf{u}} \equiv \hat{u} \mathbf{e}_x + \hat{v} \mathbf{e}_r$, we can recognize that

$\hat{v}/\hat{u} = O(Ma_w)$ and

$$\hat{u}(x, r) = -i \sum_{n=0}^{\infty} (-1)^n \frac{(\omega_l x)^{2n+1}}{(2n+1)!} R_n(r) \quad (3-126)$$

where the separated function $R_n(r)$ must be determined from

$$\begin{cases} \varepsilon \frac{d^2 R_n}{dr^2} + \frac{(\varepsilon + f)}{r} \frac{dR_n}{dr} + \left[iSt - 2(n+1) \frac{f'}{r} \right] R_n = 0; & 0 \leq r \leq 1 \\ R_n(1) = 1; & R_n'(0) = 0 \end{cases} \quad (3-127)$$

Here $St = \omega a_s / \nu_w$ stands for the Strouhal number and $\varepsilon = 1/Re$ provides a small perturbation parameter. Once $R_n(r)$ is determined, the oscillatory component of the velocity can be reconstructed from [Eq. \(3-122\)](#) using

$$u_1(x, r, t) = i \left[\sin(\omega_l x) - \sum_{n=0}^{\infty} (-1)^n \frac{(\omega_l x)^{2n+1}}{(2n+1)!} R_n(r) \right] e^{-i\omega t} \quad (3-128)$$

Being associated with a decaying oscillatory wave, several perturbation methods have been advanced to solve [Eq. \(3-127\)](#). These include multiple-scales, matched-asymptotic expansions, and the Wentzel–Kramers–Brillouin (WKB) method. A WKB expansion of $R_n(r)$ may be obtained using $R_n(r) = \exp(\delta^{-1} S_0 + S_1 + \delta S_2 + \delta^2 S_3 + \delta^3 S_4 + \dots)$, where δ is a small parameter and the functions $S_j(r)$ must be determined sequentially for $j \leq 0$. Depending on the relative sizes of ε and δ , namely, $\delta = \varepsilon, \varepsilon_1/2, \varepsilon_1/3$, etc., two fundamental distinguished limits can be identified. These are presented in the order in which they are found historically. Page 101

Type I: For $\delta = \varepsilon_1/2$ and $St = O(Re^{1/2})$, we have, following Majdalani (1995) and his sequels,

$$R_n^I(r) = (f/f_0)^{2n+2} \exp[\zeta_0 - i(\Phi_0 + \Phi_1)] + O(\varepsilon); f_0 \equiv f(1) = 1 \quad (3-129)$$

$$\begin{cases} \zeta_0 = \frac{1}{Mj} \int_1^r \frac{x^3}{f^3(x)} dx; & \Phi_0 = St \int_1^r \frac{x}{f(x)} dx \\ \Phi_1 = -\frac{St}{Re} \left\{ (2n + \frac{3}{2}) \left[\frac{1}{f_0^2} - \frac{r^2}{f^2(r)} \right] + \int_1^r \left[\frac{x(4n+5)}{f^2(x)} + \frac{2x^5}{f^5(x)Mj} \right] dx \right\} \end{cases} \quad (3-130)$$

with

Type II: For $\delta = \varepsilon$ and $St = O(Re)$, we get, as shown by Jankowski and Majdalani (2001),

$$R_n^{II} = \left(\frac{f_0^2 - 4i\varepsilon St}{f^2 - 4i\varepsilon r^2 St} \right)^{\frac{1}{4}} \left[\frac{f + \sqrt{f^2 - 4i\varepsilon r^2 St}}{r(f_0 + \sqrt{f_0^2 - 4i\varepsilon St})} \right]^{2n+\frac{5}{2}} \exp \int_1^r \left[\frac{\sqrt{f^2 - 4i\varepsilon x^2 St} - f}{2\varepsilon x} + \frac{(4n+5)f}{2x \sqrt{f^2 - 4i\varepsilon x^2 St}} \right] dx + O(\varepsilon) \quad (3-131)$$

The latter provides an alternative solution to the problem, albeit slightly more difficult to produce in closed form. For the injection case, both types can be used to provide excellent approximations. However, for the wall-suction case in porous channels and tubes, only the

type II solution is applicable, as shown by Jankowski and Majdalani (2002, 2005, 2006, 2010).

For the large Taylor–Culick injection case associated with $f(r) = \sin(\frac{1}{2}\pi r^2)$, a very accurate solution can be obtained by substituting [Eq. \(3-130\)](#) (with $n = 0$ in Φ_1) into [Eq. \(3-128\)](#) and simplifying. A closed-form solution for the oscillatory axial velocity is precipitated, namely,

$$u_1(x, r, t) = i[\sin(\omega_l x) - f \sin(\omega_l x f) \exp(\zeta_0 - i\Phi_0 - i\Phi_1)] e^{-i\omega t} \quad (3-132)$$

By keeping the real part, we have

$$u_1(x, r, t) = \sin(\omega_l x) \sin(\omega_l t) - f \sin(\omega_l x f) \exp \zeta_0 \sin(\omega_l t + \Phi_0 + \Phi_1) \quad (3-133)$$

And so, using continuity, the oscillatory radial velocity can be extracted and expressed as

$$v_1(x, r, t) = -Ma_w r^{-1} f^3 \cos(\omega_l x f) \exp \zeta_0 \cos(\omega_l t + \Phi_0 + \Phi_1) \quad (3-134)$$

which confirms the small size of the radial oscillation. At this point, the vorticity may be evaluated and collapsed into

$$\Omega_1 = r St \sin(\omega_l x f) \exp \zeta_0 \cos(\omega_l t + \Phi_0 + \Phi_1) \quad (3-135)$$

$$\text{where} \quad \begin{cases} \zeta_0 = -\frac{1}{\pi^2 Mj} \left[\csc \theta + \theta \cot \theta \csc \theta - 1 - I(\theta) + I\left(\frac{1}{2}\pi\right) \right]; & \Phi_0 = \frac{St}{\pi} \ln \left[\tan\left(\frac{1}{4}\pi r^2\right) \right] \\ \Phi_1 = \frac{St}{\pi Re} \left\{ 5 \cot \theta + 3 \left(\theta \csc^2 \theta - \frac{1}{2}\pi \right) - \frac{8}{\pi^2 Mj} \left[T(\theta) - T\left(\frac{1}{2}\pi\right) \right] \right\} \end{cases} \quad (3-136)$$

with $\theta \equiv \frac{1}{2}\pi r^2$ and two special functions:

$$I(x) = \int x \csc x dx = x + \sum_{k=1}^{\infty} (-1)^k 2(1 - 2^{2k-1}) B_{2k} x^{2k+1} / (2k+1)! = x + \frac{1}{18}x^3 + \frac{7}{1800}x^5 + \frac{31}{105840}x^7 + \dots \quad (3-137)$$

$$T(x) = \int x^2 \csc^5 x dx = \frac{1}{48} \left\{ 40 \ln \tan\left(\frac{1}{2}x\right) + 9x^2 - 2 \csc x [18x + (2 + 9x^2) \cot x] - 4x \csc^3 x (2 + 3x \cot x) \right\} \quad (3-138)$$

$$+ \frac{3}{4} \sum_{k=1}^{\infty} (-1)^k (1 - 2^{2k-1}) B_{2k} x^{2k+2} / [(2k+2)(2k)!]$$

Here, the sequence $B_{2k} = \{\frac{1}{6}, -\frac{1}{30}, \frac{1}{42}, \dots\}$ refers to the Bernoulli numbers. Note that the exponential decay of the rotational velocity wave strongly depends on Majdalani's penetration number, $Mj = Re/St^2 = Re_k/St^3 = v_w^3/(r_0 \omega^2 \nu)$, which controls the *depth of penetration* of the unsteady rotational motion, as illustrated previously in [Figs. 2-6](#) and [2-7](#). The depth of penetration, which arises in the context of oscillatory flow (Schlichting 1979), is comparable in meaning to the boundary-layer thickness. In fact, Majdalani (1995, 1999) shows that maintaining a constant penetration number results in a constant penetration depth at a given location in the tube, irrespective of the operating parameters, r_0 , ω , ν , and v_w . This can be clearly seen in [Fig. 2-6](#), where the oscillatory axial velocity given by [Eq. \(3-133\)](#) is compared to the numerical solution of the problem for the first longitudinal oscillation mode and

correlation with classic acoustic mode shapes is apparent. Maximum rotational amplitudes occur near oscillatory pressure nodes and diminish in the direction of velocity nodes. The presence of premature zero rotational amplitudes for $l = 2, 3$ in (b) and (c) is due to streaks of zero (unsteady) vorticity (chained lines) emanating from the j th internal velocity nodes located at $x/L = j/l, j < l$. Here $y = 1 - r$ represents the normalized distance above the porous wall.

$$\begin{cases} u_1^{(r)}(x, r, t) = \sin(\omega_l x) \sin(\omega_l t) - f \sin(\omega_l x f) e^{\xi_0} \sin(\Phi_0 + \Phi_1 + \omega_l t) \\ u_1^{(i)}(x, r, t) = \sin(\omega_l x) \sin(\omega_l t) - f \sin(\omega_l x f) e^{\xi_0} \cos(\Phi_0 + \Phi_1 + \omega_l t) \end{cases} \quad (3-139)$$

To further explore the behavior of the solution for the first three oscillation modes, it may be seen that the spatial patterns of $\|u_1\|$ in [Fig. 3-19](#) are clearly influenced by the classic, organ-pipe mode shapes. Rotational amplitudes are largest above the wall at oscillatory pressure nodes (or zeroes), where the corresponding velocity oscillation is most intense. Pressure nodes may be identified at $x/L = (2j - 1)/(2l)$, $1 \leq j \leq l$, for the j th internal pressure node. The additional downstream intensification of rotational amplitudes is caused by the axial convection of unsteady vorticity with the Taylor–Culick mean flow. Conversely, a weakening in vortical strength is noted during the inward wave propagation away from the injecting wall. The vortical attenuation in the radial direction can be attributed to the compounding effects of viscous diffusion and the speed reduction in the convective motion. Irrespective of the oscillation mode, one observes, near the wall, the Richardson annular effect, which is characteristic of oscillatory duct flow. At higher oscillation modes ($l > 1$), the presence of premature nodes of zero rotational amplitude is noted j times downstream of the j th internal velocity node. These irrotational points are caused by the lines of zero unsteady vorticity that originate at the oscillatory velocity nodes ($x/L = j/l$), and stretch across the solution domain (broken lines in [Fig. 3-19](#)).

Since the mean flow is solely induced by the influx at the walls, suppressing injection drastically alters our model. As we approach the limiting process of zero injection, walls become impermeable and pressure loses its mean component. The question that could be raised is: where should we stop? We find that, if v_w in the present model is made comparable to the Stokes diffusion speed, $\sqrt{2\omega\nu}$, our results will mimic [Eq. \(3-98\)](#), i.e., Sexl's exact solution for an oscillatory flow bounded by rigid walls. In this situation, dynamic similarity parameters can be chosen such that $Mj = 1/\lambda_S$, where $\lambda_S = r_0 \sqrt{\omega/(2\nu)}$ is the Stokes number. Accordingly, we get $Re = 2^{1/6} r_0 \sqrt{\omega/\nu}$ and $v_w = \sqrt{2\omega\nu}/\sqrt[3]{2}$. The wall injection velocity will thus be slightly smaller than the molecular diffusion speed, which is very small. One may interpret this condition to be reflective of virtually insignificant injection. The resulting field can be compared to [Eq. \(3-98\)](#), the exact solution given by Sexl (1930) for an oscillating fluid inside an impermeable tube. The latter is derived for an infinitely long tube and exhibits first mode oscillations that are independent of x . Due to our tube's finite length, we compare u_1 in [Fig. 3-20](#) to the exact solution at $x/L = \frac{1}{2}$ and $l = 1$. Graphically, the comparison seems to indicate a favorable agreement between asymptotic and exact predictions. In particular,

when injection is virtually absent, a reversal can be noted in the role played by viscosity. This behavior is consistent with Prandtl's classic theory foreseeing a deeper vortical presence with increased viscosity.

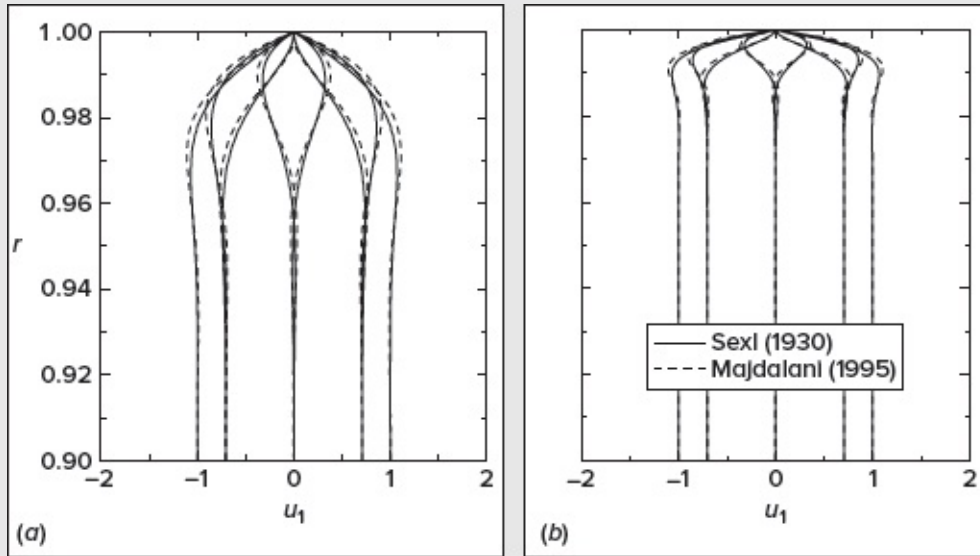


FIGURE 3-20

Velocity profiles of u_1 shown at eight successive time intervals. Results are obtained from asymptotic predictions (broken lines) and the exact formula by Sexl (full lines). Parameters correspond to $Mj = 1/\lambda_s$ for which convective and diffusive speeds are of the same order. We use $r_0\sqrt{\omega/\nu} = 100$ in (a) and $100\sqrt{10}$ in (b).

Overall, this approximate model seems to embrace Sexl's solution when injection is reduced to the diffusion speed. Since $2^{1/6} \cong 1.12$, one may set the lower limit on the wall injection Reynolds number to be $Re = r_0\sqrt{\omega/\nu} = 10$, so that $\varepsilon \leq 0.1$. This lower limit is prescribed, in part, by the desired precision in the ensuing perturbation analysis. At the lower end of the spectrum, properties must satisfy $r_0\sqrt{\omega/\nu} > 10$ and $v_w a/\nu > 10$. The corresponding model remains applicable as long as $v_w > 10\nu/a$ and $\omega > 10v_w/a$. These inequalities set the lower bounds for an open-ended range of physical parameters encompassing many realistic flows. For $10 < Re < 100$, one may substitute Berman's polynomial profile, $f = r_2(2 - r_2)$, into [Eq. \(3-130\)](#), and retrieve a suitable approximation via

$$\begin{cases} \zeta_0 = -\frac{1}{32Mj} [3\ln(2r^{-2} - 1) + 2(1 - r^{-2})(2r^4 - 3r^2 - 4)(2 - r^2)^{-2}]; & \Phi_0 = \frac{1}{4}St \ln[r^2/(2 - r^2)] \\ \Phi_1 = \frac{St}{128r^4 Re(2 - r^2)^4} [32Mj^{-1} + 2r^2(16(2 - r^2)^2(1 - r^2)[16(1 + n) - (23 + 28n)r^2 + 2(3 + 4n)r^4] \\ + Mj^{-1}\{48 + r^2[6 - r^2(3 - r^2)(84 - 65r^2 + 16r^4)]\}) + r^4(2 - r^2)^4(80 + 64n + 15Mj^{-1})\ln(2r^{-2} - 1)] \end{cases} \quad (3-140)$$

Finally, for the porous channel with an oscillatory pressure motion, similar two-dimensional approximations can be found, as detailed by Majdalani and Roh (2000) and Majdalani (2009). As such, we hope that the procedure provided here can be used in the treatment of other phenomenological problems where the mean flow is augmented by weak pressure oscillations.

3-5 UNSTEADY FLOWS WITH MOVING BOUNDARIES

A variety of solutions are known for laminar flow with moving boundaries, some of which illustrate boundary-layer behavior. Again we make the parallel-flow assumption of $u = u(y, t)$, $v = 0$, $w = 0$, so that the momentum equation (3-2) becomes

$$\frac{\partial u}{\partial t} = -\frac{1}{\rho} \frac{d\hat{p}}{dx} + \nu \frac{\partial^2 u}{\partial y^2} \quad (3-141)$$

The pressure gradient can only be a function of time for this flow and hence can be absorbed into the velocity by a change of variables. In most external flow problems, however, the pressure gradient can be dropped, thus leaving us with

$$\frac{\partial u}{\partial t} = \nu \frac{\partial^2 u}{\partial y^2} \quad (3-142)$$

Equation (3-142) is identical to the homogeneous heat-conduction equation, for which a wealth of unsteady solutions are known [see, e.g., Carslaw and Jaeger (1959)]. One of these corresponds to the motion of a fluid above an infinite plate which is moved arbitrarily. Let the plate be located at $y = 0$, so $u = u(y, t)$. The boundary conditions consist of no slip along the plate and no initial fluid motion:

$$\begin{cases} u(0, t) = U(t) & \text{for } t > 0 \\ u(y, 0) = 0 & \text{for } y > 0 \end{cases} \quad (3-143)$$

No matter how complex $U(t)$ is, the solution can be obtained from superposition of the indicial, or step-function, solution, as shown by Watson (1958). We confine ourselves to two cases:

1. Sudden acceleration of the plate to constant U .
2. Steady oscillation of the plate at $U_0 \cos \omega t$.

Case 1 is analogous to a conducting solid with a bottom plane that is suddenly reset to a different temperature. The solution is well known to be the complementary error function or probability integral

$$\text{Suddenly started plate: } \frac{u}{U} = 1 - \operatorname{erf}\left(\frac{y}{2\sqrt{\nu t}}\right) = \operatorname{erfc}\left(\frac{y}{2\sqrt{\nu t}}\right); \quad \operatorname{erf}(\beta) \equiv \frac{2}{\sqrt{\pi}} \int_0^\beta e^{-x^2} dx \quad (3-144)$$

This example is referred to as Stokes' first problem. In the above, the independent variables y and t have been combined into a single dimensionless *shape preserving* or *similarity variable*, $\eta = y/(2\sqrt{\nu t})$. Equation (3-142) can then be transformed into an ordinary differential equation for $u/U = f(\eta)$.

To justify the use of this similarity variable, we first note that the problem lacks a physical length scale because the plate is infinitely long, and the fluid is boundless. A rudimentary use of dimensional analysis starts by relating our principal parameters, $u/U = F(y, \nu, t)$, and identifying the presence of two primary dimensions, [L] and [t]. This enables us to reduce the number of functional dependencies by two parameters, namely, $u/U = F(\Pi)$, where $\Pi = y\nu^a t^b$. Then using the Buckingham Pi theorem, we deduce that $\Pi = y\nu^{-1/2} t^{-1/2}$ and so $u/U = F(y/\sqrt{\nu t})$ or, with no loss of generality, $u/U = f(\eta)$.

Since $u \neq u(x)$, one may confirm that the continuity equation reduces to $\partial v/\partial y = 0$, implying that v , which can only be a pure constant, must vanish because $v = 0$ at $y = 0$. Moreover, the y -momentum equation, which collapses into $\partial p/\partial y = 0$, reminds us that $p \neq p(y)$. In the absence of an axial pressure gradient, our Navier–Stokes equations simplify into [Eq. \(3-142\)](#). The latter may be further converted using $u = Uf$ to recover

$$\frac{\partial f}{\partial t} = \nu \frac{\partial^2 f}{\partial y^2}$$

Then using the Stokes similarity variable, $\eta = y/(2\sqrt{\nu t})$, we can readily chain-rule the derivatives to extract

$$\frac{\partial \eta}{\partial y} = \frac{1}{2\sqrt{\nu t}}, \quad \frac{\partial \eta}{\partial t} = -\frac{1}{4} y \nu^{-1/2} t^{-3/2} = -\frac{\eta}{2t}, \quad \text{and} \quad \frac{\partial^2 f}{\partial y^2} = \frac{\partial}{\partial \eta} \left(\frac{\partial f}{\partial \eta} \frac{\partial \eta}{\partial y} \right) \frac{\partial \eta}{\partial y} = \frac{1}{\nu t} \frac{\partial^2 f}{\partial \eta^2}$$

These transform our one-dimensional diffusion equation and its two boundary conditions into

$$\frac{d^2 f}{d\eta^2} + 2\eta \frac{df}{d\eta} = 0 \quad \text{with} \quad f(0) = 1 \quad (u = U \text{ at } y = 0) \quad \text{and} \quad f(\infty) = 0 \quad (u = 0 \text{ as } y \rightarrow \infty)$$

The ensuing second-order linear ODE can be integrated twice to get $f(\eta) = C_1 \int_0^\eta e^{-\eta^2} d\eta + C_2$. Further application of the boundary conditions enables us to retrieve $C_2 = 1$, $C_1 = -1/\int_0^\infty e^{-\eta^2} d\eta = -2/\sqrt{\pi}$, and so $f(\eta) = 1 - \frac{2}{\sqrt{\pi}} \int_0^\eta e^{-\eta^2} d\eta$, which is identical to [Eq. \(3-144\)](#). Values of the complementary error function are provided in [Table 3-3](#). The solution can be reversed so that the fluid is the one moving at uniform speed U_0 and the plate is suddenly decelerated to zero velocity. In this case,

TABLE 3-3

Numerical values of the complementary error function

β	$\text{erfc}(\beta)$	β	$\text{erfc}(\beta)$
0	1.0	1.1	0.11980
0.05	0.94363	1.2	0.08969
0.1	0.88754	1.3	0.06599
0.15	0.53200	1.4	0.04772
0.2	0.77730	1.5	0.03390
0.25	0.72367	1.6	0.02365
0.3	0.67137	1.7	0.01621
0.35	0.62062	1.8	0.01091
0.4	0.57161	1.9	0.00721
0.5	0.47950	2.0	0.00468
0.6	0.39615	2.5	0.000407
0.7	0.32220	3.0	0.0000221
0.8	0.25790	3.5	0.00000074
0.9	0.20309	4.0	0.00000001
1.0	0.15730	∞	0.0

Suddenly stopped plate:

$$u = U \text{erf}\left(\frac{y}{2\sqrt{\nu t}}\right) \quad (3-145)$$

Page 105 These two complementary solutions are illustrated in Fig. 3-21. While the suddenly started plate from Eq. (3-144) is shown in Fig. 3-21a, the suddenly stopped plate from Eq. (3-145) is depicted in Fig. 3-21b. The units of y are arbitrary, and the curves (a) and (b) are mirror images. In either part (a) or (b) in Fig. 3-21, the plate's effect diffuses into the fluid at a rate proportional to the square root of the kinematic viscosity. It is customary to define the shear layer *thickness* as the point where the wall effect on the fluid has dropped to 1 percent: in (a), where $u/U = 0.01$ and in (b), where $u/U = 0.99$. Both conditions lead to $\text{erfc}(\beta) = 0.01$ or $\beta \approx 1.82$. The corresponding shear layer thickness grows with

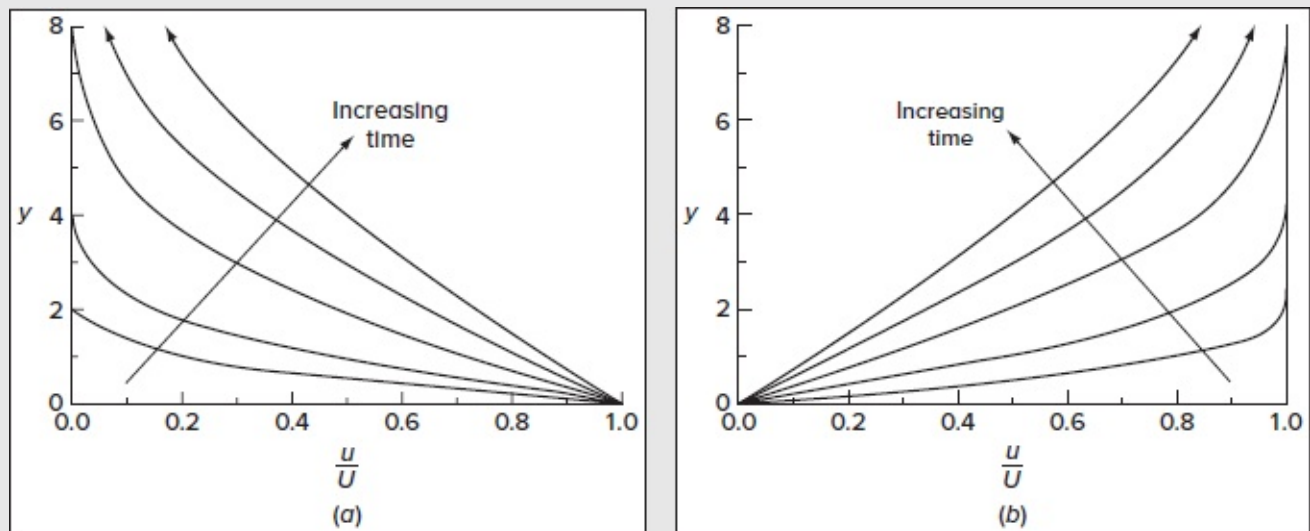


FIGURE 3-21

Stokes' first problem: (a) flow above a suddenly started plate; (b) streaming flow above a suddenly stopped plate.

$$\delta \approx 3.64 \sqrt{\nu t} \quad (3-146)$$

If we consider air at 20°C with $\nu = 1.5 \times 10^{-5} \text{ m}^2/\text{s}$, the shear thickness reaches $\delta = 11 \text{ cm}$ after 1 min.

3-5.1 Fluid Oscillation Above an Infinite Plate

Case 2, with an oscillating wall (or stream), is often called Stokes' second problem, after a celebrated paper by Stokes (1851). Here the wall is allowed to oscillate according to $u(0, t > 0) = U_0 \cos \omega t$, while the fluid in the far field remains at rest: $u(\infty, t) = 0$. The steadily oscillating solution to [Eq. \(3-142\)](#) must be of the form $u(y, t) = f(y) e_{i\omega t}$, where $i = \sqrt{-1}$. Substitution into [Eq. \(3-142\)](#) leads to the ordinary differential equation

$$\frac{d^2 f}{dy^2} - \frac{i\omega}{\nu} f = 0 \quad \text{or} \quad f = C \exp(-y \sqrt{i\omega/\nu}) \quad (3-147)$$

We may further separate $u(y, t)$ into real and imaginary parts. If the wall is oscillating, the boundary conditions dictate that

$$u_1 = U_0 \exp(-\eta) \cos(\omega t - \eta) \quad \text{where} \quad \eta = y / \sqrt{2\nu/\omega} \quad (3-148)$$

If, instead, the fluid is oscillating according to $u(\infty, 0) = U_0 \cos \omega t$ in the presence of a stationary wall with $u(0, t) = 0$, the solution becomes

$$u_2 = U_0 \cos \omega t - u_1 = U_0 [\cos \omega t - \exp(-\eta) \cos(\omega t - \eta)] \quad (3-149)$$

The instantaneous velocity profiles for the oscillating wall or fluid are illustrated in [Fig. 3-22a](#) and [b](#), respectively. The curves differ in time by $\pi/6$ during the half-cycle of sweep, from left to right, of the driving oscillation. In [Fig. 3-22a](#), the waves created in the fluid by the moving wall lag behind in phase and decay as the distance from the wall is increased. The thickness δ of the oscillating layer can again be defined where $u/U_0 = 0.01$, that is, where $u/U_0 = 0.01$. In his original paper, Stokes actually introduces a simple length scale, $\delta_s = 2\sqrt{2\nu/\omega}$, for which the amplitude of the disturbance decays to 13.53% of the driving amplitude. Since that time, a boundary layer associated with an oscillating flow is often referred to as a *Stokes layer*. In his textbook, [Page 107](#) however, Schlichting (1979) coins it *depth of penetration* and defines it as $2\pi\sqrt{2\nu/\omega}$, namely, as a wavelength separating two points that will oscillate in phase. In adherence with the standard 99% disturbance decay definition, we will continue to use the modern expression,

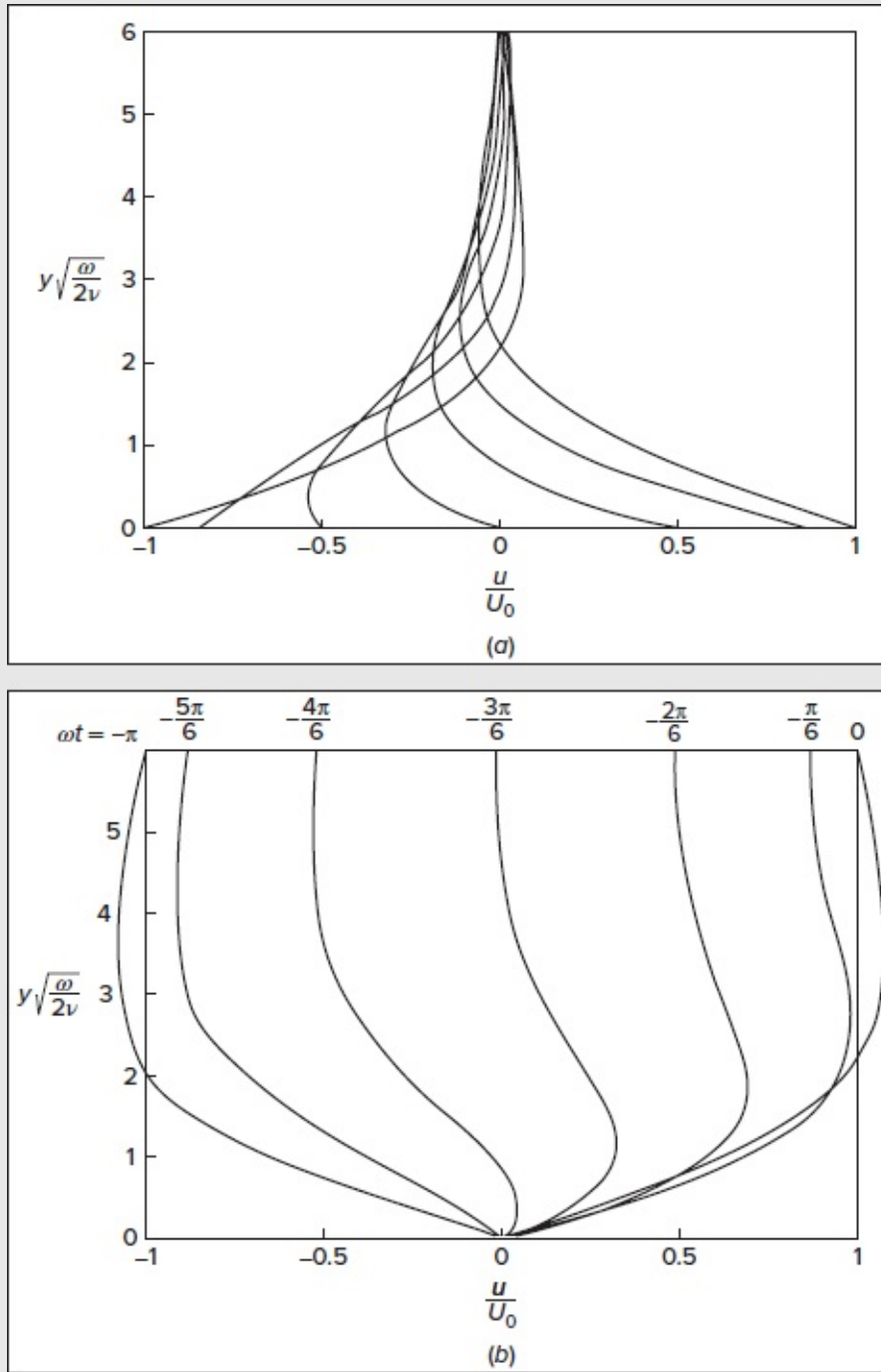


FIGURE 3-22

Stokes' second problem: (a) flow above an oscillating plate [Eq. (3-148)]; (b) an oscillating fluid above a fixed plate [Eq. (3-149)]. Velocity profiles are shown at different times that are separated by 30° increments over a half period.

$$\delta \approx 6.5\sqrt{\nu/\omega} \quad (3-150)$$

Again we have the characteristic laminar-flow dependence upon $\sqrt{\nu}$. For air at 20°C with a

plate frequency of 1 Hz ($\omega = 2\pi$ rad/s), we get $\delta \approx 1$ cm. The wall shear stress at the oscillating plate is given by

$$\tau_w = \mu \left(\frac{\partial u}{\partial y} \right)_w = U_0 \sqrt{\rho \omega \mu} \sin \left(\omega t - \frac{\pi}{4} \right) \quad (3-151)$$

and, thus, the maximum shear lags the maximum velocity by 135° .

The case of the fixed wall, [Fig. 3-22b](#), is rather different. The low-momentum fluid near the wall actually leads in phase, and we see the “Richardson” type of velocity overshoot ([Fig. 3-17](#)) at both ends of the cycle. This overshoot occurs near the wall when the contributions of the irrotational component $U_0 \cos \omega t$ (caused by the far-field reciprocating motion) and the boundary generated rotational wave, u_1 , add up. This overshoot decays quickly away from the wall along with the rotational component, u_1 , in order to restore the undisturbed far-field solution, $U_0 \cos \omega t$. Interestingly, the overshoot becomes more appreciable, approaching $2U_0$, in the presence of wall injection or blowing [e.g., Majdalani and Roh (2000)].

3-5.2 Unsteady Flow Between Two Infinite Plates

Let us revisit the linear Couette flow between a fixed and a moving plate from [Eq. \(3-6\)](#) and [Fig. 3-2a](#). More specifically, let us model the start-up of this flow from rest. Since the coordinate system of [Fig. 3-2a](#) is somewhat awkward, we will switch to the setting for [Fig. 3-23](#): At time $t = 0$, the upper plate remains fixed at $y = h$ but the lower plate at $y = 0$ begins to translate at a uniform velocity U_0 . In this setup, the final steady flow is $u = U_0(1 - y/h)$. It is convenient to work with the *difference* between u and its final steady-flow value,

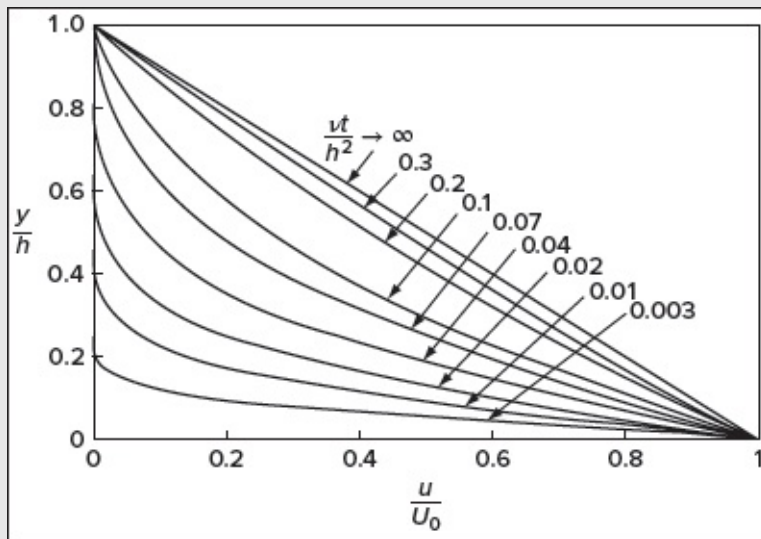


FIGURE 3-23

The development of plane Couette flow due to a suddenly accelerated lower wall

[Eq. (3-155)].

$$u_1 = u - U_0 \left(1 - \frac{y}{h}\right) \quad (3-152)$$

By adopting the dimensionless variables $u_1^* = u_1/U_0$, $y^* = y/h$, and $t^* = \nu t/h^2$, our diffusion equation (3-142) becomes

$$\frac{\partial u_1^*}{\partial t^*} = \frac{\partial^2 u_1^*}{\partial y^{*2}} \quad \text{subject to} \quad \begin{cases} u_1^*(0, t^*) = u_1^*(1, t^*) = 0 \\ u_1^*(y^*, 0) = y^* - 1 \end{cases} \quad (3-153)$$

Equation (3-153) yields to a product solution, $u_1^* = f(y^*)g(t^*)$, which leads to

$$\frac{g'}{g} = \frac{f''}{f} = -\lambda^2 \quad \text{or} \quad g = C \exp(-\lambda^2 t^*) \quad \text{and} \quad f = A \sin(\lambda y^*) + B \cos(\lambda y^*) \quad (3-154)$$

where (A, B, C) are constants. To satisfy $u_1^*(0, t^*) = 0$, we must have $B = 0$. To satisfy $u_1^*(1, t^*) = 0$, we must choose $\lambda = n\pi$, where n is an integer. Since no single sine wave will satisfy the initial condition, we form a Fourier series to require that $u_1^*(y^*, 0) = \sum A_n \sin(n\pi y^*) = y^* - 1$. The standard Fourier orthogonality condition [Kreyszig (1999)] returns

$$A_n = \int_{-1}^1 (y^* - 1) \sin(n\pi y^*) dy^* = -\frac{2}{n\pi} \quad (3-155)$$

We thus arrive at the final solution for Couette flow start-up:

$$\frac{u}{U_0} = \left(1 - \frac{y}{h}\right) - \frac{2}{\pi} \sum_{n=1}^{\infty} \frac{1}{n} \exp(-n^2 \pi^2 t^*) \sin\left(\frac{n\pi y}{h}\right) \quad (3-156)$$

Velocity profiles plotted from this expression are shown in [Fig. 3-23](#). The linear asymptote is approached at $t^* \approx 0.3$; for air at 20°C, this corresponds to $t = 2$ s if $h = 1$ cm.

Before leaving these sections on steady and unsteady Couette and Poiseuille flows, we should note that other relatively straightforward one-coordinate solutions exist for the Navier–Stokes equations. An excellent summary is given in the review article by Berker (1963). Some of these solutions will be given as problem assignments:

1. Steady Couette flow where the moving wall suddenly stops.
2. Unsteady Couette flow between a fixed and an oscillating plate. Page 108
3. Radial outflow from a porous cylinder, Prob. 3-24.
4. Radial outflow between two circular plates, Probs. 3-23 and 3-36.
5. Combined Poiseuille and Couette flow in a tube or annulus, Prob. 3-11.
6. Gravity-driven thin fluid films, Probs. 3-15 to 3-18.

7. Decay of a line Oseen–Lamb vortex, Prob. 3-14.
8. The Taylor vortex profile, Prob. 3-22.

In the next three sections, we will outline some more complex solutions, usually involving two- or three-dimensional flows.

3-6 ASYMPTOTIC SUCTION FLOWS

All solutions discussed in this chapter have had a vanishing convective acceleration, i.e., no nonlinear terms in the momentum equation. We now consider the case of simple but nonvanishing convection, i.e., flows with uniform wall suction or injection.

3-6.1 Uniform Suction on a Plane

Consider steady flow at velocity U (as $y \rightarrow \infty$) past an infinite plate (at $y = 0$). Let the plate be porous, allowing a normal, crossflow velocity through it, so that $u = 0$ but $v = v_w \neq 0$. The continuity equation for two-dimensional incompressible fluids is satisfied if $u = u(y)$ and $v = v_w = \text{const}$. The momentum equation then becomes

$$\rho v_w \frac{du}{dy} = \mu \frac{d^2 u}{dy^2} \quad \text{or} \quad \frac{d^2 u}{dy^2} - \frac{v_w}{\nu} \frac{du}{dy} = 0 \quad (3-157)$$

which is subject to $u = 0$ at $y = 0$. For a constant v_w , the convective acceleration becomes linear, and the solution may be readily retrieved,

$$u = U[1 - \exp(yv_w/\nu)] \quad (3-158)$$

Physically, v_w must be negative (wall suction), otherwise u can become unbounded at large y . As usual, the boundary-layer thickness can be prescribed by the point where $u = 0.99U$. This implies

$$\delta = -4.6(\nu/v_w) \quad (3-159)$$

This thickness is constant, being independent of y or U , because the convection toward the wall (suction or aspiration) offsets the tendency of the shear layer to grow due to viscous diffusion. For air at 20°C, if $v_w = -1$ cms, we get $\delta \approx 7$ mm. For a plate with a leading edge ($x = 0$), a laminar shear layer will develop and approach this constant value at a distance estimated by Iglisch (1944) to be $x \approx 4\nu U/v_w^2$ (see Sec. 4.4). For air at 20°C with $U = 10$ ms and $v_w = -1$ cms, this axial distance corresponds to a length of $x \approx 6$ m.

3-6.2 Flow Between Plates with Bottom Injection and Top Suction

Let us now consider the flow between two porous plates located at $y = +h$ and $y = -h$, respectively, as in [Fig. 3-24](#). Let the main flow be generated by a constant pressure gradient $-d\hat{p}/dx$. Let the porous walls be such that a uniform vertical crossflow is generated:

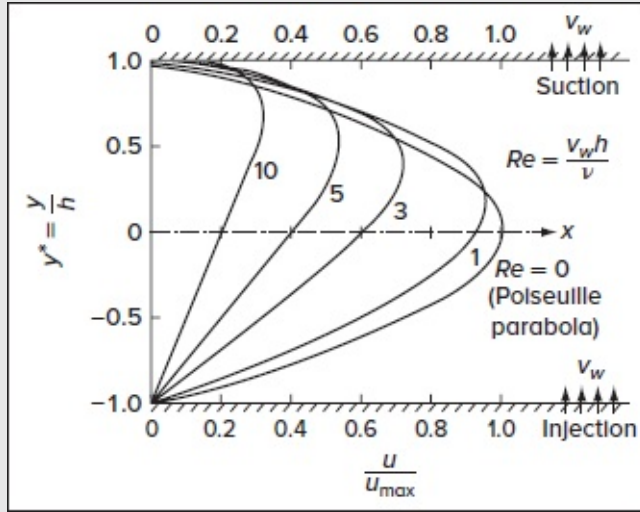


FIGURE 3-24

Velocity profiles for flow between parallel plates with equal and opposite porous walls, [Eq. \(3-163\)](#).

$$v = v_w = \text{const} \quad (3-160)$$

Then the equation of continuity with $w = 0$ requires, as before, that $u = u(y)$ only. The momentum [Eq. \(3-2\)](#) reduces to

$$\rho v_w = -\frac{d\hat{p}}{dx} + \mu \frac{d^2 u}{dy^2} \quad (3-161)$$

Since v_w is constant, this equation is linear. We retain the no-slip condition for the main flow by insisting on

$$u(+h) = u(-h) = 0 \quad (3-162)$$

Positive v_w corresponds to injection at the bottom plate and suction at the top plate ([Fig. 3-24](#)). The solution, which can be written in dimensionless form, contains the so-called *crossflow* or *wall Reynolds number* $Re = v_w h / \nu$ as a parameter. We get

$$\frac{u}{u_{\max}} = \frac{2}{Re} \left(\frac{y}{h} - 1 + \frac{e^{Re} - e^{Re y/h}}{\sinh(Re)} \right) \quad (3-163)$$

where $u_{\max} = h^2 (-d\hat{p}/dx) / (2\mu)$ is the centerline velocity for nonporous or Poiseuille flow [[Eq. \(3-44\)](#)]. For small crossflow Re , the last term in parentheses can be expanded in a power

series, and the Poiseuille solution $1 - y_2/h_2$ is reclaimed. For large Re , the same last term in parentheses yields approximately 2.0 (except in the vicinity of $y = +h$). The resulting model,

$$\frac{u}{u_{\max}} \approx \frac{2(1 + y/h)}{Re}$$

exhibits a straight-line variation that suddenly drops off to zero at the upper wall, where $u = 0$. Some velocity profiles based on [Eq. \(3-163\)](#), which illustrate this behavior, are shown in [Fig. 3-24](#). Note that the average velocity decreases with successive increases in Re , i.e., the friction factor increases as we apply more crossflow through the walls.

Similar analyses can be made with other geometries by imposing a known crossflow field, e.g., between rotating porous cylinders. The flow outside a single rotating cylinder with wall suction is given as a problem assignment; the character of this flow changes when the suction velocity v_w exceeds $2v/r_0$, with r_0 denoting the radius of the cylinder. Page 110

3-6.3 Nonlinear Effects: Flow in Porous Ducts

The previous examples were linear because of the assumption of constant crossflow velocity. If we impose more realistic boundary conditions, e.g., suction or injection at both walls, then the net mass flow will change with x , and at the very least we must have $u = u(x, y)$ and $v = v(y)$ to satisfy the continuity relation. This means that both of the axial convective acceleration terms $u \partial u / \partial x$ and $v \partial u / \partial y$ will be products of dependent variables and hence nonlinear. The solutions may be vexed with both existence and non-uniqueness problems, and it is instructive to consider an example.

For a uniformly porous duct with a constant wall velocity v_w , the average velocity \bar{u} in the duct will vary linearly with x because of the mass flow through the walls. The two most studied geometries correspond to the axisymmetric circular tube and the planar channel flow (between parallel plates). In practice, there must be an entrance region and, since the mean velocity continually varies, the question of whether a “fully developed” condition can be achieved becomes controversial.

For the present setup, let us consider incompressible channel flow between uniformly porous parallel plates, with the geometry of [Fig. 3-1](#). We assume, without proof, that we are far downstream and that the boundary conditions are

$$\begin{array}{ll} \text{At } y = +h: & u = 0 \quad v = +v_w \\ \text{At } y = -h: & u = 0 \quad v = -v_w \end{array} \quad (3-164)$$

Accordingly, the walls will have either equal suction ($v_w > 0$) or equal injection ($v_w < 0$). Let $\bar{u}(0)$ denote the average axial velocity at entry, where $x = 0$. Assuming unit width, it is clear from a gross mass balance that $\bar{u}(x)$ will differ from $\bar{u}(0)$ by the amount of mass ($-2v_w x$) injected (or removed) over a distance x , divided by the cross-sectional area ($2h$), namely, $-v_w$

$x/h > 0$, for injection. This observation led Berman (1953) to formulate the following relation for the stream function in a porous channel:

$$\psi(x, y) = [h\bar{u}(0) - v_w x]f(y^*) \quad (3-165)$$

where $y^* \equiv y/h$ and f represents a dimensionless function that is yet to be determined. The velocity components follow immediately from the definition of ψ ,

$$u(x, y^*) = \frac{\partial \psi}{\partial y} = \left[\bar{u}(0) - \frac{v_w x}{h} \right] f'(y^*) = \bar{u}(x) f'(y^*) \quad (3-166)$$

$$v(x, y^*) = -\frac{\partial \psi}{\partial x} = v_w f(y^*) = v(y) \text{ only}$$

Clearly, the function f and its derivative f' reproduce the shape of the velocity profiles independently of the axial position. The flow is hence termed *self-similar* (for more examples, see Secs. 3-8 and 4-3). The stream function must now be made to satisfy the momentum [Eq. \(3-2\)](#), for steady flow:

$$u \frac{\partial u}{\partial x} + v \frac{\partial u}{\partial y} = -\frac{1}{\rho} \frac{\partial p}{\partial x} + \nu \left(\frac{\partial^2 u}{\partial x^2} + \frac{\partial^2 u}{\partial y^2} \right) \quad u \frac{\partial v}{\partial x} + v \frac{\partial v}{\partial y} = -\frac{1}{\rho} \frac{\partial p}{\partial y} + \nu \left(\frac{\partial^2 v}{\partial x^2} + \frac{\partial^2 v}{\partial y^2} \right) \quad (3-167)$$

If we substitute u and v from (3-166) into (3-167), we find by cross-differentiation that

$$\frac{\partial^2 p}{\partial x \partial y} = 0 \quad (3-168)$$

This reminds us that, unlike the case for nonporous duct flow, the pressure gradient is *not* constant. When (3-167) and (3-168) are combined, the result is a single fourth-order ordinary nonlinear differential equation for $f(y^*)$,

$$\text{Berman's equation for porous channels:} \quad f'''' + Re(f'f'' - ff''') = 0 \quad (3-169)$$

where $Re = v_w h / \nu > 0$ (for suction) alludes to the wall or crossflow Reynolds number and primes denote differentiation with respect to y^* . Our four boundary conditions may be directly converted from (3-164) into

$$f'(-1) = 0 \quad f'(1) = 0 \quad f(-1) = -1 \quad f(1) = +1 \quad (3-170)$$

These show that $f(y^*)$ is antisymmetric about $y^* = 0$, so that at the centerline, $v = 0$ and $\partial u / \partial y = 0$, or $f(0) = f''(0) = 0$. Equation (3-169) has no known analytic closed-form solution, but it can be integrated once to obtain

$$f''' + Re(f'^2 - ff'') = k(Re) = \text{const} \quad (3-171)$$

Page 111 Further progress requires some other technique such as

1. Asymptotic solutions: Berman (1953), Sellars (1955), Yuan (1956), Terrill (1964, 1965),

Lu et al. (1992), Lu (1997), Cox and King (1997, 2004), King and Cox (2001), Saad and Majdalani (2009), and others.

2. Numerical solutions: Eckert et al. (1957), Terrill (1965), Cox (1991), and others.
3. A power-series solution: White (1959).

These are general techniques, and we shall have the opportunity to use all three of them later in analyzing problems for which the exact solution is not tractable. In fact, there are cases and ranges of the wall Reynolds number leading to multiple solutions for the laminar flow in a uniformly porous channel. These have been studied by Raithby (1971), Robinson (1976), Skalak and Wang (1978), Shih (1987), Zatorska et al. (1988), Hastings et al. (1992), MacGillivray and Lu (1994), Cox and King (1997, 2004), and many others, thus leading to the discovery of three principal types of solutions for suction (labeled I–III) and one for injection. In short, several solutions have been obtained for [Eq. \(3-169\)](#), which satisfy conditions (3-170) either identically or asymptotically. These are

$$Re = 0 \text{ (Poiseuille's profile):} \quad f = \frac{3}{2}y^* - \frac{1}{2}y^{*3} \quad (3-172a)$$

$$|Re| < 20 \text{ (Berman's small } Re \text{ profile): } f = \frac{3}{2}y^* - \frac{1}{2}y^{*3} - \frac{1}{280}Re(2 - 3y^{*2} + y^{*6})y^* + O(Re^2) \text{ [Berman (1953)]} \quad (3-172b)$$

$$Re \rightarrow +\infty \text{ (Sellars' suction profile):} \quad f = y^* \text{ [Sellars (1955)]} \quad (3-173a)$$

$$Re \gg 1 \text{ (Terrill's suction profile):} \quad f = \frac{y^* - Re^{-1}e^{-Re(1-y^*)}}{1 - Re^{-1}} + O(Re^{-2}) \text{ [Terrill (1964)]} \quad (3-173c)$$

$$Re \gg 1 \text{ (Terrill's suction profile):} \quad f = \frac{y^* - Re^{-1}e^{-Re(1-y^*)}}{1 - Re^{-1}} + O(Re^{-2}) \text{ [Terrill (1964)]} \quad (3-174a)$$

$$Re \ll -1 \text{ (Yuan's injection profile): } f = \begin{cases} \sin\phi - \frac{1}{4}\pi Re^{-1}\{(\phi \cos\phi - \sin\phi)\ln|\tan(\phi/2)| \\ + \cos\phi[C\phi - S_0(\phi)]\} + O(Re^{-2}); \quad \phi \equiv \frac{1}{2}\pi y^* \end{cases} \text{ [Yuan (1956)]} \quad (3-174b)$$

$$\text{where } S_0(x) \equiv \int_0^x z \csc z \, dz = x + 2 \sum_{k=1}^{\infty} \pi^{-2k} \frac{(1 - 2^{1-2k})}{(2k+1)} \left(\sum_{j=1}^{\infty} j^{-2k} \right) x^{2k+1}; \quad C = 2[S_0(\frac{1}{2}\pi) - 1]/\pi \approx 0.5296237$$

Note that Sellars' and Taylor's exact suction and injection profiles may be recovered from Terrill's and Yuan's asymptotic solutions as $Re \rightarrow \pm \infty$, respectively. Similarly, the Poiseuille profile, $u = \bar{u}f'(y^*)$, can be restored from Berman's small Reynolds number expansion as $Re \rightarrow 0$. For other Reynolds numbers, one could use numerical techniques, such as Runge–Kutta integration, to solve [Eq. \(3-169\)](#). Two initial conditions are unknown, i.e., if one starts at $y^* = -1$, both $f''(-1)$ and $f'''(-1)$ will have to be guessed and the solution double-integrated until $f(1) = 0$ and $f'(1) = 0$ are secured. A complete set of profiles is given by White et al. (1958) and shown here in [Fig. 3-25](#).

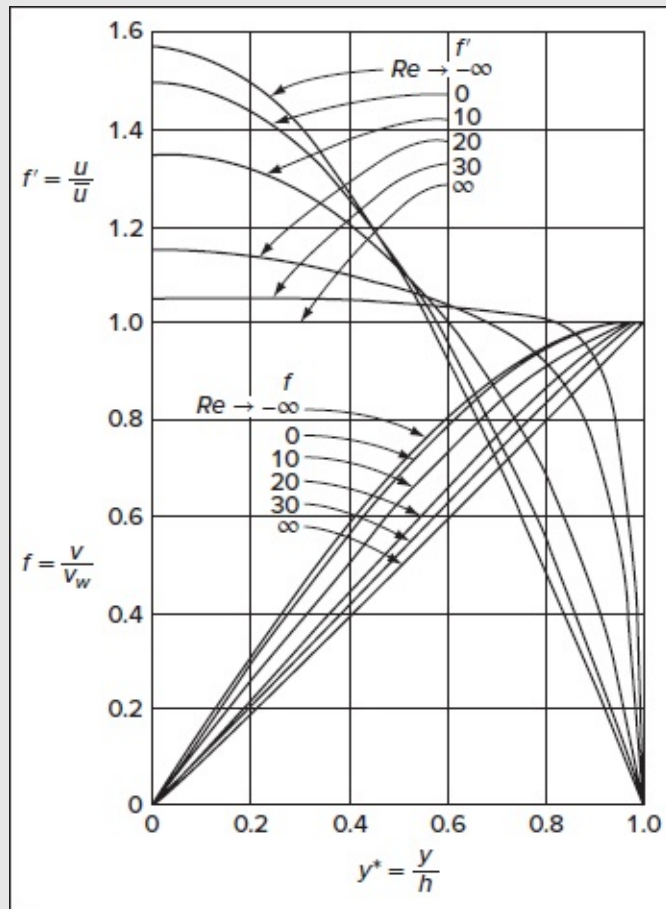


FIGURE 3-25

Similar velocity profiles for a symmetrically porous channel as a function of the wall Reynolds number $Re = v_w h / \nu$. [After White et al. (1958).]

Note that in the suction case, the velocity profiles deviate from the Poiseuille pattern by being flatter near the midsection and steeper near the walls, depending on the wall Reynolds number. In fact, the shapes change smoothly from a plug flow at $Re \rightarrow +\infty$ to Poiseuille's at $Re = 0$. In the injection case, they continue to vary, albeit more rapidly, from the Poiseuille parabola to Taylor's sinusoidal distribution, which starts to dominate as early as $Re < -100$. So while suction draws the profile closer to the wall, as illustrated in [Fig. 3-24](#), injection nudges the solution toward the midsection plane.

On the subject of solution multiplicity, which is a natural companion of nonlinear problems, Zaturka et al. (1988) are able to confirm that, for suction, one symmetric solution exists for $0 < Re < 12.165$ and three symmetric solutions for $12.165 < Re < \infty$, labeled types I–III. As for injection, Skalak and Wang (1978) showed that at most one solution could exist, and Shih (1987) later proved that this unique solution would in fact exist over the entire injection range of $Re < 0$. Interestingly, the first two of the large suction solutions (labeled I and II) exhibit the same leading-order term given by Sellars (1955) [Eq. (3-173a)], while the

type III sinusoidal form is discovered much later by Lu (1997) [Eq. (3-173c)], and further investigated by Cox and King (1997, 2004).Page 112

To further illustrate the streamline patterns associated with these solutions, we take advantage of symmetry relative to the midsection plane in [Fig. 3-26](#) and confine our domain to $0 \leq x^* \leq L_0/h$ and $0 \leq y^* \leq 1$, where L_0 denotes the length of the porous channel that is open on the right-hand side. The mean-flow streamlines are computed based on (a) the small cross flow Reynolds number expansion derived by Berman (1953) as well as the large suction solutions found by (b) Sellars (1955) and (c) Lu (1997). The latter is more closely examined in [Fig. 3-27](#) at increasing crossflow Reynolds numbers of (a) 30, (b) 60, and (c) 120. Note that in the $0 < y^* < 1 - \Delta$ interval, the flow direction switches such that fluid layers are pushed away from the porous wall as in the injection-driven problem. More specifically, the sign reversal in the normal velocity mimics the effect of injection. Clearly, the convection of the mean-flow layers away from the porous wall leads to complex streamline patterns at different suction levels. This region of nonuniformity for the type III solution expands with increasing Re . It is narrowest near $Re = 13.7$, where the largest value of $\Delta = 0.5108$ is obtained.

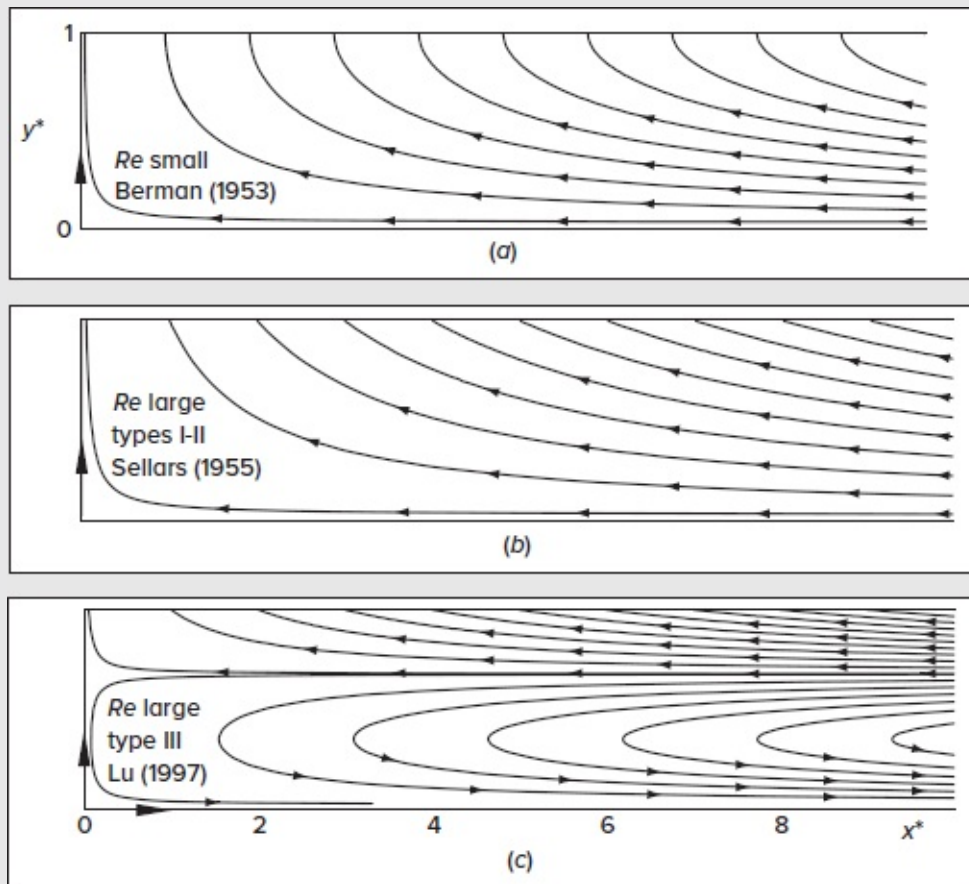


FIGURE 3-26

Streamlines corresponding to (a) Berman's small suction flow approximation as well as (b) Sellars' type I–II and (c) Lu's type III solutions for large crossflow

Reynolds numbers. Here $x^* = x/h$ denotes the dimensionless axial coordinate and the flow is allowed to enter the channel from the right-hand side.

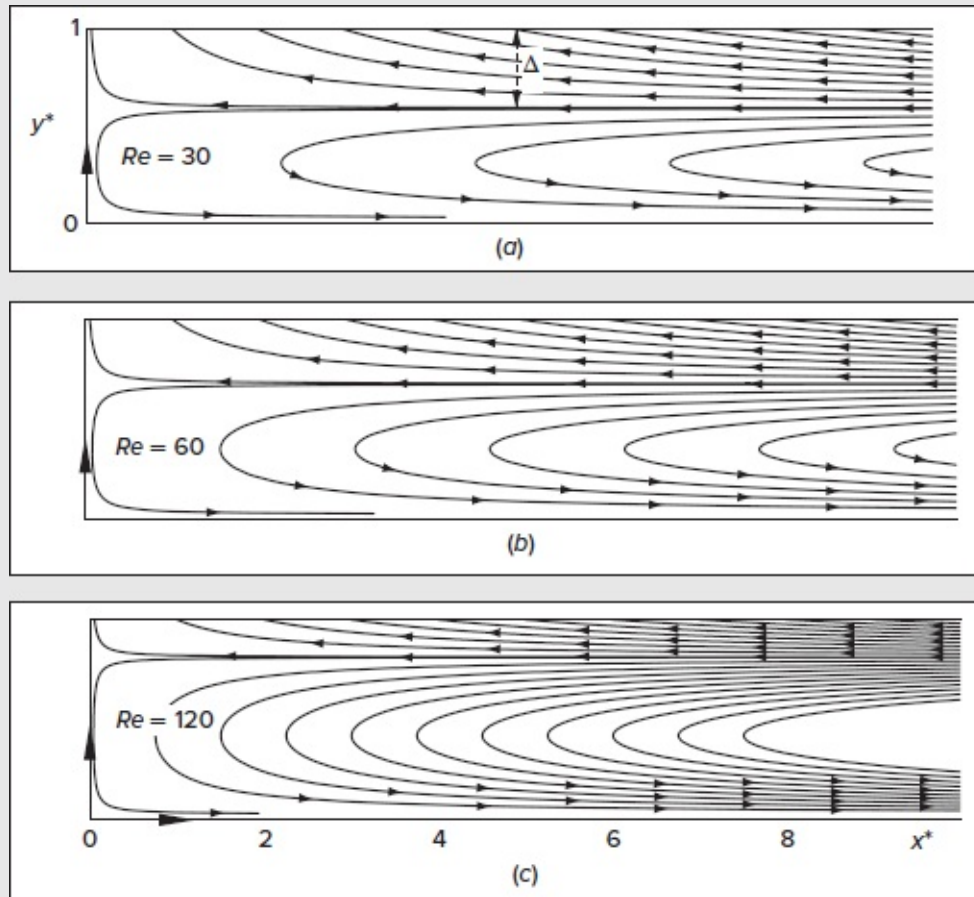


FIGURE 3-27

Streamline patterns corresponding to Lu's type III characteristic function exhibiting sharp flow turning near the wall and total flow reversal near the core ($0 < y^* < 1 - \Delta$). The figures correspond to (a) $Re = 30$, (b) $Re = 60$, and (c) $Re = 120$. Note that $\Delta \rightarrow 0$ as $Re \rightarrow \infty$.

Even more interesting behavior shows up in a uniformly porous *pipe*. In fact, White (1962a) provides an array of solutions for various values of $Re = u_w r_0/\nu$. Following several dedicated studies, it is found that two solutions for injection, one being unphysical, exist for all $Re < 0$. And despite the smooth variation of injection-driven solutions, the corresponding suction profiles exhibit the following characteristics:

1. Double solutions, one with backflow, for $0 < Re < 2.3$.
2. No solutions whatsoever in the range $2.3 < Re < 9.1$.

3. Two solutions in the range $9.1 < Re < 20.6$.
4. Four solutions for $Re > 20.6$.

It may be worth remarking that, although this section has focused on symmetric flow profiles in uniformly porous channels, an even more expansive body of literature exists for porous pipes and ducts in general with translating, rotating, and expanding or contracting walls. In addition, there are studies that consider both symmetric and asymmetric wall permeability and flow profiles under both incompressible and compressible flow conditions with and without headwall injection. Page 113 Page 114

For example, in the large injection case, axisymmetric flow analogs to those given by Eqs. (3-174) have been derived by Yuan and Finkelstein (1956), Terrill and Thomas (1969), Majdalani and Saad (2007), and Majdalani and Akiki (2010). According to the latter, we have

$$f = \sin \phi + Re^{-1} \{ 3 + (\sin \phi - \phi \cos \phi) S_1(\phi) + \cos \phi S_2(\phi) - C_1 \sin \phi - C_2 \phi \cos \phi - C_3 \cos \phi \}$$

with $\phi \equiv \frac{1}{2} \pi r^{*2}$; $C_1 = 3 + S_1(\frac{1}{2} \pi)$; $C_2 = -6\pi^{-1} - 1 - S_1(\frac{1}{2} \pi) + (2/\pi) S_2(\frac{1}{2} \pi)$; $C_3 = 3$

and $S_1(\phi) = \int_0^\phi \varphi \csc \varphi d\varphi = \phi + \sum_{k=1}^{\infty} \frac{2}{\pi^{2k}} \left(\sum_{n=1}^{\infty} \frac{1}{n^{2k}} \right) \frac{(1 - 2^{1-2k})}{(2k+1)} \phi^{2k+1}$;

$$S_2(\phi) = \int_0^\phi \varphi^2 \csc \varphi d\varphi = \frac{1}{2} \phi^2 + \sum_{k=1}^{\infty} \left(\sum_{n=1}^{\infty} n^{-2k} \right) \frac{(1 - 2^{1-2k})}{(k+1) \pi^{2k}} \phi^{2k+2}$$

(3-175)

Note that for infinitely large injection, one restores the Taylor–Culick stream function, which has been used at the basis of countless research investigations of idealized rocket chambers (see Majdalani and Saad 2007, 2012). Specifically, one gets

$$Re \rightarrow -\infty \text{ (Taylor–Culick injection profile): } f = \sin\left(\frac{1}{2} \pi r^{*2}\right) \text{ [Taylor (1956) and Culick (1966)]} \quad (3-176)$$

For small suction and injection, the axisymmetric problem has been equally examined by several investigators, including Berman (1958), Terrill and Thomas (1969), and Saad and Majdalani (2017). The latter transform Berman’s equation into

$$\text{Berman's equation for porous tubes: } 2\eta \frac{d^4 f}{d\eta^4} + 4 \frac{d^3 f}{d\eta^3} + Re \left(\frac{df}{d\eta} \frac{d^2 f}{d\eta^2} - f \frac{d^3 f}{d\eta^3} \right) = 0; \quad \eta \equiv \frac{1}{2} r^{*2} \quad (3-177)$$

with $\frac{df(\frac{1}{2})}{d\eta} = 0$ $f(\frac{1}{2}) = 1$ $f(0) = 0$ and $\lim_{\eta \rightarrow 0} \sqrt{2\eta} \frac{d^2 f}{d\eta^2} = 0$

Forthwith, a straightforward asymptotic expansion in the crossflow Reynolds number leads to

$$|Re| < 100 \quad f \approx 4\eta(1 - \eta) + \frac{1}{9}\eta(2 - 9\eta + 12\eta^2 - 4\eta^3)Re \approx 2r^{*2} - r^{*4} + \frac{1}{36}r^{*2}(4 - 9r^{*2} + 12r^{*4} - r^{*6})Re \quad (3-178)$$

This confirms Berman’s small Reynolds number solution, namely,

$$|Re| < 100 \text{ (Berman's small } Re \text{ profile): } f \approx r^{*2}(2 - r^{*2}) \quad [\text{Berman (1953)}] \quad (3-179)$$

As for the infinitely large suction approximation, it is derived by Terrill and Thomas (1969) using asymptotic tools:

$$Re \rightarrow +\infty \text{ (Terrill-Thomas suction profile): } f = r^{*2} \quad [\text{Terrill and Thomas (1969)}] \quad (3-180)$$

We close by stating that the foregoing formulations constitute only a subset of the fundamental solutions that have been advanced in the treatment of uniformly porous channels and tubes. These have given rise to a plethora of dedicated studies that remain, at the time of this writing, open areas of investigation.

3-6.4 Swirl Effects: Flow in Rotating Porous Ducts

Let us now examine the flow in a uniformly porous tube where the cylindrical wall rotates at a spinning angular rate ω_s . This model, which has been used to capture the bulk internal flow field of a spinning rocket motor (Cecil and Majdalani 2019), exhibits a finite tangential speed at the wall, v_s , as shown in [Fig. 3-28](#). It is convenient to adopt a cylindrical coordinate system anchored at the headend center, with z pointing in the axial flow direction, and (v_r, v_θ, v_z) representing the three-component velocity vector. For a constant radial injection speed at the porous wall, we can impose $v_r(r = r_0) = -v_w < 0$ for injection, where r_0 denotes the radius of the tube. Since the analysis is more easily carried out using normalized variables, we reverse our notation in this section and use asterisks to tag dimensional variables as well as a positive Reynolds number for injection. We specifically let

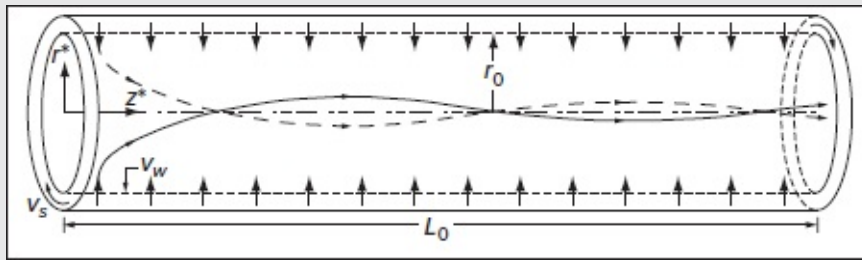


FIGURE 3-28

Porous tube with uniform wall injection speed v_w and constant tangential speed v_s .

$$r = \frac{r^*}{r_0}; \quad z = \frac{z^*}{r_0}; \quad v_r = \frac{v_r^*}{v_w}; \quad v_\theta = \frac{v_\theta^*}{v_w}; \quad v_z = \frac{v_z^*}{v_w}; \quad p = \frac{p^*}{\rho v_w^2}$$

With $Re = u_w r_0/\nu > 0$ for injection, the steady, incompressible and normalized Navier–Stokes equations simplify into

$$\begin{aligned} \frac{1}{r} \frac{\partial(rv_r)}{\partial r} + \frac{\partial v_z}{\partial z} &= 0 \\ v_r \frac{\partial v_r}{\partial r} + v_z \frac{\partial v_r}{\partial z} - \frac{v_\theta^2}{r} &= -\frac{\partial p}{\partial r} + \frac{1}{Re} \left(\frac{\partial^2 v_r}{\partial r^2} + \frac{1}{r} \frac{\partial v_r}{\partial r} + \frac{\partial^2 v_r}{\partial z^2} - \frac{v_r}{r^2} \right) \\ v_r \frac{\partial v_\theta}{\partial r} + v_z \frac{\partial v_\theta}{\partial z} + \frac{v_r v_\theta}{r} &= \frac{1}{Re} \left(\frac{\partial^2 v_\theta}{\partial r^2} + \frac{1}{r} \frac{\partial v_\theta}{\partial r} + \frac{\partial^2 v_\theta}{\partial z^2} - \frac{v_\theta}{r^2} \right) \\ v_r \frac{\partial v_z}{\partial r} + v_z \frac{\partial v_z}{\partial z} &= -\frac{\partial p}{\partial z} + \frac{1}{Re} \left(\frac{\partial^2 v_z}{\partial r^2} + \frac{1}{r} \frac{\partial v_z}{\partial r} + \frac{\partial^2 v_z}{\partial z^2} \right) \end{aligned} \quad (3-181)$$

where axisymmetric conditions (whereby $\partial/\partial\theta = 0$) have been enforced. At this juncture, a stream function that varies linearly in the flow direction may be introduced, namely,

$$\psi(r, z) = z f(r) \quad \text{with} \quad v_r = -f/r \quad \text{and} \quad v_z = z f'/r \quad (3-182)$$

After substituting these relations into the axial and radial momentum equations, the pressure can be eliminated by cross-differentiation. We are left with

$$z \frac{\partial}{\partial r} \left\{ \frac{1}{r^2} \left[f f'' - \frac{1}{r} f f' - f'^2 + \frac{1}{Re} \left(r f''' - f'' + \frac{1}{r} f' \right) \right] \right\} = \frac{2}{r} v_\theta \frac{\partial v_\theta}{\partial z} \quad (3-183)$$

Furthermore, realizing that $v_\theta = g(r)$ only, the right-hand side vanishes, which prompts us to equate the term in curly braces to a constant:

$$f f'' - \frac{1}{r} f f' - f'^2 + \frac{1}{Re} \left(r f''' - f'' + \frac{1}{r} f' \right) = r^2 C \quad (3-184)$$

The resulting expression can be further reduced by substituting $\eta \equiv r_2/2$ and differentiating once with respect to η . We thus arrive at a fourth-order, nonlinear differential equation:

$$\left(f \frac{d^3 f}{d\eta^3} - \frac{df}{d\eta} \frac{d^2 f}{d\eta^2} \right) + \frac{2}{Re} \left(\eta \frac{d^4 f}{d\eta^4} + 2 \frac{d^3 f}{d\eta^3} \right) = 0 \quad (3-185)$$

As usual, the function $f(\eta)$ is subject to the same four boundary conditions as [Eq. \(3-182\)](#). These consist of

1. Uniform radial injection: $u_r(1, z) = -1$ or $f(1/2) = 1$.
2. No axial velocity at the porous wall: $u_z(1, z) = 0$ or $\frac{df}{d\eta}(1/2) = 0$.
3. No radial crossflow at the centerline: $u_r(0, z) = 0$ or $f(0) = 0$.
4. Symmetric axial velocity at the centerline: $\partial u_z(0, z)/\partial r = 0$ or $\sqrt{2}\eta \frac{d^2 f}{d\eta^2}(0) = 0$.

After some algebra, the use of an asymptotic series expansion in the reciprocal of the wall Reynolds number leads to

$$f(r) = \sin\left(\frac{1}{2}\pi r^2\right) + \frac{1}{Re}\left\{-3 + I_1(r)\left[\frac{1}{2}\pi r^2 \cos\left(\frac{1}{2}\pi r^2\right) - \sin\left(\frac{1}{2}\pi r^2\right)\right] - I_2(r) \cos\left(\frac{1}{2}\pi r^2\right) + 3 \cos\left(\frac{1}{2}\pi r^2\right) + \frac{1}{2}\pi r^2 C_1 \cos\left(\frac{1}{2}\pi r^2\right) + C_2 \sin\left(\frac{1}{2}\pi r^2\right)\right\} + O(Re^{-2}) \quad (3-186)$$

where

$$I_1(r) = \frac{1}{2}\pi^2 \int_0^r x^3 \csc\left(\frac{1}{2}\pi x^2\right) dx, \quad I_2(r) = \frac{1}{4}\pi^3 \int_0^r x^5 \csc\left(\frac{1}{2}\pi x^2\right) dx, \quad C_1 = -\frac{1}{\pi}[6 + 7 \zeta(3)] + 2G - 1, \text{ and } C_2 = 4(3 + 2G)$$

Page 116

In the above, $G \approx 0.91596559$ returns Catalan's constant, and $\zeta(3) \approx 1.2020569$ denotes Riemann's zeta function given by $\zeta(x) = \sum_{k=1}^{\infty} k^{-x}$. At this stage, the radial and axial velocities may be deduced directly from [Eq. \(3-182\)](#). As for the tangential speed, we may insert $v_\theta = g(r)$ into the tangential momentum equation and retrieve

$$\frac{1}{r}f\left(g' + \frac{1}{r}g\right) + \frac{1}{Re}\left(g'' + \frac{1}{r}g' - \frac{1}{r^2}g\right) = 0 \quad (3-187)$$

The resulting expression can be substantially reduced when expressed in terms of the tangential angular momentum, $B(r) = rg(r)$. Equation (3-187) collapses into

$$B'' - \left(\frac{1}{r} - \frac{1}{Re} \frac{f}{r}\right)B' = 0 \quad (3-188)$$

which is subject to two basic boundary conditions:

$B(0) = 0$ (forced vortex at centerline) and $B(1) = v_s/v_w$ (tangential velocity adherence at porous wall)

Solving (3-188) while securing its two constraints leads to

$$v_\theta = \frac{\xi}{r} \frac{\int_0^r X \exp\left[-Re \int_0^X f(x)x^{-1} dx\right] dX}{\int_0^1 X \exp\left[-Re \int_0^X f(x)x^{-1} dx\right] dX}; \quad \xi \equiv \frac{v_s}{v_w} \quad (3-189)$$

Here ξ represents the ratio between the tangential and radial injection speeds at the wall. Alternatively, Cecil and Majdalani (2019) show that for $Re > 100$, a far simpler formulation can be constructed starting with an inviscid solution and then using matched-asymptotic expansions with a key viscous correction as $r \rightarrow 0$. The equivalent approximation can be expressed as

$$v_r = -\frac{1}{r} \sin\left(\frac{1}{2}\pi r^2\right), \quad v_\theta = \frac{1}{r} \xi \left[1 - \exp\left(-\frac{1}{4}\pi r^2 Re\right)\right], \text{ and } v_z = \pi z \cos\left(\frac{1}{2}\pi r^2\right) \quad [\text{Cecil and Majdalani (2019)}]$$

Figure 3-29 provides a comparison between the large Reynolds number(3-190) expansion, denoted by “LRE,” the equivalent, matched-asymptotic expansion, specified by “MAE,” and a purely computational solution labeled “CFD.” It is gratifying that an excellent agreement is observed in all reported variables both at $Re = 100$ and 2000 . Even at $Re = 100$, the difference between the asymptotic and numerical solutions is negligible.

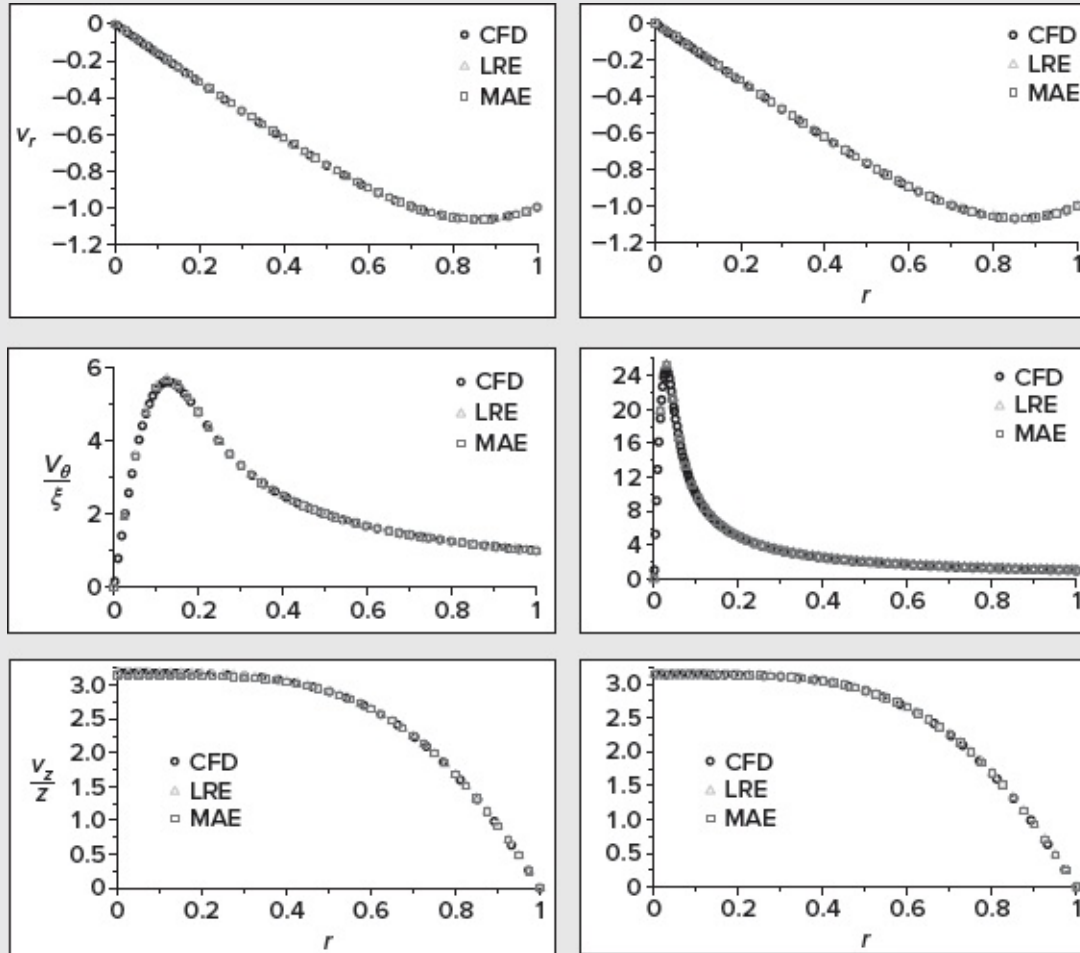


FIGURE 3-29

Normalized velocities in a rotating porous tube based on three techniques: large Reynolds number expansion (LRE), matched-asymptotic expansion (MAE), and CFD predictions for an injection Reynolds number of 100 (left) and 2000 (right). [After Cecil and Majdalani (2019).]

Based on the compact formulation, it is possible to predict the location and magnitude of the peak tangential speed. One finds

$$r_{\max} = \left[\frac{-2 - 4\text{pln}\left(-1, -\frac{1}{2}e^{-1/2}\right)}{\pi Re} \right]^{1/2} \approx \frac{1.2648}{\sqrt{Re}}; (v_{\theta})_{\max} = \xi \frac{\sqrt{\pi Re} \left\{ 1 - \exp\left[\frac{1}{2} + \text{pln}\left(-1, -\frac{1}{2}e^{-1/2}\right)\right] \right\}}{\sqrt{-2 - 4\text{pln}\left(-1, -\frac{1}{2}e^{-1/2}\right)}} \approx 0.56557\xi \sqrt{Re} \quad (3-191)$$

where $\text{pln}(x)$ denotes the product-log function. Interestingly, the location of the peak tangential velocity r_{\max} proves to be inversely proportional to the square root of the Reynolds number. Such behavior is consistent with the presence of forced vortex motion [Majdalani (2012)], where the diameter of the forced vortex is defined as twice the peak radius, i.e., $d_f = 2.5296Re^{-1/2}$. Thus, as the Reynolds number is increased, the location of $(v_{\theta})_{\max}$ shifts inwardly toward the centerline. In the same vein, the value of $(v_{\theta})_{\max}$ remains proportional to $Re^{1/2}$ and becomes larger (and closer to the centerline) with successive increases in the Reynolds number. This inward shifting and corresponding increase in $(v_{\theta})_{\max}$ are reflective of the diminishing effects of viscosity at increasing values of Re , particularly, as the forced vortex region is compressed. As the centerline is approached, it can be shown that the swirling motion will exhibit solid-body rotation of the form $v_{\theta} = \omega_f r$, which is consistent with a forced vortex rotating at a constant angular rate ω_f . This can be determined by taking

$$\lim_{r \rightarrow 0} v_{\theta} = \lim_{r \rightarrow 0} \frac{1}{r} \xi \left[1 - \left(1 - \frac{1}{4} \pi r^2 Re + \dots \right) \right] = \left(\frac{1}{4} \pi \xi Re \right) r \quad \text{and so} \quad \omega_f = \frac{1}{4} \pi Re_s; Re_s \equiv v_s r_0 / \nu. \quad (3-192)$$

The result shows that the spinning rate of the forced vortex in the core region will increase with the spinning Reynolds number, Re_s . If we actually revert back to our dimensional coordinates, we will be able to deduce that the forced vortex frequency, given in radians per second, $\omega_f^* = \frac{1}{4} \pi (v_s r_0 / \nu) (v_w / r_0) = \frac{1}{4} \pi v_s v_w / \nu$, will depend on the product of both tangential and radial wall speeds, and will further increase as the viscosity is diminished. Page 117

3-7 WIND-DRIVEN FLOWS: THE EKMAN DRIFT

A particular class of problems arises when a liquid free surface is set into motion by a gas flowing over it, e.g., wind blowing over a pond. Naturally, the shear stresses must match at the air–water interface. By setting the interface at $z = 0$, with $z > 0$ upward, the free-surface condition may be secured by requiring that

$$\tau_0 = \left(\mu \frac{\partial u}{\partial z} \right)_{\text{air}} = \left(\mu \frac{\partial u}{\partial z} \right)_{\text{water}} \quad (3-193)$$

where the motions of wind and water are assumed to point in the positive x -direction. Since $\mu_{\text{air}} \ll \mu_{\text{water}}$, it follows from the above equality that the gradient $(\partial u / \partial z)_{\text{water}}$ will be relatively small. Let us coin this water interfacial gradient $K = \tau_0 / \mu_{\text{water}}$.

3-7.1 Start-Up of Wind-Driven Surface Water

Consider water at rest that is suddenly subjected to a shearing stress τ_0 caused by sweeping wind. Assuming an unsteady parallel laminar flow, $u(z, t)$, and neglecting the Coriolis acceleration, we are left with the linear diffusion equation,

$$\frac{\partial u}{\partial t} = \nu \frac{\partial^2 u}{\partial z^2} \quad (3-194)$$

which is subject to the two boundary conditions:

$$\frac{\partial u}{\partial z}(z = 0, t) = K \quad (\text{interfacial gradient}) \quad u(z \rightarrow -\infty, t) = 0 \quad (\text{quiescent far field at great depth})$$

as well as the initial condition: $u(z < 0, 0) = 0$ (quiescent initial state)

The resulting setup is reminiscent of Stokes' first problem, which leads to a complementary error function in [Eq. \(3-144\)](#), except that the surface condition presently involves $(\partial u / \partial z)$ rather than u itself. We therefore get

$$\frac{\partial u}{\partial z} = K \left[1 + \operatorname{erf} \left(\frac{z}{2\sqrt{\nu t}} \right) \right] \quad \text{and so} \quad u(z, t) = Kz \left[1 + \operatorname{erf} \left(\frac{z}{2\sqrt{\nu t}} \right) \right] + 2K\sqrt{\frac{\nu t}{\pi}} \exp \left[- \left(\frac{z}{2\sqrt{\nu t}} \right)^2 \right] \quad (3-195)$$

This laminar-flow solution predicts that the water-interface velocity along $z = 0$ will grow as $u_0 = 2K\sqrt{\nu t/\pi}$. Using numerical estimates from the text by Roll (1965) for the wind stress over a water surface, we arrive at

$$\tau_0 \approx 0.002 \rho_{\text{air}} (V_{\text{wind}} - u_0)^2 \quad (3-196)$$

If we assume a brisk wind speed of 6 ms (about 12 knots) and an air–water interface at 20°C, we may compute from [Eqs. \(3-195\)](#) and [\(3-196\)](#) that $u_0 \approx 0.6$ ms after 1 min and 2.3 ms after 1 h. These water velocities are greatly overestimated: In an actual flow of this type, the surface-water flow would rise in about 1 h to a nearly constant velocity of 0.2 m/s, or about 3 percent of the wind speed. The main reason for the discrepancy is that both the air and water motions, in such a large-scale (high Reynolds number) flow, are turbulent. In turbulent flow, the fluid's molecular viscosity μ must be replaced by a turbulent-mixing or *eddy* viscosity, μ_t , which is much larger (see [Chap. 6](#)).

3-7.2 Coriolis Effects: The Ekman Spiral

In practical ocean flows, the wind-driven water moves at such low velocities that the Coriolis acceleration is no longer negligible. The resulting flow is steady but accelerating, i.e., the unbalanced momentum flux points in the direction of the Coriolis acceleration. The oceanographer Fridtjof Nansen (1902) found that drifting ice in the Arctic deviated from the wind direction by 20° to 40° to the right, which he correctly concluded was due to the earth's rotation. Nansen's student, Vagn Walfrid Ekman, developed a key analytical solution (1905), which laid the foundation for modern dynamic oceanography. As usual, we let (x, y) be the

plane of the horizontal, and z directed upward. For convenience, we let the applied surface wind stress τ_0 point in the y direction. Then, for steady flow with negligible pressure gradients and the acceleration given by [Eq. \(2-114\)](#), a realistic solution is possible with the horizontal velocities u and v as functions of z only. The momentum [Eq. \(3-2\)](#) simplifies into

$$\nu \frac{d^2}{dz^2}(u + iv) - 2i\omega \sin \phi (u + iv) = 0 \quad (3-197)$$

where $i = \sqrt{-1}$, ϕ gives the latitude angle, and ω supplies the angular rotational rate of earth. This differential equation yields an exponential solution if ϕ is assumed constant, i.e., localized wind drift at a given latitude. The boundary conditions consist of a y -directed shear at the surface and negligible velocity at great depth:

$$z = 0: \quad \frac{du}{dz} = 0 \quad \frac{dv}{dz} = K = \frac{\tau_0}{\mu_{\text{water}}} \quad \text{and} \quad z \rightarrow -\infty: \quad u = v = 0 \quad (3-198)$$

A solution to [Eq. \(3-197\)](#) returns the form $u + iv = C_1 e^{\beta z}$, where C_1 and β can be found from [Eq. \(3-198\)](#). The results can then be decomposed into

$$\frac{u}{V_0} = \exp \frac{\pi z}{D} \cos \left(\frac{\pi z}{D} + \frac{\pi}{4} \right) \quad \text{and} \quad \frac{v}{V_0} = \exp \frac{\pi z}{D} \sin \left(\frac{\pi z}{D} + \frac{\pi}{4} \right) \quad (3-199)$$

where V_0 stands for the surface-water speed and D denotes a vertical decay distance, often called the *penetration depth* of the wind. These are

$$V_0 = \frac{\tau_0 / \rho}{\sqrt{2\omega \nu \sin \phi}} \quad \text{and} \quad D = \pi \sqrt{\frac{\nu}{\omega \sin \phi}} \quad (\text{wind penetration depth}) \quad (3-200)$$

Equation (3-199) has several fascinating implications, particularly for engineers not used to Coriolis effects in fluid motion. First we note that, at $z = 0$, the surface-water velocities are $u = V_0 \cos (\pi/4)$ and $v = V_0 \sin (\pi/4)$, showing that the resultant surface-velocity vector is at a 45° angle to the right of the wind (in the Northern Hemisphere). As we move below the surface ($z < 0$), the resultant current vector moves uniformly to the right and decreases exponentially in magnitude, forming a logarithmic spiral, as shown in [Fig. 3-30](#), for equal-depth intervals. At $z = -3D/4$, the current is exactly opposite the wind and has a magnitude of only $V_0 e^{-3\pi/4} \approx 0.095 V_0$.

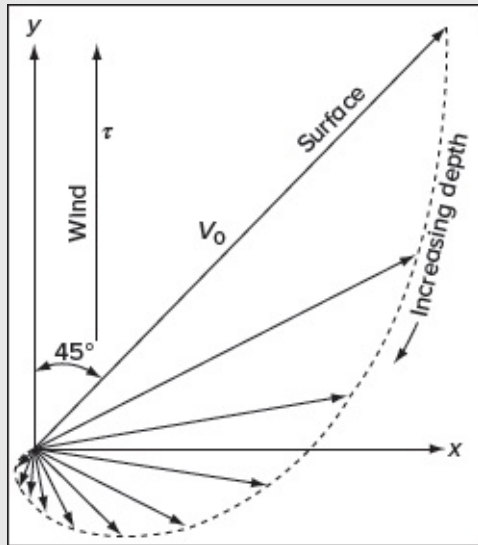


FIGURE 3-30

Wind-driven current vectors for depths of equal interval. The dashed line is a logarithmic spiral from [Eq. \(3-199\)](#). [After Ekman (1905).]

Another interesting feature may be captured by integrating the velocity distribution to determine the net mass flux. In the x and y directions, we get

$$m_x = \int_0^{-\infty} u dz = \frac{\tau_0}{2\omega \sin \phi} \quad \text{and} \quad m_y = \int_0^{-\infty} v dz = 0 \quad (3-201)$$

Page 119We thus realize that the net mass transport of water remains perpendicular to the wind direction and not dependent on v if τ_0 is known. We can explain this by noting that the x -axis, which is normal to the wind speed, coincides with the direction of the Coriolis acceleration, which is the only dynamic imbalance on the system.

As in the previous wind-start-up example, a few numbers will dispel the idea that ocean currents are laminar. Again, taking $V_{\text{wind}} = 6$ ms over a 20°C air–water interface at a latitude of 41° N (Rhode Island), [Eqs. \(3-200\)](#) predict that $V_0 = 2.7$ ms, which is far too high, and $D = 45$ cm, which is drastically low. The difficulty again is that real ocean flows are turbulent. If we scale the flow with an “eddy” viscosity as discussed in [Chap. 6](#), we obtain the realistic results of $V_0 \approx 2$ cms and $D \approx 100$ m. Thus, an actual wind-driven Ekman current provides for slow transport in a wide upper layer of the ocean. For further detail on ocean currents, wind-driven or otherwise, we refer the reader to textbooks on physical oceanography, e.g. Defant (1961) or Knauss (1978).

3-8 SIMILARITY SOLUTIONS

We complete our description of exact incompressible-flow solutions of the Navier–Stokes equations by discussing three similar flows. A *similarity solution* is one in which the number of independent variables is reduced by at least one, usually through a coordinate transformation. The idea is analogous to dimensional analysis. Instead of *parameters*, such as the Reynolds number, the *variables* themselves are collapsed into dimensionless groups.

So far, we have actually seen two similarity solutions. In Stokes’ suddenly accelerated wall problem, [Eq. \(3-144\)](#), the independent variables y and t are combined into a single similarity variable, $\eta = y/(2\sqrt{\nu t})$. The solution is then pursued analytically. In the porous-duct problem, [Eq. \(3-165\)](#), ψ is expressed as a product solution, leaving a similarity variable $f(y^*)$, where $y^* = y/h$. In both cases, partial differential equations, which are difficult to solve except by computer, are reduced to ordinary differential equations.

Similarity solutions generally require semi-infinite or infinite spatial and temporal extents. Had Stokes’ suddenly moved wall been only L long or had the wall stopped after a finite time t_0 , the similarity effort would have been compromised.

The general theory of similarity in physical problems has been examined in several textbooks: from a physical emphasis by Sedov (1959) and Hansen (1964), and from the mathematical viewpoint by Ames (1965), Bluman and Cole (1974), Dresner (1983), and Sachdev (2000). The benefits of a similarity analysis are significant: The three examples given here reduce a set of partial differential equations, which may yield only to an all-out computer assault, into ordinary differential equations, which we can handle with an elementary numerical method such as Runge–Kutta integration. These mathematical gains are accompanied by a loss of generality: Similarity solutions are, without exception, limited to certain geometries and certain boundary conditions. For example, in the porous-channel problem, the solution of [Eq. \(3-169\)](#) is invalid if v_w varies with x , and the inlet velocity profile $u(0, y)$ must have the same shape as the curves of [Fig. 3-25](#).

Let us now discuss three classic examples of laminar similarity solutions: (1) flow near a stagnation point, (2) flow near an infinite rotating disc, and (3) flow in a wedge-shaped region.

3-8.1 Viscous Flow Near a Stagnation Point

One of Prandtl’s first students, Hiemenz (1911), discovered that a stagnation-point flow can be resolved exactly by the Navier–Stokes equations.[§] We piece together here several analyses in the literature: the two-dimensional velocity distribution by Hiemenz (1911) and temperature distribution by Goldstein (1938), as well as the axisymmetric velocity distribution by Homann (1936) and temperature distribution by Sibulkin (1952). The “two-dimensional” character applies to both the velocity and temperature distributions of Hiemenz (1911) and Goldstein (1938), while the “axisymmetric” character applies to both velocity and temperature distributions of Homann (1936) and Sibulkin (1952).

The coordinate system is shown in [Fig. 3-31](#). The origin is the stagnation point (where u

$= v = 0$ in the frictionless solution), and y is the normal to the plane. For axisymmetric flow, x may be interpreted as a radial coordinate. In order to satisfy the no-slip condition for $u(x, 0)$ along the wall, a viscous region must develop near the wall. It turns out that this shear layer has a constant thickness and has the effect of “displacing” the outer inviscid flow away from the wall. Let us first consider two-dimensional flow in detail and follow with a more cursory treatment of axisymmetric flow.

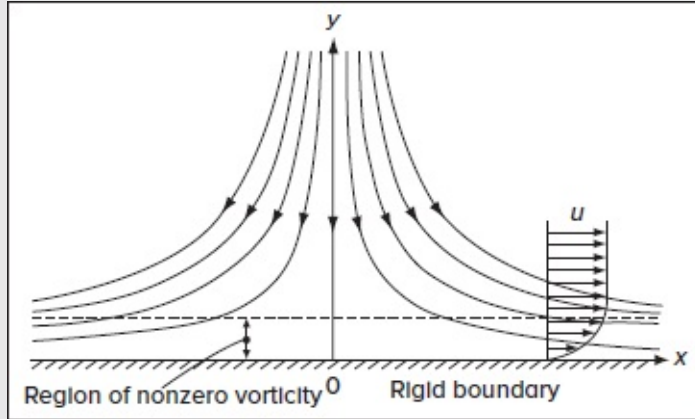


FIGURE 3-31

Stagnation flow in both planar and axisymmetric configurations. In the latter, it is customary to replace x by the radial coordinate r .

3-8.1.1 PLANE STAGNATION FLOW. For planar flow, the incompressible continuity [Eq. \(3-1\)](#) reduces to

$$\frac{\partial u}{\partial x} + \frac{\partial v}{\partial y} = 0$$

which can be satisfied by the planar stream function

$$u = \frac{\partial \psi}{\partial y} \quad \text{and} \quad v = -\frac{\partial \psi}{\partial x} \quad (3-202)$$

Note that stream functions are valid for both viscous and potential fields. Once $\psi(x, y)$ is defined, it must satisfy the steady two-dimensional momentum relations given by [Eq. \(3-2\)](#):

$$u \frac{\partial u}{\partial x} + v \frac{\partial u}{\partial y} = -\frac{1}{\rho} \frac{\partial p}{\partial x} + \nu \left(\frac{\partial^2 u}{\partial x^2} + \frac{\partial^2 u}{\partial y^2} \right) \quad \text{and} \quad u \frac{\partial v}{\partial x} + v \frac{\partial v}{\partial y} = -\frac{1}{\rho} \frac{\partial p}{\partial y} + \nu \left(\frac{\partial^2 v}{\partial x^2} + \frac{\partial^2 v}{\partial y^2} \right) \quad (3-203)$$

Inviscid motion near a stagnation point of a body is described by the simple stream function

$$\psi = Bxy \quad u = Bx \quad \text{and} \quad v = -By$$

Here B represents a positive constant that is proportional to U_0/L , where U_0 denotes the stream velocity approaching the body, and L refers to a characteristic body length [White (2016)]. This flow slips at the wall, and so $u \neq 0$ at $y = 0$. It must hence be modified to account for viscous effects.

Following Hiemenz (1911), we modify the stream function to vary with y so that the no-slip condition can be satisfied. This is accomplished by taking

$$\psi_{\text{viscous}} = Bx f(y) \quad u = \frac{\partial \psi}{\partial y} = Bx \frac{df}{dy} \quad \text{and} \quad v = -\frac{\partial \psi}{\partial x} = -Bf$$

For no slip at the wall, we would require $f(0) = f'(0) = 0$. If we substitute this $\psi(x, y)$ into the y -momentum equation in [Eq. \(3-203\)](#), we find that the pressure gradient $\partial p / \partial y = g(y)$ only. We therefore have

$$\frac{\partial^2 p}{\partial x \partial y} = 0$$

By using this condition and the same stream function in the x -momentum relation of [Eq. \(3-203\)](#), we obtain a third-order differential equation

$$f''' + \frac{B}{\nu} (ff'' - f'^2) = \text{const} = -\frac{B}{\nu} \quad (3-204)$$

The constant may be evaluated by recognizing that the form of ψ is such that, as $y \rightarrow \infty$, both f''' and f'' must vanish while f' approaches unity.

Equation (3-204) immediately tells us that Hiemenz achieved *similarity* with this stream function. The coordinate x has disappeared, leaving only a single similarity variable, y , and an ordinary differential equation. However, this equation should be nondimensionalized to eliminate the dimensional constants B and ν . There is no body-length scale “ L ” for this flow. Rather, the proper length and velocity scales are $\sqrt{\nu/B}$ and $\sqrt{\nu B}$, respectively. The appropriate dimensionless variables become

$$\text{Hiemenz's planar transformation: } \eta = y \sqrt{\frac{B}{\nu}} \quad \psi = xF(\eta) \sqrt{B\nu}$$

$$\text{and so} \quad u = Bx F'(\eta) \quad v = -F(\eta) \sqrt{B\nu} \quad (3-205)$$

where the prime denotes differentiation with respect to η . It can be readily shown that backward substitution into [Eq. \(3-204\)](#) yields a parameter-free differential equation, specifically

$$F''' + FF'' + 1 - F'^2 = 0 \quad (3-206)$$

The physical requirements include $u = v = 0$ at the wall ($\eta = 0$) and $u = Bx$ at a large distance from the wall. This assortment of boundary conditions translates into

$$F(0) = F'(0) = 0 \quad \text{and} \quad F'(\infty) = 1 \quad (3-207)$$

The two nonlinearities in (3-206) have prevented analytical solutions from being found. Instead, Hiemenz (1911) performed numerical calculations by hand. Today, it is quite straightforward to solve [Eq. \(3-206\)](#) on a computer using, say, Runge–Kutta integration. Letting $Y(1) = F''$, $Y(2) = F'$, and $Y(3) = F$, the basic (say FORTRAN) relations for [Eq. \(3-206\)](#) would be

$$F(1) = Y(2)*Y(2) - 1 - Y(1)*Y(3) \quad F(2) = Y(1) \quad F(3) = Y(2) \quad (3-208)$$

Numerically, for the initial values at $X = 0$, we can set $Y(2) = Y(3) = 0$ based on the first two conditions of [Eq. \(3-207\)](#). The problem reduces to finding the correct value of $Y(1) = F''_0$, which causes $Y(2)$ to approach unity as η becomes very large. One must first address the question of how large “infinity” needs to be taken. One answer is: when F'' becomes very small, say $<10^{-5}$. The following would be a typical asymptotic analysis: In [Eq. \(3-206\)](#), as η becomes large, $F \rightarrow a + \eta$ and $(1 - F'^2) \rightarrow 0$. Therefore, at large η , a conservative view of [Eq. \(3-206\)](#) is

$$\frac{F'''}{F''} \approx -\eta \quad \text{or} \quad F'' \approx e^{-\eta^2/2}$$

With this estimate, we are reasonably confident that $F'' < 10^{-5}$ if $\eta > 4.8$ represents the far-field “infinity.” Finally, to ensure numerical accuracy of the fourth-order-accurate Runge–Kutta method, we can select a step size of $\Delta\eta = 0.03$ so that $(\Delta\eta)^4 \leq 10^{-6}$. Using these preliminaries, the numerical solution of [Eq. \(3-206\)](#) is readily obtained by making an array of guesses ranging from $F''_0 \approx 0$ to 1.5.

The complete solution for viscous stagnation flow is shown in [Fig. 3-32](#) and tabulated in [Table 3-4](#). Also shown—and to be discussed next—is the solution for axisymmetric stagnation flow. Represented in [Fig. 3-32](#) are the characteristic stream function F , the velocity profile F' , and the shear stress F'' . The correct value of the initial guess F''_0 turns out to be 1.2326.

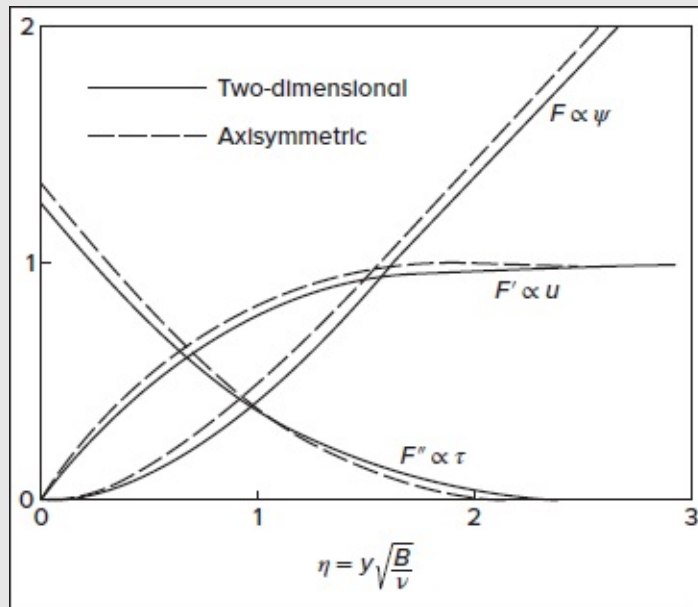


FIGURE 3-32

Numerical solutions of viscous stagnation flow for planar [Eq. (3-206)] and axisymmetric [Eq. (3-219)] conditions.

TABLE 3-4

Numerical solutions for stagnation flow

$F' = u/U$		
	Planar	Axisymmetric
	$F''(0) = 1.23259$	$F''(0) = 1.31194$
η	$\eta^* = 0.6479$	$\eta^* = 0.5689$
0.1	0.11826	0.12619
0.2	0.22661	0.24239
0.3	0.32524	0.34863
0.4	0.41446	0.44499
0.5	0.49465	0.53160
0.6	0.56628	0.60871
0.7	0.62986	0.67663
0.8	0.68954	0.73577
0.9	0.73508	0.78666
1.0	0.77787	0.82987
1.1	0.81487	0.86608
1.2	0.84667	0.89598
1.3	0.87381	0.92032
1.4	0.89681	0.93983
1.5	0.91617	0.95522
1.6	0.93235	0.96718
1.7	0.94578	0.97631
1.8	0.95684	0.98316
1.9	0.96588	0.98822
2.0	0.97322	0.99190
2.2	0.98386	0.99635
2.4	0.99055	0.99847
2.6	0.99464	0.99940
2.8	0.99705	0.99979
3.0	0.99843	0.99993

3-8.1.2 HARBINGERS OF BOUNDARY-LAYER BEHAVIOR. The stagnation flow, which constitutes an exact solution of the Navier–Stokes equations, exhibits many characteristics of thin-shear-region or *boundary-layer* behavior. The no-slip condition creates a low-velocity region that merges smoothly with the outer inviscid flow along the wall. In boundary-layer theory, the outer flow is called the “freestream” velocity, $U(x)$:

$$\text{Stagnation flow:} \quad U(x) = u(x, \infty) = Bx \quad (3-209)$$

Since the pressure decreases in the flow direction for this type of accelerating freestream, it is characterized by a *favorable* pressure gradient.

The thickness δ of this stagnation layer is defined as the point where $u/U = 0.99$, which occurs in [Table 3-4](#) when $\eta \approx 2.4 = \delta \sqrt{B/\nu}$. Thus

$$\delta \approx 2.4 \sqrt{\nu/B} \quad (3-210)$$

Page 122The boundary-layer thickness is constant in this case because the thinning due to stream acceleration exactly balances the thickening caused by viscous diffusion. In Sec. 4-3,

we will see that if $U = C x_m$, the boundary layer will grow with x when $m < 1$ and will become thinner when $m > 1$.

In typical engineering applications, the stagnation boundary layer is quite thin. For example, if we consider air at 20°C approaching a 10 cm diameter cylinder at a speed $U_0 = 10$ ms, we get $B = 4U_0/D = 400 \text{ s}^{-1}$ (see Sec. 7.3), and [Eq. \(3-210\)](#) predicts that $\delta \approx 0.46$ mm, or only 0.5 percent of the body diameter.

Another boundary-layer effect is the displacement of the outer stream by the shear layer, as hinted at in [Fig. 3-31](#). We define the *displacement thickness* δ^* as the distance the outer inviscid flow is pushed away from the wall because of the decelerating viscous layer. In terms of the stream function F , we find that

$$\lim_{\eta \rightarrow \infty} F(\eta) = \eta - \eta^* \quad \text{where} \quad \eta^* = \delta^* \sqrt{\frac{B}{\nu}} = 0.6479 \quad (3-211)$$

as shown in [Table 3-4](#). In stagnation flow, then, $\delta^* \approx 0.27\delta$.

The pressure distribution also exhibits boundary-layer behavior. With u and v known from [Eqs. \(3-205\)](#), we can return to the momentum equations (3-203) and integrate for the pressure $p(x, y)$. The result is

$$p(0, 0) - p(x, \eta) = \frac{1}{2}\rho(BxF')^2 + \frac{1}{2}B\mu F^2 + B\mu F' \quad \text{or} \quad p(0, 0) - p(x, \eta) = \frac{1}{2}\rho(u^2 + v^2) + B\mu F' \quad (3-212)$$

A useful discussion of the pressure integrability properties of the Navier–Stokes equations is given by Saad and Majdalani (2012). Note that the pressure distribution here resembles the frictionless Bernoulli equation except for the additional small term $B\mu F'$. It is instructive to calculate the pressure gradients in each direction:

$$\frac{\partial p}{\partial x} = -\rho B^2 x = -\rho U \frac{dU}{dx} \quad \text{and} \quad \frac{\partial p}{\partial y} = -\rho B \sqrt{B\nu} (FF' + F'') = O(\sqrt{\nu}) \quad (3-213)$$

Page 123Interestingly, the gradient parallel to the wall satisfies Bernoulli’s equation, whereas the gradient normal to the wall is negligibly small so long as the fluid viscosity is small. As we shall see in [Chap. 4](#), these are two of the fundamental assumptions of boundary-layer theory.

Finally, the wall shear also yields a type of boundary-layer relation. With u and v known, we readily compute

$$\tau_w = \mu \left(\frac{\partial u}{\partial y} + \frac{\partial v}{\partial x} \right) \Big|_{y=0} = \mu B x F_0'' \sqrt{\frac{B}{\nu}} = U F_0'' \sqrt{\mu \rho B} \quad (3-214)$$

In this flow, then, wall shear is proportional to the freestream velocity. If we nondimensionalize in the manner of [Eq. \(3-39\)](#), we obtain

$$C_f = \frac{2\tau_w}{\rho U^2} = \frac{2F_0''}{\sqrt{Re_x}}; \quad Re_x = \frac{Ux}{\nu} \quad (3-215)$$

We thus recover this inverse variation of skin friction with the square root of the local Reynolds number, which is very common in laminar boundary layers.

3-8.1.3 AXISYMMETRIC STAGNATION FLOW. In planar flow, the stagnation “point” is really a *line*, i.e., there is no variation in the z direction. In axisymmetric flow, stagnation is a true point, we interpret x in [Fig. 3-31](#) as the radial coordinate r , and y as the axial coordinate. The cylindrical stream function is defined differently (see App. B3) using axisymmetric continuity:

$$u = -\frac{1}{x} \frac{\partial \psi}{\partial y} \quad \text{and} \quad v = \frac{1}{x} \frac{\partial \psi}{\partial x} \quad (3-216)$$

Similarly, the x -(or radial) momentum equation becomes

$$u \frac{\partial u}{\partial x} + v \frac{\partial u}{\partial y} = -\frac{1}{\rho} \frac{\partial p}{\partial x} + \nu \left[\frac{1}{x} \frac{\partial}{\partial x} \left(x \frac{\partial u}{\partial x} \right) - \frac{u}{x^2} + \frac{\partial^2 u}{\partial y^2} \right] \quad (3-217)$$

The stream function for inviscid flow toward an axisymmetric stagnation point is given by

$$\psi = -Bx^2y \quad u = Bx \quad \text{and} \quad v = -2By \quad (3-218)$$

In comparison to the planar flow case, we observe the following: Because of the circular geometry, as the flow area increases along the wall with x , an increase in u is balanced by twice as much of a decrease in v . Following Hiemenz’s analysis, Homann (1936) defines the appropriate dimensionless variables for axisymmetric flow:

$$\text{Homann's axisymmetric transformation:} \quad \eta = y \sqrt{\frac{B}{\nu}} \quad \psi = -x^2 F(\eta) \sqrt{B\nu} \quad (3-219)$$

$$\text{and so } u = Bx F'(\eta) \quad \text{and} \quad v = -2F(\eta) \sqrt{B\nu}$$

Note the common characteristics and differences relative to the planar relations in [Eqs. \(3-205\)](#). Substitution in the y -momentum equation again yields $\partial^2 p / \partial x \partial y = 0$, and then from [Eq. \(3-217\)](#), one retrieves the axisymmetric differential equation:

$$F''' + 2FF'' + 1 - F'^2 = 0 \quad (3-220)$$

with, as before, $F(0) = F'(0) = 0$ and $F'(\infty) = 1$, which are identical to those of [Eq. \(3-207\)](#). A numerical solution can be obtained in the same manner as for the planar case, and the proper initial condition is found to be $F_0'' = 1.31194$.

The axisymmetric solutions are also shown in [Fig. 3-32](#) and cataloged in [Table 3-4](#). They differ slightly from the planar flow, specifically by displaying even smaller displacement and boundary-layer thicknesses and a bit larger wall shear stress.

3-8.1.4 STAGNATION-POINT TEMPERATURE DISTRIBUTIONS. Once the velocities are found from the previous analysis, the temperatures can be deduced from the energy equation. A similarity solution exists if the wall and stream temperatures, T_w and T_∞ , are constant—which is a realistic approximation in typical stagnation heat-transfer problems. Page 124

The planar solution for this problem is given by Goldstein (1938). The two-dimensional energy equation (3-3), with negligible mechanical dissipation, can be written as

$$\rho c_p \left(u \frac{\partial T}{\partial x} + v \frac{\partial T}{\partial y} \right) = k \left(\frac{\partial^2 T}{\partial x^2} + \frac{\partial^2 T}{\partial y^2} \right) \quad (3-221)$$

Following Goldstein (1938), we define a dimensionless temperature Θ , which vanishes at the wall and approaches unity as $y \rightarrow \infty$:

$$\Theta(\eta) = \frac{T - T_w}{T_\infty - T_w} \quad \text{where} \quad \eta = y \sqrt{\frac{B}{\nu}} \quad (3-222)$$

In other words, with constant T_w and T_∞ , the fluid temperature $T = T(\eta)$ only. With u and v known from [Eqs. \(3-205\)](#), substitution into the energy equation (3-221) yields a second-order linear equation:

$$\frac{d^2 \Theta}{d\eta^2} + Pr F(\eta) \frac{d\Theta}{d\eta} = 0 \quad (3-223)$$

with $\Theta(0) = 0$ and $\Theta(\infty) = 1$. The stream function $F(\eta)$ is known from [Fig. 3-32](#), and the Prandtl number $Pr = \mu c_p / k$ is assumed constant. Equation (3-223) is linear and has an exact solution that can be readily verified:

$$\Theta(\eta) = \frac{\int_0^\eta \exp \left(-Pr \int_0^\eta F(s) ds \right) d\eta}{\int_0^\infty \exp \left(-Pr \int_0^\eta F(s) ds \right) d\eta} \quad (3-224)$$

[Figure 3-33](#) shows the temperature profiles from this relation for various Prandtl numbers. The region of large gradients in Θ may be termed the *thermal boundary layer* and, by analogy with the velocity shear layer thickness δ_u , its thickness δ_T is the point where $\Theta \approx 0.99$. A power-law curve fit to values computed from [Fig. 3-33](#) suggests

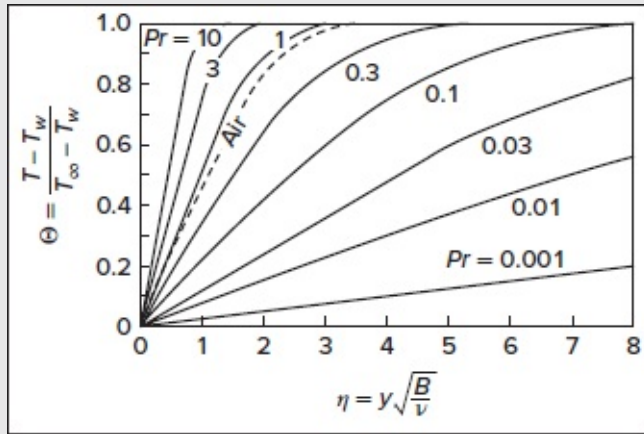


FIGURE 3-33

Stagnation-point temperature distribution for two-dimensional flow based on [Eq. \(3-224\)](#)

$$\frac{\delta_u}{\delta_T} \approx Pr^{0.4} \quad (3-225)$$

Physically, the velocity boundary layer will be thicker than the thermal boundary layer when $Pr > 1$, because viscous diffusion exceeds conduction effects. The opposite is, of course, also true. At this point, the heat transfer at the wall may be computed from Fourier's law:

$$q_w = -k \left. \frac{\partial T}{\partial y} \right|_{y=0} = -k(T_\infty - T_w)G(Pr) \sqrt{\frac{B}{\nu}} \quad (3-226)$$

where G^{-1} is the denominator in [Eq. \(3-224\)](#):

$$\frac{1}{G(Pr)} = \int_0^\infty \exp\left(-Pr \int_0^\eta F(s) ds\right) d\eta \quad (3-227)$$

We may compute G simply by adding two lines to our earlier code, (3-208), by essentially setting

$$F(4) = Y(3) \quad F(5) = \text{EXP}(-PR*Y(4))$$

Page 125The output $Y(5)$ from a Runge–Kutta solver will thus return $G(Pr)$. The corresponding effect of the Prandtl number on heat transfer is shown in [Fig. 3-34](#) and some numerical values of G for both planar and axisymmetric flows are given below:

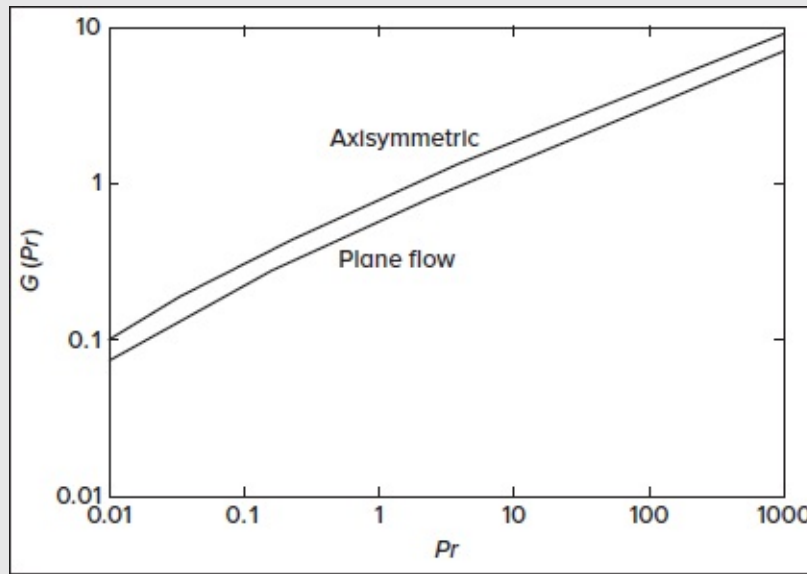


FIGURE 3-34

Variation of the heat-transfer parameter $G(Pr)$ for planar and axisymmetric stagnation flows.

Pr	G (planar)	G (axisymmetric)
0.01	0.076	0.106
0.1	0.220	0.301
1.0	0.570	0.762
10	1.339	1.752
100	2.986	3.870
1000	6.529	8.427

Note that the axisymmetric values are about one-third higher. The log–log curves in [Fig. 3-34](#) are nearly straight lines, so one can fit them into a power law, at least near a Prandtl number of unity:

$$\text{Plane flow:} \quad G \approx 0.570Pr^{0.4} \quad (3-228)$$

$$\text{Axisymmetric flow:} \quad G \approx 0.762Pr^{0.4}$$

As we move to consider the axisymmetric flow analog, the counterpart of the energy equation (3-221) becomes (App. G):

$$\rho c_p \left(u \frac{\partial T}{\partial x} + v \frac{\partial T}{\partial y} \right) = k \left[\frac{1}{x} \frac{\partial}{\partial x} \left(x \frac{\partial T}{\partial x} \right) + \frac{\partial^2 T}{\partial y^2} \right] \quad (3-229)$$

The solution is given by Sibulkin (1952), using precisely the same similarity variable $\Theta(\eta)$ from [Eq. \(3-222\)](#). However, with u and v now given by Homann's axisymmetric forms in [Eq. \(3-219\)](#), the equation for Θ becomes

$$\frac{d^2 \Theta}{d\eta^2} + 2PrF \frac{d\Theta}{d\eta} = 0 \quad (3-230)$$

The change is the factor “2” in the second term. The solutions for the temperature distribution, through [Eq. \(3-224\)](#), and heat-transfer parameter $G(Pr)$, through [Eq. \(3-227\)](#), are valid for axisymmetric flow if the Prandtl number is replaced by “ $2Pr$.” Moreover, $F(\eta)$ must be taken from the axisymmetric stream function in [Fig. 3-32](#).

The axisymmetric heat-transfer parameter $G(Pr)$ is now added to [Fig. 3-34](#). Although [Eq. \(3-226\)](#) tells the whole story, namely, that q_w is constant independently of x , it is customary to nondimensionalize q_w as a local Nusselt number by putting

$$Nu_x = \frac{q_w x}{k(T_w - T_\infty)} = G(Pr) Re_x^{1/2} \quad (3-231)$$

Page 126 where $Re_x = Ux/\nu = B x_2/\nu$ and $G(Pr)$ is given by [Fig. 3-34](#) or the power-law approximations of [Eq. \(3-228\)](#). As we discuss in [Chap. 4](#), [Eq. \(3-231\)](#) has the typical form of laminar-boundary-layer heat-transfer relations, but in the present case, it is rather misleading because it contains a useless “ x ” on each side.

3-8.1.5 THE REYNOLDS ANALOGY. Osborne Reynolds (1874) postulated an approximation, now called the *Reynolds analogy*, for estimating heat transfer in shear layers. He found that, in pipe flow and “similar” boundary layers such as stagnation flow, the wall shear and heat-transfer rate are proportional:

$$\frac{|q_w|}{\tau_w} = \frac{|k(\partial T/\partial y)_w|}{\mu(\partial u/\partial y)_w} \approx \frac{k}{\mu} \left| \frac{dT}{du} \right|_w \quad (3-232)$$

The analogy will not work unless u and T are similar in behavior, which is certainly true in stagnation flow from inspection of [Figs. 3-32](#) and [3-33](#). Since T varies with Pr and u does not, the ratio above must vary with the Prandtl number. The appropriate way to nondimensionalize [Eq. \(3-232\)](#) is to compare the friction factor C_f to the Stanton number, $C_h \equiv Nu/(RePr)$. Then, in general, the Reynolds analogy postulates that

$$\frac{C_h}{C_f} = f(Pr, \frac{x}{L}, \text{geometry}) \quad (3-233)$$

We may rewrite our stagnation-flow heat-transfer results, Eqs. (3-328) and [\(3-231\)](#), in terms of the Stanton number:

$$0.1 < Pr < 10: \quad C_h \sqrt{Re_x} \approx \begin{cases} 0.570 Pr^{-0.6} & (\text{planar}) \\ 0.762 Pr^{-0.6} & (\text{axisymmetric}) \end{cases} \quad (3-234)$$

Dividing this by the friction coefficient from [Eq. \(3-215\)](#), we obtain

$$\frac{C_h}{C_f} \approx \begin{cases} 0.23Pr^{-0.6} & \text{(planar)} \\ 0.29Pr^{-0.6} & \text{(axisymmetric)} \end{cases} \quad (3-235)$$

Thus, if C_f is known, C_h follows immediately. Comparable relations hold for turbulent shear flow over simple geometries, such as the flat plate. The drawback to [Eq. \(3-235\)](#) is that the constants (0.23, 0.29) vary markedly with the pressure gradient (Sec. 4-3). Furthermore, the Reynolds analogy deteriorates for (1) varying wall temperature and (2) nonsimilar flows.

This discussion concludes our detailed study of stagnation-flow problems, which lead to exact solutions to the Navier–Stokes equations. The results demonstrate a variety of boundary-layer phenomena: a thin viscous layer, a displacement thickness, a thin thermal layer, pressure varying with Bernoulli’s relation in the outer layer, a very small normal velocity near the wall, a very small normal pressure gradient, the Reynolds analogy, and power-law Reynolds and Prandtl number effects. The only important effect missing is shear layer *separation* (Fig. 1.11), which cannot occur in stagnation flow because the freestream velocity increases with x (“favorable” pressure gradient, [Fig. 4-5](#)). Our third example in this section, the Jeffery–Hamel wedge flow, will focus on the flow separation problem.

3-8.2 Flow Above an Infinite Rotating Disk

Consider the steady flow which results if the infinite plane at $z = 0$ rotates at constant angular speed ω about the axis $r = 0$ beneath a Newtonian viscous fluid, which would otherwise be at rest. The viscous drag of the rotating surface would set up a swirling flow toward the disk, as illustrated in [Fig. 3-35](#). All three velocity components v_r , v_θ , and v_z would be involved—a genuine three-dimensional motion—but because of radial symmetry they would be independent of θ , as would the pressure p . It is required then to solve for these four variables as functions of r and z from the continuity and Navier–Stokes equations in the r , θ , and z directions:

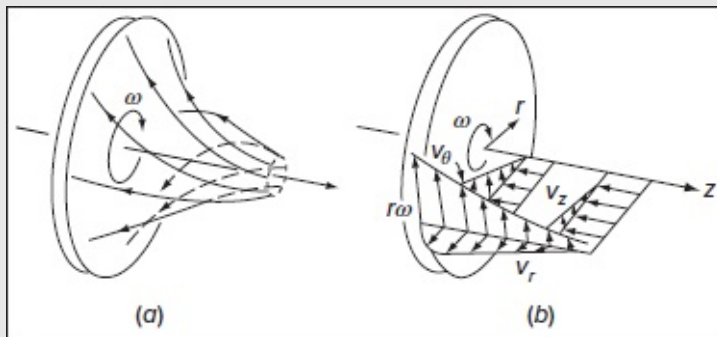


FIGURE 3-35

Laminar flow near a rotating disk: (a) streamlines and (b) velocity components.

$$\frac{1}{r} \frac{\partial}{\partial r}(rv_r) + \frac{\partial}{\partial z}(v_z) = 0 \quad (3-236)$$

$$\begin{aligned} v_r \frac{\partial v_r}{\partial r} + v_z \frac{\partial v_r}{\partial z} - \frac{v_\theta^2}{r} &= -\frac{1}{\rho} \frac{\partial p}{\partial r} + \nu \left(\frac{\partial^2 v_r}{\partial r^2} + \frac{1}{r} \frac{\partial v_r}{\partial r} + \frac{\partial^2 v_r}{\partial z^2} - \frac{v_r}{r^2} \right) \\ v_r \frac{\partial v_\theta}{\partial r} + v_z \frac{\partial v_\theta}{\partial z} + \frac{1}{r} v_r v_\theta &= \nu \left(\frac{\partial^2 v_\theta}{\partial r^2} + \frac{1}{r} \frac{\partial v_\theta}{\partial r} + \frac{\partial^2 v_\theta}{\partial z^2} - \frac{v_\theta}{r^2} \right) \\ v_r \frac{\partial v_z}{\partial r} + v_z \frac{\partial v_z}{\partial z} &= -\frac{1}{\rho} \frac{\partial p}{\partial z} + \nu \left(\frac{\partial^2 v_z}{\partial r^2} + \frac{1}{r} \frac{\partial v_z}{\partial r} + \frac{\partial^2 v_z}{\partial z^2} \right) \end{aligned}$$

The boundary conditions are no slip at the wall and no viscous effect far from the wall (except for an axial inflow):

$$\begin{aligned} \text{At } z = 0: \quad & v_r = v_z = 0 \quad v_\theta = r\omega \quad p = \text{const} = 0 \\ \text{As } z \rightarrow \infty: \quad & v_r = v_\theta = \frac{\partial v_z}{\partial z} = 0 \end{aligned} \quad (3-237)$$

This fully three-dimensional flow is often called “von Kármán’s viscous pump” [Panton (1996)]. The rotating disk sets the near-wall fluid into circumferential motion v_θ . The flow will have a tendency to move in circular streamlines when the pressure increases radially to balance the inward centripetal acceleration. But, in fact, $p = p(z)$ only, and the radial imbalance causes an outward radial flow, $v_r > 0$ (Fig. 3-35a). This outward mass flow is balanced by an inward axial flow toward the disk, $v_z < 0$.

The solution to this problem is described in a remarkable paper by Kármán (1921), who considered not only the rotating disk but also all manner of laminar and turbulent shear flows. Kármán—whose autobiography (1964) is highly recommended—was able to achieve a similarity solution after deducing that v_r/r , v_θ/r , v_z , and p are all functions of z only. This simplification reduces the problem to four coupled ordinary differential equations in the single variable z . Since the only parameters in the problem are ω and ν , it is easy to see that the correct dimensionless variable must be $z^* = z\sqrt{\omega/\nu}$. Following Kármán (1921), then, we propose the new dimensionless variables F , G , H , and P such that

$$v_r = r\omega F(z^*) \quad v_\theta = r\omega G(z^*) \quad v_z = \sqrt{\omega\nu} H(z^*) \quad p = \rho\omega\nu P(z^*) \quad (3-238)$$

We can substitute these variables into Eqs. (3-236) and obtain a coupled set of nonlinear ordinary differential equations:

$$H' = -2F, \quad F'' = -G^2 + F^2 + F'H, \quad G'' = 2FG + HG', \quad \text{and} \quad P' = 2FH - 2F' \quad (3-239)$$

where primes denote differentiation with respect to z^* . The boundary conditions from (3-237) become

$$F(0) = H(0) = P(0) = 0, \quad G(0) = 1, \quad \text{and} \quad F(\infty) = G(\infty) = 0 \quad (3-240)$$

Note that P is uncoupled: We can solve the first three equations in (3-239) for F , G , and H , and then solve for P from the fourth equation.

Kármán used this problem to illustrate his celebrated momentum-integral relation (Sec. 4-5) derived in the same 1921 paper. Later, Cochran (1934) improved the accuracy with matched-asymptotic expansions while Rogers and Lance (1960) provided very precise numerical predictions. The system in (3-239) can be solved using a Runge–Kutta solver: One simply needs to define six variables: $Y_1 = H$, $Y_2 = \bar{F}'$, $Y_3 = F$, $Y_4 = G'$, $Y_5 = G$, and $Y_6 = P$. Equations (3-239) are then simulated on a digital computer using six statements

$$\begin{aligned} F(1) &= -2.*Y(3) & F(2) &= -Y(5)*Y(5) + Y(3)*Y(3) + Y(2)*Y(1) & F(3) &= Y(2) \\ F(4) &= 2.*Y(3)*Y(5) + Y(1)*Y(4) & F(5) &= Y(4) & F(6) &= 2.*Y(3)*Y(1) - 2.*Y(2) \end{aligned} \quad (3-341)$$

The known initial conditions from [Eqs. \(3-240\)](#) are $Y_1(0) = Y_3(0) = Y_6(0) = 0$ and $Y_5(0) = 1$. The unknown conditions are $F'_0 = Y_2(0)$ and $G'_0 = Y_4(0)$, which must be chosen to make Y_3 and Y_5 vanish at large η . An appropriate step size in $\Delta\eta \leq 0.1$ and “infinity” is reached at about $\eta \approx 10$. The correct initial conditions are found to be $F'_0 = 0.5102$ and $G'_0 = -0.6159$, and the complete numerical solutions are illustrated in [Fig. 3-36](#) and [Table 3-5](#).

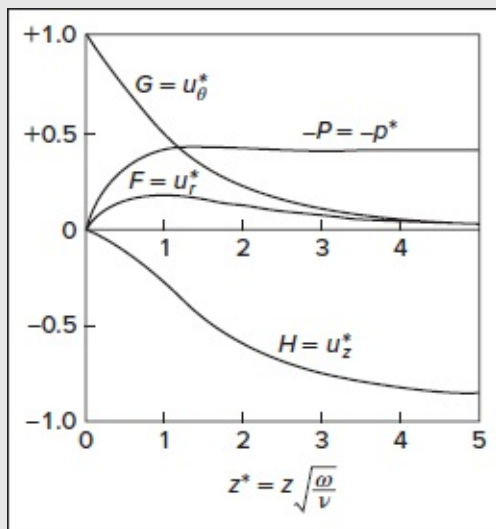


FIGURE 3-36

Numerical solutions of [Eqs. \(3-239\)](#) for the infinite rotating disk.

TABLE 3-5

Numerical solution for the rotating disk

z^*	F	F'	G	G'	H	$-P$
0.0	0.0	0.51023	1.0000	-0.61592	0.0	0.0
0.1	0.0462	0.4163	0.9386	-0.6112	-0.0048	0.0924
0.2	0.0836	0.3338	0.8780	-0.5987	-0.0179	0.1674
0.3	0.1133	0.2620	0.8190	-0.5803	-0.0377	0.2274
0.4	0.1364	0.1999	0.7621	-0.5577	-0.0628	0.2747
0.5	0.1536	0.1467	0.7075	-0.5321	-0.0919	0.3115
0.6	0.1660	0.1015	0.6557	-0.5047	-0.1239	0.3396
0.7	0.1742	0.0635	0.6067	-0.4763	-0.1580	0.3608
0.8	0.1789	0.0317	0.5605	-0.4476	-0.1933	0.3764
0.9	0.1807	0.0056	0.5171	-0.4191	-0.2293	0.3877
1.0	0.1801	-0.0157	0.4766	-0.3911	-0.2655	0.3955
1.2	0.1737	-0.0461	0.4037	-0.3381	-0.3364	0.4040
1.4	0.1625	-0.0640	0.3411	-0.2898	-0.4038	0.4066
1.6	0.1487	-0.0728	0.2875	-0.2470	-0.4661	0.4061
1.8	0.1338	-0.0754	0.2419	-0.2095	-0.5226	0.4042
2.0	0.1188	-0.0739	0.2034	-0.1771	-0.5732	0.4019
2.2	0.1044	-0.0698	0.1708	-0.1494	-0.6178	0.3997
2.4	0.0910	-0.0643	0.1433	-0.1258	-0.6568	0.3977
2.6	0.0788	-0.0580	0.1202	-0.1057	-0.6907	0.3961
2.8	0.0678	-0.0517	0.1008	-0.0888	-0.7200	0.3948
3.0	0.0581	-0.0455	0.0845	-0.0746	-0.7452	0.3938
3.2	0.0496	-0.0397	0.0709	-0.0625	-0.7666	0.3930
3.4	0.0422	-0.0344	0.0594	-0.0525	-0.7850	0.3924
3.6	0.0358	-0.0296	0.0498	-0.0440	-0.8005	0.3920
3.8	0.0303	-0.0254	0.0417	-0.0369	-0.8137	0.3917
4.0	0.0256	-0.0217	0.0349	-0.0309	-0.8249	0.3914
4.5	0.0167	-0.0144	0.0225	-0.0199	-0.8457	0.3911
5.0	0.0108	-0.0095	0.0144	-0.0128	-0.8594	0.3910
5.5	0.0070	-0.0062	0.0093	-0.0082	-0.8682	0.3910
6.0	0.0045	-0.0040	0.0059	-0.0053	-0.8739	0.3909
7.0	0.0018	-0.0017	0.0024	-0.0022	-0.8799	0.3909
8.0	0.0007	-0.0007	0.0010	-0.0009	-0.8824	0.3908
9.0	0.0002	-0.0003	0.0004	-0.0004	-0.8834	0.3908
10.0	0.0001	-0.0001	0.0001	-0.0001	-0.8838	0.3907
∞	0.0	-0.0	0.0	-0.0	-0.8838	0.3906

We may define the thickness δ as the point where the circumferential velocity v_θ drops to 1 percent of its wall value, or $G \approx 0.01$, which occurs at about $\eta \approx 5.4$. The corresponding layer thickness can be easily calculated to be

$$\delta \approx 5.4 \sqrt{\nu/\omega} \quad (3-242)$$

Page 128Page 129For a disk rotating at 1000 rpm (105 rad/s) in air at 20°C, this relation predicts a (laminar) shear layer thickness of approximately 2 mm. Moreover, we find the asymptotic value $H(\infty) = -0.8838$, which means that the disk draws fluid toward itself at the rate

$$v_z(\infty) = -0.8838 \sqrt{\omega \nu} \quad (3-243)$$

It can thus be seen that the disk's pumping action increases with both viscosity and rotation rate. For the above numerical example (1000 rpm in air), this streaming velocity will be 3.5 cm/s toward the disk. As for the circumferential wall shear stress on the disk, it can be evaluated from

$$\tau_{z\theta} = \mu \left. \frac{\partial u_\theta}{\partial z} \right|_{z=0} = \rho r G'_0 \sqrt{\nu \omega^3} \quad (3-244)$$

where $G'_0 = -0.6159$ from [Table 3-5](#). We use this result with a radial strip integration to determine the total torque required to turn a disk of radius r_0 :

$$M = \int_0^{r_0} \tau_{z\theta} r (2\pi r dr) = \frac{1}{2} \pi \rho r_0^4 G'_0 \sqrt{\nu \omega^3} \quad (3-245)$$

Clearly, the required moment increases as the fourth power of the disk radius. For our running example, 1000 rpm in air, if the disk radius is 10 cm, this torque is only 0.0005 N · m. A dimensionless torque coefficient can be defined for a disk wetted on both sides:

$$C_M = -\frac{2M}{\frac{1}{2} \rho \omega^2 r_0^5} \approx \frac{3.87}{\sqrt{Re_k}} \quad \text{where} \quad Re_k = \omega^* = \frac{\omega r_0^2}{\nu} \quad (3-246)$$

Again we have the characteristic inverse variation with the square root of the kinetic Reynolds number, which we already introduced in [Eq. \(3-100\)](#). By way of confirmation, [Eq. \(3-246\)](#) is compared in [Fig. 3-37](#) with the data of Theodorsen and Regier (1944). Although the agreement is adequate in the laminar regime, the flow becomes turbulent and follows the dashed line for $Re > 300,000$.

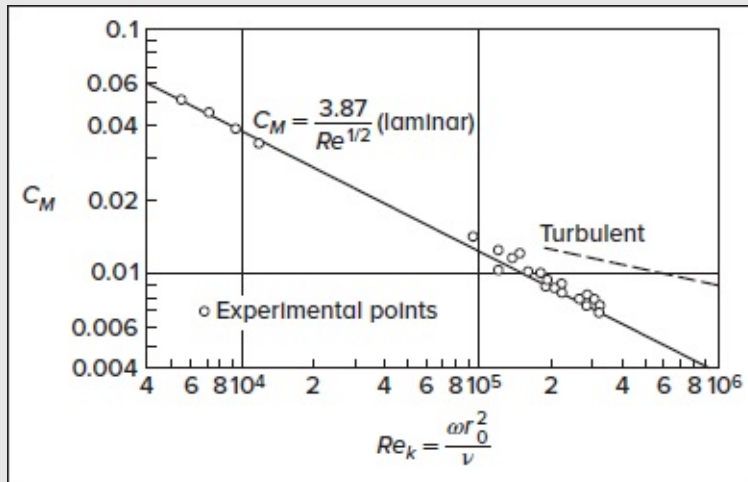


FIGURE 3-37

Theoretical and experimental torque coefficient for a rotating disk. [Data from Theodorsen and Regier (1944).]

The expected instability of laminar rotating-disk flow was clearly demonstrated in experiments carried out by Kobayashi et al. (1980). They rotated a 40 cm diameter black aluminum disk in air at 1300 to 1900 rpm, and then visualized the flow with white titanium tetrachloride gas. A numerical simulation of the flow is shown in [Fig. 3-38](#). Instability is observed at $Re_k = \omega r_2/\nu \approx 8.8 \times 10_4$. Then, at $Re \approx 3.2 \times 10_5$, turbulence ensues.

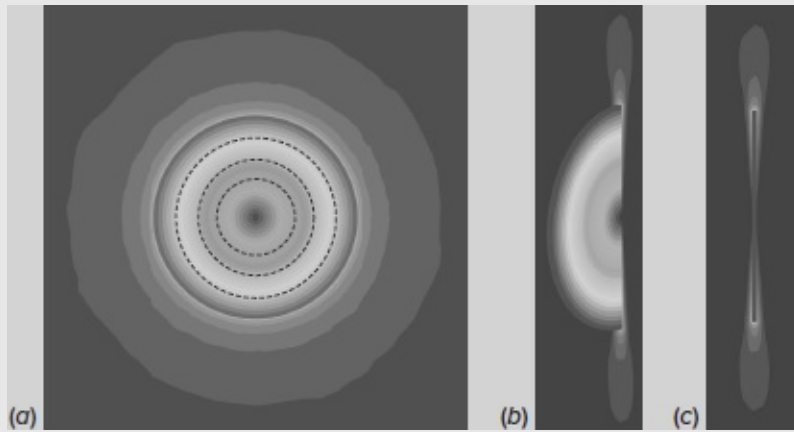


FIGURE 3-38

Flow pattern around a 40 cm disk rotating in air at 1800 rpm. Laminar flow becomes unstable at $r = 8$ cm, laminar spiral vortices form at $r = 12$ cm, and transition to turbulence occurs at $r = 16$ cm. Finite-volume simulation results show (a) top, (b) isometric, and (c) side views of the disc based on the SST $k-\omega$ turbulence model. Computations are performed by G. Sharma and J. Majdalani in a manner to replicate the experiments conducted by *Kobayashi et al. (1980)*.

Many other papers have been written about various flow problems associated with one or more circular disks. Of particular interest is rotating *flow* next to a fixed disk, first considered by Bödewadt (1940) and later by Rogers and Lance (1960). The picture is essentially reversed from [Fig. 3-35](#). The rotating outer flow sets up a radial pressure gradient which, when acting on the low-velocity fluid near the disk, causes an *inward* radial flow, called “secondary” flow. This inward motion is balanced by axial flow *away* from the disk. Secondary inward wall flow is familiar to anyone who stirs tea made with loose leaves.

3-8.3 Jeffery–Hamel Flow in a Wedge-Shaped Region

Our third and final example of an exact similarity solution focuses on the radial flow caused by a line source or sink, first discussed by Jeffery (1915) and independently by Hamel (1917). Many subsequent analyses have been devoted to this motion, and we mention especially Rosenhead (1940) and Millsaps and Pohlhausen (1953).

As shown in [Fig. 3-39](#), we consider the flow in polar coordinates (r, θ) , generated by a source (or sink) at the origin and bounded by solid walls at $\theta = \pm \alpha$, as shown. Assuming that the flow is purely radial, we can set $u_\theta = 0$. Then, from the continuity equation in polar coordinates (App. G), we have

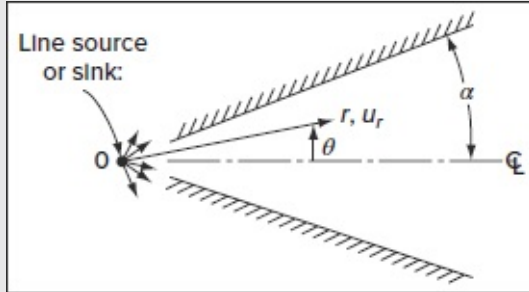


FIGURE 3-39

Geometry of the Jeffrey–Hamel flow.

$$\frac{1}{r} \frac{\partial}{\partial r} (ru_r) = 0 \quad \text{or} \quad ru_r = f(\theta) \quad (3-247)$$

We expect that u_r will have a local maximum, u_{\max} , probably at $\theta = 0$. Then a convenient nondimensionalization for this problem will entail

$$\eta = \frac{\theta}{\alpha} \quad \text{and} \quad f(\eta) = \frac{u_r}{u_{\max}} \quad (3-248)$$

Moreover, the momentum equations in polar coordinates, for $u_\theta = 0$, simplify into

$$u_r \frac{\partial u_r}{\partial r} = -\frac{1}{\rho} \frac{\partial p}{\partial r} + \nu \left(\frac{\partial^2 u_r}{\partial r^2} + \frac{1}{r} \frac{\partial u_r}{\partial r} - \frac{u_r}{r^2} + \frac{1}{r^2} \frac{\partial^2 u_r}{\partial \theta^2} \right) \quad \text{and} \quad -\frac{1}{\rho r} \frac{\partial p}{\partial \theta} + \frac{2\nu}{r^2} \frac{\partial u_r}{\partial \theta} = 0 \quad (3-249)$$

We can eliminate pressure by cross-differentiation and substitution of η and $f(\eta)$. The result is a third-order nonlinear differential equation for f :

$$f''' + 2\alpha Re f f' + 4\alpha^2 f' = 0 \quad (3-250)$$

where $Re = u_{\max} r \alpha / \nu$ is the characteristic Reynolds number. The boundary conditions consist of the no-slip condition at either wall and an assumed symmetric flow with a maximum at the centerline. These translate into

$$f(1) = f(-1) = 0 \quad \text{and} \quad f'(0) = 0 \quad (3-251)$$

We can actually replace the second condition with the symmetry requirement $f'(0) = 0$ and confine the analysis to the upper half of the wedge region.

Page 131 Since Eq. (3-250) is nonlinear, we can solve it numerically, just as we did with the stagnation flow and the rotating disk problems. Nonetheless, an analytical solution is possible here. We can start by integrating once to obtain

$$f'' + \alpha Re f^2 + 4\alpha^2 f = \text{const}$$

This equation can be multiplied by f' and integrated again, using $f(0) = 1$ and $f'(0) = 0$. We get

$$f'^2 = (1 - f) \left[\frac{2}{3} \alpha Re (f^2 + f) + 4\alpha^2 f + C \right]$$

which can be integrated once more because the variables are separable. We thus arrive at

$$\int_f^1 \frac{df}{\left\{ (1 - f) \left[\frac{2}{3} \alpha Re (f^2 + f) + 4\alpha^2 f + C \right] \right\}^{1/2}} = \eta \quad (3-252)$$

where the boundary condition $f(0) = 1$ has been implemented. As $\eta \rightarrow 1$, the lower limit approaches zero. From $f(1) = 0$ the constant C may be specified. We get

$$\int_0^1 \frac{df}{\left\{ (1 - f) \left[\frac{2}{3} \alpha Re (f^2 + f) + 4\alpha^2 f + C \right] \right\}^{1/2}} = 1 \quad (3-253)$$

Thus, Eqs. (3-252) and (3-253) represent the formal solution to this problem. The integral is an elliptical integral and can be evaluated from tables or by careful application of a numerical solver, such as Runge–Kutta's, to avoid singular behavior as $(1 - f) \rightarrow 0$.

Rosenhead (1940) made a very extensive analysis of this flow and reported the following observations:

1. For any given α and Re , there are countless solutions, both symmetric and asymmetric, corresponding to multiple regions of inflow and outflow.
2. For a given α and a specified number of inflow and outflow regions, there is a critical Re above which this specified solution is impossible.
3. For $\pi/2 < \alpha < \pi$, a solution with pure outflow is impossible, and pure-inflow solutions are limited in certain respects.
4. For $\alpha < \pi/2$, pure inflow is always possible and tends at large Re to exhibit boundary-layer behavior, whereas pure outflow is limited to certain small Re with an approximate range of $Re < 10.31/\alpha$.

Thus, once again we encounter non-uniqueness of the Navier–Stokes equations, although here it remains regular and predictable.

3.8.3.1 SOLUTION FOR SMALL WEDGE ANGLE A. The most practical

application of this flow is to the cases of large Re and small α . If both Re and α are small, we may neglect the second and third terms in [Eq. \(3-250\)](#) and integrate to

$$\alpha, \alpha Re \ll 1: \quad f = \frac{u_r}{u_{\max}} = 1 - \eta^2 \quad (3-254)$$

We thus recover the Poiseuille profile, [Eq. \(3-34\)](#), which is valid for either inflow or outflow.

Suppose instead that α is small but (αRe) is not. Then [Eq. \(3-254\)](#) reduces to

$$\left(\frac{2}{3}\alpha Re\right)^{1/2} = \int_0^1 [(1-f)(f^2 + f + K)]^{-1/2} df \quad (3-255)$$

where $K = 3C/(2\alpha Re)$. We thus can specify a range of values for K , integrate for αRe , and then deduce C from K . Values calculated in this manner are shown in [Fig. 3-40](#). For negative Re (inflow), the values approach the straight line $C = -4\alpha Re/3$, which is a boundary-layer approximation first discovered by Pohlhausen (1921). For positive Re (outflow), C drops to zero at $\alpha Re \approx 10.31$; since $C = f'^2(1)$, this must be a point of zero wall shear stress, a separation point beyond which backflow will occur at the wall. After evaluating C in this manner, Millsaps and Pohlhausen (1953) compute several velocity profiles from [Eq. \(3-252\)](#). [Figure 3-41](#) shows an array of inflow ($Re < 0$) and outflow ($Re > 0$) profiles computed in the same manner. The inflow curves become flatter and more stable as Re increases and will be discussed again in [Chap. 4](#).

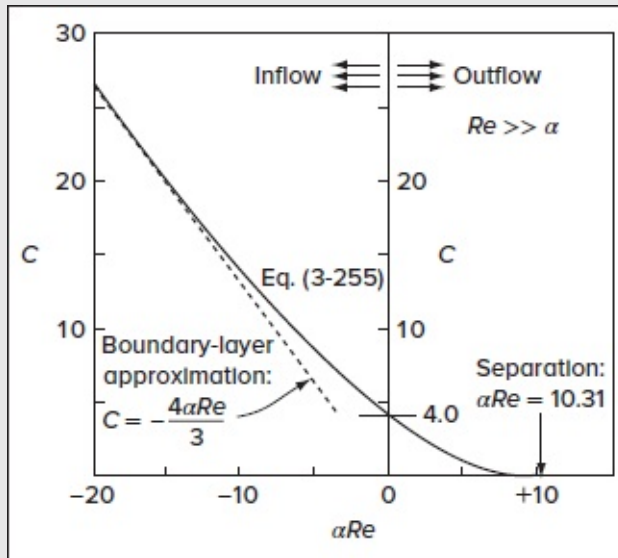


FIGURE 3-40

Values of the shear-stress constant C for wedge flow at large Reynolds numbers.

The outflow profiles become S-shaped and have zero wall shear stress (at the separation point) when $\alpha Re = 10.31$. If $\alpha Re > 10.31$, there is backflow at the wall. The difference in

profile shape is the result of the change in sign of the streamwise pressure gradient. For inflow, p decreases in the flow direction (favorable gradient), thus preventing separation. For outflow, p increases downstream (adverse gradient), a point of inflection occurs in the profile, and separation becomes imminent. Page 132

A separation criterion can be found from the pressure gradient along the centerline, which from [Eq. \(3-249\)](#) is given by

$$\frac{\partial p}{\partial r}(r, 0) \approx \frac{\rho u_{\max}^2}{r}, \quad \alpha^2 \ll 1$$

If we interpret $(r\alpha)$ as the thickness δ of the shear layer, the dimensionless form of the pressure gradient at separation would be

$$\frac{\delta^2}{\mu u_{\max}} \frac{\partial p}{\partial r}(r, 0)_{\text{separation}} \approx (\alpha Re)_{\text{separation}} = 10.31 \quad (3-256)$$

This is much more realistic than the Couette–Poiseuille flow estimate given earlier as [Eq. \(3-43\)](#). In laminar boundary layers, this quantity is related to the Kármán–Pohlhausen parameter, $-\Lambda = \delta^2(dp/dx)/(\mu U)$, which at the point of separation takes on values between 8 and 12.

With the velocity distributions given from [Fig. 3-41](#), Millsaps and Pohlhausen (1953) also solve for temperature profiles, assuming dissipation only—no hot or cold walls. For inflow, there is a region of very strong dissipation temperature rise near the wall. This example completes our overview of similar solutions to the Navier–Stokes equations. Other cases are given in the problem exercises.

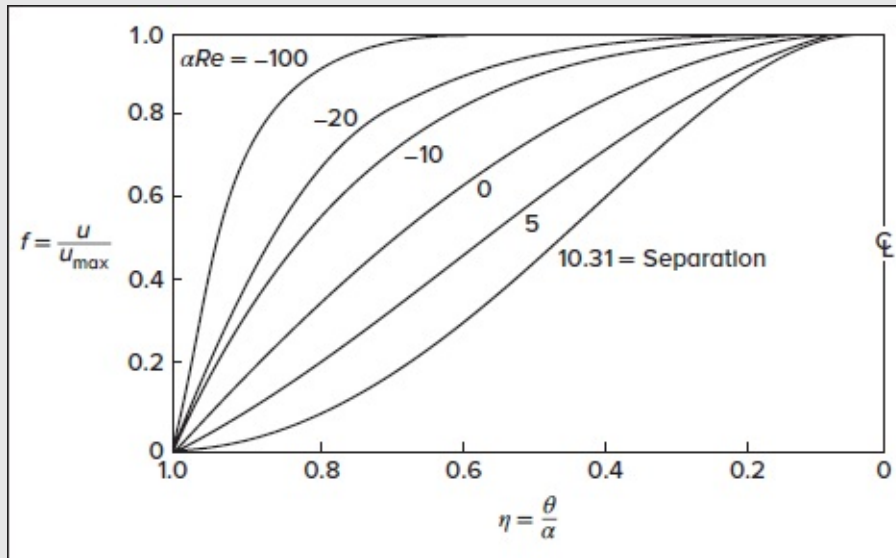


FIGURE 3-41

Velocity profiles for Jeffrey–Hamel wedge flow at large $Re \gg \alpha$, from [Eq. \(3-252\)](#). [Modified from the results of Millsaps and Pohlhausen (1953).]

3-9 LOW REYNOLDS NUMBER: LINEARIZED CREEPING MOTION

Most of the problems we have examined so far have been exact or quasi-exact solutions, valid for an arbitrary Reynolds number, until instability sets in and turbulence ensues. While interesting, these solutions lack generality. In particular, there is no known solution for the very practical problem of viscous flow past an immersed body at an arbitrary Reynolds number. Other than direct experiment, immersed-body problems are presently solvable only by three approaches: (1) digital-computer simulations; (2) boundary-layer viscous and inviscid patching schemes, as in [Chap. 4](#); and (3) the creeping-flow approximations, to be discussed here.

The basic assumption of creeping flow, developed by Stokes (1851) in a seminal paper, is that density (inertia) terms are negligible in the momentum equation. In such a flow, with stream velocity U and body length L , pressure cannot scale with the “dynamic” or inertial term ρU^2 but rather must depend upon a “viscous” scale $\mu U/L$. If we nondimensionalize the Navier–Stokes equation (3-2) with the variables

$$x^* = \frac{x}{L} \quad \mathbf{V}^* = \frac{\mathbf{V}}{U} \quad t^* = \frac{tU}{L} \quad p^* = \frac{p - p_\infty}{(\mu U/L)}$$

then the following dimensionless momentum equation is obtained:

$$Re \frac{D\mathbf{V}^*}{Dt^*} = -\nabla^* p^* + \nabla^{*2} \mathbf{V}^* \quad (3-257)$$

where $Re = \rho UL/\mu$. We can therefore neglect inertia (the left-hand side) if the Reynolds number is small. This is the creeping-flow or *Stokes flow* assumption:

$$Re \ll 1: \quad \nabla p \approx \mu \nabla^2 \mathbf{V} \quad (3-258)$$

to be combined with the incompressible continuity relation,

$$\nabla \cdot \mathbf{V} = 0 \quad (3-259)$$

Note that inertia is also negligible if there is no convective acceleration, such as in fully developed duct flow, Sec. 3-3. In such a case, the creeping-flow approximation holds with no restriction on the Reynolds number.

By taking the curl and then the gradient of [Eq. \(3-258\)](#), two additional useful relations are realized:

$$\nabla^2 \omega = 0 \quad \text{and} \quad \nabla^2 p = 0 \quad (3-260)$$

As such, both vorticity and pressure satisfy Laplace's equation in creeping motion.

Furthermore, in two-dimensional Stokes flow, we can use $\omega = -\nabla_2 \psi$, where $\psi(x, y)$ is the stream function. The vorticity equation (3-260) may be rewritten as

$$\nabla^4 \psi = 0 \quad (3-261)$$

We thus recover the *biharmonic* equation, much studied in plane elasticity problems. Typical boundary conditions for an immersed-body problem would be no slip at the body surface and uniform velocity and pressure in the freestream.

It may be worth remarking that [Eqs. \(3-258\)](#) to [\(3-261\)](#) are linear partial differential equations and thus yield many solutions in closed form. Numerical methods are also effective, including boundary-element techniques [Beer (2001) and Wrobel (2002)]. As a matter of fact, entire textbooks are written about creeping flow, notably by Happel and Brenner (1983). The drawback, of course, is that the condition $Re \ll 1$ is very restrictive and usually applies only to low-velocity, small-scale, highly viscous flows. For this reason, at least four types of creeping flow arise:

1. *Fully developed duct flow.* We have given several examples here in Sec. 3-3 and many more can be found in Berker (1963), Ladyzhenskaya (1969), and Shah and London (1978).
2. *Flow about immersed bodies.* Stokes flow is the foundation of small-particle dynamics and is treated in a text by Happel and Brenner (1983), including multiple-body interaction effects.
3. *Flow in narrow but variable passages.* First formulated by Reynolds (1886) and now known as *lubrication theory*, these flows are covered in general Stokes flow books such as Langlois (1964) and also in specialized texts such as Khonsari and Booser (2001), Szeri (1998), and Pirro et al. (2001).
4. *Flow through porous media.* This topic began with a famous treatise by Darcy (1856) and is now the subject of specialized texts such as Bear (2000), Ingham and Pop (2002), and Ehlers and Bluhm (2002). Civil engineers have long applied porous-media theory to groundwater movement [see, e.g., Charbeneau (1999)].

The fundamental principles of creeping, or small-inertia flows, are beautifully demonstrated in a 33-min color video, "Low Reynolds Number Flows," available from Encyclopedia Britannica Education Corp. The video was prepared from a color film produced over 50 years ago under the sponsorship of the National Science Foundation. It is a historical document because its narrator is Sir Geoffrey Taylor, whose collected works contain scores of important contributions to our knowledge of fluid mechanics. Today, many interesting videos can be found on YouTube.

3-9.1 Creeping Flow About Immersed Bodies: Stokes Paradox

This subject began with a solution for the flow past an immersed spherical object by Stokes (1851). Many solutions exist for three-dimensional bodies, but plane flows are fraught with paradox. As pointed out by Stokes himself, it is impossible to find a steady two-dimensional solution which satisfies both [Eq. \(3-261\)](#) and the no-slip and freestream boundary conditions. Three-dimensional flows do not have this problem, but they are slightly unrealistic in that the inertia terms are not strictly negligible in the far field of the body [Oseen (1910)].

We can illustrate the Stokes paradox with a dimensional argument: If inertia (density) is truly negligible, the force on the body must depend only upon the freestream velocity U , fluid viscosity μ , and body-length scale L :

$$\text{Two-dimensional flow:} \quad F' = \text{force per unit length} = f(U, \mu, L) \quad (3-262a)$$

$$\text{Three-dimensional flow:} \quad F = \text{total drag force} = f(U, \mu, L) \quad (3-262b)$$

Dimensional analysis of these relations leads to the force laws

$$\text{Two-dimensional:} \quad \frac{F'}{\mu U} = \text{const} \quad (3-263a)$$

$$\text{Three-dimensional:} \quad \frac{F}{\mu UL} = \text{const} \quad (3-263b)$$

The second of these is quite realistic and verified by numerous experiments, but the first is physically in error, since it implies that the drag force is independent of the size L of the body, whether huge or tiny. It follows that there must *always* be a density effect in plane creeping motion:

$$\text{Two-dimensional:} \quad F' = f(\rho, U, \mu, L) \quad \text{or} \quad \frac{F'}{\mu U} = f\left(\frac{\rho UL}{\mu}\right) \quad (3-264)$$

It can thus be seen that the Reynolds number is always important. Mathematically, the Stokes paradox means that a plane creeping solution will produce a logarithmic singularity at infinity unless inertia terms are accounted for. Physically, we can infer that a body of infinite depth produces such a profound disturbance in a viscous flow that inertia effects are always important, no matter how slow the freestream speed. Langlois (1964) explains these difficulties very well. It turns out that the Stokes paradox is not so robust for non-Newtonian fluids. With a simple analysis for power-law fluids in two-dimensional flow past a cylinder, $\tau_{xy} \approx 2K \epsilon_{xy}^n$ [Eq. (1-31a)], Tanner (1993) shows that the paradox holds only for $n = 1$ (Newtonian fluid) and for $n > 1$ (dilatant or shear-thickening fluid). Both these cases, with $n \leq 1$, have density (inertia) effects no matter how large the effective viscosity. However, for $n < 1$ (pseudoplastic or shear-thinning fluid), Tanner shows that the Stokes paradox vanishes and the creeping-flow cylinder drag becomes independent of the density.

3-9.2 Stokes' Solution for an Immersed Sphere

Consider creeping motion of a stream of speed U around a solid sphere of radius a (Fig. 3-42). It is convenient to use spherical polar coordinates (r, φ) , with the polar (or zenith) angle $\varphi = 0$ in the direction of U (defined in Chap. 2). The radial and polar velocity components u_r and u_φ are related to the Stokes stream function ψ through

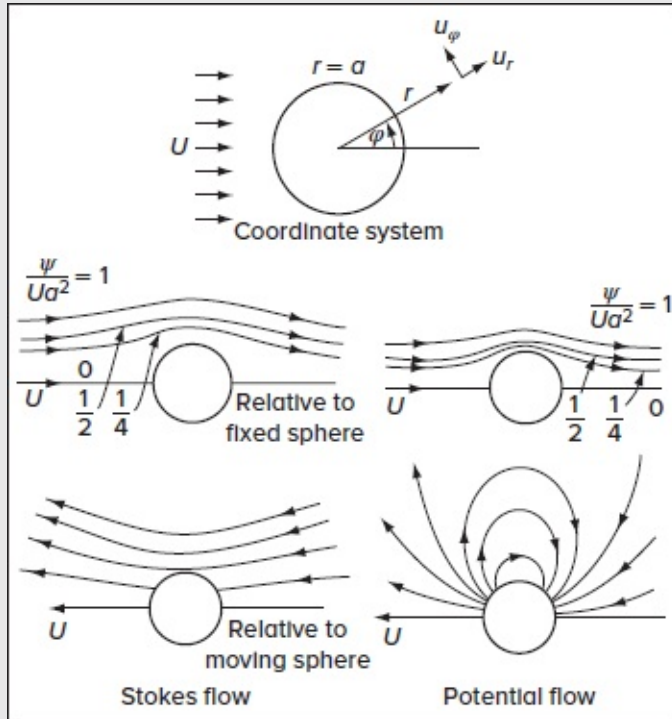


FIGURE 3-42

Comparison of creeping flow (*left*) and potential flow (*right*) past a sphere.

$$u_r = \frac{1}{r^2 \sin \varphi} \frac{\partial \psi}{\partial \varphi} \quad \text{and} \quad u_\varphi = -\frac{1}{r \sin \varphi} \frac{\partial \psi}{\partial r} \quad (3-265)$$

These satisfy the continuity relation identically. The momentum equation then becomes

$$\left(\frac{\partial^2}{\partial r^2} + \frac{1}{r^2} \frac{\partial^2}{\partial \varphi^2} - \frac{\cot \varphi}{r^2} \frac{\partial}{\partial \varphi} \right)^2 \psi = 0 \quad (3-266)$$

Page 135 Note that this is slightly more complicated than the biharmonic operator of Eq. (3-261) because of the three-dimensional geometry. The boundary conditions are

$$\text{At } r = a: \quad \frac{\partial \psi}{\partial r} = \frac{\partial \psi}{\partial \varphi} = 0 \quad \text{As } r \rightarrow \infty: \quad \psi \rightarrow \frac{1}{2} U r^2 \sin^2 \varphi + \text{const} \quad (3-267)$$

Although at first glance the problem appears to be formidable, it actually yields quite readily to a product solution of the type $\psi(r, \varphi) = f(r)g(\varphi)$. With this broad hint, we substitute in [Eq. \(3-266\)](#), satisfy [Eq. \(3-267\)](#), and reconfirm the solution obtained by Stokes (1851) for creeping motion past a sphere. This is

$$\psi = \frac{1}{4} U a^2 \sin^2 \varphi \left(\frac{a}{r} - \frac{3r}{a} + \frac{2r^2}{a^2} \right) \quad (3-268)$$

The velocity components follow immediately from [Eq. \(3-265\)](#):

$$u_r = U \cos \varphi \left(\frac{a^3}{2r^3} - \frac{3a}{2r} + 1 \right) \quad \text{and} \quad u_\theta = U \sin \varphi \left(\frac{a^3}{4r^3} + \frac{3a}{4r} - 1 \right) \quad (3-269)$$

Compared to the previous array of analyses in this chapter, this celebrated solution has several extraordinary properties:

1. The streamlines and velocities are entirely independent of the fluid viscosity. Upon reflection, we deduce that this is true of all creeping flows.
2. The streamlines possess perfect fore-and-aft symmetry: There is no wake of the type shown in [Fig. 1-5](#). It is the role of the convective acceleration terms, here neglected, to provide the strong flow asymmetry typical of high Reynolds number flows.
3. The local velocity is everywhere decelerated relative to its freestream value: There is no faster region as in the case of potential flow ([Fig. 3-42](#)) at the sphere shoulder (where $u_\theta = 1.5U$).
4. The effect of the sphere extends to enormous distances: At $r = 10a$, the velocities are still about 10 percent below their freestream values.

With u_r and u_φ known, the pressure is found by integrating the momentum relation, [Eq. \(3-258\)](#). The result is

$$p = p_\infty - \frac{3\mu a U}{2r^2} \cos \varphi \quad (3-270)$$

Page 136 where p_∞ is the uniform freestream pressure. Note that the pressure deviation is proportional to μ and antisymmetric, being positive at the front and negative at the rear of the sphere. This creates a pressure drag on the sphere. There is also a surface shear stress that induces a drag force. The shear-stress distribution in the fluid is given by

$$\tau_{r\varphi} = \mu \left(\frac{1}{r} \frac{\partial u_r}{\partial \varphi} + \frac{\partial u_\varphi}{\partial r} - \frac{u_\varphi}{r} \right) = -\frac{\mu U \sin \varphi}{r} \left(\frac{3a^3}{2r^3} \right) \quad (3-271)$$

The total drag is found by integrating the pressure and shear stress around the surface:

$$F = \int_0^\pi \tau_{r\varphi}|_{r=a} \sin \varphi \, dA - \int_0^\pi p|_{r=a} \cos \varphi \, dA, \quad dA = 2\pi a^2 \sin \varphi \, d\varphi, \quad \text{and} \quad F = 4\pi\mu Ua + 2\pi\mu Ua = 6\pi\mu Ua \quad (3-272)$$

This is the famous sphere-drag formula of Stokes (1851), which consists of *two-thirds viscous force and one-third pressure force*. The formula is strictly valid only for $Re \ll 1$ but agrees with experimental measurements up to about $Re = 1$.

The proper drag coefficient should obviously be $F/(\mu Ua) = 6\pi = \text{const}$, but everyone uses the inertia type of definition $C_D = 2F/(\rho U^2 A)$, which is nearly constant at high Reynolds numbers. Thus, the sphere drag is written as

$$C_D = \frac{F}{\frac{1}{2}\rho U^2 (\pi a^2)} = \frac{24}{Re} \quad \text{where} \quad Re = \frac{\rho U(2a)}{\mu} \quad (3-273)$$

As noted earlier, this introduces a Reynolds number effect where none exists. The formula underpredicts the actual drag when, for $Re > 1$, an asymmetrical wake forms and, for $Re > 20$, the flow separates from the rear surface, causing markedly increased pressure drag.

The Stokes flow streamlines from [Eq. \(3-268\)](#) are compared in [Fig. 3-42](#) with the streamlines for inviscid (potential) flow past a sphere, for which the classical solution is

$$\psi = \frac{1}{2} U r^2 \sin^2 \varphi \left(1 - \frac{a^3}{r^3} \right) \quad (3-274)$$

When we compare *streamlines past a fixed sphere*, the two are superficially similar, except that the Stokes streamlines are displaced further by the body. However, the difference becomes striking when we compare (as in [Fig. 3-42](#)) streamlines for a *sphere moving through a fixed fluid*, which we calculate by subtracting the freestream function $\frac{1}{2} U r^2 \sin^2 \varphi$ from [Eq. \(3-268\)](#). The sphere moving in potential flow shows circulating streamlines, thus indicating that it is merely pushing fluid out of the way. In contrast, the creeping sphere seems to drag the entire surrounding fluid with it, without causing recirculation.

3-9.3 Other Three-Dimensional Body Shapes

In principle, a Stokes flow analysis is possible for any three-dimensional body shape, provided that one has the necessary analytical skill. A few interesting shapes are discussed in the texts by Happel and Brenner (1983) and Clift et al. (1978). Of particular interest is the drag on a circular disk:

$$\text{Disk normal to the freestream:} \quad F = 16\mu Ua \quad (3-275a)$$

$$\text{Disk parallel to the freestream:} \quad F = \frac{32}{3}\mu Ua \quad (3-275b)$$

Here a is the radius of the disk. It is interesting that the values differ only by -15 and -43 percent, respectively, from the drag of a sphere, in spite of the vastly different geometry and orientation. Because the Stokes sphere law is expected to remain accurate for roughly spherical bodies, such as grains of sand or dust particles, the estimate $F = 6\pi\mu Ua$ is often used in analyzing the creeping motion of small particles.

Another shape of interest is the spheroid in [Fig. 3-43a](#). The spheroid shown is *prolate*, $a > b$; it may also be *oblate*, $a < b$. The flow may be either tangential (U_t) or normal (U_n) to the axis of revolution. In either case, the drag force has the Stokes form

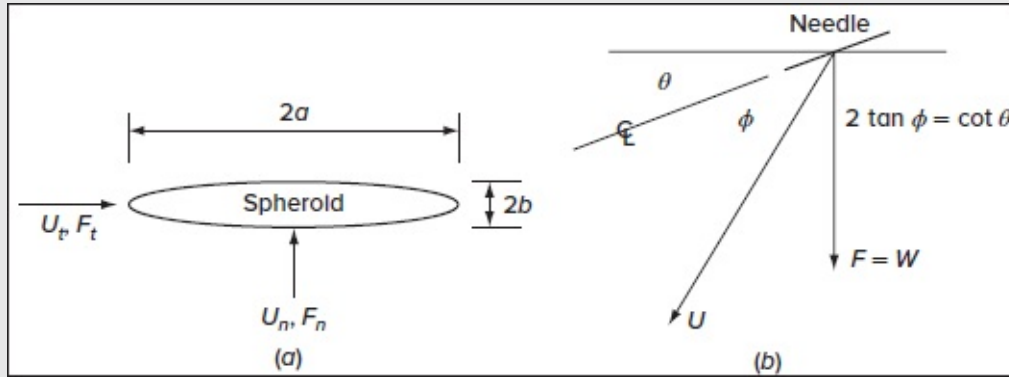


FIGURE 3-43

Forces on a body in creeping flow may be superimposed from tangential and normal components of the velocity vector: (a) an ellipsoid; (b) a nonhorizontal needle falling at an angle.

$$F = C\mu Ub \quad C = \text{const}$$

The exact solutions are rather lengthy and are given by Happel and Brenner (1983). Clift et al. (1978) propose the following curve-fit formulas:

$$C_t \approx 6\pi \frac{4 + a/b}{5} \quad C_n \approx 6\pi \frac{3 + 2a/b}{5} \quad (3-276)$$

valid to ± 10 percent error in the range $0 < a/b < 5$. When $a \gg b$, the spheroid resembles a rod or needle for which the following asymptotic expressions apply:

$$a \gg b: \quad C_t \approx \frac{4\pi a/b}{\ln(2a/b) - 0.5} \quad C_n \approx 2C_t \quad (3-277)$$

The drag on a needle is twice as large for flow normal to its axis compared to flow along its axis.

3-9.3.1 CALCULATING NORMAL AND TANGENTIAL FORCES. As alluded to earlier, the linearity of creeping motion means that normal and tangential flows may be superimposed without interaction. If the flow approaches the spheroid in [Fig. 3-43a](#) with velocity U at an angle α to its axis, one can break the velocity into components $U_n = U \sin \alpha$ and $U_t = U \cos \alpha$, and compute the force components $F_n = C_n \mu U_n b$ and $F_t = C_t \mu U_t b$. The

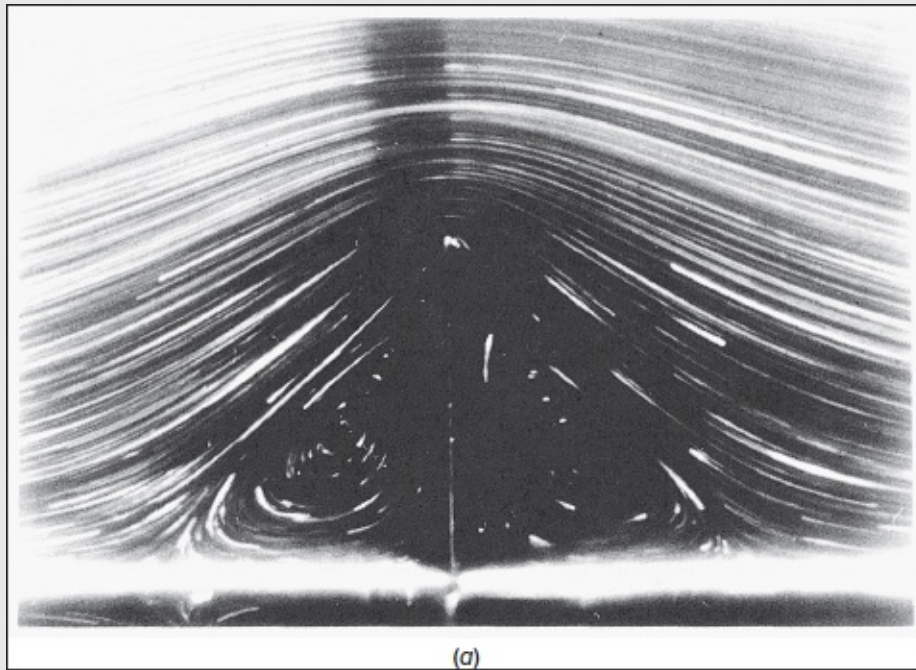
total force on the body can then be deduced from the vector sum of F_n and F_t .

When falling asymmetrically, such bodies behave in an interesting way. Consider the needle in [Fig. 3-43b](#), oriented with its axis at an angle θ to the horizontal. It must fall such that its total fluid force F is vertical to balance its body weight. Since $C_n = 2 C_t$, it falls at angle ψ with respect to its axis such that $F_n/F_t = 2 \sin \phi / \cos \phi = \tan(90^\circ - \theta)$ or

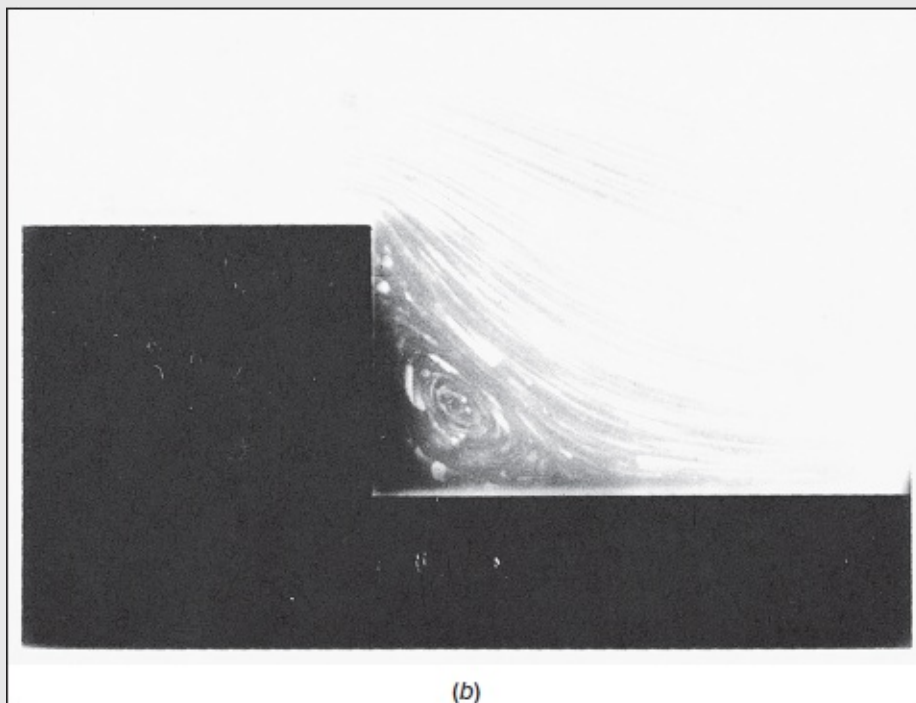
Falling rod or needle: $2 \tan \phi = \cot \theta$

This is illustrated in [Fig. 3-43b](#). For example, if $\theta = 20^\circ$, then $\phi = 54^\circ$, or the needle moves along a direction $(20^\circ + 54^\circ)$ or 74° from the horizontal. All of these forces are “in the ballpark” of the drag on a sphere of roughly the same size, i.e., shape effects do not vastly alter the drag. In fact, a remarkable theorem introduced by Hill and Power (1956) states that the Stokes drag of a body must be smaller than any circumscribed figure but larger than any inscribed figure. We can bound the drag of a particle of sand, for example, between inscribed and circumscribed spheres.

All of the immersed-body flows discussed have smooth streamlines near their surface with no separation. This is characteristic of rounded bodies in creeping flow. However, bodies with sharp corners or projecting appendages *do* show flow separation. [Figure 3-44](#) illustrates two cases realized experimentally by Taneda (1979). In [Fig. 3-44a](#), symmetric standing vortices form on either side of a plate or fence projecting into the flow. In [Fig. 3-44b](#), a standing vortex forms in the corner region of a step in a wall; like all creeping flows, the direction of the flow may be *reversed* without any change in the pattern. Note that both parts of [Fig. 3-44](#) stand in good agreement with analytical solutions for the same cases.



(a)



(b)

FIGURE 3-44

Separation occurs in creeping flow past sharp-cornered obstacles: (a) plane flow past a vertical fence at $Re = 0.014$; (b) plane flow past a step at $Re = 0.01$ (in either direction). [Taneda, S. (1979), "Visualization of Separating Stokes Flows," *J. Phys. Soc. Jpn.*, vol. 46, pp. 1935–1942.]

3-9.3.2 CREEPING FLOWS ARE KINEMATICALLY REVERSIBLE. An important aspect of creeping flow is *reversibility*. Since the basic differential equation is

linear, if a solution ψ is found, then its negative is also a solution. The streamlines can go either way. In [Fig. 3-42](#) for Stokes flow, the arrows could be reversed with no penalty. This would change the signs of the viscosity-induced pressures and shear stresses, and the drag force would act to the left and still equal $6\pi\mu Ua$. If the body is symmetric, as in flow past a sphere, the fore-and-aft streamlines would be mirror images. Note that reversibility is also true of inviscid *potential flow*, which is governed by Laplace's linear relation, [Eq. \(2-69\)](#), where ϕ denotes the velocity potential. Thus, the arrows can also be reversed on the potential flow past a sphere in [Fig. 3-42](#) and, in like manner, for the inviscid flow past a cylinder in [Fig. 1-3](#).Page 138

3-9.4 Two-Dimensional Creeping Flow: Oseen's Improvement

The Stokes paradox is that a two-dimensional creeping flow cannot satisfy all boundary conditions without including inertia. Even three-dimensional flows are not rigorously valid in the far field. Oseen (1910) overcame the paradox by adding ad hoc linearized convective acceleration to the momentum equation:

$$\rho U \frac{\partial \mathbf{V}}{\partial x} \approx -\nabla p + \mu \nabla^2 \mathbf{V} \quad (3-278)$$

where U is the stream velocity acting in the x direction. Equation (3-278) is linear and can be solved for a variety of flows, as discussed in the texts by Oseen (1927) and Lamb (1932). For an immersed body, the solutions are asymmetrical and show a wake but no separation. For flow past a sphere, the Oseen approximation adds an additional term to [Eq. \(3-273\)](#), specifically

$$C_{D \text{ sphere}} = \frac{24}{Re} \left(1 + \frac{3}{16} Re + \dots \right) \quad (3-279)$$

Page 139Other workers have used asymptotic analyses to further refine this expression. According to Proudman and Pearson (1957), the next term in parentheses should be $[9Re_2 \ln(Re)/160]$, but this diverges greatly for $Re > 3$. The idea of using creeping flow to expand into the higher Reynolds number region has not been successful.

The Stokes paradox is not really a fundamental barrier. It is a failure of the lowest order theory to match flow conditions. Oseen's ad hoc idea is worthy, but the "paradox" has now been truly resolved by the newer asymptotic methods that develop systematic analyses of the governing equations. Asymptotic methods are beyond the scope of this text and may be studied in specialized monographs such as Cebeci and Cousteix (1998) and Nayfeh (2000).

[Figure 3-45b](#) compares the Stokes [Eq. \(3-273\)](#) and Oseen [Eq. \(3-279\)](#) theories with experimental data for the drag on a sphere. For $Re > 1$, neither expression is accurate, and the measurements seem to lie in between. Since the spherical geometry is important in engineering, we offer the following curve-fit formula for the (laminar-flow) data:

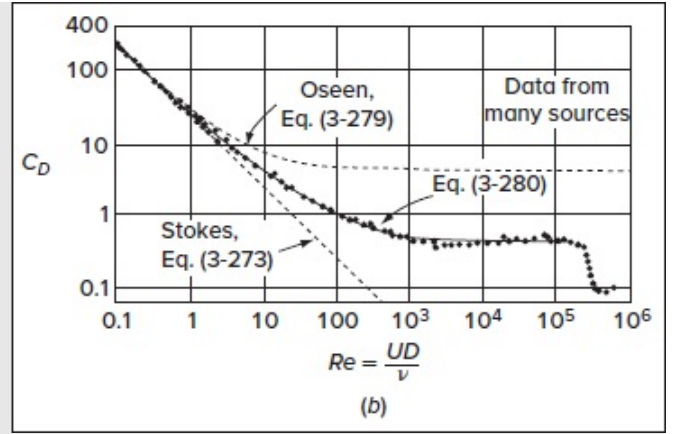
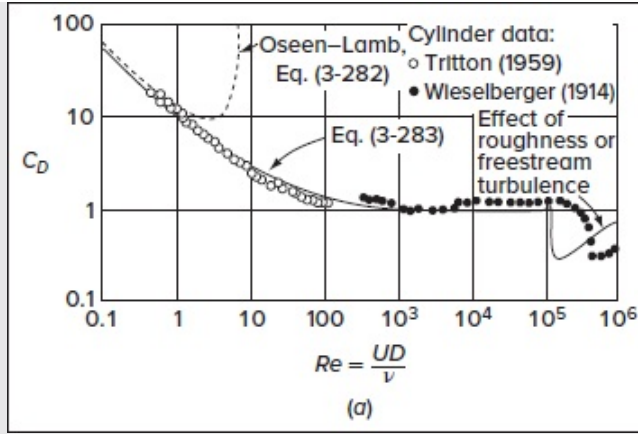


FIGURE 3-45

Comparison of experiment, theory, and empirical formulas for drag coefficients of a cylinder and a sphere (with smooth walls): (a) cylinder; (b) sphere.

$$C_{D \text{ sphere}} \approx \frac{24}{Re} + \frac{6}{1 + \sqrt{Re}} + 0.4 \quad 0 \leq Re \leq 2 \times 10^5 \quad (3-280)$$

which is also plotted in [Fig. 3-45b](#). The accuracy is ± 10 percent up to the “drag crisis,” $Re \approx 250,000$, where the boundary layer on the sphere becomes turbulent, thus markedly thinning the wake and reducing the drag. The drag crisis occurs slightly earlier with rough surfaces or a fluctuating freestream. The Oseen [Eq. \(3-278\)](#) can also be solved for various two-dimensional bodies. Of special interest is the drag on a flat plate of length L placed parallel to the stream from Lewis and Carrier (1949):

$$\text{Plate:} \quad C_D = \frac{2F'}{\rho U^2 L} = \frac{4\pi}{Re_L [1 - \Gamma + \ln(16/Re_L)]} \quad (3-281)$$

where F' is the drag per unit depth and $\Gamma = 0.577216\dots$ is Euler’s constant. Note that the drag depends upon the density no matter how small the Reynolds number.

The Oseen solution for the drag on a cylinder in crossflow is given by Tomotika and Aoi (1951):

$$\text{Cylinder:} \quad C_D = \frac{2F'}{\rho U^2 D} = \frac{8\pi}{Re_D [0.5 - \Gamma + \ln(8/Re_D)]} \quad (3-282)$$

[Figure 3-45a](#) compares this expression with data for the drag on cylinders by Tritton (1959) and Wieselberger (1914). The formula fits up to about $Re \approx 1$ and then diverges. The author earlier offered the following simple curve-fit formula:

$$C_{D \text{ cylinder}} \approx 1 + \frac{10.0}{Re_D^{2/3}} \quad (3-283)$$

which is in fair agreement up to the drag crisis, $Re \approx 250,000$. Sucker and Brauer (1975)

offered a better curve-fit formula for the same data:

$$C_{D \text{ cylinder}} \approx 1.18 + \frac{6.8}{Re_D^{0.89}} + \frac{1.96}{Re_D^{1/2}} - \frac{0.0004 Re_D}{1 + 3.64 \times 10^{-7} Re_D^2} \quad (3-284)$$

valid with good accuracy for $10^{-4} < Re_D < 2 \times 10^5$. Textbooks which cover particle drag and motion are by Clift et al. (1978) and Sirignano (1999).

3-9.5 Creeping Flow Past a Fluid Sphere

A large variety of creeping-motion solutions are given in the texts by Langlois (1964) and Happel and Brenner (1983). A particularly interesting solution is the flow past a spherical droplet of fluid. The outer stream has velocity U at infinity and viscosity μ_0 , and the droplet has viscosity μ_i and a fixed interface. The boundary conditions at the droplet interface would be (1) zero radial velocities and (2) equality of surface shear and tangential velocity on either side of the interface. The solution is provided by Rybczynski (1911) and, independently, by Hadamard (1911); accordingly, the drag on a droplet is given by

$$F = 6\pi a \mu_0 U \frac{1 + 2\mu_0/3\mu_i}{1 + \mu_0/\mu_i} \quad (3-285)$$

For $\mu_i \gg \mu_0$, this model simulates a solid sphere (Stokes solution), for which $F = 6\pi a \mu_0 U$. For $\mu_i \ll \mu_0$, the model mimics the behavior of a gas bubble in a liquid, for which $F = 6\pi a \mu_0 U$. A liquid droplet in another liquid would lie in between. Note that surface tension does not contribute to this drag force. Some streamlines of the flow are shown in [Fig. 3-46](#). These patterns are verified in experiments by Spells (1952). For higher Reynolds numbers (>1.0), the flow changes character into a nearly irrotational outer motion about a droplet that distorts gradually into nonspherical, mushroom-like shapes.

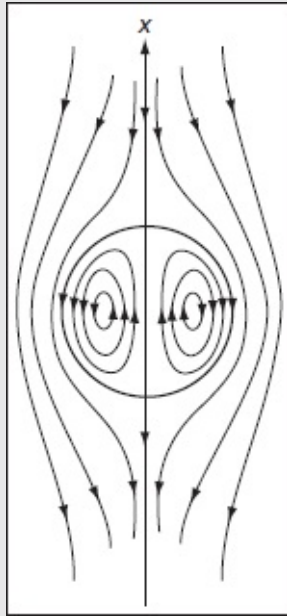


FIGURE 3-46

Streamlines for Stokes flow past a liquid droplet. See also [Fig. 3-48](#).

3-9.6 Boundary-Element CFD Creeping-Flow Solutions

Naturally most of our analytical creeping-flow solutions are for simple body shapes and walls. For more complex geometries, the boundary-element method (BEM)—see Beer (2001) or Wrobel (2002)—is ideal because the creeping-flow equations are linear. Computations are compact and economical because no internal nodes are needed. One sums elemental biharmonic or Stokesian solutions to make the element strengths match the boundary conditions (no slip or streaming flow or a porous wall, etc.). Here are some examples of BEM creeping flows.

Trogon and Farmer (1991) compute unsteady creeping flow through an orifice. Keh and Chen (2001) consider creeping flow of a droplet between plane walls. Vainshtein et al. (2002) study creeping flow near a permeable spheroid. Richardson and Power (1996) report BEM results for flow past two porous bodies of arbitrary shape. Roumeliotis and Fulford (2000) compute interactions between droplets. Lin and Han (1991) report a variety of BEM simulations: a rectangular cavity, a square bank, flow over a fence, and flow past a cylindrical arc. All these results are in good agreement with known experiments and theories. We conclude that any sensible creeping flow can be computed and analyzed with reliability and accuracy.

3-9.7 Heat Transfer in Creeping Motion

Temperature and heat transfer in Stokes flow can be computed from the linearized energy equation, including an Oseen term:

$$\rho c_p U \frac{\partial T}{\partial x} \approx k \nabla^2 T \quad (3-286)$$

where U is the (constant) freestream velocity. This relation is entirely uncoupled from the companion Stokes–Oseen velocity distribution. Typical boundary conditions include the known temperatures at the wall, T_w , and in the stream, T_∞ . Nondimensionalization of [Eq. \(3-286\)](#) yields a single parameter, the Peclet number $Pe = RePr = \rho c_p UL/k$. Furthermore, the mean Nusselt number, which is defined as

$$Nu_m = \frac{\bar{q}_w L}{k(T_w - T_\infty)}$$

varies only with the Peclet number and the geometry.

The solution for flow past a sphere ($L = 2a$) is given by Tomotika et al. (1953):

$$Nu_{m, \text{ sphere}} = 2.0 + 0.5PrRe + O(Pr^2 Re^2) \quad (3-287)$$

The first term (2.0) stems from the Stokes theory, and the second term represents the Oseen correction. When compared with the flow past a sphere data in [Fig. 3-47a](#), this formula is seen to be strictly qualitative. The curve-fit expression shown in the figure is

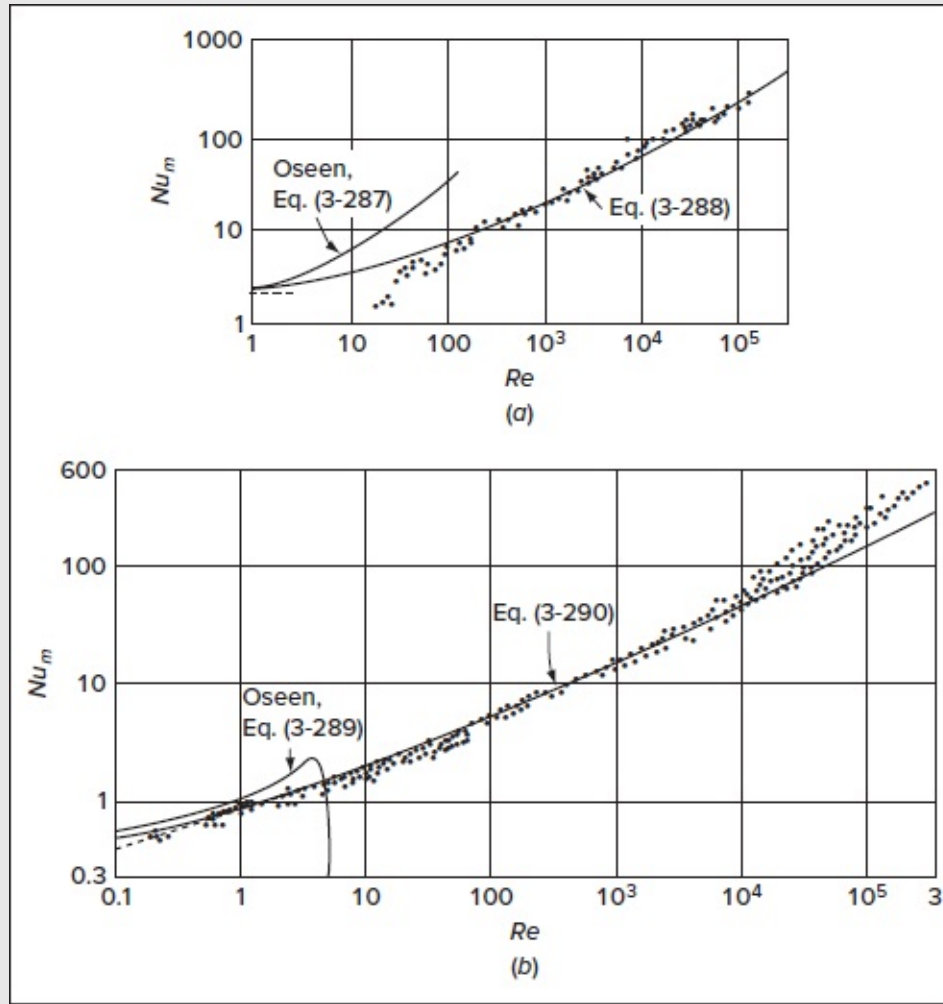


FIGURE 3-47

Comparison of theory and experiment for heat transfer from air to (a) spheres and (b) cylinders.

$$Nu_{m, \text{ sphere}} \approx 2.0 + 0.3Pr^{1/3}Re^{0.6} \quad (3-288)$$

which seems to agree with both liquid- and gas-flow data. If physical-property variations are important, it is suggested that μ , k , and c_p be evaluated at the so-called film temperature $(T_w + T_\infty)/2$.

Tomotika et al. (1953) also reproduce the Oseen solution for flow past a circular cylinder. In this case, the mean heat transfer ($L = 2a$) is given by

$$Nu_{m, \text{ cylinder}} = B - \frac{Pe^2}{12}(16 + B^2) \quad \text{where} \quad B = \frac{2}{\ln(8/Pe) - \Gamma} \quad (3-289)$$

Here $\Gamma = 0.577\dots$, as before. This formula is compared with the flow past a cylinder data for

airflow by Hilpert (1933) and is seen to be of very limited utility. A better formula is suggested by Kramers (1946) as a curve fit

$$Nu_{m, \text{cylinder}} \approx 0.42Pr^{0.2} + 0.57Pr^{1/3} Re_D^{1/2} \quad (3-290)$$

which is valid for $0.1 < Re_D < 10^4$. This formula follows *King's law*, $q_w = a + b\sqrt{U}$, predicted in an earlier study by L. V. King in 1914. It may be used to design the hot-wire anemometer, a fundamental instrument for the study of turbulence [Goldstein (1996)]. In this setup, a fine wire mounted between two needles represents the “cylinder in crossflow.” If a current I is passed through the wire and the wire placed normal to a moving stream U , then I will be a measure of U . If the wire is held at constant temperature (constant resistance), [Eq. \(3-290\)](#) predicts a relation of the form $I_2 = a + bU_1/2$, where a and b are constants. Equation (3-290) could then be used to compute a and b , but it is better to actually calibrate the hot wire in a stream of known velocity. The good agreement of Kramer's formula suggests that for air, with a typical wire diameter of 0.001 in., a hot-wire anemometer should be accurate in the velocity range suggested by Hinze (1975), namely,

$$4 \leq U < 4 \times 10^6 \text{ cm/s} \quad (3-291)$$

which extends over a wide span that is sufficient for most experimental purposes.

Note that the flow past a cylinder measurements in [Fig. 3-47b](#) fall above Kramer's formula [Eq. \(3-290\)](#) for $Re > 10^4$. This is attributed to noisiness or “freestream” turbulence in the oncoming stream approaching the cylinder. It is thought that the stream fluctuations trigger concave streamwise “Görtler vortices” (see [Fig. 5-23](#)) near the front of the body, thus increasing the nose heat transfer. Stream turbulence also hastens the onset of the drag crisis ([Fig. 3-45a](#)), which leads to increased (turbulent) heat transfer at the rear of the cylinder. This subject is discussed in detail in the monograph by Zukauskas and Ziukzda (1985).

We close this section by noting that the basic idea of Stokes or creeping flow is valid for $Re \ll 1$ but has not been successfully extended or modified into an accurate simulation of immersed-body flows when $Re > 1$. We will give a few more Stokes flow examples as problem exercises. Page 142

3-9.8 Lubrication Theory

The lubrication or friction reduction of two bodies in near contact is generally accomplished by a viscous fluid moving through a narrow but variable gap between the two bodies, with one or both bodies moving [Reynolds (1886)].

An idealization of this problem is the slipper-pad bearing shown in [Fig. 3-48](#). The bottom wall moves at velocity U and induces a Couette flow in the gap. Assuming that the upper block is fixed, the gap, which is very narrow, $h(x) \ll L$, decreases from h_0 in the entrance to h_L at the exit. The problem is to find the pressure and velocity distributions.

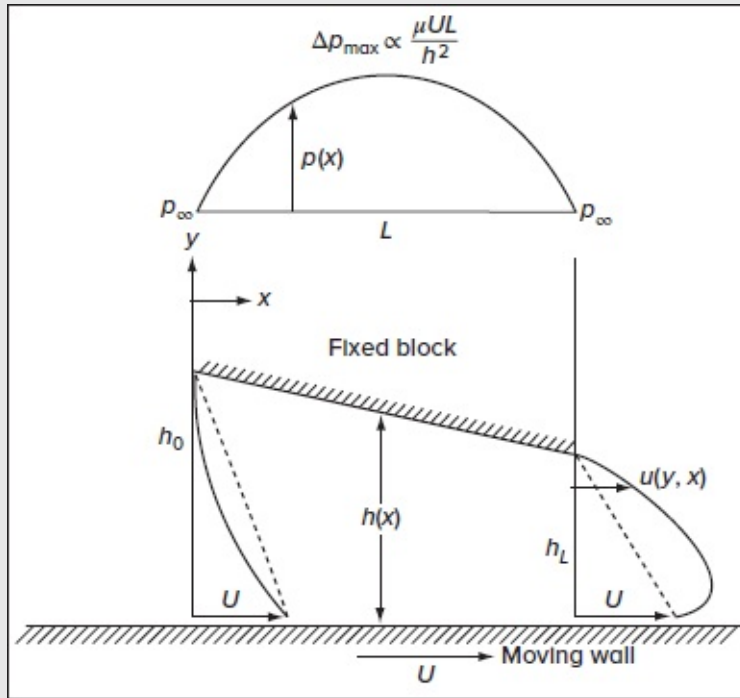


FIGURE 3-48

Low Reynolds number Couette flow in a varying gap: To maintain continuity, the gap pressure rises to a maximum and superimposes Poiseuille flow toward both ends of the gap.

Let us consider in [Fig. 3-48](#) that the flow is two-dimensional, that is, $\partial/\partial z = 0$ into the paper. Furthermore, let us assume Stokes flow, i.e., negligible inertia. This requires that $\rho u \partial u/\partial x \ll \mu \partial^2 u/\partial y^2$, or, approximately,

$$\rho U \frac{U}{L} \ll \mu \left(\frac{U}{h} \right)^2 \text{ or, finally, } \frac{\rho U L h^2}{\mu} \ll 1$$

Accordingly, the Reynolds number Re_L can be large if the gap is very small. As a practical example, take $U = 10 \text{ ms}$, $L = 4 \text{ cm}$, $h = 0.1 \text{ mm}$, and SAE 50 lubricating oil, with $\nu \approx 7 \times 10^{-4} \text{ m}^2/\text{s}$. We calculate $Re_L = 570$, although $Re_L h_2/L_2 = 0.004$. It is thus acceptable to neglect inertia in this case.

Now examine [Fig. 3-48](#). The simple linear Couette flow profiles, shown as dashed lines at the entrance and exit, are impossible for this geometry because continuity is violated. The mass flow at the entrance would exceed the exit flow. To relieve this difficulty, high pressure develops in the gap and induces a parabolic Poiseuille motion toward *both* ends of the gap, just sufficient to make the mass flow constant at every section x . At any section in the gap, then, the local velocity profile is a combined Couette–Poiseuille flow, based on [Eq. \(3-42\)](#), which is modified for the new coordinates:

$$u = \frac{1}{2\mu} \frac{\partial p}{\partial x} y(y-h) + U \left(1 - \frac{y}{h}\right) \quad (3-292)$$

Page 143 The correct distribution $p(x)$ is one that satisfies the continuity everywhere for two-dimensional flow in the gap:

$$\int_0^h \frac{\partial u}{\partial x} dy = - \int_0^h \frac{\partial v}{\partial y} dy = -v(h) + v(0) \quad (3-293)$$

where in this particular case we are assuming that the vertical velocities $v(h)$ and $v(0)$ vanish at both walls.

At this juncture, substituting for u from [Eq. \(3-292\)](#) and carrying out the integration in [Eq. \(3-293\)](#), we obtain a second-order differential equation for the pressure:

$$\frac{\partial}{\partial x} \left(h^3 \frac{\partial p}{\partial x} \right) = 6\mu U \frac{\partial h}{\partial x} \quad (3-294)$$

Here we assume U is constant and that the gap variation $h(x)$ is known. We then find $p(x)$ to secure the conditions $p(0) = p(L) = p_\infty$. Equation (3-294) is a simplified form of the Reynolds (1886) equation for lubrication. The development of [Eq. \(3-294\)](#) from [Eqs. \(3-292\)](#) and [\(3-293\)](#) is an excellent exercise, involving Leibnitz' rule, which we give as a problem assignment.

3-9.8.1 SOLUTION FOR A LINEARLY CONTRACTING GAP. Equation (3-294) may be integrated numerically for any gap variation $h(x)$. A closed-form solution is possible for a linear gap as in [Fig. 3-48](#):

$$h = h_0 + (h_L - h_0) \frac{x}{L}$$

We may substitute this expression in [Eq. \(3-294\)](#) and carry out the double integration. The algebra is quite laborious, and we give only the final result:

$$\frac{p - p_\infty}{(\mu UL/h_0^2)} = \frac{6(x/L)(1 - x/L)(1 - h_L/h_0)}{(1 + h_L/h_0)[1 - (1 - h_L/h_0)x/L]^2} \quad (3-295)$$

This expression is plotted in [Fig. 3-49](#) for various values of the gap contraction ratio h_L/h_0 . When the contraction is small, the pressure distribution is nearly symmetric, with p_{\max} at $x/L \approx 0.5$. As the degree of contraction increases, p_{\max} increases and moves toward the exit plane. The maximum pressure rise is of the order of $(\mu UL/h_0^2)$ and can be surprisingly high. For our previous example, SAE 50 oil with $U = 10$ ms, $L = 4$ cm, and $h_0 = 0.1$ mm, we may compute $(\mu UL/h_0^2) \approx 2.5 \times 10^7$ Pa, or 250 atm. This provides a high force to the slipper block, which enables it to support a large load without the block touching the wall.

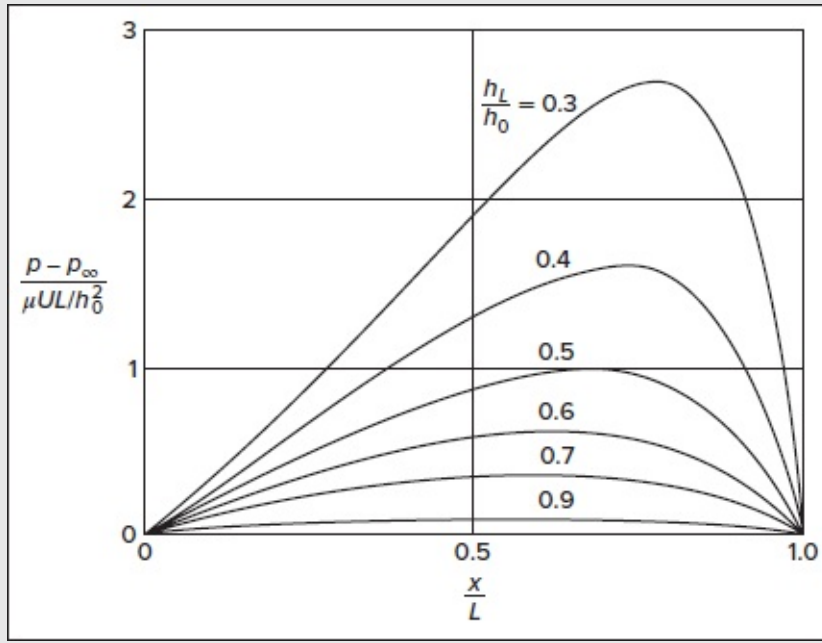


FIGURE 3-49

Pressure distribution in a two-dimensional linear-gap slider-pad bearing, from [Eq. \(3-295\)](#).

Before leaving this section, let us recall that Stokes flows, being linear, are *reversible*. If we reverse the wall in [Fig. 3-48](#) to move to the left, that is, $U < 0$, then the pressure change in [Eq. \(3-295\)](#) becomes *negative*. The fluid will not actually develop a large negative pressure but will rather cavitate and form a vapor void in the gap, as is well shown in the G. I. Taylor film “Low Reynolds Number Hydrodynamics.” Thus, flow into an expanding narrow gap may not generally bear much load or provide good lubrication. This effect is unavoidable in a rotating journal bearing, where the gap contracts and then expands, often leading to partial cavitation.

3-9.8.2 THE GENERAL REYNOLDS EQUATION. In a general lubrication problem, both the upper and lower walls in [Fig. 3-48](#) may be moving tangentially and normally, and the depth into the paper may be small, thus inducing a flow in the z direction. Assuming no translation of the walls in the z direction, the complete derivation for this case is given, for example, in the text by Szeri (1998). The pressure now varies with both x and z , while satisfying the following relation:

$$\frac{\partial}{\partial x} \left(h^3 \frac{\partial p}{\partial x} \right) + \frac{\partial}{\partial z} \left(h^3 \frac{\partial p}{\partial z} \right) = 6\mu \frac{\partial}{\partial x} \{ h[U(0) + U(h)] \} + 12\mu [V(h) - V(0)] \quad (3-296)$$

where, in general, $h = h(x, z)$. This expression represents the three-dimensional *Reynolds equation* for incompressible fluid lubrication. To achieve closure, the pressure must be known on all four open sides of the gap.

SUMMARY

It has been the intent of this chapter to present a fairly complete survey of the various types of exact or near-exact solutions presently known for incompressible (or weakly compressible) Navier–Stokes equations. Where appropriate, solutions have included not only the velocity but also the temperature and pressure distributions, and dimensionless variables have been emphasized. The various types of solutions discussed were

1. Couette flows with steadily moving surfaces
2. Poiseuille flow through ducts
3. Unsteady duct flows
4. Unsteady flows with moving boundaries
5. Asymptotic suction flows
6. Wind-driven Ekman flows
7. Similarity solutions: stagnation flow, rotating disk, wedge flow
8. Low Reynolds number (creeping) flows
9. Lubrication theory

Page 145This list seems rather substantial until we realize that none of these types possesses any degree of generality except for the computer solutions, which themselves remain limited by mesh size and Reynolds number restrictions. As the Reynolds number increases arbitrarily, laminar flows become unstable, and no method exists for exact analysis of such problems. In many flows, whether laminar or turbulent, the condition that accompanies a high Reynolds number makes certain terms in the Navier–Stokes equations negligible. What remains is a far more exploitable field of analysis: boundary-layer theory for laminar ([Chap. 4](#)), transitional ([Chap. 5](#)), turbulent ([Chap. 6](#)), and compressible ([Chap. 7](#)) motions. For nonboundary-layer flows, the use of CFD for both laminar and turbulent flows is an increasingly powerful tool.

PROBLEMS**

- 3-1. Reconsider the problem of Couette flow between parallel plates, [Fig. 3-1](#), for a power-law non-Newtonian fluid, $\tau_{xy} = K (du/dy)_n$, where $n \neq 1$. Assuming constant pressure and temperature, solve for the velocity distribution $u(y)$ between the plates with (a) $n < 1$ and (b) $n > 1$, and compare with the Newtonian solution, [Eq. \(3-6\)](#). Comment on the results.
- 3-2. Consider the axial Couette flow of [Fig. 3-3](#) with both cylinders moving. Find the velocity distribution $u(r)$ and plot it for (a) $U_1 = U_0$, (b) $U_1 = -U_0$, and (c) $U_1 = 2U_0$. Comment on the results.

- 3-3. Consider the axial Couette flow of [Fig. 3-3](#) with the inner cylinder moving at speed U_0 and the outer cylinder fixed. Solve for the temperature distribution $T(r)$ in the fluid if the inner and outer cylinder walls are held at temperatures T_0 and T_1 , respectively.
- 3-4. A long thin rod of radius R is pulled axially at speed U through an infinite expanse of still fluid. Solve the Navier–Stokes equation for the velocity distribution $u(r)$ in the fluid and comment on a possible paradox.
- 3-5. A circular cylinder of radius R is rotating at steady angular rate ω in an infinite fluid of constant ρ and μ . Assuming purely circular streamlines, find the velocity and pressure distribution in the fluid and compare with the flow field of an inviscid “potential” vortex.
- 3-6. Assuming that the velocity distribution between rotating concentric cylinders is known from [Eq. \(3-22\)](#), find the pressure distribution $p(r)$ if the pressure is p_0 at the inner cylinder.
- 3-7. An open U tube of radius r_0 filled with a length L of a viscous fluid is displaced from rest and oscillates with amplitude $X(t)$, as shown in [Fig. P3-7](#). Show with a one-dimensional integral analysis that the governing equation for $X(t)$ is

$$\frac{d^2 X}{dt^2} + \frac{C_f}{r_0} \left| \frac{dX}{dt} \right| \frac{dX}{dt} + \frac{2g}{L} X = 0$$

where C_f is the wall friction coefficient. Find the natural frequency of oscillation and the time to damp to one-half amplitude for an assumed Poiseuille-type friction factor, $C_f = 16\mu/(\rho|dX/dt|d_0)$.

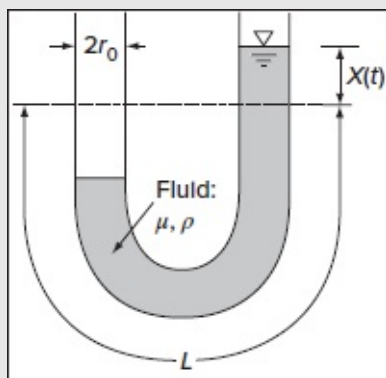


FIGURE P3.7

- 3-8. Air at 20°C and 1 atm is driven between two parallel plates 1 cm apart by an

imposed pressure gradient (dp/dx) and by the upper plate moving at 20 cms. Find (a) the volume flow rate (in cm^3/s per meter of width) if $dp/dx = -0.3 \text{ Pa/m}$ and (b) the value of dp/dx (in Pa/m), which causes the shear stress at the lower plate to vanish. Page 146

3-9. Derive the solution $u(y, z)$ for flow through an elliptical duct, [Fig. 3-9](#), by solving [Eq. \(3-30\)](#). Begin with a guessed quadratic solution, $u = A + By_2 + Cz_2$, and work your way through to the exact solution.

3-10. Air at 20°C and approximately 1 atm flows at an average velocity of 1.7 ms through a rectangular 1×4 duct. Estimate the pressure drop (in Pa/m) by (a) an exact evaluation and (b) the hydraulic diameter approximation.

3-11. Consider a swirling motion superimposed upon a circular-duct flow by letting the velocity components take the form

$$v_r = 0 \quad v_\theta = v_\theta(r, t) \quad v_z = v_z(r)$$

Show that the axial flow v_z is unaffected by the swirl, so that an arbitrary v_θ can be added without changing the Poiseuille distribution.

3-12. It is desired to measure the viscosity of light lubricating oils ($\mu \approx 0.02$ to $0.1 \text{ Pa} \cdot \text{s}$) by passing approximately $1 \text{ m}^3/\text{h}$ of fluid through an annulus of length 30 cm with inner and outer radii of 9 and 10 mm, respectively. Estimate the expected pressure drop through the device and an appropriate instrument for the pressure measurement.

3-13. Lubricating oil at 20°C [$\rho = 850 \text{ kg/m}^3$, $\mu = 0.8 \text{ Pa} \cdot \text{s}$, $k = 0.15 \text{ W/(m} \cdot \text{K)}$, $c_p = 1800 \text{ J/(kg} \cdot \text{K)}$] is to be cooled by flowing at an average velocity of 2 ms through a 3 cm diameter pipe with walls that are at 10°C . Estimate (a) the heat loss (in Wm^{-2}) at $x = 10 \text{ cm}$ and (b) the mean oil temperature at the pipe exit, $L = 2 \text{ m}$. Comment on the results.

3-14. For plane polar coordinates with circular streamlines, show that the only nonzero vorticity component, $\omega = \omega_z(r)$, satisfies the relation

$$\frac{\partial \omega}{\partial t} = \nu \left(\frac{\partial^2 \omega}{\partial r^2} + \frac{1}{r} \frac{\partial \omega}{\partial r} \right)$$

Solve this equation for the decay of a line vortex initially concentrated at the origin with circulation Γ_0 . Solve for $\omega(r, t)$ and show that

$$v_\theta = \frac{\Gamma_0}{2\pi r} \left[1 - \exp\left(-\frac{r^2}{4\nu t}\right) \right]$$

Sketch velocity profiles for a few representative times, including $t = 0$.

- 3-15.** Consider a wide liquid film of constant thickness h flowing steadily due to gravity down an inclined plane at angle θ , as shown in [Fig. P3-15](#). The atmosphere exerts constant pressure and negligible shear on the free surface. Show that the velocity distribution is given by

$$u = \frac{\rho g \sin \theta}{2\mu} y(2h - y)$$

and that the volume flow rate per unit width is $Q = \rho g h^3 \sin \theta / (3\mu)$. Compare this result with flow between parallel plates, i.e., [Eqs. \(3-44\)](#) and [\(3-45\)](#).

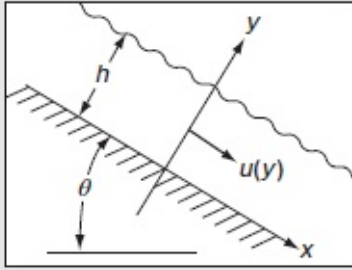


FIGURE P3.15

- 3-16.** Consider a film of liquid draining at volume flow rate Q down the outside of a vertical rod of radius a , as shown in [Fig. P3-16](#). Some distance down the rod, a fully developed region is reached where fluid shear balances gravity and the film thickness remains constant. Assuming incompressible laminar flow and negligible shear interaction with the atmosphere, find an expression for $v_z(r)$ and a relation between Q and the film radius b . Page 147

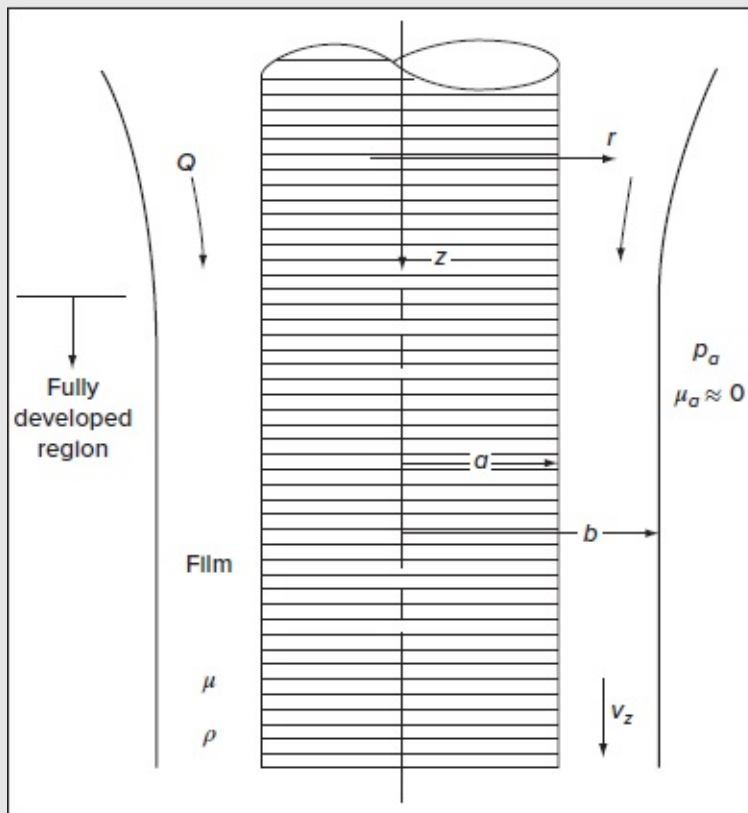


FIGURE P3.16

- 3-17. By extension to Prob. 3-15, consider a *double* layer of immiscible fluids flowing steadily down an inclined plane, as in [Fig. P3-17](#). The atmosphere exerts no shear stress on the surface and is at constant pressure. Find the laminar velocity distribution in the two layers.

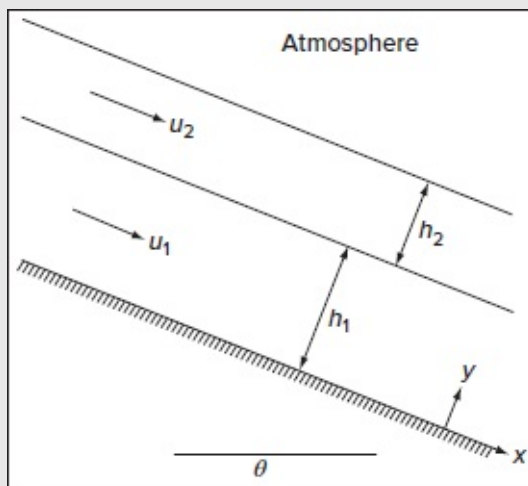


FIGURE P3.17

- 3-18.** The surface of the draining liquid film in Prob. 3-15 will become wavy and unstable at a critical Reynolds number $Re^* = hu_{\max}/\nu \approx O(10)$ that depends upon the slope θ , gravity g , density ρ , viscosity μ , and the surface tension \mathfrak{J} . Rewrite this dependence in terms of two dimensionless parameters [Fulford (1964)]. For water at 20°C, what is the numerical value of the parameter which contains viscosity?
- 3-19.** Derive [Eq. \(3-96\)](#) for start-up of flow in a circular pipe. Plot the instantaneous velocity profile for early times, $\nu t/r_0^2 = 0.005$ and 0.01.
- 3-20.** Air at 20°C and 1 atm is at rest between two fixed parallel plates 2 cm apart. At time $t = 0$ the lower plate suddenly begins to move tangentially at 30 cm/s. Compute the air velocity at the center between the plates after 2 s. When will the center velocity reach 14 cm/s?Page 148
- 3-21.** A Couette pump consists of a rotating inner cylinder and a baffled entrance and exit, as shown in [Fig. P3-21](#). Assuming zero circumferential pressure gradient and $(a - b) \ll a$, derive formulas for the volume flow and pumping power per unit depth. Illustrate for SAE oil at 20°C, with $a = 10$ cm, $b = 9$ cm, and $\omega = 600$ rpm.

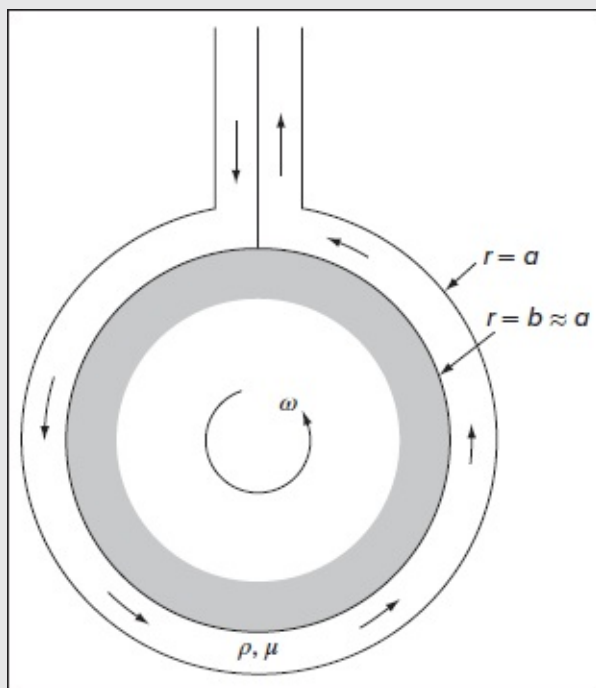


FIGURE P3.21

- 3-22. The Taylor vortex is defined by a purely circumferential flow

$$v_\theta = C \frac{r}{\nu t^2} \exp\left(-\frac{r^2}{4\nu t}\right)$$

Determine whether this vortex is an exact solution of the incompressible Navier–Stokes equations with negligible gravity. Sketch a few instantaneous velocity profiles and compare to the Oseen vortex in Prob. 3-14.

- 3-23. Consider radial outflow between two parallel disks fed by symmetric entrance holes, as shown in Fig. P3-23. Assume that $v_z = v_\theta = 0$ and $v_r = f(r, z)$, with constants ρ , μ , and $p = p(r)$ only. Neglect gravity and entrance effects at $r = 0$. Set up the appropriate differential equation and boundary conditions and solve as far as possible—numerical (e.g., Runge–Kutta) integration may be needed for a complete solution. Sketch the expected velocity profile shape.

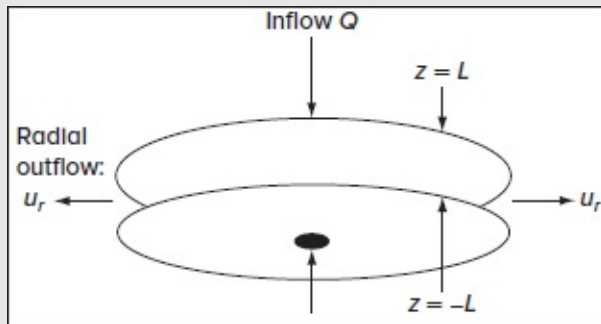


FIGURE P3.23

- 3-24. A long, uniformly porous cylinder of radius R exudes fluid at velocity U_0 into an unbounded fluid of constant ρ and μ . The pressure at the cylinder surface is p_0 . Assuming purely radial outflow with negligible gravity, find the velocity and pressure distributions in the fluid.
- 3-25. Consider the problem of steady flow induced by a circular cylinder of radius r_0 rotating at surface vorticity ω_0 and having a wall-suction velocity $v_r(r = r_0) = -v_w = \text{const}$. Set up the problem in polar coordinates assuming no circumferential variations $\partial/\partial\theta = 0$, and show that the vorticity in the fluid is given by

$$\omega = \frac{1}{r} \frac{\partial}{\partial r} (r v_\theta) = \omega_0 \left(\frac{r_0}{r} \right)^{Re}$$

Page 149 where $Re = r_0 v_w / \nu$ is the wall-suction Reynolds number of the cylinder. Integrate this relation to determine the velocity distribution $v_\theta(r)$ in the fluid and

show that the character of the solution is quite different for the three cases of the wall Reynolds number Re less than, equal to, or greater than 2.0.

- 3-26.** Consider laminar flow in a uniformly porous tube, similar to the porous-channel problem, [Eqs. \(3-167\)](#). Let the similarity variable be $\zeta = (r/r_0)^2$ and find a suitable expression for the axisymmetric stream function $\psi(x, \zeta)$, similar to [Eq. \(3-165\)](#) for the channel. Then show that the differential equation equivalent to (3-169) is

$$2\zeta g'''' + 4g''' + Re(g'g'' - gg''') = 0 \quad [\text{Yuan and Finkelstein (1956)}]$$

where $Re = v_w r_0 / \nu$ and $g = g(\zeta)$ only. This equation has no known solutions in the range $2.305 \leq Re \leq 9.105$ [White (1962a)]. Establish the proper boundary conditions on the function $g(\zeta)$.

- 3-27.** The practical difficulty with the Ekman spiral solution, [Eq. \(3-199\)](#), is that it assumes laminar flow whereas the real ocean is turbulent. One approximate remedy is to replace the kinematic viscosity ν everywhere by a (constant) turbulent or “eddy” viscosity correlated with wind shear and penetration depth using a suggestion by Clauser (1956):

$$\nu_{\text{turb}} \approx 0.04D \sqrt{\tau_0 / \rho}$$

Repeat our text example, $V_{\text{wind}} = 6$ ms over a 20°C air–water interface of 41°N latitude. Compute the penetration depth D and surface velocity V_0 .

- 3-28.** Repeat the analysis of the Ekman flow, Sec. 3-7.2, for shallow water, that is, apply the bottom boundary condition, [Eq. \(3-198\)](#), at $z = -h$. Find the velocity components and show that the surface velocity is no longer at a 45° angle to the wind but rather satisfies the equation as follows for the surface angle θ :

$$\tan \theta = \frac{\sinh(2\pi h/D) - \sin(2\pi h/D)}{\sinh(2\pi h/D) + \sin(2\pi h/D)} \quad [\text{Ekman (1905)}]$$

Find the value of h/D for which $\theta = 20^\circ$.

- 3-29.** Air at 20°C and 1 atm flows at 1 m/s across a cylinder of diameter 2 cm and wall temperature 40°C . Using inviscid theory, [Eq. \(1-2\)](#), to establish the constant B , use the results of Sec. 3-8.1 to estimate (a) the shear layer thickness δ , (b) the wall shear stress, and (c) the heat-transfer rate q_w at the front stagnation point of the cylinder.
- 3-30.** The opposite of von Kármán’s rotating disk problem is Bödewadt’s case [Rogers and Lance (1960)] of a fixed disk with a rotating outer stream, $v_\theta = r\omega$ as $z \rightarrow \infty$. Using the approach of Sec. 3-8.2, set up this problem and carry it out as far as possible, including numerical integration if a computer is available.

3-31. The rotating disk is sometimes called von Kármán's centrifugal pump, since it brings in fluid axially and throws it out radially. Consider one side of a 50 cm disk rotating at 1200 rpm in air at 20°C and 1 atm. Assuming laminar flow, compute (a) the flow rate, (b) the torque and power required, and (c) the maximum radial velocity at the disk edge.

3-32. Solve the Jeffery–Hamel wedge-flow relation, [Eq. \(3-195\)](#), for creeping flow, $Re = 0$ but $\alpha \neq 0$. Show that the proper solution is

$$f(\eta) = 1 + \frac{1}{2} \csc^2 \alpha \left[\sin\left(\frac{1}{2}\pi - 2\alpha\eta\right) - 1 \right]$$

Show also that the constant $C = 4\alpha^2 \cot^2 \alpha$ and sketch a few profiles. Show that backflow always occurs for $\alpha > 90^\circ$.

3-33. In spherical polar coordinates, where azimuthal variations $\partial/\partial\theta$ vanish due to axisymmetry, an incompressible stream function $\psi(r, \varphi)$ can be defined such that

$$u_r = \frac{\partial\psi/\partial\varphi}{r^2 \sin\varphi} \text{ (radial velocity)} \quad \text{and} \quad u_\varphi = -\frac{\partial\psi/\partial r}{r \sin\varphi} \text{ (polar velocity)}$$

The particular stream function

$$\psi(r, \varphi) = \frac{2\nu r \sin^2 \varphi}{1 + a - \cos \varphi} \quad a = \text{const}$$

is an exact solution of the Navier–Stokes equations and represents a round jet issuing from the origin. Sketch the streamlines in the upper two quadrants for a particular value of a between 0.001 and 0.1. (Various values could be distributed among a group.) Sketch the jet profile shape $u_r(1, \varphi)$, and determine how the jet width δ (where $u_r = 0.01u_{\max}$) and jet mass flow vary with r .

3-34. A sphere of specific gravity 7.8 is dropped into oil of specific gravity 0.88 and viscosity $\mu = 0.15 \text{ Pa}\cdot\text{s}$. Estimate the terminal velocity of the sphere if its diameter is (a) 0.1 mm, (b) 1 mm, and (c) 10 mm. Which of these is a creeping motion?

3-35. Verify [Eq. \(3-285\)](#) for the drag of a liquid droplet by repeating the Stokes problem with boundary conditions of zero radial velocity, equal tangential velocity, and equal shear stress at the droplet surface (assumed to be a perfect sphere, $r = a$). Page 150

3-36. Repeat the analysis of radial outflow between parallel disks, as in Prob. 3-23, for creeping flow, i.e., negligible inertia. Find the velocity and pressure distributions for this case.

3-37. Analyze the problem of creeping flow between parallel disks of radius R and separation distance L . The lower disk ($z = 0$) is fixed and the upper disk ($z = L$) rotates

at angular rate ω . Assuming that $v_\theta = rf(z)$, reduce the problem as far as possible and solve for the velocities.

3-38. Set up the method of *separation of variables* for finding $u(y, z)$ for a rectangular duct, [Fig. 3-9](#) and [Eq. \(3-48\)](#), by analyzing [Eq. \(3-30\)](#). First note that the separation will not work until one defines a new variable $U = u - F$, where $\nabla_2 F = (1/\mu) (dp/dx)$, so that $\nabla^2 U = 0$. Then separate U into x and y parts and find the form of each part. Show how an infinite series would be required to satisfy the boundary conditions, but do not determine the series coefficients.

3-39. Repeat the analysis of Sec. 3-9.7.1 for a parabolically varying gap:

$$h = h_L + (h_0 - h_L) \left(1 - \frac{x}{L}\right)^2$$

Nondimensionalize and solve for the pressure distribution similar to [Eq. \(3-295\)](#). Numerical integration may be required. Plot the resulting pressures for various h_L/h_0 and compare with [Fig. 3-49](#).

3-40. Set up Stokes' first problem of the impulsively started plane wall, [Fig. 3-21](#), for solution using a numerical method. Plot some typical velocity profiles and compare quantitatively with the exact solution, [Eq. \(3-107\)](#).

3-41. Repeat Prob. 3-40 using a numerical method.

3-42. Set up Stokes' second problem of the (long-term) oscillating wall, [Fig. 3-22a](#), for solution using a numerical method. Let the initial transient die out. Plot some typical velocity profiles and compare quantitatively with the exact solution, [Eq. \(3-111\)](#).

3-43. Repeat Prob. 3-42 using a numerical method.

3-44. The solutions $f_n(r)$ for [Eq. \(3-76\)](#) are called *Graetz functions*, but they are not tabulated. Set up a numerical solution of [Eq. \(3-76\)](#), perhaps using a Runge-Kutta solver, and solve iteratively for the first three functions f_1 –2–3 and their eigenvalues λ_1 –2–3. Compare with [Table 3-1](#), but avoid using the table for your initial guesses.

3-45. Extend Prob. 1-21, where we found only the Knudsen number, $Kn \approx 0.17$, by using all the data given there. (a) Find the Reynolds number and see if it is less than 2000 (laminar flow). (b) Estimate the required pressure gradient in Pa/m. (c) Estimate the flow rate in mm³/s.

3-46. Starting from the axial momentum equation, derive [Eqs. \(3-40\)](#) for slip flow in tubes.

- 3-47. For the geometry of [Fig. 3-1](#), assume a constant pressure gradient with both walls fixed. Solve the continuity and x momentum for laminar *slip flow* between the plates. Find the velocity distribution and the volume flow rate per unit depth. Does the Knudsen number appear?
- 3-48. Hadjiconstantinou (2003) has updated a second-order slip theory by Cercignani (2000) to give new numerical coefficients for the wall-slip velocity, to be compared with [Eq. \(1-80\)](#):

$$u_w \approx 1.11 \ell \left. \frac{\partial u}{\partial y} \right|_w - 0.61 \ell^2 \left. \frac{\partial^2 u}{\partial y^2} \right|_w$$

Repeat Prob. 3-52 with this formulation to solve continuity and x momentum for laminar *slip flow* between the plates. Find the velocity distribution and the volume flow rate per unit depth. Does the Knudsen number appear?

- 3-49. Carry out the steps that lead, for Stokes sphere flow, from [Eqs. \(3-266\)](#) to [\(3-268\)](#), by assuming a product solution $\psi(r, \theta) = f(r) g(\theta)$ separating the variables, and solving for f and g .
- 3-50. Hill and Power (1956) proved that the creeping-flow (Stokes) drag on a solid object is greater than the drag on any inscribed shape but less than the drag on any circumscribed shape. Verify this result for the spheroid of [Fig. 3-43](#) by comparing it to inscribed and circumscribed spheres. Do the relative drag forces differ markedly or by only a few percent?
- 3-51. The elemental creeping-flow solution $\psi = r \ln r \sin \theta$ is called an *Oseenlet*. Is this a solution for plane flow, [Eq. \(3-261\)](#), or axisymmetric flow, [Eq. \(3-266\)](#), or both? How might Oseenlets be used in analyzing more complex creeping flows?
- 3-52. Using a numerical method such as the Runge–Kutta scheme, solve the axisymmetric stagnation flow [Eq. \(3-220\)](#) for the function $F(\eta)$. Use an iterative scheme to determine the proper value of $F''(0)$.
- 3-53. The rotating disk of [Fig. 3-35](#) acts rather like a centrifugal pump. Consider a disk 60 cm in diameter, rotating at 120 rev/min in air at 20°C and 1 atm. Is the flow at the disk tip laminar, transitional, or turbulent? Using Karman's theory of Sec. 3-8.2, estimate the volume flow of air, in cm³/s, pumped outward by one side of the disk.
- 3-54. Consider the fully developed flow in a long axisymmetric annulus, which is driven by a pressure gradient.
- (a) Using an appropriate coordinate system, make the necessary assumptions that will simplify the incompressible Navier–Stokes equations.

- (b) Write the differential equation of motion for this problem. Page 151
- (c) Specify a judicious assortment of boundary conditions.
- (d) Solve for the steady-state velocity profile $u(r)$ for $b \leq r \leq a$.

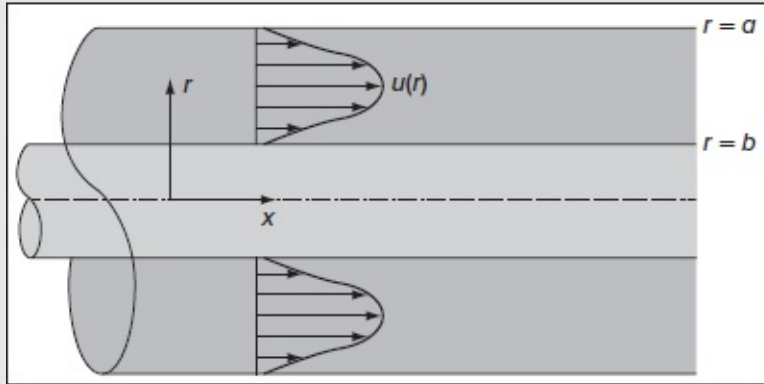


FIGURE P3.54

- 3-55. A fluid of constant thickness h flows steadily down a flat surface that is inclined at an angle θ , as shown below.
- (a) Make the necessary assumptions to reduce the Cartesian Navier–Stokes equations.
 - (b) Write the differential equation of motion for this problem.
 - (c) Specify a judicious assortment of boundary conditions.
 - (d) Solve for the steady-state velocity profile $u(y)$ for $0 \leq y \leq h$.
 - (e) Calculate the volumetric flow rate per unit width.

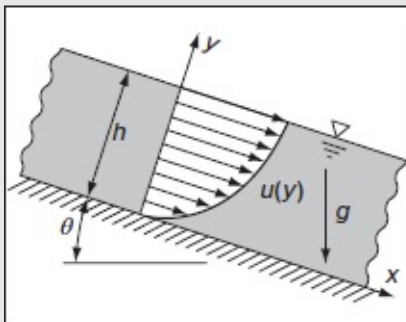


FIGURE P3.55

- 3-56.** Consider the flow configuration of two different fluid bodies that are separated by a rigid interfacial surface that can be assumed to be infinitesimally thin. The heights and dynamic viscosities of the two bodies are specified on the sketch. The upper body is bounded by a moving surface that translates in the positive x direction at a uniform speed V . What should be the axial speed of the interfacial surface in the absence of a pressure gradient in the streamwise direction?

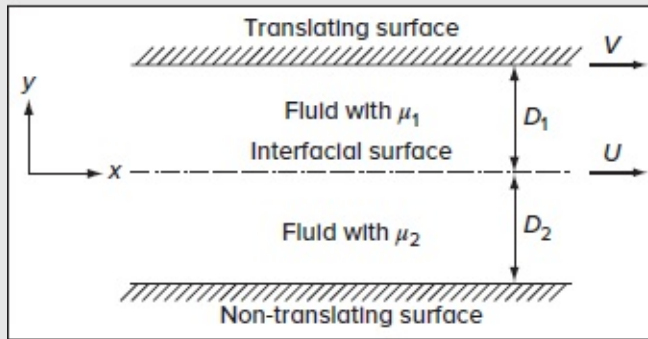


FIGURE P3.56

Page 152

- 3-57.** Consider fully developed laminar flow in the annulus between two concentric pipes as shown below. The outer pipe is stationary, and the inner pipe moves in the x -direction at a constant speed V . Assume the axial pressure gradient is zero ($dp/dx = 0$). From the differential form of the conservation laws, obtain a general expression for the velocity profile, $u(r)$ in terms of two integration constants, C_1 and C_2 . Apply the no-slip boundary conditions to solve for C_1 and C_2 . Give the final expression for $u(r)$.

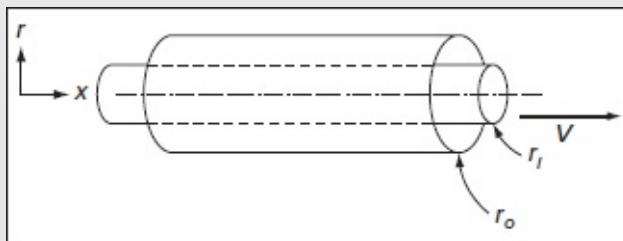


FIGURE P3.57

- 3-58.** Consider a fully developed laminar flow in the annular space formed by the two

concentric cylinders shown above, but with a stationary inner cylinder and a nonzero pressure gradient ($dp/dx \neq 0$). Let $r_o = R$ and $r_i = kR$, where $0 < k < 1$ is a constant.

- (a) Using the Navier–Stokes equations and proper boundary conditions, show that the velocity profile and volume flow rate can be written as

$$u(r) = -\frac{R^2}{4\mu} \frac{dp}{dx} \left[1 - \left(\frac{r}{R}\right)^2 + \frac{1-k^2}{\ln(1/k)} \ln\left(\frac{r}{R}\right) \right] \quad \text{and} \quad Q = -\frac{\pi R^4}{8\mu} \frac{dp}{dx} \left[1 - k^4 - \frac{(1-k^2)^2}{\ln(1/k)} \right]$$

- (b) Obtain an expression for the location of the maximum velocity as a function of k .

- (c) Obtain an expression for the average velocity in the annulus, \bar{u} .

(d) By taking the limiting case of $k \rightarrow 0$, compare your expressions to those corresponding to the Poiseuille flow in a circular pipe. Hint: They must be the same! Required integration is straightforward except for one term that must be integrated by parts:

$$\int r \ln\left(\frac{r}{R}\right) dr = R^2 \int \frac{r}{R} \ln\left(\frac{r}{R}\right) d\left(\frac{r}{R}\right) = R^2 \left[\frac{1}{2} \left(\frac{r}{R}\right)^2 \ln\left(\frac{r}{R}\right) - \frac{1}{4} \left(\frac{r}{R}\right)^2 \right]$$

3-59. Consider the problem associated with the spinning porous tube depicted in [Fig. 3-28](#) of Sec. 3-6.4. By substituting the similarity transformations given by [Eq. \(3-182\)](#) into [Eq. \(3-181\)](#), derive [Eq. \(3-183\)](#). Subsequently, recognizing that $v_\theta = g(r)$ is a function of a single variable, derive [Eq. \(3-184\)](#). Finally, introduce $\eta = \frac{1}{2}r^2$ into [Eq. \(3-184\)](#) and differentiate once to obtain [Eq. \(3-185\)](#). Verify that the four boundary conditions for this problem translate into

- | | |
|--|---|
| 1. $f\left(\frac{1}{2}\right) = 1$ from $u_r(1, z) = -1$ | (uniform radial injection at the wall) |
| 2. $f'\left(\frac{1}{2}\right) = 0$ from $u_z(1, z) = 0$ | (zero axial speed at the injecting wall) |
| 3. $f(0) = 0$ from $u_r(0, z) = 0$ | (no radial crossflow at the centerline) |
| 4. $\sqrt{2\eta}f''(0) = 0$ from $\partial u_z(0, z)/\partial r = 0$ | (symmetric axial velocity at the centerline). |

[†]There are over 100 different cases, depending on how they are classified. Many are given by Berker (1963). See also Wang (1991), Rogers (1992), Profilo et al. (1998), Drazin and Riley (2006), Dyck and Straatman (2019), and the references therein.

[‡]The duct problem is more restrictive for a multiply connected section than the torsion problem, which does not require that u vanish on the surfaces of the inner holes in the cross section.

[§]Stagnation flow also happens to be an exact solution to the simpler boundary-layer equations. It is, in fact, one of the similar solutions to be discussed in Sec. 4-3.

******Appendix I provides a collection of trigonometric identities that can be useful in solving certain problems, especially those requiring integration.

CHAPTER 4

LAMINAR BOUNDARY LAYERS

The best theory is the simplest one that still explains observations.

William of Ockham (1285–134)

4-1 INTRODUCTION

SEVERAL OF the exact solutions considered in [Chap. 3](#)—notably moving-boundary flows, oscillatory duct flows, stagnation flows, the rotating disk, convergent-wedge flow and the flat plate with asymptotic suction—have hinted strongly at boundary-layer behavior. That is, at large Reynolds numbers, the effects of viscosity become increasingly confined to narrow regions near solid walls. Digital-computer solutions also show this tendency of high-speed flows to sweep the vorticity downstream and leave the flow far from the wall essentially irrotational. Physically, this means that the rate of downstream convection is much larger than the rate of transverse viscous diffusion. Consider a flow at speed U past a thin body of length L . The time a fluid particle spends near the body is approximately L/U , while the time required for viscous effects to spread across the streamlines is of order $\sqrt{\nu L/U^3}$. This time scale can be derived directly from Majdalani's penetration number, which remains constant for a fixed penetration depth in the cross-streamwise direction, or spreading distance across streamlines (Sec. 2-9.3). By setting this dimensionless parameter equal to a constant, we get

$$Mj = \frac{U^3 \tau^2}{\nu L} = \text{const}$$

This enables us to estimate the characteristic time for crossing as $\tau \approx \sqrt{\nu L/U^3}$. According to the viscous region will be thin if the diffusion time is much shorter than the residence time:

$$\sqrt{\frac{\nu L}{U^3}} \ll \frac{L}{U} \quad \text{or} \quad \sqrt{\frac{UL}{\nu}} = \sqrt{Re_L} \gg 1 \quad (4-1)$$

Thus, a *thin boundary layer* is expected when the flow Reynolds number Re_L is large. The boundary layer is likely to be laminar at first and then, as Re_L increases, undergoes transition to turbulence. However, a thin layer is not ensured on the rear or lee side of bluff bodies. As we saw for spheres and cylinders in [Chap. 3](#), a standing eddy at moderate Re forms behind the body. As Re continues to increase, eddies are shed and scattered while a broad wake begins to develop. In this vein, the thin-boundary-layer approximations to be discussed here do not apply in the “separated” regions that occur behind bluff bodies. Boundary-layer theory will, however, be used to estimate where the point of separation occurs on the body. Analytical studies of separated flows are difficult and rare, but there is considerable experimentation and numerical modeling.

Even though standard boundary-layer analysis is not applicable to (1) low Reynolds number or (2) flow separation regions, it remains a very important subject, especially for understanding viscous flows. For this reason, the present chapter will focus on traditional boundary-layer techniques. For further study, we refer the reader to monographs that are entirely devoted to boundary-layer theory: Cebeci and Cousteix (1998), Schlichting and Gersten (2017), Schetz and Bowersox (2011), Oleinik and Samokhin (1999), and the classical monograph by Rosenhead (1963).Page 154

4-1.1 Flat-Plate Integral Analysis

Following an idea first developed by Kármán (1921), a substantial amount of quantitative information can be gained about boundary layers by performing a broad-brush momentum analysis of the flow of a viscous fluid at high Re past a flat plate. A schematic of the proposed flow configuration is given in [Fig. 4-1](#). Note that the sharp edge of the plate is set at $(x, y) = (0, 0)$ and the fluid sweeping along the plate will shear at the wall because of the no-slip condition, thus producing a drag force D . The corresponding velocity distribution $u(y)$ at any particular downstream position x will show a smooth drop-off to zero at the wall, illustrated in the figure. To satisfy conservation of mass, the streamlines will be slightly deflected away from the plate, so that the fluid pressure remains approximately constant. We have labeled the shear-layer thickness as $\delta_{99\%}$; streamlines outside this shear layer will deflect a distance δ^* (the displacement thickness), which depends only upon x . Thus, the streamline in the figure moves upward from $y = H$ at $x = 0$ to $y = \delta = H + \delta^*$ at $x = L$, where L is the length of the control volume parallel to the plate. Finally, we assume that the velocity just upstream of the sharp edge is uniform and parallel, i.e., $u = U = \text{const.}$

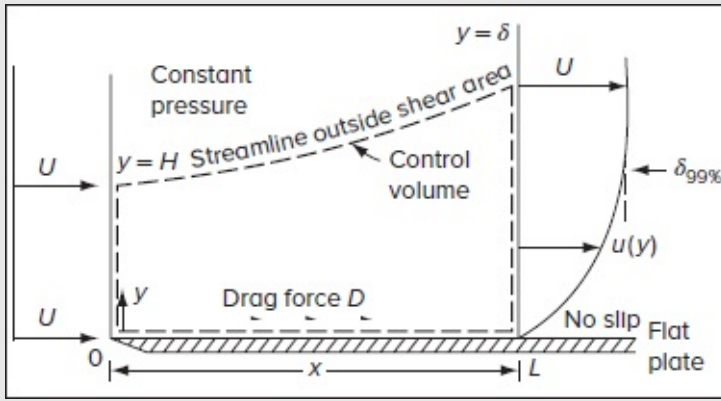


FIGURE 4-1

Definition of control volume for the analysis of flow past a flat plate.

The control volume chosen for the analysis is enclosed by dashed lines in [Fig. 4-1](#). Since velocity distributions are known only at the inlet and exit, it is helpful for the other two sides of the control volume to be streamlines that no mass or momentum can cross. The lower side is chosen to be the wall itself, thus exposing the frictional drag force. The upper side is a streamline just outside the shear layer, so that the viscous drag is zero along this line.

4-1.2 The Displacement Thickness

For steady flow, mass conservation between the (left) inlet section and the (right) outlet section of this streamline-bounded control volume can be applied, as per Eq. (2-118), to give

$$\iint_{CS} \rho \mathbf{V} \cdot d\mathbf{A} = \int_0^\delta \rho u b dy - \int_0^H \rho U b dy = 0 \quad (4-1)$$

where b is the width of the plate. For an incompressible motion with constant density, this relation simplifies into

$$U \int_0^H dy = \int_0^\delta u dy \quad \text{or} \quad H = \int_0^\delta \frac{u}{U} dy \quad (4-2)$$

Rearranging and noting that $\delta = H + \delta^*$ and, cleverly, $\delta = \int_0^\delta dy$, the displacement thickness can be deduced directly from

$$\delta^* = \delta - H = \int_0^\delta dy - \int_0^\delta \frac{u}{U} dy \quad \text{or} \quad \delta^* = \int_0^\delta \left(1 - \frac{u}{U}\right) dy \approx \int_0^\infty \left(1 - \frac{u}{U}\right) dy \quad (4-3)$$

The last approximation is permitted because of the negligible contribution of the integrand for $y > \delta$, where $u \approx U$. In fact, [Eq. \(4-3\)](#) is the formal definition of the boundary-layer displacement thickness δ^* , which holds true for any incompressible fluid, be it laminar

turbulent, with constant or variable pressure (or temperature). Physically, δ^* measures the reduction of mass transport in the axial direction due to the presence of a boundary layer (see [Fig. 4-2](#)). In other words, it represents the height of a virtual streamtube traveling at the freestream velocity U and carrying the mass deficit caused by flow deceleration inside the boundary layer—which causes the speed to vary from zero at the wall to U at the edge of the boundary layer. It, therefore, corresponds to the vertical displacement of a streamline that will preserve mass conservation in an otherwise strictly uniform flow. In [Fig. 4-2](#), the shaded areas are equal because the mass flow deficit near the wall (relative to a plug flow) is by definition equal to δ^*U . Moreover, since y variations are integrated away, δ^* remains a function of x only, although its value depends on the local velocity distribution $u(y)$.

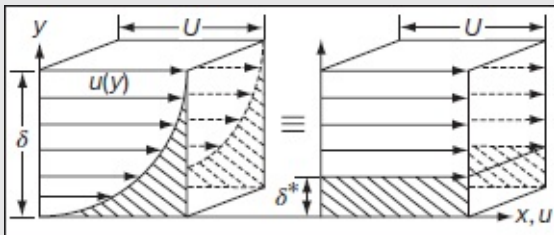


FIGURE 4-2

Vertical displacement δ^* of an inviscid, irrotational, uniform flow that will transport the same amount of mass as its corresponding sheared flow. The shaded areas, which represent the mass deficit due to flow deceleration, are equal.

The displacement thickness concept enables us to define an equivalent “effective body” that has been thickened, i.e., whose surface has been displaced by δ^* outwardly, in such a way to permit the use of a strictly inviscid flow around it, as pictured in [Fig. 4-3](#).

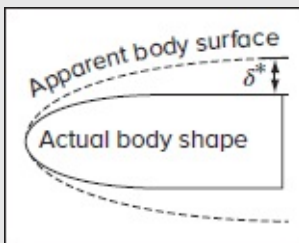


FIGURE 4-3

Sketch of an apparent (or effective) body that represents an immersed object with thickened walls, i.e., surface boundaries that have been displaced outwardly by a normal distance δ^* to permit the continual use of inviscid theory.

4-1.3 Momentum Thickness as Related to Flat-Plate Drag

Conservation of x momentum can be secured by applying [Eq. \(2-119\)](#) to our control volume. We get

$$\sum F_x = -D = \iint_{CS} u(\rho \mathbf{V} \cdot d\mathbf{A}) = \int_0^\delta u(\rho u b dy) - \int_0^H U(\rho U b dy) \quad \text{and so} \quad D = \rho U^2 H b - \int_0^\delta \rho u^2 b dy \quad (4-5)$$

Again, assuming constant ρ and recalling that $H = \int_0^\delta (u/U) dy$ from [Eq. \(4-3\)](#), we obtain

$$D = \rho b \int_0^\delta u(U - u) dy \quad \text{or} \quad \frac{D}{\rho U^2 b} = \theta = \int_0^\delta \frac{u}{U} \left(1 - \frac{u}{U}\right) dy \approx \int_0^\infty \frac{u}{U} \left(1 - \frac{u}{U}\right) dy \quad (4-6)$$

Equation (4-6) is the defining relation for a second parameter, the momentum thickness which is also a function of x only. Here θ represents the height of a virtual streamtube traveling at the freestream velocity U while carrying the net momentum deficit attributed viscous resistance. This definition for θ holds true for any incompressible boundary layer although its connection with the drag force and ρU^2 depends on the configuration at hand. For example, it will differ for a cylinder or sphere in cross flow compared to a flat-plate flow. Practically, θ measures the reduction in flow momentum due to the presence of boundary layer and is, therefore, useful in the prediction of drag. For example, based on [Eq. \(4-6\)](#), one can easily deduce the drag coefficient on a plate of length x by writing:

$$C_D(x) = \frac{D(x)}{\frac{1}{2} \rho U^2 (bx)} = \frac{2\theta(x)}{x} \quad \text{or} \quad x C_D(x) = 2\theta(x)$$

The evaluation of δ^* and θ is illustrated graphically in [Fig. 4-4](#). Clearly, δ^* is always greater than θ and their ratio, called the *shape factor*, is often used in boundary-layer analyses:

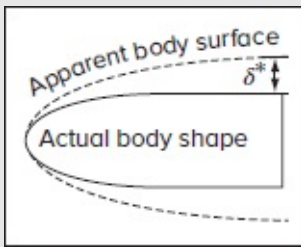


FIGURE 4-4

Momentum and displacement thickness.

$$H \equiv \frac{\delta^*}{\theta} > 1 \quad (4-7)$$

Here, H is not to be confused with the height of the inlet section in [Fig. 4-1](#). If $\tau_w(x)$ is the wall shear stress on the plate, then the total drag on one side of a plate of length L and width b is the integral of the wall shear forces:

$$D = \int_0^L \tau_w(x) b dx \quad (4-5)$$

The wall shear and drag force may be nondimensionalized in the same manner as [Chap. 3](#):

$$\text{Friction coefficient:} \quad C_f(x) = \frac{\tau_w(x)}{\frac{1}{2} \rho U^2} \quad (4-6)$$

These are general definitions. For a *flat plate*, by comparison with [Eqs. \(4-6\)](#) and [\(4-8\)](#), we get

$$\begin{aligned} C_{f, \text{plate}}(x) &= \frac{d}{dx} [x C_D(x)] = 2 \frac{d\theta}{dx} \\ C_{D, \text{plate}} &= \frac{1}{L} \int_0^L C_{f, \text{plate}}(x) dx = \frac{1}{L} \int_0^L \left(2 \frac{d\theta}{dx} \right) dx = \frac{2}{L} \theta(L) \end{aligned} \quad (4-7)$$

These two expressions were derived by Kármán (1921) in his classic paper and remain valid under both laminar and turbulent regimes. It is gratifying that flat-plate friction and drag can be estimated entirely from the momentum thickness $\theta(x)$.

4-1.4 Guessed Profiles Yield Numerical Estimates

Assuming that the inlet profile is indeed a uniform velocity U , the previous relations are exact if one uses the correct profile u . With the exact solution, though, we do not need integrals; we merely calculate the drag and wall shear directly. The beauty of Kármán's idea is that we can *guess* a reasonable form of u and extract reasonable estimates because integration tends to wash out the positive and negative deviations of the assumed profile.

To illustrate Kármán's approach, let us begin by prescribing a simple expression for $u(x, y)$ at a fixed position x in [Fig. 4-1](#). Our goal is to satisfy three fundamental physical conditions for this boundary-layer profile:

No slip at the wall: $u(x, 0) = 0$

Smooth merging with the far-field velocity or freestream:

$$u(x, \delta) = U \quad \text{and} \quad \left. \frac{\partial u}{\partial y} \right|_{y=\delta} = 0$$

Other constraints will be discussed later. We can satisfy these three conditions with a second-order polynomial of the form

$$u(x, y) \approx c_0 + c_1 y + c_2 y^2 \quad \text{or} \quad u(x, y) \approx U \left(\frac{2y}{\delta} - \frac{y^2}{\delta^2} \right) \quad (4-1)$$

where the x dependence is captured through $\delta(x)$. By inserting this approximate profile in [Eqs. \(4-4\)](#) and [\(4-6\)](#), we extract

$$\eta^* \equiv \frac{\delta^*}{\delta} \approx \frac{1}{3} \quad \theta^* \equiv \frac{\theta}{\delta} \approx \frac{2}{15} \quad \text{and} \quad H \approx \frac{5}{2} \quad (4-1)$$

Here, η^* and θ^* are used to designate the dimensionless displacement and momentum thicknesses, respectively. At this point, it proves helpful to relate the wall shear stress to the assumed shape u by differentiating the quadratic polynomial and writing

$$\tau_w = \mu \left. \frac{\partial u}{\partial y} \right|_{y=0} \approx \frac{2\mu U}{\delta} \quad (4-1)$$

Substituting [Eqs. \(4-12\)](#) and [\(4-13\)](#) into the first member of [Eqs. \(4-10\)](#), and rearranging, we obtain

$$C_f \approx \frac{2\mu U / \delta}{\frac{1}{2} \rho U^2} = 2 \frac{d\theta}{dx} \approx \frac{4}{15} \frac{d\delta}{dx} \quad \text{or} \quad \delta d\delta \approx \frac{15\mu dx}{\rho U}$$

The resulting expression can be readily integrated from $x = 0$ to any position x , while taking into account the initiation of boundary-layer growth at the leading edge, where $\delta(0) = 0$. The result is

$$\delta^2 \approx \frac{30\mu x}{\rho U} \quad \delta^2 \approx \frac{30\mu x^2}{\rho U x} \quad \text{or} \quad a \equiv \frac{\delta(x)}{x} \sqrt{Re_x} \approx 5.477 \quad (4-1)$$

where $Re_x = \rho U x / \mu$. This result is only 9.5 percent higher than the “exact” solution for laminar flat-plate flow given by Blasius (1908). Further, by substituting $\delta(x)$ from [Eq. \(4-1\)](#) into [Eqs. \(4-12\)](#) and [\(4-13\)](#), additional flat-plate characteristics can be deduced, viz.

$$b \equiv C_f \sqrt{Re_x} \approx \frac{4}{15} \frac{d\delta}{dx} \sqrt{Re_x} \approx 0.730 \quad c \equiv \frac{\delta^*}{x} \sqrt{Re_x} \approx \frac{1}{3} \sqrt{30} \approx 1.826 \quad \text{and} \quad d \equiv \frac{\theta}{x} \sqrt{Re_x} \approx \frac{2}{15} \sqrt{30} \approx 0.73 \quad (4-1)$$

The resulting constants (a , b , c , d) also fall within 10 percent of the Blasius estimates. Finally, by integrating $C_f(x)$ over the length of the plate, we obtain the total drag coefficient

$$C_D = 2C_f(L) \approx \frac{1.4605}{\sqrt{Re_L}} \quad (4-1)$$

As Kármán (1921) pointed out, these expressions can be quite easily determined compared to a full-blown attack on the continuity and momentum equations.

In fact, several momentum integral approximations for flat-plate flow, specifically those that lead to closed-form analytic expressions for u , have been pursued in the literature. Foremost among them are those devised by Pohlhausen (1921) and Schlichting (1979).

although several other formulations have become available in recent years. These can generally separated into piecewise (continuously differentiable) profiles, which are valid or within the $0 \leq y \leq \delta$ boundary-layer region, and, alternatively, into monotonically increasing continuous profiles that merge smoothly into the far field even as $y \rightarrow \infty$. We defer the discussion of continuous profiles to Sec. 4-3, where their connection to the Blasius similarity solution can be made. In the meantime, we proceed by examining five piecewise models that are defined for $0 \leq y \leq \delta$ and which are set equal to unity for $\delta < y < \infty$. These are

Pohlhausen's quadratic, cubic, and quartic profiles:

$$\frac{u}{U} = 2\frac{y}{\delta} - \frac{y^2}{\delta^2} \quad \frac{u}{U} = \frac{3}{2}\frac{y}{\delta} - \frac{1}{2}\frac{y^3}{\delta^3} \quad \text{and} \quad \frac{u}{U} = 2\frac{y}{\delta} - 2\frac{y^3}{\delta^3} + \frac{y^4}{\delta^4} \quad [\text{Pohlhausen (1921)}] \quad (4-1)$$

Schlichting's sinusoidal profile:

$$\frac{u}{U} = \sin\left(\frac{\pi y}{2\delta}\right) \quad [\text{Schlichting (1979)}] \quad (4-1)$$

Majdalani–Xuan's quartic profile:

$$\frac{u}{U} = \frac{5}{3}\frac{y}{\delta} - \frac{y^3}{\delta^3} + \frac{1}{3}\frac{y^4}{\delta^4} \quad [\text{Majdalani and Xuan (2020)}] \quad (4-1)$$

Using $\xi = y/\delta$ and $F(\xi) = u/U$ for simplicity, these profiles are collected in [Table 4-1](#) and compared to the classic solution due to Blasius (1908). Note that relative percentage errors are provided below each estimate along with the overall $L_2 = \sqrt{\int_0^1 (F - F_{\text{Blasius}})^2 d\xi}$ error across the boundary layer, to help quantify the overall deviation in each approximation from the traditionally reported Blasius values. Properties that are not shown can be easily deduced because, for laminar flow, $(\theta/x)\sqrt{Re_x} = C_f\sqrt{Re_x} = \text{const}$ (already tabulated), and $C_D\sqrt{Re_L}$ is twice this constant.

TABLE 4-1

Boundary-layer predictions from five piecewise analytic profiles with their errors relative to the classic Blasius values

Profile	$\frac{u}{U}$	$\frac{\theta}{x}\sqrt{Re_x}$	$C_f\sqrt{Re_x}$	$C_D\sqrt{Re_L}$	L_2	Relative Error (%)
Blasius	$\sum_{n=0}^{\infty} \frac{f_n}{n!} \xi^n$	0.664	0.664	1.328	0.000	0.0
Pohlhausen (Quadratic)	$2\xi - \xi^2$	0.664	0.664	1.328	0.000	0.0
Pohlhausen (Cubic)	$\frac{3}{2}\xi - \frac{1}{2}\xi^3$	0.664	0.664	1.328	0.000	0.0
Pohlhausen (Quartic)	$2\xi - 2\xi^3 + \xi^4$	0.664	0.664	1.328	0.000	0.0
Schlichting (Sinusoidal)	$\sin\left(\frac{\pi\xi}{2}\right)$	0.664	0.664	1.328	0.000	0.0
Majdalani–Xuan (Quartic)	$\frac{5}{3}\xi - \xi^3 + \frac{1}{3}\xi^4$	0.664	0.664	1.328	0.000	0.0

Page 158

$\frac{u}{U} = F(\xi)$	$\eta^* = \frac{\delta^*}{\delta}$	$\theta^* = \frac{\theta}{\delta}$	$H = \frac{\delta^*}{\theta}$	$\frac{\delta}{x} \sqrt{Re_x}$	$C_f \sqrt{Re_x}$	$\frac{\delta^*}{x} \sqrt{Re_x}$	L_2 error
$2\xi - \xi^2$	0.333 3.1%	0.133 0.25%	2.500 3.5%	5.477 9.5%	0.730 10%	1.826 6.1%	0.020
$\frac{3}{2}\xi - \frac{1}{2}\xi^3$	0.375 9.0%	0.139 4.7%	2.692 4.0%	4.641 7.2%	0.646 2.6%	1.740 1.1%	0.034
$2\xi - 2\xi^3 + \xi^4$	0.300 13%	0.118 12%	2.554 1.4%	5.836 17%	0.685 3.2%	1.751 1.8%	0.054
$\sin(\frac{1}{2} \pi \xi)$	0.363 5.6%	0.137 2.7%	2.660 2.7%	4.795 4.1%	0.655 1.3%	1.743 1.3%	0.021
$\frac{5}{3}\xi - \xi^3 + \frac{1}{3}\xi^4$	0.350 1.7%	0.134 0.52%	2.618 1.1%	4.993 0.13%	0.668 0.53%	1.748 1.6%	0.008
Blasius (1908)	0.344	0.133	2.59	5	0.664	1.72	n/a

Excluding the quartic profile due to Majdalani and Xuan (2020), the maximum error varies between 6 and 17 percent in predicting boundary-layer properties, which is typical of integral theories. However, some profiles appear to be distinctly more accurate than others, namely, in mirroring the behavior of the Blasius solution. What is most perplexing, perhaps, is what some fluid dynamicists have come to identify, rather informally, as the *Pohlhausen paradox*: the reader may notice that as we move from Pohlhausen’s second-order polynomial to his fourth-order polynomial—which is capable of securing more boundary conditions—the agreement with the Blasius solution deteriorates! From [Table 4-1](#), it can be seen that the errors in estimating the dimensionless displacement and momentum thicknesses (η^* , θ^*) jump by one order of magnitude, i.e., from (3.1, 0.25) to (13, 12) percent, while the overall L_2 error increases from 0.02 to 0.05 when Pohlhausen’s quadratic polynomial is exchanged by its quartic counterpart. The error in predicting the boundary-layer thickness also increases from 9.5 percent to a whopping 17 percent!

So, the reader may wonder, what is driving the accuracy of these profiles? For many years, it was believed that the fidelity of the guessed profiles could be improved by securing additional boundary conditions that would be representative of the Blasius model, thus making them more realistic. To this end, Pohlhausen (1921) proposed five fundamental conditions which, besides the wall adherence and smooth merging with the freestream conditions—the three constraints satisfied by the quadratic [Eq. \(4-11\)](#) earlier in this section—added on two further requirements on the shear stress: one at the wall and one at the edge of the boundary layer. In practice, the fourth condition serves to maintain the correct momentum balance at the wall between the non-vanishing components of the boundary-layer equations, namely,

$$\mu \left. \frac{\partial^2 u}{\partial y^2} \right|_{y=0} = \frac{dp}{dx} \quad (\text{boundary-layer equation at } y = 0) \quad \text{where} \quad \frac{dp}{dx} = -\rho U \frac{dU}{dx} \quad (\text{Euler's far-field equation}) \quad (4-2)$$

Here, the pressure gradient inside the boundary layer is expressed in terms of the freestream velocity using Euler’s equation for the far field. The reader may verify that only the Pohlhausen’s cubic and quartic polynomials satisfy this momentum balance.

requirement, but so do Schlichting's sinusoidal and Majdalani–Xuan's quartic profiles.

Lastly, Pohlhausen's fifth condition assumes zero shear at the edge of the boundary layer which translates into a vanishing curvature at $y = \delta$:

$$\left. \frac{\partial^2 u}{\partial y^2} \right|_{y=\delta} = 0 \quad (4-2)$$

Of the five profiles described so far, only Pohlhausen's quartic polynomial satisfies the condition identically. Incidentally, it also proves to be the most imprecise, as it leads to the largest overall L_2 error and a 17 percent discrepancy in predicting the boundary-layer thickness relative to the traditionally reported Blasius values. So what went wrong? Page 15

As it turns out, although the fifth condition holds true as $y \rightarrow \infty$, it proves to be inadequate at the edge of the boundary layer, where the velocity slope continues to change. In fact, a sufficiently resolved numerical solution to the Blasius model returns a curvature of 0.7085, which is certainly not zero, but rather of order unity.

Subjugating the quartic Pohlhausen polynomial to the fifth constraint, which happens to be off by one order of magnitude, explains, in part, its tendency to overpredict several boundary-layer properties relative to its lower-order models (cf. [Table 4-1](#)). It also leads to a higher initial slope of its velocity profile at the wall, as one may readily infer from [Fig. 4-4](#) where the analytic profiles are superimposed on the Blasius curve. In contrast, Schlichting's sinusoidal and Majdalani–Xuan's quartic profiles display slopes that are closer to the exact Blasius value of 1.630 at $y = \xi = 0$. This may be attributed to their wall gradients of $F'(0) = \pi/2 \approx 1.571$ and $5/3 \approx 1.667$, which slightly undershoot and overshoot the true slope respectively. Other deviations from the Blasius solution can be discerned graphically in the two parts of [Fig. 4-5](#). For example, the assumption that $u = U$ (and therefore $F = 1$ instead of 0.99) at $y = \delta$ (far right) can be seen to affect the piecewise approximations, but not the Blasius curve. The latter returns a value of 0.99 at $y = \delta$, which is consistent with the percent basis.

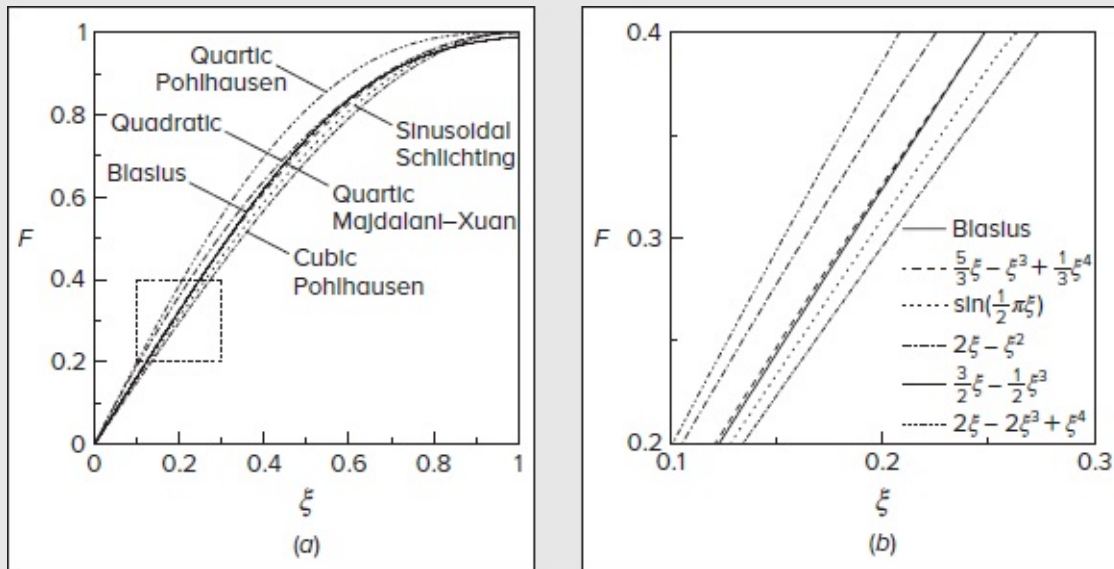


FIGURE 4-5

Comparison of five analytic approximations to the Blasius solution (solid line) including Pohlhausen’s quadratic, cubic, and quartic polynomials (chained lines) as well as Schlichting’s sinusoidal (dotted) and Majdalani–Xuan’s quartic (dashed) profiles across (a) the boundary layer and (b) a designated quadrant where individual deviations from the Blasius curve are magnified.

In the interest of clarity, the properties and conditions observed by the five analytic profiles and their derivatives at the endpoints of the viscous domain are summarized in [Table 4-2](#). Although not required, the negative curvature of the quadratic Pohlhausen profile at $\xi = 1$, which matches the curvature of the quartic Majdalani–Xuan polynomial of -2 , appears to be more in line with the Blasius “edge” curvature than its quartic companion. The characteristic feature of [Eq. \(4-11\)](#) helps to explain, in part, its improved accuracy relative to its quartic form, despite its inability to secure the momentum balance requirement at the wall, i.e., Pohlhausen’s fourth boundary condition. In fact, it is only by recognizing the various limitations that Majdalani and Xuan (2020) manage to derive a simple quartic polynomial that satisfies Pohlhausen’s four essential boundary conditions while overcoming the deficiencies that accompany Pohlhausen’s quartic solution. These, we have shown, are partly caused by a prematurely imposed zero shear-stress condition at $y = \delta$.

TABLE 4-2

Endpoint properties of the piecewise analytic velocity profiles and their corresponding Blasius values

$\frac{u}{U} = F(\xi)$	$F(0)$	$F'(0)$	$F''(0)$	$F(1)$	$F'(1)$	$F''(1)$
$2\xi - \xi^2$	0	2.000	-2	1.000	0	-2.000
$\frac{3}{2}\xi - \frac{1}{2}\xi^3$	0	1.500	0	1.000	0	-3.000
$2\xi - 2\xi^3 + \xi^4$	0	2.000	0	1.000	0	0.000
$\sin(\frac{1}{2}\pi\xi)$	0	1.571	0	1.000	0	-2.467
$\frac{5}{3}\xi - \xi^3 + \frac{1}{3}\xi^4$	0	1.667	0	1.000	0	-2.000
Blasius (1908)	0	1.630	0	0.990	0.0904	-0.709

Naturally, with the advent of a quartic polynomial that outperforms Pohlhausen's cubic and quartic formulations, the informally dubbed "Pohlhausen paradox" is finally laid to rest. Nonetheless, new challenges arise: The widely used $u = U(2\xi - 2\xi^3 + \xi^4)$ profile has been incorporated into countless viscous and thermal studies which, it stands to reason, ought to be revisited using the more precise $u = U(5\xi - 3\xi^3 + \xi^4)/3$ model. This challenge can be daunting when taking into account that, in the absence of simpler alternatives over the course of the century, Pohlhausen's quartic polynomial has become the staple of analytic approximation infusing the Kármán–Pohlhausen momentum-integral method. As such, it has formed the backbone of numerous laminar-flow solutions of viscous and thermal boundary layers, both with and without pressure gradients. Evidently, its reduced accuracy has prompted several researchers to seek alternative methods, as we shall see later in Sec. 4-6.

4-1.5 Some Insight into Boundary-Layer Approximations

The essence of the "boundary-layer approximation" is that the shear layer is thin, or $\delta \ll x$. From [Eq. \(4-14\)](#), we see that this is true if $Re_x \gg 1$. Other scaling arguments also follow from these results. First, since the velocity ratio $v/u \leq d\delta^*/dx$, which reflects the outer-streamline slope, it follows from [Eq. \(4-15\)](#) that $v \ll u$ if $Re_x \gg 1$. Second, by differentiating [Eq. \(4-11\)](#), we find that $\partial u/\partial x \ll \partial u/\partial y$ if, again, $Re_x \gg 1$, and so do the derivatives of the normal velocity v . In summary, a large Reynolds number gives rise to the following fundamental inequalities:

$$Re_x \gg 1: \quad \delta \ll x \quad v \ll u \quad \frac{\partial u}{\partial x} \ll \frac{\partial u}{\partial y} \quad \text{and} \quad \frac{\partial v}{\partial x} \ll \frac{\partial v}{\partial y} \quad (4-2)$$

In fact, all of these approximations were used by Prandtl (1904) in deriving his celebrated boundary-layer equations. Moreover, in the case of a uniform freestream for which $dp/dx = dU/dx = 0$, the boundary-layer properties can be estimated from simple relations that are fairly straightforward. For the reader's convenience, their proof is relegated to an exercise problem. In short, given a mean-flow profile $u/U = F(\xi)$, where $\xi = y/\delta$, the key boundary-layer properties can be deduced from three easy-to-evaluate constants $s = F'(0)$, $\eta^* = \int_0^1 (1 - F)d\xi$, and $\theta^* = \int_0^1 F(1 - F)d\xi$. For example, s is simply the coefficient of ξ and can be found by inspection for the entire class of polynomial approximations $F(\xi) = c_0 + s\xi + c_2\xi^2 + \dots$; the remaining constants follow straightforwardly from:

$$a = \frac{\delta}{x} \sqrt{Re_x} = \sqrt{\frac{2s}{\theta^*}}, \quad b = C_f \sqrt{Re_x} = a\theta^*, \quad c = \frac{\delta^*}{x} \sqrt{Re_x} = a\eta^*, \quad d = b = \frac{\theta}{x} \sqrt{Re_x} = a\theta^*, \quad \text{and} \quad C_{D, \text{plate}} \sqrt{Re_L} = 2at \quad (4-2)$$

Interestingly, the product of the first two constants is simply twice the slope, $ab = 2s$. These simple relations help to illuminate the source of the constants that appear in [Table 4](#) as well as the benefits of using analytic mean-flow profiles.

4-1.6 Integral Analysis of the Energy Equation

In a similar manner, the integral form of the energy equation can be used to obtain approximations for the mean and local heat transfer as well as the thickness of the thermal boundary layer, δ_T . The control volume chosen here is shown in [Fig. 4-6](#), where the back portion of the plate is heated (or cooled), for $x \leq x_0$, to a temperature T_w that is different from the boundary-layer “edge” temperature T_e in the freestream (or the leading portion of the plate). Beginning at x_0 , then, a thermal boundary layer will grow. Furthermore, considering that the upper streamline falls outside the region of shear (i.e., the viscous boundary layer), there will be no shear (or shaft) work of significance. Based on [Eq. \(2-120\)](#), we are left with

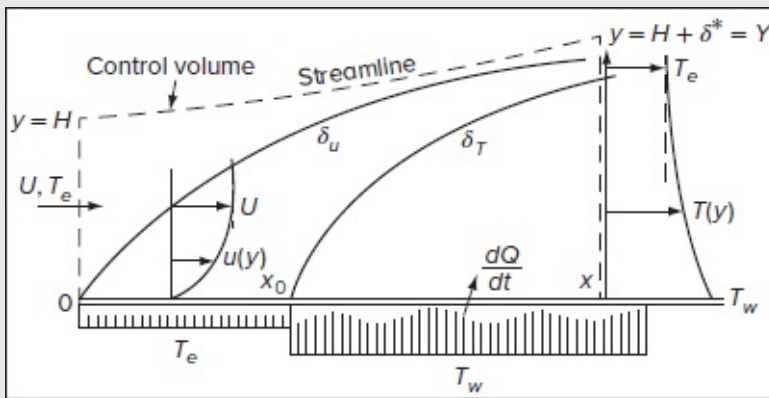


FIGURE 4-6

Sketch and control volume for the thermal boundary layer. A hot wall is shown for convenience and $\delta_u \equiv \delta$ is the viscous or velocity boundary-layer thickness.

$$\frac{dQ}{dt} = \iint_{cs} \left(e + p/\rho + gy + \frac{1}{2}u^2 + \frac{1}{2}v^2 \right) \rho \mathbf{V} \cdot d\mathbf{A} \quad (4-2)$$

At large Re_x , we have $\delta^* \ll x$ and $v \ll u$ so that the change in potential energy will be very small. In fact, by neglecting

both gy and $\frac{1}{2}v^2$, we can consolidate the quantity $(e + p/\rho)$ into the enthalpy h , and then reduce the energy equation into integrals of the *stagnation enthalpy* $h_0 = (h + \frac{1}{2}u^2)$ over the inlet and outlet sections of the domain:

$$\frac{dQ}{dt} \approx \int_0^Y \left(h + \frac{1}{2}u^2\right) \rho u b dy - \int_0^H \left(h + \frac{1}{2}u^2\right) \rho u b dy \quad (4-2)$$

Page 161 This expression applies to both incompressible and compressible motions and will be revisited in [Chap. 7](#). Here, we assume constant density and, because of the uniform conditions (h_e , T_e , U) at the inlet, we can write

$$\text{Inlet: } \int_0^H \left(h + \frac{1}{2}u^2\right) \rho u b dy = \left(h_e + \frac{1}{2}U^2\right) \rho b U H$$

Then using a mass balance similar to the one leading to [Eq. \(4-3\)](#), we can easily identify that $UH \approx \int_0^Y u dy$. This enables us to substitute $\int_0^H \left(h + \frac{1}{2}u^2\right) \rho u b dy = \int_0^Y \left(h_e + \frac{1}{2}U^2\right) \rho u b dy$ into the energy equation and write

$$\frac{dQ}{dt} = \rho \int_0^Y \left[(h - h_e) + \frac{1}{2}(u^2 - U^2)\right] u b dy \approx \rho \int_0^\infty \left[(h - h_e) + \frac{1}{2}(u^2 - U^2)\right] u b dy \quad (4-2)$$

Here too, the last approximation can be made because of the negligible value of the integrand past the edge of the composite boundary layer, i.e., for $Y \leq \max(\delta, \delta_T)$, where both $u^2 - U^2 \approx 0$ and $h - h_e \approx 0$. Essentially, one only needs to integrate up to the “edge” of the large boundary layer, although the upper bound of the integral can be formally extended out to infinity. At the left side of this *integral-energy* equation, $dQ/dt = \int q_w b dx$ can be expressed in terms of the wall heat flux q_w , and so [Eq. \(4-26\)](#) can be differentiated with respect to x and written in *local* form as:

$$q_w = \frac{d}{dx} \left[\int_0^\infty \rho u \left(h + \frac{1}{2}u^2 - h_e - \frac{1}{2}U^2\right) dy \right] = -k \left. \frac{\partial T}{\partial y} \right|_{y=0} \quad (4-2)$$

For low-speed flow, it is customary to neglect the kinetic energy per unit mass, $\frac{1}{2}u^2$ (i.e., if $Ec \ll 1$) and use $h \approx c_p T$. We are left with

$$q_w \approx \frac{d}{dx} \left[\int_0^\infty \rho c_p u (T - T_e) dy \right] \approx \frac{d}{dx} \left[\int_0^{\delta_T} \rho c_p u (T - T_e) dy \right] \quad (4-2)$$

This may be presented in dimensionless form as a Stanton number, with a local length scale termed the *enthalpy* thickness, δ_h ,

$$C_h(x) = \frac{q_w}{\rho U c_p (T_w - T_e)} = \frac{d}{dx} (x C_H) = \frac{d\delta_h}{dx} \quad (4-2)$$

$$\text{where } \delta_h = \text{enthalpy thickness} = \int_0^\infty \frac{T - T_e}{T_w - T_e} \frac{u}{U} dy \approx \int_0^{\delta_T} \frac{T - T_e}{T_w - T_e} \frac{u}{U} dy$$

Note the similarity to the local integral relation, [Eq. \(4-10\)](#). Moreover, [Eq. \(4-29\)](#) is valid for either laminar or turbulent flow.

4-1.7 Guessed Temperature Profiles Yield the Heat-Transfer Rate

We can evaluate the heat transfer for laminar flow by combining the velocity profile in the boundary layer, say [Eq. \(4-11\)](#), with a comparable second-order polynomial temperature estimate:

$$T - T_e \approx (T_w - T_e) \left[1 - \left(\frac{2y}{\delta_T} - \frac{y^2}{\delta_T^2} \right) \right] \quad (4-3)$$

By substituting these approximations into [Eqs. \(4-27\)](#) and [\(4-28\)](#), integrating over δT and simplifying, we obtain

$$q_w \approx \frac{d}{dx} \left[\rho c_p U (T_w - T_e) \delta \left(\frac{\zeta^2}{6} - \frac{\zeta^3}{30} \right) \right] \approx \frac{2k(T_w - T_e)}{\zeta \delta} \quad (4-3)$$

where $\zeta = \delta_T / \delta$ captures the ratio of boundary-layer thicknesses. Note that the term $(T_w - T_e)$ drops out assuming constant wall and stream temperatures. In this analysis, we also fix ρ , k , and c_p .

Let us illustrate two solutions of [Eq. \(4-31\)](#). First, let the thermal boundary layer start from the leading edge, with $\delta_T = 0$ at $x = 0$. Let us further assume, for convenience only, that $\delta_T < \delta$ and $U = \text{const}$ (i.e. $Pr < 1$). After substituting $\delta(x) = ax^{1/2} / \sqrt{U/\nu}$ from [Eq. \(4-14\)](#), with $a = \sqrt{30} \approx 5.477$ from [Table 4-1](#), we arrive at

$$\zeta^3 - \frac{\zeta^4}{5} = \frac{24a}{a^2 \nu} = \frac{0.8}{Pr} \quad (4-3)$$

An asymptotic solution to this polynomial, valid over a practical range of Prandtl number, may be extracted. One gets:

$$\zeta = 0.9283Pr^{-1/3} + 0.05745Pr^{-2/3} + 0.01067Pr^{-1} + O(Pr^{-4/3}) \approx Pr^{-1/3} \quad (4-3)$$

As shown with a dashed line in [Fig. 4-7](#), our $O(Pr^{-4/3})$ series expansion agrees well with the exact solution (solid line) as well as the simple, one-term, $Pr^{-1/3}$ expression (dotted line). With ζ and δ in hand, we can now proceed to construct the local Nusselt number using [Eq. \(4-31\)](#):

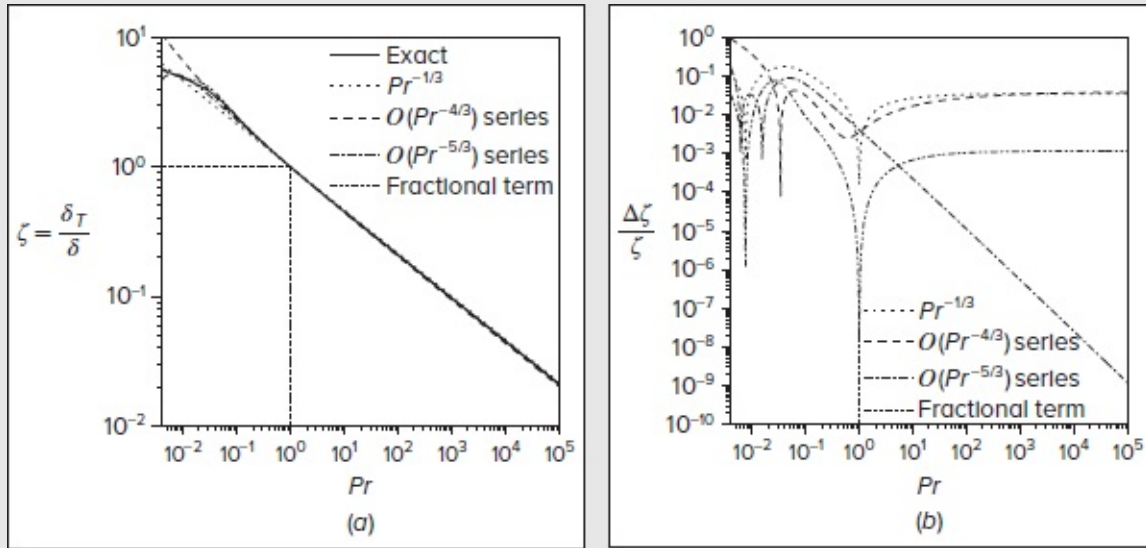


FIGURE 4-7

Comparison of several analytic approximations for $\zeta = \delta_T/\delta$ over a wide range of Prandtl numbers with (a) clear convergence characteristics for all models on the $Pr^{-1/3}$ expression for $Pr > 0.3$ and (b) well-behaved relative errors.

$$Nu_x = \frac{q_w x}{k(T_w - T_e)} = \frac{2k(T_w - T_e)x}{\zeta \delta k(T_w - T_e)} = \frac{2x}{\zeta \delta} \approx 0.365 Re_x^{1/2} Pr^{1/3} \quad (4-3)$$

The resulting estimate proves to be 10 percent higher than the exact solution for constant laminar flat-plate flow, as predicted by Pohlhausen (1921)—the correct constant being 0.35 not 0.365.

Second, let us consider an *unheated starting length*, where the wall temperature $T_w \neq$ does not begin until $x = x_0$ as per [Fig. 4-6](#). Here, $\zeta(x)$ is not constant, and [Eq. \(4-31\)](#) must be solved. After some rearrangements, we obtain

$$\zeta \delta \frac{d}{dx} \left[\delta \left(\zeta^2 - \frac{\zeta^3}{5} \right) \right] \approx \frac{12\alpha}{U} \quad \zeta = 0 \text{ at } x = x_0 \quad (4-3)$$

This differential equation can be readily handled numerically using a subroutine such as Runge–Kutta's. Alternatively, a simple solution is possible if, by noting that $\zeta < 1$ for $Pr >$ we neglect the $(\zeta^3/5)$ term and, concurrently, increase the constant 12 to 15. The differential equation becomes

$$\zeta^3 + \frac{4}{3} x \frac{d}{dx} (\zeta^3) \approx \frac{1}{Pr} \quad \text{or} \quad \zeta^3 = \frac{C}{x^{3/4}} + \frac{1}{Pr} \quad (4-3)$$

To secure $\zeta = 0$ at $x = x_0$, the constant should be $C = -x_0^{3/4}/Pr$. As usual, the final solution m

be expressed in the form of a dimensionless Nusselt number for plate flow with an unheated starting length:

$$x > x_0: \quad Nu_x = 0.365 Re_x^{1/2} Pr^{1/3} \left[1 - (x_0/x)^{3/4} \right]^{-1/3} \quad (4-3)$$

Here too, if the constant 0.365 is reduced by 10 percent to 0.332, the result will agree with the formula recommended for flat plates in most heat-transfer textbooks, including Eq. (9-2) of Kays and Crawford (1993).

Before leaving this section, it will be instructive to note that the procedure just described using Pohlhausen's quadratic polynomial can be repeated with the quartic solution due to Majdalani and Xuan (2020). To begin, Eq. (4-30) can be replaced with a fourth-order polynomial estimate for the temperature:

$$T - T_e \approx (T_w - T_e) \left[1 - \left(\frac{5y}{3\delta_T} - \frac{y^3}{\delta_T^3} + \frac{y^4}{3\delta_T^4} \right) \right] \quad (4-3)$$

Inserting this expression into the energy balance integral, which is captured through Eqs. (4-27) and (4-28), we arrive at

$$q_w \approx \rho c_p (T_w - T_e) \frac{d}{dx} \left[\int_0^{\delta_T} U \left(\frac{5y}{3\delta_T} - \frac{y^3}{\delta_T^3} + \frac{y^4}{3\delta_T^4} \right) \left[1 - \left(\frac{5y}{3\delta_T} - \frac{y^3}{\delta_T^3} + \frac{y^4}{3\delta_T^4} \right) \right] dy \right] = k(T_w - T_e) \frac{5}{3\delta_T} \quad (4-3)$$

Further expansions, integrations, and simplifications leave us with

$$\frac{3\delta_T}{5} \frac{d}{dx} \left[\left(\frac{4\zeta^2}{27} - \frac{\zeta^4}{56} + \frac{11\zeta^5}{3240} \right) U \delta \right] = \alpha \quad \text{or} \quad \zeta^3 - \frac{27\zeta^5}{224} + \frac{11\zeta^6}{480} = \frac{0.90238}{Pr} \quad (4-4)$$

The resulting expression can be put in the form $\zeta^3 - \alpha_0 \zeta^5 + \beta_0 \zeta^6 = \gamma_0 Pr^{-1}$ with $\alpha_0 = \frac{27}{224}$, $\beta_0 = \frac{11}{480}$, and $\gamma_0 = \frac{3}{420}$.

Here too, a robust approximation can be found, namely $\zeta = \gamma_0 Pr^{-1/3} + \frac{1}{3} \alpha_0 \gamma_0^3 Pr^{-1} - \frac{1}{3} \beta_0 \gamma_0^4 Pr^{-4/3} + O(Pr^{-5/3})$. More visibly, we get

$$\zeta = 0.96634 Pr^{-1/3} + 0.0362564 Pr^{-1} + 0.00666116 Pr^{-4/3} + O(Pr^{-5/3}) \approx Pr^{-1/3} \quad (4-4)$$

As illustrated with a chained (dash-dot) line in Fig. 4-7(b), this three-term perturbation series of $O(Pr^{-5/3})$ exhibits a steadily diminishing error with successive increases in the Prandtl number. It can be relied upon so long as $Pr > 0.0045$ with the knowledge that its error drops precipitously below 1 percent for $Pr > 0.45$. Another fractional approximation that outperforms the $O(Pr^{-5/3})$ series expansion in the $0.004 < Pr < 5.35962$ range can also be achieved viz.

$$\zeta = \left(\frac{1620 Pr^{1/3} - 9752 Pr - 385}{675 Pr^{1/3} - 3360 Pr - 154} \right) \frac{1}{3 Pr^{1/3}} \quad (4-4)$$

These solutions and their relative errors are showcased in [Fig. 4-7](#), along with the one-term theoretical estimate of $Pr^{-1/3}$. Despite the transcendental character of these equations, it is reassuring that they all return a root of $\zeta = 1$ for $Pr = 1$. Moreover, they all become graphically indiscernible for $Pr > 0.3$ in [Fig. 4-7\(a\)](#) as their relative errors in [Fig. 4-7\(b\)](#) drop to 4 percent or lower. These observations confirm the viability of using $\zeta \approx Pr^{-1/3}$, which entails a less than 3.3 percent error, for all gases and fluids with $Pr > 0.7$.

To complete our thermal analysis in the wake of ζ and δ , and recalling that $a \equiv \delta\sqrt{Re_x}/x = \sqrt{\frac{9450}{379}} \approx 4.9934$ from [Table 4-1](#), the local Nusselt number can be deduced systematically by taking,

$$Nu_x = \frac{q_w x}{k(T_w - T_e)} = k(T_w - T_e) \frac{5}{3\delta\zeta} \frac{x}{k(T_w - T_e)} = \frac{5x}{3\delta\zeta} \text{ and so } Nu_x = \frac{5Re_x^{1/2}Pr^{1/3}}{3a} = \frac{5Re_x^{1/2}Pr^{1/3}}{3\sqrt{\frac{9450}{379}}} \approx 0.3338Re_x^{1/2}Pr^{1/3} \quad (4-4)$$

The resulting coefficient is only 0.5 percent (not 10 percent) higher than the “exact” coefficient of 0.332 for this flow configuration. The use of the quartic Majdalani–Xu profile in lieu of Pohlhausen’s is, therefore, well justified.

In summary, we see that simple integral techniques that are based on rationally constructed velocity and temperature profiles can yield valuable approximations for either local or global friction and heat transfer coefficients with accuracies that can range from less than 1 percent to 10 percent or more. Additional examples will be provided in Sec. 4-6 for non-flat-plate flows. Page 164

4-2 LAMINAR-BOUNDARY-LAYER EQUATIONS

Integral analysis has not only led to valuable approximations, it has also yielded information about the sizes of the principal variables within the boundary layer. For example, we now know with certainty that

$$u, T, \text{ and } x = O(1) \quad v \text{ and } y = O(1/\sqrt{Re}) \quad (4-4)$$

These are solid estimates, not guesses, which can be used to derive the famous boundary layer equations first propounded by Prandtl (1904). By redefining all variables in terms of these estimates, we can quickly identify which terms in the equations of motion are negligible if Re is large. In so doing, let us confine ourselves to two-dimensional incompressible flow, for which the relevant equations reduce to

$$\frac{\partial u}{\partial x} + \frac{\partial v}{\partial y} = 0 \quad (4-4)$$

$$\frac{\partial u}{\partial t} + u \frac{\partial u}{\partial x} + v \frac{\partial u}{\partial y} = -\frac{1}{\rho} \frac{\partial p}{\partial x} + g_x \beta (T - T_0) + \nu \left(\frac{\partial^2 u}{\partial x^2} + \frac{\partial^2 u}{\partial y^2} \right)$$

$$\frac{\partial v}{\partial t} + u \frac{\partial v}{\partial x} + v \frac{\partial v}{\partial y} = -\frac{1}{\rho} \frac{\partial p}{\partial y} + g_y \beta (T - T_0) + \nu \left(\frac{\partial^2 v}{\partial x^2} + \frac{\partial^2 v}{\partial y^2} \right)$$

$$\rho c_p \left(\frac{\partial T}{\partial t} + u \frac{\partial T}{\partial x} + v \frac{\partial T}{\partial y} \right) = k \left(\frac{\partial^2 T}{\partial x^2} + \frac{\partial^2 T}{\partial y^2} \right) + \mu \left[2 \left(\frac{\partial u}{\partial x} \right)^2 + 2 \left(\frac{\partial v}{\partial y} \right)^2 + \left(\frac{\partial u}{\partial y} + \frac{\partial v}{\partial x} \right)^2 \right]$$

With our estimates from [Eq. \(4-44\)](#), we can now define dimensionless variables that will be of order unity when Re is large:

$$x^* = \frac{x}{L} \quad y^* = \frac{y}{L} \sqrt{Re} \quad t^* = \frac{tU}{L} \quad T^* = \frac{T - T_0}{T_w - T_0} \quad u^* = \frac{u}{U} \quad v^* = \frac{v}{U} \sqrt{Re} \quad p^* = \frac{p - p_0}{\rho U^2} \quad (4-4)$$

where U , L , p_0 , and T_0 are reference values and $Re = UL/\nu$ represents the characteristic Reynolds number. By substituting these variables into [Eqs. \(4-45\)](#) and taking the limit as Re becomes large, several terms drop out except for

$$\frac{\partial u^*}{\partial x^*} + \frac{\partial v^*}{\partial y^*} = 0 \quad (\text{continuity}) \quad (4-4)$$

$$\frac{\partial u^*}{\partial t^*} + u^* \frac{\partial u^*}{\partial x^*} + v^* \frac{\partial u^*}{\partial y^*} = -\frac{\partial p^*}{\partial x^*} + \frac{\beta(T_w - T_0)}{Fr_x} T^* + \frac{\partial^2 u^*}{\partial y^{*2}} \quad (x\text{-momentum})$$

$$\frac{\partial p^*}{\partial y^*} + \frac{\beta(T_w - T_0)}{Fr_y} T^* = 0 \quad (y\text{-momentum})$$

$$\frac{\partial T^*}{\partial t^*} + u^* \frac{\partial T^*}{\partial x^*} + v^* \frac{\partial T^*}{\partial y^*} = \frac{1}{Pr} \frac{\partial^2 T^*}{\partial y^{*2}} + Ec \left(\frac{\partial u^*}{\partial y^*} \right)^2 \quad (\text{energy})$$

where β represents the coefficient of thermal expansion, $Ec = U^2/[c_p(T_w - T_0)]$ denotes the Eckert number, and $Fr_i = U^2/(Lg_i)$ stands for the Froude number in each direction. All other terms end up with $1/Re$ or $(1/Re)^2$ coefficients that make them negligible. In fact, several observations can be made about this simplified set of equations:

1. The continuity equation remains unaffected by Reynolds number considerations.
2. The axial diffusion term $\partial^2 u / \partial x^2$ in the x -momentum equation disappears, and the buoyancy term can also be neglected when the Froude number is sufficiently large (with large U and small L), since $\beta(T_w - T_0) = O(1)$ or less (see [Fig. 1-24](#)). Therefore, except for small velocities and large sizes, free convection can be dismissed in the boundary layer approximation.
3. The pressure gradient in the y direction is nearly zero, being affected only by a buoyancy or stratification term that does not contribute to accelerations in the y direction. To the first intents, then, the transverse pressure gradient in a boundary layer is negligible, thus leaving us with

$$\frac{\partial p}{\partial y} \approx 0 \quad p = p(x) \text{ only} \quad (4-4)$$

This splendid observation is due to Prandtl (1904), who may have been the first to show that pressure is a *known* variable in boundary-layer analysis, with $p(x)$ being externally *impressed* upon the boundary layer by an outer inviscid flow. Consequently, the freestream velocity outside the boundary layer, $U = U(x)$, where x is the coordinate parallel to the wall, can be related to $p(x)$ through Bernoulli's theorem for incompressible flow. For steady motion, we have

$$\frac{\partial p}{\partial x} = -\rho U \frac{dU}{dx} \quad (4-4)$$

so that specifying $p(x)$ is equivalent to specifying $U(x)$ outside the boundary layer.

4. The energy equation shows that $\partial^2 T / \partial x^2$ is negligible and that only the $\partial u / \partial y$ portion of the dissipation term is important. Further, it is clear that dissipation is negligible when the Eckert number is small (e.g., for small velocities and large temperature differences).
5. A very interesting observation is that the Reynolds number does not explicitly appear in [Eqs. \(4-47\)](#). Using the judiciously posed boundary-layer coordinate transformations, the thicknesses are rescaled to order unity and, provided the flow remains laminar,[†] the Reynolds number will only appear in the characteristic length scale and velocity used to normalize the variables in the cross-streamwise direction, i.e., L / \sqrt{Re} and U / \sqrt{Re} in [Eqs. \(4-46\)](#).
6. Even more interesting, perhaps, is the elimination of all second derivatives with respect to x within the boundary-layer equations. This order reduction has two consequences: (1) the equations are now *parabolic* instead of elliptic, so that x is now a marching variable and computer solutions are relatively easier to write and (2) we are no longer in need of certain boundary conditions, notably those on v and x . More specifically, the transverse velocity v retains one derivative, $\partial v / \partial y$, and discards $\partial v / \partial x$ and its two second-order derivatives. We now need only one condition on v at one y position. The obvious condition to retain is the no-slip requirement of $v = 0$ at $y = 0$. As such, v is left free at the outer edge of the layer. Furthermore, by discarding $\partial^2 u / \partial x^2$ and $\partial^2 T / \partial x^2$, we lose one condition each on u and T ; we can disavow all knowledge of u and T at one x position, the best choice being the exit plane. Naturally, the parabolic solutions are relied upon to yield the correct values of u and T at the exit.

To sum up, the boundary-layer equations are far simpler than their parents, the Navier-Stokes equations. We can rewrite [Eqs. \(4-47\)](#) in the more common dimensional form for incompressible planar flow with constant properties:

$$\frac{\partial u}{\partial x} + \frac{\partial v}{\partial y} = 0 \quad (4-50)$$

$$\frac{\partial u}{\partial t} + u \frac{\partial u}{\partial x} + v \frac{\partial u}{\partial y} \approx \left(\frac{\partial U}{\partial t} + U \frac{dU}{dx} \right) + g_x \beta (T - T_0) + \nu \frac{\partial^2 u}{\partial y^2} \quad (4-50)$$

$$\rho c_p \left(\frac{\partial T}{\partial t} + u \frac{\partial T}{\partial x} + v \frac{\partial T}{\partial y} \right) \approx k \frac{\partial^2 T}{\partial y^2} + \mu \left(\frac{\partial u}{\partial y} \right)^2 \quad (4-50)$$

where $U = U(x, t)$, which must be given, denotes the freestream velocity just outside of the boundary layer. The full set of remaining boundary conditions can be written as:

No slip:	$u(x, 0, t) = v(x, 0, t) = 0$ and $T(x, 0, t) = T_w(x, t)$	(4-51)
Inlet condition:	$u(x_0, y, t), v(x_0, 0, t)$ and $T(x_0, y, t)$ known	
Patching to the outer layer:	$u(x, \infty, t) \rightarrow U(x, t)$ and $T(x, \infty, t) \rightarrow T_e(x, t)$	
Initial condition:	$u(x, y, 0), v(x, y, 0)$ and $T(x, y, 0)$ known.	

These equations, developed by Prandtl (1904), approximate the flow of a viscous fluid at high Reynolds numbers. They may be solved, at least numerically, for any practical distribution of stream velocity and temperature. Some important solutions will be detailed here—for additional laminar boundary layers, see the text by Rosenhead (1963).

The limitations of the boundary-layer equations are

1. The Reynolds number must be sufficiently large. In fact, there is a minimum local Reynolds number Re_x that can be estimated at any axial station.
2. If the outer flow is decelerating ($dU/dx < 0, dp/dx > 0$), a *separation point* is reached where the wall shear stress vanishes before switching direction. Unfortunately, most boundary layer approximations deteriorate beyond separation. However, some newer techniques have made headway on separated-flow analysis.
3. At some large $Re_x = O(10^6)$, the laminar solutions become unstable as the flow transitions to a turbulent state. The thin-layer approximations still hold then for the *turbulent* boundary layer.

In what follows, we present incompressible-boundary-layer relations for two-dimensional flow. These can be readily extended to three-dimensional or compressible-flow conditions.

4-2.1 Orthogonal Curvilinear Coordinates

At first glance, Eqs. (4-50a)–(4-50c) seem to be valid only for a Cartesian system (x, y) . However, they are also valid for flow along the curved wall shown in [Fig. 4-8](#), subject only to the requirement that the boundary-layer thickness δ be much smaller than the radius of curvature \mathcal{R} of the wall. The exact boundary-layer equations in such a curvilinear coordinate system are given by Tollmien (1931). After suitable order-of-magnitude assumptions, we find that the main difference between the curvilinear and the Cartesian equations lies in the pressure gradient normal to the wall, which is no longer negligibly small for a curved body:

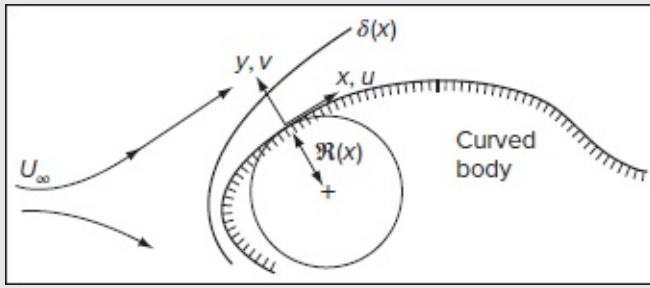


FIGURE 4-8

Boundary-layer flow over a curved body shape.

$$\frac{\partial p}{\partial y} \approx \frac{\rho}{\Re} u^2 \quad (4-5)$$

The gradient is of $O(1)$. But when integrated from $y = 0$ to $y = \delta$ assuming, say, a linear distribution $u = Uy/\delta$, we obtain

$$\frac{p(\delta) - p(0)}{\rho U^2} \approx \frac{\delta}{3\Re} \quad \text{or} \quad \Delta p^* \approx \frac{\delta}{3\Re} \quad (4-5)$$

which is negligibly small if $\delta \ll \Re$. Therefore, Eqs. (4-50a)–(4-50c) will continue to hold for curved-wall flows as long as the boundary-layer thickness remains small compared to the wall radius of curvature. This would not be true at a sharp corner, but sharp corners involve immediate flow separation and are thus to be avoided.

4-2.2 General Remarks on Flow Separation

Before we attempt actual solutions, we can spot flow-separation effects from the boundary layer equations themselves. If we apply the momentum equation at the wall, where $u = v = 0$, we find that

$$\left(\frac{\partial^2 u}{\partial y^2} \right)_{y=0} = \frac{1}{\mu} \frac{dp}{dx} \quad (4-5)$$

As such, the wall curvature has the sign of the pressure gradient, whereas further out the profile must have *negative* curvature when it merges with the freestream. Profile curvature is an indicator of possible boundary-layer *separation*. Three examples are shown in [Fig. 4-9](#). Note that for negative (favorable) pressure gradient, the curvature is negative throughout, and no flow separation can occur. For zero gradient, e.g., flat-plate flow, the curvature is zero at the wall and negative further out; there is no separation. For positive (adverse) gradient, the curvature changes sign and the profile is S-shaped. The increasing downstream pressure slows down the wall flow and can make it stop and reverse direction, thus marking the onset of flow separation.

of flow separation.

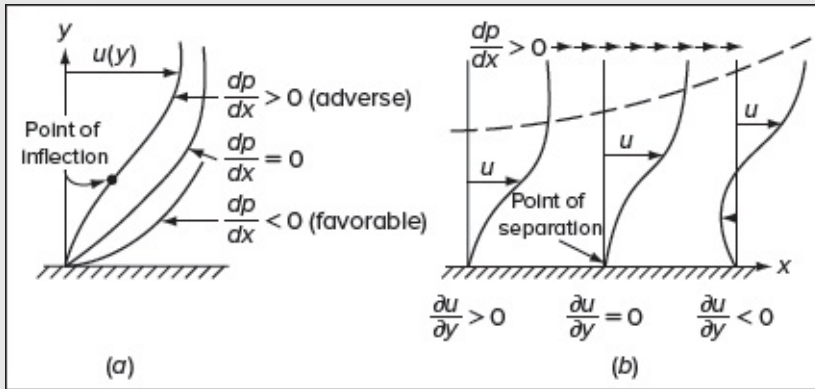


FIGURE 4-9

Geometric effects due to pressure gradient: (a) types of profile; (b) persistent adverse gradient.

[Figure 4-9b](#) illustrates the separation process. A persistently adverse gradient $\frac{dp}{dx} > 0$ makes the profile more and more S-shaped, thus reducing the wall shear to zero (at separation point) and then causing backflow, while the boundary layer becomes much thicker. Laminar flows have weak resistance to adverse gradients and separate easily. Turbulent boundary layers can resist separation longer—at the expense of increased wall friction and heat transfer. Page 167

4-2.3 Shear Stress in a Boundary Layer

After solving the boundary-layer equations, the shear stress is perhaps one of the few quantities that can be readily evaluated. In a two-dimensional setting, the stress is given by

$$\tau = \mu \left(\frac{\partial u}{\partial y} + \frac{\partial v}{\partial x} \right)$$

However, a scaling analysis shows that the term $\partial v / \partial x$ remains two orders smaller than $\partial u / \partial y$. It is, therefore, permitted in boundary-layer calculations to approximate the local shear stress using

$$\tau \approx \mu \frac{\partial u}{\partial y} \quad \text{and} \quad \tau_w \approx \mu \left(\frac{\partial u}{\partial y} \right)_{y=0} \quad (4-5)$$

Subsequently, the skin friction drag can be obtained by integrating τ_w over the wet surface area. Equation (4-55) also confirms that the point of separation in [Fig. 4-9b](#) corresponds to the point of zero shear stress, i.e., the point where τ_w switches sign.

4-3 SIMILARITY SOLUTIONS FOR STEADY TWO-DIMENSIONAL FLOW

If we neglect buoyancy effects in Eqs. (4-50a)–(4-50c), the velocity becomes uncoupled from the temperature, and this enables us to confine our attention to the momentum and continuity equations only. For steady flow, we settle on

$$\frac{\partial u}{\partial x} + \frac{\partial v}{\partial y} = 0 \quad (4-56)$$

$$u \frac{\partial u}{\partial x} + v \frac{\partial u}{\partial y} = U \frac{dU}{dx} + \nu \frac{\partial^2 u}{\partial y^2} \quad (4-56)$$

which are subject to $u(x, 0) = v(x, 0) = 0$ $u(x, \infty) = U(x)$

This is a system of partial differential equations of the parabolic type that can be solved using finite-difference techniques by marching downstream in the x direction. However, before pursuing this avenue in Sec. 4-5, let us explore the possibility of reducing these equations to *ordinary* differential equations using similarity transformations. One of our earlier similarity solutions for the full Navier–Stokes equations, discussed in Sec. 3-8, is the stagnation flow formulation, which happens to be of the boundary-layer type. In fact, there are several books that are entirely devoted to similarity techniques, such as those by Hansen (1964) and Sachdev (2000). In what follows, three similar, *shape-preserving* boundary layers will be discussed: the Blasius flat plate, the Falkner–Skan family of wedge motions, and the converging channel (sink) flow. In each case the two-dimensional equations of continuity and momentum will be reduced to a single ordinary differential equation that can be solved numerically and, at times, asymptotically.

4-3.1 The Blasius Solution for Flat-Plate Flow

Ludwig Prandtl's first student, Heinrich Blasius (1908), discovered a foundational solution for laminar-boundary-layer motion over a flat plate, which is graphically outlined in [Fig. 4-4](#). If the displacement thickness is small ($Re \gg 1$), then $U = \text{const}$ and $dU/dx = 0$ in Eq. (4-56). This can occur at zero angle of incidence in the absence of an outer pressure gradient. Here, we have a leading edge, $(x, y) = (0, 0)$, but no characteristic length “ L .” For self-preserving motion, the local velocity profiles must all have the same dimensionless shape, $u/U = f(y/\delta)$. Furthermore, based on [Eq. \(4-14\)](#) and our integral analysis, we expect $\delta/x = a/\sqrt{Re_x}$ or $\delta = a\sqrt{\nu x/U}$ ([Table 4-1](#)). We are, therefore, justified in introducing a *similarity* variable of the form y/δ , namely,

$$\eta = y \sqrt{\frac{U}{2\nu x}} \quad (4-57)$$

Note that the factor “2” is added for convenience, simply because it produces a different

equation with unitary coefficients.

An independent justification for using this similarity variable can be based on dimensional analysis: we can count two primary dimensions, [L] and [t], within the free boundary-layer parameters, $\delta = F(U, x, \nu)$. Then using (x, ν) as the so-called *repeating parameters* in conjunction with the Buckingham Pi theorem, the number of functional dependencies can be reduced by two, namely, by writing $\delta/x = F(\Pi)$, where $\Pi = Ux\nu^{-1} = Re_x^{-1/2}$. This form becomes identical to [Eq. \(4-57\)](#) when we take $F(Re_x) = CRe_x^{-1/2}$ and $\delta = C\sqrt{\nu x/U}$ or $\eta = y\sqrt{U/(2\nu x)}$ with $C = \sqrt{2}$.

Along similar lines, since no flow can cross a streamline, the spatial variation of the stream function $\psi = \int u dy|_{x=\text{const}}$ will increase with $\delta(x)$ and, as such, with $x^{1/2}$. Assuming a product solution of the form $\psi(x, \eta) = g(x)f(\eta)$, a suitable nondimensional form corresponds to $g(x) = \sqrt{2\nu Ux}$. We, therefore, have

$$\psi = \sqrt{2\nu Ux} f(\eta) \quad (4-58)$$

Here, f is a characteristic stream function that is yet to be determined and, as before, the factor “2” is used for convenience. From the definition of the stream function, we now have

$$u = \frac{\partial \psi}{\partial y} = U f'(\eta) \quad \text{and} \quad v = -\frac{\partial \psi}{\partial x} = \sqrt{\frac{\nu U}{2x}} (\eta f' - f) = \frac{U}{\sqrt{2Re_x}} (\eta f' - f) \quad (4-59)$$

where primes denote differentiation with respect to η —not to be confused with the previous variable $\xi = y/\delta$, or velocity function $F(\xi) = u/U = f'$. We may immediately confirm that u is order U while v is of smaller order, namely, $U/\sqrt{Re_x}$. We may equally verify that [Eqs. \(4-58\)](#) satisfy the continuity relation (4-56a) identically. We are left with the momentum relation (4-56b) where the substitutions of u and v from [Eqs. \(4-59\)](#) yield, after some algebra, a third-order differential equation:

$$f''' + ff'' = 0 \quad (4-60)$$

The attendant effort requires the use of several partial derivatives viz.

$$\frac{\partial \eta}{\partial x} = -\frac{\eta}{2x}, \quad \frac{\partial \eta}{\partial y} = \sqrt{\frac{U}{2\nu x}}, \quad \frac{\partial u}{\partial x} = -\frac{\eta}{2x} U f'', \quad \frac{\partial u}{\partial y} = U f'' \sqrt{\frac{U}{2\nu x}}, \quad \text{and} \quad \frac{\partial^2 u}{\partial y^2} = \frac{U^2}{2\nu x} f'''$$

As for the boundary conditions, the velocity adherence at the wall, $u(x, 0) = v(x, 0) = 0$, and the freestream-merge condition, $u(x, \infty) = U$, can be readily converted through [Eqs. \(4-58\)](#) and [\(4-59\)](#) into

$$f'(0) = f(0) = 0 \quad \text{and} \quad f'(\infty) = 1 \quad (4-61)$$

Equation (4-60) represents the illustrious *Blasius equation* for flat-plate flow. Note the strong resemblance to the nonlinear stagnation-flow relation given by Hiemenz (1911), i.e. $F''' + FF'' + 1 - F'^2 = 0$ with $F(0) = F'(0) = 0$ and $F'(\infty) = 1$ [Eq. (3-206)]. The latter contains extra terms that account for the presence of a pressure gradient.

So far, the Blasius equation has only yielded exact analytic solutions that are cast in the form of infinite series. Examples include the homotopy analysis method (HAM) series Liao (1997, 1999a, 1999b), and the Adomian decomposition of an exponentially transformed Blasius variable by Ebaid and Al-Armani (2013). Blasius himself (1908) provides asymptotic approximations for small and large η in the form of matching inner and outer series solutions. However, his power series exhibits a finite radius of convergence corresponding to $0 \leq \eta < 4.0234644935$, beyond which the solution diverges. The Blasius expansion also requires knowledge of the initial slope (of the axial velocity with respect to η), $f'(0) = \sigma$, which is also termed “*connection parameter*” or “*Blasius constant*.” Several other methods of attack are chronicled in the text by Rosenhead (1963). One method that leads to a general boundary layer technique, now outdated, is outlined in the text by Meksyn (1961).

From a historical perspective, one may find countless studies that have been advanced to better understand the asymptotic behavior of the Blasius solution since 1908. Some of these have devoted themselves to its existence and uniqueness characteristics [e.g., Weyl (1947), Callegari and Friedman (1968), Callegari and Nachman (1978), Fang et al. (2000), including its tri-pole singularity inside its semi-infinite domain [Punnis (1956a, 1956b), Boyd (1999)]. Others have attempted to overcome its singularity using Padé approximations [Boyd (1997), Ahmad and Al-Barakati (2007), Peker et al. (2011)] or Crocco variables [Callegari and Friedman (1968), Callegari and Nachman (1978), Wang (2004)], specifically, adopting a pair of coordinates, $u = f'(\eta)$ and $\tau(u) = f''(\eta)$, which transform Eq. (4-60) into a singular, second-order differential equation of the form:

$$\frac{d^2\tau}{du^2} + \frac{u}{\tau} = 0; \quad 0 \leq u < 1 \quad \text{with} \quad \left. \frac{d\tau}{du} \right|_{u=0} = 0 \quad \text{and} \quad \tau|_{u=1} = 0 \quad (4-61)$$

Coincidentally, the Crocco variable u corresponds to the axial speed normalized by the freestream velocity U while the dependent variable τ represents a normalized form of the shear stress. The first condition stems from $f'''(0) = 0$ and the absence of a pressure gradient in the far field. Physically, it can be attributed to the linearity (and thus constant slope) of the velocity profile directly above the wall. The second condition can be connected to the vanishing shear force in the far field, where $u = 1$. Clearly, Crocco’s transformation is useful in reducing the order of the Blasius equation while relocating the singularity to the outer edge of the domain, where $u = 1$ and $\tau = 0$, thus making it easier to handle.

Algebraically, the efforts to solve the Blasius equation have led to vastly dissimilar expressions that extend from simple, piecewise approximations valid up to the edge of the boundary layer, i.e., $0 \leq \eta \leq \eta_\delta$, where $\eta_\delta = \delta_{99\%} \sqrt{U/(2\nu x)}$, such as those introduced by Pohlhausen (1921) and Schlichting (1955), to infinite HAM series, such as those conceived by Liao (2010), that remain valid over the entire range of $0 \leq \eta < \infty$. They have also given rise to a plethora of analytic approximations, such as those devised by Bairstow (1921), Parlange et al. (1981), Boyd (2008), Iacono and Boyd (2015), Majdalani and Xuan (2021) and many others. In fact, impressive collections of methods have been applied to the treatment of the Blasius equation, including, but not limited to:

1. perturbation expansions [Blasius (1908), Goldstein (1930), Piercy and Preston (1933), Bender et al. (1989), Van Oudheusden (1997)];
2. Taylor series [Blasius (1908), Bairstow (1925), Parlange et al. (1981), Roman-Miller and Broadbridge (2000) with the Picard iteration method, Asaithambi (2005), Abbasbandy and Bervillier (2011)], and its related differential transformation method (DTM) with domain splitting [Yu and Chen (1998), Kuo (2003, 2004, 2005), Peker et al. (2011) including series convergence via Euler-accelerated power series or Padé approximant [Boyd (1999)];
3. homotopy analysis method (HAM) [Liao (1997, 1999a, 1999b, 2010), Allan and Syam (2005), Alizadeh-Pahlavan and Borjani-Boroujeni (2008), Zhang and Chen (2009), Zhang et al. (2013)], Adomian decomposition (ADM) [Wazwaz (2001, 2006), Wang (2006), Hashim (2006), Abbasbandy (2007), Tsai and Chen (2011), Ebaid and Al-Armani (2013), Aghakhani et al. (2015)] often mixed with homotopy or iteration perturbation methods (HPM/IPM) [He (1998, 1999a, 1999b, 2000, 2003), Esmaeilpour and Ghasemi (2007)], variational (or parameter) iteration methods (VIM) [He (1998, 1999b, 2000), Lin (1999), Wazwaz (2007)], fixed point method (FPM) integration [Xu and Guo (2011), Xu et al. (2014)], or iterative integration with Padé approximants, conformal, or Padé-Hankel mapping [Ahmad and Al-Barakati (2009), Abbasbandy and Bervillier (2011), Iacono and Boyd (2015)];
4. approximations based on intuitive basis functions in the form of logarithm, exponentials, hyperbolic cosines, hyperbolic tangents, and so on [Yun (2010, 2011), Savaş (2012), Ebaid and Al-Armani (2013), Majdalani and Xuan (2020)]; then jointly in parallel to these analyses, numerical treatment of the Blasius equation has been carried out quite effectively using pseudo-spectral techniques that are based on:
5. Chebyshev, Fourier, Gauss-Laguerre, Gegenbauer, Laguerre, Legendre, or Sinc collocation functions [Squire (1959), Boyd (1982, 1987, 2007, 2008), Khabibrakhmanov and Summers (1998), Boyd et al. (2003), Tajvidi et al. (2008), Parand and Taghavi (2009), Parand et al. (2009, 2010, 2013)], etc.

With the availability of personal computers, it is now a simple matter to program [Eqs. \(4-60\)](#) and [\(4-61\)](#) using, for example, a Runge–Kutta subroutine. Letting $f'' = Y_1$, $f' = Y_2$, and $f = Y_3$, then the proper relations become

$$F(1) = -Y(1)*Y(3) \quad F(2) = Y(1) \quad F(3) = Y(2) \quad (4-62)$$

The problem becomes that of determining the correct initial guess for $f''(0) = Y_1(\eta = 0)$ that will make $f' = Y_2 \rightarrow 1$ as $\eta \rightarrow \infty$. Practically, we find that “infinity” is approached at $\eta_\infty \approx 10$. One can compute a few solutions for several guesses of $f''(0)$ and then interpolate to find the key value of $f''(0)$ that will make $f'(\infty) \approx Y_2(10.0) \approx 1.0$. The accepted slope, correct to eight significant digits (see [Table 4-1](#)), is

$$\sigma = f''(0) = 0.46959999^\ddagger \quad \text{using} \quad \eta = y\sqrt{U/(2\nu x)} \quad (4-63)$$

Note that several studies have been devoted to the determination of the Blasius constant with increasing levels of success. For example, Bairstow (1925) and Goldstein (1930) report 0.474 and 0.470, while Falkner (1936) and Howarth (1938) obtained 0.470334 and 0.46960. With the advent of modern computers, Fazio (1992) and Boyd (1999) arrived at 12 and 15 digits of accuracy with their 0.469599988361013304509 value. The record for most significant digits is presently held by Varin (2014, 2018): he manages to secure 30 and then 100 digits (or more) while expressing $f''(0)$ in the form of a convergent series of rational numbers to arbitrary order. A sufficiently resolved numerical solution of the Blasius equation is provided in [Table 4-3](#) using the continuous Taylor series method. Based on this data, several important parameters can be computed with sufficient accuracy in all digits displayed.

TABLE 4-3

Highly resolved numerical solution of the Blasius equation for flow over a flat plate, [Eq. \(4-60\)](#)

η	$\eta/\eta_{99\%}$	$f(\eta)$	$f'(\eta)$	$f''(\eta)$	$f'''(\eta)$
0.0	0.00000	0.00000	0.00000	0.46960	0.00000
0.0	0.05761	0.00939	0.09391	0.46931	-0.00441
0.4	0.11521	0.03755	0.18761	0.46725	-0.01755
0.6	0.17282	0.08439	0.28058	0.46173	-0.03896
0.8	0.23042	0.14967	0.37196	0.45119	-0.06753
1.0	0.28803	0.23299	0.46063	0.43438	-0.10121
1.2	0.34563	0.33366	0.54525	0.41057	-0.13699
1.4	0.40324	0.45072	0.62439	0.37969	-0.17114
1.6	0.46084	0.58296	0.69670	0.34249	-0.19966
1.8	0.51845	0.72887	0.76106	0.30045	-0.21899
2.0	0.57606	0.88680	0.81669	0.25567	-0.22673
2.2	0.63366	1.05495	0.86330	0.21058	-0.22215
2.4	0.69127	1.23153	0.90107	0.16756	-0.20636
2.6	0.74887	1.41482	0.93060	0.12861	-0.18196
2.8	0.80648	1.60328	0.95288	0.09511	-0.15249
3.0	0.86408	1.79557	0.96905	0.06771	-0.12158
3.2	0.92169	1.99058	0.98036	0.04637	-0.09230
3.3	0.95049	2.08883	0.98456	0.03781	-0.07899
3.4	0.97929	2.18747	0.98797	0.03054	-0.06679
3.47 [†]	1.00000	2.25856	0.99000	0.02603	-0.05878
3.5	1.00810	2.28641	0.99071	0.02441	-0.05582
3.6	1.03690	2.38559	0.99289	0.01933	-0.04611
3.8	1.09451	2.58450	0.99594	0.01176	-0.03039
4.0	1.15211	2.78389	0.99777	0.00687	-0.01914
4.2	1.20972	2.98356	0.99882	0.00386	-0.01152
4.4	1.26732	3.18338	0.99940	0.00208	-0.00663
4.6	1.32493	3.38330	0.99970	0.00108	-0.00366
4.8	1.38253	3.58325	0.99986	0.00054	-0.00193
5.0	1.44014	3.78323	0.99994	0.00026	-0.00098
5.2	1.49774	3.98323	0.99997	0.00012	-0.00047
5.4	1.55535	4.18322	0.99999	0.00005	-0.00022
5.6	1.61296	4.38322	1.00000	0.00002	-0.00010
5.8	1.67056	4.58322	1.00000	0.00001	-0.00004
6.0	1.72817	4.78322	1.00000	0.00000	-0.00002

[†]Actual value to 16 significant digits: $\eta_\delta = 3.471886880405967$.

Interestingly, the first numerical solutions of the Blasius equation were generated manually by Töpfer (1912) and, more precisely, by Howarth (1938), and then Cortell (2001). Taking advantage of *scaled symmetry*, the problem was cleverly converted to the solution of two initial value problems that could be solved directly, with no need for shooting or iteration [cf. Töpfer (1912), Weyl (1942), Parlange et al. (1981), Fazio (1992), Yu and Chen (1993), Cortell (2005), Boyd (2008), and Fazio (2019)]. Accordingly, the Blasius equation was converted into a pair of initial value problems that are specified in terms of $F(t)$ and $f'(\eta)$, where $t = \sigma^{1/3} \eta$ and $f(\eta) = \sigma^{1/3} F(t)$. Then using $f' = \sigma^{2/3} \dot{F}$, $f'' = \sigma \ddot{F}$, and $f''' = \sigma^{4/3} \ddot{\ddot{F}}$, the final problem becomes

$$\ddot{\ddot{F}} + F\ddot{F} = 0 \quad \text{with} \quad F(0) = \dot{F}(0) = 0, \quad \ddot{F}(0) = \sigma^{-1}f''(0) = 1 \quad (\text{since } f''(0) = \sigma) \quad (4-6)$$

This enables us to determine $F(t)$ directly (without knowing σ), including its far-field value $\dot{F}(\infty)$, which happens to be $\sigma^{-2/3}\dot{F}'(\infty) = \sigma^{-2/3}$. With $\dot{F}(\infty)$ in hand, we can retrieve the Blasius constant, $\sigma = [\dot{F}(\infty)]^{-3/2}$, very precisely, and then proceed to solve for the Blasius function using

$$f''' + ff'' = 0 \quad \text{with} \quad f(0) = f'(0) = 0, \quad f''(0) = [\dot{F}(\infty)]^{-3/2} \quad (4-6)$$

[Figure 4-10a](#) describes the Blasius functions f (characteristic stream function), f' (axial velocity), and f'' (shear stress), while [Fig. 4-10b](#) compares the profile $f' = u/U$ with the experiments of Liepmann (1943). The agreement is excellent, and we may regard this first test of the boundary-layer approximation as a major success.

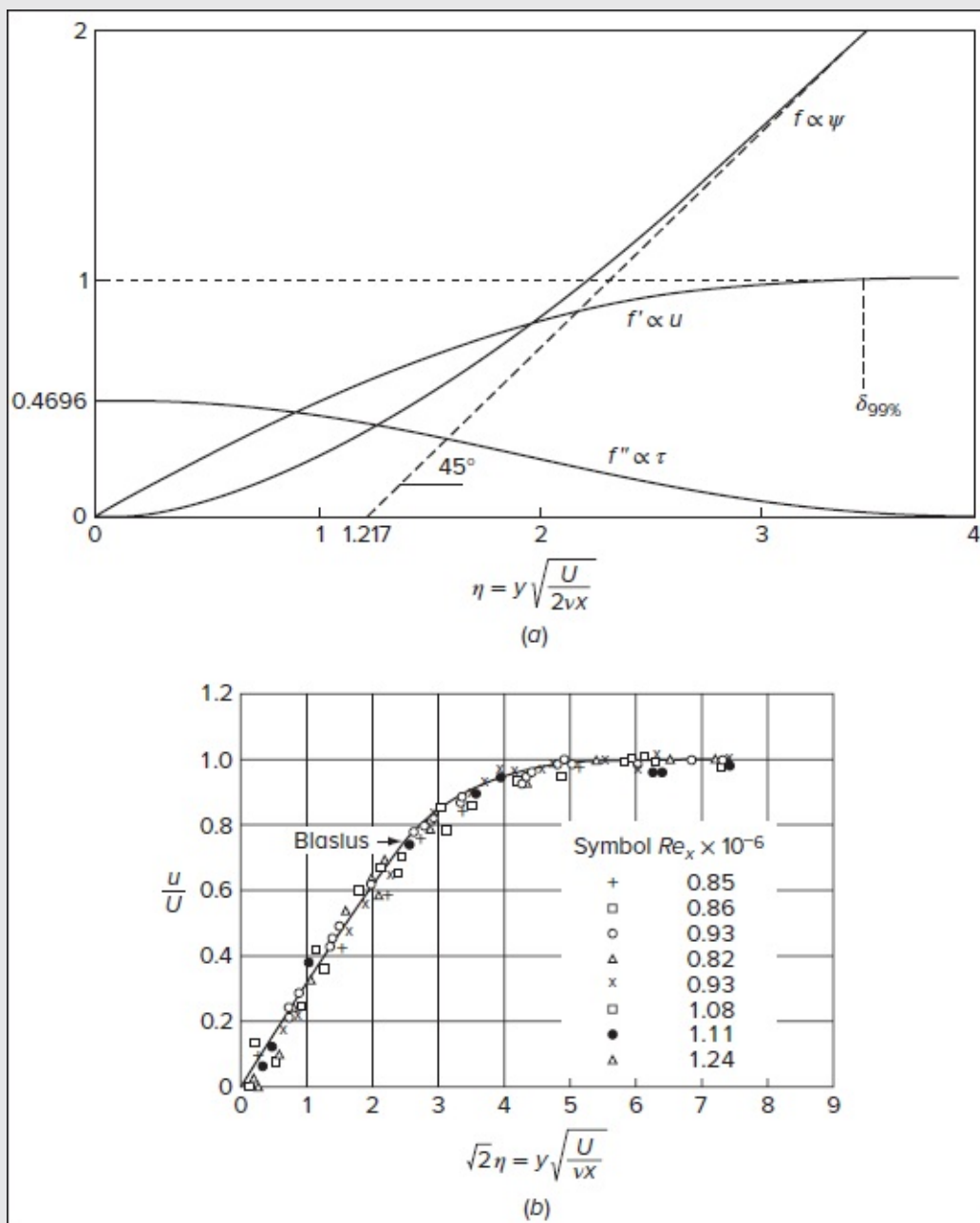


FIGURE 4-10

The Blasius solution for the flat-plate boundary layer: (a) numerical solution of [Eq. \(4-60\)](#); (b) comparison of $f' = u/U$ with experiments by Liepmann (1943).

Other properties follow from the table. We note that $f' = 0.99$ at $\eta_\delta \approx 3.47188688$. This value enables us to deduce the 99 percent boundary-layer thickness using

$$\delta_{99\%} \equiv \delta \approx 3.47189 \sqrt{\frac{2\nu x}{U}} \quad \text{or} \quad a \equiv \frac{\delta}{x} \sqrt{Re_x} \approx 4.90998951 \quad (4-6)$$

where $a = \sqrt{2}\eta_\delta \approx 4.91$ is 1.8 percent lower than the traditional value of “5” computed manually and reported in most textbooks. The displacement and momentum thicknesses are related to integrals of f' through their definitions from [Eqs. \(4-4\)](#) and [\(4-6\)](#). One gets

$$\delta^* \sqrt{\frac{U}{2\nu x}} = \int_0^\infty (1 - f') d\eta = \lim_{\eta \rightarrow \infty} (\eta - f) \approx 1.21678062 \quad \text{or} \quad c \equiv \frac{\delta^*}{x} \sqrt{Re_x} \approx 1.72078766 \quad (4-6)$$

The numerical value 1.217 is shown in [Fig. 4-10a](#) to be the η intercept of a 45° line, which is asymptotic to the curve $f(\eta)$ at large η . Since f is proportional to the stream function, the dashed 45° line represents an inviscid stream function displaced by a dimensionless amount 1.217 away from the plate. Similarly, we can calculate

$$f''(0) = \theta \sqrt{\frac{U}{2\nu x}} = \int_0^\infty f'(1 - f') d\eta \approx 0.469599988 \quad \text{or} \quad d \equiv \frac{\theta}{x} \sqrt{Re_x} \approx 0.664114672 \quad (4-6)$$

We can also calculate the wall shear stress using

$$\tau_w = \mu \left. \frac{\partial u}{\partial y} \right|_w = \frac{\mu U f''(0)}{\sqrt{2\nu x}/U} \quad \text{or} \quad C_f = \frac{2\tau_w}{\rho U^2} = \frac{\theta}{x} \approx \frac{0.664}{\sqrt{Re_x}} \quad (4-7)$$

Finally, the integrated drag coefficient on a plate of length L is

$$C_D(L) = \frac{1}{L} \int_0^L C_f dx = 2C_f(L) \approx \frac{1.328}{\sqrt{Re_L}} \quad (4-7)$$

This last expression represents the drag on one side of the plate. Experimental values in the range $1 \leq Re_L \leq 2000$ are shown in [Fig. 4-11](#) and compared with [Eq. \(4-71\)](#) along with the Oseen relation [Eq. (3-281)] discussed in [Chap. 3](#). We see that the Blasius relation is accurate for $Re_L \leq 1000$, and the Oseen theory is valid for $Re_L \leq 1$.

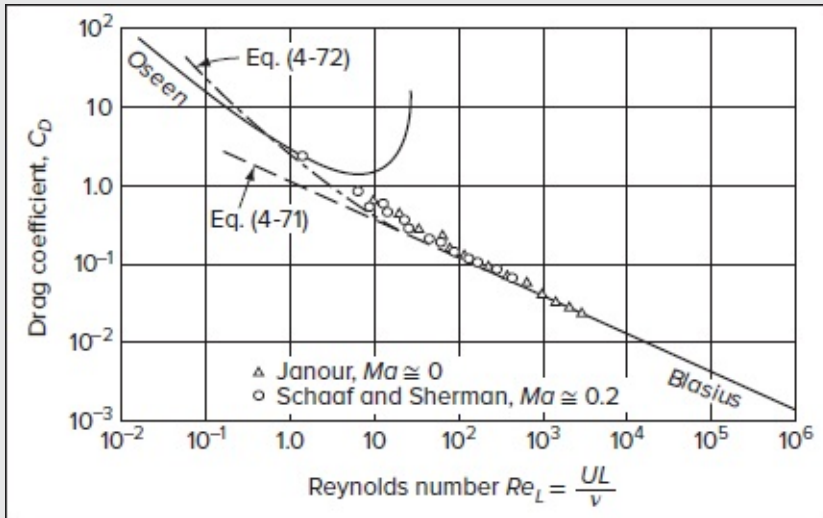


FIGURE 4-11

Theoretical and experimental drag of a flat plate.

The intermediate region $1 < Re_L < 1000$ has been the subject of many analytical and numerical studies. It may be fit reasonably well by the correction factor given in perturbation study by Imai (1957), specifically

$$C_D \approx \frac{1.328}{\sqrt{Re_L}} + \frac{2.3}{Re_L} \quad (4-7)$$

This relation is also plotted in [Fig. 4-11](#) and can be seen to fall slightly below the data.

Numerical solutions of the full Navier–Stokes equations for $0.1 < Re_L < 1000$ by Dennis and Dunwoody (1966) and by Brauer and Sucker (1976) confirm that the drag is higher than predicted by boundary-layer theory. [Figure 4-12](#) displays the computations of Dennis and Dunwoody (1966) for (a) the local friction coefficient and (b) the local surface pressure. For lower Reynolds numbers, there are appreciable effects at both the leading and trailing edges and so the boundary-layer approximation is not realized until $Re_L \leq 1000$.

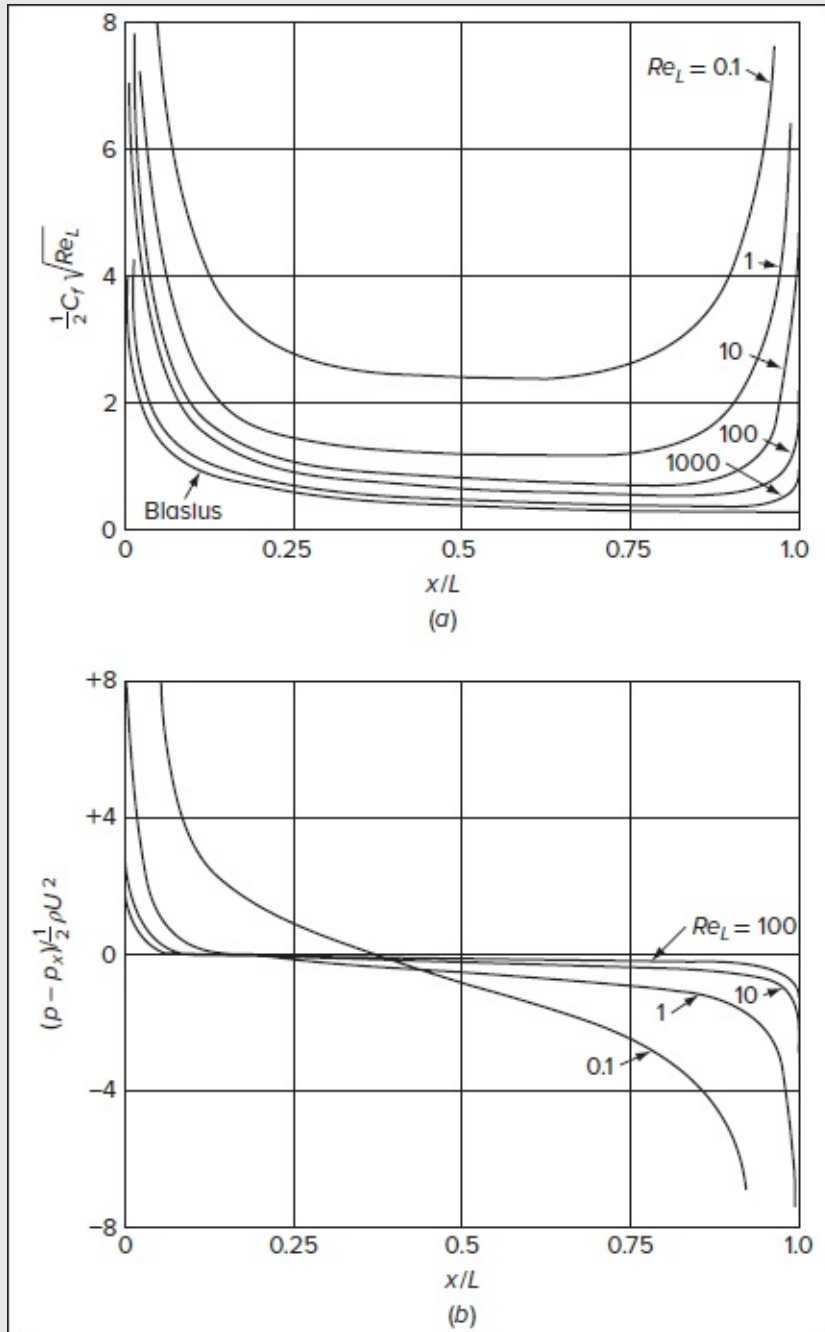


FIGURE 4-12

Numerical solution of the full Navier-Stokes equations for flat-plate flow at moderate Reynolds numbers: (a) local friction coefficient; (b) local surface pressure. [After Dennis and Dunwoody (1966).]

It is interesting that the normal velocity v is not zero at the edge of the boundary layer. Based on Eq. (4-59), one may compute, as $\eta \rightarrow \infty$,

$$\frac{v(x, \infty)}{U} = \frac{G_\infty}{\sqrt{Re_x}}; G_\infty \approx 0.86039383 \quad (4-7)$$

There is a slight upwelling of the flow because of displacement of the outer stream [Panton (1996, Sec. 20.7)].Page 173Page 174

Note that, if we were to stop at the edge of the 99% boundary layer, the normal velocity $a = \eta\delta$ is slightly lower, namely,

$$\frac{v(x, \delta)}{U} = \frac{G_\delta}{\sqrt{Re_x}}; G_\delta \approx 0.83339871$$

In fact, as shown by Majdalani and Xuan (2020), it is possible to show that for the Blasius solution, $G_\infty = a\alpha/2 = \frac{1}{2}\delta^* \sqrt{Re_x}$ and $G_\delta = \frac{1}{2}a[f'(\eta_\delta) - f'(\eta_\delta)/\eta_\delta]$. As for the piecewise analytical velocity profiles in Sec. 4-1.4, which are suddenly set equal to unity at $y = \delta$, we have

In addition to the piecewise profiles detailed in Sec. 4-1.4, several continuous velocity approximations have been developed with the goal of capturing the Blasius characteristics just described. Of those, four analytic solutions for $u/U = (df/d\eta)$ Blasius, which continue to hold past the 99 percent disturbance thickness, will be considered and compared. These have been obtained using insight into the Blasius solution, rationalization, curve-fitting conjecture, or a combination thereof:

Yun's hyperbolic tangent:

$$u/U = \tanh(\bar{s}\xi) \quad [\text{Yun (2010)}] \quad (4-7)$$

Moeini-Chamani's error function:

$$u/U = \text{erf}(1.59261\xi) \quad [\text{Moeini and Chamani (2017)}] \quad (4-7)$$

Savaş's hyperbolic tangent of fractional order:

$$u/U = [\tanh(\bar{s}\xi)^{5/3}]^{3/5} \quad [\text{Savaş (2012)}] \quad (4-7)$$

Majdalani–Xuan's decaying exponential:

$$u/U = 1 - \exp\left[-\bar{s}\xi\left(1 + \frac{1}{2}\bar{s}\xi + \xi^2\right)\right] \quad [\text{Majdalani and Xuan (2020)}] \quad (4-7)$$

where $\xi = y/\delta$ and $\bar{s} \approx 1.630398038629397$ is the Blasius constant. In the interest of clarity, the profiles are compared to the Blasius velocity function $(df/d\eta)$ in Fig. 4-13(a) for $0 \leq \xi \leq 1$ (i.e., $0 \leq \eta \leq 4.1663$), thus illustrating the degree by which they can imitate the true behavior both within the boundary layer and beyond, as $\xi \rightarrow \infty$. Graphically, it may be seen that the Majdalani–Xuan decaying exponential (dotted) is virtually indiscernible from the Blasius curve. This may be viewed as being significant, given the relative simplicity of this profile. This is followed by the Savaş hyperbolic tangent of fractional order, which can be barely distinguished from the Blasius line, even in the magnified inset of Fig. 4-13(b). Converse

Moeini-Chamani's error function and Yun's hyperbolic tangent are Page 175 shown to deviate progressively, especially in the upper $0.5 < \xi < 1$ portion of the viscous layer. In fact, a strong correlation may be seen to exist between the spatial agreement of a given flow approximation with the Blasius shape and its effectiveness at predicting the fundamental boundary-layer characteristics. This is confirmed in [Table 4-4](#), where boundary-layer predictions by the four continuous profiles are cataloged and contrasted to the computed Blasius values. As usual, the percentage error with respect to the Blasius benchmark, which accompanies each individual estimate, such as η^* , θ^* , H , $(\delta/x)\sqrt{Re_x}$, $C_f\sqrt{Re_x}$, and $(\delta^*/x)\sqrt{Re_x}$, is listed directly below it. For each profile, we also compute and display the overall L_2 error across the viscous domain, to accurately quantify the cumulative discrepancy accrued in each continuous profile. As before, only the essential properties are tabulated because other related quantities can be deduced fairly straightforwardly. Here too, $d = b = (\theta/x)\sqrt{Re_x} = C_f\sqrt{Re_x}$, and $C_D\sqrt{Re_L} = 2d$. As for the maximum normal velocity coefficient at infinity, $G_\infty = a\alpha/2$, it is simply half of the entries for $(\delta^*\sqrt{Re_x}/x)$ in [Table 4-4](#).

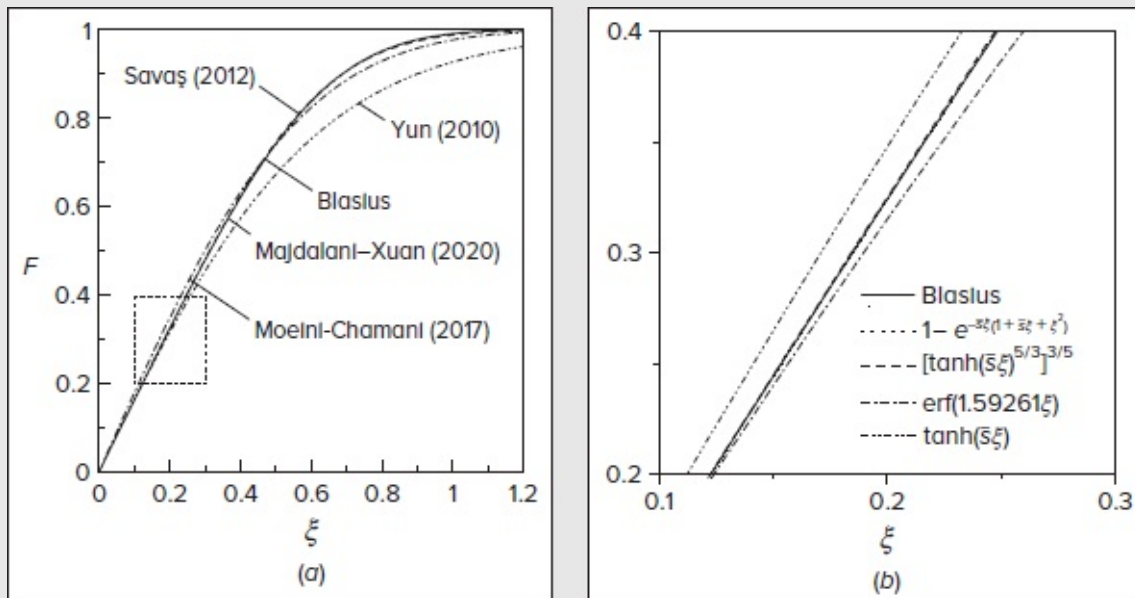


FIGURE 4-13

Comparison of four continuous approximations to the Blasius solution by Majdalani and Xuan (2020), Savaş (2012), Moeini and Chamani (2017), and Yun (2010). Results are shown (a) across the boundary-layer region into the far field, and (b) inside a designated quadrant where individual deviations from the Blasius curve are magnified $F'(0) = \sqrt{s} \approx 1.630$.

TABLE 4-4

Boundary-layer predictions from four continuous profiles with their errors relative to the computed Blasius values

$\frac{u}{U} = F(\xi) = \frac{df}{d\eta}$	$\eta^* = \frac{\delta^*}{\delta}$	$\theta^* = \frac{\theta}{\delta}$	$H = \frac{\delta^*}{\theta}$	$\frac{\delta}{x} \sqrt{Re_x}$	$C_f \sqrt{Re_x}$	$\frac{\delta^*}{x} \sqrt{Re_x}$	$\frac{v}{U} _{\delta} \sqrt{Re_x}$	$L_2 \text{ error}^\dagger$
$\tanh(\bar{s}\xi)$ Yun (2010)	0.425 21.30%	0.188 39.12%	2.259 12.81%	4.162 15.22%	0.783 17.95%	1.770 2.84%	0.805 3.45%	0.056
$\text{erf}(1.59261\xi)$ Moeini-Chamani (2017)	0.354 1.08%	0.147 8.49%	2.414 6.83%	4.494 0.80%	0.726 9.35%	1.753 1.89%	0.800 4.02%	0.016
$[\tanh(\bar{s}\xi^{5/3})]^{3/5}$ Savaş (2012)	0.351 0.12%	0.136 0.79%	2.574 0.67%	4.891 0.40%	0.667 0.40%	1.716 0.27%	0.824 1.07%	0.0020
$1 - \exp\left[-\bar{s}\xi\left(1 + \frac{1}{2}\bar{s}\xi + \xi^2\right)\right]$ Majdalani-Xuan (2020)	0.351 0.06%	0.136 0.25%	2.586 0.19%	4.904 0.12%	0.665 0.13%	1.720 0.06%	0.833 0.10%	0.00064
Blasius	0.35047	0.13526	2.59110	4.90999	0.66411	1.72079	0.83340	0

$$^\dagger L_2 = \sqrt{\int_0^1 (F - F_{\text{Blasius}})^2 d\xi}$$

Starting with the L_2 error, we compute 0.056 and 0.016 for the Yun and Moeini–Chamani profiles, respectively. These values are consistent with the level of spatial alignment between their shapes and the Blasius curve in [Fig. 4-13](#). They are also reflected by their relative variations in estimating the boundary-layer properties, which range from 2.84 to 39.12 percent in Yun’s case and from 0.8 to 9.35 percent in Moeini–Chamani’s. In hindsight, the levels are comparable to the effectiveness of the Pohlhausen polynomial profiles, with Moeini–Chamani’s results resembling those of Pohlhausen’s quadratic polynomial, $2\xi - \xi^2$ [Eq. (4-11)]. Conversely, the overall L_2 disparity falls to appreciably low levels of 2.0×10^{-4} and 6.4×10^{-4} for the Savaş and Majdalani–Xuan profiles, respectively. These appreciable orders of magnitude reductions may be viewed as being significant because the corresponding percentage errors in estimating the boundary-layer displacement, momentum and disturbance thicknesses, skin friction, and shape factor suddenly drop to virtually insignificant levels ranging from 0.12 to 0.79 percent for the Savaş profile and from 0.06 to 0.25 percent for the Majdalani–Xuan profile. These low levels can very well explain the reason why the Majdalani–Xuan exponential profile is graphically indiscernible from the Blasius solution in [Fig. 4-13](#). In fact, recalling that the Blasius equation itself is accompanied by a small truncation error that depends on the size of the flow Reynolds number, and given that the Blasius model is only valid in the laminar range, the Majdalani–Xuan exponential profile may be viewed as a simple, well-behaved, quasi-exact analytic solution to the Blasius equation in the $0 \leq \xi < \infty$ range. From an engineering perspective, however, the Majdalani–Xuan quartic polynomial, $(5\xi - 3\xi^3 + \xi^4)/3$, remains, to the authors’ knowledge, the simplest analytic profile that will readily produce accurate closed-form expressions for the boundary layer properties, albeit confined to the viscous region only. For the remaining class of continuous profiles, numerical evaluation is generally required to determine any of their integral properties.

As a final check of legitimacy of the continuous profiles, their ability to match the boundary conditions observed by the Blasius solution and its derivatives at the endpoints of the viscous domain is ascertained in [Table 4-5](#). Firstly, we are able to verify the negative $F''(1)$ curvature of all velocity profiles, consistently with the 0.709 Blasius value at the edge of the viscous

layer. Interestingly, the closest curvature corresponds to Yun's hyperbolic tangent, while the farthest stems from Savaş's hyperbolic tangent of fractional order. Secondly, we read from Table 4-4 that all models satisfy the no-slip and momentum balance requirements at the wall where $F(0) = F''(0) = 0$. Thirdly, both Majdalani–Xuan and Savaş profiles return $u/U = 99\%$ at $\xi = 1$, whereas Moeini–Chamani's and Yun's return 97.6 and 92.6 percent, respectively, at $\xi = 1.76$. As for the extraordinarily important velocity slope at the wall, all the formulations by Yun, Savaş, and Majdalani–Xuan restore the value of $F'(0) = \bar{s} \approx 1.630$. Finally, as far as matching the shear value (or velocity slope) at the edge of the viscous layer, here too, both Majdalani–Xuan and Savaş profiles predict, respectively, $F'(1) = 0.093$ and 0.0904 instead of 0.0904. These characteristic features help to explain, in part, the varying degrees of accuracy associated with each formulation, as reflected in their individual L_2 and relative errors in Table 4-4.

TABLE 4-5

Endpoint properties of the continuous analytic velocity profiles and their corresponding Blasius values

$\frac{u}{U} = F(\xi) = \frac{df}{d\eta}$	$F(0)$	$F'(0)$	$F''(0)$	$F(1)$	$F'(1)$	$F''(1)$
$\tanh(\bar{s}\xi)$	0	1.630	0	0.926	0.232	−0.701
$\text{erf}(1.59261\xi)$	0	1.797	0	0.976	0.142	−0.722
$[\tanh(\bar{s}\xi^{5/3})]^{3/5}$	0	1.630	0	0.987	0.097	−0.659
$1 - \exp[-\bar{s}\xi(1 + \frac{1}{2}\bar{s}\xi + \xi^2)]$	0	1.630	0	0.990	0.093	−0.729
Blasius (1908)	0	1.630	0	0.990	0.0904	−0.709

4-3.2 Flat-Plate Heat Transfer for Constant Wall Temperature

If T_w and T_e are constant, the temperature profiles also satisfy similarity relations. In analogy with the stagnation-flow relation, Eq. (3-222), we define a dimensionless temperature difference

$$\Theta(\eta) = \frac{T - T_e}{T_w - T_e} \quad (4-7)$$

Assuming that u and v are known from the Blasius solution, we may substitute Eq. (4-7) into the boundary-layer energy Eq. (4-50c), neglect dissipation, assuming $Ec \ll 1$, and write

$$\Theta'' + Pr f(\eta)\Theta' = 0 \quad \text{with} \quad \Theta(0) = 1 \quad \text{and} \quad \Theta(\infty) = 0 \quad (4-7)$$

The resulting expression is identical to the stagnation-flow relation, Eq. (3-223), with the boundary conditions reversed. The solution is, by analogy,

$$\Theta = \frac{\int_{\eta}^{\infty} \exp \left[-Pr \int_0^{\eta} f(s) ds \right] d\eta}{\int_0^{\infty} \exp \left[-Pr \int_0^{\eta} f(s) ds \right] d\eta} \quad (4-8)$$

The temperature profiles, first obtained by Pohlhausen (1921), can be computed from [Eq. \(80\)](#) and then displayed in [Fig. 4-14](#) for various Prandtl numbers. Since Pr is a ratio of visco to conduction effects, the higher the Prandtl number, the thinner the thermal boundary layer. The thermal to viscous thickness ratio may be approximated by

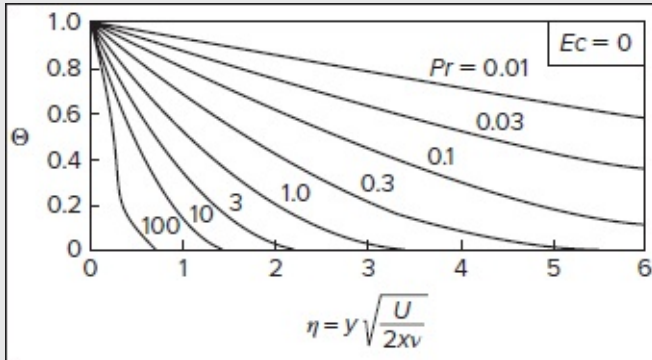


FIGURE 4-14

Flat-plate temperature profiles for zero dissipation.

$$\frac{\delta_T}{\delta} \approx Pr^{-0.4} \quad (4-8)$$

Page 177 Here, the heat transfer at the wall may be computed from Fourier's law:

$$q_w = -k \left. \frac{\partial T}{\partial y} \right|_{y=0} = -k(T_w - T_e) \Theta'(0) \sqrt{\frac{U}{2\nu x}}$$

or, in dimensionless form,

$$Nu_x = -\frac{\Theta'(0)}{\sqrt{2}} Re_x^{1/2} \quad (4-8)$$

As seen in [Fig. 4-14](#), the wall temperature slope $\Theta'(0)$ proves to be a strong function of the Prandtl number and, based on [Eq. \(4-78\)](#), may be given by

$$-\frac{1}{\Theta'(0)} = \int_0^{\infty} \exp \left[-Pr \int_0^{\eta} f(s) ds \right] d\eta \quad (4-8)$$

By direct analogy with the stagnation-flow relation (3-227), this parameter may be evaluated by adding two statements to the Blasius solver, specifically

$$F(4) = Y(3) \quad \text{and} \quad F(5) = \text{EXP}(-Pr \cdot Y(4))$$

The output $1/Y_5(\infty)$ is the desired wall slope $|\Theta'(0)|$. Some values of this thermal slope different Pr are tabulated below:

Pr	$-\Theta'(0)/\sqrt{2}$	Pr	$-\Theta'(0)/\sqrt{2}$
0.001	0.01732	10	0.72814
0.01	0.05159	100	1.5718
0.1	0.14003	1000	3.3871
1	0.33206	10,000	7.2974

For Prandtl numbers in the range $0.1 < Pr < 10,000$, a suitable curve fit to these tabulated values is $-\Theta'(0)/\sqrt{2} \approx 0.332Pr^{1/3}$. Consequently, [Eq. \(4-82\)](#) for low-speed laminar flat-plate heat transfer may be approximated as

$$Nu_x \approx 0.332Re_x^{1/2}Pr^{1/3} \quad (4-83)$$

This familiar expression has the same form as our energy integral based on an assumed polynomial profile, [Eq. \(4-34\)](#). It remains the accepted engineering approximation although overpredicts the Nusselt number for liquid metals with $Pr < 0.1$.

When dissipation is *not* neglected, the solution of the flat-plate energy equation becomes very interesting and leads to the concept of the recovery factor and the adiabatic-wall temperature. However, these concepts are realized in practice only by high-speed (compressible) boundary layers. As such, their discussion is deferred to [Chap. 7](#).

4-3.3 The Falkner–Skan Wedge Flows

The most famous family of boundary-layer similarity solutions was discovered by Falkner and Skan (1931) and later evaluated numerically by Hartree (1937). Rather than merely guessing the form of the solution as we did with the Blasius problem, it may be instructive to outline the steps leading to this similarity transformation.

To begin, we can eliminate v from the momentum equation by solving the continuity equation for v while taking into account the no-slip requirement of a vanishing velocity at the wall. Starting with $\partial v / \partial y = -\partial u / \partial x$, we may take advantage of the Leibniz rule,

$$\int_{a(x)}^{b(x)} \left[\frac{\partial}{\partial x} u(x, y) \right] dy = \frac{d}{dx} \int_{a(x)}^{b(x)} u(x, y) dy + u(x, a) \frac{da}{dx} - u(x, b) \frac{db}{dx}$$

and integrate in the vertical direction,

$$\int_0^v dv = - \int_0^y \frac{\partial u}{\partial x} dy = - \frac{\partial}{\partial x} \int_0^y u dy - u(x, y) \frac{dy}{dx} + u(x, 0) \frac{d(0)}{dx} \quad \text{or} \quad v = - \frac{\partial}{\partial x} \int_0^y u(x, y) dy \quad (4-84)$$

with the integration being carried out at constant x . The problem now reduces to a single

integrodifferential equation for u alone:

$$u \frac{\partial u}{\partial x} - \frac{\partial u}{\partial y} \left(\frac{\partial}{\partial x} \int_0^y u dy \right) = U \frac{dU}{dx} + \nu \frac{\partial^2 u}{\partial y^2} \quad (4-8)$$

Page 178 where the pressure gradient is replaced by the freestream velocity gradient using Euler's equation, $-dp/dx = \rho U dU/dx$. We now inquire: Is there any possibility of combining x and y into a single variable $\eta(x, y)$ such that the above equation becomes an ordinary differential equation in a function of η only? If so, we have achieved similarity, but only for certain special cases of the freestream velocity distribution $U(x)$. To make further headway, it is essential to generalize the Blasius solution by allowing it to accommodate a variable freestream velocity via

$$u(x, y) = U(x)f'(\eta) \quad (4-9)$$

where $\eta = \eta(x, y)$ is dimensionless. With careful chain-rule differentiation, we can substitute this expression into the momentum Eq. (4-86). For example, if $u = Uf'$, then

$$\frac{\partial u}{\partial x} = U'f' + Uf'' \frac{\partial \eta}{\partial x} \quad \text{and} \quad \frac{\partial u}{\partial y} = Uf'' \frac{\partial \eta}{\partial y} \quad (4-10)$$

and so on with the second derivatives. A particularly appealing linear form in y , which causes $\partial^2 \eta / \partial y^2$ to vanish, is:

$$\eta = yg(x) \quad (4-11)$$

In fact, one may substitute this variable into the momentum relation (4-86), evaluate the integral by parts (while availing oneself to Leibnitz' rule), and rearrange the outcome into:

$$f''' = ff'' \left(\frac{Ug'}{\nu g^3} \right) + (f'^2 - ff''' - 1) \left(\frac{dU/dx}{\nu g^2} \right) \quad (4-12)$$

Similarity is achieved if each of the two coefficients in this relation is such that occurrences of x disappear, thus leaving us only with constants. Based on Eq. (4-90), this implies that $(Ug'/g) \sim dU/dx$, or that $\ln(U)$ is proportional to $\ln(g)$, as in the case of $g(x) = Cx^a$.

Falkner and Skan (1931) found that similarity could be achieved by the variable $\eta = Cy$, which is consistent with a power-law freestream velocity distribution of the form:

$$U(x) = Kx^m; \quad m = 2a + 1 \quad (4-13)$$

The exponent m may be termed the Falkner–Skan *power-law parameter*. The constant C must make η dimensionless but is otherwise arbitrary. A good choice is to use $g(x) = Cx^a = \sqrt{(m+1)U(x)/(2\nu x)}$, with $U(x) = 2\nu C^2 x^{2a+1}/(m+1)$, thus leading to $C^2 = K(m+1)/(2\nu)$. The result is consistent with the limiting case of $m = 0$, which restores the Blasius variable

identically from [Eq. \(4-57\)](#). Accordingly, we have

$$\eta = y \sqrt{\frac{m+1}{2} \frac{U(x)}{\nu x}} \quad (4-9)$$

Substituting this similarity variable into [Eq. \(4-89\)](#) leads to the most common form of the Falkner–Skan equation:

$$f''' + ff'' + \beta(1 - f'^2) = 0; \quad \beta \equiv \frac{2m}{m+1} \quad (4-9)$$

with the same boundary conditions obtained for a flat plate,

$$f(0) = f'(0) = 0 \quad \text{and} \quad f'(\infty) = 1 \quad (4-9)$$

The parameter β is a measure of the pressure gradient dp/dx . If $\beta > 0$, the pressure gradient is negative or favorable, whereas $\beta < 0$ denotes an unfavorable pressure gradient. Naturally, $\beta = 0$ restores the “flat plate” configuration. At the onset, we expect the case of $m = -1$ ($\beta = \infty$) to be problematic, but it is not: It turns out that the case of $U = Kx^{-1}$ can be judiciously handled by a different choice of the constant C .

4-3.3.1 INVISCID FLOW PAST WEDGES AND CORNERS. The Falkner–Skan solution illustrates both favorable and adverse pressure gradients and is a realistic engineering flow pattern. The power-law freestream, $U = Kx^m$, happens to be the exact solution to inviscid flow past a wedge or corner shape. In plane polar coordinates, Laplace’s equation for the stream function $\psi(r, \theta)$, which corresponds to an irrotational motion (Appendix B4), can be written as

$$\frac{1}{r} \frac{\partial}{\partial r} \left(r \frac{\partial \psi}{\partial r} \right) + \frac{1}{r^2} \frac{\partial^2 \psi}{\partial \theta^2} = 0 \quad \text{where} \quad v_r = \frac{1}{r} \frac{\partial \psi}{\partial \theta} \quad \text{and} \quad v_\theta = -\frac{\partial \psi}{\partial r}$$

As shown in texts covering potential flow theory [e.g., White (2016)], an exact solution may be extracted in the form of

$$\psi(r, \theta) = Cr^{m+1} \sin[(m+1)\theta] \quad (4-9)$$

This expression yields certain radial streamlines that can be interpreted as the “walls” of a wedge or a corner, as shown in [Fig. 4-15](#), depending on the value of $\beta = 2m/(m+1)$. The velocity along these walls has the form $U = Kx_m$, which represents the freestream driving the boundary layer on the wall, with $x = 0$ at the tip of the wedge. The most prominent cases are:

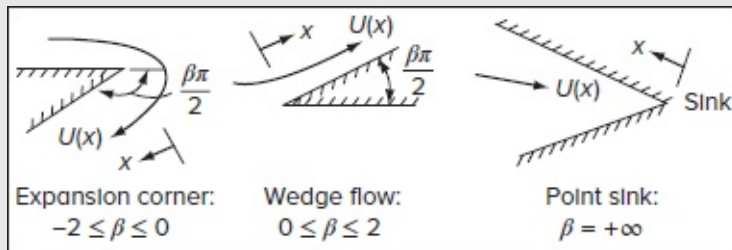


FIGURE 4-15

Some examples of Falkner–Skan potential flows.

$-2 \leq \beta \leq 0$, $-\frac{1}{2} \leq m \leq 0$: flow around an expansion corner of turning angle $\beta\pi/2$

$\beta = 0$, $m = 0$: the flat plate

$0 \leq \beta \leq +2$, $0 \leq m \leq \infty$: flow against a wedge of half-angle $\beta\pi/2$

$\beta = 1$, $m = 1$: the plane stagnation point (180° wedge)

$\beta = +4$, $m = -2$: doublet flow near a plane wall

$\beta = +5$, $m = -\frac{5}{3}$: doublet flow near a 90° corner

$\beta = +\infty$, $m = -1$: flow toward a point sink [i.e., the boundary-layer version of the Jeffery–Hamel flow in a convergent wedge (Sec. 3-8)].

These are *similar* flows, i.e., for a given β , the velocity profiles all look alike when scaled $U(x)$ and $\delta(x)$. They may also be used, with modest success, to predict the behavior of nonsimilar flows.

Equation (4-93) can be solved numerically simply by adding the term $\beta(1 - f'^2)$ to the relations of Eq. (4-63) for the Blasius equation. For example, one may use

$$F(1) = -Y(1)*Y(3) - \text{BETA}*(1. - Y(2)*Y(2)) \quad F(2) = Y(1) \quad F(3) = Y(2) \quad (4-9)$$

As before, we select β and try to find the proper value of f''_0 that makes $f'(\infty)$ asymptotically zero.

Although we could easily resolve Eq. (4-93) with our personal computers, the Falkner–Skan solutions have been well tabulated and charted [Evans (1968)]. The most important results in Fig. 4-16 span the range from the stagnation point ($\beta = m = 1$) down through flat plate flow ($\beta = m = 0$) to the separation point ($\beta = -0.19884$, $m = -0.09043$). Figure 4-1 shows the velocity profiles corresponding to $u/U = f'$, which grow thicker as β decreases. For $\beta < 0$, the profiles become S-shaped as in Fig. 4-9b before separating ($\tau_w = 0$) for $\beta = -0.19884$. Note that separation corresponds to an expansion angle in Fig. 4-15 of only 18° .

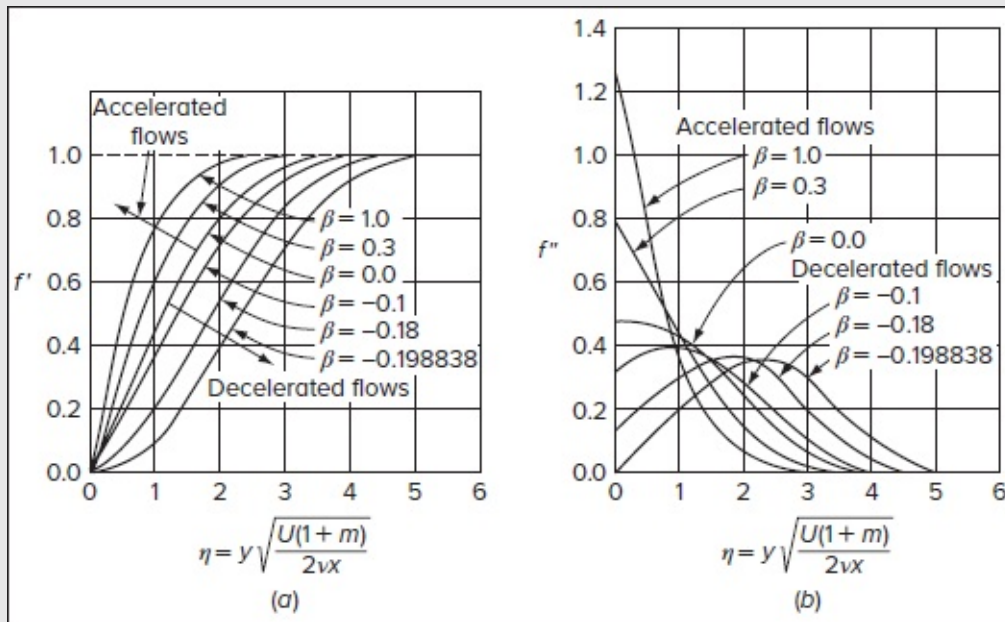


FIGURE 4-16

(a) Velocity profiles and (b) shear-stress profiles for the Falkner–Skan equation.

[Figure 4-16b](#) shows the shear-stress profiles $f''(\eta)$. Note that shear, in accelerated (favorable) flows, falls away from the wall value but instead rises from the wall for decelerated (adverse) flows. This is a consequence of the momentum equation condition $\partial\tau/\partial y|_{\text{wall}} = dp/dx$ and is true also in turbulent boundary layers. We note in passing that the solution for $\beta = \frac{1}{2}$, and $m = \frac{1}{3}$ corresponds to the axisymmetric stagnation flow from Sec. 8.1.3.

[Table 4-6](#) lists the values of $u/U = f'(\eta)$ for a variety of solutions. Also tabulated are the proper initial conditions $f''(0)$, in addition to the dimensionless displacement and momentum thicknesses:

TABLE 4-6

Numerical values of the streamwise velocity $f'(\eta)$ for Falkner–Skan similarity flows

β	-0.19884	-0.18	0.0	0.3	1.0	2.0	10.0
f_0''	0.0	0.12864	0.46960	0.77476	1.23259	1.68722	3.67523
η^*	2.35885	1.87157	1.21678	0.91099	0.64790	0.49743	0.24077
θ^*	0.58544	0.56771	0.46960	0.38574	0.29235	0.23079	0.11523
η							
0.0	0.0	0.0	0.0	0.0	0.0	0.0	0.0
0.1	0.00099	0.01376	0.04696	0.07597	0.11826	0.15876	0.31843
0.2	0.00398	0.02933	0.09391	0.14894	0.22661	0.29794	0.54730
0.3	0.00895	0.04668	0.14081	0.21886	0.32524	0.41854	0.70496
0.4	0.01591	0.06582	0.18761	0.28569	0.41446	0.52190	0.81043
0.5	0.02485	0.08673	0.23423	0.34938	0.49465	0.60964	0.87954
0.6	0.03578	0.10937	0.28058	0.40988	0.56628	0.68343	0.92414
0.7	0.04868	0.13373	0.32653	0.46713	0.62986	0.74496	0.95259
0.8	0.06355	0.15975	0.37196	0.52107	0.68594	0.79587	0.97057
0.9	0.08038	0.18737	0.41672	0.57167	0.73508	0.83767	0.98185
1.0	0.09913	0.21651	0.46063	0.61890	0.77787	0.87172	0.98888
1.2	0.14232	0.27899	0.54525	0.70322	0.84667	0.92142	0.99591
1.4	0.19274	0.34622	0.62439	0.77425	0.89681	0.95308	0.99856
1.6	0.24982	0.41691	0.69670	0.83254	0.93235	0.97269	0.99957
1.8	0.31271	0.48946	0.76106	0.87906	0.95683	0.98452	0.99998
2.0	0.38026	0.56205	0.81669	0.91509	0.97322	0.99146	0.99999
2.2	0.45097	0.63269	0.86330	0.94211	0.98385	0.99542	
2.4	0.52308	0.69942	0.90107	0.96173	0.99055	0.99761	
2.6	0.59460	0.76048	0.93060	0.97548	0.99463	0.99879	
2.8	0.66348	0.81449	0.95288	0.98480	0.99705	0.99940	
3.0	0.72776	0.86061	0.96905	0.99088	0.99842	0.99972	
3.2	0.78578	0.89853	0.98037	0.99471	0.99919	0.99987	
3.4	0.83635	0.92854	0.98797	0.99704	0.99959	0.99995	
3.6	0.87882	0.95138	0.99289	0.99840	0.99980	0.99998	
3.8	0.91315	0.96805	0.99594	0.99916	0.99991	0.99999	
4.0	0.93982	0.97975	0.99777	0.99958	0.99996		
4.5	0.97940	0.99449	0.99957	0.99994	0.99999		
5.0	0.99439	0.99997	0.99994	0.99999			

$$\eta^* = \int_0^\infty (1 - f') d\eta = (\eta - f)|_{\eta \rightarrow \infty} \quad \text{and} \quad \theta^* = \int_0^\infty f'(1 - f') d\eta = \frac{f_0'' - \beta \eta^*}{\beta + 1} \quad (4-9)$$

The ratio of these two, the shape factor H , will be especially useful in some approximate theories to be later discussed. In keeping with our constant reminders that the Navier–Stokes equations are nonunique, the boundary-layer equations also exhibit multiple solutions. Stewartson (1954) points out the following pathology of the Falkner–Skan equation for negative β :

1. For $-0.19884 \leq \beta \leq 0$, there are at least two solutions of [Eq. \(4-93\)](#) for any given β , one of which being the type shown in [Fig. 4-16a](#) and the second of which showing always backflow at the wall. The two solution types are identical at $\beta = -0.19884$ but are entirely different at $\beta = 0$.

2. For $\beta < -0.19884$, an infinity of solutions to [Eq. \(4-93\)](#) probably exists for any given value of the wall gradient f_0'' . For example, [Fig. 4-17b](#) shows a family of separating profiles with $f_0'' = 0$ computed by Libby and Liu (1967). For $\beta \approx -5.3$, -6.3 , et Stewartson (1954) has proved that all solutions in this range of β must display a velocity overshoot, that is, $f' > 1$ at some point in the boundary layer.

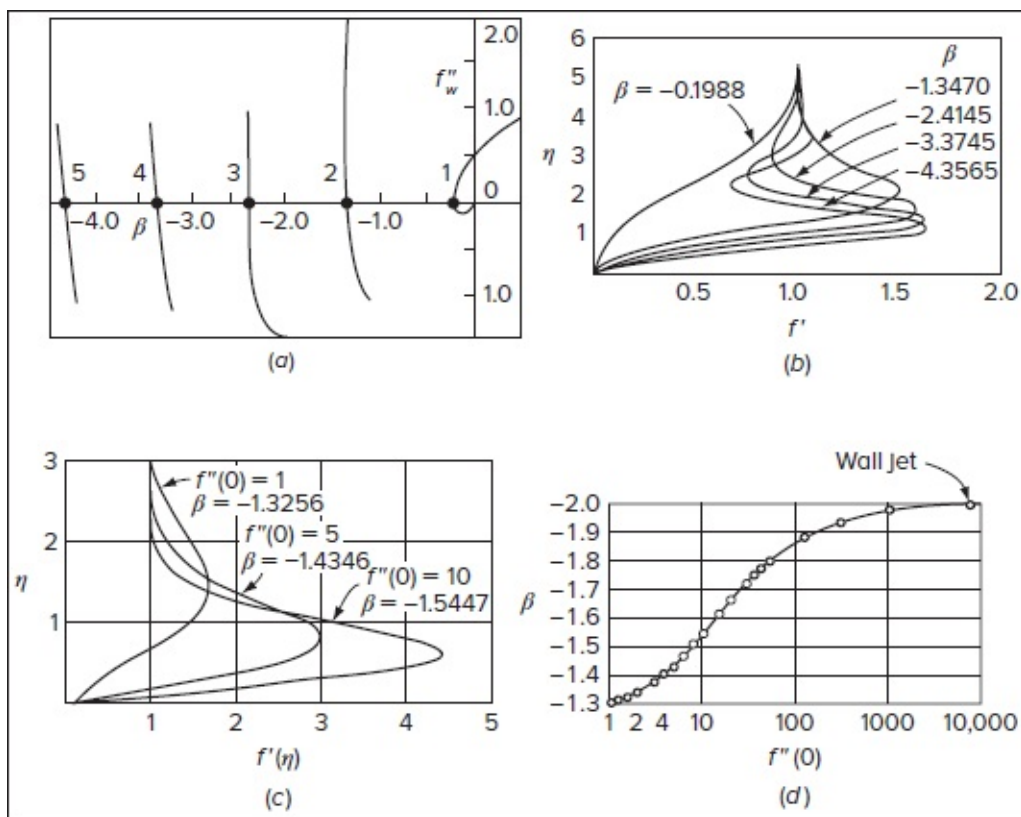


FIGURE 4-17

The multiplicity of Falkner–Skan solutions for negative β : (a) five branches of solutions for negative β , as found by Libby and Liu (1967); (b) five separating profiles corresponding to the five heavily marked intercepts in (a); (c) three overshoot profiles without backflow, calculated moving up along branch 2 [After Steinheuer (1968)]; (d) solution sets along upper branch 2 as calculated by Steinheuer (1968), showing asymptotic approach to the wall jet solution found by Glauert (1956).

The gist of these remarks is captured in [Fig. 4-17a](#), where a polar plot of β is rendered vs. f_0'' for the first five branches of solutions for negative β found by Libby and Liu (1967). [Figure 4-17c](#) illustrates some profiles for $f_0'' > 0$ along branch 2 as computed by Steinheuer (1968); these, like the separating profiles, contain an overshoot but no backflow. Libby and Liu (1967) liken these profiles to streamwise blowing into a moving stream as in the case of a wall jet. Indeed, as $f''(0)$ becomes very large along branch 2 of [Fig. 4-17a](#), β approaches 22.0 and, as pointed out by Steinheuer (1968), the velocity profile becomes identical to the pure

laminar-wall-jet solution found by Glauert (1956). This effect is shown in [Figs. 4-17c](#) and [d](#).

4-3.4 Heat Transfer for the Falkner–Skan Flows

If we neglect dissipation and assume constant wall and stream temperature, the flat-plate analysis of Sec. 4-3.2 holds in exactly the same form:

$$\Theta'' + Pr f(\eta, \beta) \Theta' = 0 \quad (4-98)$$

where $\Theta = (T - T_e)/(T_w - T_e)$ as before. Here $f(\eta, \beta)$ is the Falkner–Skan stream function—the output Y_3 from [Eq. \(4-96\)](#)—defined as

$$\psi(x, y) = \sqrt{\frac{2\nu x U(x)}{m+1}} f(\eta) \quad (4-99)$$

Note that relative to the Blasius stream function the “2” factor in [Eq. \(4-58\)](#) is now divided by $(m+1)$. The solution is given by [Eq. \(4-80\)](#), and the local Nusselt number may be written in the form of

$$Nu_x = \sqrt{\frac{1}{2}(m+1)G(Pr, \beta)Re_x^{1/2}} \quad \text{with} \quad \frac{1}{G(Pr, \beta)} = \int_0^\infty \exp\left(-Pr \int_0^\eta f ds\right) d\eta \quad (4-100)$$

Page 182 where $Re_x = xU(x)/\nu$. A plot of $G(Pr, \beta)$ for various values of β is given in [Fig. 4-18](#) and cataloged in [Table 4-7](#). For a given β , the variation with Pr is nearly a power law, as in [Eq. \(4-84\)](#). Three interesting cases include

TABLE 4-7

Numerical values of the heat-transfer parameter $G(Pr, \beta)$ from [Eq. \(4-100\)](#)

	β	-0.19884	-0.18	0.0	0.3	1.0	2.0	10.0
	f_0''	0.0	0.12864	0.46960	0.77476	1.23259	1.68722	3.67523
	η^*	2.35885	1.87157	1.21678	0.91099	0.64790	0.49743	0.24077
Air	0.001	0.02383	0.02410	0.02449	0.02467	0.02483	0.02492	0.02508
	0.003	0.03967	0.04047	0.04154	0.04206	0.04252	0.04278	0.04325
	0.006	0.05409	0.05555	0.05759	0.05859	0.05947	0.05999	0.06091
	0.01	0.06745	0.06972	0.07296	0.07455	0.07597	0.07681	0.07831
	0.03	0.10547	0.11109	0.11935	0.12353	0.12734	0.12972	0.13385
	0.06	0.13666	0.14619	0.16050	0.16791	0.17480	0.17903	0.18693
	0.1	0.16339	0.17709	0.19803	0.20908	0.21950	0.22600	0.23843
	0.3	0.23180	0.25971	0.30371	0.32783	0.35147	0.36681	0.39801
	0.6	0.28318	0.32498	0.39168	0.42892	0.46633	0.49130	0.54459
	0.72	0.29777	0.34400	0.41786	0.45929	0.50113	0.52928	0.59054
	1.0	0.32581	0.38112	0.46960	0.51952	0.57047	0.60520	0.68219
	2.0	0.39145	0.47090	0.59723	0.66905	0.74372	0.79599	0.91815
	3.0	0.43478	0.53224	0.68596	0.77344	0.86522	0.93036	1.0872
	6.0	0.51896	0.65591	0.86728	0.98727	1.1147	1.2069	1.4396
	10.0	0.59054	0.76545	1.02974	1.1791	1.3388	1.4557	1.7597
	30.0	0.77839	1.0703	1.4873	1.7198	1.9706	2.1577	2.6682
	60.0	0.92602	1.3260	1.8746	2.1776	2.5054	2.7520	3.4395
	100.0	1.0523	1.5550	2.2229	2.5892	2.9863	3.2863	4.1332
	400.0	1.4885	2.4098	3.5292	4.1331	4.7894	5.2890	6.7332
	1000.0	1.8717	3.2319	4.7901	5.6230	6.5291	7.2212	9.2401
	4000.0	2.6471	5.0631	7.6039	8.9481	10.4112	11.5320	14.8312
	10,000.0	3.3285	6.8289	10.3201	12.1577	14.1583	15.6928	20.2262

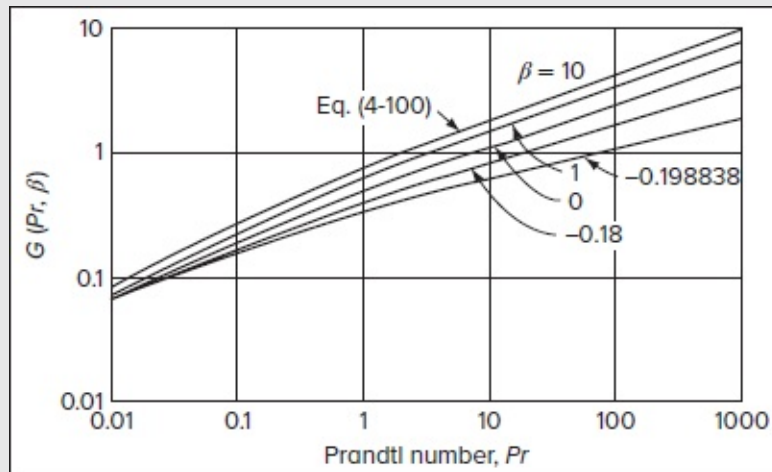


FIGURE 4-18

Heat-transfer parameter for Falkner–Skan similarity flows with constant wall temperature and negligible dissipation.

$$\frac{Nu_x}{Re_x^{1/2}} \approx \begin{cases} 0.220Pr^{0.27} & (\text{separated flow, } \beta = -0.1988) \\ 0.332Pr^{1/3} & (\text{flat plate flow, } \beta = 0) \\ 0.570Pr^{0.4} & (\text{stagnation flow, } \beta = 1) \end{cases} \quad (4-101)$$

Note that separation flow, where skin friction is *zero*, allows for considerable heat transfer. In fact, heat transfer in generally nonsimilar separated-flow regions is substantial for both laminar and turbulent flows, e.g., along the rear of bluff bodies.

Page 183

4-3.5 The Reynolds Analogy as a Function of Pressure Gradient

We saw in Sec. 3-8.1.5 that there is a proportionality between friction and heat transfer in stagnation flow. A comparable Reynolds analogy holds in flat-plate flow. If we divide [Eq. \(4-70\)](#) by [Eq. \(4-84\)](#), we obtain

$$\frac{C_f}{C_h}(\text{flat plate}) = 2Pr^{2/3} \quad (4-102)$$

This is a pure proportionality, valid for laminar or turbulent flow, irrespective of the Reynolds number. It is often used as an approximation in other (nonsimilar, non-flat-plate) configurations, such as duct flow. Nonetheless, [Eq. \(4-101\)](#) alerts us that there is a pressure gradient effect that must be judiciously accounted for.

Let us see if the Reynolds analogy holds for the Falkner–Skan solutions. The skin friction for these flows is given by

$$C_f(x) = \frac{2\mu(\partial u / \partial y)_w}{\rho U^2(x)} = f_0'' \sqrt{\frac{2(1+m)\nu}{Ux}} \quad (4-103)$$

and the Stanton number Ch is given by [Eq. \(3-15\)](#) and App. H2. If we adopt the usual power-law approximation near a Prandtl number of unity, we can put

$$G(Pr, \beta) \approx G(1, \beta)Pr^{1/3} \quad (4-104)$$

We find that the ratio of skin friction to heat transfer for the Falkner–Skan flows may be appropriately expressed as

$$\text{Gases:} \quad \frac{C_f(x)}{C_h(x)} \approx 2Pr^{2/3} \frac{f_0''}{G(1, \beta)} \quad (4-105)$$

and the simple Reynolds analogy will be valid only if the factor $f_0''/G(1, \beta)$ is unity, which is true for $\beta = 0$. However, this “analogy factor” varies strongly with β , as shown in [Fig. 4-19](#). It is zero at the separation point, where $C_f = 0$ but C_h is finite, and increases without bound as β

becomes large. The analogy is thus reliable only for modest, near-zero pressure gradients. It deteriorates for nonsimilar flows or if the wall temperature varies.

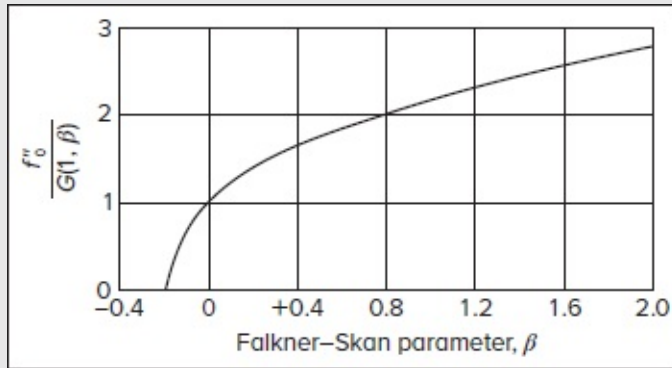


FIGURE 4-19

Variation of the Reynolds analogy from [Eq. \(4-105\)](#) with pressure gradient β for the Falkner–Skan solutions.

4-3.6 The Flat Plate with Wall Suction or Blowing

The Blasius solution can be extended to nonzero wall velocity, where $v_w \ll U$, with either positive (blowing) or negative (suction) speed. The streamwise wall velocity, $u_w = 0$, satisfies the no-slip requirement. This model has practical application to many problems involving mass transfer, drying, ablation, transpiration cooling, wall blowing, propellant burning, and boundary-layer control. For similarity, only a certain variation $v_w(x)$ is allowed. From [Eq. \(4-59\)](#), at $\eta = 0$, the wall velocity may be written as $v_w = -f(0)\sqrt{\nu U/(2x)}$. Therefore, suction and blowing can be simulated by a nonzero value of the Blasius stream function, $f(0)$, and v_w must vary as $x^{-1/2}$. We solve the Blasius [Eq. \(4-60\)](#) with

$$f'(0) = 0 \quad f''(\infty) = 1 \quad \text{and} \quad f(0) \neq 0 \quad (4-106)$$

The results will vary with the *suction-blowing parameter*, v_w^* , where

$$v_w^* = \frac{v_w}{U} \sqrt{Re_x} = \frac{-f(0)}{\sqrt{2}} \quad (4-107)$$

Page 184The corresponding momentum problem was studied by Schlichting and Bussmann (1943), with heat-transfer results added by Hartnett and Eckert (1957).

[Figure 4-20](#) illustrates the basic results for different values of v_w and Pr . Clearly, the velocity profiles in [Fig. 4-20a](#) are strongly affected by v_w^* . Suction leads to appreciable

boundary-layer thinning while greatly increasing the wall slope (i.e., friction and heat transfer). On the one hand, the suction profiles have a strong negative curvature, like a favorable gradient, and this stability causes a delay in transition (see Fig. 5-12). On the other hand, blowing thickens the boundary layer and makes the profile S-shaped, less stable, and prone to transition to turbulence (cf. [Fig. 5-12](#)). At a finite value of $v_w^* = +0.619$, the solution yields $\partial u / \partial y = 0$ at $y = 0$, with $u = 0$ for all finite y . The boundary layer is said to be “blown off” by the wall injection effect, which suppresses both heat transfer and friction. The boundary-layer approximations fail, of course, for this extreme case. [Figure 4-20b](#) displays the heat transfer $Nu_x / \sqrt{Re_x}$ versus the suction-blowing parameter. The effect of the Prandtl number is seen to be slight, at least for gases. The dash-dot lines in [Fig. 4-20b](#) also represent the skin friction $C_f/2$, especially that the Reynolds analogy becomes exact when $Pr = 1$ in flat-plate flow.

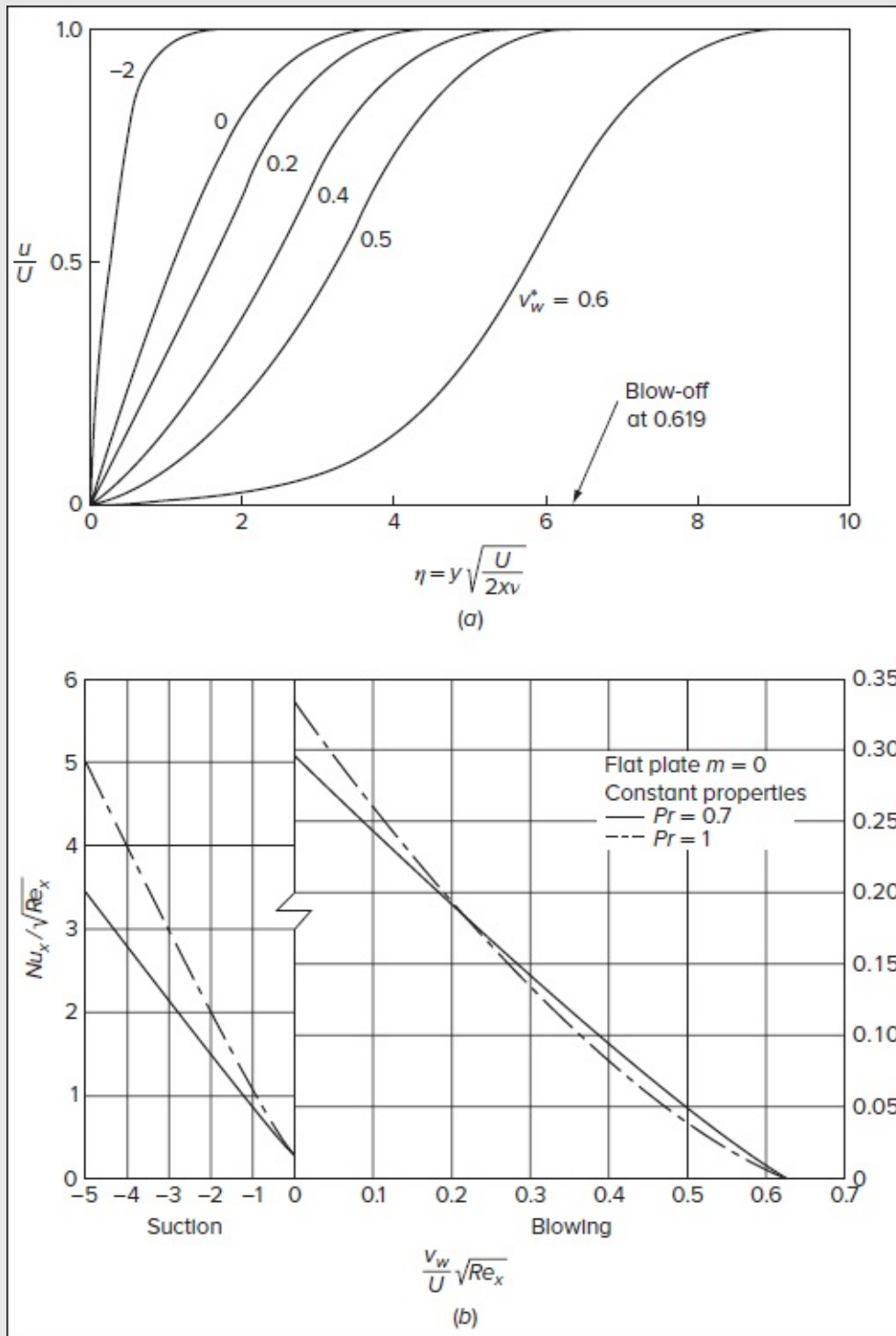


FIGURE 4-20

Flat-plate flow with suction or blowing: (a) velocity profiles; (b) local heat-transfer rates [After Hartnett and Eckert (1957).]

4-3.7 Flow Toward a Point Sink

Figure 4-15 reminds us that the limiting case of $\beta = +\infty$ at $m = -1$ corresponds to flow toward a point sink. However, the Falkner–Skan approach becomes unsuitable because the similarity variable in Eq. (4-92) vanishes for $m = -1$. The remedy is to redefine the similarity variable in this case. In fact, for the point-sink coordinates in Fig. 4-21a, it is appropriate to take

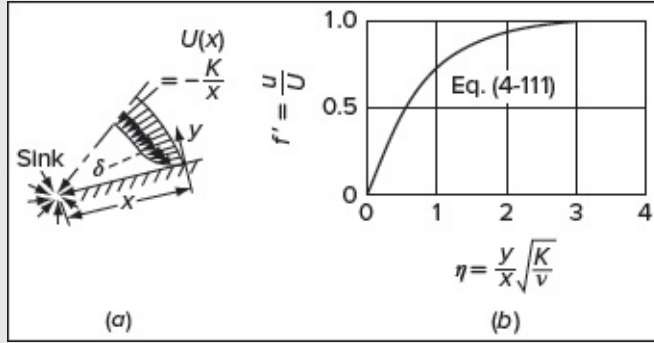


FIGURE 4-21

Boundary-layer similar solution for a point sink: (a) geometry; (b) solution.

$$U(x) = -\frac{K}{x} \quad (4-108)$$

Subsequent comparison to Eq. (4-90) reveals that similarity can be achieved if η is proportional to y/x . We, therefore, use

$$\eta_{\text{point sink}} = \sqrt{\frac{K}{\nu}} \frac{y}{x} \quad (4-109)$$

Substitution into Eq. (4-89) yields a third-order differential equation for flow into a convergent channel with three boundary conditions:

$$f''' - f'^2 + 1 = 0 \quad \text{with} \quad f(0) = f'(0) = 0 \quad \text{and} \quad f'(\infty) = 1. \quad (4-110)$$

It is gratifying that an exact solution may be extracted for this problem, namely,

$$f' = \frac{u}{U} = 3 \tanh^2 \left(\frac{\eta}{\sqrt{2}} + \tanh^{-1} \sqrt{\frac{2}{3}} \right) - 2 \quad (4-111)$$

where the constant $\tanh^{-1} \sqrt{2/3} = 1.146$. A plot of this relation is given in Fig. 4-21b, where it can be verified that $f' = 0.99$ at $\eta \approx 3.4$. This enables us to deduce the corresponding inverse square-root relation:

$$\text{Point sink:} \quad \frac{\delta}{x} = \frac{3.3913}{\sqrt{-Ux/\nu}} \quad (4-112)$$

The minus sign under the radical is a mere reminder that U is opposite to x , as shown in [Fig. 4-21a](#). Interestingly, the sink-flow profile in [Fig. 4-21b](#) reproduces the Jeffery–Hamel wedge-flow profiles of Sec. 3-8.3.1 for large negative αRe (cf. profile for $\alpha Re = -100$ in Fig. 3-41). Note, however, that η is defined quite differently for the Jeffery–Hamel motion.

4-4 FREE-SHEAR FLOWS

Free-shear layers are unaffected by walls as they can develop and spread in an open ambient fluid. They possess velocity gradients, created by some upstream mechanism that they try to smooth out by viscous diffusion in the presence of convective deceleration. Three examples are (1) the free-shear layer between parallel moving streams, (2) a jet, and (3) the wake behind a body immersed in a stream.

Let the dominant free-shear velocity be u in the x direction. If the Reynolds number is large, the boundary-layer approximations will hold with $v \ll u$, $\partial u / \partial x \ll \partial u / \partial y$, and $\partial p / \partial y \approx 0$. Furthermore, since there are no confining walls, $dp/dx \approx 0$, and so plane free-shear flows satisfy the flat-plate equations

$$\frac{\partial u}{\partial x} + \frac{\partial v}{\partial y} = 0 \quad \text{and} \quad u \frac{\partial u}{\partial x} + v \frac{\partial u}{\partial y} \approx \nu \frac{\partial^2 u}{\partial y^2} \quad (4-113)$$

except that there are no walls to enforce a no-slip condition. Page 186

Just downstream of the disturbance that causes the velocity gradients (e.g., the meeting point of the two parallel streams, the jet exit and the rear of the immersed body), the flow will be *developing* and *nonsimilar*. Further downstream, the flow will be *similar* and the velocity profiles will all look alike when suitably scaled. Here, we discuss only the similar solutions for the shear layer, the jet, and the wake.

4-4.1 The Free-Shear Layer Between Two Different Streams

[Figure 4-22a](#) shows two parallel uniform streams, U_1 (upper) and U_2 (lower), meeting at $x = 0$. As we move downstream, the discontinuity between U_1 and U_2 is smoothed out by viscosity into an S-shaped *free-shear layer* between them. The simplest application would be for $U_2 = 0$, such as a plane airflow emerging from a slot into ambient air at rest. Lock (1951) generalized this physical setting into two different fluids with physical properties (ρ_1, μ_1) and (ρ_2, μ_2) , respectively—also shown in [Fig. 4-22a](#). He defined a Blasius-type similarity variable for each stream using

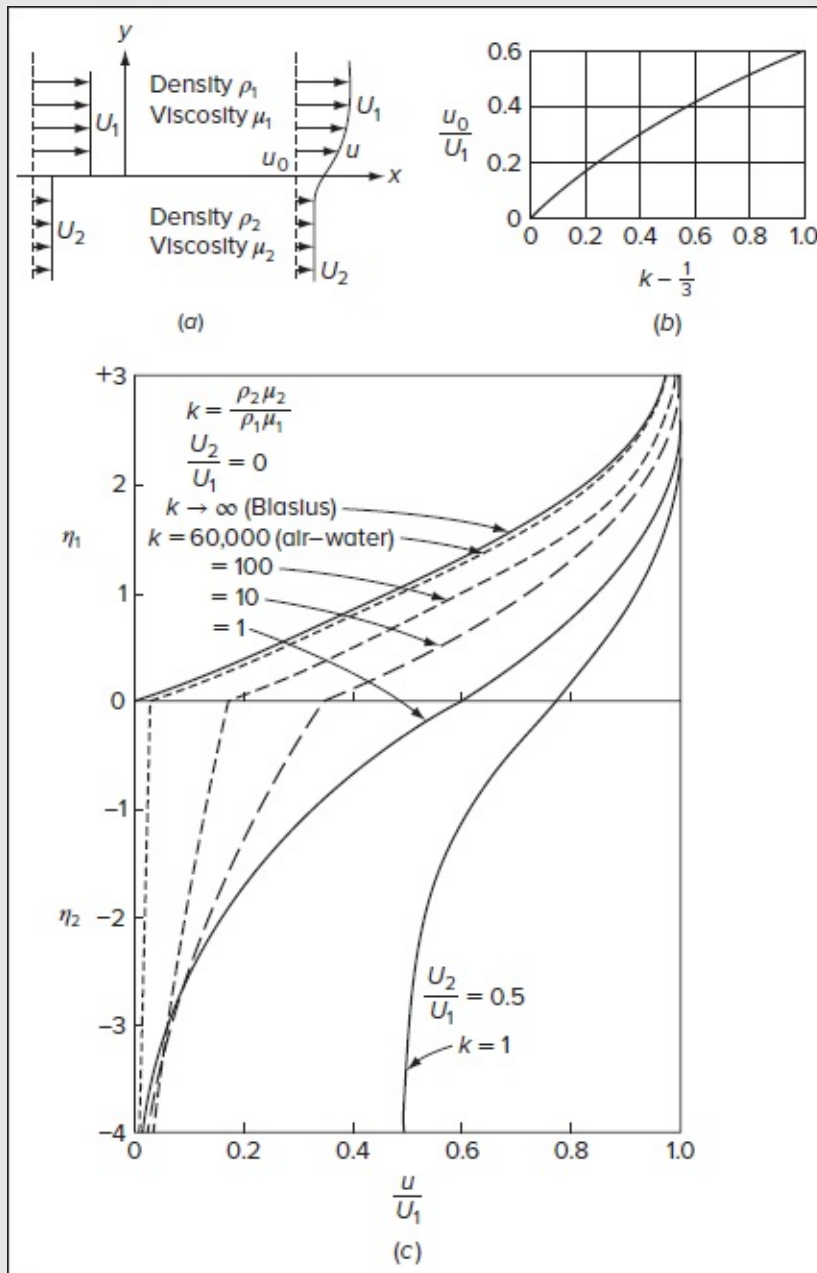


FIGURE 4-22

Velocity distribution between two parallel streams with dissimilar properties: (a) geometry; (b) velocities at the interface ($U^2 = 0$); (c) representative velocity profiles. [After Lock (1951), by permission of The Clarendon Press, Oxford.]

$$\eta_j = y \sqrt{\frac{U_1}{2x\nu_j}} \quad \text{and} \quad f'_j = \frac{u_j}{U_1}; \quad j = 1, 2 \quad (4-114)$$

Page 187Note that U_1 , not U_j , is specified in both variables. Substitution into [Eqs. \(4-114\)](#) yields a Blasius-type equation for each layer:

$$f_j''' + f_j f_j'' = 0; \quad j = 1, 2 \quad (4-115)$$

As for the boundary conditions, three types may be considered. First, one may impose the asymptotic value of the two stream velocities far away, where U_1 and U_2 are recovered above and below the free-shear layer. This condition translates into

$$f_1'(+\infty) = 1 \quad \text{and} \quad f_2'(-\infty) = U_2/U_1 \quad (4-116)$$

Second, there should be kinematic equality, $u_1 = u_2$ and $v_1 = v_2$, at the interface, where $\eta_j = 0$:

$$f_1(0) = f_2(0) = 0 \quad \text{and} \quad f_1'(0) = f_2'(0) = 0 \quad (4-117)$$

Third, there should be equality of shear stress at the interface:

$$\mu_1 \frac{\partial u_1}{\partial y}(0) = \mu_2 \frac{\partial u_2}{\partial y}(0) \quad \text{or} \quad f_1''(0) = k^{1/2} f_2''(0); \quad k = \frac{\rho_2 \mu_2}{\rho_1 \mu_1} \quad (4-118)$$

This last condition stems from the equality $y = \eta_1 \sqrt{2xv_1/U_1} = \eta_2 \sqrt{2xv_2/U_1}$, which enables us to write

$$\frac{\partial(U_1 f_1')}{\partial(\eta_1 \sqrt{2xv_1/U_1})}(0) = \frac{\mu_2}{\mu_1} \frac{\partial(U_1 f_2')}{\partial(\eta_2 \sqrt{2xv_2/U_1})}(0) \quad \text{and so} \quad \frac{d(f_1')}{d(\eta_1 \sqrt{v_1})}(0) = \frac{\mu_2}{\mu_1} \frac{d(f_2')}{d(\eta_2 \sqrt{v_2})}(0)$$

Since we are neglecting mass transfer between the two fluids, the most practical cases correspond to $k = 1$ (identical fluids) or $k \gg 1$ for a gas flowing over a liquid. For the air–water interface, $k \approx 60,000$ or $k^{1/2} \approx 245$.

Some solutions computed by Lock (1951) for different values of k are presented in [Fig. 4-22c](#). As k increases, the lower layer moves more slowly. The air–water case, with $k = 60,000$, provides a good physical picture of the slow “wind-driven” motion of the surface layer in a lake or an ocean. The interfacial velocity when $U_2 = 0$ is given in [Fig. 4-22b](#) as a function of k .

The classic case of $k = 1$ and $U_2 = 0$ in [Fig. 4-22c](#) has two interesting facets. First, it is asymmetric. The interfacial velocity is greater than $0.5U_1$ because the two layers have different convective deceleration. Second, the asymptotic value $f_2'(-\infty)/\sqrt{2} = -0.619$, which represents a flat plate at negative infinity with its boundary layer “blown off” as in [Fig. 4-20a](#).

4-4.2 The Plane Laminar Jet

Consider a plane jet emerging into a still (identical) fluid from a (two-dimensional) slot at $x = 0$, as shown in [Fig. 4-23](#). Since the jet spreads at constant pressure and there are no bounding walls, it must satisfy [Eqs. \(4-113\)](#) while maintaining a constant momentum flux across any axial station:

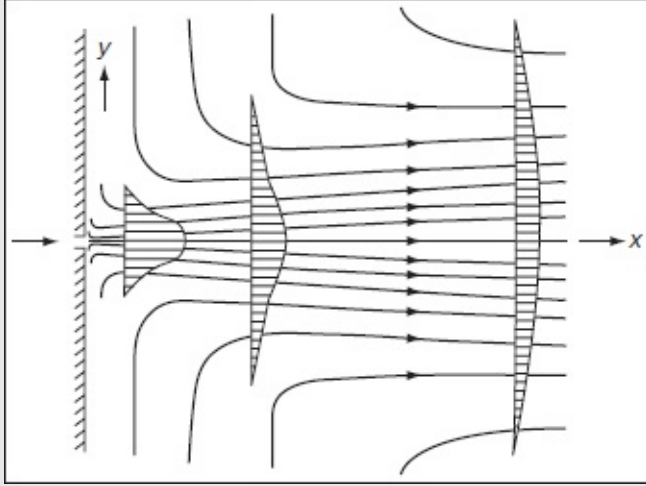


FIGURE 4-23

Definition sketch for a two-dimensional laminar free jet. [After Schlichting (1933a).]

$$J = \rho \int_{-\infty}^{+\infty} u^2 dy = \text{const} \quad (4-119)$$

Page 188 which is the zero-drag, zero-freestream version of [Eq. \(4-5\)](#) for a constant-pressure control volume. Schlichting (1933a) shows that if boundary-layer approximations are valid, the jet entrainment spreads as the cubic root of x , with the proper stream function being

$$\psi = \nu^{1/2} x^{1/3} f(\eta); \quad \eta = \frac{y}{3\nu^{1/2} x^{2/3}} \quad (4-120)$$

The corresponding velocity components may be written as

$$u = \frac{1}{3} x^{-1/3} f'(\eta) \quad \text{and} \quad v = -\frac{1}{3} \nu^{1/2} x^{-2/3} (f - 2\eta f') \quad (4-121)$$

When these expressions are substituted into [Eq. \(4-113\)](#), one gets, after some algebra:

$$f''' + ff'' + f'^2 = 0 \quad (4-122)$$

The boundary conditions for the plane laminar jet may be associated with symmetry about the x axis (i.e., $v = 0$ and $\partial u / \partial y = 0$ at $y = 0$), as well as a quiescent fluid with $u = 0$ at $y \rightarrow \infty$. These conditions translate into

$$f(0) = f''(0) = 0 \quad \text{and} \quad f'(\infty) = 0 \quad (4-123)$$

With all homogeneous boundary conditions, it looks as though we have no driving force for the equation. Upon further reflection, it may be seen that the driving potential is the

momentum flux J , analogously to the Jeffery–Hamel wedge flows of [Chap. 3](#).

Equation (4-122) contains the same two nonlinearities as the Falkner–Skan equation (4-93). In this case, however, Schlichting (1933a) is able to obtain a strikingly simple, yet exact, analytic solution:

$$f(\eta) = 2a \tanh(a\eta) \quad \text{with} \quad f'(\eta) = 2a^2 \operatorname{sech}^2(a\eta) \quad (4-124)$$

Here, the jet velocity profile has the symmetrical $\operatorname{sech}^2 y \approx 4e^{-2y}$ which is reminiscent of a Gaussian probability distribution. The constant a is determined by evaluating the momentum flux J from [Eq. \(4-119\)](#):

$$J = \rho \int_{-\infty}^{+\infty} \left(\frac{2a^2}{3x^{1/3}} \operatorname{sech}^2 a\eta \right)^2 3\nu^{1/2} x^{2/3} d\eta = \frac{16}{9} \rho \nu^{1/2} a^3 \quad \text{or} \quad a = \left(\frac{9J}{16\sqrt{\rho\nu}} \right)^{1/3} \approx 0.8255 \frac{J^{1/3}}{(\rho\nu)^{1/6}} \quad (4-125)$$

Since $\operatorname{sech}(0) = 1$, the maximum centerline velocity can be calculated to be

$$u_{\max} = \frac{2a^2}{3x^{1/3}} = \frac{2}{3} \left(\frac{9}{16} \right)^{2/3} \frac{J^{2/3}}{(\rho\nu x)^{1/3}} \approx 0.4543 \left(\frac{J^2}{\rho\nu x} \right)^{1/3} \quad (4-126)$$

Clearly, the jet spreads while its centerline speed drops off as $x^{-1/3}$. The corresponding velocity distribution may be given by

$$u(x, y) = u_{\max} \operatorname{sech}^2 a\eta = u_{\max} \operatorname{sech}^2 \left[0.2752 \left(\frac{\rho J}{\mu^2 x^2} \right)^{1/3} y \right] \quad (4-127)$$

We may define the width of the jet as twice the distance y to where $u = 0.01u_{\max}$. Noting that $\operatorname{sech}^2 3 \approx 0.01$, we have

$$\text{Jet width:} \quad b = 2y|_{1\%} \approx 21.8 \left(\frac{\mu^2}{\rho J} \right)^{1/3} x^{2/3} \quad (4-128)$$

We thus realize that the jet spreads as $x^{2/3}$. As for the mass flow rate across any vertical plane, it is given by

$$\dot{m} = \rho \int_{-\infty}^{+\infty} u dy = (36\mu\rho Jx)^{1/3} \approx 3.302(\mu\rho Jx)^{1/3} \quad (4-129)$$

which is seen to increase with $x^{1/3}$ as the jet entrains ambient fluid by dragging it along. This result is correct at large x but implies falsely that $\dot{m} = 0$ at $x = 0$, which is the slot where the jet issues. The reason is that the boundary-layer approximations fail if the Reynolds number is small, and the appropriate Reynolds number per unit depth is $\dot{m}/\mu \sim (\rho Jx/\mu^2)^{1/3}$. Since the solution deteriorates for small values of $\rho Jx/\mu^2$, we cannot ascertain the details of the flow near the jet outlet using boundary-layer theory.

Since jet velocity profiles are S-shaped with an inflection point, they are unstable and undergo transition to turbulence early—at a Reynolds number of about 30, based on exit slot width and mean slot velocity. Although there is further analysis of laminar jets in the literature [Pai (1954)], jets are more likely to be turbulent. Textbooks on turbulent-jet analysis and experiments include those by Abramovich (1963), Schetz (1980), and Morris et al. (2002). The analysis of axisymmetric (round) jets and wakes will be discussed in Sec. 4-10.

4-4.3 The Plane Laminar Wake: Far-Field Approximation

A wake is the *defect* in stream velocity behind an immersed body, as sketched in Fig. 4-24. A slender plane body with zero lift, such as the airfoil parallel to the stream in Fig. 4-24, produces a smooth wake with a velocity defect u_1 that decays monotonically downstream. A blunt body, such as a cylinder, has a wake that is distorted by an alternating shed vortex structure, such as the von Kármán vortex street—the picture in Fig. 4-24 corresponds to a time-averaged wake.

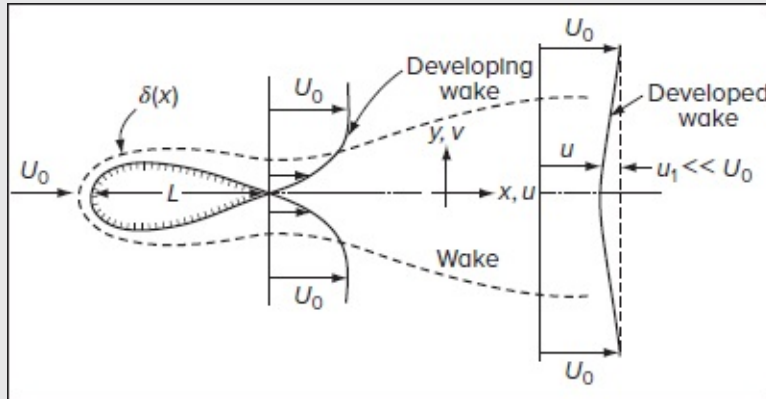


FIGURE 4-24

Flow in the wake of a body immersed in a stream.

Downstream of the body in Fig. 4-24, the wake remains nonsimilar during its development. About three body-lengths downstream, the wake develops into a self-similar profile. Here, we make only a simple far-field approximation for a developed wake by assuming that the velocity defect is very small, specifically

$$u_1(x, y) = U_0 - u(x, y) \ll U_0 \quad (4-130)$$

In this case, the convective acceleration can be linearized in conformance with the Oseen approximation [Sec. 3-9.4]. The momentum Eq. (4-113) simplifies into

$$U_0 \frac{\partial u_1}{\partial x} \approx \nu \frac{\partial^2 u_1}{\partial y^2} \quad \text{with} \quad u_1(x, \pm\infty) = 0 \quad \text{and} \quad \frac{\partial u_1}{\partial x}(x, 0) = 0 \quad (4-131)$$

The resulting linear, parabolic, heat-conduction type equation can be solved straightforwardly. We get

$$u_1 = \frac{BU_0}{\sqrt{x}} \exp\left(-\frac{U_0 y^2}{4x\nu}\right) \quad (4-132)$$

where B is a constant. In the far field, then, the wake exhibits a Gaussian velocity distribution with a centerline value that decreases as $x^{-1/2}$. The constant B can be evaluated from the condition that the body drag force F per unit depth must balance the momentum flux defect in the wake:

$$F = \int_{-\infty}^{+\infty} \rho u u_1 dy \approx \rho U_0 \int_{-\infty}^{+\infty} u_1 dy = 2\rho U_0^2 B \sqrt{\frac{\pi\nu}{U_0}} \quad (4-133)$$

Meanwhile, this force can be related to the body drag coefficient using

$$F = \frac{1}{2} C_D \rho U_0^2 L$$

By equating this expression to [Eq. \(4-133\)](#) and solving for B , the wake velocity may be written in the form

$$\frac{u_1}{U_0} = C_D \left(\frac{Re_L}{16\pi}\right)^{1/2} \left(\frac{L}{x}\right)^{1/2} \exp\left(-\frac{U_0 y^2}{4x\nu}\right) \quad (4-134)$$

Page 190 where $Re_L = U_0 L/\nu$ denotes the body Reynolds number. The wake defect is thus proportional to the body drag coefficient. For a flat plate wetted on both sides, $C_D = 2.656/\sqrt{Re_L}$ from [Eq. \(4-71\)](#), and the centerline velocity defect becomes

$$\left. \frac{u_1(x, 0)}{U_0} \right|_{\text{flat plate}} = \frac{0.664}{\sqrt{\pi}} \left(\frac{L}{x}\right)^{1/2} \quad (4-135)$$

a result given by Tollmien (1931) and valid for $x > 3L$.

A complete review of laminar wakes, including near-field and three-dimensional geometries and compressible flows, is given in the monograph by Berger (1971). Like jets, wakes are unstable and more likely in practice to be turbulent than laminar.

4-5 OTHER ANALYTIC TWO-DIMENSIONAL SOLUTIONS

It is clear that the similarity solutions of Secs. 4-3 and 4-4 are very special, in that their profile shapes remain invariant as we move downstream. It is more likely for typical flows to be nonsimilar, thus changing from adverse to favorable gradients and perhaps back again. For example, the freestream near a cylinder, which has a favorable gradient near the nose, changes continuously to an adverse gradient (with separation) as we move toward the rear.

No similarity technique can handle such a flow. However, in this personal-computer era, any practical laminar freestream distribution can be computed swiftly and accurately. In hindsight, three basic approaches have been used to model nonsimilar boundary layers:

1. Analytic continuation by series expansion, e.g., Howarth (1938), Görtler (1957), and Meksyn (1961).
2. Approximate integral methods—an extension of Sec. 4-1.1. An impressive number of these techniques are discussed by Rosenhead (1963). We will focus here on the simple and accurate laminar-flow correlation of Thwaites (1949).
3. Numerical modeling on a digital computer. Scores of these numerical techniques, which rely on finite-difference and finite-element methods, are reported in the literature [Schetz and Bowersox (2011), Cebeci and Cousteix (1998)].

Although integral and numerical methods can, with proper care, handle any new problem, two classic solutions are worth describing.

4-5.1 Linearly Decelerated Howarth Flow

A simple decelerating nonsimilar freestream distribution is considered by Howarth (1938), namely,

$$U(x) = U_0 \left(1 - \frac{x}{L}\right) \quad (4-136)$$

This profile serves to illustrate the behavior of adverse gradients and laminar-boundary-layer separation. Howarth expands the stream function into a power series in $x > L$ using coefficients that are Blasius-type functions of $y\sqrt{U_0/(\nu x)}$. He retains seven terms and plots the velocity profiles shown in Fig. 4-25. Note that the curve for $x/L = 0$ returns the Blasius profile, downstream of which the profiles become increasingly S-shaped with separation occurring at $x/L \approx 0.125$.

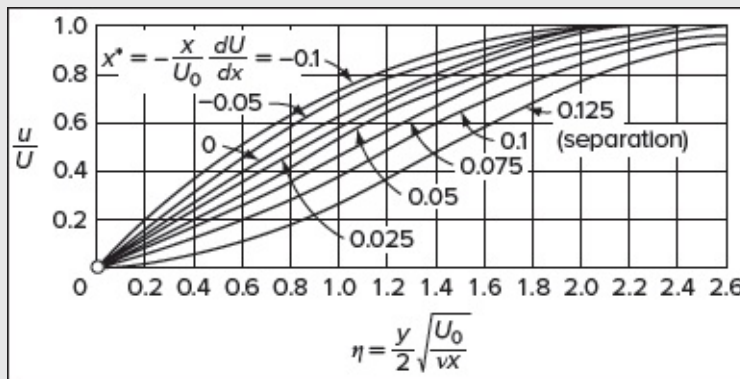


FIGURE 4-25

Velocity profiles from a series expansion of a linearly decelerated flow, $U(x) =$

Page 191The series-expansion approach is obsolete now, but even the most accurate numerical solution for boundary layers becomes invalid at separation and beyond. No matter how the external potential flow $U(x)$ varies, the wall shear stress at the separation point comes in normally to zero, that is, $\partial \tau_w / \partial n = 0$. This is known as the *Goldstein singularity*, after Goldstein (1948), who showed that, in boundary-layer theory, the wall shear stress has square-root behavior near separation:

$$\mu \left. \frac{\partial u}{\partial y} \right|_{y=0} = \text{const}(x_{\text{sep}} - x)^{1/2} \quad (4-137)$$

Though interesting mathematically, this behavior is unrealistic physically and is a fundamental limitation of boundary-layer theory. The dilemma is resolved by Sychev (1972), who shows that a *free-streamline potential theory* [Milne–Thomson (1968)], augmented by a rescaled boundary-layer approximation in the immediate vicinity of separation, removes the singularity. The wall shear stress then varies smoothly through zero. In the separated region, higher order theory and, indeed, the full Navier–Stokes equations should replace boundary-layer approximations. The Sychev–Smith theory is most appropriate for bluff-body flows, where the free streamline produces an adverse pressure gradient just sufficient to cause flow separation [cf. Chap. 14, Schlichting and Gersten (2017)].

4-5.2 Flat Plate with Uniform Wall Suction

Another series solution of an important case corresponds to the boundary-layer flow past a flat plate with uniform suction, as depicted in [Fig. 4-26](#) [Iglisch (1944)]. Since wall suction is a practical approach to delay boundary-layer transition, Iglisch solves the boundary-layer [Eqs. \(4-113\)](#) at constant pressure, with $\partial U / \partial x = 0$, and a wall-suction boundary condition:

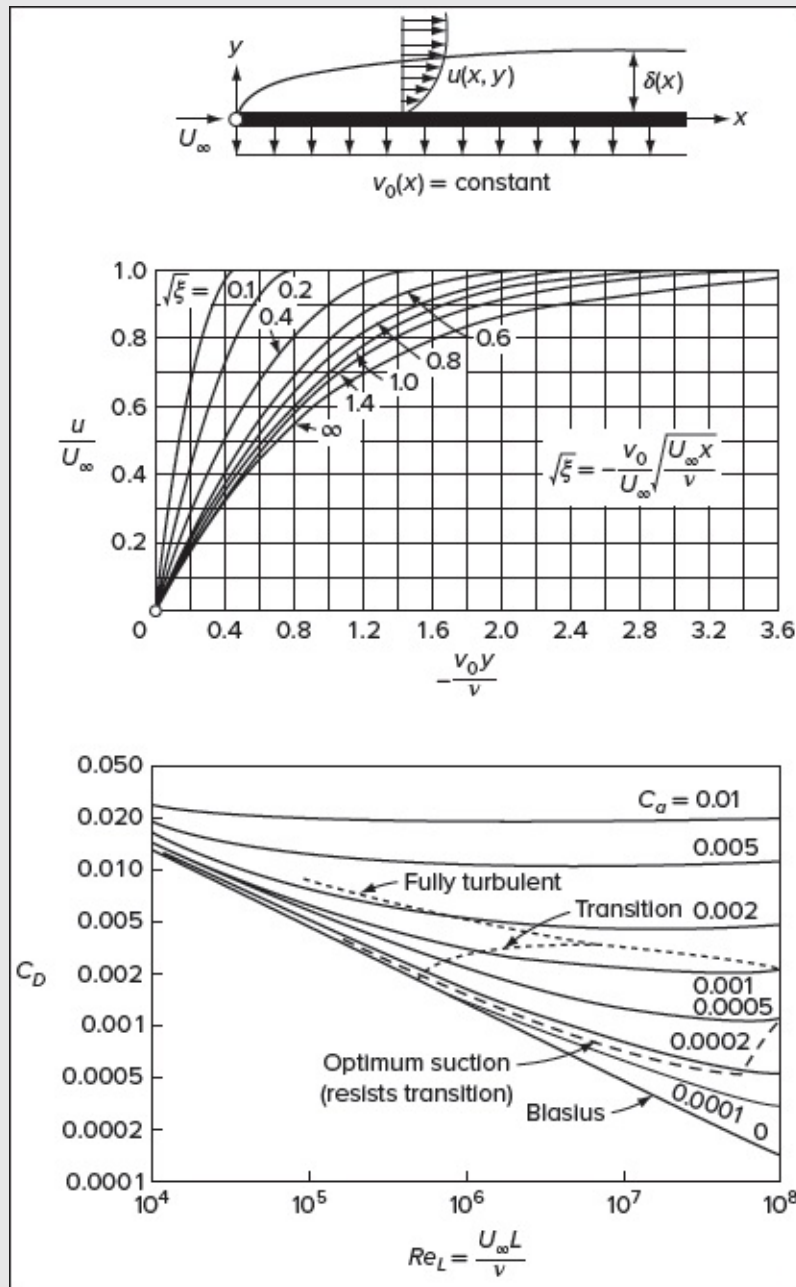


FIGURE 4-26

Velocity profile and drag coefficient of a flat plate with uniform suction. [After Iglisch (1994).]

$$u(x, 0) = 0 \quad u(x, \infty) = U_\infty \quad v(x, 0) = v_0 = \text{const} < 0 \quad (4-138)$$

The flow is nonsimilar, and the velocity profiles in [Fig. 4-26](#) gradually change from a near-Blasius shape at the leading edge to the asymptotic exponential profile of Eq. (3-158) far downstream. The asymptotic condition is reached at about $(-v_0/U_\infty)\sqrt{Re_x} \approx 2.0$. If the suction rate has a typical value of $(-v_0/U_\infty) = 0.001$ in air at 22°C with $U_\infty = 10$ m/s, this corresponds to a distance of $x = 6$ m. But the third chart in [Fig. 4-26](#) shows that increasing

suction raises the plate drag, possibly even above the turbulent-flow drag that we are trying to avoid with suction. The reader may show as an exercise (from a control volume similar to [Fig. 4-1](#)) that wall suction increases the drag coefficient on the plate by absorbing additional tangential momentum through the wall:

$$C_D = \frac{1}{L} \int_0^L C_f(x) dx + 2C_0; \quad C_0 = -\frac{v_0}{U_\infty} \quad (4-139)$$

Here, C_f refers to the local viscous shear, C_f . Iglisch's drag computations are shown in [Fig. 4-26](#). The dashed line corresponds to optimum suction, the locus of points of minimum suction required to maintain laminar flow, according to the transition theory of [Chap. 5](#) [see also Wuest in Lachmann (1961)].

4-5.3 Other Classical Analytic Solutions

There are quite a few other published classical solutions of boundary-layer equations for special profiles:

1. Tani (1949): $U = U_0(1 - x^{*n})$, $n = \{2, 4, 8\}$ and $x^* = x/L$
2. Görtler (1957): $U/U_0 = (1 - x^*)^n$, $n = \{\frac{1}{2}, 2\}$; $U/U_0 = (1 + x^*)^m$, $m = \{-1, -2, \cos x^*\}$
3. Curle (1958): $U = U_0(x^* - x^{*3} + ax^{*5})$, $a = \{0, 0.07885, -0.12156\}$
4. Terrill (1960): $U = U_0 \sin x^*$

Two of them are experiments used for comparative analysis:

5. Hiemenz (1911): Flow past a circular cylinder
6. Schubauer (1935): Flow past a slender elliptical cylinder

All of these laminar flows are driven to separation and can thus be used as effective test cases for alternative methods. Page 192

4-6 APPROXIMATE INTEGRAL METHODS

The control-volume approach of Sec. 4-1 can yield highly accurate estimates if exact velocity and temperature distributions are used. However, it becomes approximate when using intuitive or rationally conjectured profiles. While a variety of integral methods are available [Rosenhead (1963)], we limit our attention here to the Thwaites' method.

4-6.1 The Boundary-Layer Integral Equations

All integral methods use partially integrated forms of the continuity, momentum, and energy equations which, for two-dimensional incompressible flow, lead to Eqs. (4-50). Continuity is

eliminated during the derivation, so that the two basic equations are (1) the *momentum* integral relation [Kármán (1921)] and (2) the *thermal-energy* integral relation [Frankl (1934)]. Some workers also use a third, called the *mechanical-energy* integral relation [Leibenson (1935)]. The mechanical-energy equation is the x-momentum equation multiplied by u ; i.e., it simply replaces forces by the Page 193rate of work done by those forces. Although it is not a fundamental relation, it can be useful as a correlation tool, especially for turbulent boundary layers.

We may derive the integral relations by direct integration, in the y direction, of the boundary-layer equations, repeated here for convenience:

$$\text{Continuity:} \quad \frac{\partial u}{\partial x} + \frac{\partial v}{\partial y} = 0 \quad (4-50a)$$

$$\text{Momentum:} \quad \frac{\partial u}{\partial t} + u \frac{\partial u}{\partial x} + v \frac{\partial u}{\partial y} \approx \left(\frac{\partial U}{\partial t} + U \frac{\partial U}{\partial x} \right) + \frac{1}{\rho} \frac{\partial \tau}{\partial y} \quad (4-50b)$$

$$\text{Thermal energy:} \quad \rho c_v \left(\frac{\partial T}{\partial t} + u \frac{\partial T}{\partial x} + v \frac{\partial T}{\partial y} \right) \approx - \frac{\partial q}{\partial y} + \tau \frac{\partial u}{\partial y} \quad (4-50c)$$

We have neglected buoyancy and used τ and q to represent the shear stress and heat flux because, in this manner, the equations will remain valid for turbulent boundary layers. In the laminar case, we simply take $\tau = \mu \partial u / \partial y$ and $q = -k \partial T / \partial y$.

4-6.2 The Momentum-Integral Relation

To obtain the momentum-integral relation, we first multiply continuity by $u - U$ and subtract the outcome from the momentum equation. We get

$$-\frac{1}{\rho} \frac{\partial \tau}{\partial y} = \frac{\partial}{\partial t} (U - u) + \frac{\partial}{\partial x} (uU - u^2) + (U - u) \frac{\partial U}{\partial x} + \frac{\partial}{\partial y} (vU - vu) \quad (4-140)$$

We allow for unsteady flow and the possibility of a porous wall with normal velocity $v_w(x)$ (defined positive for injection). We then integrate from the wall to infinity, noting that τ vanishes at infinity in the boundary-layer approximation. The result is

$$\frac{\tau_w}{\rho} = \frac{\partial}{\partial t} \int_0^\infty (U - u) dy + \frac{\partial}{\partial x} \int_0^\infty u(U - u) dy + \frac{\partial U}{\partial x} \int_0^\infty (U - u) dy - U v_w \quad (4-141)$$

This is a fairly general form of the momentum-integral relation, often called the Kármán integral relation after Theodore von Kármán, who first suggested this approach [von Kármán (1921)]. Dividing through by U^2 , we have

$$\frac{\tau_w}{\rho U^2} = \frac{1}{U^2} \frac{\partial}{\partial t} \int_0^\infty U \left(1 - \frac{u}{U} \right) dy + \frac{1}{U^2} \frac{\partial}{\partial x} \int_0^\infty U^2 \left(\frac{u}{U} \right) \left(1 - \frac{u}{U} \right) dy + \frac{1}{U^2} \frac{\partial U}{\partial x} \int_0^\infty U \left(1 - \frac{u}{U} \right) dy - \frac{v_w}{U}$$

Moreover, by extracting $U(x)$ out of the y directed integrals, using $\partial U^2 = 2U \partial U$, and

expanding, we get

$$\frac{\tau_w}{\rho U^2} = \frac{1}{U^2} \frac{\partial}{\partial t} \underbrace{\left[U \int_0^\infty \left(1 - \frac{u}{U}\right) dy \right]}_{\delta^*} + \frac{2}{U} \frac{\partial U}{\partial x} \underbrace{\int_0^\infty \left(\frac{u}{U}\right) \left(1 - \frac{u}{U}\right) dy}_{\theta} + \frac{\partial}{\partial x} \underbrace{\int_0^\infty \left(\frac{u}{U}\right) \left(1 - \frac{u}{U}\right) dy}_{\theta} + \frac{1}{U} \frac{\partial U}{\partial x} \underbrace{\int_0^\infty \left(1 - \frac{u}{U}\right) dy}_{\delta^*} - \frac{v_w}{U}$$

As might be expected, some of the terms are equivalent to the displacement and momentum thicknesses, [Eqs. \(4-4\)](#) and [\(4-6\)](#). These enable us to simplify the momentum-integral relation into

$$\frac{\tau_w}{\rho U^2} = \frac{C_f}{2} = \frac{1}{U^2} \frac{\partial}{\partial t} (U \delta^*) + \frac{\partial \theta}{\partial x} + (2\theta + \delta^*) \frac{1}{U} \frac{\partial U}{\partial x} - \frac{v_w}{U} \quad (4-142)$$

For steady flow with an impermeable wall, [Eq. \(4-142\)](#) reduces to

$$\frac{C_f}{2} = \frac{d\theta}{dx} + (2 + H) \frac{\theta}{U} \frac{dU}{dx} \quad \text{or} \quad \frac{C_f}{2\theta^*} = \frac{d\delta}{dx} + (2 + H) \frac{\delta}{U} \frac{dU}{dx} \quad (4-143)$$

which is the most popular form of the Kármán integral relation. As mentioned earlier, the shape factor H always exceeds unity, as per [Fig. 4-4](#), and, for laminar flow, varies between 2.0 at the stagnation point to about 3.5 at separation. In turbulent flow, $1.3 \leq H \leq 2.5$. Page 194

4-6.3 The Thermal-Energy Integral Relation

The thermal-energy integral is most easily derived by first multiplying the momentum [Eq. \(4-50b\)](#) by u and adding this to the thermal-energy [Eq. \(4-50c\)](#). The result is

$$\rho \frac{\partial h_0}{\partial t} + \rho \left(u \frac{\partial h_0}{\partial x} + v \frac{\partial h_0}{\partial y} \right) = \frac{\partial}{\partial y} (-q + u\tau) \quad (4-144)$$

where $h_0 = c_p T + \frac{1}{2} u^2$ is the total, or stagnation, enthalpy of the flow—neglecting $\frac{1}{2} v^2$ naturally. This equation will have important consequences in laminar compressible flow of gases ([Chap. 7](#)). Presently, our interest lies in integrating this relation from zero to infinity, while keeping it general enough for porous walls and unsteady flows. The result is

$$q_w = \frac{\partial}{\partial t} \int_0^\infty \rho c_p T dy + \frac{\partial}{\partial x} \int_0^\infty \rho u (h_0 - h_{0e}) dy - \rho c_p v_w (T_w - T_e) \quad (4-145)$$

This general form of the thermal-energy integral relation was first derived by Frankl (1934). For steady flow with impermeable walls and negligible dissipation, we are left with

$$q_w = \frac{d}{dx} \int_0^\infty \rho c_p u (T_w - T_e) dy \quad (4-146)$$

which is valid for any low-speed laminar or turbulent boundary layer. This expression appeared earlier in our flat-plate analysis as [Eq. \(4-28\)](#).

4-6.4 The Mechanical-Energy Integral Relation

To derive the mechanical-energy integral relation, we multiply continuity by $u^2 - U^2$ and momentum by $2u$, subtract, and integrate as before from the wall to infinity. The result is

$$\frac{2}{\rho} \int_0^\infty \tau \frac{\partial u}{\partial y} dy = \frac{\partial}{\partial t} \int_0^\infty u(U - u) dy + U^2 \frac{\partial}{\partial t} \int_0^\infty \left(1 - \frac{u}{U}\right) dy + \frac{\partial}{\partial x} \int_0^\infty u(U^2 - u^2) dy - U^2 v_w \quad (4-147)$$

The integral on the left-hand side is often called the *dissipation integral*:

$$\mathcal{D} = \int_0^\infty \tau \frac{\partial u}{\partial y} dy \quad (4-148)$$

On the right-hand side, we observe the emergence of the momentum thickness, the displacement thickness, and a third integral related to the so-called *kinetic-energy thickness* (also referred to as the *dissipation thickness*):

$$\delta_3 = \int_0^\infty \frac{u}{U} \left(1 - \frac{u^2}{U^2}\right) dy \quad (4-149)$$

As usual, division by U^3 leads to

$$\frac{2\mathcal{D}}{\rho U^3} = \frac{1}{U^3} \frac{\partial}{\partial t} \underbrace{\left[U^2 \int_0^\infty \frac{u}{U} \left(1 - \frac{u}{U}\right) dy \right]}_{\theta} + \frac{1}{U} \frac{\partial}{\partial t} \underbrace{\int_0^\infty \left(1 - \frac{u}{U}\right) dy}_{\delta^*} + \frac{1}{U^3} \frac{\partial}{\partial x} \underbrace{\left[U^3 \int_0^\infty \frac{u}{U} \left(1 - \frac{u^2}{U^2}\right) dy \right]}_{\delta_3} - \frac{v_w}{U}$$

From this expansion, it can be readily seen how [Eq. \(4-147\)](#) can be rewritten as

$$C_{\mathcal{D}} = \frac{2\mathcal{D}}{\rho U^3} = \frac{1}{U} \frac{\partial}{\partial t} (\theta + \delta^*) + \frac{2\theta}{U^2} \frac{\partial U}{\partial t} + \frac{1}{U^3} \frac{\partial}{\partial x} (U^3 \delta_3) - \frac{v_w}{U} \quad (4-150)$$

This compact form represents the mechanical-energy integral relation, first derived by Leibenson (1935), for both laminar and turbulent flows. Although it has been used under laminar conditions, it has proved to be more essential in modeling turbulent motions, where an extra correlation can be viewed as a “welcome addition” to models with uncertain parameters.

4-6.5 One-Parameter Integral Methods

Although the three integral formulations derived above are exact, they are typically used in conjunction with an *approximate* method that relies either on: (1) guessed velocity and temperature profiles or (2) empirical correlations among the integral parameters. Page 195

For momentum analysis, based on [Eq. \(4-143\)](#), one can approximate u using a one-parameter family of velocity profiles:

$$u(x, y) \approx U(x)f[y/\delta, P(x)] \quad (4-151)$$

where P is a suitable dimensionless parameter. From such a profile, we could then compute $\{\theta, \delta^*, H, \tau_w\}$ and substitute the resulting expressions into [Eq. \(4-143\)](#) to obtain a first-order differential equation for, say, $\delta(x)$.

Integral methods were dominated for decades by the intuitive, guessed-profile approach, often referred to as the Kármán–Pohlhausen approach, after a seminal paper by Pohlhausen (1921) and a concurrent paper by Kármán (1921). In short, Pohlhausen proposed a fourth-order polynomial of the form

$$\frac{u}{U} \approx 2\xi - 2\xi^3 + \xi^4 + \frac{\Lambda}{6}[\xi(1 - \xi)^3]; \quad \xi \equiv \frac{y}{\delta(x)} = \frac{\eta}{\eta_\delta} \quad (4-152)$$

where the *Pohlhausen parameter* $\Lambda = \delta^2(dU/dx)/\nu$ varies with the local pressure gradient, and ξ refers to the fraction of the distance from the wall to the 99 percent edge of the boundary layer. It can also be expressed as the ratio of the Blasius similarity variable, $\eta = y\sqrt{U/(2\nu x)}$ and its edge value, $\eta_\delta = \delta\sqrt{U/(2\nu x)} \approx 3.47188688$. We are careful to use ξ instead of η to avoid confusion with the Blasius variable when derivatives are taken with respect to ξ . Equation (4-152) fits five boundary conditions and, when substituted into the momentum-integral relation (4-143), produces a differential equation that is easy to solve. Unfortunately, it is *not* very accurate, as detailed in Sec. 4-1.

There have been several other methods that rely on profile assumptions, some involving multiple parameters [Rosenhead (1963)]. In what follows, a correlation by Thwaites (1949) is presented, which is sufficiently accurate for laminar flow.

4-6.6 The Correlation Method of Thwaites

Thwaites (1949) modified and improved an idea introduced by Holstein and Bohlen (1940), who cleverly rewrote the momentum-integral [Eq. \(4-143\)](#) in terms of an effective parameter λ ,

$$\lambda = \frac{\theta^2}{\nu} \frac{dU}{dx} = \left(\frac{\theta}{\delta}\right)^2 \Lambda; \quad \Lambda = -\frac{\delta^2}{\mu U} \frac{dp}{dx} = \frac{\delta^2}{\nu} \frac{dU}{dx} \quad (4-153)$$

Their simple but inspired idea was to multiply the momentum-integral relation, [Eq. \(4-143\)](#), by $U\theta/\nu$, with the result being

$$\frac{\tau_w \theta}{\mu U} = \frac{U\theta}{\nu} \frac{d\theta}{dx} + \frac{\theta^2 U'}{\nu} (2 + H) \quad (4-154)$$

Now H and the left-hand side of this equation are dimensionless boundary-layer functions and thus, by design, are correlated reasonably well by a single parameter (λ in this case). Following Holstein and Bohlen (1940), we have

$$\frac{\tau_w \theta}{\mu U} \approx S(\lambda) \quad (\text{shear correlation}) \quad \text{and} \quad H = \frac{\delta^*}{\theta} \approx H(\lambda) \quad (\text{shape-factor correlation}) \quad (4-155)$$

Recalling that $\theta d\theta = d(\frac{1}{2}\theta^2)$, [Eq. \(4-154\)](#) may be rewritten as

$$S(\lambda) \approx \frac{U}{2} \frac{d}{dx} \left[\frac{1}{U'} \left(\frac{\theta^2 U'}{\nu} \right) \right] + 2 \left(\frac{\theta^2 U'}{\nu} \right) + \left(\frac{\theta^2 U'}{\nu} \right) H \quad \text{or} \quad S(\lambda) \approx \frac{U}{2} \frac{d}{dx} \left(\frac{\lambda}{U'} \right) + 2\lambda + \lambda H$$

where the presence of λ is evident. Rearranging, we get

$$U \frac{d}{dx} \left(\frac{\lambda}{U'} \right) \approx 2[S(\lambda) - \lambda(2 + H)] \quad \text{and so} \quad F(\lambda) \equiv \frac{U}{\nu} \frac{d\theta^2}{dx} \approx 2[S(\lambda) - \lambda(2 + H)] \quad (4-156)$$

Whereas earlier workers would have proposed a family of profiles to evaluate the parametric functions in [Eq. \(4-156\)](#), such as Pohlhausen's polynomials, Thwaites (1949) considered the entire collection of known analytic and experimental results to determine if they could be approximated by a set of average one-parameter functions. As shown in [Fig. 4-27](#), he discovered an excellent linear correlation for the function F , namely,

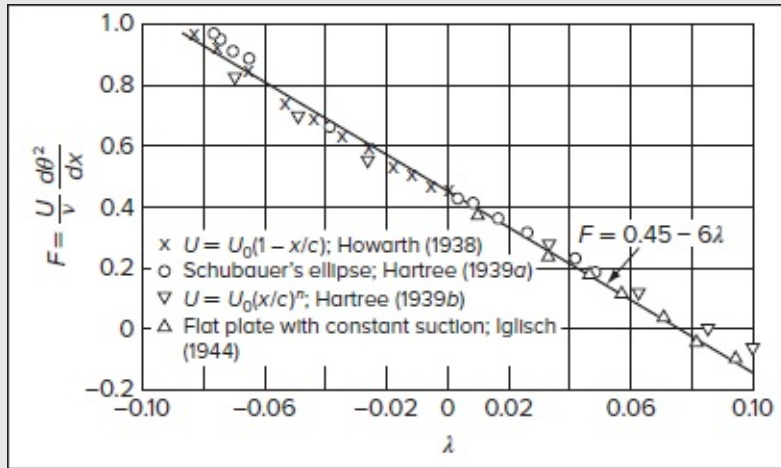


FIGURE 4-27

Empirical correlation of the boundary-layer function in [Eq. \(4-156\)](#). [After Thwaites (1949).]

$$F(\lambda) \approx 0.45 - 6.0\lambda \quad [\text{Thwaites (1949)}] \quad (4-157)$$

Moreover, if $F = a - b\lambda$ is inserted into [Eq. \(4-156\)](#), we get a closed-form solution that the reader may verify as an exercise:

$$\frac{\theta^2}{\nu} = \frac{a}{U^b} \left(\int_{x_0}^x U^{b-1} dx + C \right) \quad (4-158)$$

Page 196 If x_0 is a stagnation point, we must set $C = 0$ to avoid an infinite momentum

thickness where $U = 0$. Subsequently, Thwaites is able to show that $\theta(x)$ is predicted very accurately (within ± 3 percent), for all types of laminar boundary layers, by the simple quadrature

$$\theta^2 \approx \frac{0.45\nu}{U^6} \int_0^x U^5 dx \quad (4-159)$$

Having found θ from this relation, one is able to evaluate $\lambda = \theta^2 U' / \nu$ along with the skin friction and displacement thickness from the one-parameter correlations,

$$\tau_w = \frac{\mu U}{\theta} S(\lambda) \quad \text{and} \quad \delta^* = \theta H(\lambda) \quad (4-160)$$

Thwaites' correlations for $S(\lambda)$ and $H(\lambda)$ are provided in [Table 4-8](#) and plotted in [Fig. 4-28](#). A simple and accurate curve fit to the shear function, shown in [Fig. 4-28b](#), is

TABLE 4-8

Shear and shape functions correlated by Thwaites (1949)

λ	$H(\lambda)$	$S(\lambda)$	λ	$H(\lambda)$	$S(\lambda)$
+0.25	2.00	0.500	-0.056	2.94	0.122
0.20	2.07	0.463	-0.060	2.99	0.113
0.14	2.18	0.404	-0.064	3.04	0.104
0.12	2.23	0.382	-0.068	3.09	0.095
0.10	2.28	0.359	-0.072	3.15	0.085
+0.080	2.34	0.333	-0.076	3.22	0.072
0.064	2.39	0.313	-0.080	3.30	0.056
0.048	2.44	0.291	-0.084	3.39	0.038
0.032	2.49	0.268	-0.086	3.44	0.027
0.016	2.55	0.244	-0.088	3.49	0.015
0.0	2.61	0.220	-0.090	3.55	0.000
			(Separation)		
-0.016	2.67	0.195			
-0.032	2.75	0.168			
-0.040	2.81	0.153			
-0.048	2.87	0.138			
-0.052	2.90	0.130			

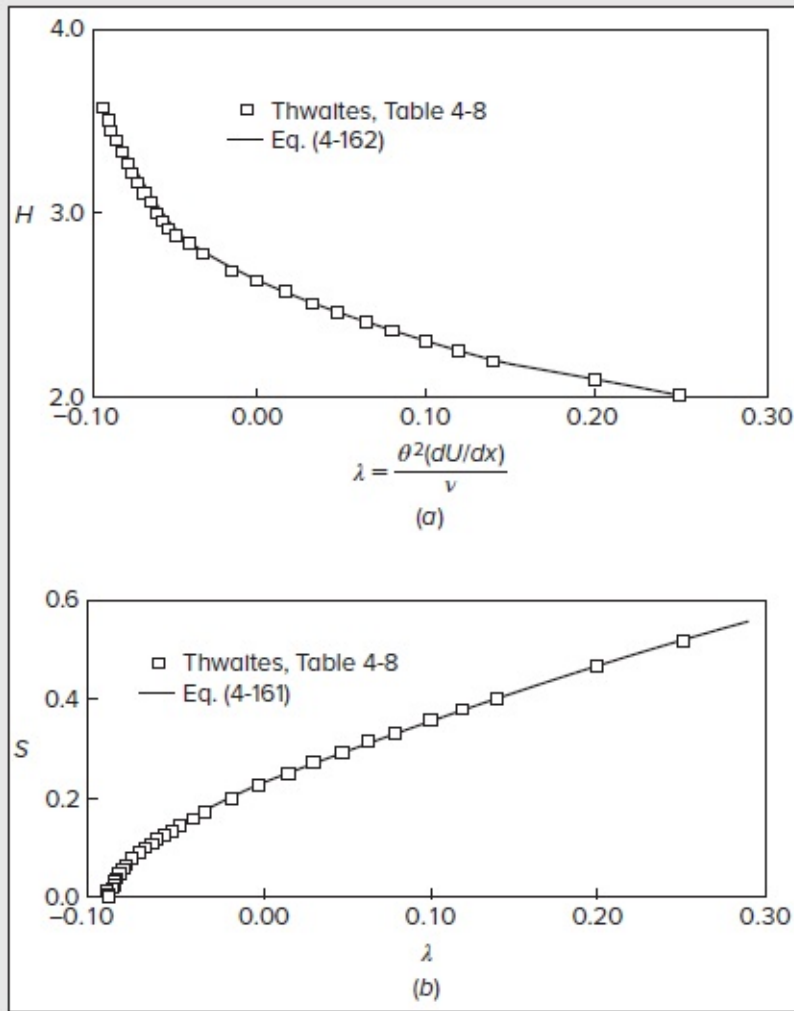


FIGURE 4-28

The laminar boundary-layer correlated functions by Thwaites (1949): (a) shape factor; (b) shear stress with curve fits.

$$S(\lambda) \approx (\lambda + 0.09)^{0.62} \quad (4-161)$$

Being unable to construct a comparably simple formula for the shape-factor function $H(\lambda)$, White (2006) offers:

$$H(\lambda) \approx 2.0 + 4.14z - 83.5z^2 + 854z^3 - 3337z^4 + 4576z^5 \quad (4-162)$$

where $z = \frac{1}{4} - \lambda$. The fit in [Fig. 4-28a](#) is adequate, though laborious. Page 197

The accuracy of the Thwaites method is about ± 5 percent for favorable or mild adverse gradients but can be as much as ± 15 percent or more near the separation point. Nevertheless, since the method is an average of several solutions, it can be regarded as a practical one-

parameter tool. If more accuracy is desired, a numerical solution is recommended.

4-6.7 Application to the Howarth Decelerating Flow

To illustrate the simplicity of Thwaites' method, we apply it to the Howarth linearly decelerating flow of [Eq. \(4-136\)](#) and [Fig. 4-25](#), with $dU/dx = -U_0/L = \text{const}$. The momentum thickness is computed, approximately, from [Eq. \(4-159\)](#):

$$\theta^2 = \frac{0.45\nu}{U_0^6(1-x/L)^6} \int_0^x U_0^5 \left(1 - \frac{x}{L}\right)^5 dx = 0.075 \frac{\nu L}{U_0} \left[\left(1 - \frac{x}{L}\right)^{-6} - 1 \right]$$

from which, by definition,

$$\lambda = \frac{\theta^2}{\nu} \frac{dU}{dx} = -0.075 \left[\left(1 - \frac{x}{L}\right)^{-6} - 1 \right] \quad (4-163)$$

With $\lambda(x)$ given by this approximate expression, we can compute the wall shear $\tau_w(x)$ from the function $S(\lambda)$ in [Table 4-8](#) or [Fig. 4-28b](#). As for the separation point, it can be predicted from $\lambda_{\text{sep}} \approx -0.09$ and so,

$$\frac{x_{\text{sep}}}{L} = 1 - (2.2)^{-1/6} \approx 0.123$$

This value falls within 3 percent of the precise finite-difference result of $x_{\text{sep}} = 0.120L$. Further, if $U(x)$ is complicated algebraically, it may be necessary to carry out the integral of U^5 in [Eq. \(4-159\)](#) numerically—which is still much simpler than a full-blown numerical simulation. Page 198

4-6.8 Application to Laminar Flow Past a Circular Cylinder

Both the accuracy and the dilemma of a bluff-body boundary-layer calculation are illustrated by the circular cylinder. In terms of the dimensionless arc length $x^* = x/a$, where a is the radius, the potential-flow velocity distribution is

$$\frac{U}{U_\infty} = 2\sin x^* = 2.0x^* - 0.333x^{*3} + 0.167x^{*5} + \dots \quad (4-164)$$

from which we can easily generate boundary-layer solutions of any type (integral, series, or digital computer). Calculations of this type have been made. Separation is predicted at an angle $x^* = \phi = 104.5^\circ$ in numerical results by Terrill (1960), which we might (mistakenly) think would be reproduced in an experimental laminar flow over a cylinder.

Unfortunately, the broad wake caused by bluff-body separation is a *first-order effect*, i.e., it is so different from potential flow predictions (e.g., [Figs. 1-5](#) and [1-6](#)) that it alters $U(x)$ everywhere, including the stagnation point. For example, the experiment of Hiemenz (1911)

for a cylinder at a Reynolds number of $Re_a = U_\infty a / \nu = 9500$ can be fitted by

$$\frac{U}{U_\infty} \approx 1.814x^* - 0.271x^{*3} - 0.0471x^{*5} \quad (4-165)$$

which is quite different from potential flow. Even the stagnation velocity gradient (1.814) is 9.3 percent less than the potential-flow value (2.0), and the maximum velocity ($1.595U_\infty$) occurs at $\phi = 71.2^\circ$, instead of $2.0U_\infty$ at $\phi = 90^\circ$. The two distributions are illustrated in [Fig. 4-29a](#), where it is clear that the potential flow is not suitable for boundary-layer calculation. Once the actual $U(x)$ is known, the various theories can be used and compared, as demonstrated in [Fig. 4-29b](#). Interestingly, the finite-difference method of Smith and Clutter (1963) places ϕ_{sep} at 80° , whereas Thwaites' integral method, [Eq. \(4-159\)](#), predicts 78.5° and a Howarth–Tifford series (including 19 terms) predicts 83° . All three are in reasonable agreement with the Hiemenz (1911) experimental observation of $\phi_{\text{sep}} \approx 80.5^\circ$. Page 199

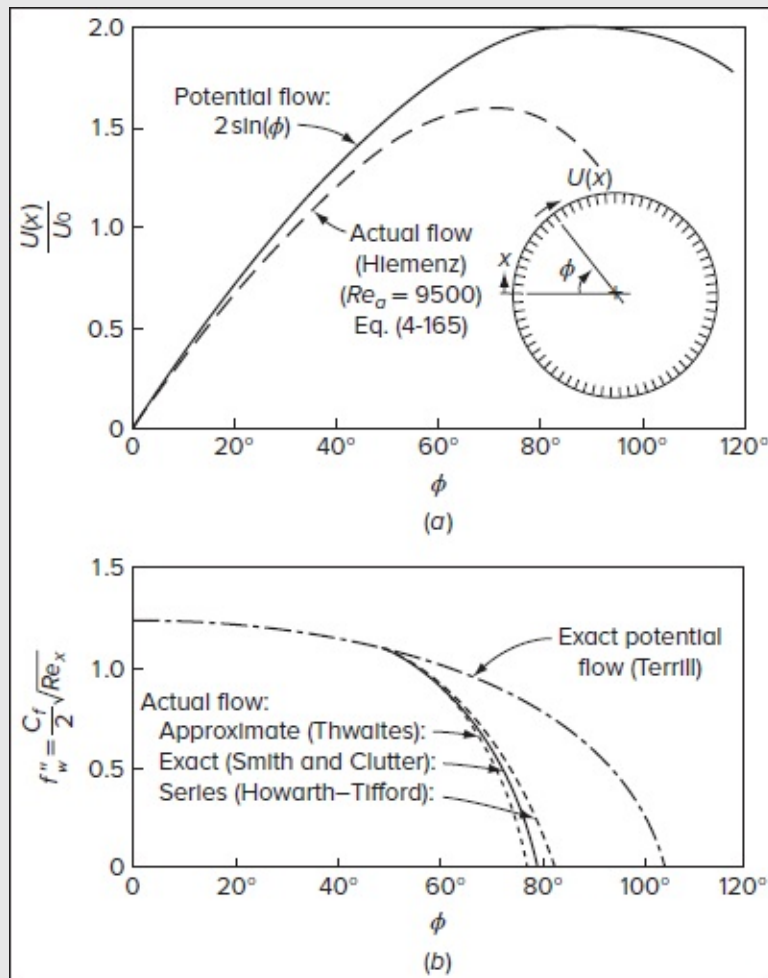


FIGURE 4-29

Comparison of potential-flow and actual-flow computations for a circular cylinder: (a) potential and actual velocity distributions; (b) potential-flow and actual-flow skin friction.

It can thus be seen that all laminar-boundary-layer estimations hinge upon knowing the correct $U(x)$ accurately. It is presently a very active area of research to develop coupled methods in which a separating boundary layer interacts with and strongly modifies the external inviscid flow.

4-6.9 Laminar-Separation-Point Prediction

One test of the general effectiveness of Thwaites' theory is to see how well [Eq. \(4-159\)](#) predicts laminar separation for a variety of $U(x)$ freestream velocity distributions. This can be accomplished by applying [Eq. \(4-159\)](#) to the distribution, computing $\theta(x)$, and noting the position where $\lambda_{\text{sep}} = \theta^2(dU/dx)/\nu \approx -0.09$. Some results are given in [Table 4-9](#) for 11 different flows with adverse pressure gradients. It is gratifying that the separation position error is less than 4 percent, although this success is tempered by our previous observation that large-scale separation alters rather substantially the external velocity and pressure distributions.

TABLE 4-9

Laminar-separation-point prediction by Thwaites' method

$U(x)$	x_{sep} (exact)	Thwaites	
		x_{sep}	Error [%]
Howarth (1938)			
$1 - x$	0.120	0.123	+2.5
Tani (1949)			
$1 - x^2$	0.271	0.268	-1.1
$1 - x^4$	0.462	0.449	-2.8
$1 - x^8$	0.640	0.621	-3.0
Terrill (1960)			
$\sin(x)$	1.823	1.800	-1.3
Curle (1958)			
$x - x^3$	0.655	0.648	-1.1
Görtler (1957)			
$\cos(x)$	0.389	0.384	-1.3
$(1 - x)^{1/2}$	0.218	0.221	+1.3
$(1 - x)^2$	0.0637	0.0652	+2.4
$(1 + x)^{-1}$	0.151	0.158	+4.6
$(1 + x)^{-2}$	0.0713	0.0739	+3.6

4-7 NUMERICAL SOLUTIONS

The integral methods discussed in Sec. 4-6 are easy to use but limited in accuracy. The similarity solutions of Sec. 4-3 are accurate but limited in applicability. If one is faced with a heavy-duty study of nonsimilar boundary layers and needs more precision, then a numerical model is suggested.

For convenience, let us repeat the two-dimensional, steady, laminar, boundary-layer equations that we wish to solve:

$$\text{Continuity:} \quad \frac{\partial u}{\partial x} + \frac{\partial v}{\partial y} = 0 \quad (4-56a)$$

$$\text{Momentum:} \quad u \frac{\partial u}{\partial x} + v \frac{\partial u}{\partial y} = U \frac{dU}{dx} + \nu \frac{\partial^2 u}{\partial y^2} \quad (4-56b)$$

These equations are *parabolic* in x , so the numerical models are all of the downstream-marching type. The usual inputs for any method are (1) known upstream profiles $u(0, y)$ and $v(0, y)$, (2) known freestream velocity $U(x)$, and (3) known wall conditions $u(x, 0) = 0$ and $v(x, 0) = v_w(x)$.

The laminar-boundary-layer equations are *parabolic* or “marching” in character and thus relatively easy to model with CFD. The literature contains scores of numerical models, many of which are summarized in three boundary-layer texts: Schetz and Bowersox (2011), Cebeci and Cousteix (1998), and Schlichting and Gersten (2017). The first two of these texts include FORTRAN codes for various boundary-layer models. Moreover, Schetz’ work has been extended, as sponsored by the National Science Foundation, in the form of Internet Boundary Layer Applets, by Devenport and Page 200Schetz (2002). These excellent Applets are JAVA codes that include laminar and turbulent flows, both incompressible and compressible. With such resources available, the present text will not attempt to become a CFD monograph. We will simply present a simple, direct boundary-layer model that is effective and useful. The reader may wish to learn from this simple method and then advance to more elaborate codes.

Two types of marching strategies exist: *explicit* and *implicit*. In the explicit scheme, the downstream profiles $u(x + \Delta x, y)$ and $v(x + \Delta x, y)$ are calculated immediately from the known upstream profiles $u(x, y)$ and $v(x, y)$ by direct application of an algebraic model of Eqs. (4-56a)–(4-56b). Explicit models are simple but become unstable numerically unless a very small step size Δx is used.

An implicit method is also an algebraic model of Eqs. (4-56a)–(4-56b), where all points on the downstream profile $u(x + \Delta x)$ are *solved simultaneously* by either iteration or matrix inversion. The computation time per step Δx can be larger than for explicit schemes, but there is no numerical instability.

The methods we will illustrate are *finite-difference* schemes, which model derivatives by differences between nodal points on a rectangular (x, y) mesh. There are also schemes that are based on the *finite-element* method [Beer (2001) or Löhner (2001)], which is quite different in principle—simulating whole fields or “elements” of flow bounded by mesh points.

4-7.1 An Explicit Finite-Difference Model for Plane Flow

For both of our methods, we use the rectangular finite-difference mesh shown in [Fig. 4-30](#).

Subscripts are convenient: $u_{m,n}$ denotes the velocity u at mesh point (m, n) , located at $(x, y) = [(m - 1)\Delta x, (n - 1)\Delta y]$. Thus $(m, n) = (1, 1)$ locates the origin, $(x, y) = (0, 0)$. The step sizes Δx and Δy need not be equal. We also locate the vertical velocity $v_{m,n}$ and (later) temperature $T_{m,n}$ at the same mesh points. All values at station m are assumed known or “previous,” as we use them to march downstream and predict the “next” local values at $(m + 1)$. Let the total mesh be $M \times N$ large, where $m = M$ is the exit, $n = N$ is the freestream, $m = 1$ is the inlet, and $n = 1$ is the wall.

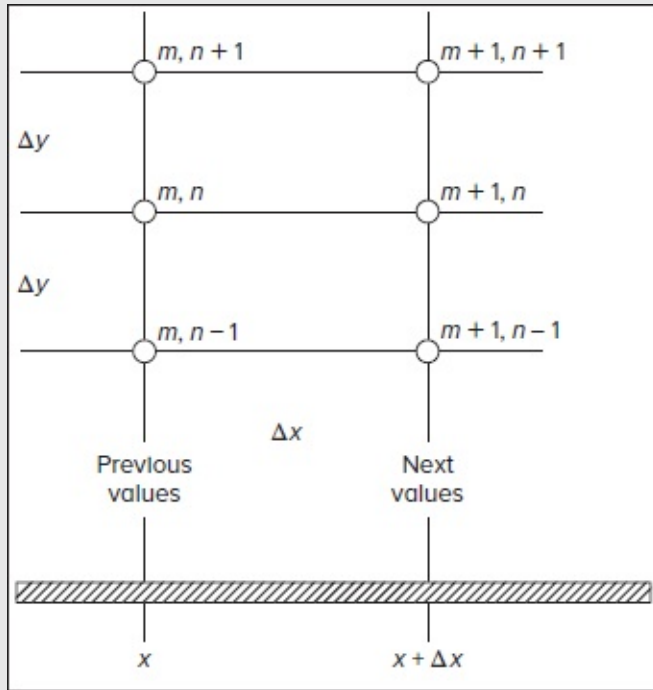


FIGURE 4-30

Finite-difference mesh for a two-dimensional boundary layer.

Let us begin by writing a finite-difference model of the momentum Eq. (4-56b), representing level n of the mesh:

$$u_{m,n} \frac{u_{m+1,n} - u_{m,n}}{\Delta x} + v_{m,n} \frac{u_{m,n+1} - u_{m,n-1}}{2\Delta y} \approx \frac{U_{m+1}^2 - U_m^2}{2\Delta x} + \nu \frac{u_{m,n+1} - 2u_{m,n} + u_{m,n-1}}{\Delta y^2} \quad (4-166)$$

Now, moving from left to right, let us describe each term. The first term uses a *forward* difference to model $\partial u / \partial x$. The second term uses a *central* difference to represent $\partial u / \partial y$, thus keeping the model at level “ n .” The third term is the pressure gradient, using the form $UdU/dx = d(\frac{1}{2}U^2)/dx$, and writing it as a forward difference—note that U_{m+1} is *known* because $U(x)$ is the freestream velocity. Finally, the fourth term is a central-difference model of $\partial^2 u / \partial y^2$.

All terms center about level “ n ,” which is good practice for numerical accuracy. The only unknown velocity in the model is $u_{m+1,n}$, which we may solve for and write as follows:

$$u_{m+1,n} \approx (\alpha - \beta)u_{m,n+1} + (1 - 2\alpha)u_{m,n} + (\alpha + \beta)u_{m,n-1} + \frac{U_{m+1}^2 - U_m^2}{2u_{m,n}} \quad \text{with} \quad \alpha = \frac{\nu \Delta x}{u_{m,n} \Delta y^2} \quad \beta = \frac{v_{m,n} \Delta x}{2u_{m,n} \Delta y} \quad (4-167)$$

The right-hand terms in [Eq. \(4-167\)](#) are all known from the “previous” station. We can solve for $u_{m+1,n}$ immediately, i.e., the model is *explicit*. However, algebraic recurrence relations such as [Eq. \(4-167\)](#) require, for numerical stability, that all coefficients in the previous u_m be positive. In this case, $\alpha < \frac{1}{2}$ and $\beta < \alpha$. The restraints limit both step sizes in the mesh:

$$\text{Numerical stability requirements:} \quad \Delta x < \frac{u_{\min} \Delta y^2}{2\nu} \quad \text{and} \quad \Delta y < \frac{2\nu}{|v_{\max}|} \quad (4-168)$$

We need the absolute value on v_{\max} because v is positive in adverse gradients but may be negative in favorable gradients. Usually u_{\min} occurs near the wall and v_{\max} near the freestream. During this explicit computation, we have to monitor $\alpha(y)$ and $\beta(y)$ to make sure that [Eqs. \(4-168\)](#) are satisfied.

With $u_{m+1,n}$ known from [Eq. \(4-167\)](#), we find $v_{m+1,n}$ by modeling the continuity Eq. (4-56a). The simplest way would be a forward difference for both terms:

$$\frac{u_{m+1,n} - u_{m,n}}{\Delta x} + \frac{v_{m+1,n} - v_{m+1,n-1}}{\Delta y} \approx 0$$

We start with $n = 2$ to compute $v_{m+1,2}$ because $v_{m+1,1} = v_w$ is known. However, numerical accuracy will be poor. Moving $\partial v / \partial y$ up to a central difference $(v_{m+1,n+1} - v_{m+1,n-1}) / (2\Delta y)$ at level n is self-defeating because we skip the value we want, $v_{m+1,n}$. Wu (1961) suggests moving $\partial u / \partial x$ down to level $n - \frac{1}{2}$ by using an average value:

$$\left. \frac{\partial u}{\partial x} \right|_{\text{avg}} \approx \frac{1}{2} \left[\frac{u_{m+1,n} - u_{m,n}}{\Delta x} + \frac{u_{m+1,n-1} - u_{m,n-1}}{\Delta x} \right]$$

We use this expression instead in the continuity model and solve explicitly for the next vertical velocity:

$$v_{m+1,n} \approx v_{m+1,n-1} - \frac{\Delta y}{2\Delta x} (u_{m+1,n} - u_{m,n} + u_{m+1,n-1} - u_{m,n-1}) \quad (4-169)$$

There is no instability in this relation other than that already required by [Eqs. \(4-168\)](#). We begin at $n = 2$ and move upward.

Equations (4-167) and (4-169) constitute a satisfactory, explicit, laminar, boundary-layer model which may be readily programmed on a personal computer. Since we are “marching,”

there is really no need to use the “ m ” subscript, e.g., to dimension $u(1000, 50)$ and $v(1000, 50)$ for 1000 downstream steps. One can merely denote station m as $up(50)$ and $vp(50)$ for “previous” and station $m + 1$ as $un(50)$ and $vn(50)$ for “next,” keep the results long enough to print them, reinitialize $up(n) = un(n)$ and $vp(n) = vn(n)$, and repeat. During the computation, one should monitor the stability conditions (4-168) and check that the outer values $u_{m,N-1}$ and $u_{m,N}$, etc., merge smoothly with the freestream velocity U_m , since the boundary-layer thickness is *a priori* unknown.

4-7.1.1 APPLICATION TO HOWARTH LINEARLY DECELERATING FLOW. For illustration, [Eqs. \(4-167\)](#) and [\(4-169\)](#) are programmed to solve the Howarth problem with $U = U_0(1 - x/L)$ from $x = 0$ until separation. Arbitrary values can be taken for U_0 , L , and ν , since the results will be nondimensionalized. [Figure 4-31](#) shows the computed values of normalized skin friction $C_f/C_f(0)$ compared with the Howarth series solution, and Thwaites’ method using $S(\lambda)$ when λ is given by [Eq. \(4-163\)](#). We see that the computer solution equals the Howarth series for $x/L \leq 0.1$ and then is more accurate near separation, $x_{\text{sep}}/L \approx 0.1$. Thwaites’ method is quite good (± 5 percent) over the entire range. The explicit computer method required 3000 steps, with Δx being extremely restricted by [Eqs. \(4-168\)](#) near separation.

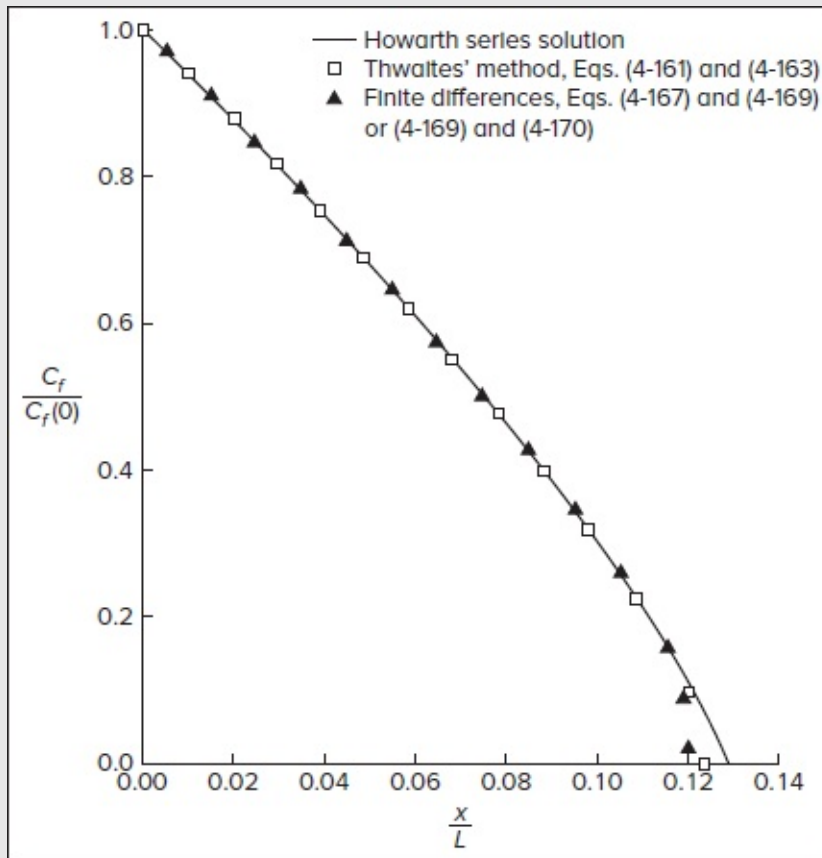


FIGURE 4-31

4-7.2 An Implicit Finite-Difference Model

In an implicit model, more of the “next” terms are used to approximate the derivatives, resulting in simultaneous algebraic equations. In the present application, we model the viscous or second-order derivative term in the momentum equation at the next station, $m + 1$, using

$$\frac{\partial^2 u}{\partial y^2} \approx \frac{u_{m+1,n+1} - 2u_{m+1,n} + u_{m+1,n-1}}{\Delta y^2}$$

By replacing the “previous” second derivative in the explicit model with this expression, the result is that each n th-level equation has three unknowns:

$$-\alpha u_{m+1,n+1} + (1 + 2\alpha)u_{m+1,n} - \alpha u_{m+1,n-1} \approx u_{m,n} - \beta(u_{m,n+1} - u_{m,n-1}) + \frac{U_{m+1}^2 - U_m^2}{2u_{m,n}} \quad (4-170)$$

where α and β have the same meaning as in [Eq. \(4-167\)](#). Now, we must solve simultaneously for the $u_{m+1,n}$ —the method is *implicit*. The benefit is that the results are unconditionally stable, regardless of the step sizes Δx and Δy . Nonetheless, it is a good habit to select Δy small enough so that at least 20 points fall within the boundary layer, and Δx should be small enough that changes in $u_{m,n}$ from station to station remain small, say, less than 5 percent.

One way to solve [Eq. \(4-170\)](#) is by Gauss–Seidel iteration: After the dominant term $u_{m+1,n}$ is computed, $u_{m+1,n\pm 1}$ is moved over, and the right-hand side is swept repeatedly until the values of u do not change. Convergence is not guaranteed unless Δx and Δy are relatively small. One may also obtain a direct solution by Gauss elimination or matrix inversion.

4-7.2.1 INVERSION OF A TRIDIAGONAL MATRIX. Assuming that $n = 1$ coincides with the wall and $n = N$ corresponds to the freestream, [Eqs. \(4-170\)](#) represent $N - 2$ equations, each with three unknowns: The matrix is thus *tridiagonal*. Such matrices are easy to invert using a *tridiagonal matrix algorithm* (TDMA) [Sec. 4.2-7, Patankar (1980)]. It works because there are only two unknowns at the bottom, $n = 2$, where $u_{n=1} = 0$ (no slip), and only two unknowns at the top, $n = N$, where $u_N = U(x)$. We can begin at the bottom and eliminate one variable at a time until we reach the top, where u_{N-1} is immediately recovered. We then work our way back to the bottom (“back substitution”), picking up u_n in terms of U_{n+1} until the final value, u_2 , is secured.

The TDMA is outlined as follows. Dropping the “ m ” subscripts as superfluous, [Eq. \(4-170\)](#) may be written, at any n , as

$$(1 + 2\alpha_n)u_n = \alpha_n u_{n+1} + \alpha_n u_{n-1} + C_n$$

where C_n denotes the entire right-hand side of [Eq. \(4-170\)](#). The desired back-substitution recurrence relation has the form

$$u_n = P_n u_{n+1} + Q_n \quad (4-171)$$

We first calculate P_n and Q_n , starting at the bottom, where $u_1 = 0$, by computing

$$P_2 = \frac{\alpha_2}{1 + 2\alpha_2} \quad \text{and} \quad Q_2 = \frac{C_2}{1 + 2\alpha_2} \quad (4-172)$$

We then evaluate the remaining values of P_n and Q_n using the recurrence relations:

$$P_n = \frac{\alpha_n}{1 + 2\alpha_n - \alpha_n P_{n-1}} \quad Q_n = \frac{C_n + \alpha_n Q_{n-1}}{1 + 2\alpha_n - \alpha_n P_{n-1}} \quad (4-173)$$

At the top, since $u_N = U$, the value of the velocity can be readily deduced:

$$u_{N-1} = \frac{\alpha_{N-1}U + \alpha_{N-1}Q_{N-2} + C_{N-1}}{1 + 2\alpha_{N-1} - \alpha_{N-1}P_{N-2}} \quad (4-174)$$

where U is the freestream velocity at that station. With u_{N-1} , P_n , and Q_n known, we can work our way downward using [Eq. \(4-171\)](#) until we reach the final unknown, u_2 . The algorithm works extremely well for a well-behaved matrix such as [Eq. \(4-170\)](#).

As shown in [Fig. 4-31](#), the implicit method was also applied to the Howarth distribution using $\Delta x/L = 0.001$, thus leading to results that are as accurate as the explicit method. Not only were the run times associated with the implicit method shorter than those of the explicit method, there were no instabilities and no special need to decrease Δx near separation.

Finally, the method was run for a circular cylinder with the Hiemenz experimental velocity distribution [Eq. (4-162)]. Resulting boundary-layer profiles are shown in [Fig. 4-32](#) at equally spaced angular increments of $\Delta\theta = 10^\circ$, as measured from the stagnation point. Separation was predicted at $\theta = 81^\circ$ (see [Fig. 4-29b](#)) and the nominal Reynolds number was taken as $U_0 R/\nu = 10^5$, to show the actual boundary-layer thickness, which is about 1 percent of the radius of the cylinder. In the favorable gradient for θ up to 60° , the profiles are strongly curved and have increasing wall shear stress. From 60° onward, as the freestream levels off and begins to decelerate, the profiles become thicker and then S-shaped, thus leading to early separation.

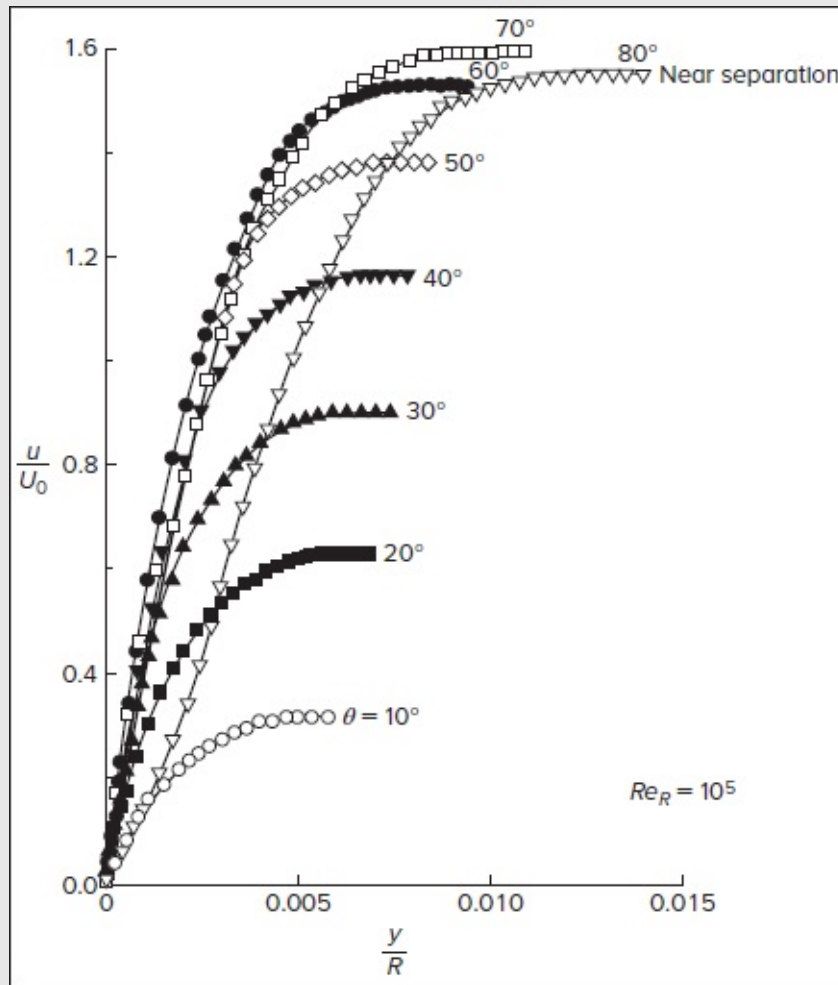


FIGURE 4-32

Laminar boundary layers on a cylinder computed by the implicit numerical method of [Eqs. \(4-169\) and \(4-170\)](#). The freestream velocity is given by [Eq. \(4-165\)](#).

4-8 THERMAL-BOUNDARY-LAYER CALCULATIONS

The previous three sections were devoted to velocity calculations, because the assumption of incompressible flow with constant viscosity uncouples the velocity and enables it to be calculated independently of the temperature. Afterward, the temperature can be obtained from the thermal-energy equation (4-50c) and the known velocity solution. Let us now review some of the methods that enable us to determine the temperature distribution under fairly arbitrary conditions.

Almost all incompressible flow analyses assume that dissipation is negligible and focus on the simplified thermal-energy equation

Differential form:

$$u \frac{\partial T}{\partial x} + v \frac{\partial T}{\partial y} \approx \frac{k}{\rho c_p} \frac{\partial^2 T}{\partial y^2} \quad (4-175a)$$

Integral form:

$$q_w = \frac{d}{dx} \left[\int_0^\infty \rho u c_p (T - T_e) dy \right] \approx \frac{d}{dx} \left[\int_0^{\delta_T} \rho u c_p (T - T_e) dy \right] \quad (4-175b)$$

Note that it is not necessary to integrate beyond the thermal boundary layer given that $T \approx T_e$ for $y > \delta_T$. Moreover, due to the linearity of the thermal-energy equation, if two solutions $T_1(x, y)$ and $T_2(x, y)$ are obtained for a given $U(x)$, then their sum $T_1 + T_2$ is also a solution. This, of course, is not true of two velocity solutions u_1 and u_2 .

As with momentum analyses, three basic approaches may be considered:

1. Series expansions [Meksyn (1961)], which are now obsolete.
2. Integral-energy methods—13 of these are discussed in an interesting review by Spalding and Pun (1962). We focus here on Thwaites' method.
3. Numerical methods—many have been proposed, including well-developed user-friendly computer codes [Tannehill et al. (1997)]. We will apply the same primitive-variable technique of Sec. 4-7.1 to the present heat-transfer problem. Finite differences are suggested when there are arbitrary variations of $U(x)$, $T_e(x)$, and $T_w(x)$.

4-8.1 One-Parameter Integral Method: Variable $U(x)$, Constant $(T_w - T_e)$

One integral approach for estimating the amount of heat transfer is to guess both velocity and temperature profiles and substitute them into Eq. (4-175b). However, favorable agreement with full-blown solutions can be achieved by a simple laminar-correlation scheme that mirrors Thwaites' momentum method described in Sec. 4-6.6.

Consider any thickness measure of a thermal boundary layer, Δ , such as the enthalpy thickness from [Eq. \(4-29\)](#). Eckert (1942) theorizes that the rate of growth of such a thickness must depend only on local stream parameters and fluid properties:

$$\frac{d\Delta}{dx} \approx f\left(\Delta, U, \frac{dU}{dx}, \nu, \frac{k}{\rho c_p}\right)$$

If the temperature difference $(T_w - T_e)$ is constant, it would have no effect, since every term in the linear Eq. (4-175a) is proportional to T . By dimensional analysis, we can rewrite the above expression as

$$\frac{U}{\nu} \frac{d\Delta^2}{dx} = f\left(\frac{\Delta^2}{\nu} \frac{dU}{dx}, Pr\right) \quad (4-176)$$

Note the close resemblance of this relation to the Holstein–Bohlen formulation, [Eq. \(4-156\)](#).

If one chooses Δ as the enthalpy thickness δ_h , a substantial amount of integration is required, thus leading to excessive charts and formulas. An elegant simplification of this procedure is proposed by Smith and Spalding (1958). With an eye toward direct computation of the heat flux, they suggest using instead the so-called conduction thickness

$$\delta_c = \frac{k(T_w - T_e)}{q_w} \quad (4-177)$$

and so,

$$\frac{U}{\nu} \frac{d\delta_c^2}{dx} = f\left(\frac{\delta_c^2 U'}{\nu}, Pr\right) \quad (4-178)$$

Page 205

where numerical values can be selected from the Falkner–Skan solutions for $U(x) = Cx^m$. In terms of m and the heat-transfer parameter $G(Pr, \beta)$ from [Eq. \(4-100\)](#), our suitable parameters become

$$\frac{U}{\nu} \frac{d\delta_c^2}{dx} = \frac{2(1-m)}{(1+m)G^2} \quad \text{and} \quad \lambda_c = \frac{\delta_c^2 U'}{\nu} = \frac{2m}{(1+m)G^2} \quad (4-179)$$

[Figure 4-33](#) shows a typical plot of [Eq. \(4-178\)](#), using these relations for $Pr = 1$. We can share Smith and Spalding's delight that the curve is nearly linear over the wide range of $-0.18 \leq \beta \leq +2.0$. Being true for all Prandtl numbers, Smith and Spalding propose a general approximation

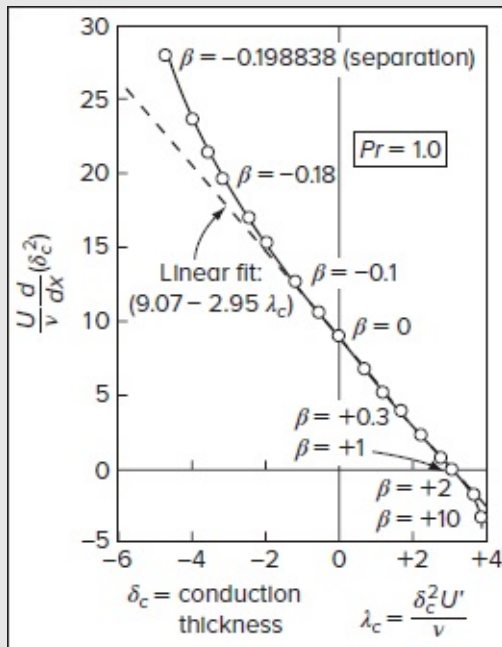


FIGURE 4-33

The correlation of [Eq. \(4-178\)](#) from the Falkner–Skan solutions ([Table 4-7](#)) compared with the linear approximation proposed by Smith and Spalding

(1958).

$$\frac{U}{\nu} \frac{d\delta_c^2}{dx} \approx a(Pr) - b(Pr)\lambda_c \quad (4-180)$$

where a and b are provided in [Table 4-10](#). Equation (4-180) is the precise analog of Thwaites' linear fit, [Eq. \(4-157\)](#), with the same exact analytic solution,

TABLE 4-10

Constants $a(Pr)$ and $b(Pr)$ for use in Eq. (4-182)

	Pr	$a^{-1/2}$	b
Air	0.0	0.0	2.0
	0.001	0.0173	2.06
	0.01	0.0760	2.17
	0.1	0.140	2.46
	0.3	0.215	2.68
	0.72	0.296	2.88
	1.0	0.332	2.95
	2.0	0.422	3.10
	3.0	0.485	3.18
	10.0	0.728	3.38
	100.0	1.572	3.61
	1000.0	3.387	3.72
	10,000.0	7.297	3.76
	∞	∞	3.81

$$\frac{\delta_c^2}{\nu} = \frac{a}{U^b} \left(\int_{x_0}^x U^{b-1} dx + C \right) \quad (4-181)$$

Page 206where, again, $C = 0$ if x_0 is the stagnation point. Since δ_c is directly related to q_w , we may readily convert [Eq. \(4-181\)](#) to a Nusselt number relation based on the local heat conductance $h = q_w/(T_w - T_e)$, a reference length L , and a velocity U_0 :

$$\frac{Nu_L}{\sqrt{Re_L}} = \frac{hL/k}{\sqrt{U_0 L/\nu}} = \left[a \left(\frac{U_0}{U} \right)^b \int_0^x \left(\frac{U}{U_0} \right)^{b-1} \frac{dx}{L} \right]^{-1/2} \quad (4-182)$$

This is an accurate and remarkably simple expression, involving only a single quadrature of the velocity distribution. From [Table 4-10](#), the terms $a(Pr)$ and $b(Pr)$ can be approximated in the range $0.1 \leq Pr \leq 10.0$ by the power laws

$$a^{-1/2} \approx 0.332 Pr^{0.35} \quad \text{and} \quad b \approx 2.95 Pr^{0.07} \quad (4-183)$$

For air, the most common case, we have $a^{-1/2} = 0.296$ and $b = 2.88$ ($Pr = 0.72$).

4-8.2 A Finite-Difference Method: Explicit or Implicit

The finite-difference momentum method outlined in Sec. 4-7.1 may be readily extended to temperature calculations. By defining the temperature at each mesh point, $T_{m,n}$, we may write the thermal-energy equation in the difference form

$$u_{m,n} \frac{T_{m+1,n} - T_{m,n}}{\Delta x} + v_{m,n} \frac{T_{m,n+1} - T_{m,n-1}}{2\Delta y} \approx \frac{k}{\rho c_p} \frac{T_{m,n+1} - 2T_{m,n} + T_{m,n-1}}{\Delta y^2}$$

where $u_{m,n}$ and $v_{m,n}$ are presumed known already from the momentum model of Sec. 4-7.1. All differences are centered about level “ n .” We can rearrange this into an explicit model for the downstream temperature:

$$T_{m+1,n} \approx (\gamma - \beta)T_{m,n+1} + (1 - 2\gamma)T_{m,n} + (\gamma + \beta)T_{m,n-1} \quad (4-184)$$

where $\gamma = \frac{k\Delta x}{\rho c_p u_{m,n} \Delta y^2}$ and $\beta = \frac{v_{m,n} \Delta x}{2u_{m,n} \Delta y}$

The stability of this explicit model is similar to the momentum formulation, that is, $\gamma < 1/2$ and $\beta < \gamma$; the step size is further limited by

$$\Delta x < \frac{\rho c_p u_{\min} \Delta y^2}{2k} \quad \text{and} \quad \Delta y < \frac{2\nu}{|v_{\max}|} \quad (4-185)$$

If $Pr < 1$, this condition on Δx is more restrictive than [Eq. \(4-168\)](#).

Equation (4-184) is to be *combined with* [Eqs. \(4-167\)](#) and [\(4-169\)](#) to form a complete numerical model that is capable of capturing explicitly the laminar boundary-layer velocity and temperature.

An implicit model can be constructed, following [Eq. \(4-170\)](#), by using a downstream central-difference model for the conduction term:

$$\frac{\partial^2 T}{\partial y^2} \approx \frac{T_{m+1,n+1} - 2T_{m+1,n} + T_{m+1,n-1}}{\Delta y^2}$$

The result is a set of simultaneous equations for the new temperatures:

$$-\gamma T_{m+1,n+1} + (1 + 2\gamma)T_{m+1,n} - \gamma T_{m+1,n-1} \approx T_{m,n} - \beta(T_{m,n+1} - T_{m,n-1}) \quad (4-186)$$

Note the strong resemblance to the implicit momentum model of [Eq. \(4-170\)](#). Since γ and β involve $u_{m,n}$ and $v_{m,n}$, [Eq. \(4-186\)](#) must be combined with [Eqs. \(4-169\)](#) and [\(4-170\)](#) to achieve closure.

Equation (4-186) can also be solved by the TDMA algorithm described in Sec. 4-7.2.1, [Eqs. \(4-171\)](#) to [\(4-174\)](#), with several modifications. Since the computation is coupled with the momentum TDMA, let us just rewrite all the recurrence relations with the new notation, as these terms must be added to the momentum analysis:

$$D_n = \text{right-hand side of Eq. (4-186)} \quad (4-187a)$$

$$T_n = R_n T_{n+1} + S_n \quad (4-187b)$$

$$R_2 = \frac{\gamma_2}{1 + 2\gamma_2} \quad S_2 = \frac{\gamma_2 T_w + D_2}{1 + 2\gamma_2} \quad (4-187c)$$

Page 207

$$R_n = \frac{\gamma_n}{1 + 2\gamma_n - \gamma_n R_{n-1}} \quad S_n = \frac{D_n + \gamma_n S_{n-1}}{1 + 2\gamma_n - \gamma_n R_{n-1}} \quad (4-187d)$$

$$T_{N-1} = \frac{\gamma_{N-1} T_e + \gamma_{N-1} S_{N-1} + D_{N-1}}{1 + 2\gamma_{N-1} - \gamma_{N-1} R_{N-1}} \quad (4-187e)$$

where T_e stands for the edge or freestream temperature. The procedure is as follows: We calculate the R_n and S_n values from the bottom up, and then deduce the temperature with Eq. (4-187b) from the top, T_{N-1} down to T_2 . As with the momentum analysis, the algorithm works well, and the results will be accurate provided that the temperature changes between steps Δx and Δy remain smaller than a few percent.

4-8.3 Experimental Thermal Boundary Layer: The Circular Cylinder

Heat transfer from a circular cylinder has been the subject of many experiments because of its relevance to the design of heat exchangers. Our focus is on the *local* Nusselt number in the laminar boundary layer on the front of a cylinder, as measured by Schmidt and Wenner (1941) as well as Giedt (1949). Here, the freestream velocity near the nose can be approximated by

$$\frac{U}{U_0} \approx 1.82 \frac{x}{R} - 0.4 \frac{x^3}{R^3} \quad (4-188)$$

where R and U_0 represent the radius of the cylinder and the approach velocity. The maximum velocity is $U/U_0 = 1.49$ at $x/R = 1.23$ ($\phi = 71^\circ$). The temperature difference ($T_w - T_e$) is constant, so that the integral method of Smith and Spalding in [Eq. \(4-182\)](#) may be used.

[Figure 4-34](#) compares the Smith–Spalding formula and our implicit finite-difference technique [Eq. (4-186)], with the local heat-transfer data. Both theories stand in good agreement with Schmidt and Wenner’s low Reynolds number data, with boundary-layer separation occurring at $\phi \approx 81^\circ$. However, Giedt’s measurements at $Re_D = 140,000$ are about 10 percent higher. In fact, there is a systematic increase in heat transfer with the Reynolds number which, at first glance, seems to defy the contention of Sec. 4-2 that laminar boundary layers should scale directly with \sqrt{Re} . Kestin et al. (1961) are able to trace this behavior to turbulence or noise in the stream approaching the cylinder. Specifically, turbulence intensifies with the Reynolds number and causes streamwise vortices in the boundary layer to enhance the heat transfer. A review of such freestream turbulence effects is

furnished by Zukauskas and Ziukzda (1985) as well as Barrett and Hollingsworth (2003), who focus on flat-plate flows.

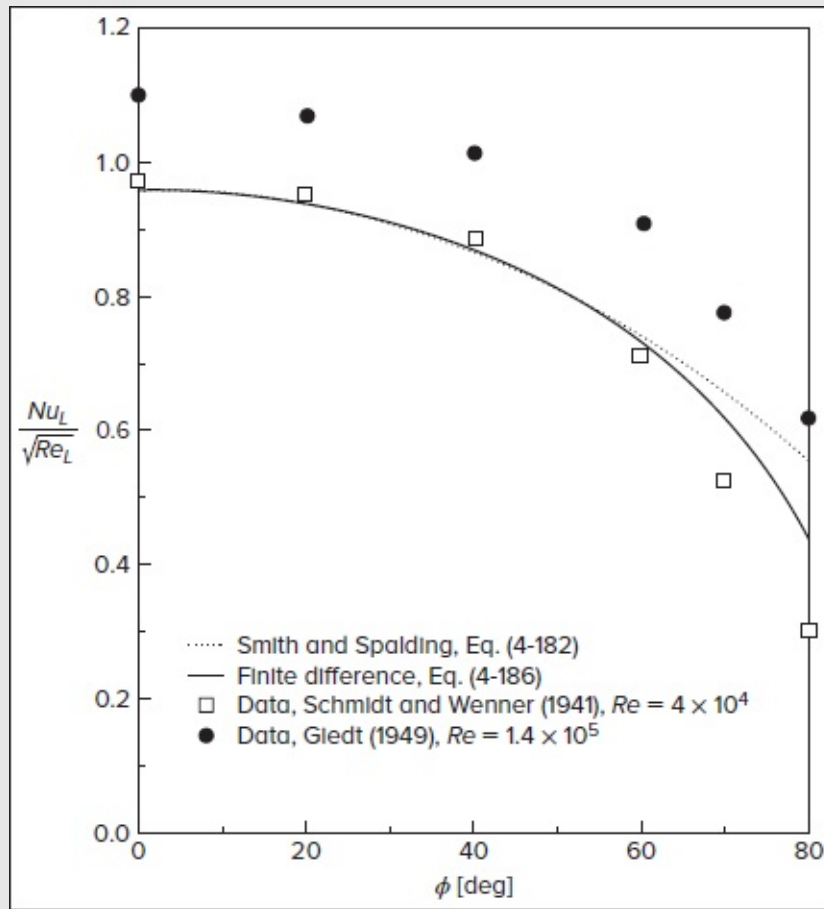


FIGURE 4-34

Comparison of theory and experiment for local heat transfer in airflow ($Pr = 0.72$) past a cylinder, constant $(T_w - T_e)$.

4-8.4 Variable Wall Temperature: Superposition of Indicial Solutions

Our previous analyses have been for a constant driving-temperature difference $(T_w - T_e)$, which is a common design assumption. For variable ΔT , our previous formulations are no longer capable of relating Nu to the *local* temperature difference. For example, if T_w drops as we move downstream, q_w will change sign before $(T_w - T_e)$, because the fluid in the local boundary layer has been warmed by the hotter upstream wall. We will demonstrate this effect with an example.

Since the thermal-energy equation is linear, a possible approach to handle a variable ($T_w - T_e$) is to use superposition of “indicial” or step-wall-change formulas for a particular $U(x)$. Let us illustrate this procedure with the common case of a flat plate with variable $\Delta T(x)$. We recall that in [Eq. \(4-37\)](#), we have presented a solution to the problem defined in [Fig. 4-6](#) for heat transfer with a discontinuity in wall temperature at $x = x_0$. The heat transfer downstream of the discontinuity was found to be

$$q_w(x_0, x) = (T_w - T_e)h(x_0, x)$$

where

$$h(x_0, x) = \frac{0.332k}{x} Pr^{1/3} Re_x^{1/2} \left[1 - \left(\frac{x_0}{x} \right)^{3/4} \right]^{-1/3} \quad (4-189)$$

is the local heat-transfer coefficient.

Imagine now that $T_w - T_e$ changes continuously with x , so that a continuous series of starting problems at successive x_0 can be constructed. If $d(T_w - T_e)$ is the change that occurs between x_0 and $x_0 + dx_0$, the wall temperature at any x can be estimated using x_0 as a dummy variable and superimposing all these infinitesimal shifts:

$$q_w(x) = \int_0^x h(x_0, x) \frac{d(T_w - T_e)}{dx_0} dx_0 \quad (4-190)$$

the integral being evaluated with x held constant.

Suppose further, for generality, that $T_w - T_e$ changes discontinuously at a certain number of points $x_0(i)$ by the amount ΔT_i . Then, we must add on to our previous solution a summation of these discrete starting solutions. The complete solution for arbitrarily variable wall temperature is, therefore,

$$q_w(x) = \int_0^x h(x_0, x) \frac{d}{dx_0} (T_w - T_e) dx_0 + \sum_{i=1}^N h[x_0(i), x] \Delta T_i \quad (4-191)$$

We must remember that the indicial solution $h(x_0, x)$ must be appropriate for the particular velocity distribution $U(x)$ of the problem.

Let us now apply this theorem to the flat plate with a polynomial distribution of $T_w - T_e$, such as

$$T_w - T_e = \sum_{j=0}^N a_j x^j = a_0 + a_1 x + a_2 x^2 + a_3 x^3 + a_4 x^4 + \dots \quad (4-192)$$

In the absence of discontinuities, [Eq. \(4-190\)](#) applies:

$$q_w(x) = \frac{0.332k}{x} Pr^{1/3} Re_x^{1/2} \int_0^x \left[1 - \left(\frac{x_0}{x} \right)^{3/4} \right]^{-1/3} \left(a_0 + \sum_{j=1}^N j a_j x_0^{j-1} \right) dx_0$$

The integrals can be readily evaluated and expressed in terms of gamma functions, specifically

$$q_w(x) = \frac{0.332k}{x} Pr^{1/3} Re_x^{1/2} \left[a_0 + \sum_{j=1}^N \frac{4}{3} j a_j x^j \frac{\Gamma(4j/3)\Gamma(2/3)}{\Gamma(4j/3 + 2/3)} \right] \quad (4-193)$$

All of the gamma functions can be determined numerically from the three known values: $\Gamma(1/3) = 2.6789385$, $\Gamma(2/3) = 1.3541179$, and $\Gamma(1) = 1$, in conjunction with the recurrence relation $\Gamma(1+k) = k\Gamma(k)$. The first five terms in the square brackets from [Eq. \(4-193\)](#) yield

$$a_0 + 1.6123a_1x + 1.9556a_2x^2 + 2.2091a_3x^3 + 2.4151a_4x^4 + \dots \quad (4-194)$$

Page 209This behavior is substantially different from q_w being proportional to the local $\Delta T = a_0 + a_1x + a_2x^2 + a_3x^3 + a_4x^4 + \dots$; to illustrate how drastically the results differ from what our intuition may be telling us, consider the linear distribution

$$T_w - T_e = \Delta T_0 \left(1 \pm \frac{x}{L} \right) \quad (4-195)$$

From [Eq. \(4-194\)](#), the Nusselt number based on ΔT_0 is

$$Nu_x = \frac{q_w}{k\Delta T_0} = 0.332Pr^{1/3} Re_x^{1/2} \left(1 \pm 1.6123 \frac{x}{L} \right) \quad (4-196)$$

It clearly exhibits strong effects due to the linear contribution. For the rising temperature difference, $1 + x/L$, the heat transfer at the trailing edge is 31 percent greater than what one may expect from the local difference of $2\Delta T_0$. For the falling case, $1 - x/L$, the heat transfer actually changes *sign* at the trailing edge, and the effect is not negligible, being 61 percent of the leading-edge heat transfer. These results are sketched in [Fig. 4-35](#).

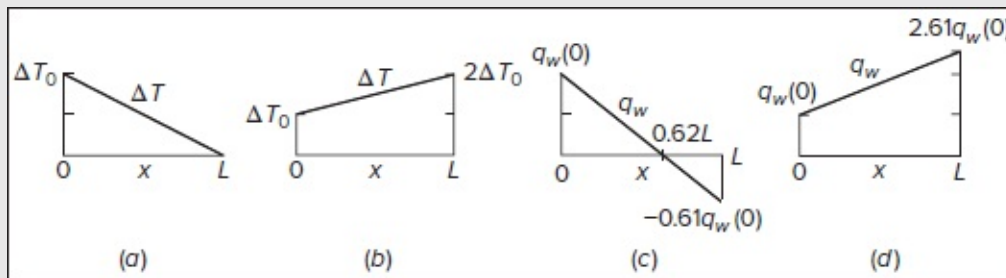


FIGURE 4-35

Local heat transfer with a linearly varying wall temperature on a flat plate, [Eq. \(4-196\)](#): (a, c) falling temperature difference; (b, d) rising temperature difference.

The finite-difference method of Sec. 4-8.2, which is valid for any $U(x)$ and $\Delta T(x)$, was applied to this particular problem of falling $\Delta T_0(1 - x/L)$. The corresponding temperature profiles are given in [Fig. 4-36](#), thus helping to illustrate the warming of the local fluid by the hot upstream wall.

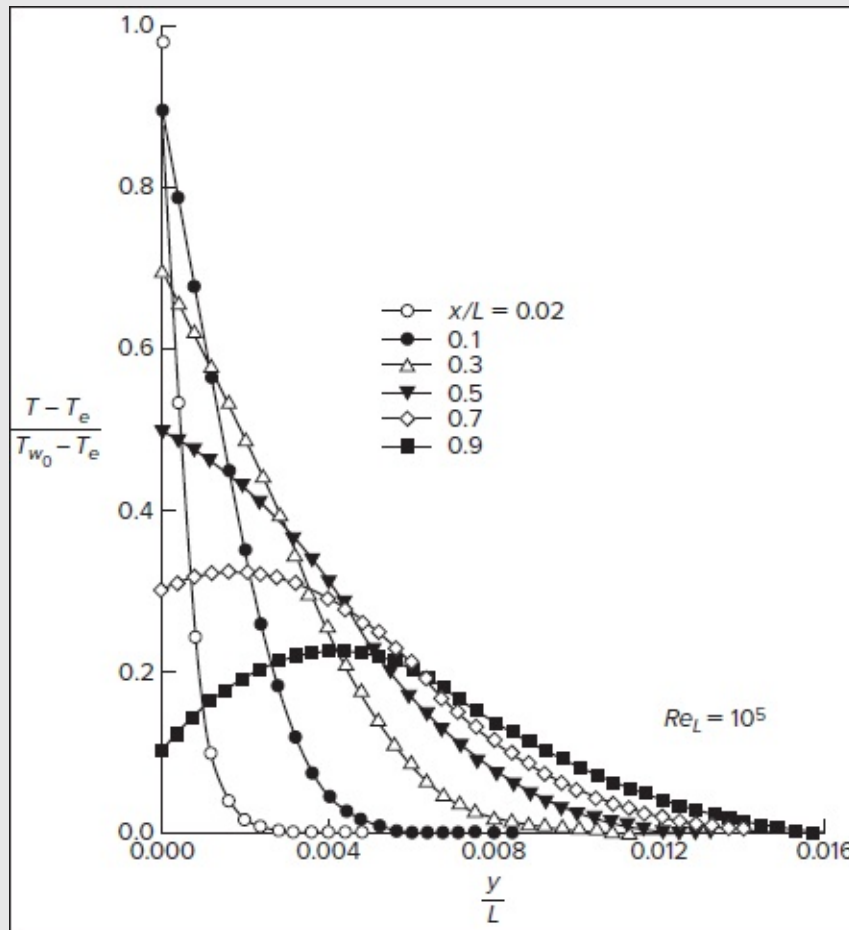


FIGURE 4-36

Finite-difference solution (Sec. 4-8.2) for temperature profiles in flat-plate flow with a linearly decreasing wall temperature. The wall heat transfer changes sign at $x/L = 0.62$.

4-9 DEVELOPING INLET FLOW IN DUCTS

The developing laminar flow in the entrance of a duct has captured the imaginations of scores of researchers. Extensive reviews are given by Schmidt and Zeldin (1969) as well as

Shah and London (1978).

The entrance-flow geometry for a pipe of radius a is shown in [Fig. 4-37](#). In a well-rounded entrance, the velocity profile at $x = 0$ is nearly uniform, $u = \bar{u} = \text{const}$, and this assumption is common in theoretical studies. A boundary layer begins to develop at the entrance with an initial behavior that resembles the Blasius flat-plate solution as long as $\delta \leq a$. However, due to continuity requirements, deceleration near the wall causes the “inviscid-core” center flow to speed up (favorable gradient), thus thinning the boundary layer more appreciably than predicted by the Blasius estimate [Eq. (4-67)]. Some distance downstream, the shear layers meet, and the duct becomes dominated by boundary-layer motion. Shortly thereafter, at $x = x_L$, the flow is essentially *developed* into the Poiseuille paraboloid. We term the region $0 \leq x \leq x_L$ the *entrance region*. Of particular engineering interest are (1) the excess pressure drop compared to Poiseuille flow and (2) the entrance length x_L/D to reach a fully developed state. Similar considerations occur in turbulent entrance flow, where the initial boundary layers are likely to be laminar and then undergo transition to turbulence before merging downstream.

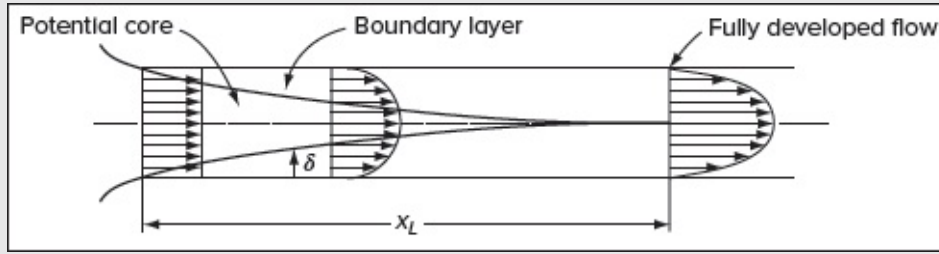


FIGURE 4-37

Laminar flow in the entrance of a duct.

Here, the excess pressure drop can be attributed to both increased shear in the boundary layers at entry and the acceleration of the core flow. Let the inlet pressure at $x = 0$ be p_0 and let $\tau_P = 4\mu\bar{u}/a$ be the shear stress in the developed Poiseuille flow region, where $u_P = 2\bar{u}(1 - r^2/a^2)$. A control-volume momentum analysis of the region between $x = 0$ and any $x \leq x_L$ yields the following balance:

$$(p_0 - p_x)\pi a^2 = 2\pi a x \tau_P + \int_0^a \rho(u_P^2 - \bar{u}^2)2\pi r dr + \int_0^x (\tau - \tau_P)2\pi a dx$$

This result may be written in dimensionless form as an “apparent” friction:

$$\frac{p_0 - p_x}{\frac{1}{2}\rho\bar{u}^2} = C_{f, \text{app}} \frac{4x}{D} = C_{fP} \frac{4x}{D} + K; \quad K = \frac{2}{3} + \int_0^{x/a} \frac{4(\tau - \tau_P)}{\rho\bar{u}^2} \frac{dx}{a} \quad (4-197)$$

Here, $C_{fp} = 16/Re_D$ is the Poiseuille friction factor from Eq. (3-39), with $D = 2a$ being the pipe diameter. The term K denotes the *excess* pressure drop due to the entrance region, where the $2/3$ contribution represents the pressure drop necessary to accelerate a uniform flow into a Poiseuille paraboloid. The integral term in K is the excess-shear contribution, approximately 0.65. Note that, for a long pipe, $x \gg D$ the term $C_f P(4x/D)$ dominates the total friction loss.

If we extend [Eq. \(4-197\)](#) into the entrance region, $K = K(x)$ increases from zero at $x = 0$ to an asymptotic constant value K_∞ in the developed region. [Figure 4-38](#) shows the finite-difference computations of Schmidt and Zeldin (1969) for $K(x)$ in pipes and between parallel plates. Note that there is only a slight Reynolds number effect, verifying the boundary-layer character of the entrance flow. Although K_∞ varies between 1.31 and 1.40 for pipe-flow computations in [Fig. 4-38](#), the experiments reviewed by Shah (1978) suggest a more realistic value of $K_\infty \approx 1.25$.

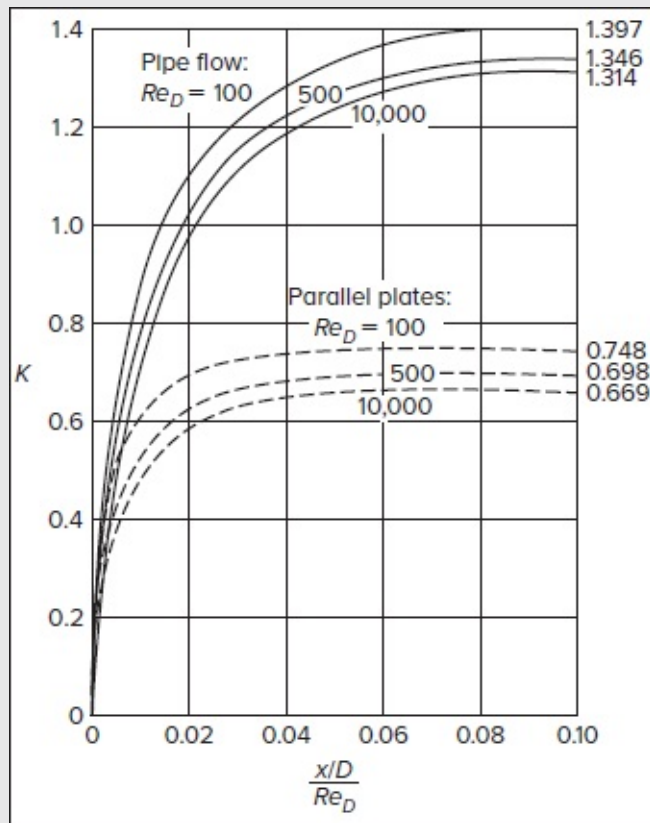


FIGURE 4-38

Pressure-drop parameter K [Eq. (4-197)] in the entrance of a duct for laminar flow. From finite-difference solutions of the full Navier–Stokes equations by Schmidt and Zeldin (1969).

The overall friction for any section of the pipe correlates with a Graetz-type variable $\zeta =$

$(x/D)/Re_D$. Shah (1978) proposes an interpolation formula that is valid within ± 2 percent for many duct shapes:

$$C_{f,app}Re \approx \frac{3.44}{\sqrt{\zeta}} + \frac{C_{fp}Re + K_{\infty}/(4\zeta) - 3.44/\sqrt{\zeta}}{1 + c/\zeta^2} \quad (4-198)$$

where C_{fp} , K_{∞} , and c correspond to the particular geometry in [Table 4-11](#). The noncircular sections use the hydraulic diameter D_h and Re_{Dh} .

TABLE 4-11

Constants to be used in [Eq. \(4-198\)](#)

b/a	$C_{fp}Re$	K_{∞}	c
Pipe or Concentric Annulus			
0.0	16.00	1.25	0.000212
0.05	21.57	0.830	0.000050
0.10	22.34	0.784	0.000043
0.50	23.81	0.688	0.000032
0.75	23.97	0.678	0.000030
1.00	24.00	0.674	0.000029
Rectangular Duct			
1.00	14.23	1.43	0.00029
0.50	15.55	1.28	0.00021
0.20	19.07	0.931	0.000076
0.00	24.00	0.674	0.000029
Equilateral Triangle			
—	13.33	1.69	0.00053

The “entrance length” x_L can be defined in various ways. [Figure 4-38](#) shows that development could be considered to occur when K approaches its final value K_{∞} at $(x/D)/Re_D \approx 0.08$ as an upper bound. A lower bound can occur when the shear layers “meet” in accordance with boundary-layer entrance theory. If we are to rely on the Page 211Blasius theory from [Eq. \(4-67\)](#), we can set the merging point at $\delta = a = c_{\text{Blasius}} \sqrt{\nu x / \bar{u}}$, or $(x/D)/Re_D = \frac{1}{4} C^{-2} \approx 0.01$ since $c_{\text{Blasius}} \approx 4.91$. This is far too low because the accelerating core thins the shear layer.

Shah and London (1978) define x_L as the point where the developing centerline velocity reaches 99 percent of the Poiseuille value u_{max} and recommend the following correlation for the entrance length:

$$\frac{x_L}{D} \approx \frac{0.6}{1 + 0.035Re_D} + 0.056Re_D \quad (4-199)$$

The entrance length does not vanish as Re approaches zero. It still takes about 0.6 diameters for a uniform, non-inertial creeping flow to morph into a parabolic profile.

4-10 ROTATIONALLY SYMMETRIC BOUNDARY LAYERS

So far, all of our boundary-layer solutions have been focused on planar motions. Let us now consider the rotationally symmetric case, as a preliminary to more general three-dimensional boundary layers. By rotationally symmetric, we mean flow in cylindrical polar coordinates (r, θ, z) , where none of the variables $(v_r, v_\theta, v_z, p, T)$ depend on θ . The circumferential component $v_\theta(r, z)$ is called the *swirl velocity*. If $v_\theta = 0$ everywhere, the flow reduces to the case of *axisymmetric flow*, where the streamlines remain in meridian planes.

We have already considered several rotationally symmetric flows in [Chap. 3](#): pipe flow (including uniform swirl), Couette flow between rotating cylinders, Taylor-Culick flow in spinning porous cylinders, axisymmetric stagnation flow, and flow near an infinite rotating disk. The boundary-layer equations under rotational symmetry were first given by Mangler (1945) in the form we use today. Mangler chose the curvilinear coordinates (x, y, θ) with corresponding velocity components (u, v, w) shown in [Fig. 4-39](#). The boundary-layer equations then become

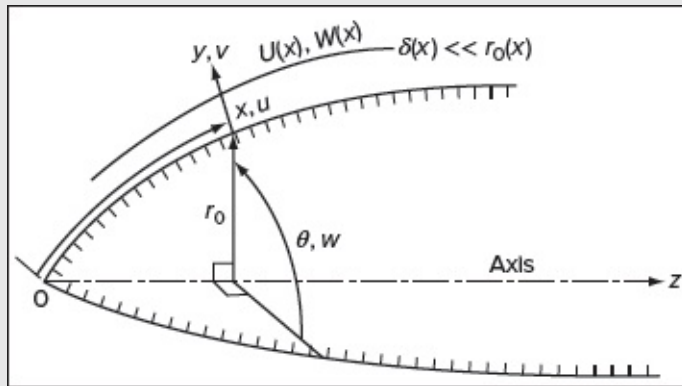


FIGURE 4-39

Coordinate system for rotationally symmetric flow, Eqs. (4-200a)–(4-200d).

Continuity:

$$\frac{\partial}{\partial x}(r_0 u) + r_0 \frac{\partial v}{\partial y} = 0 \quad (4-200a)$$

x -momentum:

$$\frac{\partial u}{\partial t} + u \frac{\partial u}{\partial x} + v \frac{\partial u}{\partial y} - \frac{w^2}{r_0} \frac{dr_0}{dx} = -\frac{1}{\rho} \frac{\partial p}{\partial x} + \nu \frac{\partial^2 u}{\partial y^2} \quad (4-200b)$$

y -momentum:

$$\frac{\partial p}{\partial y} = 0 \quad (4-200c)$$

$$\theta\text{-momentum:} \quad \frac{\partial w}{\partial t} + u \frac{\partial w}{\partial x} + v \frac{\partial w}{\partial y} + \frac{uw}{r_0} \frac{dr_0}{dx} = \nu \frac{\partial^2 w}{\partial y^2} \quad (4-200d)$$

Here $r_0(x)$ is the local surface radius, measured from the axis (*not* the radius of curvature of the surface). The derivation further assumes that r_0 is much larger than the boundary-layer thickness δ so that variations in r_0 through the boundary layer can be neglected. At the edge of the boundary layer, the freestream velocity is $U(x)$ and the swirl is $W(x)$, which can be related to the pressure by the potential-flow relations

$$\frac{\partial U}{\partial t} + U \frac{\partial U}{\partial x} - \frac{W^2}{r_0} \frac{dr_0}{dx} = -\frac{1}{\rho} \frac{\partial p}{\partial x} \quad \text{and} \quad \frac{\partial W}{\partial t} + U \frac{\partial W}{\partial x} + \frac{UW}{r_0} \frac{dr_0}{dx} = 0 \quad (4-201)$$

The boundary conditions can include, for generality, a porous surface rotating about its axis at angular speed $\Omega(t)$:

$$\begin{aligned} \text{At } y = 0: & \quad u = 0 \quad v = v_w(x, t) \quad w = r_0 \Omega(t) \\ \text{At } y \rightarrow \infty: & \quad u = U(x, t) \quad w = W(x, t) \\ \text{At } x = 0: & \quad u(0, y, t), v(0, y, t), w(0, y, t) \text{ (specified leading edge values)} \\ \text{At } t = 0: & \quad u(x, y, 0), v(x, y, 0), w(x, y, 0) \text{ (specified initial values)} \end{aligned} \quad (4-202)$$

As with two-dimensional boundary-layer problems, we neglect the normal pressure gradient in the y direction.

4-10.1 Axisymmetric Boundary Layers: Similarity Solutions

A much simpler special case is that of steady axisymmetric flow ($w = 0$) for which a great deal of work has been reported. Equations (4-200a)–(4-200d) reduce to

Page 213

$$\begin{aligned} \frac{\partial}{\partial x}(r_0 u) + r_0 \frac{\partial v}{\partial y} &= 0 \\ u \frac{\partial u}{\partial x} + v \frac{\partial u}{\partial y} &= U \frac{dU}{dx} + \nu \frac{\partial^2 u}{\partial y^2} \end{aligned} \quad (4-203)$$

with with
$$u(x, 0) = 0 \quad v(x, 0) = v_w(x) \quad u(x, \infty) \rightarrow U(x)$$

Assuming that the body shape $r_0(x)$ is known, a family of similarity solutions to [Eqs. \(4-203\)](#) may be found if the freestream velocity is of the power-law form

$$U(x) = C x^n \quad (4-204)$$

These correspond to potential flow at zero angle of attack past a cone of half-angle ϕ . An extensive discussion is given by Evans (1968), and the half-angles which relate to different values of n , are organized in [Table 4-12](#). It is not a simple relation, such as the Falkner–Skan plane wedge flows, where $\phi_{\text{wedge}} = m\pi/(1 + m)$.

TABLE 4-12**Variation of the cone half-angle ϕ with the velocity parameter n**

n	ϕ [deg]	n	ϕ [deg]
0.0	0.0	1.2	97.01
0.05	19.10	1.4	102.99
0.1	27.73	1.6	108.12
0.15	34.52	1.8	112.61
0.2	40.33	2.0	116.58
0.3	50.11	2.5	124.60
0.4	58.22	3.0	130.89
0.5	65.20	4.0	139.90
0.6	71.31	5.0	146.12
0.7	76.84	6.0	150.71
0.8	81.60	7.0	154.12
0.9	86.00	8.0	156.86
1.0	90.00	9.0	159.70

The proper similarity variables for these cone flows are

$$u(x, y) = U(x)f'(\eta); \quad \eta = y\sqrt{\frac{(3+n)U(x)}{2\nu x}} \quad (4-205)$$

Backward substitution in [Eqs. \(4-203\)](#) leads to a third-order, ordinary differential equation

$$f''' + ff'' + \frac{2n}{3+n}(1 - f'^2) = 0 \quad (4-206)$$

with with

$$f(0) = f'(0) = 0 \quad \text{and} \quad f'(\infty) = 1$$

The resulting expression is identical to the Falkner–Skan relation, [Eq. \(4-93\)](#), except that the equivalent value of β is different. If we equate the two parameters, we find that any given cone flow is equivalent mathematically to a certain wedge flow:

$$\beta_{\text{cone}} = \frac{2n}{3+n} = \beta_{\text{wedge}} = \frac{2m}{1+m} \quad \text{or} \quad m_{\text{wedge}} = \frac{1}{3}n_{\text{cone}} \quad (4-207)$$

As such, cone flows with $U = Cx^n$ will possess identical properties to wedge flows with $U = C'x'^{n/3}$; both types can be determined from the Falkner–Skan solution. Note that C and x for the cone are not the same as C' and x' for the wedge, i.e., the pressure gradients are quite different for the two flows. The equivalence is only through the similarity solutions, e.g., the solution for axisymmetric stagnation flow ($n = 1$) can be taken directly from the known similar solution for a 90° wedge ($m = 1/3$). In fact, the cone-wedge equivalence is not accidental. Mangler (1948) deduces an extraordinary transformation,

$$x' = \frac{1}{L^2} \int_0^x r_0^2 dx \quad y' = \frac{r_0 y}{L} \quad u' = u \quad U'(x') = U(x) \quad \text{and} \quad v' = \frac{L}{r_0} \left(v + \frac{yu}{r_0} \frac{dr_0}{dx} \right) \quad (4-208)$$

where L is a reference length, which converts [Eqs. \(4-203\)](#) directly into an equivalent plane-boundary-layer flow [[Eqs. \(4-56a\)–\(4-56b\)](#)]. The advantage is that plane-flow methods may be used for (x', y', u', v') but in turn the transformed pressure gradient $U'(x')$ may result in a complicated function. Sometimes the Mangler transformation is highly effective. Consider the cone of [Eq. \(4-205\)](#), where $r_0 = x \sin \phi$. The transformation through [Eqs. \(4-208\)](#) predicts $x' = (\text{const})x^3$. Thus, $U = C x_n$ for the cone is equivalent to plane flow with $U = C' x'^{n/3}$, as shown in [Eq. \(4-207\)](#). Since the Falkner–Skan results are well established, no new calculations are needed for cone flow analysis.

4-10.2 A Thwaites-Type Method for Axisymmetric Flow

We may bypass the Mangler transformation and convert [Eqs. \(4-203\)](#) directly into integral form. The derivation follows the procedure described in Sec. 4-6.2 for plane flow; we get

$$\frac{C_f}{2} = \frac{1}{U^2} \frac{\partial}{\partial t} (U\delta^*) + \frac{2\theta + \delta^*}{U} \frac{\partial u}{\partial x} + \frac{\partial \theta}{\partial x} + \frac{\theta}{r_0} \frac{dr_0}{dx} - \frac{v_w}{U} \quad (4-209)$$

The only difference from plane flow is the term involving dr_0/dx , which is prescribed by the surface geometry. As usual, the derivation assumes that $\delta \ll r_0$. For steady axisymmetric flow with an impermeable wall, this reduces to

$$\frac{\tau_w}{\rho} = \frac{1}{r_0} \frac{d}{dx} (r_0 U^2 \theta) + U \frac{dU}{dx} \delta^* \quad (4-210)$$

By exact analogy with [Eq. \(4-155\)](#) for plane flow, we regroup this relation in terms of the Thwaites or Holstein–Bohlen parameter, $\lambda = \theta^2(dU/dx)/\nu$. The result is

$$\frac{U}{r_0^2} \frac{d}{dx} \left(\frac{r_0^2 \lambda}{dU/dx} \right) = 2S - 2\lambda(2 + H) = F(\lambda) \approx 0.45 - 6\lambda \quad (4-211)$$

where $S(\lambda)$ and $H(\lambda)$ have the same meanings and correlations as in plane flow [Sec. 4-6.6]. Again, by analogy with plane flow's [Eq. \(4-159\)](#), we can integrate [Eq. \(4-211\)](#) directly to find:

$$\theta^2 \approx \frac{0.45\nu}{r_0^2 U^6} \int_0^x r_0^2 U^5 dx \quad (4-212)$$

with separation again assumed to occur at $\lambda = -0.09$. This expression was developed by Rott and Crabtree (1952). If r_0 is constant or much larger than x , [Eq. \(4-212\)](#) reduces to the Thwaites' plane-flow method. The expected accuracy is ± 5 percent.

4-10.3 Axisymmetric Finite-Difference Methods

Since the main difference between plane and axisymmetric boundary layers is the presence of $r_0(x)$ in the continuity [Eq. \(4-203\)](#), very little modification is needed to the numerical techniques described in Sec. 4-7.

For axisymmetric flow, both the explicit x -momentum model, [Eq. \(4-167\)](#), and its implicit sibling, [Eq. \(4-170\)](#), remain valid, along with the stability constraints on the explicit model [[Eqs. \(4-168\)](#)]. Only the continuity relation [Eq. \(4-169\)](#) must be changed by introducing $r_0(x)$, which we denote as r_m . This minor modification can be accommodated by taking

$$v_{m+1,n} \approx v_{m+1,n-1} - \frac{\Delta y}{2\Delta x r_{m+1}} [r_{m+1}(u_{m+1,n} + u_{m+1,n-1}) - r_m(u_{m,n} + u_{m,n-1})] \quad (4-213)$$

This relation is used to compute the next column of vertical velocities once the new $u_{m+1,n}$ are known from either the explicit or implicit models.

4-10.4 Application to Flow Past a Sphere

Consider a sphere of radius a immersed in a stream of velocity U_0 . If ϕ is the angle measured from the nose, the potential-flow surface-velocity distribution is [White (2016), Sec. 8.8, Eq. (8.87)]

$$U = \frac{3}{2} U_0 \sin \phi = \frac{3}{2} U_0 \sin (x/a) \quad (4-214)$$

We may test this theoretical freestream distribution against our two methods: (1) the Rott–Crabtree modification of Thwaites’ method, prescribed by [Eq. \(4-212\)](#); and (2) a finite-difference method, based on [Eqs. \(4-170\)](#) and [\(4-213\)](#). Page 215The results for predicted skin friction are shown in [Fig. 4-40](#). The Rott–Crabtree method predicts separation at $\phi = 103.6^\circ$, and the most exact finite-difference computation yields $\phi_{\text{sep}} = 105.5^\circ$.

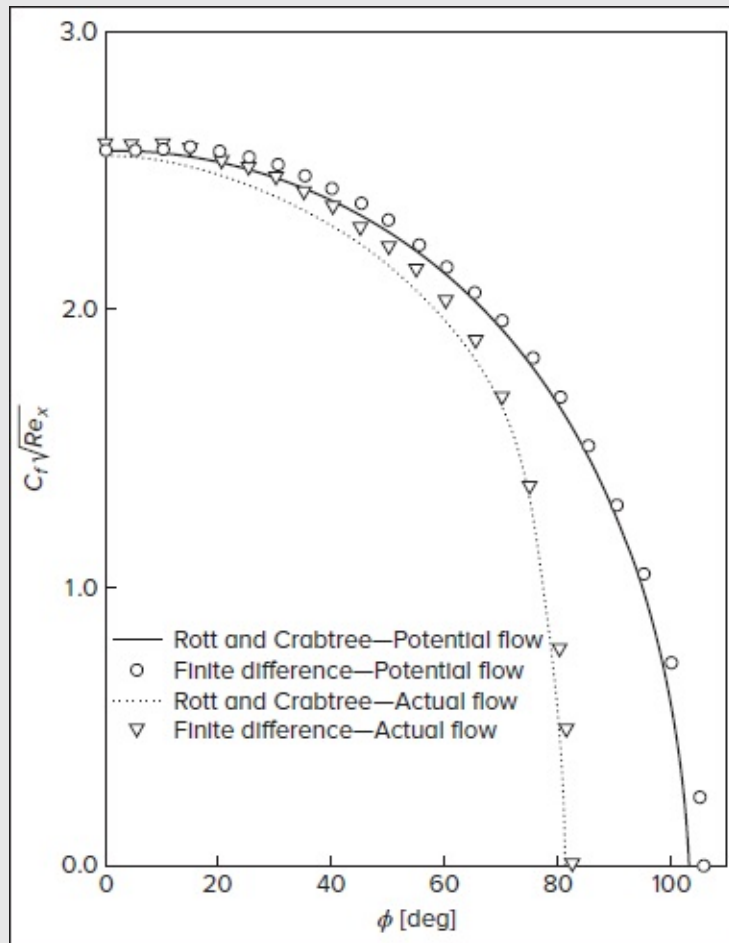


FIGURE 4-40

Comparison of the Rott–Crabtree (1952) integral method and a finite-difference computation for skin friction in sphere flow.

As in the flow past a cylinder problem, potential flow calculations are not reliable here because of first-order flow-separation effects. The actual velocity distribution measured by Fage (1936) at $Re_a \approx 200,000$ fits the curve

$$\frac{U}{U_0} \approx 1.5 \frac{x}{a} - 0.4371 \left(\frac{x}{a}\right)^3 + 0.1481 \left(\frac{x}{a}\right)^5 - 0.0423 \left(\frac{x}{a}\right)^7 \quad 0 \leq \frac{x}{a} \leq 1.48 \quad (4-215)$$

This relation drops off much faster than the potential flow estimate, reaching a maximum of $U/U_0 = 1.274$ at $x/a = 1.291$ ($\phi = 74^\circ$), whereas the potential flow has a maximum of $U/U_0 = 1.5$ at $\phi = 90^\circ$.

[Figure 4-40](#) also compares the two methods for this experimental $U(x)$ distribution. Again the two sets of results are acceptably close—the separation angles are 81.1° for the Rott–Crabtree method and 82.4° for the (nearly exact) finite-difference computations. The numerical method used was implicit, based on a step size of $\Delta\theta = 0.5^\circ$.

4-10.5 Thick Axisymmetric Boundary Layers

This section has so far considered only “thin” boundary layers, where $\delta \ll r_0$. If a cylindrical body is long enough, however, there must be some point downstream where this assumption fails, and the boundary-layer thickness becomes of the order of the body diameter or greater. A long towed cable is an important practical example. The main effect of a thick axisymmetric boundary layer is that the cylindrical geometry must be taken into account; hence, the term *transverse-curvature effect* is often used to describe these flows.

We now consider the problem of the axisymmetric laminar boundary layer along an extremely long cylinder of constant radius a . The pressure gradient is negligible ($U = U_0 \approx \text{const}$) and the boundary-layer approximations apply Page 216 if the square root of the Reynolds number Re_x is large. Using the “wall” coordinate $y = r - a$, $dy = dr$, the axisymmetric boundary-layer equations become

$$\frac{\partial u}{\partial x} + \frac{1}{a+y} \frac{\partial}{\partial y}[(a+y)v] = 0 \quad (4-216a)$$

$$u \frac{\partial u}{\partial x} + v \frac{\partial u}{\partial y} = \frac{\nu}{a+y} \frac{\partial}{\partial y} \left[(a+y) \frac{\partial u}{\partial y} \right] \quad (4-216b)$$

Note that if $y \ll a$ these equations reduce to the flat-plate equations, so that the boundary layer on a short cylinder follows the Blasius solution.

There have been many studies of this problem, notably by Glauert and Lighthill (1955), who manage to produce an approximate solution that applies over an extensive range of cylinder lengths, i.e., from short to very long cylinders. They also point out that, for $\delta \gg a$, the convective acceleration becomes negligible and the momentum Eq. (4-216b) can be solved for the velocity directly:

$$u(x, y) \approx \frac{a}{\mu} \tau_w(x) \ln \left(1 + \frac{y}{a} \right) \quad (4-217)$$

Interestingly, this solution remains valid for both laminar and turbulent regimes along a very long cylinder. Glauert and Lighthill then extend their expression with the shear-related parameter $\alpha(x) = \mu U_0 / (a \tau_w)$ to obtain the approximate profiles

$$u = \begin{cases} \frac{U_0}{\alpha} \ln \left(1 + \frac{y}{a} \right) & \text{for } y \leq \delta = a(e^\alpha - 1) \\ U_0 & \text{for } y \geq \delta \end{cases} \quad (4-218)$$

In this context, the steady cylindrical momentum integral relation becomes

$$\tau_w = \frac{d}{dx} \left[\int_0^\delta \rho u (U_0 - u) \left(1 + \frac{y}{a} \right) dy \right] \quad (4-219)$$

This integral can be evaluated using u from [Eq. \(4-218\)](#) to retrieve an algebraic expression

for the local shear $\alpha(x)$. One gets:

$$\frac{1}{4} \left[e^{2\alpha} + 3 - \frac{2}{\alpha}(e^{2\alpha} - 1) + \int_0^{2\alpha} \frac{e^z - 1}{z} dz \right] = \frac{\nu x}{U_0 a^2} \quad (4-220)$$

So, by computing the exponential integral numerically, [Eq. \(4-220\)](#) can be used to relate $\alpha(x)$ to the *long-cylinder* parameter,

$$\xi(\alpha) = \sqrt{\frac{\nu x}{U_0 a^2}} = \frac{x/a}{\sqrt{Re_x}} = \frac{1}{2} \sqrt{e^{2\alpha} + 3 - \frac{2}{\alpha}(e^{2\alpha} - 1) + \int_0^{2\alpha} \frac{e^z - 1}{z} dz} \quad (4-221)$$

With $\xi(\alpha)$ known from [Eq. \(4-221\)](#), Glauert and Lighthill are able to tabulate shear, drag, and thickness parameters, which are plotted in [Fig. 4-41](#). Note that, for a “very long” cylinder with $\xi > 100$, the skin friction and drag approach the asymptotic result of $C_f \sqrt{Re_x} \approx 2\xi/\ln(2\xi)$. Conversely, for $\xi < 0.01$, the Blasius solution is recovered.

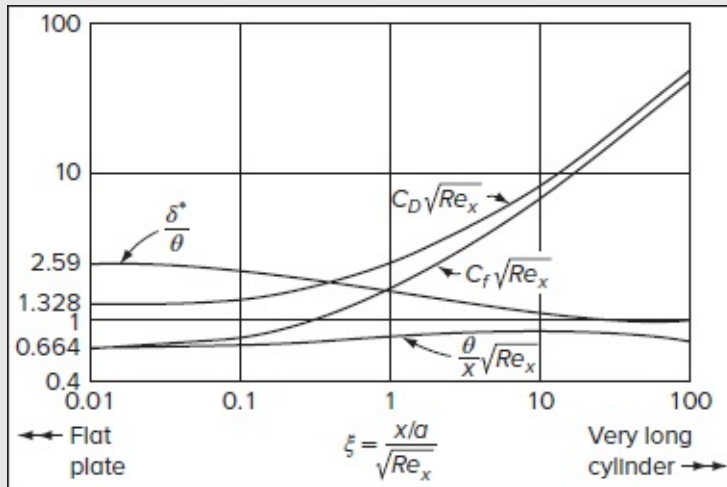


FIGURE 4-41

Boundary-layer parameters for steady laminar flow past the outside of an extremely long cylinder. Computed from the theory of Glauert and Lighthill (1955).

Although the results shown in [Fig. 4-41](#) are approximate, they remain accurate when compared to finite-difference computations. In fact, Eqs. (4-216a)–(4-216b) are parabolic and easily amenable to the numerical techniques of Sec. 4-7.

4-10.6 The Narrow Axisymmetric Jet

If a round jet emerges from a circular hole with sufficient momentum, it remains narrow and grows slowly, the radial change $\partial/\partial r$ being much larger than the axial change $\partial/\partial x$. Schlichting (1933a) found a solution for a narrow jet that satisfies the axisymmetric boundary-layer equations, particularly,

$$\text{Continuity:} \quad \frac{\partial u}{\partial x} + \frac{1}{r} \frac{\partial}{\partial r}(rv) = 0 \quad (4-222a)$$

$$\text{x-momentum:} \quad u \frac{\partial u}{\partial x} + v \frac{\partial u}{\partial r} = \frac{\nu}{r} \frac{\partial}{\partial r} \left(r \frac{\partial u}{\partial r} \right) \quad (4-222b)$$

Schlichting reasoned that the jet thickness grew linearly, so that the proper similarity variable was r/x . He defined a stream function

$$\psi(r, x) = \nu x F(\eta); \quad \eta = \frac{r}{x} \quad (4-223)$$

from which the axisymmetric velocity components may be deduced as

$$u = \frac{1}{r} \frac{\partial \psi}{\partial r} = \frac{\nu F'}{r} \quad \text{and} \quad v = -\frac{1}{r} \frac{\partial \psi}{\partial x} = \frac{\nu}{r} (\eta F' - F) \quad (4-224)$$

Substitution into the axial momentum equation (4-222b) leads to the following third-order nonlinear differential equation:

$$\frac{d}{d\eta} \left(F'' - \frac{F'}{\eta} \right) = \frac{1}{\eta^2} (FF' - \eta F'^2 - \eta FF'') \quad (4-225)$$

Since the outcome is devoid of x and r , a similarity solution has been achieved. As for the boundary conditions, they translate into $F(0) = F'(0) = F'(\infty) = 0$. Here too, Schlichting (1933a) is able to identify an exact solution of the form

$$F = \frac{(C\eta)^2}{1 + (C\eta/2)^2} \quad (4-226)$$

where the constant C must be prescribed by the momentum of the jet, analogously to the plane jet of Sec. 4-4.2:

$$J = \rho \int_0^\infty u^2(2\pi r) dr = \frac{16}{3} \pi \rho C^2 \nu^2 \quad \text{or} \quad C = \left(\frac{3J}{16\pi\rho\nu^2} \right)^{1/2} \quad (4-227)$$

With C in hand, the axial jet velocity can be retrieved from [Eq. \(4-224\)](#), namely,

$$u = \frac{3J}{8\pi\mu x} \left(1 + \frac{C^2\eta^2}{4} \right)^{-2} \quad (4-228)$$

The term in parentheses represents the jet profile, which differs from the (sech^2) shape of the plane jet [Eq. (4-124)]. The jet centerline velocity drops off as x^{-1} and the mass flow rate across any axial section of the jet can be determined from

$$\dot{m} = \rho \int_0^{\infty} u(2\pi r) dr = 8\pi\mu x \quad (4-229)$$

Clearly, the mass flow rate increases with x irrespective of the jet momentum J ; the latter only affects the width of the jet through C .

[Figure 4-42](#) displays the jet streamlines associated with [Eq. \(4-226\)](#) for $C = 1$ and 4. We note that the $C = 1$ case is not “narrow,” which weakens the boundary-layer approximation. However, the case of $C \leq 4$ leads to a narrow jet with $\partial/\partial r \gg \partial/\partial x$ and a Reynolds number of $J/(\rho v^2) > 250$, based on [Eq. \(4-227\)](#).

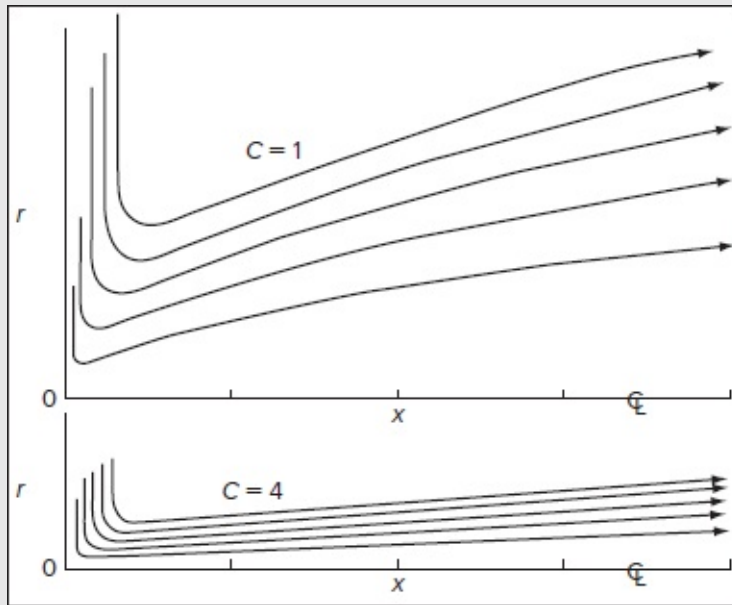


FIGURE 4-42

Streamlines of a round jet for two cases, from the boundary-layer theory of [Eq. \(4-226\)](#).

4-10.7 Axisymmetric Wakes

The plane wake discussed in Sec. 4-4.3 uses an Oseen-type linearization of the convective acceleration. We refer back to [Fig. 4-24](#) for the wake geometry, where the wake velocity defect $u_1 = (U_0 - u)$ is assumed to be small. For axisymmetric flow, the momentum Eq. (4-222b) can be reduced to

$$U_0 \frac{\partial u_1}{\partial x} \approx \frac{\nu}{r} \frac{\partial}{\partial r} \left(r \frac{\partial u_1}{\partial r} \right) \quad \text{with} \quad \frac{\partial u_1}{\partial r}(0, x) = 0, \quad u_1(\pm\infty, x) = 0, \quad \text{and} \quad u_1(r, \infty) = 0 \quad (4-230)$$

As we have seen before in [Eq. \(4-132\)](#), the solution is a Gaussian wake-velocity distribution of the form,

$$\frac{u_1}{U_0} = \frac{C}{x} \exp\left(-\frac{U_0 r^2}{4\nu x}\right) \quad (4-231)$$

Page 218 where C is a constant related to the drag force on the body, viz.

$$F \approx \rho U_0 \int_0^\infty u_1(2\pi r) dr = \rho U_0^2 C \frac{4\pi\nu}{U_0} = \frac{1}{2} C_D \rho U_0^2 L^2 \quad \text{or} \quad C = \frac{C_D U_0 L^2}{8\pi\nu}$$

where L corresponds to a body reference length. The wake defect velocity becomes

$$\frac{u_1}{U_0} = \frac{C_D}{8\pi} \left(\frac{U_0 L}{\nu}\right) \frac{L}{x} \exp\left(-\frac{U_0 r^2}{4\nu x}\right) \quad (4-232)$$

These similar profiles occur in the far-field wake, at least three body-lengths downstream of the trailing edge.

[Figure 4-43](#) displays five typical wake-velocity profiles based on [Eq. \(4-232\)](#), thus illustrating the decay of the centerline velocity defect and the spreading of the wake. For further details on laminar wakes, the reader is referred to Berger (1971).

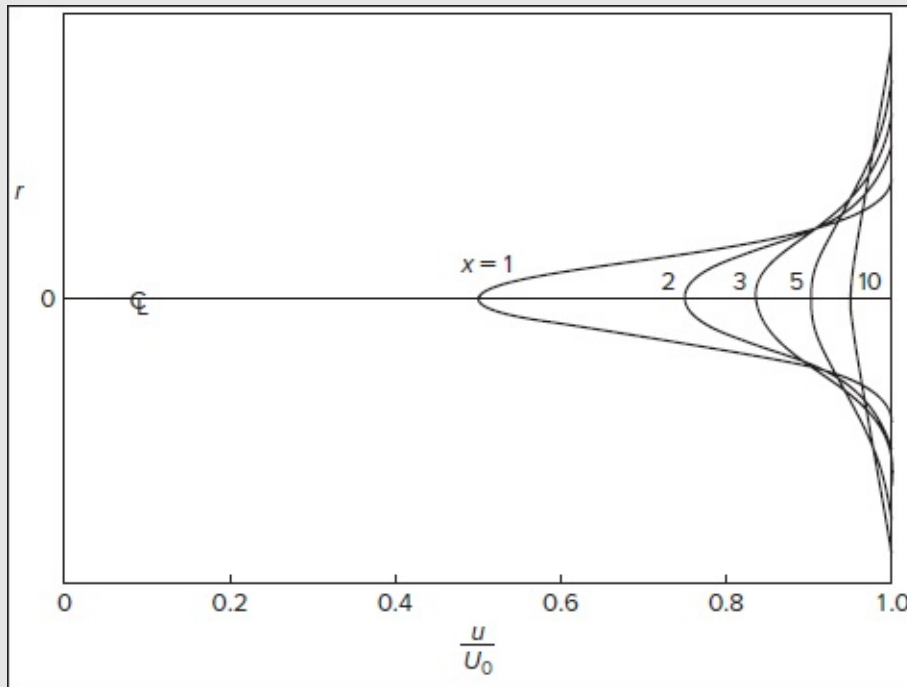


FIGURE 4-43

Velocity profiles illustrating the decay of a round wake from [Eq. \(4-232\)](#). Units on x and r are arbitrary.

4-11 THREE-DIMENSIONAL LAMINAR BOUNDARY LAYERS

This text is primarily concerned with two-dimensional boundary layers—including axisymmetric flows, which can readily be interpreted using two-dimensional concepts. However, many real-world problems are three-dimensional: swept finite wings, corners, turbine blades, slender bodies at an angle of attack, spinning projectiles, curved ducts, and wing–body junctions. The theory of laminar three-dimensional boundary layers is well developed but limited to unseparated flows. Flow separation in three-dimensional space leads to a complex topological problem [Tobak and Peake (1982), Wang (1997)]. Progress in modeling turbulent three-dimensional flows has been slow because of the lack of detailed data. Nonetheless, there have been several reviews of three-dimensional boundary-layer physics, mainly, in the context of turbulent flows: Eichelbrenner (1973), Cebeci (1984), Cousteix (1986), and Bradshaw (1987).

In general, the boundary layer can develop over an arbitrarily curved surface S , as in [Fig. 4-4](#). We may choose orthogonal curvilinear coordinates (x_1, x_2, x_3) with x_3 everywhere perpendicular to S . The boundary-layer velocities are (u_1, u_2, u_3) . We consider two freestream velocity components, U_1 and U^2 while assuming that the boundary layer is thin, so that $u_3 \ll u_1, u_2$. In orthogonal coordinates, the element of arc length ds is related to (x_1, x_2, x_3) through *stretching* or *scaling* factors h_1, h_2 and h_3 , which are detailed in Sec. 2-7. Accordingly, we have

$$(ds)^2 = (h_1 dx_1)^2 + (h_2 dx_2)^2 + (h_3 dx_3)^2 \quad (4-233)$$

However, since x_3 is everywhere normal to the wall, we can take $h_3 \equiv 1$ everywhere. If the scaling factors are not known, they can be determined by relating (x_1, x_2, x_3) to any convenient Cartesian system (x, y, z) , using

$$h_1^2 = \left(\frac{\partial x}{\partial x_1}\right)^2 + \left(\frac{\partial y}{\partial x_1}\right)^2 + \left(\frac{\partial z}{\partial x_1}\right)^2 = \left[\left(\frac{\partial x_1}{\partial x}\right)^2 + \left(\frac{\partial x_1}{\partial y}\right)^2 + \left(\frac{\partial x_1}{\partial z}\right)^2\right]^{-1} \quad (4-234)$$

with exactly similar expressions for h_2 and h_3 . Again, we are choosing the particular case of $h_3 \equiv 1$. In these coordinates, the incompressible continuity equation becomes

$$\frac{1}{h_1 h_2} \left[\frac{\partial}{\partial x_1} (h_2 u_1) + \frac{\partial}{\partial x_2} (h_1 u_2) + \frac{\partial}{\partial x_3} (h_1 h_2 u_3) \right] = 0 \quad (4-235)$$

which is still exact. In the boundary-layer approximation, the third term may be equated to $u_3 / \partial x_3$. As hoped for, a thin boundary layer enables us to neglect the normal pressure gradient $\partial p / \partial x_3$. The remaining boundary-layer momentum equations become

$$\frac{Du_1}{Dt} + \frac{u_1 u_2}{h_1 h_2} \frac{\partial h_1}{\partial x_2} - \frac{u_2^2}{h_1 h_2} \frac{\partial h_2}{\partial x_1} \approx -\frac{1}{\rho h_1} \frac{\partial p}{\partial x_1} + \nu \frac{\partial^2 u_1}{\partial x_3^2} \quad \text{and} \quad \frac{Du_2}{Dt} - \frac{u_1^2}{h_1 h_2} \frac{\partial h_1}{\partial x_2} + \frac{u_1 u_2}{h_1 h_2} \frac{\partial h_2}{\partial x_1} \approx -\frac{1}{\rho h_2} \frac{\partial p}{\partial x_2} + \nu \frac{\partial^2 u_2}{\partial x_3^2} \quad (4-236)$$

where $\frac{D}{Dt} = \frac{\partial}{\partial t} + \frac{u_1}{h_1} \frac{\partial}{\partial x_1} + \frac{u_2}{h_2} \frac{\partial}{\partial x_2} + u_3 \frac{\partial}{\partial x_3}$

The boundary-layer thermal-energy equation can be written in terms of the total enthalpy, $H \approx c_p T + \frac{1}{2}(u_1^2 + u_2^2)$:

$$\frac{DH}{Dt} \approx \frac{1}{\rho} \frac{\partial p}{\partial t} + \frac{\alpha}{Pr} \frac{\partial^2}{\partial x_3^2} \left[H + \frac{1}{2}(Pr - 1)(u_1^2 + u_2^2) \right] \quad (4-237)$$

Page 220 where $\alpha = k/(\rho c_p)$. From this equation, we note that in steady flow with $Pr = 1$, the total enthalpy H is constant everywhere in the boundary layer if the wall is insulated, i.e., Crocco's relation is not affected by three dimensionality.

The pressure gradients in [Eqs. \(4-236\)](#) must be matched to the freestream velocity, which has two components $U_1(x_1, x_2, t)$ and $U^2(x_1, x_2, t)$. The proper matching is given by Euler's relations for inviscid flow

$$\begin{cases} -\frac{1}{\rho h_1} \frac{\partial p}{\partial x_1} = \frac{\partial U_1}{\partial t} + \frac{U_1}{h_1} \frac{\partial U_1}{\partial x_1} + \frac{U_2}{h_2} \frac{\partial U_1}{\partial x_2} + \frac{U_1 U_2}{h_1 h_2} \frac{\partial h_1}{\partial x_2} - \frac{U_2^2}{h_1 h_2} \frac{\partial h_2}{\partial x_1} \\ -\frac{1}{\rho h_2} \frac{\partial p}{\partial x_2} = \frac{\partial U_2}{\partial t} + \frac{U_1}{h_1} \frac{\partial U_2}{\partial x_1} + \frac{U_2}{h_2} \frac{\partial U_2}{\partial x_2} + \frac{U_1 U_2}{h_1 h_2} \frac{\partial h_2}{\partial x_1} - \frac{U_1^2}{h_1 h_2} \frac{\partial h_1}{\partial x_2} \end{cases} \quad (4-238)$$

Finally, the boundary conditions, including a porous wall, are

$$\begin{array}{llll} \text{At } x_3 = 0: & u_1 = u_2 = 0 & u_3 = v_w(x_1, x_2, t) & T = T_w \\ \text{As } x_3 \rightarrow \infty: & u_1 \rightarrow U_1 & u_2 \rightarrow U_2 & T = T_e \end{array} \quad (4-239)$$

As for the shear stress, two components must be considered in a three-dimensional boundary layer, namely,

$$\tau_1 = \mu \frac{\partial u_1}{\partial x_3} \quad \text{and} \quad \tau_2 = \mu \frac{\partial u_2}{\partial x_3} \quad (4-240)$$

These expressions continue to hold at the wall where, generally speaking, the resultant wall shear may not be in the same direction as the resultant freestream velocity.

4-11.1 Cartesian Coordinates: Secondary Flow and Skewing

In Cartesian coordinates, $h_1 = h_2 = 1$ and we may choose y as normal to the wall. The boundary-layer continuity and momentum equations, for steady flow with constant density and viscosity, become

$$\frac{\partial u}{\partial x} + \frac{\partial v}{\partial y} + \frac{\partial w}{\partial z} = 0 \quad (4-241)$$

$$u \frac{\partial u}{\partial x} + v \frac{\partial u}{\partial y} + w \frac{\partial u}{\partial z} = U \frac{\partial U}{\partial x} + W \frac{\partial U}{\partial z} + \nu \frac{\partial^2 u}{\partial y^2} \quad u \frac{\partial w}{\partial x} + v \frac{\partial w}{\partial y} + w \frac{\partial w}{\partial z} = U \frac{\partial W}{\partial x} + W \frac{\partial W}{\partial z} + \nu \frac{\partial^2 w}{\partial z^2}$$

where $U(x, z)$ and $W(x, z)$ are the freestream velocity components. These equations, like their curvilinear counterparts in [Eqs. \(4-236\)](#), are parabolic in (x, z) and can be marched downstream from known initial values, if U and W are known. The initial conditions are not limited to a single “entrance,” $x = 0$, but extend along the *sides* of the computational field. Such side conditions, for example, $(x, y, z) = (x, y, 0)$ and (x, y, L) , are often not well known or well modeled. Dwyer (1981) takes care to point out that the “region of influence” of a point in a three-dimensional boundary layer is affected by both convection and diffusion, especially strong when there is large crossflow convection, as in a spinning rocket.

Suppose that U is locally aligned with the mainstream direction. Then $w(x, y, z)$ is called the crossflow or *secondary flow* and is strongly dependent on the curvature of the main streamlines and the associated crossflow pressure gradients. Two different types of motions are shown in [Fig. 4-45](#). In [Fig. 4-45a](#), the crossflow is unidirectional, implying a uniformly positive crossflow pressure gradient, similar to the rotating disk flow $v_r(z)$ in [Fig. 3-35](#). An effective vectorial visualization of this three-dimensional motion is through a hodograph of w vs. u , as in [Fig. 4-45c](#). Johnston (1960) suggests that a triangular hodograph shape is suitable for many unidirectional crossflows. Thus, if we model the main flow U by, say, a two-dimensional velocity profile and correlate W with U through the hodograph, we may approximate such problems with integral methods.

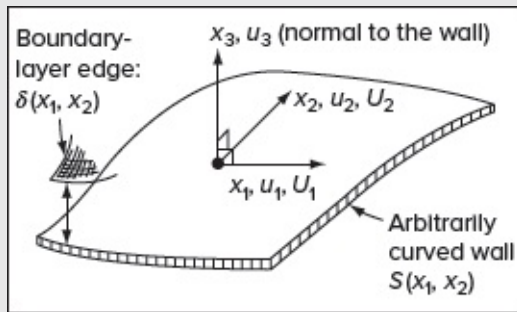


FIGURE 4-44

Orthogonal coordinate system for a three-dimensional boundary layer.

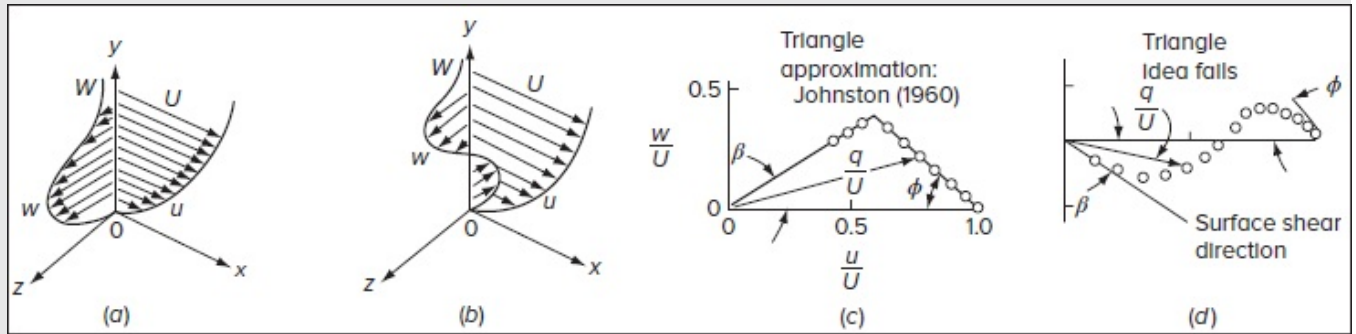


FIGURE 4-45

Unidirectional and bidirectional skewing in three-dimensional pressure-driven boundary layers: (a) unidirectional skewing; (b) bidirectional skewing; (c) unidirectional hodograph; (d) bidirectional hodograph.

A second type of crossflow is bidirectional, as shown in [Fig. 4-45b](#). This could be caused, for example, by a reversal in outer streamline curvature. The associated hodograph, [Fig. 4-45d](#), is S-shaped, which causes the triangular approximation to fail. Since such a shape is not well correlated with the outer stream conditions, integral analysis can also suffer.

Note that, in [Figs. 4-45c](#) and [d](#), the surface streamline appears at an angle β with respect to the main freestream. As such, it can be related to the surface shear stresses by

$$\tan \beta = \frac{\tau_{zy, \text{wall}}}{\tau_{xy, \text{wall}}} \quad (4-242)$$

In our numerical solution for the rotating disk, Table 3-5, the surface streamline lay at an angle of $\beta = 39.6^\circ$ compared to purely circumferential “mainstream” motion.

4-11.2 Flat-Plate Flow with a Parabolic Freestream

A simple example of secondary motion was given by Loos (1955), who envisioned a sharp flat plate immersed in a freestream that moves in parabolic curves across the plate, as shown in [Fig. 4-46](#). The velocity components are^s

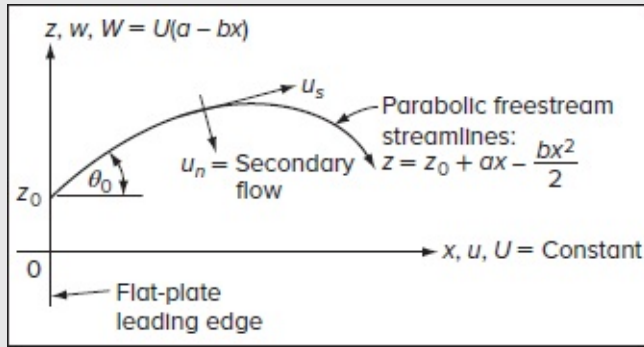


FIGURE 4-46

Definition sketch for parabolic flow over a flat plate.

$$U = \text{const}, \quad W = U(a - bx)$$

Here, a is the initial slope, and b is the curvature of the outer streamlines, as we can confirm from the geometric relation

$$\left. \frac{dz}{dx} \right|_{\text{streamline}} = \frac{W}{U} = a - bx \quad \text{or} \quad z = z_0 + ax - \frac{1}{2}bx^2 \quad (4-243)$$

As shown in [Fig. 4-46](#), z_0 is where the streamline intercepts the plate's leading edge ($x = 0$), $a = \tan \phi_0$ is the leading-edge streamline slope, and $-b = z''_{\text{streamline}}$ streamline represents the curvature of the parabolic streamlines. A good choice of coordinates here is the Cartesian system (x, y, z) with (u, v, w) velocities. For this parabolic freestream, [Eqs. \(4-241\)](#) reduce to

$$\frac{\partial u}{\partial x} + \frac{\partial v}{\partial y} = 0 \quad u \frac{\partial w}{\partial x} + v \frac{\partial w}{\partial y} = -bU^2 + \nu \frac{\partial^2 w}{\partial y^2} \quad u \frac{\partial u}{\partial x} + v \frac{\partial u}{\partial y} = \nu \frac{\partial^2 u}{\partial y^2} \quad (4-244)$$

Page 222 since the flow is everywhere independent of z . The boundary conditions are

$$y = 0: \quad u = v = w = 0; \quad y \rightarrow \infty: \quad u \rightarrow U \quad w \rightarrow W \quad (4-245)$$

By way of confirmation, it can be seen that [Eq. \(4-244\)](#) restores the Blasius model for $b = 0$, because its $-bU^2$ term captures the curvature effect that is responsible for inducing the secondary motion. Even if $a \neq 0$, the solution will still be a Blasius motion along the slanted straight lines corresponding to $dz/dx = a = \tan \phi_0$. In other words, the flow along a flat plate is not affected by the direction with which the freestream crosses the leading edge.

An exact solution to this problem can be obtained using a Blasius-type similarity variable,

$$\eta = \frac{1}{2}y\sqrt{U/(\nu x)}$$

from which the velocities can be related to three characteristic functions f , g , and h :

$$u = \frac{1}{2} U f'(\eta) \quad v = \frac{1}{2} (\eta f' - f) \sqrt{U\nu/x} \quad \text{and} \quad w = U[ag(\eta) - cxh(\eta)] \quad (4-246)$$

Substitution into [Eqs. \(4-244\)](#) yields three ordinary differential equations

$$f''' + ff'' = 0 \quad (4-246a)$$

$$g'' + fg' = 0 \quad (4-246b)$$

$$h'' + fh' - 2f'h = 0 \quad (4-246c)$$

$$\text{with} \quad f(0) = f'(0) = g(0) = h(0) = 0 \quad f'(\infty) = 2 \quad \text{and} \quad g(\infty) = h(\infty) = 1 \quad (4-248)$$

Equation (4-247a) is the Blasius equation for two-dimensional flat-plate flow. Equation (4-247b) can be integrated to give

$$g = \frac{1}{2} f' \quad (4-249)$$

This is again the Blasius solution for that portion of the spanwise flow w not associated with curvature—another verification of the independence principle. Finally, with $f(\eta)$ known, Eq. (4-247c), which is linear, can be readily solved. Sowerby (1954) computes a preemptive numerical solution to complete the problem.

To illustrate the behavior of the secondary motion, we can resolve the flow into velocity components parallel and normal to the outer streamlines (see [Fig. 4-46](#)). We get

$$\frac{u_s}{U_0} = \frac{1}{2} f' + (a - bx) \left(\frac{1}{2} a f' - cxh \right) \quad \text{and} \quad \frac{u_n}{U_0} = cx \left(h - \frac{1}{2} f' \right) \quad \text{where} \quad U_0 = U [1 + (a - bx)^2]^{-1/2} \quad (4-250)$$

Here, u_n is positive if directed toward the center of curvature of the streamlines. Since $h - \frac{1}{2} f' > 0$, the secondary flow is always toward the center of curvature.

[Figure 4-47](#) depicts a numerical example for $a = +1$, $bx = +2$, where the resultant freestream velocity is $U = U_0 \sqrt{2}$. It is seen that the secondary flow is substantial, with a maximum of 64 percent of U_0 . The streamwise component u_s has an overshoot, another aspect of curving boundary layers. The angle of deviation of the resultant velocity from the outer streamline is also substantial, being 38° at the wall. The equivalent wall angle for a rotating disk ([Chap. 3](#)) is 39.6° .

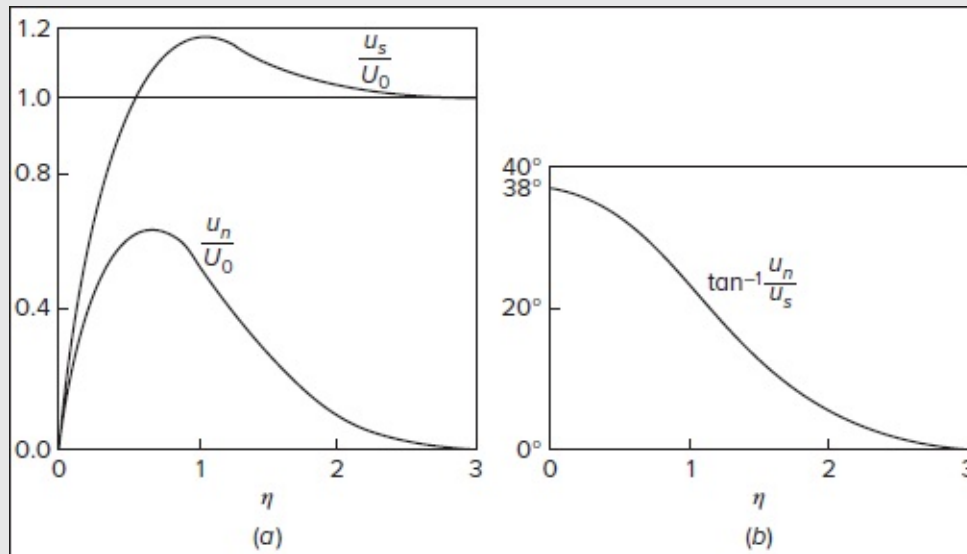


FIGURE 4-47

Laminar-boundary-layer solution for parabolic flow over a flat plate for $a = +1$, $bx = +2$: (a) velocity components; (b) deviation from external streamlines. [After Sowerby (1954).]

4-11.3 Boundary Layer on a Yawed Infinite Cylinder

The practical problem of designing swept-back wings for aircraft has led to the need for analysis of flow over a body whose leading edge is not normal to the oncoming stream. It is known that fluid in the boundary layer near the trailing edge moves outward along the wing axis toward the rearward part of the wing. This is another example of secondary flow.

For finite-span swept (possibly tapered) wings, no similarity relations can be obtained. Analysis is possible only through computer simulations. However, some illumination is possible if we assume an infinite-span wing of constant cross section, as sketched in [Fig. 4-48](#). This flow is three-dimensional, but its velocities are independent of the spanwise coordinate z . It is convenient to split the freestream into components $U(x)$ and $W(x)$ normal and parallel to the leading edge, respectively. Since the velocities do not vary with z , the boundary-layer [Eqs. \(4-235\)](#) and [\(4-236\)](#) reduce to

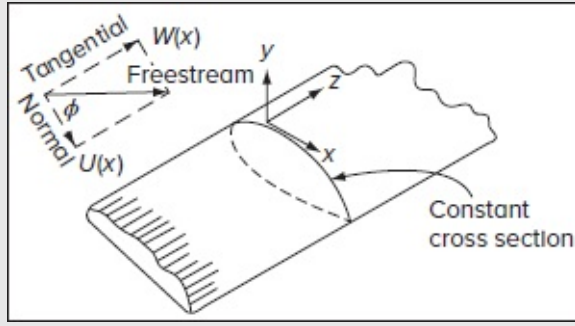


FIGURE 4-48

Coordinate system for a yawed infinite cylinder.

$$\frac{\partial u}{\partial x} + \frac{\partial v}{\partial y} = 0 \quad (4-251a)$$

$$u \frac{\partial u}{\partial x} + v \frac{\partial u}{\partial y} = U \frac{\partial U}{\partial x} + \nu \frac{\partial^2 u}{\partial y^2} \quad (4-251b)$$

$$u \frac{\partial w}{\partial x} + v \frac{\partial w}{\partial y} = \nu \frac{\partial^2 w}{\partial y^2} \quad (4-251c)$$

The boundary conditions consist of no slip at the wall and velocity matching in the freestream:

$$u(x, 0) = v(x, 0) = w(x, 0) = 0 \quad u(x, \infty) = U(x) \quad \text{and} \quad w(x, \infty) = W(x) \quad (4-252)$$

These equations were first deduced by Prandtl (1945b) in a pioneering attempt to model three-dimensional boundary layers.

Because Eqs. (4-251a) (4-251b) are independent of w , they can be solved for u and v in a two-dimensional-type analysis. The splitting of u and v from w conforms to the *independence principle*, first noted by Prandtl (1945b). If separation occurs, it is due to adverse gradients in the normal component $U(x)$. The separation “line” is illustrated in the two particular examples computed in [Fig. 4-49](#). Using approximate two-dimensional methods, Wild (1949) computed the flow over a 45° yawed 6:1 elliptical cylinder at $\alpha = 7^\circ$, and Sears (1948) computed the case of $U = C(x - x_3)$. In both configurations, the surface streamline turns asymptotically toward the separation line. Such spanwise surface motion occurs for finite wings also, and it is customary to provide chordwise boundary-layer “fences” on swept wings to avoid loss of aileron effectiveness from this crossflow.

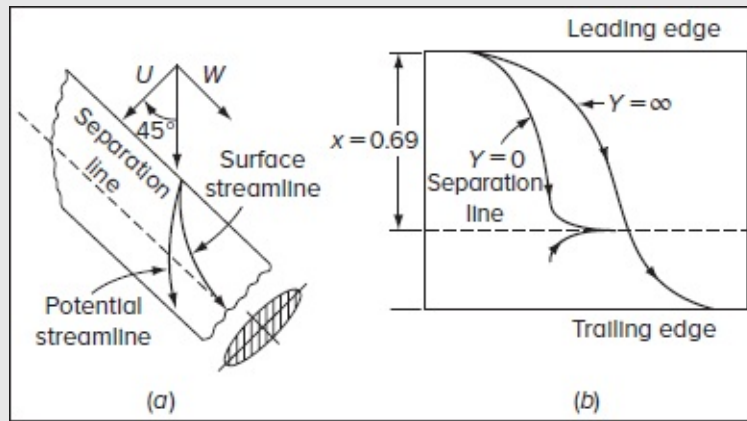


FIGURE 4-49

Two examples of outer potential flow and limiting surface streamlines for separating flow over an infinite yawed cylinder: (a) elliptical cylinder (1:6), $\phi = 45^\circ$ [after Wild (1949)]; (b) $U = C(x - x_3)$, $W = W_0$ [after Sears (1948).]

Another interesting example of three-dimensional boundary layers is the corner flow between intersecting bodies. Even the limiting case of intersecting sharp flat plates still requires three independent velocity components. In his study of flat-plate corners, Gersten (1959) predicts the three-dimensional friction drag to be lower than in the case of two independent plates of the same area:

$$C_{D, \text{corner}} \approx \frac{1.328}{Re_L^{1/2}} - \frac{C(\alpha)}{Re_L} \quad (4-253)$$

Page 224 where α is the corner angle. Gersten reports $C(90^\circ) \approx 5.76$. Experimental measurements on flat-plate corners are typically taken under turbulent-flow conditions [Nakayama and Rahai (1984)].

Further, in his study of the flow along the roots of an airfoil cascade, Gersten points out that the dual resistance of the walls causes the low-momentum corner flow to separate almost immediately in adverse gradients, as illustrated in [Fig. 4-50](#). Also shown is a separation zone which forms in the front of such round-nosed junctions and, as nose bluntness increases, grows into a horseshoe-shaped “junction vortex.”

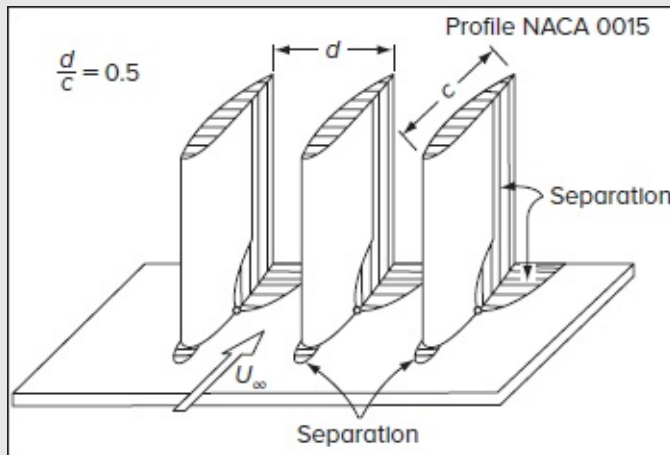


FIGURE 4-50

Separation regions in corner flow between airfoils. [After Gersten (1959).]

4-11.4 Separation Geometry in Three-Dimensional Flow

Two-dimensional separation has a simple geometry, as in [Fig. 4-9b](#). The entire boundary-layer motion breaks away at the point of zero wall shear stress and, having no way to diverge left or right, has to divert itself up and over the resulting separation bubble or wake. The ability to separate in three dimensions leads to more freedom and breakaway options. For example, the surface streamlines in [Fig. 4-49](#) move tangentially toward the separation line while the outer flow climbs up and over the bubble.

According to active research in the mathematical topology of three-dimensional separation zones [Tobak and Peake (1982), Wang (1997)], four different points in separation can be distinguished:

1. A *nodal point*, where an infinite number of surface streamlines (“skin-friction lines”) merge tangentially to the separation line.
2. A *saddle point*, where only two surface streamlines intersect and all others divert to either side.
3. A *focus*, or spiral node, which forms near a saddle point and around which an infinite number of surface streamlines swirl.
4. A *three-dimensional singular point*, not on the wall, where the velocity is zero, but serving as the center for a horseshoe vortex.

A classic example is the boundary-layer motion on the wall near a round-nosed obstacle in [Fig. 4-51](#), as studied by Johnston (1960). Because the obstacle creates an adverse gradient on the wall in front of it, the flow must separate, and the resulting bubble wraps itself around the obstacle in a U-shaped junction or horseshoe vortex. In the Tobak–Peake notation, the

point S in [Fig. 4-51](#) denotes a nodal point of separation. Inside the bubble, on the center plane between S and the obstacle, a three-dimensional singular point occurs where the vortex center forms. In the rear of such obstacles (not shown), a nodal attachment point and twin foci may also form. Baker (1979) reports experiments on the laminar horseshoe vortex. Since most practical applications (turbomachinery blade roots, wing-body junctions, control surfaces on ships) correspond to high Reynolds numbers, research on turbulent junction vortices continues [Menna and Pierce (1988)].

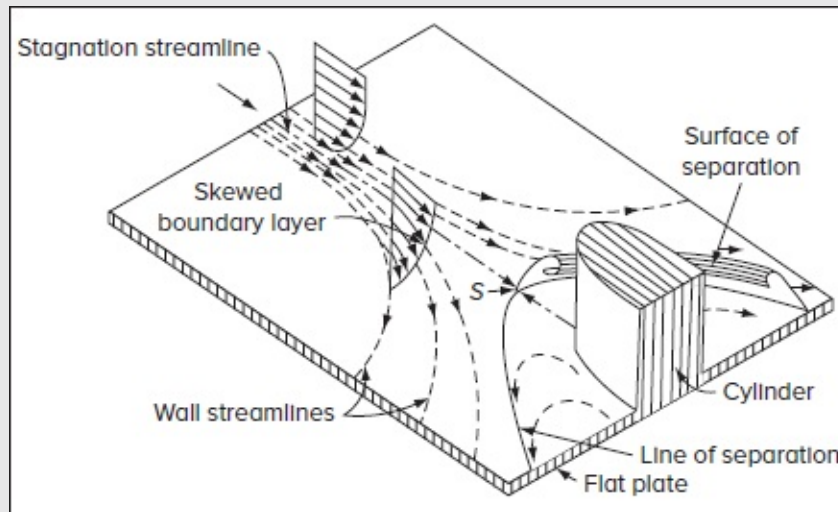


FIGURE 4-51

Three-dimensional separation in flat-plate flow against a cylindrical obstacle.
[After Johnston (1960).]

Another example of laminar three-dimensional separation is the flow past a round-nosed body at an angle of attack, sketched in [Fig. 4-52](#) and first described by Legendre (1965). In the Tobak–Peake (1981) notation, point A constitutes a nodal attachment point, point S defines a saddle point, and point F (always near S) specifies the focus of separation. In [Fig. 4-52](#), instead of forming a bubble or streamwise vortex, the separated flow breaks away from the surface in what Wang (1997) calls a *tornado-like vortex*. This behavior stands in contrast to the “open” or nonbubble separation on a prolate spheroid, where flow from upstream may enter the separated region. Though experimentation has been the key to such complex flow descriptions, mega-mesh CFD models can now simulate three-dimensional flow separation.

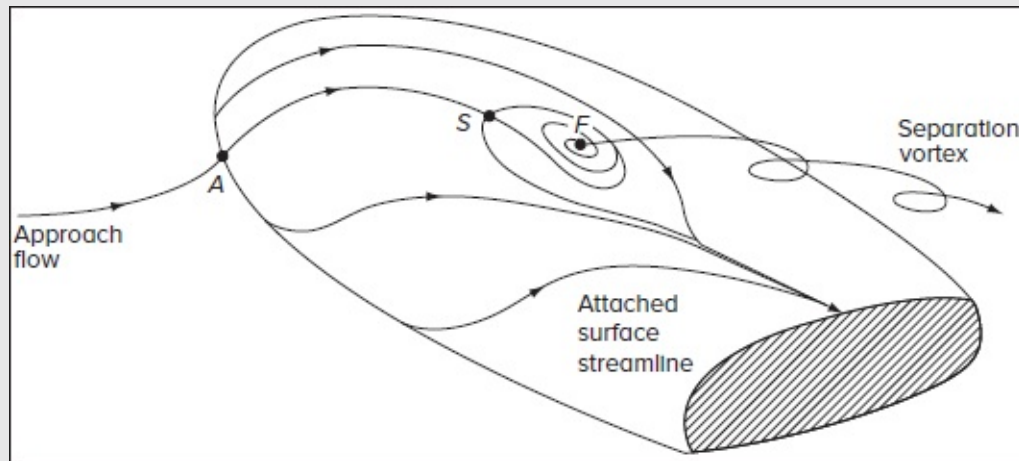


FIGURE 4-52

Three-dimensional separation on a round-nosed body at an angle of attack, first described by Legendre (1965). Points A, S, and F represent a nodal attachment point, a saddle point, and a focus of separation point, respectively.

4-12 UNSTEADY BOUNDARY LAYERS: SEPARATION ANXIETY

Unsteady flows are typically associated with (1) start-up of a flow or (2) periodic flow. Chapter 3 presented some exact unsteady Navier–Stokes solutions: in Sec. 3-4, pipe flow with a pressure gradient suddenly applied (start-up flow) or oscillating (periodic flow). Section 3-5 illustrated Stokes’ solutions for a suddenly accelerated plate (start-up flow) and an oscillating plate (periodic flow). None of these examples encountered flow separation, but many unsteady boundary layers do separate.

4-12.1 Start-Up Flows

Consider the start-up motion that occurs when a cylinder at rest suddenly begins to move at speed U . An interesting sequence ensues, as in [Fig. 4-53](#). Initially [[Fig. 4-53a](#)], the flow is inviscid and matches the classical potential-flow pattern of [Fig. 1-4](#). At $Ut/R \approx 0.35$ the shear stress vanishes at the rear stagnation point and separation begins [[Fig. 4-53b](#)]. However, boundary-layer theory predicts no Goldstein-type singularity at this time. Later, at about $Ut/R \approx 1.5$, a large standing double-vortex layer forms [[Fig. 4-53c](#)]. Much later, the alternating Kármán vortex street forms, as the final flow pattern, with separation occurring on the front of the cylinder at about 81° from the front stagnation point [[Fig. 4-53d](#)].

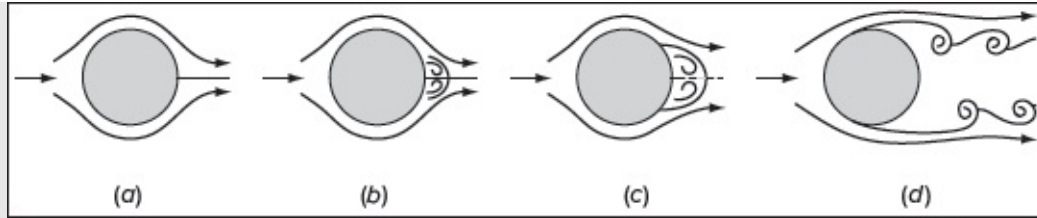


FIGURE 4-53

Start-up of viscous flow past a cylinder accelerated from rest: (a) Initial flow is nearly inviscid, resembling Fig. 1-4; (b) later, separation begins on the rear surface; (c) still later, separation extends up the rear surface in a symmetric vortex pattern; (d) finally, the double vortex becomes unstable, leading to an alternating Kármán vortex street, with the separation point on the front of the body.

The profound flow-pattern changes in [Fig. 4-53](#) prompt the questions: (1) how is separation defined in unsteady flow and (2) can boundary-layer theory still be useful? In the 1950s, Moore, Rott, and Sears [in Moore (1958)] independently proposed that unsteady separation is signaled by a singular point $[x_s(t), y_s(t)]$ in the flow where the velocity relative to the moving point s , the shear stress, and the vorticity all vanish:

$$u_s = \frac{dx_s}{dt} = 0 \quad \text{and} \quad \tau_s = \omega_s = \left. \frac{du}{dy} \right|_s = 0$$

This is now known as the MRS criterion and is the unsteady version of the Goldstein steady-flow singularity, [Eq. \(4-137\)](#). The point s need not be at the wall, and there need not be any reverse flow. Later, in the 1980s, the exact behavior of the boundary layer on the impulsively started cylinder of [Fig. 4-53](#), became controversial, as discussed in the monographs by Cebeci (1982) and Telionis (1981). Van Dommelen and Shen (1981, 1982) give a good explanation in a careful numerical study. Using Lagrangian coordinates and a fine mesh, they calculate a non-Goldstein singularity, at about 111° from the front, in the form of a nearly inviscid “peel-off” of a vorticity layer from the wall. The wall shear stress is not necessarily zero at this point. In Van Dommelen’s words, “the boundary layer is ejected away from the wall after a finite time” of order $Ut/R \approx 1.5$. Thus, boundary-layer theory is also fundamentally limited in unsteady separated flow [Koumoutsakos and Leonard (1995), Haller (2004)].

4-12.2 Periodic Flows: Acoustic Streaming

The second important type of unsteady viscous flow is an oscillatory boundary layer. An illustrative case occurs when a cylindrical body of length L oscillates in a fluid at rest, with a small oscillatory amplitude, $A \ll L$. If, in steady freestream flow, the body has the potential flow distribution $U_0(x)$, the oscillating body will create a potential flow that is given by

$$U(x, t) = U_0(x)\cos(\omega t)$$

Page 227 Thus, the boundary layer is driven by an oscillating freestream, much like the flat wall in Stokes' second problem, Sec. 3-5.1. For a circular cylinder oscillating at high frequency, Schlichting (1932) provides a solution in series form. The first-order solution is identical to Eq. (3-149) for Stokes' second problem:

$$u_0(x, t) = U_0(x)[\cos(\omega t) - e^{-\eta}\cos(\omega t - \eta)]; \quad \eta = y\sqrt{\frac{\omega}{2\nu}}$$

The second-order solution $u_1(x, t)$ turns out to have a finite, non-vanishing value in the freestream

$$u_1(x, \infty) = -\frac{3}{4} \frac{U_0}{\omega} \frac{dU_0}{dx}$$

This term occurs because the convective acceleration terms, such as $u_0(\partial u_0 / \partial x)$, have a nonzero mean value when they oscillate. The term $u_1(x, \infty)$ is thus called *acoustic streaming*, a motion toward decreasing the freestream velocity $U_0(x)$, created by the body oscillation. Schlichting's solution explains the formation of dust patterns in a Kundt tube when standing waves occur, as first studied by Lord Rayleigh in 1883. [Figure 4-54](#) shows Schlichting's sketches of acoustic streaming caused by an oscillating cylinder. This concept of periodic motions causing nonzero mean convective terms will be very important in flow stability ([Chap. 5](#)) and turbulent flow ([Chap. 6](#)). Further studies of unsteady viscous flows are given in the monograph by Telionis (1981).

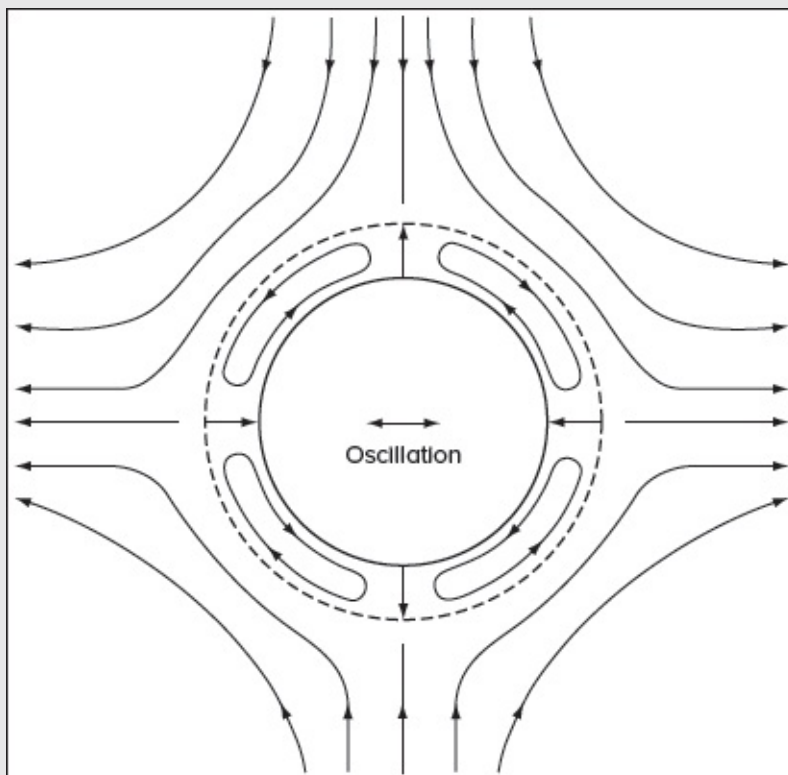


FIGURE 4-54

Streamlines for acoustic streaming in the outer flow about an oscillating circular cylinder. [After Schlichting (1932).]

4-13 FREE-CONVECTION BOUNDARY LAYERS

Although we have included body forces in the derivation of the basic equations, we have not yet considered any solutions of flow with buoyancy effects. The purpose of this section is to discuss some examples of natural-convection boundary layers. There are many practical cases of buoyant flow in both engineering (heat exchangers, computer chips, fires, and plumes) and geophysics (ocean and atmosphere). For further reading, see the monographs by Jaluria (1980) and by Kakaç et al. (1985).

4-13.1 Velocity Scales: The Grashof Number

We consider purely buoyant flows, i.e., with no superimposed freestream or “forced” motion. With no stream velocity U_∞ as a reference, we must scale the flow velocities with the body force. We further restrict ourselves to single-phase flows, thus excluding problems associated with condensation and melting. Page 228

If a fluid contains density differences $\Delta\rho$, arising from temperature or concentration differences, a gravitational body force $g\Delta\rho$ will drive the motion. For example, in flow next to a hot vertical wall, the average buoyant force in the near-wall layers will be $g(\rho_\infty - \rho_w)/2$. If the lighter fluid rises, from rest, a distance L , it will (approximately) lose potential energy and gain kinetic energy or motion. We thus maintain a crude energy balance

$$\frac{1}{2}\Delta\rho gL \approx \frac{1}{2}\rho V^2 \quad \text{or} \quad V \approx \sqrt{gL \frac{\Delta\rho}{\rho}} \quad (4-254)$$

The quantity V is the appropriate velocity scale for free convection. In this vein, an equivalent Reynolds number squared can be defined for buoyant flows:

$$Re_{\text{effective}}^2 = \left(\frac{VL}{\nu}\right)^2 = \frac{gL^3}{\nu^2} \frac{\Delta\rho}{\rho} = Gr_L \quad (4-255)$$

This new parameter Gr , the *Grashof number*, takes the place of the Reynolds number (squared) in free convection. In the common case of buoyancy caused by temperature differences, $\Delta\rho$ can be related to ΔT through the coefficient of thermal expansion β and a linear approximation:

$$\Delta\rho \approx \rho\beta\Delta T \quad \text{or} \quad Gr_L = \frac{g\beta\Delta TL^3}{\nu^2} \quad (4-256)$$

By comparing the relative sizes of Grashof and Reynolds numbers, we may determine when free-convection effects are important:

$Gr \ll Re^2$:	forced convection dominates
$Gr \gg Re^2$:	free convection dominates
$Gr = O(Re^2)$:	“mixed” free and forced convection

For a given size and temperature difference, the fluid buoyancy parameter ($g\beta/\nu^2$) determines the strength of the Grashof number. According to the values given in [Table 4-13](#), viscous oils have poor buoyancy, gases have moderate to good levels, and light liquids and liquid metals have high buoyancy potential.

TABLE 4-13

Buoyancy parameter of various fluids at 20°C and 1 atm earth gravity

Fluid	$g\beta/\nu^2 [\text{K}^{-1}\text{m}^{-3}]$
Glycerin	3.2×10^3
Engine oil	7.9×10^3
Helium	2.4×10^6
Hydrogen	3.1×10^6
Air	1.5×10^8
Carbon dioxide	5.3×10^8
Water	2.0×10^9
Ethyl alcohol	4.5×10^9
Mercury	1.4×10^{11}

4-13.2 Two-Dimensional Steady-Free Convection

Let us now reconsider the boundary-layer equations from Eqs. (4-50a)–(4-50c) for steady flow with constant properties and nonnegligible buoyancy:

$$\begin{aligned}
 \frac{\partial u}{\partial x} + \frac{\partial v}{\partial y} &= 0 \\
 u \frac{\partial u}{\partial x} + v \frac{\partial u}{\partial y} &= g_x \beta (T - T_0) + \nu \frac{\partial^2 u}{\partial y^2} \\
 u \frac{\partial T}{\partial x} + v \frac{\partial T}{\partial y} &= \alpha \frac{\partial^2 T}{\partial y^2}
 \end{aligned}
 \tag{4-257}$$

Page 229 where $\alpha = k/(\rho c_p)$ is the (constant) thermal diffusivity. Note that we have neglected dissipation. We have also assumed no forced motion and dropped the external pressure gradient UdU/dx . Since buoyancy is proportional to g_x , the component of gravity parallel to the solid boundary, it may be important to account for geometric changes in g_x if the surface is curved or inclined.

The usual boundary conditions consist of no slip or temperature jumps at the wall and a

fluid at rest under ambient temperature at infinity:

$$u(x, 0) = v(x, 0) = u(x, \infty) = 0 \quad T(x, 0) = T_w(x) \quad \text{and} \quad T(x, \infty) = T_\infty = \text{const} \quad (4-258)$$

There are many analyses of these equations in the literature for various geometric flow configurations and applications. An excellent treatment, both broad and deep, is given by Gebhart et al. (1988).

4-13.3 Free Convection along a Vertical Isothermal Plate

For a vertical plate with $g_x = g$, let us assume constant T_w . If we ignore the anomalous case of water near freezing, where β may be negative, all common fluids have low density at a hot wall. Buoyant motion and free convection are both upward along a hot vertical plate, and the leading edge $x = 0$ starts at the bottom. For a cold plate, buoyancy is downward and $x = 0$ is located at the top of the plate. The coordinate y is normal to the plate.

Since the local Grashof number Gr_x plays the role of Re_x^2 in buoyant motion, we can guess (correctly) that the boundary-layer thickness δ/x will be proportional to $Gr_x^{1/4}$. Indeed, the “scale analysis” in the text by Bejan (1994) predicts that δ will be proportional to $x^{1/4}$. For vertical plate flow, velocity and thickness scales are prescribed by Schmidt et al. (1930) in an assortment of similarity variables:

$$\eta = \left(\frac{Gr_x}{4}\right)^{1/4} \frac{y}{x} \quad Gr_x = \frac{\beta g(T_w - T_\infty)x^3}{\nu^2} \quad u = 2\sqrt{x\beta g(T_w - T_\infty)}f' \quad v = \left[\frac{\beta g(T_w - T_\infty)\nu^2}{4x}\right]^{1/4} (\eta f' - 3f) \quad \Theta = \frac{T - T_\infty}{T_w - T_\infty} \quad (4-259)$$

The reader can verify that u and v satisfy continuity and that these variables will reduce momentum and energy relations to the two coupled nonlinear ordinary differential equations

$$f''' + 3ff'' - 2f'^2 + \Theta = 0 \quad \text{and} \quad \Theta'' + 3Prf\Theta' = 0 \quad (4-260)$$

subject to the boundary conditions

$$f(0) = f'(0) = f'(\infty) = 0 \quad \text{and} \quad \Theta(0) = 1 \quad \Theta(\infty) = 0 \quad (4-261)$$

Note that [Eqs. \(4-260\)](#) are coupled and must be solved simultaneously, which is always the case in free-convection problems. Since no analytic solution is known, numerical integration is necessary. There are two unknown initial values at the wall. One must find the proper values of $f''(0)$ and $\Theta'(0)$, which cause the velocity and temperature to vanish for large η .

The original approximate solutions given by Pohlhausen in 1930 are improved in the digital-computer solutions provided by Ostrach (1953) and others. Some accurate initial values are listed in [Table 4-14](#). Velocity and temperature profiles are shown in [Fig. 4-55](#) for various Prandtl numbers. Except for $Pr \ll 1$, the velocity layers are thicker than the temperature layers. These theoretical profiles stand in good agreement with experimental

laminar free-convection data on vertical surfaces.

TABLE 4-14

Computed parameters from [Eqs. \(4-260\)](#) for free convection on a vertical isothermal plate

Pr	$f''(0)$	$-\Theta'(0)$	$Nu_x/Gr_x^{1/4}$
0.01	0.9873	0.0807	0.0571
0.1	0.8591	0.2301	0.1627
0.72	0.6760	0.5046	0.3568
1.0	0.6422	0.5671	0.4010
2.0	0.5713	0.7165	0.5066
3.0	0.5309	0.8155	0.5767
6.0	0.4649	1.0075	0.7124
10.0	0.4192	1.1693	0.8268
30.0	0.3312	1.5891	1.1237
100.0	0.2517	2.1913	1.5495
1000.0	0.1449	3.9650	2.8037

Page 230

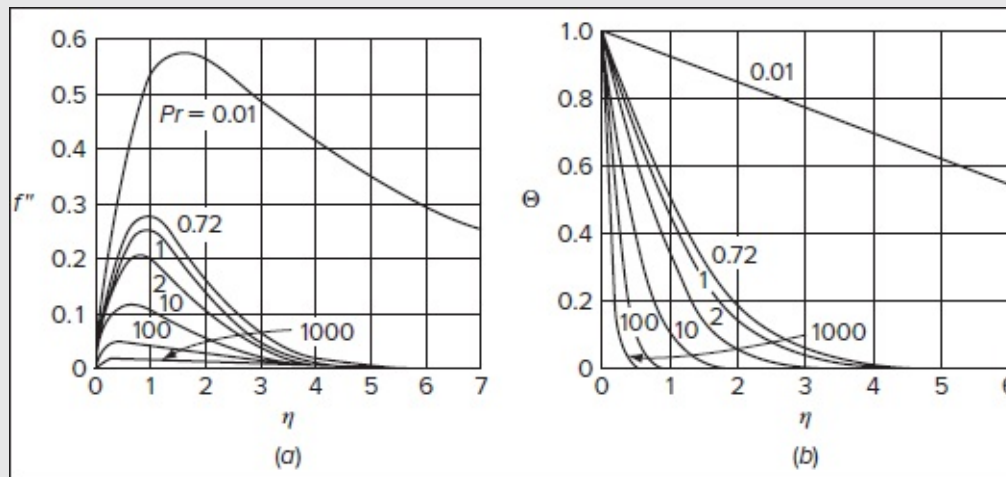


FIGURE 4-55

(a) Velocity and (b) temperature profiles for free convection on a vertical plate. Computed by Ostrach (1953) from the differential [Eqs. \(4-260\)](#) of Pohlhausen.

The most important results of the analysis are the dimensionless heat-transfer rates, or Nusselt numbers:

$$Nu_x = \frac{xq_w}{k(T_w - T_\infty)} \text{ (local)} \quad Nu_m = \frac{1}{L} \int_0^L Nu_x dx \text{ (mean)} \quad (4-262)$$

From the definition of Θ , we have $Nu_x(4/Gr_x)^{1/4} = -\Theta(0) = F(Pr)$, where Gr_x is the local Grashof number defined in [Eq. \(4-259\)](#). Since q_w varies as $x^{-1/4}$, it follows that the two Nusselt numbers are related simply by $Nu_x(L) = \frac{3}{4}Nu_m$. Some numerical values of $Nu_x/Gr_x^{1/4}$ are listed in [Table 4-14](#). For gases with Pr near unity, a simple power law is sufficient. One gets

$$Nu_x \approx 0.4Ra_x^{1/4} \quad \text{with} \quad Ra_x = Gr_x Pr \quad (4-263)$$

where Ra_x is called the *Rayleigh number* of the flow. Meanwhile, Churchill and Usagi (1972) propose the following curve-fit formula which is valid within ± 0.5 percent accuracy over the entire range of Prandtl numbers:

$$Nu_x \approx \frac{0.503Ra_x^{1/4}}{[1 + (0.492/Pr)^{9/16}]^{4/9}} \quad [\text{Churchill and Usagi (1972)}] \quad (4-264)$$

This formula is limited to isothermal walls and the laminar free-convection flow regime, with $10^5 < Ra_x < 10^9$. It predicts Nu_x varying as $(Gr_x Pr^2)^{1/4}$ for very small Pr $(Gr_x Pr)^{1/4}$ for very large Pr , which can be proved asymptotically.

The stability and transition of free-convection flows are reviewed by Gebhart and Majahan (1982) as well as Gebhart et al. (1988). Boundary-layer instability begins for Grashof numbers as low as 400, and fully turbulent flow generally develops by $Gr_x \approx 10^9$. The local Nusselt numbers in turbulent flow then vary approximately as $Gr_x^{1/3}$. Although the local heat flux may change sharply during transition, the overall heat transfer rate increases gradually and is well represented by the curve-fit correlation of Churchill and Chu (1975):

$$Nu_L^{1/2} = 0.825 + \frac{0.387Ra_L^{1/6}}{[1 + (0.492/Pr)^{9/16}]^{8/27}} \quad Ra_L \leq 10^{12}, \forall Pr \quad (4-265)$$

which is valid for isothermal walls regardless of the Prandtl number.

The related problem of laminar free convection on a vertical surface with uniform heat flux was solved by Sparrow and Gregg (1956). Their computational results for the local heat transfer are fitted by Churchill and Ozoe (1973) into the formula

$$Nu_x \approx \left(\frac{Gr_x^* Pr^2}{4 + 9Pr^{1/2} + 10Pr} \right)^{1/5} \quad 10^5 < Gr_x^* < 10^{12}, \forall Pr \quad (4-266)$$

The quantity $Gr_x^* = Gr_x Nu_x = g\beta q_w x^4 / (k\nu^2)$ is termed the modified or “heat-flux” Grashof number. For overall heat transfer in both laminar and turbulent flow, Churchill and Chu (1975) propose the curve-fit:

$$Nu_L^{1/2} = 0.825 + \frac{0.387(Gr_L Pr)^{1/6}}{[1 + (0.437/Pr)^{9/16}]^{8/27}} \quad 1 < Gr_L Pr < 10^{11}, \forall Pr \quad (4-267)$$

Page 231 Interestingly, this correlation uses the traditional rather than the modified Grashof number and, therefore, must be iterated with the relation $Gr_L = Gr_L^* / Nu_L$ since the temperature difference varies over the surface.

4-13.4 Other Geometries

If a plane surface in free convection is inclined from the vertical by an angle ϕ , the first-order theoretical effect is to decrease the gravitational force (per unit mass) from g to $g \cos\phi$. The second-order effect depends on whether the lateral buoyancy component is toward or away from the plate surface. In the latter case, the flow tends to separate away from the plate. The overall conclusion of many experiments [Gebhart et al. (1988, Sec. 5.2)] is that, if $|\phi| \leq 60^\circ$, the heat transfer may be computed by evaluating the vertical-surface formulas at the effective Grashof number of $Gr_x \cos \phi$.

The laminar-flow solution for a vertical cylinder is given by Sparrow and Gregg (1956). The heat transfer is increased if the boundary layer becomes thick compared to the radius of the cylinder. The appropriate parameter here is $\zeta = (L/D)Ra_L^{-1/4}$, and an approximate correction relates the overall heat transfer to a vertical plate of the same length using

$$Nu_{L, \text{cylinder}} \approx Nu_{L, \text{plate}} (1 + 1.3\zeta^{0.9}) \quad (4-268)$$

where the plate Nusselt number is taken from [Eq. \(4-265\)](#).

Perhaps the most practical shape is the horizontal cylinder, which occurs so often in heat-exchanger design. The first theory is by Hermann (1936), who uses the boundary-layer [Eqs. \(4-257\)](#) with gravity varying as $g_x = g \sin(x/R)$. Moreover, Kuehn and Goldstein (1980) have reported fully elliptic Navier–Stokes computations for this case. Their computed and experimental isotherms for $Ra_D = 10^5$ are shown in [Fig. 4-56](#). Note that, unlike forced motion past a cylinder, there is no separation at the rear of the body. Rather, the flow at the rear gradually spreads and turns to form a plume above the cylinder. At lower Rayleigh numbers, $Ra_D < 10^4$ [Kuehn and Goldstein (1980)], the entire flow resembles a plume near a hot “source” and is much larger in extent than the body radius.

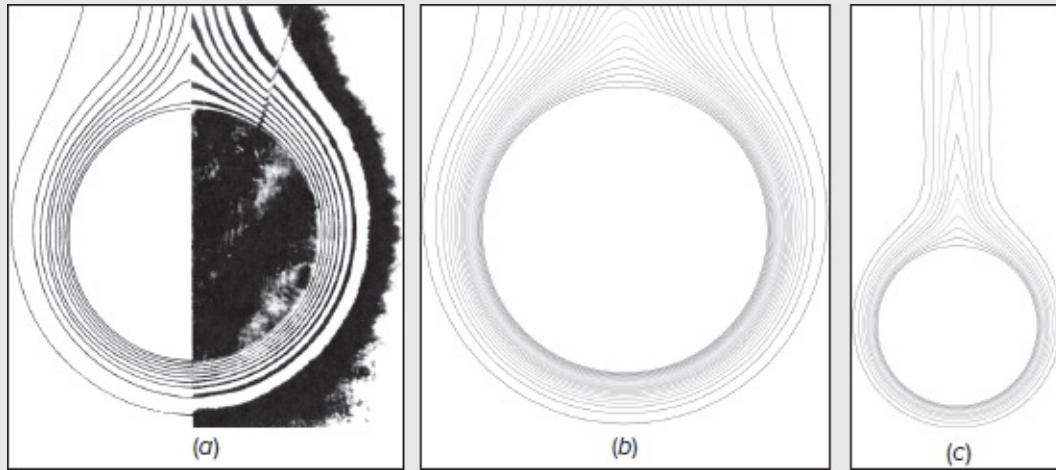


FIGURE 4-56

Comparison of isotherms in free convection near a heated horizontal cylinder showing (a) both experimental and fully elliptic Navier–Stokes computations (mirrored right and left); [from Kuehn and Goldstein (1980), courtesy of the authors.] (b) independent computations using a finite-volume Navier-Stokes solver with a zoomed-out view in (c) [replicated by G. Sharma and J. Majdalani].

Along similar lines, free-convection heat transfer on a horizontal cylinder can be approximated by a vertical plate of length $\pi D/2$, the “length of travel” of a particle in the boundary layer. Churchill and Chu (1975) recommend the following general curve-fit for cylinders:

$$Nu_D^{1/2} = 0.60 + \frac{0.387 Ra_D^{1/6}}{[1 + (0.559/Pr)^{9/16}]^{8/27}} \quad 10^{-5} < Ra_D < 10^{12}, \forall Pr \quad (4-269)$$

Note the similarity to [Eq. \(4-256\)](#) for a vertical plate. A more accurate regime-specific correlation is recommended by Goldstein et al. (2019), namely,

$$\text{Laminar:} \quad (Nu_D)_{\text{lam}} = \frac{2}{\ln \left[1 + \frac{2.7}{f(Pr) Ra_D^{1/4}} \right]}; f(Pr) = \frac{0.701}{\left[1 + \left(\frac{1}{2Pr} \right)^{10/17} \right]^{4/9}} \quad Ra_D < 10^6, \forall Pr \quad (4-270)$$

$$\text{Turbulent:} \quad (Nu_D)_{\text{turb}} = 0.1 Ra_D^{1/3} \quad Ra_D > 10^9, \forall Pr \quad (4-271)$$

This correlation turns into a blending function within the intermediate or transitional $10^6 < Ra_D < 10^9$ range, specifically, $(Nu_D)_{\text{tr}} = [(Nu_D)_{\text{lam}}^{12} + (Nu_D)_{\text{turb}}^{12}]^{1/12}$. For further studies of buoyant free- or mixed-convection flows, see Gebhart et al. (1988).

SUMMARY

This chapter reviews in some detail the many different types of laminar-boundary-layer flows, with emphasis upon both velocity and temperature distributions. The simple integral momentum and energy analyses of Sec. 4-1 lead into the full boundary-layer equations of Sec. 4-2. A variety of similarity solutions are discussed in Sec. 4-3, followed by free-shear flows (mixing layers, jets, and wakes) in Sec. 4-4 and a few nonsimilar flows in Sec. 4-5. Among the similarity solutions, a strong emphasis is placed on the Blasius equation and the various analytical and numerical methods that can be used to solve it. Methods of analysis for general boundary-layer motions are introduced in Sec. 4-6, with a focus on integral techniques, such as Kármán's momentum-integral approach and Thwaites' one-parameter technique; these are then augmented in Sec. 4-7 with finite-difference methods that are suitable for boundary-layer treatment. In this process, a simplification of Kármán's momentum-integral approach is provided along with an explanation of the paradoxical behavior of Pohlhausen's polynomial approximations, which has intrigued the fluid mechanics community for over 100 years. Thermal boundary layers are analyzed in Sec. 4-8 by both integral and finite-difference methods. Section 4-9 provides a brief treatment of flow in the inlets of ducts, and Sec. 4-10 presents a variety of axisymmetric boundary-layer solutions for round jets and wakes. The chapter ends with discussions of three-dimensional boundary layers (Sec. 4-11), unsteady boundary layers (Sec. 4-12), and free-convection flows (Sec. 4-13).

We should emphasize that laminar flows inevitably break down at some critical Reynolds number and that the ensuing motion will be turbulent ([Chap. 6](#)). In this vein, [Chap. 5](#) will examine the stability and transition of laminar flows and the techniques used to predict the onset of instability. So why should we dwell on laminar flows, when turbulence is so often the actual state of affairs? The answer is simple: laminar theory is far more advanced than turbulent-boundary-layer theory, and the many phenomena that we have just described—similarity, momentum balance, separation, favorable gradients, free convection, three-dimensional flow—are representative of the general behavior of boundary layers. For this reason, the tools that we have learned in this chapter will better prepare us to explore the world of turbulence. Often the only differences between laminar and turbulent-flow correlations will be seen in the numerical values of their coefficients and exponents.

PROBLEMS

- 4-1.** Repeat the momentum-integral analysis of the flat plate in Sec. 4-1 for Pohlhausen's cubic polynomial profile

$$\frac{u}{U} = \frac{3}{2}\left(\frac{y}{\delta}\right) - \frac{1}{2}\left(\frac{y}{\delta}\right)^3$$

where $\delta(x)$ is the boundary-layer or disturbance thickness as pictured in [Fig. P4-1](#). Is this profile any more (or less) realistic than the approximation of [Eq. \(4-11\)](#)? For the above profile, compute (a) $(\theta/x)\sqrt{Re_x}$; (b) $(\delta^*/x)\sqrt{Re_x}$; (c) $(\delta/x)\sqrt{Re_x}$; (d) $C_f\sqrt{Re_x}$; (e) $C_D\sqrt{Re_x}$.

Answers: (a) 0.646, (b) 1.740, (c) 4.64, (d) 0.646, (e) 1.293

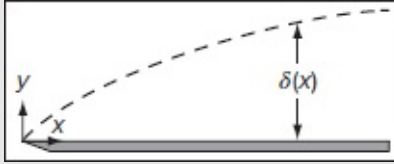


Figure P4.1

- 4-2. Repeat the integral heat-transfer analysis of Sec. 4-1.7 by replacing Eq. (4-30) by the quartic temperature profile approximation

$$T - T_e \approx (T_w - T_e)(1 - 2\zeta + 2\zeta^3 - \zeta^4)$$

What boundary conditions does this profile satisfy? Compare your results with [Eqs. \(4-32\)](#) and [\(4-33\)](#).

- 4-3. Schlichting (1979, p. 206) points out that the simple flat-plate velocity profile approximation

$$u \approx U \sin\left(\frac{\pi y}{2\delta}\right) \quad [\text{Schlichting (1979)}]$$

gives much better accuracy for C_f , θ , and δ^* (± 2 percent) than Pohlhausen's parabolic profile

$$u(y) \approx U\left(\frac{2y}{\delta} - \frac{y^2}{\delta^2}\right) \quad [\text{Pohlhausen (1921)}]$$

Page 233

Verify this statement by computing C_f . Does Schlichting's sine-wave shape satisfy any additional boundary conditions compared to Pohlhausen's parabolic profile?

- 4-4. Air at 20°C and 1 atm flows past a smooth flat plate as in [Fig. P4-4](#). A pitot stagnation tube, placed 2 mm from the wall, develops a water manometer head $h = 21$ mm. Use this information with the Blasius solution, [Table 4-3](#), to estimate the position x of the pitot tube. Check to see if the flow is laminar.

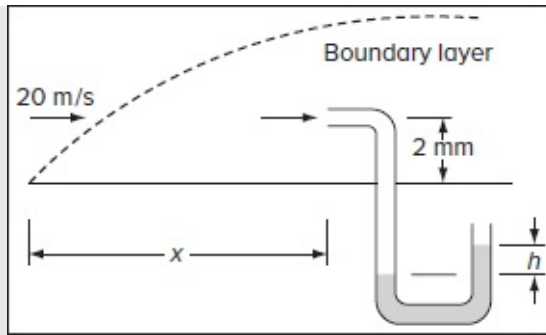


Figure P4.4

- 4-5. In the unheated-starting-length analysis that led to [Eq. \(4-37\)](#), a term $(\zeta^3/5)$ is neglected in the integral-energy equation. Without neglecting this term, solve the differential equation numerically (e.g., with Runge–Kutta) for $1 < x < 5$, $x_0 = 1$ and the special case of $Pr = 1$. Compare your numerical results with [Eq. \(4-37\)](#).
- 4-6. Develop a numerical solution (e.g., using Runge-Kutta integration), and [Eqs. \(4-63\)](#), that will iterate the Blasius equation from an initial guess $f''(0) = 0.3$ and converge to the exact value $f''(0) = 0.4696$.
- 4-7. Consider a long flat plate emerging from a wall at velocity U as in [Fig. P4-7](#). There is no freestream. Show that the Blasius [Eq. \(4-60\)](#) holds for this case, with $f(0) = 0$, $f'(0) = 1$, and $f'(\infty) = 0$. Solve the equation numerically and show that $C_f \approx 0.444/R e_{x1}/2$. Also evaluate $u(\infty)$ and discuss. [Hint: Note that $f''(0)$ is negative.]

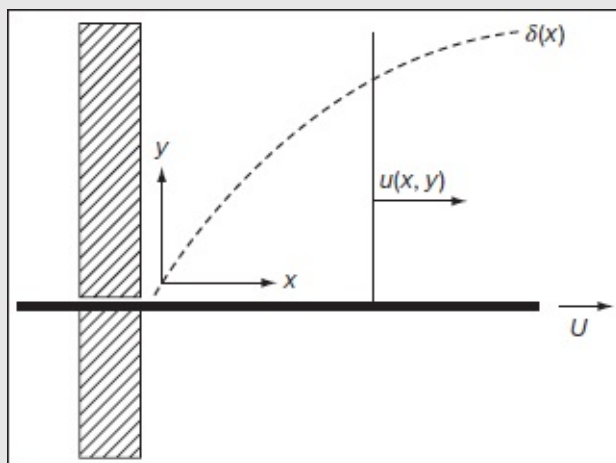


Figure P4.7

- 4-8. Develop a numerical solution (e.g., using Runge–Kutta integration), and [Eqs. \(4-](#)

96), which will iterate the Falkner–Skan Eq. (4-93), for any fixed value of $\beta \neq 0$, from an initial guess for $f''(0)$ to the precise value of $f''(0)$ within a user-defined error tolerance. Compare your results with Fig. 4-16.

- 4-9. The Blasius Eq. (4-60) must be iterated to find the value of $f''(0)$, which causes $f'(\infty)$ to equal 1.0. Töpfer (1912) and then Weyl (1942), Parlange et al. (1981), Panton (1996), and Fazio (2019) suggest the following to avoid iteration: Define

$$f(\eta) = \alpha F(\alpha\eta), \text{ where } \alpha \text{ is a constant}$$

- (a) Show that the function F also satisfies the Blasius equation. (b) If we arbitrarily set an initial condition $F''(0) = 1.0$, explain how α can be found without iteration. (c) Even with α found, explain why the solution for F is difficult to align with Table 4-3. (d) If an integration (not required of you) then yields $F'(\infty) = 1.65519036$, what is the proper value of α ? (e) Show that the value of α from part (d) leads to the result $f''(0) = 0.4696$.

Page 234

- 4-10. The quantity $(\delta^*/\tau_w)(dp/dx)$ is called Clauser's parameter. It compares an external pressure gradient to wall friction and is very useful for turbulent boundary layers (Chap. 6). (a) Show that this parameter is a constant for a given laminar Falkner–Skan wedge-flow boundary layer. (b) What value does this parameter have at the separation condition?

Answers: (a) $-2m\eta^*/[(m+1)f''(0)]$, (b) positive infinity.

- 4-11. If, instead of Eq. (4-92), we choose the Falkner–Skan similarity variable $\eta = y\sqrt{|U|/(\nu x)}$, the Falkner–Skan equation becomes

$$f''' + \frac{1}{2}(m+1)ff'' + m(f^2 - 1) = 0$$

subject to the same boundary conditions Eq. (4-94). Examine this relation for the special case of $U = -K/x$ and show that a closed-form solution may be obtained.

Answer: $u/U = 3 \tanh^2[(y/x)\sqrt{K/(2\nu)} + \tanh\sqrt{2/3}] - 2$

- 4-12. A thin equilateral triangle plate is immersed parallel to a 12 m/s stream of air at 20°C and 1 atm, as in Fig. P4-12. Assuming laminar flow, estimate the drag of this plate (in N).

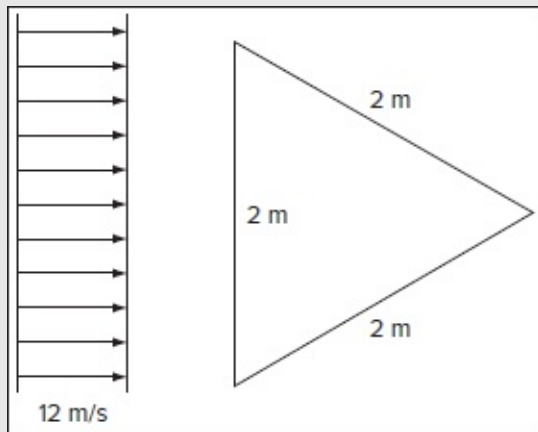


Figure P4.12

- 4-13.** Flow straighteners consist of arrays of narrow ducts placed in a flow to remove swirl and other transverse (secondary) velocities. One element can be idealized as a square box with thin sides as in [Fig. P4-13](#). Using laminar flat-plate theory, derive a formula for the pressure drop ΔP across an $N \times N$ bundle of such boxes.

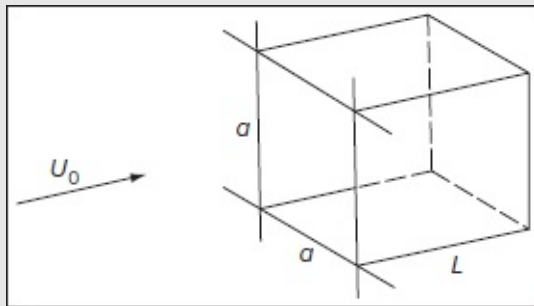


Figure P4.13

- 4-14.** Develop a numerical solution for the Blasius equation with wall suction or blowing, for a particular value $v_w^* \neq 0$, and compare your results with [Fig. 4-20](#).
- 4-15.** Derive a relation for the skin-friction coefficient C_f as a function of the local Reynolds number Re_x for boundary-layer flow toward a point sink, [Eq. \(4-111\)](#). Compare your result with the stagnation flow solution with a strong favorable gradient.
- 4-16.** Develop a numerical solution for a laminar mixing layer between parallel streams, for a particular value of k , and compare with [Fig. 4-17](#).

- 4-17.** Air at 20°C and 1 atm issues from a narrow slot and forms a two-dimensional laminar jet. At 50 cm downstream of the slot, the maximum velocity is 20 cm/s. Estimate, at this position, (a) the jet width, (b) the jet mass flow per unit depth, and (c) an appropriate Reynolds number for the jet.

Answers: (a) 0.09 m, (b) 0.0072 kg/(m · s), (c) 1200

Page 235

- 4.18.** Air at 20°C and 1 atm flows at 1 m/s past a slender two-dimensional body, of length $L = 30$ cm, whose drag coefficient is 0.05 based on a “plan” area (bL). Assuming laminar flow at a point 3 m downstream of the trailing edge, estimate (a) the maximum wake velocity defect (in m/s), (b) the “one percent” wake thickness (in m), and (c) the wake-thickness Reynolds number.

Answers: (a) 0.32 m/s, (b) 0.029 m, (c) 600

- 4-19.** Derive the steady-flow version of the momentum-integral relation, [Eq. \(4-142\)](#) or its equivalent, including wall suction or blowing, by making a mass and force balance on the differential boundary-layer control volume shown in [Fig. P4-19](#).

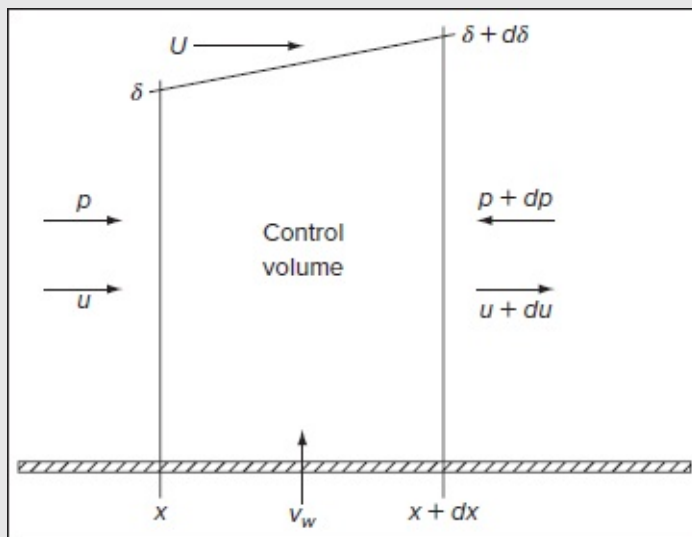


Figure P4.19

- 4-20.** Solve the integral relation [Eq. \(4-142\)](#), with $v_w \neq 0$ and a velocity profile given by [Eq. \(4-11\)](#), by assuming that both δ and $1/v_w$ are proportional to $x^{1/2}$. Compare the computed wall friction with [Fig. 4-20b](#) for $Pr = 1$, assuming that $Nu_x/Re_x = C_f/2$.
- 4-21.** Improve Prob. 4-20 by developing a parametric polynomial velocity profile which

accounts for blowing and suction in the manner of [Fig. 4-20a](#). Match your profile at the wall to the boundary-layer equations. Hint: At $y = 0$, although the no-slip condition still holds, with $u = 0$, blowing or suction require satisfying an additional relation at the wall, namely

$$\rho v_w \frac{\partial u}{\partial y} = \mu \frac{\partial^2 u}{\partial y^2}$$

- 4-22.** Modify Prob. 4-20 by using the same profile [Eq. \(4-11\)](#) but letting the suction or blowing v_w be constant. Solve for $C_f(x)$ and $\delta(x)$, and compare the asymptotic results with [Fig. 4-26](#) and Eq. (3-158).
- 4-23.** Apply the method of Thwaites, Sec. 4-6.6, to boundary-layer flow on a cylinder, using either the inviscid [Eq. \(4-164\)](#) or measured [Eq. \(4-165\)](#) freestream velocity distributions. Compare the computed local wall friction with [Fig. 4-29b](#).
- 4-24.** Apply the Thwaites' integral method to one of the laminar-flow test cases in [Table 4-9](#) (for best results have each member of the class take a different case). Compute and plot the local friction distribution $C_f \sqrt{Re_x}$ and compare the predicted separation point with [Table 4-9](#).
- 4-25.** Consider a two-dimensional flat-walled diffuser, as in [Fig. P4-25](#). Assume incompressible flow with a one-dimensional freestream velocity $U(x)$ and entrance velocity $U_0(x)$. The entrance height is W and the constant depth into the paper is b . Using Thwaites' method, (a) find an expression for the angle θ at which separation will occur at $x = L$. (b) What is the value of θ if $L = 1.5W$?

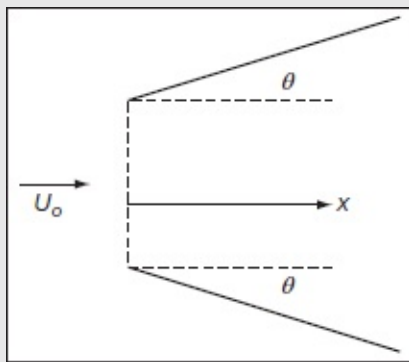


Figure P4.25

Answers: (a) $\theta_{sep} = \tan^{-1}(0.079W/L_{sep})$, (b) 3.0°

- 4-26. Apply the explicit finite-difference model, Sec. 4-7.1, to boundary-layer flow on a cylinder, using either the inviscid, Eq. (4-164), or measured, Eq. (4-165), freestream velocity distributions. Compare the computed local wall friction with [Fig. 4-29b](#).
- 4-27. Modify Prob. 4-26 by instead using the implicit finite-difference model of Sec. 4-7.2.
- 4-28. Investigate the use of the Crank–Nicolson (1947) method for computer analysis of a laminar boundary layer. What are its numerical advantages and disadvantages?
- 4-29. Apply the explicit finite-difference method of Sec. 4-7.1 to one of the laminar-flow test cases in [Table 4-9](#) (for best results have each member of the class take a different case). Compute and plot the local friction distribution $C_f\sqrt{Re_x}$ and compare the predicted separation point with [Table 4-9](#).
- 4-30. Sherman (1990) gives a CFD solution for laminar flow due to a freestream U_0 approaching a parabolic cylinder, as in [Fig. P4-30](#). The cylinder surface is defined by $y/R = (2x/R)_1/2$, where R is the cylinder nose radius. The arc length S along the surface is defined by $ds = R(1 + \zeta^2)^{1/2}d\zeta$, where $\zeta = y/R$. From potential theory, the surface velocity is $U = U_0\zeta/(1 + \zeta^2)^{1/2}$. (a) Show that the surface velocity approaches the stream velocity U_0 as one moves up the surface. (b) Using Thwaites' method, estimate the distance s/R along the surface where $\tau\theta/(\mu U)$ is within 10 percent of the flat-plate value of 0.22.

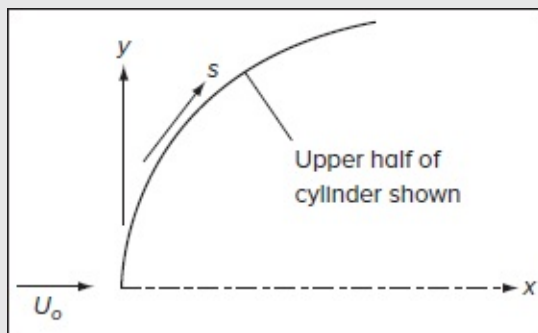


Figure P4.30

- 4-31. Apply the Smith and Spalding thermal-integral method of [Eq. \(4-182\)](#) for $Pr = 1$ to the Howarth velocity distribution, [Eq. \(4-136\)](#), with constant wall temperature, computing the local heat-transfer rate up to the point of separation. Also compute the Reynolds analogy factor, $\frac{1}{2}C_f(x)/C_h(x)$, and relate this to [Fig. 4-19](#).
- 4-32. Modify Prob. 4-31 by using instead the explicit or implicit finite-difference

method of Sec. 4-8.2.

4-33. Apply the Smith and Spalding thermal-integral method of [Eq. \(4-182\)](#) for $Pr = 0.72$ to flow past an isothermal circular cylinder, [Eq. \(4-188\)](#), and compare your results with [Fig. 4-30](#).

4-34. In [Eq. \(4-165\)](#) for $Re_a = 9500$, $U/U_\infty \approx 1.814x/a$ near the front of the cylinder. For air at 20°C and 1 atm, this corresponds approximately to $a = 5$ cm and $U_\infty = 2.85$ m/s. Using the Falkner–Skan theory, [Tables 4-6](#) and [4-7](#), and a temperature difference $T_w - T_\infty = 12^\circ\text{C}$, estimate (a) the momentum thickness in mm and (b) the heat-transfer rate in W/m^2 at the front of this cylinder.

Answers: (a) $\theta = 0.11$ mm, (b) 410 W/m^2

4-35. For a flat plate, $U = U_0$, and a wall temperature distribution $T_w - T_e = \Delta T_0[1 - (x/L)^3]$, use the superposition method of Sec. 4-8.4 to compute the value of x at which the local heat transfer q_w changes sign.

Answer: 0.768

4-36. Modify Prob. 4-35 by using instead the explicit or implicit finite-difference method of Sec. 4-8.2.

4-37. Carry out an integral analysis of laminar flow in the entrance between impermeable parallel plates a distance $2H$ apart, analogous to [Fig. 4-37](#) [Sparrow (1955)]. At any x , let the velocity profile consist of (a) a potential core $U(x)$ that satisfies Bernoulli's equation and (b) a parabolic boundary-layer profile, extending out to distance $\delta \leq H$. Use

$$\frac{u(x, y)}{U(x)} = 2\frac{y}{\delta} - \left(\frac{y}{\delta}\right)^2, \quad \delta = \delta(x)$$

The flow enters with a flat profile $U = U_0$. Apply the steady-flow momentum-integral relation (4-141), along with mass conservation across the entire channel, to compute $\delta(x)$ and $U(x)$. Find the entrance length x_e .

$$\text{Answer: } \frac{x_e/(2H)}{U_0(2H)/\nu} = \frac{3}{40} \left(9 \frac{U}{U_0} - 16 \ln \frac{U}{U_0} - 7 \frac{U_0}{U} - 2 \right) \bigg|_{U=1.5U_0} \approx 0.0259$$

4-38. For potential freestream flow past a sphere, $U = 1.5U_0 \sin(x/a)$, use the Rott–Crabtree integral method, [Eq. \(4-212\)](#), to compute the point of laminar-boundary-layer separation. Compare with [Fig. 4-40](#). Page 237

4-39. In the spirit of Eq. (4-167) for two-dimensional flow, develop an explicit finite-

difference model for the thick axisymmetric flow momentum relation, Eq. (4-216b). Use the same mesh as shown in [Fig. 4-30](#), with y_n as the radial coordinate, but do not analyze the axisymmetric continuity Eq. (4-216a). Do the parameters α and β still appear? Note that there is no pressure gradient, $U_{m+1} = U_m$.

- 4-40.** Air at 20°C and 1 atm issues from a circular hole and forms a round laminar jet. At 20 cm downstream of the hole, the maximum velocity is 35 cm/s. Estimate, at this position, (a) the “one percent” jet thickness, (b) the jet mass flow, and (c) an appropriate Reynolds number for the jet.

Answers: (a) 0.05 m, (b) 9.05×10^{-5} kg/s, (c) 1160

- 4-41.** Air at 20°C and 1 atm flows at 1 m/s past a slender body of revolution, of length $L = 15$ cm, whose drag coefficient is 0.008 based on area L^2 . Assuming laminar flow at a point 3 m downstream of the trailing edge, estimate (a) the maximum wake velocity defect (in cm/s), (b) the “one percent” wake thickness (in cm), and (c) the wake-thickness Reynolds number.

Answers: (a) 16 cm/s, (b) 58 cm, (c) 610

- 4-42.** Given a streamlined airfoil as pictured in [Fig. P4-42a](#), axial velocity profiles may be measured at both the upstream and downstream sections labeled 1 and 2 using a *streamline-bounded* control volume (i.e., one that forms a streamtube). Assuming equal pressure around the control volume and symmetry with respect to the midsection plane, determine (a) the half height of the upstream station, H , and (b) the drag coefficient on this airfoil if the vertical dimension at the downstream station is $Y = \phi c$, where c is the cord. The downstream velocity is given by $u = U \left[1 - \frac{1}{2} \cos\left(\frac{1}{2} \pi y / Y\right) \right]$. Hint: You may take advantage of symmetry by selecting a control volume as pictured in Fig. P4-42b.

Answers: (a) $H = (\pi - 1)Y/\pi$, (b) $\phi(8 - \pi)/(2\pi)$

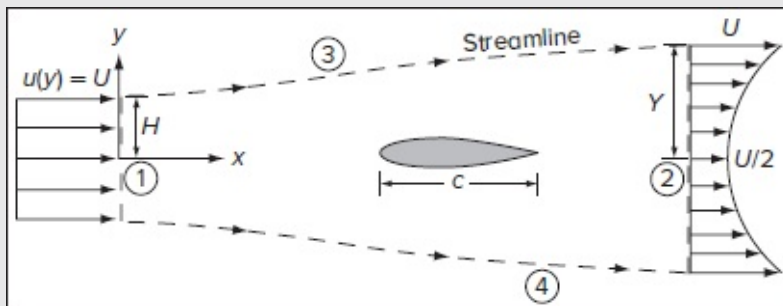


Figure P4.42a

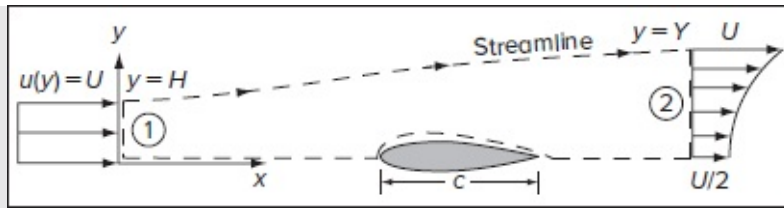


Figure P4.42b

- 4-43.** Consider the steady, incompressible, and two-dimensional flow past a circular cylinder of diameter d , as pictured in [Fig. P4-43](#). The upstream velocity U may be taken to be uniform while the downstream velocity may be set to be

$$\frac{u(y)}{U} = \begin{cases} \sin\left(\frac{\pi y}{2\delta}\right); & +0 \leq y \leq +\delta \\ 1; & +\delta < y < +\infty \end{cases}$$

where both U and d are known. Calculate (a) δ and (b) the drag coefficient C_D .

Answers: (a) $\delta = \pi d/2$, (b) $C_D = 4\theta/d = 4 - \pi$

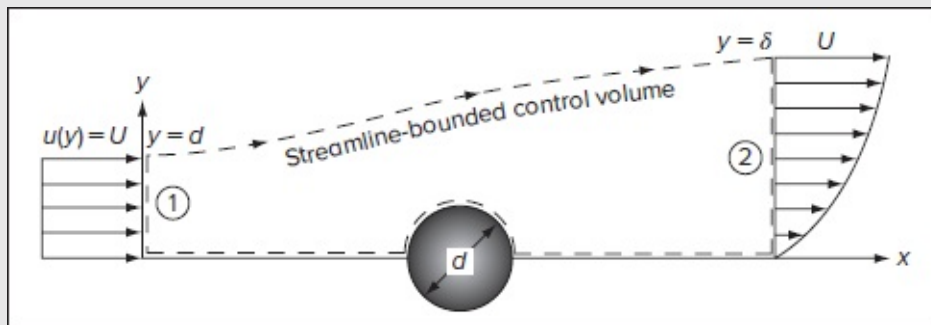


Figure P4.43

- 4-44.** The rotating-disk laminar boundary layer of Sec. 3-8.2 is fully three-dimensional. By changing the frame of reference of v_θ so that it is zero at the wall (i.e., subtracting v_θ from $r\omega$), plot the results of Table 3-5 in the form of a hodograph, with v_θ as the “streamwise” flow. Find the angle β and compare the results with [Fig. 4-45c](#).
- 4-45.** Verify that the similarity variables of [Eq. \(4-259\)](#) do indeed lead to the coupled ordinary differential [Eqs. \(4-260\)](#).
- 4-46.** Develop a numerical solution for the vertical free-convection [Eqs. \(4-260\)](#) and (4-

261). Take any Prandtl number not listed in Table 4-14 (such as $Pr = 8$, or each class member can choose a different case). The iteration can be challenging because there are two unknown conditions, $f''(0)$ and $\Theta'(0)$. Compute the Nusselt number and compare with Eq. (4-264).

Answers: For $Pr = 8$, $f''(0) = 0.4386$, $\Theta'(0) = -1.0957$, and $Nu/Gr^{1/4} = 0.775$

- 4-47. A vertical isothermal plate 40 cm high and 30 cm wide is immersed in air at 20°C and 1 atm. Each side of the plate is to dissipate 100 W of heat to the air. Calculate (a) the wall temperature (in °C) and (b) the Grashof number. Is the flow laminar? Hint: Assuming an average wall-fluid (film) temperature of 100°C, evaluate the necessary thermophysical properties, and repeat until the properties no longer change.

Answers: For $Pr = 0.71$, (a) $T_w = 170^\circ\text{C}$, (b) $Gr = 5.2 \times 10^8$

- 4-48. A horizontal pipe of outer diameter 5 cm is immersed in air at 20°C and 1 atm. If the cylinder surface is at 300°C, how much heat (in W) is lost to the air per meter of pipe length? Hint: Evaluate the necessary thermophysical properties at the average film temperature.

Answers: For $Pr = 0.71$, $q_w = 400 \text{ W/m}$

- 4-49. A model two-dimensional airfoil has the following theoretical potential-flow surface velocities on its upper surface at a small angle of attack:

x/C	0.0	0.025	0.05	0.1	0.2	0.3	0.4	0.6	0.8	1.0
v/U_∞	0.0	0.97	1.23	1.28	1.29	1.29	1.24	1.14	0.99	0.82

The stream velocity U_∞ is variable. The chord length C is 30 cm. The fluid is air at 20°C and 1 atm. Assume that x is a good approximation of the arc length along the upper surface. Using any laminar-boundary-layer method of your choice, find the predicted separation point, if any, for (a) $Re_C = 10^6$; and (b) $Re_C = 4 \times 10^5$.

Answer: $x/C = 0.45$ irrespective of Re_C

- 4-50. Air at about 1 atm and 20°C flows through a 12 cm square duct at 0.4 m³/s, as in Fig. P4-50. Two hundred thin flat plates of 1 cm chord length are stretched across the duct at random positions. They do not interfere with each other. How much additional pressure drop do these plates contribute to the duct flow loss?

Answer: $\Delta p \approx 150 \text{ Pa}$

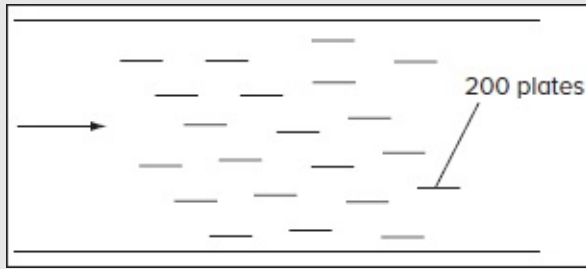


Figure P4.50

- 4-51.** Nondimensionalize Thwaites' method, using U_0 and L as reference values, for laminar-boundary-layer flow with an external potential-flow distribution $U(x)$. Show that the predicted separation point is independent of the Reynolds number $U_0 L/\nu$. Apply this conclusion to discuss the expected results for Prob. 4-49.

Answer: Using $V = U/U_0$ and $\xi = x/L$, show that Thwaites' parameter only depends on the dimensionless velocity and

position, and is thus independent of viscosity and the Reynolds number:

$$\lambda(\xi) = 0.45(dV/d\xi)V^{-6} \int_0^\xi V^5 d\xi = -0.09.$$

- 4-52.** A conical diffuser of initial radius R expands at a uniform angle θ , as in [Fig. P4-52](#). The flow enters at a uniform velocity U_0 . Assuming a one-dimensional freestream, use any laminar-boundary-layer method of your choosing (such as the Rott-Crabtree axisymmetric modification) to estimate the angle θ for which flow separation occurs at $x = 2R$.

Answer: $\theta = 1.13^\circ$

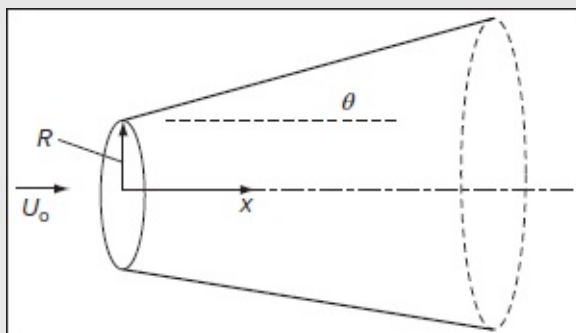


Figure P4.52

- 4-53. Show that the point-sink boundary-layer solution of Eqs. (4-108) and (4-111) may be interpreted through Thwaites' method as a constant value of Thwaites' parameter, $\lambda = 9/80$. How does this value of λ compare to two-dimensional stagnation flow?

Answer: The comparable Thwaites' estimate for plane stagnation flow is approximately 0.075 or 33 percent lower.

- 4-54. Show that the exact Falkner–Skan solutions for two-dimensional stagnation flow are equivalent to Thwaites' method parameters of $\lambda = 0.0855$, $S = 0.360$, and $H = 2.216$. How do these values compare with values from the use of Thwaites' method for the freestream $U = Bx$?

- 4-55. When a jet is formed parallel to a wall, it is called a *wall jet*, as shown in [Fig. P4-55](#). The jet origin can be thought of as a source of momentum, and further down the wall the velocity profiles are similar. Glauert (1956) showed that both plane and axisymmetric wall jets satisfy the same ordinary differential equation for laminar flow:

$$\frac{d^3 f}{d\eta^3} + f \frac{d^2 f}{d\eta^2} + 2 \left(\frac{df}{d\eta} \right)^2 = 0$$

where $\eta \propto y$, $f \propto \psi$, $f' \propto u$ and $f'' \propto \tau$. The boundary-layer thickness δ is proportional to $x^{3/4}$. (a) Verify Glauert's choice of boundary conditions: $f(0) = f'(0) = f'(\infty) = 0$. (b) To enforce the normalized condition $f(\infty) = 1$, Glauert showed that $f''(0) = 2/9$. For this value, numerically integrate the similarity equation out to $\eta = 8$ and plot both $f(\eta)$ and $f'(\eta)$. Hint: Read Glauert's paper.

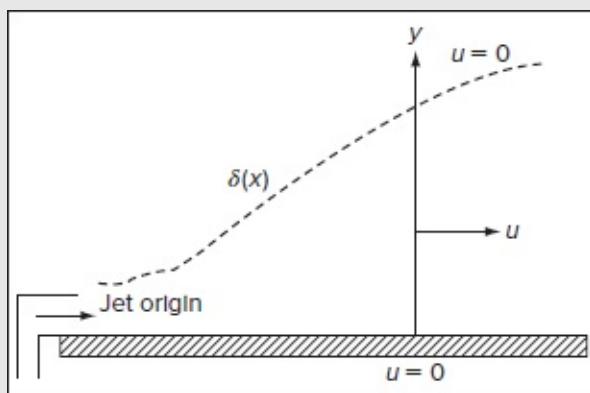


Figure P4.55

- 4-56. Consider the steady two-dimensional flow past a circular cylinder of diameter d , as

pictured in [Fig. P4-56](#). The upstream velocity U may be taken to be uniform while the downstream velocity is allowed to vary from $U/2$ to U according to the following symmetric profile:

$$\frac{u(y)}{U} = \begin{cases} \frac{1}{2} \left[1 + \sin\left(\frac{\pi y}{2\delta}\right) \right]; & 0 \leq y \leq \delta \\ 1; & \delta < y < \infty \end{cases} \quad \text{or} \quad \frac{u(\xi)}{U} = \begin{cases} \frac{1}{2} \left[1 + \sin\left(\frac{1}{2}\pi\xi\right) \right]; & 0 \leq \xi \leq 1 \\ 1; & 1 < \xi < \infty \end{cases}$$

where both U and d are known. Calculate (a) δ as a function of d and (b) the drag coefficient C_D . Here, $\xi = y/\delta$.

Answers: (a) $\delta = 2\pi d/(2 + \pi)$, (b) $C_D = \pi/(2 + \pi)$

Page 240

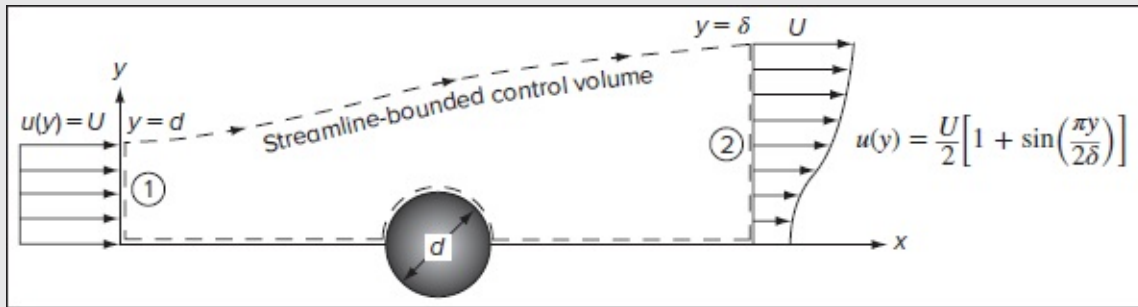


Figure P4.56

4-57. Repeat the previous problem using the following polynomial profile at the downstream section of the control volume:

$$\frac{u(y)}{U} = \begin{cases} 1; & -\infty < y < -\delta \\ \frac{1}{2} \left(1 + \frac{y^2}{\delta^2} \right); & -\delta \leq y \leq +\delta \\ 1; & +\delta < y < +\infty \end{cases} \quad \text{or} \quad \frac{u(\xi)}{U} = \begin{cases} 1; & -\infty < \xi < -1 \\ \frac{1}{2} (1 + \xi^2); & -1 \leq \xi \leq +1 \\ 1; & +1 < \xi < +\infty \end{cases}$$

Answers: (a) $\delta = 3d/2$, (b) $C_D = 1.2$

4-58. Consider the steady, incompressible, and two-dimensional flow past an ellipsoidal cylinder with unit depth W in the z -direction. The upstream velocity, U , may be taken to be uniform while the downstream velocity varies from $U/2$ until it reaches U according to the following profile:

$$\frac{u(y)}{U} = \begin{cases} 1; & -\infty < y < -Y \\ \frac{1}{2} \left(1 + \frac{y^4}{Y^4} \right); & -Y \leq y \leq +Y \\ 1; & +Y < y < +\infty \end{cases} \quad \text{or} \quad \frac{u(\xi)}{U} = \begin{cases} 1; & -\infty < \xi < -1 \\ \frac{1}{2} (1 + \xi^4); & -1 \leq \xi \leq +1 \\ 1; & +1 < \xi < +\infty \end{cases}$$

where U is known and Y defines the edge of the boundary-layer region. Calculate (a) Y in terms of H and (b) the drag coefficient C_D using the major axis of the ellipse as the characteristic length. You may use half of the domain shown below for simplicity.

Answers: (a) $Y = 5 H/3$, (b) $C_D = 20 H/(27b)$

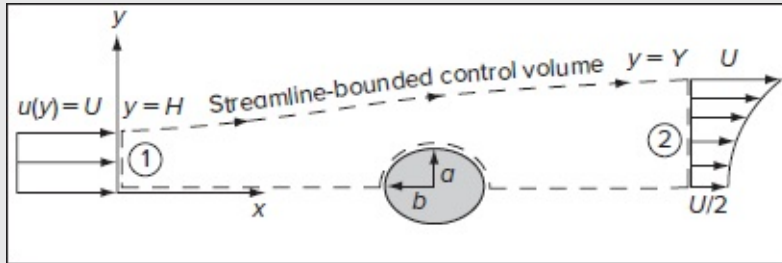


Figure P4.58

4-59. The Blasius equation can be expressed as:

$$\frac{f'''}{f''} + f = 0$$

where the primes denote differentiation with respect to $\eta = y/\sqrt{U/(2\nu x)}$. Given that the Blasius constant is $\sigma = f'(0)$, show that an integrodifferential form of the solution consists of

$$f''(\eta) = \sigma \exp \left[- \int_0^\eta f(t) dt \right]$$

4-60. The Blasius solution arises in the context of laminar, incompressible, constant property, boundary-layer flow over a flat plate, where the freestream velocity above the plate is U . As usual, the boundary-layer equations for flow over a flat plate reduce to Page 241

$$\begin{cases} \frac{\partial u}{\partial x} + \frac{\partial v}{\partial y} = 0 \\ u \frac{\partial u}{\partial x} + v \frac{\partial u}{\partial y} = \nu \frac{\partial^2 u}{\partial y^2} \end{cases} \quad \text{with} \quad u(x, 0) = 0, \quad u(x, \delta) = U, \quad \text{and} \quad \left. \frac{\partial u}{\partial y} \right|_{y=\delta} = 0$$

An equally common form of the Blasius similarity variable does not carry the arbitrary “2” factor under the radical. More specifically, the Blasius equation can be rederived using the following transformations:

$$\eta = \sqrt{\frac{U}{\nu x}} y, \quad \psi = \sqrt{\nu x U} f, \quad \text{and} \quad \frac{u(x, y)}{U} = \frac{df(\eta)}{d\eta}$$

Show that the corresponding Blasius equation becomes $f''' + \frac{1}{2}ff'' = 0$ with the same boundary conditions as before.

4-61. Use the Runge–Kutta method with shooting to solve the Blasius equation $f''' + \frac{1}{2}ff'' = 0$ and thus capture the flat plate boundary layer using $\eta = y\sqrt{U/(2\nu x)}$. Use the far-field value of $\eta_\infty = 6$ and a step size of $\Delta\eta = 0.02$.

- Select $f''(0) = \{0.3, 0.4\}$ as the first two guesses for the unknown initial condition. Report the number of additional guesses required to converge on $f'(\infty) \approx 1$ within an absolute tolerance of $\epsilon = 10^{-5}$.
- Plot f , f' , and f'' versus η . Tabulate f , f' , and f'' for increments of $\Delta\eta = 0.2$ (i.e., every tenth data point). Feel free to check your results against [Table 4-3](#).
- Use the 99 percent definition of the boundary-layer thickness to estimate the value of $\eta = \eta_\delta$ that corresponds to the “edge” of the boundary layer.
- Compute the parameters:

$$\frac{\delta^*}{x}\sqrt{Re_x}, \quad \frac{\theta}{x}\sqrt{Re_x}, \quad \text{and} \quad C_f\sqrt{Re_x}$$

4-62. Under standard temperature and pressure conditions, consider a laminar, incompressible flow of air over a flat plate, as pictured in [Fig. P4-1](#), where the velocity may be taken to be *linear*, specifically, $u(y) = Uy/\delta$. Using von Kármán’s -momentum-integral approach, evaluate (a) the fundamental boundary-layer properties, δ , δ^* , θ and τ_w ; (b) the drag force per unit width (F_D/b) as well as the drag coefficient, $C_D = 2F_D/(\rho U^2 L b)$. You may use a constant freestream velocity, $U = 10\text{ m/s}$, $b = 1\text{ m}$, and $L = 1\text{ m}$.

Answers:

$$(a) \delta(x) = \frac{3.46}{\sqrt{Re_x}}x, \quad \delta^* = \frac{1.73}{\sqrt{Re_x}}x, \quad \theta = \frac{0.58}{\sqrt{Re_x}}x, \quad \tau_w = \frac{2.89\mu}{x}\sqrt{Re_x}; \quad (b) \frac{F_D}{b} = 18.278\sqrt{\rho\mu}, \quad C_D = 0.3656\sqrt{\nu}$$

4-63. Under standard temperature and pressure conditions, consider a laminar, incompressible flow over a flat plate where the velocity may be taken to be of the Pohlhausen type, specifically, $u/U = c_0 + c_1\xi + c_2\xi^2 + c_3\xi^3 + c_4\xi^4$; $\xi \equiv y/\delta$. Evaluate (a) the fundamental boundary-layer properties, δ , δ^* , θ and τ_w ; (b) the drag force per unit width (F_D/b) as well as the drag coefficient, $C_D = 2F_D/(\rho U^2 L b)$. Assume a uniform freestream velocity with no pressure gradient.

4-64. (a) Consider steady, incompressible, laminar flow over a flat plate at 20°C , 1 atm, and 0.1 m/s. Does water or air produce a thicker boundary layer at the trailing edge?

Show your work and any assumptions that you need to make.

Fluid	ρ [kg/m ³]	μ [N·s/m ²]
Air	1.214	1.812×10^{-5}
Water	998.0	1.002×10^{-3}

(b) Consider the attached two-dimensional laminar motion over two streamlined airfoils as pictured below.

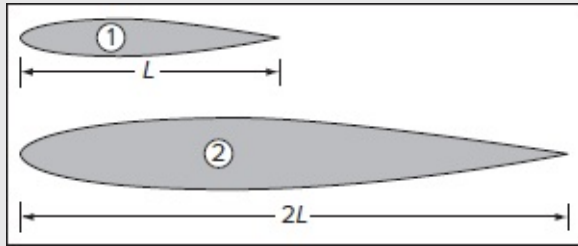


Figure P4.64

If the only difference between the two airfoils is that Airfoil # 1 has twice the length of Airfoil # 2, what is the relation between their boundary-layer thicknesses at the trailing edge? You may treat the two airfoils as two-dimensional flat plates. You may also resort to any suitable laminar correlation.

Answers: (a) $\delta_{\text{air}} = 3.86\delta_{\text{water}}$, (b) $\delta_2 = \sqrt{2}\delta_1$

Page 242

4-65. For nearly a century, the boundary-layer problem for flow over a flat plate, which was first reduced to a third-order nonlinear differential equation by Blasius (1908), could only be solved numerically or through the use of infinite series. In seeking practical alternatives, several polynomial approximations have been attempted, and these are mainly attributed to Pohlhausen (1921). Because the polynomial profiles are intended to capture the flow behavior inside the boundary layer only, the profiles are expressed as piecewise solutions of the form:

$$\frac{u}{U} = \begin{cases} c_0 + c_1 \frac{y}{\delta} + c_2 \left(\frac{y}{\delta}\right)^2 + c_3 \left(\frac{y}{\delta}\right)^3 + c_4 \left(\frac{y}{\delta}\right)^4; & 0 \leq y \leq \delta \\ 1; & \delta < y < \infty \end{cases}$$

To ensure smooth merging between the velocity in the boundary layer (u) and the outer, freestream velocity (U), several boundary conditions have been suggested by Pohlhausen (1921). These are:

(1) No slip condition at the wall: $u(x, 0) = 0$

(2) Matching the far-field velocity at the boundary-layer edge: $u(x, \delta) = U$

(3) Smooth merging with the far field, where the shear vanishes: $\frac{\partial u}{\partial y}\bigg|_{y=\delta} = 0$

(4) Axial momentum balance at the wall: $\mu \frac{\partial^2 u}{\partial y^2}\bigg|_{y=0} = \frac{dp}{dx}$, which is recovered from the boundary-layer equation, and where

the pressure gradient $\frac{dp}{dx} = -\rho U \frac{dU}{dx}$ in conformance with Euler's far-field equation

(5) No further variations in the slope of the velocity at the boundary-layer edge (zero curvature): $\frac{\partial^2 u}{\partial y^2}\bigg|_{y=\delta} = 0$

Note that in the case of a zero pressure gradient, which corresponds to the Blasius problem, condition # 4 reduces to $\frac{\partial^2 u}{\partial y^2}\bigg|_{y=0} = 0$. For this particular case, determine which of the five boundary conditions (1–5) are satisfied by the following

Pohlhausen profiles:

(a) Second-order, quadratic polynomial: $\frac{u}{U} = 2\frac{y}{\delta} - \frac{y^2}{\delta^2}$

(b) Third-order, cubic polynomial: $\frac{u}{U} = \frac{3y}{2\delta} - \frac{y^3}{2\delta^3}$

(c) Fourth-order, quartic polynomial: $\frac{u}{U} = 2\frac{y}{\delta} - 2\frac{y^3}{\delta^3} + \frac{y^4}{\delta^4}$

Hint: Although condition # 5 is true as $y \rightarrow \infty$, it proves to be inaccurate at the edge of the boundary layer, where the slope is still changing. Fortunately, this condition only affects the quartic Pohlhausen polynomial, which explains why it tends to be less precise in predicting boundary-layer characteristics than its lower-order counterparts (cf. [Table 4-1](#)).

4-66. Consider the quartic Pohlhausen profile for the laminar, incompressible flow over a flat plate with a nonzero pressure gradient:

$$\frac{u}{U} = c_0 + c_1\xi + c_2\xi^2 + c_3\xi^3 + c_4\xi^4, \quad 0 \leq \xi \leq 1 \quad \text{where} \quad \xi = \frac{y}{\delta}$$

(a) Apply Pohlhausen's five boundary conditions to show that the unknown coefficients must be

$$c_0 = 0, \quad c_1 = 2 + \frac{1}{6}\Lambda, \quad c_2 = -\frac{1}{2}\Lambda, \quad c_3 = \frac{1}{2}\Lambda - 2, \quad \text{and} \quad c_4 = 1 - \frac{1}{6}\Lambda \quad \text{where} \quad \Lambda = -\frac{\delta^2}{\mu U} \frac{dp}{dx} = \frac{\rho \delta^2}{\mu} \frac{dU}{dx}$$

Here Λ represents the *Pohlhausen pressure gradient parameter*. Simplify your solution into the form:

$$u/U = 2\xi - 2\xi^3 + \xi^4 + \frac{1}{6}\Lambda\xi(1 - \xi)^3$$

- (b) For what value of Λ will flow separation occur? Recall that separation occurs when $\partial u / \partial y = 0$ at $y = 0$.
- (c) Plot u/U versus ξ for $\Lambda = \{-12, -6, 0, +6, +12\}$.

4-67. Consider the quartic Pohlhausen profile for the laminar, incompressible flow over a flat plate at zero incidence and with no pressure gradient. Using dimensionless variables, we have:

$$F(\xi) = \frac{u}{U} = \begin{cases} 2\xi - 2\xi^3 + \xi^4; & 0 \leq \xi \leq 1 \\ 1; & 1 < \xi < \infty \end{cases} \quad \text{where} \quad \xi = \frac{y}{\delta}$$

- (a) Show that the dimensionless displacement thickness, momentum thickness, and shape factor lead to:

$$\eta^* = \frac{\delta^*}{\delta} = \int_0^1 \left(1 - \frac{u}{U}\right) d\xi = 0.3 \quad \theta^* = \frac{\theta}{\delta} = \int_0^1 \frac{u}{U} \left(1 - \frac{u}{U}\right) d\xi = 0.1175 \quad \text{and} \quad H = \frac{\delta^*}{\theta} = 2.554$$

Page 243

- (b) Show that the Kármán–Pohlhausen momentum-integral equation reduces to

$$\frac{\tau_w}{\rho} = U^2 \theta^* \frac{d\delta}{dx} = \frac{\nu U}{\delta} s; \quad s \equiv \left. \frac{dF}{d\xi} \right|_{\xi=0} = \text{dimensionless velocity slope at the wall}$$

- (c) After separating variables and integrating from $\delta(0) = 0$ to $\delta(x)$, show that the boundary-layer thickness can be written as a function of the local Reynolds number, $Re_x = Ux/\nu$, specifically,

$$\frac{\delta}{x} = \frac{a}{\sqrt{Re_x}}; \quad a = 5.836$$

- (d) Recalling that the friction coefficient is $C_f = 2\tau_w/(\rho U^2) = 2\theta^* d\delta/dx$, and that $\delta = ax^{1/2}/\sqrt{U/\nu}$, show that

$$\frac{d\delta}{dx} = \frac{(a/2)}{\sqrt{Re_x}} \quad \text{and} \quad C_f = \frac{b}{\sqrt{Re_x}}; \quad b = a\theta^* = 0.6855$$

- (e) Recalling that the displacement thickness can be deduced from $\delta^*/x = \eta^* \delta/x$, show that

$$\frac{\delta^*}{x} = \frac{c}{\sqrt{Re_x}}; \quad c = a\eta^* = 1.751$$

(f) Recalling that the momentum thickness can be deduced from $\theta/x = \theta^*\delta/x$, show that

$$\frac{\theta}{x} = \frac{d}{\sqrt{Re_x}}; \quad d = a\theta^* = 0.6855$$

(g) Using continuity, $\frac{v}{U} = -\frac{\partial}{\partial x} \int_0^y \frac{u}{U} dy$, integrate the axial profile to show that the transverse velocity can be written as

$$\frac{v}{U} = \left(\xi^2 - \frac{3}{2}\xi^4 + \frac{4}{5}\xi^5 \right) \frac{(a/2)}{\sqrt{Re_x}} = \left(\xi^2 - \frac{3}{2}\xi^4 + \frac{4}{5}\xi^5 \right) \frac{2.9178}{\sqrt{Re_x}}$$

(h) Show that the maximum transverse velocity occurs at the edge of the boundary layer where it can be obtained from

$$\left. \frac{v}{U} \right|_{\max} = \left. \frac{v}{U} \right|_{y=\delta} = \frac{(3a/20)}{\sqrt{Re_x}} = \frac{0.8753}{\sqrt{Re_x}}$$

(i) Verify that the errors in predicting δ/x and C_f are 17 and 3.2 percent relative to the classic Blasius results.

4-68. Consider the quartic Majdalani–Xuan profile for the laminar, incompressible flow over a flat plate:

$$F(\xi) = \frac{u}{U} = \begin{cases} \frac{5}{3}\xi - \xi^3 + \frac{1}{3}\xi^4, & 0 \leq \xi \leq 1 \\ 1, & 1 < \xi < \infty \end{cases} \quad \text{where} \quad \xi = \frac{y}{\delta} \quad [\text{Majdalani and Xuan (2020)}]$$

(a) Show that the dimensionless displacement thickness, momentum thickness, and shape factor lead to:

$$\eta^* = \frac{\delta^*}{\delta} = \int_0^1 \left(1 - \frac{u}{U} \right) d\xi = 0.3500, \quad \theta^* = \frac{\theta}{\delta} = \int_0^1 \frac{u}{U} \left(1 - \frac{u}{U} \right) d\xi = 0.1337, \quad \text{and} \quad H = \frac{\delta^*}{\theta} = 2.618$$

(b) Show that

$$a = \delta \sqrt{Re_x}/x = 4.993, \quad b = C_f \sqrt{Re_x} = \theta \sqrt{Re_x}/x = 0.6676, \quad \text{and} \quad c = \delta^* \sqrt{Re_x}/x = 1.748$$

(c) Calculate the total skin friction force and the drag coefficient for a plate of length L . Express your result in terms of $Re_L = UL/\nu$.

(d) Using the continuity equation, integrate the axial velocity profile to show that

$$\frac{v}{U} = \left(\xi^2 - \frac{3}{2}\xi^4 + \frac{4}{5}\xi^5 \right) \frac{(a/2)}{\sqrt{Re_x}} = \left(\xi^2 - \frac{3}{2}\xi^4 + \frac{4}{5}\xi^5 \right) \frac{2.9178}{\sqrt{Re_x}}$$

- (e) Show that the maximum transverse velocity occurs at the edge of the boundary layer where it can be obtained from

$$\frac{v}{U}|_{\max} = \frac{v}{U}|_{y=\delta} = \frac{(7a/40)}{\sqrt{Re_x}} = \frac{0.8738}{\sqrt{Re_x}}$$

- (f) Verify that the errors in predicting δ/x and C_f are 1.7 and 0.53 percent relative to the classic Blasius results in [Table 4-1](#).

- (g) Show that the quartic Majdalani–Xuan profile satisfies all of the fundamental boundary conditions except for the vanishing curvature at the edge of the boundary layer. Explain why better predictions are obtained when this condition is relaxed. Hint: Although the zero-curvature boundary condition is true as $y \rightarrow \infty$, it is inaccurate at the edge of the boundary layer, where the velocity slope continues to change. By relaxing this condition, Majdalani and Xuan (2020) are able to derive a simple approximation that is more accurate than Pohlhausen’s quartic polynomial by one order of magnitude. Consequently, the Majdalani–Xuan polynomial profile may be viewed as a practical equivalent to the Blasius solution in several engineering applications. Page 244

- 4-69.** Consider the continuous Majdalani–Xuan exponential profile for the laminar, incompressible flow over a flat plate:

$$\frac{u}{U} = 1 - e^{-\bar{s}\xi(1+\frac{1}{2}\bar{s}\xi+\xi^2)}, \quad \xi = \frac{y}{\delta}, \quad \bar{s} = \frac{\sigma a}{\sqrt{2}} = \sigma \frac{\delta}{x} \sqrt{\frac{Re_x}{2}} \approx 1.63040, \quad 0 \leq \xi < \infty \quad [\text{Majdalani and Xuan (2020)}]$$

- (a) Show that the dimensionless displacement thickness, momentum thickness, and shape factor lead to:

$$\eta^* = \int_0^\infty \left(1 - \frac{u}{U}\right) d\xi = 0.35068, \quad \theta^* = \int_0^\infty \frac{u}{U} \left(1 - \frac{u}{U}\right) d\xi = 0.13559, \quad \text{and} \quad H = 2.5862$$

- (b) Show that

$$\delta\sqrt{Re_x}/x = 4.9039, \quad C_f\sqrt{Re_x} = \theta\sqrt{Re_x}/x = 0.66494, \quad \text{and} \quad \delta^*\sqrt{Re_x}/x = 1.7197$$

- (c) Verify that the errors in predicting δ/x , C_f , and δ^*/x are negligible, being, respectively, 0.12, 0.13, and 0.06 percent relative to the

accurately computed Blasius solution in [Table 4-4](#).

(d) In addition to the fundamental boundary conditions that are satisfied by this profile, verify that the continuous Majdalani–Xuan exponential profile captures the behavior of the Blasius solution very robustly: (1) it exhibits the same slope as the exact Blasius solution at the wall, (2) it equals, as it should, $0.99U$ at $y = \delta$, (3) it matches the slope of the Blasius velocity profile at the edge of the boundary layer with reasonable accuracy, and (4) it approximates the curvature of the exact Blasius solution at $y = \delta$, where the Blasius curvature does not vanish.

(e) Contrary to the piecewise approximations that are confined to the $0 \leq \xi < 1$ range, this profile remains valid beyond the edge of the boundary layer, specifically as $\xi \rightarrow \infty$, with $u/U \rightarrow 1$ asymptotically, as it should, thus allowing for the smooth and seamless merging of the viscous solution with the far-field freestream. Explain why this simple analytic profile is practically equivalent to the “exact” Blasius solution given the small truncation error entailed in the derivation of the Blasius equation itself.

(f) By writing $\eta = y\sqrt{U/(2\nu x)} = C_{\eta\xi}\xi$, and recalling that $\delta = a\sqrt{\nu x/U}$, show that the conversion constant between the Blasius similarity variable and ξ is simply $C_{\eta\xi} = a/\sqrt{2} \approx 3.47$.

(g) Plot this solution for $0 \leq \xi \leq \xi_\infty$, where $\xi_\infty = 1.5$ corresponds to $\eta_\infty \approx 5.2$ written in terms of the Blasius variable. Add to your plot the Blasius derivative function $df/d\eta$, which represents the normalized axial velocity.

4-70. Consider the sinusoidal Schlichting profile for the laminar, incompressible flow over a flat plate:

$$\frac{u}{U} = \sin\left(\frac{\pi y}{2\delta}\right); \quad 0 \leq y \leq \delta \quad [\text{Schlichting (1979)}]$$

(a) Using continuity, $\frac{v}{U} = -\frac{\partial}{\partial x} \int_0^y \frac{u}{U} dy$, integrate the axial profile to show that the transverse velocity can be written as

$$\frac{v}{U} = \left[\cos\left(\frac{\pi y}{2\delta}\right) + \frac{\pi y}{2\delta} \sin\left(\frac{\pi y}{2\delta}\right) - 1 \right] \frac{a}{\pi\sqrt{Re_x}}; \quad a = \frac{\delta\sqrt{Re_x}}{x}$$

(b) Plot u/U and v/U versus y/δ and show that the maximum transverse velocity occurs at the edge of the boundary layer where it can be obtained from

$$\frac{v}{U}|_{\max} = \frac{v}{U}|_{y=\delta} = \frac{\pi-2}{\pi} \frac{(a/2)}{\sqrt{Re_x}} = \frac{0.871264}{\sqrt{Re_x}}$$

Page 245

- (c) Evaluate at $(v/U)_{\max}$ at $x = 0.6$ m and $\delta = 0.006$ m. Hint: First show that, irrespective of the Reynolds number,

$$\frac{v}{U}|_{\max} = \frac{\pi-2}{2\pi} \frac{\delta}{x}$$

Answer: (c) $(v/U)_{\max} = 0.182\%$

- 4-71.** Consider the cubic Pohlhausen profile for the laminar, incompressible flow over a flat plate:

$$\frac{u}{U} = \frac{3y}{2\delta} - \frac{y^3}{2\delta^3}; \quad 0 \leq y \leq \delta \quad [\text{Pohlhausen (1921)}]$$

- (a) Using continuity, integrate the axial profile to show that the transverse velocity can be written as

$$\frac{v}{U} = \frac{3}{16} \left(2 \frac{y^2}{\delta^2} - \frac{y^4}{\delta^4} \right) \frac{a}{\sqrt{Re_x}} = \frac{3}{16} \left(2 \frac{y^2}{\delta^2} - \frac{y^4}{\delta^4} \right) \frac{\delta}{x}$$

- (b) Plot u/U and v/U versus y/δ and show that the maximum transverse velocity occurs at the edge of the boundary layer where it can be obtained from

$$\frac{v}{U}|_{\max} = \frac{v}{U}|_{y=\delta} = \frac{3a}{16\sqrt{Re_x}} = \frac{0.8702}{\sqrt{Re_x}}$$

- (c) Evaluate $(v/U)_{\max}$ at $x = 0.7$ m and $\delta = 0.007$ m.

Answer: (c) $(v/U)_{\max} = 0.188\%$

- 4-72.** Consider the continuous, one-parameter, tangent hyperbolic Yun profile for laminar flow over a flat plate:

$$\frac{u}{U} = \tanh(\bar{s}\xi); \quad \xi = \frac{y}{\delta}, \quad \bar{s} = 1.6304, \quad 0 \leq \xi < \infty \quad [\text{Yun (2010)}]$$

- (a) Show that the dimensionless displacement thickness, momentum thickness, and shape factor lead to:

$$\eta^* = \int_0^\infty \left(1 - \frac{u}{U}\right) d\xi = 0.4251, \quad \theta^* = \int_0^\infty \frac{u}{U} \left(1 - \frac{u}{U}\right) d\xi = 0.1882, \quad \text{and} \quad H = 2.2589$$

(b) Show that

$$\delta\sqrt{Re_x}/x = 4.1624, \quad C_f\sqrt{Re_x} = \theta\sqrt{Re_x}/x = 0.7834, \quad \text{and} \quad \delta^*\sqrt{Re_x}/x = 1.7696$$

(c) Verify that the errors in predicting δ/x and C_f are 15.2 and 18 percent relative to the computed Blasius values in [Table 4-4](#).

4-73. Consider the continuous, two-parameter tangent hyperbolic Savaş profile for laminar flow over a flat plate:

$$\frac{u}{U} = [\tanh(\varphi\xi)^{5/3}]^{3/5}; \quad \xi = \frac{y}{\delta}, \quad \varphi = \bar{s} = 1.6304, \quad 0 \leq \xi < \infty \quad [\text{Savaş (2012)}]$$

(a) Show that the dimensionless displacement thickness, momentum thickness, and shape factor lead to:

$$\eta^* = \int_0^\infty \left(1 - \frac{u}{U}\right) d\xi = 0.3509, \quad \theta^* = \int_0^\infty \frac{u}{U} \left(1 - \frac{u}{U}\right) d\xi = 0.1363, \quad \text{and} \quad H = 2.5738$$

(b) Show that

$$\delta\sqrt{Re_x}/x = 4.8906, \quad C_f\sqrt{Re_x} = \theta\sqrt{Re_x}/x = 0.6667, \quad \text{and} \quad \delta^*\sqrt{Re_x}/x = 1.7161$$

(c) Verify that the errors in predicting δ/x and C_f are 0.40 and 0.40 percent relative to the computed Blasius solution in [Table 4-4](#).

4-74. Consider the continuous, one-parameter Moeini–Chamani profile for laminar flow over a flat plate:

$$\frac{u}{U} = \text{erf}(\varphi\xi); \quad \xi = \frac{y}{\delta}, \quad \varphi = 1.59261, \quad 0 \leq \xi < \infty \quad [\text{Moeini and Chamani (2017)}]$$

(a) Show that the dimensionless displacement thickness, momentum thickness, and shape factor lead to:

$$\eta^* = \int_0^\infty \left(1 - \frac{u}{U}\right) d\xi = 0.3543, \quad \theta^* = \int_0^\infty \frac{u}{U} \left(1 - \frac{u}{U}\right) d\xi = 0.1467, \quad \text{and} \quad H = 2.4142$$

(b) Show that

$$\delta\sqrt{Re_x}/x = 4.9491, \quad C_f\sqrt{Re_x} = \theta\sqrt{Re_x}/x = 0.7262, \quad \text{and} \quad \delta^*\sqrt{Re_x}/x = 1.7532$$

(c) Verify that the errors in predicting δ/x and C_f are 0.80 and 9.4 percent relative to the computed Blasius solution in [Table 4-4](#).

4-75. Because of the popularity of approximate profiles in laminar boundary-layer

studies, let us consider a quartic mean flow in the case of no pressure gradient:

$$F(\xi) = \frac{u}{U} = c_0 + s\xi + c_2\xi^2 + c_3\xi^3 + c_4\xi^4; \quad \xi = \frac{y}{\delta} \quad 0 \leq \xi \leq 1$$

where ξ represents the fractional distance within the laminar boundary layer, and $s \equiv c_1 = F'(0)$ is the axial velocity slope at the wall, also known as the *Blasius constant* or *connection parameter*.

- (a) Show that the particular profile that will satisfy Pohlhausen's four essential conditions described in Sec. 4-1 must be:

$$F(\xi) = \xi s + (4 - 3s)\xi^3 + (2s - 3)\xi^4$$

Hint: These conditions translate into $F(0) = F'(1) = F''(0) = 0$ and $F(1) = 1$.

- (b) Show that the normalized boundary-layer properties, η^* , θ^* , and H , can be written as a direct function of s :

$$\begin{cases} \eta^* \equiv \frac{\delta^*}{\delta} = \int_0^1 (1 - F) d\xi = \frac{3}{20}(4 - s) & \text{(normalized displacement thickness)} \\ \theta^* \equiv \frac{\theta}{\delta} = \int_0^1 F(1 - F) d\xi = \frac{4}{35} + \frac{13s}{210} - \frac{19s^2}{630} & \text{(normalized momentum thickness)} \\ H \equiv \frac{\delta^*}{\theta} = \frac{\eta^*}{\theta^*} = \frac{189(4 - s)}{144 + 78s - 38s^2} & \text{(momentum shape factor)} \end{cases}$$

Page 246

- (c) Making use of $C_f = 2d\theta/dx$, show that the wall shear stress and skin friction coefficient can be written as

$$\tau_w = \frac{\mu U}{\delta} s \quad \text{and} \quad C_f = \frac{2\nu s}{\delta U} = 2 \left(\frac{4}{35} + \frac{13s}{210} - \frac{19s^2}{630} \right) \frac{d\delta}{dx}$$

- (d) Use separation of variables to identify

$$\delta d\delta = \frac{630s}{72 + 39s - 19s^2} \frac{\nu}{U} dx$$

- (e) After integrating from $\delta(0) = 0$ to $\delta(x)$, show that the boundary-layer thickness and its derivative can be written as functions of the local Reynolds number, $Re_x = Ux/\nu$, and the slope s :

$$\frac{\delta}{x} = \frac{a}{\sqrt{Re_x}}; \quad a = \sqrt{\frac{1260s}{72 + 39s - 19s^2}} \quad \text{and} \quad \frac{d\delta}{dx} = \frac{(a/2)}{\sqrt{Re_x}}$$

- (f) Using the definition of the friction coefficient, $C_f = 2\tau_w/(\rho U^2)$, show that

$$C_f = \frac{b}{\sqrt{Re_x}}; \quad b = \sqrt{\frac{s}{315}(72 + 39s - 19s^2)}$$

- (g) Recalling that the displacement thickness may be specified as $\delta^* = \delta\eta^*$, show that

$$\frac{\delta^*}{x} = \frac{c}{\sqrt{Re_x}}; \quad c = \frac{3a}{20}(4 - s)$$

- (h) Recalling that the momentum thickness may be deduced from $\theta = \delta\theta^*$, show that

$$\frac{\theta}{x} = \frac{d}{\sqrt{Re_x}}; \quad d = a\theta^* = b$$

- (i) Using the continuity equation $v = -\frac{\partial}{\partial x} \int_0^y u dy$, show that the transverse velocity component becomes

$$\frac{v}{U} = \left[\frac{s}{4}\xi^2 + \frac{3}{8}(4 - 3s)\xi^4 + \frac{2}{5}(2s - 3)\xi^5 \right] \frac{a}{\sqrt{Re_x}}$$

- (j) Show that the maximum value of the transverse velocity occurs at the edge of the boundary layer where

$$\left(\frac{v}{U} \right)_{\max} = \frac{v}{U} \Big|_{y=\delta} = \frac{G_\delta}{\sqrt{Re_x}}; \quad G_\delta = \left(1 - \frac{1}{4}s \right) \sqrt{\frac{567s}{360 + 195s - 95s^2}}$$

- (k) Calculate (a, b, c, d, e) for the two values of $s = 2$ and $5/3$, which correspond to the quartic Pohlhausen and Majdalani–Xuan profiles, respectively. Compare your results to the classic Blasius values in [Table 4-1](#).

4-76. Because of the popularity of approximate solutions in laminar boundary-layer studies, let us consider a quartic mean-flow profile in the presence of a pressure gradient:

$$F(\xi) = \frac{u}{U} = c_0 + s\xi + c_2\xi^2 + c_3\xi^3 + c_4\xi^4; \quad \xi = \frac{y}{\delta} \quad 0 \leq \xi \leq 1$$

where ξ represents the fractional distance within the laminar boundary layer, and $s \equiv c_1 = F'(0)$ is the axial velocity slope at the wall which can be written as function of the zero-pressure slope s_0 and a pressure gradient correction:

$$s = s_0 + s_1\Lambda$$

- (a) Show that the particular profile that will satisfy Pohlhausen's four

essential conditions with a non-vanishing pressure gradient [Sec. 4-1] must be:

$$F(\xi) = s\xi - \frac{1}{2}\Lambda\xi^2 + (4 - 3s + \Lambda)\xi^3 + \left(2s - 3 - \frac{1}{2}\Lambda\right)\xi^4; \Lambda = -\frac{\delta^2}{\mu U} \frac{dp}{dx} = \frac{\rho\delta^2}{\mu} \frac{dU}{dx}$$

Hint: These translate into $F(0) = F'(1) = 0$, $F(1) = 1$ and $F''(0) = -\Lambda$, where Λ is Pohlhausen's pressure parameter.

(b) Show that flow separation will occur for $\Lambda = -s_0/s_1$. Recall that separation occurs when $\partial u/\partial y = 0$ at $y = 0$.

(c) Show that the normalized boundary-layer properties, η^* , θ^* , and H , can be written as a function of s and Λ :

$$\eta^* = \frac{1}{60}(36 - 9s + \Lambda) \quad (\text{normalized displacement thickness})$$

$$\theta^* = -\frac{19s^2}{630} - \frac{(\Lambda - 12)(24 + \Lambda)}{2520} + \frac{s(156 + 17\Lambda)}{2520} \quad (\text{normalized momentum thickness})$$

$$H = \frac{2520(9s - 36 - \Lambda)}{76s^2 + (\Lambda - 12)(24 + \Lambda) - s(156 + 17\Lambda)} \quad (\text{momentum shape factor})$$

Page 247

(d) Making use of $C_f = 2\theta^* d\delta/dx + 2(2 + H)\theta^*(U'/U)\delta$, where $U' = dU/dx$, show that the wall shear stress and skin friction coefficient can be written as

$$\tau_w = \frac{\mu U}{\delta} s \quad \text{and so} \quad C_f = \frac{\tau_w}{\frac{1}{2}\rho U^2} = \frac{2\nu}{U\delta} s = 2\theta^* d\delta/dx + 2(2 + H)\theta^*(U'/U)\delta$$

$$\text{or} \quad U \frac{d}{dx} \left(\frac{\Lambda}{U'} \right) = 2(2 + H)\Lambda - \frac{2s}{\theta^*} = 4 \frac{\Lambda^3 - (17s + 1248)\Lambda^2 + (76s^2 + 11184s - 45648)\Lambda + 1260s}{\Lambda^2 + (12 - 17s)\Lambda + 76s^2 - 156s - 288}$$

(e) For the case of Hiemenz flow where the velocity outside the boundary layer is given by $U = ax$ and $V = -ay$ in Sec. 3-8.1, the analytic solution leads to a constant boundary-layer thickness, show that $\Lambda = (\delta^2/\nu)U' = \text{const.}$

(f) Using Pohlhausen's quartic profile with $s = 2 + \Lambda/6$, determine Λ and the corresponding skin friction coefficient, $\tau_w \sqrt{\nu/U'} / (\mu U)$, for the Hiemenz flow; compare your predictions to those obtained from the numerical solution provided in Table 3-4. Show that:

$$\Lambda_{\text{Pohlhausen}} = 7.052 \text{ and } \frac{\tau_w}{\mu U} \sqrt{\frac{\nu}{U'}} = \frac{s}{\sqrt{\Lambda}} = 1.196 \quad \text{versus} \quad \text{the numerical value of}$$

$$\Lambda_{\text{Hiemenz}} = 5.760 \text{ and } \frac{\tau_w}{\mu U} \sqrt{\frac{\nu}{U'}} = 1.233$$

The latter appears as " $f''(0)$ " in Table 3-4.

- (g) Using Majdalani–Xuan’s quartic profile with $s = 5/3 + 0.2075\Lambda$, determine Λ and the corresponding skin friction coefficient, $\tau_w \sqrt{\nu/U'} / (\mu U)$, for the Hiemenz flow; compare your predictions to those in Part (f). Show that:

$\Lambda_{\text{Majdalani-Xuan}} = 5.761$ matches the Hiemenz value and $\frac{\tau_w}{\mu U} \sqrt{\frac{\nu}{U}} = \frac{s}{\sqrt{\Lambda}} = 1.192$ is off by 3.33 percent.

- (h) Use Thwaites’ approach to predict the value of λ and the corresponding skin friction coefficient $\tau_w \sqrt{\nu/U} / (\mu U)$ by applying [Eqs. \(4-160\)](#) and [\(4-161\)](#). Compare the skin friction coefficient predicted by Thwaites’ approach to the one obtained from the numerical solution provided in [Table 3-4](#). Show that

$$\lambda = 0.075, \quad S(\lambda) = 0.3272, \quad \text{and} \quad \frac{\tau_w}{\mu U} \sqrt{\frac{\nu}{U}} = S(\lambda) \sqrt{\frac{6}{0.45}} = 1.195$$

- (i) Compute the normalized displacement and momentum thicknesses as well as the shape factor using Pohlhausen’s quartic profile for the Hiemenz flow. Show that $\eta^* = 0.241$, $\theta^* = 0.105$, and $H = 2.308$.
- (j) Compute the normalized displacement and momentum thicknesses as well as the shape factor using Majdalani–Xuan’s quartic profile for the Hiemenz flow. Show that $\eta^* = 0.267$, $\theta^* = 0.115$, and $H = 2.318$.

Hint: The reference Hiemenz solutions obtained by numerical integration are $\eta^* = 0.270$, $\theta^* = 0.122$, and $H = 2.219$.

- 4-77.** Consider a shape-preserving mean-flow profile in the laminar boundary layer over a flat plate with no pressure gradient:

$$\frac{u}{U} = F(\xi); \quad \xi = \frac{y}{\delta} \quad 0 \leq \xi \leq 1$$

As usual, let $s = F'(0)$ denote the axial velocity slope at the wall. For an arbitrary profile $F(\xi)$, the normalized boundary-layer properties, $\eta^* = \delta^*/\delta$, $\theta^* = \theta/\delta$, and $H = \eta^*/\theta^*$, consist of pure constants that can be determined from their defining integrals once $F(\xi)$ is specified.

- (a) Recalling that $C_f = 2d\theta/dx$, show that the wall shear stress and skin friction coefficient can be reduced to:

$$\tau_w = \frac{\mu U}{\delta} s \quad \text{and} \quad C_f = \begin{cases} \frac{2\nu s}{\delta U} & \text{(definition)} \\ 2\theta^* \frac{d\delta}{dx} & \text{(momentum-integral relation)} \end{cases}$$

- (b) By equating the defining expression for C_f and its momentum-integral relation to θ , show that

$$\delta d\delta = \frac{\nu s}{U\theta^*} dx$$

- (c) By integrating from the plate's leading edge to any station x , show that $\delta(x)$ and its derivative can be expressed in terms of $Re_x = Ux/\nu$, θ^* , and the slope s :

$$\frac{\delta}{x} = \frac{a}{\sqrt{Re_x}}; \quad a = \sqrt{\frac{2s}{\theta^*}} \quad \text{and} \quad \frac{d\delta}{dx} = \frac{(a/2)}{\sqrt{Re_x}}$$

Page 248

- (d) Using the defining expression for the friction coefficient, $C_f = 2\tau_w/(\rho U^2)$, show that

$$C_f = \frac{b}{\sqrt{Re_x}}; \quad b = \sqrt{2s\theta^*}$$

- (e) Prove the two identities $ab = 2s$ and $b/a = \theta^*$.

- (f) Recalling that the displacement and momentum thicknesses may be specified as $\delta^* = \delta\eta^*$ and $\theta = \delta\theta^*$, show that

$$\frac{\delta^*}{x} = \frac{c}{\sqrt{Re_x}}; \quad c = a\eta^* \quad \text{and} \quad \frac{\theta}{x} = \frac{d}{\sqrt{Re_x}}; \quad d = a\theta^* = b$$

- (g) Using $C_{D, \text{plate}} = 2\theta(L)/L$ from [Eq. \(4-10\)](#) and $\theta(x)$ above, show that

$$C_{D, \text{plate}} = \frac{2a\theta^*}{\sqrt{Re_L}}$$

- (h) Evaluate (a, b, c) for the Majdalani–Xuan quartic profile and compare your results to the classic Blasius values.

[‡]This value shifts to $\sigma/\sqrt{2} \approx 0.3320573362151963$ when the similarity variable and stream function are written slightly differently as $\eta = y\sqrt{U/(\nu x)}$ and $\psi = \sqrt{\nu U x} f(\eta)$. The corresponding Blasius equation becomes $f''' + \frac{1}{2}ff'' = 0$ with the same $f'(0) = f(0) = 0$ and $f'(\infty) = 1$. The same slope changes to $\bar{s} = dF(0)/d\xi = \sigma\alpha/\sqrt{2} \approx 1.630398038629397$ when written as the wall derivative of the velocity function $F(\xi) = u/U$ of Sec. 4-1 (cf. Table 4-1), where $\xi = y/\delta$.

[†]In turbulent flows (Sec. 6-4), the Reynolds number remains as a parameter because the turbulent inertia terms cannot be scaled by the square root of Re .

[§]Note that this freestream is a rotational flow, that is, $\partial U/\partial z - \partial W/\partial x \neq 0$. This can be ignored; the illustration of secondary

flow is what matters.

CHAPTER 5

THE STABILITY OF LAMINAR FLOWS

In order to shake a hypothesis, it is sometimes not necessary to do anything more than push as far as it will go.

Denis Diderot (1713–1784)

0

5-1 INTRODUCTION: THE CONCEPT OF SMALL-DISTURBANCE STABILITY

CHAPTERS 3 and 4 have tackled a wide variety of laminar-flow problems. [Chapter 3](#) has considered the full Navier–Stokes equations and a host of simple flow geometries. [Chapter 4](#) has introduced the Prandtl boundary-layer approximation that has enabled us to explore a wider class of realistic flows, subject only to accurate knowledge of the inviscid outer flow distribution. One way or another, available methodologies have allowed us to resolve, to reasonable accuracy, almost any laminar-flow problem. However, although a laminar solution may exist, it will not necessarily develop unless it represents a stable solution over some range of its operating parameters. By devoting itself to the issue of stability, this chapter will therefore complement the previous two chapters, which focused on the issue of existence.

Why? Laminar flows have a known physical limitation, which is a tendency to break apart at high Reynolds numbers. For any given laminar flow, there is a finite value of its Reynolds number beyond which coherent motion cannot be sustained. Since this *critical Reynolds number* has only a modest value, being of the order of 1000 when referring to a transverse thickness, it follows that laminarity is the exception rather than the rule in most engineering applications. At high Reynolds numbers, the motion becomes turbulent, i.e., disorderly, randomly unsteady, and usually impossible to track precisely, although it remains

amenable to analysis based on its average characteristics ([Chap. 6](#)).

Since laminar-flow instability depends on the value of a critical Reynolds number, low-viscosity fluids such as water, mercury, ammonia, gases, etc., are ordinarily turbulent, not laminar. Coffee stirred in a cup mixes turbulently. Smoke rises turbulently from a chimney. Water in a bathroom shower pipe flows turbulently.[†] The boundary layer on a commercial jet airplane wing is turbulent. Any river worthy of its name flows turbulently. Meanwhile, laminar flows should not be disregarded, because many practical situations arise that are indeed laminar, such as low-speed flows, small-scale bodies, substantially viscous fluids, and both boundary-layer and leading-edge flows.

The two key words in this chapter are *stability* and *transition*. The general concept of stability has been discussed many times, probably never more eloquently than by Cunningham (1963). The discussion always boils down to one question: Can a given physical state withstand a disturbance and still return to its original state? If so, it is *stable*. If not, that particular state is unstable. It is therefore incumbent upon the stability analyst to test the effect of a particular disturbance.

A simple example is shown in [Fig. 5-1](#), where a ball lies at rest under various conditions. In [Fig. 5-1a](#), its position is unconditionally stable, because it would return to its initial position even if disturbed by a large displacement. Conversely, [Fig. 5-1b](#) depicts an unstable state, since any slight disturbance would topple the ball, never to return. A flat tabletop, as in [Fig. 5-1c](#), constitutes an example of neutral stability, because the ball will rest anywhere it is displaced. Finally, [Fig. 5-1d](#) illustrates a more complicated case, where the ball is stable for small displacements but will diverge if disturbed far enough to drop over the edge. This is often the case in boundary layers, where a large trip wire can cause an otherwise stable laminar flow to become turbulent. Note that stability requires simply a yes or no answer. One can prove that a physical state is unstable without being able to determine to what eventual state the disturbance will lead. In viscous flow, we can prove that laminar flow is unstable above certain Reynolds numbers, but that is the extent of our predictive insight. The analysis does *not* predict turbulence. Turbulence is an experimentally observed fact. It has never been proved mathematically that turbulent flow is the proper stable state at high Reynolds numbers. Thus, we can discuss only qualitatively our second key word, *transition*, which is defined as the change, over space and time and a certain Reynolds number range, of a laminar flow into a turbulent flow.[‡] Although small-disturbance stability theory has been widely accepted for 50 years and many transition-related measurements have been accumulated, there is still no theory of transition,[§] although there is, as we shall see, a modestly successful empirical prediction of transition based on the spatial amplification rates obtained from the linearized stability theory. It is also possible, at least for moderate Reynolds numbers, to use computational fluid dynamics (CFD) to predict flow instability and transition. This continually evolving field is called *direct numerical simulation* (DNS), which relies on the size and speed of the newest computers to simulate all important scales of a flow, including turbulent fluctuations. Today, DNS has become a numerical experiment for investigating stability, transition, and low Reynolds number turbulence, as reviewed by Moin and Mahesh (1998), Pirozzoli (2011), Zhong and Wang (2012), and Elghobashi (2019).

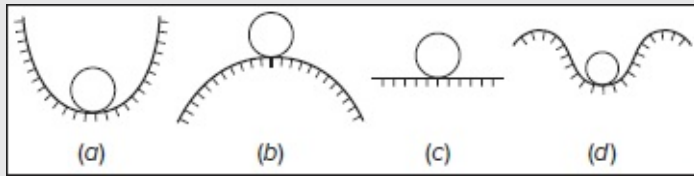


FIGURE 5-1

Relative stability of a ball at rest: (a) stable; (b) unstable; (c) neutrally stable; (d) stable for small disturbances but unstable for large ones.

Page 250

The present chapter undertakes a comprehensive review of the subject, but there are several complete monographs for further reading. Two classic analytical texts are by Lin (1955) and Chandrasekhar (1961). Betchov and Criminale (1967) cover the linear stability of parallel flows, and Joseph (1976) emphasizes nonlinear theories. Drazin and Reid (1981) cover the subject broadly, including numerical methods. Other relevant texts are by Godreche and Manneville (1998), Riahi (2000), Schmid and Henningson (2001), and Drazin and Reid (2004). For pure enjoyment of this very interesting subject, the writer recommends the short text by Philip Drazin (2002), regrettably the last of his many excellent textbooks.

5-1.1 Outline of a Typical Stability Analysis

All small-disturbance stability analyses follow the same general framework, which may be captured in seven steps.

1. We seek to examine the stability of a basic solution Q_0 (or \bar{Q}), to a general physical problem, which may be a scalar quantity or a vector function.
2. We add a generic disturbance \hat{q} and substitute the total generic variable ($\tilde{Q} = Q_0 + \hat{q}$) into the basic equations of motion. Here the circumflex and tilde are used to denote fluctuating and instantaneous quantities, respectively.
3. From the equations resulting from step 2, we subtract the basic terms that the basic solution Q_0 satisfies identically. What remains is called the *disturbance equation* or, more generally, *equations*.
4. We linearize the disturbance equations by assuming *small* disturbances, that is, $|\hat{q}| \ll |Q_0|$, and neglect higher-order terms such as \hat{q}^2 and \hat{q}^3 , etc.
5. If the linearized disturbance equations are complicated and multidimensional, they can be simplified by assuming a spatial form for the disturbance, such as a traveling wave or a perturbation in one or more spatial directions.
6. The linearized disturbance equations should be homogeneous and have homogeneous boundary conditions. They can be solved only for certain specific values of the

equations' parameters. In other words, they result in an *eigenvalue* problem.

7. The eigenvalues found in step 6 are examined to determine when they grow (are unstable), decay (are stable), or remain constant (neutrally stable). The ensuing analysis will generally result in a set of *eigensolutions* (or *eigenfunctions*) that can be displayed for each eigenvalue and a chart showing regions of stability separated from unstable regions by *neutral curves*.

To illustrate this process, we consider a classical example that is more than a century old.

5-1.2 Wind-Generated Waves: The Kelvin–Helmholtz Instability

Page 251

Our first example is very important yet not too difficult mathematically, with no computer required. The reader knows from experience that a wind of sufficient velocity will form waves on a calm water surface. The air–water interface is *unstable* under certain conditions. Hermann von Helmholtz posed the problem physically in 1868, and his friend, Lord Kelvin, set it up mathematically and gave the solution in 1871.

The mathematical model is shown in [Fig. 5-2](#). In this problem, a horizontal interface divides two uniform flows having different velocities and densities. Kelvin assumed that both the lower (region 1) and upper (region 2) flows were incompressible, irrotational, and inviscid.** As such, both *basic flows* (step 1 of Sec. 5-1.1) possess a velocity potential and a hydrostatic pressure distribution that may be described using

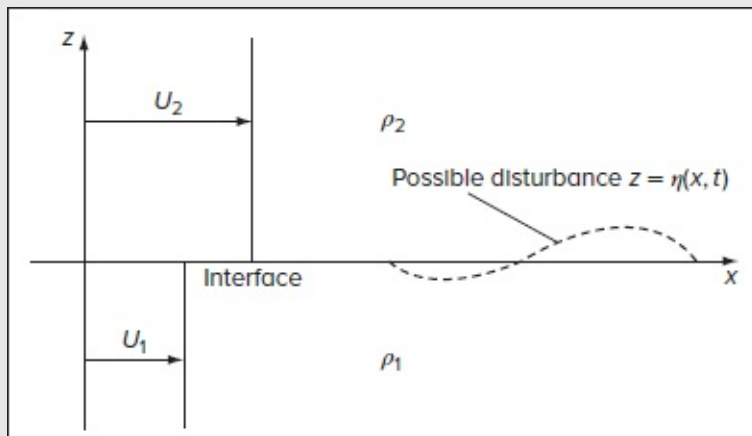


FIGURE 5-2

Sketch and nomenclature for the Kelvin-Helmholtz interfacial instability.

$$z < 0: \quad \phi_1 = U_1 x \quad p_1 = p_0 - \rho_1 g z \quad \text{and} \quad z > 0: \quad \phi_2 = U_2 x \quad p_2 = p_0 - \rho_2 g z \quad (5-1)$$

We allow tangential slip at the interface, which is a *vortex sheet* with a discontinuity in velocity. Step 2 of Sec. 5-1.1 then prompts us to apply a disturbance to both variables, denoted here by the circumflex, or “hat”:

$$\phi_1 = U_1 x + \hat{\phi}_1(x, z, t) \quad \phi_2 = U_2 x + \hat{\phi}_2(x, z, t) \quad (5-2)$$

The interface is disturbed also, to $z = \eta(x, t)$, as shown in [Fig. 5-2](#). The pressure becomes unsteady when the flow is disturbed and satisfies the unsteady Bernoulli relation, [Eq. \(2-95\)](#):

$$p_j = C_j - \rho_j \frac{\partial \phi_j}{\partial t} - \frac{\rho_j}{2} |\nabla \phi_j|^2 - \rho_j g z \quad \text{for regions } j = 1, 2 \quad (2-95)$$

For this expression to be valid at $z = 0$ in the absence of disturbances, one must have $C_1 - \frac{1}{2} \rho_1 U_1^2 = C_2 - \frac{1}{2} \rho_2 U_2^2$. One boundary condition is that the pressure must be continuous across the interface:

$$\text{At } z = \eta: \quad C_1 - \rho_1 \frac{\partial \phi_1}{\partial t} - \frac{\rho_1}{2} |\nabla \phi_1|^2 - \rho_1 g \eta = C_2 - \rho_2 \frac{\partial \phi_2}{\partial t} - \frac{\rho_2}{2} |\nabla \phi_2|^2 - \rho_2 g \eta$$

A second condition is that the vertical velocities must each match the interfacial motion:

$$\text{At } z = \eta: \quad w_j = \frac{\partial \phi_j}{\partial z} = \frac{d\eta}{dt} = \frac{\partial \eta}{\partial t} + \frac{\partial \phi_j}{\partial x} \frac{\partial \eta}{\partial x} \quad \text{for } j = 1, 2$$

The other two conditions require that the disturbances die out far from the interface:

$$\nabla \hat{\phi}_2 \rightarrow 0 \quad \text{as } z \rightarrow +\infty \quad \text{and} \quad \nabla \hat{\phi}_1 \rightarrow 0 \quad \text{as } z \rightarrow -\infty \quad (5-3)$$

Step 3 of Sec. 5-1.1 consists of subtracting the basic flow equation to reveal the *disturbance equation*. This is easy for our inviscid flow because the disturbance terms also satisfy Laplace’s equation:

$$\nabla^2 \hat{\phi}_1 = 0 \quad \text{and} \quad \nabla^2 \hat{\phi}_2 = 0 \quad (5-4)$$

Step 4 is to linearize the problem by assuming that the disturbances are weaker (i.e., much smaller in size) than the basic flow. First, the interface is assumed to have small displacements and small slopes:

$$g\eta \ll U_j^2 \quad \frac{\partial \eta}{\partial x} \ll 1$$

Page 252

This enables us to approximate the interfacial conditions at $z = \eta \approx 0$. Second, the disturbance velocities are assumed to be small: $|\nabla \hat{\phi}_j| \ll U_j$. This enables us to linearize the interfacial conditions, namely,

$$\begin{aligned}
\text{Pressure:} \quad & \rho_1 \left(U_1 \frac{\partial \hat{\phi}_1}{\partial x} + \frac{\partial \hat{\phi}_1}{\partial t} + g\eta \right) \approx \rho_2 \left(U_2 \frac{\partial \hat{\phi}_2}{\partial x} + \frac{\partial \hat{\phi}_2}{\partial t} + g\eta \right) \quad \text{at} \quad z \approx 0 \quad (5-5) \\
\text{Kinematic:} \quad & \frac{\partial \hat{\phi}_1}{\partial x} \approx \frac{\partial \eta}{\partial t} + U_1 \frac{\partial \eta}{\partial x} \quad \text{and} \quad \frac{\partial \hat{\phi}_2}{\partial x} \approx \frac{\partial \eta}{\partial t} + U_2 \frac{\partial \eta}{\partial x} \quad \text{at} \quad z \approx 0
\end{aligned}$$

Although the equations and boundary conditions are now linear, they are still difficult to handle for an arbitrary disturbance $\eta(x, t)$. Thus, step 5 of Sec. 5-1.1 suggests assuming a simple form for the disturbances, namely, two-dimensional traveling waves or *normal modes*:

$$\eta = \eta_0 e^{i(\alpha x - \sigma t)} = \eta_0 e^{i[\alpha x - (\sigma_r + \sigma_i)t]} \quad \hat{\phi}_j = \hat{\phi}'_j(z) e^{i(\alpha x - \sigma t)} \quad \text{for regions} \quad j = 1, 2$$

where $i = \sqrt{-1}$. Note that the wave number α is real, but the frequency σ represents a complex number, and so the disturbance $\eta = \eta_0 e^{\sigma_i t} e^{i(\alpha x - \sigma_r t)}$ will be temporally *unstable* (grow without bound) when its imaginary part σ_i is positive.

Step 6 of Sec. 5-1.1: We solve the Laplacian given by [Eqs. \(5-4\)](#), retrieve exponential disturbances of the form $e^{\pm kz}$, and then use the far-field boundary conditions of [Eqs. \(5-3\)](#) to reduce the solutions to

$$\phi'_1 = A_1 e^{kz} \quad \text{and} \quad \phi'_2 = A_2 e^{-kz} \quad (5-6)$$

At this point, substitution back into the interfacial conditions of [Eqs. \(5-5\)](#) gives rise to three linear homogeneous equations for the three constants η_0 , A_1 , and A_2 . The results are

$$A_1 = i\eta_0 \left(U_1 - \frac{\sigma}{\alpha} \right) \quad \text{and} \quad A_2 = -i\eta_0 \left(U_2 - \frac{\sigma}{\alpha} \right)$$

This specifies the coefficients in the disturbance *eigenfunctions* of [Eqs. \(5-6\)](#). These are proportional to η_0 , which is arbitrary but small. The *eigenvalues* σ are found from the pressure condition, [Eq. \(5-5\)](#), which is a quadratic equation with the solution:

$$\sigma = \alpha \frac{\rho_1 U_1 + \rho_2 U_2}{\rho_1 + \rho_2} \pm \left[\frac{\alpha^2 \rho_1 \rho_2 (U_1 - U_2)^2}{(\rho_1 + \rho_2)^2} - \frac{\alpha g (\rho_1 - \rho_2)}{(\rho_1 + \rho_2)} \right]^{1/2}$$

The key to stability is encapsulated within the square bracket $[\]$. The disturbance will be stable, neutral, or unstable when the bracketed term is negative, zero, or positive. The unstable condition is thus

$$\alpha \rho_1 \rho_2 (U_1 - U_2)^2 > g(\rho_1^2 - \rho_2^2) \quad \text{or} \quad \alpha = \frac{2\pi}{\lambda} \quad (5-7)$$

where λ is the wavelength of the disturbance. This condition is always true for large enough α , or small enough λ , so, at this level of approximation, vortex sheets are always unstable.

A more realistic result is obtained by adding linearized surface (interfacial) tension to the analysis, using [Eq. \(1-87\)](#). The final result is

$$\sigma = \alpha \frac{\rho_1 U_1 + \rho_2 U_2}{\rho_1 + \rho_2} \pm \left[\frac{\alpha^2 \rho_1 \rho_2 (U_1 - U_2)^2}{(\rho_1 + \rho_2)^2} - \frac{\alpha [g(\rho_1 - \rho_2) + \alpha^2 \mathfrak{S}]}{(\rho_1 + \rho_2)} \right]^{1/2} \quad (5-8)$$

where \mathfrak{S} is the surface-tension coefficient. The bracketed term $[\]$ is positive (i.e., unstable) when

$$(U_1 - U_2)^2 > \frac{[g(\rho_1 - \rho_2) + \alpha^2 \mathfrak{S}](\rho_1 + \rho_2)}{\alpha \rho_1 \rho_2} \quad (5-9)$$

Unlike [Eq. \(5-7\)](#), which neglects surface tension, [Eq. \(5-9\)](#) requires a finite velocity difference to cause waves to form. The reader may show as an exercise that the right-hand side of [Eq. \(5-9\)](#) reaches a minimum when $\alpha = [g(\rho_1 - \rho_2)/\mathfrak{S}]^{1/2}$. As an example, let us consider air at 20 °C and 1 atm blowing over a fresh water surface. From Tables C-1 and C-2 in App. C, $\rho_{\text{water}} = 998 \text{ kg/m}^3$, $\rho_{\text{air}} = 1.20 \text{ kg/m}^3$, and $\mathfrak{S} = 0.0727 \text{ N/m}$. The minimum value of $(U_1 - U_2)^2$ occurs at $\alpha \approx 367 \text{ m}^{-1}$. Then [Eq. \(5-9\)](#) predicts that waves will begin to form at a critical value $|U_1 - U_2| \approx 6.67 \text{ m/s} = 15 \text{ mph}$, for which the critical wavelength is 0.0171 m. This calculation is merely an estimate, ± 50 percent. The actual critical velocity difference will depend on the viscosity, wind nonuniformity, and turbulence.

Page 253



FIGURE 5-3

Kelvin-Helmholtz breaking waves outlined by a billow-cloud formation. [*John Davidson Photos.Alamy Stock Photo*].

The final step 7 of Sec. 5-1.1 suggests drawing a chart showing regions of flow stability and instability. This is appropriate for the complex computer solutions of the next section, but here we derived a formula, [Eq. \(5-9\)](#), which makes a chart unnecessary.

Although modified by viscosity, Kelvin-Helmholtz instability is common in the atmosphere and the oceans in particular, where the wind-generated surface waves are visible. Deep in the ocean, there are internal waves at density interfaces, as explained by Phillips (1978). In the atmosphere, wind shear, which is the bane of pilots, generates waves that are generally invisible. But sometimes cloud and light conditions reveal the waves, as shown in [Fig. 5-3](#), which depicts beautiful rolled-up waves caused by the naturally occurring Kelvin-Helmholtz instability.

5-2 LINEARIZED STABILITY OF PARALLEL VISCOUS FLOWS

We now use the same method of Sec. 5-1 to study viscous-flow instability. Here, both the basic solution and its assumed disturbances will generally be three-dimensional unsteady functions. The same seven steps apply:

1. Select a basic solution flow.
2. Add a disturbance.
3. Find the disturbance equations.
4. Linearize in the presence of a small disturbance.
5. Simplify the spatial disturbance form (by setting it, in this case, to a traveling wave).
6. Solve for the eigenvalues and corresponding eigensolutions.
7. Identify and interpret the stability conditions and draw a chart showing the neutral curves and the growth and decay rates.

5-2.1 Derivation of the Orr–Sommerfeld Equation

Let us now carry out the seven steps for incompressible laminar flow with constant (ρ, μ, k, c_p) and no buoyancy effects. This enables us to explore the stability of the continuity and Navier–Stokes relations for the two instantaneous variables $\tilde{\mathbf{v}}$ and \tilde{p} :

$$\nabla \cdot \tilde{\mathbf{v}} = 0 \quad \frac{D\tilde{\mathbf{v}}}{Dt} = -\frac{1}{\rho} \nabla \tilde{p} + \nu \nabla^2 \tilde{\mathbf{v}} \quad (5-10)$$

Let us assume that we have extracted, by the methods of [Chap. 3](#) or 4, an analytical or numerical laminar-flow solution (often called the *basic flow*), to these equations: $\mathbf{V}_0 = \mathbf{V}_0(\mathbf{x}, t) = (U, V, W)$ and $P_0(\mathbf{x}, t)$. To determine whether the base flow is stable, we add the small-disturbance variables $\hat{\mathbf{v}}(\mathbf{x}, t) = (\hat{u}, \hat{v}, \hat{w})$ and $\hat{p}(\mathbf{x}, t)$. We substitute the superimposed variables $\tilde{\mathbf{v}} = \mathbf{V}_0 + \hat{\mathbf{v}}$ and $\tilde{p} = P_0 + \hat{p}$ into [Eqs. \(5-10\)](#), subtract the original \mathbf{V}_0 and P_0 equalities, and then dismiss higher-order terms and products of $\hat{\mathbf{v}}$, which occur only in one place, the (nonlinear) convective acceleration term. The reader may readily verify the following linearized disturbance equations, written out in full:

$$\begin{aligned} \frac{\partial \hat{u}}{\partial t} + \frac{\partial \hat{v}}{\partial y} + \frac{\partial \hat{w}}{\partial z} &= 0 \\ \frac{\partial \hat{u}}{\partial t} + U \frac{\partial \hat{u}}{\partial x} + \hat{u} \frac{\partial U}{\partial x} + V \frac{\partial \hat{u}}{\partial y} + \hat{v} \frac{\partial U}{\partial y} + W \frac{\partial \hat{u}}{\partial z} + \hat{w} \frac{\partial U}{\partial z} &= -\frac{1}{\rho} \frac{\partial \hat{p}}{\partial x} + \nu \nabla^2 \hat{u} \\ \frac{\partial \hat{v}}{\partial t} + U \frac{\partial \hat{v}}{\partial x} + \hat{u} \frac{\partial V}{\partial x} + V \frac{\partial \hat{v}}{\partial y} + \hat{v} \frac{\partial V}{\partial y} + W \frac{\partial \hat{v}}{\partial z} + \hat{w} \frac{\partial V}{\partial z} &= -\frac{1}{\rho} \frac{\partial \hat{p}}{\partial y} + \nu \nabla^2 \hat{v} \\ \frac{\partial \hat{w}}{\partial t} + U \frac{\partial \hat{w}}{\partial x} + \hat{u} \frac{\partial W}{\partial x} + V \frac{\partial \hat{w}}{\partial y} + \hat{v} \frac{\partial W}{\partial y} + W \frac{\partial \hat{w}}{\partial z} + \hat{w} \frac{\partial W}{\partial z} &= -\frac{1}{\rho} \frac{\partial \hat{p}}{\partial z} + \nu \nabla^2 \hat{w} \end{aligned} \quad (5-11)$$

These are formidable but *linear* partial differential equations for the perturbed variables, $(\hat{u}, \hat{v}, \hat{w}, \hat{p})$, because U, V , and W represent known functions that merely serve as variable

Equations (5-11) can be systematically reduced to a single ordinary differential equation by assuming a locally parallel basic flow. If y refers to the coordinate normal to the wall or across the shear layer, an assumption can be made that the component V across the layer is negligibly small, as in duct flow, and further assume that $U \approx U(y)$ and $W \approx W(y)$. This scenario will eliminate 10 convective terms on the left-hand sides and leave us with

$$\begin{aligned}\frac{\partial \hat{u}}{\partial x} + \frac{\partial \hat{v}}{\partial y} + \frac{\partial \hat{w}}{\partial z} &= 0 \\ \frac{\partial \hat{u}}{\partial t} + U \frac{\partial \hat{u}}{\partial x} + \hat{v} \frac{\partial U}{\partial y} + W \frac{\partial \hat{u}}{\partial z} &= -\frac{1}{\rho} \frac{\partial \hat{p}}{\partial x} + \nu \nabla^2 \hat{u} \\ \frac{\partial \hat{v}}{\partial t} + U \frac{\partial \hat{v}}{\partial x} + W \frac{\partial \hat{v}}{\partial z} &= -\frac{1}{\rho} \frac{\partial \hat{p}}{\partial y} + \nu \nabla^2 \hat{v} \\ \frac{\partial \hat{w}}{\partial t} + U \frac{\partial \hat{w}}{\partial x} + W \frac{\partial \hat{w}}{\partial z} &= -\frac{1}{\rho} \frac{\partial \hat{p}}{\partial z} + \nu \nabla^2 \hat{w}\end{aligned}$$

At this juncture, the disturbances can be assumed to be parallel. In fact, a reasonable form of a three-dimensional disturbance $(\hat{u}, \hat{v}, \hat{w})$ is that of a wave traveling along the wall at an angle ϕ with respect to the x -axis with an amplitude that varies with y . Taking advantage of the complex notation, we specify each generic disturbance \hat{q} using $\hat{q} = q(y)\exp[i\alpha(x \cos \phi + z \sin \phi - ct)]$, namely,

$$(\hat{u}, \hat{v}, \hat{w}, \hat{p}) = [u(y), v(y), w(y), p(y)] \exp[i\alpha(x \cos \phi + z \sin \phi - ct)] \quad (5-12)$$

where $i = \sqrt{-1}$. Accordingly, all disturbances travel at a wave number α , propagation speed c , and frequency $\omega = \alpha c$. They are historically referred to as Tollmien–Schlichting waves, which are the first (infinitesimal) indications of laminar-flow instability. If we substitute [Eqs. \(5-12\)](#) into the resulting equations above, we obtain the following linear ordinary differential equations with complex coefficients:

$$i\alpha u \cos \phi + v' + i\alpha w \sin \phi = 0 \quad (5-13)$$

$$i\alpha u(U \cos \phi + W \sin \phi - c) + U'v = -\frac{i}{\rho} \alpha p \cos \phi + \nu(u'' - \alpha^2 u) \quad (5-14)$$

$$i\alpha v(U \cos \phi + W \sin \phi - c) = -\frac{1}{\rho} p' + \nu(v'' - \alpha^2 v) \quad (5-15)$$

$$i\alpha w(U \cos \phi + W \sin \phi - c) + W'v = -\frac{i}{\rho} \alpha p \sin \phi + \nu(w'' - \alpha^2 w) \quad (5-16)$$

where the primes denote differentiation with respect to y . As expected, our system is second order in u , v , w and first order in p . We may assume that the disturbances grow either spatially (when α is complex and $\omega = \alpha c$ is real) or else temporally (for real α and complex ω). Note that by deliberately aligning the x -axis with the traveling wave motion, one recovers $\hat{q} = q(y)\exp[i\alpha(x - ct)]$ and a simplified form of the eigenvalue problem, namely,

$$\begin{aligned}
iau + v' &= 0 \\
iau(U - c) + U'v &= -\frac{i}{\rho}\alpha p + \nu(u'' - \alpha^2 u) \\
iav(U - c) &= -\frac{1}{\rho}p' + \nu(v'' - \alpha^2 v) \\
iaw(U - c) + W'v &= \nu(w'' - \alpha^2 w)
\end{aligned}$$

A more elegant way of formulating this problem while retaining its general character is to multiply [Eq. \(5-14\)](#) by $\cos \phi$ and [Eq. \(5-16\)](#) by $\sin \phi$ before adding the two equations. Further, we can introduce the compact notation

$$u_0 = u \cos \phi + w \sin \phi \quad \text{and} \quad U_0 = U \cos \phi + W \sin \phi \quad (5-17)$$

We find ourselves left with only three equations in three variables, u_0 , v , and p :

$$iau_0 + v' = 0 \quad (5-18)$$

$$iau_0(U_0 - c) + U'_0 v = -\frac{i}{\rho}\alpha p + \nu(u''_0 - \alpha^2 u_0) \quad (5-19)$$

$$iav(U_0 - c) = -\frac{1}{\rho}p' + \nu(v'' - \alpha^2 v) \quad (5-20)$$

These are two-dimensional equations whose components u_0 and U_0 are parallel to the direction of propagation ϕ of the traveling waves, as seen from [Eqs. \(5-17\)](#). Thus, the stability of any parallel flow in any direction ϕ can be found from a two-dimensional analysis for the effective basic flow $U_0(y)$ in that direction. This vital conclusion was first deduced by Dunn and Lin (1955) and later used by Gregory et al. (1955) to derive general results for the stability of three-dimensional flows, particularly the rotating disk flow of Sec. 3-8.

Page 255

Now suppose further that W is identically zero, i.e., the basic flow is purely two-dimensional. Then the shape of the profile $U_0(y)$ becomes independent of ϕ , which means that the stability computation is no longer dependent on ϕ , except for the scale factor $\cos \phi$. Therefore, for an oblique disturbance, the basic flow $U \cos \phi$ is relatively slower and hence more stable than when the disturbance propagates parallel to $U(y)$. This result was deduced by Squire (1933) in his now famous theorem.

Squire's theorem. For a two-dimensional parallel flow $U(y)$, the minimum critical unstable Reynolds number occurs for a two-dimensional disturbance propagating in the same direction ($\phi = 0$).

In considering only two-dimensional disturbances, Squire's theorem is concerned with the minimum Reynolds number, which occurs when $\phi = 0$. However, in his review, Stuart (1987) points out that maximum wave *amplification* occurs for $\phi \neq 0$, such that three-dimensional disturbances do indeed affect the growth and shape of an unstable disturbance.

Let us now drop the subscript 0 in [Eqs. \(5-18\)–\(5-20\)](#). It is possible to eliminate any two of the three variables u , v , and p . If we eliminate u , we obtain a simple equation for the pressure fluctuation:

$$p'' - \alpha^2 p = -2i\alpha\rho U'v \quad (5-21)$$

Thus, the pressure satisfies a Poisson equation with a source term that is proportional to the product of the mean shear and the longitudinal variation of the normal velocity fluctuation,

$$\frac{dU}{dy} \frac{\partial \hat{v}}{\partial x}$$

In the outer freestream, where $U' \approx 0$, the solution must be of the form

$$p = ae^{-\alpha y} + be^{+\alpha y} \quad (5-22)$$

Since the disturbance is assumed to vanish at infinity, it follows that $b = 0$ and the pressure fluctuation is damped exponentially.

It is relatively difficult to eliminate v and p from these equations. The result will be the same mathematically if we eliminate u and p , with the outcome being the celebrated Orr–Sommerfeld relation:

$$(U - c)(v'' - \alpha^2 v) - U''v + \frac{i\nu}{\alpha}(v''' - 2\alpha^2 v'' + \alpha^4 v) = 0 \quad (5-23)$$

The secrets of infinitesimal laminar-flow instability lie within this fourth-order linear homogeneous equation, first derived independently by Orr (1907) and Sommerfeld (1908). The boundary conditions are that the disturbances u and v must vanish at infinity and at any walls (no slip). The continuity relation in [Eq. \(5-18\)](#) shows that $u = 0$ implies $v' = 0$. Hence, the proper conditions on the Orr–Sommerfeld equation are of the following types:

$$\text{Duct flows:} \quad v(\pm h) = v'(\pm h) = 0 \quad (5-24)$$

$$\text{Boundary layers:} \quad v(0) = v'(0) = 0 \quad v(\infty) = v'(\infty) = 0$$

$$\text{Free-shear layers:} \quad v(\pm\infty) = v'(\pm\infty) = 0$$

Since the equation and its boundary conditions are both homogeneous, they give rise to an eigenvalue problem. The Orr–Sommerfeld equation has three parameters: α , c , and ν (or, better, a Reynolds number $Re = U\delta / \nu$). For a given profile $U(y)$ and $U''(y)$, only a certain continuous but limited sequence of these parameters (the eigenvalues) will satisfy [Eqs. \(5-23\)](#) and [\(5-24\)](#). The mathematical problem becomes that of finding this sequence, which has a different functional form for the spatial versus temporal growth of disturbances:

$$\text{Temporal growth:} \quad f(Re, \alpha, c_r, c_i) = 0 \quad (c_i > 0: \text{temporally unstable}) \quad (5-25)$$

$$\text{Spatial growth:} \quad f(Re, \alpha_r, \alpha_i, \omega) = 0 \quad (\alpha_i < 0: \text{spatially unstable}) \quad (5-26)$$

where the subscripts r and i denote real and imaginary parts, respectively. Of particular

interest is the case of neutral stability: $c_i = 0$ for the temporal case and $\alpha_i = 0$ for spatial neutral growth. The locus of these neutral points forms the boundary between stability and instability. The solutions $v(y)$ associated with the eigenvalues in [Eqs. \(5-25\)–\(5-26\)](#) represent the problem's eigenfunctions or eigensolutions.

5-2.2 Inviscid-Stability Theory

A limiting but very instructive case is that of an infinite Reynolds number or negligible viscosity, for which we can drop the term involving ν in the Orr–Sommerfeld relation, [Eq. \(5-23\)](#). The resulting inviscid-disturbance relation,

Page 256

$$v'' - \left(\frac{U''}{U - c} + \alpha^2 \right) v = 0 \quad (5-27)$$

is named in honor of Lord Rayleigh, who first studied this equation in a series of papers between 1878 and 1915, all of which are now collected in six volumes of his “Scientific Papers.” The Rayleigh equation is second order, and hence we can no longer maintain conditions on the tangential velocity u (or v'). We retain two conditions on the normal velocity v , for example,

$$v(0) = v(\infty) = 0 \quad (5-28)$$

Numerous inviscid analyses are reported in the literature, and an excellent discussion is given in the text by Drazin and Reid (2004). Rayleigh's theory provides good insight into profile shape effects on stability, and some workers have used the two “inviscid” solutions to help generate two additional “viscous” solutions of the full Orr–Sommerfeld equation.

The Rayleigh [Eq. \(5-27\)](#) can be readily solved either analytically or numerically. There is a singularity on the real axis at the point, $c = c_r$, where the velocity $U = c_r$. The analytical behavior of v near this singularity was established in pioneering work by Tollmien (1929).

Five important theorems on inviscid stability follow:

Theorem 1 [Rayleigh (1880)]. A necessary (but not sufficient) condition for instability is for the velocity profile to have an inflection point.

Theorem 2 [Fjørtoft (1950)]. It is further necessary that the numerical value $|U''|$ of the vorticity be a maximum at the point of inflection.

Theorem 3 [Fjørtoft (1950)]. If a point of inflection exists, it is further necessary that $U''(U - U_{PI}) < 0$ somewhere on the profile, where U_{PI} is the velocity at the point of inflection.

Theorem 4 [Lin (1955)]. If $U(y)$ possesses an inflection point at $y = y_c$, a neutral disturbance ($c_i = 0$) may exist whose phase velocity is $c_r = U(y_c)$.

Theorem 5 [Rayleigh (1880)]. The phase velocity c_r of an amplified disturbance must always lie between the minimum and maximum values of $U(y)$.

Rayleigh's result, Theorem 1, led workers for many years to believe that real (viscous) profiles without a point of inflection, such as channel flows and boundary layers with favorable pressure gradients, would be stable. It remained for Prandtl (1921) to show that viscosity can indeed be destabilizing for certain wave numbers at finite Reynolds numbers.

[Figure 5-4](#) introduces four different velocity profiles to be evaluated for inviscid instability. The first three are unconditionally stable; only the fourth is possibly unstable by virtue of Fjortoft's Theorem 3. Meanwhile, all four possess viscous instability at a finite Reynolds number.

Some actual profiles, which resemble [Fig. 5-4d](#)—and are unstable even in the inviscid limit—include boundary layers with adverse pressure gradients, shear layers between parallel streams, jets, and wakes.

5-2.3 Viscous Stability: Solution of the Orr–Sommerfeld Equation

The Rayleigh equation reveals the point of inflection to be a source of possible instability as Re approaches infinity; however, it is clear from experiments that all types of laminar profiles become unstable at finite Reynolds numbers, as predicted physically by Prandtl (1921) and first shown mathematically by Tollmien (1929). These instabilities are manifested in the eigenvalues of the Orr–Sommerfeld equation, written here in dimensionless form:

$$(U^* - c^*)(\phi'' - \alpha_\delta^2 \phi) - U^{*''} \phi + \frac{i}{\alpha_\delta Re_\delta} (\phi''' - 2\alpha_\delta^2 \phi'' + \alpha_\delta^4 \phi) = 0 \quad (5-29)$$

where

$$\phi = \frac{v}{U_e} \quad U^* = \frac{U}{U_e} \quad c^* = \frac{c}{U_e} \quad \alpha_\delta = \alpha \delta \quad Re_\delta = \frac{U_e \delta}{\nu}$$

Here, the non-dimensional normal coordinate is taken to be $\xi = y/\delta$ and U_e is used to represent the speed at the edge of the boundary layer. The boundary conditions have the same homogeneous form as in [Eq. \(5-24\)](#).

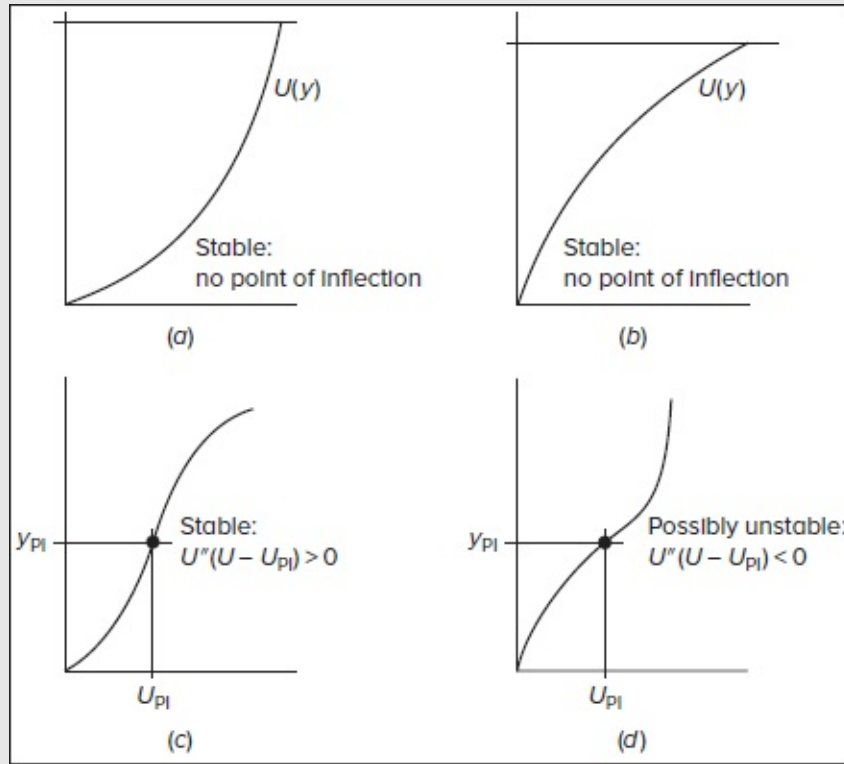


FIGURE 5-4

Four inviscid velocity profiles evaluated for stability pursuant to Theorems 1 and 3 of Sec. 5-2.2.

Page 257

For a given velocity profile $U(y)$, [Eq. \(5-29\)](#) can be solved for its eigenvalues α_δ which vary with Re_δ . The problem can be solved for either temporal stability (real α_δ), or spatial stability (real $\omega^* = \alpha_\delta c^*$). The solution will be unstable if we find eigenvalues such that

$$\text{Temporal instability:} \quad c_i^* > 0 \quad (5-30)$$

$$\text{Spatial instability:} \quad \alpha_{\delta i} < 0 \quad (5-31)$$

To satisfy the freestream boundary conditions $\phi(\infty) = \phi'(\infty) = 0$, we set $U^{*''} = 0$ and $U' = U_e^*$, so that [Eq. \(5-29\)](#) can be solved for damped exponential behavior:

$$\text{Freestream, } \xi \gg 1: \quad \phi = C_1 e^{-\alpha_\delta \xi} + C_2 e^{-\zeta \xi}; \quad \zeta^2 = \alpha_\delta^2 + i \alpha_\delta Re_\delta (U_e^* - c^*) \quad (5-32)$$

The constants C_1 and C_2 are unimportant because the differential equation and boundary conditions are homogeneous. This asymptotic behavior reveals a formidable numerical difficulty in the solution of the Orr–Sommerfeld equation. Since α_δ and c^* are of order unity and $Re_\delta \gg 1, 1$, the two rates of change in [Eq. \(5-32\)](#) are quite different; generally speaking,

regardless of the velocity profile shape,

$$|\zeta| \gg |\alpha_\delta| \quad (5-33)$$

Thus, of the four independent solutions of [Eq. \(5-29\)](#), two of them (associated with $e^{\alpha_\delta \delta}$) grow slowly, whereas two of them (associated with $e^{\zeta \delta}$) grow rapidly. The fast-growing solutions tend to contaminate and smear the slower pair, so that accurate eigenvalues cannot easily be found.

5-2.3.1 NUMERICAL METHODS. The Rayleigh inviscid-stability [Eq. \(5-27\)](#) is only moderately difficult to model numerically and hence is suitable for problem assignments. However, the viscous Orr–Sommerfeld [Eq. \(5-29\)](#), with competing small and large solutions, requires a substantially greater effort. Orr–Sommerfeld programs are lengthy and sophisticated. The pioneers were Tollmien (1929) and Schlichting (1933b), who developed analytical (noncomputer) methods. By the 1950s, digital-computer methods were tried but proved inaccurate. Kaplan (1964) made a breakthrough with a “purification” scheme to keep slow- and fast-moving solutions separate, as described in the text by Betchov and Criminale (1967). Wazzan et al. (1968a) used Gram–Schmidt orthonormalization to ensure accuracy up to $Re_{\delta^*} \approx 10^5$. Modern methods use either spectral techniques or finite differences, as described in the text by Drazin and Reid (1981). Sherman (1990) and Cebeci and Cousteix (1998) provide FORTRAN programs, whereas Schmid and Henningson (2001) employ MATLAB programs in stability calculations. In view of these, the transition-prediction methods of Sec. 5-4 will avoid lengthy Orr–Sommerfeld computations.

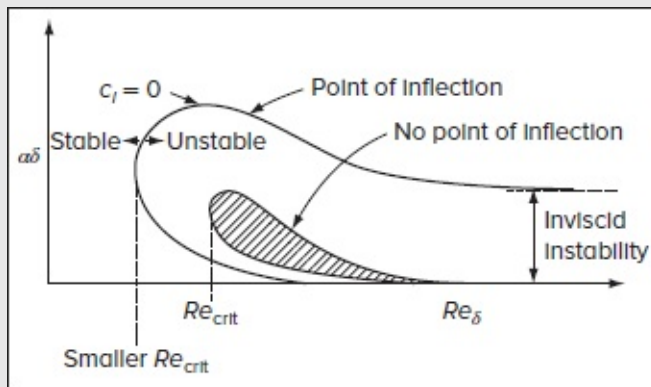


FIGURE 5-5

Neutral curves of the Orr-Sommerfeld equation

The viscous theories predict a finite region at low Reynolds numbers (of the order of $Re_\delta \approx 1000$) where infinitesimal disturbances are amplified ($c_i > 0$). The boundary of this

region is the so-called *neutral curve*, which is the locus of points where $c_i = 0$. From their shapes, they are called *thumb curves*, and two examples are sketched in [Fig. 5-5](#). Outside the thumb, all disturbances are damped. If the profile $U(y)$ has no point of inflection, the thumb disappears at a large Reynolds number, in accordance with the Rayleigh criterion. In contrast, if $U(y)$ has a point of inflection, the thumb curve remains open at infinity. The lowest Reynolds number to which the thumb protrudes is called Re_{crit} , and typically the inflection profile has a smaller Re_{crit} , and a bigger thumb all around. The point Re_{crit} denotes the smallest Reynolds number at which disturbances can be amplified. It *should not* be confused with the point of transition to turbulence, which occurs some 10 to 20 times the distance x_{crit} further downstream in the boundary layer. In practice, the values of c_i and $\alpha\delta$ within the thumb tend to be more important than Re_{crit} because these determine the spatial and temporal growth rates that are responsible for the onset of turbulent motion.

5-2.4 Stability of the Blasius and Falkner–Skan Profiles

Most of the classical velocity profiles have now been studied and their eigenvalues tabulated and charted. Early work concentrated on *temporal* stability, [Eq. \(5-25\)](#). In the 1960s, emphasis shifted to *spatial* stability, in the form of [Eq. \(5-26\)](#), which is a more realistic model of disturbances in a boundary layer growing and propagating downstream. Review articles such as Wazzan (1975) and Arnal (1984) discuss a wide variety of profiles such as the Falkner–Skan flows, the plane jet, the plane wake, the free-shear layer, Poiseuille pipe and channel flows, and many nonsimilar flows.

Accurate stability computations for the Blasius profile, assuming parallel flow, are shown in [Figs. 5-6a](#) and [b](#), from Wazzan et al. (1968a). Note the difference in viewpoint between *temporal* instability ([Fig. 5-6a](#)), where unstable contours of $c_i > 0$ are plotted, and *spatial* instability ([Fig. 5-6b](#)), where values of $\alpha_i < 0$ are contoured. The neutral curves corresponding to $c_i = \alpha_i = 0$ have the same physical meaning, although they are correlated differently. The following details are listed:

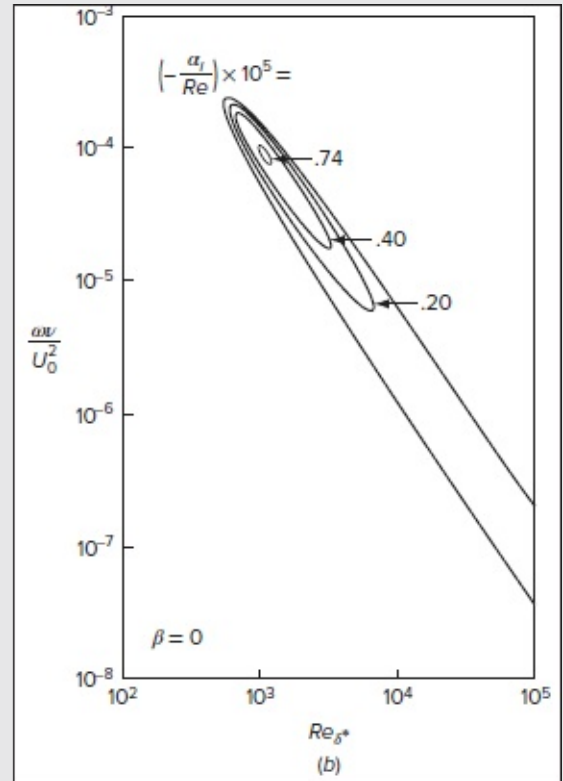
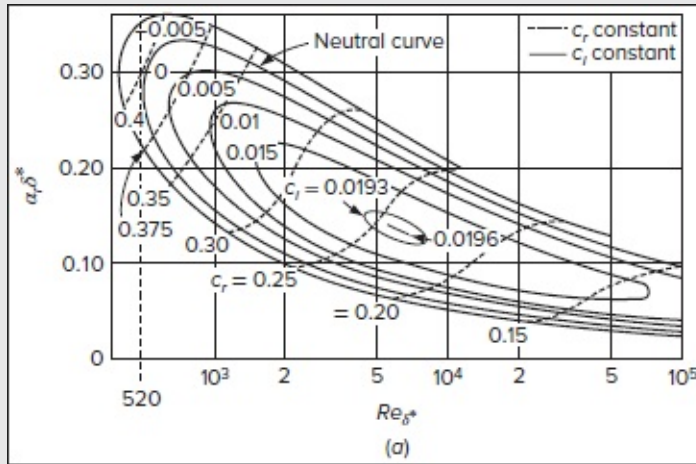


FIGURE 5-6

Amplification curves for the Blasius flat-plate boundary layer from the point of view of (a) temporal stability and (b) spatial stability. [After Wazzan *et al.* (1968a)].

1. The minimum or *critical* Reynolds number for initial instability is $Re_{\delta^*, \text{crit}} = 520$ or $Re_{x, \text{crit}} \approx 91,000$. (Nonparallel-flow effects reduce these further to about 400 and 54,000, respectively.)
2. At Re_{crit} , the wave parameters, as calculated by Jordinson (1970), are $\alpha \delta^* = 0.3012$, $c_r/U_0 = 0.3961$, and $Re_w^{-1} = \omega \nu / U_0^2 = 2.29 \times 10^{-4}$, where $Re_w = MjSt$ denotes the wave Reynolds number, i.e., the product of $Mj = U_0^3 / (\omega^2 \nu L)$ and $St = \omega L / U_0$ (App. H2).
3. The maximum wave number for instability is $\alpha \delta^* \approx 0.35$; hence, the smallest unstable wavelength is $\lambda_{\min} = 2\pi \delta^* / 0.35 \approx 18\delta^* \approx 6\delta$. Thus, unstable Tollmien–Schlichting waves are long relative to the boundary-layer thickness.
4. The maximum temporal growth rate is $c_i/U_0 \approx 0.0196$.
5. The maximum spatial growth rate is $\alpha_i \nu / U_0 \approx -0.74 \times 10^{-5}$.
6. The maximum phase velocity of unstable waves is $c_r/U_0 \approx 0.4$; hence, Tollmien–Schlichting waves travel rather slowly and tend to arise *near the wall*.
7. Compared to $Re_{x, \text{crit}} \approx 91,000$, the point of final transition to turbulence is at about Re

$x_{tr} \approx 3 \times 10^6$, or about 30 times further downstream.

Figure 5-7 shows neutral curves for Falkner–Skan wedge-flow profiles as computed by Wazzan (1968b). The parameter β has the same meaning as in the Falkner–Skan Eq. (4-93). We see a very strong pressure gradient effect: a stagnation flow with $\beta = 1.0$ can be hundreds of times more stable than a separating flow with $\beta = -0.1988$. This is true not only of Re_{crit} but also of the maximum spatial amplification rates, as shown in Table 5-1. Note how the curves for $\beta < 0$ (adverse gradients) remain open at large Reynolds numbers, since they have a point of inflection and hence are prone to inviscid instability.

Page 259

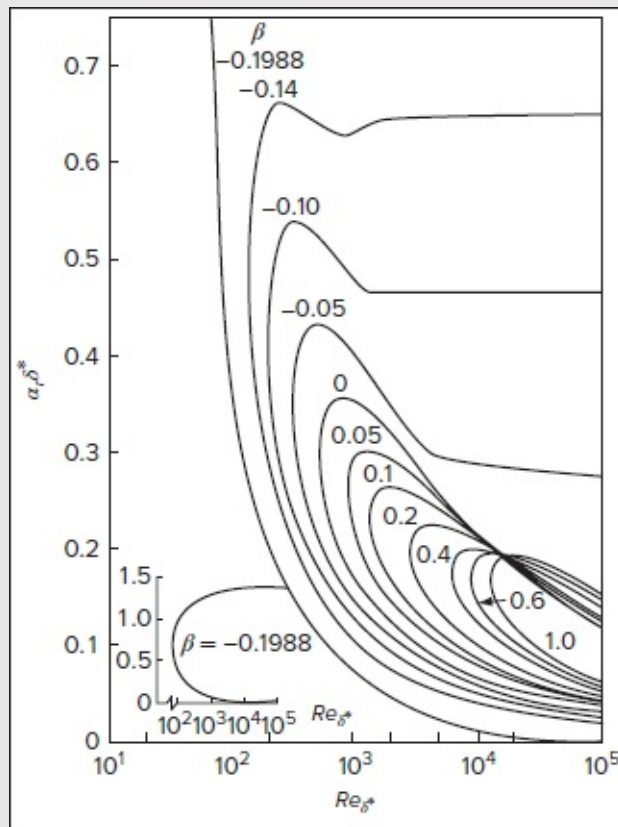


FIGURE 5-7

Neutral stability curves for Falkner–Skan boundary-layer profiles. [After Wazzan et al. (1968b)].

TABLE 5-1

Spatial stability parameters for Falkner-Skan profiles

β	$Re_{\delta^*, \text{crit}}$	$Re_{\theta, \text{crit}}$	$c_{i,\text{max}}$	$\left(\frac{\alpha\delta^*}{Re_{\delta^*}}\right)_{\text{max}} \times 10^7$
+1.0	12,490	5,636	0.0065	1.14
0.8	10,920	4,874	0.0070	1.35
0.6	8,890	3,909	0.0075	1.67
0.5	7,680	3,344	0.0080	1.92
0.4	6,230	2,679	0.0085	2.42
0.3	4,550	1,927	0.0095	3.45
0.2	2,830	1,174	0.0104	6.0
0.1	1,380	556	0.0129	15.7
0.05	865	342	0.0154	32
0.0	520	201	0.0196	74
-0.05	318	119	0.0275	186
-0.1	199	71	0.0388	450
-0.14	138	47	0.0525	963
-0.1988	67	17	0.12	5,600

Source: Computations by Wazzan et al. (1968b).

5-2.5 Comparison of Stability Theory with Experiment

Page 260

Although the concepts of instability and transition were well established by Reynolds (1883), stability theory did not receive wide acceptance at first. Early wind tunnel transition experiments by Burgers (1924) reported $Re_{x,\text{crit}} \approx 350,000$ for flat plates and did not detect any Tollmien–Schlichting waves. Even after the hot-wire anemometer was invented, careful measurements by Dryden (1934) confirmed the onset of turbulent fluctuations but did not detect Tollmien–Schlichting waves. These experiments were contaminated by the very noisy turbulence and the acoustics in the wind tunnels of the day.

Then, in 1940, the U.S. National Bureau of Standards, under the direction of H. L. Dryden, constructed a new wind tunnel with the extremely small freestream turbulence level of 0.02 percent†† [compared to about 1.2 percent for Burgers' (1924) tunnel]. In this 1940–1941 tunnel (reported after World War II), the classic experiment of Schubauer and Skramstad (1947) was performed. First, hot-wire measurements were acquired to determine flat-plate transition in the presence of random fluctuations in the freestream. These results are shown in [Fig. 5-8](#). At $x < 7$ ft from the leading edge, the velocity oscillations are negligibly small. At 8 ft, selective amplification clearly occurs. At 9 ft, the amplitudes of certain sinusoidal components become quite large. At 10 ft, nonlinear processes begin to dominate, and the fluctuations become more random. At 11 ft, the flow is fully turbulent and the scale of motion changes drastically. Relevant frequencies are now in thousands instead of tens of hertz. This information would not have been possible had the freestream been noisy.

Page 261

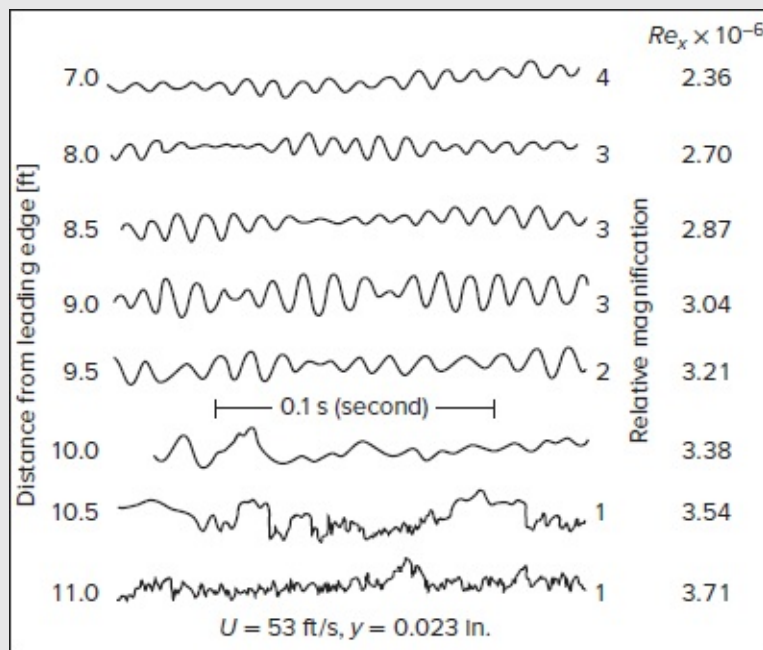


FIGURE 5-8

Hot-wire oscillograms showing natural transition from laminar to turbulent flow on a flat plate. [After Schubauer and Skramstad (1947)].

Figure 5-8 shows the effect of natural disturbances. To determine the effect of specific sinusoidal components, Schubauer and Skramstad placed a metal ribbon 0.1 inch wide and 0.002 inch thick across the flat plate at a distance of 0.005 inch from the wall and oscillated it electromagnetically. In this way, they could introduce disturbances of any frequency into the boundary layer. For example, at a given Reynolds number, one could start from zero and slowly increase the oscillation frequency of the ribbon. At first, the downstream hot wire showed insignificant natural oscillations, until a frequency was reached where definite sinusoidal components appeared. This constituted the lower boundary of the neutral curve. As the frequency increased, the sinusoidal oscillations grew to a maximum amplitude and then decreased, finally disappearing at a higher finite frequency, along the upper boundary of the thumb curve. In this way, one could establish the entire neutral curve by varying the Reynolds number of the flow.

The neutral curve measured in this classic controlled experiment is shown in Fig. 5-9, where it is compared to stability theories assuming (1) parallel flow [Wazzan et al. (1968a)] and (2) nonparallel flow [Saric and Nayfeh (1975)]. The effect of nonparallel flow—boundary-layer growth $U(x, y)$ and $V(x, y)$ —is seen to be significant at the lower Reynolds numbers and is in good agreement with the experiment. Saric and Nayfeh (1975) also use their “method of multiple scales” to investigate nonparallel flow behavior with pressure gradients. As expected, favorable gradients ($\beta > 0$) grow slowly and show small effects on the neutral curve. Conversely, rapidly growing adverse gradients ($\beta < 0$) show large effects

that are difficult to assess.

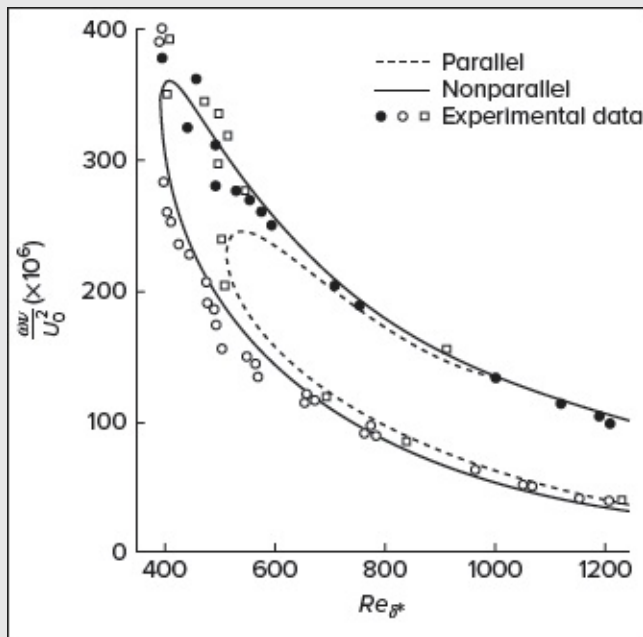


FIGURE 5-9

Comparison of theory and experiment for the neutral curves of the Blasius flat-plate boundary layer: \square data of Schubauer and Skramstad (1947); \circ upper branch and \bullet lower branch data by Ross and Barnes (1970). [After Saric and Nayfeh (1975)].

The good agreement between theory and experimental stability measurements for the phase velocities and eigenfunctions helps to legitimize the use of linear instability theory [Kaplan (1964)].

5-3 PARAMETRIC EFFECTS IN THE LINEAR STABILITY THEORY

The success of the stability theory means that we can analytically predict the effect of various parameters such as the Mach number, wall temperature, and wall suction on laminar-flow stability. A great many such analyses have now appeared, mostly using the newer digital-computer techniques of handling the Orr–Sommerfeld equation. In [Fig. 5-7](#), we saw the computed effect of the pressure gradient on Falkner–Skan profiles, showing that favorable (or adverse) gradients increase (or decrease) stability. This effect was qualitatively verified in the same experiment of Schubauer and Skramstad (1947), as shown in [Fig. 5-10](#). Moving down from the top, we see that an established unstable flow is completely damped by a favorable gradient (downstream pressure drop) and then the instabilities appear even stronger when the pressure rises (adverse gradient). A pressure gradient influences not only the initial

linear instability but also the final breakdown into turbulence, as reviewed in detail by Tani (1969). In a near-separating flow, this final process is abrupt.

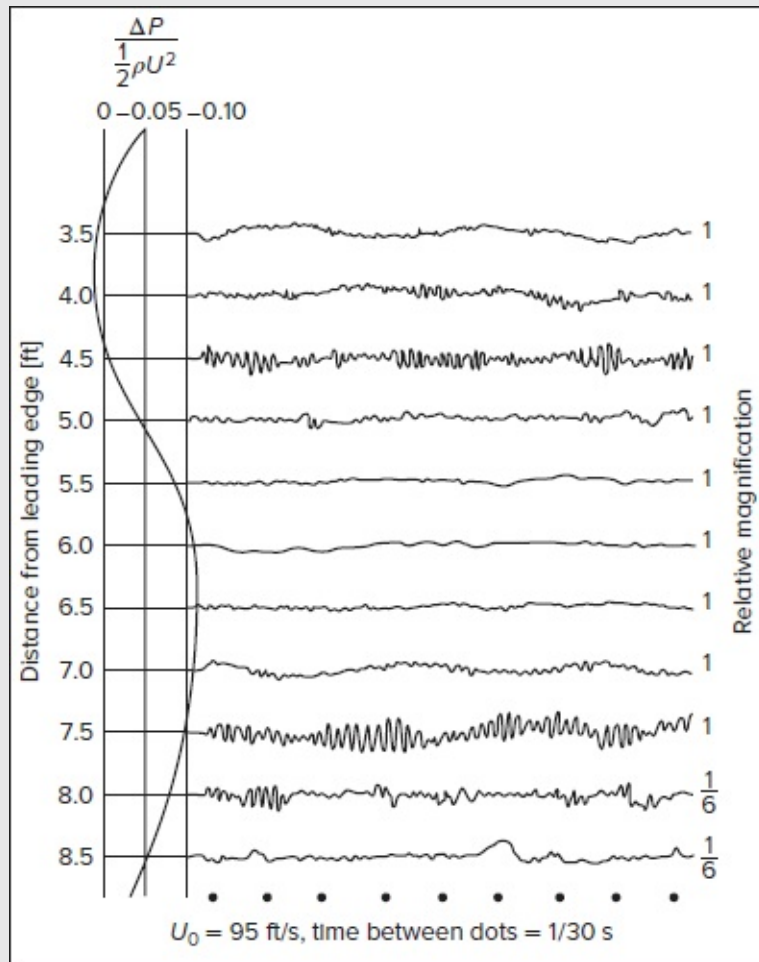


FIGURE 5-10

Pressure gradient effect on laminar-boundary-layer oscillations. [After Schubauer and Skramstad (1947)].

5-3.1 Classical Laminar-Flow Profiles

The linear stability of the classical Poiseuille and Couette flow profiles from [Chap. 3](#) is analyzed in a number of papers.

The parabolic Poiseuille channel flow due to a pressure gradient (Fig. 3-8) has the form $U = U_0 (1 - y^2/L^2)$ and is studied as one of the last of the asymptotic analyses by Shen (1954). His computed amplification curves, shown in [Fig. 5-11](#), are accurate to about 5 percent. A subsequent machine calculation by Nachtsheim (1964) predicts $Re_{crit} = 5767$ and $\alpha L = 1.02$,

which are labeled on the figure. Apparently, linear instability does *not* control this flow because channels typically show transition to turbulence at about $Re_L \approx 1000$, far less than the critical value in Fig. 5-11. The most probable explanation is that *large* disturbances cause the transition, but it may be possible that the developing-flow profiles in the channel entrance become unstable.

Even more paradoxical is the axisymmetric Poiseuille pipe flow, with the paraboloidal profile $U = U_0 (1 - r^2/r_0^2)$. All known papers report the same result: no apparent linear instability at any Reynolds number. Yet we know since the work of Reynolds (1883) that transition to turbulence typically occurs at about $Re D \approx 2300$. Here again it is thought that the instability is due to large disturbances in the entrance, since with proper care one can maintain laminar flow in a smooth pipe up to $Re D \approx 10^5$. Tatsumi (1952) shows that the developing pipe entrance profiles become unstable at about $Re D \approx 10^4$. Alternatively, Meseguer (2003) analyzes the *streak breakdown* process that, in conjunction with finite disturbances, is a possible path toward pipe-flow transition. For further details, see Drazin and Reid (1981) or Sec. 9.3 of Schmid and Henningson (2001).

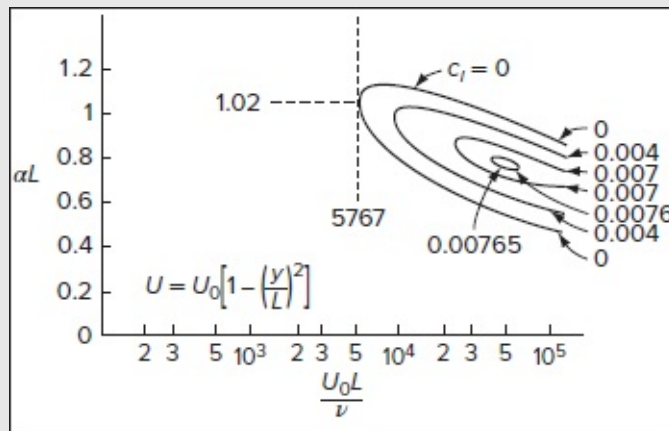


FIGURE 5-11

Stability diagram for the plane Poiseuille flow. [After Shen (1954).]

The case of the linear Couette profile $U = U_0 y/L$ generated between a fixed and a moving plate (Fig. 3-1) is apparently completely stable for all infinitesimal disturbances. Yet we know from experiment that turbulent flow ensues if $Re = U_0 L/\nu > 1500$ [see Fig. 19.3 of Schlichting (1979)]. Once again it is held that Couette flow becomes unstable due either to (1) large disturbances or (2) Tollmien–Schlichting waves in the developing transient profiles.

PSEUDORESONANCE. As mentioned earlier, no unstable normal-mode traveling waves have been found for either plane Couette flow or Poiseuille pipe flow. The linear

theory is stable, and large disturbances are necessary to trigger turbulence. Meanwhile, Trefethen et al. (1993, 1999) reported an entirely different linear stability approach that predicts large-amplitude growth, if not actual instability. The theory employs spectral methods to generate a continuous set of linear three-dimensional perturbations. Part of this *pseudospectrum* is highly amplified, especially at higher Reynolds numbers, and certain small disturbances can grow by three or four orders of magnitude. Presumably, some of these amplified disturbances spur nonlinear effects that lead to instability.

5-3.2 Instability of Suction Profiles: A Shape Factor Correlation

The asymptotic (exponential) suction profile of [Fig. 4-26](#) displays excellent stability characteristics. Hughes and Reid (1965) report for this condition that

$$U(y) = U_0(1 - e^{-y}) \quad Re_{crit} = \frac{U_0 \delta^*}{\nu} = 46,000 \quad (5-34)$$

This is 90 times greater than the Blasius value. The profile also has one of the smallest laminar shape factors $H = \delta^* / \theta = 2$. Recall from Sec. 4-6.2 that $2 \leq H \leq 3.5$ for laminar flows. Suction profiles, with no inflection point and U'' positive everywhere, are very stable and are used to delay transition in aerodynamic and hydrodynamic applications. The dashed line labeled “optimum suction” on the drag curve in [Fig. 4-26](#) was computed from the suction stability theory. Obviously, there is a large decrease from the turbulent-flow drag curve.

If the values of Re_{crit} from [Table 5-1](#) were plotted versus the boundary-layer shape factor $H = \delta^* / \theta$, a smooth curve would result, as shown in Obremski et al. (1969). Even more interesting, stability results for nonsimilar profiles fall close to this curve. This is shown in [Fig 5-12](#) from Wazzan et al. (1979). The points on the curve include Falkner–Skan wedge flows from [Table 5-1](#), flat-plate suction and blowing stability computations from Tsou and Sparrow (1979), and wedge flows with hot walls and variable viscosity from Wazzan et al. (1979). Wazzan hence proposes that [Fig. 5-12](#) is a universal correlation, so that the shape factor H is all that is needed for an engineering estimate of boundary-layer instability. For example, one can compute $H(\lambda)$ from Thwaites’ method, Table 4-8.

5-3.3 Wakes, Jets, and Shear Layers

When no wall or pressure gradient is present, the so-called free-shear layers always possess strong curvature and one or more points of inflection, e.g., the shear layer ([Fig. 4-22](#) with $k = 1$), the laminar jet ([Fig. 4-23](#)), and the developed wake ([Fig. 4-24](#)). Thus, they are relatively unstable.

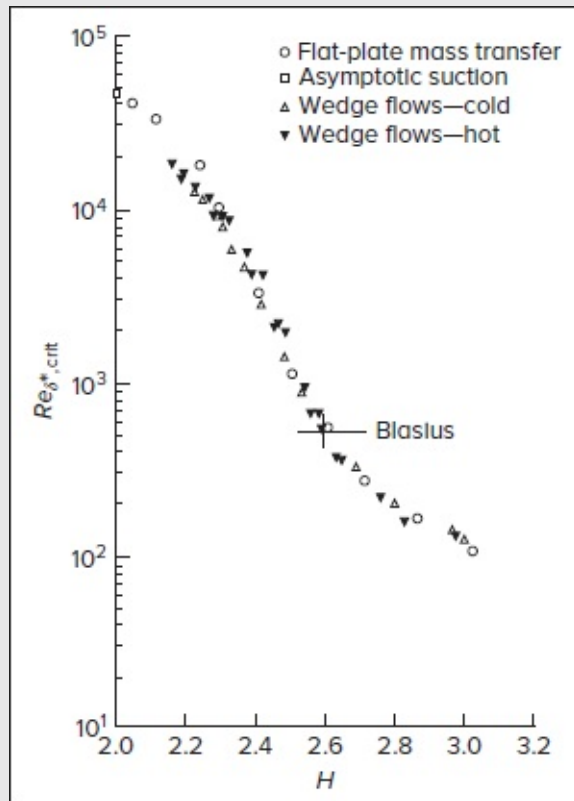


FIGURE 5-12

Correlation between the critical Reynolds number and the boundary-layer shape factor that may be used as an engineering estimate of initial instability. [After Wazzan *et al.* (1979)].

Page 264

The two-dimensional jet has the profile shape $U = U_0 \text{sech}^2 y$ and has been analyzed by many workers. [Figure 5-13](#) shows the jet eigenvalues computed by Kaplan (1964). Instability occurs very early given

$$\text{Jet:} \quad Re_{\text{crit}} \approx 4 \quad \text{at} \quad \alpha \approx 0.2 \quad (5-35)$$

Similarly, the two-dimensional wake has a reverse-jet appearance and has been analyzed by, among others, Mattingly and Criminale (1972). The velocity profile has the approximate form given by $U = 1 + (U_0 - 1) \text{sech}^2 y$ and, much like the jet, exhibits a critical Reynolds number of approximately 4.

The two-dimensional shear layer may be represented by $U = U_0 \tanh(y/L)$ and, according to Betchov and Szewczyk (1963), has a critical Reynolds number of

$$Re_{\text{crit}} = 0 \quad \text{and} \quad C_{i,\text{max}} = 0.19 \quad \text{at} \quad \alpha L = 0.5 \quad (5-36)$$

The shear layer between streams of different velocity is hence unconditionally unstable for all Reynolds numbers. However, these jet, wake, and shear-layer calculations assume parallel flow and should be corrected for nonparallel effects that clearly occur at such low Reynolds numbers. These flows are discussed in detail by Betchov and Criminale (1967) and Drazin and Reid (1981).

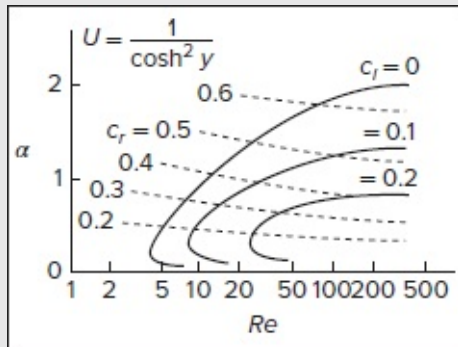


FIGURE 5-13

Eigenvalues for a two-dimensional jet. [After Kaplan (1964)].

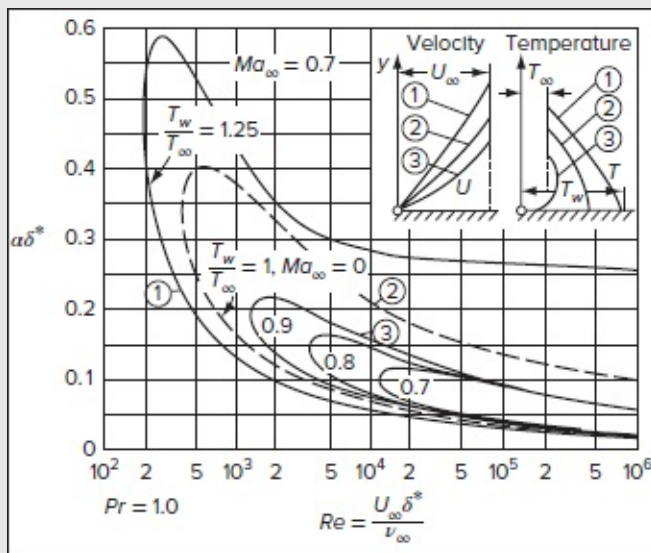


FIGURE 5-14

Wall temperature effect on the stability of a subsonic gas boundary layer. [After Lees and Lin (1946)].

5-3.4 Effect of Wall Temperature

Real fluids have viscosities that vary with temperature. Therefore, the viscosity near the wall, and thereby the near-wall profile shape, can be influenced by heat transfer. Generally speaking, boundary-layer stability is enhanced by increasing the near-wall negative curvature $U''(0)$. As pointed out by Reshotko (1987), if $\mu = \mu(T)$, the boundary-layer equation at the wall, with no slip, yields the curvature expression

$$\left. \frac{\partial^2 u}{\partial y^2} \right|_{y=0} = \frac{1}{\mu_w} \left(\frac{dp}{dx} - \frac{d\mu}{dT} \frac{\partial T}{\partial y} \right)_{y=0} \left. \frac{\partial u}{\partial y} \right|_{y=0} \quad (5-37)$$

As already seen, we can make $U''(0)$ more negative by imposing a negative (favorable) pressure gradient $dp/dx < 0$. Equation (5-37) shows an additional effect due to heat transfer. Since $\partial u / \partial y > 0$, the second term on the right will be negative under two different conditions:

$$\text{Gases:} \quad \frac{d\mu}{dT} > 0 \quad \left. \frac{\partial T}{\partial y} \right|_{y=0} > 0: \quad \text{Cold wall} \quad (5-38)$$

$$\text{Liquids:} \quad \frac{d\mu}{dT} < 0 \quad \left. \frac{\partial T}{\partial y} \right|_{y=0} < 0: \quad \text{Hot wall} \quad (5-39)$$

Thus, gases, whose viscosity can only increase with temperature, are stabilized by cooling and liquids, whose viscosity decreases with temperature, by wall heating.

If we continue to assume parallel, incompressible flow but allow for a variable viscosity $\mu(y)$ due to temperature variations, the Orr–Sommerfeld [Eq. \(5-29\)](#) changes to

$$(U - c)(\phi'' - \alpha_\delta^2 \phi) - U''\phi = -\frac{i}{\alpha_\delta Re_\delta} [\mu(\phi'''' - 2\alpha_\delta^2 \phi'' + \alpha_\delta^4 \phi) + 2\mu'(\phi''' - \alpha_\delta^2 \phi') + \mu''(\phi'' + \alpha_\delta^2 \phi)] \quad (5-40)$$

where the two added terms involve μ' and μ'' . When applied to a gas in a subsonic flow, [Eq. \(5-40\)](#) reveals a very strong effect on both the neutral curves and the amplification factors. For example, [Fig. 5-14](#) illustrates the computations of Lees and Lin (1946) at a freestream Mach number of 0.7. Reduction in wall temperature to $T_w = 0.7T_\infty$ leads to a 30-fold increase in the critical Reynolds number and a similar decrease in the growth rate c_i .

Exactly the opposite effect is reported by Wazzan et al. (1968a) in studies of flat-plate flow with water, whose viscosity drops sharply with temperature. Their computations, assuming $T_e = T_\infty = 60^\circ\text{F}$ and varying T_w , are given in [Table 5-2](#). The most stable condition corresponds to a hot wall with $T_w = 135^\circ\text{F}$, which has a critical Reynolds number 22 times larger and a spatial amplification factor 63 times smaller than the Blasius (isothermal) boundary layer.

Further stability computations involving liquids are discussed in the review article by Wazzan et al. (1979).

TABLE 5-2**Stability of flat-plate flow with water at $T_\infty \equiv T_e = 60^\circ\text{F}$**

$T_w, ^\circ\text{F}$	$Re_{\delta, \text{crit}}$	$\left(\frac{\alpha_i \delta^* c_i}{U_e}\right)_{\text{max}}$	$\left(\frac{\alpha_i \delta^*}{Re_{\delta^*}}\right)_{\text{max}} \times 10^5$
32	240	0.0131	4.80
45	280	0.00780	2.50
60	520	0.00355	0.740 [†]
75	1680	0.00135	0.105
90	5200	0.00080	0.028
105	8925	0.00067	0.016
120	10,750	0.00060	0.0125
135	11,400	0.00057	0.0117 [‡]
140	11,440	0.00057	0.0120
150	11,300	0.00058	0.0130
175	9600		0.0166
200	8200		0.0200
250	5500		0.0295
300	3700		0.0405

Source: Computations by Wazzan et al. (1968a).

5-3.5 Stability of Compressible Flows

Page 266

The addition of gas compressibility to a stability problem greatly increases its complexity. Since pressure is now coupled to temperature and density through the equation of state, one must add the fluctuating variables $\rho(y)$ and $T(y)$ to the quartet (u, v, w, p) considered previously in [Eq. \(5-12\)](#) and resulting in a sixth-order set of differential equations. A detailed discussion of this problem is given in the text by Betchov and Criminale (1967, Chap. 8) and in the extensive notes and reviews by Mack (1969, 1984, 1987).

Lees and Lin (1946) developed the inviscid compressible stability theory and Brown (1962) obtained the first numerical solutions of the viscous theory. Numerical studies since that time have revealed a variety of interesting phenomena, such as unstable supersonic waves. The field has progressed to the point that laminar-flow control can be estimated in compressible flow design studies using computer codes.

Let us briefly discuss some significant results. [Figure 5-15](#) shows experimental data compared with theories for the neutral curve on an adiabatic flat plate in air at $Ma_e = 2.2$. We see that the approximate analysis of Dunn and Lin (1955), either in its asymptotic or numerically integrated form, is not in good agreement with the data. The full multivariable stability equations are needed for accuracy. Some further calculations of Mack (1969) for an adiabatic plate are shown in [Fig. 5-16](#). At first glance it appears that compressibility is stabilizing, since $Re_{x, \text{crit}}$ is increasing with the Mach number. Actually, great changes are taking place in the character of the instabilities. The amplification rates and the general shape of the curves are changing greatly with both the Mach number and the Reynolds number.

Note that the curve for $Ma_e = 1.6$ is of the incompressible thumb-curve type. At $Ma_e = 2.2$, a local minimum appears in the upper branch of the curve, indicating that viscosity has become stabilizing in the higher range of Reynolds numbers. This minimum moves further to the right as Ma_e increases and disappears at about $Ma_e = 3.0$, above which viscosity is stabilizing for all Reynolds numbers. At $Ma_e = 3.8$, the neutral curve has the general shape of the separation profile in [Fig. 5-7](#), with the maximum instability in the inviscid limit. The temporal amplification rates for $Ma_e = 3.8$ are given in [Fig. 5-17](#), showing that inviscid rates are the highest.

Page 267

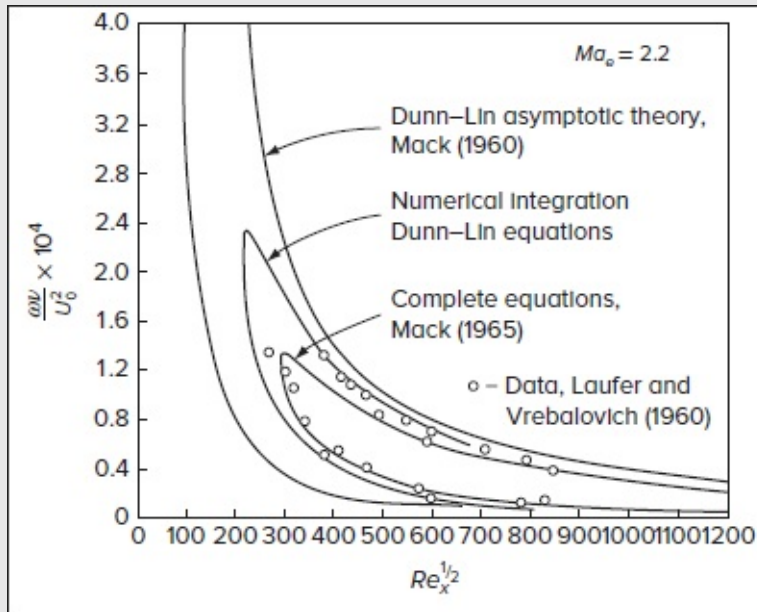


FIGURE 5-15

Comparison of three stability theories for the neutral curve on an adiabatic flat plate at $Ma_e = 2.2$. [After Mack (1969)].

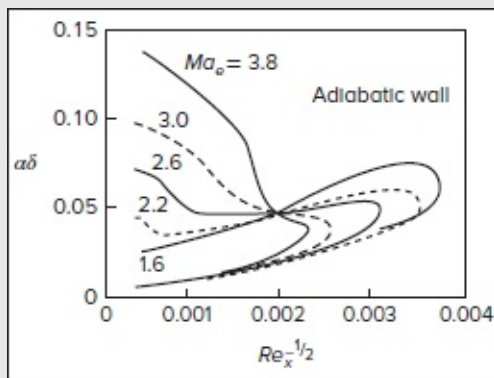


FIGURE 5-16

Computer solutions by Mack (1969) for the neutral curves in supersonic adiabatic flow over a flat plate (perfect gas). [Courtesy of the Jet Propulsion Laboratory, California Institute of Technology].

For Ma_e greater than about 3.0, higher modes appear. These modes occur when the disturbance phase velocity is supersonic relative to the wall, with $c_r > a_w$. The second mode appears at very high frequency and is insignificantly weak until about $Ma_e = 3.7$. It becomes stronger and moves downward with increasing Mach number, merging with the first mode at about $Ma_e = 4.8$. This effect is illustrated by the neutral curves for $Ma_e = 4.5$ and 4.8 in [Fig 5-18](#). The merging of modes is even more complete at higher Mach numbers, and the two modes are indistinguishable at $Ma_e = 7$. Regretfully, the higher modes are not damped by wall cooling, unlike the first-mode effect shown in [Fig. 5-14](#). Calculations by Mack (1969) suggest that amplification rates of the higher modes are slightly increased by wall cooling.

Still another interesting facet of compressibility is that Squire's theorem no longer holds: The most unstable waves need not be parallel to the freestream. In fact, as dissipation becomes important at high Mach numbers, it is not quite correct to treat a three-dimensional disturbance by an equivalent two-dimensional approximation, as was done for the incompressible case. This was first shown by Dunn and Lin (1955), who demonstrated that viscous and conduction terms transform properly to an equivalent two-dimensional system but that dissipation terms do not. Some results of Mack (1969) for amplification rates and the most unstable wave angle ϕ [from [Eq. \(5-12\)](#)] on a flat plate are illustrated in [Fig. 5-19](#). Squire's theorem ($\phi = 0$) holds for the first mode up to about $Ma_e = 0.7$, after which the critical angle jumps to $\phi = 45\text{--}65^\circ$. The second mode satisfies Squire's theorem throughout. Note that the second mode quickly assumes prominence at $Ma_e = 4$ and becomes the more unstable mode.

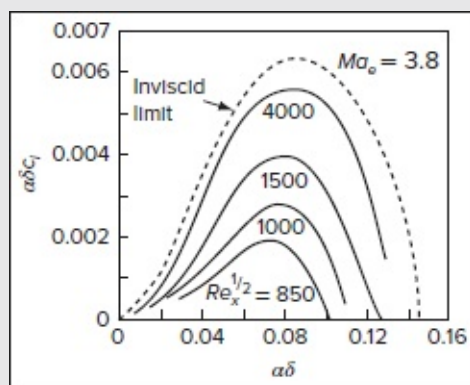


FIGURE 5-17

Reynolds number effect on the first-mode amplification rates at $Ma_e = 3.8$ on an

adiabatic flat plate. [Courtesy of the Jet Propulsion Laboratory, California Institute of Technology, after Mack (1969)].

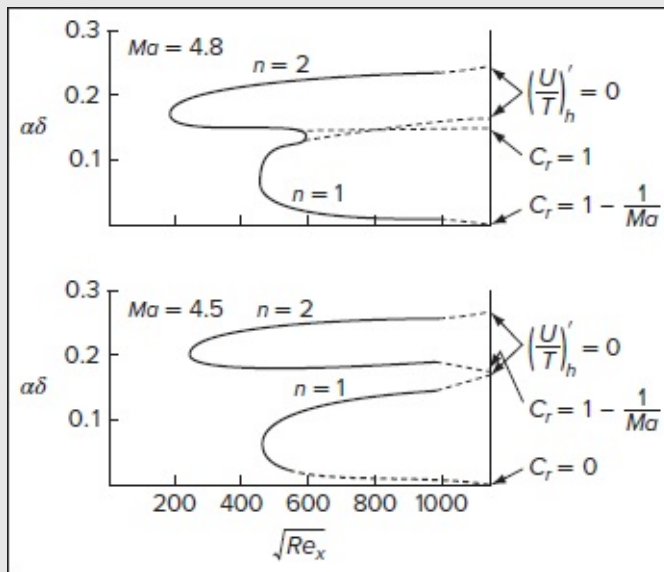


FIGURE 5-18

Neutral curves for supersonic, adiabatic flat plate flow illustrating the appearance of higher modes. [After Mack (1969)].

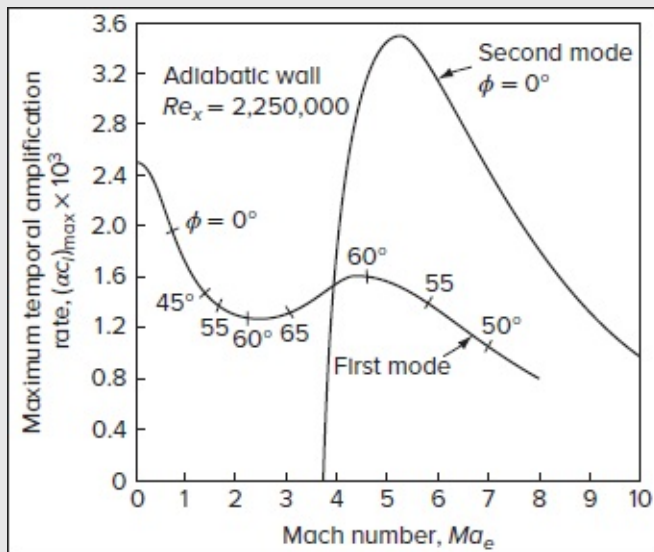


FIGURE 5-19

Temporal amplification rates and the most unstable wave direction ϕ for adiabatic flow past a flat plate. [Courtesy of the Jet Propulsion Laboratory,

The stability of high Mach number (hypersonic) flows, both theoretical and experimental, is the subject of many studies, notably Stetson (1988), Lachowicz et al. (1996), and Cassel et al. (1996). The dominant instability is the second mode, whose growth rates compare reasonably well with linear theory. High-frequency disturbances are detected in the experiments and imply strong nonlinear effects in hypersonic stability.

Page 268

5-3.6 Stability with Compliant Boundaries

All results discussed so far are for rigid walls, where a simple no-slip condition holds. A number of important examples occur when the wall is flexible: (1) panel flutter, (2) motion of liquid films, (3) growth of ocean waves, (4) rubber-coated instruments such as sonar domes, (5) cardiovascular flow, and (6) the skin of a swimming fish. The thesis of Kaplan (1964), which led to the purification breakthrough in numerical analysis, was in fact a study of compliant boundaries. His work was triggered by some intriguing experiments by Kramer (1957), which indicated a reduction in drag on bodies towed in water if their surfaces were coated with a compliant material such as natural rubber. Kramer speculated that the drag reduction was due to a delay in transition to turbulence caused by compliant boundaries. Subsequently, Benjamin (1960) showed analytically that compliant walls were potentially stabilizing in some cases and that there were three types of unstable waves: class A (Tollmien–Schlichting waves); class B (aeroelastic boundary flutter), and class C (Kelvin–Helmholtz instability). Class A waves are typically damped and stabilized by the compliant wall, but class B waves are often destabilized by compliance and become the critical case. Class C waves are analogous to inviscid instability and can cause problems in the fabrication and maintenance of the coating.

Kaplan (1964) reported numerical stability solutions for some specific compliant walls. His results for a membrane surface with a Blasius boundary layer are shown in [Fig. 5-20](#). The constants (C_0 , d_0 , ω_0 , m_0 , R) are characteristics of the particular membrane. Both class A and B waves appear, and the critical Reynolds number for class A waves is 2150, about 40 percent higher than for the rigid wall case (Fig. 5-6). Class B waves become unstable at about $Re_{crit} \approx 3800$ and have higher growth rates and phase speeds than class A waves.

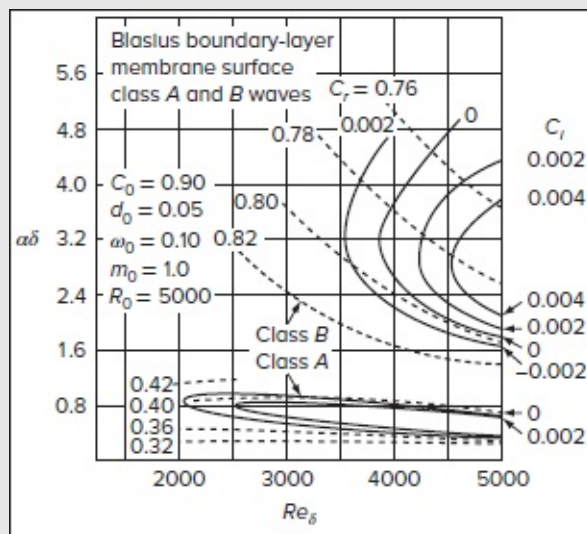


FIGURE 5-20

Amplification rates and phase speeds for flow over a compliant membrane surface. [After Kaplan (1964)].

Although Kramer's experiments were provocative and supported qualitatively by theory, the promise of compliant-surface transition delay and drag reduction has not been too fruitful, and no reliable engineering designs have been reported.

Page 269

5-3.7 Stability of Free-Convection Flows

Free or buoyant convection constitutes an excellent medium for studying laminar instability. The varying temperature field allows for flow visualization through the interferometric techniques pioneered by Eckert and Soehngen [see the text by Eckert and Drake (1972)]. An excellent review of the subject is given by Gebhart (1969) and in Chap. 11 of the text by Gebhart et al. (1988).

The free-convection equivalent to the Orr–Sommerfeld relation was derived by Plapp (1957). Comparable to the boundary-layer relations themselves [Eqs. (4-257)], these equations incorporate velocity and temperature coupling—but because of the small-disturbance assumption, they remain linear. Computer solutions of Plapp's fully coupled equations were given by Nachtsheim (1963), and the results shown in Fig. 5-21 agree well with experiments. Instability occurs very early because the velocity profiles have a point of inflection (see Fig. 4-55a). In Fig. 5-21, we see that the critical Grashof numbers are about 2500 for water and 50,000 for gases, which correspond to equivalent values of $Re_{crit} \approx 50$ and 700, respectively. Growth rates are moderate, so that final transition to turbulence does not occur until a local Grashof number of $Gr_x \approx 10^9$, or about 30–70 times further downstream.

Note from [Fig. 5-21b](#) that the neutral curve for gases has two modes, the upper and lower humps corresponding to velocity and temperature fluctuations, respectively.

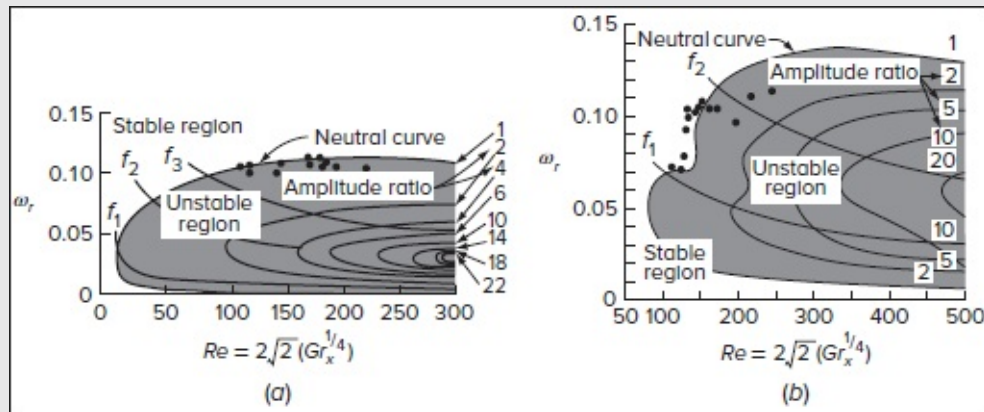


FIGURE 5-21

Amplification curves for free-convection flow on a vertical: (a) water: $Pr = 6.7$; • = data from Knowles and Gebhart (1968); (b) gases: $Pr = 0.7$; • = data from Polymeropoulos and Gebhart (1967).

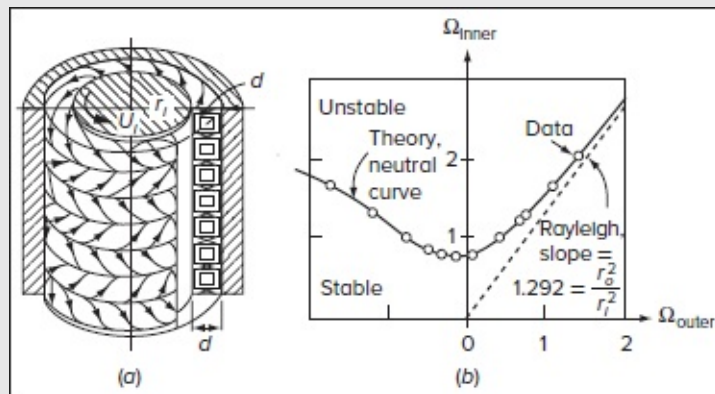


FIGURE 5-22

Classical theory and experiment by Taylor (1923) for the instability of Couette flow between rotating cylinders: (a) Taylor vortices and (b) theory and experiment for $r_o = 4.035$ cm and $r_i = 3.55$ cm.

5-3.8 Centrifugal Instability

The previous stability examples have all been parallel viscous flows. A somewhat different

but related case corresponds to that of centrifugal instability of rotating flows. In this context, we recall that the classic Couette flow between rotating cylinders, [Eq. \(3-22\)](#), breaks down for a finite configuration of rotational speeds and radii. As illustrated in Fig. 5-22a, the flow that ensues is *not* turbulent but rather stable laminar flow of rows of circumferential toroidal vortices, called *Taylor vortices*, after G. I. Taylor (1923). Turbulence does not appear until much higher rotational rates.

Page 271

A criterion for inviscid rotational instability was deduced by Rayleigh (1916): “An inviscid rotating flow is unstable if the square of its circulation decreases outward.” In other words, stability is ensured if

$$\frac{d}{dr} (rv_\theta)^2 > 0$$

For Couette flow between cylinders [[Eq. \(3-22\)](#)], this reduces to

$$\text{Stability:} \quad \Omega_o r_o^2 > \Omega_i r_i^2 \quad (5-41)$$

where the subscripts i and o denote the inner and outer surfaces, respectively. From this condition, we deduce the following intriguing predictions:

1. Inner cylinder rotating, outer cylinder at rest: *unstable*
2. Inner cylinder at rest, outer cylinder rotating: *stable*
3. Cylinders rotating in opposite directions: *unstable*

Actually, viscosity tends to stabilize and smudge these boundaries somewhat. Viscous instability is studied by allowing the basic flow, given by [Eq. \(3-22\)](#), to be perturbed with small disturbances in v_r , v_θ , v_z , and p . This analysis was performed by Taylor (1923) in a two-pronged experimental and analytical study. By assuming that the clearance, $C = (r_o - r_i)$, is small relative to r_i , Taylor simplified the problem so that stability became dependent only on Ω_o/Ω_i and a dimensionless parameter, now called the *Taylor number*:

$$Ta = \frac{r_i C^3 (\Omega_i^2 - \Omega_o^2)}{\nu^2} \quad (5-42)$$

Note that small-gap stability theory predicts that, for $0 \leq \Omega_o/\Omega_i \leq 1$, instability occurs at

$$Ta_{\text{crit}} \approx 1708 \quad \text{and} \quad \alpha C \approx 3.12 \quad (5-43)$$

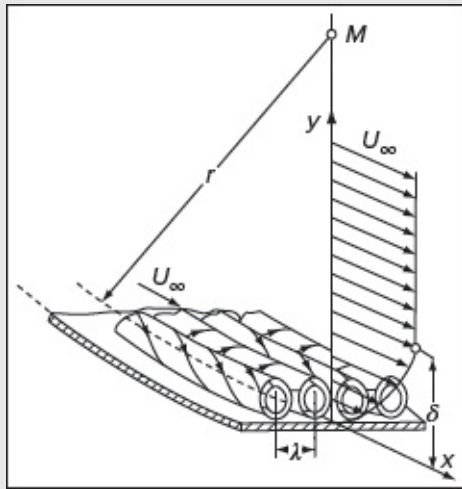


FIGURE 5-23

Longitudinal vortices in concave-wall flow. [After Görtler (1955)].

Page 272

The critical wave number of 3.12 is nearly π , i.e., the toroidal vortices that form in [Fig. 5-22a](#) are nearly square. These results are in good agreement with the careful experiments of Coles (1965). As Ta increases, the laminar vortices begin to develop circumferential waves while remaining laminar. At $Ta \approx 160,000$ turbulence ensues. Photographs of these toroidal vortices are given in the photo album of van Dyke (1982).

Experimental results for turbulent Couette flow at very high Taylor numbers, $8 \times 10^7 < Ta < 4 \times 10^9$, are reported by Townsend (1984).

In a related example, Görtler (1955) pointed out the existence of longitudinal vortex instability in boundary-layer flow along a concave wall, as illustrated in [Fig. 5-23](#). For small $\delta/r \approx 0.020.1$, these paired streamwise vortices begin to form at about $U_\infty \delta/\nu \approx 5$. They are thought to have a strong influence on early transition to turbulence on concave walls.

Still another example of centrifugal instability is the flow over a rotating disk, which was discussed in Sec. 3-8.2. The experiments of Gregory et al. (1955) showed unstable logarithmic-spiral vortices in a finite-thickness ring on the disk, as in [Fig. 3-38](#). The three-dimensional disturbance equations were found by Malik (1986) to be unstable at a kinetic Reynolds number corresponding to $Re_\omega = r^2(\omega/\nu) \approx 81,200$. Lingwood (1995) then found a point of *absolute* (multidirectional, nonconvective) instability at $ReRe_\omega \approx 260,000$. Her experiments then showed that absolute instability is immediately followed by transition [Lingwood (1996)].^{‡‡}

In fact, excellent reviews of centrifugal instability are given by Drazin and Reid (1981) and Koschmieder (1993).

5-4 TRANSITION TO TURBULENCE

The linearized stability theory of the previous two sections predicts the demise of laminar flow at some finite Reynolds number. It *does not* predict the onset of turbulence. Following the initial breakdown of laminar flow through amplification of infinitesimal disturbances, the flow passes through a complicated sequence of spatial changes; the result is the unsteady and disorderly but strangely rational and marvelously stable phenomenon known as turbulence. The evolutionary process from laminar to turbulent flow is termed transition.

After a century of research on the transition process, there has been significant progress, especially in visualization of unstable waves, but the mechanisms are still not completely understood. Historically, opinions about transition have shifted from one concept to another. The Rayleigh inviscid theories of 1880 obscured the real problem in boundary layers: viscous instability of infinitesimal disturbances. Then, when the viscous Tollmien–Schlichting waves were predicted in 1929, researchers doubted them because the (noisy) experiments of the day pointed clearly to transition as a three-dimensional “explosion” into turbulence. Twenty years later, when Schubauer and Skramstad and also Liepmann documented the Tollmien–Schlichting waves, the rush of opinions to embrace the two-dimensional cause was so great that Liepmann’s clear indication of spanwise fluctuations was entirely ignored. A decade later, Emmons (1951) accidentally noticed sporadic turbulent spots on shallow running water; two-dimensionality was abandoned, and suddenly, as Morkovin (1969) wryly notes, “everyone was seeing spots.” It was another decade before Klebanoff et al. (1962) clarified the essential intermediate process involving longitudinal vorticity and spanwise energy exchange. Added to this is the annoying unit Reynolds number effect, by which transition processes differ among the various experimental facilities, indicating a strong role for the initial disturbance spectrum (freestream turbulence, radiated noise, surface roughness) on the actual paths toward turbulence. The complexities of these parameters and their interactions continue to discourage our hopes for a definitive picture of the transition process.

Page 273

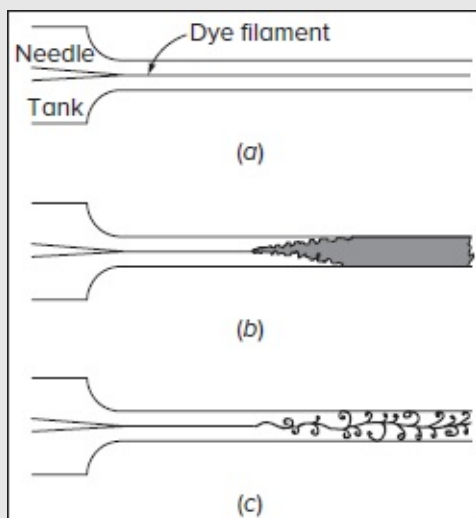


FIGURE 5-24

The classic pipe-flow dye experiment of Reynolds (1883): (a) low speed: laminar flow; (b) high speed: turbulent flow; (c) spark photograph of condition (b).

A dramatic example of our limited knowledge is the fact that the original transition experiment (pipe flow) is still not well understood. Reynolds (1883) conducted the classic experiment of introducing dye into the entrance of a circular pipe, as in [Fig. 5-24](#). By varying the flow speed at constant diameter and viscosity, Reynolds was in effect varying the dimensionless parameter $Re = u \bar{Re} = \bar{u}d/\nu$, later named after him. At low speed ($Re < 2000$), the flow remained laminar, and the dye filament stayed along a nearly straight and distinct streamline, as in [Fig. 5-24a](#). As speed was increased to a value of Re between 2000 and 13,000, depending upon the smoothness of entrance conditions, the filament broke up somewhere downstream and mixed rapidly with surrounding water to color the tube completely, as in [Fig. 5-24b](#). The flow in the well-mixed region was turbulent, but a spark photograph ([Fig. 5-24c](#)) revealed that the instantaneous filament was actually still confined to a relatively distinct set of curls and eddies. These eddies and associated fluid parcels appeared in rapid three-dimensional motion at frequencies up to thousands of hertz, thereby producing a color-blurred effect to the naked eye ([Fig. 5-24b](#)). It was also found that no transition occurred for $Re < 2000$, no matter how rough and noisy the entrance conditions were made.

Some other facts regarding [Fig. 5-24](#) are worth noting: (1) the transition occurs downstream, not in the pipe entrance, with the actual point tending to move toward the entrance with successive increases in the Reynolds number; (2) there is a clear region of amplification from laminar flow into turbulence, and far downstream the turbulence reaches a fully developed equilibrium state of balance between production and decay independently of the initial disturbance; (3) at the beginning of the turbulent zone, the flow is only *intermittently* turbulent, interspersed with laminar-flow spots. For example, in the measurements of Rotta (1956), at $Re = 2500$, the flow is about 50 percent turbulent (*intermittency factor* $\gamma = 0.5$) at $x/d = 200$ and still only about 85 percent turbulent ($\gamma = 0.85$) at $x/d = 500$. The same phenomenon of intermittency occurs in boundary-layer flow, where it delineates a rather sharp interface between turbulent-boundary-layer flow and nearly nonturbulent outer flow ([Fig. 6-5](#)).

5-4.1 Development of Spanwise Vorticity

If the initial disturbance spectrum is nearly infinitesimal and random (with no discrete frequency peaks), theory predicts and experiment validates that the initial instability will occur as two-dimensional Tollmien–Schlichting waves, traveling in the mean-flow direction so long as compressibility is unimportant. However, three-dimensionality soon appears as the Tollmien–Schlichting waves rather quickly begin to show spanwise variations. This tendency

toward three-dimensionality was not predicted or expected until the experiments of the 1960s. In this context, Klebanoff et al. (1962) showed that a shear layer in the unstable region has a strong propensity to amplify any slight three-dimensionality, which surely must be present in any natural-disturbance spectrum. [Figure 5-25](#) shows the rapid development of spanwise peaks and valleys in the streamwise velocity fluctuations downstream of a vibrating ribbon containing spacers. The spanwise variation is slight downstream, but 11 cm later, the peaks are 4 times as strong as the valleys. Similar variations (not shown) develop in the lateral and vertical fluctuations, and the flow approaches a condition of thorough three-dimensionality so characteristic of fully turbulent flow. The flow in [Fig. 5-25](#), however, is still laminar.

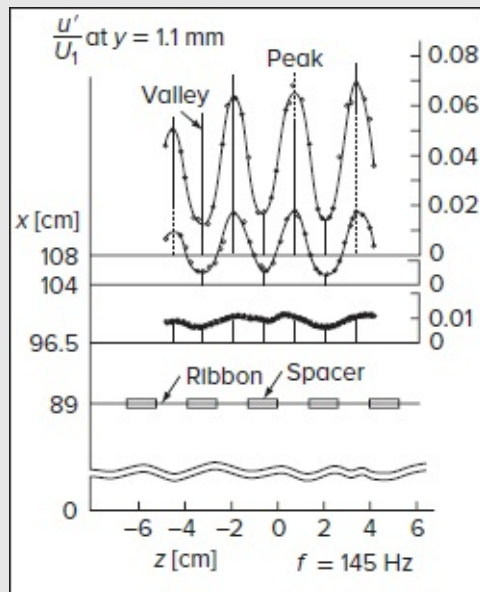


FIGURE 5-25

Flow past a thin airfoil: (a) low incidence angle, smooth flow, no separation; (b) high incidence angle, upper surface separates or “stalls,” lift decreases.

The 1980s have produced excellent visualizations of the growth process of Tollmien–Schlichting waves. There are many excellent discussions by various authors in the monograph edited by Tatsumi (1984). In particular, Saric and Thomas (1984) use smoke-wire visualization of flat-plate flow to demonstrate three different types of Tollmien–Schlichting wave breakdown. Whereas Klebanoff et al. (1962) use a ribbon with spacers, Saric and Thomas (1984) use an unadorned ribbon and then vary the rms amplitude and frequency of its vibrations. The results are shown in [Fig. 5-26](#) and are called Λ vortices.

Figure 5-26a shows in-phase Λ vortices—i.e., peak-following-peak—which have the same wavelength as a Tollmien–Schlichting wave and arise at fluctuation amplitudes of

approximately 1 percent of U_∞ . These waves are identical to those in [Fig. 5-25](#) and are hence called K-type vortices, after Klebanoff. The spanwise wavelength λ_z is about one-half of the streamwise value, λ_x .

At lower amplitudes (≈ 0.3 percent of U_∞), a structure of staggered waves, with peak-following-valley, appears as in [Fig. 5-26b](#). The streamwise wave number and frequency are approximately one-half of a Tollmien–Schlichting wave, and $\lambda_z \approx 1.5\lambda_x$. The pattern constitutes a *subharmonic* unstable wave, now called a C-type vortex after Craik (1971), who first explained its structure as a superposition of a wave triad.

Finally, [Fig. 5-26c](#) shows a second type of staggered (subharmonic) vortex pattern with $\lambda_x \approx 2\lambda_{TS}$ but with short span, $\lambda_z \approx 0.7\lambda_x$. These waves occur at an intermediate fluctuation amplitude of about 0.6 percent of U_∞ and are called H waves, after Herbert (1983), who showed that they arise from a secondary instability of Tollmien–Schlichting waves to three-dimensional disturbances.

It can therefore be seen that there are many paths from Tollmien–Schlichting waves to turbulence, and many of them are explained by the nonlinear theories of flow instability, as reviewed by Stuart (1987) and in [Chap. 5](#) of the text by Schmid and Henningson (2001). However, the nonlinear theories are beyond the scope of the present text.

5-4.2 Turbulent Spots: The Final Transition Process

We have seen that a shear layer develops viscous instability and forms Tollmien–Schlichting waves that grow, while still laminar, into finite amplitude (1–2 percent) three-dimensional fluctuations in velocity and pressure. From then on, the process is more akin to a breakdown than a growth. The longitudinally stretched vortices undergo a cascading breakdown into smaller units, until the relevant frequencies and wave numbers approach randomness. Then, in this diffusely fluctuating state, intense local changes occur at random times and locations in the shear layer near the wall. Turbulence bursts forth in the form of growing and spreading *spots*, first noticed by Emmons (1951) on the surface of a shallow-water channel. Since then, many workers have been able to generate artificial spots using, for example, an electric spark.

Page 275

[Figure 5-27](#) shows a compilation of various observations of the growth and shape of turbulent spots. Viewed from above—[Figs. 5-27a](#) and [c](#)—a spot looks like an arrowhead moving downstream and spreading at a half-angle that is typically reported between 8° and 12° . The leading edge travels at about $0.9 U_\infty$ whereas the trailing edge propagates more slowly, at about $0.5U_\infty$. Thus, the spot grows in size but its normalized shape remains unchanged, as confirmed in [Fig. 5-27b](#) at five different x positions. The disorderly patterns in [Fig. 5-27c](#) suggest that the spot is fully turbulent. Its detailed structure becomes finer as the Reynolds number increases—see, e.g., photos 111 in van Dyke (1982). For [Fig. 5-27c](#), $Re_x \approx 400,000$ at the center of the spot.

Carlson et al. (1982) use a visualization method to capture the traveling spot itself. Their photos show strong oblique waves at both the front and the rear “wings” of the arrowhead. The results also suggest that unstable wave breakdown continues to play a role even after the spot is formed.

Since the spots grow and remain intensely turbulent, they must entrain the surrounding laminar fluid to maintain themselves. Wygnanski et al. (1976) report that the strongest entrainment occurs at the leading edge as well as the upper surface of the trailing edge.

In boundary-layer flow, spots form randomly and naturally in what Dhawan and Narasimha (1958) report as a narrow transverse band Δx , which remains small compared to the length of the transition zone. Since the spots spread downstream, they inevitably coalesce into a region where they continually evolve and prosper. The flow downstream is then said to be fully turbulent and, as will be seen in [Chap. 6](#), is scaled by modeling laws that are entirely different from those of laminar flow.

Our overall picture of the transition process in boundary-layer flow past a smooth surface hence consists of the following processes:

1. Stable laminar flow near the leading edge.
2. Unstable two-dimensional Tollmien–Schlichting waves.
3. Development of three-dimensional unstable waves and hairpin eddies.
4. Vortex breakdown at regions of high localized shear.
5. Cascading vortex breakdown into fully three-dimensional fluctuations.
6. Formation of turbulent spots at locally intense fluctuations.
7. Coalescence of spots into fully turbulent flow.

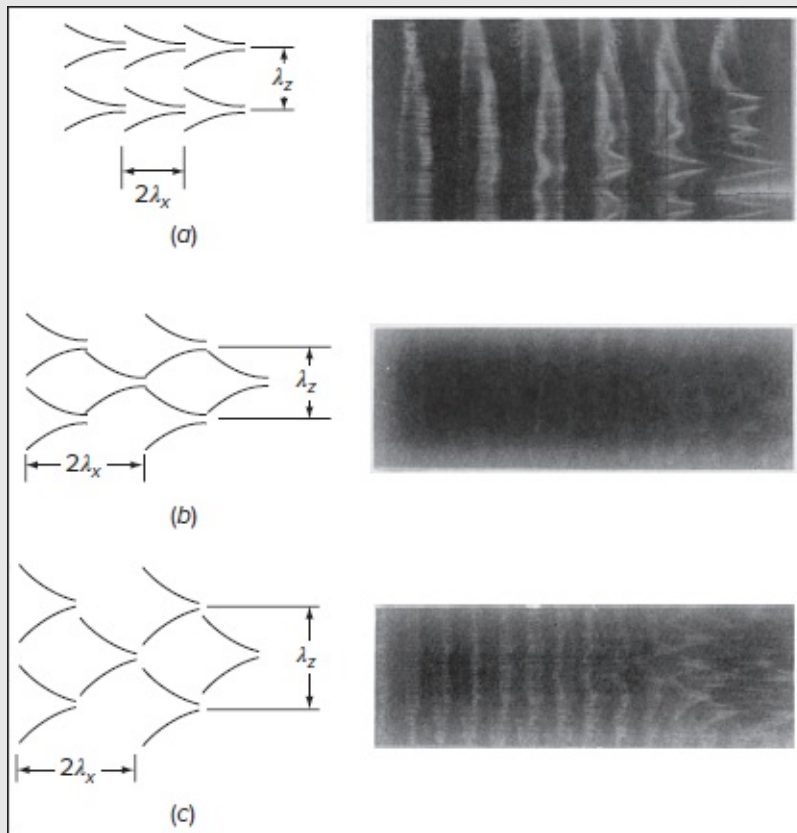


FIGURE 5-26

Patterns of unstable vortex breakdown in a boundary layer: (a) K-type ($u' / U_\infty \approx 1$ percent) aligned in-phase and similar to a Tollmien–Schlichting wave; (b) C-type (0.3 percent) staggered subharmonic with $\lambda_z \approx 1.5\lambda_x$; (c) H-type (0.6 percent) staggered subharmonic with $\lambda_z \approx 0.7\lambda_x$. [Courtesy of Dr. William S. Saric].

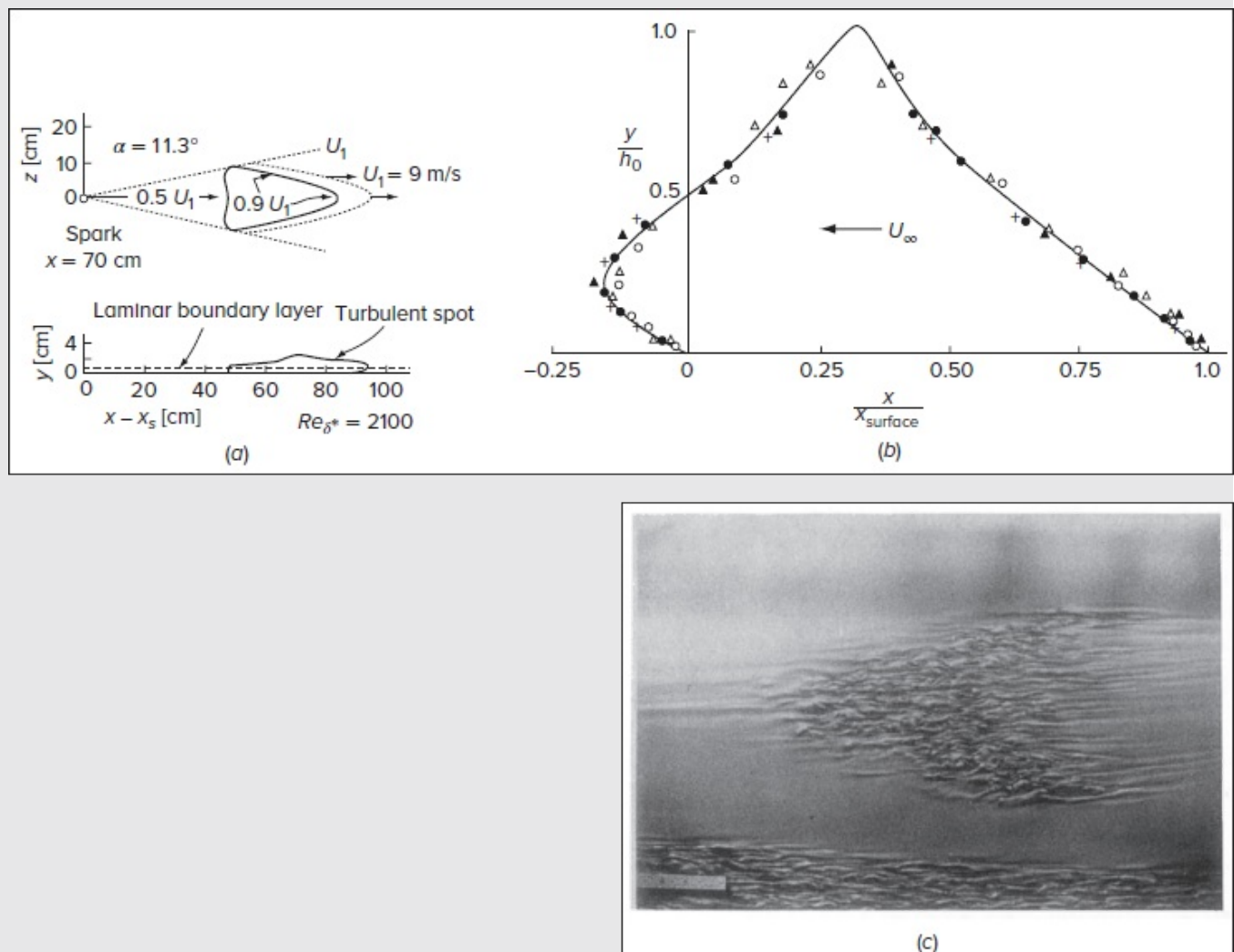


FIGURE 5-27

Observations of turbulent spot growth: (a) plan and elevation sketches [after Schubauer and Klebanoff (1995)]; (b) normalized measured shape [after Wygnanski *et al.* (1976)]; and (c) visualization by aluminum flakes in a water channel [Cantwell, B., Coles, D. and Dimotakis, P., "Structure and Entrainment in the Plane of Symmetry of a Turbulent Spot," *Journal of Fluid Mechanics*, 87 (1978): 641–72].

These phenomena are sketched as an idealized flat-plate flow in [Fig. 5-28a](#), which also illustrates the contamination effect of the lateral edges of the plate. The edges simulate a finite disturbance which, if severe enough, can cause immediate transition to turbulent flow (without spots). [Figure 5-28b](#) confirms this picture with a smoke-flow visualization of transition on the straight cylindrical portion of a body of revolution.

Qualitatively similar effects occur in the presence of mild pressure gradients. A motion

with a strong adverse gradient, being both unstable and subject to flow separation, may short-circuit some steps and instead form a separation bubble, with the reattached flow downstream being fully turbulent.

5-4.3 Classification of Boundary-Layer Transition Processes

There are three types of wall-bounded transition processes in fluids engineering. An interesting chart was given by Morkovin (1969b), and the subject was reviewed by Mayle (1991) in his IGTI Scholar Lecture related to gas turbine engines. The three scenarios are:

1. *Natural transition.* This is the gradual process of [Fig. 5-28](#), caused by infinitesimal disturbances. The flow changes from TS waves to three-dimensional waves, vortex breakdown, turbulent spots, and fully turbulent flow, in this sequence. The stream should be quiet and the walls smooth.
2. *Bypass transition.* If the walls are rough, the freestream noisy, the surface vibrating, or the stream subject to acoustic waves, the flow may skip the early stages of natural instability and go directly to vortex breakdown or turbulent spot production. Large disturbances cause the bypass.
3. *Separated-flow transition.* If a laminar boundary layer separates and forms a separation bubble, it will likely reattach as a turbulent fluid. Some or all of the natural transition processes of [Fig. 5-28](#) may occur in the region of the bubble.

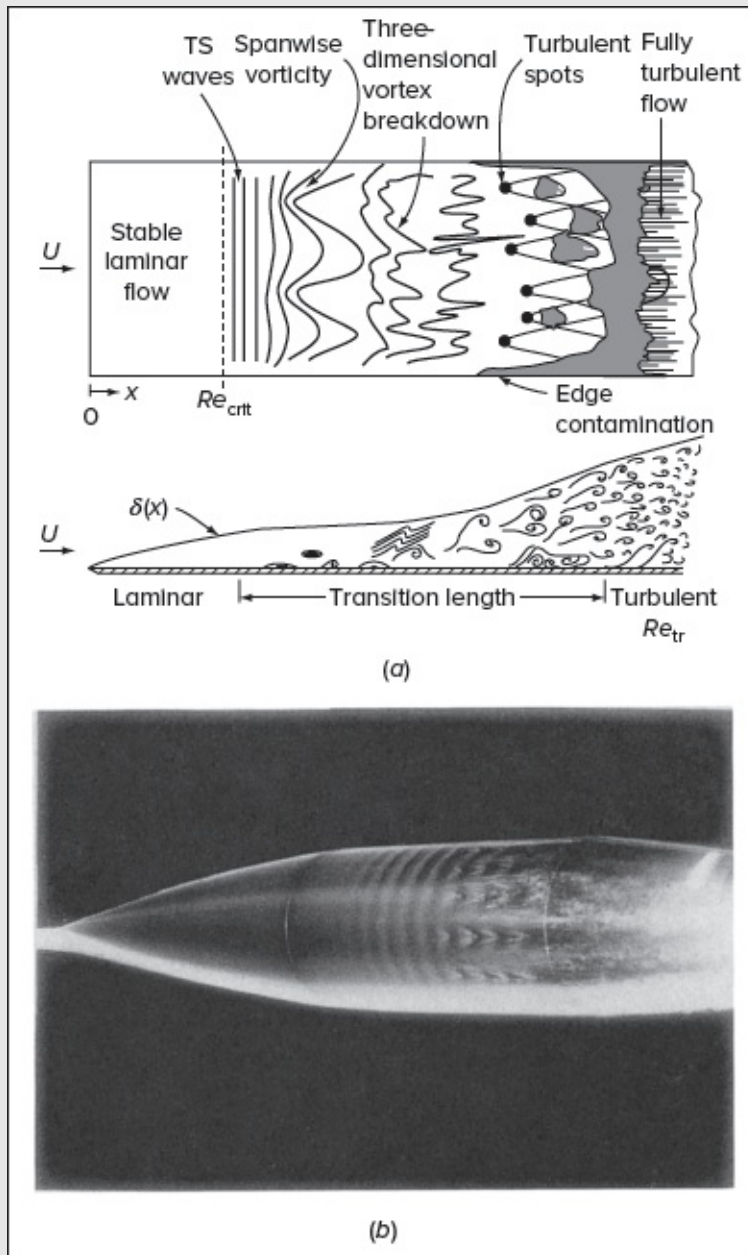


FIGURE 5-28

Description of the boundary-layer transition process: (a) idealized sketch of flat-plate flow and (b) smoke visualization of flow with transition induced early by acoustic input at $Re_L = 814,000$ and 500 Hz. [Courtesy of J.T. Kegelman and T.J. Mueller, University of Notre Dame].

5-4.3.1 BOUNDARY-LAYER RECEPTIVITY. Bypass transition is not just a sudden change. It may take a number of different paths, usually called *transient growth*, on the way to transition. Finding these paths by theory, CFD simulations, or experiment is a field of research called *boundary-layer receptivity*, reviewed by Saric et al. (2002).

5-5 ENGINEERING PREDICTION OF TRANSITION

There is no fundamental *theory* of transition, but there are experiments and correlations which try to predict the final onset of fully turbulent flow, such as $Re_{x,tr}$ or $Re_{\theta,tr}$, as a function of the following parameters:

1. Pressure gradient.
2. Freestream turbulence.
3. Wall roughness.
4. Mach number.
5. Wall suction or blowing.
6. Wall heating or cooling.

Understandably, most of the approximations deal with only one or two of these parameters.

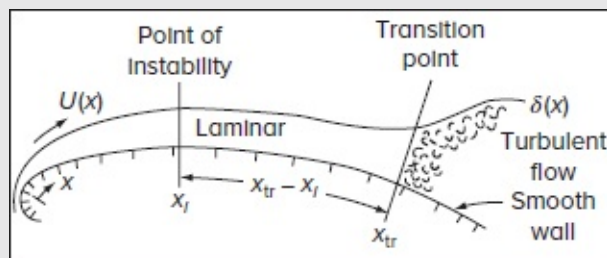


FIGURE 5-29

The two-step calculation of the transition point.

5-5.1 Effect of Pressure Gradient

Consider the problem sketched in [Fig. 5-29](#). We assume that $U(x)$ is known, with zero freestream turbulence, and that the walls are smooth, impermeable, and unheated. The boundary layer will be initially laminar and becomes unstable at point x_i , where undamped Tollmien–Schlichting waves first appear. These waves will grow and distort, in the manner of [Fig. 5-28](#), until the point of *transition* or fully turbulent flow, x_{tr} , is reached. We wish to predict x_{tr} , using x_i as an input if necessary. We briefly look at four methods.

5-5.1.1 THE TWO-STEP METHOD OF GRANVILLE. An early and still popular method of Granville (1953) requires the computation of x_i first, perhaps by following $H(\lambda)$ from Thwaites' method until it hits the Re_{crit} correlation of Fig. 5-12. Then,

while continuing to monitor $Re_\theta(x)$, Granville suggests computing a mean Thwaites' parameter,

$$\lambda_m = \frac{1}{(x_{tr} - x_i)} \int_{x_i}^{x_{tr}} \lambda(x) dx \quad (5-44)$$

where $\lambda = \theta^2(dU/dx)/\nu$. We can assume that x_{tr} occurs when Re_θ strikes Granville's transition data, which can be fit to the following formula:

$$Re_\theta(x_{tr}) \approx Re_\theta(x_i) + 450 + 400e^{60\lambda_m}; \quad \lambda < 0.04 \quad (5-45)$$

For an adverse gradient ($\lambda \approx -0.1$), the last term is negligible and transition is very near to x_i . For a favorable gradient, the last term is very large and transition moves far downstream.

5-5.1.2 THE ONE-STEP METHOD OF MICHEL. An extremely simple but effective method was proposed by Michel (1952) in the form of a correlation based on local values of momentum thickness and position. One ignores x_i and simply computes $\theta(x)$ from, say, Thwaites' method, [Eq. \(4-159\)](#), until we strike Michel's "transition line"

$$Re_{\theta, tr} \approx \frac{U(x)\theta(x)}{\nu} \approx 2.9Re_{x, tr}^{0.4} \quad (5-46)$$

The computed $Re_\theta(x)$ should approach this curve unambiguously from below.

5-5.1.3 THE ORR–SOMMERFELD METHOD OF JAFFE ET AL. In the same paper in which [Eq. \(5-46\)](#) was proposed, Michel (1952) noted that the transition points in his data compilation seemed to correspond to total amplification of Tollmien–Schlichting waves equal to about $A/A_0 \approx 10^4$, where A_0 represented the initial amplitude. This fact inspired workers in computational stability to evaluate the eigenvalues of various boundary-layer profiles and then compute the total wave growth at a given frequency. In this way, Smith and Gamberoni (1956) and, independently, van Ingen (1956) verified that temporal stability theory, when applied to these experiments, would predict a total growth of

$$\frac{A}{A_0} = \exp \left[\int_{x_i}^{x_{tr}} \alpha c_i dt \right] \approx e^9 \quad (5-47)$$

This method became quickly known as the " e^9 " method. Later, Jaffe et al. (1970) showed that a more realistic procedure would be to use *spatial* stability theory to evaluate the overall growth rate. Their computations with the exact velocity profiles, rather than with local-similarity approximations, gave good agreement with transition measurements when the growth rate was spatially integrated and set equal to

$$\frac{A}{A_0} = \exp \left[\int_{x_i}^{x_{tr}} (-\alpha_i) dx \right] \approx e^{10} \quad (5-48)$$

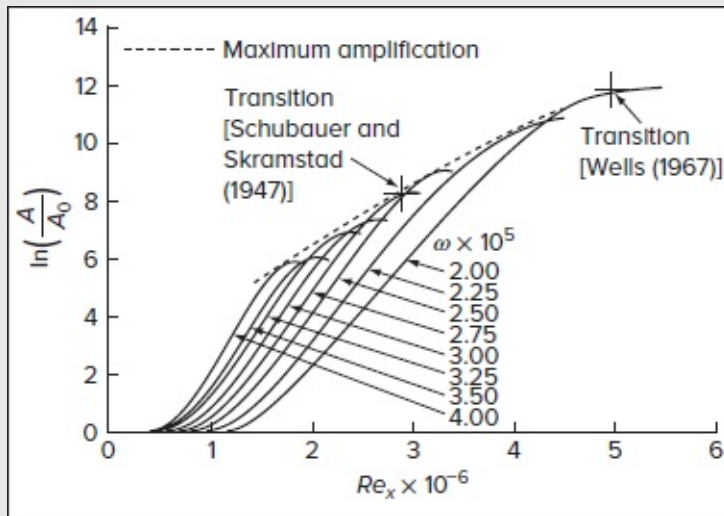


FIGURE 5-30

Constant-frequency amplification curves for flat-plate flow from linear stability theory [Eq. (5-48)]. Each curve represents a slice through the Blasius thumb curves of Fig. 5-6b. [After Jaffe et al. (1970)].

Page 279

Thus, one also hears of the “ e^{10} ” method. An example of their calculations of constant-frequency growth curves for the Blasius profile is shown in Fig. 5-30. Although Gaster (1962) proposed a transformation to relate temporal and spatial growth rates and propagation speeds, the accuracy was only fair and thus Eq. (5-48) prevailed.

Subsequently, in the spirit of Michel’s formula given by Eq. (5-46), Cebeci and Smith (1974) suggested that the e^9 computations be correlated using

$$Re_{\theta, tr} \approx 1.174 \left[1 + \left(\frac{22,400}{Re_{x, tr}} \right) \right] Re_{x, tr}^{0.46} \quad (5-49)$$

which is claimed to be somewhat more accurate than Michel’s relation.

5-5.1.4 THE ONE-STEP METHOD OF WAZZAN ET AL The success of Fig. 5-12 in correlating Re_{crit} to H for widely different cases led Wazzan et al. (1979, 1981) to propose a similar correlation for the transition Reynolds number. These researchers found that the e^9 method gave the same result for parameters such as the pressure gradient, suction and blowing, or heating and cooling, if plotted in terms of the transition shape factor. Their correlation is shown as the upper curve in Fig. 5-31. The lower curve gives Re_{crit} computed from Fig. 5-12 by converting Re_{θ} to Re_x . To use Fig. 5-31, one computes $H(\lambda)$ by any laminar-boundary-layer method, e.g., Thwaites’. Transition is predicted when this locus $H(Re_x)$, rising from below, intersects the upper curve. Wazzan et al. (1981) suggested the

following curve fit for the upper curve:

$$\begin{cases} \log_{10}(Re_{x,tr}) \approx -40.4557 + 64.8066H - 26.7538H^2 + 3.3819H^3 \\ \text{or} \\ \ln(Re_{x,tr}) \approx -93.1527 + 149.223H - 61.6029H^2 + 7.7871H^3 \end{cases} \quad (5-50)$$

for $2.1 < H < 2.8$. This method is not well validated experimentally, but is attractive nonetheless because of the widespread acceptance of the e^9 method.

5-5.1.5 COMPARISON FOR FLAT-PLATE FLOW. As a preliminary comparison, we can compute $Re_{x, tr}$ for flat-plate flow by each of the four previous methods and tabulate them as follows:

Method	Equation	$Re_{x, tr}$ (predicted)
Granville (1953)	(5-45)	2,505,000
Michel (1952)	(5-46)	2,525,000
Smith and Gamberoni (1956)	(5-49)	2,027,000
Wazzan et al. (1981)	(5-50)	4,753,000 (in a quieter experiment)

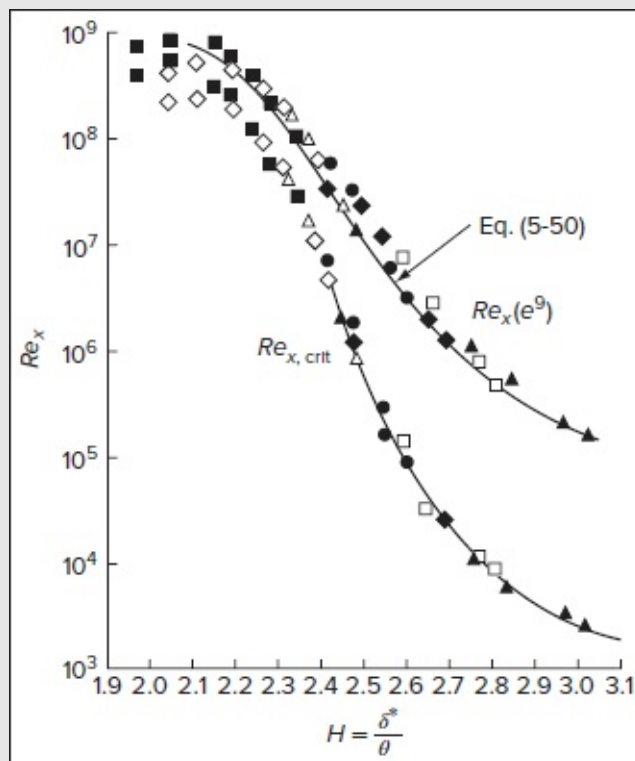


FIGURE 5-31

Correlation of critical and transition Reynolds numbers versus boundary-layer shape factors. [After Wazzan et al. (1981)].

Obviously, there is a sharp difference between the older methods and Wazzan et al. (1981). One reason might be seen in the two flat-plate sets of data points compared quietly but provocatively in [Fig. 5-31](#). The older methods were turned toward the experiment of Schubauer and Skramstad (1947), which reported $Re_{x, \text{tr}} \approx 2.8 \times 10^6$ at 0.02 percent turbulence. Later, Wells (1967) extended the transition point to $Re_{x, \text{tr}} \approx 4.9 \times 10^6$ by eliminating acoustic disturbances present in the Schubauer–Skramstad data. The Wazzan estimate reflects this quieter experiment. Because transition is so sensitive to various types of disturbances, it is doubtful if a simple theory can resolve these effects.

5-5.1.6 COMPARISON FOR THE FALKNER–SKAN FLOWS. As a further comparison of pressure gradient effects, in the absence of freestream turbulence or wall roughness and heat transfer, the four theories above, plus two others to be discussed, were applied to the Falkner–Skan wedge flows. Where necessary, $Re_\theta(x)$ was computed using [Eq. \(4-159\)](#) of Thwaites’ method. The results are plotted in [Fig. 5-32](#). Mindful of the log scale, we see that all six methods are comparable for $\beta = 0$ and fairly consistent for adverse gradients ($\beta < 0$). However, they differ by five orders of magnitude for strong favorable gradients ($\beta > 0.5$). One surmises that these methods are not well calibrated for favorable gradients, although many such cases occur in fluids engineering. It is recommended that - Wazzan’s relation [Eq. \(5-50\)](#) be used in such cases.

5-5.1.7 DIRECT NUMERICAL SIMULATION OF TRANSITION. The formulas recommended in this section are correlations, not theories. There is no pure theory of transition, but numerical methods are making inroads. The DNS technique, reviewed by Moin and Mahesh (1998), solves the full time-dependent Navier–Stokes equations, without “closure” models, thereby accounting for all important scales of the flow. In this vein, as the Reynolds number increases, the number of CFD mesh points must increase rapidly. To avoid a googol of nodes, the foreseeable limit is a low-turbulent Reynolds number. This will be sufficient for a DNS study of transition that focuses on simulating disturbances such as vibrating ribbons, freestream turbulence, and wall roughness. Kleiser and Zang (1991) review results through 1990. Rist and Fasel (1995) use an improved spatial (as opposed to temporal) computation and replicate transition experiments. Bake et al. (2002) model a vibrating-ribbon disturbance, and their results agree well with Klebanoff (K-type) transition experiments ([Fig. 5-26a](#)). At the time of this writing, DNS computations continue to predict transition for a variety of geometries and disturbances.

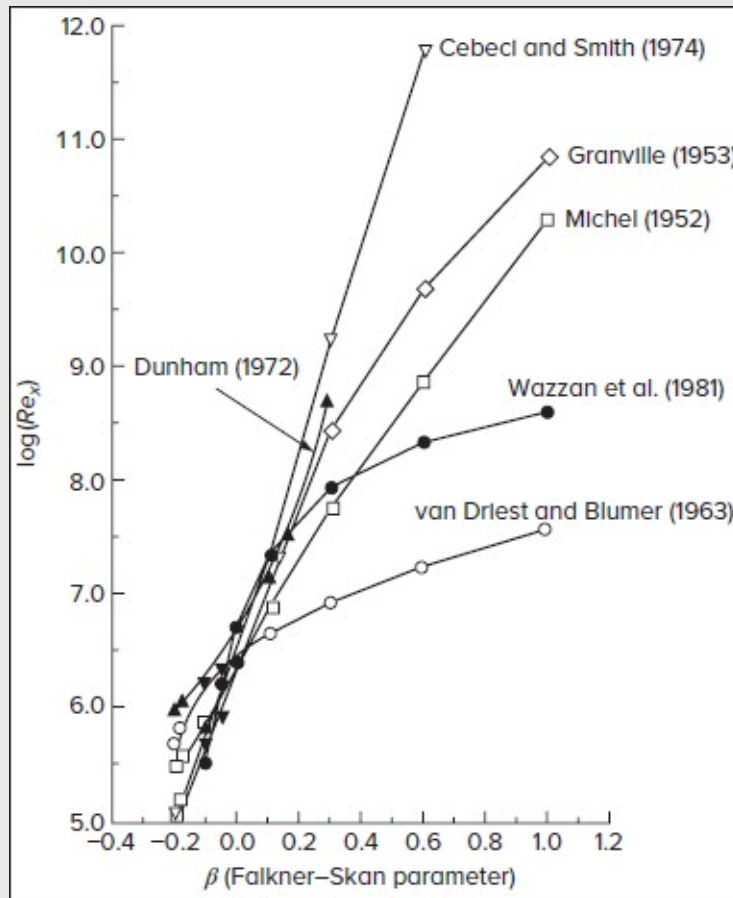


FIGURE 5-32

Transition Reynolds numbers for the Falkner-Skan wedge flows as predicted by six different methods.

5-5.2 Effect of Freestream Turbulence

We have already discussed the fact that a noisy freestream hastens the transition process and, in the early days, has masked the initial role of Tollmien-Schlichting waves. The parameter characterizing freestream turbulence level is defined as

$$T = \frac{q}{U}; \quad q = \left[\frac{1}{3} (\overline{u'^2} + \overline{v'^2} + \overline{w'^2}) \right]^{1/2} \quad (5-51)$$

in which U denotes the mean freestream velocity, and u' , v' , and w' represent the fluctuating velocities in the freestream.

The notation $\overline{u'^2}$ stands for the mean square fluctuation, which is averaged over a sufficiently long period of time (see Sec. 6-1 for the rules of time averaging). The effect of T on

transition is very strong: At $T = 0.35$ percent, Re_{tr} is already 50 percent lower than its “quiet” value corresponding to the experiment of Schubauer and Skramstad (1947).

It should be noted that the term “freestream disturbances” is somewhat ambiguous. Different effects occur when the disturbances are due to (1) grid-generated turbulence, (2) acoustic noise, (3) excited standing waves, and (4) excited traveling waves. This is illustrated in [Fig. 5-33](#) for flat-plate flow experiments. The experiment of Wells (1967), which was free of acoustic noise but contained standing waves, gave a high “quiet” value $Re_{tr} \approx 4.9 \times 10^6$. When grids were added to produce freestream turbulence, Wells’ data dropped down to meet those of Schubauer and Skramstad (1947), whose data are thought to contain acoustic noise. The latter reported a quiet Re_{tr} of only 2.8×10^6 . Spangler and Wells (1968) then used Wells’ facility to stimulate the boundary layer with excited acoustic waves of specific frequencies known to be unstable based on the Orr–Sommerfeld equation (see [Fig. 5-9](#)). In this work, standing waves were suppressed and traveling waves at 82 Hz (above the thumb curve) caused no effect, but waves at 27, 43, and 76 Hz caused rapid decreases in $Re_{x,tr}$ as seen in [Fig. 5-33](#). Here the use of grids (open circles) was far more effective than in Wells’ (1967) experiment. Spangler and Wells also reported that the spectral density distribution of the disturbances was significant. Such experimental disparities would later prompt Arnal (1984) to remark, “There is no universal $Re_{x,tr}(T)$ curve.”

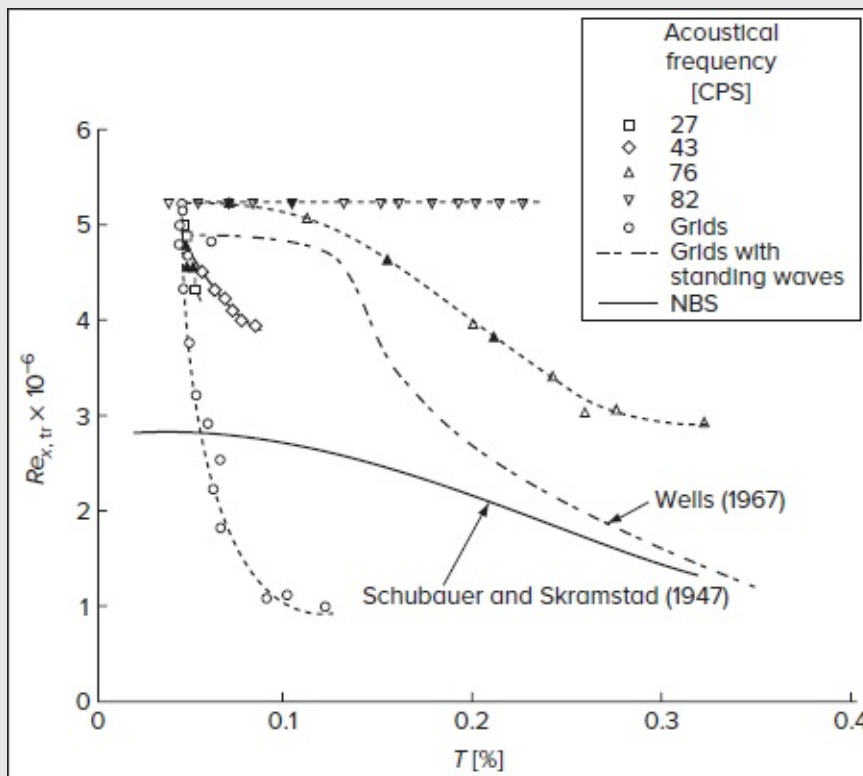


FIGURE 5-33

Measured effect of various types of freestream disturbances on the flat-plate transition point. [After Spangler and Wells (1968)].

5-5.2.1 THE CORRELATION OF VAN DRIEST AND BLUMER. Following a suggestion given by Liepmann in 1943, van Driest and Blumer (1963) theorized that transition occurs when the Reynolds number associated with maximum vorticity in the boundary layer, namely,

$$Re_{\omega} = \left(\frac{\omega y^2}{\nu} \right)_{\max}$$

Page 282

reaches a critical value that can be correlated with freestream turbulence. By relating Re_{ω} to the shape of the profile and fitting its critical value to the data of Schubauer and Skramstad (1947), van Driest and Blumer derived the following correlation for flat-plate transition:

$$Re_{x, \text{tr}}^{1/2} = \frac{-1 + \sqrt{1 + 132,500 T^2}}{39.2 T^2}; T = \sqrt{\frac{1}{3} \left(\frac{\overline{u'^2} + \overline{v'^2} + \overline{w'^2}}{U^2} \right)} \quad (5-52)$$

where T is to be taken as a fraction, not a percentage. Equation (5-52) stands in excellent agreement with the solid line of [Fig. 5-33](#) and, in fact, was “tuned” to the Schubauer and Skramstad data.

To illustrate the combined effect of freestream turbulence and pressure variation, van Driest and Blumer evaluated Re_{ω} for the Falkner–Skan wedge flows with $U = C x^m$ and arrived at the following expression:

$$\frac{1690}{Re_{x, \text{tr}}^{1/2}} \approx 0.312(m + 0.11)^{-0.528} + 1.6\eta_{\delta}^2 Re_{x, \text{tr}}^{1/2} T^2 \quad (5-23)$$

where η_{δ} is the 99 percent boundary-layer thickness in terms of the similarity variable from [Eq. \(4-92\)](#). Equation (5-53) includes the flat-plate correlation, [Eq. \(5-52\)](#), as the special case for which $m = 0$ and $\eta_{\delta} = 3.5$.

Figure 5-34a is a plot of Eq. (5-53), showing that both freestream turbulence and pressure gradient have strong effects on transition. This formula, with $T = 0$, is also displayed for comparison in [Fig. 5-32](#) and is seen to predict early transition for strong favorable gradients.

5-5.2.2 THE CORRELATION OF DUNHAM. In studying boundary-layer transition on turbomachinery blades, Dunham (1972) collected data on combined freestream turbulence and pressure gradient effects in the following correlation:

$$Re_{\theta, \text{tr}} \approx (0.27 + 0.73e^{-80T}) \left[550 + \frac{680}{(1 + 100T - 21\lambda_{\text{tr}})} \right]; \lambda < 0.04 \quad (5-54)$$

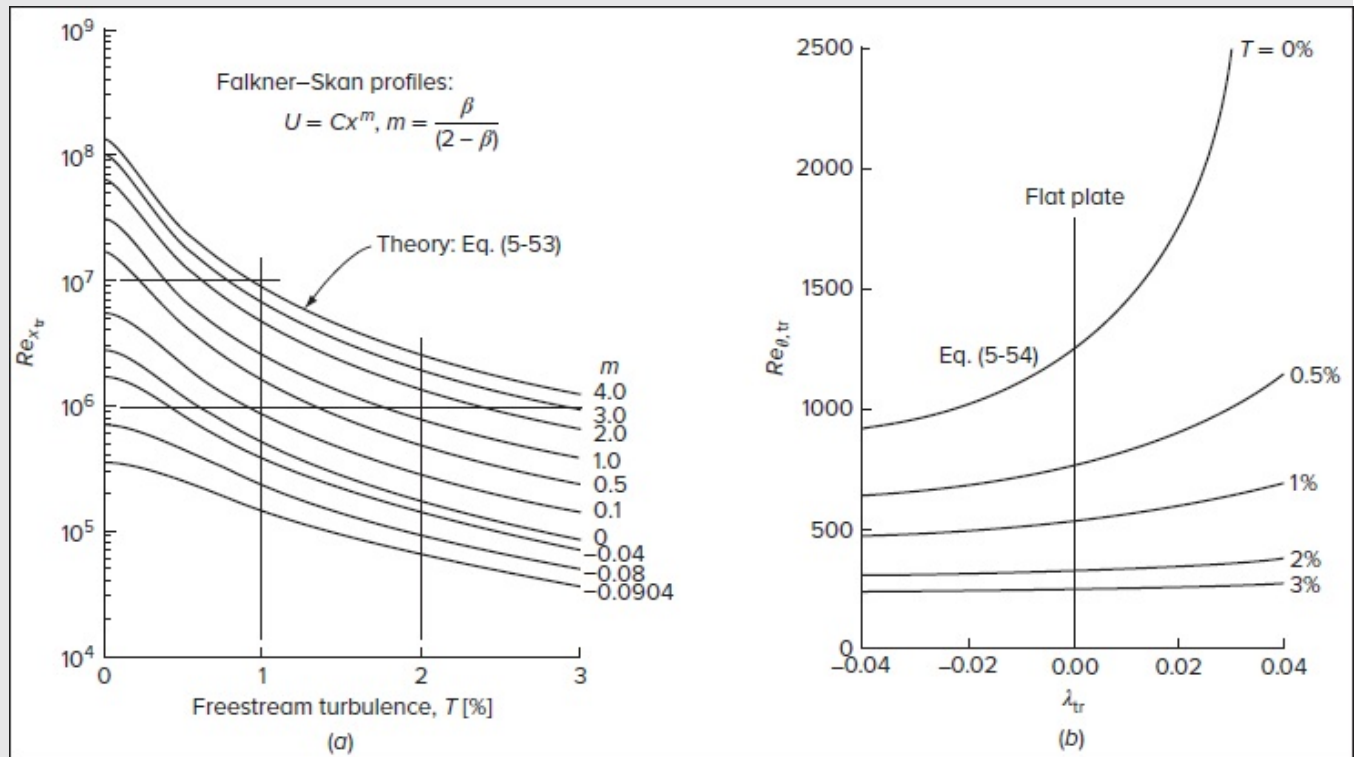


FIGURE 5-34

Combined effects of freestream turbulence and pressure gradient on transition: (a) the correlation of van Driest and Blumer (1963) for wedge flows and (b) the correlation of Dunham (1972).

where $\lambda = \theta^2(dU/dx)/\nu$ is the Thwaites parameter. This expression is plotted in Fig. 5-34b and is seen to predict a strong stabilizing effect of favorable gradients when T is small. Note also that Dunham's correlation predicts a weak effect of pressure gradients at high turbulence levels. Moreover, Eq. (5-54) with $T = 0$ can be converted to Re_x from the Falkner-Skan relations as already displayed in Fig. 5-32. And had we plotted Eq. (5-53) in Fig. 5-33 for $\lambda = 0$, its predictions would have fallen about 10 percent higher than the curve labeled Schubauer and Skramstad (1947).

Page 283

5-5.2.3 MACK'S MODIFICATION OF THE e^9 METHOD. One limitation in the correlations of Eqs. (5-53) and (5-54) is that one gets no feedback for the effect of freestream turbulence on the spectrum of disturbances or their subsequent amplification. Mack (1977) suggested that turbulence might be related to the initial disturbance level, which would then modify the e^9 method into an " e^N " prediction, where $N = N(T) \leq 9$. Accordingly, he proposed:

$$N \approx -8.43 - 2.4 \ln(T)$$

which is valid for $0.0007 \leq T \leq 0.0298$. For example, for $T = 0.0015$, we get $N = 7.2$. For $T = 0.0298$, we find $N \approx 0$, thus indicating that transition occurs right at Re_{crit} . However, to use this expression, one has to integrate the amplitude ratios from the Orr–Sommerfeld results using [Eq. \(5-47\)](#) or (5-48). Alternatively, one could modify Wazzan’s method in [Fig. 5-31](#) to include lower levels of e^N [see, for example, Fig. 25 of Wazzan et al. (1979)].

5-5.2.4 HIGH FREESTREAM TURBULENCE: A BYPASS FORMULA. A glance at [Fig. 5-34b](#) shows that, for freestream turbulence above 1 percent, transition becomes virtually insensitive to the pressure gradient. When the disturbance is sufficiently large, the flow can thus bypass the natural transition process. Using an optimal-growth criterion that is proportional to the Reynolds number, Schmid and Henningson (2001) provide a simple but elegant dimensionless formula for bypass transition, specifically,

$$T(Re_{x,tr})^{1/2} \approx 1200 \pm 200 \quad (5-55)$$

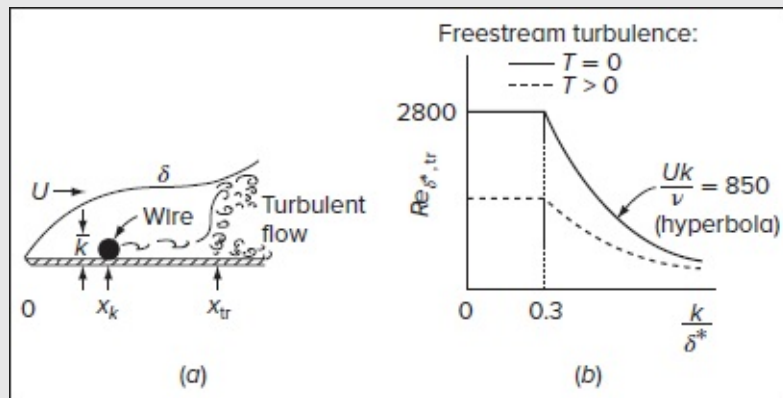


FIGURE 5-35

Idealized effect of two-dimensional roughness on transition: (a) flat plate with trip wire and (b) transition data.

where the freestream turbulence T is expressed in percent. Schmid and Henningson point out that this relation is analogous to Eq. (5-53) of van Driest and Blumer. However, Eq. (5-53) retains a substantial pressure gradient effect, even at T as high as 3 percent [Fig. 5-34a].

5-5.3 Effect of Surface Roughness on Transition

Page 284

The results so far correspond to smooth walls. The introduction of roughness or projection at the wall will generally cause earlier transition because of the additional disturbances that surface irregularities feed into the boundary layer. We should distinguish between two different geometries: (1) two-dimensional roughness, a wire or cylinder stretched across the

flow; and (2) three-dimensional roughness, a sphere or spike or a single grain of sand. These are considered *single* roughnesses. There is also the possibility of *distributed* roughness such as sandpaper or rows of cylinders or multiple rivets.

Two- and three-dimensional roughnesses have distinctly different effects. [Figure 5-35a](#) shows an idealized two-dimensional element—a transverse wire on a flat plate. As discussed by Klebanoff and Tidstrom (1972), the wire wake introduces disturbances that raise the level of the Tollmien–Schlichting waves growing downstream. If the wire height k is much smaller than the local displacement thickness $\delta^*(x_k)$, there is little effect and transition occurs at the smooth-wall location x_{tr} correlated, for example, in [Fig. 5-33](#). As U (or k) increases until k/δ^* exceeds 0.3, the point x_{tr} moves upstream toward the roughness element, and the value of $Re_{\delta^*,tr}$ drops along a hyperbolic curve, as shown in [Fig. 5-35b](#). Thus, a criterion for a wire to “trip” a flow into turbulence is

$$Uk/\nu \approx 850 \quad [\text{Gibbings (1959)}] \quad (5-56)$$

When freestream turbulence is present, both the smooth-wall and roughness-affected transition values decrease, as shown in the dashed line of [Fig. 5-35b](#). The value $Re_{\delta^*,tr}(k = 0)$ can be estimated from [Fig. 5-33](#). As Dryden (1953) pointed out, the effect of freestream turbulence in [Fig. 5-35b](#) can be suppressed by normalizing the abscissa with its “quiet” value. The outcome, as correlated by Dryden (1953), is shown in [Fig. 5-36a](#) to be a nearly universal curve.

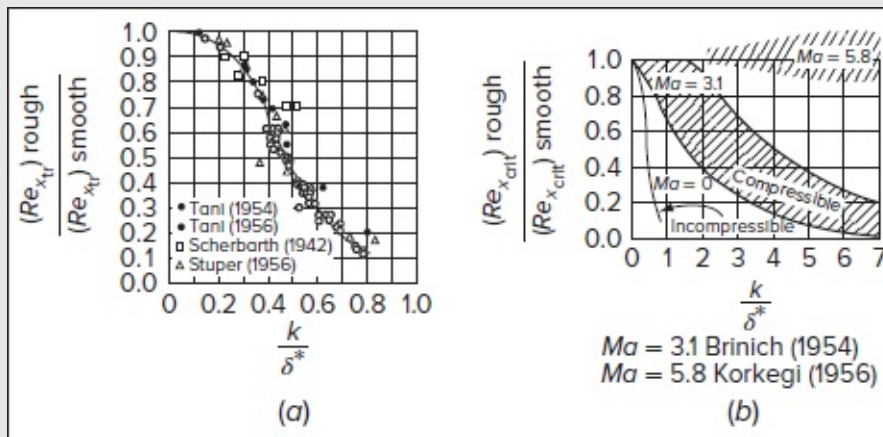


FIGURE 5-36

Flat-plate, two-dimensional roughness transition data normalized to eliminate freestream turbulence effects: (a) incompressible flow [after Dryden (1953)] and (b) compressible flow.

At higher Mach numbers, a two-dimensional trip is much less effective. [Figure 5-36b](#) shows normalized transition data for $Ma = 0$ (from [Fig. 5-36a](#)), $Ma = 3.1$ [Brinich (1954)], and $Ma = 5.8$ [Korkegi (1956)]. In this case, much larger roughness heights are required for effective tripping, as predicted by Gibbings (1959):

Flat-plate Mach number	$\frac{Uk}{\nu}$
0.0	850
2.0	2000
4.0	10,000
6.0	∞

A single three-dimensional roughness element gives rise to a zone of spreading disturbances in its wake. There is little effect on the transition point until $k/\delta^* \approx 0.6$, ≈ 0.6 , after which there is a sharp drop in $Re_{\delta^*,tr}$. At a local roughness Reynolds number of $u(k)k/\nu \approx 600$, a low-speed boundary layer is considered “tripped,” and the flow downstream of the element may be viewed as a wedge of continuous turbulence. As the Mach number increases, the element remains an effective trip until $Ma > 4$, after which the necessary roughness height increases markedly. Whitfield and Iannuzzi (1969) conducted experiments at hypersonic Mach numbers and gave a general transition correlation for spherical elements from $Ma = 0$ to $Ma = 16$.

Distributed roughness has been less studied. Results for sand-grain roughness reported by Feindt in 1957 [see Fig. 17.45 of Schlichting (1979)] show no effect on transition until $Uk/\nu \approx 120$, in both favorable and adverse pressure gradients. However, for $Re_k > 120$, the transition point x_{tr} decreases markedly with Re_k .

5-5.4 Transition of Unsteady Flows

All the discussions in this section have described transition in steady shear flows. Additional parameters appear in unsteady flows, to which the symposium edited by Dwoyer and Hussaini (1987) was devoted. Usually a dimensionless time or frequency is added to the correlation.

5-5.4.1 OSCILLATING BOUNDARY LAYERS. Obremski and Fejer (1967) experimented with flat-plate airflow whose stream velocity varied approximately sinusoidally about a mean:

$$U = U_0(1 + N_A \sin \omega t) \quad (5-57)$$

The amplitude ratio N_A varied from 0.014 to 0.27, and the frequency ω (4.5 to 62 Hz) was kept below the range of expected unstable Tollmien–Schlichting waves. Initial instability began in the low-velocity trough of the cycle ($\omega t \approx 3\pi/2$). In addition to the usual $Re_{x,tr}$, Obremski and Fejer defined a “nonsteady Reynolds number,” $Re_{ns} = N_A U_0^2 / (\omega \nu)$, and found that $Re_{ns} \approx 26,000$ was a critical point. As shown in [Fig. 5-37a](#), for $Re_{ns} > 25,000$,

there was no effect of the oscillations on the transition point $Re_{x, \text{tr}} \approx 1.6 \times 10^6$. However, for $Re_{\text{ns}} > 27,000$, the transition point moved rapidly forward as $N A$ increases.

Two additional results, characteristic of unsteady instability, were reported by Obremski and Fejer: (1) unstable wave packets were formed at the velocity trough for all values of Re_{ns} , but only for $Re_{\text{ns}} > 27,000$ did these packets burst into turbulence; and (2) at certain times during transition, the wave packet interface appeared to move upstream—something that had not been observed in steady-flow instability. By evaluating the Orr–Sommerfeld eigenvalues of the instantaneous velocity profiles and following their paths, Obremski and Morkovin (1969) were able to propose a quasi-steady theory which explained these results. The subject of time-periodic flow stability is reviewed by Davis (1976).

5-5.4.2 ACCELERATING FLOW IN A PIPE. Lefebvre and White (1989, 1991) experimented with water flow accelerated linearly from rest in a 30 m long pipe with $D = 5$ cm and (later) 9 cm. The flow began as laminar, underwent transition abruptly and almost globally (within 30 ms), then became fully turbulent. The laminar velocity profiles were in agreement with the classic solution of Szymanski (1932) from Sec. 3-4 (Fig. 3-16). Compared to steady pipe flow, transition occurred at very high Reynolds numbers, $2 \times 10^5 \leq Re_{D, \text{tr}} \leq 1.1 \times 10^6$, for accelerations from 0.2 to 11.8 ms^{-2} . The comparison is misleading because the velocity profiles are not parabolas but rather resemble the earliest profile in [Fig. 3-16](#), with thin boundary layers and a flat core. The laminar profiles burst globally into turbulence at a transition time t_{tr} which is a function of the pipe diameter D , acceleration a , and kinematic viscosity ν . By dimensional analysis, we realize that

$$t_{\text{tr}} \left(\frac{a^2}{\nu} \right)^{1/3} = f \left[D \left(\frac{a}{\nu^2} \right)^{1/3} \right] \quad (5-58)$$

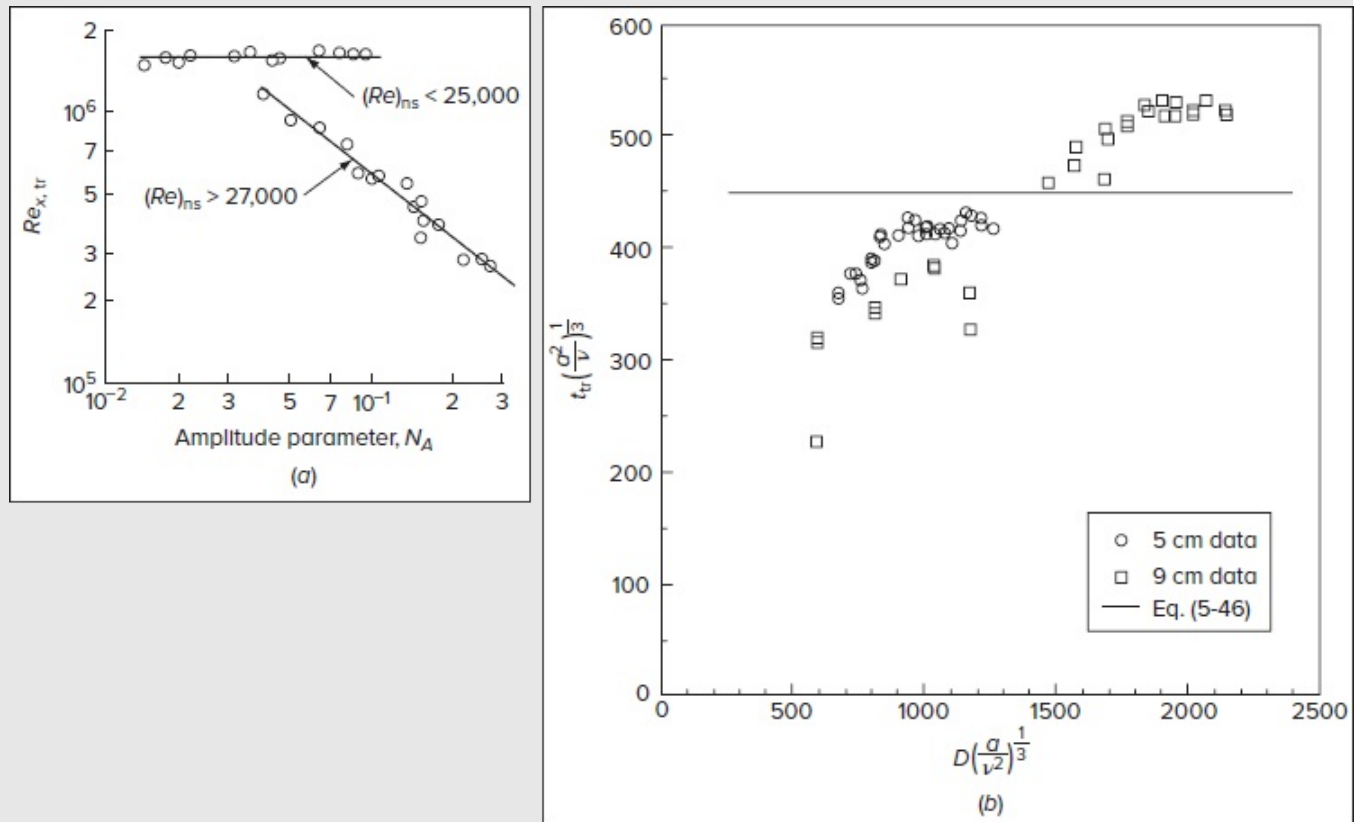


FIGURE 5-37

Transition in unsteady shear flows: (a) on a flat plate with oscillating freestream [after Obremski and Fejer (1967)] and (b) in pipe flow accelerated linearly from rest [after Lefebvre and White (1991)].

Page 286

The transition-time data for two different pipe sizes are shown in [Fig. 5-37b](#). As an approximate comparison, Lefebvre and White (1991) noted that Michel's steady-flow criterion, [Eq. \(5-46\)](#), gave the simplest result. This is also shown in [Fig. 5-37b](#). The data are more closely fit by a square-root relation, $t_{tr} \propto \sqrt{D}$.

5-5.5 Control of Boundary-Layer Transition

Although existing theories are not definitive, we know enough about transition to make some serious attempts at designing systems that *control* transition. This subject is reviewed by Reshotko (1987), who also covers the concept of *receptivity*, the means by which freestream disturbances enter the boundary layer and excite its “normal modes” or Tollmien–Schlichting waves. For example, with reference to [Fig. 5-33](#), why is the boundary layer so *receptive* to certain types of grid turbulence?

Basically, boundary layers are stabilized or transition delayed by increasing the negative

curvature of the profile. Reshotko (1987) extends [Eq. \(5-37\)](#) to include a nonzero wall velocity:

$$\mu_w \left. \frac{\partial^2 u}{\partial y^2} \right|_{y=0} = \frac{dp}{dx} + \left(\rho v_w - \left. \frac{d\mu}{dT} \frac{\partial T}{\partial y} \right|_{y=0} \right) \left. \frac{\partial u}{\partial y} \right|_{y=0} \quad (5-59)$$

From this expression it may be seen that the effects that make the right-hand side more negative (stable) are

1. Favorable pressure gradient: $dp/dx < 0$.
2. Wall suction: $v_w < 0$.
3. Cooling of gases: $d\mu/dT > 0$, $\partial T/\partial y > 0$.
4. Heating of liquids: $d\mu/dT < 0$, $\partial T/\partial y < 0$.

Delaying transition (maintaining laminar flow) will lower the drag of vehicles—about 60 percent of the drag of aircraft and 90 percent of the drag of underwater bodies are due to wall friction. Reshotko (1987) reviews work to date on the above effects, which we summarize here.

A favorable pressure gradient (effect 1) is achieved by “shaping” the body so that its point of maximum velocity moves far aft. One is then faced with designing the (short) tail of the body to avoid extensive flow separation.

Wall suction (effect 2) has long been known to keep the boundary layer laminar, reducing drag, and delaying separation (thus achieving higher lift). Pfenniger and Reed (1966) summarize research on airfoil suction. Suction is often less effective for swept wings, where turbulence from the fuselage tends to spread out along the leading edge. Wagner and Fischer (1984) summarize efforts to keep leading edges free from such contamination.

Cooling of gases (effect 3) is very effective (Fig. 5-14) but expensive, requiring cryogenic equipment for application to aircraft. Nevertheless, Reshotko (1979) shows that drag reductions of 20–25 percent might be a practical and achievable goal.

Page 287

Surface heating of water flows (effect 4) definitely stabilizes boundary layers. By overheating a body of revolution in a water flow to 25°C above ambient, Lauchle and Gurney (1984) showed that $Re_{x_{tr}}$ increased from 4.5×10^6 to 3.64×10^7 . Heating power requirements are large (approximately 100 kWm²) because of the high heat capacity and thermal conductivity of water.

There is much research on *active control* of boundary layers to delay transition or otherwise improve flow conditioning. A general review is given by Gad-el-Hak (1996). One method is *wave cancellation*, wherein growing disturbances are detected and the control system generates opposing waves that are 180° out of phase to cancel them. This idea is surveyed by Joslin et al. (1996).

A second active-control proposal, useful in both transitional and turbulent boundary layers, is to cover the surface with an array of *piezoelectric actuators* that generate counterrotating motions to cancel the streamwise vortices that feed turbulence. This idea is reviewed by Jacobson and Reynolds (1998).

All of the above laminar-flow-control techniques suffer from environmental factors—such as ice crystals, rain, dirt, and sediment depositions or small organisms in water—which may bypass the control and cause disturbances that are sufficient to trigger turbulence.

5-5.6 Chaos and Turbulence

In 1963, E. N. Lorentz, while analyzing a system of first-order differential equations simulating atmospheric behavior, discovered that these apparently deterministic equations led to disorderly solutions, now termed *chaos*. These findings have triggered an explosion of chaos research by physicists, mathematicians, and engineers. Many physical systems are found to be chaotic.

For example, consider the *logistic equation*, a simple algebraic formula for predicting the growth of a population x of a biological species:

$$x_{\text{new}} = rx_{\text{old}}(1 - x_{\text{old}}) \quad (5-60)$$

where $1 < r < 4$ is a parameter. Let us begin with any initial guess $0 < x < 1$ and iterate this equation for a given value of r . For $1 < r < 3$, the iterates converge to a single stable curve. At $r = 3$, the iterates bifurcate into two curves. Two more bifurcations occur at $r = 3.5$ and 3.6 . Then, for $r > 3.6$, the iterates spread chaotically throughout the region between the highest and lowest bifurcations. Such behavior is illustrated graphically in [Fig. 5-38](#) and is characteristic of many seemingly deterministic dynamical systems.

The chief requirement for chaos to occur in a dynamical system is its *extreme sensitivity to initial conditions*. Slight changes in initial data will create a trajectory that eventually diverges completely from neighbors with nearly the same starting conditions. The trajectories will often circle near a point, not periodically (i.e., a limit cycle) but rather wandering through changing layers that, in time, pass near every part of the region. These points are called *strange attractors* and have a “fractal” dimension greater than the perceived geometric dimensions of the region.

Chaos theory is now a mature science covered in several textbooks. It bears a strong similarity to transition, as one can imagine by viewing [Figs. 5-28a](#) and [5-38](#). Both processes involve multiple bifurcations and lead toward random content but, as discussed in Chap. 9 of Drazin (2002), it is an oversimplification to match the two. Transition is too diverse, with too many parameters and paths toward turbulence. Chaos and transition were first compared in books by Tatsumi (1984), Swinney and Gollub (1985), and Chevray (1989). It is known that certain laminar flows—Couette flow, Bénard convection, and fluid mixing—exhibit chaotic behavior. Certain turbulent structures—the edges of jets and shear layers—have a fractal (noninteger) dimension. Chaos and transition are not analogous, but their parallelism remains

intriguing and, as such, has become the subject of recent books by Favre (1995), Branover et al. (1999), and Debnath and Riahi (2000).

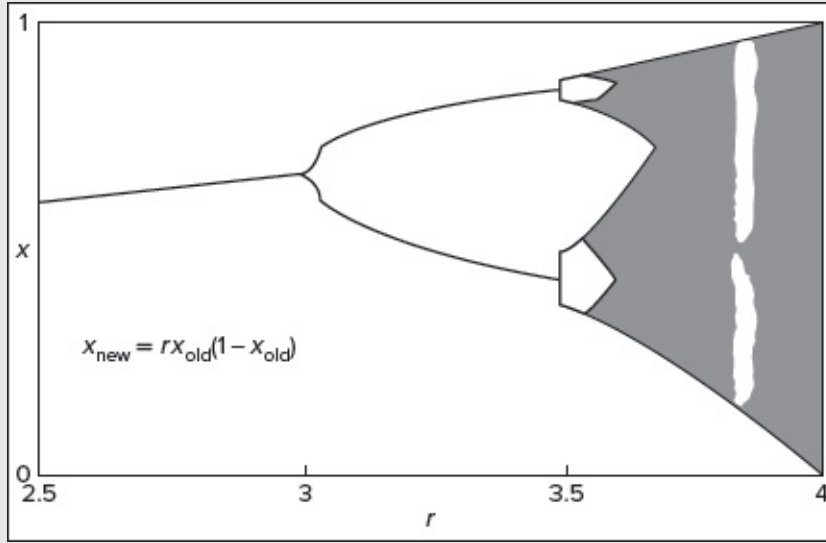


FIGURE 5-38

Iterates of the logistic formula, [Eq. \(5-60\)](#). Bifurcations occur at $r = 3.0$, 3.5 , and 3.6 . For $r > 3.6$, solutions become chaotic.

5-6 BIGLOBAL STABILITY OF INCOMPRESSIBLE VISCOUS FLOW

So far, we have assumed that two-dimensional disturbances can be suitably represented by traveling waves $\hat{q} = q(y)\exp[i(\alpha x - \sigma t)] = q(y)e^{\sigma_i t} e^{i(\alpha x - \sigma_r t)}$, where α denotes the spatial wave number in the x -direction and, based on temporal stability theory, $\sigma = \alpha c$ represents a complex angular frequency. Accordingly, a flow will be unstable when $\sigma_i = \alpha c_i > 0$. In modeling three-dimensional flows that exhibit rapid changes in the transverse, or cross-streamwise direction y , this traveling wave form becomes

$$\hat{q}(x, y, z, t) = q(y)e^{\sigma_i t} e^{i(\alpha x + n z - \sigma_r t)} \quad (\text{Cartesian}) \quad (5-61)$$

where x and z represent the streamwise and spanwise directions with their corresponding wave numbers α and n , respectively. In cylindrical polar coordinates, we equivalently have

$$\hat{q}(r, \theta, z, t) = q(r)e^{\sigma_i t} e^{i(\alpha z + m \theta - \sigma_r t)} \quad (\text{Cylindrical}) \quad (5-62)$$

where m denotes the tangential (or azimuthal) mode number. Such models are appropriate for

mostly parallel flows that are weakly dependent on the streamwise coordinate, namely, for which,

$$\left| \frac{\partial Q_0}{\partial x} \right|, \left| \frac{\partial Q_0}{\partial z} \right| = \left| \frac{\partial Q_0}{\partial y} \right| \quad (\text{Cartesian}) \quad \text{or} \quad \left| \frac{\partial Q_0}{\partial \theta} \right|, \left| \frac{\partial Q_0}{\partial z} \right| = \left| \frac{\partial Q_0}{\partial r} \right| \quad (\text{Cylindrical}) \quad (5-63)$$

In seeking greater generality, a biglobal form of the disturbance amplitude may be implemented, specifically

$$\hat{q}(x, y, z, t) = q(x, y) e^{\sigma_i t} e^{i(nz - \sigma_r t)} \quad \text{or} \quad \hat{q}(r, \theta, z, t) = q(r, z) e^{\sigma_i t} e^{i(m\theta - \sigma_r t)} \quad (5-64)$$

By expressing the disturbance amplitude as a function of two spatial coordinates—instead of one only—the resulting framework is no longer restricted to a purely exponential form in prescribing spatial amplification or attenuation. Consequently, instabilities of the basic flow can be more accurately identified at user-specified values of the wave number n or m in the third spatial direction, z or θ , respectively.

In this section, we explore some of the characteristics of the biglobal stability framework when used in conjunction with the Navier–Stokes equations. For more detail, see Theofilis (2011), Chedevergne et al. (2012), Boyer et al. (2013), or Elliott and Gibson (2019).

5-6.1 Linearized Disturbance Relations Based on the Incompressible Navier–Stokes Equations

To initiate the stability analysis, we use the instantaneous variables $\tilde{\mathbf{V}} = \mathbf{V}_0 + \hat{\mathbf{v}}$ and $\tilde{P} = P_0 + \hat{p}$. As such, a generic variable $\tilde{Q} = Q_0 + \hat{q}$ may be decomposed into its basic form plus a small disturbance, which can be taken as a first-order perturbation of the basic motion. When inserted into a nonlinear operator, such as the Navier–Stokes equations given by [Eq. \(5-10\)](#), one obtains $(Q_0 + \hat{q}) = 0$. The latter can be further expanded into $(Q_0) = 0$, which is generally satisfied by the *basic motion*, plus a linearized operator acting on \hat{q} of the form $\mathcal{L}(Q_0) \cdot \hat{q} + O(\hat{q}^2) = 0$. This linearized Navier–Stokes operator, $\mathcal{L}(Q_0)$, which dictates the behavior of \hat{q} , leads to the so-called disturbance equation(s).

Page 289

We illustrate this procedure using the three-dimensional forms of the incompressible Navier–Stokes equations. Starting with [Eq. \(5-10\)](#) and using an instantaneous velocity vector $\tilde{\mathbf{V}} = (\tilde{U}, \tilde{V}, \tilde{W})$, the continuity, axial, transverse, and spanwise momentum equations become

$$\frac{\partial \tilde{U}}{\partial x} + \frac{\partial \tilde{V}}{\partial y} + \frac{\partial \tilde{W}}{\partial z} = 0 \quad (\text{continuity}) \quad (5-65)$$

$$\frac{\partial \tilde{U}}{\partial t} + \tilde{U} \frac{\partial \tilde{U}}{\partial x} + \tilde{V} \frac{\partial \tilde{U}}{\partial y} + \tilde{W} \frac{\partial \tilde{U}}{\partial z} + \frac{1}{\rho} \frac{\partial \tilde{P}}{\partial x} = \nu \left(\frac{\partial^2 \tilde{U}}{\partial x^2} + \frac{\partial^2 \tilde{U}}{\partial y^2} + \frac{\partial^2 \tilde{U}}{\partial z^2} \right) \quad (\text{x-mom.}) \quad (5-66)$$

$$\frac{\partial \tilde{V}}{\partial t} + \tilde{U} \frac{\partial \tilde{V}}{\partial x} + \tilde{V} \frac{\partial \tilde{V}}{\partial y} + \tilde{W} \frac{\partial \tilde{V}}{\partial z} + \frac{1}{\rho} \frac{\partial \tilde{P}}{\partial y} = \nu \left(\frac{\partial^2 \tilde{V}}{\partial x^2} + \frac{\partial^2 \tilde{V}}{\partial y^2} + \frac{\partial^2 \tilde{V}}{\partial z^2} \right) \text{ (y-mom.)} \quad (5-67)$$

$$\frac{\partial \tilde{W}}{\partial t} + \tilde{U} \frac{\partial \tilde{W}}{\partial x} + \tilde{V} \frac{\partial \tilde{W}}{\partial y} + \tilde{W} \frac{\partial \tilde{W}}{\partial z} + \frac{1}{\rho} \frac{\partial \tilde{P}}{\partial z} = \nu \left(\frac{\partial^2 \tilde{W}}{\partial x^2} + \frac{\partial^2 \tilde{W}}{\partial y^2} + \frac{\partial^2 \tilde{W}}{\partial z^2} \right) \text{ (z-mom.)} \quad (5-68)$$

In cylindrical polar coordinates, we may comparably take $\tilde{\mathbf{V}} = (\tilde{U}_r, \tilde{U}_\theta, \tilde{U}_z)$ and transform [Eq. \(5-10\)](#) into

$$\frac{\partial \tilde{U}_r}{\partial r} + \frac{\tilde{U}_r}{r} + \frac{1}{r} \frac{\partial \tilde{U}_\theta}{\partial \theta} + \frac{\partial \tilde{U}_z}{\partial z} = 0 \text{ (continuity)} \quad (5-69)$$

$$\frac{\partial \tilde{U}_r}{\partial t} + \tilde{U}_r \frac{\partial \tilde{U}_r}{\partial r} + \frac{\tilde{U}_\theta}{r} \frac{\partial \tilde{U}_r}{\partial \theta} - \frac{\tilde{U}_\theta^2}{r} + \tilde{U}_z \frac{\partial \tilde{U}_r}{\partial z} + \frac{1}{\rho} \frac{\partial \tilde{P}}{\partial r} = \nu \left(\frac{\partial^2 \tilde{U}_r}{\partial r^2} + \frac{1}{r} \frac{\partial \tilde{U}_r}{\partial r} - \frac{\tilde{U}_r}{r^2} + \frac{1}{r^2} \frac{\partial^2 \tilde{U}_r}{\partial \theta^2} - \frac{2}{r^2} \frac{\partial \tilde{U}_\theta}{\partial \theta} + \frac{\partial^2 \tilde{U}_r}{\partial z^2} \right) \text{ (r-mom.)} \quad (5-70)$$

$$\frac{\partial \tilde{U}_\theta}{\partial t} + \tilde{U}_r \frac{\partial \tilde{U}_\theta}{\partial r} + \frac{\tilde{U}_\theta}{r} \frac{\partial \tilde{U}_\theta}{\partial \theta} + \frac{\tilde{U}_r \tilde{U}_\theta}{r} + \tilde{U}_z \frac{\partial \tilde{U}_\theta}{\partial z} + \frac{1}{\rho r} \frac{\partial \tilde{P}}{\partial \theta} = \nu \left(\frac{\partial^2 \tilde{U}_\theta}{\partial r^2} + \frac{1}{r} \frac{\partial \tilde{U}_\theta}{\partial r} - \frac{\tilde{U}_\theta}{r^2} + \frac{1}{r^2} \frac{\partial^2 \tilde{U}_\theta}{\partial \theta^2} + \frac{2}{r^2} \frac{\partial \tilde{U}_r}{\partial \theta} + \frac{\partial^2 \tilde{U}_\theta}{\partial z^2} \right) \text{ (\theta-mom.)} \quad (5-71)$$

$$\frac{\partial \tilde{U}_z}{\partial t} + \tilde{U}_r \frac{\partial \tilde{U}_z}{\partial r} + \frac{\tilde{U}_\theta}{r} \frac{\partial \tilde{U}_z}{\partial \theta} + \tilde{U}_z \frac{\partial \tilde{U}_z}{\partial z} + \frac{1}{\rho} \frac{\partial \tilde{P}}{\partial z} = \nu \left(\frac{\partial^2 \tilde{U}_z}{\partial r^2} + \frac{1}{r} \frac{\partial \tilde{U}_z}{\partial r} + \frac{1}{r^2} \frac{\partial^2 \tilde{U}_z}{\partial \theta^2} + \frac{\partial^2 \tilde{U}_z}{\partial z^2} \right) \text{ (z-mom.)} \quad (5-72)$$

For the reader's convenience, both Cartesian and cylindrical forms are presented side by side, or else deferred to an exercise problem. After substituting the decomposed variables, $\tilde{\mathbf{V}} = \mathbf{V}_0 + \hat{\mathbf{v}}$ and $\tilde{P} = P_0 + \hat{p}$, and dismissing terms of order $\hat{\mathbf{v}}^2$, \hat{p}^2 , and higher, the linearized stability equations that control the evolution of unsteady disturbances can be retrieved. These are called the disturbance equations for $\hat{\mathbf{v}}$, where the components of the basic flow, \mathbf{V}_0 , appear as predetermined coefficients. In Cartesian coordinates, where $\hat{\mathbf{v}} = (\hat{u}, \hat{v}, \hat{w})$ and $\mathbf{V}_0 = (U, V, W)$, these relations become

$$\frac{\partial \hat{u}}{\partial x} + \frac{\partial \hat{v}}{\partial y} + \frac{\partial \hat{w}}{\partial z} = 0 \text{ (continuity)} \quad (5-73)$$

$$\frac{\partial \hat{u}}{\partial t} + \frac{\partial U}{\partial x} \hat{u} + \frac{\partial U}{\partial y} \hat{v} + \frac{\partial U}{\partial z} \hat{w} + U \frac{\partial \hat{u}}{\partial x} + V \frac{\partial \hat{u}}{\partial y} + W \frac{\partial \hat{u}}{\partial z} + \frac{1}{\rho} \frac{\partial \hat{p}}{\partial x} = \nu \left(\frac{\partial^2 \hat{u}}{\partial x^2} + \frac{\partial^2 \hat{u}}{\partial y^2} + \frac{\partial^2 \hat{u}}{\partial z^2} \right) \text{ (x-mom.)} \quad (5-74)$$

$$\frac{\partial \hat{v}}{\partial t} + \frac{\partial V}{\partial x} \hat{u} + \frac{\partial V}{\partial y} \hat{v} + \frac{\partial V}{\partial z} \hat{w} + U \frac{\partial \hat{v}}{\partial x} + V \frac{\partial \hat{v}}{\partial y} + W \frac{\partial \hat{v}}{\partial z} + \frac{1}{\rho} \frac{\partial \hat{p}}{\partial y} = \nu \left(\frac{\partial^2 \hat{v}}{\partial x^2} + \frac{\partial^2 \hat{v}}{\partial y^2} + \frac{\partial^2 \hat{v}}{\partial z^2} \right) \text{ (y-mom.)} \quad (5-75)$$

$$\frac{\partial \hat{w}}{\partial t} + \frac{\partial W}{\partial x} \hat{u} + \frac{\partial W}{\partial y} \hat{v} + \frac{\partial W}{\partial z} \hat{w} + U \frac{\partial \hat{w}}{\partial x} + V \frac{\partial \hat{w}}{\partial y} + W \frac{\partial \hat{w}}{\partial z} + \frac{1}{\rho} \frac{\partial \hat{p}}{\partial z} = \nu \left(\frac{\partial^2 \hat{w}}{\partial x^2} + \frac{\partial^2 \hat{w}}{\partial y^2} + \frac{\partial^2 \hat{w}}{\partial z^2} \right) \text{ (z-mom)} \quad (5-76)$$

Note that the basic flow components (U, V, W) must be known, computed, or specified beforehand. In cylindrical coordinates, we may use $\mathbf{V}_0 = (U_r, U_\theta, U_z)$, $\hat{\mathbf{v}} = (\hat{u}_r, \hat{u}_\theta, \hat{u}_z)$, and expand the disturbance equations into

$$\frac{\partial \hat{u}_r}{\partial r} + \frac{\hat{u}_r}{r} + \frac{1}{r} \frac{\partial \hat{u}_\theta}{\partial \theta} + \frac{\partial \hat{u}_z}{\partial z} = 0 \text{ (continuity)} \quad (5-77)$$

$$\begin{aligned} \frac{\partial \hat{u}_r}{\partial t} + U_r \frac{\partial \hat{u}_r}{\partial r} + \hat{u}_r \frac{\partial U_r}{\partial r} + \frac{U_\theta}{r} \frac{\partial \hat{u}_r}{\partial \theta} + \frac{\hat{u}_\theta}{r} \frac{\partial U_r}{\partial \theta} - \frac{2 U_\theta \hat{u}_\theta}{r} + U_z \frac{\partial \hat{u}_r}{\partial z} + \hat{u}_z \frac{\partial U_r}{\partial z} + \frac{1}{\rho} \frac{\partial \hat{p}}{\partial r} \\ = \nu \left(\frac{\partial^2 \hat{u}_r}{\partial r^2} + \frac{1}{r} \frac{\partial \hat{u}_r}{\partial r} - \frac{\hat{u}_r}{r^2} + \frac{1}{r^2} \frac{\partial^2 \hat{u}_r}{\partial \theta^2} - \frac{2}{r^2} \frac{\partial \hat{u}_\theta}{\partial \theta} + \frac{\partial^2 \hat{u}_r}{\partial z^2} \right) \quad (r\text{-mom.}) \end{aligned} \quad (5-78)$$

$$\begin{aligned} \frac{\partial \hat{u}_\theta}{\partial t} + U_r \frac{\partial \hat{u}_\theta}{\partial r} + \hat{u}_r \frac{\partial U_\theta}{\partial r} + \frac{U_\theta}{r} \frac{\partial \hat{u}_\theta}{\partial \theta} + \frac{\hat{u}_\theta}{r} \frac{\partial U_\theta}{\partial \theta} + \frac{U_r \hat{u}_\theta}{r} + \frac{\hat{u}_r U_\theta}{r} + U_z \frac{\partial \hat{u}_\theta}{\partial z} + \hat{u}_z \frac{\partial U_\theta}{\partial z} + \frac{1}{\rho r} \frac{\partial \hat{p}}{\partial \theta} \\ = \nu \left(\frac{\partial^2 \hat{u}_\theta}{\partial r^2} + \frac{1}{r} \frac{\partial \hat{u}_\theta}{\partial r} - \frac{\hat{u}_\theta}{r^2} + \frac{1}{r^2} \frac{\partial^2 \hat{u}_\theta}{\partial \theta^2} + \frac{2}{r^2} \frac{\partial \hat{u}_r}{\partial \theta} + \frac{\partial^2 \hat{u}_\theta}{\partial z^2} \right) \quad (\theta\text{-mom.}) \end{aligned} \quad (5-79)$$

$$\begin{aligned} \frac{\partial \hat{u}_z}{\partial t} + U_r \frac{\partial \hat{u}_z}{\partial r} + \hat{u}_r \frac{\partial U_z}{\partial r} + \frac{U_\theta}{r} \frac{\partial \hat{u}_z}{\partial \theta} + \frac{\hat{u}_\theta}{r} \frac{\partial U_z}{\partial \theta} + U_z \frac{\partial \hat{u}_z}{\partial z} + \hat{u}_z \frac{\partial U_z}{\partial z} + \frac{1}{\rho} \frac{\partial \hat{p}}{\partial z} \\ = \nu \left(\frac{\partial^2 \hat{u}_z}{\partial r^2} + \frac{1}{r} \frac{\partial \hat{u}_z}{\partial r} + \frac{1}{r^2} \frac{\partial^2 \hat{u}_z}{\partial \theta^2} + \frac{\partial^2 \hat{u}_z}{\partial z^2} \right) \quad (z\text{-mom.}) \end{aligned} \quad (5-80)$$

Page 290

5-6.2 Biglobal Expansion and Eigenvalue Problem Formulation

At this juncture, the unsteady disturbances can be modeled using a biglobal form, i.e., one that does not restrict the spatial amplitude of the disturbances in two of the three spatial directions. This is accomplished by letting

$$\hat{q} = q(x, y) \exp(\sigma_i t) \exp[i(nz - \sigma_r t)] \quad \text{or} \quad \hat{q} = q(r, z) \exp(\sigma_i t) \exp[i(m\theta - \sigma_r t)] \quad (5-81)$$

where n and m represent the spanwise and tangential mode numbers in Cartesian and cylindrical coordinates, respectively. As usual, the complex eigenmode, $\sigma = \sigma_r + i \sigma_i$, encapsulates both the stability growth rate, σ_i , and the circular frequency, σ_r . A similar ansatz is effectively used by Chedevergne et al. (2012) to investigate the hydrodynamic stability characteristics of the Taylor–Culick profile in a porous tube. Generally speaking, the flow will be stable when the unsteady disturbances about the basic motion decay over time, or when $\sigma_i < 0$.

Using $(\hat{u}, \hat{v}, \hat{w}, \hat{p}) = (u, v, w, p) \exp[i(nz - \sigma t)]$, [Eqs. \(5-73\)–\(5-76\)](#) become

$$\frac{\partial u}{\partial x} + \frac{\partial v}{\partial y} + inw = 0 \quad (5-82)$$

$$-i\sigma u + \frac{\partial U}{\partial x} u + \frac{\partial U}{\partial y} v + \frac{\partial U}{\partial z} w + U \frac{\partial u}{\partial x} + V \frac{\partial u}{\partial y} + inWu + \frac{1}{\rho} \frac{\partial p}{\partial x} = \nu \left(\frac{\partial^2 u}{\partial x^2} + \frac{\partial^2 u}{\partial y^2} - n^2 u \right) \quad (5-83)$$

$$-i\sigma v + \frac{\partial V}{\partial x} u + \frac{\partial V}{\partial y} v + \frac{\partial V}{\partial z} w + U \frac{\partial v}{\partial x} + V \frac{\partial v}{\partial y} + inWv + \frac{1}{\rho} \frac{\partial p}{\partial y} = \nu \left(\frac{\partial^2 v}{\partial x^2} + \frac{\partial^2 v}{\partial y^2} - n^2 v \right) \quad (5-84)$$

$$-i\sigma w + \frac{\partial W}{\partial x} u + \frac{\partial W}{\partial y} v + \frac{\partial W}{\partial z} w + U \frac{\partial w}{\partial x} + V \frac{\partial w}{\partial y} + inWw + in \frac{p}{\rho} = \nu \left(\frac{\partial^2 w}{\partial x^2} + \frac{\partial^2 w}{\partial y^2} - n^2 w \right) \quad (5-85)$$

In like manner, using $(\hat{u}_r, \hat{u}_\theta, \hat{u}_z, \hat{p}) = (u_r, u_\theta, u_z, p) \exp[i(m\theta - \sigma t)]$, [Eqs. \(5-77\)–\(5-80\)](#) reduce to

$$\frac{\partial u_r}{\partial r} + \frac{u_r}{r} + im \frac{u_\theta}{r} + \frac{\partial u_z}{\partial z} = 0 \quad (\text{continuity}) \quad (5-86)$$

$$\begin{aligned} -i\sigma u_r + U_r \frac{\partial u_r}{\partial r} + u_r \frac{\partial U_r}{\partial r} + im \frac{U_\theta u_r}{r} + \frac{u_\theta}{r} \frac{\partial U_r}{\partial \theta} - \frac{2U_\theta u_\theta}{r} + U_z \frac{\partial u_r}{\partial z} + u_z \frac{\partial U_r}{\partial z} + \frac{1}{\rho} \frac{\partial p}{\partial r} \\ = \nu \left[\frac{\partial^2 u_r}{\partial r^2} + \frac{1}{r} \frac{\partial u_r}{\partial r} - (1 + m^2) \frac{u_r}{r^2} - \frac{2im}{r^2} u_\theta + \frac{\partial^2 u_r}{\partial z^2} \right] \quad (r\text{-mom.}) \end{aligned} \quad (5-87)$$

$$\begin{aligned} -i\sigma u_\theta + U_r \frac{\partial u_\theta}{\partial r} + u_r \frac{\partial U_\theta}{\partial r} + im \frac{U_\theta u_\theta}{r} + \frac{u_\theta}{r} \frac{\partial U_\theta}{\partial \theta} + \frac{U_r u_\theta}{r} + \frac{u_r U_\theta}{r} + U_z \frac{\partial u_\theta}{\partial z} + u_z \frac{\partial U_\theta}{\partial z} + i \frac{m}{\rho r} p \\ = \nu \left[\frac{\partial^2 u_\theta}{\partial r^2} + \frac{1}{r} \frac{\partial u_\theta}{\partial r} - (1 + m^2) \frac{u_\theta}{r^2} + \frac{2im}{r^2} u_r + \frac{\partial^2 u_\theta}{\partial z^2} \right] \quad (\theta\text{-mom.}) \end{aligned} \quad (5-88)$$

$$\begin{aligned} -i\sigma u_z + U_r \frac{\partial u_z}{\partial r} + u_r \frac{\partial U_z}{\partial r} + im \frac{U_\theta u_z}{r} + \frac{u_\theta}{r} \frac{\partial U_z}{\partial \theta} + U_z \frac{\partial u_z}{\partial z} + u_z \frac{\partial U_z}{\partial z} + \frac{1}{\rho} \frac{\partial p}{\partial z} \\ = \nu \left(\frac{\partial^2 u_z}{\partial r^2} + \frac{1}{r} \frac{\partial u_z}{\partial r} - \frac{m^2}{r^2} u_z + \frac{\partial^2 u_z}{\partial z^2} \right) \quad (z\text{-mom.}) \end{aligned} \quad (5-89)$$

Page 291

In two-dimensional and axisymmetric flows, it is possible to manipulate and consolidate these sets of equations into a single stream function formulation, using similar steps to those undertaken to derive the Orr–Sommerfeld equation. The corresponding effort is relegated to the problems section. However, by retaining the generality of the velocity-pressure expansion, the ensuing framework will be fundamentally three-dimensional and capable of accommodating basic flows with three nonvanishing velocity components. To this end, it is helpful to rewrite the resulting equations in operator form starting with [Eqs. \(5-82\)–\(5-85\)](#), which can be rearranged into

$$\left(\frac{\partial}{\partial x} \right) u + \left(\frac{\partial}{\partial y} \right) v + (in)w = 0 \quad (\text{continuity}) \quad (5-90)$$

$$\left[\frac{\partial U}{\partial x} + U \frac{\partial}{\partial x} + V \frac{\partial}{\partial y} + inW - \nu \left(\frac{\partial^2}{\partial x^2} + \frac{\partial^2}{\partial y^2} - n^2 \right) \right] u + \left(\frac{\partial U}{\partial y} \right) v + \left(\frac{\partial U}{\partial z} \right) w + \left(\frac{1}{\rho} \frac{\partial}{\partial x} \right) p = (i\sigma)u \quad (x\text{-mom.}) \quad (5-91)$$

$$\left(\frac{\partial V}{\partial x} \right) u + \left[\frac{\partial V}{\partial y} + U \frac{\partial}{\partial x} + V \frac{\partial}{\partial y} + inW - \nu \left(\frac{\partial^2}{\partial x^2} + \frac{\partial^2}{\partial y^2} - n^2 \right) \right] v + \left(\frac{\partial V}{\partial z} \right) w + \left(\frac{1}{\rho} \frac{\partial}{\partial y} \right) p = (i\sigma)v \quad (y\text{-mom.}) \quad (5-92)$$

$$\left(\frac{\partial W}{\partial x} \right) u + \left(\frac{\partial W}{\partial y} \right) v + \left[\frac{\partial W}{\partial z} + U \frac{\partial}{\partial x} + V \frac{\partial}{\partial y} + inW - \nu \left(\frac{\partial^2}{\partial x^2} + \frac{\partial^2}{\partial y^2} - n^2 \right) \right] w + \left(\frac{in}{\rho} \right) p = (i\sigma)w \quad (z\text{-mom.}) \quad (5-93)$$

Similarly, [Eqs. \(5-86\)–\(5-89\)](#) in cylindrical coordinates may be regrouped into operators and written as

$$\left(\frac{\partial}{\partial r} + \frac{1}{r} \right) u_r + \left(\frac{im}{r} \right) u_\theta + \left(\frac{\partial}{\partial z} \right) u_z = 0 \quad (\text{continuity}) \quad (5-94)$$

$$\left[U_r \frac{\partial}{\partial r} + \frac{\partial U_r}{\partial r} + im \frac{U_\theta}{r} + U_z \frac{\partial}{\partial z} - \nu \left(\frac{\partial^2}{\partial r^2} + \frac{1}{r} \frac{\partial}{\partial r} - \frac{1+m^2}{r^2} + \frac{\partial^2}{\partial z^2} \right) \right] u_r + \left(\frac{1}{r} \frac{\partial U_r}{\partial \theta} - \frac{2U_\theta}{r} + \frac{2\nu im}{r^2} \right) u_\theta + \left(\frac{\partial U_r}{\partial z} \right) u_z + \left(\frac{1}{\rho} \frac{\partial}{\partial r} \right) p = (i\sigma) u_r \quad (r\text{-mom.}) \quad (5-95)$$

$$\left(\frac{\partial U_\theta}{\partial r} + \frac{U_\theta}{r} - \frac{2\nu im}{r^2} \right) u_r + \left[U_r \frac{\partial}{\partial r} + \frac{im U_\theta}{r} + \frac{1}{r} \frac{\partial U_\theta}{\partial \theta} + \frac{U_r}{r} - \nu \left(\frac{\partial^2}{\partial r^2} + \frac{1}{r} \frac{\partial}{\partial r} - \frac{1+m^2}{r^2} + \frac{\partial^2}{\partial z^2} \right) + U_z \frac{\partial}{\partial z} \right] u_\theta + \left(\frac{\partial U_\theta}{\partial z} \right) u_z + \left(\frac{im}{\rho r} \right) p = (i\sigma) u_\theta \quad (\theta\text{-mom.}) \quad (5-96)$$

$$\left(\frac{\partial U_z}{\partial r} \right) u_r + \left(\frac{1}{r} \frac{\partial U_z}{\partial \theta} \right) u_\theta + \left[U_r \frac{\partial}{\partial r} + im \frac{U_\theta}{r} + U_z \frac{\partial}{\partial z} + \frac{\partial U_z}{\partial z} - \nu \left(\frac{\partial^2}{\partial r^2} + \frac{1}{r} \frac{\partial}{\partial r} - \frac{m^2}{r^2} + \frac{\partial^2}{\partial z^2} \right) \right] u_z + \left(\frac{1}{\rho} \frac{\partial}{\partial z} \right) p = (i\sigma) u_z \quad (z\text{-mom.}) \quad (5-97)$$

The PDEs prescribed by [Eqs. \(5-90\)–\(5-93\)](#) or, alternatively, [Eqs. \(5-94\)–\(5-97\)](#), comprise four equations with four unknowns, (u, v, w, p) or (u_r, u_θ, u_z, p) . The coefficients of these variables can be collected and used to form a generalized eigenvalue problem of the type

$$A_{ij} f_i = \sigma B_{ij} f_i \quad (5-98)$$

where σ and f_i denote the eigenvalues and corresponding eigenvectors, while A_{ij} and B_{ij} refer to the operator matrices in the continuity and three momentum equation projections:

$$A_{ij} = \begin{bmatrix} A_{c,u} & A_{c,v} & A_{c,w} & A_{c,p} \\ A_{x,u} & A_{x,v} & A_{x,w} & A_{x,p} \\ A_{y,u} & A_{y,v} & A_{y,w} & A_{y,p} \\ A_{z,u} & A_{z,v} & A_{z,w} & A_{z,p} \end{bmatrix} \quad \text{and} \quad B_{ij} = \begin{bmatrix} B_{c,u} & B_{c,v} & B_{c,w} & B_{c,p} \\ B_{x,u} & B_{x,v} & B_{x,w} & B_{x,p} \\ B_{y,u} & B_{y,v} & B_{y,w} & B_{y,p} \\ B_{z,u} & B_{z,v} & B_{z,w} & B_{z,p} \end{bmatrix} \quad (5-99)$$

Page 292

For example, based on [Eqs. \(5-90\)–\(5-93\)](#), the operator matrices can be populated using

$$\left\{ \begin{array}{l} A_{c,u} = \frac{\partial U}{\partial x} \\ A_{c,v} = \frac{\partial}{\partial y} \\ A_{c,w} = in \\ A_{c,p} = 0 \end{array} \right\} \left\{ \begin{array}{l} A_{x,u} = \frac{\partial U}{\partial x} + inW - \nu \left(\frac{\partial^2}{\partial x^2} + \frac{\partial^2}{\partial y^2} - n^2 \right) \\ A_{x,v} = \frac{\partial U}{\partial y} \\ A_{x,w} = \frac{\partial U}{\partial z} \\ A_{x,p} = \frac{1}{\rho} \frac{\partial}{\partial x} \end{array} \right\} \left\{ \begin{array}{l} A_{y,u} = \frac{\partial V}{\partial x} \\ A_{y,v} = \frac{\partial V}{\partial y} + U \frac{\partial}{\partial x} + V \frac{\partial}{\partial y} \\ A_{y,w} = \frac{\partial V}{\partial z} \\ A_{y,p} = \frac{1}{\rho} \frac{\partial}{\partial y} \end{array} \right\} \left\{ \begin{array}{l} A_{z,u} = \frac{\partial W}{\partial x} \\ A_{z,v} = \frac{\partial W}{\partial y} \\ A_{z,w} = \frac{\partial W}{\partial z} + U \frac{\partial}{\partial x} + V \frac{\partial}{\partial y} \\ A_{z,p} = \frac{in}{\rho} \end{array} \right\} \quad (5-100)$$

Additionally, it can be seen that $B_{x,u} = B_{y,v} = B_{z,w} = i$, with all other terms in B_{ij} being

null. Similar operators associated with [Eqs. \(5-94\)–\(5-97\)](#) are deferred to a self-contained problem.

5-6.3 Numerical Strategy and Chebyshev Spectral Collocation Scheme

In practice, each of the operator matrices must be evaluated over the solution domain, thus giving rise to block matrices that depend on the number of spatial dimensions that the user retains. Since the operators contain several spatial derivatives, the numerical scheme of choice must be capable of high spatial resolution, especially near the boundaries. Given the nature of the resulting PDEs, many researchers have turned their attention to efficient, high-order, spectral collocation methods, particularly those that can provide vantage points over other discretization approaches [Boyd (2000), Trefethen (2005), and Theofilis (2011)]. The selection of a suitable polynomial collocation is prompted by the need to control the local grid resolution, numerical stability, and overall accuracy. In fact, algebraic polynomials based on power series can be constructed in a variety of clever ways including Lagrange polynomials, Newton divided differences, Padé approximations, and so on. In this context, trigonometric and orthogonal polynomial interpolators, such as the set of Chebyshev and Legendre families, stand to offer unique advantages. Their nonuniformly spaced stencils are often considered in boundary-layer discretization because of their inherent ability to impose fine grid spacings near the wall, or the region of nonuniformity, and coarser distributions elsewhere. Moreover, uniformly spaced stencils are generally susceptible to the undesirable Gibbs phenomenon, which plagues Fourier-type spectral approximations, and the equivalent Runge phenomenon, which undermines equispaced algebraic interpolators [Runge (1901)]. The advantage of using Chebyshev collocation in overcoming the endpoint Runge oscillations associated with equispaced, algebraic polynomial interpolators is illustrated in [Fig. 5-39](#) [Trefethen (2005)]. Note that the inaccuracy in evaluating first derivatives only worsens as the number of interpolation points increases. To avoid such discrepancies, a global discretization that incorporates the Chebyshev collocation approach is adopted here, i.e., with the Chebyshev polynomials forming the basis functions for spectral interpolation and differentiation.

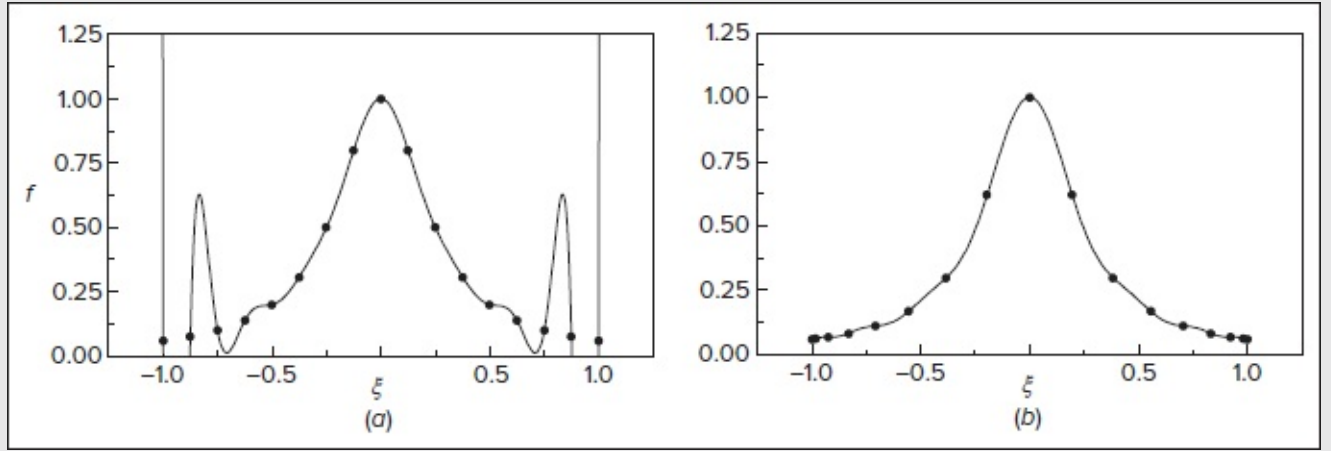


FIGURE 5-39

Characteristic results of interpolation schemes based on (a) equispaced and (b) unequally spaced Chebyshev stencils. Endpoint Runge oscillations accompany the uniformly spaced polynomial interpolator in (a).

The Chebyshev collocation approach is initiated with the selection of a stencil of order N . Because an exact polynomial representation of a function $f(\xi)$ of degree infinity is designated as $\mathcal{P}_\infty f(\xi_\infty)$, a discrete Chebyshev polynomial of degree N may be written as

$$\mathcal{P}_N f(\xi) = \sum_{i=1}^N f(\xi_i) \lambda_i(\xi) \quad (5-101)$$

Here ξ_i reproduces the collocation points at nodes $i = 1, \dots, N$, whereas $\lambda_i(\xi)$ stands for the appropriate weight function. For Chebyshev polynomials, the weight functions may be retrieved from

$$\lambda_i(\xi) = (-1)^i \left(\frac{1 - \xi^2}{\xi - \xi_i} \right) \left[\frac{T'_{N-1}(\theta)}{d_i (N-1)^2} \right] \quad \text{with} \quad \begin{cases} \xi_i = \cos \left[\frac{(i-1)\pi}{N-1} \right] \\ \theta = \arccos \xi \end{cases} \quad (5-102)$$

where

$$d_i = \begin{cases} 2; & i = 1 \text{ or } N \\ 1; & \text{otherwise} \end{cases} \quad (5-103)$$

In the interest of clarity, the collocation points ξ_i are shown below for $N \leq 5$:

M_i	1	2	3	4	5
1	0				
2	1	-1			
3	1	0	-1		
4	1	0.5	-0.5	-1	
5	1	0.7071	0	-0.7071	-1

The Chebyshev discretization scheme leads to a system of N equations and N unknowns that can be solved simultaneously for the discrete values of the spectral function $f(\xi_i)$. The polynomials are subsequently constructed from the weight functions multiplied by the functional value at each of the collocation points. In this effort, the first derivative of f may be approximated at the collocation nodes $\{\xi_1, \dots, \xi_N\}$ using the first derivative of $\mathcal{P}_N f(\xi)$. In this process, a polynomial

representation of a derivative may be given by $\mathcal{D}_N f(\xi) = [\mathcal{P}_N f(\xi)]' = \sum_{i=1}^N f(\xi_i) \lambda'_i(\xi)$ and so $f'(\xi_i) = D_N f(\xi_i)$. Moreover,

the weight function derivatives, $\lambda'_i(\xi)$, can be evaluated upfront and stored in the so-called *pseudo-spectral differentiation matrix*, $\{D_{ij}\}$, where $D_{ij} = \lambda'_j(\xi_i)$ for $i, j = 1, \dots, N$. By differentiating the N th-order Chebyshev polynomial and resolving the coefficients at all collocation points, a general expression for the differentiation matrix may be arrived at. This matrix D_N , which contains $N \times N$ rows and columns [Voigt et al. (1984)], is defined for each $N \leq 1$ using

$$\begin{cases} (D_N)_{11} = \frac{2(N-1)^2 + 1}{6} & (D_N)_{NN} = -\frac{2(N-1)^2 + 1}{6} \\ (D_N)_{ii} = \frac{-\xi_i}{2(1-\xi_i^2)} & i = 2, \dots, N-1 \\ (D_N)_{ij} = \frac{(-1)^{i+j}}{(\xi_i - \xi_j)} \frac{d_i}{d_j} & i \neq j, \quad i, j = 2, \dots, N-1 \end{cases} \quad (5-104)$$

Higher-order derivatives may be generated straightforwardly by raising the first-order differentiation matrix to the corresponding power,

$$\frac{d}{d\xi} \rightarrow (D_N)^1 = D_N, \quad \frac{d^2}{d\xi^2} \rightarrow (D_N)^2 = D_N \times D_N, \quad \text{and} \quad \frac{d^n}{d\xi^n} \rightarrow (D_N)^n = \underbrace{D_N \times D_N \times \dots \times D_N}_{\times n} \quad (5-105)$$

A valuable collection of spectral differentiation and integration codes is described by Weideman and Reddy (2000).

5-6.4 Coordinate Transformation and Grid Conditioning

Since the N collocation points as well as the n th-order Chebyshev differentiation matrix extend over the $[-1, 1]$ interval, it is necessary to linearly adjust other solution domains to the same interval. For example, if we consider a traditional two-dimensional problem with variables $x \in [a, b]$ and $y \in [c, d]$, a dual coordinate transformation will require the

installation of two auxiliary variables, ξ and η , that will recondition the problem using

$$\begin{cases} x = \frac{b}{2}(\xi + 1) - \frac{a}{2}(\xi - 1) & \xi = \frac{2x - (a + b)}{b - a} \\ y = \frac{d}{2}(\eta + 1) - \frac{c}{2}(\eta - 1) & \eta = \frac{2y - (c + d)}{d - c} \end{cases} \quad \text{and} \quad \begin{cases} \frac{\partial}{\partial x} = \frac{2}{b - a} \frac{\partial}{\partial \xi} \\ \frac{\partial}{\partial y} = \frac{2}{d - c} \frac{\partial}{\partial \eta} \end{cases} \quad (5-106)$$

Accordingly, a domain that consists of $0 \leq x \leq X_N$ and $0 \leq y \leq 1$ may be reconditioned using

$$\begin{aligned} x &= \frac{1}{2}X_N(\xi + 1) & \xi &= \frac{2}{X_N}x - 1 \\ y &= \frac{1}{2}(\eta + 1) & \eta &= 2y - 1 \end{aligned} \quad \text{and} \quad \begin{aligned} \frac{\partial}{\partial x} &= \frac{2}{X_N} \frac{\partial}{\partial \xi} \\ \frac{\partial}{\partial y} &= 2 \frac{\partial}{\partial \eta} \end{aligned} \quad (5-107)$$

Page 294

Moreover, a two-dimensional problem requires a two-dimensional grid that is based on directionally independent Chebyshev points. Such a tensor product grid will enable two independent variables to coexist in the same matrix operator [Trefethen (2000)]. Tensor product grids require the use of what is known as *Kronecker products*. Strictly speaking, the Kronecker product of two matrices, designated as $A_{ij} \otimes B_{mn} = C_{ijmn}$, leads to a block matrix C_{ijmn} , with each block being constituted of $\{a_{ij}B_{mn}\}$ terms. In this case, the Kronecker product yields

$$A_{ij} \otimes B_{mn} = \begin{pmatrix} a_{11}B_{mn} & \cdots & a_{1j}B_{mn} \\ \vdots & \ddots & \vdots \\ a_{i1}B_{mn} & \cdots & a_{ij}B_{mn} \end{pmatrix} \quad (5-108)$$

where each element of A_{ij} is multiplied by the entire matrix B_{mn} . In order to specify derivatives in two directions, the Kronecker product is applied to the differentiation matrix. In this vein, derivatives with respect to η can be taken as $(I_N) \otimes (D_N)^n$, while derivatives with respect to ξ can be written as $(D_N)^n \otimes (I_N)$, where (I_N) is the $N \times N$ identity matrix. In solving a two-dimensional problem with two spatial directions, each operator matrix, such as $A_{x,u}$ in [Eq. \(5-99\)](#), will give rise to a block matrix that is $N \times N$ large. At the outset, the A_{ij} and B_{ij} matrices will be $4N^2 \times 4N^2 = 16N^4$ in size, because an N^2 block matrix exists for each of the four variables (columns) and equations of motion (rows). In three-dimensional space, the size can rise to $4N^3 \times 4N^3 = 16N^6$, assuming that only four equations of motion are being used in conjunction with our quartet of unknown variables, (u, v, w, p) .

At this juncture, we may apply the domain mapping and differentiation matrices to [Eq. \(5-100\)](#) and extract the block matrices, which may be discretely specified using

$$\begin{cases} A_{c,u} = \bar{D}_N^x \\ A_{c,v} = \bar{D}_N^y \\ A_{c,w} = inI_N \\ A_{c,p} = 0 \end{cases} \begin{cases} A_{x,u} = U_{ii}\bar{D}_N^x + V_{ii}\bar{D}_N^y + \left(\frac{\partial U}{\partial x}inW\right)_{ii} \\ -\nu[(\bar{D}_N^x)^2 + (\bar{D}_N^y)^2 - n^2I_N] \\ A_{x,v} = \left(\frac{\partial U}{\partial y}\right)_{ii} \\ A_{x,w} = \left(\frac{\partial U}{\partial z}\right)_{ii} \\ A_{x,p} = \frac{1}{\rho}\bar{D}_N^x \end{cases} \begin{cases} A_{y,u} = \left(\frac{\partial V}{\partial x}\right)_{ii} \\ A_{y,v} = \left(\frac{\partial V}{\partial y} + inW\right)_{ii} \\ + U_{ii}\bar{D}_N^x + V_{ii}\bar{D}_N^y \\ -\nu[(\bar{D}_N^x)^2 + (\bar{D}_N^y)^2 - n^2I_N] \\ A_{y,w} = \left(\frac{\partial V}{\partial z}\right)_{ii} \\ A_{y,p} = \frac{1}{\rho}\bar{D}_N^y \end{cases} \begin{cases} A_{z,u} = \left(\frac{\partial W}{\partial x}\right)_{ii} \\ A_{z,v} = \left(\frac{\partial W}{\partial y}\right)_{ii} \\ A_{z,w} = \left(\frac{\partial W}{\partial z} + inW\right)_{ii} \\ + U_{ii}\bar{D}_N^x + V_{ii}\bar{D}_N^y \\ -\nu[(\bar{D}_N^x)^2 + (\bar{D}_N^y)^2 - n^2I_N] \\ A_{z,p} = \frac{in}{\rho}I_N \end{cases} \quad (5-109)$$

In [Eq. \(5-109\)](#), the overbar is used as a reminder that the spectral operators are mapped to the physical domain under consideration, such as $x \in [a, b]$ and $y \in [c, d]$. In addition to [Eq. \(5-109\)](#), all terms in the right-hand-side matrix $\{B_{ij}\}$ vanish except for $B_{x,u} = B_{y,v} = B_{z,w} = iI_N$. The effort to formulate the equivalent block matrices associated with cylindrical polar operators in [Eqs. \(5-94\)–\(5-97\)](#) is provided as an exercise problem.

5-6.5 Boundary Conditions and Numerical Solvers

Boundary conditions associated with biglobal stability problems tend to be homogeneous except at inflow and outflow sections, where different ideas have been suggested. Conditions may be specified by suppressing the velocity fluctuations at solid boundaries and acoustically closed surfaces, imposing symmetry conditions along midsection planes and centerlines, ensuring zero wall gradients by equating wall values to their nearest neighbors, maintaining flow continuance using exit point extrapolation, equating the normal stress to zero at the outflow location, and specifying adjoint exit conditions [Boyer et al. (2013)]. In fact, the development of a well-posed adjoint problem leads to conditions that prove essential to the modeling of viscous fluids using finite elements. As shown by Boyer et al. (2013), two main choices of boundary conditions are available when analyzing incompressible flows. These consist of an imposed velocity for the inflow and an imposed normal stress for the outflow. The most notable of these requirements is a vanishing stress tensor in the streamwise direction, a condition that leads to

Page 295

$$\tilde{\sigma}(\tilde{\mathbf{V}}, \tilde{P}) \cdot \mathbf{e}_x = [-\tilde{P}\boldsymbol{\delta} + \mu(\nabla\tilde{\mathbf{V}} + \nabla\tilde{\mathbf{V}}^T)] \cdot \mathbf{e}_x = 0 \quad (\text{at outflow}) \quad (5-110)$$

where \mathbf{e}_x (or \mathbf{e}_z) represents the normal unit vector in the streamwise direction and $\boldsymbol{\delta}$ alludes to the identity matrix. Term by term, we have

$$\begin{cases} \nabla\tilde{\mathbf{V}} \cdot \mathbf{e}_x = \frac{\partial\tilde{U}}{\partial x}\mathbf{e}_x + \frac{\partial\tilde{U}}{\partial y}\mathbf{e}_y + \frac{\partial\tilde{U}}{\partial z}\mathbf{e}_z, & \nabla\tilde{\mathbf{V}}^T \cdot \mathbf{e}_x = \frac{\partial\tilde{U}}{\partial x}\mathbf{e}_x + \frac{\partial\tilde{V}}{\partial x}\mathbf{e}_y + \frac{\partial\tilde{W}}{\partial x}\mathbf{e}_z \quad (\text{Cartesian}) \\ \nabla\tilde{\mathbf{V}} \cdot \mathbf{e}_z = \frac{\partial\tilde{U}_z}{\partial r}\mathbf{e}_r + \frac{1}{r}\frac{\partial\tilde{U}_z}{\partial\theta}\mathbf{e}_\theta + \frac{\partial\tilde{U}_z}{\partial z}\mathbf{e}_z, & \nabla\tilde{\mathbf{V}}^T \cdot \mathbf{e}_z = \frac{\partial\tilde{U}_r}{\partial z}\mathbf{e}_r + \frac{\partial\tilde{U}_\theta}{\partial z}\mathbf{e}_\theta + \frac{\partial\tilde{U}_z}{\partial z}\mathbf{e}_z \quad (\text{Cylindrical}) \end{cases} \quad (5-111)$$

In order to satisfy [Eq. \(5-110\)](#), we must account for the three spatial projections in each of the

coordinate systems:

$$\begin{cases} 2\mu \frac{\partial \tilde{U}}{\partial x} - \tilde{P} = 0; & \frac{\partial \tilde{U}}{\partial y} + \frac{\partial \tilde{V}}{\partial x} = 0; & \frac{\partial \tilde{U}}{\partial z} + \frac{\partial \tilde{W}}{\partial x} = 0 & \text{(Cartesian)} \\ \frac{\partial \tilde{U}_z}{\partial r} + \frac{\partial \tilde{U}_r}{\partial z} = 0; & \frac{1}{r} \frac{\partial \tilde{U}_z}{\partial \theta} + \frac{\partial \tilde{U}_\theta}{\partial z} = 0; & 2\mu \frac{\partial \tilde{U}_z}{\partial z} - \tilde{P} = 0 & \text{(Cylindrical)} \end{cases} \quad (5-112)$$

When these conditions are applied to the flow disturbances, we recover

$$\begin{cases} 2\mu \frac{\partial u}{\partial x} - p = 0; & \frac{\partial u}{\partial y} + \frac{\partial v}{\partial x} = 0; & \frac{\partial u}{\partial z} + \frac{\partial w}{\partial x} = 0 & \text{(Cartesian)} \\ \frac{\partial u_z}{\partial r} + \frac{\partial u_r}{\partial z} = 0; & \frac{1}{r} \frac{\partial u_z}{\partial \theta} + \frac{\partial u_\theta}{\partial z} = 0; & 2\mu \frac{\partial u_z}{\partial z} - p = 0 & \text{(Cylindrical)} \end{cases} \quad (5-113)$$

Moreover, when considering planar or axisymmetric disturbances with no spanwise or azimuthal variations, [Eq. \(5-113\)](#) may be further reduced into

$$\begin{cases} 2\mu \frac{\partial u}{\partial x} - p = 0; & \frac{\partial u}{\partial y} + \frac{\partial v}{\partial x} = 0; & \frac{\partial w}{\partial x} = 0 & \text{(Cartesian)} \\ \frac{\partial u_z}{\partial r} + \frac{\partial u_r}{\partial z} = 0; & \frac{\partial u_\theta}{\partial z} = 0; & 2\mu \frac{\partial u_z}{\partial z} - p = 0 & \text{(Cylindrical)} \end{cases} \quad (5-114)$$

To illustrate the application of these conditions to a problem with a simple geometric configuration, consider a rectangular fluid domain that extends over $0 \leq x \leq X_N$ and $0 \leq y \leq 1$, with infinite impedance (hardwall) boundaries everywhere except at $x = X_N$, where an outflow condition exists. Combining the commonly used conditions with those derived above, one can use

$$\begin{cases} u(x,0) = 0 \\ u(x,1) = 0 \\ u(0,y) = 0 \\ \frac{\partial u(X_N,y)}{\partial x} = \frac{p}{2\mu} \end{cases} \quad \begin{cases} v(x,0) = 0 \\ v(x,1) = 0 \\ v(0,y) = 0 \\ \frac{\partial v(X_N,y)}{\partial x} = -\frac{\partial u(X_N,y)}{\partial y} \end{cases} \quad \begin{cases} w(x,0) = 0 \\ w(x,1) = 0 \\ w(0,y) = 0 \\ \frac{\partial w(X_N,y)}{\partial x} = 0 \end{cases} \quad \begin{cases} \frac{\partial p(x,0)}{\partial y} = 0 \end{cases} \quad (5-115)$$

Note that the boundary conditions add to the sparsity of the matrices to be handled. At this juncture, having specified all of the terms that feed into the block matrices, including their boundary values, a suitable eigensolver is needed. Depending on the solver, the matrices may require preconditioning and norm reduction to mitigate roundoff errors and reduce the effect of zero elements. Some transformations reduce both A_{ij} and B_{ij} to triangular forms in which the eigenvalues appear as diagonal elements. This is generally achieved using the QZ or LZ algorithms for dense matrices, and the Arnoldi algorithm for sparse matrices. Arnoldi's strategy is to compute a predetermined number of eigenvalues that are located around a guess value [Chedevergne et al. (2012)]. Some eigensolvers can be found in the newmat11 library for C++, LAPACK for FORTRAN, GNU Scientific Library for C, and the core library in MATLAB. In fact, MATLAB implements the QZ and Arnoldi solvers with the simple commands `eig(A, B)` and `eigs(A, B)`, respectively. Several examples that illustrate the

application of the biglobal stability framework to incompressible viscous-flow profiles are provided in the problems section.

Page 296

5-7 BIGLOBAL STABILITY OF COMPRESSIBLE VISCOUS FLOW

The biglobal stability scheme has enabled us to identify the conditions leading to hydrodynamic breakdown of an incompressible viscous motion along with the characteristics of the corresponding hydrodynamic disturbance waves, which travel at speeds that are comparable to those of the basic flow. Many cases exist where the additional presence of pressure-induced oscillations, or acoustic waves, which travel near the speed of sound, is particularly important. For example, in studies related to rocket and gas turbine engine flow stability, the ability to capture acoustic wave characteristics often overweighs the need to identify hydrodynamic stability modes.

Among the earliest stability techniques used to predict the onset of oscillations in simulated rocket chambers, one can cite the Orr–Sommerfeld approach discussed in Sec. 5-2. This method, however, was quickly dismissed in favor of the local nonparallel approach, which enabled the retention of all velocity components in the Navier–Stokes formulation [Varapaev and Yagodkin (1969)]. The local approach was further developed by Casalis et al. (1998), Griffond et al. (2000), and Griffond and Casalis (2001), who considered both planar and axisymmetric chamber configurations associated with the Taylor (1956) and Taylor–Culick (1966) basic motions in porous channels and tubes. Such idealizations have often been relied on to mimic the bulk injection-driven flow of an internally burning slab or right-cylindrical rocket chamber with constant cross section. Supported by a series of experiments, the resulting studies have helped to identify several essential stability features, such as the critical distances from the chamber headwall beyond which flow instabilities emerged [Avalon et al. (1998), Avalon and Lambert (2001), Fabignon et al. (2003)].

In seeking to develop a model that remained unhampered by the parallel-flow assumption, the biglobal stability framework was explored by Chedevergne et al. (2006) in the context of porous tubes with sidewall injection. Using an incompressible vorticity-streamfunction formulation of the Taylor–Culick instability problem, these researchers managed to reconcile between the spatial features of the eigenmodes measured experimentally by Avalon et al. (1998) and those predicted theoretically. In a follow-up study by Chedevergne et al. (2012), it was confirmed that direct numerical simulations of the Taylor–Culick motion stood in favorable agreement with the oscillatory wave composition obtained by consolidating the incompressible biglobal stability predictions of the hydrodynamic waves with the vorticoacoustic fluctuations generated, for example, using the closed-form approximations of Majdalani and Van Moorhem (1998). Nonetheless, these and other such investigations (e.g. Boyer et al. 2013) required decomposing the disturbances into incompressible, hydrodynamic waves (obtained from an incompressible solver), which could

be subsequently combined with the compressible acoustic eigenmodes and their corresponding rotational fluctuations generated at the domain's boundaries.

Following this continually evolving line of research progress, this section focuses on the use of the biglobal stability framework in partnership with the fully compressible Navier–Stokes equations. Although this effort will increase the number of variables as well as the mathematical complexity of the equations to be solved, it will eliminate the need to decompose the flow at the forefront of the analysis. Instead, the vorticoacoustic and hydrodynamic eigenmodes will be shown to be retrievable simultaneously using the compressible biglobal stability framework. In short, the compressible biglobal stability framework will be shown to represent an eigenvalue problem that is capable of producing accurate predictions of vorticoacoustic and hydrodynamic eigenmodes, their associated mode shapes, and the rich structures that they engender [Majdalani et al. (2016)].

5-7.1 Linearized Disturbance Relations Based on the Compressible Navier–Stokes Equations

As before, we use the instantaneous variables $\tilde{\mathbf{V}} = \mathbf{V}_0 + \hat{\mathbf{v}}$ and $\tilde{P} = P_0 + \hat{p}$ with the addition of the density and temperature, $\tilde{\rho} = \rho_0 + \hat{\rho}$ and $\tilde{T} = T_0 + \hat{T}$. We initiate this procedure using the three-dimensional form of the compressible Navier-Stokes equations in concert with the energy and state equations:

$$\frac{\partial \tilde{\rho}}{\partial t} + \nabla \cdot (\tilde{\rho} \tilde{\mathbf{V}}) = 0 \quad (5-116)$$

$$\tilde{\rho} \left[\frac{\partial \tilde{\mathbf{V}}}{\partial t} + (\tilde{\mathbf{V}} \cdot \nabla) \tilde{\mathbf{V}} \right] = -\nabla \tilde{P} + \mu \left[\nabla^2 \tilde{\mathbf{V}} + \frac{1}{3} \nabla (\nabla \cdot \tilde{\mathbf{V}}) \right] \quad (5-117)$$

$$\tilde{\rho} c_p \left[\frac{\partial \tilde{T}}{\partial t} + (\tilde{\mathbf{V}} \cdot \nabla) \tilde{T} \right] = \frac{\partial \tilde{P}}{\partial t} + \tilde{\mathbf{V}} \cdot \nabla \tilde{P} + \tilde{\Phi} + k \nabla^2 \tilde{T} \quad (5-118)$$

$$\tilde{P} = \tilde{\rho} R \tilde{T} \quad (5-119)$$

Page 297

Here $\tilde{\Phi}$ denotes the mechanical dissipation function. Subsequently, the substitution of the decomposed variables leads to the linearized compressible stability equations in which second-order fluctuations of the type $\hat{\mathbf{v}}^2, \hat{p}^2, \hat{\rho}^2, \hat{T}^2, \hat{\rho}\hat{T}$ and higher are suppressed. The result is

$$\frac{\partial \hat{\rho}}{\partial t} + \nabla \cdot (\rho_0 \hat{\mathbf{v}} + \hat{\rho} \mathbf{V}_0) = 0 \quad (5-120)$$

$$\rho_0 \left[\frac{\partial \hat{\mathbf{v}}}{\partial t} + (\mathbf{V}_0 \cdot \nabla) \hat{\mathbf{v}} + (\hat{\mathbf{v}} \cdot \nabla) \mathbf{V}_0 \right] + \hat{\rho} \left[\frac{\partial \mathbf{V}_0}{\partial t} + (\mathbf{V}_0 \cdot \nabla) \mathbf{V}_0 \right] = -\nabla \hat{p} + \mu \nabla^2 \hat{\mathbf{v}} + \frac{1}{3} \mu \nabla (\nabla \cdot \hat{\mathbf{v}}) \quad (5-121)$$

$$\rho_0 c_p \left[\frac{\partial \hat{T}}{\partial t} + (\mathbf{V}_0 \cdot \nabla) \hat{T} + (\hat{\mathbf{v}} \cdot \nabla) T_0 \right] + \hat{\rho} c_p \left[\frac{\partial T_0}{\partial t} + (\mathbf{V}_0 \cdot \nabla) T_0 \right] = \frac{\partial \hat{p}}{\partial t} + (\mathbf{V}_0 \cdot \nabla) \hat{p} + \hat{\mathbf{v}} \cdot \nabla p_0 + \hat{\Phi} + k \nabla^2 \hat{T} \quad (5-122)$$

$$\hat{p} = \rho_0 R \hat{T} + \hat{\rho} R T_0$$

(5-123)

Now using Cartesian coordinates, where $\tilde{\mathbf{V}} = (\tilde{U}, \tilde{V}, \tilde{W})$, all but the ideal gas equation can be further expanded and rearranged into

$$\frac{\partial \hat{p}}{\partial y} + \frac{\partial}{\partial x}(\rho_0 \hat{u}) + \frac{\partial}{\partial y}(\rho_0 \hat{v}) + \frac{\partial}{\partial z}(\rho_0 \hat{w}) + U \frac{\partial \hat{p}}{\partial y} + V \frac{\partial \hat{p}}{\partial y} + W \frac{\partial \hat{p}}{\partial z} + \hat{p} \left(\frac{\partial U}{\partial x} + \frac{\partial V}{\partial y} + \frac{\partial W}{\partial z} \right) = 0 \quad (\text{continuity}) \quad (5-124)$$

$$\begin{aligned} \rho_0 \left(\frac{\partial \hat{u}}{\partial t} + U \frac{\partial \hat{u}}{\partial x} + V \frac{\partial \hat{u}}{\partial y} + W \frac{\partial \hat{u}}{\partial z} + \hat{u} \frac{\partial U}{\partial x} + \hat{v} \frac{\partial U}{\partial y} + \hat{w} \frac{\partial U}{\partial z} \right) + \hat{p} \left(\frac{\partial U}{\partial t} + U \frac{\partial U}{\partial x} + V \frac{\partial U}{\partial y} + W \frac{\partial U}{\partial z} \right) \\ = -\frac{\partial \hat{p}}{\partial x} + \mu \left(\frac{\partial^2 \hat{u}}{\partial x^2} + \frac{\partial^2 \hat{u}}{\partial y^2} + \frac{\partial^2 \hat{u}}{\partial z^2} \right) + \frac{1}{3} \mu \left(\frac{\partial^2 \hat{u}}{\partial x^2} + \frac{\partial^2 \hat{v}}{\partial x \partial y} + \frac{\partial^2 \hat{w}}{\partial x \partial z} \right) \end{aligned} \quad (\text{x-mom.}) \quad (5-125)$$

$$\begin{aligned} \rho_0 \left(\frac{\partial \hat{v}}{\partial t} + U \frac{\partial \hat{v}}{\partial x} + V \frac{\partial \hat{v}}{\partial y} + W \frac{\partial \hat{v}}{\partial z} + \hat{u} \frac{\partial V}{\partial x} + \hat{v} \frac{\partial V}{\partial y} + \hat{w} \frac{\partial V}{\partial z} \right) + \hat{p} \left(\frac{\partial V}{\partial t} + U \frac{\partial V}{\partial x} + V \frac{\partial V}{\partial y} + W \frac{\partial V}{\partial z} \right) \\ = -\frac{\partial \hat{p}}{\partial y} + \mu \left(\frac{\partial^2 \hat{v}}{\partial x^2} + \frac{\partial^2 \hat{v}}{\partial y^2} + \frac{\partial^2 \hat{v}}{\partial z^2} \right) + \frac{1}{3} \mu \left(\frac{\partial^2 \hat{u}}{\partial x \partial y} + \frac{\partial^2 \hat{v}}{\partial y^2} + \frac{\partial^2 \hat{w}}{\partial y \partial z} \right) \end{aligned} \quad (\text{y-mom.}) \quad (5-126)$$

$$\begin{aligned} \rho_0 \left(\frac{\partial \hat{w}}{\partial t} + U \frac{\partial \hat{w}}{\partial x} + V \frac{\partial \hat{w}}{\partial y} + W \frac{\partial \hat{w}}{\partial z} + \hat{u} \frac{\partial W}{\partial x} + \hat{v} \frac{\partial W}{\partial y} + \hat{w} \frac{\partial W}{\partial z} \right) + \hat{p} \left(\frac{\partial W}{\partial t} + U \frac{\partial W}{\partial x} + V \frac{\partial W}{\partial y} + W \frac{\partial W}{\partial z} \right) \\ = -\frac{\partial \hat{p}}{\partial z} + \mu \left(\frac{\partial^2 \hat{w}}{\partial x^2} + \frac{\partial^2 \hat{w}}{\partial y^2} + \frac{\partial^2 \hat{w}}{\partial z^2} \right) + \frac{1}{3} \mu \left(\frac{\partial^2 \hat{u}}{\partial x \partial z} + \frac{\partial^2 \hat{v}}{\partial y \partial z} + \frac{\partial^2 \hat{w}}{\partial z^2} \right) \end{aligned} \quad (\text{z-mom.}) \quad (5-127)$$

and

$$\begin{aligned} \rho_0 c_p \left(\frac{\partial \hat{T}}{\partial t} + U \frac{\partial \hat{T}}{\partial x} + V \frac{\partial \hat{T}}{\partial y} + W \frac{\partial \hat{T}}{\partial z} + \hat{u} \frac{\partial T_0}{\partial x} + \hat{v} \frac{\partial T_0}{\partial y} + \hat{w} \frac{\partial T_0}{\partial z} \right) + \hat{p} c_p \left(\frac{\partial T_0}{\partial t} + U \frac{\partial T_0}{\partial x} + V \frac{\partial T_0}{\partial y} + W \frac{\partial T_0}{\partial z} \right) \\ = \frac{\partial \hat{p}}{\partial t} + U \frac{\partial \hat{p}}{\partial x} + V \frac{\partial \hat{p}}{\partial y} + W \frac{\partial \hat{p}}{\partial z} + \hat{u} \frac{\partial P_0}{\partial x} + \hat{v} \frac{\partial P_0}{\partial y} + \hat{w} \frac{\partial P_0}{\partial z} + \hat{\Phi} + k \left(\frac{\partial^2 \hat{T}}{\partial x^2} + \frac{\partial^2 \hat{T}}{\partial y^2} + \frac{\partial^2 \hat{T}}{\partial z^2} \right) \end{aligned} \quad (\text{energy}) \quad (5-128)$$

where the dissipation function, which is coordinate specific, becomes

$$\begin{aligned} \hat{\Phi} = \frac{4}{3} \left[\left(2 \frac{\partial U}{\partial x} - \frac{\partial V}{\partial y} - \frac{\partial W}{\partial z} \right) \frac{\partial \hat{u}}{\partial x} + \left(2 \frac{\partial V}{\partial y} - \frac{\partial U}{\partial x} - \frac{\partial W}{\partial z} \right) \frac{\partial \hat{v}}{\partial y} + \left(2 \frac{\partial W}{\partial z} - \frac{\partial U}{\partial x} - \frac{\partial V}{\partial y} \right) \frac{\partial \hat{w}}{\partial z} \right] \\ + 2 \left[\left(\frac{\partial U}{\partial y} + \frac{\partial V}{\partial x} \right) \left(\frac{\partial \hat{u}}{\partial y} + \frac{\partial \hat{v}}{\partial x} \right) + \left(\frac{\partial U}{\partial z} + \frac{\partial W}{\partial x} \right) \left(\frac{\partial \hat{u}}{\partial z} + \frac{\partial \hat{w}}{\partial x} \right) + \left(\frac{\partial V}{\partial z} + \frac{\partial W}{\partial y} \right) \left(\frac{\partial \hat{v}}{\partial z} + \frac{\partial \hat{w}}{\partial y} \right) \right] \end{aligned} \quad (5-129)$$

In cylindrical polar coordinates, we equivalently take $\tilde{\mathbf{V}} = (\tilde{U}_r, \tilde{U}_\theta, \tilde{U}_z)$ and write

$$\begin{aligned} \frac{\partial \hat{p}}{\partial t} + \hat{u}_r \frac{\partial \rho_0}{\partial r} + \frac{\hat{u}_\theta}{r} \frac{\partial \rho_0}{\partial \theta} + \hat{u}_z \frac{\partial \rho_0}{\partial z} + U_r \frac{\partial \hat{p}}{\partial r} + \frac{U_\theta}{r} \frac{\partial \hat{p}}{\partial \theta} + U_z \frac{\partial \hat{p}}{\partial z} + \rho_0 \left(\frac{\partial \hat{u}_r}{\partial r} + \frac{\hat{u}_r}{r} + \frac{1}{r} \frac{\partial \hat{u}_\theta}{\partial \theta} + \frac{\partial \hat{u}_z}{\partial z} \right) \\ + \hat{p} \left(\frac{\partial U_r}{\partial r} + \frac{U_r}{r} + \frac{1}{r} \frac{\partial U_\theta}{\partial \theta} + \frac{\partial U_z}{\partial z} \right) = 0 \end{aligned} \quad (\text{continuity}) \quad (5-130)$$

$$\begin{aligned}
& \rho_0 \left(\frac{\partial \hat{u}_r}{\partial t} + U_r \frac{\partial \hat{u}_r}{\partial r} + \frac{U_\theta}{r} \frac{\partial \hat{u}_r}{\partial \theta} + U_z \frac{\partial \hat{u}_r}{\partial z} - \frac{2 U_\theta \hat{u}_\theta}{r} + \hat{u}_r \frac{\partial U_r}{\partial r} + \frac{\hat{u}_\theta}{r} \frac{\partial U_r}{\partial \theta} + \hat{u}_z \frac{\partial U_r}{\partial z} \right) \\
& + \hat{\rho} \left(\frac{\partial U_r}{\partial t} + U_r \frac{\partial U_r}{\partial r} + \frac{U_\theta}{r} \frac{\partial U_r}{\partial \theta} + U_z \frac{\partial U_r}{\partial z} - \frac{U_\theta^2}{r} \right) \\
& = -\frac{\partial \hat{p}}{\partial r} + \frac{\mu}{3} \left[4 \left(\frac{\partial^2 \hat{u}_r}{\partial r^2} + \frac{1}{r} \frac{\partial \hat{u}_r}{\partial r} - \frac{\hat{u}_r}{r^2} \right) + 3 \left(\frac{1}{r^2} \frac{\partial^2 \hat{u}_r}{\partial \theta^2} + \frac{\partial^2 \hat{u}_r}{\partial z^2} \right) - \frac{7}{r^2} \frac{\partial \hat{u}_\theta}{\partial \theta} + \frac{1}{r} \frac{\partial^2 \hat{u}_\theta}{\partial r \partial \theta} + \frac{\partial^2 \hat{u}_z}{\partial r \partial z} \right] \quad (r\text{-mom.})
\end{aligned} \tag{5-131}$$

$$\begin{aligned}
& \rho_0 \left(\frac{\partial \hat{u}_\theta}{\partial t} + U_r \frac{\partial \hat{u}_\theta}{\partial r} + \frac{U_\theta}{r} \frac{\partial \hat{u}_\theta}{\partial \theta} + U_z \frac{\partial \hat{u}_\theta}{\partial z} + \frac{U_r \hat{u}_\theta}{r} + \frac{\hat{u}_r U_\theta}{r} + \hat{u}_r \frac{\partial U_\theta}{\partial r} + \frac{\hat{u}_\theta}{r} \frac{\partial U_\theta}{\partial \theta} + \hat{u}_z \frac{\partial U_\theta}{\partial z} \right) \\
& + \hat{\rho} \left(\frac{\partial U_\theta}{\partial t} + U_r \frac{\partial U_\theta}{\partial r} + \frac{U_\theta}{r} \frac{\partial U_\theta}{\partial \theta} + U_z \frac{\partial U_\theta}{\partial z} + \frac{U_r U_\theta}{r} \right) \\
& = -\frac{1}{r} \frac{\partial \hat{p}}{\partial \theta} + \frac{\mu}{3} \left[3 \left(\frac{\partial^2 \hat{u}_\theta}{\partial r^2} + \frac{1}{r} \frac{\partial \hat{u}_\theta}{\partial r} - \frac{\hat{u}_\theta}{r^2} + \frac{\partial^2 \hat{u}_\theta}{\partial z^2} \right) + \frac{4}{r^2} \frac{\partial^2 \hat{u}_\theta}{\partial \theta^2} + \frac{7}{r^2} \frac{\partial \hat{u}_r}{\partial \theta} + \frac{1}{r} \frac{\partial^2 \hat{u}_r}{\partial r \partial \theta} + \frac{1}{r} \frac{\partial^2 \hat{u}_z}{\partial z \partial \theta} \right] \quad (\theta\text{-mom.})
\end{aligned} \tag{5-132}$$

$$\begin{aligned}
& \rho_0 \left(\frac{\partial \hat{u}_z}{\partial t} + U_r \frac{\partial \hat{u}_z}{\partial r} + \frac{U_\theta}{r} \frac{\partial \hat{u}_z}{\partial \theta} + U_z \frac{\partial \hat{u}_z}{\partial z} + \hat{u}_r \frac{\partial U_z}{\partial r} + \frac{\hat{u}_\theta}{r} \frac{\partial U_z}{\partial \theta} + \hat{u}_z \frac{\partial U_z}{\partial z} \right) + \hat{\rho} \left(\frac{\partial U_z}{\partial t} + U_r \frac{\partial U_z}{\partial r} + \frac{U_\theta}{r} \frac{\partial U_z}{\partial \theta} + U_z \frac{\partial U_z}{\partial z} \right) \\
& = -\frac{\partial \hat{p}}{\partial z} + \frac{\mu}{3} \left[3 \left(\frac{\partial^2 \hat{u}_z}{\partial r^2} + \frac{1}{r} \frac{\partial \hat{u}_z}{\partial r} + \frac{1}{r^2} \frac{\partial^2 \hat{u}_z}{\partial \theta^2} \right) + 4 \frac{\partial^2 \hat{u}_z}{\partial z^2} + \frac{1}{r} \left(\frac{\partial \hat{u}_r}{\partial z} + \frac{\partial^2 \hat{u}_\theta}{\partial \theta \partial z} \right) + \frac{\partial^2 \hat{u}_r}{\partial r \partial z} \right] \quad (z\text{-mom.})
\end{aligned} \tag{5-133}$$

and

$$\begin{aligned}
& \rho_0 c_p \left(\frac{\partial \hat{T}}{\partial t} + U_r \frac{\partial \hat{T}}{\partial r} + \frac{U_\theta}{r} \frac{\partial \hat{T}}{\partial \theta} + U_z \frac{\partial \hat{T}}{\partial z} + \hat{u}_r \frac{\partial T_0}{\partial r} + \frac{\hat{u}_\theta}{r} \frac{\partial T_0}{\partial \theta} + \hat{u}_z \frac{\partial T_0}{\partial z} \right) + \hat{\rho} c_p \left(\frac{\partial T_0}{\partial t} + U_r \frac{\partial T_0}{\partial r} + \frac{U_\theta}{r} \frac{\partial T_0}{\partial \theta} + U_z \frac{\partial T_0}{\partial z} \right) \\
& = \frac{\partial \hat{p}}{\partial t} + U_r \frac{\partial \hat{p}}{\partial r} + \frac{U_\theta}{r} \frac{\partial \hat{p}}{\partial \theta} + U_z \frac{\partial \hat{p}}{\partial z} + \hat{u}_r \frac{\partial P_0}{\partial r} + \frac{\hat{u}_\theta}{r} \frac{\partial P_0}{\partial \theta} + \hat{u}_z \frac{\partial P_0}{\partial z} + \hat{\Phi} + k \left(\frac{\partial^2 \hat{T}}{\partial r^2} + \frac{1}{r} \frac{\partial \hat{T}}{\partial r} + \frac{1}{r^2} \frac{\partial^2 \hat{T}}{\partial \theta^2} + \frac{\partial^2 \hat{T}}{\partial z^2} \right) \quad (\text{energy})
\end{aligned} \tag{5-134}$$

where the cylindrical dissipation function is given by

$$\begin{aligned}
\frac{\hat{\Phi}}{\mu} &= \frac{4}{3} \left[\left(2 \frac{\partial U_r}{\partial r} - \frac{U_r}{r} - \frac{1}{r} \frac{\partial U_\theta}{\partial \theta} - \frac{\partial U_z}{\partial z} \right) \frac{\partial \hat{u}_r}{\partial r} + \left(\frac{2}{r} \frac{\partial U_\theta}{\partial \theta} + 2 \frac{U_r}{r} - \frac{\partial U_r}{\partial r} - \frac{\partial U_z}{\partial z} \right) \left(\frac{\hat{u}_r}{r} + \frac{1}{r} \frac{\partial \hat{u}_\theta}{\partial \theta} \right) + \left(2 \frac{\partial U_z}{\partial z} - \frac{\partial U_r}{\partial r} - \frac{U_r}{r} - \frac{1}{r} \frac{\partial U_\theta}{\partial \theta} \right) \frac{\partial \hat{u}_z}{\partial z} \right] \\
&+ 2 \left\{ \left[\frac{\partial U_\theta}{\partial r} + \frac{1}{r} \left(\frac{\partial U_r}{\partial \theta} - U_\theta \right) \right] \left[\frac{\partial \hat{u}_\theta}{\partial r} + \frac{1}{r} \left(\frac{\partial \hat{u}_r}{\partial \theta} - \hat{u}_\theta \right) \right] + \left(\frac{\partial U_z}{\partial r} + \frac{\partial U_r}{\partial z} \right) \left(\frac{\partial \hat{u}_z}{\partial r} + \frac{\partial \hat{u}_r}{\partial z} \right) + \left(\frac{1}{r} \frac{\partial U_z}{\partial \theta} + \frac{\partial U_\theta}{\partial z} \right) \left(\frac{1}{r} \frac{\partial \hat{u}_z}{\partial \theta} + \frac{\partial \hat{u}_\theta}{\partial z} \right) \right\}
\end{aligned} \tag{5-135}$$

Page 298

Note that the last term in the continuity equation vanishes when the basic flow satisfies $\nabla \cdot \mathbf{V}_0 = 0$. Moreover, the incompressible disturbance equations of the previous section for the Cartesian and cylindrical polar formulations can be readily recovered from [Eqs. \(5-124\)–\(5-127\)](#) and [Eqs. \(5-130\)–\(5-133\)](#), respectively.

5-7.2 Biglobal Expansion and Compressible Eigenvalue Problem Formulation

In order to introduce the biglobal disturbance form, we find it convenient to write

$$\begin{cases} (\hat{\rho}, \hat{u}, \hat{v}, \hat{w}, \hat{T}, \hat{\Phi}) = (\rho, u, v, w, T, \Phi) \exp(\sigma_i t) \exp[i(nz - \sigma_r t)] & \text{(Cartesian)} \\ (\hat{\rho}, \hat{u}_r, \hat{u}_\theta, \hat{u}_z, \hat{T}, \hat{\Phi}) = (\rho, u_r, u_\theta, u_z, T, \Phi) \exp(\sigma_i t) \exp[i(m\theta - \sigma_r t)] & \text{(Cylindrical)} \end{cases} \quad (5-136)$$

where n or m represents the user-specified spanwise or tangential mode number and, as usual, $\sigma = \sigma_r + i \sigma_i$ incorporates both the stability growth rate, σ_i , and the circular frequency, σ_r . Apart from the ideal gas equation, which becomes $p = \rho_0 RT + \rho RT_0$, the biglobal ansatz enables us to transform the linearized disturbance equations, starting with the Cartesian assortment of [Eqs. \(5-124\)–\(5-129\)](#), into

$$\begin{aligned} -i\sigma\rho + \frac{\partial}{\partial x}(\rho_0 u) + \frac{\partial}{\partial y}(\rho_0 v) + \frac{\partial}{\partial z}(\rho_0 w) + U \frac{\partial \rho}{\partial x} + V \frac{\partial \rho}{\partial y} + W \frac{\partial \rho}{\partial z} + \rho \left(\frac{\partial U}{\partial x} + \frac{\partial V}{\partial y} + \frac{\partial W}{\partial z} \right) &= 0 \quad \text{(continuity)} \\ \rho_0 \left(-i\sigma u + U \frac{\partial u}{\partial x} + V \frac{\partial u}{\partial y} + inWu + u \frac{\partial U}{\partial x} + v \frac{\partial U}{\partial y} + w \frac{\partial U}{\partial z} \right) + \rho \left(\frac{\partial U}{\partial t} + U \frac{\partial U}{\partial x} + V \frac{\partial U}{\partial y} + W \frac{\partial U}{\partial z} \right) & \\ = -R \left(\frac{\partial \rho}{\partial x} T_0 + \frac{\partial T_0}{\partial x} \rho + \frac{\partial \rho_0}{\partial x} T + \frac{\partial T}{\partial x} \rho_0 \right) + \frac{\mu}{3} \left(4 \frac{\partial^2 u}{\partial x^2} + 3 \frac{\partial^2 u}{\partial y^2} - 3n^2 u + \frac{\partial^2 v}{\partial x \partial y} + in \frac{\partial w}{\partial x} \right) & \quad \text{(x-mom.)} \end{aligned} \quad (5-137)$$

$$\begin{aligned} \rho_0 \left(-i\sigma v + U \frac{\partial v}{\partial x} + V \frac{\partial v}{\partial y} + inWv + u \frac{\partial V}{\partial x} + v \frac{\partial V}{\partial y} + w \frac{\partial V}{\partial z} \right) + \rho \left(\frac{\partial V}{\partial t} + U \frac{\partial V}{\partial x} + V \frac{\partial V}{\partial y} + W \frac{\partial V}{\partial z} \right) & \\ = -R \left(\frac{\partial \rho}{\partial y} T_0 + \frac{\partial T_0}{\partial y} \rho + \frac{\partial \rho_0}{\partial y} T + \frac{\partial T}{\partial y} \rho_0 \right) + \frac{\mu}{3} \left(3 \frac{\partial^2 v}{\partial x^2} + 4 \frac{\partial^2 v}{\partial y^2} - 3n^2 v + \frac{\partial^2 u}{\partial x \partial y} + in \frac{\partial w}{\partial y} \right) & \quad \text{(y-mom.)} \end{aligned} \quad (5-138)$$

$$\begin{aligned} \rho_0 \left(-i\sigma w + U \frac{\partial w}{\partial x} + V \frac{\partial w}{\partial y} + inWw + u \frac{\partial W}{\partial x} + v \frac{\partial W}{\partial y} + w \frac{\partial W}{\partial z} \right) + \rho \left(\frac{\partial W}{\partial t} + U \frac{\partial W}{\partial x} + V \frac{\partial W}{\partial y} + W \frac{\partial W}{\partial z} \right) & \\ = -R \left(inT_0 \rho + \frac{\partial T_0}{\partial z} \rho + \frac{\partial \rho_0}{\partial z} T + in\rho_0 T \right) + \frac{\mu}{3} \left(3 \frac{\partial^2 w}{\partial x^2} + 3 \frac{\partial^2 w}{\partial y^2} - 4n^2 w + in \frac{\partial u}{\partial x} + in \frac{\partial v}{\partial y} \right) & \quad \text{(z-mom.)} \end{aligned} \quad (5-139)$$

and

$$\begin{aligned} \rho_0 c_p \left(-i\sigma T + U \frac{\partial T}{\partial x} + V \frac{\partial T}{\partial y} + inWT + u \frac{\partial T_0}{\partial x} + v \frac{\partial T_0}{\partial y} + w \frac{\partial T_0}{\partial z} \right) + \rho c_p \left(\frac{\partial T_0}{\partial t} + U \frac{\partial T_0}{\partial x} + V \frac{\partial T_0}{\partial y} + W \frac{\partial T_0}{\partial z} \right) & \\ = R \left(-i\sigma + U \frac{\partial}{\partial x} + V \frac{\partial}{\partial y} \right) (\rho_0 T + T_0 \rho) + RW \left(inT_0 \rho + \frac{\partial T_0}{\partial z} \rho + \frac{\partial \rho_0}{\partial z} T + in\rho_0 T \right) & \\ + u \frac{\partial P_0}{\partial x} + v \frac{\partial P_0}{\partial y} + w \frac{\partial P_0}{\partial z} + \Phi + k \left(\frac{\partial^2 T}{\partial x^2} + \frac{\partial^2 T}{\partial y^2} - n^2 T \right) & \quad \text{(energy)} \end{aligned} \quad (5-140)$$

where

$$\begin{aligned} \frac{\Phi}{\mu} = \frac{4}{3} \left[\left(2 \frac{\partial U}{\partial x} - \frac{\partial V}{\partial y} - \frac{\partial W}{\partial z} \right) \frac{\partial u}{\partial x} + \left(2 \frac{\partial V}{\partial y} - \frac{\partial U}{\partial x} - \frac{\partial W}{\partial z} \right) \frac{\partial v}{\partial y} + \left(2 \frac{\partial W}{\partial z} - \frac{\partial U}{\partial x} - \frac{\partial V}{\partial y} \right) inw \right] & \\ + 2 \left[\left(\frac{\partial U}{\partial y} + \frac{\partial V}{\partial x} \right) \left(\frac{\partial u}{\partial y} + \frac{\partial v}{\partial x} \right) + \left(\frac{\partial U}{\partial z} + \frac{\partial W}{\partial x} \right) \left(inu + \frac{\partial w}{\partial x} \right) + \left(\frac{\partial V}{\partial z} + \frac{\partial W}{\partial y} \right) \left(inv + \frac{\partial w}{\partial y} \right) \right] & \quad \text{(dissipation)} \end{aligned} \quad (5-141)$$

Similarly, using cylindrical polar coordinates, [Eqs. \(5-130\)–\(5-135\)](#) simplify into

$$\begin{aligned}
 -i\sigma\rho + u_r \frac{\partial\rho_0}{\partial r} + \frac{u_\theta}{r} \frac{\partial\rho_0}{\partial\theta} + u_z \frac{\partial\rho_0}{\partial z} + U_r \frac{\partial\rho}{\partial r} + \frac{im}{r} U_\theta \rho + U_z \frac{\partial\rho}{\partial z} + \rho_0 \left(\frac{\partial u_r}{\partial r} + \frac{u_r}{r} + \frac{im}{r} u_\theta + \frac{\partial u_z}{\partial z} \right) \\
 + \rho \left(\frac{\partial U_r}{\partial r} + \frac{U_r}{r} + \frac{1}{r} \frac{\partial U_\theta}{\partial\theta} + \frac{\partial U_z}{\partial z} \right) = 0 \quad (\text{continuity})
 \end{aligned} \tag{5-143}$$

$$\begin{aligned}
 \rho_0 \left(-i\sigma u_r + U_r \frac{\partial u_r}{\partial r} + \frac{im}{r} U_\theta u_r + U_z \frac{\partial u_r}{\partial z} - \frac{2U_\theta u_\theta}{r} + u_r \frac{\partial U_r}{\partial r} + \frac{u_\theta}{r} \frac{\partial U_r}{\partial\theta} + u_z \frac{\partial U_r}{\partial z} \right) \\
 + \rho \left(\frac{\partial U_r}{\partial t} + U_r \frac{\partial U_r}{\partial r} + \frac{U_\theta}{r} \frac{\partial U_r}{\partial\theta} + U_z \frac{\partial U_r}{\partial z} - \frac{U_\theta^2}{r} \right) = -R \left(\frac{\partial\rho}{\partial r} T_0 + \frac{\partial T_0}{\partial r} \rho + \frac{\partial\rho_0}{\partial r} T + \frac{\partial T}{\partial r} \rho_0 \right) \\
 + \frac{\mu}{3} \left[4 \left(\frac{\partial^2 u_r}{\partial r^2} + \frac{1}{r} \frac{\partial u_r}{\partial r} - \frac{u_r}{r^2} \right) + 3 \left(\frac{\partial^2 u_r}{\partial z^2} - \frac{m^2}{r^2} u_r \right) - 7 \frac{im}{r^2} u_\theta + \frac{im}{r} \frac{\partial u_\theta}{\partial r} + \frac{\partial^2 u_z}{\partial r \partial z} \right] \quad (r\text{-mom.})
 \end{aligned} \tag{5-144}$$

$$\begin{aligned}
 \rho_0 \left(-i\sigma u_\theta + U_r \frac{\partial u_\theta}{\partial r} + \frac{im}{r} U_\theta u_\theta + U_z \frac{\partial u_\theta}{\partial z} + \frac{U_r u_\theta}{r} + \frac{u_r U_\theta}{r} + u_r \frac{\partial U_\theta}{\partial r} + \frac{u_\theta}{r} \frac{\partial U_\theta}{\partial\theta} + u_z \frac{\partial U_\theta}{\partial z} \right) \\
 + \rho \left(\frac{\partial U_\theta}{\partial t} + U_r \frac{\partial U_\theta}{\partial r} + \frac{U_\theta}{r} \frac{\partial U_\theta}{\partial\theta} + U_z \frac{\partial U_\theta}{\partial z} + \frac{U_r U_\theta}{r} \right) = -\frac{R}{r} \left(im T_0 \rho + \frac{\partial T_0}{\partial\theta} \rho + \frac{\partial\rho_0}{\partial\theta} T + im \rho_0 T \right) \\
 + \frac{\mu}{3} \left[3 \left(\frac{\partial^2 u_\theta}{\partial r^2} + \frac{1}{r} \frac{\partial u_\theta}{\partial r} - \frac{u_\theta}{r^2} + \frac{\partial^2 u_\theta}{\partial z^2} \right) - \frac{4m^2}{r^2} u_\theta + 7 \frac{im}{r^2} u_r + \frac{im}{r} \frac{\partial u_r}{\partial r} + \frac{im}{r} \frac{\partial u_z}{\partial z} \right] \quad (\theta\text{-mom.})
 \end{aligned} \tag{5-145}$$

$$\begin{aligned}
 \rho_0 \left(-\sigma u_z + U_r \frac{\partial u_z}{\partial r} + \frac{im}{r} U_\theta u_z + U_z \frac{\partial u_z}{\partial z} + u_r \frac{\partial U_z}{\partial r} + \frac{u_\theta}{r} \frac{\partial U_z}{\partial\theta} + u_z \frac{\partial U_z}{\partial z} \right) \\
 + \rho \left(\frac{\partial U_z}{\partial t} + U_r \frac{\partial U_z}{\partial r} + \frac{U_\theta}{r} \frac{\partial U_z}{\partial\theta} + U_z \frac{\partial U_z}{\partial z} \right) = -R \left(\frac{\partial\rho}{\partial z} T_0 + \frac{\partial T_0}{\partial z} \rho + \frac{\partial\rho_0}{\partial z} T + \frac{\partial T}{\partial z} \rho_0 \right) \\
 + \frac{\mu}{3} \left[3 \left(\frac{\partial^2 u_z}{\partial r^2} + \frac{1}{r} \frac{\partial u_z}{\partial r} - \frac{m^2}{r^2} u_z \right) + 4 \frac{\partial^2 u_z}{\partial z^2} + \frac{1}{r} \left(\frac{\partial u_r}{\partial z} + im \frac{\partial u_\theta}{\partial z} \right) + \frac{\partial^2 u_r}{\partial r \partial z} \right] \quad (z\text{-mom.})
 \end{aligned} \tag{5-146}$$

and

$$\begin{aligned}
 \rho_0 c_p \left(-i\sigma T + U_r \frac{\partial T}{\partial r} + \frac{im}{r} U_\theta T + U_z \frac{\partial T}{\partial z} + u_r \frac{\partial T_0}{\partial r} + \frac{u_\theta}{r} \frac{\partial T_0}{\partial\theta} + u_z \frac{\partial T_0}{\partial z} \right) + \rho c_p \left(\frac{\partial T_0}{\partial t} + U_r \frac{\partial T_0}{\partial r} + \frac{U_\theta}{r} \frac{\partial T_0}{\partial\theta} + U_z \frac{\partial T_0}{\partial z} \right) \\
 = R \left(-i\sigma + U_r \frac{\partial}{\partial r} + U_z \frac{\partial}{\partial z} \right) (\rho_0 T + T_0 \rho) + R \frac{U_\theta}{r} \left(im T_0 \rho + \frac{\partial T_0}{\partial\theta} \rho + im \rho_0 T + \frac{\partial\rho_0}{\partial\theta} T \right) \\
 + u_r \frac{\partial P_0}{\partial r} + \frac{u_\theta}{r} \frac{\partial P_0}{\partial\theta} + u_z \frac{\partial P_0}{\partial z} + \Phi + k \left(\frac{\partial^2 T}{\partial r^2} + \frac{1}{r} \frac{\partial T}{\partial r} - \frac{m^2}{r^2} T + \frac{\partial^2 T}{\partial z^2} \right) \quad (\text{energy})
 \end{aligned} \tag{5-147}$$

where the dissipation function may be evaluated from

$$\begin{aligned}
 \frac{\Phi}{\mu} = \frac{4}{3} \left[\left(2 \frac{\partial U_r}{\partial r} - \frac{U_r}{r} - \frac{1}{r} \frac{\partial U_\theta}{\partial\theta} - \frac{\partial U_z}{\partial z} \right) \frac{\partial u_r}{\partial r} + \frac{u_r}{r} \left(\frac{2}{r} \frac{\partial U_\theta}{\partial\theta} + \frac{2U_r}{r} - \frac{\partial U_r}{\partial r} - \frac{\partial U_z}{\partial z} \right) + \left(2 \frac{\partial U_z}{\partial z} - \frac{\partial U_r}{\partial r} - \frac{U_r}{r} - \frac{1}{r} \frac{\partial U_\theta}{\partial\theta} \right) \frac{\partial u_z}{\partial z} \right] \\
 + 2 \left[\left(\frac{\partial U_\theta}{\partial r} + \frac{1}{r} \frac{\partial U_r}{\partial\theta} - \frac{U_\theta}{r} \right) \left(\frac{\partial u_\theta}{\partial r} + \frac{im u_r - u_\theta}{r} \right) + \left(\frac{\partial U_z}{\partial r} + \frac{\partial U_r}{\partial z} \right) \left(\frac{\partial u_z}{\partial r} + \frac{\partial u_r}{\partial z} \right) + \left(\frac{1}{r} \frac{\partial U_z}{\partial\theta} + \frac{\partial U_\theta}{\partial z} \right) \left(\frac{im}{r} u_z + \frac{\partial u_\theta}{\partial z} \right) \right]
 \end{aligned} \tag{5-148}$$

Here too, the incompressible set of disturbance equations given by [Eqs. \(5-82\)–\(5-85\)](#) as well as [Eqs. \(5-86\)–\(5-89\)](#) may be restored from their compressible counterparts embodied within [Eqs. \(5-137\)–\(5-140\)](#) and [Eqs. \(5-143\)–\(5-146\)](#), respectively.

At this stage, it is helpful to regroup the foregoing relations in operator form starting with [Eqs. \(5-137\)–\(5-142\)](#); these can be rearranged into

$$\begin{aligned} & \left(\frac{\partial U}{\partial x} + \frac{\partial V}{\partial y} + \frac{\partial W}{\partial z} + U \frac{\partial}{\partial x} + V \frac{\partial}{\partial y} + inW \right) \rho \\ & + \left(\frac{\partial \rho_0}{\partial x} + \rho_0 \frac{\partial}{\partial x} \right) u + \left(\frac{\partial \rho_0}{\partial y} + \rho_0 \frac{\partial}{\partial y} \right) v + \left(\frac{\partial \rho_0}{\partial z} + in \rho_0 \right) w = (i\sigma) \rho \end{aligned} \quad \text{(continuity)} \quad (5-149)$$

$$\begin{aligned} & \left[\left(\frac{\partial U}{\partial t} + U \frac{\partial U}{\partial x} + V \frac{\partial U}{\partial y} + W \frac{\partial U}{\partial z} \right) \frac{1}{\rho_0} + \frac{R}{\rho_0} \frac{\partial T_0}{\partial x} + \frac{R T_0}{\rho_0} \frac{\partial}{\partial x} \right] \rho + \left[\frac{\partial U}{\partial x} + U \frac{\partial}{\partial x} + V \frac{\partial}{\partial y} + inW - \frac{\mu}{\rho_0} \left(\frac{4}{3} \frac{\partial^2}{\partial x^2} + \frac{\partial^2}{\partial y^2} - n^2 \right) \right] u \\ & + \left(\frac{\partial U}{\partial y} - \frac{\mu}{3 \rho_0} \frac{\partial^2}{\partial x \partial y} \right) v + \left(\frac{\partial U}{\partial z} - \frac{in \mu}{3 \rho_0} \frac{\partial}{\partial x} \right) w + \left(R \frac{\partial}{\partial x} + \frac{R}{\rho_0} \frac{\partial \rho_0}{\partial x} \right) T = (i\sigma) u \end{aligned} \quad \text{(x-mom.)} \quad (5-150)$$

$$\begin{aligned} & \left[\frac{1}{\rho_0} \left(\frac{\partial V}{\partial t} + U \frac{\partial V}{\partial x} + V \frac{\partial V}{\partial y} + W \frac{\partial V}{\partial z} \right) + \frac{R T_0}{\rho_0} \frac{\partial}{\partial y} + \frac{R}{\rho_0} \frac{\partial T_0}{\partial y} \right] \rho + \left(\frac{\partial V}{\partial x} - \frac{\mu}{3 \rho_0} \frac{\partial^2}{\partial x \partial y} \right) u \\ & + \left[\frac{\partial V}{\partial y} + U \frac{\partial}{\partial x} + V \frac{\partial}{\partial y} + inW - \frac{\mu}{\rho_0} \left(\frac{\partial^2}{\partial x^2} + \frac{4}{3} \frac{\partial^2}{\partial y^2} - n^2 \right) \right] v + \left(\frac{\partial V}{\partial z} - \frac{in \mu}{3 \rho_0} \frac{\partial}{\partial y} \right) w + \left(\frac{R}{\rho_0} \frac{\partial \rho_0}{\partial y} + R \frac{\partial}{\partial y} \right) T = (i\sigma) v \end{aligned} \quad \text{(y-mom.)} \quad (5-151)$$

$$\begin{aligned} & \left[\frac{1}{\rho_0} \left(\frac{\partial W}{\partial t} + U \frac{\partial W}{\partial x} + V \frac{\partial W}{\partial y} + W \frac{\partial W}{\partial z} \right) + \frac{R}{\rho_0} \left(in T_0 + \frac{\partial T_0}{\partial z} \right) \right] \rho + \left(\frac{\partial W}{\partial x} - \frac{in \mu}{3 \rho_0} \frac{\partial}{\partial x} \right) u + \left(\frac{\partial W}{\partial y} - \frac{in \mu}{3 \rho_0} \frac{\partial}{\partial y} \right) v \\ & + \left[\frac{\partial W}{\partial z} + U \frac{\partial}{\partial x} + V \frac{\partial}{\partial y} + inW - \frac{\mu}{\rho_0} \left(\frac{\partial^2}{\partial x^2} + \frac{\partial^2}{\partial y^2} - \frac{4}{3} n^2 \right) \right] w + R \left(in + \frac{1}{\rho_0} \frac{\partial \rho_0}{\partial z} \right) T = (i\sigma) w \end{aligned} \quad \text{(z-mom.)} \quad (5-152)$$

and

$$\begin{aligned} & \left[c_p \frac{\partial T_0}{\partial t} + c_v \left(U \frac{\partial T_0}{\partial x} + V \frac{\partial T_0}{\partial y} + W \frac{\partial T_0}{\partial z} \right) - R T_0 \left(U \frac{\partial}{\partial x} + V \frac{\partial}{\partial y} + inW \right) \right] \rho + \left(\rho_0 c_p \frac{\partial T_0}{\partial x} - \frac{\partial P_0}{\partial x} - \Phi_u \right) u \\ & + \left(\rho_0 c_p \frac{\partial T_0}{\partial y} - \frac{\partial P_0}{\partial y} - \Phi_v \right) v + \left(\rho_0 c_p \frac{\partial T_0}{\partial z} - \frac{\partial P_0}{\partial z} - \Phi_w \right) w + \left[\rho_0 c_v \left(U \frac{\partial}{\partial x} + V \frac{\partial}{\partial y} + inW \right) \right. \\ & \left. - R \left(U \frac{\partial \rho_0}{\partial x} + V \frac{\partial \rho_0}{\partial y} + W \frac{\partial \rho_0}{\partial z} \right) - k \left(\frac{\partial^2}{\partial x^2} + \frac{\partial^2}{\partial y^2} - n^2 \right) \right] T = (i\sigma) (\rho_0 c_v T - R T_0 \rho) \end{aligned} \quad \text{(energy)} \quad (5-153)$$

where

$$\begin{aligned} \Phi_u &= 2\mu \left[\frac{2}{3} \left(2 \frac{\partial U}{\partial x} - \frac{\partial V}{\partial y} - \frac{\partial W}{\partial z} \right) \frac{\partial}{\partial x} + \left(\frac{\partial U}{\partial y} + \frac{\partial V}{\partial x} \right) \frac{\partial}{\partial y} + in \left(\frac{\partial U}{\partial z} + \frac{\partial W}{\partial x} \right) \right] \\ \Phi_v &= 2\mu \left[\frac{2}{3} \left(2 \frac{\partial V}{\partial y} - \frac{\partial U}{\partial x} - \frac{\partial W}{\partial z} \right) \frac{\partial}{\partial y} + \left(\frac{\partial U}{\partial y} + \frac{\partial V}{\partial x} \right) \frac{\partial}{\partial x} + in \left(\frac{\partial V}{\partial z} + \frac{\partial W}{\partial y} \right) \right] \\ \Phi_w &= 2\mu \left[\frac{2in}{3} \left(2 \frac{\partial W}{\partial z} - \frac{\partial U}{\partial x} - \frac{\partial V}{\partial y} \right) + \left(\frac{\partial U}{\partial z} + \frac{\partial W}{\partial x} \right) \frac{\partial}{\partial x} + \left(\frac{\partial V}{\partial z} + \frac{\partial W}{\partial y} \right) \frac{\partial}{\partial y} \right] \end{aligned} \quad (5-154)$$

Similarly, the operators in the cylindrical polar [Eqs. \(5-143\)–\(5-148\)](#) may be collected and segregated into

$$\left(\frac{\partial U_r}{\partial r} + \frac{U_r}{r} + \frac{1}{r} \frac{\partial U_\theta}{\partial \theta} + \frac{\partial U_z}{\partial z} + U_r \frac{\partial}{\partial r} + \frac{im}{r} U_\theta + U_z \frac{\partial}{\partial z}\right) \rho \quad (5-155)$$

$$+ \left[\frac{\partial \rho_0}{\partial r} + \rho_0 \left(\frac{\partial}{\partial r} + \frac{1}{r} \right) \right] u_r + \frac{1}{r} \left(\frac{\partial \rho_0}{\partial \theta} + im \rho_0 \right) u_\theta + \left(\frac{\partial \rho_0}{\partial z} + \rho_0 \frac{\partial}{\partial z} \right) u_z = i \sigma \rho \quad (\text{continuity})$$

$$\begin{aligned} & \left[\left(\frac{\partial U_r}{\partial t} + U_r \frac{\partial U_r}{\partial r} + \frac{U_\theta}{r} \frac{\partial U_r}{\partial \theta} + U_z \frac{\partial U_r}{\partial z} - \frac{U_\theta^2}{r} \right) + R \left(\frac{\partial T_0}{\partial r} + T_0 \frac{\partial}{\partial r} \right) \right] \rho \\ & + \left\{ \rho_0 \left(U_r \frac{\partial}{\partial r} + im \frac{U_\theta}{r} + U_z \frac{\partial}{\partial z} + \frac{\partial U_r}{\partial r} \right) - \mu \left[\frac{4}{3} \left(\frac{\partial^2}{\partial r^2} + \frac{1}{r} \frac{\partial}{\partial r} - \frac{1}{r^2} \right) + \left(\frac{\partial^2}{\partial z^2} - \frac{m^2}{r^2} \right) \right] \right\} u_r \\ & + \left[\frac{\rho_0}{r} \left(\frac{\partial U_r}{\partial \theta} - 2 U_\theta \right) - \frac{im\mu}{3r} \left(\frac{\partial}{\partial r} - \frac{7}{r} \right) \right] u_\theta + \left(\rho_0 \frac{\partial U_r}{\partial z} - \frac{\mu}{3} \frac{\partial^2}{\partial r \partial z} \right) u_z + R \left(\frac{\partial \rho_0}{\partial r} + \rho_0 \frac{\partial}{\partial r} \right) T = i \rho_0 \sigma u_r \quad (r\text{-mom.}) \end{aligned} \quad (5-156)$$

$$\begin{aligned} & \left[\left(\frac{\partial U_\theta}{\partial t} + U_r \frac{\partial U_\theta}{\partial r} + \frac{U_\theta}{r} \frac{\partial U_\theta}{\partial \theta} + U_z \frac{\partial U_\theta}{\partial z} + \frac{U_r U_\theta}{r} \right) + \frac{R}{r} \left(im T_0 + \frac{\partial T_0}{\partial \theta} \right) \right] \rho + \left[\rho_0 \left(\frac{U_\theta}{r} + \frac{\partial U_\theta}{\partial r} \right) - \frac{im\mu}{3r} \left(\frac{7}{r} + \frac{\partial}{\partial r} \right) \right] u_r \\ & + \left[\rho_0 \left(U_r \frac{\partial}{\partial r} + \frac{im U_\theta}{r} + U_z \frac{\partial}{\partial z} + \frac{1}{r} \frac{\partial U_\theta}{\partial \theta} \right) - \mu \left(\frac{\partial^2}{\partial r^2} + \frac{1}{r} \frac{\partial}{\partial r} - \frac{1}{r^2} + \frac{\partial^2}{\partial z^2} - \frac{4m^2}{3r^2} \right) \right] u_\theta \\ & + \left(\rho_0 \frac{\partial U_\theta}{\partial z} - \frac{im\mu}{3r} \frac{\partial}{\partial z} \right) u_z + \frac{R}{r} \left(im \rho_0 + \frac{\partial \rho_0}{\partial \theta} \right) T = i \rho_0 \sigma u_\theta \quad (\theta\text{-mom.}) \end{aligned} \quad (5-157)$$

$$\begin{aligned} & \left[\left(\frac{\partial U_z}{\partial t} + U_r \frac{\partial U_z}{\partial r} + \frac{U_\theta}{r} \frac{\partial U_z}{\partial \theta} + U_z \frac{\partial U_z}{\partial z} \right) + R \left(\frac{\partial T_0}{\partial z} + T_0 \frac{\partial}{\partial z} \right) \right] \rho + \left[\rho_0 \frac{\partial U_z}{\partial r} - \frac{\mu}{3} \left(\frac{1}{r} \frac{\partial}{\partial z} + \frac{\partial^2}{\partial r \partial z} \right) \right] u_r + \left(\frac{\rho_0}{r} \frac{\partial U_z}{\partial \theta} - \frac{im\mu}{3r} \frac{\partial}{\partial z} \right) u_\theta \\ & + \left[\rho_0 \left(U_r \frac{\partial}{\partial r} + \frac{im}{r} U_\theta + U_z \frac{\partial}{\partial z} + \frac{\partial U_z}{\partial z} \right) - \mu \left(\frac{\partial^2}{\partial r^2} + \frac{1}{r} \frac{\partial}{\partial r} - \frac{m^2}{r^2} + \frac{4}{3} \frac{\partial^2}{\partial z^2} \right) \right] u_z \\ & + R \left(\frac{\partial \rho_0}{\partial z} + \rho_0 \frac{\partial}{\partial z} \right) T = i \rho_0 \sigma u_z \quad (z\text{-mom.}) \end{aligned} \quad (5-158)$$

$$\begin{aligned} & \left[c_p \frac{\partial T_0}{\partial t} + c_v \left(U_r \frac{\partial T_0}{\partial r} + \frac{U_\theta}{r} \frac{\partial T_0}{\partial \theta} + U_z \frac{\partial T_0}{\partial z} \right) - R T_0 \left(U_r \frac{\partial}{\partial r} + U_z \frac{\partial}{\partial z} + \frac{im}{r} U_\theta \right) \right] \rho + \left(\rho_0 c_p \frac{\partial T_0}{\partial r} - \frac{\partial P_0}{\partial r} - \Phi_r \right) u_r \\ & + \left(\frac{\rho_0 c_p}{r} \frac{\partial T_0}{\partial \theta} - \frac{1}{r} \frac{\partial P_0}{\partial \theta} - \Phi_\theta \right) u_\theta + \left(\rho_0 c_p \frac{\partial T_0}{\partial z} - \frac{\partial P_0}{\partial z} - \Phi_z \right) u_z \\ & + \left[\rho_0 c_v \left(U_r \frac{\partial}{\partial r} + \frac{im}{r} U_\theta + U_z \frac{\partial}{\partial z} \right) - R \left(U_r \frac{\partial \rho_0}{\partial r} + U_z \frac{\partial \rho_0}{\partial z} + \frac{U_\theta}{r} \frac{\partial \rho_0}{\partial \theta} \right) - k \left(\frac{\partial^2}{\partial r^2} + \frac{1}{r} \frac{\partial}{\partial r} - \frac{m^2}{r^2} + \frac{\partial^2}{\partial z^2} \right) \right] T \\ & = i \sigma (\rho_0 c_v T - R T_0 \rho) \quad (\text{energy}) \end{aligned} \quad (5-159)$$

where the three arms of the dissipation function may be calculated using

$$\begin{aligned} \frac{\Phi_r}{\mu} = & \frac{4}{3} \left[\left(2 \frac{\partial U_r}{\partial r} - \frac{U_r}{r} - \frac{1}{r} \frac{\partial U_\theta}{\partial \theta} - \frac{\partial U_z}{\partial z} \right) \frac{\partial}{\partial r} + \frac{1}{r} \left(2 \frac{\partial U_\theta}{\partial \theta} + 2 \frac{U_r}{r} - \frac{\partial U_r}{\partial r} - \frac{\partial U_z}{\partial z} \right) \right] \\ & + 2 \left[\frac{im}{r} \left(\frac{\partial U_\theta}{\partial r} + \frac{1}{r} \frac{\partial U_r}{\partial \theta} - \frac{U_\theta}{r} \right) + \left(\frac{\partial U_z}{\partial r} + \frac{\partial U_r}{\partial z} \right) \frac{\partial}{\partial z} \right] \end{aligned}$$

$$\frac{\Phi_\theta}{\mu} = \frac{4im}{3r} \left(\frac{2}{r} \frac{\partial U_\theta}{\partial \theta} + 2 \frac{U_r}{r} - \frac{\partial U_r}{\partial r} - \frac{\partial U_z}{\partial z} \right) + 2 \left[\left(\frac{\partial U_\theta}{\partial r} + \frac{1}{r} \frac{\partial U_r}{\partial \theta} - \frac{U_\theta}{r} \right) \left(\frac{\partial}{\partial r} - \frac{1}{r} \right) + \left(\frac{1}{r} \frac{\partial U_z}{\partial \theta} + \frac{\partial U_\theta}{\partial z} \right) \frac{\partial}{\partial z} \right] \quad (5-160)$$

$$\frac{\Phi_z}{\mu} = \frac{4}{3} \left(2 \frac{\partial U_z}{\partial z} - \frac{\partial U_r}{\partial r} - \frac{U_r}{r} - \frac{1}{r} \frac{\partial U_\theta}{\partial \theta} \right) \frac{\partial}{\partial z} + 2 \left[\left(\frac{\partial U_z}{\partial r} + \frac{\partial U_r}{\partial z} \right) \frac{\partial}{\partial r} + \frac{im}{r} \left(\frac{1}{r} \frac{\partial U_z}{\partial \theta} + \frac{\partial U_\theta}{\partial z} \right) \right]$$

Page 302

The ensuing system of PDEs in each coordinate system comprises six equations with six unknowns. However, since the pressure can be linearly related to the temperature and density through the ideal gas equation, it may be entirely eliminated from the momentum and energy equations. This leaves us with five equations with the five remaining scalar variables (i.e., the density, the three velocity components, and the temperature). The corresponding PDEs may be rendered in operator form and written as a generalized eigenvalue problem of the type $A_{ij} f_i = \sigma B_{ij} f_i$, where, as before, σ and f_i represent the eigenvalue and eigenvector, while A_{ij} and B_{ij} refer to the operator matrices. Each operator matrix may be further subdivided into individual sets that contain the coefficients of the five dependent variables. In this manner, each subset will supply the multipliers at every grid point as shown in the illustrative matrix diagram below:

$$\text{Cartesian: } A_{ij} = \begin{bmatrix} A_{c,\rho} & A_{c,u} & A_{c,v} & A_{c,w} & A_{c,T} \\ A_{x,\rho} & A_{x,u} & A_{x,v} & A_{x,w} & A_{x,T} \\ A_{y,\rho} & A_{y,u} & A_{y,v} & A_{y,w} & A_{y,T} \\ A_{z,\rho} & A_{z,u} & A_{z,v} & A_{z,w} & A_{z,T} \\ A_{e,\rho} & A_{e,u} & A_{e,v} & A_{e,w} & A_{e,T} \end{bmatrix} \begin{matrix} \rightarrow \text{continuity} \\ \rightarrow x\text{-momentum} \\ \rightarrow y\text{-momentum} \\ \rightarrow z\text{-momentum} \\ \rightarrow \text{energy} \end{matrix} \quad B_{ij} = \begin{bmatrix} B_{c,\rho} & B_{c,u} & B_{c,v} & B_{c,w} & B_{c,T} \\ B_{x,\rho} & B_{x,u} & B_{x,v} & B_{x,w} & B_{x,T} \\ B_{y,\rho} & B_{y,u} & B_{y,v} & B_{y,w} & B_{y,T} \\ B_{z,\rho} & B_{z,u} & B_{z,v} & B_{z,w} & B_{z,T} \\ B_{e,\rho} & B_{e,u} & B_{e,v} & B_{e,w} & B_{e,T} \end{bmatrix} \quad (5-161)$$

$$\text{Cylindric: } A_{ij} = \begin{bmatrix} A_{c,\rho} & A_{c,u_r} & A_{c,u_\theta} & A_{c,u_z} & A_{c,T} \\ A_{r,\rho} & A_{r,u_r} & A_{r,u_\theta} & A_{r,u_z} & A_{r,T} \\ A_{\theta,\rho} & A_{\theta,u_r} & A_{\theta,u_\theta} & A_{\theta,u_z} & A_{\theta,T} \\ A_{z,\rho} & A_{z,u_r} & A_{z,u_\theta} & A_{z,u_z} & A_{z,T} \\ A_{e,\rho} & A_{e,u_r} & A_{e,u_\theta} & A_{e,u_z} & A_{e,T} \end{bmatrix} \begin{matrix} \rightarrow \text{continuity} \\ \rightarrow r\text{-momentum} \\ \rightarrow \theta\text{-momentum} \\ \rightarrow z\text{-momentum} \\ \rightarrow \text{energy} \end{matrix} \quad B_{ij} = \begin{bmatrix} B_{c,\rho} & B_{c,u_r} & B_{c,u_\theta} & B_{c,u_z} & B_{c,T} \\ B_{r,\rho} & B_{r,u_r} & B_{r,u_\theta} & B_{r,u_z} & B_{r,T} \\ B_{\theta,\rho} & B_{\theta,u_r} & B_{\theta,u_\theta} & B_{\theta,u_z} & B_{\theta,T} \\ B_{z,\rho} & B_{z,u_r} & B_{z,u_\theta} & B_{z,u_z} & B_{z,T} \\ B_{e,\rho} & B_{e,u_r} & B_{e,u_\theta} & B_{e,u_z} & B_{e,T} \end{bmatrix} \quad (5-162)$$

For instance, when using $N \times N$ collocation points, the operator matrices A_{ij} and B_{ij} will contain $5 N 2 \times 5 N 2 = 25 N 4$ elements, because an $N 2$ block matrix may be generated for each of the five variables (columns) and equations (rows). In three-dimensional space, assuming that only five equations are being solved in the five unknown variables, such as (ρ, u, v, w, T) , the matrix size becomes $5 N 3 \times 5 N 3 = 25 N^6$. Presently, adopting a stencil of 40 or 60 points in two-dimensional space will entail the progressive use of 64 and 324 million elements. Then, given the improved speed and memory allocations of available computational resources, one may use the QZ algorithm, instead of Arnoldi's, and solve the resulting eigenvalue problem at increasing values of N . This can be carried out to ensure that reported results are grid independent.

Based on [Eqs. \(5-149\)–\(5-154\)](#), the Cartesian operator matrices can be generated using

$$\begin{aligned}
& \left\{ \begin{aligned} A_{c,p} &= \frac{\partial U}{\partial x} + \frac{\partial V}{\partial y} + \frac{\partial W}{\partial z} + U \frac{\partial}{\partial x} + V \frac{\partial}{\partial y} + inW \\ A_{x,p} &= \frac{1}{\rho_0} \left(\frac{\partial U}{\partial t} + U \frac{\partial U}{\partial x} + V \frac{\partial U}{\partial y} + W \frac{\partial U}{\partial z} \right) + \frac{R}{\rho_0} \left(\frac{\partial T_0}{\partial x} + T_0 \frac{\partial}{\partial x} \right) \\ A_{y,p} &= \frac{1}{\rho_0} \left(\frac{\partial V}{\partial t} + U \frac{\partial V}{\partial x} + V \frac{\partial V}{\partial y} + W \frac{\partial V}{\partial z} \right) + \frac{R}{\rho_0} \left(\frac{\partial T_0}{\partial y} + T_0 \frac{\partial}{\partial y} \right) \\ A_{z,p} &= \frac{1}{\rho_0} \left(\frac{\partial W}{\partial t} + U \frac{\partial W}{\partial x} + V \frac{\partial W}{\partial y} + W \frac{\partial W}{\partial z} \right) + \frac{R}{\rho_0} \left(\frac{\partial T_0}{\partial z} + inT_0 \right) \\ A_{e,p} &= c_p \frac{\partial T_0}{\partial t} + c_v \left(U \frac{\partial T_0}{\partial x} + V \frac{\partial T_0}{\partial y} + W \frac{\partial T_0}{\partial z} \right) \\ &\quad - RT_0 \left(U \frac{\partial}{\partial x} + V \frac{\partial}{\partial y} + inW \right) \end{aligned} \right. & \left\{ \begin{aligned} A_{c,u} &= \frac{\partial \rho_0}{\partial x} + \rho_0 \frac{\partial}{\partial x} \\ A_{x,u} &= \frac{\partial U}{\partial x} + U \frac{\partial}{\partial x} + V \frac{\partial}{\partial y} + inW \\ &\quad - \frac{\mu}{\rho_0} \left(\frac{4}{3} \frac{\partial^2}{\partial x^2} + \frac{\partial^2}{\partial y^2} - n^2 \right) \\ A_{y,u} &= \frac{\partial V}{\partial x} - \frac{\mu}{3\rho_0} \frac{\partial^2}{\partial x \partial y} \\ A_{z,u} &= \frac{\partial W}{\partial x} - \frac{in\mu}{3\rho_0} \frac{\partial}{\partial x} \\ A_{e,u} &= \rho_0 c_p \frac{\partial T_0}{\partial x} - \frac{\partial P_0}{\partial x} - \Phi_u \end{aligned} \right. \\
& \left\{ \begin{aligned} A_{c,v} &= \frac{\partial \rho_0}{\partial y} + \rho_0 \frac{\partial}{\partial y} \\ A_{x,v} &= \frac{\partial U}{\partial y} - \frac{\mu}{3\rho_0} \frac{\partial^2}{\partial x \partial y} \\ A_{y,v} &= \frac{\partial V}{\partial y} + U \frac{\partial}{\partial x} + V \frac{\partial}{\partial y} + inW \\ &\quad - \frac{\mu}{\rho_0} \left(\frac{\partial^2}{\partial x^2} + \frac{4}{3} \frac{\partial^2}{\partial y^2} - n^2 \right) \\ A_{z,v} &= \frac{\partial W}{\partial y} - \frac{in\mu}{3\rho_0} \frac{\partial}{\partial y} \\ A_{e,v} &= \rho_0 c_p \frac{\partial T_0}{\partial y} - \frac{\partial P_0}{\partial y} - \Phi_v \end{aligned} \right. & \left\{ \begin{aligned} A_{c,w} &= \frac{\partial \rho_0}{\partial z} + in\rho_0 \\ A_{x,w} &= \frac{\partial U}{\partial z} - \frac{in\mu}{3\rho_0} \frac{\partial}{\partial x} \\ A_{y,w} &= \frac{\partial V}{\partial z} - \frac{in\mu}{3\rho_0} \frac{\partial}{\partial y} \\ A_{z,w} &= \frac{\partial W}{\partial z} + U \frac{\partial}{\partial x} + V \frac{\partial}{\partial y} + inW \\ &\quad - \frac{\mu}{\rho_0} \left(\frac{\partial^2}{\partial x^2} + \frac{\partial^2}{\partial y^2} - \frac{4n^2}{3} \right) \\ A_{e,w} &= \rho_0 c_p \frac{\partial T_0}{\partial z} - \frac{\partial P_0}{\partial z} - \Phi_w \end{aligned} \right. & \left\{ \begin{aligned} A_{c,T} &= 0 \quad A_{x,T} = R \frac{\partial}{\partial x} + \frac{R}{\rho_0} \frac{\partial \rho_0}{\partial x} \\ A_{y,T} &= R \frac{\partial}{\partial y} + \frac{R}{\rho_0} \frac{\partial \rho_0}{\partial y} \\ A_{z,T} &= inR + \frac{R}{\rho_0} \frac{\partial \rho_0}{\partial z} \\ A_{e,T} &= \rho_0 c_v \left(U \frac{\partial}{\partial x} + V \frac{\partial}{\partial y} + inW \right) \\ &\quad - k \left(\frac{\partial^2}{\partial x^2} + \frac{\partial^2}{\partial y^2} - n^2 \right) \\ &\quad - R \left(U \frac{\partial \rho_0}{\partial x} + V \frac{\partial \rho_0}{\partial y} + W \frac{\partial \rho_0}{\partial z} \right) \end{aligned} \right. \\
& \hspace{15em} (5-163)
\end{aligned}$$

Additionally, it can be seen that $B_{c,p} = B_{r,u} = B_{\theta,v} = B_{z,w} = i$, $B_{e,T} = i\rho_0 c_v$, and $B_{e,p} = -iRT_0$, with all other terms in B_{ij} being null. Similar operators associated with [Eqs. \(5-155\)–\(5-160\)](#) are deferred to an exercise problem.

5-7.3 Numerical Strategy and Boundary Conditions

The same Chebyshev-based spectral collocation and grid preconditioning procedures described in Secs. 5-6.3 and 5-6.4 for the treatment of the incompressible Navier-Stokes equations can be used here. By applying the domain mapping and differentiation matrices to [Eq. \(5-163\)](#), the block matrices in Cartesian coordinates may be discretely specified using

$$\begin{cases}
A_{c,\rho} = \left(\frac{\partial U}{\partial x} + \frac{\partial V}{\partial y} + \frac{\partial W}{\partial z} + inW \right)_{ii} + U_{ii} \bar{D}_N^x + V_{ii} \bar{D}_N^y \\
A_{x,\rho} = \frac{1}{(\rho_0)_{ii}} \left(\frac{\partial U}{\partial t} + U \frac{\partial U}{\partial x} + V \frac{\partial U}{\partial y} + W \frac{\partial U}{\partial z} \right)_{ii} + \frac{R}{(\rho_0)_{ii}} \left[\left(\frac{\partial T_0}{\partial x} \right)_{ii} + (T_0)_{ii} \bar{D}_N^x \right] \\
A_{y,\rho} = \frac{1}{(\rho_0)_{ii}} \left(\frac{\partial V}{\partial t} + U \frac{\partial V}{\partial x} + V \frac{\partial V}{\partial y} + W \frac{\partial V}{\partial z} \right)_{ii} + \frac{R}{(\rho_0)_{ii}} \left[\left(\frac{\partial T_0}{\partial y} \right)_{ii} + (T_0)_{ii} \bar{D}_N^y \right] \\
A_{z,\rho} = \frac{1}{(\rho_0)_{ii}} \left(\frac{\partial W}{\partial t} + U \frac{\partial W}{\partial x} + V \frac{\partial W}{\partial y} + W \frac{\partial W}{\partial z} \right)_{ii} + \frac{R}{(\rho_0)_{ii}} \left[\left(\frac{\partial T_0}{\partial z} \right)_{ii} + in(T_0)_{ii} \right] \\
A_{e,\rho} = c_p \left(\frac{\partial T_0}{\partial t} \right)_{ii} + c_v \left(U \frac{\partial T_0}{\partial x} + V \frac{\partial T_0}{\partial y} + W \frac{\partial T_0}{\partial z} \right)_{ii} \\
\quad - R(T_0)_{ii} (U_{ii} \bar{D}_N^x + V_{ii} \bar{D}_N^y + inW_{ii})
\end{cases}
\begin{cases}
A_{c,u} = \left(\frac{\partial \rho_0}{\partial x} \right)_{ii} + (\rho_0)_{ii} \bar{D}_N^x \\
A_{x,u} = \left(\frac{\partial U}{\partial x} \right)_{ii} + U_{ii} \bar{D}_N^x + V_{ii} \bar{D}_N^y + inW_{ii} \\
\quad - \frac{\mu}{(\rho_0)_{ii}} \left[\frac{4}{3} (\bar{D}_N^x)^2 + (\bar{D}_N^y)^2 - n^2 I_N \right] \\
A_{y,u} = \left(\frac{\partial V}{\partial x} \right)_{ii} - \frac{\mu \bar{D}_N^x \bar{D}_N^y}{3(\rho_0)_{ii}} \\
A_{z,u} = \left(\frac{\partial W}{\partial x} \right)_{ii} - \frac{in\mu \bar{D}_N^x}{3(\rho_0)_{ii}} \\
A_{e,u} = \left(\rho_0 c_p \frac{\partial T_0}{\partial x} - \frac{\partial P_0}{\partial x} \right)_{ii} - \bar{\Phi}_u
\end{cases}$$

$$\begin{cases}
A_{c,v} = \left(\frac{\partial \rho_0}{\partial y} \right)_{ii} + (\rho_0)_{ii} \bar{D}_N^y \\
A_{x,v} = \left(\frac{\partial U}{\partial y} \right)_{ii} - \frac{\mu \bar{D}_N^x \bar{D}_N^y}{3(\rho_0)_{ii}} \\
A_{y,v} = \left(\frac{\partial V}{\partial y} \right)_{ii} + U_{ii} \bar{D}_N^x + V_{ii} \bar{D}_N^y + inW_{ii} \\
\quad - \frac{\mu}{(\rho_0)_{ii}} \left[(\bar{D}_N^x)^2 + \frac{4}{3} (\bar{D}_N^y)^2 - n^2 I_N \right] \\
A_{z,v} = \left(\frac{\partial W}{\partial y} \right)_{ii} - \frac{in\mu \bar{D}_N^y}{3(\rho_0)_{ii}} \\
A_{e,v} = \left(\rho_0 c_p \frac{\partial T_0}{\partial y} - \frac{\partial P_0}{\partial y} \right)_{ii} - \bar{\Phi}_v
\end{cases}
\begin{cases}
A_{c,w} = \left(\frac{\partial \rho_0}{\partial z} \right)_{ii} + in(\rho_0)_{ii} I_N \\
A_{x,w} = \left(\frac{\partial U}{\partial z} \right)_{ii} - \frac{in\mu \bar{D}_N^x}{3(\rho_0)_{ii}} \\
A_{y,w} = \left(\frac{\partial V}{\partial z} \right)_{ii} - \frac{in\mu \bar{D}_N^y}{3(\rho_0)_{ii}} \\
A_{z,w} = \left(\frac{\partial W}{\partial z} \right)_{ii} + U_{ii} \bar{D}_N^x + V_{ii} \bar{D}_N^y + inW_{ii} \\
\quad - \frac{\mu}{(\rho_0)_{ii}} \left[(\bar{D}_N^x)^2 + (\bar{D}_N^y)^2 - \frac{4}{3} n^2 I_N \right] \\
A_{e,w} = \left(\rho_0 c_p \frac{\partial T_0}{\partial z} - \frac{\partial P_0}{\partial z} \right)_{ii} - \bar{\Phi}_w
\end{cases}
\begin{cases}
A_{c,T} = 0 \quad A_{x,T} = R \bar{D}_N^x + \frac{R}{(\rho_0)_{ii}} \left(\frac{\partial \rho_0}{\partial x} \right)_{ii} \\
A_{y,T} = R \bar{D}_N^y + \frac{R}{(\rho_0)_{ii}} \left(\frac{\partial \rho_0}{\partial y} \right)_{ii} \\
A_{z,T} = inR I_N + \frac{R}{(\rho_0)_{ii}} \left(\frac{\partial \rho_0}{\partial z} \right)_{ii} \\
A_{e,T} = (\rho_0)_{ii} c_v (U_{ii} \bar{D}_N^x + V_{ii} \bar{D}_N^y + inW_{ii} I_N) \\
\quad - k \left[(\bar{D}_N^x)^2 + (\bar{D}_N^y)^2 - n^2 I_N \right] \\
\quad - R \left(U \frac{\partial \rho_0}{\partial x} + V \frac{\partial \rho_0}{\partial y} + W \frac{\partial \rho_0}{\partial z} \right)_{ii}
\end{cases}$$

(5-164)

where

$$\begin{aligned}
\bar{\Phi}_u &= 2\mu \left[\frac{2}{3} \left(2 \frac{\partial U}{\partial x} - \frac{\partial V}{\partial y} - \frac{\partial W}{\partial z} \right)_{ii} \bar{D}_N^x + \left(\frac{\partial U}{\partial y} + \frac{\partial V}{\partial x} \right)_{ii} \bar{D}_N^y + \left(\frac{\partial U}{\partial z} + \frac{\partial W}{\partial x} \right)_{ii} in I_N \right] \\
\bar{\Phi}_v &= 2\mu \left[\frac{2}{3} \left(2 \frac{\partial V}{\partial y} - \frac{\partial U}{\partial x} - \frac{\partial W}{\partial z} \right)_{ii} \bar{D}_N^y + \left(\frac{\partial U}{\partial y} + \frac{\partial V}{\partial x} \right)_{ii} \bar{D}_N^x + \left(\frac{\partial V}{\partial z} + \frac{\partial W}{\partial y} \right)_{ii} in I_N \right] \\
\bar{\Phi}_w &= 2\mu \left[\frac{2}{3} \left(2 \frac{\partial W}{\partial z} - \frac{\partial U}{\partial x} - \frac{\partial V}{\partial y} \right)_{ii} in I_N + \left(\frac{\partial U}{\partial z} + \frac{\partial W}{\partial x} \right)_{ii} \bar{D}_N^x + \left(\frac{\partial V}{\partial z} + \frac{\partial W}{\partial y} \right)_{ii} \bar{D}_N^y \right]
\end{aligned}$$

(5-165)

In addition to [Eq. \(5-164\)](#), all terms in the right-hand-side matrix $\{B_{ij}\}$ vanish except for $B_{c,\rho} = B_{x,u} = B_{y,v} = B_{z,w} = in I_N$, $B_{e,T} = ip_0 c_v I_N$, and $B_{e,\rho} = -iR T_0 I_N$. Corresponding boundary conditions typically require that all three velocity eigenfunctions vanish at the physical boundaries of the solution domain. A bounded domain may also be assumed to be acoustically closed such that $\mathbf{n} \cdot \nabla p = 0$ can be set at all boundaries, which translates into $\mathbf{n} \cdot \nabla T = \mathbf{n} \cdot \nabla \rho = 0$ conditions on the temperature and density. Since the pressure can be deduced straightforwardly from the ideal gas equation using $p = p_0 RT + \rho R T_0$, no boundary conditions are needed for the pressure. At the outflow section, however, different conditions may be enforced, including non-reflecting conditions on the velocities, such as a linear extrapolation in the streamwise direction (say x or z) to allow the flow to

seamlessly transition out of the domain.

Page 304

$$\text{At outflow: } \frac{\partial^2 u}{\partial x^2} = 0, \quad \frac{\partial^2 v}{\partial x^2} = 0, \quad \frac{\partial^2 w}{\partial x^2} = 0 \quad (\text{Cartesian}) \quad \text{or} \quad \frac{\partial^2 u_r}{\partial z^2} = 0, \quad \frac{\partial^2 u_\theta}{\partial z^2} = 0, \quad \frac{\partial^2 u_z}{\partial z^2} = 0 \quad (\text{Cylindrical}) \quad (5-166)$$

The development of equivalent block matrices with the cylindrical polar operators associated with [Eqs. \(5-155\)–\(5-159\)](#) is assigned to an example problem. In what follows the application of this approach to the compressible Taylor–Culick profile in a porous tube will be briefly outlined and discussed.

5-7.4 Stability Analysis of the Compressible Taylor–Culick Flow

As schematically illustrated in [Fig. 5-40](#), a solid rocket motor may be idealized as a right-cylindrical tube of porous length Z_N and radius a . The porous wall mimics the burning surface of a solid propellant grain by its ability to sustain a constant mass injection rate. In fact, a uniform injection (or blowing) speed at the wall, V_w , is often taken to represent the inward injection of a single-phase gaseous substance across a non-regressing porous wall [Saad and Majdalani (2017)].

In this problem, the intervals $0 \leq r \leq a$, $0 \leq \theta \leq 2\pi$, and $0 \leq z \leq Z_N$ may be used to delineate the domain boundaries. However, axisymmetry enables us to limit our analysis to half of the chamber, i.e., to a domain that extends horizontally from $z = 0$ to $z = Z_N$ and vertically from $r = 0$ to $r = a$. It is also convenient to set the chamber aspect ratio as $L = Z_N/a$ and use the subscript ‘w’ to denote reference properties taken at the porous wall. For this configuration, a closed-form analytical solution is available for the mean flow pursuant to a Rayleigh–Janzen expansion in the wall Mach number squared [Majdalani (2007)]. Assuming a sound propagation speed c_s , a wall Mach number of $Ma_w = V_w/c_s$, and $\eta \equiv \frac{1}{2}\pi(r/a)^2$, the basic flow stream function may be approximated by

$$\psi_0(r, z) = V_w a z \sin(\eta) \left(1 - \frac{1}{4} \left\{ \pi^2 (z/a)^2 \left[1 + \frac{1}{3} \cos(2\eta) \right] + 2 \right\} Ma_w^2 \right) \quad (5-167)$$

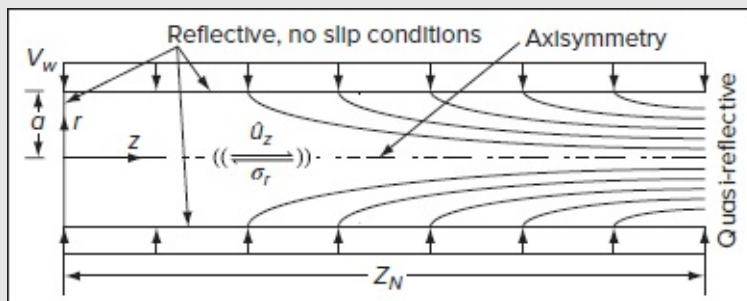


FIGURE 5-40

Schematics of a right-cylindrical, internal burning rocket modeled as a porous tube with sidewall injection.

and so, for the basic flow velocity components, we have

$$U_r = -V_w(a/r) \sin(\eta) \left(1 - \frac{1}{4} \left\{ \pi^2(z/a)^2 [1 + \cos(2\eta)] - (a/r)^2 [1 - \cos(2\eta)] + 2 \right\} Ma_w^2 \right) \quad (5-168)$$

$$U_z = V_w \pi(z/a) \cos(\eta) \left(1 + \frac{1}{4} \left\{ \pi^2(z/a)^2 \left[\frac{5}{3} - \cos(2\eta) \right] + (a/r)^2 [1 - \cos(2\eta)] - 2 \right\} Ma_w^2 \right) \quad (5-169)$$

The corresponding density, temperature, and pressure distributions may be expressed in terms of η and expanded as

Page 305

$$\rho_0 = \rho_w \left(1 - \frac{1}{2} \pi \left[\pi(z/a)^2 + \frac{1}{2} \eta^{-1} \sin^2 \eta \right] Ma_w^2 - \frac{1}{8} \pi^2 \left\{ \frac{1}{3} \pi^2(z/a)^4 (3\gamma - 2) + \pi(z/a)^2 \left[\eta + \eta^{-1} (\gamma - 1) \sin^2 \eta - 4/\pi \right] - 2\eta/\pi + \frac{3}{4} \eta^2 + \frac{1}{4} \eta^{-2} (\gamma - 1) \sin^4 \eta \right\} Ma_w^4 \right) \quad (5-170)$$

$$T_0 = T_w \left\{ 1 - \frac{1}{2} \pi (\gamma - 1) \left[\pi(z/a)^2 + \frac{1}{2} \eta^{-1} \sin^2 \eta \right] Ma_w^2 - \frac{1}{8} \pi^2 (\gamma - 1) \left[\frac{4}{3} \pi^2(z/a)^4 + \pi(z/a)^2 (\eta + \eta^{-1} \sin^2 \eta - 4/\pi) - 2\eta/\pi + \frac{3}{4} \eta^2 + \frac{1}{4} \eta^{-2} (\gamma - 1) \sin^4 \eta \right] Ma_w^4 \right\} \quad (5-171)$$

and

$$P_0 \approx \rho_w R T_w \left\{ 1 - \frac{1}{2} \pi \gamma \left[\pi(z/a)^2 + \frac{1}{2} \eta^{-1} \sin^2 \eta \right] Ma_w^2 - \frac{1}{8} \pi^2 \gamma \left[\frac{1}{3} \pi^2(z/a)^4 + (z/a)^2 (\pi \eta - 4) + \frac{1}{4} \eta (3\eta - 8/\pi) \right] Ma_w^4 \right\} \quad (5-172)$$

As for the boundary conditions, they can be specified at the headwall, sidewall, centerline, and outflow section labeled endwall. For the reader's convenience, these conditions are summarized in [Table 5-3](#).

Given the complexity of programming [Eqs. \(5-155\)–\(5-159\)](#), a simple simulation can be used to verify the procedure's accuracy and robustness in resolving the acoustic pressure waves in the absence of wall injection. In this case, the conventional wave equation in a quiescent medium may be used, namely,

$$\frac{\partial^2 \hat{p}}{\partial t^2} - c_s^2 \nabla^2 \hat{p} = 0 \quad (5-173)$$

In practical systems, the mean flow will also affect the chamber's acoustic frequencies, which may be determined using the Convected Wave Equation described, for example, by Campos (2007). However, because well-known benchmark cases that describe resonant acoustic frequencies with mean-flow effects are not widely available in the literature, it is helpful to demonstrate the effectiveness of the present scheme in reproducing pure acoustic tones. To isolate the acoustic waveforms, the method is first applied to a circular port motor

with an aspect ratio of $L = 5$, in a chamber with no injection or viscosity. In the absence of a mean flow, the theoretical acoustic frequencies may be readily evaluated using the standard relations,

$$\sigma_r = \alpha c_s = (k_{lmn}/a)c_s = (c_s/a)\sqrt{k_l^2 + k_{mn}^2} \quad \text{or} \quad \sigma_r^*|_{Ma_w=0} = \frac{\sigma_r}{(c_s/a)} = k_{lmn} = \sqrt{k_l^2 + k_{mn}^2} \text{ for an } (l, m, n) \text{ mode} \quad (5-174)$$

where σ_r^* represents the dimensionless frequency while $k_l = l\pi/L$ and k_{mn} denote the longitudinal and transverse wave numbers, respectively. Time may also be normalized with respect to (a/c_s) , which is the average time it takes for a sound wave to cross the chamber's characteristic length, a . By taking $t^* = t c_s/a$, the normalizing values for the circular frequency and time become reciprocals, thus leading to the convenient outcome, $\sigma_r t = \sigma_r^* t^*$. As for k_{mn} , it may be determined from the sequential roots of $J'_m(k_{mn}) = 0$. For the purely radial waveforms, one obtains, as usual,

$$(k_{01}, k_{02}, k_{03}, k_{04}, k_{05}) \approx (3.8317, 7.0156, 10.1735, 13.3237, 16.4706) \quad (5-175)$$

TABLE 5-3

Summary of boundary conditions imposed on the various eigenfunctions

	ρ	u_r	u_θ	u_z	T
Headwall ($z = 0$)	$\frac{\partial}{\partial z} = 0$	0	0	0	$\frac{\partial}{\partial z} = 0$
Sidewall ($r = 1$)		0	0	0	$\frac{\partial}{\partial r} = 0$
Centerline ($r = 0$)	$\frac{\partial}{\partial r} = 0$	$\frac{\partial}{\partial r} = 0$	$\frac{\partial}{\partial r} = 0$	$\frac{\partial}{\partial r} = 0$	$\frac{\partial}{\partial r} = 0$
Endwall ($z = Z_N$)		$\frac{\partial^2}{\partial z^2} = 0$	$\frac{\partial^2}{\partial z^2} = 0$	$\frac{\partial^2}{\partial z^2} = 0$	$\frac{\partial^2}{\partial z^2} = 0$

Page 306

and, conversely, for the purely tangential modes, one regains the complementary eigenvalues given by

$$(k_{10}, k_{20}, k_{30}, k_{40}, k_{50}) \approx (1.8412, 3.0542, 4.2012, 5.3175, 6.4156) \quad (5-176)$$

The corresponding pressure wave with a characteristic amplitude A_{lmn} may be expressed as

$$\hat{p} = A_{lmn} \cos(k_l z/a) J_m(k_{mn} r/a) \cos(m\theta) \cos(\sigma_r t) \quad (5-177)$$

As an aside, it may be instructive to note that in static rocket motor firings, longitudinal and tangential modes tend to be more frequently encountered than radial modes because of their reduced energy requirements. Conversely, radial modes, which exhibit pressure antinodes at $r = 0$, require an energy source along the axis of the chamber, which is an unlikely occurrence in solid rocket motors. With the principal source of energy being situated near the grain

surface, tangential mode oscillations, which confront less resistance and damping, are more easily driven and sustained. This may explain why, in analyzing experimental measurements, it is quite common to identify not only hydrodynamic modes, but also combined k_{lmn} modes that showcase contributions from both axial and transverse wave motions. However, in the present biglobal stability approach, tangential modes are prescribed by the tangential mode number m . By setting $m = 0$, the eigenmodes are restricted to longitudinal and radial wave excursions only. If tangential eigenmodes are sought, the desired mode number m has to be explicitly provided. In contrast, a triglobal solver, which is not covered here, can capture both radial and tangential modes simultaneously. Bearing these factors in mind, we proceed by first exploring the longitudinal and tangential mode predictions at $m = 0$.

A comparison between theoretical predictions for inviscid, isentropic flow and acoustic frequencies produced by the eigensolver for the first five longitudinal modes is showcased in [Table 5-4](#) using a large acoustic Reynolds number $Re = c_s a / \nu$, of 2×10^{20} , $\gamma = 1.4$, $Pr = 0.7$ and two successive values of $N = 30$ and 40 . A very large acoustic Reynolds number is chosen specifically to recreate conditions for which viscosity is negligible. Also displayed are the relative differences between the eigensolver and strictly theoretical predictions. In these ten cases, no manifestation of transverse mode oscillations can be seen, with the outcome being $k_{mn} = k_{00} = 0$ and $\sigma_r^* = k_{lmn} = \sqrt{k_l^2 + k_{00}^2} = k_l = l\pi / L$.

The corresponding Hertzian frequencies are readily calculated from $f_r = \sigma_r^* c_s / (2\pi a) = lc_s / (2aL) = \frac{1}{2} lc_s / Z_N$ for a closed-closed configuration.

In addition to the strong agreement between theory and simulations, the tabulated differences show a negligible disparity between the computed frequencies and those evaluated analytically, owing no doubt to the high degree of precision associated with the Chebyshev discretization scheme. Furthermore, the numerical discrepancies, which typically increase at higher frequencies, become virtually insignificant at $N = 40$ and above. The corresponding eigensolutions for the pressure fluctuations, which are featured in [Fig. 5-41](#) for the first four eigenmodes, follow purely sinusoidal mode shapes that align very well with [Eq. \(5-177\)](#). The latter reduces in this case to the classical irrotational and inviscid form, $\hat{p} = \cos(k_l z) \cos(\sigma_r t)$, where we have used $A_{lmn} = a = 1$ for simplicity. For each axial mode, multiple timelines are displayed firstly with no mean flow and secondly with a mean flow Mach number of $Ma_w = 0.05$ to help identify the effects of the mean flow on the vorticoacoustic disturbances. In the presence of a mean flow, it is clear that the spatial mode shapes are amplified, namely, by exhibiting spatial growth in the streamwise direction. Such spatial growth is a well-known property of the Taylor–Culick profile (see Chedevergne et al. 2012).

TABLE 5-4

Computed axial frequencies with $Ma_w = 0$ versus pure acoustic modes in a chamber with $L = 5$

Benchmark		$N = 30$		$N = 40$	
Mode l	$l\pi/L$	Eigenvalue	Difference	Eigenvalue	Difference
1	0.6283	0.6281	0.0318%	0.6282	0.0159%
2	1.2566	1.2558	0.0636%	1.2562	0.0318%
3	1.8850	1.8839	0.0583%	1.8844	0.0318%
4	2.5133	2.5117	0.0636%	2.5124	0.0358%
5	3.1416	3.1398	0.0572%	3.1406	0.0318%

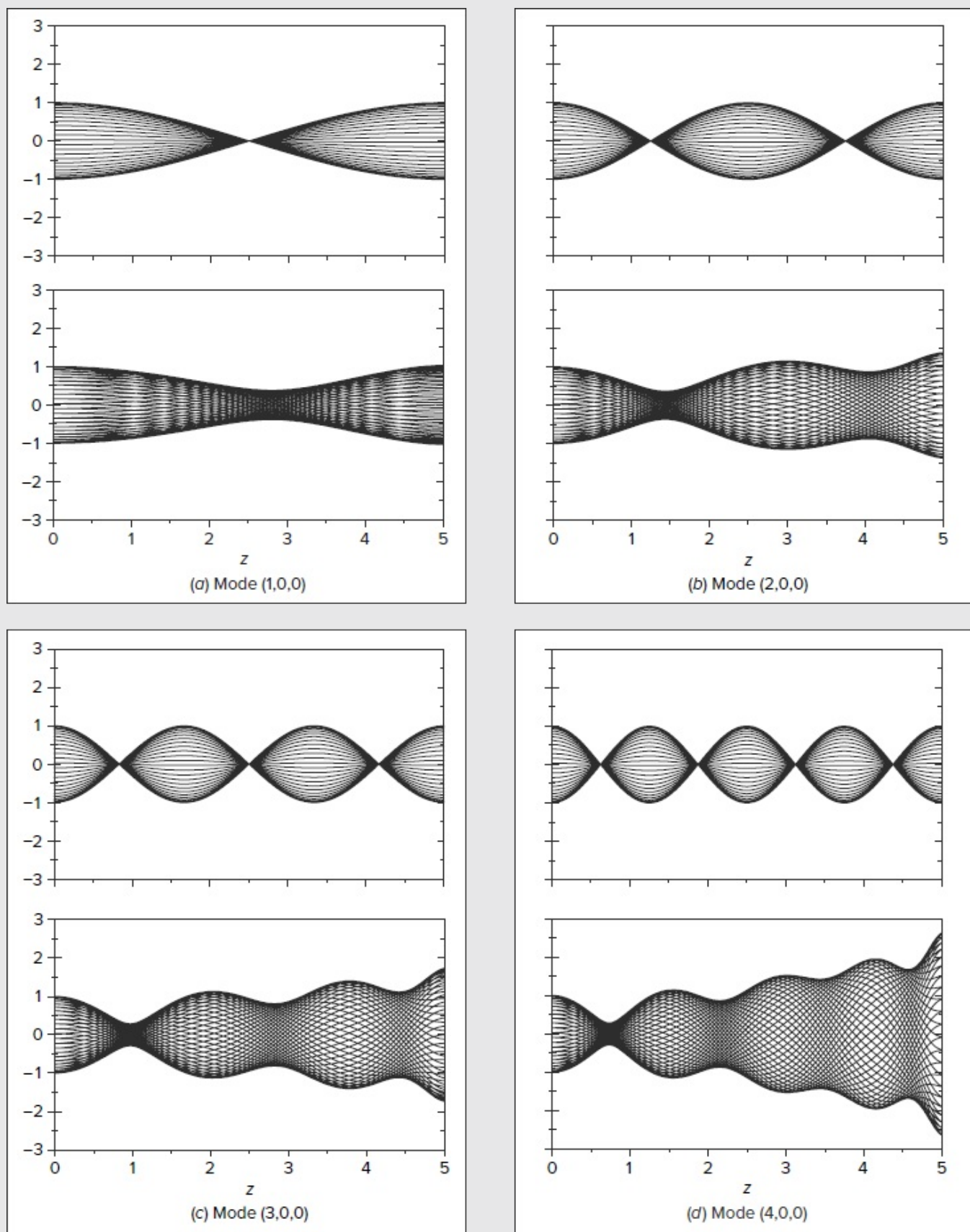


FIGURE 5-41

Modulus of the pressure waveform \hat{p} for the first four longitudinal modes $l =$

{1, 2, 3, 4} with $Ma_w = 0$ (top) and 0.05 (bottom) and a radial station of $r/a = 0.5$. The compressible biglobal stability solver accurately reproduces the acoustic modes in a quiescent medium in all cases considered.

TABLE 5-5

Computed radial frequencies with $Ma_{ew} = 0$ versus pure acoustic modes in a chamber with $L = 5$

Benchmark		$N = 30$		$N = 40$	
Radial mode n	k_{0n}	Eigenvalue	Difference	Eigenvalue	Difference
1	3.8317	3.8311	1.5721%	3.83158	0.5198%
2	7.0156	7.0143	1.8510%	7.0151	0.7091%
3	10.1735	10.1710	2.4601%	10.1728	0.6911%
4	13.3237	13.3190	3.5290%	13.3218	1.4289%

TABLE 5-6

Computed tangential frequencies with $Ma_w = 0$ versus acoustic modes in a chamber with $L = 5$

Benchmark		$N = 30$		$N = 40$	
Tangential m	k_{m0}	Eigenvalue	Difference	Eigenvalue	Difference
1	1.8419	1.8416	1.6310%	1.8481	0.5392%
2	3.0543	3.0539	1.3098%	3.0541	0.6479%
3	4.2012	4.1998	3.3287%	4.2009	0.7009%
4	5.3176	5.3151	4.7011%	5.3171	0.9312%

Similar comparisons between theory and computations for the radial and tangential eigenmodes are featured in Tables 5-5 and 5-6, where the first four tangential eigenvalues are showcased including their relative differences at two successive discretization schemes of $N = 30$ and 40. As one would expect of the radial oscillations, an excellent agreement between computed eigenmodes and theoretical k_{0n} values is realized for $n = \{1, 2, 3, 4\}$. For the tangential modes, the method is applied while specifying the tangential mode number $m = \{1, 2, 3, 4\}$ explicitly in the biglobal solver. Here too, the computed eigenmodes are seen to mirror their theoretical k_{m0} projections. In comparison to the axially dominated oscillations, the discrepancy relative to theoretical modes rapidly diminishes as the number of Chebyshev points is increased.

To further illustrate this behavior, spatial mode shapes of the pressure waves are

displayed in [Fig. 5-42](#) for the first four radial modes at a polar slice that is located midway in the chamber at $z/Z_N = \frac{1}{2}$. The evolution of the solution in the radial direction exhibits well-defined nodal points that correspond quite closely to the $J_0(k_{0n}r/a)$ dependence embedded in the analytical waveform of [Eq. \(5-177\)](#). From a three-dimensional perspective, each nodal point that appears along the radial axis gives rise to a concentric nodal circle that revolves around the z -axis. In the presence of a mean flow, a small frequency and therefore time shift relative to the case with no mean flow may be detected. In short, the observations confirm the ability of the compressible biglobal approach to recover the pure acoustic tones associated with wave propagation in a typical enclosure.

Let us now proceed to examine more closely the effects of the mean flow on acoustic frequencies using both the biglobal approach and the strictly irrotational convective wave equation, which can only partially account for mean-flow effects. To elaborate, we make use of the same geometric configuration, albeit with the inclusion of a steady-state motion that is driven by a wall Mach number of 0.05 and an acoustic Reynolds number of 200. We also hold the Prandtl number and ratio of specific heats constant at 0.7 and 1.4, respectively. Subsequent results, which are cataloged in Tables 5-7 and 5-8, display a downward shift in both longitudinal and radial frequencies of up to 6.6 percent. Overall, the biglobal solver is seen to predict a larger frequency shift than the strictly irrotational convective wave equation. This is due to the ability of the biglobal solver to account for the two-way coupling that exists between unsteady pressure and vorticity disturbances, unlike the convective wave equation, which only accounts for unsteady pressure disturbances. Although not shown, it can be demonstrated that lowering the acoustic Reynolds number, which can be achieved by increasing the viscosity, leads to a larger frequency shift. Conversely, boosting the Reynolds number by one order of magnitude, i.e., to 2000, leads to roughly half of the frequency shift observed at $Re = 200$. This can be attributed to the pure acoustic tones being derived in the context of a strictly inviscid, irrotational, isentropic, and injection-free environment. In practice, the scale of the frequency shifts may be viewed as being characteristic of those observed in experimental measurements [Gazanion et al. (2014)]. In a rocket-related acoustic stability investigation, the radial frequency shifts remain smaller than their longitudinal counterparts due to the lower radial velocities relative to the axial mean-flow speed. However, as the acoustic Reynolds number is decreased, the radial frequency shifts become more appreciable. As usual, pressure mode shapes may be readily extracted from the computed eigenfunctions and illustrated graphically. They are shown here in [Figs. 5-41](#) and [5-42](#), where their strong spatial resemblance to those obtained with no mean flow is confirmed.

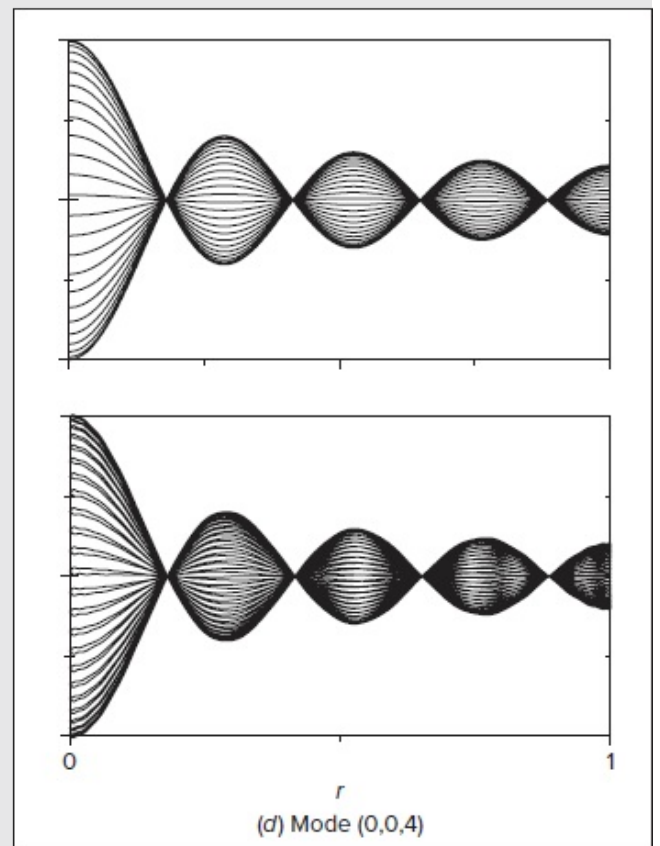
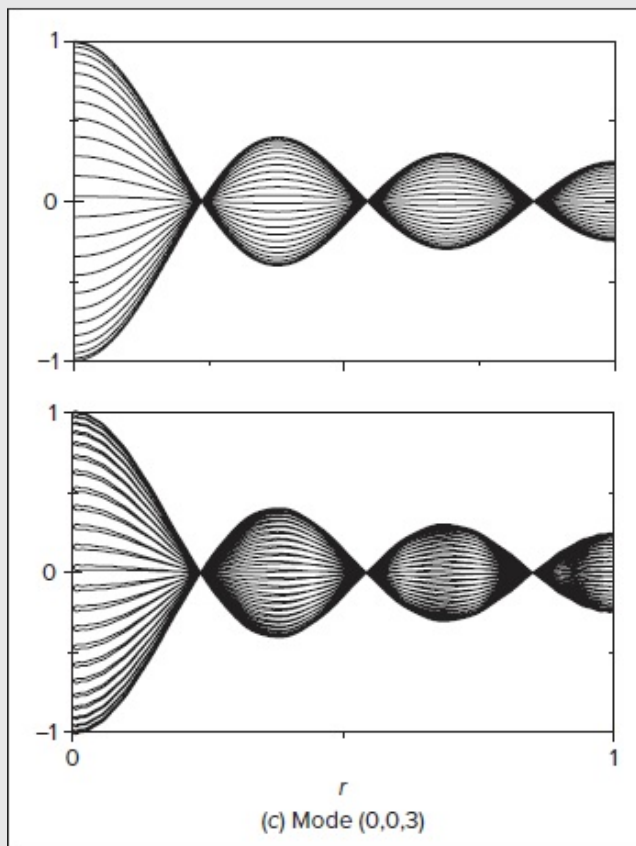
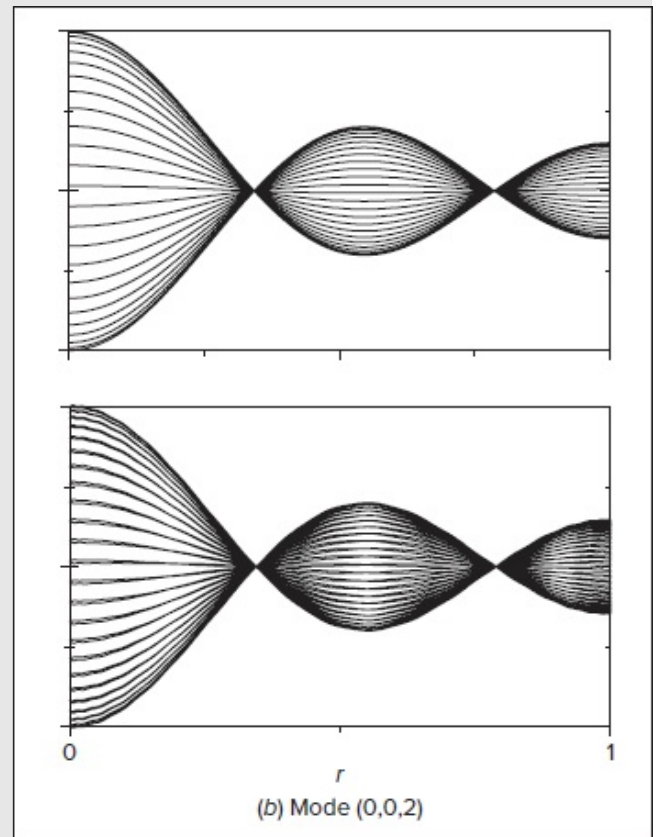
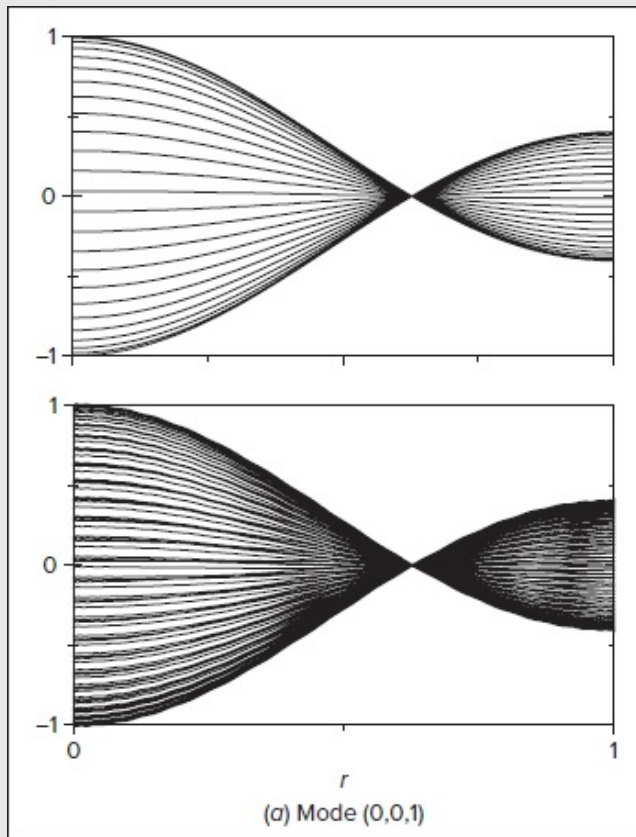


FIGURE 5-42

Pressure waveform \hat{p} for the first four radial modes with $Ma_w = 0$ (top) and

TABLE 5-7

Computed axial frequencies versus pure acoustic modes for $Ma_w = 0.05$, $N = 40$, $L = 5$, and $Re = 200$

Benchmark		Convective Wave Equation		Compressible Biglobal Solver	
Mode l	$l\pi/L$	Eigenvalue	Frequency shift	Eigenvalue	Frequency shift
1	0.6283	0.571	9.20%	0.586	6.61%
2	1.2566	1.124	10.52%	1.176	6.35%
3	1.8850	1.670	11.40%	1.767	6.26%
4	2.5133	2.202	12.39%	2.387	5.02%
5	3.1416	2.719	13.44%	2.966	4.61%

TABLE 5-8

Computed radial frequencies versus pure acoustic modes for $Ma_w = 0.05$, $N = 40$, $L = 5$, and $Re = 200$

Benchmark		Convective Wave Equation		Compressible Biglobal Solver	
Radial mode n	k_{0n}	Eigenvalue	Frequency shift	Eigenvalue	Frequency shift
1	3.8317	3.823	0.23%	3.803	0.75%
2	7.0156	6.995	0.29%	6.944	0.72%
3	10.1735	10.132	0.41%	10.098	0.74%
4	13.3237	13.251	0.55%	13.249	0.56%

To illustrate the effect of the azimuthal wave number, the tangential mode number can be reset from zero to $m = \{1, 2, 3, 4\}$ and the compressible solver can be rerun one azimuthal case at a time. This enables us to capture the excursion in tangential frequencies caused by the mean flow. Using the same wall Mach number as before, the frequencies obtained from the biglobal eigensolver as well as the convective wave equation are cataloged in [Table 5-9](#) for the first four modes, an acoustic Reynolds number of 200, and $N = 40$. Here too, the tangential excursions predicted by the convective wave equation remain substantially smaller than those computed using the compressible biglobal solver. However, both remain noticeably smaller than the longitudinal frequency shifts. Such behavior may be attributed to the absence of a tangential mean-flow component and to the axisymmetric nature of the motion. These factors reduce the sensitivity of the tangential frequency on the mean flow, viscosity and, as such, the acoustic Reynolds number.

TABLE 5-9
Computed tangential frequencies versus pure acoustic modes for $Ma_w = 0.05$, $N = 40$, $L = 5$, and $Re = 200$

Benchmark		Convective Wave Equation		Compressible Biglobal Solver	
Tangential mode m	k_{m0}	Eigenvalue	Frequency shift	Eigenvalue	Frequency shift
1	1.8419	1.839	0.13%	1.783	3.19%
2	3.0543	3.052	0.09%	2.974	2.63%
3	4.2012	4.198	0.07%	4.135	1.58%
4	5.3176	5.315	0.05%	5.273	0.84%

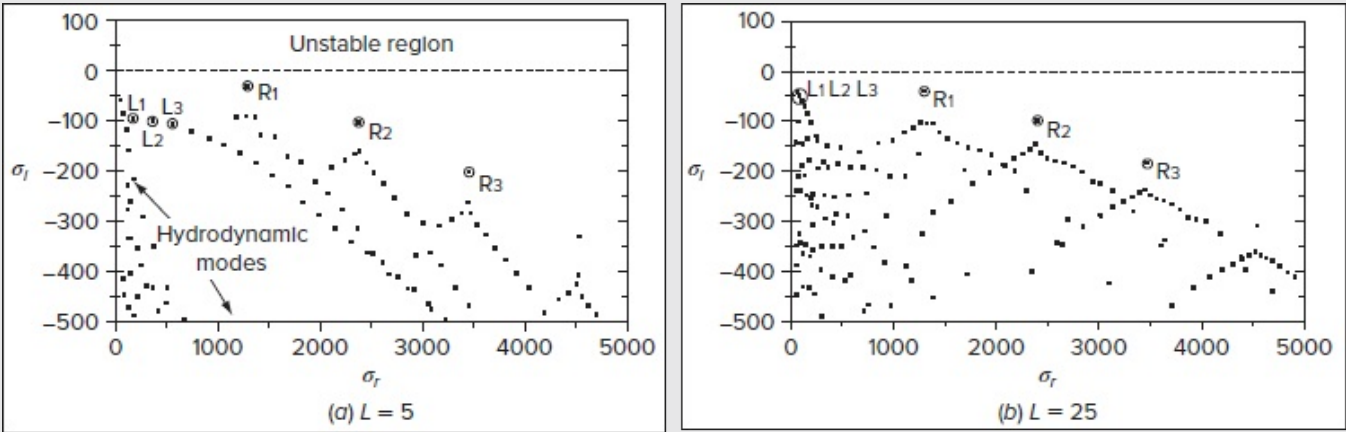


FIGURE 5-43
Typical frequency spectrum for a cylindrical rocket motor with $Re = 200$, $N = 40$, $m = 0$, $Ma_w = 0.05$ and both (a) $L = 5$ and (b) 25.

As we turn our attention to the complex frequencies generated by the compressible biglobal solver, these can be split into real and imaginary parts. As depicted in [Fig. 5-43](#), the real component, σ_r , represents the frequency of oscillations, whereas the imaginary component, determines the growth rate which, in turn, controls the temporal amplification of the principal eigensolutions. Unstable modes may hence be associated with a positive σ_i where the amplitude function increases continuously in a linear system. In these particular runs, the tangential mode number is taken to be $m = 0$, which excludes variations in the θ -direction by restricting the transverse modes to radial oscillations only.

Using $Ma_w = 0.05$ and $Re = 200$, typical frequency spectra are overlaid in [Fig. 5-43](#) for a motor with length-to-radius aspect ratios of 5 and 25 in [Figs. 5-43a](#) and [5-43b](#), respectively. Based on these graphs, one may readily infer the presence of a series of characteristic

frequencies starting with the first three longitudinal modes that are labeled L1 through L3. Also shown are the first three radial modes, labeled as R1–R3, with trailing modes emanating from each. The trailing points represent mixed modes that combine both longitudinal and radial contributions. Conversely, the modes appearing at the lower left corner of the graph allude to the hydrodynamic modes which, for the configuration at hand, remain temporally damped because of their negative growth rates. Not only do the hydrodynamic modes associated with mean-flow breakdown appear at lower frequencies, but their negative growth rates remain smaller than those associated with vorticoacoustically coupled modes.

In conclusion, the use of a compressible biglobal stability procedure enables us to capture the characteristic frequencies and growth rates associated with both hydrodynamic and acoustic disturbances in a compressible viscous fluid with no need for flow decomposition. It thus leads to a comprehensive view of the disturbances that can evolve in a viscous fluid.

SUMMARY

As far as we know, all laminar flows eventually become unstable and develop or “transition” into turbulence at a sufficiently high speed parameter appropriate to the flow such as the Reynolds, Grashof, or Taylor numbers.

The stability of any flow can be studied by superimposing small disturbances on a basic laminar motion. For boundary-layer flows, the linearized disturbance relation in the form of the Orr–Sommerfeld equation has been solved for a variety of flows. Based on a multitude of experimental studies and computer simulations, several stabilizing parameters have been identified, and these include favorable pressure gradients, wall suction, wall compliance, heating of liquids, and cooling of gases.

Experiments show that the unstable, plane traveling Tollmien–Schlichting waves, predicted by the Orr–Sommerfeld analysis, grow downstream and become three-dimensional, thus ultimately causing vortex breakdown and formation of turbulent spots that coalesce into a fully turbulent motion. Several empirical correlations have been advanced for the prediction of this final *transition point*. Transition is strongly affected by freestream turbulence, acoustic excitations, and wall roughness. After a brief discussion of transition in unsteady shear flows, a description of some possible design criteria for controlling the onset of transition is provided. The chapter ends with a discussion of the biglobal stability approach, which is gaining widespread use in the fluid dynamics community, as it can be applied to both incompressible and compressible flows.

Page 312

PROBLEMS

- 5-1. While holding $(g, \rho_1, \rho_2, \mathfrak{F})$ constant, show that the right-hand side of [Eq. \(5-9\)](#) has a minimum at the wave number $\alpha = [g(\rho_1 - \rho_2)/\mathfrak{F}]^{1/2}$. Find experimental data somewhere

and estimate this “critical” wavelength and velocity difference for air blowing over gasoline. For further discussion, see Drazin (2002), p. 57.

- 5-2. Show that, if the upper and lower velocities in [Fig. 5-2](#) are negligible and if surface tension is ignored, a disturbance of the interface will propagate at the phase speed

$$c = \sqrt{\frac{g\lambda(\rho_1 - \rho_2)}{2\pi(\rho_1 + \rho_2)}}$$

where λ is the wavelength of the disturbance. Discuss what might happen if $\rho_1 < \rho_2$. Estimate this propagation speed for an air–water interface when the wavelength is 3 m.

- 5-3. Derive a linearized disturbance equation for the celebrated (nonlinear) van der Pol equation,

$$\frac{d^2 X}{dt^2} + C(X^2 - 1)\frac{dX}{dt} + X = 0$$

where C is a constant. Assume that $X_0(t)$ is a known exact solution. Comment on the disturbance equation but do not solve it.

- 5-4. Verify the Orr–Sommerfeld [Eq. \(5-23\)](#) by eliminating p and u from [Eqs. \(5-18\)–\(5-20\)](#).

- 5-5. Consider Rayleigh’s inviscid stability [Eq. \(5-27\)](#). The perturbation amplitude $v(y)$ is complex, and, for temporal stability analysis, α is real and c is complex. Show that Rayleigh’s equation may be split into real and imaginary parts, as follows:

$$\begin{aligned} v_r'' - \left[\alpha^2 + \frac{U''(U - c_r)}{(U - c_r)^2 + c_i^2} \right] v_r + \frac{U'' c_i}{(U - c_r)^2 + c_i^2} v_r &= 0 \\ v_i'' - \left[\alpha^2 + \frac{U''(U - c_r)}{(U - c_r)^2 + c_i^2} \right] v_i - \frac{U'' c_r}{(U - c_r)^2 + c_i^2} v_i &= 0 \end{aligned}$$

Explain, in words, a possible method for solving this system numerically for a given $U(y)$.

- 5-6. Consider Pohlhausen’s quartic-polynomial profile that provides a rough approximation for the velocity distribution over a flat plate with no pressure gradient:

$$\frac{u}{U} = 2\xi - 2\xi^3 + \xi^4 \quad \xi = \frac{y}{\delta}$$

Solve the Orr–Sommerfeld [Eq. \(5-23\)](#) numerically for the inviscid case with $\nu = 0$. Begin at $y = 2\delta$ assuming that $v \approx e^{-\alpha y}$ and integrate inwardly to satisfy the wall conditions $v = v' = 0$ at $y = 0$. Assuming temporal amplification, find some (damped)

eigenvalues and plot c_i versus α in dimensionless form.

- 5-7. For stagnation boundary-layer flow, $U = Kx$, estimate the position Re_x where instability first occurs.

Page 313

- 5-8. For the separating Falkner–Skan wedge-flow boundary layer, $\beta = -0.19884$, estimate the position Re_x where instability first occurs.
- 5-9. For the Howarth freestream velocity $U = U_0(1 - x/L)$, if $U_0 L/\nu = 10^6$, estimate the point (x/L) where boundary-layer instability first occurs. Assume a low subsonic Mach number.
- 5-10. Generalize Prob. 5-9 to calculate and plot the instability point $(x/L)_{crit}$ as a function of $U_0 L/\nu$.
- 5-11. For potential freestream flow across a cylinder, $U = 2U_0 \sin(x/a)$, if $Re_D = 10^6$, estimate the position $(x/a)_{crit}$ where boundary-layer instability first occurs.
- 5-12. Using the guidance of Probs. 5-5 and 5-6 and any numerical method of your choosing, solve the Rayleigh [Eq. \(5-27\)](#) for simplified boundary-layer flow, $U = \tanh(y)$, $0 \leq y \leq \infty$, with a typical value of $\alpha \approx 0.2$ to 0.3 . Do you expect any inviscid instability? If time permits, plot some computed values of c_r and α . [Hint: Begin at large $y \leq 4$ with the exponential approximation of [Eq. \(5-6\)](#) and integrate backward to the wall.]
- 5-13. Using the guidance of Probs. 5-5 and 5-6 and any numerical method of your choosing, solve the Rayleigh [Eq. \(5-27\)](#) for the Blasius boundary-layer flow, which you should generate from [Eqs. \(4-60\)](#) and [\(4-61\)](#). Do you expect any inviscid instability? Select a value of α in the range 0.2 to 0.3 . [Hint: Begin at large $\eta \leq 5$ with the exponential approximation of [Eq. \(5-6\)](#) and integrate backward to the wall.]
- 5-14. For stagnation boundary-layer flow, $U = Kx$, estimate the position Re_x where transition first occurs, using the method of Michel given by [Eq. \(5-46\)](#). What makes the correlation of Granville (Sec. 5-5.1.1) inappropriate? Assume negligible freestream turbulence.
- 5-15. For the separating Falkner–Skan wedge-flow boundary layer, $\beta = -0.19884$, use any appropriate correlation to estimate the position Re_x where transition first occurs. Neglect freestream turbulence. Compare your result with [Fig. 5-32](#).
- 5-16. For the Howarth freestream velocity $U = U_0(1 - x/L)$, if $U_0 L/\nu = 4 \times 10^6$, use the

correlation of Michel, given by [Eq. \(5-46\)](#), to estimate the point (x/L) where boundary-layer transition occurs. Neglect freestream turbulence. Compare your result with [Fig. 5-31](#).

- 5-17. Generalize Prob. 5-16 into a parametric computer study to compute and plot $(x/L)_{tr}$ versus $U_0 L / \nu$.
- 5-18. For potential freestream flow across a cylinder, $U = 2 U_0 \sin (x/a)$, if $Re_D = 2 \times 10^6$, use the correlation of Michel given by [Eq. \(5-46\)](#) to estimate the position $(x/a)_{tr}$ where boundary-layer transition first occurs. Neglect freestream turbulence. Compare your result with [Fig. 5-31](#).
- 5-19. Air at 20°C and 1 atm flows quietly toward a wedge of half-angle 36°, thus resulting in a power-law freestream and a laminar boundary layer along the surface. Use Wazzan's method given by [Eq. \(5-50\)](#) to estimate the transition Reynolds number $Re_{x, tr}$.
- 5-20. Modify Prob. 5-14 for a freestream turbulence level of 1 percent.
- 5-21. Modify Prob. 5-15 for a freestream turbulence level of 1 percent.
- 5-22. Modify Prob. 5-16 for a freestream turbulence level of 1 percent.
- 5-23. Modify Prob. 5-18 for a freestream turbulence level of 1 percent.
- 5-24. For a pipe flow started from rest with acceleration a , as in [Fig. 5-37b](#), the momentum thickness initially grows according to the formula $\theta \approx 0.35(\nu t)^{1/2}$. Apply this relation to Michel's steady-flow transition correlation, [Eq. \(5-46\)](#), assuming that " U " and " x " are given by constant-acceleration formulas. Show that the result is a constant value of the dimensionless transition time $t_{tr}(a^2/\nu)^{1/3}$. Why does the diameter D not appear?
- 5-25. Air at 20°C and 1 atm flows at $U = 12$ m/s past a smooth flat plate. It is desired to trip the boundary layer to turbulence by stretching a 1 mm diameter wire across the plate at the wall. Where will transition occur if the wire is placed at $x = 1$ m? What wire location x will cause the earliest transition?
- 5-26. Repeat Prob. 5-25 if the freestream turbulence level is 1 percent.
- 5-27. The narrow vertical white band in the chaotic area of the logistic map in [Fig. 5-38](#) lies in the region $3.825 < r < 3.865$. Beginning at $r = 3.825$ with an initial guess $x = 0.5$, make repeated computer iterations, for small increments $\Delta r \leq 0.0005$, of the logistic relation given by [Eq. \(5-60\)](#) and plot the results on an expanded abscissa for this region. Comment on the remarkable pattern you find.

- 5-28. Repeat Prob. 5-19 if the freestream has a turbulence level of 4 percent. Find the estimated transition Reynolds number $Re_{x_{tr}}$ by two different methods and compare.
- 5-29. The famous neutral curve of Taylor (1923), for Couette flow between rotating cylinders, is shown in [Fig. 5-22b](#). The region above the curve is simply labeled *unstable*. Some amazingly diverse flow regimes lie in this region, as shown in a wonderful chart by Andereck et al. (1986). Describe this chart and its many unstable flow patterns.
- 5-30. For two-dimensional inviscid flow, the vorticity transport [Eq. \(2-103\)](#) may be written as

$$\frac{\partial \omega}{\partial t} + u \frac{\partial \omega}{\partial x} + v \frac{\partial \omega}{\partial y} = 0$$

where

$$\omega = \frac{\partial v}{\partial x} - \frac{\partial u}{\partial y} = -\nabla^2 \psi$$

Defining a basic flow by its mean-flow stream function, velocity, and vorticity components (Ψ, U, V, Ω), and their corresponding disturbances (ψ', u', v', ω'), derive a linearized disturbance equation for this flow. Then assume normal modes as traveling waves:

$$(\psi', u', v', \omega') = [\hat{\psi}(y), \hat{u}(y), \hat{v}(y), \hat{\omega}(y)] \exp[i\alpha(x - ct)]$$

Derive the disturbance equations and, if possible, combine them to obtain a single differential equation for a single disturbance amplitude.

- 5-31. Use the airfoil surface-velocity data of Prob. 4.49 and Michel's method, given by [Eq. \(5-46\)](#), to estimate the position of transition to turbulence if $Re_c = 2 \times 10^6$. Assume air at 20°C and 1 atm. If you note an ambiguity in the results, please criticize them.
- 5-32. Consider the cubic flat-plate velocity distribution:

$$\frac{u}{U} = \frac{3}{2}\xi - \frac{1}{2}\xi^3 \quad \xi = \frac{y}{\delta}$$

Solve the Orr–Sommerfeld [Eq. \(5-23\)](#) numerically for the inviscid case with $\nu = 0$. Begin at $y = 2\delta$ assuming that $v \approx e^{-\alpha y}$ and integrate inwardly to satisfy the wall conditions $v = v' = 0$ at $y = \xi = 0$. Assuming temporal amplification, find some (damped) eigenvalues and plot c_i versus α in dimensionless form.

- 5-33. Consider the sinusoidal flat-plate velocity distribution:

$$\frac{u}{U} = \sin\left(\frac{\pi\xi}{2}\right) \quad \xi = \frac{y}{\delta}$$

Solve the Orr–Sommerfeld [Eq. \(5-23\)](#) numerically for the inviscid case with $\nu = 0$. Begin at $y = 2\delta$ assuming that $u \approx e^{-\alpha y}$ and integrate inwardly to satisfy the wall conditions $u = u' = 0$ at $y = \xi = 0$. Assuming temporal amplification, find some (damped) eigenvalues and plot c_i versus α in dimensionless form.

- 5-34. Consider the Majdalani–Xuan polynomial profile, which represents a surprisingly simple and precise quartic velocity approximation to the Blasius boundary-layer problem:

$$\frac{u}{U} = \frac{5}{3}\xi - \xi^3 + \frac{1}{3}\xi^4 \quad \xi = \frac{y}{\delta}$$

Solve the Orr–Sommerfeld [Eq. \(5-23\)](#) numerically for the inviscid case with $\nu = 0$. Begin at $y = 2\delta$ assuming that $u \approx e^{-\alpha y}$ and integrate inwardly to satisfy the wall conditions $u = u' = 0$ at $y = \xi = 0$. Assuming temporal amplification, find some (damped) eigenvalues and plot c_i versus α in dimensionless form.

- 5-35. Consider the Majdalani–Xuan exponential profile, which represents a highly accurate velocity approximation to the Blasius boundary-layer problem:

$$\frac{u}{U} = 1 - \exp\left[-\bar{s}\xi\left(1 + \frac{1}{2}\bar{s}\xi + \xi^2\right)\right] \quad \xi = \frac{y}{\delta}$$

where $\bar{s} = 1.630398038629397$ denotes the Blasius slope at the wall, also known as the *Blasius constant* or *connection parameter*. Solve the Orr–Sommerfeld [Eq. \(5-23\)](#) numerically for the inviscid case with $\nu = 0$. Begin at $y = 2\delta$ assuming that $u \approx e^{-\alpha y}$ and integrate inwardly to satisfy the wall conditions $u = u' = 0$ at $y = \xi = 0$. Assuming temporal amplification, find some (damped) eigenvalues and plot c_i versus α in dimensionless form.

- 5-36. Determine whether the following profiles are prone to instability in the context of an inviscid, incompressible, external fluid domain ($0 \leq y \leq \infty$):

$$(a) U = 1 + y^2; (b) U = y^3; (c) U = y^4; (d) U = e^{-y}; (e) U = e^{-y^2}; (f) U = e^{-y^2} \cos(y); (g) U = \tanh(y)$$

- 5-37. Given an inviscid motion $U(y)$, show that if σ represents an eigenvalue of the Rayleigh equation given by [Eq. \(5-27\)](#) then so does its complex conjugate.

- 5-38. Compare the benefits and deficiencies of the Orr–Sommerfeld equation to the e^N method in the treatment of boundary-layer instability.

- 5-39. Discuss the implications of Squire’s theorem on the stability of two-dimensional planar motions that are subject to three-dimensional disturbances under (a) inviscid

and (b) viscous conditions.

- 5-40.** Rayleigh's criterion for rotational instability states that "*an inviscid rotating flow is unstable if the square of its circulation decreases outward.*" Using cylindrical polar coordinates (r, θ, z) , consider the motion of an inviscid rotating field prescribed by $\mathbf{V}(r) = [0, V_\theta(r), 0]$ over a finite interval $r_i \leq r \leq r_o$, where the vorticity retains a single nonzero component in the z -direction, namely, $\omega = (0, 0, \omega_z)$. (a) Show that

$$\omega_z = \frac{1}{r} \frac{d}{dr}(rV_\theta); \quad \frac{d\omega_z}{dr} < 0; \quad \text{and} \quad \frac{d(r^2 V_\theta^2)}{dr} < 0$$

Is the flow stable or unstable?

(b) Assuming Couette flow [Eq. (3-22)] between two long cylinders where the subscripts i and o denote the inner and outer surfaces rotating at angular speeds Ω_i and Ω_o , show that a condition leading to instability corresponds to

$$\Omega_i r_i^2 > \Omega_o r_o^2$$

From this condition, what can you say about the stability of the motion if the outer cylinder is stationary and the inner cylinder is rotating? Conversely, what happens if the inner cylinder is stationary and the outer cylinder is rotating? Finally, what happens anytime the two cylinders rotate in opposite directions?

- 5-41.** Consider the following time-dependent convective equation for $u(x, t)$,

$$\frac{\partial u}{\partial t} + c \frac{\partial u}{\partial x} = \sigma u$$

where c and σ are positive constants. (a) Show that any disturbance of the form $u(x, t) = \epsilon e^{\sigma t} f(x - ct)$ represents a valid solution. (b) By specifying disturbances to the zeroth-order solution $U_0 = 0$ using the normal mode form $u(x, t) = \epsilon e^{\sigma t} \exp[i\alpha(x - ct)]$, determine the condition for stability. (c) Assuming $u(x, t) = \epsilon e^{\sigma t} \text{sech}^2(x - ct)$, illustrate the behavior of this disturbance graphically. (d) How does the solution behave as $t \rightarrow \infty$ at a fixed point in space? (e) After a very long time, if u becomes unbounded at a fixed point in space, it will signal the presence of an absolute instability. Show that this disturbance becomes absolutely unstable for $\sigma > 2c$.

Page 315

- 5-42.** Consider the following time-dependent convection-diffusion equation for $u(x, t)$,

$$\frac{\partial u}{\partial t} + c \frac{\partial u}{\partial x} = \frac{\partial^2 u}{\partial x^2} + (\sigma - \sigma_0)u$$

where c , σ , and σ_0 are positive constants. (a) Show that the flow will be stable so

long as $\sigma < \sigma_0$. (b) If, instead, we have $\sigma > \sigma_0$, find the range of c that will give rise to convectively unstable disturbances as well as the range that will trigger a case of absolute instability.

- 5-43.** Using cylindrical polar coordinates (r, θ, z) in conjunction with a velocity vector $\mathbf{V} = (v_r, v_\theta, v_z)$ and pressure P , the continuity and momentum equations for inviscid, incompressible motion reduce to

$$\begin{aligned} \rho \left(\frac{\partial v_r}{\partial t} + v_r \frac{\partial v_r}{\partial r} + \frac{v_\theta}{r} \frac{\partial v_r}{\partial \theta} + v_z \frac{\partial v_r}{\partial z} - \frac{v_\theta^2}{r} \right) &= -\frac{\partial P}{\partial r} \\ \frac{1}{r} \frac{\partial}{\partial r} (r v_r) + \frac{1}{r} \frac{\partial v_\theta}{\partial \theta} + \frac{\partial v_z}{\partial z} &= 0 \quad \text{and} \quad \rho \left(\frac{\partial v_\theta}{\partial t} + v_r \frac{\partial v_\theta}{\partial r} + \frac{v_\theta}{r} \frac{\partial v_\theta}{\partial \theta} + v_z \frac{\partial v_\theta}{\partial z} + \frac{v_r v_\theta}{r} \right) = -\frac{1}{r} \frac{\partial P}{\partial \theta} \\ \rho \left(\frac{\partial v_z}{\partial t} + v_r \frac{\partial v_z}{\partial r} + \frac{v_\theta}{r} \frac{\partial v_z}{\partial \theta} + v_z \frac{\partial v_z}{\partial z} \right) &= -\frac{\partial P}{\partial z} \end{aligned}$$

Let us now consider the case of a rotating axisymmetric flow between two concentric cylinders, where the velocity field can be prescribed by $\mathbf{V} = \mathbf{V}_0 + \epsilon \mathbf{v}^*(\mathbf{x}, t)$ with $0 < \epsilon \ll 1$. The basic motion in this problem may be captured by a strictly swirling (azimuthal) velocity component of the form, $\mathbf{V}_0(r) = [0, V(r), 0]$. (a) Start by writing the disturbances as $\mathbf{v}^*(\mathbf{x}, t) = (u^*, v^*, w^*) = (u, v, w)e^{i\alpha z + \alpha c_i t}$ and show that the radial disturbance must satisfy a linear, second-order, differential equation, namely,

$$\frac{d^2 u}{dr^2} + \frac{1}{r} \frac{du}{dr} - \frac{u}{r^2} - \left(\alpha^2 + \frac{B}{c_i^2} \right) u = 0 \quad \text{where } B = \frac{1}{r^3} \frac{d}{dr} (r^2 V^2)$$

(b) A journal bearing may be modeled as being composed of an inner cylinder of radius r_i , and an outer cylinder of radius $r_o > r_i$. Assuming that the steady viscous motion in the cylindrical annulus is expressible as $V(r) = C_1 r + C_2 r^{-1}$, determine the appropriate constants and then proceed to deduce B .

(c) By fixing the longitudinal wavenumber α , and assuming that B can be negative, discuss the stability characteristics of this motion.

- 5-44.** Assuming strictly two-dimensional flow conditions with a spanwise wave number of $n = 0$ in the z direction and a basic motion that is prescribed by a two-component velocity vector of the form $\mathbf{V}_0(x, y) = [U(x, y), V(x, y), 0]$, (a) show that the linearized Navier–Stokes equations with biglobal stability disturbance modes, given by [Eqs. \(5-82\)–\(5-85\)](#), can be readily reduced into

$$\frac{\partial u}{\partial x} + \frac{\partial v}{\partial y} = 0 \quad (\text{continuity})$$

$$-i\sigma u + \frac{\partial U}{\partial x} u + \frac{\partial U}{\partial y} v + U \frac{\partial u}{\partial x} + V \frac{\partial u}{\partial y} + \frac{1}{\rho} \frac{\partial p}{\partial x} = \nu \left(\frac{\partial^2 u}{\partial x^2} + \frac{\partial^2 u}{\partial y^2} \right) \quad (\text{x-mom.})$$

$$-i\sigma v + \frac{\partial V}{\partial x} u + \frac{\partial V}{\partial y} v + U \frac{\partial v}{\partial x} + V \frac{\partial v}{\partial y} + \frac{1}{\rho} \frac{\partial p}{\partial y} = \nu \left(\frac{\partial^2 v}{\partial x^2} + \frac{\partial^2 v}{\partial y^2} \right) \quad (\text{y-mom.})$$

where $\hat{p}(x, y, z, t) = p(x, y)e^{-i\sigma t}$ and $\hat{\mathbf{v}}(x, y, z, t) = (\hat{u}, \hat{v}, 0) = [u(x, y), v(x, y), 0]e^{-i\sigma t}$.

(b) Using a disturbance stream function that satisfies the linearized continuity equation identically, eliminate u and v from the remaining momentum equations by substituting

$$u = \frac{\partial \psi}{\partial y} \quad \text{and} \quad v = -\frac{\partial \psi}{\partial x}$$

Show that the resulting momentum equations can be rearranged into

$$\frac{1}{\rho} \frac{\partial p}{\partial x} = i\sigma \frac{\partial \psi}{\partial y} - \frac{\partial U}{\partial x} \frac{\partial \psi}{\partial y} + \frac{\partial U}{\partial y} \frac{\partial \psi}{\partial x} - U \frac{\partial^2 \psi}{\partial x \partial y} - V \frac{\partial^2 \psi}{\partial y^2} + \nu \left(\frac{\partial^3 \psi}{\partial x^2 \partial y} + \frac{\partial^3 \psi}{\partial y^3} \right) \quad (\text{x-mom.})$$

$$\frac{1}{\rho} \frac{\partial p}{\partial y} = -i\sigma \frac{\partial \psi}{\partial x} - \frac{\partial V}{\partial x} \frac{\partial \psi}{\partial y} + \frac{\partial V}{\partial y} \frac{\partial \psi}{\partial x} + U \frac{\partial^2 \psi}{\partial x^2} + V \frac{\partial^2 \psi}{\partial x \partial y} - \nu \left(\frac{\partial^3 \psi}{\partial x^3} + \frac{\partial^3 \psi}{\partial x \partial y^2} \right) \quad (\text{y-mom.})$$

(c) The pressure can be eliminated by taking the partial derivative of the x-momentum pressure gradient with respect to y and setting it equal to the partial derivative of the y-pressure gradient with respect to x . Bearing in mind that the basic flow motion represented by (U, V) must satisfy continuity, show that the two momentum equations can be consolidated into a single fourth-order partial differential equation for the disturbance stream function viz.

Page 316

$$\begin{aligned} i\sigma \left(\frac{\partial^2 \psi}{\partial x^2} + \frac{\partial^2 \psi}{\partial y^2} \right) &= \left(\frac{\partial^2 V}{\partial x \partial y} - \frac{\partial^2 U}{\partial y^2} \right) \frac{\partial \psi}{\partial x} + \left(\frac{\partial^2 U}{\partial x \partial y} - \frac{\partial^2 V}{\partial x^2} \right) \frac{\partial \psi}{\partial y} \\ &+ U \left(\frac{\partial^3 \psi}{\partial x^3} + \frac{\partial^3 \psi}{\partial x \partial y^2} \right) + V \left(\frac{\partial^3 \psi}{\partial y^3} + \frac{\partial^3 \psi}{\partial x^2 \partial y} \right) - \nu \left(\frac{\partial^4 \psi}{\partial x^4} + \frac{\partial^4 \psi}{\partial y^4} + 2 \frac{\partial^4 \psi}{\partial x^2 \partial y^2} \right) \end{aligned}$$

5-45. . The Taylor profile, which has been used to describe the ideal gaseous motion in slab-type rocket motors (Taylor 1956), corresponds to a two-dimensional self-similar profile in a porous channel [Griffond and Casalis (2006)]. When the channel half height is taken to be unity, the basic flow stream function may be written as $\psi_0(x, y) = x \sin(\frac{1}{2}\pi y)$ for $0 \leq x \leq X_N, 0 \leq y \leq 1$ where X_N represents the length of the porous channel (see Fig. P5-45).

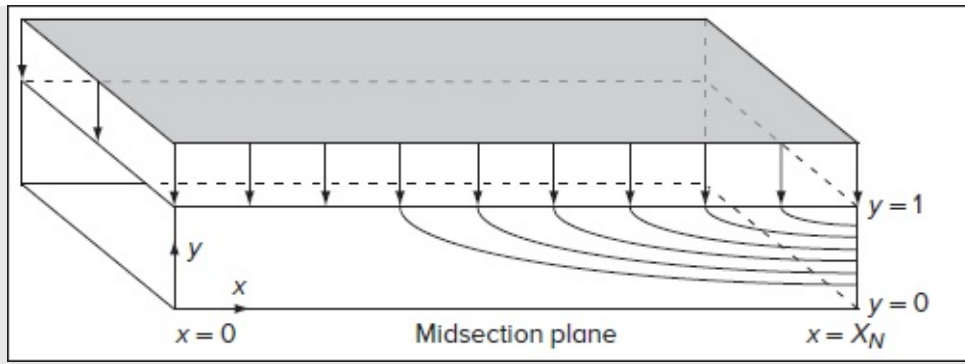


FIGURE P5-45

Assuming a wall injection speed of unity, the basic flow velocity may be expressed as $\mathbf{V}_0(x, y) = U(x, y)\mathbf{i} + V(y)\mathbf{j}$ with $U = \frac{1}{2}\pi x \cos(\frac{1}{2}\pi y)$ and $V = -\sin(\frac{1}{2}\pi y)$. As shown in the problem above, the linearized Navier–Stokes equations with

two-dimensional biglobal stability disturbance modes (and $n = 0$ in the z direction) can be consolidated into a single, fourth-order, partial differential equation for the disturbance stream function $\hat{\psi} = \psi(x, y)e^{-i\sigma t}$. Since $V(y)$ is independent of x , the stream function formulation can be further reduced into

$$i\sigma \left(\frac{\partial^2 \psi}{\partial x^2} + \frac{\partial^2 \psi}{\partial y^2} \right) = -\frac{\partial^2 U}{\partial y^2} \frac{\partial \psi}{\partial x} + \frac{\partial^2 U}{\partial x \partial y} \frac{\partial \psi}{\partial y} + U \left(\frac{\partial^3 \psi}{\partial x^3} + \frac{\partial^3 \psi}{\partial x \partial y^2} \right) + V \left(\frac{\partial^3 \psi}{\partial y^3} + \frac{\partial^3 \psi}{\partial x^2 \partial y} \right) - \nu \left(\frac{\partial^4 \psi}{\partial x^4} + \frac{\partial^4 \psi}{\partial y^4} + 2 \frac{\partial^4 \psi}{\partial x^2 \partial y^2} \right)$$

The basic flow boundary conditions require uniform wall-normal injection, no slip at the headwall, and symmetry with respect to the midsection plane, $y = 0$, specifically:

$$\begin{cases} \frac{\partial \psi_0}{\partial x}(x, 1) = 1; & \frac{\partial \psi_0}{\partial y}(x, 1) = 0 & \text{(wall-normal injection)} \\ \frac{\partial \psi_0}{\partial x}(0, y) = \frac{\partial \psi_0}{\partial y}(0, y) = 0 & & \text{(no slip at headwall)} \\ \frac{\partial \psi_0}{\partial x}(x, 0) = \frac{\partial^2 \psi_0}{\partial y^2}(x, 0) = 0 & & (V = \partial U / \partial y = 0 \text{ at } y = 0) \end{cases}$$

(a) Recalling that the instantaneous motion is recoverable from $\psi \sim \psi_0 + \hat{\psi}$, and that disturbances are not allowed to alter the basic flow conditions at the boundaries, show that the disturbances must satisfy:

$$\begin{cases} \frac{\partial \psi}{\partial x}(x, 1) = \frac{\partial \psi}{\partial y}(x, 1) = 0 & \text{(wall-normal injection)} \\ \frac{\partial \psi}{\partial x}(0, y) = \frac{\partial \psi}{\partial y}(0, y) = 0 & \text{(no slip at headwall)} \\ \frac{\partial \psi}{\partial x}(x, 0) = \frac{\partial^2 \psi}{\partial y^2}(x, 0) = 0 & \text{(midsection symmetry)} \end{cases}$$

You may also impose the outflow condition suggested by Theofilis, Duck, and Owen (2004) by setting a simple extrapolation relation at the domain's exit plane, $x = X_N$, namely,

$$\psi(X_N, y) = \frac{X_N - X_{N-2}}{X_{N-1} - X_{N-2}} \psi(X_{N-1}, y) + \frac{X_{N-1} - X_N}{X_{N-1} - X_{N-2}} \psi(X_{N-2}, y)$$

(b) Using the Taylor basic flow profile and a numerical solver of your choice, find the eigenvalues for $n = 0$, $X_N = 8$, and $\nu = 1/900 = 1.11 \times 10^{-3} \text{ m}^2/\text{s}$.

(c) Optional: Compare your findings to those of Griffond and Casalis (2001), “On the nonparallel stability of the injection induced two-dimensional Taylor flow.”

5-46. Assuming strictly axisymmetric flow conditions with an azimuthal wave number of $m = 0$ and a basic motion that is prescribed by a two-component velocity vector of the form $\mathbf{V}_0(r, z) = [U_r(r), 0, U_z(r, z)]$, (a) show that the linearized Navier–Stokes equations with biglobal stability disturbance modes, which are given by [Eqs. \(5-86\)–\(5-89\)](#), can be readily reduced into

$$\begin{aligned} \frac{\partial u_r}{\partial r} + \frac{u_r}{r} + \frac{\partial u_z}{\partial z} &= 0 \text{ (continuity)} \\ -i\sigma u_r + U_r \frac{\partial u_r}{\partial r} + u_r \frac{\partial U_r}{\partial r} + U_z \frac{\partial u_r}{\partial z} - \nu \left(\frac{\partial^2 u_r}{\partial r^2} + \frac{1}{r} \frac{\partial u_r}{\partial r} - \frac{u_r}{r^2} + \frac{\partial^2 u_r}{\partial z^2} \right) &= -\frac{1}{\rho} \frac{\partial p}{\partial r} \text{ (r-mom.)} \\ -i\sigma u_z + U_r \frac{\partial u_z}{\partial r} + u_r \frac{\partial U_z}{\partial r} + U_z \frac{\partial u_z}{\partial z} + u_z \frac{\partial U_z}{\partial z} - \nu \left(\frac{\partial^2 u_z}{\partial r^2} + \frac{1}{r} \frac{\partial u_z}{\partial r} + \frac{\partial^2 u_z}{\partial z^2} \right) &= -\frac{1}{\rho} \frac{\partial p}{\partial z} \text{ (z-mom.)} \end{aligned}$$

where $\hat{p}(r, \theta, z, t) = p(r, z)e^{-i\sigma t}$ and $\hat{\mathbf{v}}(r, \theta, z, t) = (\hat{u}_r, 0, \hat{u}_z) = [u_r(r, z), 0, u_z(r, z)]e^{-i\sigma t}$.

(b) Using a disturbance stream function that satisfies the linearized continuity equation identically, eliminate u_r and u_z from the remaining radial and axial momentum equations by substituting

$$u_r = -\frac{1}{r} \frac{\partial \psi}{\partial z} \quad \text{and} \quad u_z = \frac{1}{r} \frac{\partial \psi}{\partial r}$$

(c) The pressure can be eliminated by taking the partial derivative of the radial pressure gradient with respect to z and setting it equal to the partial derivative of the axial pressure gradient with respect to r . Show that the problem reduces to a single fourth-order partial differential equation for the disturbance stream function, namely, the one advanced by Chedevergne et al. (2006):

$$\begin{aligned}
i\sigma \left(\frac{\partial^2 \psi}{\partial r^2} - \frac{1}{r} \frac{\partial \psi}{\partial r} + \frac{\partial^2 \psi}{\partial z^2} \right) &= U_r \frac{\partial^3 \psi}{\partial r^3} + \left(\frac{\partial U_r}{\partial r} + \frac{\partial U_z}{\partial z} - \frac{2U_r}{r} \right) \frac{\partial^2 \psi}{\partial r^2} + U_z \frac{\partial^3 \psi}{\partial z^3} + \left(\frac{2U_r}{r^2} - \frac{1}{r} \frac{\partial U_r}{\partial r} + \frac{\partial^2 U_z}{\partial r \partial z} - \frac{1}{r} \frac{\partial U_z}{\partial z} \right) \frac{\partial \psi}{\partial r} \\
&+ U_r \frac{\partial^3 \psi}{\partial r \partial z^2} + \left(-\frac{U_r}{r} + \frac{\partial U_r}{\partial r} + \frac{\partial U_z}{\partial z} \right) \frac{\partial^2 \psi}{\partial z^2} + \left(\frac{1}{r} \frac{\partial U_z}{\partial r} - \frac{\partial^2 U_z}{\partial r^2} \right) \frac{\partial \psi}{\partial z} - \frac{U_z}{r} \frac{\partial^2 \psi}{\partial r \partial z} + U_z \frac{\partial^3 \psi}{\partial r^2 \partial z} \\
&- \nu \left(\frac{\partial^4 \psi}{\partial r^4} - \frac{2}{r} \frac{\partial^3 \psi}{\partial r^3} + \frac{3}{r^2} \frac{\partial^2 \psi}{\partial r^2} - \frac{3}{r^3} \frac{\partial \psi}{\partial r} + 2 \frac{\partial^4 \psi}{\partial r^2 \partial z^2} - \frac{2}{r} \frac{\partial^3 \psi}{\partial r \partial z^2} + \frac{\partial^4 \psi}{\partial z^4} \right)
\end{aligned}$$

5-47. The Taylor–Culick profile, which has been repeatedly used to describe the ideal gaseous motion in solid rocket motors (Culick 1966), corresponds to an axisymmetric, self-similar profile in a porous tube. When the tube radius is taken to be unity, the basic flow stream function may be written as $\psi_0 = z \sin \left(\frac{1}{2} \pi r^2 \right)$ for $0 \leq r \leq 1$ and $0 \leq z \leq Z_N$, where Z_N represents the length of the porous tube (see Fig. P5-47a).

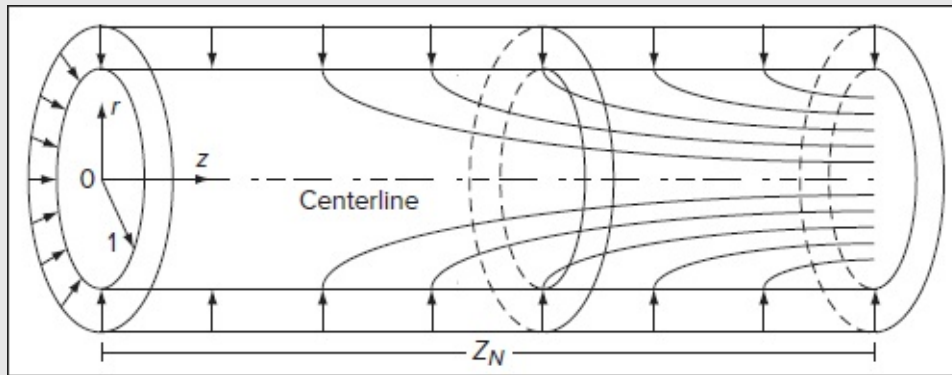


FIGURE P5-47a

Assuming a wall injection speed of unity, the basic flow velocity may be expressed as $\mathbf{V}_0(r, z) = U_r \mathbf{e}_r + U_z \mathbf{e}_z$

with $U_r = -r^{-1} \sin(\frac{1}{2} \pi r^2)$ and $U_z = \pi z \cos(\frac{1}{2} \pi r^2)$. As shown in the problem above, the linearized Navier–Stokes equations

with biglobal stability disturbance modes can be reduced into a single, fourth-order, partial differential equation for the disturbance stream function $\hat{\psi}$, where $\hat{\psi} = \psi(r, z)e^{-i\sigma t}$. Following Chedevergne et al. (2012), the basic flow boundary conditions require uniform wall-normal injection, no slip at the headwall, and axisymmetry with respect to $r = 0$, specifically:

$$\begin{cases} \frac{\partial \psi_0}{\partial r}(1, z) = 0; \quad \frac{\partial \psi_0}{\partial z}(1, z) = 1 & \text{(wall-normal injection)} \\ \frac{\partial \psi_0}{\partial r}(r, 0) = \frac{\partial \psi_0}{\partial z}(r, 0) = 0 & \text{(no slip at headwall)} \\ \frac{\partial^3 \psi_0}{\partial r^3}(0, z) = \frac{\partial \psi_0}{\partial r}(0, z) = \frac{\partial \psi_0}{\partial z}(0, z) = 0 & (U_r = \partial U_z / \partial r = 0) \end{cases}$$

(a) Recalling that the instantaneous motion is recoverable from $\psi \sim \psi_0 + \psi^*$, and that disturbances must be prevented from altering the basic flow conditions at the boundaries, show that the disturbances must satisfy:

$$\begin{cases} \frac{\partial \psi}{\partial r}(1, z) = \frac{\partial \psi}{\partial z}(1, z) = 0 & \text{(wall-normal injection)} \\ \frac{\partial \psi}{\partial r}(r, 0) = \frac{\partial \psi}{\partial z}(r, 0) = 0 & \text{(no slip at headwall)} \\ \frac{\partial^3 \psi}{\partial r^3}(0, z) = \frac{\partial \psi}{\partial r}(0, z) = \frac{\partial \psi}{\partial z}(0, z) = 0 & \text{(axisymmetry)} \end{cases}$$

You may also impose the outflow condition suggested by Theofilis, Duck, and Owen (2004) by setting a simple extrapolation relation at the domain's exit plane, $z = Z_N$, namely,

$$\psi(r, Z_N) = \frac{Z_N - Z_{N-2}}{Z_{N-1} - Z_{N-2}} \psi(r, Z_{N-1}) + \frac{Z_{N-1} - Z_N}{Z_{N-1} - Z_{N-2}} \psi(r, Z_{N-2})$$

(b) Using the Taylor–Culick basic flow and a numerical solver of your choice, show that one of the eigenvalues for $m = 0, Z_N = 8$ and $\nu = 1/1975 \text{ m}^2/\text{s} \approx 5 \times 10^{-4} \text{ m}^2/\text{s}$ is approximately $\sigma = 40.4 - 9.16i$.

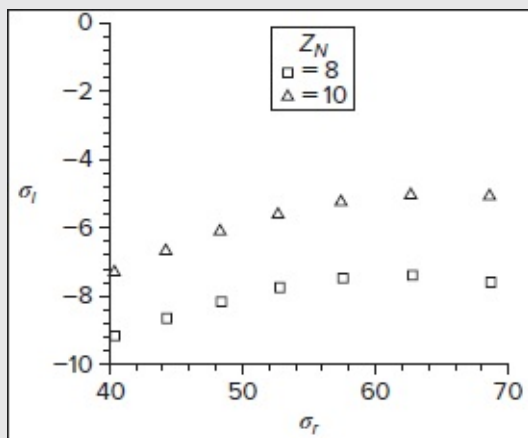


FIGURE P5-47b

(c) Obtain the “boomerang” set of eigenvalues for $Z_N = 8$ and $Z_N = 10$ using $\nu = 5 \times 10^{-4} \text{ m}^2/\text{s}$.

(d) Compare your results to those of Chedevergne et al. (2012) provided in Fig. P5-47b and explain the differences.

5-48. Identify the operators that appear in the biglobal stability disturbance equations using cylindrical polar coordinates, which are given by [Eqs. \(5-94\)–\(5-97\)](#), in order to provide the source coefficients for the eigenvalue problem represented by $A_{ij} f_i = \sigma B_{ij} f_i$, denote the eigenvalues and corresponding eigenvectors, while A_{ij} and B_{ij} refer to

$$A_{ij} = \begin{bmatrix} A_{c,u_r} & A_{c,u_\theta} & A_{c,u_z} & A_{c,p} \\ A_{r,u_r} & A_{r,u_\theta} & A_{r,u_z} & A_{r,p} \\ A_{\theta,u_r} & A_{\theta,u_\theta} & A_{\theta,u_z} & A_{\theta,p} \\ A_{z,u_r} & A_{z,u_\theta} & A_{z,u_z} & A_{z,p} \end{bmatrix} \quad \text{and} \quad B_{ij} = \begin{bmatrix} B_{c,u_r} & B_{c,u_\theta} & B_{c,u_z} & B_{c,p} \\ B_{r,u_r} & B_{r,u_\theta} & B_{r,u_z} & B_{r,p} \\ B_{\theta,u_r} & B_{\theta,u_\theta} & B_{\theta,u_z} & B_{\theta,p} \\ B_{z,u_r} & B_{z,u_\theta} & B_{z,u_z} & B_{z,p} \end{bmatrix}$$

Show that

$$\begin{cases} A_{c,u_r} = \frac{\partial}{\partial r} + \frac{1}{r} \\ A_{c,u_\theta} = \frac{im}{r} \\ A_{c,u_z} = \frac{\partial}{\partial z} \\ A_{c,p} = 0 \end{cases} \quad \begin{cases} A_{r,u_r} = U_r \frac{\partial}{\partial r} + \frac{\partial U_r}{\partial r} + im \frac{U_\theta}{r} + U_z \frac{\partial}{\partial z} \\ \quad - \nu \left(\frac{\partial^2}{\partial r^2} + \frac{1}{r} \frac{\partial}{\partial r} - \frac{1+m^2}{r^2} + \frac{\partial^2}{\partial z^2} \right) \\ A_{r,u_\theta} = \frac{1}{r} \frac{\partial U_r}{\partial \theta} - \frac{2U_\theta}{r} + 2\nu \frac{im}{r^2} \\ A_{r,u_z} = \frac{\partial U_r}{\partial z} \quad A_{r,p} = \frac{1}{\rho} \frac{\partial}{\partial r} \end{cases} \quad \begin{cases} A_{\theta,u_r} = \frac{\partial U_\theta}{\partial r} + \frac{U_\theta}{r} - 2\nu \frac{im}{r^2} \\ A_{\theta,u_\theta} = U_r \frac{\partial}{\partial r} + \frac{1}{r} \frac{\partial U_\theta}{\partial \theta} + \frac{U_r}{r} + U_z \frac{\partial}{\partial z} + im \frac{U_\theta}{r} \\ \quad - \nu \left(\frac{\partial^2}{\partial r^2} + \frac{1}{r} \frac{\partial}{\partial r} - \frac{1+m^2}{r^2} + \frac{\partial^2}{\partial z^2} \right) \\ A_{\theta,u_z} = \frac{\partial U_\theta}{\partial z} \quad A_{\theta,p} = \frac{im}{\rho r} \end{cases}$$

$$\text{and} \quad \begin{cases} A_{z,u_r} = \frac{\partial U_z}{\partial r} \quad A_{z,u_\theta} = \frac{1}{r} \frac{\partial U_z}{\partial \theta} \\ A_{z,u_z} = U_r \frac{\partial}{\partial r} + U_z \frac{\partial}{\partial z} + \frac{\partial U_z}{\partial z} + im \frac{U_\theta}{r} \\ \quad - \nu \left(\frac{\partial^2}{\partial r^2} + \frac{1}{r} \frac{\partial}{\partial r} - \frac{m^2}{r^2} + \frac{\partial^2}{\partial z^2} \right) \quad A_{z,p} = \frac{1}{\rho} \frac{\partial}{\partial z} \end{cases}$$

and that the only nonvanishing values of B_{ij} are $B_{r,u_r} = B_{\theta,u_\theta} = B_{z,u_z} = i$.

5-49. Using [Eq. \(5-106\)](#), provide the linear coordinate transformations that are needed to map an axisymmetric problem defined in the (r, z) domain from the $0 \leq r \leq 1$ and $0 \leq z \leq Z$ N intervals to the Chebyshev domain of $[-1, 1]$.

5-50. Using [Eq. \(5-106\)](#), provide the linear coordinate transformations that are needed to map a cylindrical polar problem defined in the (r, θ, z) domain from the $0 \leq r \leq 1$, $0 \leq \theta \leq 2\pi$, and $0 \leq z \leq Z$ N intervals to the Chebyshev domain of $[-1, 1]$.

5-51. Identify the block matrices that must be used to convert the biglobal stability disturbance equations in cylindrical polar coordinates, based on [Eqs. \(5-94\)–\(5-97\)](#), to an eigenvalue problem of the form $A_{ij} f_i = \sigma B_{ij} f_i$, where σ and f_i denote the eigenvalues and corresponding eigenvectors. The block matrices appear as

$$A_{ij} = \begin{bmatrix} A_{c,u_r} & A_{c,u_\theta} & A_{c,u_z} & A_{c,p} \\ A_{r,u_r} & A_{r,u_\theta} & A_{r,u_z} & A_{r,p} \\ A_{\theta,u_r} & A_{\theta,u_\theta} & A_{\theta,u_z} & A_{\theta,p} \\ A_{z,u_r} & A_{z,u_\theta} & A_{z,u_z} & A_{z,p} \end{bmatrix} \quad \text{and} \quad B_{ij} = \begin{bmatrix} B_{c,u_r} & B_{c,u_\theta} & B_{c,u_z} & B_{c,p} \\ B_{r,u_r} & B_{r,u_\theta} & B_{r,u_z} & B_{r,p} \\ B_{\theta,u_r} & B_{\theta,u_\theta} & B_{\theta,u_z} & B_{\theta,p} \\ B_{z,u_r} & B_{z,u_\theta} & B_{z,u_z} & B_{z,p} \end{bmatrix}$$

Show that the only nonvanishing values of B_{ij} are $B_{r,u_r} = B_{\theta,u_\theta} = B_{z,u_z} = iI_N$ and that

$$\begin{cases} A_{c,u_r} = \bar{D}_N^r + \frac{1}{r_{ii}} \\ A_{c,u_\theta} = \frac{im}{r_{ii}} \\ A_{c,u_z} = \bar{D}_N^z \\ A_{c,p} = 0 \end{cases} \quad \begin{cases} A_{r,u_r} = (U_r)_{ii} \bar{D}_N^r + (U_z)_{ii} \bar{D}_N^z + \left(\frac{\partial U_r}{\partial r} + im \frac{U_\theta}{r} \right)_{ii} \\ \quad - \nu \left[(\bar{D}_N^r)^2 + \frac{\bar{D}_N^r}{r_{ii}} - \frac{1+m^2}{r_{ii}^2} + (\bar{D}_N^z)^2 \right] \\ A_{r,u_\theta} = \left(\frac{1}{r} \frac{\partial U_r}{\partial \theta} - 2 \frac{U_\theta}{r} \right)_{ii} + 2\nu \frac{im}{r_{ii}^2} \\ A_{r,u_z} = \left(\frac{\partial U_r}{\partial z} \right)_{ii} \quad A_{r,p} = \frac{1}{\rho} \bar{D}_N^r \end{cases} \quad \begin{cases} A_{\theta,u_r} = \left(\frac{\partial U_\theta}{\partial r} + \frac{U_\theta}{r} \right)_{ii} - 2\nu \frac{im}{r_{ii}^2} \\ A_{\theta,u_\theta} = (U_r)_{ii} \bar{D}_N^r + \left(\frac{1}{r} \frac{\partial U_\theta}{\partial \theta} \right)_{ii} \\ \quad + \left(\frac{U_r}{r} + im \frac{U_\theta}{r} \right)_{ii} + (U_z)_{ii} \bar{D}_N^z \\ \quad - \nu \left[(\bar{D}_N^r)^2 + \frac{\bar{D}_N^r}{r_{ii}} - \frac{1+m^2}{r_{ii}^2} + (\bar{D}_N^z)^2 \right] \\ A_{\theta,u_z} = \left(\frac{\partial U_\theta}{\partial z} \right)_{ii} \quad A_{\theta,p} = \frac{im}{\rho r_{ii}} \end{cases}$$

$$\text{and} \quad \begin{cases} A_{z,u_r} = \left(\frac{\partial U_z}{\partial r} \right)_{ii} \quad A_{z,u_\theta} = \left(\frac{1}{r} \frac{\partial U_z}{\partial \theta} \right)_{ii} \\ A_{z,u_z} = (U_r)_{ii} \bar{D}_N^r + (U_z)_{ii} \bar{D}_N^z + \left(\frac{\partial U_z}{\partial z} + im \frac{U_\theta}{r} \right)_{ii} \\ \quad - \nu \left[(\bar{D}_N^r)^2 + \frac{1}{r_{ii}} \bar{D}_N^r - \frac{m^2}{r_{ii}^2} + (\bar{D}_N^z)^2 \right] \quad A_{z,p} = \frac{1}{\rho} \bar{D}_N^z \end{cases}$$

Page 320

- 5-52. Reduce the block matrices of [Eqs. \(5-94\)–\(5-97\)](#) that you just derived assuming axisymmetric disturbances with no azimuthal variations and $m = 0$.
- 5-53. Consider a problem with a simple axisymmetric viscous-flow configuration, namely, a cylindrical fluid domain that extends over $0 \leq r \leq 1$ and $0 \leq z \leq Z_N$. Assume infinite impedance (hardwall) boundaries everywhere along $r = 0$, $r = 1$, and $z = 0$, and that an outflow condition exists at $z = Z_N$, where a zero normal stress requirement based on [Eq. \(5-114\)](#) translates into

$$\frac{\partial u_z}{\partial r} + \frac{\partial u_r}{\partial z} = 0; \quad \frac{\partial u_\theta}{\partial z} = 0; \quad 2\mu \frac{\partial u_z}{\partial z} - p = 0$$

Show that the boundary conditions on the (u_r, u_θ, u_z, p) disturbance eigenfunctions can be written as

$$\begin{cases} u_r(0, z) = 0 & u_\theta(0, z) = 0 & \frac{\partial u_z}{\partial r}(0, z) = 0 & \frac{\partial p(0, z)}{\partial r} = 0 & \text{(centerline)} \\ u_r(1, z) = 0 & u_\theta(1, z) = 0 & u_z(1, z) = 0 & \text{---} & \text{(sidewall)} \\ u_r(r, 0) = 0 & u_\theta(r, 0) = 0 & u_z(r, 0) = 0 & \text{---} & \text{(headwall)} \\ \frac{\partial u_r}{\partial z}(r, Z_N) = -\frac{\partial u_z}{\partial r}(r, Z_N) & \frac{\partial u_\theta}{\partial z}(r, Z_N) = 0 & \frac{\partial u_z}{\partial z}(r, Z_N) = \frac{p(r, Z_N)}{2\mu} & \text{---} & \text{(exit plane)} \end{cases}$$

- 5-54. Using the cylindrical polar formulation of Probs. 5-51–5-53 and a numerical solver of your choice, investigate the stability of the Taylor–Culick profile corresponding to $\psi_0 = z \sin(\frac{1}{2}\pi r^2)$ for $0 \leq r \leq 1, 0 \leq z \leq Z_N$. Here $\mathbf{V}_0(r, z) = U_r \mathbf{e}_r + U_z \mathbf{e}_z$ with $U_r = -r^{-1} \sin(\frac{1}{2}\pi r^2)$ and $U_z = \pi z \cos(\frac{1}{2}\pi r^2)$. Using $m = 0$ and $\nu = 5 \times 10^{-4} \text{ m}^2/\text{s}$ find the spectrum of eigenvalues for $Z_N = 8$ and $Z_N = 10$. Compare your results to those of Chedevergne et al. (2012) provided in Fig. P5-47b.
- 5-55. Using the cylindrical polar formulation of Probs. 5-51–5-53, investigate the stability of the Cecil–Majdalani profile, which extends the Taylor–Culick motion to spinning rocket motors (see [Fig. P5-55](#)). As shown by Cecil and Majdalani (2017) in their AIAA award-winning paper, the basic motion can be described using $\mathbf{V}_0(r, z) = U_r \mathbf{e}_r + U_\theta \mathbf{e}_\theta + U_z \mathbf{e}_z$ with $U_r = -r^{-1} \sin(\frac{1}{2}\pi r^2)$, $U_\theta = \xi r^{-1} [1 - \exp(-\frac{1}{4}\pi r^2 Re)]$, and $U_z = \pi z \cos(\frac{1}{2}\pi r^2)$ for $0 \leq r \leq 1, 0 \leq \theta \leq 2\pi$, and $0 \leq z \leq Z_N$. Here $\xi = V_s/V_w$ represents the tangential speed of the spinning chamber relative to the wall injection speed, and $Re = V_w a/\nu$ stands for the injection Reynolds number based on the wall injection speed V_w , chamber radius a , and kinematic viscosity ν . When the injection speed and chamber radius are taken to be unity, the Reynolds number becomes equivalent to the reciprocal of the kinematic viscosity, $Re = 1/\nu$ and the Hertzian frequency of rotation may be deduced from $f_s = V_s/(2\pi a)$. Using $m = 0$ and $\nu = 5 \times 10^{-4} \text{ m}^2/\text{s}$, find the spectrum of eigenvalues for $Z_N = 8$ and $Z_N = 10$. By comparing your results to those of Chedevergne et al. (2012) in Fig. P5-47b, what can you say about the effect of axial rotation on the stability of the basic motion? You may use the boundary conditions described in Prob. 5-53.

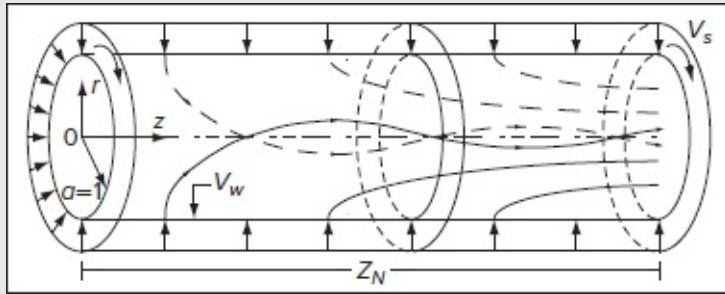


FIGURE P5-55

- 5-56. Identify the operators that appear in the compressible biglobal stability disturbance equations in cylindrical polar coordinates, which are given by [Eqs. \(5-155\)–\(5-160\)](#), in order to provide the source coefficients for the eigenvalue problem represented by $A_{ij} f_i = \sigma B_{ij} f_i$, where σ and f_i denote the eigenvalues and corresponding eigenvectors,

while A_{ij} and B_{ij} refer to

$$A_{ij} = \begin{bmatrix} A_{c,\rho} & A_{c,u_r} & A_{c,u_\theta} & A_{c,u_z} & A_{c,T} \\ A_{r,\rho} & A_{r,u_r} & A_{r,u_\theta} & A_{r,u_z} & A_{r,T} \\ A_{\theta,\rho} & A_{\theta,u_r} & A_{\theta,u_\theta} & A_{\theta,u_z} & A_{\theta,T} \\ A_{z,\rho} & A_{z,u_r} & A_{z,u_\theta} & A_{z,u_z} & A_{z,T} \\ A_{e,\rho} & A_{e,u_r} & A_{e,u_\theta} & A_{e,u_z} & A_{e,T} \end{bmatrix} \quad \text{and} \quad B_{ij} = \begin{bmatrix} B_{c,\rho} & B_{c,u_r} & B_{c,u_\theta} & B_{c,u_z} & B_{c,T} \\ B_{r,\rho} & B_{r,u_r} & B_{r,u_\theta} & B_{r,u_z} & B_{r,T} \\ B_{\theta,\rho} & B_{\theta,u_r} & B_{\theta,u_\theta} & B_{\theta,u_z} & B_{\theta,T} \\ B_{z,\rho} & B_{z,u_r} & B_{z,u_\theta} & B_{z,u_z} & B_{z,T} \\ B_{e,\rho} & B_{e,u_r} & B_{e,u_\theta} & B_{e,u_z} & B_{e,T} \end{bmatrix}$$

Show that

$$\begin{cases} A_{c,\rho} = \frac{\partial U_r}{\partial r} + \frac{U_r}{r} + \frac{1}{r} \frac{\partial U_\theta}{\partial \theta} + \frac{\partial U_z}{\partial z} + U_r \frac{\partial}{\partial r} + im \frac{U_\theta}{r} + U_z \frac{\partial}{\partial z} \\ A_{r,\rho} = \left(\frac{\partial U_r}{\partial t} + U_r \frac{\partial U_r}{\partial r} + \frac{U_\theta}{r} \frac{\partial U_r}{\partial \theta} + U_z \frac{\partial U_r}{\partial z} - \frac{U_\theta^2}{r} \right) + R \left(\frac{\partial T_0}{\partial r} + T_0 \frac{\partial}{\partial r} \right) \\ A_{\theta,\rho} = \left(\frac{\partial U_\theta}{\partial t} + U_r \frac{\partial U_\theta}{\partial r} + \frac{U_\theta}{r} \frac{\partial U_\theta}{\partial \theta} + U_z \frac{\partial U_\theta}{\partial z} + \frac{U_r U_\theta}{r} \right) + \frac{R}{r} \left(im T_0 + \frac{\partial T_0}{\partial \theta} \right) \\ A_{z,\rho} = \left(\frac{\partial U_z}{\partial t} + U_r \frac{\partial U_z}{\partial r} + \frac{U_\theta}{r} \frac{\partial U_z}{\partial \theta} + U_z \frac{\partial U_z}{\partial z} \right) + R \left(\frac{\partial T_0}{\partial z} + T_0 \frac{\partial}{\partial z} \right) \\ A_{e,\rho} = c_p \frac{\partial T_0}{\partial t} + c_v \left(U_r \frac{\partial T_0}{\partial r} + \frac{U_\theta}{r} \frac{\partial T_0}{\partial \theta} + U_z \frac{\partial T_0}{\partial z} \right) - RT_0 \left(U_r \frac{\partial}{\partial r} + U_z \frac{\partial}{\partial z} + im \frac{U_\theta}{r} \right) \end{cases} \quad (\text{density terms})$$

$$\begin{cases} A_{c,u_r} = \frac{\partial \rho_0}{\partial r} + \rho_0 \left(\frac{\partial}{\partial r} + \frac{1}{r} \right) \\ A_{r,u_r} = \rho_0 \left(U_r \frac{\partial}{\partial r} + im \frac{U_\theta}{r} + U_z \frac{\partial}{\partial z} + \frac{\partial U_r}{\partial r} \right) - \mu \left[\frac{4}{3} \left(\frac{\partial^2}{\partial r^2} + \frac{1}{r} \frac{\partial}{\partial r} - \frac{1}{r^2} \right) + \frac{\partial^2}{\partial z^2} - \frac{m^2}{r^2} \right] \\ A_{\theta,u_r} = \rho_0 \left(\frac{U_\theta}{r} + \frac{\partial U_\theta}{\partial r} \right) - \mu \frac{im}{3r} \left(\frac{7}{r} + \frac{\partial}{\partial r} \right) \\ A_{z,u_r} = \rho_0 \frac{\partial U_z}{\partial r} - \mu \left(\frac{1}{r} \frac{\partial}{\partial z} + \frac{\partial^2}{\partial r \partial z} \right) \quad A_{e,u_r} = \rho_0 c_p \frac{\partial T_0}{\partial r} - \frac{\partial P_0}{\partial r} - \Phi_r \end{cases} \quad (\text{radial terms})$$

$$\begin{cases} A_{c,u_\theta} = \frac{1}{r} \frac{\partial \rho_0}{\partial \theta} + \rho_0 \frac{im}{r} \quad A_{r,u_\theta} = \frac{\rho_0}{r} \left(\frac{\partial U_r}{\partial \theta} - 2U_\theta \right) - \mu \frac{im}{3r} \left(\frac{\partial}{\partial r} - \frac{7}{r} \right) \\ A_{\theta,u_\theta} = \rho_0 \left(U_r \frac{\partial}{\partial r} + \frac{im U_\theta}{r} + \frac{U_r}{r} + U_z \frac{\partial}{\partial z} + \frac{1}{r} \frac{\partial U_\theta}{\partial \theta} \right) - \mu \left(\frac{\partial^2}{\partial r^2} + \frac{1}{r} \frac{\partial}{\partial r} - \frac{1}{r^2} + \frac{\partial^2}{\partial z^2} - \frac{4m^2}{3r^2} \right) \\ A_{z,u_\theta} = \frac{\rho_0}{r} \frac{\partial U_z}{\partial \theta} - \mu \frac{im}{3r} \frac{\partial}{\partial z} \quad A_{e,u_\theta} = \frac{\rho_0 c_p}{r} \frac{\partial T_0}{\partial \theta} - \frac{1}{r} \frac{\partial P_0}{\partial \theta} - \Phi_\theta \end{cases} \quad (\text{tangential terms})$$

$$\begin{cases} A_{c,u_z} = \frac{\partial \rho_0}{\partial z} + \rho_0 \frac{\partial}{\partial z} \quad A_{r,u_z} = \rho_0 \frac{\partial U_r}{\partial z} - \frac{\mu}{3} \frac{\partial^2}{\partial r \partial z} \quad A_{\theta,u_z} = \rho_0 \frac{\partial U_\theta}{\partial z} - \mu \frac{im}{3r} \frac{\partial}{\partial z} \\ A_{z,u_z} = \rho_0 \left(U_r \frac{\partial}{\partial r} + im \frac{U_\theta}{r} + U_z \frac{\partial}{\partial z} + \frac{\partial U_z}{\partial z} \right) - \mu \left(\frac{\partial^2}{\partial r^2} + \frac{1}{r} \frac{\partial}{\partial r} - \frac{m^2}{r^2} + \frac{4}{3} \frac{\partial^2}{\partial z^2} \right) \\ A_{e,u_z} = \rho_0 c_p \frac{\partial T_0}{\partial z} - \frac{\partial P_0}{\partial z} - \Phi_z \end{cases} \quad (\text{axial terms})$$

and

$$\begin{cases} A_{c,T} = 0 \quad A_{r,T} = R \left(\frac{\partial \rho_0}{\partial r} + \rho_0 \frac{\partial}{\partial r} \right) \quad A_{\theta,T} = \frac{R}{r} \left(im \rho_0 + \frac{\partial \rho_0}{\partial \theta} \right) \quad A_{z,T} = R \left(\frac{\partial \rho_0}{\partial z} + \rho_0 \frac{\partial}{\partial z} \right) \\ A_{e,T} = \rho_0 c_v \left(U_r \frac{\partial}{\partial r} + im \frac{U_\theta}{r} + U_z \frac{\partial}{\partial z} \right) - R \left(U_r \frac{\partial \rho_0}{\partial r} + U_z \frac{\partial \rho_0}{\partial z} + \frac{U_\theta}{r} \frac{\partial \rho_0}{\partial \theta} \right) - k \left(\frac{\partial^2}{\partial r^2} + \frac{1}{r} \frac{\partial}{\partial r} - \frac{m^2}{r^2} + \frac{\partial^2}{\partial z^2} \right) \end{cases} \quad (\text{temperature terms})$$

where the dissipation function may be reconstructed from

$$\begin{aligned}\frac{\Phi_r}{\mu} &= \frac{4}{3} \left\{ \left(2 \frac{\partial U_r}{\partial r} - \frac{U_r}{r} - \frac{1}{r} \frac{\partial U_\theta}{\partial \theta} - \frac{\partial U_z}{\partial z} \right) \frac{\partial}{\partial r} + \frac{1}{r} \left[2 \left(\frac{\partial U_\theta}{\partial \theta} + U_r \right) - \frac{\partial U_r}{\partial r} - \frac{\partial U_z}{\partial z} \right] \right\} \\ &\quad + 2 \left\{ \frac{im}{r} \left[\frac{\partial U_\theta}{\partial r} + \frac{1}{r} \left(\frac{\partial U_r}{\partial \theta} - U_\theta \right) \right] + \left(\frac{\partial U_z}{\partial r} + \frac{\partial U_r}{\partial z} \right) \frac{\partial}{\partial z} \right\} \\ \frac{\Phi_\theta}{\mu} &= \frac{4}{3} \left[\frac{2}{r} \left(\frac{\partial U_\theta}{\partial \theta} + U_r \right) - \frac{\partial U_r}{\partial r} - \frac{\partial U_z}{\partial z} \right] \frac{im}{r} + 2 \left\{ \left[\frac{\partial U_\theta}{\partial r} + \frac{1}{r} \left(\frac{\partial U_r}{\partial \theta} - U_\theta \right) \right] \left(\frac{\partial}{\partial r} - \frac{1}{r} \right) + \left(\frac{1}{r} \frac{\partial U_z}{\partial \theta} + \frac{\partial U_\theta}{\partial z} \right) \frac{\partial}{\partial z} \right\} \\ \frac{\Phi_z}{\mu} &= \frac{4}{3} \left(2 \frac{\partial U_z}{\partial z} - \frac{\partial U_r}{\partial r} - \frac{U_r}{r} - \frac{1}{r} \frac{\partial U_\theta}{\partial \theta} \right) \frac{\partial}{\partial z} + 2 \left[\left(\frac{\partial U_z}{\partial r} + \frac{\partial U_r}{\partial z} \right) \frac{\partial}{\partial r} + \left(\frac{1}{r} \frac{\partial U_z}{\partial \theta} + \frac{\partial U_\theta}{\partial z} \right) \frac{im}{r} \right]\end{aligned}$$

Page 322

and that the only nonvanishing values of B_{ij} are $B_{c,\rho} = i$, $B_{r,u_r} = B_{\theta,u_\theta} = B_{z,u_z} = i\rho_0$, $B_{e,T} = i\rho_0 c_v$, and $B_{e,\rho} = -iRT_0$.

5-57. Identify the block matrices that must be used to convert the compressible biglobal stability disturbance equations in cylindrical polar coordinates, based on [Eqs. \(5-155\)–\(5-160\)](#), to an eigenvalue problem of the form $A_{ij}f_i = \sigma B_{ij}f_i$, where σ and f_i denote the eigenvalues and corresponding eigenvectors. The block matrices appear as

$$A_{ij} = \begin{bmatrix} A_{c,\rho} & A_{c,u_r} & A_{c,u_\theta} & A_{c,u_z} & A_{c,T} \\ A_{r,\rho} & A_{r,u_r} & A_{r,u_\theta} & A_{r,u_z} & A_{r,T} \\ A_{\theta,\rho} & A_{\theta,u_r} & A_{\theta,u_\theta} & A_{\theta,u_z} & A_{\theta,T} \\ A_{z,\rho} & A_{z,u_r} & A_{z,u_\theta} & A_{z,u_z} & A_{z,T} \\ A_{e,\rho} & A_{e,u_r} & A_{e,u_\theta} & A_{e,u_z} & A_{e,T} \end{bmatrix} \quad \text{and} \quad B_{ij} = \begin{bmatrix} B_{c,\rho} & B_{c,u_r} & B_{c,u_\theta} & B_{c,u_z} & B_{c,T} \\ B_{r,\rho} & B_{r,u_r} & B_{r,u_\theta} & B_{r,u_z} & B_{r,T} \\ B_{\theta,\rho} & B_{\theta,u_r} & B_{\theta,u_\theta} & B_{\theta,u_z} & B_{\theta,T} \\ B_{z,\rho} & B_{z,u_r} & B_{z,u_\theta} & B_{z,u_z} & B_{z,T} \\ B_{e,\rho} & B_{e,u_r} & B_{e,u_\theta} & B_{e,u_z} & B_{e,T} \end{bmatrix}$$

Show that the only nonvanishing values of B_{ij} are $B_{c,\rho} = iI_N$, $B_{r,u_r} = B_{\theta,u_\theta} = B_{z,u_z} = i\rho_0 I_N$, $B_{e,T} = i\rho_0 c_v I_N$, $B_{e,\rho} = -iRT_0 I_N$ and that

$$\left\{ \begin{aligned} A_{c,\rho} &= \left(\frac{\partial U_r}{\partial r} + \frac{U_r}{r} + \frac{1}{r} \frac{\partial U_\theta}{\partial \theta} + \frac{\partial U_z}{\partial z} + im \frac{U_\theta}{r} \right)_{ii} + (U_r)_{ii} \bar{D}'_N + (U_z)_{ii} \bar{D}^z_N \\ A_{r,\rho} &= \left(\frac{\partial U_r}{\partial t} + U_r \frac{\partial U_r}{\partial r} + \frac{U_\theta}{r} \frac{\partial U_r}{\partial \theta} + U_z \frac{\partial U_r}{\partial z} - \frac{U_\theta^2}{r} \right)_{ii} + R \left[\left(\frac{\partial T_0}{\partial r} \right)_{ii} + (T_0)_{ii} \bar{D}'_N \right] \\ A_{\theta,\rho} &= \left(\frac{\partial U_\theta}{\partial t} + U_r \frac{\partial U_\theta}{\partial r} + \frac{U_\theta}{r} \frac{\partial U_\theta}{\partial \theta} + U_z \frac{\partial U_\theta}{\partial z} + \frac{U_r U_\theta}{r} \right)_{ii} + \frac{R}{r_{ii}} \left[im (T_0)_{ii} + \left(\frac{\partial T_0}{\partial \theta} \right)_{ii} \right] \\ A_{z,\rho} &= \left(\frac{\partial U_z}{\partial t} + U_r \frac{\partial U_z}{\partial r} + \frac{U_\theta}{r} \frac{\partial U_z}{\partial \theta} + U_z \frac{\partial U_z}{\partial z} \right)_{ii} + R \left[\left(\frac{\partial T_0}{\partial z} \right)_{ii} + (T_0)_{ii} \bar{D}^z_N \right] \\ A_{e,\rho} &= c_p \left(\frac{\partial T_0}{\partial t} \right)_{ii} + c_v \left(U_r \frac{\partial T_0}{\partial r} + \frac{U_\theta}{r} \frac{\partial T_0}{\partial \theta} + U_z \frac{\partial T_0}{\partial z} \right)_{ii} - R (T_0)_{ii} \left[(U_r)_{ii} \frac{\partial}{\partial r} + (U_z)_{ii} \frac{\partial}{\partial z} + im \left(\frac{U_\theta}{r} \right)_{ii} \right] \end{aligned} \right. \quad (\text{density terms})$$

$$\left\{ \begin{aligned} A_{c,u_r} &= \left(\frac{\partial \rho_0}{\partial r} \right)_{ii} + (\rho_0)_{ii} \left(\bar{D}'_N + \frac{1}{r_{ii}} \right) \\ A_{r,u_r} &= (\rho_0)_{ii} \left[(U_r)_{ii} \bar{D}'_N + im \left(\frac{U_\theta}{r} \right)_{ii} + (U_z)_{ii} \bar{D}^z_N + \left(\frac{\partial U_r}{\partial r} \right)_{ii} \right] - \mu \left\{ \frac{4}{3} \left[(\bar{D}'_N)^2 + \frac{1}{r_{ii}} \bar{D}'_N - \frac{1}{r_{ii}^2} \right] + (\bar{D}^z_N)^2 - \frac{m^2}{r_{ii}^2} \right\} \\ A_{\theta,u_r} &= (\rho_0)_{ii} \left(\frac{U_\theta}{r} + \frac{\partial U_\theta}{\partial r} \right)_{ii} - \mu \frac{im}{3} \left(\frac{7}{r_{ii}^2} + \frac{1}{r_{ii}} \bar{D}'_N \right) \\ A_{z,u_r} &= (\rho_0)_{ii} \left(\frac{\partial U_z}{\partial r} \right)_{ii} - \frac{\mu}{3} \left(\frac{\bar{D}^z_N}{r_{ii}} + \bar{D}'_N \bar{D}^z_N \right) \quad A_{e,u_r} = (\rho_0)_{ii} c_p \left(\frac{\partial T_0}{\partial r} \right)_{ii} - \left(\frac{\partial P_0}{\partial r} \right)_{ii} - \bar{\Phi}_r \end{aligned} \right. \quad (\text{radial terms})$$

$$\left\{ \begin{aligned} A_{c,u_\theta} &= \frac{1}{r_{ii}} \left(\frac{\partial \rho_0}{\partial \theta} + im \rho_0 \right)_{ii} \quad A_{r,u_\theta} = (\rho_0)_{ii} \left(\frac{1}{r} \frac{\partial U_r}{\partial \theta} - \frac{2 U_\theta}{r} \right)_{ii} - \mu \frac{im}{3} \left(\frac{1}{r_{ii}} \bar{D}'_N - \frac{7}{r_{ii}^2} \right) \\ A_{\theta,u_\theta} &= (\rho_0)_{ii} \left[(U_r)_{ii} \bar{D}'_N + \frac{im (U_\theta)_{ii} + (U_r)_{ii}}{r_{ii}} + (U_z)_{ii} \bar{D}^z_N + \frac{1}{r_{ii}} \left(\frac{\partial U_\theta}{\partial \theta} \right)_{ii} \right] \\ &\quad - \mu \left[(\bar{D}'_N)^2 + \frac{\bar{D}'_N}{r_{ii}} - \frac{1}{r_{ii}^2} + (\bar{D}^z_N)^2 - \frac{4 m^2}{3 r_{ii}^2} \right] \\ A_{z,u_\theta} &= \frac{(\rho_0)_{ii}}{r_{ii}} \left(\frac{\partial U_z}{\partial \theta} \right)_{ii} - \mu \frac{im}{3 r_{ii}} \bar{D}^z_N \quad A_{e,u_\theta} = c_p \frac{(\rho_0)_{ii}}{r_{ii}} \left(\frac{\partial T_0}{\partial \theta} - \frac{\partial P_0}{\partial \theta} \right)_{ii} - \bar{\Phi}_\theta \end{aligned} \right. \quad (\text{tangential terms})$$

$$\left\{ \begin{aligned} A_{c,u_z} &= \left(\frac{\partial \rho_0}{\partial z} \right)_{ii} + (\rho_0)_{ii} \bar{D}^z_N \quad A_{r,u_z} = (\rho_0)_{ii} \left(\frac{\partial U_r}{\partial z} \right)_{ii} - \frac{\mu}{3} \bar{D}'_N \bar{D}^z_N \\ A_{\theta,u_z} &= (\rho_0)_{ii} \left(\frac{\partial U_\theta}{\partial z} \right)_{ii} - \mu \frac{im}{3 r_{ii}} \bar{D}^z_N \\ A_{z,u_z} &= (\rho_0)_{ii} \left[(U_r)_{ii} \bar{D}'_N + im \left(\frac{U_\theta}{r} \right)_{ii} + (U_z)_{ii} \bar{D}^z_N + \left(\frac{\partial U_z}{\partial z} \right)_{ii} \right] \\ &\quad - \mu \left[(\bar{D}'_N)^2 + \frac{\bar{D}'_N}{r_{ii}} - \frac{m^2}{r_{ii}^2} + \frac{4}{3} (\bar{D}^z_N)^2 \right] \quad A_{e,u_z} = \left(\rho_0 c_p \frac{\partial T_0}{\partial z} - \frac{\partial P_0}{\partial z} \right)_{ii} - \Phi_z \end{aligned} \right. \quad (\text{axial terms})$$

and

$$\left\{ \begin{aligned} A_{c,T} &= 0 \quad A_{r,T} = R \left[\left(\frac{\partial \rho_0}{\partial r} \right)_{ii} + (\rho_0)_{ii} \bar{D}'_N \right] \\ A_{\theta,T} &= \frac{R}{r_{ii}} \left(im \rho_0 + \frac{\partial \rho_0}{\partial \theta} \right)_{ii} \quad A_{z,T} = R \left[\left(\frac{\partial \rho_0}{\partial z} \right)_{ii} + (\rho_0)_{ii} \bar{D}^z_N \right] \\ A_{e,T} &= (\rho_0)_{ii} c_v \left[(U_r)_{ii} \bar{D}'_N + im \left(\frac{U_\theta}{r} \right)_{ii} + (U_z)_{ii} \bar{D}^z_N \right] \\ &\quad - R \left(U_r \frac{\partial \rho_0}{\partial r} + U_z \frac{\partial \rho_0}{\partial z} + \frac{U_\theta}{r} \frac{\partial \rho_0}{\partial \theta} \right)_{ii} - k \left[(\bar{D}'_N)^2 + \frac{\bar{D}'_N}{r_{ii}} - \frac{m^2}{r_{ii}^2} + (\bar{D}^z_N)^2 \right] \end{aligned} \right. \quad (\text{temperature terms})$$

where the dissipation function may be reconstructed from

$$\frac{\Phi_r}{\mu} = \frac{4}{3} \left[\left(2 \frac{\partial U_r}{\partial r} - \frac{U_r}{r} - \frac{1}{r} \frac{\partial U_\theta}{\partial \theta} - \frac{\partial U_z}{\partial z} \right) \bar{D}_N^r + \left(\frac{2}{r} \frac{\partial U_\theta}{\partial \theta} + 2 \frac{U_r}{r} - \frac{\partial U_r}{\partial r} - \frac{\partial U_z}{\partial z} \right) \frac{1}{r} \right]$$

†The shower spray is also turbulent but not continuous. When viewed under stroboscopic light, it shows a striking pattern of irregular droplets.

§It can be stated, however, that transition never occurs for $Re < Re_{crit}$.

**Later work has added viscous effects to the analysis. See the text by Phillips (1978).

††Using u' , v' , and w' to denote the velocity fluctuations, the turbulence level is defined as

$$T = \frac{1}{U_0} \left[\frac{1}{3} \left(\overline{u'^2} + \overline{v'^2} + \overline{w'^2} \right) \right]^{1/2}$$

‡‡Absolute instability refers to the case for which disturbances start and continue to grow from the same initiation point in space, before spreading elsewhere. Convective instability refers to the case for which disturbances grow while moving away from their initiation source.

CHAPTER 6

INCOMPRESSIBLE TURBULENT MEAN FLOW

I am an old man now, and when I die and go to Heaven there are two matters on which I hope for enlightenment. One is quantum electrodynamics and the other is the turbulent motion of fluids. And about the former I am really rather optimistic.

Horace Lamb (1849–1934)

6-1 PHYSICAL AND MATHEMATICAL DESCRIPTION OF TURBULENCE

CHAPTER 5 showed that smooth, orderly laminar flow is strictly limited to finite values of critical parameters—Reynolds number, Grashof number, Taylor number, Richardson number, etc. Beyond that, laminar flow is unstable and will evolve to a new flow regime if the critical parameter is large enough. That new regime, not predicted by stability theory but nevertheless inevitable, is a fluctuating, disorderly motion called *turbulence*. Because turbulence is so complex, its complete analysis and quantification will probably never be achieved. Turbulent flow will remain the subject of research in the foreseeable future, thus leading to hundreds of published papers and articles every year.

Much is known now about the structure of turbulence, due to excellent experimental techniques. First, there is advanced flow visualization, as described in the monographs by van Dyke (1982), Merzkirch (1987), Nakayama (1988), Yang (1989, 1994), Nakayama and Tanida (1996), and Smits and Lim (2000). In addition to still images, there is an outstanding list of fluid-flow videotapes and movies given by Carr and Young (1996). The flow-visualization community meets regularly. Second, there is superb modern miniature instrumentation: hot-wires (Bruun 1995), laser-Doppler systems (Durst 1992), particle image velocimetry (Raffel et al. 1998), and other measurement techniques including, but not limited to, ultrasound, X-ray, computed tomography, holography, and magnetic resonance velocimetry (Goldstein 1996).

The present chapter provides a modest survey of incompressible turbulent flow. There are

many advanced monographs on the subject, in chronological order: Hinze (1975), Libby (1996), Schmitt (1997), Wilcox (1998), Mathieu and Scott (2000), Pope (2000), Launder and Sandham (2001), Bernard and Wallace (2002), Cebeci (2003), and Tzabiras (2003).

6-1.1 Physical Description

A provocative visualization of transitional and turbulent flat-plate flow is described by Nakayama (1988) and reproduced computationally in [Fig. 6-1](#). Air ($\nu \approx 1.5 \times 10^{-5} \text{ m}^2/\text{s}$) flows at 3.3 m/s past a plate 2.4 m long and 1.2 m wide. The shear-layer motion is visualized by smoke introduced at the leading edge. Spots form and merge, and transition to turbulence occurs at about $x = 90 \text{ cm}$, which corresponds to a local Reynolds number of $Re_x \approx 2 \times 10^5$. After this point, the boundary layer is much thicker and quite disorderly. The disorder is not merely white noise. It has clear spatial structure and may be described by the following characteristics:

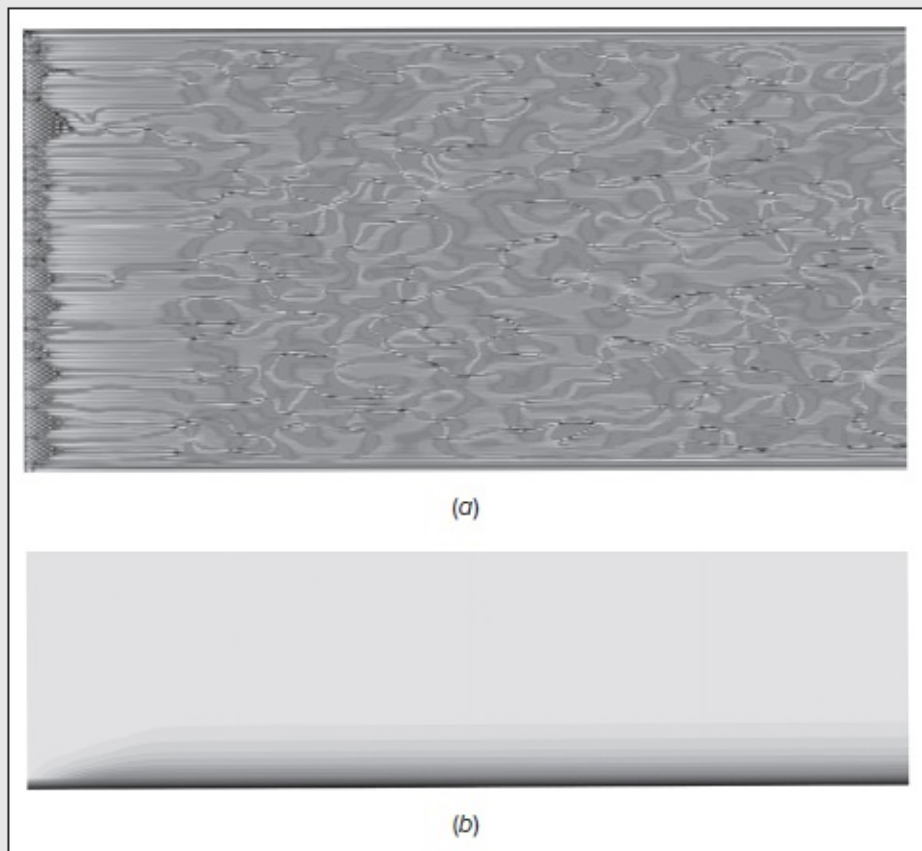


FIGURE 6-1

Numerical simulation of airflow at 3.3 m/s past a flat plate based on the Reynolds Stress Turbulence Model: (a) top view; (b) side view. Transition is at $x \approx 90 \text{ cm}$ or $Re_x \approx 2 \times 10^5$. [Produced by G. Sharma and J. Majdalani using a finite-volume solver and 4 million hexahedral cells.]

1. *Fluctuations* in pressure and velocity (and also temperature when there is heat transfer). The velocity fluctuates in all three directions. Fluctuations are superimposed upon a mean value of each property.
2. *Eddies* or fluid packets of many sizes that intermingle and fill the shear layer. The eddy size varies continuously from a shear-layer thickness δ (about 40 mm in this case) down to the so-called Kolmogorov length scale, $L = (\nu^3 \delta / U^3)^{1/4}$, or about 0.05 mm in this case.

Page 324

3. *Random* variations in fluid properties which have a particular form (not white noise). Each property has a specific continuous energy spectrum that drops off to zero at high wave numbers (small eddy size).
4. *Self-sustaining* motion. Once triggered, turbulent flow can maintain itself by producing new eddies to replace those lost by viscous dissipation. This is especially true in wall-bounded flows. Turbulence production is not generally related to the original instability mechanisms such as Tollmien–Schlichting waves.
5. *Mixing* that is much stronger than that due to laminar (molecular) action. Turbulent eddies actively spread in three dimensions and cause rapid diffusion of mass, momentum, and energy. Moreover, ambient fluid from nonturbulent zones is strongly entrained in a turbulent flow. Heat transfer and friction are greatly enhanced when compared to laminar flow, and turbulent mixing is associated with a gradient in the time-mean flow.

These are typical descriptors for turbulence: a spatially varying mean flow with superimposed three-dimensional random fluctuations that are self-sustaining and enhance mixing, diffusion, entrainment, and dissipation.

It is not necessary to have a nearby wall to generate turbulence. Boundary-free motions—jets, wakes, mixing layers—may also be turbulent and have all the characteristics mentioned above. In addition, turbulent flows that interface with a nonturbulent fluid may contain visible patterns called *coherent structures*. An example is shown in [Fig. 6-2](#) of turbulent flow in the mixing layer between two parallel streams of unequal velocity. Note that a coherent pattern of paired vortices that grow linearly downstream may be identified within the disorderly small-eddy motions, namely, one that is associated with the Kelvin–Helmholtz instability of an inviscid mixing layer [see Fig. 5-3]. Related coherent structures may also be found at the edges of turbulent jets, wakes, and boundary layers [Hussain (1986), Holmes et al. (1998)].

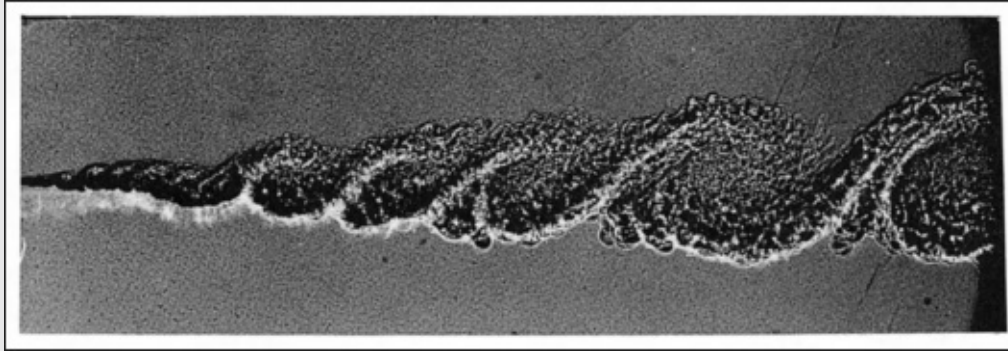


FIGURE 6-2

Spark shadowgraph of turbulent flow in the mixing layer between unequal parallel streams. A large coherent vortical structure is embedded within the random turbulent eddies. [After Brown and Roshko (1974).]

Since turbulence involves a wide spectrum of properties with random length and timescales, describing it can be difficult. The present chapter will concentrate on engineering estimates of time-mean velocity, pressure, temperature, shear stress, and heat transfer. There are many other worthy measures of turbulent flow. Chapter 2 of Bernard and Wallace (2002), for example, details the properties of integral microscales, Reynolds stress, turbulent kinetic energy, turbulent dissipation, turbulent transport, pressure–strain correlations, vorticity, and enstrophy. In fluid dynamics, the enstrophy is the quantity directly related to the kinetic energy in the flow model that corresponds to dissipation effects in the fluid.

Page 325

6-1.2 Mathematical Description

Visualizations such as those by Nakayama (1988) are illuminating, but fail to provide much quantitative information. At a minimum, one wishes in a turbulent-flow analysis to be able to predict (1) velocity and/or temperature profiles and (2) wall friction and/or heat transfer distributions. Additional information on the statistical properties of turbulence is desirable, albeit impossible to *predict* the structures in [Fig. 6-1](#) using purely theoretical arguments.

As far as we know, the Navier–Stokes equations from [Chap. 3](#) do apply to turbulent flow, and these equations can be modeled on a digital computer by finite differences or finite elements. Such frontal attacks on turbulence constitute the basis for the new research field on *direct numerical simulation* or DNS (Moin and Mahesh 1998). Because of the wide range of flow scales involved, DNS solutions require supercomputers and, even then, are limited to very low Reynolds numbers. A flow such as [Fig. 6-1](#) is out of the question—the smallest eddy size is about 0.04 mm, hence simulation of a shear layer 10 cm high on a 1.2×2.4 m

plate would require 5 trillion mesh points, which still exceed the capacity of most computers. The largest meshes achieved thus far are only sufficient to model transitional and low-turbulent flows ($Re \leq 10^4$), although they are capable of yielding much needed information for modeling higher Reynolds numbers.

Let us recall that, at one point in time, DNS turbulence computation was thought to be impossible. Emmons (1970) estimated that prediction of fine details of turbulent pipe flow would require 10^{22} numerical operations, far beyond the capability of any single supercomputer. Since then, *parallel* computation using CPU and GPU platforms, which combine the efforts of a multitude of single computers, has enabled researchers to exceed Emmons' estimate by several orders of magnitude.

6-1.3 Fluctuations and Time Averaging

Since actual computation of a raw velocity component $u(x, y, z, t)$ is not possible in high Reynolds number flow, the standard analysis of turbulence separates the fluctuating property from its time-mean value.

Figure 6-3 shows time traces, taken by a hot-wire, of a single velocity component in a turbulent flow. Trace *a* was taken deep within a shear layer and shows continuous random fluctuations of 5–10 percent about a mean value. Trace *b* was taken near the edge of a jet flow and shows intermittent regimes of turbulent and nonturbulent flow. The flow is seen to be turbulent about 20 percent of the time—hence we define the *intermittency factor*, $\gamma = (\text{turbulent time})/(\text{total time}) = 0.2$. Note that the mean flow has been subtracted for convenience in trace *b*. The intermittency occurs because the edge of a turbulent jet is sharp and ragged and regions of turbulent and nonturbulent flow alternately pass over the probe.

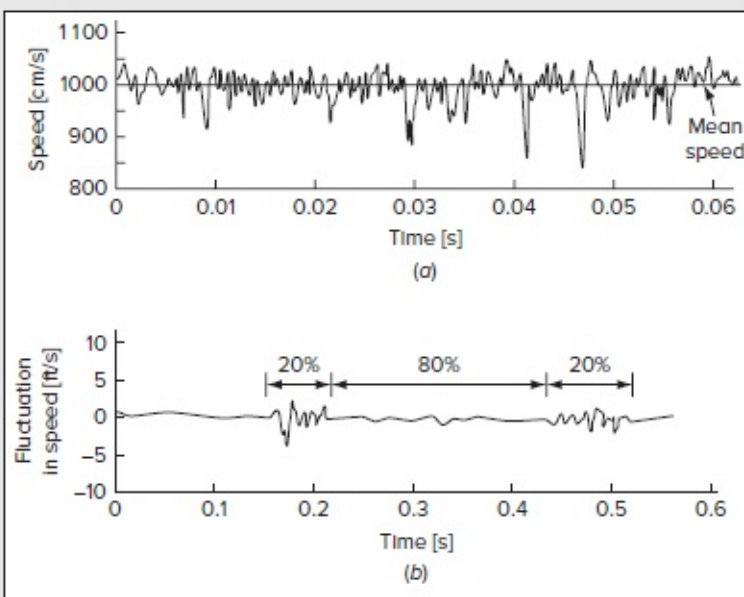


FIGURE 6-3

Hot-wire measurements showing turbulent velocity fluctuations: (a) typical trace of a single velocity component in a turbulent flow; (b) trace showing intermittent turbulence at the edge of a jet.

When analyzed for energy content, the frequency spectrum of trace *a* is found to be continuous (random), with significant energy in the range of 1–10⁵ Hz. The same is true of the turbulent portions of trace *b*. Other properties—pressure, temperature, and the remaining two velocity components—show more or less the same behavior as in [Fig. 6-3](#).

Suppose that trace *a* in [Fig. 6-3](#) represents $u(t)$ at a particular spot (x, y, z). Then the time average of u is defined as

$$\bar{u} = \frac{1}{T} \int_{t_0}^{t_0+T} u dt \quad (6-1)$$

Page 326

where the integration interval T is chosen to be larger than any significant period of the fluctuations in u . We may then define the fluctuation, u' , as the remainder when the mean flow is subtracted:

$$u' = u - \bar{u} \quad (6-2)$$

The fluctuation alone is shown in trace *b* of [Fig. 6-3](#). Based on this definition, it may be easily shown that the mean fluctuation is strictly zero: $\overline{u'} = 0$. Therefore, to characterize the magnitude of the fluctuation, we evaluate its mean-square value:

$$\overline{u'^2} = \frac{1}{T} \int_{t_0}^{t_0+T} u'^2 dt \quad (6-3)$$

The root-mean-square (rms) value of u' is defined as $u'_{\text{rms}} = \sqrt{\overline{u'^2}}$. Furthermore, if the integrals in [Eqs. \(6-1\)](#) and [\(6-3\)](#) are independent of the starting time t_0 , the fluctuations are said to be statistically *stationary*.

There are two paths to turbulent-flow analysis: (1) a statistical theory of turbulent correlation functions and (2) a semiempirical modeling of turbulent mean quantities. The former approach focuses on the statistical properties of the fluctuations: their frequency correlations, space–time correlations, and interactions with one another. The latter approach emphasizes the turbulent properties of most engineering significance: mean velocity and temperature profiles, wall friction and heat transfer, shear-layer thickness parameters, and rms fluctuation profiles. With the increased sophistication in recent turbulent-modeling research, the two paths are beginning to overlap. This text will primarily emphasize the second approach, which is focused on semiempirical modeling of engineering problems. The

statistical theory is treated in several excellent texts: Monin and Yaglom (1972), Tennekes and Lumley (1972), Hinze (1975), and Heinz (2003).

6-1.4 Illustration: Turbulence Measurements in Flat-Plate Flow

Throughout boundary-layer theory, we shall adopt coordinates (u, v, w) such that u is parallel to the freestream, v is

normal to the wall, and w is lateral to the freestream. [Figure 6-4](#) shows measured values of $(\sqrt{u'^2}, \sqrt{v'^2}, \sqrt{w'^2})$ and the covariance $\overline{u'v'}$, which is called the *turbulent shear stress* for reasons we shall soon see, in a turbulent boundary layer on a flat plate at a Reynolds number $Re_x \approx 10^7$, after Klebanoff (1955). Note that the fluctuations are quite large, up to 11 percent of the freestream speed. The presence of the wall makes the fluctuations different in magnitude (anisotropy, typical of all shear flows) for clear geometric and physical reasons. The longitudinal fluctuation u' is largest, being unimpeded by the wall and slightly reinforced by the freestream. The term v' is smallest, being directly impeded by the presence of the wall, and reaches its maximum much farther out than u' or w' . The lateral component w' is intermediate and quite large. The reader may perhaps be struck by this evidence that even the most “two-dimensional” of turbulent boundary layers has a thoroughly three-dimensional set of velocity fluctuations. However, w' does not directly influence the mean flow in this case. Finally, the turbulent shear $\overline{u'v'}$ is much smaller but of fundamental importance to later analysis. Determining its characteristics is the central problem in our analysis of turbulent shear flows.

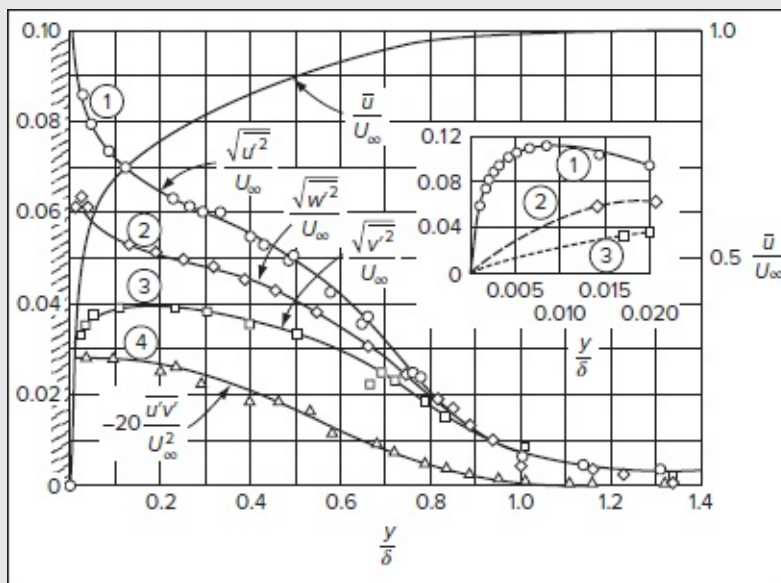


FIGURE 6-4

Flat-plate measurements of the fluctuating velocities u' (streamwise), v' (normal), and w' (lateral) and the turbulent shear $u'v'$. [After Klebanoff (1955).]

[Figure 6-4](#) has other interesting features. First, near the wall, all fluctuations (u' , v' , w') should vanish due to the no-slip condition. Yet the large-scale graph ($0 < y / \delta < 1$) shows the mean flow \bar{u} dropping to zero but not the fluctuations, which require an expanded inset scale to demonstrate no slip. Turbulence is quite resistant to wall damping, and measurements in thick boundary layers show significant fluctuations, even at $y / \delta = 0.0001$.

Second, at large y , we see that the fluctuations extend *outside* the point normally designated at the boundary-layer “edge” $y = \delta$, where $\bar{u} \approx U_\infty$. This is associated with the intermittency of the outer layer. Klebanoff (1955) demonstrated that a sharp interface or *superlayer* exists between turbulent and nonturbulent regions of the flow. This interface has a ragged shape and undulates while traveling downstream, as sketched in [Fig. 6-5b](#). The superlayer varies between about 0.4δ and 1.2δ while propagating downstream at about $0.94U_\infty$. The interface exhibits *fractal* behavior, i.e., its length and surface area rise at a faster rate than its basic size would predict [see, e.g., Chevray (1989)].

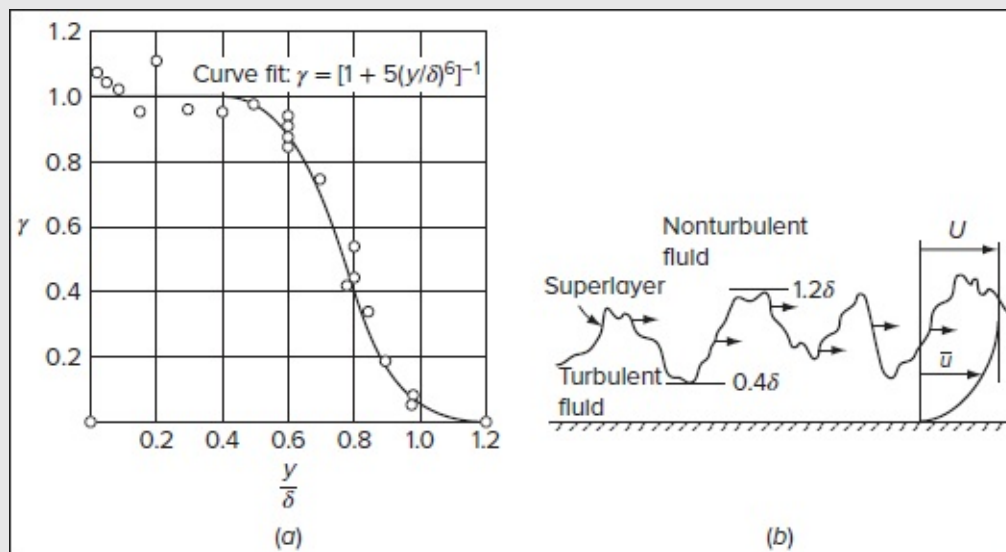


FIGURE 6-5

The phenomenon of intermittency in a turbulent boundary layer: (a) measured intermittency factors [after Klebanoff (1955)]; (b) the superlayer interface between turbulent and nonturbulent fluid.

Klebanoff measured the intermittency (percentage of time the flow is turbulent) in the boundary layer, with results shown in [Fig. 6-5a](#). The oddity of data points where $\gamma > 1$ (near the wall) is explained by Klebanoff’s use of a statistical formula, rather than the more recent technique of conditioned sampling with an instrument that discriminates between laminar and turbulent flow [Kovaznay et al. (1970)]. The curve-fit formula in [Fig. 6-5a](#) is often used in empirical theories, Klebanoff showed that the intermittency distribution is almost exactly

Gaussian in the rangePage 328 between $y / \delta = 0.4$ and 1.2. Similar measurements by Corrsin and Kistler (1955) show the same Gaussian intermittency for turbulent jets and wakes. Klebanoff estimated the dominant wavelength of the superlayer to be about 2δ . The mean position of this interface (where $\gamma \approx 0.5$) is at 0.78δ .

Note from [Fig. 6-4](#) that the rms fluctuations (u' , v' , w') become approximately equal for $y / \delta \geq 0.8$, where the turbulence becomes *isotropic* [see, e.g., Bernard and Wallace (2002)]. Near the wall, however, the flow is strongly anisotropic, and this is the region where most of the production and dissipation of turbulence energy take place.

Finally, Klebanoff (1955) also measured the energy content or turbulence *spectrum*. His results for the wave-number spectrum of the streamwise fluctuation u' are shown in [Fig. 6-6](#). The area under these curves is a measure of the total mean-square fluctuation:

$$\overline{u'^2} = \int_0^\infty F_u(k_u) dk_u \quad (6-4)$$

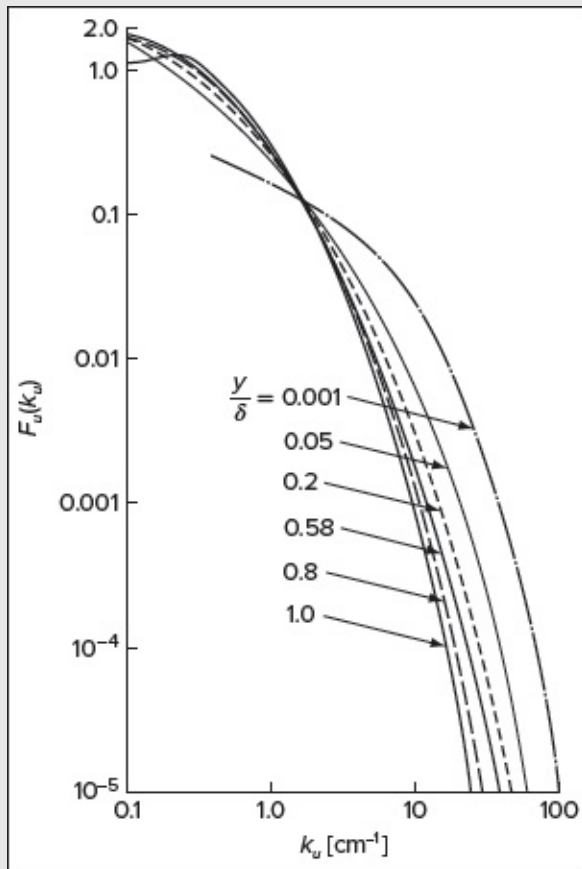


FIGURE 6-6

The wave-number spectrum of the streamwise turbulent velocity fluctuation in flat-plate flow. [Adapted from Klebanoff (1955).]

We see that, for positions near the wall, there is more energy at a high wave number (small

eddies), whereas away from the wall, the large eddies dominate the spectrum.

6-2 THE REYNOLDS EQUATIONS OF TURBULENT MOTION

Although statistical theories and numerical simulations are viable options, most research on turbulent-flow analysis in the past century has used the concept of time averaging. Applying time averaging to the basic equations of motion leads to the Reynolds equations, which involve both mean and fluctuating quantities. One then attempts to model the fluctuating terms by relating them to mean properties or their gradients. This approach may now be yielding diminishing returns. Lumley (1989) provides a stimulating discussion of how time averaging might outlive its usefulness. Nonetheless, the Reynolds equations are far from obsolete, and continue to form the basis of most engineering analyses of turbulent flow.

Following the original idea of Reynolds (1895), we assume that the fluid exists in a randomly unsteady turbulent state to justify the use of the time-averaged or mean equations of motion. In this vein, any variable Q may be resolved into a mean quantity \bar{Q} and a fluctuating value Q' where, by definition,

$$\bar{Q} = \frac{1}{T} \int_{t_0}^{t_0+T} Q dt \quad (6-5)$$

Page 329

Here the period over which integration is carried out, T , must be sufficiently large compared to the relevant period of the fluctuations. The mean value \bar{Q} itself may vary slowly with time, as sketched in [Fig. 6-7](#), and we speak of this case as an *unsteady* turbulent flow. For example, in a tidal estuary, the velocities can have turbulent components in the 1 Hz range superimposed on a tidal variation with a 12 or 24 h period. After time averaging, the mean flow can still oscillate with tidal periods.

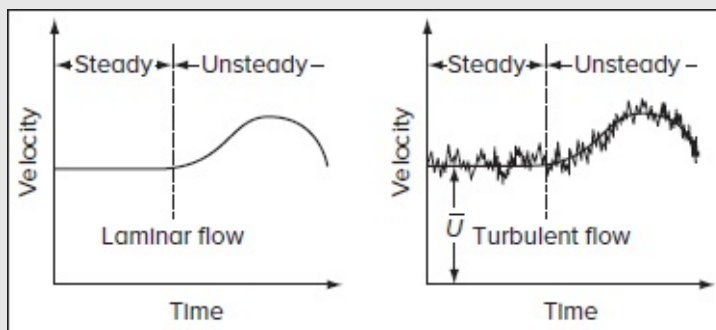


FIGURE 6-7

Steady and unsteady laminar and turbulent flow.

To initiate this analysis, let us consider incompressible turbulent flow with constant transport properties and possible fluctuations in its velocity, pressure, and temperature. The flow variables may be decomposed into

$$\begin{cases} u = \bar{u} + u' \\ v = \bar{v} + v' \\ w = \bar{w} + w' \end{cases} \begin{cases} p = \bar{p} + p' \\ T = \bar{T} + T' \end{cases} \quad (6-6)$$

Before substituting these expansions into the basic equations, we can verify from [Eq. \(6-5\)](#) that the following rules of averaging apply to any two turbulent quantities f and g :

$$\begin{aligned} \overline{f'} &= 0 & \overline{\bar{f}} &= \bar{f} & \overline{fg} &= \bar{f}\bar{g} & \overline{f'g'} &= 0 & \overline{f+g} &= \bar{f} + \bar{g} \\ \frac{\partial \bar{f}}{\partial s} &= \frac{\partial \bar{f}}{\partial s} & \overline{fg} &= \bar{f}\bar{g} + \overline{f'g'} & \overline{\int f ds} &= \int \bar{f} ds \end{aligned} \quad (6-7)$$

As for the incompressible continuity equation,

$$\nabla \cdot \mathbf{V} = 0 \quad (6-8)$$

we can substitute in it the decomposed forms of u , v , and w from [Eqs. \(6-6\)](#) and take the time average of the resulting equation. Realizing that the time average of the partial derivatives of all fluctuations drop out, one is left with

$$\frac{\partial \bar{u}}{\partial x} + \frac{\partial \bar{v}}{\partial y} + \frac{\partial \bar{w}}{\partial z} = 0 \quad (6-9)$$

Now by subtracting [Eq. \(6-9\)](#) from [Eq. \(6-8\)](#), we deduce an important condition on the fluctuating variables, namely,

$$\frac{\partial u'}{\partial x} + \frac{\partial v'}{\partial y} + \frac{\partial w'}{\partial z} = 0 \quad (6-10)$$

In short, the mean and fluctuating velocity components each must separately satisfy the same form of the continuity equation. This would not be true if we were to account for density fluctuations, because terms involving $\overline{\rho' u'_i}$ would couple the two relations. As we make further headway, we will concentrate on the mean-flow relation [[Eq. \(6-9\)](#)], in lieu of the fluctuations [[Eq. \(6-10\)](#)].

Next, we attempt the same procedure with the incompressible Navier–Stokes equations, specifically,

$$\begin{cases} \rho \frac{D\mathbf{V}}{Dt} = \rho \mathbf{g} - \nabla p + \mu \nabla^2 \mathbf{V} & \text{(vector form)} \\ \rho \frac{Du_i}{Dt} = \rho g_i - \nabla_i p + \mu \nabla^2 u_i & \text{or} & \rho \left(\frac{\partial u_i}{\partial t} + u_j \frac{\partial u_i}{\partial x_j} \right) = \rho g_i - \frac{\partial p}{\partial x_i} + \mu \frac{\partial^2 u_i}{\partial x_j \partial x_j} & \text{(indicial form)} \end{cases} \quad (6-11)$$

For the reader's convenience, both vector and indicial forms are provided in parallel. Before substituting for u , v , w , and p , we can avoid unnecessary churning by noting the following rather clever rearrangement of the convective-acceleration term:

$$\mathbf{v} \cdot \nabla Q = u \frac{\partial Q}{\partial x} + v \frac{\partial Q}{\partial y} + w \frac{\partial Q}{\partial z} = \frac{\partial}{\partial x}(uQ) + \frac{\partial}{\partial y}(vQ) + \frac{\partial}{\partial z}(wQ) - Q \left(\frac{\partial u}{\partial x} + \frac{\partial v}{\partial y} + \frac{\partial w}{\partial z} \right) = \frac{\partial}{\partial x}(uQ) + \frac{\partial}{\partial y}(vQ) + \frac{\partial}{\partial z}(wQ)$$

The ensuing equality stems from the incompressible continuity relation [Eq. (6-8)]. It can be readily leveraged in Eq. (6-11) which, when time averaged, yields

$$\begin{cases} \rho \frac{D\bar{\mathbf{V}}}{Dt} + \rho \nabla \cdot (\bar{\mathbf{u}'\mathbf{u}'}') = \rho \mathbf{g} - \nabla \bar{p} + \mu \nabla^2 \bar{\mathbf{V}} \\ \rho \frac{D\bar{u}_i}{Dt} + \rho \nabla_j (\bar{u'_i u'_j}) = \rho g_i - \nabla_i \bar{p} + \mu \nabla^2 \bar{u}_i \end{cases} \quad \text{or} \quad \rho \left(\frac{\partial \bar{u}_i}{\partial t} + \bar{u}_j \frac{\partial \bar{u}_i}{\partial x_j} \right) + \rho \frac{\partial (\bar{u'_i u'_j})}{\partial x_j} = \rho g_i - \frac{\partial \bar{p}}{\partial x_i} + \mu \frac{\partial^2 \bar{u}_i}{\partial x_j \partial x_j} \quad (6-12)$$

Note that the mean momentum equation is complicated by a new term involving the turbulent-inertial tensor $\bar{u'_i u'_j}$. This new term is extraordinarily important and constitutes the source of our difficulties because its mathematical form is not known beforehand. In essence, the time-averaging procedure introduces nine new variables (i.e., the tensor components) that can be defined only through (unavailable) knowledge of the detailed turbulent structure. The components of $\bar{u'_i u'_j}$ relate not only to fluid physical properties but also to local flow conditions such as the velocity, geometry, surface roughness, and upstream conditions. In a two-dimensional turbulent boundary layer ($\bar{w} = 0, \partial/\partial z = 0$), the only significant term reduces to $\bar{u'v'}$, but even this single term requires extensive speculation to achieve its closure in the form of a mathematical correlation that is semiempirical at best. Fortunately, some empirical approaches have been successful, though rather thinly formulated from nonrigorous postulates.

A slight amount of illumination is thrown upon Eq. (6-12) if it is rearranged to display the turbulent-inertial terms as if they were stresses. In this context, we write

$$\begin{cases} \rho \frac{D\bar{\mathbf{V}}}{Dt} = \rho \mathbf{g} - \nabla \bar{p} + \nabla \cdot \boldsymbol{\tau} \\ \rho \frac{D\bar{u}_i}{Dt} = \rho g_i - \nabla_i \bar{p} + \nabla_j \tau_{ij} \end{cases} \quad \text{or} \quad \rho \left(\frac{\partial \bar{u}_i}{\partial t} + \bar{u}_j \frac{\partial \bar{u}_i}{\partial x_j} \right) = \rho g_i - \frac{\partial \bar{p}}{\partial x_i} + \frac{\partial \tau_{ij}}{\partial x_j} \quad (6-13)$$

where

$$\tau_{ij} = \underbrace{\mu \left(\frac{\partial \bar{u}_i}{\partial x_j} + \frac{\partial \bar{u}_j}{\partial x_i} \right)}_{\text{Laminar}} - \underbrace{\rho \bar{u'_i u'_j}}_{\text{Turbulent}}$$

Mathematically, then, the turbulent-inertial terms behave as if the total stress on the system were composed of Newtonian viscous stresses that are augmented by an additional or apparent turbulent-stress tensor $-\rho \bar{u'_i u'_j}$. In boundary-layer analysis, the dominant term $-\rho \bar{u'v'}$ is coined *turbulent shear*.

Now consider the energy equation (i.e., first law of thermodynamics) for incompressible flow with constant properties

$$\rho c_p \frac{DT}{Dt} = k \nabla^2 T + \Phi \quad (6-14)$$

where Φ is the dissipation function given by [Eq. \(2-46\)](#). Taking the time average, we obtain the mean-energy equation

$$\rho c_p \frac{D\bar{T}}{Dt} = -\frac{\partial q_i}{\partial x_i} + \bar{\Phi} \quad (6-15)$$

where

$$\bar{\Phi} = \frac{\mu}{2} \overline{\left(\frac{\partial \bar{u}_i}{\partial x_j} + \frac{\partial \bar{u}'_i}{\partial x_j} + \frac{\partial \bar{u}_j}{\partial x_i} + \frac{\partial \bar{u}'_j}{\partial x_i} \right)^2} \quad \text{and} \quad q_i = \underbrace{-k \frac{\partial \bar{T}}{\partial x_i}}_{\text{Laminar}} + \underbrace{\rho c_p \overline{u'_i T'}}_{\text{Turbulent}}$$

By analogy with our rearrangement of the momentum equation, we have collected conduction and turbulent convection terms into a total-heat-flux vector q_i , which combines both the molecular flux and the *turbulent flux* $\rho c_p \overline{u'_i T'}$. The total-dissipation term Φ is obviously complex in the general case but in two-dimensional turbulent-boundary-layer flow, it reduces approximately to

$$\bar{\Phi} \approx \frac{\partial \bar{u}}{\partial y} \left(\mu \frac{\partial \bar{u}}{\partial y} - \rho \overline{u'v'} \right)$$

Page 331

[Equations \(6-9\)](#), [\(6-13\)](#), and [\(\(6-15\)\)](#) represent the Reynolds-averaged basic differential equations for turbulent mean continuity, mean momentum, and mean thermal energy. They contain several new unknowns involving time-averaged correlations of fluctuating velocities and temperature. Therefore, solutions cannot be pursued without additional relations or empirical modeling ideas to achieve the necessary closure.

6-2.1 The Turbulence Kinetic-Energy Equation

Many attempts have been made to add “turbulence conservation” relations to the time-averaged continuity, momentum, and energy equations above. The most obvious single addition is a relation for the *turbulence kinetic energy* K of the fluctuations, defined by

$$K = \frac{1}{2} (\overline{u'u'} + \overline{v'v'} + \overline{w'w'}) = \frac{1}{2} \overline{u'_i u'_i} \quad (6-16)$$

Here we have introduced for convenience the Einstein summation notation, where $u_i = (u_1, u_2, u_3) = (u, v, w)$ and a repeated subscript implies summation (App. D). For example, $u_i u_i = u_1^2 + u_2^2 + u_3^2$. If turbulence is to be described by only one velocity scale, it should be $K^{1/2}$.

A conservation relation for K can be derived by forming the mechanical-energy equation, i.e., the dot product of u_i and the i th momentum equation. Then, following Prandtl (1945a), we subtract the instantaneous mechanical energy from its time-averaged value. The result is

the *turbulence kinetic-energy* relation for an incompressible fluid:

$$\frac{DK}{Dt} = \underbrace{-\frac{\partial}{\partial x_i} \left[u'_i \left(\frac{1}{2} u'_j u'_j + \frac{p'}{\rho} \right) \right]}_{\text{I}} - \underbrace{\overline{u'_i u'_j} \frac{\partial \bar{u}_j}{\partial x_i}}_{\text{II}} + \underbrace{\frac{\partial}{\partial x_i} \left[\overline{v u'_j} \left(\frac{\partial u'_i}{\partial x_j} + \frac{\partial u'_j}{\partial x_i} \right) \right]}_{\text{IV}} - \underbrace{\nu \frac{\partial u'_j}{\partial x_i} \left(\frac{\partial u'_i}{\partial x_j} + \frac{\partial u'_j}{\partial x_i} \right)}_{\text{V}} \quad (6-17)$$

We have labeled this relation with Roman numerals to describe the relation in words. The rate of change of turbulent energy (I) is equal to its convective diffusion (II), plus its production (III), plus the work done by turbulent viscous stresses (IV), plus turbulent viscous dissipation (V). The terms in this relation are so complex that they cannot be computed from first principles. For this reason, modeling ideas are considered.

6-2.2 The Reynolds Stress Equation

From [Eq. \(6-3\)](#), the turbulent or “Reynolds” stresses have the form $S_{ij} = (-\rho \overline{u'_i v'_j})$. From this point of view, turbulence kinetic energy is actually proportional to the sum of the three turbulent normal stresses, $K = S_{ii} / (2\rho)$. Of more importance to the engineer are the turbulent shear stresses, where $i \neq j$. It is possible to develop a conservation equation for a single Reynolds stress and the derivation involves subtracting the time-averaged momentum [Eq. \(6-12\)](#) from its instantaneous value, in both the i and j directions. In this manner, the i th result is multiplied by u_j and added to the j th result multiplied by u_i . This relation is then time averaged to yield the *Reynolds stress equation*:

$$\underbrace{\frac{D \overline{u'_i u'_j}}{Dt}}_{\text{I}} = - \underbrace{\left[\overline{u'_j u'_k} \frac{\partial \bar{u}_i}{\partial x_k} + \overline{u'_i u'_k} \frac{\partial \bar{u}_j}{\partial x_k} \right]}_{\text{II}} - \underbrace{2\nu \frac{\partial u'_i}{\partial x_k} \frac{\partial u'_j}{\partial x_k}}_{\text{III}} + \underbrace{\frac{p'}{\rho} \left(\frac{\partial u'_i}{\partial x_j} + \frac{\partial u'_j}{\partial x_i} \right)}_{\text{IV}} - \underbrace{\frac{\partial}{\partial x_k} \left[\overline{u'_i u'_j u'_k} - \nu \frac{\partial \overline{u'_i u'_j}}{\partial x_k} + \frac{p'}{\rho} (\delta_{jk} u'_i + \delta_{ik} u'_j) \right]}_{\text{V}} \quad (6-18)$$

Here the Roman numerals denote the following: (I) rate of change of Reynolds stress, (II) generation of stress, (III) dissipation, (IV) pressure–strain effects, and (V) diffusion of Reynolds stress.

In their full three-dimensional form, [Eqs. \(6-17\)](#) and [\(6-18\)](#) are extremely complex, with many unknown correlations to model. We will confine our attention in subsequent sections to the much simpler two-dimensional boundary-layer forms of these relations.

If buoyancy and temperature dependence of fluid properties are neglected, we may uncouple the mean-energy [Eq. \(6-15\)](#) and solve for mean temperature later. The mean velocity and pressure $(\bar{u}, \bar{v}, \bar{w}, \bar{p})$ may be solved from the continuity and momentum relations [[Eqs. \(6-9\)](#) and [\(6-13\)](#)], given a judicious set of turbulence modeling assumptions.

BOUNDARY-LAYER EQUATIONS

We must face the fact that our chief success in turbulent-flow analysis lies with two-dimensional boundary layers. If we define a boundary layer as one in which large lateral (cross-streamwise) changes occur relative to the longitudinal (streamwise) changes in flow properties, our definition would then include not only wall flows but also pipe flow, channel flow, wakes, and jets.

As usual, we let x be the freestream or streamwise direction and y be normal to the wall. By analogy with laminar boundary-layer analysis, we can assume the boundary-layer thickness $\delta(x) \ll x$ and write

$$\bar{v} \ll \bar{u} \quad \frac{\partial}{\partial x} \ll \frac{\partial}{\partial y} \quad (6-19)$$

In addition, the mean-flow structure may be considered to be two-dimensional such that

$$\bar{w} = 0 \quad \frac{\partial}{\partial z} = 0 \quad (6-20)$$

In this case, the mean lateral turbulence is actually not zero, $\overline{w'^2} \neq 0$, but its z derivative may be ignored. Then we can easily verify that the basic turbulent [Eqs. \(6-9\)](#), [\(6-13\)](#), and [\(6-15\)](#) reduce to the boundary-layer approximations for incompressible turbulent flow, specifically,

$$\text{Continuity:} \quad \frac{\partial \bar{u}}{\partial x} + \frac{\partial \bar{v}}{\partial y} = 0 \quad (6-21a)$$

$$\text{Axial momentum:} \quad \bar{u} \frac{\partial \bar{u}}{\partial x} + \bar{v} \frac{\partial \bar{u}}{\partial y} \approx U_\epsilon \frac{dU_\epsilon}{dx} + \frac{1}{\rho} \frac{d\tau}{dy} \quad (6-21b)$$

$$\text{Thermal energy:} \quad \rho c_p \left(\bar{u} \frac{\partial \bar{T}}{\partial x} + \bar{v} \frac{\partial \bar{T}}{\partial y} \right) \approx \frac{\partial q}{\partial y} + \tau \frac{\partial \bar{u}}{\partial y} \quad (6-21c)$$

where $U_\epsilon(x)$ represents the freestream velocity and where we have adopted the short notation

$$\tau = \mu \frac{\partial \bar{u}}{\partial y} - \rho \overline{u'v'} \quad q = -k \frac{\partial \bar{T}}{\partial y} - \rho c_p \overline{v'T'} \quad (6-22)$$

We see that Eqs. (6-21a) to (6-21c) closely resemble the laminar-flow equations from [Chap. 4](#), except that q and τ contain a turbulent heat flux and turbulent shear stress, respectively, which must be modeled.

The y -momentum equation reduces to

$$\frac{\partial p}{\partial y} \approx -\rho \frac{\partial \overline{v'^2}}{\partial y}$$

which may be integrated across the boundary layer to yield

$$p \approx p_e(x) - \rho \overline{v'^2} \quad (6-23)$$

Thus, unlike laminar flow, the pressure slightly varies across the boundary layer due to velocity fluctuations normal to the wall. From [Fig. 6-4](#), the rms v' fluctuations are no more than 4 percent of the stream velocity and the pressure differs from freestream pressure by no more than about 0.4 percent of the freestream dynamic pressure, a negligible variation. Note that, due to the no-slip condition, the wall pressure equals the freestream pressure.

Since Bernoulli's relation is assumed to hold in the (inviscid) freestream, we can write

$$dp_e \approx -\rho U_e dU_e \quad (6-24)$$

This relation has, in fact, been used in Eq. (6-21b). Considering that the freestream conditions $U_e(x)$ and $T_e(x)$ are known, the boundary conditions become

$$\text{No slip, no jump:} \quad \bar{u}(x, 0) = \bar{v}(x, 0) = 0 \quad \bar{T}(x, 0) = T_w(x) \quad (\text{at the wall}) \quad (6-25)$$

$$\text{Freestream matching:} \quad \bar{u}(x, \delta) = U_e(x) \quad \bar{T}(x, \delta_T) = T_e(x) \quad (\text{at the boundary layer edge})$$

Here too, the velocity and thermal boundary-layer thicknesses (δ , δ_T) are not necessarily equal depending on the Prandtl number, as in laminar-flow analysis. Equations (6-21a) and (6-21b) can be solved for \bar{u} and \bar{v} if a suitable correlation for the total shear τ is known. Subsequently, the temperature \bar{T} can be found from Eq. (6-21c) if the turbulent heat flux q can be correlated.

Page 333

6-3.1 Turbulent Energy and Reynolds Stress

Since Eqs. (6-21) contain the two new unknowns, q and τ , they need to be supplemented in order to achieve mathematical closure. One avenue is through the boundary-layer forms of the turbulence equations.

The turbulence kinetic-energy [Eq. \(6-17\)](#) has the two-dimensional boundary-layer form

$$\bar{u} \frac{\partial K}{\partial x} + \bar{v} \frac{\partial K}{\partial y} \approx -\frac{\partial}{\partial y} \left[\overline{v' \left(\frac{1}{2} u'_i u'_i + \frac{p'}{\rho} \right)} \right] + \frac{\tau}{\rho} \frac{\partial \bar{u}}{\partial y} - \epsilon \quad (6-26)$$

$$\text{where} \quad \epsilon = -\nu \frac{\partial u'_i}{\partial x_j} \frac{\partial u'_j}{\partial x_i} = \text{turbulent dissipation}$$

Unfortunately, this introduces two additional turbulence parameters, the pressure-strain term and the dissipation, which also require some modeling, as we will see later in this chapter.

The two-dimensional boundary-layer form of the Reynolds stress [Eq. (6-18)] becomes

$$\bar{u} \frac{\partial \bar{u}' v'}{\partial x} + \bar{v} \frac{\partial \bar{u}' v'}{\partial y} \approx 2 \bar{u}' v' \frac{\partial \bar{u}}{\partial y} - \frac{\partial}{\partial y} \left(\overline{u' v'^2} + \frac{p' u'}{\rho} \right) - 2 \bar{v} \frac{\partial \bar{u}' v'}{\partial x} + \frac{p'}{\rho} \left(\frac{\partial \bar{u}'}{\partial y} + \frac{\partial \bar{v}'}{\partial x} \right) + \bar{v} \frac{\partial^2 \bar{u}' v'}{\partial y^2} \quad (6-27)$$

Again, several new turbulence correlations are introduced that will need to be, and have been, successfully modeled.

6-3.2 Turbulent-Boundary-Layer Integral Relations

The momentum-integral, energy, etc., relations for turbulent flow may be derived by using continuity Eq. (6-21a) to eliminate \bar{v} in favor of \bar{u} and then integrating the result across the boundary layer. Alternatively, one may use a control volume of width dx and height δ .

The momentum-integral equation was first derived by Kármán (1921) and has a form identical to the laminar-flow relation (4-122):

$$\frac{d\theta}{dx} + (2 + H) \frac{\theta}{U_e} \frac{dU_e}{dx} = \frac{\tau_w}{\rho U_e^2} = \frac{C_f}{2} \quad (6-28)$$

where

$$\delta^* = \int_0^\infty \left(1 - \frac{\bar{u}}{U_e} \right) dy = \delta \eta^* \quad \eta^* = \int_0^1 \left(1 - \frac{\bar{u}}{U_e} \right) d\left(\frac{y}{\delta}\right) \quad (\text{displacement thickness})$$

$$\theta = \int_0^\infty \frac{\bar{u}}{U_e} \left(1 - \frac{\bar{u}}{U_e} \right) dy = \delta \theta^* \quad \theta^* = \int_0^1 \frac{\bar{u}}{U_e} \left(1 - \frac{\bar{u}}{U_e} \right) d\left(\frac{y}{\delta}\right) \quad (\text{momentum thickness})$$

$$H = \frac{\delta^*}{\theta} = \frac{\eta^*}{\theta^*} \quad (\text{momentum shape factor})$$

This equation contains three variables, θ , H , and C_f . In laminar flow, we can relate these three quantities reasonably well with one-parameter velocity profile approximations such as those given in Table 4-1. The turbulent-flow profile is, however, more complicated in shape, and many different correlations or additional relations have been proposed to achieve closure in [Eq. \(6-28\)](#). There are over 50 different ideas in the literature.

In a likewise manner, the two-dimensional turbulent integral-energy equation is identical to its laminar counterpart, [Eq. \(4-145\)](#). For steady flow with impermeable walls, it may be written as

$$q_w = \frac{d}{dx} \left[\int_0^\infty \rho \bar{u} (\bar{h}_0 - \bar{h}_{0e}) dy \right] \quad \text{where} \quad \bar{h}_0 \approx c_p \bar{T} + \frac{1}{2} \bar{u}^2 \quad (\text{mean stagnation enthalpy}) \quad (6-29)$$

Equation (6-29) can be used to develop approximate theories for turbulent heat convection by making suitable assumptions about the form of the (turbulent) velocity and temperature profiles.

Since the momentum-integral relation [Eq. \(6-28\)](#) contains unknown functions, it has often been supplemented by additional integral relations. One of these uses “mechanical energy” and is formed by multiplying Eq. (6-21b) by \bar{u} and integrating across the layer. The result is the two-dimensional *mechanical-energy integral relation*, which takes the same form

for either laminar or turbulent flow:

$$\frac{\rho}{2} \frac{d}{dx} \left[U_e \int_0^\infty \bar{u} (U_e^2 - \bar{u}^2) dy \right] = \int_0^\infty \tau \frac{\partial \bar{u}}{\partial y} dy \quad (6-30)$$

Page 334

The right hand side of Eqn. (6-30) is called the *dissipation integral* and, for turbulent flow, contains new information that can be used for closure. Kline et al. (1968) discuss seven integral-boundary-layer methods that use this relation.

Finally, some workers use the integrated form of the continuity relation (6-21a), which becomes, for an impermeable wall,

$$v_e = - \int_0^\infty \frac{\partial \bar{u}}{\partial x} dy = \frac{d}{dx} \left(\int_0^\infty \bar{u} dy \right) + U_e \frac{d\delta}{dx}$$

where Leibnitz' rule is used to evaluate the integral. By introducing δ^* from the definition of displacement thickness in [Eq. \(6-28\)](#), we may rewrite this expression as

$$\frac{d\delta}{dx} - \frac{v_e}{U_e} = \frac{1}{U_e} \frac{d}{dx} [U_e (\delta - \delta^*)] \quad (6-31)$$

The result represents the rate at which the outer fluid is brought into the boundary layer. It is called the *entrainment relation*, valid for either laminar or turbulent flow, and was first derived by Head (1958). Kline et al. (1968) outline four turbulent-flow methods that use this relation.

Turbulent-boundary-layer integral methods were once the mainstay of design calculations, but now they have mostly been replaced by commercial CFD turbulence-modeling codes, assisted by large-eddy simulation (LES) and DNS. Integral methods are reviewed by Cousteix in Kline et al. (1982, vol. 2, pp. 650–671), and some excellent integral methods are incorporated into the online Java applets (Boundary Layer Applets) of Devenport and Schetz (2002). The advantage of integral methods includes their ease of implementation on simple spreadsheets.

6-4 VELOCITY PROFILES: THE INNER, OUTER, AND OVERLAP LAYERS

Now let us consider velocity profiles $\bar{u}(x, y)$ for turbulent flow. First, what do they look like? [Figure 6-8](#) shows some experimental profiles of \bar{u}/U_e versus y/δ for various pressure gradients in turbulent flow. The profiles have a distinctive look about them that seems to spell analytic trouble. They are about as nonlaminar as they can possibly be. They seem to smash up against the wall as if there were velocity slip at the wall; actually, they drop linearly to zero within a thickness that is hardly measurable. For the uppermost profile, for example, the

linear (viscous) drop-off occurs in the region $0 \leq y / \delta < 0.002$. The profiles also seem to have a characteristic concavity near $y / \delta \approx 0.2$, as if a gremlin were sitting upon them. This is the beginning of the wakelike behavior of the outer (fully turbulent) layer.

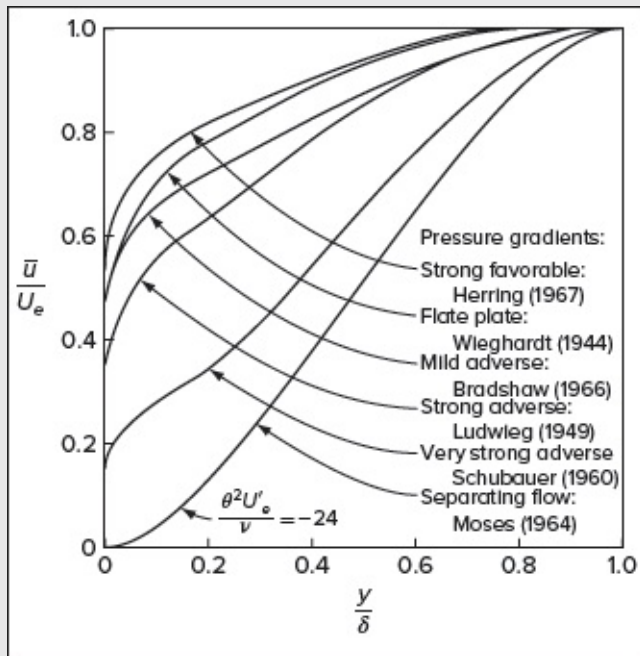


FIGURE 6-8

Experimental turbulent-boundary-layer velocity profiles for various pressure gradients. [Data from Coles and Hirst (1968).]

For the key to profile shape, we are indebted to the physical insight of Ludwig Prandtl and Theodore von Kármán. They deduced that the profile consists of an inner and an outer layer, plus an intermediate overlap between the two:

Inner layer: viscous (molecular) shear dominates.

Outer layer: turbulent (eddy) shear dominates.

Overlap layer: both types of shear are important, and the profile smoothly connects the inner and outer regions.

Page 335

For the inner law, Prandtl reasoned in 1933 that the profile would depend upon wall shear stress, fluid properties, and distance y from the wall, but not upon the freestream parameters. He proposed:

Inner law:

$$\bar{u} = f(\tau_w, \rho, \mu, y)$$

Conversely, for the outer layer, Kármán deduced in 1930 that the wall acts merely as a source of resistance, reducing local velocity $\bar{u}(y)$ below the stream velocity U_ϵ in a manner independent of viscosity μ but dependent upon the wall shear stress, layer thickness, and freestream pressure gradient:

$$\text{Outer law:} \quad U_\epsilon - \bar{u} = f\left(\tau_w, \rho, y, \delta, \frac{dp_\epsilon}{dx}\right) \quad (6-33)$$

Finally, for the overlap layer, we simply specify that the inner and outer functions merge together seamlessly over some finite intermediate region:

$$\text{Overlap law:} \quad \bar{u}_{\text{inner}} = \bar{u}_{\text{outer}} \quad (6-34)$$

Interestingly, the physical characteristics of the problem determine the mathematical form of this overlap profile.

6-4.1 Dimensionless Profiles

The functional forms in [Eqs. \(6-32\)](#) to [\(6-34\)](#) are guided by dimensional analysis and determined from experiment. These relations contain three primary dimensions (mass, length, and time). Therefore, [Eq. \(6-32\)](#), with five variables, reduces to $5 - 3 = 2$ dimensionless parameters. The reader may show that the proper dimensionless inner law is

$$\text{Inner law:} \quad \frac{\bar{u}}{v^*} = f\left(\frac{yv^*}{\nu}\right) \quad v^* = \left(\frac{\tau_w}{\rho}\right)^{\frac{1}{2}} \quad (6-35)$$

The variable v^* has units of velocity and is called the *wall-friction velocity*. We shall use v^* over and over again in our turbulent-flow analyses.

In like manner, [Eq. \(6-33\)](#) may be nondimensionalized using

$$\text{Outer law:} \quad \frac{U_\epsilon - \bar{u}}{v^*} = g\left(\frac{y}{\delta}, P\right) \quad P = \frac{\delta}{\tau_w} \frac{dp_\epsilon}{dx} \quad (6-36)$$

This is often called the *velocity-defect law*, with $U_\epsilon - \bar{u}$ being the “defect” or retardation of the flow due to wall effects. At any given position x , the defect shape $g(y / \delta)$ will depend upon the local pressure gradient P . Note that the definition of P resembles Clauser’s, Pohlhausen’s, or Thwaites’ pressure parameters (App. H2).

The overlap function follows immediately by setting the inner and outer profiles equal in the intermediate region where they both share the same pressure gradient P :

$$\text{Overlap law:} \quad \frac{\bar{u}}{v^*} = f\left(\frac{\delta v^* y}{\nu}\right) = \frac{U_\epsilon}{v^*} - g\left(\frac{y}{\delta}\right) \quad (6-37)$$

The resulting expression is supposedly an *identity*, yet the function f contains a multiplicative constant and the function g an additive constant. Using functional analysis, it can be shown

that the expression will be true only if both f and g are *logarithmic* functions of the form

$$\text{Inner variables:} \quad \frac{\bar{u}}{v^*} = \frac{1}{\kappa} \ln \frac{yv^*}{\nu} + B \quad (6-38a)$$

$$\text{Outer variables:} \quad \frac{U_e - \bar{u}}{v^*} = -\frac{1}{\kappa} \ln \frac{y}{\delta} + A \quad (6-38b)$$

where κ and B are near-universal constants for turbulent flow past smooth, impermeable walls and A varies mainly with the pressure gradient P . The original pipe-flow measurements in 1930 by Prandtl's student J. Nikuradse suggested that $\kappa \approx 0.40$ and $B \approx 5.5$, but later data correlations, e.g., Coles and Hirst (1968), adjust these values to

$$\kappa \approx 0.41 \quad B \approx 5.0 \quad (6-39)$$

which are adopted in this text.

The validity of the inner law, including the logarithmic overlap, is quickly established by replotting the velocity profiles from [Fig. 6-8](#) in terms of the inner variables, $u^+ = \bar{u}/v^*$ and $y^+ = yv^*/\nu$. This is done in [Fig. 6-9](#), with smashing success. With the exception of the separating flow, all of the curves, which looked so different in [Fig. 6-8](#), now collapse into a single logarithmic relation in the overlap region $35 \leq y^+ \leq 350$, corresponding roughly to the range $0.02 \leq y/\delta \leq 0.2$, after which the curves either turn upward in the outer (wakelike) layer or turn downward in the inner (viscous) layer.

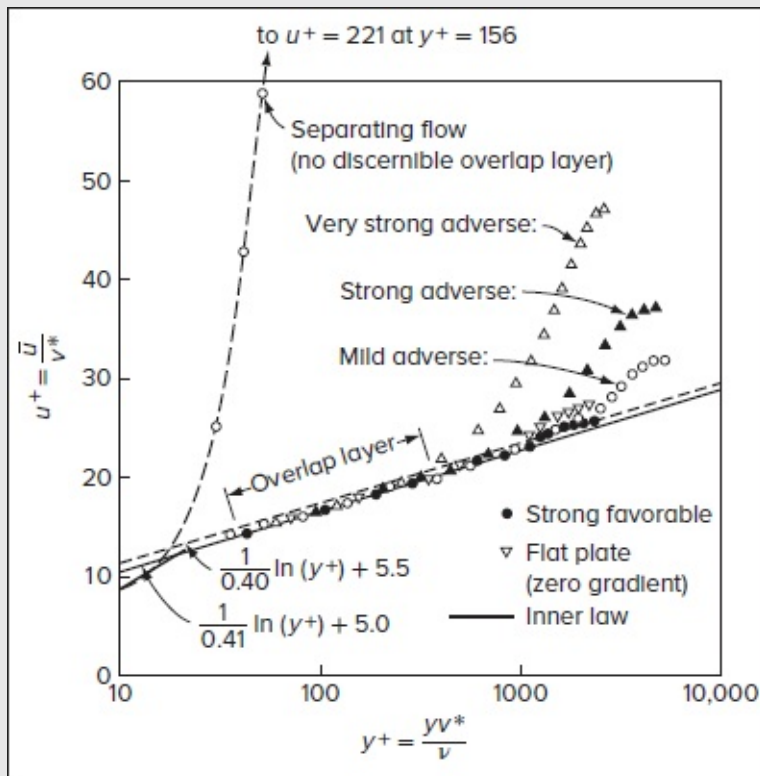


FIGURE 6-9

Replot of the velocity profiles of [Fig. 6-8](#) using inner law variables y^+ and u^+ .

The near-separating flow profile in [Fig. 6-9](#) zooms to the left and up off the chart because v^* approaches zero and hence u^+ becomes very large and y^+ very small. Near separation, then, scaling based on wall shear stress deteriorates. The outer law holds, but the inner and overlap layers become vanishingly small.

Note also from [Fig. 6-9](#) that there is little to choose between (0.40, 5.5) or (0.41, 5.0) for the logarithmic-law constants κ and B . The latter values will be used here when numerical results are needed.

The validity of the outer law [Eq. (6-36)] becomes less evident when the profiles from [Fig. 6-8](#) are replotted using the outer variables of velocity defect versus y / δ . The result is shown as [Fig. 6-10](#). At first glance, we may be momentarily distressed by the fact that the profiles do not collapse into a single “universal” curve. Upon closer scrutiny, it becomes apparent that the graphical disparities can be attributed to the differences in the pressure gradient parameter, P , which accompanies each of the profiles:

Strong favorable:	−4.8	Mild adverse:	+6.3
Flat plate:	0.0	Strong adverse:	+29

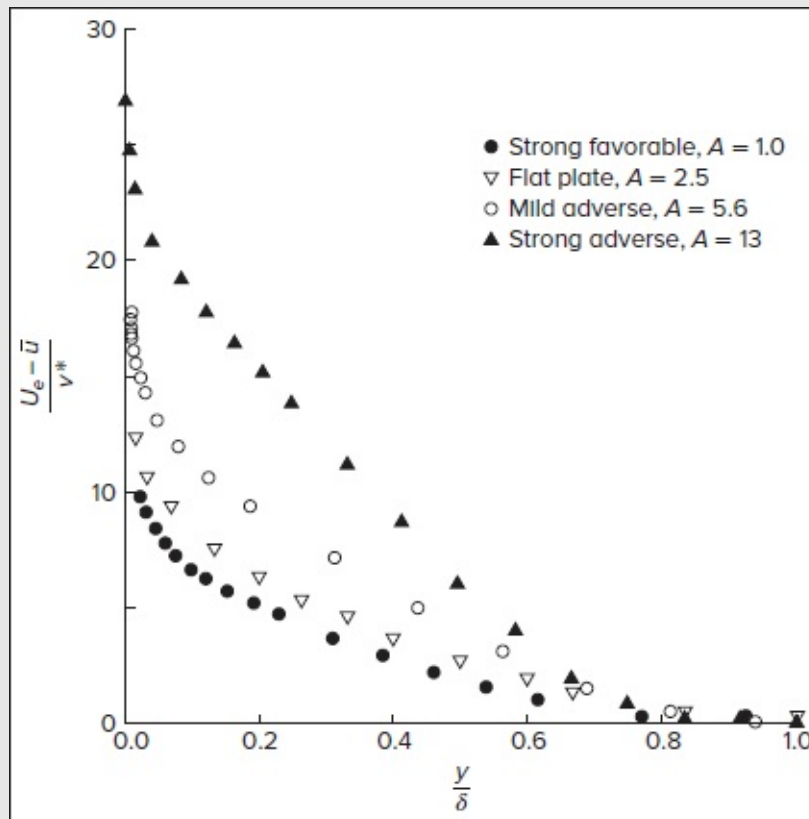


FIGURE 6-10

Replot of the velocity profiles of [Fig. 6-8](#) using outer law variables from [Eq. \(6-36\)](#). Success is not evident because each profile has a different value of the pressure gradient parameter P .

According to [Fig. 6-10](#), each shape is different depending on the value of its constant A . As such, the overlap laws do not collapse either. However, for a given P , a nearly unique profile develops. For example, all flat-plate data fall near the open-triangle points in [Fig. 6-10](#).

6-4.2 Inner Layer Details: The Law of the Wall

From [Fig. 6-9](#), we see that the inner law, [Eq. \(6-35\)](#), rises from no slip at the wall to merge smoothly, at about $y^+ \approx 30$, with the overlap log-law, [Eq. \(6-38a\)](#). Not shown in the figure is the behavior very near the wall, where turbulence is damped out and the boundary layer is dominated by viscous shear. At very small y , the velocity profile is linear:

$$y^+ \leq 5: \quad \tau_w = \frac{\mu \bar{u}}{y} \quad \text{or} \quad u^+ = y^+ \quad (6-40)$$

This (very thin) region near the wall is called the *viscous sublayer*. Its thickness is, by general agreement, $\delta_{\text{sub}} = 5\nu / v^*$, and the quantity (ν / v^*) is often called the *viscous length scale* of a turbulent boundary layer. For Wieghardt's Page 337 flat-plate airflow data in [Fig. 6-8](#), for example, with $v^* = 1.24$ m/s and $\nu_{\text{air}} \approx 1.51 \times 10^{-5}$ m² / s, we find $\delta_{\text{sub}} = 5(1.51 \times 10^{-5}) / 1.24 \approx 0.06$ mm, which is 500 times thinner than the 3 cm boundary-layer thickness.

Between $5 \leq y^+ \leq 30$, the so-called *buffer layer*, the velocity profile is neither linear nor logarithmic, but rather a smooth blend of the two regions. For decades, separate relations were assigned to the sublayer, the buffer layer, and the log layer, until Spalding (1961) [Eqn. 6-41](#) is the log law of the wall deduced a single composite formula that covered the entire wall-related region:

$$y^+ = u^+ + e^{-\kappa B} \left[e^{\kappa u^+} - 1 - \kappa u^+ - \frac{1}{2}(\kappa u^+)^2 - \frac{1}{6}(\kappa u^+)^3 \right] \quad (6-41)$$

This expression represents an excellent fit to inner law data all the way from the wall to the point (usually at $y^+ = 100$) where the outer layer begins to rise above the logarithmic curve.

It should be noted that for decades, there were no mean-velocity data close enough to the wall to test the inner law, until Lindgren (1965), testing a smooth pipe with distilled water, provided the data shown in [Fig. 6-11](#). Clearly, the agreement with Spalding's formula [Eq. \(6-41\)](#) is excellent even past $y^+ > 300$, where the outer law begins. This outer “wake” is very slight because fully developed pipe flow has a favorable gradient with $P \approx -2$, or about halfway between the “favorable” and “flat-plate” data in [Fig. 6-9](#). Note the (acceptable) use in [Fig. 6-11](#) of the older log constants $(\kappa, B) = (0.40, 5.5)$.

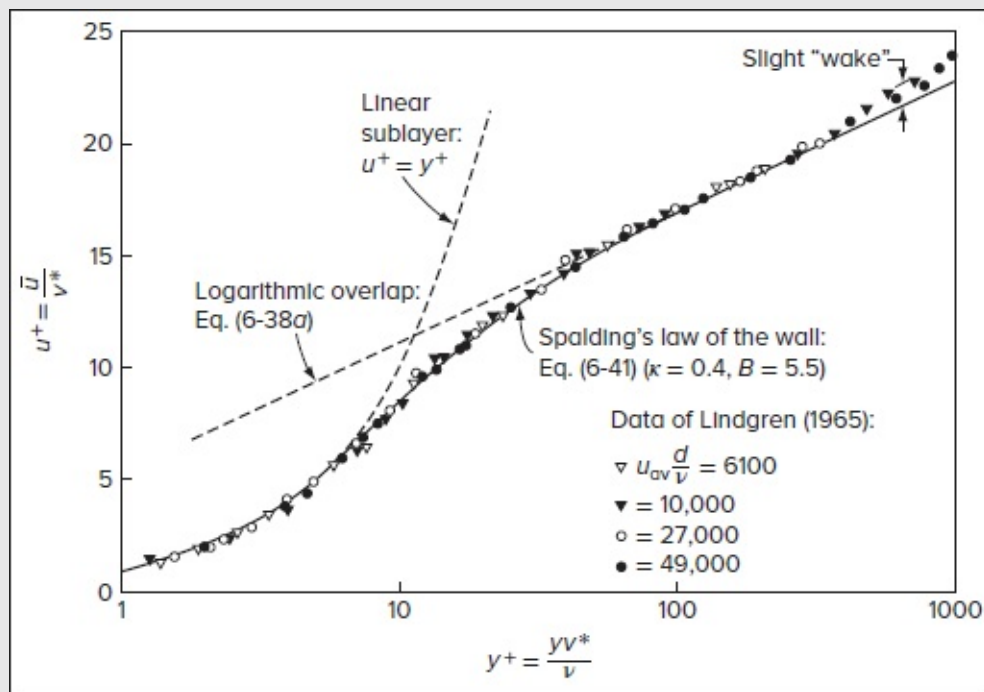


FIGURE 6-11

Comparison of Spalding's inner law expression with the pipe-flow data of Lindgren (1965).

6-4.3 Outer Layer Details: Equilibrium Turbulent Flows

The inner law may be viewed as a complete success for smooth-wall turbulent flow, namely, [Eq. \(6-41\)](#) or its equivalent. The outer law, though, is highly sensitive to the pressure gradient parameter $P = (\delta / \tau_w)(d p_e / dx)$ and its variation with x , as shown by [Eq. \(6-36\)](#) and [Fig. 6-10](#).

In two classic papers, Clauser (1954, 1956) developed the idea of specific cases for which P is constant, that he termed *equilibrium turbulent flows*. Clauser replaced the fuzzily defined thickness δ by the rigorously defined displacement thickness, thus leading to a dimensionless equilibrium pressure gradient parameter, specifically

$$\text{Clauser's equilibrium parameter:} \quad \beta \equiv \frac{\delta^*}{\tau_w} \frac{dp_e}{dx} = P\eta^* \quad (6-42)$$

Page 338

It turns out that constant- β flows correspond to a power-law freestream distribution for which $U_e = C x^m$, strikingly analogous to the laminar Falkner–Skan similarity flows of Sec. 4-3.4.

With considerable experimental effort, Clauser (1954) shows that a boundary layer with variable $p_e(x)$ but constant β can achieve turbulent equilibrium in the sense that all gross properties of that boundary layer can be scaled with a single parameter. The most relevant characteristic length for equilibrium flow is determined by Clauser to be the *defect thickness* Δ

$$\Delta = \int_0^\infty \frac{U_e - \bar{u}}{v^*} dy = \delta^* \lambda \quad (6-43)$$

where $\lambda = \sqrt{2/C_f}$ is a measure of the local skin friction (λ will be very useful in some approximate analyses which follow). Velocity profiles can thus be scaled with y / Δ ; a shape factor G that remains constant in an equilibrium boundary layer is also defined by Clauser using

$$G = \frac{1}{\Delta} \int_0^\infty \left(\frac{U_e - \bar{u}}{v^*} \right)^2 dy \quad (6-44)$$

The conventional Kármán-type shape factor, $H = \delta^* / \theta$, can be related to G via

$$H = \frac{\lambda}{\lambda - G} \quad (6-45)$$

We remark that since the skin friction varies with x , H is *not* constant in an equilibrium boundary layer.

There is no longer any doubt about the validity of Clauser's outer layer structural assumptions. [Figure 6-12](#) shows the outer layer defect profile for a flat plate ($\beta = 0$), including data for rough walls. The data can be seen to collapse beautifully about the eddy-viscosity calculations of Mellor and Gibson (1966). Also shown are the two equilibrium adverse gradients generated in the original experiments by Clauser (1954), again with excellent agreement. The two distributions are now commonly called Clauser I ($\beta \approx 1.8$, $G \approx 10.1$) and Clauser II ($\beta \approx 8.0$, $G \approx 19.3$). The equilibrium concept is even valid at the ultimate limit ($\beta \rightarrow \infty$), as measured, for example, by Stratford (1959). Finally, the case of negative β (favorable gradient) stands in equally good agreement with experiments, as shown by Herring and Norbury (1967), among others.

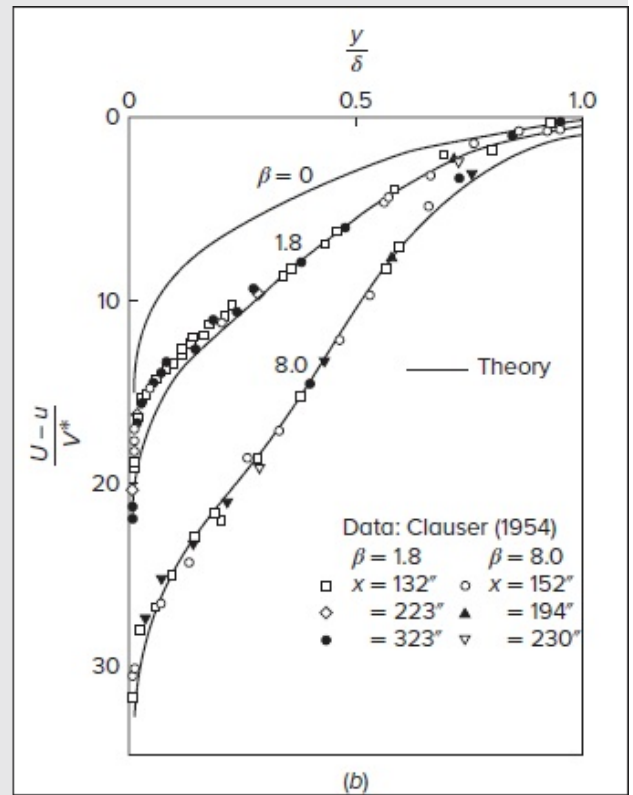
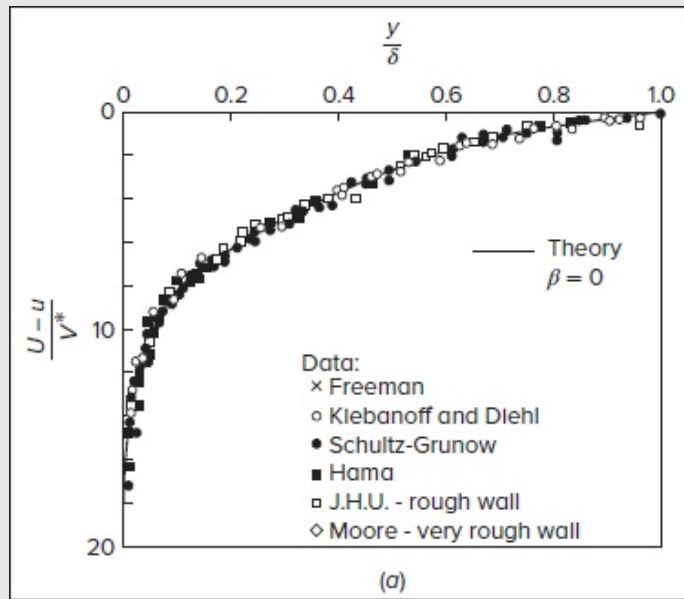


FIGURE 6-12

Equilibrium-defect profiles, as correlated by the Clauser parameter β and the theory of Mellor and Gibson (1966): (a) flat-plate data; (b) equilibrium adverse gradients.

6-4.4 An Alternative View: Coles' Law of the Wake

From an application point of view, there are two difficulties with the outer layer approach of Clauser: (1) nonequilibrium flows deviate in shape from the “similarity” profiles of [Fig. 6-12](#), and (2) even the equilibrium shapes have noPage 339 simple analytical forms to use in an engineering theory. These points were resolved by Coles (1956), who noted that the *deviations* or excess velocity of the outer layer above the log layer (see [Fig. 6-9](#)) have a wakelike shape when viewed from the freestream. If normalized by the maximum deviation at $y = \delta$, the data nearly collapse into a unique function of y / δ . In other words, Coles proposed that

$$\frac{u^+ - u_{\log\text{-law}}^+}{U_e^+ - u_{\log\text{-law}}^+(y = \delta)} \approx f\left(\frac{y}{\delta}\right)$$

where the *wake function* f is normalized to be zero at the wall and unity at $y = \delta$. Two popular curve fits are used for the S-shape expected for the wake function:

$$f\left(\frac{y}{\delta}\right) \approx \sin^2\left(\frac{\pi y}{2\delta}\right) \approx 3\left(\frac{y}{\delta}\right)^2 - 2\left(\frac{y}{\delta}\right)^3 \quad (6-46)$$

The polynomial fit is, of course, easier to use in an integral formulation.

By adding the wake to the log-law, we arrive at an accurate approximation for both the overlap and outer layers:

$$u^+ \approx \frac{1}{\kappa} \ln(y^+) + B + \frac{2\Pi}{\kappa} f\left(\frac{y}{\delta}\right) \quad (6-47)$$

The quantity $\Pi = \kappa A / 2$, called *Coles' wake parameter*, is directly related to the previously defined outer constant A . It is also approximately related to Clauser's equilibrium parameter β (see [Fig. 6-27](#)). For equilibrium flows, Π should vary only with β .

The beauty of [Eq. \(6-47\)](#) is that it represents a complete and reasonably accurate expression for any two-dimensional turbulent-boundary-layer profile, whether in equilibrium or not. If $y^+ < 30$, one should omit the wake and proceed to compute u^+ from [Eq. \(6-41\)](#). The efficacy of [Eq. \(6-47\)](#) is seen from the representative profiles plotted in [Fig. 6-13](#), demonstrating the idea of adding an S-shaped wake function to the pure law of the wall ($\Pi = 0$). These represent very realistic shapes that are easy to compute. If normalized to u / U_e and replotted, they closely resemble the profiles shown in [Fig. 6-8](#).

Page 340

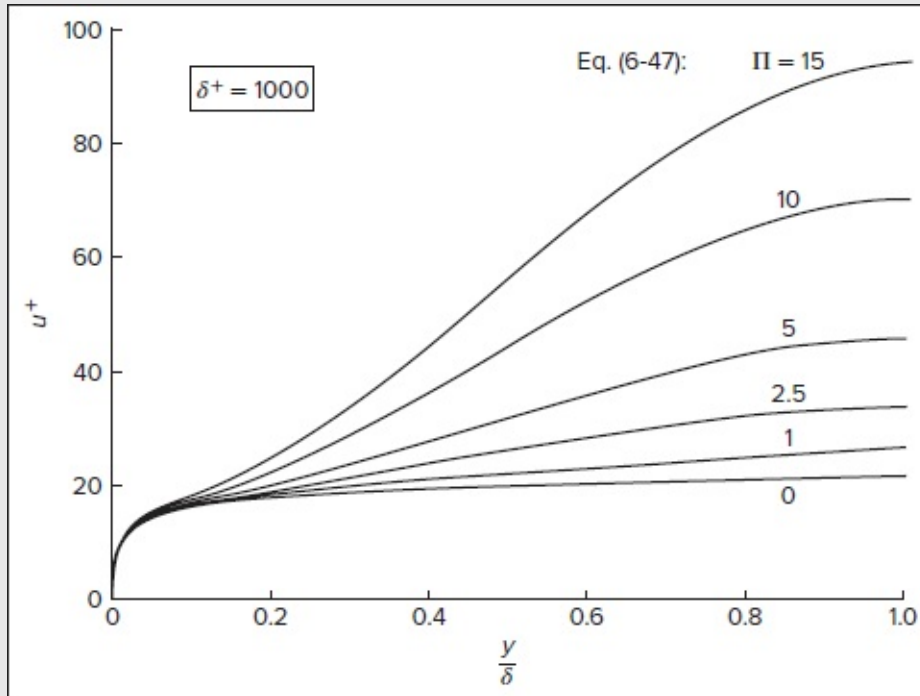


FIGURE 6-13

Turbulent velocity profiles computed from the Coles' wall-wake formula, [Eq.](#)

(6-47), assuming $\delta^+ = 1000$. The curve for $\Pi = 0$ is the pure law of the wall from Eq. (6-41).

The wall–wake composite profile can be used in several types of turbulent shear-flow theories. Its admirable simplicity, for example, results in concise formulas for integral parameters. By integrating Eq. (6-47) across the boundary layer, we obtain

$$\frac{\delta^*}{\delta} \approx \frac{1 + \Pi}{\kappa \lambda} \quad \lambda = \left(\frac{2}{C_f} \right)^{1/2} \quad \frac{\theta}{\delta} \approx \frac{\delta^*}{\delta} - \frac{2 + 3.2\Pi + 1.5\Pi^2}{\kappa^2 \lambda^2} \quad (6-48)$$

Similarly, the local skin-friction coefficient, $C_f = 2\tau_w/(\rho U_e^2)$, may be related to Π and the local Reynolds number, $Re_\delta = U_e \delta / \nu$, by evaluating the wall–wake law through Eq. (6-47) at the edge of the boundary layer. We obtain

$$\frac{U_e}{v^*} = \lambda = \left(\frac{2}{C_f} \right)^{1/2} = \frac{1}{\kappa} \ln \left(\frac{Re_\delta}{\lambda} \right) + B + \frac{2\Pi}{\kappa} \quad (6-49)$$

We will use this simple algebraic approach for some practical turbulent shear-flow problems in the next sections. Huang and Bradshaw (1995) discuss the effect of the pressure gradient.

6-4.5 The Alternative Power-Law Overlap: A Controversy

Fluids engineering is a collaborative field of study. Researchers usually make incremental gains and seldom argue, except about calculation methods. Thus, when Barenblatt et al. (1997) proposed a new nonlogarithmic formula for the overlap law, it became surprisingly controversial. Newspapers carried the headline “Law of the Wall Toppled.” By this they meant the logarithmic-law of the wall, Eq. (6-38a), which had been accepted for 70 years. The reporter, Kathleen Stein, quoted the authors that “Engineering and aerodynamics textbooks, and design software will have to be rewritten.” George and Castillo (1997) and others, notably Zagarola and Smits (1998), seconded the demise of the log-law. The alternative overlap formula, proposed for both pipe flow and flat-plate flow, is a *power law* of the form

$$u^+ \approx C(y^+)^{\alpha} \quad \text{where} \quad C \approx 3 + 0.62 \ln(Re_\theta) \quad \text{and} \quad \alpha \approx \frac{1.24}{\ln(Re_\theta)} \quad (6-50)$$

Unlike the classical log-law, with $\kappa \approx 0.41$ and $B \approx 5.0$, the constants C and α were acknowledged to vary with the Reynolds number. The idea recalls the original observation in 1921 by Prandtl (1961, vol. II, pp. 620–626) that pipe-flow velocities approximated a one-seventh power law.

One might assume that the fluids community would now accept two viable overlap laws?

Instead, the controversy escalated into fierce arguments at several international conferences. A good effort to resolve the debate was finally offered by Buschmann and Gad-el-Hak (2003), who analyzed 109 different zero-pressure-gradient data sets by both log and power formulas. They included newer data by Österlund (1999), which extended to $Re_\theta = 27,000$, much higher than data for which the log-law had been matched. They concluded that the two laws provided comparable agreement and neither was statistically superior. The power law is poorer near the wall, and the log-law is poorer near the wake region. [Figure 6-14](#) shows the best fit values of log-law and power-law “constants” as a function of the Reynolds number. We see that all coefficients vary slightly with Re_θ . It is generally agreed that the log-law should be valid as $Re_\theta \rightarrow \infty$, where Buschmann and Gad-el-Hak (2003) suggest the limiting values of $\kappa \approx 0.38$ and $B \approx 4.08$.

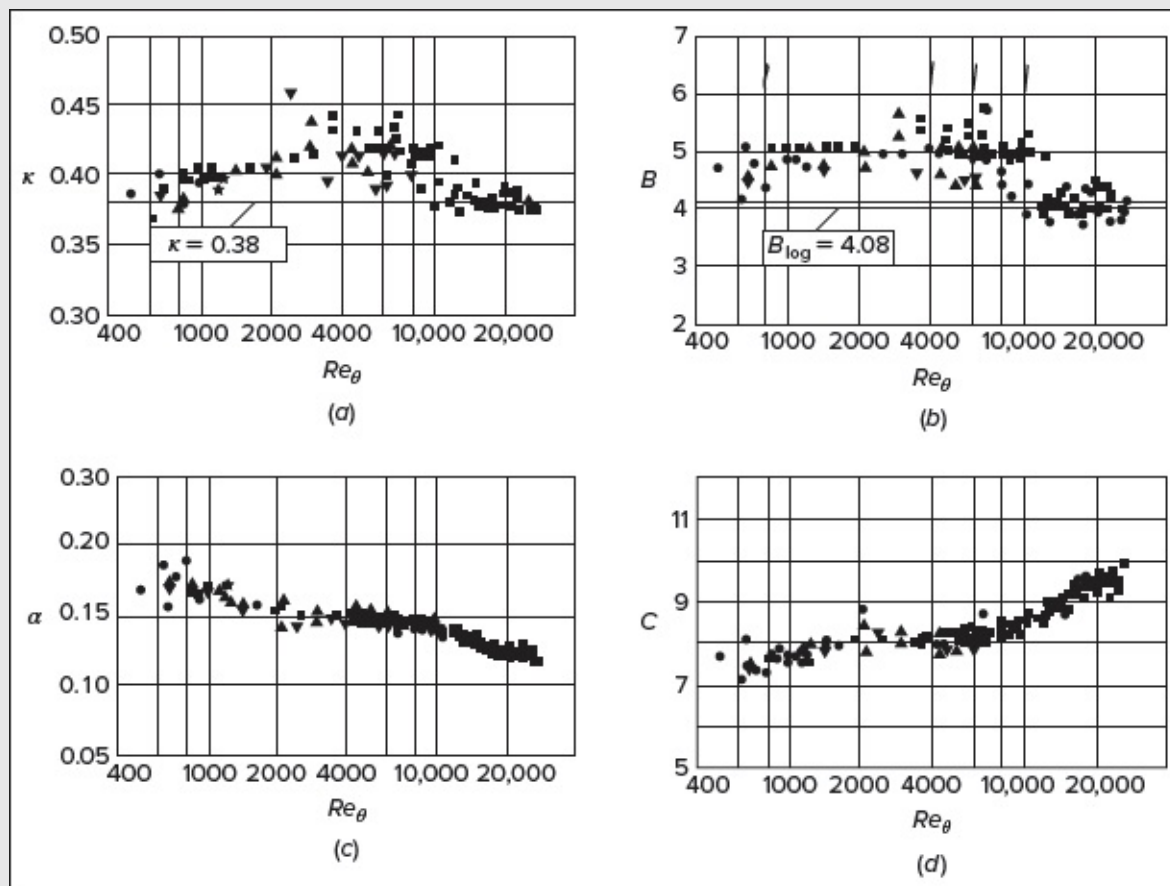


FIGURE 6-14

Overlap law constants as correlated by Buschmann and Gad-el-Hak (2003): (a, b) log-law, Eq. (6-38a); (c, d) power law, [Eq. \(6-50\)](#). [Reprinted by permission of the American Institute of Aeronautics and Astronautics.]

It is interesting that, for all the discussions and graphs given in Sec. 6-4, there was actually no underlying theory. No equations were solved and all of the velocity profiles were correlations, i.e., the outcome of physically meaningful dimensional analysis. We can now proceed from these algebraic expressions to solve simple problems, without any extensive use of “theory.” Here we discuss fully developed flow in ducts.

6-5.1 The Circular Pipe

Let us consider the case of a fully developed pipe flow, assumed far downstream of the entrance, where the velocity no longer depends on the axial distance x . The laminar-flow analysis, Sec. 3-3.1, predicts a parabolic velocity distribution, Eq. (3-34), along with a friction factor of $C_f = 16 / Re_D$, which was illustrated in [Fig. 3-7](#). Laminar motion becomes unstable at about $Re_D = 2000$ and a fully turbulent flow ensues at $Re_D \approx 4000$. At higher Reynolds numbers, Page 342 the data in [Fig. 3-7](#) follow a curve labeled “Blasius,” which is not a theory but rather a curve fit to smooth-wall data collected in 1913 by Prandtl’s student H. Blasius:

$$C_f(\text{pipe}) = \frac{2\tau_w}{\rho u_{av}^2} \approx 0.0791 Re_D^{-1/4} \quad 4000 < Re_D < 10^5 \quad (6-51)$$

The Blasius formula was one of the first modern applications of the technique of dimensional analysis; however, it has a limited range of applicability.

A better result follows from the wall law, [Eq. \(6-41\)](#) or (6-38a). Pipe flow, having a favorable pressure gradient, should resemble the upper velocity profile in [Fig. 6-8](#). Denoting the pipe radius by a , the wall coordinate becomes

$$y = a - r \quad dy = -dr$$

With the profile known, we may evaluate the average pipe velocity:

$$u_{av} = \frac{Q}{A} = \frac{1}{\pi a^2} \int_0^a \bar{u}(2\pi r) dr = \frac{2}{a^2} \int_0^a \bar{u}(a - y) dy \quad (6-52)$$

[Figure 6-11](#) shows clearly that turbulent pipe flow has an insignificant wake, that is, $\Pi \approx 0$. Consequently, the law of the wall remains accurate all the way across the pipe. Furthermore, we may neglect the (very thin) viscous sublayer and substitute the simple log-law, Eq. (6-38a), with the result

$$u_{av} = v^* \left(\frac{1}{\kappa} \ln \frac{av^*}{\nu} + B - \frac{3}{2\kappa} \right) \quad (6-53)$$

Now, from the definition of pipe-friction factor, $C_f = 2\tau_w / (\rho u_{av}^2)$, and the following identities hold:

$$\frac{u_{av}}{v^*} = \left(\frac{2}{C_f}\right)^{1/2} \quad \frac{av^*}{\nu} = Re_D \left(\frac{C_f}{8}\right)^{1/2} \quad Re_D = \frac{2au_{av}}{\nu}$$

This piques our interest, revealing that [Eq. \(6-53\)](#) is actually a friction factor relation. Introducing base-10 logarithms, with $\ln(x) = \ln(10)\log_{10}(x)$, along with $\kappa = 0.41$ and $B = 5.0$, we may rearrange [Eq. \(6-53\)](#) into

$$\frac{1}{\Lambda^{1/2}} = 1.99\log_{10}(Re_D \Lambda^{1/2}) - 1.02$$

where $\Lambda = 4 C_f$ is the Darcy friction factor. This formula was derived by Prandtl in 1935. Since he neglected the sublayer and wake regions, Prandtl slightly adjusted the constants to fit pipe-friction data more effectively, especially at lower Reynolds numbers. The final formula is

$$\frac{1}{\Lambda^{1/2}} = 2.0\log_{10}(Re_D \Lambda^{1/2}) - 0.8 \quad (6-54)$$

This expression is valid for smooth-wall turbulent pipe flow at any Reynolds number greater than 4000. It supplants the Blasius correlation given by [Eq. \(6-51\)](#).

[Figure 6-15](#) shows the laminar and turbulent friction factor formulas plotted versus the Reynolds number. Note that the Blasius formula [Eq. \(6-51\)](#) falls too low for $Re_D > 10^5$, thus unpredicting the effect of friction. However, the Blasius formula can be used to reveal interesting trends by rewriting it in terms of the wall shear stress,

$$\tau_w \approx 0.0396\rho^{3/4}u_{av}^{7/4}\mu^{1/4}D^{-1/4} \quad (6-55)$$

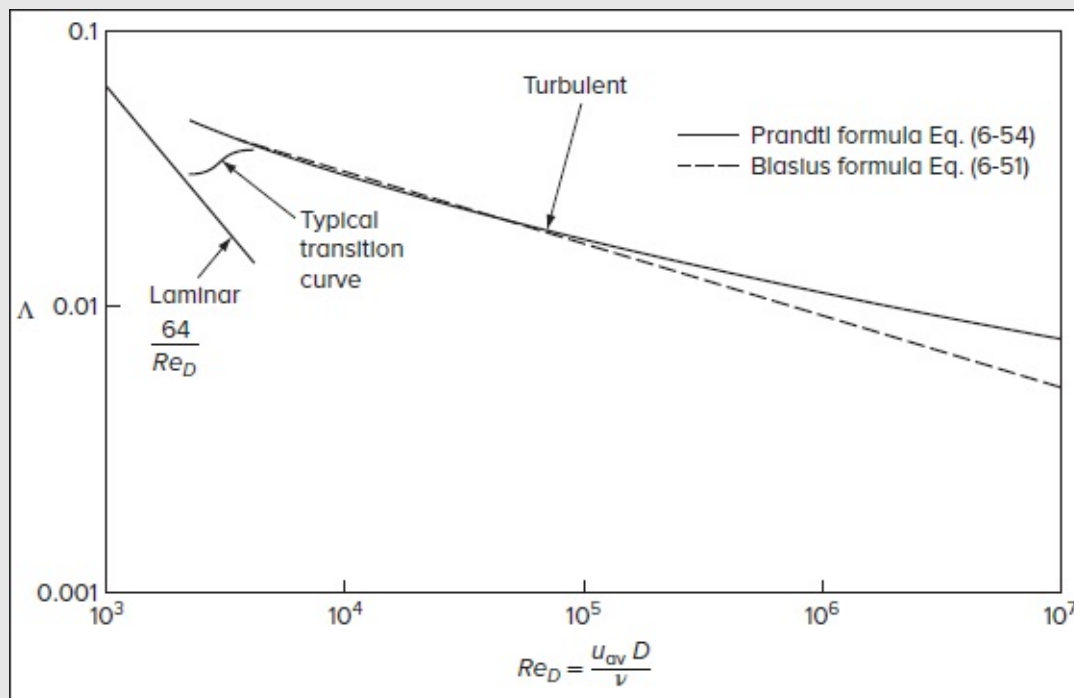


FIGURE 6-15

Analytical friction factor formulas for fully developed pipe flow. Compare with the data in [Fig. 3-7](#).

Thus, in turbulent pipe flow, wall shear increases nearly linearly with the density, almost quadratically with the velocity, very weakly with the viscosity, and decreases weakly with the pipe size. The transition curve in [Fig. 6-15](#) is typical of the change from laminar to turbulent flow between $Re_D = 2000$ and 4000 . This region is rather uncertain, and the flow pulsates as turbulent “slugs” propagate through the pipe. It should be avoided in the design of a pipe-flow system.

6-5.2 Channel Flow between Parallel Plates

The case of a fully developed laminar flow between parallel plates was solved as Eq. (3-44), resulting in a parabolic velocity distribution $u(y)$ and a friction factor $C_f = 6/Re_h$, where h denotes the half-width between plates. The geometry is shown in [Fig. 6-16](#) and illustrates the contrast between laminar and turbulent velocity profiles. Also shown is the total shear-stress distribution $\tau(y)$, which, like pipe flow, drops linearly from the wall value to zero at the centerline.

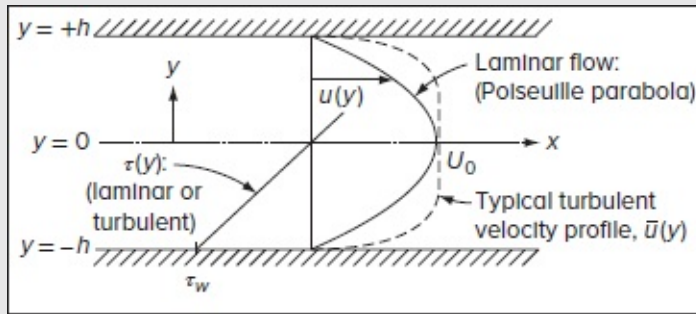


FIGURE 6-16

Fully developed laminar and turbulent flow in a channel.

Here too, the wake is small and the sublayer negligible, so it is possible to use the log-law Eq. (6-38a) to represent the velocity profile across the entire channel. Using a wall variable of $Y = (h - y)$, the average velocity may be approximated from the log-law:

$$u_{av} = \frac{1}{h} \int_0^h \bar{u} dY \approx v^* \left(\frac{1}{\kappa} \ln \frac{h v^*}{\nu} + B - \frac{1}{\kappa} \right)$$

Since $u_{av}/v^* = (8/\Lambda)^{1/2} = (2/C_f)^{1/2}$, we can now solve for the corresponding friction factor.

For a channel, it is convenient to employ the hydraulic diameter concept from [Eq. \(3-55\)](#) and write

$$Re_{D_h} = \frac{u_{av} D_h}{\nu} \quad D_h = \frac{4A}{\mathcal{P}} = 4h \quad (6-56)$$

where A and \mathcal{P} denote the flow area and wetted perimeter, respectively. Introducing these definitions into the expression for u_{av} , using base-10 logarithms, and rearranging, we obtain, for smooth-wall turbulent channel flow,

$$\frac{1}{\Lambda^{1/2}} = 2.0 \log_{10}(Re_{D_h} \Lambda^{1/2}) - 1.19 \quad (6-57)$$

The result is strikingly similar to the pipe relation, [Eq. \(6-54\)](#), but predicts a slightly higher Λ , namely, 7 percent at $Re = 10^5$ and down to 4 percent at $Re = 10^8$.

Page 344

Note that by using the law of the wall to analyze pipe and channel flows, the evaluation of u_{av} leads to the final result straightforwardly. No differential equations are solved, and no theoretical arguments are made.

6-5.3 The Effective Diameter for Turbulent Noncircular Duct Flow

The channel-flow relation [Eq. \(6-57\)](#) is close enough to the pipe-flow result that it substantiates the common engineering practice [e.g., White (2012, p. 373–374)] of computing noncircular duct friction by using the hydraulic diameter D_h and the pipe-friction relation [Eq. \(6-54\)](#). Indeed, experiments with turbulent flow through triangular, square, rectangular, and annular ducts [see Schlichting (1979, Fig. 20.12)] show only a few percent error when this scheme is adopted. As such, the hydraulic diameter approximation is much better for turbulent than for laminar flow (recall [Fig. 3-13](#) for comparison).

A further improvement may be obtained by modifying D_h using laminar duct theory for the same cross section. For example, [Eq. \(6-57\)](#) for the channel will resemble the circular pipe law [Eq. \(6-54\)](#) if rewritten as

$$\frac{1}{\Lambda^{1/2}} (\text{channel}) = 2.0 \log_{10}(0.64 Re_{D_h} \Lambda^{1/2}) - 0.8 \quad (6-58)$$

The best agreement between channel and pipe configurations is predicted when we use $(0.64 D_h)$ as the *effective diameter* of the channel. Recall that in laminar flow, $C_f(\text{pipe}) = 16 / Re_D$ and $C_f(\text{channel}) = 24 / Re_{D_h}$, and so the ratio of these two is $16 / 24 = 0.667$, which is quite near the prediction of 0.64. This is no coincidence. A general rule for estimating turbulent friction in noncircular ducts is to use the pipe-friction law [Eq. \(6-54\)](#) based on an

effective Reynolds number

$$Re_{D_{\text{eff}}} = \frac{u_{\text{av}} D_{\text{eff}}}{\nu} \quad \text{where} \quad D_{\text{eff}} = D_h \frac{16}{(C_f Re_{D_h})_{\text{laminar}}} \quad (6-59)$$

This concept was proposed and proved experimentally by O. C. Jones in tests involving rectangular [Jones (1976)] and concentric annular ducts [Jones and Leung (1981)]. One could take $(C_f Re)_{\text{laminar}}$ for the given section from the results in Sec. 3-3.3. In fact, the method should work well for any squatty or blocky cross section, i.e., with no unusually thin regions. For example, an experiment by Eckert and Irvine (1957) on a 12 o isosceles triangle gave poorer results, because the flow in the 12 o corner remained laminar up to surprisingly high Reynolds numbers. Obot (1988) reviewed the entire subject of noncircular ducts, including small apex angles and rough walls. While agreeing with the effective diameter scheme, Obot went further and proposed a “critical friction” or transition-oriented method for correlating the data in any duct.

6-5.4 Turbulent Flow in Rough Pipes

The previous formulas are valid only for smooth-wall turbulent duct flow. Although wall roughness has little bearing on laminar flow, even a small degree of roughness will break up the thin viscous sublayer and greatly increase the wall friction in turbulent flow. Denoting the average roughness height by k , the wall law and friction law become, respectively,

$$u^+ = f(y^+, k^+) \quad \text{where} \quad k^+ = \frac{k v^*}{\nu} \quad \text{and} \quad \Lambda = f\left(Re_D, \frac{k}{D}\right)$$

The logarithmic overlap layer still exists but, as k^+ increases, the intercept B begins to move downward monotonically and the effective “wall” position begins to move outwardly:

$$u_{\text{overlap}}^+ = \frac{1}{\kappa} \ln \frac{y v^*}{\nu} + B - \Delta B(k^+) \quad (6-60)$$

As illustrated in [Fig. 6-17](#), the downward shift can be large, with a correspondingly large increase in friction. While Kármán’s constant $\kappa \approx 0.41$ does not change with roughness, ΔB proves to be a non-unique function of k^+ , which varies with the *type* of roughness (uniform sand, sand mixtures, rivets, threads, spheres, etc.). This is seen in [Fig. 6-18](#), taken from a compilation by Clauser (1956). Although a substantial variation occurs at small k^+ , the asymptotic variation at large k^+ is logarithmic with a slope of $1 / \kappa$ in all cases considered. Note that the *outer* or defect layer is not affected by wall roughness (the data in [Fig. 6-12a](#) include rough and very rough surfaces!).

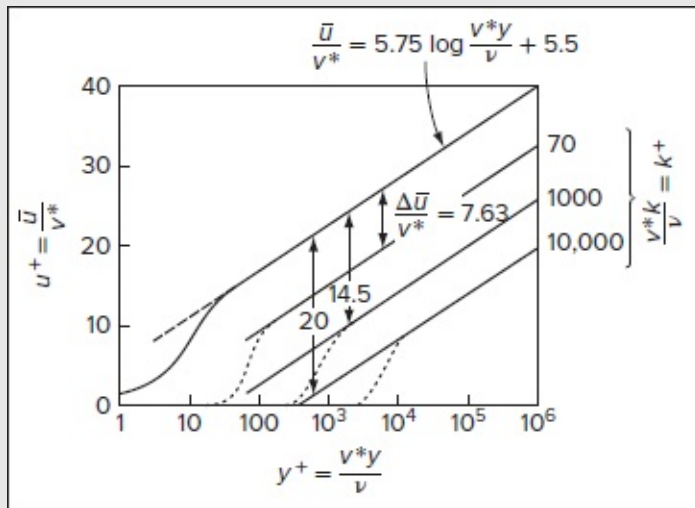


FIGURE 6-17

Experimental rough-pipe velocity profiles, showing the downward shift ΔB of the logarithmic overlap layer.

The dashed line in [Fig. 6-18](#) denotes the classic Prandtl–Schlichting sand-grain roughness curve. For $k^+ < 4$, there is no roughness effect, and for $k^+ > 60$, ΔB is logarithmic. This defines the three roughness regimes:

$$k^+ < 4 : \text{hydraulically smooth wall}$$

$$4 < k^+ < 60 : \text{transitional-roughness regime}$$

$$k^+ > 60 : \text{fully rough flow (no } \mu \text{ effect)}$$

(6-61)

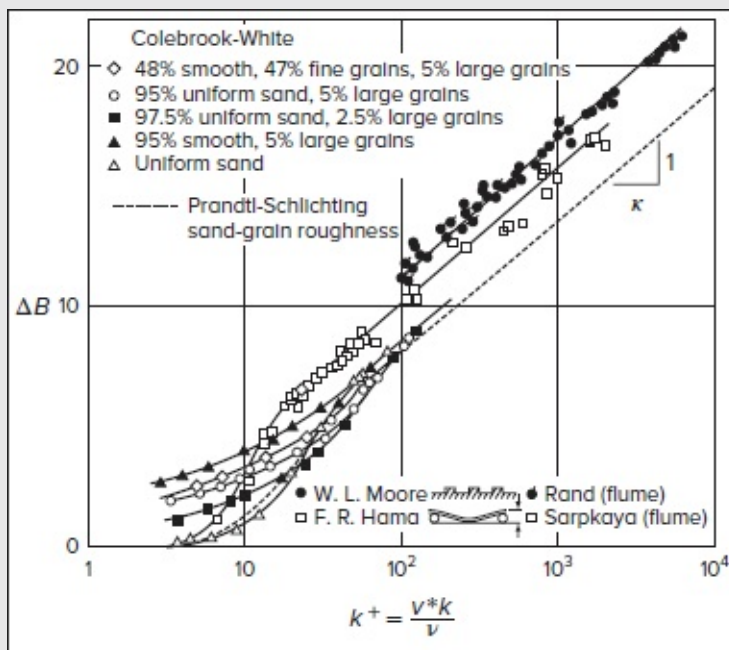


FIGURE 6-18

Composite plot of the profile-shift parameter $\Delta B(k^+)$ for various roughness geometries, compiled by Clauser (1956).

To derive a pipe-friction formula with sand-grain roughness, we may curve fit the dashed curve in [Fig. 6-18](#) with the following expression:

$$\Delta B_{\text{sand grains}} \approx \frac{1}{\kappa} \ln(1 + 0.3k^+) \quad (6-62)$$

When this relation is substituted back into [Eq. \(6-60\)](#), it reduces to

$$\text{Fully rough flow:} \quad u^+ = \frac{1}{\kappa} \ln\left(\frac{y}{k}\right) + 8.5; k^+ > 60 \quad (6-63)$$

In this condition, there is no effect of viscosity on the velocity profile.

Page 346

Similarly, the introduction of $(B - \Delta B)$ into the pipe-friction formula (6-53) yields, after rearranging and introducing base-10 logarithms,

$$\frac{1}{\Lambda^{1/2}} \approx 2.0 \log \left[\frac{Re_D \sqrt{\Lambda}}{1 + 0.1k/D Re_D \sqrt{\Lambda}} \right] - 0.8 \quad (6-64)$$

This expression should be viewed as a suitable representation of sand-grain pipe friction over the entire turbulent-flow regime. The denominator term shows that if

$$\begin{aligned} \left(\frac{k}{D}\right) Re_D < 10: & \quad \text{inconsequential roughness} \\ \left(\frac{k}{D}\right) Re_D > 1000: & \quad \text{dominant roughness; "fully rough" flow independently of } Re_D \end{aligned}$$

Commercial pipes have roughnesses that do not precisely follow sand-grain behavior, so C. F. Colebrook in 1939 devised a formula, different from [Eq. \(6-64\)](#), which was plotted by Moody (1944) and shown in [Fig. 6-19](#). The Colebrook interpolation formula is

$$\frac{1}{\Lambda^{1/2}} \approx -2.0 \log_{10} \left(\frac{k/D}{3.7} + \frac{2.51}{Re_D \sqrt{\Lambda}} \right) \quad (6-65)$$

proposed by Haaland (1983):

$$\frac{1}{\Lambda^{1/2}} \approx -1.8 \log_{10} \left[\frac{6.9}{Re_D} + \left(\frac{k/D}{3.7} \right)^{1.11} \right] \quad \text{or} \quad \Lambda = \frac{1.6364}{\ln^2 \left[\frac{6.9}{Re} + \frac{(k/D)^{1.11}}{3.7} \right]} \quad (6-66)$$

This relation varies by less than ± 2 percent from [Eq. \(6-65\)](#) and enables us to evaluate the friction factor directly (see App. E).

6-6 THE TURBULENT BOUNDARY LAYER ON A FLAT PLATE

The problem of flow past a sharp flat plate at high Reynolds numbers has been extensively studied, and numerous formulas have been proposed for the corresponding friction factor. The studies vary in sophistication from data curve fits, use of the Kármán integral relation and/or law of the wall, to numerical simulations using models of turbulent shear (Sec. 6-7).

6-6.1 Momentum-Integral Analysis

An integral approach is ideally suited for this problem. The pressure gradient is zero, and the momentum-integral relation (6-28) reduces to

$$C_f = 2 \frac{d\theta}{dx} \quad (6-67)$$

Since this is an equilibrium flow ($\beta = 0$), the velocity profile is well approximated by the wall–wake law [Eq. \(6-47\)](#) with $\Pi \approx 0.45$. Evaluation of the profile function (6-47) at $y = \delta$ then gives

$$\frac{U_e}{v^*} = \left(\frac{2}{C_f} \right)^{1/2} = \frac{1}{\kappa} \ln \frac{\delta v^*}{\nu} + B + \frac{2\Pi}{\kappa} \approx 2.44 \ln \left[Re_\delta \left(\frac{C_f}{2} \right)^{1/2} \right] + 7.2$$

By analogy with [Eq. \(6-53\)](#), this relation represents a friction relation between C_f and Re_δ . It is laborious algebraically, so we may proceed to substitute several values for C_f from 0.001 to 0.005, and then construct an excellent power-law curve-fit approximation:

$$C_f \approx 0.020 Re_\delta^{-1/6} \quad \text{or, in terms of the wall shear stress, } \tau_w = 0.010 \rho u_{av}^2 \left(\frac{\nu}{u_{av} \delta} \right)^{1/6} \quad (6-68)$$

This secures the left-hand side of [Eq. \(6-67\)](#).

To evaluate the momentum thickness without undue algebra, Prandtl suggested in 1921 [Prandtl (1961, vol. II, pp. 620–626)] a simple one-seventh power-law profile, taken from pipe data:

$$\frac{\bar{u}}{U_e} \approx \left(\frac{y}{\delta}\right)^{1/7} \quad \text{hence} \quad \frac{\theta}{\delta} \approx \frac{7}{72} \quad (6-69)$$

Substitution of [Eqs. \(6-68\)](#) and [\(6-69\)](#) in [Eq. \(6-67\)](#) leads to the simple first-order ordinary differential equation

$$0.020 Re_\delta^{-1/6} \approx 2 \frac{d}{dx} \left(\frac{7\delta}{72} \right) = \frac{7}{36} \frac{dRe_\delta}{dRe_x}$$

Integrating with the knowledge that $\delta = 0$ at $x = 0$, we extract

$$Re_\delta \approx 0.16 Re_x^{6/7} \quad \frac{\delta}{x} \approx \frac{0.16}{Re_x^{1/7}} \quad \text{and} \quad C_f \approx \frac{0.027}{Re_x^{1/7}} \quad (6-70)$$

These simple power-law expressions prove to be in favorable agreement with turbulent flat-plate data and are recommended for general use.

A slightly more detailed relation can be obtained using the wall-wake momentum thickness result, [Eq. \(6-48\)](#), with $\kappa = 0.41$ and $\Pi \approx 0.45$:

$$\frac{\theta}{\delta} \approx \frac{3.54}{\lambda} - \frac{22.21}{\lambda^2} \quad \text{where} \quad \lambda = \left(\frac{2}{C_f} \right)^{1/2} \quad (6-71)$$

Page 348

Unfortunately, the use of this expression in [Eq. \(6-67\)](#) leads to results that are not any more accurate than [Eq. \(6-71\)](#). We give this analysis as a problem exercise.

Meanwhile, Prandtl in 1927 used $\tau_w = 0.0233 \rho u_{av}^2 [\nu / (u_{av} \delta)]^{1/4}$ or, alternatively, $C_f \approx 0.0466 Re_\delta^{-1/4}$, to produce the power-law approximations

$$\frac{\delta}{x} \approx \frac{0.37}{Re_x^{1/5}} \quad \text{and} \quad C_f \approx \frac{0.058}{Re_x^{1/5}} \quad (6-72)$$

These relations, though often quoted in the literature, were developed from very limited low Reynolds number data.

Because of the popularity of power-law profiles in turbulent boundary layer studies, a generalization of the foregoing solutions is warranted. As shown by Majdalani in his 2018 class notes, this can be readily accomplished by applying von Kármán's momentum-integral analysis to a normalized velocity profile of the form

$$\frac{\bar{u}}{U_e} = \left(\frac{y}{\delta} \right)^{1/q} \quad \xi \equiv \frac{y}{\delta}$$

where ξ represents the fractional distance within the velocity boundary layer and $q = \{5, 6, 7, 8, 9\}$ sets the power-law exponent that best reflects the motion under consideration. Then based on [Eq. \(6-28\)](#), it can be readily shown that the normalized displacement and

momentum thicknesses, η^* and θ^* , as well as the shape factor H , can be expressed as direct functions of q , namely,

$$\begin{cases} \eta^* \equiv \frac{\delta^*}{\delta} = \int_0^1 \left(1 - \frac{\bar{u}}{U_e}\right) d\xi = \frac{1}{q+1} & \text{(normalized displacement thickness)} \\ \theta^* \equiv \frac{\theta}{\delta} = \int_0^1 \frac{\bar{u}}{U_e} \left(1 - \frac{\bar{u}}{U_e}\right) d\xi = \frac{q}{(q+1)(q+2)} & \text{(normalized momentum thickness)} \\ H \equiv \frac{\delta^*}{\theta} = \frac{\eta^*}{\theta^*} = \frac{q+2}{q} & \text{(momentum shape factor)} \end{cases}$$

For example, using $q = 7$, one gets $\eta^* = 1/8$, $\theta^* = 7/72$, and $H = 9/7$. To make further headway, it is essential to specify

the wall shear stress as a function of Re_δ . In fact, both [Eqs. \(6-68\)](#) and [\(6-72\)](#), which are associated with the wall–wake and Prandtl’s power law approximations, depend on a shear stress correlation of the form

$$\tau_w = C_w \rho u_{av}^2 \left(\frac{\nu}{u_{av} \delta} \right)^{1/m} \quad \text{or} \quad C_f = \frac{2C_w}{Re_\delta^{1/m}}$$

where the empirical constants C_w and m are characteristics of the problem under consideration. For example, Prandtl’s 1927 model uses $m = 4$ whereas the wall–wake power-law formulation relies on $m = 6$. In all such cases, the momentum-integral balance, given by [Eq. \(6-67\)](#) for a zero pressure gradient, leads to

$$\frac{d\theta}{dx} = \theta^* \frac{d\delta}{dx} = \frac{C_w}{Re_x^{1/m}}, \quad \theta^* \frac{dRe_\delta}{dRe_x} = \frac{C_w}{Re_x^{1/m}}, \quad \text{or} \quad Re_\delta^{1/m} dRe_\delta = \frac{C_w}{\theta^*} dRe_x$$

Using our initial condition of $\delta(0) = 0$, we can integrate straightforwardly to obtain

$$\int_0^{Re_\delta} Re_\delta^{1/m} dRe_\delta = \frac{C_w}{\theta^*} \int_0^{Re_x} dRe_x \quad \text{or} \quad Re_\delta = \frac{u_{av} \delta}{\nu} = \left(\frac{C_w m + 1}{\theta^* m} \right)^{\frac{m}{m+1}} Re_x^{\frac{m}{m+1}}$$

Solving for $\delta(x)$, rearranging, and simplifying, we have

$$\frac{\delta}{x} = \left(\frac{C_w m + 1}{\theta^* m} \right)^{\frac{m}{m+1}} \frac{1}{Re_x^{\frac{1}{m+1}}} \quad C_f = \frac{2C_w}{Re_\delta^{1/m}} = \frac{2}{Re_x^{\frac{1}{m+1}}} \left(\frac{m\theta^* C_w^m}{m+1} \right)^{\frac{1}{m+1}}$$

and

$$\frac{\delta^*}{x} = \eta^* \frac{\delta}{x} = \frac{1}{q+1} \left(\frac{C_w m + 1}{\theta^* m} \right)^{\frac{m}{m+1}} \frac{1}{Re_x^{\frac{1}{m+1}}} \quad \frac{\theta}{x} = \theta^* \frac{\delta}{x} = \frac{q}{(q+1)(q+2)} \left(\frac{C_w m + 1}{\theta^* m} \right)^{\frac{m}{m+1}} \frac{1}{Re_x^{\frac{1}{m+1}}}$$

These relations may be conveniently expressed as

$$\frac{\delta}{x} = \frac{a}{Re_x^{\frac{1}{m+1}}} \quad C_f = \frac{b}{Re_x^{\frac{1}{m+1}}} \quad \frac{\delta^*}{x} = \frac{c}{Re_x^{\frac{1}{m+1}}} \quad \text{and} \quad \frac{\theta}{x} = \frac{d}{Re_x^{\frac{1}{m+1}}}$$

where

$$a \equiv \left(\frac{C_w m + 1}{\theta^* m} \right)^{\frac{m}{m+1}} \quad b \equiv 2 \left(\frac{m \theta^* C_w^m}{m+1} \right)^{\frac{1}{m+1}} \quad c \equiv \frac{1}{q+1} \left(\frac{C_w m + 1}{\theta^* m} \right)^{\frac{m}{m+1}} \quad \text{and} \quad d \equiv \frac{q}{(q+1)(q+2)} \left(\frac{C_w m + 1}{\theta^* m} \right)^{\frac{m}{m+1}}$$

The validity of these expressions can be confirmed by taking Prandtl's $C_w = 0.0233$, $q = 7$, and $m = 4$ to reproduce, within the round-off error affecting [Eq. \(6-72\)](#), the following correlations:

$$\frac{\delta}{x} = \frac{0.381}{Re_x^{\frac{1}{5}}} \quad C_f = \frac{0.0593}{Re_x^{\frac{1}{5}}} \quad \frac{\delta^*}{x} = \frac{0.0477}{Re_x^{\frac{1}{5}}} \quad \text{and} \quad \frac{\theta}{x} = \frac{0.0371}{Re_x^{\frac{1}{5}}}$$

The same may be repeated for the wall-wake law. Using $C_w = 0.010$, $q = 7$, and $m = 6$, we may bypass intermediate calculations and recover

$$\frac{\delta}{x} = \frac{0.162}{Re_x^{\frac{1}{7}}} \quad C_f = \frac{0.0271}{Re_x^{\frac{1}{7}}} \quad \frac{\delta^*}{x} = \frac{0.0203}{Re_x^{\frac{1}{7}}} \quad \text{and} \quad \frac{\theta}{x} = \frac{0.0158}{Re_x^{\frac{1}{7}}}$$

which coincide with the expressions given by [Eq. \(6-70\)](#). Note that the transverse velocity can be obtained from the continuity equation, namely,

$$\frac{\bar{v}}{U_e} = -\frac{\partial}{\partial x} \int_0^y \frac{\bar{u}}{U_e} dy = -\frac{\partial}{\partial x} \int_0^y \left(\frac{y}{\delta} \right)^{1/q} dy \quad \text{and so} \quad \frac{\bar{v}}{U_e} = \frac{m}{(m+1)(q+1)} \frac{y}{x} \left(\frac{y}{\delta} \right)^{1/q} = \begin{cases} \frac{y}{10x} \left(\frac{y}{\delta} \right)^{1/7}; & \text{Prandtl's} \\ \frac{3}{28x} \left(\frac{y}{\delta} \right)^{1/7}; & \text{wall-wake law} \end{cases}$$

6-6.2 Flat-Plate Computation Using Inner Variables

A very interesting alternative approach was suggested by Kestin and Persen (1962). The idea is to assume that the streamwise velocity u in the boundary layer is correlated by inner variables:

$$\frac{\bar{u}(x, y)}{v^*(x)} = u^+ \approx f(y^+) \quad y^+ = \frac{y v^*(x)}{\nu} \quad (6-73)$$

The wall function $f(y^+)$ could be Spalding's formula [Eq. \(6-41\)](#)—it is not necessary to specify at this point. The wake component ($\Pi W / \kappa$) can be neglected, albeit not strictly necessary. Then the normal velocity may be retrieved through straightforward integration of the continuity equation:

$$\bar{v} = -\int_0^y \frac{\partial \bar{u}}{\partial x} dy = -\frac{\nu}{v^*} \int_0^{y^+} \frac{\partial}{\partial x} (v^* u^+) dy = -\frac{\nu}{v^*} \frac{\partial v^*}{\partial x} u^+ y^+ \quad (6-74)$$

Kestin and Persen (1962) substituted these velocity assumptions directly into the streamwise boundary-layer momentum equation, with $d U_e / dx = 0$:

$$\bar{u} \frac{\partial \bar{u}}{\partial x} + \bar{v} \frac{\partial \bar{u}}{\partial y} = \frac{1}{\rho} \frac{\partial \tau}{\partial y}$$

The result can be expressed entirely in terms of inner variables:

$$v^* \frac{\partial v^*}{\partial x} u^{+2} \approx \frac{v^*}{\mu} \frac{\partial \tau}{\partial y^+}$$

This relation can then be integrated across the entire boundary layer, from $y^+ = 0$ to $y^+ = \delta^+$, while noting that $\tau = 0$ at $y = \delta$. The result is

$$\tau_w = \rho v^{*2} = -\mu \frac{dv^*}{dx} G(\lambda) \quad \text{where} \quad G = \int_0^{\delta^+} u^{+2} dy^+ \quad (6-75)$$

and $\lambda = (2 / C_f)^{1/2}$, as in [Eq. \(6-71\)](#). This is a first-order differential equation for the distribution of wall-friction velocity $v^*(x)$ or, equivalently, $\tau_w(x)$. Before integrating, we replace v^* by the dimensionless variable $\lambda = U_e / v^*$. The result can be integrated once again to obtain:

$$\frac{U_e}{\nu} = G(\lambda) \frac{d\lambda}{dx} \quad \text{or} \quad Re_x = \frac{U_e x}{\nu} = \int_0^\lambda G(\zeta) d\zeta \quad (6-76)$$

Page 350

where we have assumed that the turbulent boundary layer begins at $x = 0$. Kestin and Persen evaluated the integral from Spalding's wall formula [Eq. \(6-41\)](#), with a somewhat algebraically involved but very accurate result:

$$\begin{cases} G(\lambda) = \int_0^\lambda u^{+2} dy^+ = \frac{1}{3} \lambda^3 + \frac{e^{-\kappa B}}{\kappa^2} \left[e^Z (Z^2 - 2Z + 2) - 2 - \frac{Z^3}{3} - \frac{Z^4}{4} \right] \\ Re_x = \int_0^\lambda G d\lambda = \frac{1}{12} \lambda^4 + \frac{e^{-\kappa B}}{\kappa^3} \left[e^Z (Z^2 - 4Z + 6) - 6 - 2Z - \frac{Z^4}{12} - \frac{Z^5}{20} \right] \end{cases} \quad (6-77)$$

where $Z = \kappa \lambda$. Since $\lambda = (2 / C_f)^{1/2}$, [Eq. \(6-77\)](#) encapsulates the desired flat-plate wall-friction law for turbulent flow. However, it is implicit in C_f and therefore awkward to evaluate. White (1969) noted that the function G , in its practical range $20 < \lambda < 40$, is well approximated by an exponential:

$$G(\lambda) \approx 8.0 e^{0.48 \lambda}$$

By introducing this approximation into [Eq. \(6-76\)](#), integrating, and rearranging, we obtain the desired explicit formula:

$$\text{Flat plate:} \quad C_f \approx \frac{0.455}{\ln^2(0.06 Re_x)} \quad [\text{White (1969)}] \quad (6-78)$$

This simpler expression falls within ± 1 percent of [Eq. \(6-77\)](#) and is recommended as a more

or less “exact” engineering relation for flat-plate turbulent skin friction, especially that its maximum error remains smaller than the error associated with the model itself.

[Figure 6-20](#) shows laminar and turbulent theories for $C_f(Re_x)$, with transition occurring around $Re_x \approx 5 \times 10^5$. We see that Prandtl’s traditional power-law expression (6-72) deteriorates very rapidly past $Re_x \approx 6 \times 10^6$. We also see that the newer power-law theory of [Eq. \(6-70\)](#) remains in favorable agreement with the “exact” solution—so why bother with the more complicated inner variable theory? The answer is that the latter can be readily extended to variable pressure gradients.

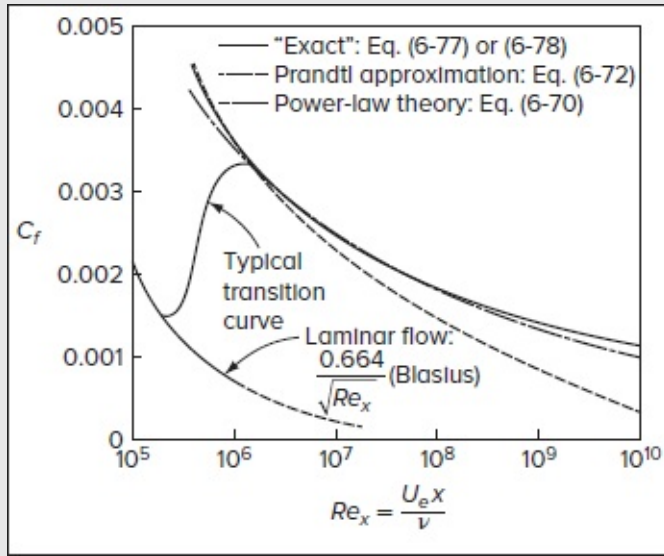


FIGURE 6-20

Local skin friction on a smooth flat plate for turbulent flow, showing several theories.

Other formulas for flat-plate skin friction that are of comparable accuracy abound in the literature [Chap. XXIa, Schlichting (1979)]. Note that the foregoing formulas assume turbulent flow beginning at $x = 0$. If there is a laminar-flow segment that is followed by transition, one should interpolate to estimate the “effective” turbulent point of origin.

6-6.3 Total Friction Drag of a Flat Plate

Let F be the total drag force per unit width on one side of a plate of length L and width b . As in laminar flow, F may be calculated by integrating the local wall shear stress:

$$F = \int_0^L \tau_w b dx \quad \text{or} \quad C_D = \frac{F}{\frac{1}{2} \rho U_e^2 L b} = \int_0^1 C_f d\left(\frac{x}{L}\right) \quad (6-79)$$

where C_D is called the *drag coefficient*. In this particular case of a thin plate at zero incidence, there is no *form drag* because all pressure forces remain normal to the freestream.

By introducing our power law, [Eq. \(6-70\)](#), into [Eq. \(6-79\)](#) and integrating, we find that C_D is one-sixth larger than the trailing-edge value of C_f :

$$C_{D,\text{plate}} \approx 0.031 Re_L^{-1/7} = \frac{7}{6} C_f(L) \quad (6-80)$$

This simple approximation remains valid over the whole Reynolds number range in turbulent smooth-wall flow.

Alternatively, the log-squared law given by [Eq. \(6-78\)](#) may be integrated, albeit vexing analytically. The result can be approximated as

$$C_{D,\text{plate}} \approx 1.15 C_f(L) \approx \frac{0.523}{\ln^2(0.06 Re_L)} \quad (6-81)$$

This relation is quite accurate and practically equivalent to [Eq. \(6-80\)](#). Here too, a plethora of comparable formulas may be found in the literature, but we will use [Eq. \(6-81\)](#) as our standard.

6-6.4 Turbulent Flow Past a Rough Plate

Suppose now that the plate has a uniform average roughness height k , and we wish to know the spatial wall-friction variation $C_f(Re_x, k/x)$. The inner variable approach works for this case also, if we assume that, say, the sand-grain correlation (6-62) holds locally in the boundary layer:

$$u^+ = \frac{\bar{u}(x, y)}{v^*(x)} \approx \frac{1}{\kappa} \ln(y^+) + B - \frac{1}{\kappa} \ln(1 + 0.3k^+)$$

Substitution in the streamwise boundary-layer momentum equation yields

$$v^* \frac{dv^*}{dx} \left[u^{+2} - \frac{0.3k^+}{\kappa(1 + 0.3k^+)} \left(u^+ - \frac{1}{\kappa} \right) \right] = \frac{v^*}{\mu} \frac{\partial \tau}{\partial y^+}$$

Following the same procedure as Sec. 6-6.3, this relation may be integrated twice, nondimensionalized, and rearranged as

$$Re_x \approx 1.73(1 + 0.3k^+) e^Z \left[Z^2 - 4Z + 6 - \frac{0.3k^+}{1 + 0.3k^+} (Z - 1) \right] \quad (6-82)$$

where

$$Z = \kappa \lambda \quad \lambda = \left(\frac{2}{C_f} \right)^{1/2} \quad \text{and} \quad k^+ = \frac{kv^*}{\nu} = \frac{Re_x(k/x)}{\lambda}$$

This result, although implicit in all three variables (Re_x , C_f , k/x), is valid for uniform sand-grain roughness over the complete range of hydraulically smooth, transitional, and fully rough walls in turbulent flat-plate flow. Some numerical values of C_f are plotted in [Fig. 6-21](#) for various (x/k) and Re_x . These values may not be accurate for other types of roughness elements such as spheres or rivets.

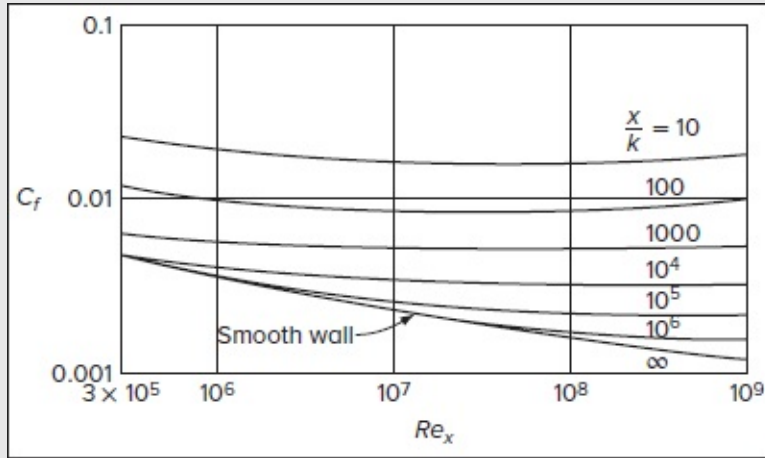


FIGURE 6-21

Local skin friction on a uniformly rough plate, from [Eq. \(6-82\)](#).

Page 352

As k^+ becomes large, the effect of the Reynolds number vanishes and the flow becomes fully rough. An approximation of [Eq. \(6-82\)](#) for this case is

$$\text{Fully rough:} \quad C_f \approx \left[1.4 + 3.7 \log_{10} \left(\frac{x}{k} \right) \right]^{-2} \quad \text{for} \quad \frac{x}{k} > \frac{Re_x}{1000} \quad (6-83)$$

This expression stands in good agreement with experiments on sand-roughened plates by Nikuradse (1933), for which Schlichting (1979, p. 654) recommends the following curve-fit relations:

$$\text{Fully rough:} \quad C_f \approx \left[2.87 + 1.58 \log_{10} \left(\frac{x}{k} \right) \right]^{-2.5} \quad (6-84a)$$

$$C_D \approx \left[1.89 + 1.62 \log_{10} \left(\frac{L}{k} \right) \right]^{-2.5} \quad (6-84b)$$

These correlations may not be accurate for other than sand-grain roughness types.

A general review of rough-wall effects is given by Raupach et al. (1991). Although the roughness log-law shift ΔB is employed in turbulence modeling, it is judiciously criticized by

Patel (1998), who points out that there is “uncertainty in the dependence of ΔB on the size and type of roughness and the effective location of the fictitious wall.” Schlichting and Gersten (2000, Chap. 17) classify a number of roughness element shapes. For uniform periodic roughness, such as ribs and grooves, CFD results by Grégoire et al. (2003) show that the fictitious wall ($y = 0$) is close to the crests of the elements. An alternative approach called the *discrete-element model*, Taylor et al. (1985, 1988), makes direct calculations of the form drag and blockage of individual elements. Finally, although the computational effort is large and the Reynolds numbers low, it is now possible to simulate rough-wall flows by either LES [Lee (2002)] or DNS tools [Miyake et al. (2001)].

6-6.5 Turbulent Flow with Continuous Wall Suction or Blowing

An effect as strong as roughness is that of nonzero normal velocity at the wall (also called crossflow, transverse, or radial, depending on the geometry and fluid dynamics community): $v_w < 0$ (suction) or $v_w > 0$ (blowing). Such a crossflow component adds a strong streamwise convective acceleration, $v_w \partial \bar{u} / \partial y$, to the near-wall boundary layer. If we assume zero pressure gradient (flat-plate) flow, the momentum equation in the direct vicinity of the wall becomes

$$\rho v_w \frac{\partial \bar{u}}{\partial y} \approx \frac{\partial \tau}{\partial y} \quad \text{or} \quad \tau \approx \tau_w + \rho v_w \bar{u} \quad (6-85)$$

We see that wall transpiration changes the shear distribution significantly. By matching [Eq. \(6-85\)](#) to an “eddy-viscosity” model of turbulent shear (see Sec. 6-7), Stevenson (1963) derived the following modification of the logarithmic-law of the wall with suction or blowing:

$$\frac{2}{v_w^+} \left[(1 + v_w^+ u^+)^{1/2} - 1 \right] \approx \frac{1}{\kappa} \ln(y^+) + B \quad (6-86)$$

where $v_w^+ = v_w / v^*$. We assign this derivation as a problem exercise. When $v_w = 0$, this expression reduces to the impermeable law of the wall given by [Eq. \(6-38a\)](#). The typical range of v_w^+ is ± 0.06 .

[Figure 6-22](#) shows some law of the wall profiles plotted from [Eq. \(6-86\)](#)—the sublayer is not shown. Recalling that $C_f = 2v^{*2} / U_e^2$, we see that a small amount of wall transpiration causes a large friction change. For example, if $\delta^+ = 1000$, the impermeable wall friction is $C_f \approx 0.0042$. For moderate blowing, $v_w^+ = +0.02$, $C_f \approx 0.0034$, or 19 percent lower; for equivalent suction, $v_w^+ \approx -0.02$, $C_f \approx 0.0053$, or 26 percent higher. So while suction increases the degree of friction at the wall, injection decreases it. In fact, the viscous layer at the wall can be entirely blown off to an unlocalized region in the case of large injection (also called *hard blowing*), as shown by Cole and Aroesty (1968).

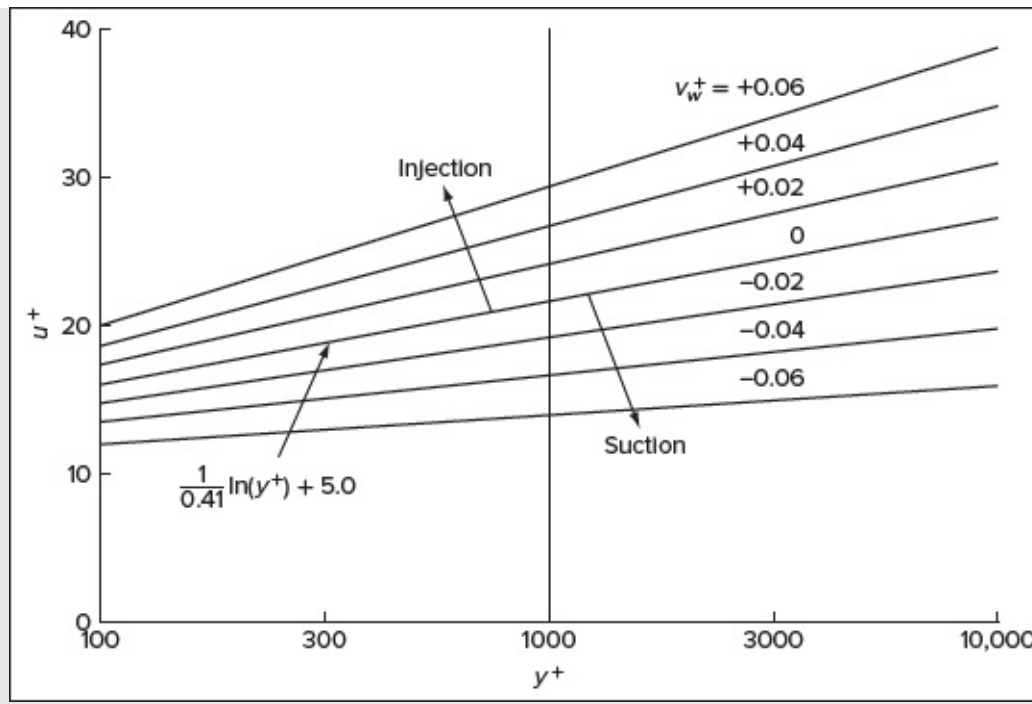


FIGURE 6-22

Illustration of the effect of suction and blowing on the law of the wall, using the correlation of Stevenson (1963), [Eq. \(6-86\)](#).

[Figure 6-22](#), though satisfying physically, does not depict an exact correlation. Schetz (1984, pp. 151–155) criticizes both Stevenson’s law [Eq. \(6-86\)](#) and a comparable law proposed by Simpson (1968) on the grounds that they do not collapse all available porous flat-plate data. One problem is that real porous walls are rough, at least slightly, so multiple effects can occur. However, Schetz’ own data suggest that even a very smooth porous wall will *increase* skin friction over the impermeable case. Thus, if one is trying to reduce friction (or heat transfer) by blowing, a certain amount of blowing is needed just to bring one back to the nonporous condition.

Suction and blowing have little effect on the outer defect law, so one can add, say, the Coles’ wake function [Eq. \(6-47\)](#) to [Eq. \(6-86\)](#) to simulate the full velocity profile of a transpired boundary layer.

Page 353

Overall, Stevenson’s algebraic formula (6-86) remains quite adequate for engineering estimates of turbulent wall suction and blowing (and for homework assignments). Further details of suction/blowing effects can be found in CFD studies. Turbulence modeling yields satisfactory results, as reported, for example, by Sofialidis and Primos (1996, 1997). Furthermore, DNS measurements that are limited to low-turbulence Reynolds numbers can assist in model improvement and flow visualization [Sumitani and Kasagi (1995) and Kim et al. (2002)].

6-7 TURBULENCE MODELING

Very quickly we run out of simple turbulent shear-flow cases for which we can use the wall-wake law [Eq. (6-47)], and a bit of algebra, to wrap up the whole problem. What are we to do for arbitrarily variable: (1) pressure gradients, (2) wall roughness, or (3) blowing and suction? What can we do if asked for more details than just the wall friction, for example: (1) the complete velocity profile, (2) the turbulent shear stress, or (3) the rms turbulent fluctuations? The answers lie in turbulence modeling.

Turbulence modeling has become a mature field and has spawned several monographs, notably by Wilcox (1998), Chen and Jaw (1997), Durbin and Pettersson (2001), Piquet et al. (2001), Launder and Sandham (2001), Gross and Burchard (2002), and Cebeci (2003). Many commercial CFD turbulence codes are now available and are being (slowly) merged with computer-aided design (CAD) systems [Thilmany (2003)]. The present chapter merely highlights modeling concepts and leaves CFD programs for advanced reading.

A hierarchy of turbulence models exists, ranging from the simplest algebraic correlations to full-blown unsteady Navier–Stokes treatment. Wilcox (1998) gives an excellent discussion. Here the term “*n*-Equation” model means that, in addition to the time-mean continuity and momentum relations, *n* time-mean partial differential equations have been added. The six different classifications, in order of increasing complexity, are as follows:

1. *Zero-equation* model: simply adds algebraic eddy-viscosity formulas to the system.
2. *One-equation* model: adds the time-mean equation of either (1) turbulence kinetic energy or (2) eddy viscosity to the system, plus some algebraic formulas to model its various terms. This idea has not been too successful but is still used today.
3. *Two-equation* model: adds turbulent kinetic energy and a second partial differential equation, usually involving time-mean turbulence dissipation, to the system, plus more algebraic modeling formulas.
4. *Second-moment closure* model: This is the most complex time-mean turbulence model. It skips the turbulent kinetic-energy equation, keeps the dissipation equation, and models the full Reynolds stress relation [Eq. (6-18)].

Page 354

5. *Large-eddy simulation* (LES): Carries out full unsteady Navier–Stokes calculations for motion scales of the order of the grid size or larger, then uses a turbulence model for the smaller sub-grid-scale motions. The system is computationally intensive and limited to moderate Reynolds numbers. See, for example, the review by Lesieur and Métais (1996) or the monographs by Sagaut and Germano (2002), Geurts (2003), or Volker (2003).
6. *Direct numerical simulation* (DNS): Attacks the full unsteady Navier–Stokes equations for all turbulence scales using no model at all. It is limited to low-turbulent Reynolds numbers. A very important use of DNS is to provide details for improving turbulence

models. See the review by Moin and Mahesh (1998) or the monographs by Baritaud (1996) or Geurts (2003).

6-7.1 Zero-Equation Models: The Eddy Viscosity

In two-dimensional turbulent-boundary-layer flow, the only additional unknown in the momentum equation is turbulent shear $(-\rho\overline{u'v'})$. The traditional modeling assumption, following J. Boussinesq in 1877, is to make this a gradient diffusion term, analogous to molecular shear:

$$\tau_t = -\rho\overline{u'v'} = \mu_t \frac{\partial \bar{u}}{\partial y} \quad \text{where} \quad \mu_t = \text{eddy viscosity} \quad (6-87)$$

The eddy viscosity μ_t has the same dimensions as μ , although it is *not* a fluid property; it varies with flow conditions and geometry. In like manner, we will define an eddy conductivity later for turbulent heat transfer.

The first thing to notice is that μ_t is positive, i.e., the shear correlation $(\overline{u'v'})$ is negative. To explain this, consider a position y in shear flow where $\partial \bar{u} / \partial y > 0$. An eddy coming down ($v' < 0$) to position y will generally bring with it a higher streamwise velocity ($u' > 0$). Similarly, a slower eddy moving up from below ($v' > 0$) will cause a decrement in velocity ($u' < 0$). Thus, the majority of eddy motions are associated with a negative correlation $(\overline{u'v'})$.

The second point is that gradient diffusion of eddies is only an approximation, albeit a reasonable one. In a typical boundary layer, $\bar{u}(y)$ increases monotonically to U_e , hence $\partial \bar{u} / \partial y > 0$ throughout and approaches zero in the freestream, where $\tau_t \rightarrow 0$ also. The whole profile supports a plausible (positive) correlation between τ_t and $(\partial \bar{u} / \partial y)$. There are some profiles, however, that exhibit a local maximum (or minimum), e.g., a wall jet (or an asymmetrical wake). The turbulent shear changes sign, and the measured values of τ_t are not necessarily zero where $(\partial \bar{u} / \partial y)$ vanishes. The trend is right, though, and the use of the eddy-viscosity concept should not cause any serious concern in such cases.

6-7.1.1 MIXING-LENGTH THEORY. A very popular approach is the *mixing-length* concept of Prandtl (1925), who, by analogy with kinetic theory, proposed that each turbulent fluctuation could be related to a length scale and a velocity gradient. He proposed

$$-\overline{u'v'} \approx (\text{const}) u'_{\text{rms}} v'_{\text{rms}} \approx (\text{const}) \left(l_1 \frac{\partial \bar{u}}{\partial y} \right) \left(l_2 \frac{\partial \bar{u}}{\partial y} \right)$$

where the scales l_1 and l_2 are called *mixing lengths*, which represent some mean eddy size much larger than the fluid's mean-free path. For convenience, one may replace $(\text{const}) (l_1 l_2)$ by a single scale ℓ^2 , where ℓ represents the characteristic distance over which a given turbulent eddy will travel while retaining its momentum, before dispersing. In other words, the mixing length scales with the distance over which a fluid eddy will retain its original

characteristics before dispersing them into the surrounding fluid. When Prandtl's expression is compared with [Eq. \(6-87\)](#), one deduces

$$\text{Mixing-length model:} \quad \mu_t \approx \rho \ell^2 \left| \frac{\partial \bar{u}}{\partial y} \right| \quad (6-88)$$

The model is complete if we can relate the mixing length ℓ to the flow conditions. The primary effect is the distance y from the wall. Prandtl and Kármán took turns with these estimates and arrived at the following:

$$\text{In the sublayer:} \quad \ell \approx y^2 \quad (6-89a)$$

$$\text{In the overlap layer:} \quad \ell \approx \kappa y \quad (6-89b)$$

$$\text{In the outer layer:} \quad \ell \approx \text{constant} \quad (6-89c)$$

Page 355

It is possible to merge all three conditions into one single magnificent composite function. However, most researchers merge only (a) and (b) and then transfer to (c) at some matching condition. The most popular composite for (a) and (b) is due to van Driest (1956a), who added a “damping factor” to condition (b) to take care of (a):

$$\ell_{a,b} \approx \kappa y \left[1 - \exp\left(-\frac{y^+}{A}\right) \right] \quad A \approx 26 \text{ for flat-plate flow} \quad (6-90)$$

where, as usual, $y^+ = yv^* / \nu$. The van Driest *damping factor* in brackets [] is derived from oscillating laminar flow near a wall, Eq. (3-111). The dimensionless damping constant A varies with flow conditions such as the pressure gradient, wall roughness, and blowing or suction. For a smooth, impermeable wall with zero pressure gradient, $A \approx 26$.

In the outer layer, condition (6-89c) is satisfied by relating the mixing length to the boundary-layer thickness. The most popular model is

$$\ell_{\text{outer layer}} \approx 0.09\delta \quad (6-91)$$

This same idea of a mixing length that is proportional to a layer thickness is used in the analysis of jets, wakes, and free-shear layers. The crossover point between [Eqs. \(6-90\)](#) and [\(6-91\)](#) occurs, where $\kappa y \approx 0.09\delta$, or $y_{\text{match}} \approx 0.22\delta$.

These models enable us to introduce

$$\tau = (\mu + \mu_t) \frac{\partial \bar{u}}{\partial y}$$

into the momentum Eq. (6-21b). With μ_t calculated from [Eqs. \(6-90\)](#) and [\(6-91\)](#), these models lead to an excellent prediction for the complete velocity profile in the linear sublayer, buffer layer, log layer, and wavelike outer layer.

6-7.1.2 MODELING WITHOUT THE MIXING LENGTH. It is possible to estimate the eddy viscosity directly without the mixing-length concept, in both inner and outer layers. For example, the inner layer model, which Spalding (1961) used to derive [Eq. \(6-41\)](#)—see [Fig. 6-11](#)—was

$$\mu_t \approx \mu \kappa e^{-\kappa B} \left(e^Z - 1 - Z - \frac{1}{2}Z^2 \right) \quad Z = \kappa u^+ = \kappa \bar{u} / v^* \quad (6-92)$$

Despite the absence of a mixing length or velocity gradient, the agreement with the data in [Fig. 6-11](#) is excellent.

Similarly, a popular outer layer formulation by Clauser (1956) is

$$\mu_{t, \text{outer}} \approx C \rho U_e \delta^* \quad C \approx 0.016 \quad (6-93)$$

or, equivalently, $\mu_t / \mu \approx 0.016 Re_\delta^*$. This type of model is also used in simulating jets, wakes, and free-shear layers.

One can mix and match also: Equations (6-90) and (6-93) are the basis of the widely used Cebeci–Smith model outlined in their text [Cebeci and Smith (1974)] and at the Stanford 1968 Conference [Kline et al. (1968, pp. 346–355)]. They modified the outer law to account for intermittency near the edge of the boundary layer (see [Fig. 6-5a](#)):

$$\mu_{t, \text{outer}} \approx \frac{0.016 \rho U_e \delta^*}{[1 + 5.5(y/\delta)^6]} \quad (6-94)$$

[Figure 6-23](#) illustrates these composite models, [Eqs. \(6-92\)](#) and [\(6-93\)](#) or [Eq. \(6-94\)](#), for three different local Reynolds numbers. We see that μ_t remains linear in the inner region—except for a nearly invisible region near the origin where damping reduces μ_t to a cubic function of y . Although [Eqs. \(6-88\)](#) and [\(6-92\)](#) have completely different formulations and parameters, both reduce in the inner layer to the linear relation

$$\mu_t \approx \kappa \rho v^* y \quad \text{or} \quad \frac{\mu_t}{\mu} \approx \kappa y^+ \quad (6-95)$$

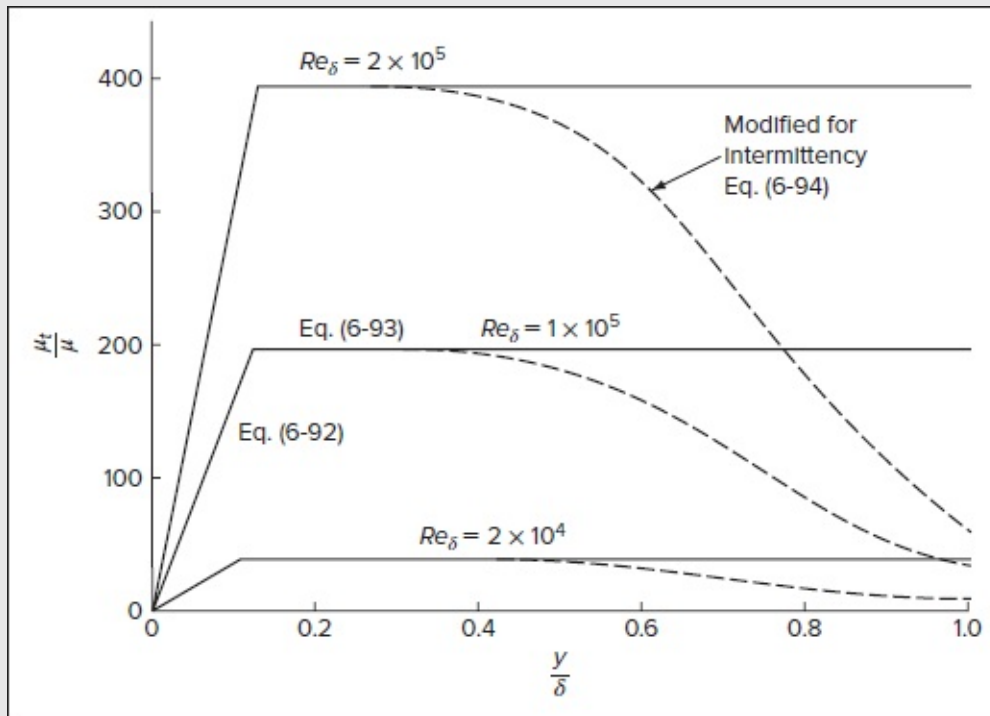


FIGURE 6-23

Eddy-viscosity distribution in a turbulent boundary layer computed from the inner law [Eq. \(6-92\)](#) and outer law (6-93). An expanded view near the origin ($y / \delta < 0.01$) would be needed to show the cubic damping effect.

except, as noted, in the sublayer region.

In the outer layer, [Fig. 6-23](#) shows that, depending on the local Reynolds number, μ_t is tens or even hundreds of times greater than the molecular viscosity. A turbulent shear layer basically has a high outer and low inner effective viscosity, which is why turbulent velocity profiles are so steep at the wall and so flat further out.

A display of μ_t by the mixing-length formulas [Eqs. \(6-90\)](#) and [\(6-91\)](#) would be similar, but not identical, to [Fig. 6-23](#). Either approach—or a mixture of the two—will lead to an adequate prediction of a turbulent-boundary-layer velocity profile.

6-7.1.3 APPLICATION TO FLAT-PLATE FLOW. When the pressure gradient is zero, the total shear stress becomes constant near the wall, and one can immediately compute the overlap layer from the definition of eddy viscosity and, say, the mixing-length model in [Eq. \(6-90\)](#):

$$\tau \approx \tau_w = (\mu + \mu_t) \frac{\partial \bar{u}}{\partial y} \approx \rho \kappa^2 y^2 \left| \frac{\partial \bar{u}}{\partial y} \right| \frac{\partial \bar{u}}{\partial y} = \rho v^{*2}$$

where we have neglected $\mu \ll \mu_t$. Taking the square root, separating and integrating this relation, we obtain

$$\frac{\bar{u}}{v^*} = \frac{1}{\kappa} \ln\left(\frac{yv^*}{\nu}\right) + B$$

The overlap law (6-38a) is hence reproduced faithfully by the mixing-length theory, which was probably Prandtl's goal in proposing the model. We have no "boundary condition" for the constant $B \approx 5.0$, so an experiment would be needed. If we further incorporate the molecular viscosity term and the van Driest damping term from [Eq. \(6-90\)](#), then we may integrate all the way from the wall, using the no-slip condition. After considerable algebra, we get

$$u^+ = \int_0^{y^+} \frac{2dy^+}{1 + \left\{ 1 + 4\kappa^2 y^{+2} [1 - \exp(-y^+/A)] \right\}^2}^{1/2} \quad (6-96)$$

If we choose the particular value of $A = 26$, the entire inner law—sublayer, buffer layer, and overlap—can be accurately reproduced with the correct log-law constant $B \approx 5.0$. If we choose the wrong A , we get the wrong B . If we add other effects, e.g., pressure gradient, to the analysis, we have to modify A as shown in the next section.

In like manner, if we choose, instead, Spalding's expression [Eq. \(6-92\)](#) for μ_t and keep the molecular viscosity term, integration will yield Spalding's law of the wall [Eq. (6-41)], which is also a complete expression for the inner law. Both approaches are very successful for impermeable flat-plate flow.

6-7.1.4 MODIFICATION FOR PARAMETRIC EFFECTS. The eddy-viscosity model has to be modified for pressure gradients or blowing or suction. Early efforts centered about changing only the damping constant A in [Eq. \(6-90\)](#). Later it was realized that the linear variation (κy) itself needed changing because the total shear stress was no longer constant near the wall. With a pressure gradient or nonzero wall velocity, the variation of shear stress near the wall is, to first order,

$$\tau \approx \tau_w + \frac{dp_e}{dx} y + \rho v_w \bar{u} + \dots \quad (6-97)$$

Page 357

The changes in slope near the wall are substantial. Thomas and Hasani (1989) extended [Eq. \(6-97\)](#) into an interpolation formula for $\tau(y)$, which is reasonably accurate across the entire boundary layer:

$$\frac{\tau}{\tau_w} \approx 1 + P \frac{y}{\delta} + \varphi \frac{\bar{u}}{U_e} - (3 + 2P + 3\varphi) \left(\frac{y}{\delta}\right)^2 + (2 + P + 2\varphi) \left(\frac{y}{\delta}\right)^3; P = \frac{\delta}{\tau_w} \frac{dp_e}{dx} \varphi = v_w^+ U_e^+ \quad (6-98)$$

This relation is plotted in [Fig. 6-24](#) for an impermeable wall ($\varphi = 0$) and three simple cases of: (1) flat plate, $P = 0$; (2) a moderate adverse pressure gradient, $P = +4$; and (3) a strong favorable gradient, $P = -3$. The purpose of the figure is to illustrate the strong effect of pressure gradients on the shear stress. To account for these effects, Galbraith et al. (1977) show convincingly that [Eq. \(6-90\)](#) should be modified by the square root of the shear:

$$\ell_{inner} \approx \kappa y \left(\frac{\tau}{\tau_w}\right)^{1/2} \left[1 - \exp\left(-\frac{y^+}{A}\right)\right] \quad (6-99)$$

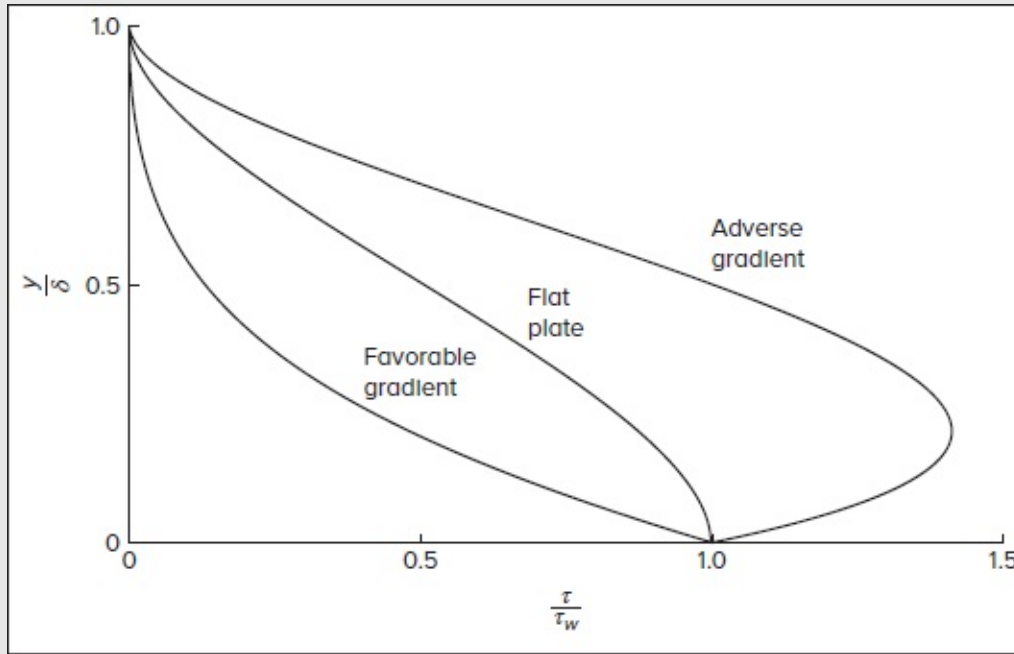


FIGURE 6-24

Illustration of the effect of a pressure gradient on the shear-stress distribution in a turbulent boundary layer. Plotted from [Eq. \(6-98\)](#) for an impermeable wall ($\varphi = 0$).

Such an adjustment causes the profile to start well for any pressure gradient. To merge into the log layer smoothly, however, one needs to modify A . Granville (1989) suggests that the smoothest merge (with the log-law intercept *and* its slope) can be accomplished by the following damping-constant variation:

$$A \approx \frac{26}{(1 + bp^+)^{1/2}} \quad p^+ = \frac{\nu}{\rho v_*'^3} \frac{dp_e}{dx} \quad (6-100)$$

where $b = 12.6$ if $p^+ > 0$ and $b = 14.76$ if $p^+ < 0$. Equations (6-99) and (6-100) are

recommended for general use in turbulent boundary layers with impermeable walls.

6-7.1.5 THE BALDWIN–LOMAX MODEL. When using the previous eddy-viscosity models, iteration is always required, even when marching downstream with, say, an explicit finite-difference procedure. The chief reason is that the inner law is correlated with wall shear stress τ_w or its equivalent, u^* , which is unknown. A second reason is that the outer law formulas also contain unknowns: δ for the mixing-length model [Eq. (6-91)] and δ^* for the Clauser model [Eq. (6-93)]. To avoid this second iteration, Baldwin and Lomax (1978) proposed an entirely different model for the outer law, eliminating δ or δ^* in favor of a certain maximum function in the boundary layer. In their notation,

$$\mu_{t,outer} \approx \frac{0.016 C_{cp} \rho y_{max} F_{max}}{1 + 5.5 (C_{kleb} y / y_{max})^6} \quad \text{with} \quad F_{max} = \max \left[y \left| \frac{\partial \bar{u}}{\partial y} \right| (1 - e^{-y/\Lambda}) \right] \quad (6-101)$$

and where y_{max} specifies the value of y corresponding to F_{max} . The parameters C_{cp} and C_{kleb} were suggested to be constants of the order of unity. This model has become especially popular in the aerospace literature. However, it results in discrepancies with other generally accepted outer layer relations, such as Coles' law of the wake.

Granville (1987) suggested that the “constants” should really be variables that can be retrofitted to known properties of Coles' wake law and equilibrium pressure gradients. His suggested correlations consist of

$$C_{kleb} \approx \frac{2}{3} - \frac{0.01312}{0.1724 + \beta^*} \quad \beta^* = \frac{y_{max}}{u^*} \frac{dU_e}{dx} \quad C_{cp} \approx \frac{3 - 4C_{kleb}}{2C_{kleb}(2 - 3C_{kleb} + C_{kleb}^3)} \quad (6-102)$$

It is believed that this modification will give the Baldwin–Lomax model accuracy comparable to the mixing-length and Clauser iterative models.

6-7.2 Higher Order Modeling

The eddy-viscosity approach adds *zero* equations and leads to a direct algebraic correlation for Reynolds stresses in the momentum equation. Although it can be pruned and tuned for various types of flows, it remains limited to only one type of output: the mean velocities \bar{u} and \bar{v} as well as the turbulent shear, $(-\overline{u'v'})$. It cannot compute the turbulent energy K or any of its fluctuating components $(u', v', w')_{rms}$. Additional partial differential equations are therefore needed. Modeling of the fluctuations began with Prandtl in 1945 and has taken many paths: kinetic energy, turbulent dissipation, turbulence length scale, vorticity fluctuations, dissipation time scale, pressure–strain correlations, and various stress relations. There are excellent monographs on turbulence modeling, such as Wilcox (1998), Piquet et al. (2001), and Cebeci (2003).

Turbulence modeling with CFD was in its infancy at the seminal 1968 Stanford Conference on Turbulent Boundary Layers [Kline et al. (1968)]. Now, nearly 40 years later,

hundreds of modeling papers and their applications are published each year. The most popular two-equation models are available in commercial CFD codes and are widely used. One can contrast the many CFD vendors by perusing any issue of the *Mechanical Engineering Magazine*. Eight different commercial codes are compared in an interesting paper by Freitas (1995).

6-7.2.1 ONE-EQUATION MODEL: TURBULENT KINETIC ENERGY. For convenience, let us repeat here the two-dimensional boundary-layer form of the turbulent kinetic-energy equation:

$$\bar{u} \frac{\partial K}{\partial x} + \bar{v} \frac{\partial K}{\partial y} \approx -\frac{\partial}{\partial y} \left[\overline{v' \left(\frac{1}{2} u_i' u_i' + \frac{p'}{\rho} \right)} \right] + \frac{\tau}{\rho} \frac{\partial \bar{u}}{\partial y} - \epsilon \quad (6-26)$$

where $K = (\overline{u_i' u_i'}) / 2$ denotes the kinetic energy and ϵ stands for the turbulent dissipation with units of power per unit mass or velocity³/length.

Let L be a turbulence length scale or effective eddy size. Such an eddy would have a velocity scale of $K^{1/2}$. Its dissipation should then scale, by dimensional reasoning, as

$$\epsilon \approx (\text{const}) \frac{K^{3/2}}{L} \quad (6-103)$$

It follows that if an eddy of size L travels at a speed $K^{1/2}$, the power it dissipates per unit mass must be proportional to

$$\frac{\text{drag} \times \text{velocity}}{\text{mass}} \approx \frac{[(\text{const}) \rho K L^2] K^{1/2}}{(\text{const}) \rho L^3} \approx (\text{const}) \frac{K^{3/2}}{L}$$

The second or “production” term on the right-hand side of [Eq. \(6-26\)](#) has already been modeled by eddy viscosity, $\tau = (\mu + \mu_t) \partial \bar{u} / \partial y$. The first or “convective diffusion” term on the right-hand side is vexing because it cannot be measured in a boundary layer. The reason is that, although small flush-mounted sensors do measure *wall* pressure fluctuations, there is presently no instrument which measures fine-scale fluctuations p' in the fluid body itself. By analogy with turbulent shear stress, it is reasonable to assume that this term is akin to gradient diffusion, i.e.,

$$-\overline{v' \left(\frac{1}{2} u_i' u_i' + \frac{p'}{\rho} \right)} \approx (\text{const}) \frac{\partial K}{\partial y}$$

Then our generic model for the turbulent kinetic-energy equation simplifies into

$$\bar{u} \frac{\partial K}{\partial x} + \bar{v} \frac{\partial K}{\partial y} \approx \frac{\partial}{\partial y} \left[(\text{const}) \frac{\partial K}{\partial y} \right] + \nu_t \left(\frac{\partial \bar{u}}{\partial y} \right) - (\text{const}) \frac{K^{3/2}}{L} \quad (6-104)$$

This relation is to be paired with the continuity and momentum Eqs. (6-21a) and (6-21b). However, closure is not obtained until the length scale L is suitably modeled. Three of the differential methods at the 1968 Stanford Conference [Kline et al. (1968)] used [Eq. \(6-104\)](#) with algebraic correlations for L . The results were satisfactory but, apparently, no better than the best zero-equation models, which merely used a conjectured relation for eddy viscosity. This fact, coupled with the extreme difficulty of extending a length-scale correlation to complex flows, led to the realization that a one-equation model could not be widely adopted.

6-7.2.2 TWO EQUATIONS: THE $K - \epsilon$ MODEL. The turbulent kinetic-energy [Eq. \(6-104\)](#) performs better if coupled with a second equation that models the rate of change of either (1) the dissipation ϵ or (2) the turbulent length scale L . Dissipation is very popular, perhaps, because of a seminal paper by Jones and Launder (1972), which opened up the field of turbulence modeling to users as opposed to specialists. These researchers modeled the complete dissipation equation [found in Tennekes and Lumley (1972)] in a manner similar to [Eq. \(6-104\)](#). The resulting two models are given for fully elliptical (nonboundary-layer) high Reynolds number flow as

$$\text{Energy:} \quad \frac{DK}{Dt} \approx \frac{\partial}{\partial x_j} \left(\frac{\nu_t}{\sigma_K} \frac{\partial K}{\partial x_j} \right) + \nu_t \frac{\partial \bar{u}_i}{\partial x_j} \left(\frac{\partial \bar{u}_i}{\partial x_j} + \frac{\partial \bar{u}_j}{\partial x_i} \right) - \epsilon \quad (6-105a)$$

$$\text{Dissipation:} \quad \frac{D\epsilon}{Dt} \approx \frac{\partial}{\partial x_j} \left(\frac{\nu_t}{\sigma_\epsilon} \frac{\partial \epsilon}{\partial x_j} \right) + C_1 \nu_t \frac{\epsilon}{K} \frac{\partial \bar{u}_i}{\partial x_j} \left(\frac{\partial \bar{u}_i}{\partial x_j} + \frac{\partial \bar{u}_j}{\partial x_i} \right) - C_2 \frac{\epsilon^2}{K} \quad (6-105b)$$

where σ_K and σ_ϵ are effective “Prandtl numbers” that relate eddy diffusion of K and ϵ to the momentum eddy viscosity: $\sigma_K = \nu_t / \nu_K$ and $\sigma_\epsilon = \nu_t / \nu_\epsilon$. The eddy viscosity itself is modeled using

$$\nu_t \approx \frac{C_\mu K^2}{\epsilon} \quad (6-106)$$

The five empirical constants that appear in these relations have the following recommended values for attached boundary-layer calculations:

$$C_\mu = 0.09 \quad C_1 = 1.44 \quad C_2 = 1.92 \quad \sigma_K = 1.0 \quad \sigma_\epsilon = 1.3 \quad (6-107)$$

These values are, unfortunately, *not universal* but have to be modified for other problems such as jets, wakes, and recirculating flows.

Equations (6-105) to (6-107), combined with continuity and momentum Eqs. (6-21a, b), form the complete $K - \epsilon$ model for analysis of two-dimensional turbulent shear flow. Except for flat-plate flow, to which the constants in [Eq. \(6-107\)](#) are tuned, accuracy is often only fair. For this reason, other researchers have proposed different, but related, two-equation models:

(1) The $K - \epsilon$ model using Renormalization Group methods by Yakhot and Smith (1992).

(2) The $K - \omega$ model by Prandtl (1945a) and Wilcox (1998).

(3) The $K-L$ model by Rotta (1986).

(4) The $K - \omega^2$ model by Wilcox and Rubesin (1980).

In the same spirit is a $K - \epsilon$ model with two additional equations, i.e., a *four-equation* model, namely:

(5) The $K - \epsilon - v'^2 - f$ model, sometimes simply called the $v'^2 - f$ model by Durbin (1995).

In this fifth model, v'^2 represents the fluctuating normal velocity, and f denotes its rate of production. Recall that L captures the turbulence length scale, and ω refers to the dissipation per unit turbulent kinetic energy, as modeled by the relation $\omega = \epsilon / (KC_\mu)$. Both L and ω require their own partial differential equations to join the equation for K [see detail in the text by Wilcox (1998)]. The five models above are generally more accurate than the standard $K - \epsilon$ model for adverse pressure gradients, low Reynolds numbers, and separated flows [Wilcox (1998)]. But the standard model is still widely used and is qualitatively satisfactory.

A stringent case for testing these models is reported by Iaccarino (2001) for flow through an asymmetrical two-dimensional diffuser with a flat upper wall and a lower wall expanding at a 10° angle. The Reynolds number, based on inlet channel height, is 20,000, for which experimental data are available from Obi et al. (1993). Iaccarino uses a grid of 124 streamwise and 65 transverse nodes, packed especially closely near the walls.

[Figure 6-25](#) shows the computed isovelocity contours for (1) the $v'^2 - f$ model and (2) the $K - \epsilon$ model with low Reynolds number corrections. The $v'^2 - f$ model predicts a long thin separation bubble in the corner (the dashed lines), which proves to be in excellent agreement with experiments. The $K - \epsilon$ model does not predict separation, but is otherwise qualitatively correct.

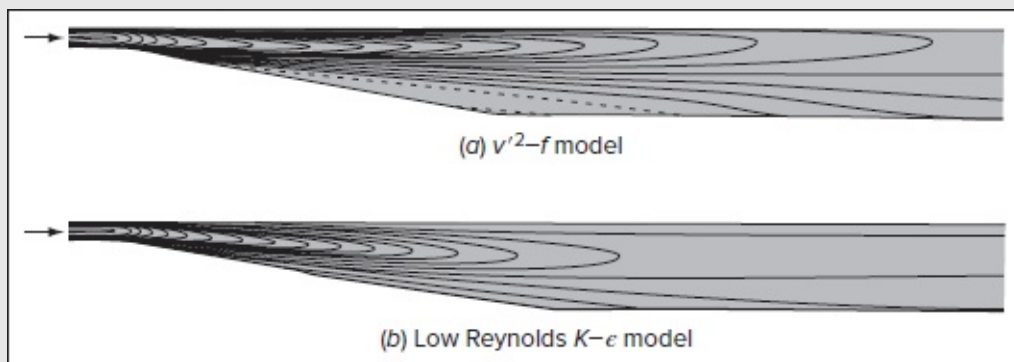


FIGURE 6-25

Turbulence modeling isovelocity contours of an asymmetrical diffuser with a 10°

lower wall expansion at $Re \approx 20,000$: (a) the $u'^2 - f$ model correctly predicts the experimental separation bubble (dashed lines); (b) the $K - \epsilon$ model fails to predict separation but is qualitatively reasonable. [From Iaccarino (2001), with permission of the author].

6-7.2.3 WALL FUNCTIONS AND LOW REYNOLDS NUMBER MODIFICATIONS. Most standard two-equation models are developed for “high Reynolds numbers.” Note that the $K - \epsilon$ model Eqs. (6-105a)–(6-105b) to (6-106) do not contain the molecular viscosity μ . The model is meant to be applied in the fully turbulent region away from any viscosity-dominated near-walls. Two options are possible for the near-wall regions: (1) use of *wall-function* inner law relations that patch into the first computational node in the overlap region or (2) add viscosity and damping terms to the model itself and use a fine mesh right up to the wall.

The wall-function formulas are essentially log-law relations tailored to the $K - \epsilon - \omega$ parameters. For example, if y_p denotes the grid point nearest to the wall, we could specify

$$\frac{\bar{u}_p}{v^*} = \frac{1}{\kappa} \ln\left(\frac{v^* y_p}{\nu}\right) + B \quad K_p = \frac{v^{*2}}{C_\mu^{1/2}} \quad \epsilon_p = \frac{v^{*3}}{\kappa y_p} \quad \omega_p = \frac{C_\mu^{3/4} K^{3/2}}{\kappa y_p} \quad (6-108)$$

This approach is generally satisfactory, certainly for qualitative calculations. Unfortunately, the results are numerically sensitive to the position of the match point y_p and are often inaccurate in separated-flow and corner-flow regions. The advantage, of course, is the gratifying increase in grid size. A substantial improvement is reported by Craft et al. (2002), who derive new analytical wall-function formulas for velocity, temperature, and dissipation rate. Their approach accounts for buoyancy, pressure gradient, and molecular transport property variations.

The second near-wall option is to add molecular viscosity and damping terms and then use a fine mesh that accounts for local dynamics. Jones and Launder (1973) add these terms directly to both the K and ϵ differential equations. The fine grid should reach into the viscous sublayer with points as close as $y^+ < 1$. Jones and Launder suggest the following modifications to (6-105a)–(6-105b):

$$\bar{u} \frac{\partial K}{\partial x} + \bar{v} \frac{\partial K}{\partial y} \approx \frac{\partial}{\partial y} \left[\left(\nu + \frac{\nu_t}{\sigma_K} \right) \frac{\partial K}{\partial y} \right] + \nu_t \left(\frac{\partial \bar{u}}{\partial y} \right)^2 - \epsilon \quad (6-109a)$$

$$\bar{u} \frac{\partial \epsilon}{\partial x} + \bar{v} \frac{\partial \epsilon}{\partial y} \approx \frac{\partial}{\partial y} \left[\left(\nu + \frac{\nu_t}{\sigma_\epsilon} \right) \frac{\partial \epsilon}{\partial y} \right] + C_1 \frac{\epsilon \nu_t}{K} \left(\frac{\partial \bar{u}}{\partial y} \right)^2 - C_2 \frac{\epsilon^2}{K} \quad (6-109b)$$

where we have added viscosity μ and the “constants” C_1 , C_2 , and C_μ can now vary near the wall. In addition to the Jones and Launder (1973) formulation, Wilcox (1998) discusses three other low Reynolds number models and compares them to data for 12 different boundary-

layer experiments from Coles and Hirst (1968). All four models have defects, whereas the $K - \omega$ model performs quite well for all 12 flows. The review by Patel et al. (1985) tests seven low Reynolds number models, along with the $K - \omega^2$ model of Wilcox and Rubesin (1980), and finds that all have inaccuracies, especially for favorable pressure gradients. Wilcox (1998) speculates that the inaccuracy occurs because the ϵ relation in Eq. (6-105b) is improperly formulated.

A variation on low Reynolds number modifications is the $v'^2 - f$ model of Durbin (1995) that uses no damping or wall functions. Rather, it uses the fact that the normal velocity v'^2 is a natural damper, as one approaches the wall. Modeled correctly, it reproduces the sublayer and inner layer quite well. The equation modeled by Durbin can be written as:

$$\bar{u} \frac{\partial v'^2}{\partial x} + \bar{v} \frac{\partial v'^2}{\partial y} \approx K f_{22} - \frac{\epsilon}{K} v'^2 + \frac{\partial}{\partial y} \left[\left(\nu + \frac{\nu_t}{\sigma_K} \right) \frac{\partial v'^2}{\partial y} \right] \quad (6-110)$$

Page 361

where the term f_{22} represents the *source*, or rate of production, of v'^2 and can be modeled by a relaxation-type differential equation. In addition to $(C_1, C_2, C_\mu, \sigma_K, \sigma_\epsilon)$ from the $K - \epsilon$ equations, Durbin introduces three more tuned constants to complete the model. Durbin's examples and those of Iaccarino (2001) lead to reasonably accurate models that hold great promise for separation bubbles, backstep flows, and even vortex shedding from bluff bodies.

6-7.2.4 REYNOLDS STRESS MODELS. The modeling of Reynolds stresses $(-\rho \overline{u'v'})$ is a level higher than the previous schemes and is usually called a *second-order closure*. The eddy viscosity and velocity gradient approaches are discarded, and the stresses computed directly by either (1) an algebraic stress model or (2) a differential equation for the rate of change of stress. The modeling itself is carried out at a higher level that is rather complex and computationally intensive.

This subject is reviewed by Rodi (1984), Launder et al. (1975), and Wilcox (1998). Following the discussion by Rodi [Kline et al. (1982, pp. 681–690)], one breaks the Reynolds stress equation into separate terms. Using the indicial summation notation, we have

$$\frac{\partial (\overline{u'_i u'_j})}{\partial t} + u_k \frac{\partial (\overline{u'_i u'_j})}{\partial x_k} = D_{ij} + P_{ij} + \pi_{ij} - \epsilon_{ij} + \nu \frac{\partial^2 \overline{u'_i u'_j}}{\partial x_k \partial x_k} \quad (6-111)$$

where

$$D_{ij} = -\frac{\partial}{\partial x_k} \left(\overline{u'_i u'_j u'_k} + \frac{\overline{p' u'_i}}{\rho} \delta_{jk} + \frac{\overline{p' u'_j}}{\rho} \delta_{ki} \right) \quad (\text{turbulent transport})$$

$$P_{ij} = -\overline{u'_i u'_k} \frac{\partial \bar{u}_j}{\partial x_k} - \overline{u'_j u'_k} \frac{\partial \bar{u}_i}{\partial x_k} \quad (\text{production})$$

$$\pi_{ij} = \frac{\overline{p'}}{\rho} \left(\frac{\partial u'_i}{\partial x'_j} + \frac{\partial u'_j}{\partial x'_i} \right) \quad (\text{pressure-strain})$$

$$\epsilon_{ij} = 2\nu \overline{\frac{\partial u'_i}{\partial x'_k} \frac{\partial u'_j}{\partial x'_k}} \quad (\text{dissipation})$$

This equation is to be used in concert with relations for K and ϵ (it does not replace them).

The production term P_{ij} is already in Reynolds stress form, but one must model the other three terms: dissipation, turbulent transport, and pressure–strain. We observe that all three are complex statistical correlations, difficult or even impossible (pressure–strain) to measure. Wilcox (1998) discusses these subtleties nicely, projecting a bright future for second-order closure.

Since dissipation is isotropic away from the wall and anisotropic near the wall, Hanjalic and Launder (1976) suggest the following model:

$$\epsilon_{ij} = \frac{2\epsilon}{3} \delta_{ij} + f_s \epsilon \left(-\frac{\overline{u'_i u'_j}}{2K} + \frac{1}{3} \delta_{ij} \right) \quad (6-112)$$

where the overall dissipation and turbulence intensity, ϵ and K , continue to be calculated from their particular differential relations, such as Eqs. (6-105a)–(6-105b). As for the coefficient f_s , it represents a damping function.

The turbulent transport term $D_{ij} = -\partial (\beta_{ijk}) / \partial x_k$ has been studied by DNS calculations, e.g., Moin and Mahesh (1998), which support a model by Hanjalic and Launder (1976). For convenience, we denote $S_{ij} \equiv -\overline{u'_i u'_j}$. Then their model for the three-term quantity β_{ijk} becomes

$$\beta_{ijk} = C_s \frac{K}{\epsilon} \left(S_{im} \frac{\partial S_{jk}}{\partial x_m} + S_{jm} \frac{\partial S_{ik}}{\partial x_m} + S_{km} \frac{\partial S_{ij}}{\partial x_m} \right) \quad (6-113)$$

with a constant $C_s \approx 0.11$. This model is used in the popular Launder–Reece–Rodi (LRR) (1975) and Speziale–Sarkar–Gatski (SSG) (1991a) approaches.

Finally, the pressure–strain term π_{ij} is still undergoing intensive evolution because it is (1) unmeasurable and (2) difficult to model. The SSG version, for example, contains 11 terms and seven empirical constants. The Wilcox and Rubesin (1980) model encompasses eight terms and five constants. A simpler model is due to Rodi (1984), specifically,

$$\pi_{ij} \approx -C_1 \frac{\epsilon}{K} \left(\overline{u'_i u'_j} - \frac{2}{3} K \delta_{ij} \right) - C_7 \left(P_{ij} - \frac{1}{3} P_{ii} \delta_{ij} \right) \quad (6-114)$$

These terms may be collected into the Reynolds stress relation (6-106) and solved simultaneously with the continuity, momentum, and rate equations for the dissipation ϵ . The eddy-viscosity model in [Eq. \(6-111\)](#) is also discarded, since turbulent shear may be computed directly. Modifications are necessary to use the model in the direct vicinity of the wall.

The constants suggested for use in this model are:

$$C_s \approx 0.25 \quad C_1 \approx 1.5 \quad C_\gamma \approx 0.6 \quad (6-115)$$

Note that Reynolds stress modelers often use $K - \epsilon$ models that are different from those presented here in Sec. 6-7.2.2 [see Rodi (1984) for more detail].

6-7.2.5 ALGEBRAIC STRESS MODELS. Although Reynolds stress closure models constitute an improvement, in principle, over one- and two-equation models, they involve three to six additional partial differential equations and are thus computationally intensive. Beginning with Hanjalic and Launder (1972), many researchers have proposed replacing the *differential* [Eq. \(6-111\)](#) with an algebraic stress model (ASM) that mimics the dissipation, turbulent transport, and pressure-strain effects captured by [Eq. \(6-111\)](#). For example, Rodi (1976) proposes the nonlinear relation:

$$\frac{\tau_{ij}}{\rho K} \left(\tau_{mn} \frac{\partial \bar{u}_m}{\partial x_n} - \rho \epsilon \right) \approx -\tau_{ik} \frac{\partial \bar{u}_j}{\partial x_k} - \tau_{jk} \frac{\partial \bar{u}_i}{\partial x_k} - \epsilon_{ij} - \pi_{ij} \quad (6-116)$$

to be supplemented by extremely complex three-dimensional correlations for the dissipation ϵ_{ij} and pressure-strain π_{ij} terms. The idea here is comparable to a nonlinear eddy-viscosity model. However, ASMs are not popular, especially for separating and reattaching flows.

It should be clear that the present Sec. 6-7 only offers a brief overview of the extensively broad research area of turbulence modeling. For a detailed discussion, see Wilcox (1998), Bernard and Wallace (2002), or Cebeci (2003).

6-8 ANALYSIS OF TURBULENT BOUNDARY LAYERS WITH A PRESSURE GRADIENT

Using the tools outlined earlier in this chapter, a variety of methods have been developed to analyze turbulent boundary layers under fairly arbitrary conditions. Among those, two basic groups can be identified along with their subcategories:

1. *Integral* methods, which are based on (1) the Kármán integral relation or (2) inner variables.
2. *Finite-difference* (differential) methods, which are based on (1) eddy viscosity, (2)

turbulence kinetic energy, (3) two equations, e.g., energy (K) and dissipation ϵ , or (4) Reynolds stress equations.

Integral methods, being averaged across the boundary layer, lead to ordinary differential equations that yield gross parameters such as skin friction and momentum thickness information. Differential methods yield those same parameters and also the complete profiles of velocity, turbulent shear, and whatever else is being modeled. However, integral methods are easy to program, unlike differential methods, which usually require the use or development of complex computer codes. Both types of methods can provide accurate predictions for a variety of problems.

Let us discuss these methods now for variable pressure gradients but limit ourselves to two-dimensional steady turbulent flow with smooth impermeable walls.

6-8.1 Methods Using the Kármán Integral Relation

Most integral methods in the literature rely on the famous momentum relation of Kármán (1921), which we repeat here for convenience:

$$\frac{d\theta}{dx} + (2 + H)\frac{\theta}{U_e} \frac{dU_e}{dx} = \frac{C_f}{2} \quad (6-28)$$

With $U_e(x)$ assumed known, there are three unknowns— θ , H , and C_f —hence at least two additional relations are necessary. One of these is a purely algebraic relation that arises because the wall–wake law [Eq. \(6-47\)](#) fits the profile data so well. Ludwig and Tillmann (1949) found the following classic correlation simply by relating measured values of (θ, H, C_f) in a variety of flows:

$$\text{Ludwig–Tillmann relation:} \quad C_f \approx 0.246 \left(\frac{U_e \theta}{\nu} \right)^{-0.268} 10^{-0.678H} \quad (6-117)$$

Page 363

When compared to data, the accuracy is ± 10 percent; Separation is not predicted; that is, C_f does not tend toward zero for finite H . Many similar correlations have since been proposed, as reviewed by Cousteix [Kline et al. (1982, p. 657)]. For example, Felsch et al. [Kline et al. (1968, p. 170)] propose

$$C_f \approx 0.058 Re_\theta^{-0.268} (0.93 - 1.95 \log_{10} H)^{1.705} \quad (6-118)$$

Accordingly, separation ($C_f = 0$) is predicted at $H = 3.0$, which is quite reasonable.

The validity of all such correlations rests upon the excellence of the Coles wall–wake law, whose integral parameters are provided in [Eqs. \(6-48\)](#). Let us rearrange those formulas as follows:

$$\lambda = a(\Pi) \frac{H}{H-1}$$

where

$$a(\Pi) = \frac{2 + 3.179(\Pi) + 1.5\Pi^2}{\kappa(1 + \Pi)} \quad (6-119a)$$

$$Re_\theta = \frac{1 + \Pi}{\kappa H} \exp(\kappa\lambda - \kappa B - 2\Pi) \quad (6-119b)$$

If we eliminate Π between these two formulas, we obtain a unique relation among $C_f = 2/\lambda^2$, H , and Re_θ . The results are plotted in [Fig. 6-26](#) and have been curve-fitted quite accurately (± 3 percent) by the following relation:

$$C_f \approx \frac{0.3e^{-1.33H}}{(\log_{10} Re_\theta)^{1.74+0.31H}} \quad (6-120)$$

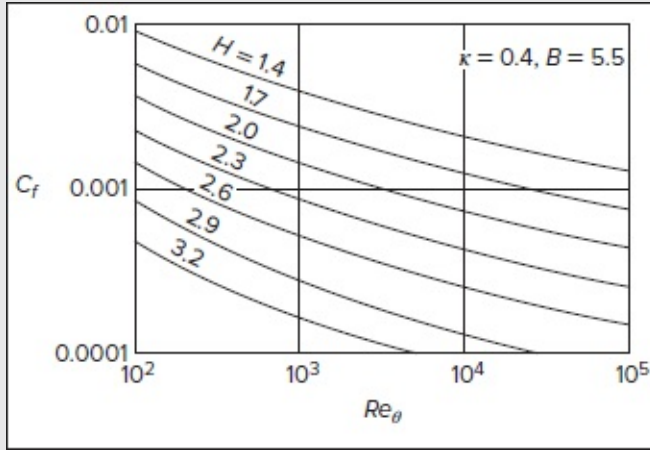


FIGURE 6-26

Computations from the law of the wake, [Eqs. \(6-119a\)–\(6-119b\)](#), for skin friction as a function of momentum thickness and shape factor.

This correlation stands among the most accurate to use in conjunction with Kármán-based methods.

6-8.1.1 SIMPLE KÁRMÁN-TYPE CLOSURE WITH A $\Pi - B$ CORRELATION. The approximate correlation between Coles' wake parameter Π and the Clauser parameter β , discussed earlier in Sec. 6-4.4, can be used to close the Kármán-type integral method. The first edition of this text proposed the simple formula $\Pi = 0.8 (\beta + 0.5)^{3/4}$, which fits a limited number of experimental equilibrium flows. Since then, Das (1987) has correlated hundreds of data points from the 1968 Stanford Conference [Coles and Hirst (1968)] into the following polynomial correlation:

$$\beta \approx -0.4 + 0.76\Pi + 0.42\Pi^2 \quad (6-121)$$

This formula is compared with equilibrium and nonequilibrium data in [Fig. 6.27](#). The considerable scatter of data does not invalidate the formula's quite serviceable use in an integral method. The large scatter for negative β (favorable gradients) is not due to experimental error; it results from subtracting numbers that are nearly equal when Π is very small.

Although [Eq. \(6-121\)](#) provides a “third relation,” it introduces new parameters, Π and β , that must be related to (C_f, H, Re_q) . The resolution is straightforward: Π is already related to C_f and H through [Eq. \(6-119a\)](#), and β can be easily determined from its defining expression:

$$\beta = \frac{\delta^*}{\tau_w} \frac{dp_e}{dx} = -\lambda^2 H \frac{\theta}{U_e} \frac{dU_e}{dx} \quad (6-122)$$

Page 364

To proceed, one solves [Eqs. \(6-28\)](#), [\(6-119a\)](#), [\(6-120\)](#), [\(6-121\)](#), and [\(6-122\)](#) simultaneously using, say, a Runge–Kutta method to integrate $d\theta / dx$. The initial conditions are known $C_f(0)$ and $\theta(0)$ at, say, $x = 0$. At each step ($x + \Delta x$), iteration is required to compute H , C_f , etc., among the four algebraic relations, after which one can step forward to the next position ($x + 2\Delta x$). Although this method has no pedigree, it makes quite adequate predictions for both favorable and adverse pressure gradients.

6-8.1.2 ENTRAINMENT INTEGRAL METHODS. Many workers believe that the “third relation” should not be an algebraic correlation but rather a second differential equation, namely, the entrainment relation discussed earlier:

$$E = \frac{1}{U_e} \frac{d}{dx} [U_e (\delta - \delta^*)] \quad (6-31)$$

To be useful, E needs to be correlated with other integral parameters. The original method of Head (1958) defines a new shape factor

$$H_1 = \frac{\delta - \delta^*}{\theta}$$

and writes [Eq. \(6-31\)](#) as a curve-fit correlation in terms of this factor:

$$\frac{d}{dx} (U_e \theta H_1) = U_e F(H_1) \quad F(H_1) \approx 0.0306 (H_1 - 3.0)^{-0.6169} \quad (6-123)$$

Head then showed that H_1 is related to the standard shape factor H , and his correlation is later curve-fitted to the following formulas:

$$H_1 \approx \begin{cases} 3.3 + 0.8234(H - 1.1)^{-1.287} & \text{for } H \leq 1.6 \\ 3.3 + 1.5501(H - 0.6778)^{-3.064} & \text{for } H \geq 1.6 \end{cases} \quad (6-124)$$

[Equations \(6-28\)](#), [\(6-120\)](#), [\(6-123\)](#), and [\(6-124\)](#) constitute a closed system to be solved for $(\theta,$

C_f , H , H_1) with a known freestream velocity $U_e(x)$. The agreement is favorable except for separating flows.

For strong adverse gradients and separating flows, Ferziger et al. (1982) suggest reformulating the entrainment in terms of the shape factor

$$\eta^* = \frac{\delta^*}{\delta}$$

Their entrainment correlation takes the form

$$\frac{d}{dx} \left[U_e H \theta \left(\frac{1}{\eta^*} - 1 \right) \right] = U_e f(\eta^*) \quad f(\eta^*) \approx 0.0083 (1 - \eta^*)^{-2.5} \quad (6-125)$$

Page 365

In addition, Ferziger et al. (1982) discount the Ludwig–Tillmann relation in favor of a skin-friction correlation that is directly related to η^* :

$$C_f \approx 0.1017 |1 - 2\eta^*|^{1.732} \left(\frac{\eta^*}{H Re_\theta} \right)^{0.268} \text{sgn}(1 - 2\eta^*) \quad (6-126)$$

Accordingly, separation ($C_f = 0$) occurs at a value of $\eta^* = \frac{1}{2}$. This expression can be used even *past* the separation point, where $C_f < 0$ and the wall flow is reversed. Finally, they relate η^* to C_f and H by manipulating the Coles' wall–wake law [Eq. (6-49)] into the following correlation:

$$\frac{H-1}{H} \approx 1.5\eta^* + 0.309 C_f^{1/2} + 0.955 \frac{C_f}{\eta^*} \quad (6-127)$$

[Equations \(6-28\)](#), [\(6-125\)](#), [\(6-126\)](#), and [\(6-127\)](#) may be solved simultaneously for (θ, C_f, H, η^*) : The agreement is satisfactory for adverse gradients but, unfortunately, unreliable for favorable gradients.

6-8.2 An Inner Variable Integral Method

The inner variable method that led to [Eq. \(6-76\)](#) for a flat plate can be extended to pressure gradient conditions by adding a wake component. The result is a first-order ordinary differential equation with known algebraic coefficients for the skin friction $C_f(x)$.

An early attempt by White (1969), using a wake that varied linearly with y , was reasonably effective—even for hand calculation. It has been supplanted, however, by a more accurate model by Das (1988), who uses Coles' wall–wake velocity profile in the form:

$$\frac{\bar{u}(x, y)}{v^*(x)} \approx \frac{1}{\kappa} \ln y^+ + B + \frac{2\Pi}{\kappa} (3\xi^2 - 2\xi^3) \quad (6-128)$$

where

$$v^* = \left(\frac{\tau_w}{\rho} \right)^{1/2} \quad \xi = \frac{y^+}{\delta^+} \quad \text{and} \quad y^+ = \frac{y v^*}{\nu}$$

The polynomial wake, suggested by Moses [Kline et al. (1968, p. 78)], replaces the sine-squared law of [Eq. \(6-46\)](#) to simplify the integration.

With \bar{u} known from [Eq. \(6-128\)](#), the normal velocity component follows from continuity [Eq. (6-21a)]. We get

$$\bar{v} \approx -\frac{\nu}{v^*} \int_0^{y^+} \frac{\partial \bar{u}}{\partial x} dy^+ \quad (6-129)$$

In a similar—but algebraically more complicated—fashion to Sec. 6-6.2, \bar{u} and \bar{v} can be substituted into the momentum Eq. (6-21b) and integrated across the boundary layer from ($y^+ = 0, \tau = \tau_w$) to the edge of the layer at ($y^+ = \delta^+, \tau = 0$). The result of this intermediate step is

$$A_1 \frac{dv^*}{dx} + A_2 \frac{d\Pi}{dx} + A_3 \frac{d\delta^+}{dx} \approx \delta^+ U_e \frac{dU_e}{dx} - \frac{v^* \tau_w}{\mu} \quad (6-130)$$

where coefficients $A_{1,2,3}$ are given by Das (1988). To eliminate $d\delta^+ / dx$ from [Eq. \(6-130\)](#), we use the differential form of the wall–wake friction law of [Eq. \(6-49\)](#) and rearrange terms such that:

$$\frac{d\delta^+}{dx} \approx \frac{\kappa \delta^+}{v^*} \frac{dU_e}{dx} - \frac{\delta^+}{v^*} (\ln \delta^+ + \kappa B + 2\Pi) \frac{dv^*}{dx} - 2\delta^+ \frac{d\Pi}{dx} \quad (6-131)$$

To further eliminate $d\Pi / dx$ from [Eq. \(6-130\)](#), we first recall the definition of the Clauser parameter,

$$\beta = \frac{\delta^*}{\tau_w} \frac{dp_e}{dx} = -\frac{\delta U_e}{v^{*2}} \frac{dU_e}{dx} \frac{\delta^*}{\delta} \quad \frac{\delta^*}{\delta} \approx \frac{(1 + \Pi)v^*}{\kappa U_e} \quad (6-132)$$

where the latter follows from [Eq. \(6-48\)](#). Finally, we relate β to Π , approximately, by the polynomial fit of [Eq. \(6-121\)](#), as shown in [Fig. 6-27](#). In this way, $d\Pi / dx$ is also eliminated from [Eq. \(6-130\)](#). The result is a (dimensional) differential equation containing only dv^* / dx . Finally, Das (1988) nondimensionalizes this relation by defining

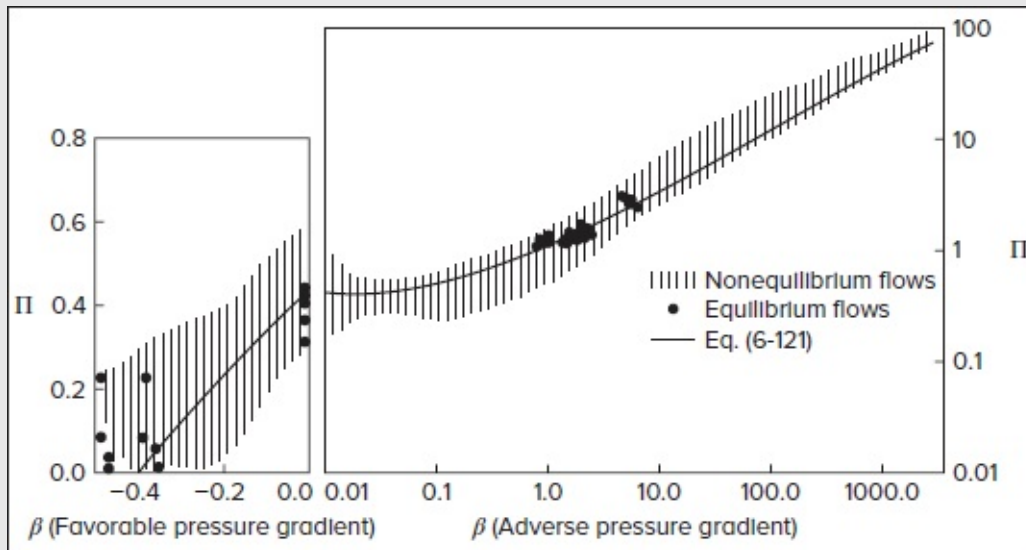


FIGURE 6-27

Correlation of the Coles' wake parameter with the Clauser parameter for equilibrium and nonequilibrium boundary layers. [After Das (1987).]

$$x^* = \frac{x}{L} \quad V = \frac{U_\epsilon}{U_0} \quad \text{and} \quad \zeta = \frac{v^*(x)}{U_\epsilon(x)} \quad (6-133)$$

where L and U_0 stand for any convenient reference length and velocity, respectively.

Page 366

The final differential equation has the form

$$\frac{d\zeta}{dx^*} = -\frac{\zeta}{V} \frac{dV}{dx^*} + \frac{1}{V} \frac{T_1 - T_2 + R_L T_3 (T_4 - R_L T_5)}{R_L T_3 (T_6 + T_7) + T_8 + T_9} \quad (6-134)$$

where $R_L = U_0 L / \nu$ and the dimensionless coefficients T_{1-9} are given in Table 6-2. A known initial value $\zeta(0)$ is necessary. Once $\zeta(x^*)$ is computed, the skin friction follows from the identity $C_f = 2\zeta^2$. If desired, one can calculate estimates of $\delta^*(x)$, $H(x)$, and $\theta(x)$ from the wall-wake law:

TABLE 6-2

The coefficient functions T_i for use in [Eq. \(6-134\)](#) [After Das (1988).]

$$T_1 = \delta^+ [F_1] \left[\frac{1}{V} \left(\frac{dV}{dx^*} \right)^2 \right]$$

where $F_1 = \zeta(6.25 \ln \delta^+ + 8.54 + 6.42\Pi^2) + \zeta\Pi(12.5 \ln \delta^+ + 18.97)$

$$T_2 = 2.5\delta^+ \zeta [F_1] \left(-\frac{d^2V}{dx^{*2}} \right)$$

$$T_3 = \frac{[F_2]\zeta^2}{(1 + \Pi)^2} - \frac{5\delta^+}{R_L V^2} \left(\frac{dV}{dx^*} \right)$$

where $F_2 = 1.16 + 0.84\Pi + 0.42\Pi^2$

$$T_4 = [\zeta(1.28\Pi^2) + \zeta\Pi(2.5 \ln \delta^+ + 2.58) + 1] \left(V \frac{dV}{dx^*} \right)$$

$$T_5 = \frac{\zeta^3 V^3}{\delta^+}$$

$$T_6 = [\zeta(6.25 \ln^2 \delta^+ + 8.75 \ln \delta^+ + 14.0) + \zeta\Pi^2(3.21 \ln \delta^+ + 7.06) + \zeta\Pi(6.25 \ln \delta^+ + 20.2 \ln \delta^+ + 21.48)]V$$

$$T_7 = [\zeta\Pi(12.5 \ln \delta^+ + 15.0 + 6.42\Pi^2) + \zeta(6.25 \ln \delta^+ + 1.25) + \zeta\Pi^2(12.5 \ln \delta^+ + 22.18)]V$$

$$T_8 = \delta^+(2.5 \ln \delta^+ + 5.5)[F_1] \left(\frac{1}{V} \frac{dV}{dx^*} \right)$$

$$T_9 = 5\delta^+(\Pi + 1)[F_1] \left(\frac{1}{V} \frac{dV}{dx^*} \right)$$

$$\frac{1}{\kappa} \ln \delta^+ + B + \frac{2\Pi}{\kappa} = \frac{1}{\zeta} \quad \beta = -\frac{\delta^+(1 + \Pi)}{\kappa \zeta^2 R_L} V \frac{dV}{dx^*} \quad (6-135)$$

This method requires a reasonably smooth function for the freestream velocity $V(x^*)$ and its first two derivatives in order to perform adequately.

A related, and slightly simpler, polynomial-shear integral method is proposed by Thomas and Kadry (1990). Also, the method of Das [Eq. (6-134)] is extended to wall transpiration by Oljaca and Sucec (1997). Their results, which are straightforward but lengthier than Table 6-2, stand in excellent agreement with blowing/suction experiments.

6-8.2.1 RELAXATION EFFECTS: LAG EQUATIONS. Most integral methods employ correlations developed from equilibrium turbulent flows such as the flat plate configuration. They perform well in nonequilibrium flows if the changes are gradual. When changes become rapid, the actual integral parameters will lag behind the equilibrium prediction. For example, [Fig. 6-28](#) shows a *relaxing* boundary layer, where a strong adverse pressure gradient is suddenly removed. The wall region reacts quickly, but the outer wake slowly relaxes toward equilibrium over a distance of five to ten boundary-layer thicknesses. A theory tied directly to the sudden change from large positive β to, say, $\beta = 0$ leads to premature predictions that do not actually occur until further downstream. To avoid premature changes, some workers use an exponential-type “lag equation” of the form

$$\frac{dQ}{dx} = \frac{C}{\delta} (Q_{eq} - Q) \quad (6-136)$$

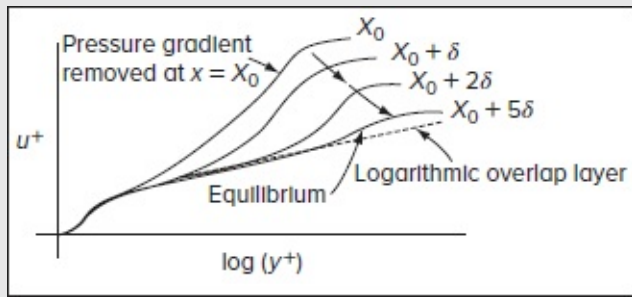


FIGURE 6-28

Schematic of the relaxation zone following a sudden removal of a pressure gradient.

where Q represents any integral property (H , Π , etc.), C denotes a dimensionless constant, and Q_{eq} captures the downstream asymptote. For example, in their entrainment method from Sec. 6-8.1.2, Ferziger et al. (1982)Page 367 suggest that [Eq. \(6-136\)](#) be used in certain rapidly changing pressure gradients, where Q is taken to be E and $C \approx 0.025$.

6-8.3 Finite-Difference Analysis of Boundary Layers

The integral methods discussed above lead to ordinary differential equations that are solved in the streamwise direction for parameters such as $C_f(x)$ and $\theta(x)$. Details of the flow field can be deduced only from algebraic approximations. In contrast, *differential* methods consider the full partial differential equations of motion and compute flow-field ingredients such as $\bar{u}(x, y)$, $\bar{v}(x, y)$, $K(x, y)$, $\epsilon(x, y)$, etc. In principle, they tend to be more accurate than integral methods. In practice, being based on modeling assumptions rather than pure physics, they often show deviations from experimental data.

All of the aforementioned methods require a digital computer and a two-dimensional (or three-dimensional) nodal mesh. Such a mesh must be finer near the wall, where changes in turbulent flow occur very rapidly. In modeling swirling flows, it is necessary to refine the mesh both at the wall and around the axis of rotation. Although the finite-element method [Löhner (2001)] is applicable to this problem, such as the method of Hytopoulos et al. (1993), most schemes presently use either finite differences or the finite-volume method popularized by Patankar (1980). A variety of boundary-layer computation schemes are discussed in the texts by Schetz (1992), Cebeci and Cousteix (1998), and Schlichting and Gersten (2000). Furthermore, the boundary-layer Applet codes of Devenport and Schetz (2002) are available for direct use over the Internet.

6-8.3.1 ZERO-EQUATION MODELS. These methods use the eddy-viscosity concept to solve the continuity and momentum Eqs. (6-21a) and (6-21b) with no additional

differential equations. In a method discussed in detail in their text, Cebeci and Smith (1974) use the van Driest inner layer model of [Eq. \(6-90\)](#) and the Clauser outer layer model of [Eq. \(6-93\)](#) to capture the eddy viscosity. In this context, the damping constant A in [Eq. \(6-90\)](#) is adjusted for the pressure gradient in a manner similar to [Eq. \(6-100\)](#). Moreover, Cebeci and Smith use a Blasius-type coordinate across the boundary layer, namely,

$$d\eta = \left(\frac{U_\epsilon}{\nu x} \right)^{1/2} dy$$

which makes the same method very convenient for laminar boundary layers. For turbulent motion, they use a mesh size $\Delta\eta$ that is very fine near the wall, becoming coarser in the outer layer. Their computer code has been tested for a variety of parametric conditions—rough walls, suction and blowing, low Reynolds numbers, free convection—and has been popular since its inception.

6-8.3.2 TWO-EQUATION MODELS. The $K - \epsilon$ method of Sec. 6-7.2.2 is the best known two-equation model, although numerous other formulations have been advanced. Jones and Launder (1972) used the Patankar–Spalding stream function variable with 100 cross-stream steps $\Delta\omega$ and a streamwise step of $\Delta x \approx 0.3\delta$, with satisfactory results for boundary layers. It is less accurate for recirculating flows, i.e., flows with separated (backflow) regions.

Wilcox (1998) has shown, by comparison to numerous data sets, that the $K - \omega$ model is superior to the $K - \epsilon$ model for boundary layers, especially with adverse pressure gradients. Two-equation models can be extended to separated, wall blowing/suction, and high-speed compressible flows.

Page 368

6-8.3.3 REYNOLDS STRESS MODELS. The best of these RSM models are superior for complex flows, such as separation and reattachment, and they even surpass the $K - \omega$ model in the treatment of attached boundary layers. The RSM can easily account for gravity and wall curvature and extend rather seamlessly to three-dimensional flows, albeit with much computational effort. Since LES and DNS tools are limited to low Reynolds numbers, RSM will probably remain a dominant CFD approach, as speculated by Speziale (1991b), Hanjalic (1994), and Wilcox (1998).

6-8.4 Turbulent Flow Past a Flat Plate

A simple but important test of any model is the flat-plate flow measured by Wieghardt and Tillmann (1951). In this problem, air with $\nu \approx 1.51 \times 10^{-5} \text{ m}^2/\text{s}$ flows at $U_\epsilon \approx 33 \text{ m/s}$ past a 5 m long waxed plywood plate. The flow is tripped at the leading edge so that the first measurement station, $x = 0.087 \text{ m}$, is barely turbulent ($Re_x \approx 1.9 \times 10^5$, $Re_\theta \approx 460$) and very thin ($\delta \approx 4 \text{ mm}$); so only five velocity profile data points are taken. In fact, for all stations

with $x < 0.8$ m, there is considerable uncertainty in both the velocity profiles and the skin-friction coefficient. In spite of this defect, the experiment constitutes an excellent preliminary test for any predictive tool.

[Figure 6-29](#) provides a side-by-side comparison of skin friction and momentum thickness data using four different methods described earlier: Head (1958) and Ferziger et al. (1982) from Sec. 6-8.1.2, Das (1988) from Sec. 6-8.2, and Cebeci and Smith (1974) from Sec. 6-8.3.1. To avoid some of the data uncertainty, the prediction is initiated at the fourth station, $x = 0.387$ m. All four methods are found to be fairly accurate except that Head (1958) predicts low values of C_f , the problem being that the given (uncertain) initial values of C_f , H , and θ are incompatible with the algebraic correlations of [Eq. \(6-117\)](#) or (6-120). For example, when compared with [Eq. \(6-78\)](#), the experimental value $C_f(0) = 0.00364$ proves to be compatible with an effective origin $x(0) = -0.15$ m. When compared with [Eq. \(6-70\)](#), the experimental value $\theta(0) = 0.092$ cm proves to be compatible with a different origin, $x(0) = -0.09$ m.

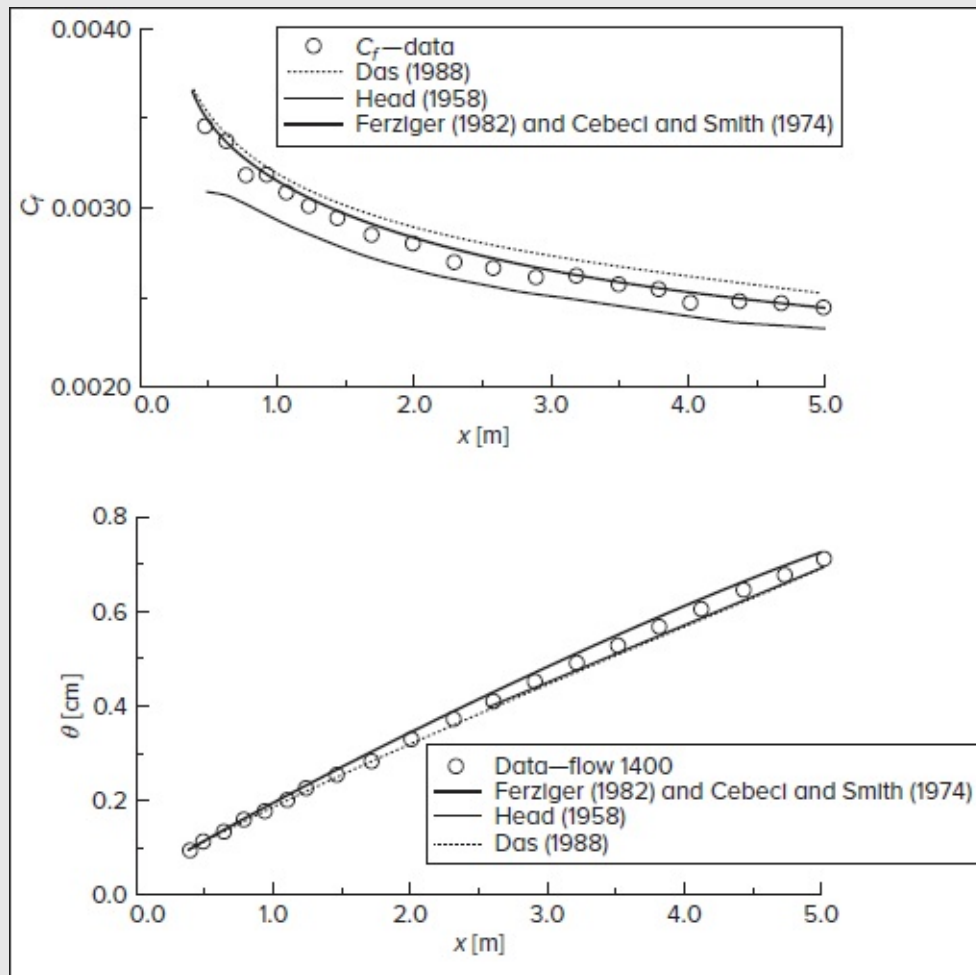


FIGURE 6-29

Comparison of four boundary-layer prediction methods with the flat-plate data of Wieghardt [flow 1400 of Coles and Hirst (1968)].

To avoid clutter in [Fig. 6-29](#), we omit the Kármán-based method of Sec. 6-8.1.1 [results similar to Das (1988)] or the $K - \omega$ and Reynolds stress models [Kline et al. (1982, pp. 1249–1250)], all of which show favorable agreement. The differential models, being field methods, can also predict the velocity profiles $\bar{u}(x, y)$ with adequate precision. This test shows that all of the previously mentioned integral and differential methods are reasonably accurate and well behaved for flat-plate flow.

6-8.4.1 VISUALIZATION AND SIMULATION OF FLAT-PLATE FLOW.

The results shown in [Fig. 6-29](#) are typical of “boundary-layer analyses” that predict time-mean properties such as $C_f(x)$, $\theta(x)$ and, in the case of the differential methods, $\bar{u}(x, y)$, $K(x, y)$ or $\overline{u'v'}(x, y)$. The time-varying fluctuations themselves—or the unsteady flow field—are *not* computed. But the instantaneous turbulent flow field can be photographed and now, with the advent of supercomputers, simulated numerically.

For example, hydrogen bubble visualizations of water flow past a flat plate have been reported by Hirata and colleagues at the University of Tokyo [see also Nakayama (1988, p. 27)]. [Figure 6-30a](#) shows the mean velocity profile at five dissimilar locations corresponding to Hirata’s experiment. The latter captures the sublayer and shows a characteristic spanwise variation of fast and slow “streaks” of streamwise vorticity. In the buffer layer, the flow mixes better and the streaks become less pronounced. In the log layer, mixing is thorough and the streaks disappear. In the outer (wake) layer, the scale of the eddies becomes much larger and the flow is slightly intermittent. Unfortunately, these experimental observations are lost when the time-mean is taken in [Fig. 6-30a](#).

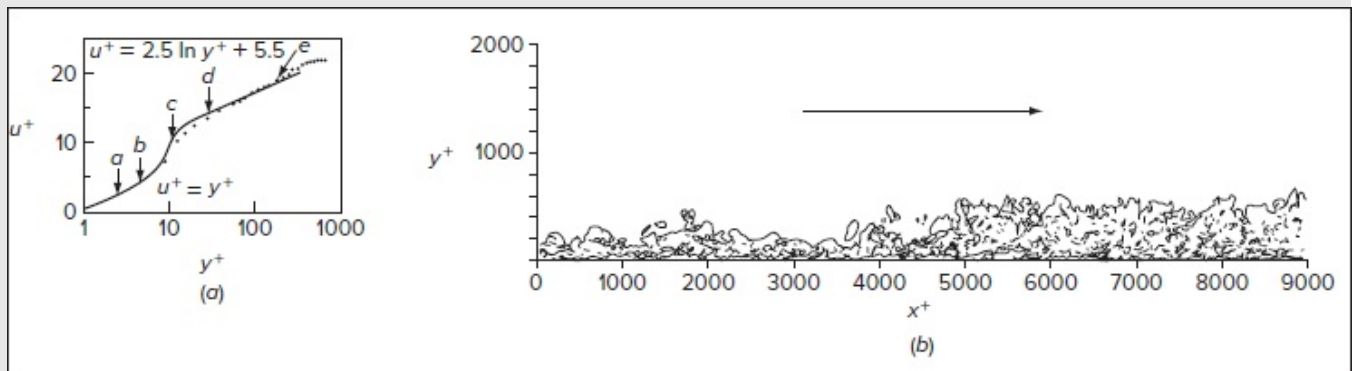


FIGURE 6-30

Flat-plate flow results showing: (a) velocity profile based on 5 dissimilar locations; (b) supercomputer simulation of vorticity contours at $Re_\theta = 1410$. [From Spalart (1988).]

Along similar lines, Spalart (1988) solves the three-dimensional time-dependent Navier–Stokes equations with a spectral method for flat plate flow at $Re_\theta = 225, 300, 670$, and 1410. This well-known DNS study uses the NASA-Ames Laboratory supercomputer with 10 million mesh points. [Figure 6-30b](#) shows the computed instantaneous vorticity contours at the highest Reynolds number. When those 10 million point-values are correlated over time and space, Spalart is able to verify the following results:

1. Friction coefficients and shape factors accurate to ± 5 percent.
2. Velocity profiles that verify the inner law, the log-law with $\kappa \approx 0.41$ and $B \approx 5.0$, and an outer wake with Π slightly lower than Coles' (1956).
3. Accurate estimates of Reynolds stress and rms fluctuations of both velocity and pressure.
4. Reasonably accurate frequency spectra of both velocity and pressure whose trends agree with statistical theories [Hinze (1975)].

Although the computed Reynolds numbers are small, of low turbulence, the value of such simulations in providing a wealth of space–time information about turbulent flows is striking and bringing engineering analysis of turbulent flow to a new level.

6-8.5 Equilibrium Flow with an Adverse Pressure Gradient

A more difficult case than flat-plate flow is flow 2200 of Coles and Hirst (1968), from the experiments of Clauser (1954), who was first to demonstrate the properties of equilibrium turbulent boundary layers. The flow was meant to have constant $\beta \approx 1.8$ [Eq. (6-42)], but in fact the measured β increased from about 1.4 to 2.3 over a 25 ft distance. The flow was a thick boundary layer in a narrow wind tunnel and almost certainly contained three-dimensional effects.

[Figure 6-31a](#) shows the measured freestream velocity which, as expected for equilibrium flows, fits a power-law distribution quite well. [Figure 6-31b](#) compares the measured skin-friction coefficients with the same four theories used in [Fig. 6-29](#) along with the Kármán-based method of Sec. 6-8.1.1. The Kármán-based and Das predictions yield the best agreement, as might be expected, since both use an equilibrium correlation [Eq. (6-121)]. The other methods consistently predict friction far too low.

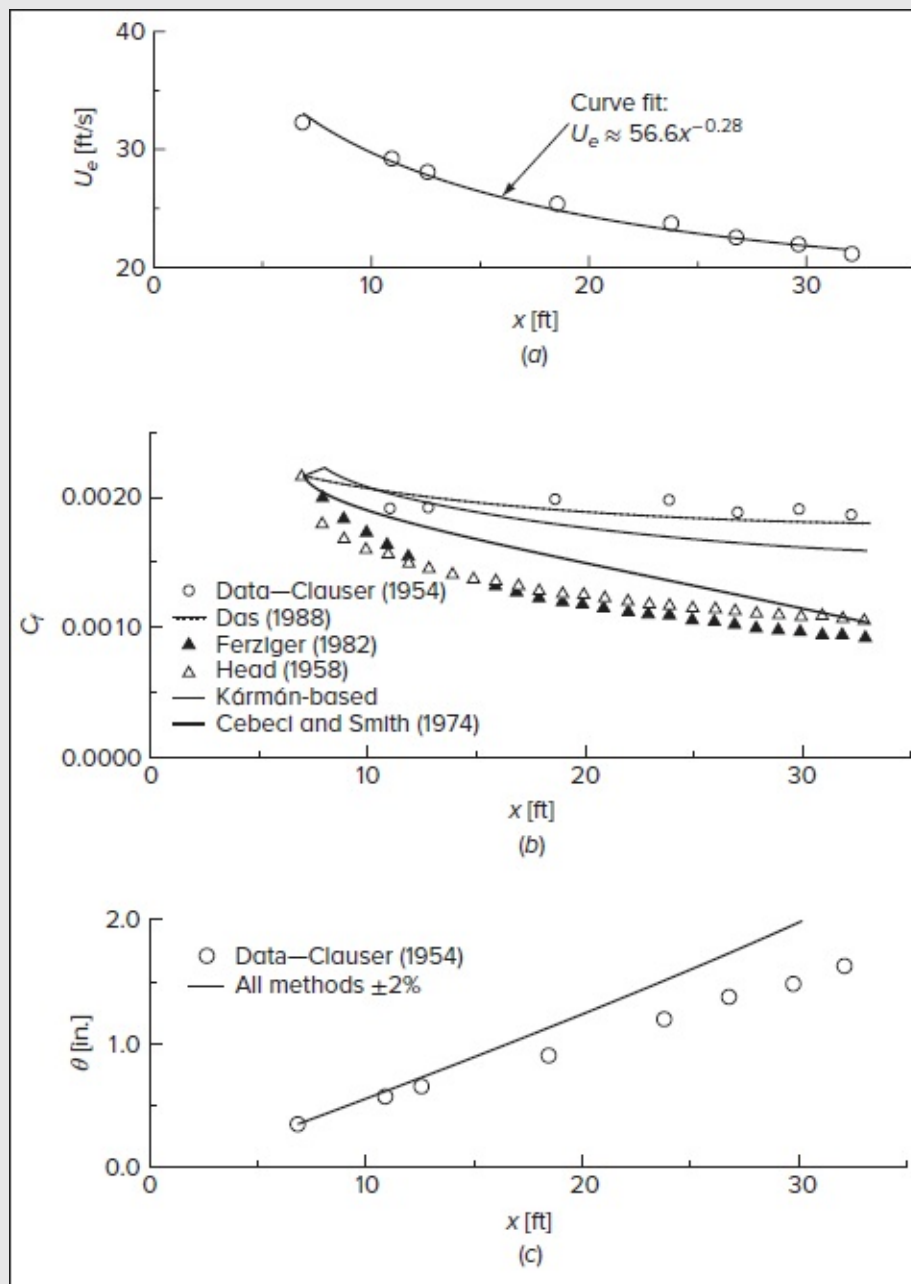


FIGURE 6-31

Comparison of theory and experiment for the equilibrium flow of Clauser (1954), flow 2200 of Coles and Hirst (1968).

[Figure 6-31c](#) compares the computed and measured momentum thickness variations. All five methods lead to similar overpredictions—perhaps another indication of unknown effects in the data. However, an excellent prediction of $\theta(x)$ for flow 2200 resulted from a one-equation turbulent kinetic-energy method by Bradshaw and Ferriss [Kline et al. (1968, pp. 264–274)].

6-8.6 Nonequilibrium Separating Flow: The Newman Airfoil

Newman (1951) carried out a wind tunnel study of flow at 120 ft/s past an airfoil section. The measurements on the upper (suction) surface proceed along an adverse pressure gradient toward separation at $x \approx 5$ ft. [Figure 6-32a](#) shows the measured freestream velocity, which fits a least-squares cubic polynomial quite well. Approximately one-third of the methods used in Kline et al. (1968) rendered reasonably accurate predictions for this nonequilibrium flow.

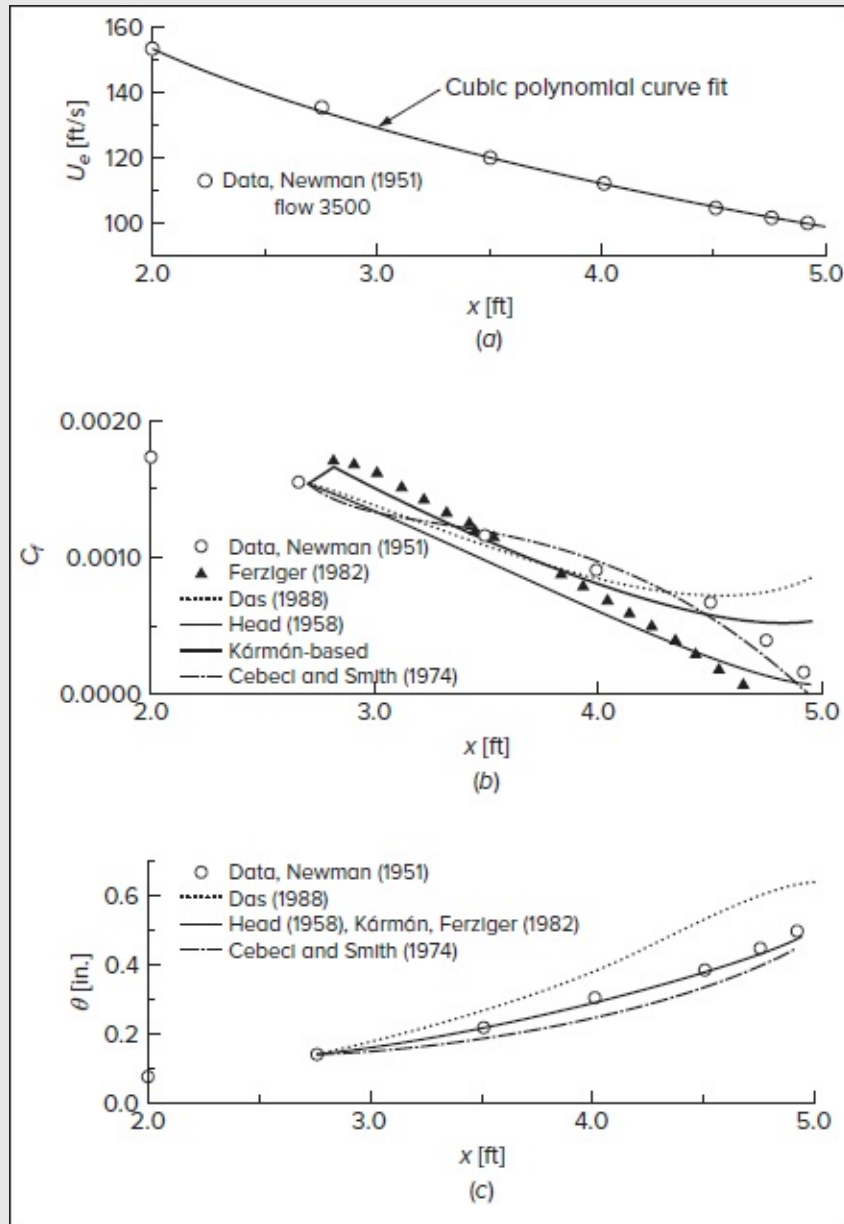


FIGURE 6-32

Comparison of theory and experiment for the separating airfoil flow of Newman (1951), flow 3500 of Coles and Hirst (1968).

[Figure 6-32b](#) shows the skin-friction data compared to our five methods. The Das and Kármán-based equilibrium-oriented methods lead to (unrealistic) relaxation of C_f before separation. Ferziger et al. (1982) predict separation too early. Head (1958) appears to be reasonable but too low. Only the Cebeci and Smith (1974) predictions stand in very good agreement.

[Figure 6-32c](#) shows the prediction and data for momentum thickness. Although Das' projection is too high, the other four methods give reasonable agreement. In fact, the typical trend of being more accurate at predicting $\theta(x)$ than $C_f(x)$ seems to be a general characteristic of the methods under consideration. We conclude that, although the techniques presented here seem “adequate” for engineering use in turbulent boundary-layer prediction, no single method can be reliably adopted to provide consistent agreement with all available data.

6-8.6.1 SEPARATING FLOWS: INVERSE TECHNIQUES. Near separation, $C_f \rightarrow 0$, β and Π approach infinity, and most boundary-layer methods become inaccurate—primarily because of heightened sensitivity to the freestream velocity $U_e(x)$. After separation, τ_w and v^* turn negative, the displacement thickness becomes very large, and the boundary-layer approximations become inaccurate; normal velocity and streamwise gradients become much larger. Under these conditions, the most fundamental approach is to solve, with finite differences, the full equations of motion in thePage 372 whole flow field—freestream and wall regions—a computer-intensive procedure. Yet boundary-layer theory can still be used effectively in an “inverse” mode.

The appropriate interaction near separation is to assume that the displacement thickness distribution $\delta^*(x)$ is known and the freestream velocity $U_e(x)$ is unknown—hence the term *inverse* method. With this modification, satisfactory agreement with measured separating flows can be obtained by both finite-difference methods [Pletcher (1978)] and integral methods [Moses et al. (1979) and Strawn and Kline (1983)].

Das (1987) modifies the “direct” inner variable method of Sec. 6-8.2 into an inverse technique most elegantly. First the wall–wake law [Eq. \(6-128\)](#) is written in terms of a wake velocity $v_\beta = \Pi v^*$:

$$\bar{u} = \frac{v^*}{\kappa} \ln\left(\frac{yv^*}{\nu}\right) + Bv^* + \frac{v_\beta}{\kappa}(6\xi^2 - 4\xi^3) \quad \xi \equiv \frac{y}{\delta} \quad (6-137)$$

The advantage is that v_β remains finite and positive throughout separation, whereas v^* changes sign and Π becomes singular. The new form of the momentum-integral relation in [Eq. \(6-130\)](#) becomes

$$A_{11} \frac{dv^*}{dx} + A_{12} \frac{dv_\beta}{dx} + A_{13} \frac{d\delta^+}{dx} + A_{14} \frac{dU_e}{dx} = A_{15} \quad (6-138)$$

where A_{ij} are given by Das (1987). The derivative form of the wall–wake law in [Eq. \(6-131\)](#)

also takes the form of [Eq. \(6-138\)](#),

$$\left(\frac{1}{\kappa} \ln \delta^+ + B\right) \frac{dv^*}{dx} + \frac{2}{\kappa} \frac{dv_\beta}{dx} + \frac{v^*}{\kappa \delta^+} \frac{d\delta^+}{dx} + \frac{dU_e}{dx} = 0 \quad (6-139)$$

Equation (6-132) is combined with the $\Pi - \beta$ correlation [Eq. (6-121)] and retained as a third relation for dU_e / dx , except that $(1 + \Pi)v^*$ is replaced by $(v^* + v_\beta)$, in the following rearrangement,

$$\frac{dU_e}{dx} = - \frac{\kappa |v^*| [-0.4v^{*2} + 0.76v_\beta |v^*| + 0.42v_\beta^2]}{v\delta^+(v_\beta + v^*)} \quad (6-140)$$

Finally, the derivative form of [Eq. \(6-132\)](#) yields a fourth differential equation,

$$\frac{dv_\beta}{dx} = B_1 \frac{dv^*}{dx} + B_2 \frac{d\delta^+}{dx} + B_3 \frac{dU_e}{dx} + B_4 \quad (6-141)$$

where B_i are given by Das (1987).

Equations (6-138) to (6-141) are four first-order ordinary differential equations to be solved for U_e , v^* , v_β , and δ^+ , assuming a known input distribution $\delta^*(x)$. For example, when this inverse scheme is applied to the Newman airfoil problem of [Fig. 6-32](#) (for which the direct inner variable method is not very accurate), the results agree well with the measurements for U_e , C_f and $\theta(x)$ —even in the separated-flow region. Other satisfactory examples are given by Das (1987). In principle, such inverse methods can be used to design “tailored” flows to, say, avoid separation or reduce body drag.

6-8.7 Complex Turbulent Flows

Although the emphasis in this section has been on developing relatively simple turbulent-boundary-layer methods for engineering use, there are complex motions for which such methods fail. In the late 1970s, many computer-oriented methods were developed to analyze such complicated flows. Such efforts continue to this day. Simply put, a “complex” turbulent flow is one that is more complicated than the two-dimensional, steady, incompressible, and attached thin shear layers that are thoroughly covered in the literature. Three-dimensionality is the most obvious complexity. Other contributing factors include:

1. Fluid effects: polymer additives, chemical reactions, multiple phases, compressibility, surface tension, and non-Newtonian behavior.
2. Fluctuations, turbulence, and periodicity in the freestream.
3. Wall effects: irregular geometry, suction and blowing, roughness, compliance, and moving walls.
4. Body forces, especially due to streamline curvature.

5. Strain interactions, especially in three dimensions.

Page 373

One straightforward example is an *irregular geometry*. As illustrated in [Fig. 6-33](#), right-angle variations in the wall or body shape will immediately cause the flow to separate and, if wall length permits, to reattach further downstream. The separation “bubble” does not exhibit a boundary-layer character and interacts strongly with the freestream. A full flow-field computation is required to predict each of the seven examples in [Fig. 6-33](#).

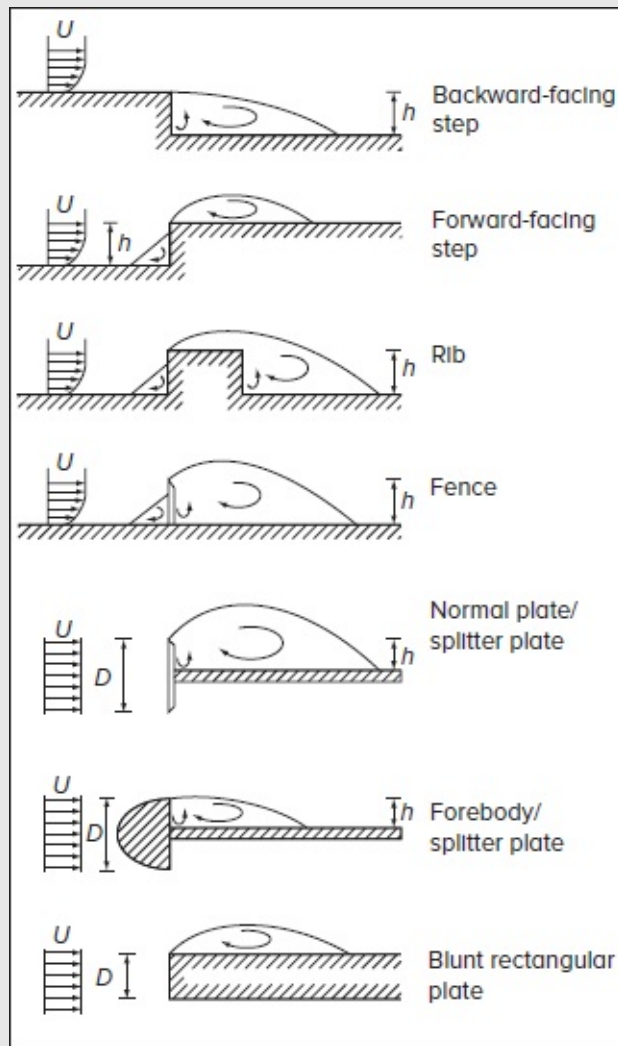


FIGURE 6-33

Seven examples of right-angle wall- and body-shape configurations which cause two-dimensional flow separation and reattachment. [Courtesy of I. S. Gartshore and N. Djilali, University of British Columbia.]

The question of whether a sufficient number of reliable data sets could be assembled in a

timely fashion to study a given problem turns out to be a moot point. A total of 66 test cases, including 26 incompressible-flow and 18 compressible-flow experiments, are incorporated in vol. II of Kline et al. (1982), many of which have multiple cases. Among the incompressible-flow experiments are the following typical problems:

1. Corner flows.
2. Diffuser flows.
3. Freestream turbulence.
4. Curved streamlines.
5. Suction or blowing.
6. Separated flows.
7. Wall jets.
8. Relaminarizing flows.
9. Wakes—near and far.
10. Decay of grid turbulence.
11. Backward-facing steps ([Fig. 6-33a](#)).
12. Secondary flows.

Needless to say, no single method could successfully handle the complete spectrum of this rich variety of cases.

Page 374

A total of 35 computer groups are featured in these studies, using 67 methods in all, including (1) integral methods, (2) eddy viscosity, (3) two-equation models, (4) algebraic stress models, and (5) differential Reynolds stress models. To quote from the Evaluation Committee report [Kline et al. (1982, pp. 979–986)]: “No method had any significant universality. Likewise, no method proved to be universally bad.” Because different methods worked in different cases, they recommended that all methods receive further attention and refinement. Best progress toward predictive accuracy seems to have occurred in separated flows, shock-wave–boundary-layer interactions, calculation of fluctuating velocities (u' , v' , w'), decay of turbulence toward laminar flow, and transonic flow. Further conclusions consist of:

1. The weakest part of two-equation models is the ϵ relation. Agreement in particular cases may be found by “tweaking its constants,” but in general a better dissipation model is needed.
2. Algebraic stress models, though expected to be better than eddy-viscosity closures, do not yield significant improvements.
3. Differential methods that integrate down to the wall yield better results than “wall functions.”
4. Grid spacing and numerical uncertainty are often inadequate.

5. In some difficult cases—transonic airfoils, curved walls, and diffusers—the simplest (integral) methods are, vexingly, the most accurate. In general, there is no correlation between the complexity of the models used and their actual predictive capability.
6. Predictive accuracy for separated flows, e.g., [Fig. 6-33](#), is substantially worse than that for the corresponding attached flows.

The present status is one of uncertainty as to whether we will ever achieve “universal” models that handle all (or most) turbulent flows, or whether instead we should assemble groups of *zonal* models that are each effective for certain regions, classes, or types of motion.

6-8.7.1 RELAMINARIZATION. An intriguing test case—not computed by many researchers—corresponds to flows that undergo reverse transition or *relaminarization*. About 30 experiments in the literature, reviewed by Narasimha and Sreenivasan (1979), Sreenivasan (1982), Warnack (1998), and Majdalani et al. (2002), have studied this interesting phenomenon.

Disregarding special effects due to buoyancy and electromagnetic forces, there are two fluid-flow mechanisms causing reversion of turbulent to laminar flow. These consist of strong convective acceleration of a boundary layer ([Fig. 6-34a](#)), and gradual expansion of fully developed duct flow ([Fig. 6-34b](#)).

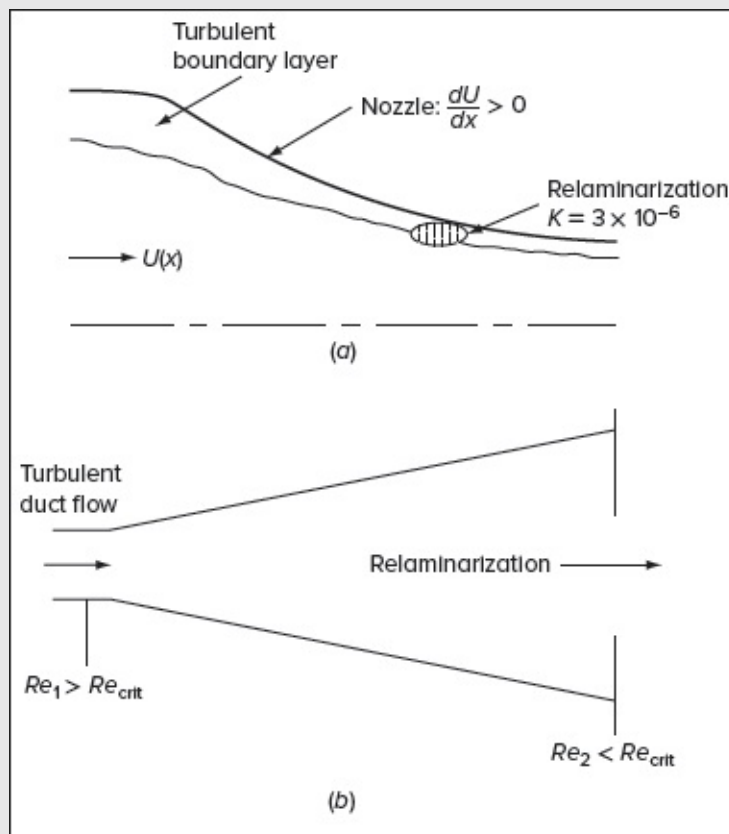


FIGURE 6-34

Two examples of reverse transition experiments: (a) convective acceleration of an initially turbulent boundary layer; (b) reduction of duct Reynolds number due to gradual (unstalled) expansion.

In [Fig. 6-34a](#), “weak” laminarization occurs, in the sense that the turbulence does not disappear, but mean parameters such as the velocity profile and skin friction approach laminar values. Turbulence becomes smaller only in an absolute sense: $(-\overline{u'v'})$ remains almost constant during the laminarization process but becomes a sharply decreasing fraction of the stream energy U_e^2 . Although it is thought that turbulence cannot exist for Reynolds numbers $Re_\theta < 300$, this critical value does *not* correlate laminarization in [Fig. 6-34a](#). The proposed critical parameter is a dimensionless acceleration, specifically,

$$K_{\text{crit}} = \frac{\nu}{U_e^2} \frac{dU_e}{dx} \approx 3 \times 10^{-6} \quad (6-142)$$

Typically, this value is reached about 20 boundary-layer thicknesses after acceleration begins. However, Sreenivasan (1982) points out that K cannot truly be a fundamental parameter since it contains no boundary-layer information.

The case of [Fig. 6-34b](#) may be called “strong” laminarization because, far downstream, the turbulence disappears altogether. For a small ($1 - 2^\circ$) expansion angle, the duct Reynolds number drops gradually until turbulent flow can no longer be sustained. Turbulent shear decreases faster than the rms fluctuations, but both decay slowly over tens or even hundreds of diameters. As this expansion occurs, dissipation will exceed turbulent production to the extent that [Fig. 6-34b](#) may be viewed as a “viscous” laminarization, whereas in [Fig. 6-34a](#), where dissipation remains small, the reversion may be attributed to the stabilizing effect of acceleration on the flow field. According to Kline et al. (1982, p. 1165), few methods could predict relaminarization very effectively, although the original $K - \epsilon$ model of Jones and Launder (1972) was developed for this purpose. Later, however, it has become possible to predict this effect, both with a second-moment closure [Shima (1993)] and also with DNS calculations [Iida and Nagano (1998)].

Page 375

6-9 FREE TURBULENCE: JETS, WAKES, AND MIXING LAYERS

The previous sections have been concerned with wall-bounded flows, where the interaction between an inner and outer layers is crucial to rational analysis. We now turn our attention to consider *free turbulence*, which refers to high Reynolds number shear flow in an open ambient fluid (i.e., unconfined and uninfluenced by walls). Several monographs and reviews are devoted to free turbulent flows, notably, those by Pai (1954), Abramovich (1963), List

(1982), Ho and Huerre (1984), Sherman (1990), Middleman (1995), Morris et al. (2002), Lee and Chu (2003), and others. [Figure 6-35](#) shows the three most common types of free turbulence: (1) a mixing layer between two streams of different velocity, (2) a jet issuing into a still (quiescent) or moving stream, and (3) a wake behind a body. In all three cases, there is a characteristic velocity scale, $U_{\max}(x)$ or $\Delta u_{\max}(x)$, and a characteristic shear-layer width, $b(x)$. Since these flows are “free,” or unconfined, the pressure is approximately constant throughout the flow, except for (small) turbulent fluctuations within the layer.

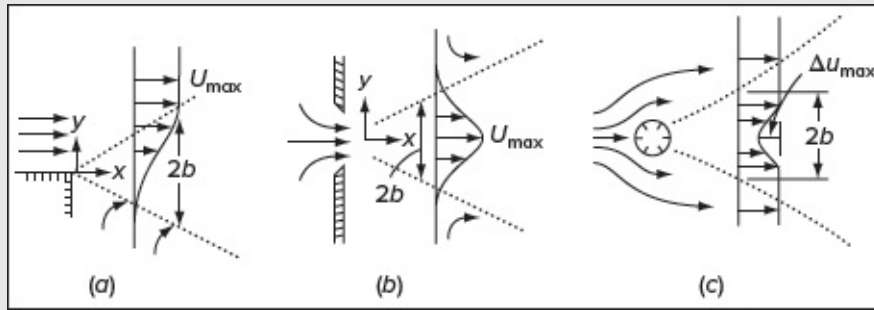


FIGURE 6-35

Three types of free turbulent flow: (a) mixing layer; (b) free jet; (c) wake of a body.

In [Fig. 6-35](#), we are looking at the asymptotic downstream behavior of free turbulence, traditionally assumed to be independent of the type of source that generated the flow. The source, thus ignored, is also assumed to be symmetrical, so that the shear layer is not *skewed* in shape. One then analyzes the asymptotic behavior of width and velocity scales and the velocity profile, $\bar{u}(x, y)$, for plane flow or $\bar{u}(x, r)$ for axisymmetric flow. Actually, there are certain effects, to be discussed, of the precise form of the jet source or the body creating the wake.

Page 376

[Figure 6-36](#) shows the details of the initial formation of a jet, assuming a still ambient fluid. The figure is valid only for similar jet and ambient fluids, e.g., air-into-air, not water-into-air. Velocity profiles are shown as thick dark lines across the flow. The jet typically issues at a nearly flat, fully developed, turbulent velocity U_{exit} . Mixing layers form at the lip of the exit, as in [Fig. 6-35a](#), growing between the still ambient and the nearly inviscid *potential core* flowing at velocity U_{exit} . The potential core vanishes quickly at a distance of about one diameter from the exit, where the velocity profile loses its mixing-layer–flat-core shape. Downstream of the core, the flow begins to develop into the distinctive Gaussian-type shape we think of as a “jet.” Finally, at about 20 diameters downstream of the exit, the velocity profile reaches and maintains a *self-preserving* shape,

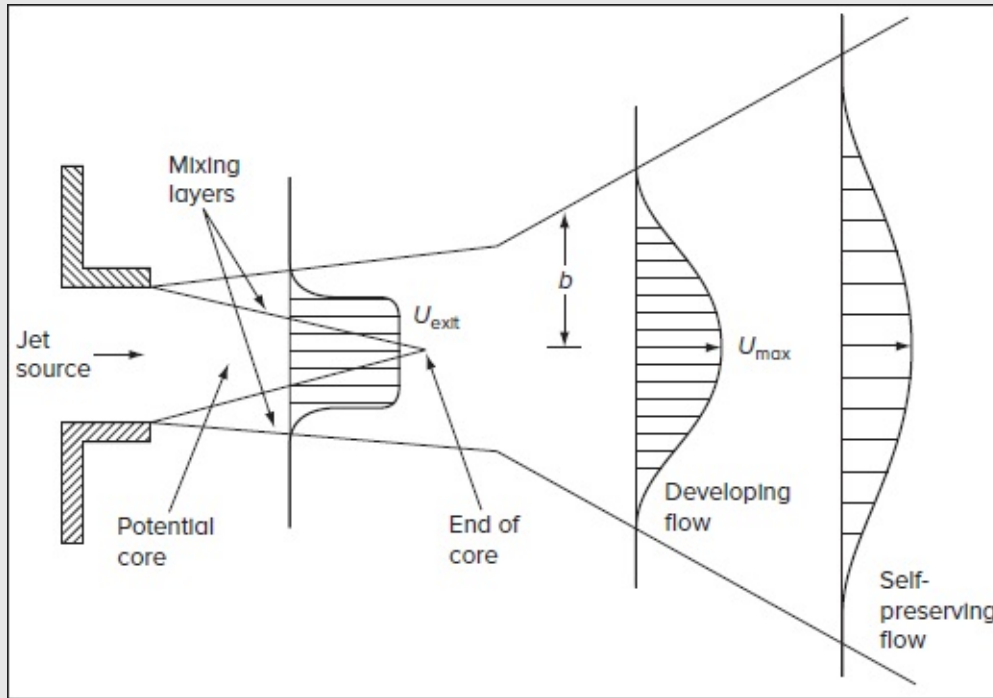


FIGURE 6-36

Details of the early development of a real jet.

$$\frac{\bar{u}}{U_{\max}} \approx F\left(\frac{y}{b}\right) \quad \text{or} \quad F\left(\frac{r}{b}\right) \quad (6-143)$$

depending upon whether the jet is plane or axisymmetric. It is this asymptotic self-similar form of free turbulent flows that we wish to study here. Equation (6-143) is satisfying physically but hardly surprising. Most curves of this shape—falling from a maximum through a point of inflection to approach zero—will collapse together reasonably well when normalized with their maximum values and their characteristic widths. The developed or self-similar region seems to grow from an “apparent origin” in front of the exit, as sketched in [Fig. 6-36](#).

Note that the velocity profiles in [Fig. 6-36](#) possess the same momentum but *not* the same mass flow. Fluid is entrained in the jet from the ambient region and the jet mass flow increases downstream. One should also emphasize that [Fig. 6-36](#) is a schematic of the time-mean flow field—the instantaneous flow might resemble the unsteady structure depicted in [Fig. 6-2](#).

6-9.1 Self-Similarity of Turbulent Jets

Assuming that we are sufficiently downstream for the jet velocity to become self-similar, as in [Eq. \(6-143\)](#), the jet momentum J must remain constant at each cross section in the absence

of a pressure gradient [recall Eq. (4-125) for laminar jets]:

$$J = \int_{-\infty}^{+\infty} \rho \bar{u}^2 dA = \begin{cases} (\text{const}) \rho b U_{\max}^2 & (\text{plane jet}) \\ (\text{const}) \rho b^2 U_{\max}^2 & (\text{axisymmetric}) \end{cases} \quad (6-144)$$

In the self-similar region, the centerline velocity and jet width should depend only upon jet momentum, density, and distance, but *not* upon molecular viscosity since there are no walls:

$$U_{\max} = F(x, J, \rho) \quad b = g(x, J, \rho)$$

Page 377

By dimensional analysis, the width can only grow linearly, and so one can take $b = (\text{const}) x$ for both plane and axisymmetric configurations. Recall from [Chap. 4](#) that this was also true for a laminar circular jet, [Fig. 4-37](#), but there the constant depended upon jet momentum and molecular viscosity. Here the constant is unique: a single growth rate for all self-similar turbulent jets, regardless of the Reynolds number. Also recall that the growth of a plane laminar jet, Eq. (4-128), is $b = C x^{2/3}$.

Dimensional analysis of U_{\max} leads to the following two relations:

$$\begin{aligned} \text{Plane flow:} \quad U_{\max} &= (\text{const}) \left(\frac{J}{\rho} \right)^{1/2} x^{-1/2} \\ \text{Axisymmetric flow:} \quad U_{\max} &= (\text{const}) \left(\frac{J}{\rho} \right)^{1/2} x^{-1} \end{aligned}$$

Unlike laminar flow, the constants here are unique, independent of the Reynolds number, and often determined from experimental data. An elegant discussion of the restrictions on these self-preserving assumptions is given by George (1989).

Page 378

6-9.1.1 THEORETICAL VELOCITY PROFILE FOR A PLANE JET. With the forms of $b(x)$ and $U_{\max}(x)$ established by dimensional analysis, the jet profile shape may be captured by solving the turbulent-boundary-layer continuity and momentum relations with a zero pressure gradient:

$$\frac{\partial \bar{u}}{\partial x} + \frac{\partial \bar{v}}{\partial y} = 0 \quad \text{and} \quad \bar{u} \frac{\partial \bar{u}}{\partial x} + \bar{v} \frac{\partial \bar{u}}{\partial y} = \frac{1}{\rho} \frac{\partial \tau}{\partial y} \quad (6-145)$$

As suggested by Prandtl in 1926, shear stress can be modeled by an eddy viscosity that depends only upon x and has the form of Clauser's outer wake model for a boundary layer [Eq. (6-93)]:

$$\mu_t(\text{jet}) \approx K \rho U_{\max} b = (\text{const}) x^{1/2} \quad K \approx 0.016 \quad (6-146)$$

where the $x^{1/2}$ variation follows from our dimensional analysis. Görtler (1942) made the same assumption for a plane jet and defined the following similarity variables:

$$\bar{u} = U_0 \left(\frac{x_0}{x} \right)^{1/2} f'(\eta) \quad v_t = KU_0 b_0 \left(\frac{x}{x_0} \right)^{1/2} \quad \eta = \sigma \frac{y}{x} \quad (6-147)$$

where σ denotes an arbitrary constant and (U_0, b_0) represent the values of (U_{\max}, b) at an initial reference point x_0 . Substitution of [Eqs. \(6-146\)](#) and [\(6-147\)](#) into [Eqs. \(6-145\)](#) yields a similarity differential equation for the characteristic function f :

$$\frac{1}{2} f''' + f f'' + f'^2 = 0 \quad (6-148)$$

where the coefficient $\frac{1}{2}$ has been chosen for convenience by specifying that

$$\frac{4Kb_0\sigma^2}{x_0} = 1 \quad \text{or} \quad \sigma = \frac{1}{2} \sqrt{\frac{x_0}{Kb_0}} \quad (6-149)$$

Equation (6-148) is subject to symmetry at the centerline, where $\bar{v} = \partial \bar{u} / \partial y = 0$ at $y = 0$, and a vanishing velocity \bar{u} as $y \rightarrow \infty$. These conditions translate into

$$f(0) = f''(0) = f'(\infty) = 0 \quad (6-150)$$

We also recognize that $f'(0) = 1$ from the velocity definition in [Eq. \(6-147\)](#). Comparing these with their laminar-jet equivalents, [Eqs. \(4-124\)](#) and [\(4-127\)](#), we see that the solution for a turbulent plane jet is

$$f(\eta) = \tanh(\eta) \quad \frac{\bar{u}}{U_{\max}} = \text{sech}^2(\eta) \quad (6-151)$$

This distribution proves to be in excellent agreement with experiments for plane jets. Görtler (1942) matched the data at the *half-velocity point*, $y_{1/2}$, where $\bar{u} = U_{\max}/2$ and $\eta_{1/2} = \text{sech}^{-2}(0.5) = 0.88$, thereby obtaining the estimate

$$\sigma_{\text{plane jet}} \approx 7.67$$

The “width” of the jet remains ill-defined, since the velocity drops asymptotically to zero at large y . If we define $b = 2y_{1/2}$, then the jet grows as

$$\frac{b}{x} = \frac{1.76}{7.67} = \tan(13^\circ) \quad \text{with} \quad K = \frac{x}{4b\sigma^2} = 0.018$$

Thus, a turbulent plane jet grows at a half-angle of 13° , independently of the Reynolds number; as for the eddy viscosity, it stands in reasonable agreement with Clauser’s formula given by [Eq. \(6-93\)](#).

6-9.1.2 SOLUTION FOR A CIRCULAR JET. The analysis for a round jet is quite

similar, except that one takes U_{\max} to be proportional to x^{-1} and uses the axisymmetric boundary-layer relations specified by Eqs. (4-222). The Görtler (1942) theory for this case leads to the profile

$$\frac{\bar{u}}{U_{\max}} \approx \left(1 + \frac{\eta^2}{4}\right)^{-2} \quad \eta \approx 15.2 \frac{y}{x} \quad \text{and} \quad U_{\max} \approx 7.4 \frac{(J/\rho)^{1/2}}{x} \quad (6-152)$$

This motion has the same form as the laminar round jet corresponding to Eq. (4-228). When this solution is compared to experimental measurements in [Fig. 6-37a](#), a reasonable agreement is found except in the outer region of the jet, where the velocity overshoot may be attributed to intermittency of turbulence near the jet edge [Corrsin and Kistler (1955)].

Page 379

A better formula for the round jet is found simply by carrying over the plane-jet solution with a different value of σ :

$$\text{Round jet:} \quad \frac{\bar{u}}{U_{\max}} \approx \text{sech}^2\left(10.4 \frac{y}{x}\right) \quad (6-153)$$

This expression is seen in [Fig. 6-37a](#) to be in excellent agreement with the data of Wygnanski and Fiedler (1969). Self-similarity in the velocity profile occurs for $x/D > 20$, where D is the source diameter. At the centerline, U_{\max} decreases with x^{-1} as if the flow begins from a virtual origin approximately seven diameters downstream of the actual source.

The unsteady fluctuations take longer to develop than the mean velocity. [Figure 6-37b](#) shows the measured streamwise velocity fluctuation, which is nonsimilar at $x/D = 20$ and does not become self-similar until $x/D = 50$. Note the very high levels of turbulence (30 percent) compared to boundary layers ([Fig. 6-4](#)). The transverse components, v'_{rms} and w'_{rms} , do not become similar until $x/D = 70$, at which point the round jet becomes truly *self-preserving*. Even at $x/D = 100$, the components v' and w' remain smaller than u' , indicating that turbulence has not become isotropic.

Turbulence in free-shear flows can be predicted by higher order theories, such as the $K - \epsilon$ model of Sec. 6-7.2.2, but the “constants” in [Eqs. \(6-107\)](#) have to be modified to improve the agreement, as reviewed by Rodi (1984) and Taulbee (1989). The models predict mean velocities very well, growth rates and shear stresses moderately well, and are only fair to poor for the turbulence components. See Wilcox (1998) for further discussion.

If the jet issues at velocity U_j into a *co-flowing* stream of velocity U_e , the development of self-similarity is strongly affected, as shown by the data of Antonia and Bilger (1973). The mean-velocity difference scales well with $y/y_{1/2}$, as in [Fig. 6-37a](#), and is well approximated by

$$\frac{\bar{u} - U_e}{U_j - U_e} \approx \cos^2\left(\frac{\pi}{4} \frac{y}{y_{1/2}}\right) \quad 0 < y < 2y_{1/2}$$

Here the growth rate $y_{1/2}(x)$ is smaller and decidedly nonlinear as U_e / U_j increases. This behavior is evident in [Fig. 6-37a](#) at $U_e = 0$, where $y_{1/2} / D \approx 25$ at $x / D = 300$. However, from the measurements of Antonia and Bilger (1973) for $U_e / U_j = 1 / 3$ and $x / D = 300$, one finds $y_{1/2} D \approx 3.2$, or eight times smaller. The mean velocity becomes self-similar for $x / D > 40$, but the streamwise turbulence $u'_{\text{rms}} / U_{\text{max}}$ continues to develop even at $x / D = 266$.

6-9.2 The Plane Mixing Layer

Using an eddy-viscosity analysis, Görtler (1942) also solves for the planar velocity profile in a mixing layer between parallel streams, including the case where the upper stream moves at speed U^2 and the lower stream at U_1 . The corresponding motion is slightly antisymmetric about the midpoint, with boundary conditions

$$\bar{u}(-\infty) = U_1 \quad \bar{u}(+\infty) = U_2 \quad \bar{u}(0) = \frac{1}{2}(U_1 + U_2)$$

The solution given by Görtler (1942) is

$$u^* = \frac{\bar{u} - U_1}{U_2 - U_1} = \frac{1}{2} \left[1 + \operatorname{erf} \left(\frac{\sigma y}{x} \right) \right] \quad \sigma \approx 13.5 \quad (6-154)$$

If we define the layer half-thickness as the point where $u^* = 0.99$, then $\sigma b / x \approx 1.64$ or $b / x \approx 0.121 = \tan (7^\circ)$. Equation (6-154) stands in good agreement with experiments such as Plesniak and Johnston (1988), whose measurements shown in [Fig. 6-38a](#) are taken in a water channel with $U_1 / U_2 = 0.5$. The abscissa in [Fig. 6-38](#) is not y / x but rather y nondimensionalized by a “shear thickness” δ_s equal to $(U_2 - U_1)$ divided by the slope $(\partial \bar{u} / \partial y)_{\text{max}}$ at the center point ($y = 0$).

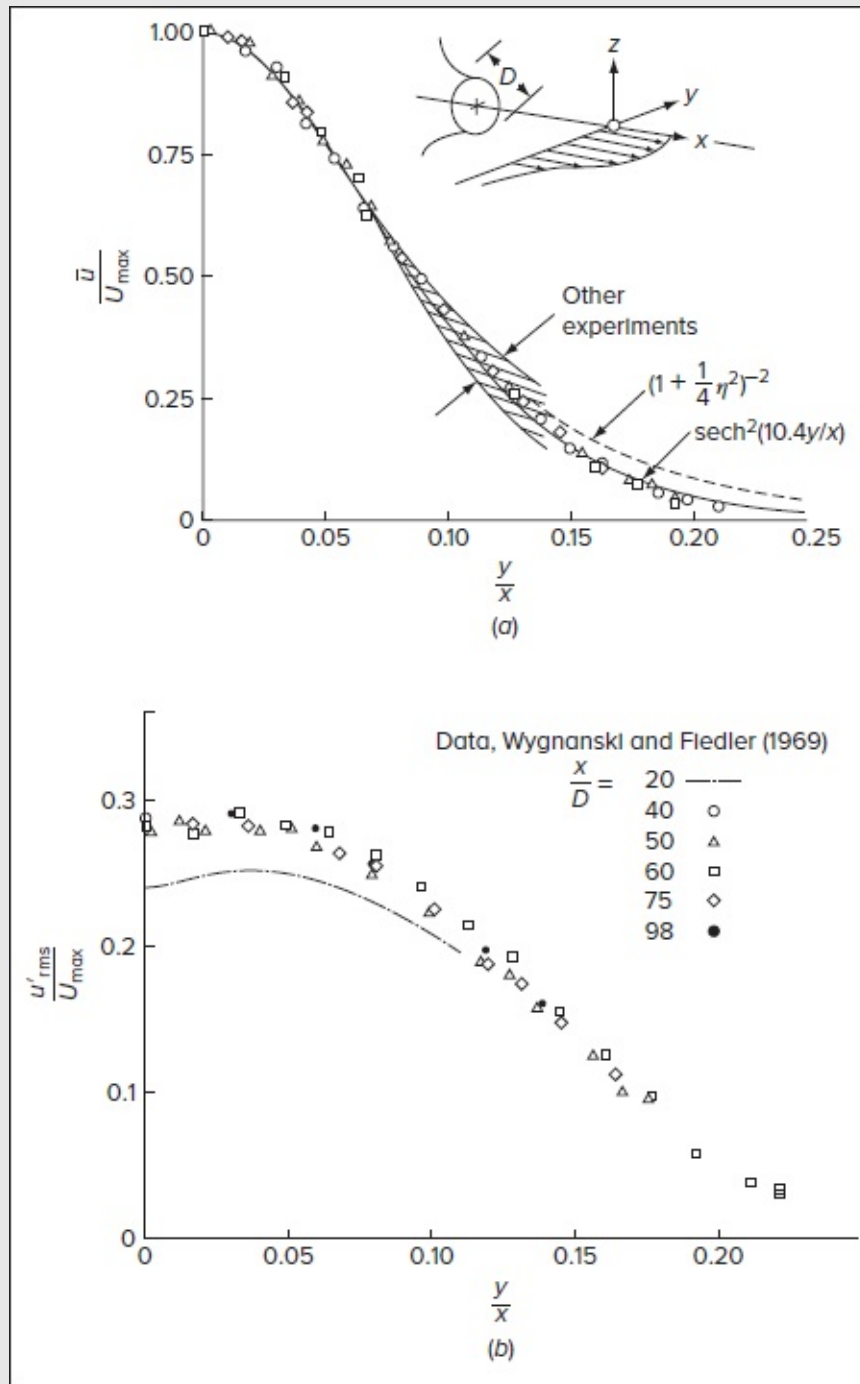


FIGURE 6-37

Experimental data for a circular jet, verifying the approach to self-similarity: (a) mean velocity; (b) streamwise fluctuation. [After Wygnanski and Fiedler (1969).]

Note in [Fig. 6-38](#), as with jet flow, the staged development of self-similarity. The mean velocity in [Fig. 6-38a](#) develops at $x = 30$ cm, whereas u'_{rms} in [Fig. 6-38b](#) keeps developing until $x = 70$ cm. Finally, u'_{rms} in [Fig. 6-38c](#) is not similar within the distance where the measurements are taken and is not as large as the streamwise fluctuation. Plesniak and

Johnston (1988) further show that the mixing layer is strongly affected by streamline curvature, being stabilized or destabilized depending upon the angular momentum ratio of the upper and lower streams.

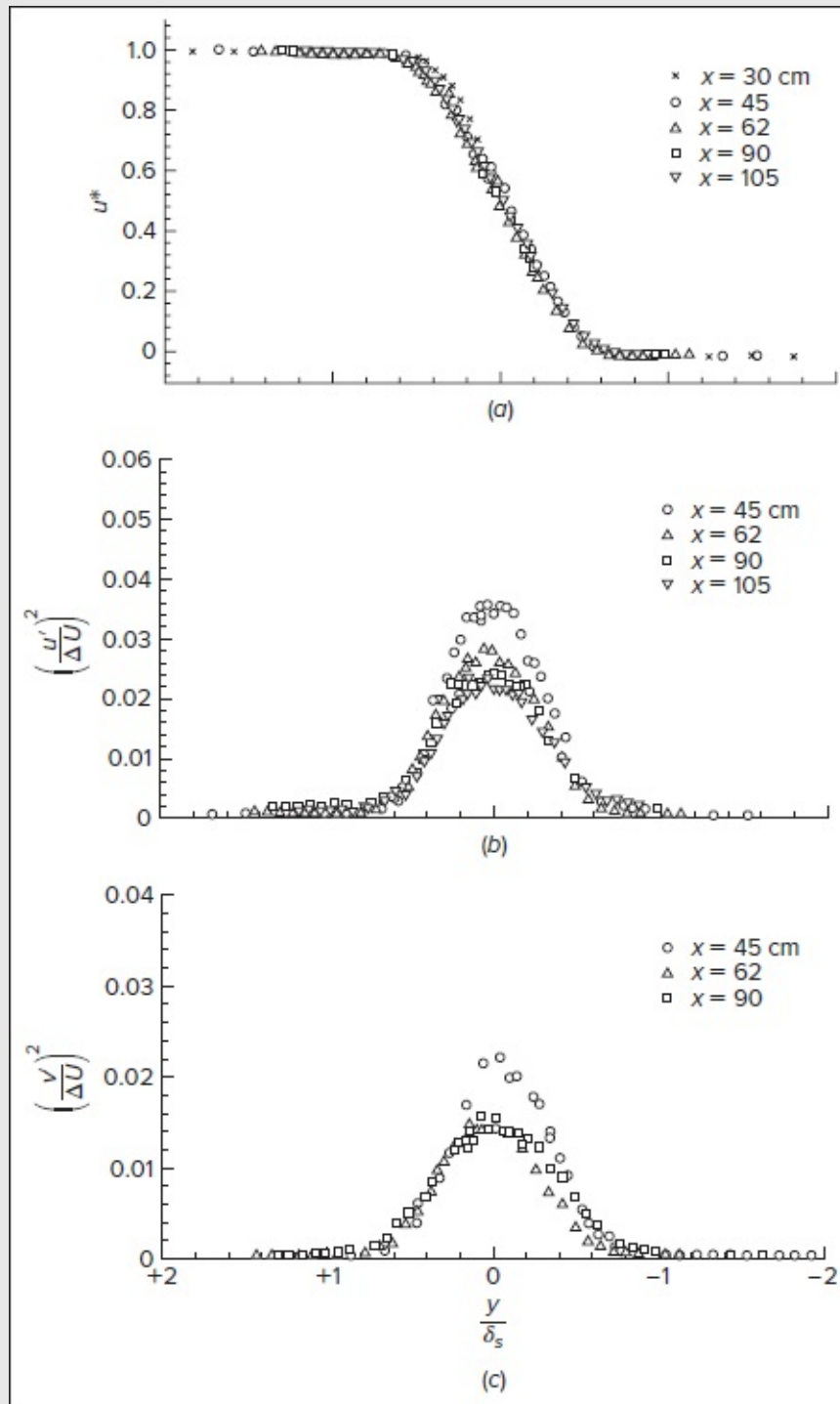


FIGURE 6-38

Measurements in a plane mixing layer: (a) mean velocity; (b) longitudinal fluctuation; (c) transverse fluctuation. [After Plesniak and Johnston (1988).]

The plane mixing layer at low Reynolds numbers is an excellent test case for direct simulation of turbulence by supercomputers. By way of example, Sandham and Reynolds (1987) use a spectral method (with 1024 longitudinal and 256 transverse mesh points) to compute a turbulent mixing layer with $U_1/U_2 = 0.5$ and an inlet profile with $Re_{\theta 1} = 100$. In their simulation, vortex pairing and turbulence are triggered by forcing the inlet profile with three of its unstable frequencies. Interestingly, a strictly periodic forcing is found to produce erratic, anomalous results. However, by “jittering” the inlet forcing, i.e., randomly varying the phases of the exciting modes, very realistic results are obtained, as shown in [Fig. 6-39](#). Note how these “numerical snapshots” resemble the visualization of a real mixing layer in [Fig. 6-2](#).

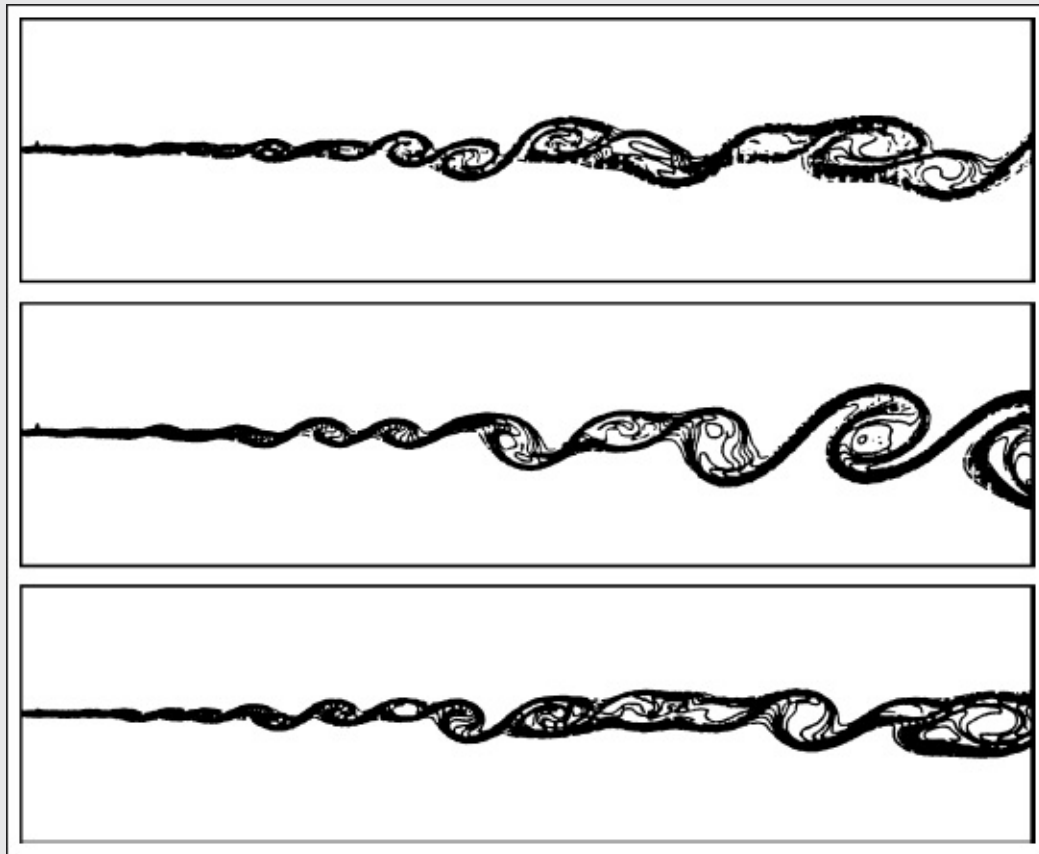


FIGURE 6-39

Three instantaneous snapshots of passive-scalar contours in a supercomputer simulation of a turbulent mixing layer. Compare with [Fig. 6-2](#). [After Sandham and Reynolds (1987).]

When time-averaged, the simulations in [Fig. 6-39](#) yield a mean-velocity profile that is almost identical to [Fig. 6-38a](#) or [Eq. \(6-154\)](#). However, the agreement is not as favorable for turbulence components, and the mean scalar fluxes seem to have the wrong sign near the layer edges. It is clear that DNS prediction of turbulence is a fruitful research field that will

continue to evolve.

Page 381

6-9.3 Turbulent Wakes

The wake in [Fig. 6-35c](#) resembles a jet carved out of a uniform stream. Since a wake constitutes a “defect” in a moving stream, it has a much stronger effect than a jet because of convective acceleration. Naturally, its resulting formulas are quite dissimilar from those of a jet. Far downstream, we assume self-similarity and write

$$\frac{\Delta u}{\Delta u_{\max}(x)} = f\left[\frac{y}{b(x)}\right] \quad (6-155)$$

As with jet flow, the pressure in the wake is nearly constant—except for turbulent fluctuation effects—because of the open environment. This time, the momentum theorem states that the drag force F associated with the wake profile is independent of x :

$$F = \int_{-\infty}^{+\infty} \rho \bar{u} \Delta u dA \approx \begin{cases} (\text{const}) \rho U \Delta u_{\max} b & \text{(plane wake)} \\ (\text{const}) \rho U \Delta u_{\max} b^2 & \text{(round wake)} \end{cases} \quad (6-156)$$

where U is the stream velocity outside the wake, assumed uniform. The last two results in [Eq. \(6-156\)](#) follow from the small-defect assumption, $\Delta u \ll U$. Thus, unlike the jet, Δu_{\max} is proportional to b^{-1} (plane) and to b^{-2} (circular wake). When these relations are substituted into the boundary-layer equations with the small-defect assumption $u(\partial u / \partial x) \approx U(\partial u / \partial x)$, we find that similarity cannot be achieved unless

$$\begin{array}{ll} \text{Plane wake:} & b = (\text{const}) x^{1/2} \quad \Delta u_{\max} = (\text{const}) x^{-1/2} \\ \text{Circular wake:} & b = (\text{const}) x^{1/3} \quad \Delta u_{\max} = (\text{const}) x^{-2/3} \end{array} \quad (6-157)$$

This information enables us to solve for the velocity-defect similarity profiles. If we use the Clauser-type eddy-viscosity distribution [Eq. (6-146)], and take “ b ” as the half-velocity point, the solution becomes a Gaussian distribution [Eq. (4-231)]:

$$\frac{\Delta u}{\Delta u_{\max}} = \exp\left(-0.693 \frac{y^2}{y_{1/2}^2}\right) \quad (6-158)$$

The constants in [Eqs. \(6-157\)](#) that determine the variations of Δu_{\max} and $y^{1/2}$ must be established by experiment. This is difficult because of the large-scale structures, e.g., Kármán vortex streets, in typical wakes—similarity may not develop until up to 1000 diameters downstream. Using a dual-plate “small-disturbance” wake generator, Sreenivasan and Narasimha (1982) propose the following growth-rate expressions for a plane wake:

$$y_{1/2} \approx 0.30 (x\theta)^{1/2} \quad \Delta u_{\max} \approx 1.63 U \left(\frac{\theta}{x}\right)^{1/2} \quad (6-159)$$

where θ is the momentum thickness of the wake, which is independent of x :

$$\theta = \int_{-\infty}^{+\infty} \frac{\Delta u}{U} \left(1 - \frac{\Delta u}{U} \right) dy = \text{const}$$

Wynnganski et al. (1986) measured the plane wakes behind various types of bodies—cylinders, high-solidity screens, strips, and airfoils—with the results shown in [Fig. 6-40](#). The flows did not become self-similar until hundreds of momentum thicknesses downstream of the bodies.

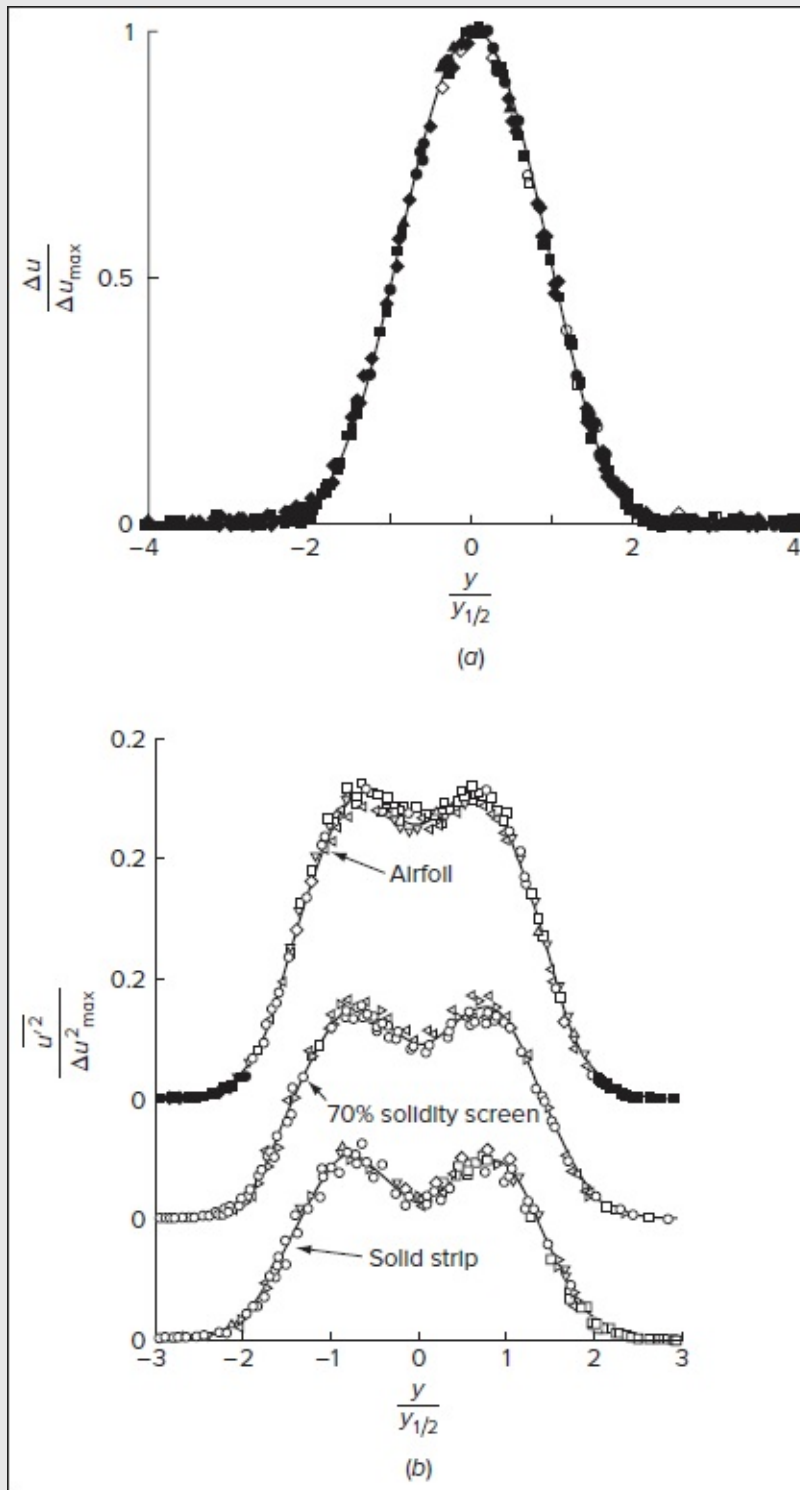


FIGURE 6-40

Measurements of plane wakes behind various-shaped bodies: (a) mean-velocity defect; (b) streamwise turbulent fluctuation. The data are taken for $x / \theta = 200$ to 700. [After Wygnanski et al. (1986).]

The mean-velocity defect measurements in [Fig. 6-40a](#) appear to be in good agreement with the Gaussian [Eq. \(6-158\)](#), except near the edge of the planar wake (not shown). For cylindrical wakes, the growth rate constants are slightly different from those in [Eq. \(6-159\)](#), namely, (0.275, 1.75) in lieu of (0.30, 1.63). Moreover, [Fig. 6-40b](#) shows that the streamwise fluctuation behind each reaches self-similarity, but the distributions do not agree with each other. Even the normalized turbulent shear, $(-\overline{u'v'})/\Delta u_{\max}^2$, is not the same behind the various body shapes. Wygnanski et al. (1986) conclude that there is no “universal” state of similarity for two-dimensional wakes except for the mean-velocity defect.

The various cases of free turbulent flows just discussed have their growth rates and velocity decay rates summarized in Table 6-3.

TABLE 6-3

Power laws for jets and wakes

	Laminar flow		Turbulent flow	
	Growth of width b	Velocity decay of \bar{u} or Δu	Growth of width b	Velocity decay of \bar{u} or Δu
Mixing zone	$x^{1/2}$	1.0	x	1.0
Plane jet	$x^{2/3}$	$x^{-1/3}$	x	$x^{-1/2}$
Circular jet	x	x^{-1}	x	x^{-1}
Plane wake	$x^{1/2}$	$x^{-1/2}$	$x^{1/2}$	$x^{-1/2}$
Circular wake	$x^{1/2}$	x^{-1}	$x^{1/3}$	$x^{-2/3}$

6-10 TURBULENT CONVECTIVE HEAT TRANSFER

As in laminar incompressible flow, the heat transfer seems to arise as an afterthought, because the velocity profiles, skin friction, and other flow ingredients can be determined independently of the temperature. Then, with velocities known, the temperature can, in theory, be deduced from the thermal-energy equation for turbulent boundary layers

$$\rho c_p \left(\bar{u} \frac{\partial \bar{T}}{\partial x} + \bar{v} \frac{\partial \bar{T}}{\partial y} \right) = \frac{\partial \bar{q}}{\partial y} + \tau \frac{\partial \bar{u}}{\partial y} \quad (6-160)$$

where

$$\tau = \mu \frac{\partial \bar{u}}{\partial y} - \rho \overline{u'v'} \quad \text{and} \quad \bar{q} = k \frac{\partial \bar{T}}{\partial y} - \rho c_p \overline{v'T'}$$

The difficulty, as usual, stems from the turbulent-inertial terms.

This section presents a brief overview of turbulent convective heat transfer, a popular subject in many textbook and monograph authors. In chronological order, they are Arpaci (1984), Kays and Crawford (1993), Burmeister (1993), Bejan (1994), Kakac and Yener (1994), Oosthuizen (1999), and Kaviani (2001). Some authors specialize in the computational aspects of the subject: Jaluria and Torrance (1986), Nakayama (1995), Tannehill et al. (1997), and Comini and Sunden (2000), to name a few. All types of

turbulence models, from zero- and one- and two-equation models to second-moment closures, LES, and DNS methods, have been applied to turbulent heat transfer.

6-10.1 Turbulent Eddy Conductivity

We may formally express the Boussinesq analogy for eddy viscosity and eddy conductivity using:

$$\tau_{\text{total}} = (\mu + \mu_t) \frac{\partial \bar{u}}{\partial y} \quad q_{\text{total}} = -(k + k_t) \frac{\partial \bar{T}}{\partial y} \quad (6-22)$$

Although μ_t and k_t are not fluid properties, they can be formed into a dimensionless ratio called the *turbulent Prandtl number*:

$$Pr_t = \frac{c_p \mu_t}{k_t} \quad (6-161)$$

Page 384

Since the turbulent-flux terms $\overline{v'u'}$ and $\overline{v'T'}$ are due to the same mechanism of time-averaged convection, it follows that their ratio Pr_t ought to be of order unity. This idea is essentially that of Reynolds (1874), who considers turbulent momentum and heat fluxes to be equivalent phenomena. Hence, one can take

$$Pr_t = f(Pr) = O(1)$$

This is one form of the celebrated Reynolds analogy for turbulent flow. Even today, over 100 years later, the turbulent Prandtl number, which surely must vary somewhat with local conditions, is taken to be a constant or at most a function of the molecular Prandtl number Pr . Even the latest digital-computer programs for computing turbulent heat transfer take advantage of this assumption.

Much of our experimental database for turbulent forced convection here stems from the Stanford University group, reviewed by Moffat and Kays (1984). In this context, [Fig. 6-41](#) reports the data of Blackwell (1973) for the turbulent Prandtl number of air in positive, zero, and negative pressure gradients. In all cases considered, Pr_t decreases from about 1.5 in the sublayer to 0.7 at the outer edge of the boundary layer. The increase near the wall is not too important, since both μ_t and k_t remain locally small; so it is not necessary to curve-fit the data. Instead, it is common to assume a constant value of $O(1)$:

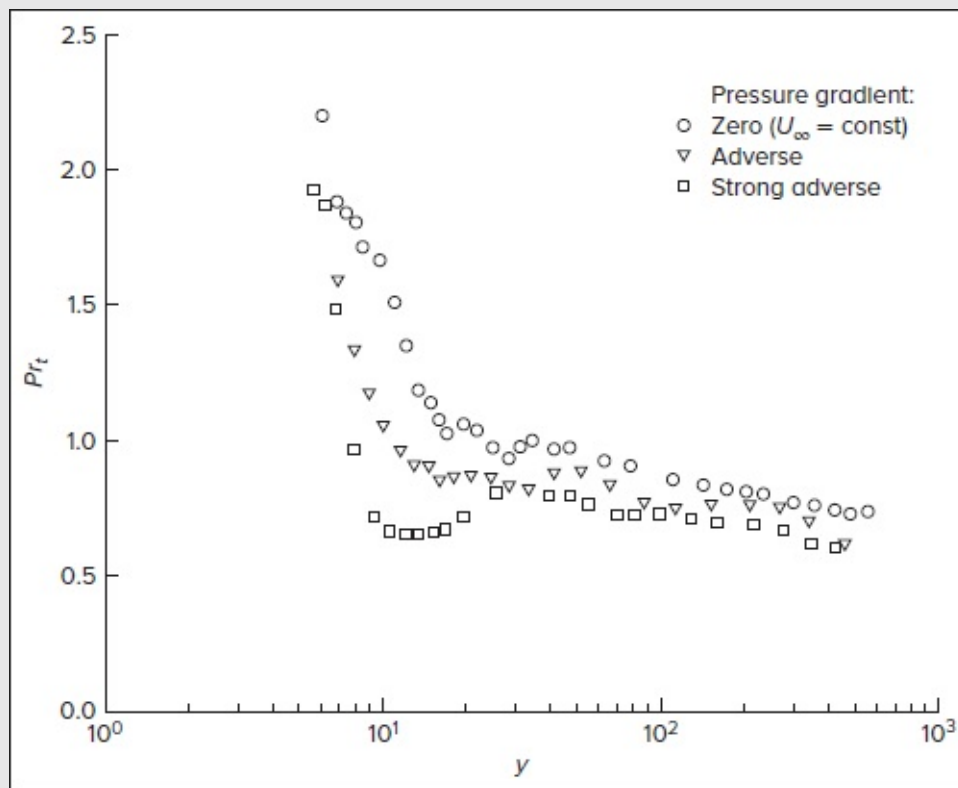


FIGURE 6-41

Experimental measurements of the turbulent Prandtl number in a boundary layer with pressure gradients. [After Blackwell (1973).]

$$Pr > 0.7: \qquad \qquad \qquad Pr_t \approx 0.9 \text{ or } 1.0 \qquad \qquad \qquad (6-162)$$

Additional experiments with wall suction and blowing [Simpson et al. (1970)] indicate no additional effects, so that the assumption in [Eq. \(6-162\)](#) can still be used. Presumably the data uncertainty in [Fig. 6-41](#) is large, since numerical differentiation of both velocity and temperature profiles is involved. In practice, the use of a constant Pr_t has been very successful in theoretical models. Also, in free turbulence (jets, wakes, mixing layers), one should take $Pr_t \approx 0.7$, as suggested by the data of [Fig. 6-41](#).

With Pr_t known, we have $k_t = c_p \mu_t / Pr_t$ and μ_t can be correlated by the usual eddy viscosity models, e.g., through [Eqs. \(6-92\)](#) and [\(6-93\)](#). Subsequently, the mean temperature and wall heat transfer profiles can be determined with no further assumptions. All turbulence models can be readily augmented by thermal calculations.

6-10.2 The Temperature Law of the Wall

Although a pressure gradient affects the near-wall shear stress $\tau(y)$ —see [Eq. \(6-98\)](#) and [Fig. 6-24](#)—it does not affect, to first order, the near-wall heat flux. To see this, consider the

energy Eq. (6-21c) for small y , with $\bar{u} \approx 0$ and either suction or blowing, i.e., $v \approx v_w \neq 0$. We may resolve this “Couette flow” approximation by integrating:

$$\frac{\partial q}{\partial y} \approx \rho c_p v_w \frac{\partial \bar{T}}{\partial y} \quad \text{or} \quad q \approx q_w + \rho c_p v_w (\bar{T} - T) + \dots \quad (6-163)$$

Page 385

Near an impermeable wall, then, $q \approx q_w \approx \rho c_p (v/Pr + \nu_t/Pr_t)(\partial \bar{T}/\partial y)$, which we can separate and integrate using the law-of-the-wall variable y^+ :

$$T^+ = \frac{T_w - \bar{T}}{T^*} = \int_0^{y^+} \frac{dy^+}{1/Pr + \mu_t/(\mu Pr_t)} \quad (6-164)$$

where $T^* = q_w / (\rho c_p v^*)$ represents a wall-conduction temperature that is analogous to the wall-friction velocity v^* . This term defines the *temperature law of the wall*, first proposed by Kármán (1939).

Assuming constant Pr and Pr_t , [Eq. \(6-164\)](#) may be integrated numerically using, say, [Eq. \(6-92\)](#) for the eddy viscosity μ_t / μ . Results are shown in [Fig. 6-42](#) for $Pr_t = 1.0$ and various molecular Prandtl numbers. In the immediate vicinity of the wall, the thermal sublayer has the form $T^+ = Pr y^+$. Further away from the wall, a logarithmic layer develops, namely,

$$T^+ \approx \frac{Pr_t}{\kappa} \ln y^+ + A(Pr) \quad (6-165)$$

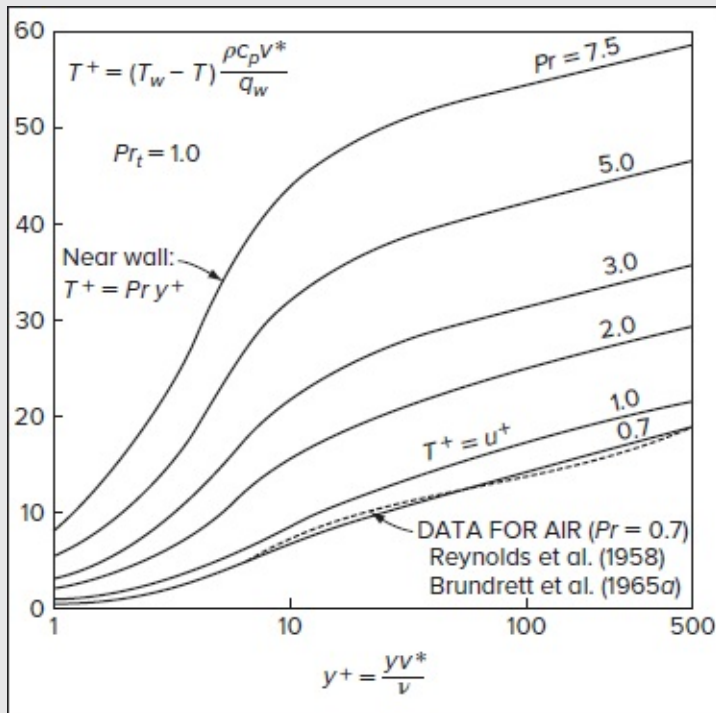


FIGURE 6-42

The temperature law of the wall for fluids with a Prandtl number greater than 0.7, from [Eqs. \(6-92\)](#) and [\(6-164\)](#).

The intercept $A(Pr)$ varies strongly with Pr as shown in [Fig. 6-42](#). In fact, an easy-to-remember curve-fit expression is

$$A(Pr) \approx 13Pr^{2/3} - 7 \quad Pr \geq 0.7 \quad (6-166)$$

Kader (1981) reports a more complicated curve fit that remains valid even for liquid metals with low Prandtl numbers ranging from 0.001 to 0.03:

$$A(Pr) \approx (3.85Pr^{1/3} - 1.3)^2 + 2.12\ln(Pr) \quad (6-167)$$

Kader finds this fit to be in good agreement with his survey of temperature profiles measured in air, water, ethylene glycol, and oil, over a substantial range of $0.7 \leq Pr \leq 170$. He also constructs curve fits for the entire temperature profile—sublayer, overlap layer, and outer layer—for zero and moderate pressure gradients. Kays and Crawford (1993) report a similar data survey. Other T^+ (y^+) models have been proposed. Sucec (1999) uses a power law, $T^+ \approx 6(y^+)^{0.17} + 13.2Pr - 9.37$. Volino and Simon (1997) avoid the Couette flow approximation of [Eq. \(6-163\)](#), and include a pressure gradient and convection in their near-wall analysis. Their formula for T^+ , which proves to be complex and implicit (not in closed form), stands in good agreement with experimental measurements. Huang and Bradshaw (1995) analyze pressure gradient effects and find their best results with the $K - \omega$ two-equation model. Cruz and Silva-Freire (2002) develop a thermal law of the wall for separating and recirculating flow. These correlations correspond to smooth, impermeable walls. Wall transpiration, especially blowing, has a very strong effect, as discussed by Faraco-Medeiros and Silva-Freire (1992). Hollingsworth et al. (1992) also analyze and characterize the effect of surface curvature.

6-10.3 The Reynolds Analogy for Stanton Number

We begin by recalling that in laminar-boundary-layer flow, [Chap. 4](#), a proportionality is established between the skin friction and heat transfer coefficients for flat-plate flow, namely,

$$C_h \approx \frac{C_f}{2Pr^{2/3}} \quad (4-80)$$

Similar approximations are possible for turbulent flat-plate and pipe flows because the velocity and temperature wakes are negligible. We simply evaluate the two log-laws at the edges of the boundary layer:

$$\frac{T_w - T_\epsilon}{T^*} \approx \frac{Pr_t}{\kappa} \ln \frac{\delta_T v^*}{\nu} + A \quad \frac{U_\epsilon}{v^*} \approx \frac{1}{\kappa} \ln \frac{\delta v^*}{\nu} + B$$

where δ and δ_T denote the velocity and thermal boundary-layer thicknesses, respectively. Assuming that $Pr_t \approx 1$ and $\delta \approx \delta_T$, we may subtract these two expressions and write:

$$\frac{q_w}{\rho c_p U_e (T_w - T_e)} \left[\frac{U_e}{v^*} + (A - B) \right] \approx \frac{v^*}{U_e}$$

We can hence identify the Stanton number in the left-hand-side coefficient and $(C_f / 2)^{1/2}$ on the right-hand side. With A from [Eq. \(6-166\)](#), we can then rewrite this expression as an approximate Reynolds analogy for turbulent flat-plate flow via

$$Pr \geq 0.7: \quad C_h \approx \frac{C_f / 2}{1 + 13(Pr^{2/3} - 1)(C_f / 2)^{1/2}} \quad (6-168)$$

For Pr near unity, this expression is well approximated by [Eq. \(4-102\)](#) and is valid only for smooth, impermeable, and isothermal walls. As for the skin-friction coefficient for a smooth flat plate, it may be evaluated using White's [Eq. \(6-78\)](#).

6-10.3.1 FULLY DEVELOPED TURBULENT PIPE FLOW. In pipe flow, the heat-transfer coefficient is based not on the centerline temperature but rather on the bulk or *cup-mixing* temperature, as in [Chap. 3](#), for constant c_p :

$$T_m = \frac{\int \rho \bar{u} \bar{T} dA}{\int \rho \bar{u} dA} \quad (3-65)$$

The pipe Stanton number is defined as

$$C_h = \frac{q_w}{\rho c_p u_{av} (T_w - T_m)}$$

Note that u_{av} for fully developed turbulent pipe flow has already been evaluated from the log-law in [Eq. \(6-53\)](#). If we now substitute the velocity log-law [Eq. \(6-38a\)](#) and temperature log-law [Eq. \(6-165\)](#) into [Eq. \(3-65\)](#) to evaluate T_m , the result, after substantial manipulation, can be expressed as

$$C_{h,pipe} \approx \frac{\Lambda / 8}{1 + 13(Pr^{2/3} - 1)(\Lambda / 8)^{1/2}} \quad 0.5 \leq Pr \leq 10^5 \quad (6-169)$$

where $\Lambda = 4C_f$ is the pipe-friction factor, to be evaluated from [Eq. \(6-54\)](#). This formula, first proposed by Petukhov (1970), is valid only for smooth walls with no blowing or suction.

Since it is customary to formulate pipe heat-transfer correlations in the form of a Nusselt number rather than a Stanton number, we have

$$Nu_D = \frac{q_w D}{k(T_w - T_m)} = C_h Re_D Pr$$

Page 387

For liquid metals ($Pr < 0.1$), where [Eq. \(6-169\)](#) is not valid, an alternative experimental correlation is provided by Sleicher and Rouse (1975):

$$Pr < 0.1: \quad Nu_D = 6.3 + 0.00167 Re_D^{0.85} Pr^{0.93} \quad (6-170)$$

[Figure 6-43](#) illustrates the variation of the Nusselt number with the Reynolds number at fixed values of Pr based on [Eqs. \(6-169\)](#) and [\(6-170\)](#). These predictions are found to be in fair agreement with fully developed pipe-flow experiments for constant wall temperature and heat flux. Note that the Nusselt number is typically higher in the entrance of the pipe. For more detail, Kays and Crawford (1993, Chap. 14) provide an excellent summary of the available data and theories in the entry region.

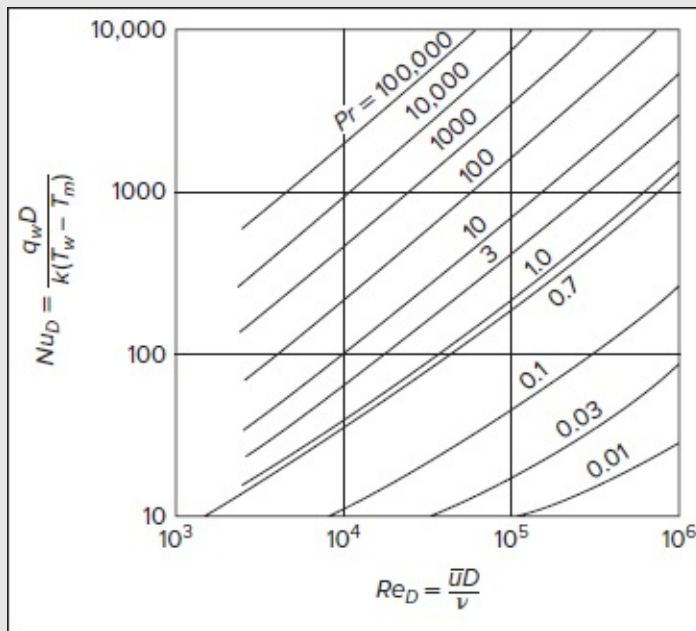


FIGURE 6-43

Nusselt numbers for fully developed turbulent flow in pipes, from [Eqs. \(6-169\)](#) and [\(6-170\)](#).

6-10.4 Turbulent Convection with Suction or Blowing

Wall transpiration has a strong effect on turbulent heat transfer, as reported by Moffat and Kays (1984). [Figure 6-44](#) displays some measurements of velocity and temperature profiles in flat-plate flow at $Re_x \approx 2 \times 10^6$ for different values of the suction or blowing parameter, F

$= v_w / U_e$. The velocity profiles in [Fig. 6-44a](#) rise dramatically with the blowing rate, not because of any striking changes in turbulent momentum transfer but rather because of changes in the shear-stress distribution according to [Eq. \(6-83\)](#). The effect of wall suction ($v_w < 0$) is minor, and the measured profile for $v_w / U_e = -0.0024$ agrees well with Stevenson's law of the wall [Eq. (6-86)]. However, [Eq. \(6-86\)](#) overpredicts u^+ in the blowing case, thus leading Simpson (1968) to propose an alternative law of the wall with transpiration, namely,

$$\frac{2}{v_w^+} [(1 + v_w^+ u^+)^{1/2} - (1 + 11v_w^+)^{1/2}] = \frac{1}{\kappa} \ln\left(\frac{y^+}{11}\right) \quad (6-171)$$

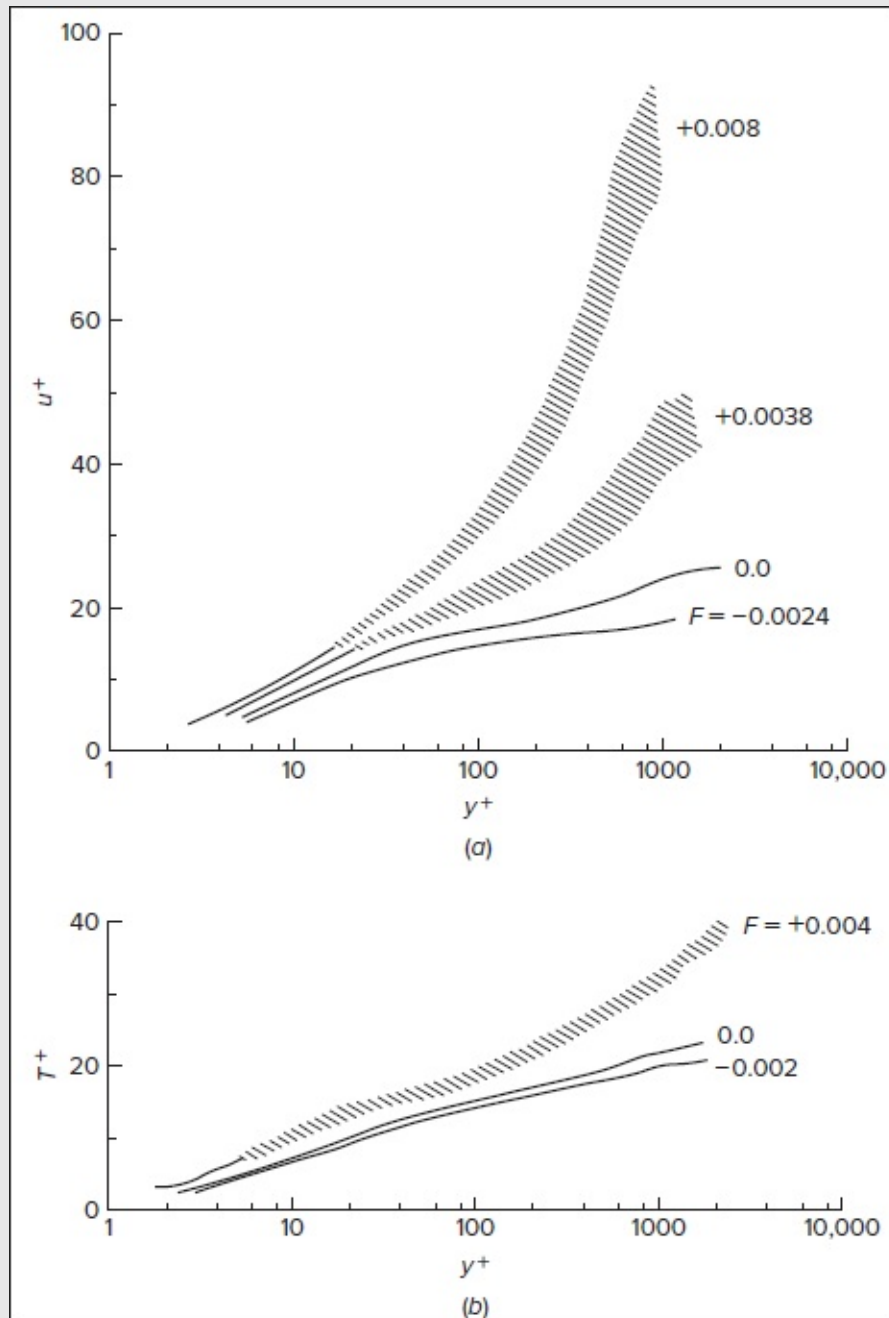


FIGURE 6-44

Experimental (a) velocity and (b) temperature profiles in flat-plate flow with suction and blowing. The parameter $F = v_w / U_e$. [After Moffat and Kays (1984).]

Equation (6-171) is formulated so that all profiles start at $(u^+, y^+) = (11, 11)$. It agrees with the two blowing curves in [Fig. 6-44a](#)—that have considerable scatter because of the difficulty of measuring skin friction—but not with other data, where Stevenson’s law in [Eq. \(6-86\)](#) still outperforms [Eq. \(6-171\)](#). This controversy—still unresolved—between two competing wall-blowing velocity correlations is discussed in detail by Schetz (1980, pp. 151–155).

[Figure 6-44b](#) presents the temperature profiles in wall coordinates, showing much less of an effect of suction and blowing compared to [Fig. 6-44a](#). The same trends would be true if we had added the pressure gradient as a parameter: a major effect on u^+ would be experienced, especially with freestream deceleration, and only a minor effect on T^+ [Moffat and Kays (1984)].

Page 388

Naturally, wall transpiration has a strong effect on both skin friction and heat transfer coefficients. [Figure 6-45](#) compiles measurements reported by Moffat and Kays (1984) of the local Stanton number in turbulent flat-plate flow with blowing and suction. We see that suction (or blowing) can cause an order of magnitude increase (or decrease) in wall heat transfer. By integrating [Eqs. \(6-97\)](#) and [\(6-163\)](#) and across the boundary layer and assuming that eddy viscosity is not affected by transpiration, Kays and Crawford (1980, pp. 180–182) offer the following correlation for flat-plate flow:

$$\frac{C_f(Re_x, v_w / U_e)}{C_f(Re_x, 0)} \approx \frac{C_h(Re_x, v_w / U_e)}{C_h(Re_x, 0)} \approx \frac{\zeta}{e^\zeta - 1} \quad (6-172)$$

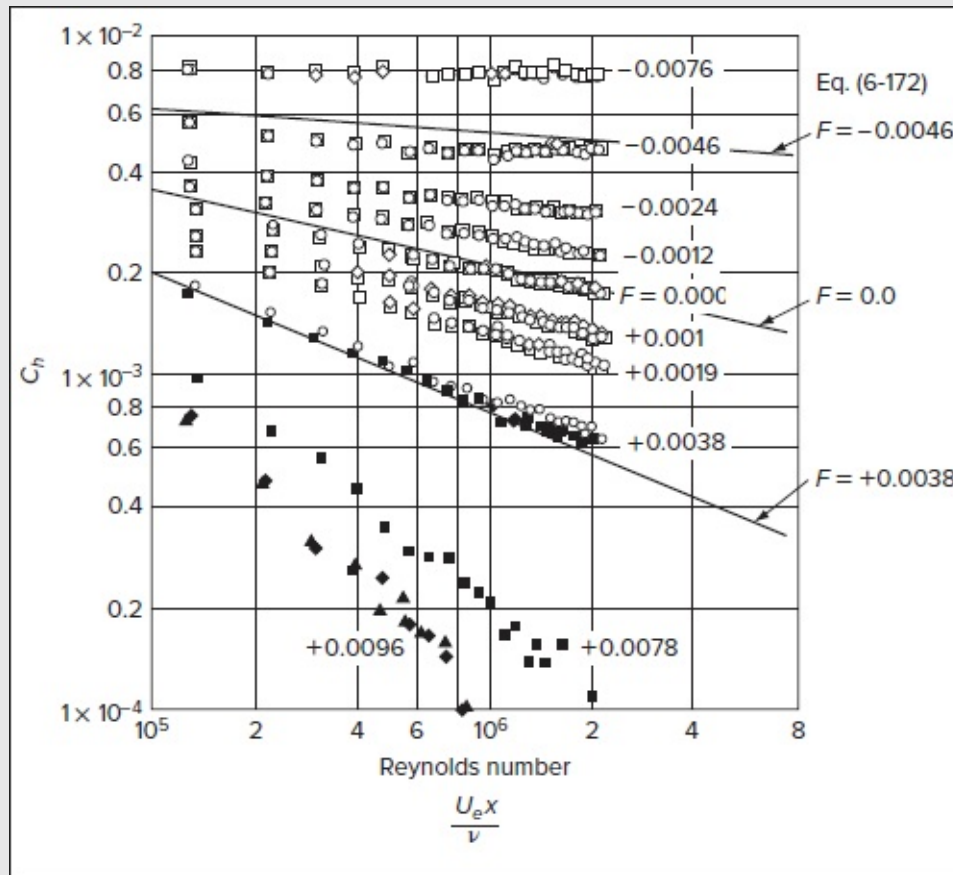


FIGURE 6-45

Measured local Stanton numbers for turbulent flat-plate flow with uniform suction or blowing, where $F = v_w/U_e$. The theory for $F = 0$ uses [Eqs. \(6-78\)](#) and [\(6-168\)](#). [After Moffat and Kays (1984).]

where $\zeta = 2(v_w/U_e)/C_f(Re_x, 0)$ or $(v_w/U_e)/C_h(Re_x, 0)$ for wall friction and heat transfer, respectively. The reference value $C_f(Re_x, 0)$ is computed from [Eq. \(6-78\)](#), after which the Stanton number $C_h(Re_x, 0)$ is determined for a given Prandtl number from [Eq. \(6-168\)](#). [Figure 6-45](#) illustrates the results of three representative calculations, i.e., for suction ($F = -0.0046$), impermeable wall ($F = 0$), and blowing ($F = +0.0038$). It is gratifying that the agreement is satisfactory for all three cases and indeed fits the available data. Also note that, for strong suction, the Stanton number asymptotically approaches $C_h = -F$ with successive increases in Re_x .

6-10.5 Flat-Plate Heat Transfer with Varying Wall Temperature

The previous analyses are for constant temperature difference $T_w - T_e$, whereas in practical

applications, the wall temperature is often variable. One approach is to superimpose a series of step changes as was done for laminar flow in Sec. 4-8.4. A comprehensive study of turbulent flat-plate flow with variable $T_w(x)$ is provided in four reports by Reynolds et al. (1958). Suppose that the flow is isothermal, $T_w = T_e$, until a position $x = x_0$, where the wall temperature suddenly changes to $T_w \neq T_e$. Reynolds et al. carried out an integral analysis, similar to the development of [Eq. \(4-28\)](#) for laminar flow, assuming that both u and $T - T_w$ vary with $y^{1/7}$. Their expression for the local Stanton number aft of x_0 consists of

$$C_h(x, x_0) \approx C_h(x, 0) \left[1 - \left(\frac{x_0}{x} \right)^{9/10} \right]^{-1/9} \quad (6-173)$$

where $C_h(x, 0)$ represents the isothermal solution from, say, [Eq. \(6-168\)](#). This result agrees well with their experiments on step changes in wall temperature [Reynolds et al. (1958, part 2)]. Now suppose that $(T_w - T_e)$ varies continuously with x . By analogy with the laminar-flow analysis [Eq. (4-190)], the total heat transfer over a plate of length x is given by

$$q_w(x) = \int_0^x h(x, x_0) d(T_w - T_e) \quad h(x, x_0) = \frac{q_w(x, x_0)}{T_w - T_e} \quad (6-174)$$

Page 390

If the temperature difference contains a number of discontinuities ΔT_i at points $x_0(i)$, [Eq. \(6-174\)](#) separates into a Riemann integral plus a summation of indicial functions, exactly as with Eq. (4-191):

$$q_w(x) = \int_0^x h(x, x_0) \frac{d}{dx_0} (T_w - T_e) dx_0 + \sum_{i=1}^N h[x, x_0(i)] \Delta T_i \quad (6-175)$$

This development mirrors its laminar-flow counterpart (Sec. 4-8.4). To provide a numerical example for turbulent flow, suppose that ΔT is a polynomial of the form

$$T_w - T_e = a_0 + a_1 x + a_2 x^2 + a_3 x^3 + \dots$$

Then the Stanton number referenced to the local temperature difference will be

$$\frac{C_{h,\text{actual}}}{C_{h,\text{plate at } \Delta T}} = \frac{1}{\Delta T(x)} \int_0^x \left[1 - \left(\frac{x_0}{x} \right)^{9/10} \right]^{-1/9} \left(a_0 + \sum_{j=1}^N j a_j x_0^{j-1} \right) dx_0$$

As before, the integrals are readily evaluated in terms of gamma functions:

$$\frac{C_{h,\text{actual}}}{C_{h,\text{plate at } \Delta T}} = \frac{1}{\Delta T(x)} \left[a_0 + \sum_{j=1}^N \frac{10}{9} j a_j x^j \frac{\Gamma(10j/9) \Gamma(8/9)}{\Gamma(10j/9 + 8/9)} \right] \quad (6-176)$$

By evaluating $\Gamma\left(\frac{8}{9}\right) = 1.07776$, for example, we can write the first five terms

$$\frac{C_{h,\text{actual}}}{C_{h,\text{plate at } \Delta T}} = \frac{a_0 + 1.1340a_1x + 1.2026a_2x^2 + 1.2497a_3x^3 + 1.2858a_4x^4 + \dots}{a_0 + a_1x + a_2x^2 + a_3x^3 + a_4x^4 + \dots} \quad (6-177)$$

It can be seen that the wall heat transfer varies at a faster rate than one would estimate by simply applying the isothermal-wall formula at the local $\Delta T(x)$. However, the equivalent changes under laminar conditions [Eq. (4-192)] are much greater. Reynolds et al. (1958, part 3) also study other cases of varying wall temperature, such as a delayed ramp or a suddenly insulated wall. Note that the previous solution is valid only for flat-plate flow with a smooth, impermeable wall. The same superposition scheme applies to other conditions, such as favorable or adverse pressure gradients, but new indicial functions analogous to [Eq. \(6-173\)](#) would have to be found and integrated.

6-10.6 Turbulent Convection with Pressure Gradients

For turbulent heat transfer with both wall temperature *and* freestream velocity varying, several analyses are possible: (1) a remarkably simple quadrature scheme; (2) an inner variable integral method; or (3) various differential methods, including eddy conductivity computations and the $K - \epsilon$ two-equation approach. Fundamentally, the temperature plays the role of a passive scalar in the energy Eq. (6-21c), which can be added to the continuity and momentum relations.

In this case, a simple and reliable theory is due to Ambrok (1957), who solves a modeled energy-integral equation so that the local turbulent Stanton number can be calculated by simple quadrature using

$$C_h(x) \approx 0.0295Pr^{-0.4} \frac{r_0^{0.25}(T_w - T_e)^{0.25} \mu^{0.2}}{\left[\int_0^x r_0^{1.25}(T_w - T_e)^{1.25} \rho U_e dx \right]^{0.2}} \quad (6-178)$$

where $r_0(x)$ denotes the surface radius of an axisymmetric body ([Fig. 4-39](#)). If the body is two-dimensional, one simply drops out the r_0 terms. Note that in the limit of constant $T_w - T_e$ and constant U and r_0 , [Eq. \(6-178\)](#) reduces to

$$C_h \approx 0.0295Pr^{-0.4}Re_x^{-0.2} \approx \frac{C_f}{2Pr^{0.4}} \quad (6-179)$$

This is approximately the same as the traditional Reynolds analogy in Sec. 6-10.3.

By extending the momentum method of Das (1988) to the thermal-energy equation, Sucec (1999) develops an inner variable, turbulent-boundary-layer integral method for heat transfer. Its outcome consists of an added “thermal” first-order differential equation for temperature parameters, similar to [Eq. \(6-130\)](#). The corresponding analysis includes variable wall blowing and suction, and the results agree quite well with heat-transfer data for flat plates and for pressure gradients.

Another inner variable integral method that includes both skin friction and wall heat flux is developed by White et al. (1973). By defining and integrating simplified wall functions for velocity and temperature, two coupled first-order ordinary differential equations are expressed in terms of two dimensionless variables:

$$\lambda_1 = \frac{U_e}{v^*} \left(\frac{T_w}{T_e} \right)^{1/2} \quad \lambda_2 = \frac{q_w}{\rho U_e^3} \frac{T_e}{T_w} \quad (6-180)$$

Assuming known $U_e(x)$, $T_e(x)$, and $T_w(x)$ —an arbitrary Mach number $Ma_e(x)$ is also allowed—one solves for $\lambda_1(x)$ and $\lambda_2(x)$, and then deduces $v^*(x)$ and $q_w(x)$.

Differential methods can be easily extended to include heat transfer by finite-difference solutions of the energy Eq. (6-21c), using the known velocity components from the momentum analysis of Sec. 6-8.3.1 and the assumption of constant Pr_t , so that the eddy conductivity may be estimated from $k_t = c_p \mu_t / Pr_t$. The overlap and outer layer eddy-viscosity models of Fig. 6-23 still hold, even in the presence of heat transfer, pressure gradients, and wall transpiration. This is confirmed through the mixing-length measurements reported by Moffat and Kays (1984) in Fig. 6-46. The experimental data sets shown therein are well approximated by $\ell = \kappa y$ in the overlap layer and $\ell = 0.09\delta$ in the outer wake.

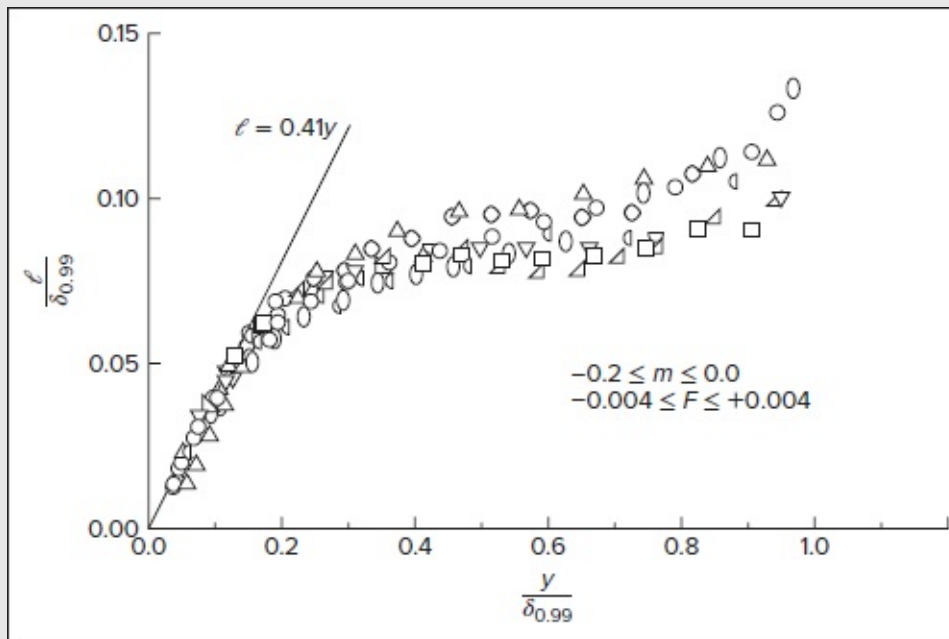


FIGURE 6-46

Measured values of turbulent mixing length for decelerating flows, $U_e = Cx_m$, and for wall blowing and suction, $F = v_w / U_e$. [After Moffat and Kays (1984).]

Although the mixing length varies near the wall, the graphical scale of [Fig. 6-46](#) is insufficient to depict the rapid changes in the sublayer damping constant A as predicted from [Eq. \(6-90\)](#). Moffat and Kays (1984) recommend an empirically based algebraic correlation for the van Driest damping constant, specifically:

$$A \approx \frac{26}{1 + a[v_w^+ + bp^+/(1 + cv_w^+)]} \quad (6-181)$$

where p^+ is prescribed by [Eq. \(6-100\)](#) and where

$$\begin{cases} a = 7.10 & \text{if } v_w^+ \geq 0 & \text{and} & a = 9.0 & \text{if } v_w^+ < 0 \\ b = 5.24 & \text{if } p^+ \leq 0 & \text{and} & b = 2.9 & \text{if } p^+ > 0 \\ c = 10.0 & \text{if } p^+ \leq 0 & \text{and} & c = 0.0 & \text{if } p^+ > 0 \end{cases}$$

It should be noted that the two-equation methods can also accommodate the energy equation for heat-transfer computations. Jones and Launder (1972) report good agreement of their $K - \epsilon$ model with four different runs in the experiments of Moretti and Kays (1965) for varying $U_e(x)$ and $T_w(x)$.

[Figure 6-47](#) compares theory and experiment corresponding to one run of Moretti and Kays (1965) for which the freestream velocity has a favorable gradient and the wall temperature changes abruptly in the middle of the run. Good agreement is achieved in [Fig. 6-47](#) with the theories of Ambrok (1957), White et al. (1973), and Herring and Mellor (1968). Jones and Launder (1972) do not report results for this particular run but show excellent results for four related tests.

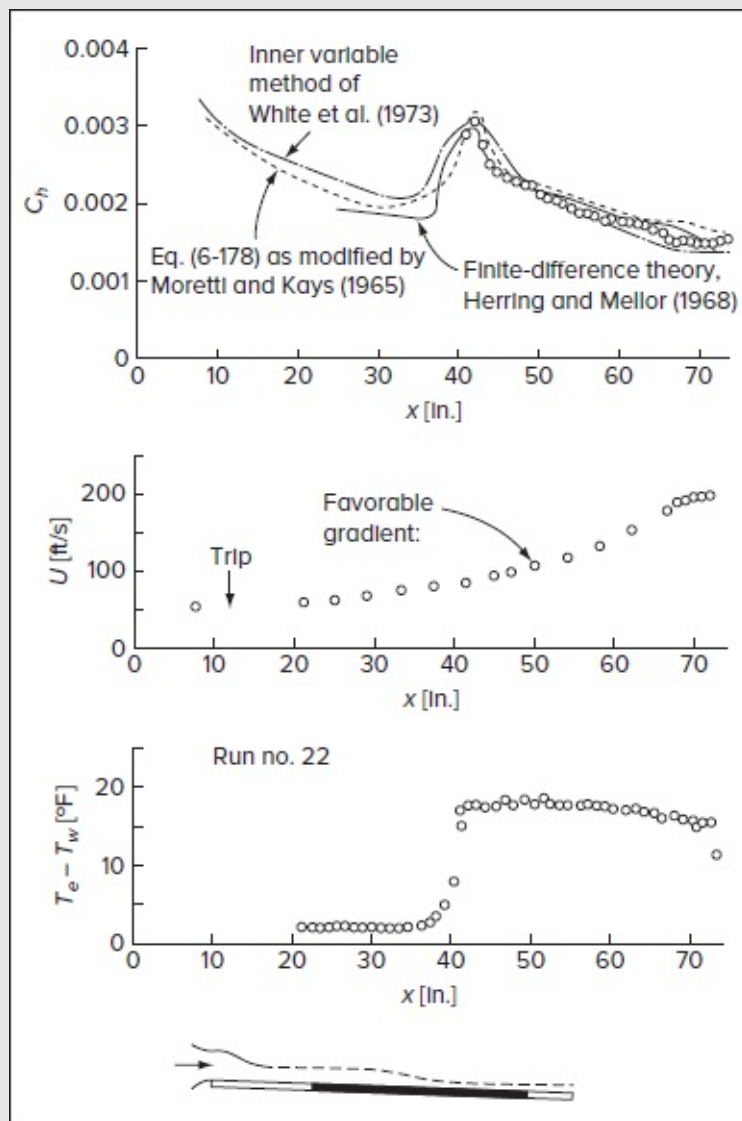


FIGURE 6-47

Comparison of theory and experiment for the variable-velocity and wall temperature experiment of Moretti and Kays (1965).

SUMMARY

This chapter presents an introduction to the analysis of turbulent time-averaged flows. No detailed treatment is given of the statistical theory of turbulence. The discussion emphasizes engineering properties of turbulent shear layers, such as mean velocity and temperature profiles, wall friction, flow separation, and heat transfer.

After deriving the Reynolds time-averaged equations of turbulent flow, semiempirical correlations are presented for the inner, outer, and overlap velocity layers in wall-related

flows. Simple analyses are then performed for turbulent flow in ducts and past flat plates. For more complex flows, turbulence *modeling* is introduced through the concepts of eddy viscosity, mixing length, $K - \epsilon$ closure, Reynolds stress, and algebraic stress formulations.

Turbulent boundary layers with pressure gradients are studied by both integral and finite-difference methods. Free turbulence—jets, wakes, and mixing layers—are then discussed. The subject of turbulent heat transfer is briefly treated by introducing and applying the temperature law of the wall, the turbulent Prandtl number, the eddy conductivity, and the Reynolds analogy; other parametric effects due to variable pressure gradients, wall suction and blowing, and surface temperatures are also considered and discussed.

Because of its practical importance and inherent complexity, turbulent-flow research is the most active field in fluid mechanics. Since turbulent fluctuation length scales and frequencies cover such a broad spectrum, present supercomputers—or even mega-supercomputers—are still struggling to resolve the full details of high Reynolds number flows. In the immediate future, we anticipate turbulence research to continue to concentrate on detailed experiments and improved semiempirical models of turbulent flow.

Page 393

PROBLEMS

- 6-1. By direct substitution of the fluctuation definitions [Eqs. \(6-6\)](#) and the use of averaging rules given by [Eqs. \(6-7\)](#), develop the three-dimensional time-averaged x -momentum equation and show what reductions occur in a steady two-dimensional turbulent boundary layer.
- 6-2. Using the Navier–Stokes equations for cylindrical coordinates from App. G and the concepts of [Eqs. \(6-6\)](#) and [\(6-7\)](#), develop a three-dimensional Reynolds stress z -momentum relation for turbulent flow. Simplify this to axial boundary-layer flow along the outside of a cylinder.
- 6-3. Consider turbulent flow past an isothermal flat plate of width b and length L with constant (ρ, μ, C_p, k) . Assume $\delta u \approx \delta T$, that is, $Pr \approx 1$. At $x = 0$, the flow has uniform velocity U and temperature T_e . At $x = L$, the mean flow may be approximated by the one-seventh power-law profiles:

$$\frac{u}{U} \approx \frac{T - T_w}{T_e - T_w} \approx \left(\frac{y}{\delta}\right)^{1/7}$$

There is no information about the flow structure between the leading and trailing edges. Use a control-volume analysis to estimate, on one side of the plate, (a) the total friction drag and (b) the total heat transfer in terms of the boundary-layer thickness.

- 6-4. The experiment of Clauser (1954), flow 2200 of Coles and Hirst (1968), used air at

24°C and 1 atm. At the first station, $x = 6.92$ ft, the turbulent-boundary-layer velocity data are as follows:

y [in]	u [ft/s]	y [in]	u [ft/s]
0.1	16.14	0.8	22.88
0.15	17.02	0.9	23.70
0.2	17.54	1.0	24.38
0.25	18.16	1.25	26.51
0.3	18.69	1.5	28.21
0.4	19.60	2.0	31.22
0.5	20.49	2.5	32.27
0.6	21.24	3.0	32.44
0.7	22.03	3.5	32.50

The boundary-layer thickness was 3.5 in, and the local freestream velocity gradient was $dU / dx \approx -1.06 \text{ s}^{-1}$. Analyze these measurements with suitable plots and formulas to establish (a) the inner law and wall shear stress, (b) the outer law with Clauser's parameter β and the Coles wake parameter Π , and (c) the logarithmic overlap.

- 6-5.** Analyze the velocity data of Prob. 6-4 to achieve a power-law overlap approximation, as in [Eq. \(6-50\)](#). Find α and C and compare with [Eq. \(6-50\)](#). To save work, use [Eq. \(6-69\)](#) to estimate the momentum thickness. At this station, the wall shear stress is approximately 0.0027 lbf /ft². (Hint: Use only the first 10 data points, the rest are well into the wake region.)
- 6-6.** For developed turbulent smooth wall pipe flow, assuming that the log-law analysis of Sec. 6-5.1 is valid with $\kappa = 0.41$, show that the maximum pipe velocity may be computed from

$$\frac{u_{\max}}{u_{\text{av}}} \approx 1 + 1.29\Lambda^{1/2}$$

where Λ is the Darcy friction factor.

- 6-7.** Water at 20°C flows through a smooth pipe of diameter 3 cm at 30 m³ /h. Assuming developed flow, estimate (a) the wall shear stress (in Pa), (b) the pressure drop (in Pa/m), and (c) the centerline velocity in the pipe. What is the maximum flow rate for which the flow would be laminar? What flow rate would give $\tau_w = 100$ Pa?
- 6-8.** The overlap region of Clauser's velocity profile in Prob. 6-4 may be fitted by a power-law estimate $u^+ \approx 7.5(y^+)^{1/6}$. Use this result to estimate the wall shear stress in lbf /ft² and the shape factor H .
- 6-9.** Consider fully developed turbulent flow through a duct of square cross section. Taking advantage of the double symmetry, analyze this problem using the log-law,

Eq. (6-38a), and a suitable assumption regarding the variation of shear stress around the cross section. Compare your result for Λ with the hydraulic-radius concept.

- 6-10.** In the overlap layer, turbulent shear is dominant, and the effect of viscosity is small. Suppose that we neglect μ and replace [Eq. \(6-32\)](#) by the approximate gradient relationship

$$\frac{d\bar{u}}{dy} \approx f(y, \tau_w, \rho)$$

Show, by dimensional analysis, that this relation leads directly to the logarithmic overlap law, Eq. (6-38a).

- 6-11.** Use the log-law of Eq. (6-38a) to analyze turbulent flow through a smooth concentric annulus of inner radius r_i and outer radius r_o . Find expressions for the velocity distribution $u(r)$ and the friction factor Λ . Compare your friction result with thePage 394 hydraulic-radius approximation. (The maximum velocity does not occur midway in the annular region but could be so assumed as a first approximation.)
- 6-12.** Modify the flat-plate integral analysis of Sec. 6-6.1 by using [Eq. \(6-71\)](#) rather than [Eq. \(6-69\)](#) to combine with [Eq. \(6-67\)](#). (Numerical integration may be necessary.) Compare your results for the friction factor and boundary-layer thickness with [Eqs. \(6-70\)](#).
- 6-13.** The flat-plate formulas of Sec. 6-6 assume turbulent flow beginning at the leading edge ($x = 0$). More likely, there is an initial region of laminar flow, as in [Fig. P6-13](#).

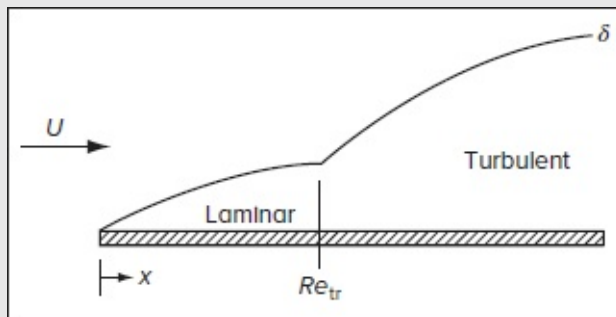


FIGURE P6.13

Devise a scheme to compare $\delta(x)$ and $C_f(x)$ in the turbulent region, $Re > Re_{tr}$, by accounting for the laminar part of the flow.

- 6-14.** Water at 20°C and 1 atm flows at 6 m/s past a smooth flat plate 1 m long and 60 cm wide. Estimate (a) the trailing-edge displacement thickness, (b) the trailing-edge

wall shear stress, and (c) the drag of one side of the plate, if $Re_{x, tr} = 10^6$.

- 6-15.** Modify Prob. 6-14 to pose the same questions if the plate has an average roughness height of 0.1 mm. Also estimate the value of the log-law shift ΔB at the trailing edge.
- 6-16.** Derive Stevenson's law of the wall with suction or blowing, [Eq. \(6-86\)](#).
- 6-17.** Rewrite Stevenson's relation [Eq. \(6-86\)](#) in the form of a wall-friction law with suction or blowing. Show that the ratio of C_f to the impermeable wall value C_{f0} is approximately a function only of a "blowing parameter" $B = (2v_w)/(U_e C_f)$. Plot C_f/C_{f0} vs. B in the range $-0.5 < B < 2.0$ and compare your results with the correlation $[\ln(1 + B)]/B$ recommended by Kays and Crawford (1980, p. 181).
- 6-18.** Water at 20°C flows through a smooth permeable pipe of diameter 8 cm. The volume flow rate is 0.06 m³/s. Estimate the wall shear stress, in pascals, if the wall velocity is (a) 0.01 m/s blowing, (b) 0 m/s, and (c) 0.01 m/s suction. To avoid excessive iteration, assume that the ratio of average to centerline velocity is 0.85.
- 6-19.** Use Stevenson's [Eq. \(6-86\)](#) to develop a formula for wall friction in pipe flow with blowing or suction. Apply your result to Prob. 6-7 modified so that the wall blowing rate is 3 cm/s.
- 6-20.** As an alternative to [Eq. \(6-62\)](#), Bergstrom et al. (2002) suggest the following formula for the downshift of the log-law of [Eq. \(6-60\)](#) due to uniform surface roughness of height k :

$$\Delta B \approx \frac{1}{k^+} \ln(k^+) - 3.5 \quad \text{for } k^+ \geq 4.2$$

First compare this correlation, using a sketch or graph, to [Eq. \(6-62\)](#). Then apply this correlation to derive a formula for the pipe-friction factor Λ , similar to [Eq. \(6-64\)](#).

- 6-21.** Use numerical quadrature to evaluate and sketch [Eq. \(6-96\)](#) for zero pressure gradients. Compare your results with [Eq. \(6-41\)](#) and [Fig. 6-11](#).
- 6-22.** Use the log-law, [Eq. \(6-38a\)](#), to analyze Couette flow between parallel plates a distance $2h$ apart, with the upper plate moving at velocity U . Show that the turbulent-flow velocity profile is S-shaped, as in [Fig. 3-5](#). Sketch the profile for $Uh/\nu = 10^5$ and compute the ratio $\tau_w h / (\mu U)$ for this condition.
- 6-23.** Use the log-law [Eq. \(6-38a\)](#) to analyze steady turbulent flow about a long cylinder of radius R rotating at an angular rate ω in an infinite fluid. Derive the skin friction, $C_f = 2\tau_w / (\rho \omega^2 R^2)$, and sketch its variation vs. $Re = \omega R^2 / \nu$.

- 6-24.** Consider the flat-plate flow of Prob. 6-14. Use any integral method from Sec. 6-8 to predict the distribution of $\tau_w(x)$, $\delta^*(x)$, and $H(x)$ along the plate surface. Compare your results with the traditional algebraic flat-plate formulas. For simplicity, neglect the laminar region and begin at $x = 4$ cm with $C_f \approx 0.005$.
- 6-25.** To illustrate the increased resistance of a turbulent boundary layer to separation, compute the Howarth freestream velocity distribution, $U = U_0 (1 - x / L)$, using an integral method from Sec. 6-8. Assume turbulent flow from the leading edge ($x = 0$) and find the separation point x_{sep} / L for $U_0 L / \nu = (a) 10^6$, $(b) 10^7$, and $(c) 10^8$.

Page 395

- 6-26.** Assume potential flow past a cylinder, $U = 2U_0 \sin(x / a)$, with a turbulent boundary layer starting from the stagnation point. Use any turbulent-boundary-layer integral method to compute the value of the separation point ϕ_{sep} for a Reynolds number $U_0 a / \nu$ equal to $(a) 10^6$, $(b) 10^7$, and $(c) 10^8$. Compare with the laminar value $\phi_{\text{sep}} \approx 105^\circ$.
- 6-27.** Use an integral method of Sec. 6-8 to compute the skin-friction distribution for experiment II of Clauser (1956), flow 2300 of Coles and Hirst (1968). The experimental freestream velocity and skin friction are tabulated. The kinematic viscosity of the fluid (air) was $0.000165 \text{ ft}^2 / \text{s}$. Compare your computed results with the experiment. The average deviation of the seven “good” methods at the Stanford Conference for this experiment was approximately ± 15 percent.

x [ft]	U [ft/s]	C_f (exp)
7.5	26.1	0.00127
9.0	24.8	0.00115
11.0	23.5	0.00110
12.67	22.8	0.00104
16.17	21.3	0.00105
19.17	20.2	0.00105
23.92	18.9	0.00095
26.67	18.1	0.00085

- 6-28.** Use any integral method from Sec. 6-8 to compute $C_f(x)$ for the experiment of Moses, case 5 [flow 4000 of Coles and Hirst (1968)]. The fluid is air with $\nu = 0.000166 \text{ ft}^2 / \text{s}$. The experimental freestream velocity and skin-friction data are tabulated. Plot your computer results and compare with the experimental measurements.

x , ft	U , ft/s	C_f (exp)
0.0	82.00	0.00471
0.162	76.26	0.00429
0.323	69.09	0.00347
0.484	61.36	0.00233
0.646	55.49	0.00146
0.865	51.14	0.00090
1.058	49.54	0.00090
1.303	48.93	0.00156
1.516	48.65	0.00215
1.734	48.79	0.00251
1.979	48.86	0.00278
2.198	48.51	0.00280
2.438	48.86	0.00294
2.683	49.13	0.00306
2.928	48.16	0.00305

- 6-29.** Using the similarity concepts of Sec. 6-9, derive power-law expressions, similar to Table 6-3, for the variation of the total mass flux with x in the developed region of (a) a plane jet, (b) a circular jet, and (c) a plane mixing layer. Compare these with laminar-flow results.
- 6-30.** At a certain cross section in a developed turbulent plane water jet, the maximum velocity is 3 m/s and the mass flow is 800 kg/s per meter of width. Estimate (a) the jet width, (b) the maximum velocity, and (c) the total mass flow at a position 2 m further downstream.
- 6-31.** Air at 20°C and 1 atm issues at 0.001 kg/s from a 4 mm diameter orifice into still air. At a section in the jet 1 m downstream of the orifice, estimate (a) the maximum velocity, (b) the jet width, and (c) the ratio μ_t/μ .
- 6-32.** As part of a low-temperature thermal-power design, a long 5 m diameter vertical cylinder is placed in the ocean. The current across the cylinder is 60 cm/s. At a point 1 km downstream of the cylinder, estimate (a) the wake width (in m) and (b) the maximum velocity defect (in cm/s).
- 6-33.** Evaluate the temperature law of the wall, [Eq. \(6-164\)](#), numerically, using the van Driest eddy viscosity per [Eq. \(6-90\)](#), for $Pr_t = 1.0$ and various values of Pr . Compare your results with [Eqs. \(6-165\)](#) and [\(6-166\)](#).
- 6-34.** Air at 20°C and 1 atm flows at 60 m/s past a smooth flat plate 1 m long and 60 cm wide. The plate surface temperature is 50°C. Estimate the total heat loss (in W) from one side of the plate.
- 6-35.** Modify Prob. 6-34 if the fluid is water flowing at 6 m/s.
- 6-36.** Modify Prob. 6-34 (for airflow) if the plate is permeable, with a uniform blowing

velocity of 2 cm/s.

- 6-37.** Water at 20°C and 1 atm flows at 4 kg/s into a smooth tube of diameter 3 cm and length 2 m. If the tube wall temperature is 40°C, estimate the average outlet temperature of the water.

Page 396

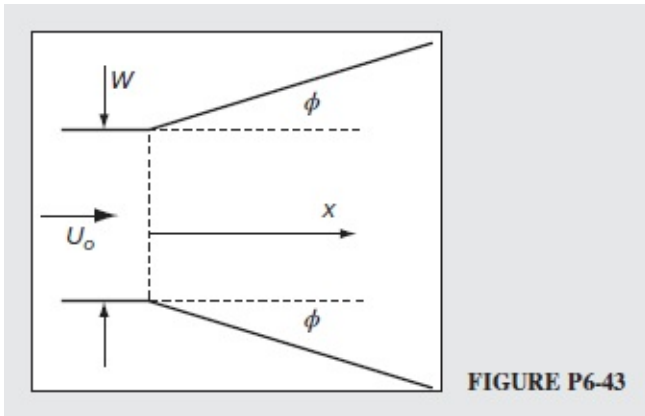
- 6-38.** Reconsider the liquid film flowing down an inclined plane from Prob. 3-15. This time, let the flow be *turbulent* and of constant depth h . Using the log-law for the velocity, (a) find an expression for the bottom wall shear stress as related to ρ , g , μ , θ , h and the surface velocity U_s . (b) Find a formula for the flow rate Q per unit width and compare to laminar flow, $Q \propto h^3$.
- 6-39.** Use the method of Ambrok, [Eq. \(6-178\)](#), to estimate the heat transfer from an isothermal cylinder at $Re_D = 10^6$ and $Pr = 1.0$. Compare your overall Nusselt number with the experimental value of $Nu_D \approx 1400$.
- 6-40.** Investigate the possibility of modifying the explicit or implicit finite-difference boundary-layer methods of Secs. 4-7.1 and 4-7.2 to a two-dimensional *turbulent* boundary layer, using an eddy-viscosity model. Explain any difficulties that arise.
- 6-41.** Assuming eventual success with the development of a turbulent finite-difference technique in Prob. 6-40, apply the method to compute $C_f(x)$ in flat-plate flow at $Re_L = 10^6$. Take the flow to be turbulent starting at the leading edge.
- 6-42.** Use the log-law of [Eq. \(6-38a\)](#) to analyze turbulent flow near a rotating disk of radius R and angular velocity ω . Let the crossflow velocity w be given by a parabolic hodograph assumption:

$$\bar{w} \approx \bar{u} \left(1 - \frac{y}{\delta}\right)^2 \tan \beta \quad \beta \approx 12^\circ$$

Recall the hodograph concept of [Fig. 4-45](#). Derive expressions for the skin friction C_f and the moment coefficient $C_M = 4M / (\rho \omega^2 R^5)$ as a function of the disk Reynolds number $Re = \omega R^2 / \nu$. Compare your results with the formulas given by Kármán (1921): $C_f \approx 0.053/Re^{1/5}$ and $C_M \approx 0.1463/Re^{1/5}$. See [Fig. 3-37](#), which contains data from Theodorsen and Regier (1944).

- 6-43.** Consider a two-dimensional flat-walled diffuser, as in [Fig. P6-43](#). Assume incompressible flow with a one-dimensional freestream velocity $U(x)$ and entrance velocity U_0 at $x = 0$. The entrance height is W and the constant depth into the paper is $b = 4W$. Assume turbulent flow at $x = 0$, with momentum thickness $\theta/W = 0.02$, $H(0)$

$= 1.3$, and $U_0 W / \nu = 10^5$. Using the method of Head, Sec. 6-8.1.2, numerically estimate the angle ϕ for which separation will occur at $x = 1.5W$.



- 6-44.** Solve Prob. 6-43 instead by the Kármán method of Sec. 6-8.1.1. Investigate the behavior of the solution for three different Reynolds numbers of $U_0 W / \nu = 10^5$, 10^6 , and 10^7 . Do you expect the separation angle ϕ to increase as the Reynolds number increases?
- 6-45.** Solve Prob. 6-43 again by Head's method if the diffuser is an expanding *cone* with an inlet pipe of diameter W . This time there is no “depth into the paper b .” For a given Reynolds number, do you expect a cone to have a smaller separation angle ϕ than a flat-walled diffuser?
- 6-46.** The sink flow of [Fig. 4-21](#), if begun far out with a turbulent boundary layer, may relaminarize as it approaches the origin. Show that the acceleration parameter K_{crit} relates to the sink flow and also relates to the Reynolds number of the flow. According to K_{crit} data, what Reynolds number should cause the sink flow to relaminarize?
- 6-47.** As an improvement on Stevenson's inner velocity law with suction and blowing, given by [Eq. \(6-86\)](#), Oljaca and Sucec (1997) offer the following inner/overlap/outer velocity profile formula based on wall transpiration data compiled by Donald Coles in 1971:

$$u^+ \approx \sigma + \frac{2\Pi}{\kappa} f + \frac{v_w^+}{4} \left(\sigma^2 + \frac{4\Pi}{\kappa} \sigma f + \frac{4\Pi^2}{\kappa^2} f^2 \right); \quad \sigma = \frac{1}{\kappa} \ln(y^+) + A$$

The function $f \approx 3 (y / \delta)^2 - 2 (y / \delta)^3$ defines the wake shape, as in [Eq. \(6-46\)](#) and the constant $A \approx 5$ for moderate blowing or suction. Show how this profile differs from the [Fig. 6-22](#) curves for $v_w^+ = \pm 0.02$ and also compare it with [Fig. 6-44a](#) for $v_w^+ = \pm 0.0038$.

6-48. Consider as a starting point the shear stress expression in the viscous sublayer, i.e.

$$\tau = \mu \frac{\partial \bar{u}}{\partial y} - \rho \bar{u}'\bar{v}' = \text{const}$$

Make the necessary assumptions and simplifications leading to the linear relation, $u^+ = y^+$.

6-49. Consider as a starting point the shear stress expression in the log layer, i.e.

$$\tau = \mu \frac{\partial \bar{u}}{\partial y} - \rho \bar{u}'\bar{v}' = \text{const}$$

Make the necessary assumptions and simplifications, including the mixing-length approximation, that result in the logarithmic relation, $u^+ = \kappa^{-1} \ln y^+ + B$.

6-50. The average velocity for a turbulent pipe flow can be evaluated using the expression,

$$u_{av} = \frac{Q}{A} = \frac{1}{\pi a^2} \int_0^a \bar{u}(r) dA = \frac{1}{\pi a^2} \int_0^a \bar{u}(r) 2\pi r dr = \frac{2}{a^2} \int_0^a \bar{u}(y)(a-y) dy$$

where the simple $y = a - r$ coordinate transformation is used, with y being the dimensional distance from the wall. Assuming that the law of the wall is accurate all the way to the wall, i.e., neglecting the very thin viscous sublayer, substitute the log-law, $u^+ = \kappa^{-1} \ln y^+ + B$, into the average velocity definition to prove that

$$\frac{u_{av}}{v^*} = \frac{1}{\kappa} \ln \left(\frac{av^*}{\nu} \right) + B - \frac{3}{2\kappa}$$

Hint: Before substituting $u^+ = \kappa^{-1} \ln y^+ + B$ into the average velocity integral, express it first as

$$\frac{\bar{u}(y)}{v^*} = \frac{1}{\kappa} \ln \left(\frac{yv^*}{\nu} \right) + B$$

6-51. The wall-friction factor in a pipe of radius a is defined as

$$C_f = \frac{\Lambda}{4} \equiv \frac{2\tau_w}{\rho u_{av}^2}$$

where Λ is the Darcy friction factor. (a) Show that the following identities hold:

$$\frac{u_{av}}{v^*} = \sqrt{\frac{2}{C_f}} \quad \text{and} \quad \frac{av^*}{\nu} = Re_D \sqrt{\frac{C_f}{8}}, \quad \text{where} \quad Re_D = \frac{(2a)u_{av}}{\nu}$$

(b) Substitute these identities into our previous result, namely,

$$\frac{u_{av}}{v^*} = \frac{1}{\kappa} \ln \left(\frac{av^*}{\nu} \right) + B - \frac{3}{2\kappa}$$

Then using $\kappa = 0.41$, $B = 5.0$, and $\log_{10}(x) = \ln(x)/\ln 10$, derive Prandtl's 1935 Darcy friction factor formula for smooth pipes, namely,

$$1/\sqrt{\Lambda} = 1.99 \log_{10}(Re_D \sqrt{\Lambda}) - 1.02; \quad \Lambda \equiv 4C_f$$

Note that Prandtl slightly adjusted the constants in this correlation to better fit pipe-friction measurements at low Reynolds numbers, thus leading to [Eq. \(6-54\)](#).

- 6-52.** One of the simplest ways to recapture the Reynolds stress is to time-average the conservation form of the axial momentum equation in Cartesian coordinates. (a) Start by expanding

$$\frac{\partial(u^2)}{\partial x} + \frac{\partial(uv)}{\partial y} = -\frac{1}{\rho} \frac{dp}{dx} + \nu \frac{\partial^2 u}{\partial y^2} \text{ (axial momentum in conservation form)}$$

Then using the continuity equation, show that the result is identical to the traditional form:

$$u \frac{\partial u}{\partial x} + v \frac{\partial u}{\partial y} = -\frac{1}{\rho} \frac{dp}{dx} + \nu \frac{\partial^2 u}{\partial y^2} \text{ (steady, incompressible, axial momentum form)}$$

(b) By substituting the Reynolds decomposed variables, $u = \bar{u} + u'$, $v = \bar{v} + v'$, $p = \bar{p} + p'$, into the conservation form, time-averaging, cancelling terms that average out, and assuming that streamwise variations in $\overline{u'u'}$ are much slower than the cross-streamwise variations in $\overline{u'u'}$, show that

$$\bar{u} \frac{\partial \bar{u}}{\partial x} + \bar{v} \frac{\partial \bar{u}}{\partial y} = -\frac{1}{\rho} \frac{d\bar{p}}{dx} + \nu \frac{\partial^2 \bar{u}}{\partial y^2} + \frac{\partial}{\partial y}(-\overline{u'v'})$$

Page 398

Hint: The time-averaged products of mean and fluctuating quantities, such as $\overline{uu'}$, $\overline{uv'}$, $\overline{vu'}$, and $\overline{vv'}$, all vanish identically. Similarly, the time-averaged fluctuating quantities vanish unless they are squared or multiplied by other fluctuating quantities. Finally, the time-averaged mean quantities are the mean quantities.

- 6-53.** The average velocity for a turbulent channel flow can be evaluated using the expression,

$$u_{av} = \frac{Q}{A} = \frac{1}{h} \int_0^h \bar{u}(y) dy$$

where h represents the distance from the wall to the midsection plane of the channel. Assuming that the law of the wall is accurate all the way to the wall, i.e., neglecting the very thin viscous sublayer, substitute the log-law, $u^+ = \kappa^{-1} \ln y^+ + B$, into the average velocity definition to prove that

$$\frac{u_{av}}{v^*} = \frac{1}{\kappa} \ln\left(\frac{h v^*}{\nu}\right) + B - \frac{1}{\kappa}$$

- 6-54.** Because a channel is not round, it is necessary to use the concept of a hydraulic diameter on which the Reynolds number can be based. For a sufficiently wide channel of height $2h$, (a) show that the hydraulic diameter is $D_h = 4A/P = 4h$. Next, (b) using $Re_D h = (4h)u_{av}/\nu$, and recalling that $u_{av}/v^* \equiv (8/\Lambda)^{1/2}$, show that

$$\frac{h v^*}{\nu} = \frac{1}{8} \frac{4h u_{av}}{\nu} \sqrt{\frac{\Lambda}{2}} = \frac{1}{8\sqrt{2}} Re_{D_h} \sqrt{\Lambda}$$

(c) In addition, by substituting $\kappa = 0.41$, $B = 5.0$, and $\log_{10}(x) = \ln(x)/\ln 10$ into

$$\frac{u_{av}}{v^*} = \frac{1}{\kappa} \ln\left(\frac{h v^*}{\nu}\right) + B - \frac{1}{\kappa}$$

derive the Darcy friction factor formula for smooth channels, namely,

$$1/\sqrt{\Lambda} = 2.0 \log_{10}(Re_{D_h} \sqrt{\Lambda}) - 1.19$$

- 6-55.** Determine the beginning, ending and maximum entrance lengths in a circular duct of diameter $D = 0.03$ m with air flowing between 1 m/s (beginning) and 50 m/s (ending). Repeat the analysis in a square duct of 0.03 m height. For air, use a density of 1.2 kg/m^3 and a viscosity of $1.8 \times 10^{-5} \text{ kg/(m} \cdot \text{s)}$. Recall that the hydraulic diameter can be calculated using $D_h = 4A/P$. Calculate the velocity leading to the maximum entrance lengths in both circular and square ducts.

- 6-56.** Because of the popularity of power-law profiles in turbulent boundary layer studies, Majdalani (2018) introduced a generic mean-flow pattern of the form:

$$\frac{\bar{u}}{U_e} \equiv F(\xi) = \xi^{1/q}$$

where $\xi \equiv y/\delta$ represents the fractional distance within the turbulent boundary layer and the power-law exponent $q = \{5, 6, 7, 8, 9\}$ can be used to prescribe the value that best captures the motion under consideration.

(a) Based on [Eq. \(6-28\)](#), show that the normalized displacement and momentum thicknesses, η^* and θ^* , as well as the shape factor H , can be expressed as direct functions of q , namely,

$$\begin{cases} \eta^* \equiv \frac{\delta^*}{\delta} = \int_0^1 (1 - F) d\xi = \frac{1}{q+1} & \text{(normalized displacement thickness)} \\ \theta^* \equiv \frac{\theta}{\delta} = \int_0^1 F(1 - F) d\xi = \frac{q}{(q+1)(q+2)} & \text{(normalized momentum thickness)} \\ H \equiv \frac{\delta^*}{\theta} = \frac{\eta^*}{\theta^*} = \frac{q+2}{q} & \text{(momentum shape factor)} \end{cases}$$

(b) Recognizing that most wall shear stress correlations, such as [Eqs. \(6-68\)](#) and [\(6-](#)

72), can be specified as functions of Re_δ , Majdalani wrote a generic expression of the form

$$\tau_w = C_w \rho u_{av}^2 \left(\frac{\nu}{u_{av} \delta} \right)^{1/m} \quad \text{or} \quad C_f = \frac{2C_w}{Re_\delta^{1/m}}$$

where C_w and m are characteristics of the problem at hand. Assuming no pressure gradients, apply the momentum-integral relation, given by Eq. (6-67), to obtain

$$\frac{d\delta}{dx} = \frac{C_w}{\theta^*} \left(\frac{\nu}{u_{av} \delta} \right)^{1/m}$$

Page 399

(c) After separating variables and integrating from $\delta(0) = 0$ to $\delta(x)$, show that the boundary layer thickness may be written as a function of the local Reynolds number, $Re_x = u_{av}x / \nu$, namely,

$$\frac{\delta}{x} = \frac{a}{Re_x^{1/(m+1)}}; \quad a \equiv \left(\frac{C_w m + 1}{\theta^* m} \right)^{\frac{m}{m+1}}$$

(d) Recalling that the friction coefficient may be defined as $C_f = 2\tau_w / (\rho u_{av}^2)$, show that

$$C_f = \frac{b}{Re_x^{1/(m+1)}}; \quad b \equiv 2 \left(\frac{m\theta^* C_w^m}{m+1} \right)^{\frac{1}{m+1}}$$

(e) Recalling that the displacement thickness may be specified as $\delta^* = \delta \int_0^1 (1 - F) d\xi$, show that

$$\frac{\delta^*}{x} = \frac{c}{Re_x^{1/(m+1)}}; \quad c \equiv \frac{1}{q+1} \left(\frac{C_w m + 1}{\theta^* m} \right)^{\frac{m}{m+1}}$$

(f) Recalling that the momentum thickness may be deduced from $\theta = \delta \int_0^1 F(1 - F) d\xi$, show that

$$\frac{\theta}{x} = \frac{d}{Re_x^{1/(m+1)}}; \quad d \equiv \frac{q}{(q+1)(q+2)} \left(\frac{C_w m + 1}{\theta^* m} \right)^{\frac{m}{m+1}}$$

(g) Using the continuity equation $\bar{v} = -\frac{\partial}{\partial x} \int_0^y \bar{u} dy$, integrate the axial velocity profile to show that

$$\frac{\bar{v}}{U_e} = e \frac{y}{x} \left(\frac{y}{\delta} \right)^{1/q}; \quad e \equiv \frac{m}{(m+1)(q+1)}$$

(h) Recognizing that Prandtl's 1927 power-law model uses $C_w = 0.0233$, $q = 7$, and m

= 4, determine the characteristic coefficients (a, b, c, d, e) and compare your results to [Eq. \(6-72\)](#).

(i) Recognizing that the wall–wake law of Coles uses $C_w = 0.010$, $q = 7$, and $m = 6$, determine the characteristic coefficients (a, b, c, d, e) and compare your results to [Eq. \(6-70\)](#).

CHAPTER 7

COMPRESSIBLE BOUNDARY-LAYER FLOW

I am, and ever will be, a white-socks, pocket-protector, nerdy engineer, born under the second law of thermodynamics, steeped in steam tables, in love with free-body diagrams, transformed by Laplace and propelled by compressible flow.

Neil Armstrong (1930–2012)

7-1 INTRODUCTION: THE COMPRESSIBLE-BOUNDARY-LAYER EQUATIONS

So far most of the text has been devoted to the analysis of incompressible viscous flow. If we allow the compressibility of a fluid to be a factor, density becomes a new important variable. In a compressible boundary layer, accelerations are significant and continuity is no longer trivial. Further, even in a compressible boundary layer, the normal pressure gradient is usually neglected, and $p \approx p_e(x)$, so that both pressure and density vary along with the temperature, which must also vary according to the thermodynamic state relation $T = T(p, \rho)$. Since most compressible flows are gases, by far the most common state relation is the perfect-gas relation $p = \rho RT$, and we must be careful to note that T in most models corresponds to the absolute temperature.

In deriving the two-dimensional compressible, laminar, boundary-layer equations, with (x, y) being parallel and normal to the wall, the same approximations hold: $v \ll u$ and $\partial/\partial x \ll \partial/\partial y$. We only need to remember that density is variable and that the dependence of k and μ on temperature can be important. Then, the two-dimensional boundary-layer equations for an arbitrary compressible fluid may be written as

$$\text{Continuity:} \quad \frac{\partial \rho}{\partial t} + \frac{\partial}{\partial x}(\rho u) + \frac{\partial}{\partial y}(\rho v) = 0 \quad (7-1a)$$

$$\text{x-momentum:} \quad \rho \left(\frac{\partial u}{\partial t} + u \frac{\partial u}{\partial x} + v \frac{\partial u}{\partial y} \right) \approx - \frac{\partial p_e}{\partial x} + \frac{\partial}{\partial y} \left(\mu \frac{\partial u}{\partial y} \right) \quad (7-1b)$$

$$\text{y-momentum:} \quad \frac{\partial p}{\partial y} \approx 0 \quad (7-1c)$$

$$\text{Energy:} \quad \rho \left(\frac{\partial h}{\partial t} + u \frac{\partial h}{\partial x} + v \frac{\partial h}{\partial y} \right) \approx \frac{\partial p_e}{\partial t} + u \frac{\partial p_e}{\partial x} + \frac{\partial}{\partial y} \left(k \frac{\partial T}{\partial y} \right) + \mu \left(\frac{\partial u}{\partial y} \right)^2 \quad (7-1d)$$

where $h = e + p/\rho$ is the enthalpy. The y-momentum equation is included simply as a reminder that the pressure variation is prescribed by the freestream. At this point, we have three equations in five unknowns (u , v , ρ , h , T) and therefore need two supplementary relations to correlate the two extra thermodynamic variables

$$T = T(p, \rho) \quad h = h(p, \rho)$$

Also, the freestream pressure gradient may be related to the velocity and enthalpy gradients through the Bernoulli equation for inviscid nonconducting flow

$$\frac{\partial p_e}{\partial x} = -\rho_e \left(\frac{\partial U_e}{\partial t} + U_e \frac{\partial U_e}{\partial x} \right) = \frac{\rho_e}{U_e} \frac{\partial h_e}{\partial t} + \rho_e \frac{\partial h_e}{\partial x} - \frac{1}{U_e} \frac{\partial p_e}{\partial t} \quad (7-2)$$

Page 401

Finally, it is assumed that we know how the transport coefficients vary

$$\mu = \mu(T) \quad k = k(T)$$

through, say, the power law or the Sutherland formulas discussed in [Chap. 1](#). The boundary conditions are, as usual, the no slip ($u = v = 0$) and the no temperature jump ($T = T_w$) at the surface and, at the outer edge, a smooth blending with the freestream conditions, ($u \rightarrow U_e$, $T \rightarrow T_e$, $h \rightarrow h_e$), with no requirement on v at the outer edge.

An equivalent relation that will shortly be shown to be useful can be realized by rewriting the energy Eq. (7-1d) in terms of the total enthalpy $H = h + u^2/2$ ($v^2/2$ being entirely negligible):

$$\mu \frac{DH}{Dt} = \frac{\partial p_e}{\partial t} + \frac{\partial}{\partial y} \left(k \frac{\partial T}{\partial y} + \mu u \frac{\partial u}{\partial y} \right) \quad (7-3)$$

This is seldom analyzed under unsteady conditions.

This chapter will concentrate on concepts and theories associated with viscous compressible flow. For further reading, several monographs on this subject may be consulted: Park (1990), Smits and Dussage (1996), Oosthuizen and Carscallen (1997), Laney (1998), Anderson (2000, 2002), Chattot (2002), Felcman et al. (2003), and Ockendon and Ockendon (2004). Somewhat to our disadvantage, the primary emphasis of these texts is on inviscid flow. There is a specialized book on supersonic jet flow, by Morris et al. (2002), and comprehensive review articles by Bradshaw (1977), Spina et al. (1994), and Monnoyer

(1997). Moreover, at least two boundary-layer texts, Schetz and Bowersox (2011) and Schlichting and Gersten (2017), have excellent sections on compressible motions.

7-1.1 Steady Isentropic Flow of a Perfect Gas

We are concerned here with *viscous* flow of gases. However, the freestream outside a compressible boundary layer is generally frictionless and adiabatic, thus often isentropic. Although one can deal computationally with an imperfect gas, here we assume an ideal gas with the following standard properties:

$$\begin{aligned} p &= \rho RT & R &= \text{specific gas constant} \approx 287 \text{ J/(kg} \cdot \text{K)} \text{ for air} \\ dh &= c_p dT & c_p(T) &= c_v(T) + R & \gamma(T) &= c_p/c_v \end{aligned} \quad (7-4)$$

If we further assume constant specific heats, then $h = c_p T$ and $\gamma = \text{constant} \approx 1.40$ for air. For steady flow with negligible friction and heat transfer, [Eq. \(7-3\)](#) may be integrated into

$$H = h + u^2/2 = c_p T + u^2/2 = \text{constant} \quad \text{or} \quad T_0 = \frac{H}{c_p} = T + \frac{u^2}{2c_p} = \text{constant} \quad (\text{stagnation temperature})$$

We have assumed *adiabatic* flow, which is generally true only in the freestream, where $u = U$. Substituting the ideal-gas relations $c_p = \gamma R/(\gamma - 1)$ and $a = \sqrt{\gamma RT}$ for the speed of sound, we obtain

$$\frac{T_0}{T} = \left(\frac{a_0}{a}\right)^2 = 1 + \frac{\gamma - 1}{2} Ma^2 \quad Ma = \frac{U}{a} \text{ (Mach number)} \quad (7-5)$$

Thus, for *adiabatic* flow, as the Mach number and kinetic energy increase, the freestream temperature and speed of sound decrease, slowly at first, then more rapidly, as shown in [Fig. 7.1](#). If we further assume *isentropic* conditions, then the pressure and density may be expressed using analogous relations, namely,

$$\frac{p_0}{p} = \left(\frac{T_0}{T}\right)^{\gamma/(\gamma-1)} = \left(1 + \frac{\gamma - 1}{2} Ma^2\right)^{\gamma/(\gamma-1)} \quad \frac{\rho_0}{\rho} = \left(\frac{T_0}{T}\right)^{1/(\gamma-1)} = \left(1 + \frac{\gamma - 1}{2} Ma^2\right)^{1/(\gamma-1)} \quad (7-6)$$

These two relations are plotted in [Fig. 7-1](#) and are seen to drop off faster with the Mach number. We will later compare these isentropic trends with the viscous boundary-layer behavior.

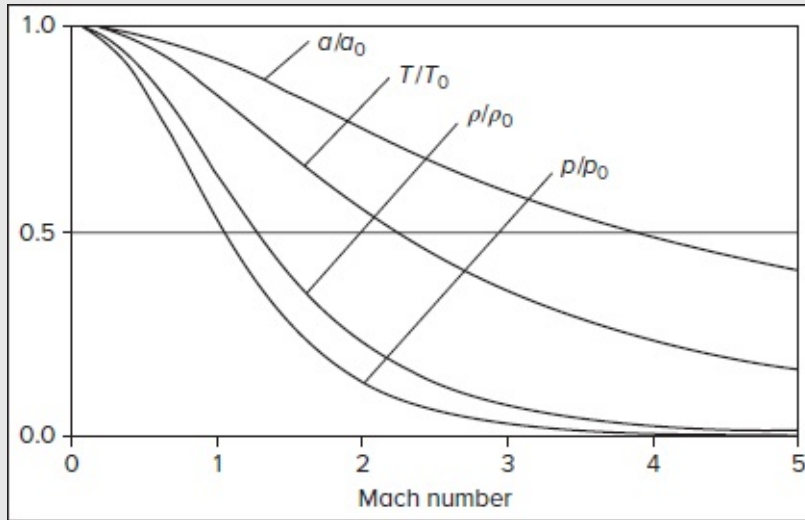


FIGURE 7-1

Adiabatic (T/T_0 and a/a_0) and isentropic (p/p_0 and ρ/ρ_0) perfect-gas properties versus Mach number for $\gamma = 1.4$.

Equations (7-5) and (7-6) are often solved numerically or, more traditionally, their predictions for a particular value of γ are tabulated over a range of Mach numbers for use in miscellaneous compressible flow calculations [Anderson (2003)]. More recently, Majdalani and Maicke (2012) showed that these equations could be combined with Stodola's area–Mach number relation and inverted analytically. Stodola's relation prescribes the area ratio as a function of the local Mach number,

$$\text{Stodola's relation: } \left(\frac{A}{A_t}\right)^2 = \frac{1}{Ma^2} \left\{ \frac{2}{\gamma+1} \left[1 + \frac{1}{2}(\gamma-1)Ma^2 \right] \right\}^{\frac{\gamma+1}{\gamma-1}} \quad \text{or} \quad \varepsilon^{\frac{1}{2}} = \frac{Ma \left[\frac{1}{2}(\gamma+1) \right]^{\frac{\gamma+1}{2(\gamma-1)}}}{\left[1 + \frac{1}{2}(\gamma-1)Ma^2 \right]^{\frac{\gamma+1}{2(\gamma-1)}}} \quad (7-7)$$

Page 402

where $\varepsilon \equiv (A_t/A)^2$ denotes the area ratio squared; the latter is based on the throat area A_t divided by the local area A in an isentropic expansion process. Since two roots exist for each area ratio, the corresponding subsonic and supersonic solutions must be sought separately. A highly accurate three-term approximation for the subsonic root is provided by Majdalani and Maicke (2013) as a direct function of the area ratio:

$$Ma_{\text{sub}} = \left(\frac{2}{\gamma+1} \right)^{\frac{\gamma+1}{2(\gamma-1)}} \frac{A_t}{A} + \frac{1}{4} \left(\frac{2}{\gamma+1} \right)^{\frac{\gamma+5}{2(\gamma-1)}} \left(\frac{A_t}{A} \right)^3 + \left[2^{\frac{15-5\gamma}{2(\gamma-1)}} (\gamma+1)^{\frac{3\gamma+7}{2-2\gamma}} (3\gamma+7) \right] \left(\frac{A_t}{A} \right)^5 + O \left[\left(\frac{A_t}{A} \right)^7 \right] \quad (7-8)$$

In most practical applications, a one-term expansion, namely, $Ma_{\text{sub}} \approx [2/(\gamma+1)]^{\frac{1}{2}(\gamma+1)/(\gamma-1)} A_t/A$ is sufficient, as it entails a less than 5% error for operational area ratios not exceeding 0.47 and

$\gamma = 1.7$. The use of three terms extends this range substantially to $A_t/A = 0.88$ using a conservative value of $\gamma = 1.2$. Given a fixed error bracket, reducing the value of γ increases the maximum value of A_t/A for which the approximation will continue to hold. Nonetheless, using Bürmann's theorem, Majdalani and Maicke (2013) show that the subsonic Mach number can be extracted to any desired order of accuracy using a simple recursive formula, namely,

$$Ma_{\text{sub}}^{(N)} = \sum_{n=0}^N \frac{(\gamma-1)^n \varepsilon^{n+\frac{1}{2}}}{(2n+1)! \left(\frac{1}{2}\gamma + \frac{1}{2}\right)^{(n+\frac{1}{2})\frac{\gamma+1}{\gamma-1}}} \frac{(2n)!}{n! 2^n} \prod_{m=0}^{n-1} \left[\left(n + \frac{1}{2}\right) \frac{\gamma+1}{\gamma-1} - m \right] + O(\varepsilon^{N+\frac{3}{2}}) \quad (7-9)$$

The corresponding subsonic approximations for the classical temperature, pressure, and density ratios may be expressed directly as a function of $\varepsilon = (A_t/A)^2$ using

$$\bar{T}_{\text{sub}} = \frac{T}{T_0} = 1 + 2^{\frac{2}{\gamma-1}} (1-\gamma)(1+\gamma)^{\frac{1+\gamma}{1-\gamma}} \varepsilon + 2^{\frac{3+\gamma}{\gamma-1}} (1-\gamma)(1+\gamma)^{\frac{2(\gamma+1)}{1-\gamma}} \varepsilon^2 + O(\varepsilon^3) \quad (7-10)$$

$$\bar{p}_{\text{sub}} = \frac{p}{p_0} = 1 - 2^{\frac{2}{\gamma-1}} \gamma (1+\gamma)^{\frac{1+\gamma}{1-\gamma}} \varepsilon - 3\gamma 2^{\frac{5-\gamma}{\gamma-1}} (1+\gamma)^{\frac{2(1+\gamma)}{1-\gamma}} \varepsilon^2 + O(\varepsilon^3) \quad (7-11)$$

and

$$\bar{\rho}_{\text{sub}} = \frac{\rho}{\rho_0} = 1 - 2^{\frac{2}{\gamma-1}} (1+\gamma)^{\frac{1+\gamma}{1-\gamma}} \varepsilon - 2^{\frac{5-\gamma}{\gamma-1}} (2+\gamma)(1+\gamma)^{\frac{2(\gamma+1)}{1-\gamma}} \varepsilon^2 + O(\varepsilon^3) \quad (7-12)$$

Majdalani and Maicke (2012) also show that all relations in [Eqs. \(7-5\)](#) and [\(7-6\)](#) can be cleverly consolidated into a single, universal expression, namely,

$$\varepsilon \xi = \bar{x} - \bar{x}^{\frac{\gamma+1}{2}} = \left\{ \frac{\bar{T}^{2/(\gamma-1)} - \bar{T}^{(\gamma+1)/(\gamma-1)}}{\bar{p}^{2/\gamma} - \bar{p}^{(\gamma+1)/\gamma}} \right\} \quad \text{where} \quad \bar{x} = \left\{ \frac{\bar{T}^{2/(\gamma-1)}}{\bar{p}^{2/\gamma}} \right\} \quad \text{and} \quad \xi \equiv \frac{\gamma-1}{\gamma+1} \left(\frac{2}{\gamma+1} \right)^{\frac{2}{\gamma-1}} \quad (7-13)$$

Page 403

The advantage here is that, by solving the universal expression for \bar{x} under subsonic or supersonic conditions, one directly unravels a generic solution to all three thermodynamic properties. For example, a substantially accurate five-term approximation may be expressed using,

$$\bar{x}_{\text{sub}} = 1 - 2^{\frac{\gamma+1}{\gamma-1}} (1+\gamma)^{\frac{1+\gamma}{1-\gamma}} \varepsilon - 2^{\frac{4}{\gamma-1}} (1+\gamma)^{\frac{3+\gamma}{1-\gamma}} \varepsilon^2 - \frac{1}{3} 2^{\frac{5+\gamma}{\gamma-1}} (3+\gamma)(1+\gamma)^{\frac{2(\gamma+2)}{1-\gamma}} \varepsilon^3 - 2^{\frac{9-\gamma}{\gamma-1}} (2+\gamma)(5+\gamma)(1+\gamma)^{\frac{5+3\gamma}{1-\gamma}} \varepsilon^4 + O(\varepsilon^5) \quad (7-14)$$

or, to an arbitrary truncation order,

$$\bar{x}_{\text{sub}} = \left\{ \frac{\bar{T}_{\text{sub}}^{2/(\gamma-1)}}{\bar{p}_{\text{sub}}^{2/\gamma}} \right\} = \sum_{n=0}^N \frac{\prod_{m=1}^{n-1} \left[n - 1 + \frac{1}{2} m(\gamma-1) \right]}{(-1)^{1+(2n)!} n!} \left(\frac{2\varepsilon \xi}{\gamma-1} \right)^n + O(\varepsilon^{N+1}) \quad (7-15)$$

This universal solution is surprisingly accurate as it entails a relative error of less than 1% for area ratios up to 0.637 using only the $N = 1$ term. Moreover, the error remains bounded by 5% up to an area ratio of 0.846. A comparable, though technically more sophisticated expansion, leads to the supersonic roots. One finds

$$\bar{x}_{\text{sup}} = \left\{ \begin{matrix} \bar{T}_{\text{sub}}^{2/(\gamma-1)} \\ \bar{p}_{\text{sub}}^{-2/\gamma} \\ \bar{\rho}_{\text{sub}}^{-2} \end{matrix} \right\} = \bar{x}_0 + \sum_{n=1}^N \bar{x}_n + O(\varepsilon^{\kappa_N}); \quad \bar{x}_0 = \varepsilon \xi; \quad \bar{x}_n = \frac{X_n - (X_n)^{\frac{1}{2}\gamma + \frac{1}{2}} - \varepsilon \xi}{\frac{1}{2}(\gamma + 1)(X_n)^{\frac{1}{2}\gamma - \frac{1}{2}} - 1}; \quad X_n = \sum_{m=0}^{n-1} \bar{x}_m \quad (7-16)$$

with a universal truncation order of

$$\kappa_N = \begin{cases} \frac{1}{2}(\gamma + 1) & N = 0 \\ \frac{1}{2}[(2^{N+2} - 5)\gamma + 7 - 2^{N+2}] & N \geq 1 \end{cases} \quad (7-17)$$

Although the truncation order remains invariant for all three variables, the temperature approximation exhibits the lowest relative error. For this reason, it is often sufficient to use two corrections for the temperature and three corrections for the pressure and density. Alternatively, a property-specific approximation can be constructed to arbitrary order. Accordingly, a two-term approximation for the supersonic properties may be written as

$$\bar{T}_{\text{sup}} = \frac{T}{T_0} = (\varepsilon \xi)^{\frac{1}{2}(\gamma-1)} \left[1 + \frac{(\gamma-1)}{2(\varepsilon \xi)^{\frac{1}{2}(1-\gamma)} - (\gamma+1)} \right] + O[\varepsilon^{\frac{1}{2}(3\gamma-1)}], \quad \bar{p}_{\text{sup}} = \frac{p}{p_0} = (\varepsilon \xi)^{\frac{1}{2}\gamma} \left[1 + \frac{1}{2(\varepsilon \xi)^{\frac{1}{2}-\frac{1}{2}\gamma} - (\gamma+1)} \right] + O[\varepsilon^{\frac{1}{2}(3\gamma-1)}]$$

and

$$\bar{\rho}_{\text{sup}} = \frac{\rho}{\rho_0} = (\varepsilon \xi)^{\frac{1}{2}} \left[1 + \frac{1}{2(\varepsilon \xi)^{\frac{1}{2}-\frac{1}{2}\gamma} - (\gamma+1)} \right] + O[\varepsilon^{\frac{1}{2}(3\gamma-1)}] \quad (7-18)$$

As for the supersonic Mach number evaluation, Stodola's relation can be first rewritten as

$$(\gamma + 1)Ma^{2\kappa} - (\gamma - 1)\varepsilon^\kappa Ma^2 - 2\varepsilon^\kappa = 0; \quad \kappa \equiv \frac{\gamma - 1}{\gamma + 1} \quad (7-19)$$

where $0 \leq \kappa \leq \frac{1}{4}$ for $1 \leq \gamma \leq \frac{5}{3}$. Then using the method of successive approximations, Majdalani and Maicke (2013) show that

$$Ma_{\text{sup}} = Ma_0 + Ma_1 + \dots = \underbrace{\left(\frac{\gamma + 1}{\gamma - 1} \right)^{\frac{1}{4}(\gamma+1)} \frac{1}{\varepsilon^{\frac{1}{4}(\gamma-1)}}}_{Ma_0} + \underbrace{\left(\frac{\gamma + 1}{\gamma - 1} \right)^{\frac{1}{4}(3-\gamma)} \frac{\varepsilon^{\frac{\gamma^2-1}{4(\gamma+1)}}}{(\gamma-1)}}_{Ma_1} + O[\varepsilon^{\frac{3}{4}(\gamma-1)}] \quad (7-20)$$

As such, through the tools of asymptotic theory, the supersonic Mach number can be evaluated as a direct function of γ and the area ratio to any desired level of precision. One finds

$$Ma_{\text{sup}} = Ma_0 + \sum_{n=1}^N Ma_n; \quad Ma_n = \frac{2\varepsilon^\kappa - (\gamma + 1)[Ma_{\text{sup}}^{(n-1)}]^{2\kappa} + (\gamma - 1)\varepsilon^\kappa [Ma_{\text{sup}}^{(n-1)}]^2}{2\kappa(\gamma + 1)[Ma_{\text{sup}}^{(n-1)}]^{2\kappa-1} - 2(\gamma - 1)\varepsilon^\kappa Ma_{\text{sup}}^{(n-1)}}; \quad Ma_{\text{sup}}^{(n-1)} = \sum_{m=0}^{n-1} Ma_m \quad (7-21)$$

For further detail on these relations, see Majdalani and Maicke (2012, 2013).

Page 404

7-1.2 Steady Viscous Flow: The Crocco–Busemann Relations

Compressible boundary-layer flow is neither adiabatic nor isentropic. Even if the wall and the freestream are adiabatic, the boundary layer between them is not, as it will generally generate heat dissipation. However, certain ideal-gas assumptions lead to interesting energy integrals.

It is not necessary to assume constant specific heats in what follows. If we consider only steady flow, the boundary-layer equations reduce to

$$\frac{\partial}{\partial x}(\rho u) + \frac{\partial}{\partial y}(\rho v) = 0 \quad (7-22a)$$

$$\rho u \frac{\partial u}{\partial x} + \rho v \frac{\partial u}{\partial y} = -\frac{dp_e}{dx} + \frac{\partial}{\partial y}\left(\mu \frac{\partial u}{\partial y}\right) \quad (7-22b)$$

$$\rho u \frac{\partial h}{\partial x} + \rho v \frac{\partial h}{\partial y} = u \frac{dp_e}{dx} + \frac{\partial}{\partial y}\left(\frac{\mu}{Pr} \frac{\partial h}{\partial y}\right) + \mu \left(\frac{\partial u}{\partial y}\right)^2 \quad (7-22c)$$

where we have introduced the Prandtl number, $Pr = \mu c_p/k$, into the energy equation. The total enthalpy relation [Eq. (7-3)] takes on a particularly interesting form, viz.

$$\rho u \frac{\partial H}{\partial x} + \rho v \frac{\partial H}{\partial y} = \frac{\partial}{\partial y}\left(\frac{\mu}{Pr} \frac{\partial H}{\partial y}\right) + \frac{\partial}{\partial y}\left[\left(1 - \frac{1}{Pr}\right)\mu u \frac{\partial u}{\partial y}\right] \quad (7-23)$$

If the Prandtl number is unity (a fair approximation for gases), the last term vanishes, and this relation then admits to a particular solution $H = \text{const}$ throughout the boundary layer. However, since $H = h + u^2/2$, setting $H = \text{const}$ implies that $\partial h/\partial y = 0$ at the wall where $u = 0$ (no slip). Thus, our particular solution corresponds to zero heat transfer at the wall and is the first of two energy integrals discovered by Busemann (1931) and independently by Crocco (1932):

$$Pr = 1, \text{ adiabatic wall:} \quad H = h + \frac{1}{2}u^2 = \text{const} \quad (7-24)$$

Thus, $Pr = 1$ leads to a perfect balance between viscous dissipation and heat conduction so as to keep the stagnation enthalpy constant in an adiabatic boundary layer, just as it would be true in outer potential flow. Note that the pressure gradient (if any) is immaterial and there is no requirement for constant μ , k , or c_p . However, the fluid must be an ideal gas or at least satisfy $dh = c_p dT$ to good approximation.

A second energy integral is possible for $Pr = 1$ and the further restriction of a zero pressure gradient. We may note that the momentum and energy relations, given by Eqs. (7-

22b) and (7-22c), are similar in mathematical character if the pressure gradient vanishes, and it almost seems as if u and h could be interchanged except for the dissipation term. In other words, we may test the particular solution $h = h(u)$ by noting, for example, that

$$\frac{\partial h}{\partial y} = \frac{dh}{du} \frac{\partial u}{\partial y}$$

Substituting into the energy relation and assuming $Pr = 1$, we have, for a zero pressure gradient:

$$\frac{dh}{du} \left[\rho u \frac{\partial u}{\partial x} + \rho v \frac{\partial u}{\partial y} - \frac{\partial}{\partial y} \left(\mu \frac{\partial u}{\partial y} \right) \right] = \left(1 + \frac{d^2 h}{du^2} \right) \mu \left(\frac{\partial u}{\partial y} \right)^2 \quad (7-25)$$

The left-hand side vanishes by virtue of the momentum relation of Eq. (7-22b). As such, the right-hand side must follow suit, namely,

$$\frac{d^2 h}{du^2} = -1 \quad \text{or} \quad h = -\frac{u^2}{2} + C_1 u + C_2 \quad (7-26)$$

By inspection, $C_2 = h_w$ since $u = 0$ at the wall. The constant C_1 may be related to either the wall heat transfer or the freestream conditions. Choosing the latter, we see that $h = h_e$ at $u = U_e$ or $C_1 = (h_e + U_e^2/2 - h_w)/U_e$. Collecting terms into the final relation and rearranging, we arrive at the *second* Crocco–Busemann energy integral, namely,

$$\text{For } Pr = 1, \frac{dp}{dx} = 0: \quad H = h + \frac{u^2}{2} = h_w + (H_e - h_w) \frac{u}{U_e} \quad (7-27)$$

Thus, the total enthalpy varies linearly with the velocity across the boundary layer. Note that the *first* Crocco–Busemann relation for an adiabatic wall may be restored from [Eq. \(7-27\)](#) as a special case with $H_e = h_w = H = \text{const.}$

If we further require constant c_p , so that $h = c_p T + \text{const}$, then [Eq. \(7-27\)](#) becomes a relation between temperature and velocity

$$\text{For } Pr = 1, \frac{dp}{dx} = 0, c_p = \text{const:} \quad T = T_w + \left(T_e + \frac{U_e^2}{2c_p} - T_w \right) \frac{u}{U_e} - \frac{u^2}{2c_p} \quad (7-28)$$

Page 405

Equation (7-28) is a temperature–velocity relation, which is very useful in formulating approximate theories of the compressible boundary layer when Pr is near unity (gases) and dp/dx is not too large. Noting that $T_e + U_e^2/(2c_p)$ is the adiabatic-wall temperature T_{aw} , we can rewrite the relation as

$$T = T_w + (T_{aw} - T_w) \frac{u}{U_e} - \frac{u^2}{2c_p} \quad (7-29)$$

Then by differentiating, we can relate the wall heat flux and skin-friction coefficient using

$$\frac{q_w}{k_w} = \left(\frac{\partial T}{\partial y} \right)_w = \frac{T_{aw} - T_w}{U_e} \left(\frac{\partial u}{\partial y} \right)_w - \left(\frac{u}{c_p} \frac{\partial u}{\partial y} \right)_w = \frac{(T_{aw} - T_w)\tau_w}{U_e \mu_w}$$

and so, the Stanton number emerges as

$$C_h = \frac{q_w}{\rho_e U_e c_p (T_{aw} - T_w)} = \frac{C_f}{2Pr} \quad (7-30)$$

which is a reflection of the Reynolds analogy. It is strictly valid only for $Pr = 1$ and zero pressure gradients but is a good approximation for gases under both laminar and turbulent conditions, particularly if we modify the correction factor from Pr to $Pr^{2/3}$.

The Prandtl number also affects the insulated-wall temperature in high-speed flow. When the (inviscid) freestream is adiabatically decelerated to zero velocity, its temperature approaches the “ideal” stagnation temperature T_{0e} , which, for an ideal gas with constant c_p , can be expressed as $T_e + U_e^2/(2c_p)$. However, when a viscous high-speed boundary-layer flow is decelerated to zero velocity at an insulated wall, it approaches an adiabatic wall temperature T_{aw} , which differs from T_{0e} as defined by a dimensionless *recovery factor*, r :

$$r = \frac{T_{aw} - T_e}{T_{0e} - T_e} \approx f(Pr) \quad (7-31)$$

Clearly, accurately evaluating r is important, because q_w in high-speed flow is proportional to $(T_{aw} - T_w)$, not to $(T_w - T_e)$, as we shall see. The Crocco integral and recovery factor concepts have been extended by Van Oudheusden (1997, 2004).

7-2 SIMILARITY SOLUTIONS FOR COMPRESSIBLE LAMINAR FLOW

The compressible-boundary-layer relations in Eqs. (7-22a) to (7-22c) are formidably coupled nonlinear partial differential equations. They can be resolved using finite-difference methods, but analytic techniques lead to deeper physical understanding. Since the classic compressible-flow analyses originated in the precomputer era, a great deal of sophisticated effort was applied to simplifying these equations. Early workers developed a number of beautiful transformations relating compressible boundary layers to equivalent incompressible models. A variety of similarity variables were also found to reproduce ordinary differential equations for certain freestream and wall conditions. We discuss only one of these transformations attributed to Illingworth (1950).

7-2.1 The Illingworth Transformation

The stream function $\psi(x, y)$ for compressible flow is defined as

$$\frac{\partial \psi}{\partial y} = \rho u \quad \frac{\partial \psi}{\partial x} = -\rho v \quad (7-32)$$

This eliminates the continuity relation identically. It immediately suggests that the variable $\int \rho$ should replace the incompressible y in compressible flow. Then the general idea followed by early workers is to presuppose the existence of *two* similarity variables (ξ, η) and to see whether ψ and u could take the following “split” forms:

$$\psi(\xi, \eta) = \int \rho u \, dy = G(\xi)f(\eta) \quad u(\xi, \eta) = U_e(\xi)f'(\eta) \quad (7-33)$$

Then one substitutes into the momentum Eq. (7-22b) and tries to enforce the requirement that the resulting differential equation *be independent of ξ* . Here the analysis can follow several paths and lead to dissimilar transformations. The path taken here was discovered by Illingworth (1950), who found that it was convenient to account for viscosity effects in ξ and for density effects in η , using the dual variable transformations:

$$\xi(x) = \int_0^x \rho_e(x) U_e(x) \mu_e(x) \, dx \quad \text{and} \quad \eta(x, y) = \frac{U_e}{\sqrt{2\xi}} \int_0^y \rho \, dy \quad (7-34)$$

Page 406

When these transformations are substituted into the momentum Eq. (7-22b), the following ordinary differential equation for $f(\eta)$ is obtained:

$$(Cf'')' + ff'' + \frac{2\xi}{U_e} \frac{dU_e}{d\xi} \left(\frac{\rho_e}{\rho} - f'^2 \right) = 0 \quad \text{with} \quad C = \frac{\rho}{\rho_e} \frac{\mu}{\mu_e} \approx C(\eta) \quad (7-35)$$

Here primes denote differentiation with respect to η . By examining (7-33), we see that the boundary conditions for an impermeable wall are

$$f(0) = f'(0) = 0 \text{ (no slip)} \quad f'(\infty) = 1 \text{ (freestream)} \quad (7-36)$$

Two special cases of (7-35) immediately come to mind. First, for a flat plate at low speed and modest heat transfer, U_e , ρ , and μ are constant. Subsequently, we can take $C \approx 1$, $dU_e/d\xi = 0$, and write

$$f''' + ff'' = 0 \quad (7-37)$$

which we recognize as the Blasius equation (4-60). Second, if ρ and μ are constant but the freestream varies as $U_e = Kx^m$, then $C \approx 1$ and we extract

$$f''' + ff'' + \frac{2m}{m+1} (1 - f'^2) = 0 \quad (7-38)$$

which is identical to the Falkner–Skan equation (4-93). In both situations, we recover the

corresponding incompressible relations as special cases.

The boundary-layer energy equation (7-22c) also reduces to an ordinary differential equation if we split the enthalpy into a magnitude multiplied by a shape function,

$$h(x, y) = h_e(\xi)g(\eta) \quad (7-39)$$

In fact, backward substitution into Eq. (7-22c) yields an ordinary differential equation for $g(\eta)$, namely,

$$\left(\frac{C}{Pr}g'\right)' + fg' = \left(\frac{\xi}{H_e} \frac{dH_e}{d\xi}\right)f' \left(2g + \frac{U_e^2}{h_e}f'^2\right) - \frac{U_e^2}{h_e}Cf'^2 \quad (7-40)$$

where $H_e = h_e + U_e^2/2$ is the freestream stagnation enthalpy. For a perfect gas with constant specific heats, the Eckert-type parameter, U_e^2/h_e , can be converted to a Mach number squared:

$$\frac{U_e^2}{h_e} = \frac{U_e^2}{c_p T_e} = \frac{(\gamma - 1)U_e^2}{\gamma R T_e} = (\gamma - 1)Ma_e^2 \quad (7-41)$$

In many cases, the entire right-hand side of [Eq. \(7-40\)](#) is neglected. For example, in low-speed flow near a stagnation point, $Ma_e \approx 0$ and $H_e \approx \text{const}$, with $C \approx 1$ and $Pr \approx \text{const}$, so that [Eq. \(7-40\)](#) reduces to

$$g'' + Prfg' \approx 0 \quad (7-42)$$

which we recognize as (3-223) for incompressible stagnation-flow heat transfer. The boundary conditions on $g(\eta)$ can accommodate either adiabatic or heat-transfer conditions:

$$\text{Adiabatic wall:} \quad g(0) = g_w \quad g'(0) = 0 \quad g(\infty) = 1 \quad (7-43a)$$

$$\text{Heat transfer:} \quad g(0) = g_w \quad g'(0) \neq 0 \quad g(\infty) = 1 \quad (7-43b)$$

For adiabatic flow, the problem consists of finding the correct value of g_w , whereas for heat transfer, g_w is specified, and one must find the correct value of $g'(0)$.

Examining [Eqs. \(7-35\)](#) and [\(7-40\)](#), we see that similarity is not achieved unless certain coefficients are constant or functions only of η :

1. $C = \text{const}$ or related to f and g .
2. $Pr = \text{const}$ or related to f and g .
3. ρ_e/ρ related to f and g .
4. $\frac{2\xi}{U_e} \frac{dU_e}{d\xi} = \text{const}$.
5. $\frac{U_e^2}{h_e} = \text{const}$ (e.g., for $Pr = 1$) or negligible (for small Mach numbers).
6. $\frac{2\xi}{H_e} \frac{dH_e}{d\xi} = \text{const}$.

Although this set prescribes a wide variety of conditions, most of them are reasonable. Conditions 1–3 are satisfied if we make the ideal-gas assumption. Recalling that the pressure is nearly constant across the boundary layer, we can put

$$\frac{\rho_e}{\rho(y)} = \frac{T(y)}{T_e} \approx \frac{h(y)}{h_e} \quad (7-44)$$

This means that C and the density can be related approximately to g :

$$\frac{\rho_e}{\rho} \approx g(\eta) \quad \text{and} \quad \frac{h_e \mu}{h \mu_e} \approx \left(\frac{h}{h_e} \right)^{n-1} = g^{n-1} = C(\eta) \quad (7-45)$$

where we have made a power-law approximation for the viscosity–temperature relation of gases. Values of n are given in Table 1-2. For air, $n \approx \frac{2}{3}$, hence $C \approx g^{-1/3}$. Further, from [Fig. 1-17](#), the Prandtl number is approximately constant for most gases, which takes care of condition 2. Conditions 4 and 5 are satisfied by the Falkner–Skan distributions

$$U_e \sim \xi^m \quad \text{and} \quad H_e \sim \xi^j \quad (7-46)$$

The most common assumptions are constant freestream stagnation temperature ($j = 0$) and flat-plate ($m = 0$) or stagnation flow ($m = 1$). Finally, condition 5 is satisfied for flat-plate ($U_e^2/h_e \approx \text{const}$) and stagnation flow ($U_e^2/h_e \approx 0$), but not in general. In the Falkner–Skan problem, U_e^2/h_e will vary with ξ unless $j = 2m$, which is unlikely; we will have to neglect this term by making the assumption of $U_e^2 \ll h_e$.

We should also note that similarity is violated unless the wall enthalpy $g_w = g(0)$ is fixed, independently of ξ . Thus, in the majority of cases, our solutions are valid only for constants H_e and T_w .

By taking all of these simplifying assumptions into consideration, we can finally rewrite [Eqs. \(7-35\)](#) and [\(7-41\)](#) for laminar flow of an ideal gas in the following similarity form:

$$\text{Momentum:} \quad (Cf'')' + ff'' = \beta(f'^2 - g) \quad (7-47a)$$

$$\text{Energy:} \quad (Cg')' + Prfg' = -PrC(\gamma - 1)Ma_e^2 f''^2 \quad (7-47b)$$

$$\text{where} \quad \beta = \frac{2\xi}{Ma_e} \frac{dMa_e}{d\xi} \quad \text{and} \quad C = \frac{\rho\mu}{\rho_e\mu_e} \approx g^{n-1} \approx g^{-1/3} \quad \text{for air}$$

Note that, except for the variable parameter $C(\eta)$, Eqs. (7-47a) and (7-47b) resemble the Falkner–Skan incompressible-flow solutions from Secs. 4-3.4 and 4-3.5. Compressible similarity solutions of these—and related—equations have been advanced by a number of investigators, as detailed in the monograph by Stewartson (1964). Here we limit our discussion, in Sec. 7-4, to the Falkner–Skan-type solutions found by Cohen and Reshotko (1956).

7-3 SOLUTIONS FOR LAMINAR FLAT-PLATE AND STAGNATION-POINT FLOW

The two most relevant applications of laminar, compressible, boundary-layer theory are (1) flat-plate flow (for estimating the friction and heat transfer on slender bodies) and (2) stagnation-point flow (where the heat-transfer rate is usually the highest on blunt bodies). Both cases give insight into the general effect of compressibility on boundary-layer flows.

7-3.1 Approximate Analysis of the Flat-Plate Recovery Factor

Consider flat-plate flow ($\beta = 0$) with constant wall temperature. Further assume that $C = 1$, that is, μ proportional to T , because the dependence of the recovery factor on the temperature and Mach number is extremely weak. Then Eqs. (7-47a) and (7-47b), for an adiabatic wall, reduce to

$$f''' + ff'' \approx 0 \quad (7-48a)$$

$$g'' + Prfg' = -Bf'^2 \quad (7-48b)$$

with $f(0) = f'(0) = g'(0) = 0$ and $f'(\infty) = g(\infty) = 1$. For brevity, we have defined $B = Pr(\gamma - 1)Ma_e^2$. These are the Blasius relations, and $f(\eta)$ is already known from [Fig. 4-10](#) and Table 4-3. The solution of the (linear, nonhomogeneous) energy Eq. (7-48b) becomes

$$g = g_w + A \int_0^\eta G d\zeta + \int_0^\eta G \left(\int_0^\zeta \frac{f'^2}{G} d\lambda \right) d\zeta; \quad G(\eta, Pr) = \exp \left(-Pr \int_0^\eta f(\zeta) d\zeta \right) \quad (7-49)$$

Page 408

This solution was first given by Pohlhausen (1921). The constant A must be such that $g(\infty) = 1$. Further, for an *adiabatic* wall, the requirement that $g'(0) = 0$ means that $A = 0$, as can be seen by differentiating [Eq. \(7-49\)](#). For this case, then, $g_w = T_{aw}/T_e$, and so the rearrangement of [Eq. \(7-49\)](#) yields

$$T_{aw} = T_e + r \frac{U_e^2}{2c_p} \quad \text{and} \quad r = 2Pr \int_0^\infty G \left(\int_0^\zeta \frac{f'^2}{G} d\lambda \right) d\zeta \quad (7-50)$$

Thus, we can take $r \approx r(Pr)$ with great accuracy. For $Pr = 1$ and $r = 1$, the plate recovers the freestream stagnation temperature at an adiabatic wall because conduction and dissipation are precisely balanced in the boundary layer. For $Pr \neq 1$, the integral in [Eq. \(7-50\)](#) may be evaluated by adding three more statements to the computer program for the Blasius solution from [Eq. \(4-63\)](#):

$$F(4) = Y(3) \quad F(5) = Y(1) * Y(1) * \text{EXP}(PR * Y(4)) \quad F(6) = 2 * PR * \text{EXP}(-PR * Y(4)) * Y(5) \quad (7-51)$$

The output variable $Y(6)$ approaches r , as η becomes large. Some computed recovery factors are listed in Table 7-1. Note that two curve-fit approximations to these results are

$$0.1 < Pr < 3.0: \quad r \approx \sqrt{Pr} \quad (7-52a)$$

$$Pr > 3.0: \quad r \approx 1.905 Pr^{1/3} - 1.15 \quad (7-52b)$$

TABLE 7-1

Flat-plate recovery factors from [Eqs. \(7-49\)](#) and [\(7-50\)](#)

Pr	$r(Pr)$	Pr	$r(Pr)$
0.001	0.02946	1.0	1.0
0.003	0.05125	2.0	1.4089
0.006	0.07279	3.0	1.7088
		6.0	2.3571
0.01	0.09434	10.0	2.9622
0.03	0.16534	30.0	4.7238
0.06	0.23610	60.0	6.2467
0.1	0.30731		
0.3	0.54197	100.0	7.6272
0.6	0.77286	300.0	11.5483
Air 0.72	0.84771	600.0	14.881
		1000.0	17.881

These are plotted, along with the exact values, in [Fig. 7-2](#). In practice, only formula Eq. (7-52a) is important, and since most compressible-flow problems involve air or gases, one may use $Pr \approx 0.72$ or $r \approx 0.85$.

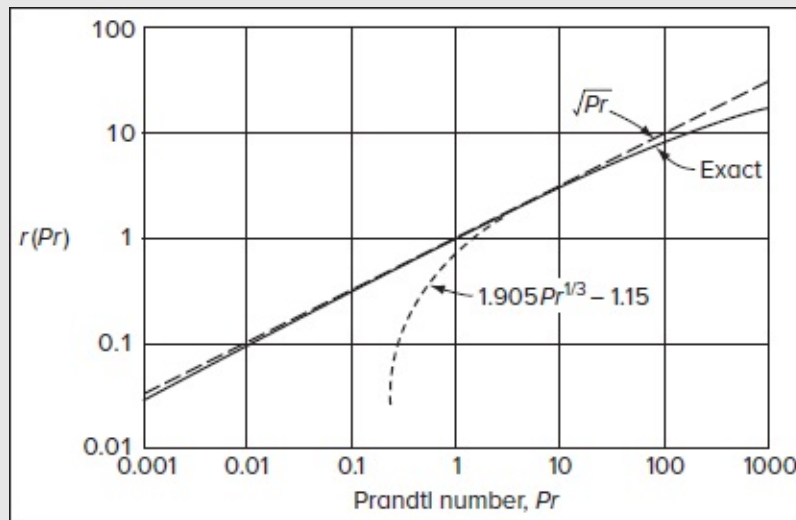


FIGURE 7-2

Flat-plate recovery factors (exact and approximate).

7-3.2 Laminar Flat-Plate Friction at High Mach Numbers

The quantity $C = \rho\mu/(\rho_e \mu_e)$, which is coined the *Chapman–Rubesin parameter* after a pioneering paper by Chapman and Rubesin (1949), has little effect on the recovery factor but does affect friction and heat transfer. The following simplified analysis explains how. For a flat plate, $\beta = 0$ and Eq. (7-48a) becomes

$$(Cf'')' + ff'' = 0$$

The variables may be separated and integrated twice across the boundary layer with the outcome

$$\int_0^\infty Cf'' d\eta = C_w f''(0) \int_0^\infty \exp\left(-\int_0^\eta \frac{f}{C} d\zeta\right) d\eta$$

An approximate solution can be found with the near-wall simplifications

$$C \approx C_w \approx \text{const} \quad f \approx \frac{1}{2}f''(0)\eta^2 + \dots$$

The integrals may then be evaluated for the approximate result of

$$C_w \approx \frac{C_w f''(0)}{3} \left[\frac{6C_w}{f''(0)} \right]^{1/3} \Gamma\left(\frac{1}{3}\right) \quad \text{or} \quad f''(0) \approx \frac{0.48}{\sqrt{C_w}} \quad (7-53)$$

In a more accurate analysis, the constant 0.48 would be the Blasius value for incompressible flow, $f''(0)_{\text{Blasius}} = \sigma \approx 0.4696$. Since $f''(0)$ is proportional to the wall shear stress, we may convert [Eq. \(7-53\)](#) into a skin-friction approximation for compressible flat-plate flow using:

$$C_f = \frac{2\tau_w}{\rho_e U_e^2} \approx \frac{0.664 C_w^{1/2}}{Re_x^{1/2}} \quad (7-54)$$

where $C_w = \rho_w \mu_w / \rho_e \mu_e \approx (T_w / T_e)^{-1/3}$ for gases. Similarly, the Stanton number, or the dimensionless wall heat transfer coefficient, may be estimated from $C_h \approx C_{h, Ma=0} \sqrt{C_w}$. The resulting agreement is valid for adiabatic walls but deteriorates for heated or cooled walls.

7-3.3 The Reference Temperature Concept

It was found in the 1950s that the simplified expression (7-54) could be modified to achieve good accuracy for all flat-plate compressible gas flows by evaluating the fluid properties (ρ , μ , c_p , k) at a *reference temperature*, T^* , which varies with the Mach number and wall temperature. Accordingly, the Chapman–Rubesin parameter can be evaluated as

$$C^* = \frac{\rho^* \mu^*}{\rho_e \mu_e} \approx \left(\frac{T_e}{T^*} \right)^{1/3} \quad (7-55)$$

The flat-plate formulas, modified with the reference temperature, become

$$\frac{T_{aw}}{T_e} \approx 1 + \sqrt{Pr^*} \frac{\gamma - 1}{2} Ma_e^2 \quad (\text{laminar recovery factor}) \quad (7-56a)$$

$$\frac{2\tau_w}{\rho_e U_e^2} \approx \frac{0.664 \sqrt{C^*}}{\sqrt{Re_{xe}}} \quad (\text{laminar plate flow}) \quad (7-56b)$$

$$\frac{C_{fe}}{2C_{he}} \approx Pr^{*2/3} \quad (\text{laminar or turbulent}) \quad (7-56c)$$

The most popular correlation for T^* is due to Eckert (1955):

$$\frac{T^*}{T_e} \approx 0.5 + 0.039 Ma_e^2 + 0.5 \frac{T_w}{T_e} \quad (7-57)$$

Although [Eq. \(7-57\)](#) is originally proposed as an empirical correlation, Dorrance (1962) proves that the reference temperature is a direct consequence of the similarity relations for compressible motion. Equation (7-57) may also be used to modify *turbulent* flat-plate formulas, although better approximations are possible in that case.

Page 410

7-3.4 Exact Laminar Flat-Plate Solutions

We may compare our approximate flat-plate compressible-flow formulas with an array of exact numerical laminar-flow computations by van Driest (1952a). The calculations assume $Pr = 0.75$ and Sutherland's viscosity law for air, [Eq. \(1-34\)](#):

$$\mu = \frac{0.006584}{T + 110.6} \left(\frac{T}{273.1} \right)^{1.5}$$

Similar formulas for $c_p(T)$ and $k(T)$ are also used. The theory uses a different coordinate transformation from [Eqs. \(7-34\)](#), although the basic idea is nearly the same.

Figure 7-3 displays the computed velocity, temperature, and Mach number profiles in the boundary layer for an adiabatic wall. The velocity profiles in [Fig. 7-3a](#) are nearly straight lines at high Mach numbers, an approximation often used in hypersonic flow analyses, e.g., Truitt (1960, art. 5-3). The temperature profiles show the dramatic heating effect of viscous dissipation in the boundary layer at high Mach numbers. If the velocity is known, the temperature in [Fig. 7-3b](#) is well approximated by [Eq. \(7-28\)](#) for $T_w = T_{aw}$, as follows:

$$\frac{T}{T_e} \approx 1 + Pr^{1/2} \left(\frac{\gamma - 1}{2} \right) Ma_e^2 \left(1 - \frac{u^2}{U_e^2} \right) \quad (7-58)$$

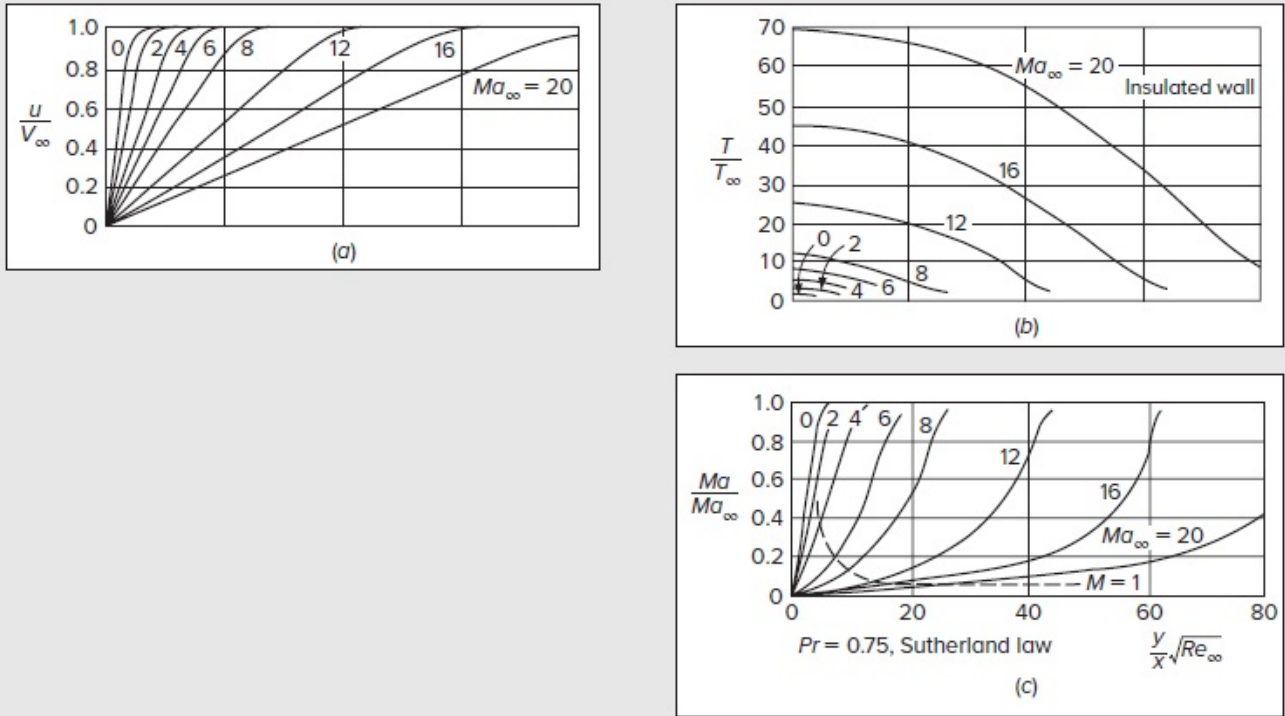


FIGURE 7-3

Calculations of the laminar, compressible, boundary layer on an insulated flat plate by van Driest (1952a): (a) velocity profiles; (b) temperature profiles; (c) Mach number profiles.

The recovery factor relation $r \approx Pr^{1/2}$ is quite accurate. For example, at $Ma_e = 20$, $r = 0.75^{1/2}$ predicts $T_{aw}/T_e = 70.3$, which is in excellent agreement with [Fig. 7-3b](#). Finally, the Mach number profiles in [Fig. 7-3c](#) show that the majority of a high-velocity boundary layer sustains supersonic conditions.

Figure 7-4 reproduces the flat-plate computations by van Driest (1952a) for a very cold wall, with $T_w = T_e/4$. The velocity profiles remain rounded even at a Mach number of 20 and, we recall from [Chap. 5](#), that such profiles are more resistant to transition. If the velocity is known, then the temperature profiles can be well fit by the Crocco–Busemann relation [Eq. (7-28)].

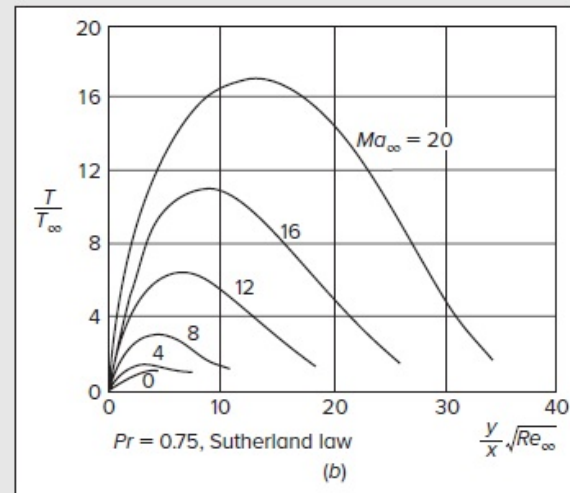
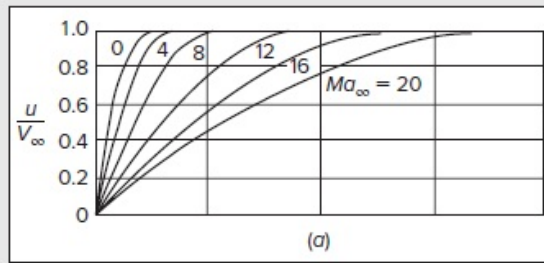


FIGURE 7-4

Calculations by van Driest (1952a) of the compressible, laminar, boundary layer on a cold flat plate ($T_w = \frac{1}{4}T_e$): (a) velocity profiles; (b) temperature profiles.

Figure 7-5 illustrates van Driest's calculations for laminar, flat-plate parameters such as the total drag ($C_D = 2 C_f$), local Stanton number (C_h), and boundary-layer thickness (δ). Note that the Stanton number for compressible flow is defined as

$$C_h = \frac{q_w}{\rho_e U_e C_{pe} (T_{aw} - T_w)} \quad (7-59)$$

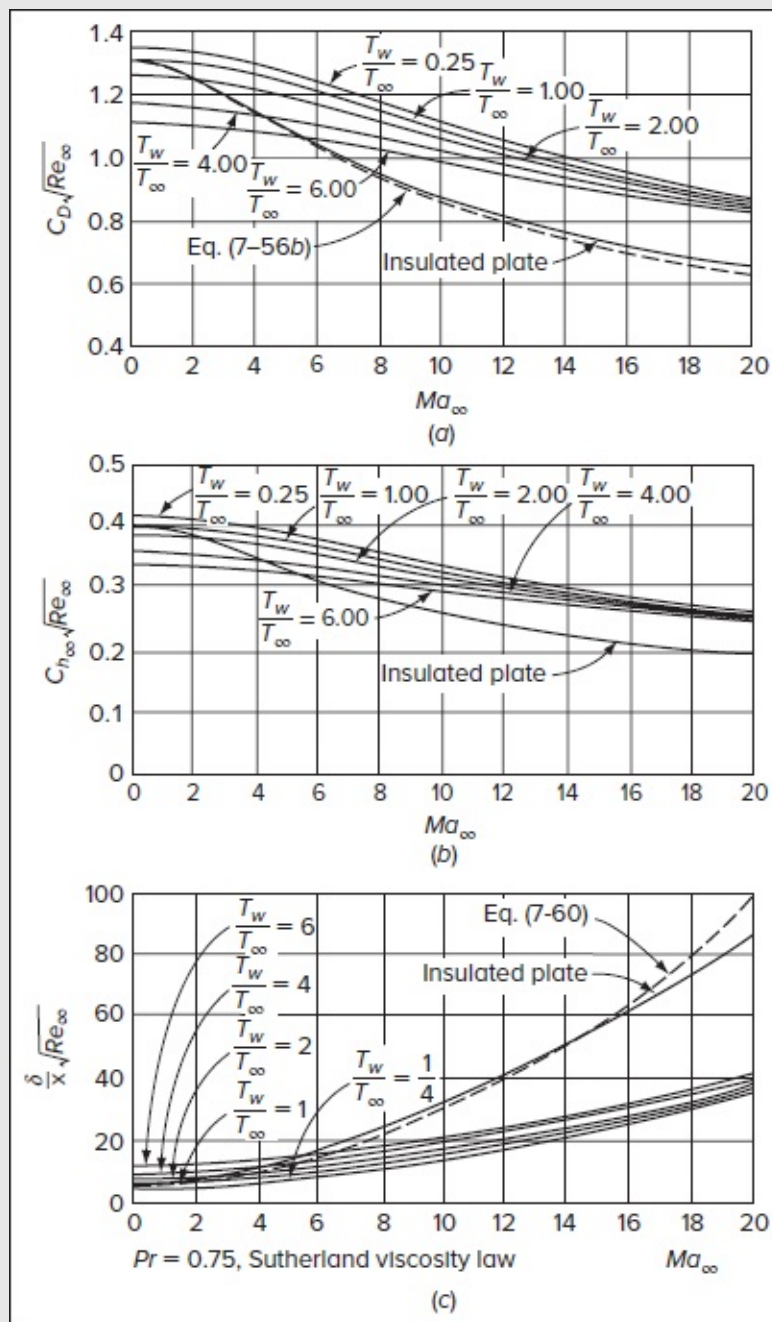


FIGURE 7-5

Calculations by van Driest (1952a) of the drag, heat transfer, and velocity thickness of a laminar, flat-plate, compressible, boundary layer: (a) total drag coefficient $C_D = 2C_f$; (b) local Stanton number; (c) boundary-layer thickness.

with q_w positive for a cold wall. As the Mach number approaches zero, the temperature difference $(T_{aw} - T_w)$ approaches the value $(T_e - T_w)$ used for incompressible motion. Both

C_D and C_h are well approximated by the reference temperature formulas (7-56a) to (7-56c). For example, at $Ma_e = 10$ and $T_w/T_e = 4$, we read $C_h\sqrt{Re_{xe}} \approx 0.30$ from Fig. 7-5b. By comparison, the reference temperature for this case, based on Eq. (7-57), is $T^*/T_e \approx 5.9$, whence $C^* \approx 0.58$ and Eq. (7-56c) predicts $C_h\sqrt{Re_{xe}} \approx 0.306$, only 2 percent higher. This result is typical of the accuracy that accompanies reference temperature formulas.

As we move to Fig. 7-5c, it may be seen that the dimensionless boundary-layer thickness grows with the Mach number for both adiabatic and nonadiabatic walls. A semiempirical formula to approximate this thickness is given by

$$\frac{\delta}{x} Re_{xe}^{1/2} \approx C_w^{1/2} \left[5 + \left(0.2 + 0.9 \frac{T_w}{T_{aw}} \right) (\gamma - 1) Ma_e^2 \right] \quad (7-60)$$

The accuracy of Eq. (7-60) is only adequate, judging by its prediction for an adiabatic wall in Fig. 7-5c, where it is represented by a dashed curve.

Van Driest's calculations of the recovery factor, $r \approx Pr^{1/2}$, and the Reynolds analogy factor, $C_f/(2C_h) \approx Pr^{2/3}$, show an insignificant drop-off with the Mach number. Note, however, that these traditional approximations stand for *flat-plate flows* with no pressure gradients. Calculations by Van Oudheusden (1997, 2004) and others show a strong effect of a pressure gradient on the recovery factor. For compressible heat transfer with pressure gradients, an accurate CFD result is preferred to Prandtl number formulas.

7-3.5 High-Speed Plane Stagnation Flow

We can readily extend our previous discussion to stagnation flow. Here, the external temperature T_e refers to the stagnation, or adiabatic-wall temperature, and the difference between T_e and T_w represents the correct driving temperature for heat transfer. The similarity equations for $\beta = 1$ and $Ma_e \approx 0$ are

$$(Cf'')' + ff'' + g - f'^2 = 0 \quad (7-61a)$$

$$(Cg')' + Prfg' = 0 \quad (7-61b)$$

$$U_\epsilon = Kx \quad (7-61c)$$

where K denotes the stagnation velocity gradient. The stagnation region is subsonic and, if T_w is not too different from T_e , we have $C \approx 1$ and $g \approx 1$, so that the momentum Eq. (7-61a) reduces to the incompressible Hiemenz solution, Eq. (3-206) or Table 3-4, with $f''(0) \approx 1.2326$. The energy Eq. (7-61b) can be separated and integrated once to obtain

$$Cg' = Cwg'(0) \exp\left(-Pr \int_0^\eta \frac{f}{C} d\zeta\right)$$

Using the same approximations which led to [Eq. \(7-53\)](#), we may integrate again from zero to infinity, with the result

$$C_w[1 - g(0)] \approx g'(0)C_w\Gamma\left(\frac{4}{3}\right)\left[\frac{6C_w}{Prf''(0)}\right]^{4/3} \quad f''(0) \approx 1.2326$$

where

$$g'(0) \approx 0.66[1 - g(0)]\left(\frac{Pr}{C_w}\right)^{1/3}$$

This is the correct theoretical formulation, but the numerical constants in it are slightly off. Extensive computations by Fay and Riddell (1958), using the Sutherland viscosity law, have led to slightly adjusted constants:

$$g'(0) \approx 0.570[1 - g(0)]\left(\frac{Pr}{C_w}\right)^{0.4} \quad [\text{Fay and Riddell (1958)}] \quad (7-62)$$

We recognize the constant 0.570 from the Hiemenz solution for incompressible plane stagnation flow in [Chap. 3](#). Since $g'(0) \sim q_w$ and $[1 - g(0)] \sim (h_e - h_w)$, [Eq. \(7-62\)](#) is equivalent to specifying a heat-transfer rate for stagnation flows:

$$q_w = 0.570 Pr^{-0.6}(\rho_e \mu_e K)^{1/2} \left(\frac{\rho_w \mu_w}{\rho_e \mu_e}\right)^{0.1} (h_e - h_w) \quad (\text{plane flow}) \quad (7-63a)$$

$$q_w = 0.763 Pr^{-0.6}(\rho_e \mu_e K)^{1/2} \left(\frac{\rho_w \mu_w}{\rho_e \mu_e}\right)^{0.1} (h_e - h_w) \quad (\text{axisymmetric flow}) \quad (7-63b)$$

Page 413

Since the local Mach number is negligible, the only perceptible difference between plane and axisymmetric motions appears in the coefficient (0.570 versus 0.763) and the fact that the local velocity gradient K may differ. The heat transfer depends strongly upon K , and no practical computations can be made unless K is known from external considerations. For flow past a typical aerodynamic body (cylinder or sphere, for example) of finite size D and approach velocity V_∞ (see [Fig. 7-6](#)), the local velocity gradient K at the stagnation point will depend upon both D and V_∞ and, to a lesser extent, upon the approach Mach number Ma_∞ and the particular body shape. According to dimensional analysis, we expect

$$\frac{KD}{V_\infty} = f(Ma_\infty, \text{body shape}) \quad (7-64)$$

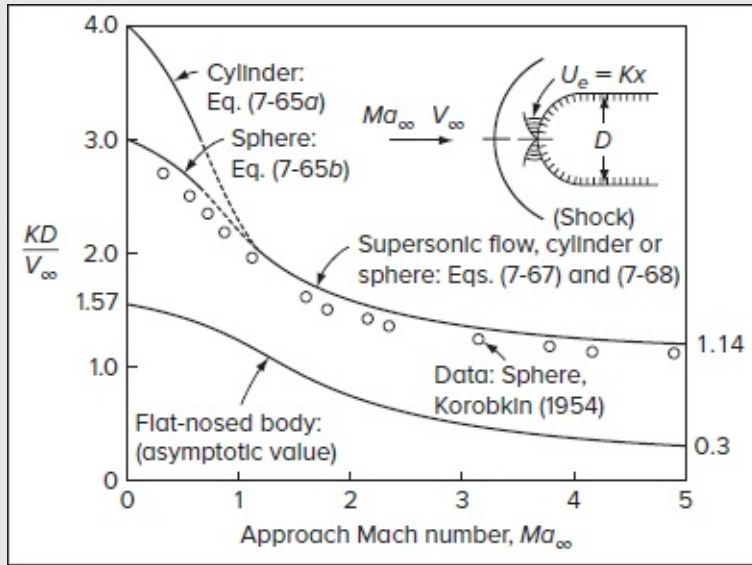


FIGURE 7-6

Theoretical, experimental, and estimated stagnation-point velocity gradients on cylinders, spheres, and flat noses.

At low speeds (subsonic flow), first-order calculations can be performed using the Rayleigh–Janzen Mach number expansion procedure [Shapiro (1953, Chap. 12)]. Some results are

$$\frac{KD}{V_\infty} = 4(1 - 0.461Ma_\infty^2 - 0.164Ma_\infty^4 + \dots) \quad (\text{cylinder}) \quad (7-65a)$$

$$\frac{KD}{V_\infty} = 3(1 - 0.252Ma_\infty^2 - 0.0175Ma_\infty^4 + \dots) \quad (\text{sphere}) \quad (7-65b)$$

$$\frac{KD}{V_\infty} = \frac{\pi}{2}(1 - \dots) \quad (\text{flat-nosed cylinder}) \quad (7-65c)$$

A flat-nosed cylinder has a considerably smaller gradient, and one can therefore reduce the stagnation-point heat flux by flattening the nose. At supersonic speeds, where these formulas are invalid [Anderson (2000)], the gradient may be estimated from Newtonian impact theory, which predicts the surface-pressure distribution as

$$\frac{p - p_\infty}{\rho_\infty U_\infty^2} \approx \cos^2 \theta \quad (7-66a)$$

$$\text{or} \quad \left. \frac{dp}{dx} \right|_{x \rightarrow 0} = -\rho_\infty K^2 x = -2\rho_\infty V_\infty^2 \theta \frac{d\theta}{dx} \quad (7-66b)$$

where θ is the angle between the surface normal and the approaching freestream; for example, $\theta = 0$ at the nose. For a circular nose of diameter D , planar or spherical, we can substitute $\theta = 2x/D$ in Eq. (7-66b) and cancel x to obtain

$$\frac{KD}{V_\infty} \approx \sqrt{\frac{8\rho_\infty}{\rho_e}} \quad (\text{round nose at supersonic speed}) \quad (7-67)$$

Remembering that, in this case, the subscript e denotes stagnation conditions, we can compute ρ_∞/ρ_e from normal shock-wave theory and, for an ideal gas, we get

$$\frac{\rho_e}{\rho_\infty} = \frac{(\gamma + 1)Ma_\infty^2}{2 + (\gamma - 1)Ma_\infty^2} \left[1 + \frac{\gamma - 1}{2} \frac{(\gamma - 1)Ma_\infty^2 + 2}{2\gamma Ma_\infty^2 - \gamma + 1} \right]^{1/(\gamma - 1)} \quad (7-68)$$

Page 414

This expression, though impressive, is slowly varying. For $\gamma = 1.4$, [Fig. 7-6](#) shows that KD/V_∞ from [Eq. \(7-67\)](#) decreases from 2.25 at $Ma = 1$ to about 1.12 at an infinite Mach number. These values merge for subsonic flow with the low-speed formulas in Eqs. (7-65a) and (7-65b). Data taken by Korobkin at the Naval Ordnance Laboratory (Report 3841) agree with this trend but fall consistently about 10 percent lower.

Equation (7-67) is not valid for flat noses, where it predicts $K = 0$ as D approaches infinity. Were it true, a flat nose would have eliminated stagnation-point heat transfer! However, there is no question that flat noses *reduce* K , and an estimated flat-nose curve is shown in [Fig. 7-6](#), based on asymptotic values at $Ma = 0$ and $Ma = \infty$.

Equation (7-67) is best applied to a round nose that merges smoothly with the afterbody, such as a hemispherical cylinder. Meanwhile, a flat nose reduces stagnation-point heat transfer by up to 50 percent, since q_w is proportional to $K^{1/2}$. In between these two cases is a hybrid body consisting of a shallow spherical cap attached to a cylinder, resulting in a sharp corner at the shoulder. [Figure 7-7](#) shows hypersonic velocity gradient data for such bodies, as given by Trimmer (Report AEDC-TR-68-99, 1968). For shallow noses with $R/r > 1.42$, the sonic point occurs at the sharp shoulder, and the Newtonian (supersonic) theory predicts too low of a gradient. For rounder noses, $1 < R/r < 1.42$, the sonic point occurs at $\theta \approx 45^\circ$ and $KD/V_\infty \approx 1.12$, as predicted by [Eq. \(7-67\)](#) for hypersonic flow.

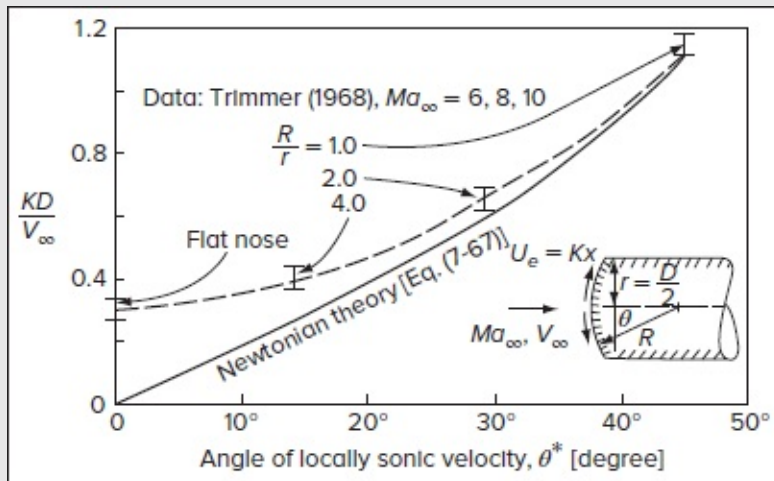


FIGURE 7-7

Comparison of theory and experiment for the stagnation-point velocity gradient K on cylinders with spherical noses.

Assuming that K is known, the stagnation-point theory for heat-flux prediction appears to be in excellent agreement with experiments. [Figure 7-8](#) provides a comparison of Eq. (7-63b) with shock-tube experiments by Rose and Stark (1958) on a hemispherical cylinder at hypersonic speeds approximating reentry conditions. It is speculated that discrepancies, if any, are due almost entirely to the difficulty of estimating gas viscosity at the very high temperatures associated with the stagnation point at hypersonic conditions.

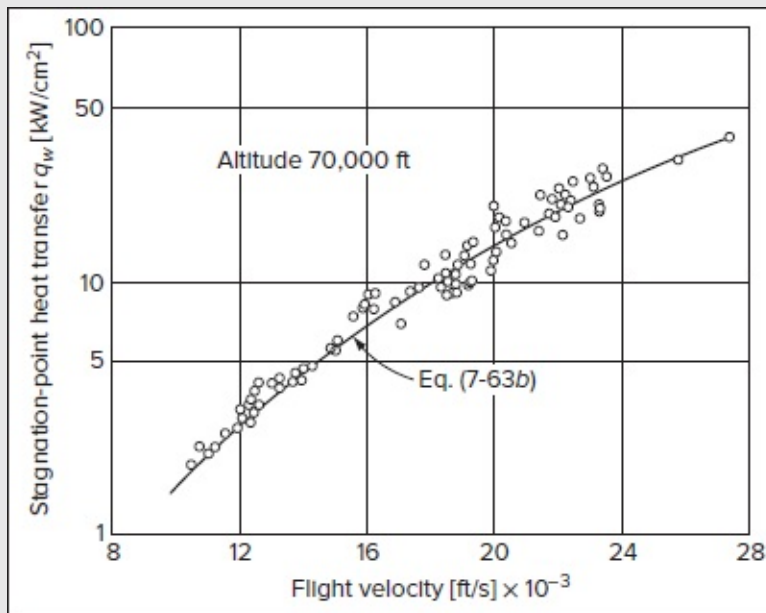


FIGURE 7-8

Theoretical stagnation-point heat flux compared with shock-tube experiments by Rose and Stark (1958) on a hemispherical cylinder.

7-4 COMPRESSIBLE LAMINAR BOUNDARY LAYERS UNDER ARBITRARY CONDITIONS

Although the flat plate and stagnation-point problems lead to the most important compressible-flow solutions, there are practical problems of variable velocity $U_e(x)$ and

temperature $T_e(x)$ or $T_w(x)$ that require a numerical method to compute, at least approximately, the wall skin-friction and heat-flux distributions. The English translation of the monograph by Walz (1969) is essentially devoted to the development of such approximate computations, mainly for laminar but also for turbulent boundary layers. Moreover, the monograph by Stewartson (1964) may be an excellent source for approximate theories that apply to compressible, laminar, boundary layers.

At least three possible strategies may be pursued in the development of an approximate laminar-flow theory:

1. Modification and extension of the compressible similarity solutions of Eqs. (7-47a) and (7-47b).
2. Extension to the integral momentum and energy relations of compressible flow.
3. Finite-difference computations of the exact, compressible, laminar equations.

Let us have a brief look at each of these approaches.

7-4.1 Modification of Compressible Similar Solutions

A complete assortment of velocity and stagnation enthalpy distributions is provided by Cohen and Reshotko (1956) for Falkner–Skan-type compressible similar flows. In this context, the simplifying assumptions $C = Pr = 1$ are made so that variable viscosity effects are only approximate and Prandtl number effects are absent. Consequently, our similarity Eqs. (7-47a) and (7-47b) reduce to

$$\text{Momentum:} \quad f''' + ff'' + \beta(g - f'^2) = 0 \quad (7-69a)$$

$$\text{Enthalpy:} \quad g'' + fg' = -(\gamma - 1)Ma_e^2 f'^2 \quad (7-69b)$$

$$\text{Stagnation enthalpy:} \quad S'' + fS' = 0 \quad S = \frac{H}{H_e} - 1 \quad (7-69c)$$

Cohen and Reshotko employ the stagnation enthalpy variable S because, for a unit Prandtl number, S no longer depends on the Mach number, but rather on the wall heat transfer S_w and the pressure gradient parameter β . Their computed velocity profiles are shown in [Fig. 7-9](#) for a hot wall ($S_w = +1.0$) and a cold wall ($S_w = -1.0$). An insulated adiabatic wall lies in between ($S_w = 0$ or $H = \text{const}$) and is identical to the incompressible Falkner–Skan profiles ([Fig. 4-16a](#)). Page 416 Note that the similarity coordinate is of the Falkner–Skan type and not the same as η defined here [Eq. (7-34)]. At least two observations about these curves are of interest:

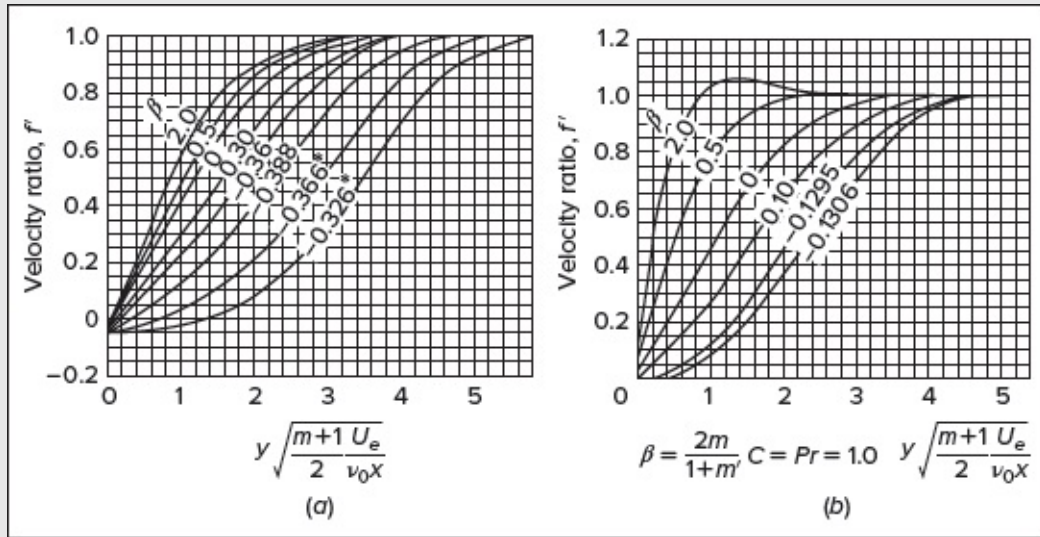


FIGURE 7-9

Similarity solutions for a compressible, laminar, boundary layer: (a) cold wall ($S_w = -1.0$); (b) hot wall ($S_w = +1.0$). [After Cohen and Reshotko (1956).]

1. The separation point is affected by heat transfer, β_{sep} being -0.326 for the cold wall ($S_w = 1.0$), -0.1988 for the insulated wall ($S_w = 0$), and -0.1305 for the hot wall ($S_w = +1.0$). Hot walls suffer earlier separation, and cold walls resist it, as we have seen before.
2. Hot-wall profiles overshoot the freestream velocity for positive β (favorable gradient). This is obvious for $\beta = 2.0$ and barely visible for $\beta = 0.5$.

We should also remark that the coordinate $y\sqrt{(m+1)U_e/(2\nu_0x)}$ in [Fig. 7-9](#) contains the quantity ν_0 , which denotes the kinematic viscosity evaluated at the freestream stagnation temperature T_0 .

An extensive set of tables of compressible similarity solutions can be found in the paper (and related report) by Bae and Emanuel (1989).

Figure 7-10 shows the computed wall shear stress function $f''(0)$ and the Reynolds analogy factor $C_f/(C_h Pr^{2/3})$ as a function of β and S_w . We see that both pressure gradient and wall temperature give strong effects.

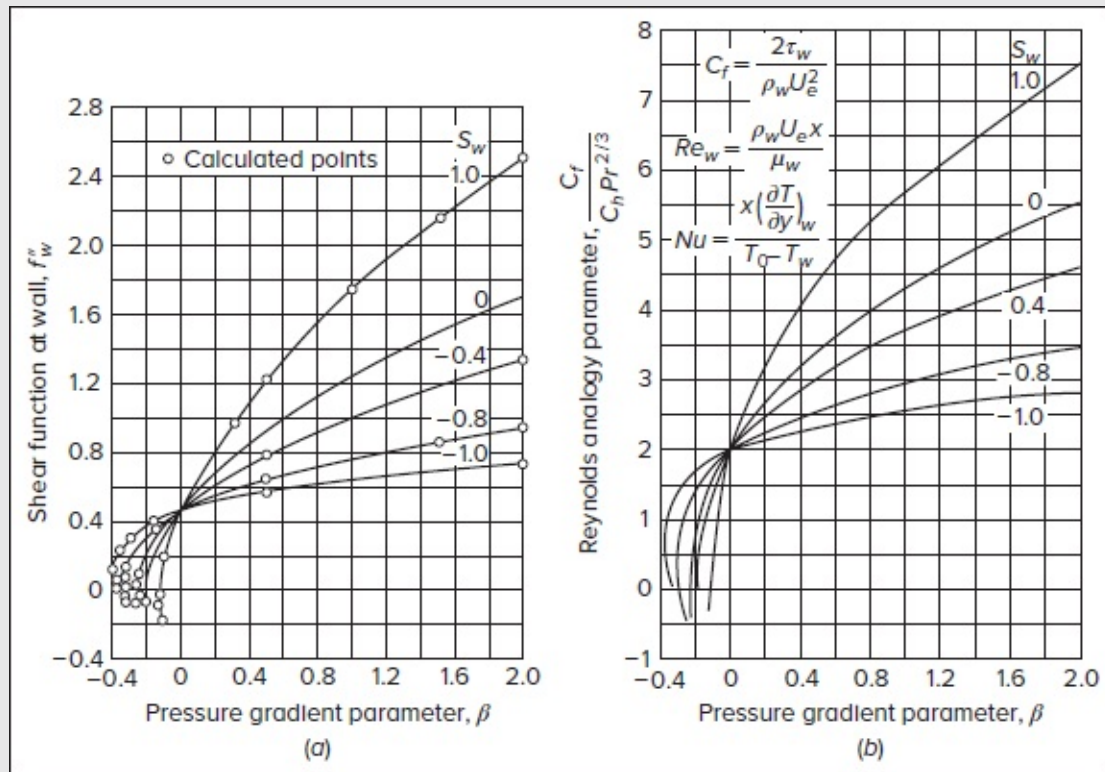


FIGURE 7-10

Computations of (a) skin friction $f''(0)$ and (b) the Reynolds analogy parameter for laminar compressible similar flows. [After Cohen and Reshotko (1956).]

For nonsimilar flows, it seems reasonable as a first approximation to compute the local value of $\beta(x)$ and use [Fig. 7-10](#) to estimate the wall heat flux and skin friction. This was suggested by Lees (1956), who also performed a clever approximate analysis for the forward region of a blunt body. As we move away from the stagnation point of a cylinder or sphere, the heat flux drops off, but not as any simple function of x or ϕ . The local Falkner–Skan parameter is

$$\beta(x) = \frac{2\xi}{U_e} \frac{dU_e}{d\xi} \quad \text{where} \quad \xi = \int_0^x \rho_e U_e \mu_e dx \quad (7-70)$$

For a perfect gas, we can compute $U_e(x)$ from the relation $U_e = Ma_e \sqrt{\gamma R T_e}$, and the Mach number $Ma_e(x)$ can be estimated from the Newtonian approximation given by Eqs. (7-66a) if the approaching flow is supersonic:

$$\frac{p_e(x)}{p_0} \approx \frac{p_\infty}{p_0} [1 + Ma_\infty^2 \cos^2 \theta(x)] \quad (7-71)$$

The ratio $p_0/p_\infty \approx 1 + \gamma Ma_e^2$ from normal-shock theory at high Mach numbers, e.g., White (2016, p. 615). Therefore, since $\theta = 2x/D$ for a round nose, [Eq. \(7-71\)](#) is a formula to predict surface Mach number Ma_e^2 , supplemented by the ideal-gas isentropic relations

$$\frac{p_0}{p_e} = \left[1 + \frac{1}{2}(\gamma - 1)Ma_e^2 \right]^{\gamma/(\gamma-1)} \quad \text{and} \quad \frac{T_0}{T_e} = 1 + \frac{1}{2}(\gamma - 1)Ma_e^2 \quad (7-72)$$

For a round-nosed blunt body, Lees (1956) combines these approximations with a modified form of the Illingworth transformation in [Eq. \(7-34\)](#) and uses the concept of “local similarity,” which enables us to determine the heat transfer $q_w(x)$ from the local gradient $\beta(x)$ through [Eq. \(7-70\)](#). The result is the following formula for the local heat flux:

$$\frac{q_w(x)}{q_w(0)} \approx \frac{F(x)}{(2^{j+1}K/U_\infty)^{1/2}}; \quad F(x) = \frac{(C_e U_e / C_0 U_\infty) r_0^j}{\int_0^x (C_e U_e / C_0 U_\infty) r_0^{2j} dx} \quad [\text{Lees (1956)}] \quad (7-73)$$

We recall that K represents the stagnation-point velocity gradient ([Figs. 7-6](#) and [7-7](#)), and $r_0(x)$ stands for the body surface radius, with $j = 1$ for axisymmetric flow and $j = 0$ for planar flow. Also, $C = \rho\mu / (\rho_e \mu_e)$ is the Chapman–Rubesin parameter; hence $C_e/C_0 = \rho_e \mu_e / (\rho_0 \mu_0)$, where the subscript “0” refers to the stagnation point. This formula is quite simple in appearance, but the required quadrature is somewhat tedious. Shortly thereafter, Kemp et al. (1959) slightly refined the analysis and proposed adding a correction factor in the form of a multiplier,

$$\frac{q_w(x)}{q_w(0)} \approx \left[\frac{q_w(x)}{q_w(0)} \right]_{\text{Lees}} [0.936 + 0.090\sqrt{\beta(x)}] \quad (7-74)$$

This relation leads to about a 10 percent correction at the most. In either [Eqs. \(7-73\)](#) or (7-74), one should estimate $q_w(0)$ as accurately as possible, using, say, [Eqs. \(7-63a\)](#) and (7-63b).

Figure 7-11 compares these two formulas with experimental heat-flux measurements taken on a hemisphere in hypersonic flow. Both appear to be in favorable agreement.

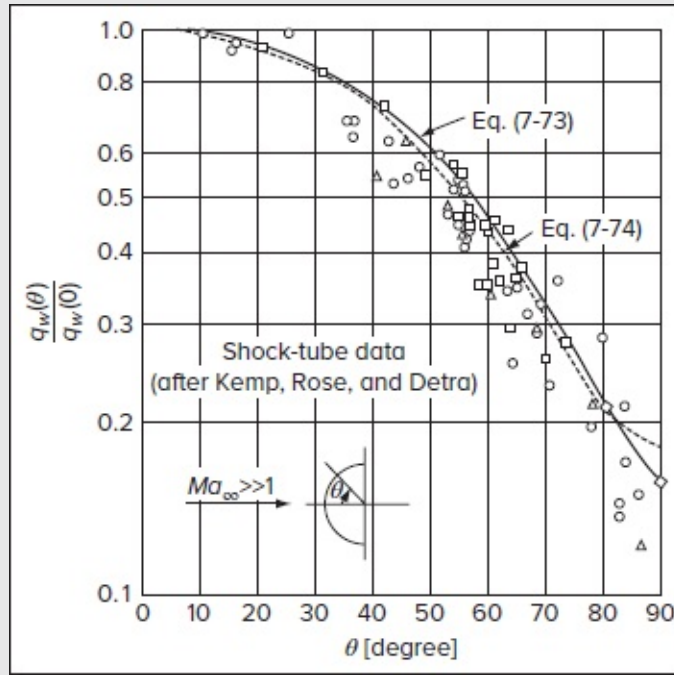


FIGURE 7-11

Comparison of theory and experiment for local heat transfer in hypersonic laminar flow past a hemisphere.

7-4.2 Integral Relations for a Compressible Boundary Layer

A second possible approach to an arbitrary, compressible, boundary layer is through the Kármán-type momentum-integral relations, similar to the incompressible-flow theories developed in Sec. 4-6. The approach is nearly unchanged, but the integral relations must be rederived from the compressible, boundary-layer Eqs. (7-22a), (7-22b), and (7-22c); Page 418 the velocity v is eliminated through the continuity Eq. (7-22a) and then Eqs. (7-22b) and (7-22c) are integrated outwardly from the wall to infinity. The first result is the momentum-integral relation

$$\frac{d\theta}{dx} + \frac{\theta}{U_e} \frac{dU_e}{dx} \left(2 + H + \frac{U_e}{\rho_e} \frac{d\rho_e}{dU_e} \right) + \frac{1}{\rho_e U_e^2} \frac{d}{dx} \left(p_e \delta - \int_0^\delta p \, dy \right) = \frac{C_f}{2} \quad (7-75)$$

where

$$C_f = \frac{2\tau_w}{\rho_e U_e^2} \quad H = \frac{\delta^*}{\theta}$$

$$\delta^* = \int_0^\infty \left(1 - \frac{\rho}{\rho_e} \frac{u}{U_e} \right) dy \quad (\text{compressible displacement thickness})$$

$$\theta = \int_0^\infty \frac{\rho}{\rho_e} \frac{u}{U_e} \left(1 - \frac{u}{U_e} \right) dy \quad (\text{compressible momentum thickness})$$

and, for an adiabatic freestream,

$$\frac{U_e}{\rho_e} \frac{d\rho_e}{dU_e} \equiv -Ma_e^2$$

This relation is valid for either laminar or turbulent flow. For low-speed motion at constant density, [Eq. \(7-75\)](#) reduces to the Kármán momentum-integral relation [Eq. \(4-143\)](#). The effect of compressibility adds three complicating factors to the analysis: (1) the density variation must be included in the definition of the integral thicknesses, (2) the freestream Mach number is an important part of the pressure gradient term, and (3) at high speeds, the pressure variation integrated across the boundary layer [last term on the left of [Eq. \(7-75\)](#)] may be too large to neglect.

7-4.3 The Laminar Boundary Layer

For laminar flow, it is customary to neglect the cross-streamwise pressure variation and consider only adiabatic freestreams, for which [Eq. \(7-75\)](#) reduces to

$$\frac{d\theta}{dx} + \frac{\theta}{U_e} \frac{dU_e}{dx} (2 + H - Ma_e^2) \approx \frac{C_f}{2} \quad (7-76)$$

In computing θ and δ^* from their definitions in (7-75), we can avoid the energy equation by substituting the ideal gas expression, $\rho_e T_e \approx \rho T$, into the Crocco–Busemann relation, (7-29), which can be expanded as

$$T = T_w + (T_{aw} - T_w) \frac{u}{U_e} - \frac{U_e^2}{2c_p} \left(\frac{u}{U_e} \right)^2 = T_w + (T_{aw} - T_w) \frac{u}{U_e} - (T_{aw} - T_e) \left(\frac{u}{U_e} \right)^2 \quad (7-77)$$

since $U_e^2/(2c_p) = T_{aw} - T_e$. In terms of the density ratio, we have

$$\frac{\rho_e}{\rho} = \frac{T}{T_e} = \frac{T_w}{T_e} + \frac{T_{aw} - T_w}{T_e} \frac{u}{U_e} - \frac{T_{aw} - T_e}{T_e} \left(\frac{u}{U_e} \right)^2 = T_w^* + (T_{aw}^* - T_w^*)F - (T_{aw}^* - 1)F^2 \quad (7-78)$$

where the normalized velocity and wall temperatures refer to $F \equiv u/U_e$, $T_w^* \equiv T_w/T_e$, and $T_{aw}^* \equiv T_{aw}/T_e$. In this manner, the density ratio can be entirely eliminated in the displacement and momentum thickness integrals; the latter become expressible directly as functions of the normalized velocity and wall temperatures, specifically,

$$\delta^* = \int_0^\infty \left[1 - \frac{F}{T_w^* + (T_{aw}^* - T_w^*)F - (T_{aw}^* - 1)F^2} \right] dy \quad \text{and} \quad \theta = \int_0^\infty \frac{F(1 - F)}{T_w^* + (T_{aw}^* - T_w^*)F - (T_{aw}^* - 1)F^2} dy \quad (7-79)$$

Naturally, these extended integrals are easier to evaluate, provided the temperatures are known. Moreover, the incompressible forms of δ^* and θ can be restored as special cases for which $T_{aw}^* = T_w^* = 1$ or $T_w = T_e$.

The text by Walz (1969) discusses several approaches to the solution of [Eq. \(7-76\)](#). Here we present only the method of Gruschwitz (1950), who extends the classic Kármán–

Pohlhausen technique by approximating both velocity and density as polynomials in y/δ . The single parameter is the dimensionless pressure gradient, λ or Λ :

$$\lambda = \frac{T_w \theta^2}{T_e \nu_e} \frac{dU_e}{dx} = \Lambda \left(\frac{\theta}{\Delta} \right)^2 \quad [\text{Pohlhausen (1921)}] \quad (7-80)$$

where

$$\Delta = \int_0^\delta \frac{\rho}{\rho_e} dy \quad \text{and} \quad \frac{\theta}{\Delta} = \frac{37 - \Lambda/3 - 5\Lambda^2/144}{315}$$

Page 419

Note that for low-speed adiabatic flow, $\rho \approx \rho_e$, $\Delta \approx \delta$, and Λ reduces to Pohlhausen's original parameter $(\delta^2/\nu) dU/dx$. Gruschwitz substitutes his polynomial distributions in the momentum-integral and mechanical-energy integral relations and finds, after considerable algebra, that the problem reduces to a single first-order differential equation for the momentum thickness $\theta(x)$, specifically

$$\frac{\theta U_e}{\nu_e} \frac{d\theta}{dx} = F_1(\lambda) - \lambda \frac{T_e}{T_w} [2 - Ma_e^2 F_2(\lambda)] \quad (7-81)$$

It is assumed that the variation of U_e , ν_e , Ma_e , and T_e/T_w are known functions of x . Gruschwitz then proceeds to specify polynomial expressions for F_1 and F_2 , which include the Prandtl number and specific-heat ratio as parameters:

$$F_1 = 2 \frac{\theta}{\Delta} \left(1 - \frac{\Lambda}{15} + \frac{\Lambda^2}{240} \right) \approx 0.235 \exp(-5.4\lambda) \quad F_2 = 1 - \frac{\gamma - 1}{2} \frac{\Delta}{\theta} \left[\frac{\delta_3}{\Delta} - \frac{Pr(12 + \Lambda)^2}{2160} \right] \approx 0.78 \exp(1.5\lambda) \quad (7-82)$$

where

$$\frac{\delta_3}{\Delta} = \frac{798,048 - 4,656\Lambda - 758\Lambda^2 - 7\Lambda^3}{4,324,320}$$

The exponential approximations are for the special case of $Pr = 0.72$, $\gamma = 1.4$, which corresponds to air quite closely and avoids unnecessary algebra. Again, it is believed that this method of Gruschwitz is equivalent in accuracy to several more sophisticated techniques.

Once $\lambda(x)$ is found from the (numerical) solutions of [Eqs. \(7-81\)–\(7-82\)](#), and $\Lambda(x)$ is computed from [Eq. \(7-80\)](#), the local skin friction and separation point may be estimated from

$$C_f = \frac{2\tau_w(x)}{\rho_e U_e^2} \approx \frac{4\nu_e}{U_e \Delta} \left(1 + \frac{\Lambda}{7} \right) \quad (\text{skin friction}) \quad \lambda \approx -0.1 \quad \Lambda \approx -7 \quad (\text{separation}) \quad (7-83)$$

These equations, though algebraically complicated, are easy to program and solve numerically. For further detail on the laminar-flow method by Gruschwitz (1950), see Schreier (1982).

7-4.4 Finite-Difference Methods for Compressible Laminar Flow

Since the laminar-boundary-layer equations are well defined and essentially free from empiricism, they are, in principle, solvable by finite-difference or finite-element methods. Many workers have suggested numerical approaches, and some of these are discussed in the texts by Cebeci and Smith (1974), Schreier (1982), and Anderson (2000). Most of the published methods use coordinate transformations before applying numerical approximations. Here we present a finite-difference approach in the raw variables (u, v, ρ, p, T) as an extension of the incompressible-flow methods of Sec. 4-7. The results are easy to understand and program.

We consider only two-dimensional, steady, compressible flow. We denote the (x, y) location of a mesh point by subscripts (m, n) as in [Fig. 7-12](#), which is a convenient repetition of [Fig. 4-30](#). The variables at each node are denoted by $u_{m,n}$, $v_{m,n}$, $\rho_{m,n}$, and $T_{m,n}$. The transport properties $\mu_{m,n}$, $k_{m,n}$, and $c_{pm,n}$ also vary because of temperature variations. The freestream properties are assumed to be known functions of x with only one coordinate subscript: $U_{e,m}$, $T_{e,m}$, $p_{e,m}$, and $\rho_{e,m}$. The Prandtl number is assumed constant.

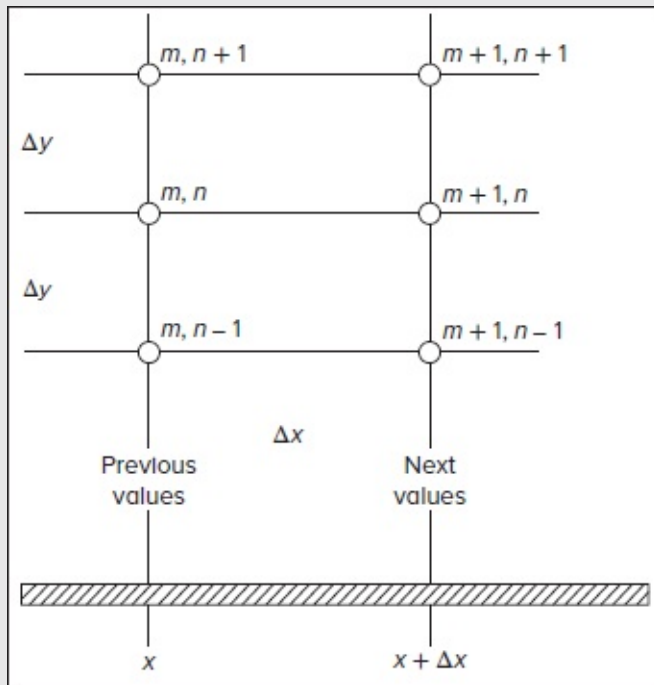


FIGURE 7-12

Finite-difference mesh for a two-dimensional boundary layer.

7-4.4.1 AN EXPLICIT MODEL. The steady form of the x -momentum Eq. (7-1b) can be expressed as

$$\rho u \frac{\partial u}{\partial x} + \rho v \frac{\partial u}{\partial y} = \rho_e U_e \frac{dU_e}{dx} + \frac{\partial \mu}{\partial y} \frac{\partial u}{\partial y} + \mu \frac{\partial^2 u}{\partial y^2} \quad (7-84)$$

where we have broken up the viscous term into two parts. By analogy with the development of Sec. 4-7.1, the finite-difference model of this equation may be written as

$$\rho_{m,n} u_{m,n} \frac{u_{m+1,n} - u_{m,n}}{\Delta x} + \rho_{m,n} v_{m,n} \frac{u_{m,n+1} - u_{m,n-1}}{2\Delta y} \approx \frac{\rho_{e,m}(U_{m+1}^2 - U_m^2)}{2\Delta x} + \frac{(\mu_{m,n+1} - \mu_{m,n-1})(u_{m,n+1} - u_{m,n-1})}{(2\Delta y)^2} + \mu_{m,n} \frac{u_{m,n+1} - 2u_{m,n} + u_{m,n-1}}{\Delta y^2}$$

If we clean this up and solve for the (single) downstream velocity, we obtain

$$u_{m+1,n} \approx (\alpha^* - \beta + \zeta) u_{m,n+1} + (1 - 2\alpha^*) u_{m,n} + (\alpha^* + \beta - \zeta) u_{m,n-1} + \frac{\rho_{e,m}(U_{m+1}^2 - U_m^2)}{2\rho_{m,n} u_{m,n}} \quad (7-85)$$

Page 420

where

$$\alpha^* = \frac{\mu_{m,n} \Delta x}{\rho_{m,n} u_{m,n} \Delta y^2} \quad \beta = \frac{v_{m,n} \Delta x}{2u_{m,n} \Delta y} \quad \zeta = \frac{(\mu_{m,n+1} - \mu_{m,n-1}) \Delta x}{4\rho_{m,n} u_{m,n} \Delta y^2}$$

Equation (7-85) represents the compressible analog of the incompressible formula given by [Eq. \(4-167\)](#).

Next, we consider the steady form of the energy Eq. (7-1d), namely,

$$\rho u c_p \frac{\partial T}{\partial x} + \rho v c_p \frac{\partial T}{\partial y} = u \frac{dp_e}{dx} + \mu \left(\frac{\partial u}{\partial y} \right)^2 + \frac{\partial k}{\partial y} \frac{\partial T}{\partial y} + k \frac{\partial^2 T}{\partial y^2} \quad (7-86)$$

As we mimic the development of Sec. 4-8.2, an explicit finite-difference model of this equation can be written as

$$(\rho u c_p)_{m,n} \frac{T_{m+1,n} - T_{m,n}}{\Delta x} + (\rho v c_p)_{m,n} \frac{T_{m,n+1} - T_{m,n-1}}{2\Delta y} \approx - \frac{u_{m,n} \rho_{e,m}(U_{m+1}^2 - U_m^2)}{2\Delta x} + \mu_{m,n} \left(\frac{u_{m,n} - u_{m,n-1}}{\Delta y} \right)^2 + \frac{(k_{m,n+1} - k_{m,n-1})(T_{m,n+1} - T_{m,n-1})}{(2\Delta y)^2} + k_{m,n} \frac{T_{m,n+1} - 2T_{m,n} + T_{m,n-1}}{\Delta y^2}$$

This may be rearranged into the following explicit scheme:

$$T_{m+1,n} \approx \left(\frac{\alpha^*}{Pr} - \beta + \frac{\zeta}{Pr} \right) T_{m,n+1} + \left(1 - \frac{2\alpha^*}{Pr} \right) T_{m,n} + \left(\frac{\alpha^*}{Pr} + \beta - \frac{\zeta}{Pr} \right) T_{m,n-1} - \frac{\rho_{e,m}(U_{m+1}^2 - U_m^2)}{2(\rho u c_p)_{m,n}} + \frac{\alpha^*}{c_{p,m,n}} (u_{m,n} - u_{m,n-1})^2 \quad (7-87)$$

This is the compressible analog of [Eq. \(4-184\)](#) Finally, continuity in Eq. (7-1a) may be discretized as

$$\frac{(\rho u)_{m+1,n} - (\rho u)_{m,n}}{2\Delta x} + \frac{(\rho u)_{m+1,n-1} - (\rho u)_{m,n-1}}{2\Delta x} + \frac{(\rho v)_{m+1,n} - (\rho v)_{m+1,n-1}}{\Delta y} \approx 0$$

and then rearranged to solve for the normal velocity at the next mesh point:

$$v_{m+1,n} \approx \frac{(\rho v)_{m+1,n-1}}{\rho_{m+1,n}} - \frac{\Delta y}{2\rho_{m+1,n}\Delta x} [(\rho u)_{m+1,n} - (\rho u)_{m,n} + (\rho u)_{m+1,n-1} - (\rho u)_{m,n-1}] \quad (7-88)$$

This expression corresponds to [Eq. \(4-169\)](#). The density values at $(m + 1)$ can be computed directly from the ideal-gas law, once the temperatures are known from [Eq. \(7-87\)](#). In general, we have

$$\frac{\rho_{m,n}}{\rho_e} = \frac{T_e}{T_{m,n}} \quad (7-89)$$

Page 421

The transport properties can be computed from the known temperature. For air, for example, power-law approximations may be used from Tables 1-1 and 1-2 to give

$$\frac{\mu_{m,n}}{\mu_e} \approx \left(\frac{T_{m,n}}{T_e} \right)^{0.666} \quad \frac{k_{m,n}}{k_e} \approx \left(\frac{T_{m,n}}{T_e} \right)^{0.81} \quad (7-90)$$

Subsequently, $c_{pm,n} = k_{m,n} Pr/\mu_{m,n}$ can be deduced. Equations (7-85) and (7-87)–[\(7-90\)](#) must be solved collectively for $(u, T, v, \rho, \mu, k, c_p)$ at the new point $(m + 1, n)$. Since the method is explicit, the following inequalities must hold for numerical stability, assuming a gas with $Pr < 1$:

$$\frac{\alpha^*}{Pr} < 0.5 \quad \beta < \frac{\alpha^*}{Pr} \quad \frac{\zeta}{Pr} < \beta \quad (7-91)$$

These parameters should be monitored during the computation to ensure convergence.

7-4.4.2 AN IMPLICIT MODEL. By analogy with Sec. 4-7.2, an implicit finite-difference scheme may be established by evaluating the second derivatives of u and T at the next station, $(m + 1)$. We then obtain two tridiagonal relations:

$$-\alpha^* u_{m+1,n+1} + (1 + 2\alpha^*) u_{m+1,n} - \alpha^* u_{m+1,n-1} \approx u_{m,n} + \frac{\rho_{e,m}(U_{m+1}^2 - U_m^2)}{2\rho_{m,n}u_{m,n}} - (\beta - \zeta)(u_{m,n+1} - u_{m,n-1}) \quad (7-92)$$

$$\begin{aligned} -\frac{\alpha^*}{Pr} T_{m+1,n+1} + \left(1 - \frac{2\alpha^*}{Pr}\right) T_{m+1,n} - \frac{\alpha^*}{Pr} T_{m+1,n-1} \approx T_{m,n} + \frac{\alpha^*}{c_{p,m,n}} (u_{m,n} - u_{m,n-1})^2 - \frac{\rho_{e,m}(U_{m+1}^2 - U_m^2)}{2(\rho u c_p)_{m,n}} \\ - \left(\beta - \frac{\zeta}{Pr}\right) (T_{m,n+1} - T_{m,n-1}) \end{aligned} \quad (7-93)$$

These can be solved, in conjunction with [Eq. \(7-88\)](#), for the new velocities and temperatures, using the tridiagonal matrix algorithm described in Sec. 4-7.2.1. Generally, this implicit computation, though more complex algebraically, is faster for a given accuracy than the explicit formulation. The density and transport properties are again computed by [Eqs. \(7-89\)](#) and [\(7-90\)](#).

The boundary conditions for either the explicit or implicit method are

$$\text{Known freestream conditions:} \quad U_e, T_e, \text{ and } \rho_e \quad (7-94a)$$

$$\text{No slip:} \quad u_{m,1} = v_{m,1} = 0 \quad (7-94b)$$

$$\text{No temperature jump:} \quad T_{m,1} = T_w \quad (7-94c)$$

$$\text{Known wall heat flux:} \quad T_{m,2} \approx T_{m,1} + \frac{q_w \Delta y}{k_{m,1}} \quad (7-94d)$$

$$\text{Known initial profiles:} \quad u_{1,n}, v_{1,n}, \text{ and } T_{1,n} \quad (7-94e)$$

The implicit method has no stability limitations, but a small mesh size (Δx , Δy) should nevertheless be chosen in order to cap the resulting truncation errors.

7-4.4.3 EXAMPLE: A FLAT PLATE WITH ADIABATIC WALL. The finite-difference marching methods discussed before can be applied, in principle, to any laminar, compressible, boundary layer with known freestream and wall-temperature conditions. As an example, let us consider flow over a flat-plate with $Ma_e = 3.0$, assuming air with a freestream temperature of 300 K and a Prandtl number of 0.71. Viscosity and thermal conductivity are readily computed by the power-law approximations in (7-90). The transverse mesh size Δy can be chosen such that the velocity profile will contain about 40 points. The streamwise step size Δx can be chosen so that velocities and temperatures change by no more than 5 percent with each step. To avoid instability, the implicit method of Sec. 7-4.4.2 can be readily implemented.

Figure 7-13 shows the computed results for both an adiabatic and a cold wall ($T_w = T_e$). In comparison to the exact analytical results of [Figs. 7-3](#) and [7-4](#), the adiabatic-wall temperature is slightly lower, corresponding to a recovery factor $r \approx 0.81$. The cold wall greatly suppresses the high temperatures generated by viscous dissipation and creates a thinner, more rounded velocity profile that is more stable (i.e., resistant to transition). The computed values of $C_D \sqrt{Re_x} \approx 1.18$ and 1.28 for adiabatic and cold walls, respectively, are very close to the exact values of [Fig. 7-5a](#). The numerical approach is judged to be a reasonable success.

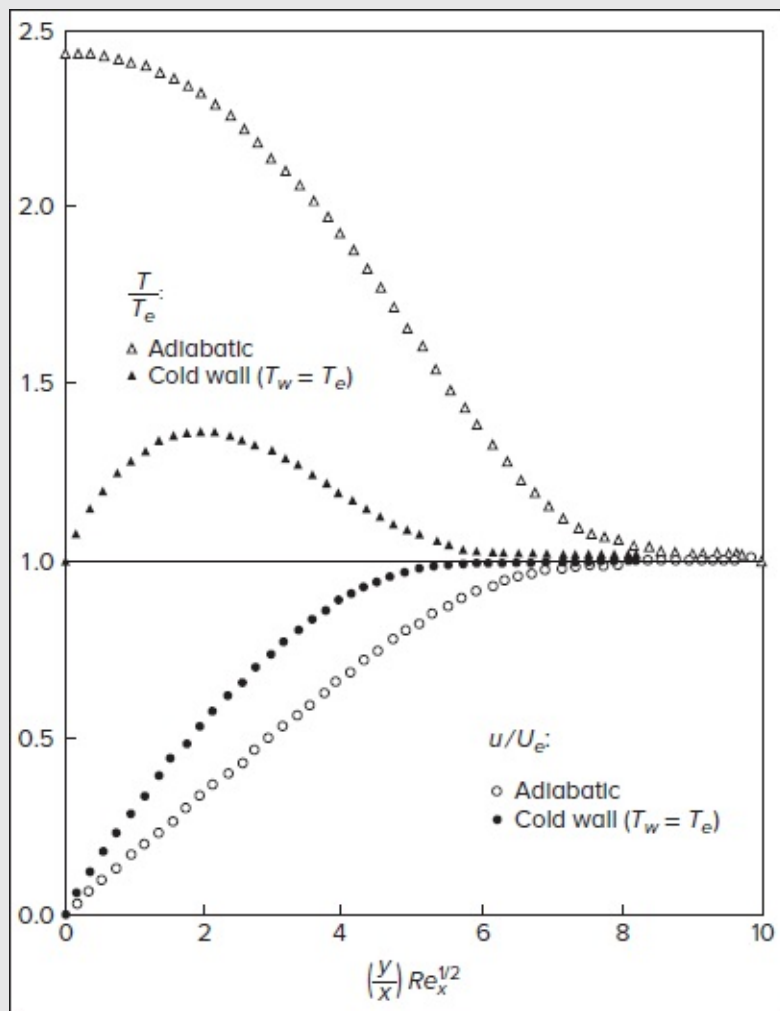


FIGURE 7-13

Digital-computer results for velocity and temperature profiles in flat-plate flow at $Ma = 3.0$, from [Eqs. \(7-88\)](#), [\(7-92\)](#), and [\(7-93\)](#).

7-4.4.4 EXAMPLE: SUPERSONIC LINEARLY DECELERATING FLOW.

As a second example involving an adverse pressure gradient, let us consider an extension of the Howarth flow from Sec. 4-5.1, where $U = U_0 (1 - x/L)$, to a compressible, linearly decreasing, freestream Mach number with:

$$Ma_e(x) = Ma_0 \left(1 - \frac{x}{L}\right) \quad (7-95)$$

For incompressible conditions, $Ma_0 \ll 1$, this laminar motion separates at $x/L \approx 0.12$ (see [Figs. 4-25](#) or [4-31](#)). For higher Mach numbers, let us assume an adiabatic wall and compare the predictions of our integral method to those of a finite-difference solution. Again let us

take the freestream as air at 300 K with $Pr = 0.71$.

It is quite easy to use [Eq. \(7-95\)](#) in conjunction with the Gruschwitz integral method, [Eq. \(7-81\)](#). One needs only an estimate for the wall temperature, which could be supplied by assuming a “local” recovery factor of $r \approx \sqrt{Pr} \approx 0.84$:

$$\frac{T_w}{T_e} \approx 1 + (0.71)^{1/2} \left(\frac{1.4 - 1}{2} \right) Ma_e^2 = 1 + 0.1685 Ma_e^2 \quad (7-96)$$

Integration of [Eq. \(7-81\)](#) by, say, the Runge–Kutta method, will readily produce $\theta(x)$, which then enables us to deduce $\lambda(x)$ and $C_f(x)$ directly from [Eqs. \(7-80\)](#) and [\(7-83\)](#), respectively.

Alternatively, the implicit numerical method of Sec. 7-4.4.2 can be programmed using [Eq. \(7-95\)](#), with an adiabatic-wall ($q_w = 0$) approximation and $T_{m,2} = T_{m,1}$. In this vein, the boundary layer can be discretized with at least 40 mesh points Δy at each x station. The local skin friction predicted by each method is reported in [Fig. 7-14](#). The case of $Ma_0 = 0$ corresponds to our earlier study and [Fig. 4-31](#). We see that compressibility, in this case, causes earlier separation of the laminar boundary layer. If we assume that the numerical results in [Fig. 7-14](#) are trustworthy, then the integral method of Gruschwitz may be characterized as being qualitatively correct but imprecise at increasing Mach numbers.

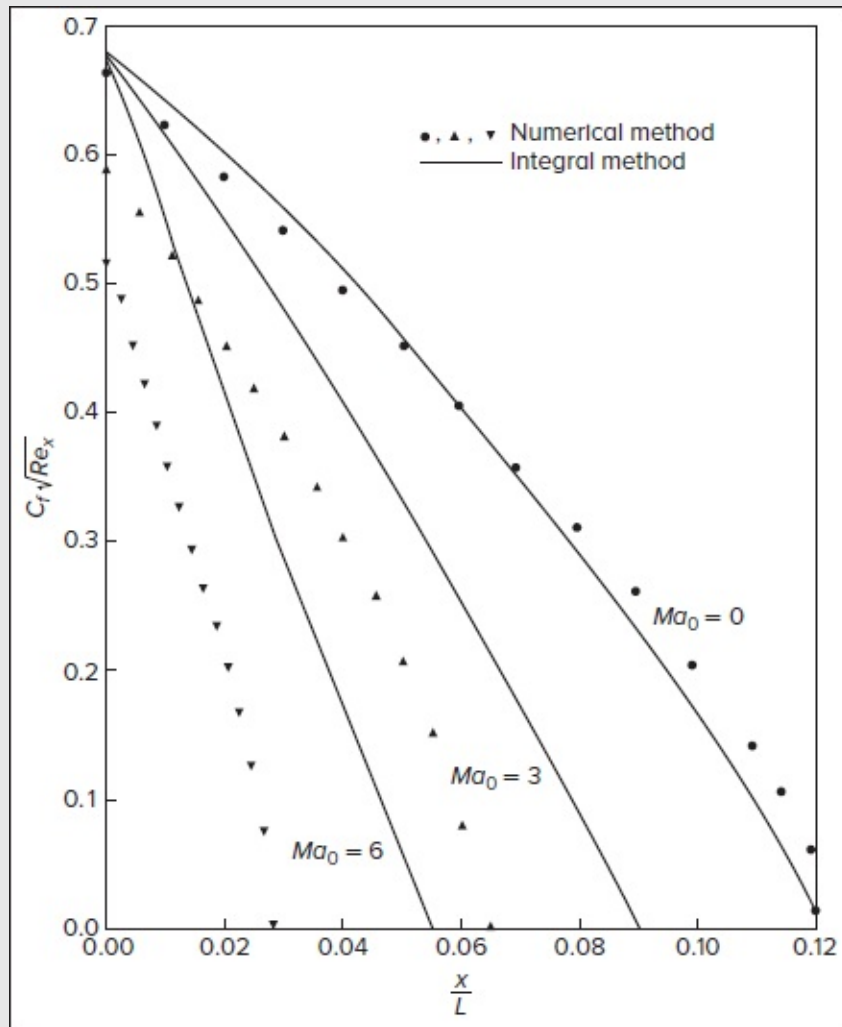


FIGURE 7-14

Boundary layer with linearly decreasing freestream Mach number: comparison of an integral method [Eq. (7-81)], with an implicit finite-difference method [Eqs. (7-88), (7-92), and (7-93)].

An interesting sidelight of this example is that the computed adiabatic-wall temperatures prove to be lower than expected, especially near separation. The following table of computed recovery factors near separation illustrates this point:

Ma_0	0	1	2	3	4	5	6
r_{sep}	0.84	0.82	0.75	0.68	0.61	0.55	0.51

The reason for this behavior is that, for a given value of U_e , the near-wall shear stresses near separation decrease, and the viscous dissipation term $[\mu (\partial u / \partial y)^2]$ becomes smaller, hence

generating less internal energy compared to $U_e^2/(2c_p)$. This lowering of T_{aw}/T_e is difficult to estimate beforehand and so it cannot be reasonably preprogrammed into the Gruschwitz method of [Eq. \(7-81\)](#).

7-4.4.5 OTHER NUMERICAL SOLUTIONS. The aerospace industry has developed many CFD approaches for compressible viscous flows. Laminar flow is especially successful, even for three-dimensional geometries, since supercomputers can now supply billions of mesh points. One can now compute the supersonic flow field around a complex aircraft shape, as reviewed by Agarwal (1999). However, the turbulence-modeled portions of aircraft flow are not so accurate. Compressible-flow CFD methods, primarily inviscid, are reviewed in monographs by Laney (1998), Anderson (2002), Chattot (2002), and Felcman et al. (2003). Shock-wave discontinuities are often present and difficult to predict, although excellent shock-capturing and shock-fitting CFD schemes have been developed. Most boundary-layer calculations use finite differences, but the finite-element method is also successful [Hytopoulos et al. (1993)]. Compressible-boundary-layer integral methods are also available from the Internet Applets of Devenport and Schetz (2002).

Boundary-layer computations began in the 1960s with the work of A. M. O. Smith and colleagues at McDonnell-Douglas Corp. [Figure 7-15](#) depicts the computations of Smith and Clutter (1965) for hypersonic flow past a flat-nosed cylinder with a rounded shoulder. It may be readily seen that the agreement with data from Kemp et al. (1959) is adequate. The simple correlations of [Eqs. \(7-73\)](#) and [\(7-74\)](#) from Lees (1956) are also quite reasonable. Such results require a preliminary inviscid calculation to yield accurate freestream distributions for $U_e(x)$ and $T_e(x)$.

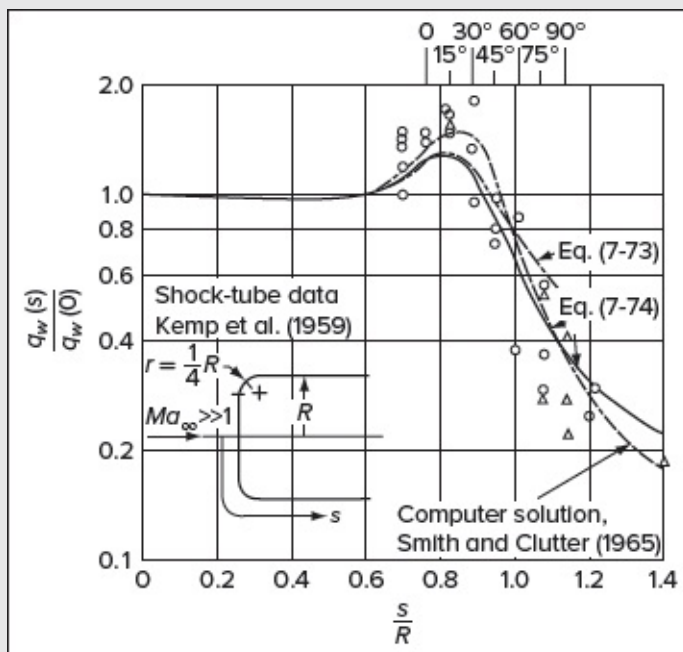


FIGURE 7-15

Comparison of theory and experiment for surface heat flux in laminar hypersonic flow past a flat-nosed cylinder.

7-5 SPECIAL TOPICS IN COMPRESSIBLE LAMINAR FLOW

The subject of compressible (supersonic) viscous flow is a broad one, as there are many topics under investigation, including, for example: (1) high-temperature breakdown of air into separate species, notably the dissociation of oxygen and nitrogen, with resulting species diffusion; (2) combustion, ionization, and other nonequilibrium thermodynamic processes; (3) radiation from a hot-gas boundary layer; and (4) foreign-gas injection into the boundary layer. Here we briefly discuss two of these topics. For further reading, see Anderson (2000).

7-5.1 The Laminar Supersonic Cone Rule

Let us consider the case of an inviscid supersonic flow past a cone at zero incidence [e.g., Shapiro (1954, Chap. 17)]; for $Ma_\infty > 1.2$ and a cone half-angle below 55° , the resulting shock wave remains attached to the cone vertex, and the flow at the cone surface has constant velocity, pressure, and temperature. As such, the boundary layer in supersonic cone flow at zero incidence exhibits properties akin to those associated with flat-plate flow. In addition to a zero pressure gradient, let us assume that T_w is constant.

The boundary-layer flow is axisymmetric, and Lees (1956) modified the applicable Illingworth transformation through [Eqs. \(7-34\)](#) as follows:

$$\xi = \int_0^x \rho_e U_e \mu_e r_0^{2j} dx \quad \text{and} \quad \eta = \frac{\rho_e U_e r_0^j}{\sqrt{2\xi}} \int_0^y \frac{\rho}{\rho_e} dy \quad (7-97)$$

where $r_0(x)$ stands for the body surface radius while the exponent $j = 1$ stays for axisymmetric flow and $j = 0$ for planar motion. Note the resemblance to the incompressible Mangler transformation embodied in Eqs. (4-208). When substituted into the boundary-layer momentum and energy equations, the similarity relations given by Eqs. (7-47a) and (7-47b) are obtained.

Now let us define a cone of half-angle ϕ and $r_0 = bx$, where $b = \tan^{-1} \phi$. Then the variables ξ and η become

$$\xi_{\text{cone}} = \frac{\rho_e U_e \mu_e b^2 x^3}{3} \quad \text{and} \quad d\eta_{\text{cone}} = \left(\frac{3\rho_e U_e}{2x\mu_e} \right)^{1/2} \rho dy \quad (7-98)$$

From the expression for $d\eta/dy$, we can then compute the skin-friction coefficient at the surface

$$C_{f, \text{cone}} = \frac{2\tau_w}{\rho_e U_e^2} = \frac{\sqrt{6} C_w f''(0)}{(\rho_e U_e x / \mu_e)^{1/2}} = \frac{\sqrt{6} C_w f''(0)}{(Re_{xe})^{1/2}} \quad (7-99)$$

Page 425

where C denotes the Chapman–Rubesin parameter and $f''(0)$ may be computed from the similarity Eqs. (7-47a) and (7-47b) for zero pressure gradients with $\beta = 0$.

If we carry out the same analysis for flat-plate flow with constant wall temperature, we obtain

$$\xi_{\text{plate}} = \rho_e U_e \mu_e x, \quad d\eta_{\text{plate}} = \left(\frac{\rho_e U_e}{2x \mu_e} \right)^{1/2} \rho dy \quad \text{and} \quad C_{f, \text{plate}} = \frac{\sqrt{2} C_w f''(0)}{(\rho_e U_e x / \mu_e)^{1/2}} = \frac{\sqrt{2} C_w f''(0)}{(Re_{xe})^{1/2}} \quad (7-100)$$

Interestingly, if a cone and a plate have the same T_w/T_e , then C_w will be the same for both; furthermore, if the Mach number and specific-heat ratio are the same for both, then $f''(0)$ will be the same, because it originates from identical similarity equations for $\beta = 0$. So by comparing the two C_f expressions, a cone-to-plate rule may be readily identified for laminar compressible flow. We may take at least two points of view:

$$\text{If } Re_{xe, \text{cone}} = Re_{xe, \text{plate}} \quad \text{then} \quad C_{f, \text{cone}} = \sqrt{3} C_{f, \text{plate}} \quad (7-101a)$$

$$\text{If } C_{f, \text{cone}} = C_{f, \text{plate}} \quad \text{then} \quad Re_{xe, \text{cone}} = 3 Re_{xe, \text{plate}} \quad (7-101b)$$

The view in Eq. (7-101a) is the usual one stated in the literature: If a cone and a plate have the same local Reynolds number, Mach number, and wall-temperature ratio, then the cone skin friction is 73.2 percent higher than the plate's local friction. Further, if both have the same Prandtl number, then the cone local heat flux is also 73.2 percent higher than the plate's. This behavior follows from the Reynolds analogy [Eq. (7-56c)]. There is also a turbulent cone rule (Sec. 7-8.4), but in this case the ratio of cone to plate C_f and C_h is only about 1.1–1.15, not a simple square root, 1.732. For this reason, a Reynolds number ratio based on Eq. (7-101b) is the way a turbulent cone rule is specified.

7-5.2 Hypersonic Flow: Shock-Wave Boundary-Layer Interactions

As supersonic flow increases to *hypersonic* conditions, interactions between the boundary layer and the freestream become important. As Anderson (2002) remarks, the definition of hypersonic (Greek, *hyper*: over, above, excessive) is flexible, although it usually corresponds to $Ma > 5$. The key indicator depends on the shock-wave boundary-layer interactions. If they are strong, the flow is hypersonic.

Interactions can be classified depending on (1) pressure induced by the displacement effect of the boundary layer, (2) blast-wave effects due to blunting of a leading edge, (3) flow separation in a supersonic compression corner, (4) a shock wave impinging on a boundary layer, and (5) boundary layer changes due to vorticity introduced from a curved upstream shock wave. The interaction problem is intriguing, because it requires the outer inviscid and inner viscous-flow equations to be solved simultaneously. Reviews of hypersonic flow theory are given in the classic texts by Hayes and Probstein (1959), Dorrance (1962), as well as Rasmussen (1994), Smits and Dussauge (1996), and Anderson (2000).

Let us consider the specific problem of supersonic flow past a sharp-edged flat plate, as shown in [Fig. 7-16](#). The boundary layer has a finite but small displacement effect $\delta^*(x)$ that is negligible at low speeds but causes a significant induced leading-edge shock wave to appear at high speeds. The shock increases the pressure $p_e(x)$ over the leading-edge region, as sketched in [Fig. 7-16](#). Associated with this pressure rise are increased skin friction and surface heat transfer.

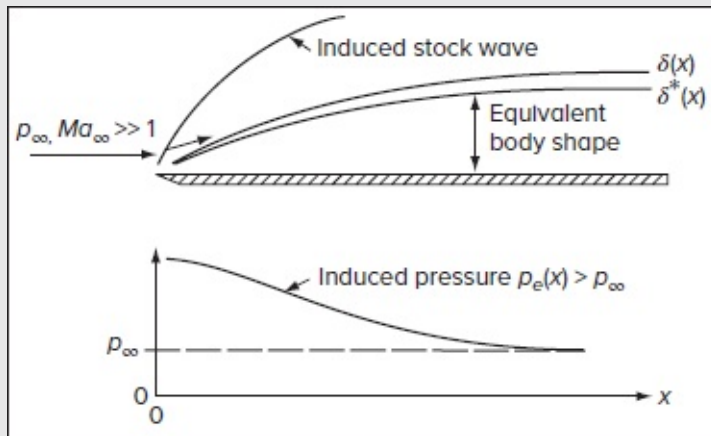


FIGURE 7.16

Flat-plate leading-edge shock wave and pressure distribution induced by boundary-layer displacement.

Page 426

In a hypersonic boundary layer, near-wall temperatures are high and densities low compared to the freestream. Thus, since $\rho/\rho_e \ll 1$, the displacement thickness $\delta^* = \int_0^\delta [1 - \rho u / (\rho_e U_e)] dy \approx \delta$. Subsequently, our [Eq. \(7-60\)](#) will indicate that, if $Ma_e \approx Ma_\infty \gg 1$,

$$\frac{\delta^*}{x} \approx \frac{\delta}{x} \approx \frac{C_w^{1/2}}{Re_{xe}^{1/2}} \left[\left(0.2 + 0.9 \frac{T_w}{T_{aw}} \right) (\gamma - 1) Ma_e^2 \right] \approx (\text{const}) Ma_\infty^2 \left(\frac{C_w}{Re_x} \right)^{1/2} \quad (7-102)$$

The displacement thickness represents a growing “body shape” to the approaching supersonic flow, which must deflect by a local angle $\phi \approx d\delta^*/dx$. If $Ma_\infty \gg 1$, the oblique-shock formulas [e.g., White (2016, Chap. 9)] show that the pressure rise across the shock is approximately a function only of the specific-heat ratio and the single parameter $K = Ma_\infty \phi$:

$$\frac{p_e}{p_\infty} \approx 1 + \frac{\gamma}{4}(\gamma + 1)K^2 + \gamma K \left\{ 1 + \left[\frac{(\gamma + 1)K}{4} \right]^2 \right\}^{1/2} \quad (7-103)$$

This formula is valid whenever $K = O(1)$ and $\phi < 20^\circ$.

Differentiation of [Eq. \(7-102\)](#) shows that $d\delta^*/dx$ is also proportional to $Ma_\infty^2 (C_w/Re_x)^{1/2}$. Then the parameter K may be written as

$$K = Ma_\infty \left(\frac{d\delta^*}{dx} \right) = (\text{const})\chi \quad \chi = Ma_\infty^3 \left(\frac{C_w}{Re_{x_\infty}} \right)^{1/2} \quad (7-104)$$

The new grouping, χ , is called the *hypersonic-interaction parameter*. The strength of the leading-edge interactions in [Fig. 7-16](#) depends on the size of this parameter. The following order-of-magnitude estimates apply:

$\chi \ll 1$: negligible interaction effects.

$\chi = O(1)$: weak interaction; can be computed by simply assuming supersonic inviscid flow over the (uncoupled) body shape $\delta^*(x)$.

$\chi \gg 1$: strong interaction; $\delta^*(x)$ and the external supersonic flow are strongly interdependent and must be solved simultaneously.

As it turns out, one can derive an ordinary differential equation valid for all these regimes, and therefore there is no real need to distinguish between weak and strong interactions. An excellent review of this type of theory is given by Bertram and Blackstock (1961).

Since $p_e(x)$ decreases with x , as shown in [Fig. 7-16](#), the pressure gradient is favorable, which tends to slightly decrease the displacement thickness. Extensive calculations by Bertram and Blackstock (1961) have resulted in the following algebraic correlation for flat plates:

$$\frac{\delta^*}{x} \approx 0.85 \left(\frac{T_w}{T_{aw}} + 0.35 \right) (\gamma - 1) Ma_\infty^2 \left(\frac{C_w p_\infty}{Re_{x_\infty} p_e} \right)^{1/2} \quad (7-105)$$

Differentiating with respect to x and evaluating [Eq. \(7-104\)](#), we obtain a more precise estimate for the parameter K :

$$K = \frac{a\chi}{\sqrt{P}} \left(1 + \frac{\chi}{2P} \frac{dP}{d\chi} \right) \quad P = \frac{P_e}{P_\infty} \quad a = 0.425 \left(\frac{T_w}{T_{aw}} + 0.35 \right) (\gamma - 1) \quad (7-106)$$

Equations (7-104) and (7-106) may be solved simultaneously for the shock-induced pressure distribution $P(\chi)$, with the initial condition $P(0) = 1$. A numerical solution is necessary, but the results are nearly linear with χ . Thus, a linear approximation is sufficient, namely,

$$P \approx 1 + a\chi \left[\frac{9}{8} \gamma (\gamma + 1) \right]^{1/2} \quad (7-107)$$

To this approximation order, then, the hypersonic-interaction parameter χ successfully correlates the leading-edge induced pressures. For $\gamma = 1.4$ and an adiabatic wall, $a \approx 0.23$ and so [Eq. \(7-107\)](#) becomes

$$\frac{P_e}{P_\infty} \approx 1 + 0.45\chi \quad (7-108)$$

This simple expression is compared with experimental data for adiabatic flat plates in [Fig. 7-17](#). The theory somewhat underestimates the data for very strong interactions, but the linear behavior is evident. For further details, see Bertram and Blackstock (1961).

Page 427

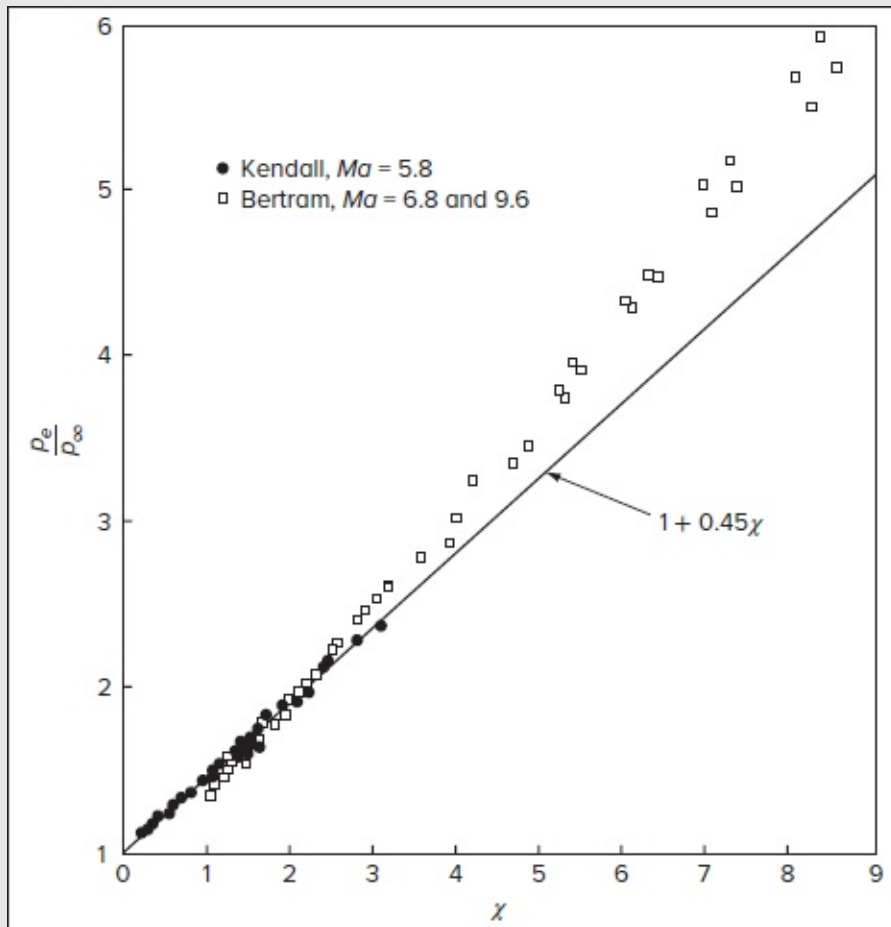


FIGURE 7-17

Correlation of measured shock-induced pressures on an adiabatic flat plate in air at high Mach numbers. [After Bertram (1958).]

This theory has been extended by White (1962*b*) to a flat surface at an angle of attack. The results are in good agreement with hypersonic force measurements on wedges at angles of attack. Anderson (2000) gives an interesting discussion of viscous interactions on various hypersonic vehicles. Generally speaking, the higher pressures induced by viscous displacement increase the body drag force more than its lift, thereby decreasing its lift–drag ratio.

7-5.3 Weakly Compressible Duct Flow: The Unsteady Water Hammer Problem

Consider an initially steady or unsteady hydraulic motion in a long pipe that contains a valve somewhere in the system (Fig. 7-18). The so-called water hammer can be triggered by a sudden closure of the valve. When this occurs, the flow upstream of the valve will be stagnated, hence building a pressure peak that propagates as a left traveling wave toward the left inlet. At the same time, the flow downstream of the valve gains a sudden pressure drop that will first propagate downstream until it reaches the open outlet, reflect back, and then travel back upstream with a high-pressure peak that impacts the valve just like a hammer. This to-and-fro motion is, of course, repeated cyclically, with the pressure waves reflecting at the open ends while undergoing each time a 180-degree phase change. With each phase change, a low-pressure wave reverses to a high-pressure wave, and vice-versa. Naturally, the alternating collisions and periodic pressure surges lead to strong vibrations and steep intermittent noise that can cause structural damage and failures in the valve, fittings, sensors, and piping system.

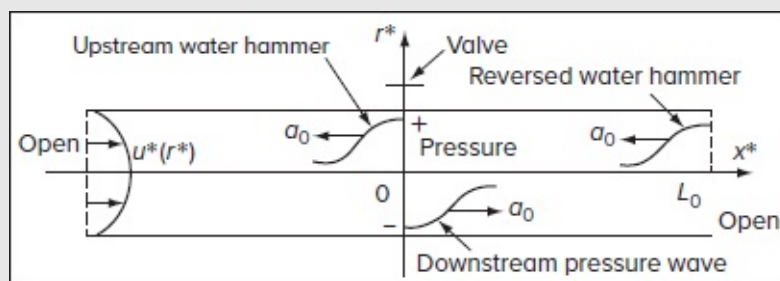


FIGURE 7-18

Sketch of the weakly compressible water hammer motion. [After Xuan *et al.* (2012).]

Studies of the water hammer problem date back to 1883, specifically to Johannes von

Kries (1883) and his investigation of pulsation in blood vessels. The problem is later revisited by N. Y. Joukowsky (1898), who manages to determine the strength of the water hammer for inviscid flow. In the following 120 years, several researchers tackle this problem using either theoretical or numerical techniques; however, an exact solution remains intractable. In 2011, Li-Jun Xuan develops a theoretical framework based on Green's functions, thus leading to a very accurate analytical solution for the water hammer problem under both laminar and turbulent conditions. In what follows, a synopsis of Xuan's integrodifferential solution under laminar conditions is described.

To start, we consider the unsteady compressible Navier–Stokes equations for axisymmetric flow. The motion in question is confined to a circular pipe of finite length L_0 and radius r_0 , with a slender geometric ratio of $\ell = r_0/L_0 \ll 1$. For simplicity, we label our dimensional pressure, density, and both axial and radial velocity components with asterisks, i.e., p^* , ρ^* , u^* , and v^* , which, as usual, depend on the dimensional coordinates (x^*, r^*, t^*) (see Fig. 7-18). The valve is located at $x^* = 0$ and the weak compressibility of the problem enables the use of a linear state equation of the form, $p^* - p_0 = a_0^2(\rho^* - \rho_0)$, where p_0 , ρ_0 , and a_0 denote the constant pressure, density, and speed of sound in the fluid at a reference state. With these parameters in hand, a judicious scaling analysis leads to the following dimensionless variables:

$$\begin{cases} x = x^*/L_0, & r = r^*/r_0, & t = t^*a_0/L_0 \\ u = u^*/u_{\max}, & v = v^*L_0/(u_{\max}r_0) \\ p = (p^* - p_0)/(\rho_0 a_0 u_{\max}), & \rho = (\rho^* - \rho_0)/(\rho_0 Ma) \end{cases} \quad (7-109)$$

where u_{\max} stands for the maximum initial velocity and $Ma = u_{\max}/a_0 \ll 1$ represents the largest Mach number. In view of the slender ratio of the pipe as well as the small size of the Mach number, a Rayleigh–Janzen perturbation expansion in the Mach number can be implemented. Subsequently, by neglecting terms of order $O(Ma, \ell^2)$ and noting that the normalized density and pressure $\rho(x, t) = p(x, t)$ are both equal and independent of r , one can extract the leading-order linearized equations

$$\begin{cases} \left\{ \frac{\partial p}{\partial t} + 2 \frac{\partial}{\partial x} \int_0^1 r u dr = 0 \right. & \text{(continuity)} \\ \left. \frac{\partial u}{\partial t} + \frac{\partial p}{\partial x} - \frac{1}{r} \frac{\partial}{\partial r} \left(\varepsilon r \frac{\partial u}{\partial r} \right) = 0 \right. & \text{(axial momentum)} \end{cases} \quad (7-110)$$

where $\varepsilon \equiv 1/(\ell Re)$, with the acoustic Reynolds number being defined as $Re = a_0 r_0/\nu$. This set of linearized relations is accompanied by several initial and boundary conditions. Specifically, we have

$$\begin{aligned} \frac{\partial u}{\partial r}(x, 0, t) = u(x, 1, t) = 0 & \quad \text{(zero shear at the centerline and no slip at the wall)} \\ u_i(x, r) = u(x, r, 0) & \quad \text{(prescribed initial velocity)} \\ p_i(x) = p(x, 0), \quad p(1, t) = 0 & \quad \text{(prescribed initial and fixed-point pressure)} \end{aligned} \quad (7-111)$$

To make further headway, the velocity is decomposed into $u(x, r, t) = u_1(x, r, t) + u_2(x, r, t)$ such that the axial momentum relation can be split into two sub-problems:

$$\begin{cases} \frac{\partial u_1}{\partial t} - \frac{1}{r} \frac{\partial}{\partial r} \left(\epsilon r \frac{\partial u_1}{\partial r} \right) = 0, & u_1(x, r, 0) = u_0(x, r) \\ \frac{\partial u_2}{\partial t} - \frac{1}{r} \frac{\partial}{\partial r} \left(\epsilon r \frac{\partial u_2}{\partial r} \right) = -\frac{\partial p}{\partial x}, & u_2(x, r, 0) = 0 \end{cases} \quad (7-112)$$

Naturally, both u_1 and u_2 must satisfy the homogeneous boundary conditions prescribed for u at $r = 0$ and $r = 1$. In view of this decomposition, a Bessel functional expansion can be used to extract u_1 from

$$u_1(x, r, t) = \sum_{n=1}^{\infty} a_n(x) J_0(\lambda_n r) e^{-\epsilon \lambda_n^2 t} \quad (7-113)$$

where $J_0(r)$ represents the zeroth-order Bessel function, λ_n reproduces its n th root, and $a_n(x)$ denotes the n th coefficient of the Bessel expansion of the initial velocity

$$a_n(x) = 2 J_1^{-2}(\lambda_n) \int_0^1 r J_0(\lambda_n r) u_i(x, r) dr \quad (7-114)$$

Page 429

with J_1 being the first-order Bessel function. On the other hand, u_2 , which is prescribed by a non-homogenous equation, can be derived using Green's functional method starting with

$$u_2(x, r, t) = - \int_0^t W(r, t - \tau) \frac{\partial p}{\partial x}(x, \tau) d\tau \quad (7-115)$$

where $W(r, t)$ can be determined from

$$\frac{\partial W}{\partial t} - \frac{1}{r} \frac{\partial}{\partial r} \left(\epsilon r \frac{\partial W}{\partial r} \right) = \delta(t); \quad W(r, 0) = W(1, t) = \frac{\partial W}{\partial r}(0, t) = 0 \quad (7-116)$$

Here $\delta(t)$ symbolizes the Dirac delta function. At this juncture, with the velocity $u(x, r, t)$ in hand, one can revisit the continuity equation to deduce an integrodifferential relation for the pressure. One gets

$$\frac{\partial p}{\partial t} - \int_0^1 \frac{\partial^2 p}{\partial x^2}(x, \tau) F_\epsilon(t - \tau) d\tau = -2 \frac{\partial}{\partial x} \left[\int_0^1 r u_1(x, r, t) dr \right] \quad (7-117)$$

where $F_\epsilon(t) = 2 \int_0^1 r W(r, t) dr = 4 \sum_{n=1}^{\infty} \lambda_n^{-2} e^{-\epsilon \lambda_n^2 t}$. Then, through the use of Laplace transforms, a general solution to this equation can be obtained, as shown by Xuan et al. (2012). For the special case of an initially steady pipe flow with a constant pressure gradient of the form $\partial p / \partial x = -C$, $C > 0$, one is left with

$$p(x, t) = - \int_0^t \frac{\partial p}{\partial x}(0, \tau) H_\varepsilon(x, t - \tau) d\tau + C(1 - x) \quad (7-118)$$

where Green's function, $H_\varepsilon(z, t)$, can be evaluated from

$$\frac{\partial H_\varepsilon}{\partial t} - \int_0^t \frac{\partial^2 H_\varepsilon}{\partial x^2}(x, \tau) F_\varepsilon(t - \tau) d\tau = 0; \quad H_\varepsilon(x, 0) = 0, \quad \frac{\partial H_\varepsilon}{\partial x}(0, t) = -\delta(t), H_\varepsilon(1, t) = 0 \quad (7-119)$$

The last step is to extract $H_\varepsilon(x, t)$ using a numerical technique or an inverse Laplace transform, namely,

$$H_\varepsilon(x, t) = L^{-1} \left\{ \frac{\sinh[G(1 - x)]}{G \cosh G} \right\}, \quad G = \sqrt{\frac{s}{\hat{F}_\varepsilon(s)}}, \quad \hat{F}_\varepsilon(s) = \sum_{n=1}^{\infty} \frac{1}{\lambda_n^2(s + \varepsilon \lambda_n^2)} \quad (7-120)$$

To illustrate the accuracy of this solution, the theoretical prediction of the pressure history at $x = 0$ is compared in [Fig. 7-19](#) to DNS results for the case of $u_{\max} = 10$ m/s, $L_0 = 800$ m, $r_0 = 1$ m, $\nu = 0.2$ m²/s and $a_0 = 1450$ m/s, where the valve is suddenly closed. The DNS results are acquired using an implicit time-marching scheme in a commercial finite-volume solver. To verify grid convergence, two grids are used: Grid 1 with 6400×40 ($x \times r$) points and a time step of 0.016 s and grid 2, with 800×40 points and a time step of 0.002 s. As it may be surmised from [Fig. 7-19](#), both numerical simulations agree very well with Xuan's theoretical prediction.

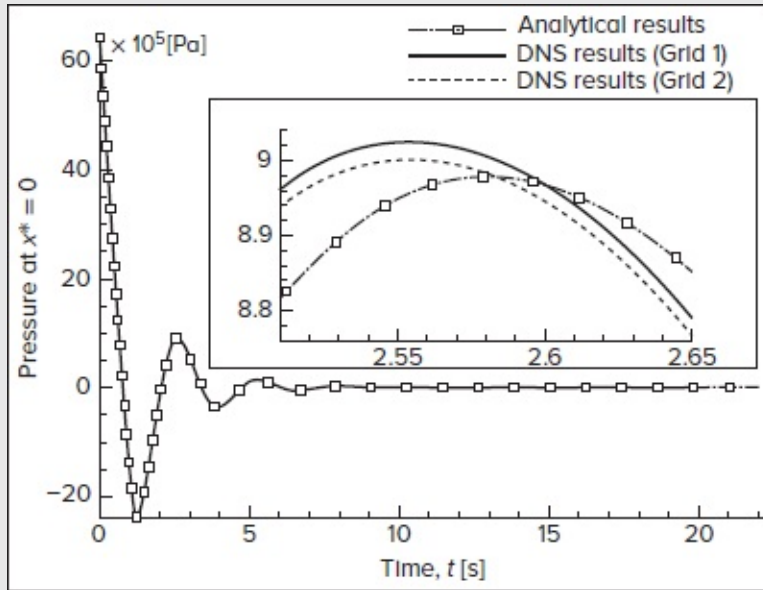


FIGURE 7-19

Comparison of $p^*(0, t^*)$ obtained using [Eq. \(7-118\)](#) and two DNS solutions carried out using ($x \times r$) grid resolutions of 6400×40 (grid 1) and 800×40 (grid 2). [After Xuan et al. (2012).]

7-6 THE COMPRESSIBLE-TURBULENT-BOUNDARY-LAYER EQUATIONS

As in laminar flows, turbulent compressible flows have variable density and need supplementing by an equation of state. Turbulent motion also has the additional complication of having to account for density fluctuations

$$\rho = \bar{\rho} + \rho' \quad (7-121)$$

with the usual notation of a bar for average values and a prime for fluctuating values. Since density keeps occurring together with other variables, additional time-averaged quantities are obtained, involving products of fluctuating variables. For example, all three conservation relations contain the axial mass flux ρu , which becomes, after time averaging,

$$\overline{\rho u} = \bar{\rho} \bar{u} + \overline{\rho' u'} \quad (7-122)$$

The quantity \bar{u} , when broken out from density, is called the *mass-averaged* velocity, also known as *Favre-averaging*, after the original derivation by Favre (1965). Smits and Dussauge (1996) present the complete Favre-averaged equations of three-dimensional, compressible, turbulent flow. Here we study only turbulent-boundary-layer equations.

Another complication of compressible turbulent flows is that density fluctuations automatically imply temperature fluctuations through the equation of state. Then, if $T = \bar{T} + T'$ and T' is important, there is a possibility that fluctuations in the transport properties, which depend upon T , will also be important. These include

$$\mu(T) = \bar{\mu} + \mu' \quad k(T) = \bar{k} + k' \quad c_p(T) = \bar{c}_p + c'_p \quad Pr(T) = \bar{Pr} + Pr' \quad (7-123)$$

This added complication would have been certainly discouraging, albeit not entirely infeasible; fortunately, it turns out that transport-property fluctuations can be neglected.

7-6.1 Morkovin's Hypothesis: The Boundary-Layer Equations

In studying supersonic flow, Morkovin (1962) postulated that “the essential dynamics of compressible shear flows will follow the incompressible pattern,” that is, fluctuations in density and enthalpy will not modify the turbulence structure as long as Mach number fluctuations remain much smaller than unity. Subsequent experiments verify this hypothesis for Mach numbers as high as 5. Thus, most of our concepts from incompressible turbulence ([Chap. 6](#)) will continue to hold.

A visual demonstration of Morkovin's hypothesis is shown in [Fig. 7-20](#), which is a schlieren image of a Mach 3 boundary layer from Garg and Settles (1998). By comparing the

patterns here with the low-speed smoke-flow image in [Fig. 6-1b](#), we see that the structures and length scales are more or less similar, thus indicating that compressible and incompressible-flow dynamics are analogous.

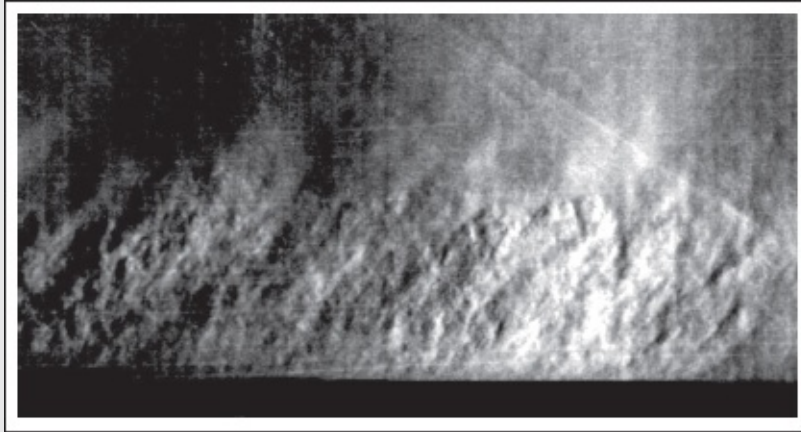


FIGURE 7-20

Visual support for Morkovin’s hypothesis: focusing schlieren image of a Mach 3 turbulent boundary layer from Garg and Settles (1998). Compare this to [Fig. 6-1b](#). [Reprinted by permission of the authors and the journal “Experiments in Fluids.”]

The derivation of the compressible two-dimensional turbulent-boundary-layer equations uses the same order-of-magnitude considerations as laminar flow, with the additional assumption that the fluctuations are small, specifically

$$\begin{cases} \bar{v} \ll \bar{u} & \frac{\partial}{\partial x} \ll \frac{\partial}{\partial y} \\ Q' \ll \bar{Q} & \text{for all } Q \end{cases} \quad (7-124)$$

Page 431

These conditions were first applied to the compressible Navier–Stokes equations by van Driest (1951) in a stunning display of expertise in handling time-averaged quantities. The boundary-layer equations that follow include

$$\text{Continuity:} \quad \frac{\partial}{\partial x}(\bar{\rho}u) + \frac{\partial}{\partial y}(\bar{\rho}v) = 0 \quad (7-125a)$$

$$\text{x- momentum:} \quad \bar{\rho}u \frac{\partial \bar{u}}{\partial x} + \bar{\rho}v \frac{\partial \bar{u}}{\partial y} = \rho_e U_e \frac{dU_e}{dx} + \frac{\partial \tau}{\partial y} \quad (7-125b)$$

$$\text{y- momentum:} \quad \frac{\partial \bar{p}}{\partial y} = -\frac{\partial}{\partial y}(\bar{\rho}v'v') \ll \left| \frac{\partial \bar{p}}{\partial x} \right| \quad (7-125c)$$

$$\text{Energy:} \quad \bar{\rho} \bar{u} \frac{\partial \bar{h}}{\partial x} + \bar{\rho} \bar{v} \frac{\partial \bar{h}}{\partial y} = \bar{u} \frac{\partial \bar{p}}{\partial x} + \frac{\partial q}{\partial y} + \tau \frac{\partial \bar{u}}{\partial y} \quad (7-125d)$$

where

$$\tau = \bar{\mu} \frac{\partial \bar{u}}{\partial y} - \overline{\rho u' v'} \quad q = \bar{k} \frac{\partial \bar{T}}{\partial y} - \overline{\rho v' h'}$$

Again, as for incompressible flow, there is a slight pressure gradient in the y direction that can be ignored in the present context (hence $\partial \bar{p} / \partial x \approx -\rho_e U_e dU_e / dx$) but becomes important in a Kármán-type integral method, for example, [Eq. \(7-75\)](#). Note that the turbulent-shear and heat-flux terms become triple correlations due to a varying density; nonetheless, such a complication proves to be nearly inconsequential to the semiempirical treatment of these terms.

In analyzing these relations, the typical first step is to eliminate $\bar{\rho} \bar{v}$ from momentum and energy through the use of the continuity relation, leaving only two equations in the three variables \bar{p} , \bar{u} , and \bar{T} . Naturally, another relation is needed, such as the equation of state. It is sufficient for our purposes to adopt the ideal-gas approximation

$$\begin{aligned} \bar{p} &= \bar{\rho} R \bar{T} & R &= \text{specific gas constant} \\ d\bar{h} &= c_p d\bar{T} & c_p &\approx \text{const} \end{aligned} \quad (7-126)$$

Since \bar{p} is nearly constant across the boundary layer, the density profile can be directly related to the temperature profile through the perfect-gas law

$$\frac{\bar{\rho}(y)}{\rho_e} \approx \frac{T_e}{\bar{T}(y)} \quad (7-127)$$

which simplifies the algebra greatly. The boundary conditions are the usual:

At the wall ($y = 0$):

$$\bar{u} = \bar{v} = 0 \quad \bar{T} = T_w \quad \bar{p} = \rho_w \quad (7-128a)$$

At the outer edge ($y \rightarrow \infty$):

$$\bar{u} \rightarrow U_e(x) \quad \bar{T} \rightarrow T_e(x) \quad \bar{p} \rightarrow \rho_e(x) \quad (7-128b)$$

When the turbulent shear and heat flux are properly correlated, these equations and boundary conditions become well defined and solvable parabolically, similarly to their laminar counterparts. Moreover, eddy viscosity and eddy conductivity assumptions remain reasonably effective so long as the density variation is properly modeled.

7-6.2 The Turbulent Crocco–Busemann Relation

It is possible to introduce eddy transport definitions that mirror those for incompressible motion. Particularly, we let

$$-\overline{\rho u'v'} = \mu_t \frac{\partial \bar{u}}{\partial y} \quad \text{and} \quad -\overline{\rho v'h'} = k_t \frac{\partial \bar{T}}{\partial y} \quad (7-129)$$

We can then proceed to rewrite the momentum equation in terms of μ_t and the energy equation in terms of $H = \bar{h} + \bar{u}^2/2$:

Momentum:

$$\bar{\rho} \bar{u} \frac{\partial \bar{u}}{\partial x} + \bar{\rho} \bar{v} \frac{\partial \bar{u}}{\partial y} = -\frac{d\bar{p}}{dx} + \frac{\partial}{\partial y} \left[(\mu + \mu_t) \frac{\partial \bar{u}}{\partial y} \right]$$

Energy:

$$\bar{\rho} \bar{u} \frac{\partial H}{\partial x} + \bar{\rho} \bar{v} \frac{\partial H}{\partial y} = \frac{\partial}{\partial y} \left[\left(\frac{\mu}{Pr} + \frac{\mu_t}{Pr_t} \right) \frac{\partial H}{\partial y} \right] + \frac{\partial}{\partial y} \left[\mu \left(1 - \frac{1}{Pr} \right) + \mu_t \left(1 - \frac{1}{Pr_t} \right) \right] \frac{\partial}{\partial y} \left(\frac{\bar{u}^2}{2} \right) \quad (7-130)$$

Page 432

where $Pr_t = \mu_t c_p / k_t$ is the turbulent Prandtl number. It is immediately obvious that if one makes the standard assumption of $Pr \approx Pr_t \approx 1$ (which is quite reasonable for air) and if the pressure gradient is negligible, the previous two equations become identical in mathematical form, thus leading to a particular solution,

$$H = C_1 + C_2 \bar{u} \quad \text{or} \quad \bar{h} = C_1 + C_2 \bar{u} - \frac{1}{2} \bar{u}^2 \quad (7-131)$$

This expression is identical to the laminar [Eq. \(7-26\)](#) discussed earlier. When the boundary conditions at the wall and outer edge are used, we obtain

$$Pr = Pr_t \approx 1 \quad \frac{d\bar{p}}{dx} \approx 0 \quad \bar{T} \approx T_w + (T_{aw} - T_w) \frac{\bar{u}}{U_e} - \frac{r \bar{u}^2}{2 c_p} \quad (7-132)$$

It can therefore be seen that the Crocco–Busemann relation between temperature and velocity can be extended with good accuracy to turbulent flows with negligible pressure gradients, although it also represents a reasonable approximation with pressure gradients. Note that we have assumed constant c_p (so that $\bar{h} = c_p \bar{T}$) and incorporated the recovery factor r to achieve better accuracy. For turbulent gaseous flow, one may use $r = Pr^{1/3} \approx 0.89$ for air, and the use of [Eq. \(7-132\)](#) will be illustrated in the analyses that follow.

The integral momentum relation for compressible turbulent flow is identical to the laminar formula when time-averaged velocity, density, and temperature are used. The integral-energy equation is also the same for either laminar or turbulent motion:

$$q_w = \frac{d}{dx} \left[\int_0^\infty \bar{\rho} \bar{u} \left(\bar{h} + \frac{1}{2} \bar{u}^2 - h_e - \frac{1}{2} U_e^2 \right) dy \right] \quad (7-133)$$

One may, in principle, solve these integral relations by introducing suitable approximations for the (turbulent) velocity, density, and enthalpy profiles.

7-7 WALL AND WAKE LAWS FOR TURBULENT COMPRESSIBLE FLOW

Assuming fully turbulent flow, we recall from [Figs. 5-15](#) to [5-19](#) that (1) laminar compressible flows have more than one mode of instability; (2) as Ma increases, the first mode can be unstable in many different (transverse) directions; and (3) for $Ma > 4$, the second mode is the most unstable. Compressible and incompressible transition processes are similar, as predicted by Morkovin's hypothesis. DNS results for flat-plate flow at $Ma = 4.5$, by Adams and Kleiser (1993), predict second-mode instability that develops into subharmonic staggered Λ -vortices and then into detached high-shear layers. Fully turbulent compressible flow is hence anticipated for all developing compressible, laminar, boundary layers.

In [Chap. 6](#), we developed accurate law-of-the-wall and law-of-the-wake relations for incompressible turbulent mean flow. In keeping with Morkovin's hypothesis that compressible boundary-layer flows "follow the incompressible pattern," we can find modified wall and wake laws up to at least $Ma \approx 5$. The results seem quite reasonable when compared with the gold mine of incompressible- and compressible-flow data compiled by Fernholz and Finley (1980, 1996).

7-7.1 Compressible Law of the Wall: The van Driest Transformation

This subject is thoroughly reviewed by Bradshaw (1977) and Smits and Dussauge (2000). Realizing that density and viscosity vary across the boundary layer, it is helpful to define inner law dimensionless variables based on *wall* values of density and viscosity:

$$u^+ = \frac{\bar{u}}{v^*} \quad y^+ = \frac{yv^*}{\nu_w} \quad v^* = \left(\frac{\tau_w}{\rho_w} \right)^{1/2} \quad (7-134)$$

This also ensures that, in the linear viscous sublayer, we recover $u^+ = y^+$ without any extraneous coefficients.

Edward R. van Driest (1951) anticipated Morkovin's insight with a near-wall mixing-length theory that accounted for variable density. Neglecting the sublayer, he assumed

$$\tau \approx \tau_t = \bar{\rho} \ell^2 \left(\frac{d\bar{u}}{dy} \right)^2 \quad \ell \approx \kappa y \quad (7-135)$$

To relate density to velocity, van Driest further assumed an ideal gas and adopted the Crocco–Busemann approximation given by (7-132) for a unit Prandtl number,

$$\frac{\rho_w}{\bar{\rho}} = \frac{\bar{T}}{T_w} = 1 + \left(\frac{T_{aw}}{T_w} - 1 \right) \frac{\bar{u}}{U_e} - \frac{\gamma - 1}{2} Ma_e^2 \frac{T_e}{T_w} \left(\frac{\bar{u}}{U_e} \right)^2 \quad (7-136)$$

By substituting (7-136) into (7-135) and applying Prandtl's original assumption that $\tau \approx \tau_w$ (which is accurate for a flat plate), van Driest (1951) was able to integrate and retrieve $\bar{u}(\bar{y})$ in closed form:

$$u_{eq} = \frac{U_\epsilon}{a} \left(\sin^{-1} \frac{2a^2 \bar{u}/U_\epsilon - b}{Q} + \sin^{-1} \frac{b}{Q} \right) = v^* \left(\frac{1}{\kappa} \ln y^+ + B \right) \quad (7-137)$$

where

$$a = \left(\frac{\gamma - 1}{2} Ma_\epsilon^2 \frac{T_\epsilon}{T_w} \right)^{1/2} \quad b = \left(\frac{T_{aw}}{T_w} - 1 \right) \quad Q = (b^2 + 4a^2)^{1/2}$$

Here v^* and y^+ are defined precisely as in (7-134). The right-hand side of (7-137) represents the ordinary incompressible law of the wall. The left-hand side has been given the symbol u_{eq} , the van Driest *effective velocity*.

For zero heat transfer, $b = 0$, $Q = 2a$, and the effective velocity becomes

$$\text{Adiabatic walls:} \quad u_{eq} = \frac{U_\epsilon}{a} \sin^{-1} \left(\frac{a \bar{u}}{U_\epsilon} \right) \quad a^2 = 1 - \frac{T_\epsilon}{T_{aw}} \quad (7-138)$$

To first order, the van Driest effective velocity correlates supersonic and hypersonic near-wall flows with $\kappa \approx 0.41$ and $B \approx 5.0$, as in incompressible flow. It can also be used to define a compressible “defect law” by analogy with (6-36).

The success of van Driest's effective velocity is seen in [Fig. 7-21](#), reproduced from Fernholz and Finley (1980). For Mach numbers between 3.5 and 7.2, the raw velocities \bar{u} (solid symbols) are too low for near-adiabatic flow and too high for cold-wall flow. When transformed to u_{eq} from (7-137), all data cling nicely to the incompressible log-law up to $y^+ \approx 400$, above which they form a law-of-the-wake shape.

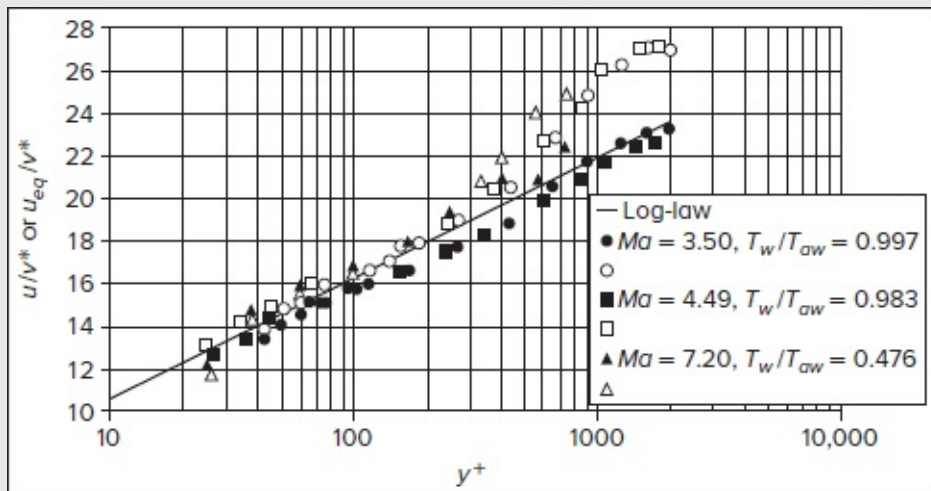


FIGURE 7-21

Verification of the van Driest transformation, Eq. (7-137), for compressible, turbulent, boundary layers: natural velocity (solid symbols) and effective velocity (open symbols). [After Fernholz and Finley (1980).]

So et al. (1994) use the inner–outer matching procedure of Sec. 6-4.1 to show that the effective velocity fits log-laws in both the overlap layer and the outer defect layer. However, the log-law constants (k , B , A) are found to vary with Mach number, heat flux, and ratio of specific heats.

7-7.2 Compressible Law of the Wake

It turns out that the van Driest transformation makes compressible-flow data fit Coles' incompressible law of the wake [Eq. (6-47)]; if one defines v^* based on wall properties and replaces \bar{u} by u_{eq} , the resulting wake expression becomes valid:

$$\frac{u_{eq}}{v^*} \approx \frac{1}{\kappa} \ln\left(\frac{yv^*}{\nu_w}\right) + B + \frac{2\Pi}{\kappa} w\left(\frac{y}{\delta}\right), \quad w \approx 3\left(\frac{y}{\delta}\right)^2 - 2\left(\frac{y}{\delta}\right)^3 \quad (7-139)$$

where $\kappa \approx 0.41$ and $B \approx 5$. For flat-plate data with $1.7 < Ma_e < 10.3$, Fernholz and Finley (1980) show that $\Pi \approx 0.55 \pm 0.05$ for $Re_\theta > 2000$, just as Coles (1956) had shown for incompressible, turbulent flow. Similarly, for $Re_\theta < 2000$, the value of Π drops off slowly to zero, just as Coles showed. For compressibility, it is postulatedPage 434 that Π varies with the pressure gradient, freestream turbulence, and wall heat flux, although verification data - measurements remain scarce. For further discussion, see Sec. 7.4 of Smits and Dussauge (1996).

The van Driest transformation is equivalent to modifying the velocity by the square root of the integrated density ratio:

$$\bar{u}_{\text{effective}} = \int_0^{\bar{u}} \left(\frac{\bar{\rho}}{\rho_\epsilon}\right)^{1/2} d\bar{u} \quad (7-140)$$

This type of velocity correlates supersonic data up to Mach 7 and for walls as cold as $T_w/T_{aw} = 0.3$. Meanwhile, the success of the Lees–Illingworth coordinate transformations in laminar compressible flow has prompted several attempts to pursue similar models for turbulent flows. Bradshaw (1977) reviews these alternate transformations, which have not been widely accepted compared to the van Driest approach.

7-7.3 A Compressible Law of the Wall with Heat Transfer and a Pressure Gradient

The van Driest transformation, (7-137), is elegant but complicated algebraically and difficult to implement in a compressible boundary-layer calculation procedure. The present subsection describes another algebraic compressible law of the wall that accounts for three important effects, as shown by White and Christoph (1972). It is intended for preliminary engineering calculations and problem assignments.

The three effects considered are the pressure gradient, compressibility, and wall heat flux. They are nondimensionalized using wall variables as follows:

$$\alpha = \frac{\nu_w}{\tau_w v^*} \frac{dp_\epsilon}{dx} \quad (\text{pressure gradient}) \quad \beta = \frac{q_w \nu_w}{T_w k_w v^*} \quad (\text{heat flux}) \quad \gamma = \frac{r v^{*2}}{2 c_p T_w} \quad (\text{compressibility}) \quad (7-141)$$

where, as before, r denotes the recovery factor and $q_w > 0$ for a cold wall. All three parameters typically take on small (fractional) numerical values. As shown in [Fig. 7-22](#), the effect of positive α and β is to raise the profile above the incompressible log-law, whereas γ and negative α and β tend to lower the profile.

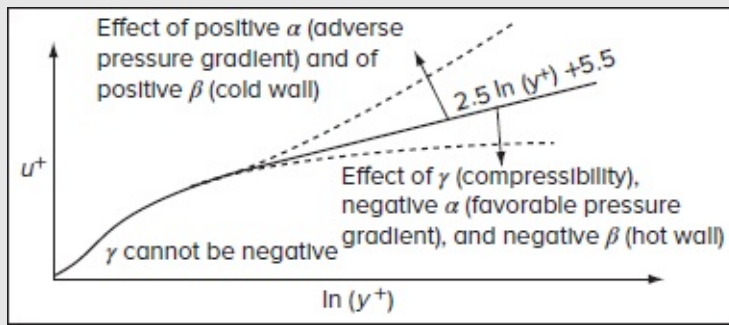


FIGURE 7-22

Sketch illustrating the effect of various parameters on the law of the wall for compressible turbulent flow. [After White and Christoph (1972).]

White and Christoph (1972) use the mixing-length approximation, (7-135), and introduce the near-wall effect of a pressure gradient by setting:

$$\tau \approx \tau_w + \frac{dp_\epsilon}{dx} y + O(y^3) = \bar{\rho} \kappa^2 y^2 \left(\frac{d\bar{u}}{dy} \right)^2 \quad (7-142)$$

They then rewrite the Crocco–Busemann relation, (7-132), in terms of wall variables:

$$\frac{\rho_w}{\bar{\rho}} = \frac{\bar{T}}{T_w} \approx 1 + \beta u^+ - \gamma u^{+2} \quad (7-143)$$

where β and γ are defined by (7-141). Combining (7-142) and (7-143), solving for the velocity derivative, and rewriting in wall variables, one gets

$$\frac{du^+}{dy^+} = \frac{(1 + \alpha y^+)^{1/2}}{\kappa y^+ (1 + \beta u^+ - \gamma u^{+2})^{1/2}} \quad (7-144)$$

where α is the same pressure gradient parameter in (7-141). Note that this differential equation contains no overt thickness parameter (δ , δ^* , etc.) and, consequently, it can be integrated indefinitely from the wall outwardly.

Page 435

More specifically, (7-144) may be separated and integrated in closed form, starting at an initial point (u_0^+, y_0^+) , with the result,

$$u^+(y^+, \alpha, \beta, \gamma) = \frac{1}{2\gamma} \left(\beta + Q \sin \left\{ \phi + \frac{\sqrt{\gamma}}{\kappa} \left[2(S - S_0) + \ln \left(\frac{S-1}{S+1} \frac{S_0+1}{S_0-1} \right) \right] \right\} \right) \quad (7-145)$$

where

$$\phi = \sin^{-1} \frac{2\gamma u_0^+ - \beta}{Q} \quad Q = (\beta^2 + 4\gamma)^{1/2} \quad S = (1 + \alpha y^+)^{1/2}$$

Note that this formula does not account for the viscous sublayer, nor does the van Driest theory from Sec. 7-7.2. The initial conditions are chosen so that the expression reduces to the low-speed logarithmic law $[u^+ = (1/\kappa) \ln(y^+) + B]$ when $\alpha = \beta = \gamma = 0$. We choose the point where the log-law goes to zero:

$$u_0^+ = u^+(y^+, 0, 0, 0) = 0 \quad (7-146)$$

$$y_0^+ = e^{-\kappa B} = 0.1287 \quad \text{for } \kappa = 0.41 \quad \text{and } B = 5.0$$

Some special cases of (7-145) for zero pressure gradient, zero wall heat flux, and zero compressibility lead to

$$u^+(y^+, 0, \beta, \gamma) = \frac{1}{2\gamma} \left[\beta + Q \sin \left(\phi + \frac{\sqrt{\gamma}}{\kappa} \ln \frac{y^+}{y_0^+} \right) \right] \quad (7-147a)$$

$$u^+(y^+, 0, \beta, 0) = \frac{1}{\kappa} \ln \frac{y^+}{y_0^+} + \frac{\beta}{4\kappa^2} \ln^2 \frac{y^+}{y_0^+} \quad (7-147b)$$

$$u^+(y^+, 0, 0, \gamma) = \frac{1}{\sqrt{\gamma}} \sin \left(\frac{\sqrt{\gamma}}{\kappa} \ln \frac{y^+}{y_0^+} \right) \quad (7-147c)$$

$$u^+(y^+, 0, 0, 0) = \frac{1}{\kappa} \ln \frac{y^+}{y_0^+} = \frac{1}{\kappa} \ln y^+ + B \quad (7-147d)$$

These will be very useful, for example, in studying flat-plate flow in the next section.

Some of the typical effects contained within (7-145) are illustrated in [Fig. 7-23](#). The left chart shows the effect of both compressibility γ and an adverse pressure gradient ($\alpha > 0$) on the law of the wall, compared with the low-speed logarithmic law, which is the straight line labeled (0, 0, 0). Note that, with or without a pressure gradient, compressibility drives the

profiles downward, in perfect agreement with experimental trends. Also note that as we move out along the lowest curve $(0, 0, 0.002)$, the effective freestream Mach number is continuously increasing, from about 3.8 (for air) at $y^+ = 1000$ to about 19.8 at $y^+ = 10^5$. In other words, this single curve is equivalent to an infinite spectrum of adiabatic compressible flat-plate turbulent flows. The utility of the law of the wall as an analytical tool for turbulent flows is truly gratifying in this case.

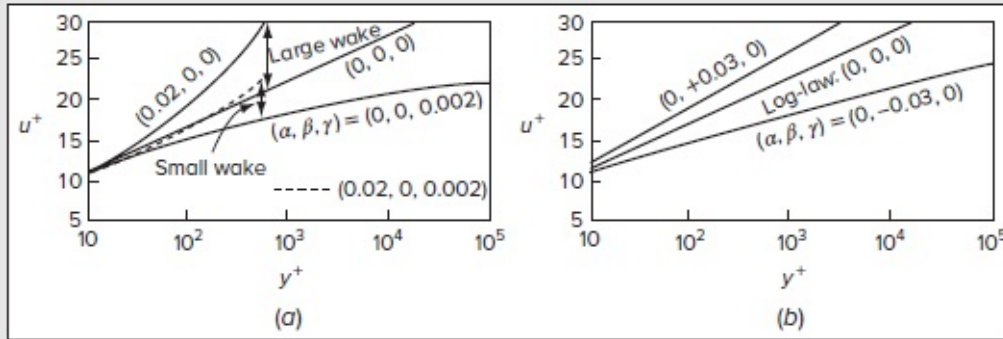


FIGURE 7-23

Law of the wall for compressible flow, from the first-order mixing-length theory, (7-145): (a) effect of compressibility and adverse pressure gradient; (b) effect of wall heat flux in low-speed flow. Note: β is positive for a cold wall.

A second concept in [Fig. 7-23a](#), shown by the arrows, is that compressibility reduces the outer “wake” effect. The dashed-line high-speed wake ($\gamma = 0.002$) is approximately one-half of the low-speed ($\gamma = 0$) wake for the same value of α . In fact, as γ increases to 0.005 (hypersonic flow), the same wake becomes negligibly small. It may be thus inferred that the wall-related theory of pressure gradient effects in supersonic flow may be more accurate than its already successful counterpart in incompressible flow.

Figure 7-23b shows the effect of cold and hot walls on the law of the wall in low-speed flow with a zero pressure gradient, as computed from (7-145).

7.8 COMPRESSIBLE TURBULENT FLOW PAST A FLAT PLATE

A classic problem to consider is that of compressible turbulent flow past a flat plate at arbitrary Mach numbers and wall temperatures. Practically everyone in the field has had a try at it. [Figure 7-24](#) shows a classic display of the 21 adiabatic-wall theories in existence in 1953; Spalding and Chi (1964) reviewed and discussed 32 theories. Now, several decades

later, there are over 50 theories and countless computations.

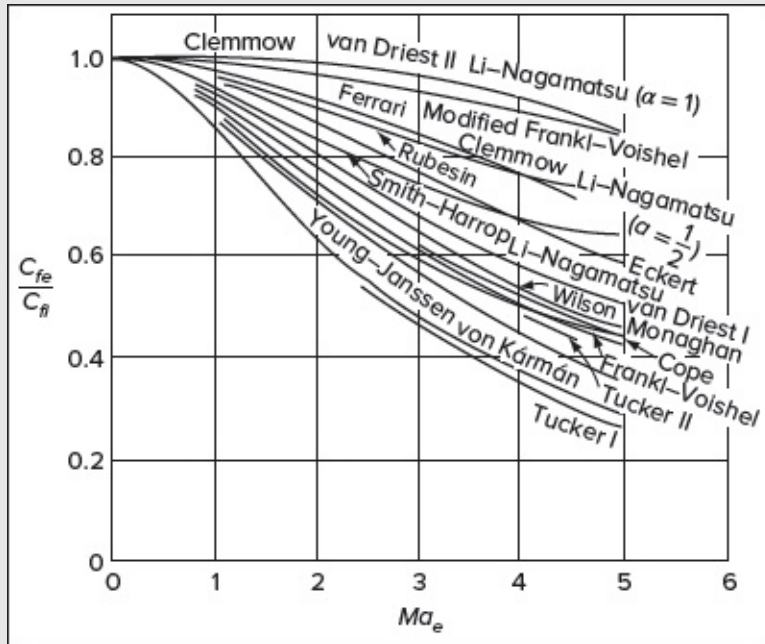


FIGURE 7-24

An array of adiabatic flat-plate theories compiled by Chapman and Kester (1953).

The ordinate in [Fig. 7-24](#) is the ratio of the skin-friction coefficient at a given Mach number and Reynolds number to the skin friction at the same Reynolds number and $Ma_e = 0$. Clearly the coefficient decreases with Ma_e (although the wall shear itself increases because τ_w is nondimensionalized by U_e^2). The 21 theories are supposed to predict the same behavior, namely, adiabatic skin friction. Typical data measurements—which can be quite sensitive to the Reynolds number—fall along the curve labeled “Frankl–Voishel,” which does not correspond to a formula but rather some tabulated values. [Figure 7-24](#) does not tell the whole story, because as the Reynolds number varies from 10^5 to 10^8 , the skin friction will vary up to 25 percent.

7-8.1 The Flat-Plate Theory of van Driest (1956)

The theory labeled “van Driest II” in [Fig. 7-24](#) appears to be ineffective, but in fact it was plotted for an incorrect viscosity–temperature relation: μ proportional to T rather than $T^{0.67}$ for air. Later, van Driest (1956) modified the theory and derived a corrected formula that remains one of the most popular and dependable.

These early theories all used the Kármán integral relation (7-75) that reduces, for zero

pressure gradient, to

$$C_f = 2 \frac{d\theta}{dx} \quad \theta = \int_0^\infty \frac{\bar{\rho}}{\rho_e} \frac{\bar{u}}{U_e} \left(1 - \frac{\bar{u}}{U_e}\right) dy \quad (7-148)$$

To compute $\theta(x)$, van Driest (1956) uses the density and velocity profiles from [Eqs. \(7-136\)–\(7-137\)](#). The resulting integration, which involves a complicated quotient of polynomial, trigonometric, and logarithmic functions, is approximated in series form and adjusted into the following expression for the local skin friction:

$$\frac{\sin^{-1} A + \sin^{-1} B}{\sqrt{C_{fe}(T_{aw}/T_e - 1)}} \approx 4.15 \log\left(Re_x C_{fe} \frac{\mu_e}{\mu_w}\right) + 1.7; \quad A = \frac{2a^2 - b}{(b^2 + 4a^2)^{1/2}}, \quad B = \frac{b}{(b^2 + 4a^2)^{1/2}} \quad (7-149)$$

The parameters a and b are defined in (7-137). For low-speed flow ($Ma_e \approx 0$), (7-149) reduces to the Kármán–Schoenherr incompressible relation,

$$\frac{1}{\sqrt{C_f}} \approx 4.15 \log(Re_x C_f) + 1.7 \quad [\text{Schoenherr (1932)}] \quad (7-150)$$

Page 437

which is still the formula of choice for naval architects estimating the skin friction of ship hulls.

Equation (7-149) can be interpreted as an incompressible approximation, which has been “stretched” by compressibility and viscosity effects. It can be rewritten in a canonical manner using:

$$C_{fe} = \frac{1}{F_c} C_{f_{inc}}(Re_x F_{Re_x}) = \frac{1}{F_c} c_{f_{inc}}(Re_{\theta e} F_{Re_x} F_c); \quad F_c = \frac{T_{aw}/T_e - 1}{(\sin^{-1} A + \sin^{-1} B)^2}, \quad F_{Re_x} F_c = \frac{\mu_e}{\mu_w} \quad (7-151)$$

This generic form, common to many flat-plate theories, was suggested by Spalding and Chi (1964) as a *compressibility transformation* for flat-plate friction. Accordingly, one computes an equivalent incompressible Reynolds number $Re_x F_{Re_x}$ and uses one’s favorite incompressible skin-friction formula to compute $C_{f_{inc}}$, then dividing the result by F_c to obtain the desired (compressible) C_f . The local Stanton number follows from the Reynolds analogy, namely,

$$C_{he} = \frac{q_w}{\rho_e U_e c_p (T_{aw} - T_w)} \approx \frac{C_{fe}}{2Pr^{2/3}} = 0.62 C_{fe} \quad (\text{air}) \quad (7-152)$$

[Figure 7-25](#) displays computed Stanton numbers on an adiabatic flat plate for both laminar and turbulent flows, using [Eqs. \(7-56c\)](#), [\(7-149\)](#), and [\(7-152\)](#).

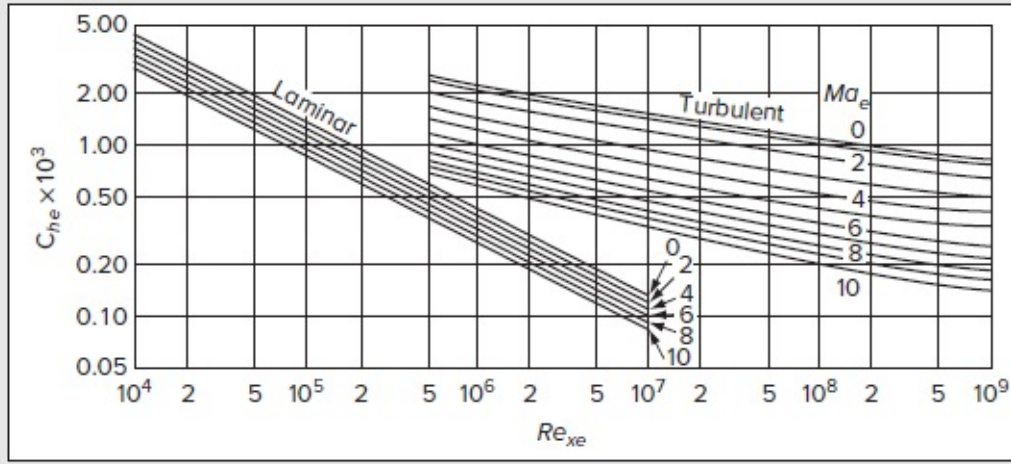


FIGURE 7-25

Theoretical local-wall, heat-flux coefficients on an adiabatic flat plate at high Mach numbers; laminar: Eq. (7-56b); turbulent: [Eq. \(7-149\)](#).

Moreover, van Driest (1956) shows that the same stretched variables are applicable for estimating the total drag on a plate:

$$\frac{\sin^{-1} A + \sin^{-1} B}{\sqrt{C_{De}(T_{aw}/T_e - 1)}} \approx 4.13 \log \left(Re_{Le} C_{De} \frac{\mu_e}{\mu_w} \right) \quad (7-153)$$

At low speed, this relation reduces to the Kármán–Schoenherr incompressible drag formula, $C_D^{-1/2} \approx 4.13 \log(Re_x C_D)$.

In one of his review articles, Bradshaw (1977) asserts that, compared to available data, the van Driest II solution in (7-149) proves to be the most accurate of all popular formulas for compressible, flat-plate, skin friction.

7-8.2 Compressible Flat-Plate Flow Using Inner Variables

Alternatively, a very accurate method by White and Christoph (1972) leverages the inner (or law-of-the-wall) variables to extend the analysis of Sec. 6-6.2 to compressible motions. Accordingly, the velocity profile is correlated by the wall law given by [Eq. \(7-145\)](#) with $\alpha = 0$:

$$u^+ = \frac{\bar{u}(x, y)}{v^*(x)} = f(y^+, \beta, \gamma) \quad (7-154)$$

Now the continuity Eq. (7-125a) is satisfied by the compressible stream function $\psi(x, y)$ using

$$\frac{d\psi}{dy} = +\bar{\rho}\bar{u} \quad \text{and} \quad \frac{d\psi}{dx} = -\bar{\rho}\bar{v} \quad (7-155)$$

Page 438

When we introduce Crocco's approximation for $\bar{\rho}$ and the law of the wall for \bar{u} , the stream function also emerges as a law-of-the-wall variable, specifically

$$\psi = \mu_w \int_0^{y^+} \frac{u^+ dy^+}{1 + \beta u^+ - \gamma u^{+2}} = \psi(y^+, \beta, \gamma) \quad (7-156)$$

Introducing these variables into the momentum Eq. (7-125b) for zero pressure gradient yields

$$\rho v^* u^+ \frac{\partial}{\partial x} (v^* u^+) - \frac{\partial \psi}{\partial x} \frac{v^*}{\nu_w} \frac{\partial}{\partial y^+} (v^* u^+) = \frac{v^*}{\nu_w} \frac{\partial \tau}{\partial y^+} \quad (7-157)$$

Although differentiation with respect to y^+ is left untouched, differentiation with respect to x is carried out using the chain rule

$$\frac{\partial}{\partial x} = \frac{\partial}{\partial y^+} \frac{\partial y^+}{\partial x} + \frac{\partial}{\partial \beta} \frac{\partial \beta}{\partial x} + \frac{\partial}{\partial \gamma} \frac{\partial \gamma}{\partial x}$$

Subsequently, in harmony with Sec. 6-6.2, we can integrate (7-157) with respect to y^+ from the wall ($y = 0, \tau = \tau_w$) to the boundary layer edge ($y = \delta, \tau = 0$). In this process, we employ the same dimensionless variables as before

$$x^* = \frac{x}{L} \quad \lambda = \sqrt{\frac{2}{C_f}} \quad V = \frac{U_e}{U_0} \text{ (1.0 here)} \quad (7-158)$$

These transformations turn [Eq. \(7-157\)](#) into

$$G \frac{d\lambda}{dx^*} = Re_L = \frac{U_0 L}{\nu_e} \frac{\mu_e}{\mu_w} \left(\frac{T_e}{T_w} \right)^{1/2} \quad (7-159)$$

where

$$G(\lambda, \beta, \gamma) = \int_0^{\delta^+} \frac{\bar{\rho}}{\rho_w} \left(u^{+2} - \beta u^+ \frac{\partial u^+}{\partial \beta} + 2\gamma u^+ \frac{\partial u^+}{\partial \gamma} + \frac{\beta}{\mu_w} \frac{\partial \psi}{\partial \beta} \frac{\partial u^+}{\partial y^+} - \frac{\gamma}{\mu_w} \frac{\partial \psi}{\partial \gamma} \frac{\partial u^+}{\partial y^+} \right) dy^+$$

This form is identical to the incompressible relation, (6-76), except that (1) the nominal Reynolds number Re_L contains additional viscosity and temperature terms (here assumed constant) and (2) the function G contains more terms than its incompressible counterpart. Evaluation of G is merely a matter of dogwork quadrature and curve fitting, and this has been accomplished by White and Christoph (1972), who propose

$$G(\lambda, \beta, \gamma) \approx 8.0 \exp \frac{0.48\lambda}{S}; \quad S = \frac{(T_{aw}/T_e - 1)^{1/2}}{\sin^{-1} A + \sin^{-1} B} \quad (7-160)$$

Note that S is the square root of van Driest's parameter F_c from (7-151). It expresses the combined effect of compressibility and heat transfer without bringing in β or γ explicitly. In fact, β and γ may be related to $U_e^+ = \gamma(T_e/T_w)^{1/2}$ by rewriting their definitions from (7-141) using

$$\gamma U_e^{+2} = \frac{T_{aw} - T_e}{T_w} \quad \text{and} \quad \beta U_e^+ = \frac{T_{aw}}{T_w} - 1 \quad (7-161)$$

As in the incompressible analysis of [Chap. 6](#), we see that (7-159) can be integrated immediately to yield a flat-plate, skin-friction relation

$$Re_{xe} = \frac{U_e x}{\nu_e} = \frac{\mu_w}{\mu_e} \left(\frac{T_w}{T_e} \right)^{1/2} \int_0^{\lambda} G(\lambda, \beta, \gamma) d\lambda$$

Substituting for G from (7-160), integrating, and rearranging to solve for the skin-friction coefficient $C_{fe} = 2/\lambda^2$, we obtain the following simple formula for turbulent skin friction on a flat plate:

$$C_{fe} \approx \frac{0.455}{S^2 \ln^2 \left(\frac{0.06}{S} Re_{xe} \frac{\mu_e}{\mu_w} \sqrt{\frac{T_e}{T_w}} \right)} \quad (7-162)$$

This expression is very accurate over the entire practical range of turbulent Reynolds numbers, Mach numbers, and wall temperatures. By comparing (7-162) with the incompressible formula (6-78), we see that the same compressibility-transformation of van Driest's method holds:

$$C_{f, \text{comp}} = \frac{1}{F_c} C_{f, \text{incomp}}(Re_x F_{Re_x}) \quad [\text{White and Christoph (1972)}] \quad (7-163)$$

Page 439

As mentioned previously, others have tackled the compressible, turbulent, flat-plate problem. Huang et al. (1993) couple the van Driest transformed velocity (expressed as a wall-wake formula) and a clever form of the Crocco-law, temperature-velocity relation, to obtain

$$T = T_w - \frac{Pr_t q_w \bar{u}}{c_p \tau_w} - \frac{Pr_t \bar{u}^2}{2 c_p} \quad (7-164)$$

These allow for the variation of Coles' wake parameter Π with $Re \theta$ while outlining an iterative numerical integration that yields values of C_f and the Stanton number. No algebraic friction formula results, but the agreement with experimental data is excellent for air and

helium up to $Ma = 11$. Along similar lines, Barnwell and Wahls (1991) combine a wall–wake law with the equilibrium power-law defect stream function of Clauser (1956) to derive skin friction for adiabatic flow with pressure gradients. Their flat-plate formula agrees well with experiments but appears to be quite complicated algebraically.

We close this section with [Fig. 7-26](#), required for any textbook, showing the approximate effect of the Mach number and the wall temperature on flat-plate skin friction. The chart is strictly valid for $Re_x = 10^7$ and will vary by about ± 20 percent over the range $10^6 < Re_x < 10^9$.

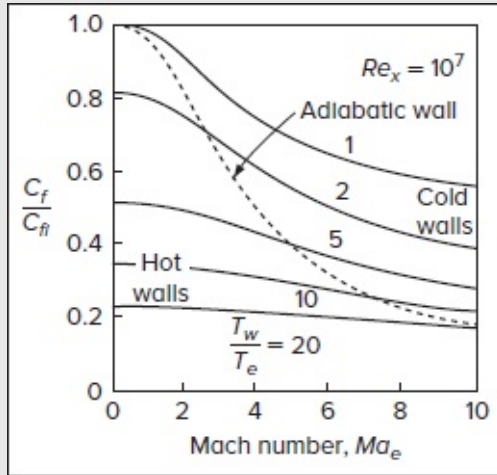


FIGURE 7-26

Ratio of turbulent, flat-plate, skin friction $C_f (M_e, T_w/T_e, Re_{xe})$ to the incompressible value $C_f(0, 1, Re_{xe})$ for $Re_x = 10^7$, as computed by the method of White and Christoph (1972) for air, using [Eq. \(7-162\)](#).

7-8.3 The Flat-Plate Turbulent Recovery Factor

In laminar flat-plate flow, the recovery factor is an output of the quasi-exact similarity analysis leading to (7-50). In turbulent flow, the theory is not so well developed. Dorrance (1962) develops a simple but effective model by breaking the law of the wall into three parts: a linear layer for $y^+ < 5$, a buffer layer for $5 < y^+ < 30$, and a log layer for $y^+ > 30$. By assuming a constant turbulent Prandtl number, Dorrance integrates the velocity and temperature profiles to obtain the following estimate for the turbulent recovery factor:

$$r_{\text{turb}} \approx Pr_t + (Pr - Pr_t) \left(\frac{11.5}{U_\epsilon^+} \right)^2 \quad (7-165)$$

There is no overt effect of the Mach number predicted. From [Fig. 7-23a](#) for compressible flow (nonzero γ), a typical value of U_ϵ^+ is about 20. If $Pr_t \approx 1$, then [Eq. \(7-165\)](#) becomes

$$r \approx 1 + (Pr - 1) \left(\frac{11.5}{20} \right)^2 \approx 1 + 0.33(Pr - 1)$$

If Pr is near unity (gases), these are the first two terms in the binomial expansion of the cube root of Pr . Therefore we adopt the customary approximation for the turbulent flat-plate recovery factor:

$$r_{\text{turb}} \approx Pr^{1/3} \quad [\text{Dorrance (1962)}] \quad (7-166)$$

Page 440

The accuracy of this expression will deteriorate for flow with strong favorable or adverse pressure gradients, as we have seen for laminar flow in Sec. 7-4.4.4. A formula to account for pressure gradient effects will be an excellent addition to our repertoire of engineering approximations.

Figure 7-27 displays recovery factors measured in supersonic flow at zero incidence past cones with adiabatic surfaces, after Mack (1954). Transition to turbulence occurs at Reynolds numbers between 2×10^6 and 4×10^6 , depending partly upon the Mach number and partly upon the particular disturbances in the flow. We see that the simple estimates, $r_{\text{lam}} \approx Pr^{1/2} \approx 0.84$ and $r_{\text{turb}} \approx Pr^{1/3} \approx 0.89$, stand in good agreement with these measurements.

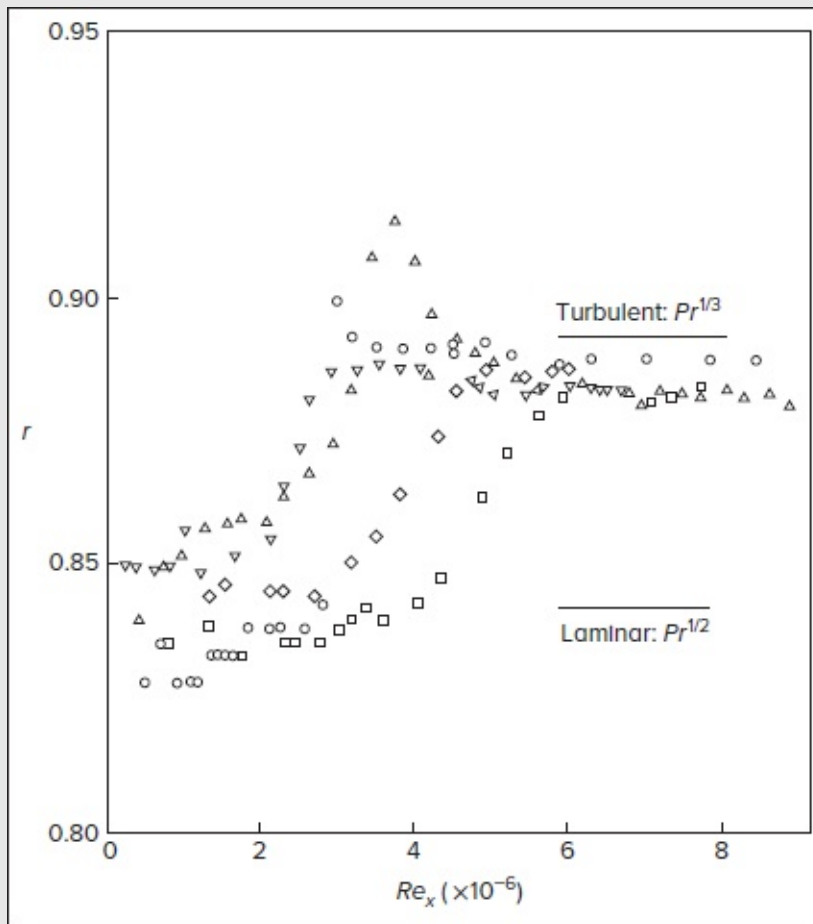


FIGURE 7-27

Measured recovery factors on cones at Mach numbers from 1.2 to 6.0, for air, $Pr = 0.71$. [Data from Mack (1954).]

7-8.4 The Turbulent Cone Rule

As mentioned before, supersonic flow past a cone at zero incidence generally results in an attached shock wave and a zero surface-pressure gradient. For laminar flow, we derive an exact cone rule leading to Eqs. (7-101a) and (7-101b). For turbulent flow, van Driest (1952b) derives an approximate cone rule, using the axisymmetric momentum-integral relation with a zero pressure gradient:

$$\frac{d\theta}{dx} + \frac{\theta}{r_0} \frac{dr_0}{dx} = \frac{1}{2} C_f \quad (7-167)$$

where $r_0(x)$ denotes the surface radius. For a cone of half-angle ϕ , we have $r_0 = x \sin \phi$, and so [Eq. \(7-167\)](#) becomes

Cone flow:
$$C_f = \frac{2}{x} \frac{d}{dx}(x\theta)$$

If we assume that friction and momentum thickness can be related by a power law, $C_f = (\text{const})\theta^{-m}$, where $m = 1$ for laminar flow and $\frac{1}{8} < m < \frac{1}{4}$ for turbulent flow, we may integrate in closed form and compare the cone to the plate. The result is a cone rule in terms of the Reynolds number:

$$\text{If } C_{f, \text{cone}} = C_{f, \text{plate}} \quad \text{then} \quad Re_{xe, \text{cone}} = (2 + m) Re_{xe, \text{plate}} \quad (7-168)$$

Page 441

The case of $m = 1$ corresponds to the previous laminar expression given by Eq. (7-101b). The result can also be expressed as a skin-friction ratio. If $Re_{xe, \text{cone}} = Re_{xe, \text{plate}}$, then, for turbulent flow,

$$\frac{C_{f, \text{cone}}}{C_{f, \text{plate}}} \approx (2 + m)^{m/(m+1)} = \begin{cases} 1.087 & m = \frac{1}{8} \\ 1.176 & m = \frac{1}{4} \end{cases} \quad (7-169)$$

Thus, as mentioned earlier, the effect for turbulent flow is only a 10–15 percent increase in friction and heat transfer, whereas in laminar flow ($m = 1$), the increase is $\sqrt{3}$ or 73 percent.

7-9 COMPRESSIBLE-TURBULENT-BOUNDARY-LAYER CALCULATION WITH A PRESSURE GRADIENT

Different methods are available to calculate compressible, turbulent, boundary layers with a pressure gradient. Here we present only a single Kármán-based method, after Walz (1969), and an inner variable approach, after White and Christoph (1972). Other methods are reviewed by Delery and Marvin (1986) and in the texts by Schetz (1992), Cebeci and Cousteix (1998), Schlichting and Gersten (2017), and Cebeci (2003). The Internet Applets of Devenport and Schetz (2002) include compressible, turbulent-flow, integral methods. Moreover, compressible two-equation and second-moment models are reviewed by Wilcox (1998) while progress on DNS predictions of shock-wave, boundary-layer interactions is reported by Yoon and Chung (1996).

7-9.1 The Kármán-Based Method of Walz (1969)

As an illustration of a momentum-thickness approach, we select the method developed by Walz (1969) and co-workers. As variables, a momentum-thickness parameter and a shape factor are defined, namely,

$$Z = \theta \left(\frac{\rho_e U_e \theta}{\mu_w} \right)^n \quad W = \frac{\delta_3}{\theta} \quad (7-170)$$

where $n = 0.268$ for turbulent flow and δ_3 is the (compressible) kinetic-energy thickness:

$$\delta_3 = \int_0^\infty \frac{\rho}{\rho_e} \frac{\bar{u}}{U_e} \left(1 - \frac{\bar{u}^2}{U_e^2} \right) dy \quad (7-171)$$

Substitution into the momentum- and mechanical-energy integral relations leads to two coupled first-order differential equations:

$$\text{Momentum:} \quad \frac{dZ}{dx} + \frac{F_1}{U_e} \frac{dU_e}{dx} Z = F_2 \quad (7-172a)$$

$$\text{Mechanical-energy:} \quad \frac{dW}{dx} + \frac{F_3}{U_e} \frac{dU_e}{dx} W = \frac{F_4}{Z} \quad (7-172b)$$

The four variables F_i are algebraic functions of the Mach number, Re_θ , shape factor $H = \delta^*/\theta$, and reduced temperature $\Theta(x)$, assumed known:

$$\Theta(x) = \frac{T_{aw}(x) - T_w(x)}{T_{aw}(x) - T_e(x)} \quad (7-173)$$

To simplify these expressions, two intermediate parameters, a and b , are defined and used to correlate the skin friction, viz.

$$C_f(x) \approx 2 \frac{a}{b} \left(\frac{\rho_e U_e \theta}{\mu_w} \right)^{-0.268}; \quad a \approx 0.0394(W - 1.515)^{0.7}, \quad b \approx 1 + 0.88 \frac{\gamma - 1}{2} Ma_e^2 (W - \Theta)(2 - W) \quad (7-174)$$

Then the functions F_1 to F_4 given by Walz (1969) may be written as

$$F_1 = 2.268 + 1.268H - Ma_e^2, \quad F_2 = 1.268 \frac{a}{b}, \quad F_3 = 1 - H + 0.88(\gamma - 1)Ma_e^2 \left(1 - \frac{\Theta}{W}\right), \quad F_4 = \frac{1}{b} \left[2\beta \left(\frac{\rho_e U_e \theta}{\mu_w} \right)^{0.168} - aW \right]$$

where $H \approx 1 + 1.48(2 - W) + 104(2 - W)^{6.7}$ and $\beta = \left[\frac{1 + 0.587(\gamma - 1)Ma_e^2(1 - 0.75\Theta)}{1 + 0.44Ma_e^2(1 - \Theta)(\gamma - 1)} \right]^n$; $n \approx 0.7$

(7-175)

Page 442

Note that the exponent n in the definition of β is the viscosity–temperature exponent, which is about 0.67 for air.

In this formulation, separation, if it occurs, is defined by $a = 0$, or $W = 1.515$. Initial values are needed for $Z(0)$ and $W(0)$. In practice, Eqs. (7-172a)–(7-175) may be integrated rather straightforwardly by any standard numerical technique.

7-9.2 An Inner Variable Approach

The flat-plate theory, which led to Eqs. (7-159) and (7-162), was extended by White and Christoph (1972) to pressure gradients by including the parameter $\alpha(x)$ and letting $u^+ = f(y^+, \alpha, \beta, \gamma)$ as per Eq. (7-145). In this process, the momentum Eq. (7-157) is extended to include pressure gradients:

$$\rho v^* u^+ \frac{\partial}{\partial x} (v^* u^+) - \frac{\partial \psi}{\partial x} \frac{v^*}{\nu_w} \frac{\partial}{\partial y^+} (v^* u^+) = \rho_e U_e \frac{dU_e}{dx} + \frac{v^*}{\nu_w} \frac{\partial \tau}{\partial y^+} \quad (7-176)$$

Also, the chain rule must be extended to include the effect of $\alpha(x)$:

$$\frac{\partial}{\partial x} = \frac{\partial}{\partial y^+} \frac{\partial y^+}{\partial x} + \frac{\partial}{\partial \alpha} \frac{\partial \alpha}{\partial x} + \frac{\partial}{\partial \beta} \frac{\partial \beta}{\partial x} + \frac{\partial}{\partial \gamma} \frac{\partial \gamma}{\partial x} \quad (7-177)$$

Now, exactly as in the previous procedure (Sec. 7-8.2), we carry out the differentiation with respect to x and then integrate the entire equation across the boundary layer from $y^+ = 0$ to $y^+ = \delta^+$, writing the final result in terms of the same dimensionless variables defined by Eqs. (7-158). We obtain

$$(G - 3\alpha H) \frac{d\lambda}{dx^*} + \frac{V^*}{V} \lambda (\lambda^2 \delta^+ - G) - \lambda^4 \frac{H(1/V)^*}{Re_L} = Re_L V \quad (7-178)$$

$$H = H(\lambda, \alpha, \beta, \gamma) = \int_0^{\delta^+} \frac{\rho}{\rho_w} \left(u^+ \frac{\partial u^+}{\partial \alpha} - \frac{1}{\mu_w} \frac{\partial \psi}{\partial \alpha} \frac{\partial u^+}{\partial y^+} \right) dy^+$$

The functions Re_L and G are defined exactly as before in Eq. (7-159), except that now u^+ and ψ must also vary with α and so the final result becomes $G = G(\lambda, \alpha, \beta, \gamma)$. Since the functions F and G are difficult to evaluate under general conditions and no accurate curve-fit correlation could be devised, White and Christoph (1972) chose to rearrange the basic

differential [Eq. \(7-178\)](#) into a two-part approximate form, using the van Driest parameter S from [Eq. \(7-160\)](#) and a “stretched” Reynolds number Re^* related to the pressure gradient:

$$Re^* = \frac{Re_L}{Y''}; \quad Y \equiv \frac{1}{V} = \frac{U_0}{U_e} \quad (7-179)$$

The separation point is defined as a large but finite value of λ , where $d\lambda/dx$ becomes unbounded:

$$\text{Separation:} \quad \lambda = \lambda_{\max} = 8.7S \log(Re^*) \quad (7-180)$$

Depending upon λ/λ_{\max} , the basic differential equation takes on two different forms:

$$\frac{\lambda}{\lambda_{\max}} > 0.36: \quad \frac{d\lambda}{dx^*} \approx \frac{6.25}{f^* S^3} \left[\frac{Y''}{Y} (1 + 9S^{-2} g^* Re^{*0.07}) + \frac{Y'''}{Y''} (3S^2 g^* Re^{*0.07}) \right] \quad (7-181a)$$

$$\frac{\lambda}{\lambda_{\max}} < 0.36 \text{ or } Re^* < 0: \quad \frac{d\lambda}{dx^*} \approx \frac{1}{8} \frac{Re_L}{Y'} \exp\left(-0.48 \frac{\lambda}{S}\right) + 5.5 \frac{Y''}{Y} \quad (7-181b)$$

The functions f^* and g^* depend only upon λ/λ_{\max} and may be curve fit as follows:

$$\frac{\lambda}{\lambda_{\max}} \geq 0.36: \quad \begin{cases} f^* = (2.434Z + 1.443Z^2)\exp(-44Z^6) \\ g^* \approx 1 - 2.3Z + 1.76Z^3; \quad Z = 1 - \lambda/\lambda_{\max} \end{cases} \quad (7-182)$$

Equations (7-181a) and (7-181b) may be solved by any standard numerical method such as Runge–Kutta integration. It is assumed that $U_e(x)$, $Ma_e(x)$, T_e , and T_w are known. Once $\lambda(x)$ is computed, the local skin friction follows from $C_f(x) = 2/\lambda^2$. To avoid ragged behavior of the solution, the freestream velocity $V(x^*)$ should be fit to a continuous analytic function, so that Y' and Y'' are smooth functions. The freestream Mach number $Ma_e(x)$ and the ratio T_w/T_e can be approximated more crudely.

Page 443

7-9.3 The Experiment of Zwarts

In his thesis, Zwarts (1970) produces a supersonic motion that is sharply decelerated from Mach 4 to Mach 3 in about 8 inches, thereafter remaining nearly constant at Mach 3. The corresponding freestream velocity and Mach number distributions are illustrated in [Fig. 7-28](#). With $U_0 = 2204$ ft/s, White and Christoph (1972) propose two different curve fits to the velocity distribution:

$$V \approx 1.0013 - 0.00051x^* - 0.003885x^{*2} + 0.0004466x^{*3} - 0.0000139x^{*4} \quad (7-183a)$$

$$V \approx 0.9165 + 0.0835\exp(-0.03x^* - 0.05x^{*2}) \quad (7-183b)$$

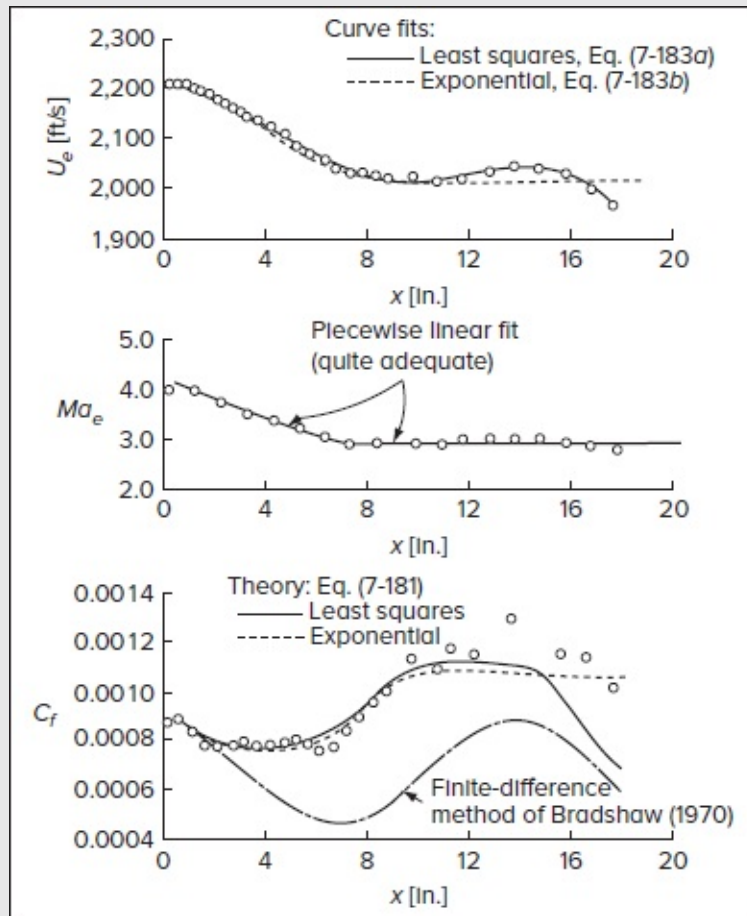


FIGURE 7-28

Comparison of theory with the supersonic relaxing-flow experiment of Zwarts (1970). [After White and Christoph (1972).]

where x^* is in inches. The polynomial is seen to be an excellent fit, whereas the exponential form does not reproduce the final curvature at the end of the run. The Mach number $Ma_e(x^*)$ is fitted by two piecewise-straight lines, as shown in Fig. 7-28. The wall temperature is approximately adiabatic, which justifies using $T_w/T_e \approx 1 + r(\gamma - 1)Ma_e^2/2$. These formulas are applied to Eqs. (7-181a) and (7-181b), and the computed skin friction is overlaid in Fig. 7-28. Both curve fits are seen to be in good agreement with the data.

Figure 7-28 shows that skin-friction predictions based on the White–Christoph method are somewhat sensitive to the quality of the curve fit of $U_e(x)$, as was the incompressible inner variable method of Das (1988) discussed in Sec. 6-8.2. The method avoids the use of momentum thickness or shape factor, so no predictions of these parameters are made. Meanwhile, the method of Walz from Sec. 7-9.1 cannot be programmed for this flow, because Zwarts (1970) does not report data for the kinetic-energy thickness $\delta_3(x)$. Other theories have been applied to Zwarts' experiment, notably the turbulent-energy differential

method of Bradshaw and Ferriss (1971). At the Stanford Conference [Kline et al. (1982, pp. 1263–1264)], four competitors—all with multi-equation differential models—attempted to predict this flow, called case 8411. Of the four predictions, two were excellent for skin friction and two were poor, but all four were excellent for predicting the shape factor, and none could reproduce the measured momentum-thickness distribution!

Page 444

7-10 COMPRESSIBLE-FLOW APPROXIMATIONS FOR QUASI-VISCOUS FLOWS

Exact solutions to compressible-flow problems are often difficult to achieve in all but the simplest of geometries and physical settings. One possible alternative is to pursue compressible-flow approximations using small parameter perturbation theory. Perturbation methods rely on asymptotic expansions of the variables of interest using series of diminishing terms that are structured according to

$$p = p_0 + \varepsilon p_1 + \varepsilon^2 p_2 + \cdots \quad (7-184)$$

where ε represents a small parameter, such as the reciprocal of the Reynolds number. When the variables of interest are expanded within the equations of motion, a linearized system is realized. Terms of equal order in ε are subsequently collected into separate equations and solved sequentially. This procedure enables us to determine a leading-order, basic solution that is followed by multiple corrections. Naturally, with each successive correction, the truncation error is reduced, and the overall solution is improved.

For slightly compressible flows, the Mach number (squared) can be used as a perturbation parameter. At the conclusion of this process, one can generally verify that the incompressible solution is recovered at the leading order. As such, all asymptotic corrections can be directly attributed to the effects of compressibility. Approximations of this sort are dubbed Rayleigh–Janzen expansions in honor of Lord Rayleigh and Oskar Janzen, who both employed this methodology in the early 20th century. To showcase the Rayleigh–Janzen procedure, two quasi-viscous solutions involving porous duct flows are presented here and discussed. These solutions are sometimes referred to as *quasi-viscous*, because of their observance of the no-slip condition at the porous wall even in their inviscid forms.

7-10.1 The Compressible Taylor Flow in a Porous Channel

In pursuing a solution for the compressible flow in a porous channel with sidewall injection, the vorticity-stream function approach may be used. The problem arises in the context of a rectangular channel of length L_0 and half height h [Maicke and Majdalani (2008)]. Along the top and bottom sidewalls, the flow enters the channel isentropically at a uniform injection

speed V_w . The origin of the coordinate system is located at the headwall's dead center and, using the tilde to denote dimensional variables, \tilde{x} and \tilde{y} , can be taken to be the directions parallel and normal to the midsection plane, respectively. The channel width is assumed to be at least 4 times larger than its height, hence rendering variations in the spanwise direction \tilde{z} inconsequential. To make further headway, all variables and operators are normalized using

$$x = \frac{\tilde{x}}{h}, \quad y = \frac{\tilde{y}}{h}, \quad u = \frac{\tilde{u}}{V_w}, \quad v = \frac{\tilde{v}}{V_w}, \quad p = \frac{\tilde{p}}{p_0}, \quad T = \frac{\tilde{T}}{T_0}, \quad \rho = \frac{\tilde{\rho}}{\rho_0}, \quad \psi = \frac{\tilde{\psi}}{\rho_0 h V_w}, \quad \omega = \frac{\tilde{\omega} h}{V_w}, \quad \nabla = h \tilde{\nabla}, \quad L = \frac{L_0}{h} \quad (7-185)$$

where ψ stands for the stream function, L denotes the channel's aspect ratio, and the subscript "0" describes a reference condition at the headwall. Taking advantage of symmetry, a solution can be obtained for the top half portion of the channel, namely, $0 \leq x \leq L$ and $0 \leq y \leq 1$, as illustrated in [Fig. 7-29](#), and then mirrored across the midsection plane. The two-dimensional velocity vector can be represented by $\mathbf{v} = (u, v, 0)$ while its corresponding vorticity, which carries only one non-vanishing component, by $\boldsymbol{\omega} = \nabla \times \mathbf{v} = (0, 0, \omega)$. The velocity components can be related to the compressible stream function using

$$u = \frac{1}{\rho} \frac{\partial \psi}{\partial y} \quad \text{and} \quad v = -\frac{1}{\rho} \frac{\partial \psi}{\partial x} \quad (7-186)$$

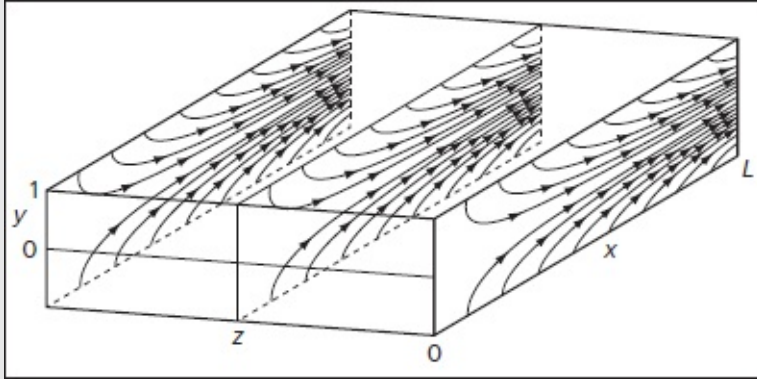


FIGURE 7-29

Schematic of a two-dimensional porous channel with wall-normal injection.

When substituted into the vorticity definition, one arrives at the first fundamental equation relating the vorticity to the stream function,

$$\frac{\partial^2 \psi}{\partial x^2} + \frac{\partial^2 \psi}{\partial y^2} = \frac{1}{\rho} (\nabla \rho \cdot \nabla \psi) - \omega \rho \quad (\text{vorticity}) \quad (7-187)$$

A second relation between ψ and ω is, of course, necessary. One can reproduce the vorticity transport equation by taking the curl of the momentum equation and putting

$$\nabla \times (\mathbf{v} \times \boldsymbol{\omega}) = -\frac{1}{\gamma Ma_w^2 \rho^2} \nabla \rho \times \nabla p \quad (\text{vorticity transport}) \quad (7-188)$$

Page 445

Conservation of momentum can also be used to determine the pressure once the stream function and vorticity are determined, specifically from

$$-\frac{\nabla p}{\gamma Ma_w^2} = \rho \nabla \left[\frac{1}{2\rho^2} (\nabla \psi \cdot \nabla \psi) \right] + \omega \nabla \psi \quad (\text{momentum}) \quad (7-189)$$

Finally, since the flow is isentropic, it is possible to relate the thermodynamic variables using

$$\rho = p^{1/\gamma} \quad \text{and} \quad T = p^{(\gamma-1)/\gamma} \quad (\text{isentropic relations}) \quad (7-190)$$

The boundary conditions stem from the need to prevent axial flow at the headwall and sidewall, maintain the same normal velocity at the sidewall, and disallow crossflow about the midsection plane. These conditions translate into

$$u(0, y) = 0, \quad u(x, 1) = 0, \quad v(x, 1) = -1, \quad v(x, 0) = 0 \quad (7-191)$$

In fact, the quasi-viscous character of the solution may be directly attributed to the enforcement of the no-slip condition at the sidewall, namely, $u(x, 1) = 0$.

To solve [Eqs. \(7-187\)–\(7-190\)](#), a Rayleigh–Janzen expansion is introduced. As such, the variables of interest are expanded in terms of the Mach number squared according to

$$\begin{aligned} u(x, y) &= u_0 + Ma_w^2 u_1 + O(Ma_w^4) & \rho(x, y) &= 1 + Ma_w^2 \rho_1 + Ma_w^4 \rho_2 + O(Ma_w^6) \\ v(x, y) &= v_0 + Ma_w^2 v_1 + O(Ma_w^4) & p(x, y) &= 1 + Ma_w^2 p_1 + Ma_w^4 p_2 + O(Ma_w^6) \\ \psi(x, y) &= \psi_0 + Ma_w^2 \psi_1 + O(Ma_w^4) & T(x, y) &= 1 + Ma_w^2 T_1 + Ma_w^4 T_2 + O(Ma_w^6) \\ \omega(x, y) &= \omega_0 + Ma_w^2 \omega_1 + O(Ma_w^4) \end{aligned} \quad (7-192)$$

The expanded terms are then substituted into [Eqs. \(7-187\)–\(7-190\)](#) and sorted in orders of the Mach number. At the leading order, one recovers the incompressible Taylor flow equations:

$$u_0 = \frac{\partial \psi_0}{\partial y} \quad v_0 = -\frac{\partial \psi_0}{\partial x} \quad (7-193)$$

$$\frac{\partial^2 \psi_0}{\partial x^2} + \frac{\partial^2 \psi_0}{\partial y^2} = -\omega_0 \quad (7-194)$$

$$\nabla \times (\mathbf{v}_0 \times \boldsymbol{\omega}_0) = 0 \quad (7-195)$$

$$-\nabla p_1 / \gamma = \nabla \left[\frac{1}{2} (\nabla \psi_0 \cdot \nabla \psi_0) \right] + \omega_0 \nabla \psi_0 \quad (7-196)$$

$$\rho_1 = p_1 / \gamma \quad \text{and} \quad T_1 = (\gamma - 1) p_1 / \gamma \quad (7-197)$$

These relations are equivalent to those considered when analyzing the incompressible flow in a channel with sidewall injection. Along similar lines, the first-order equations, which encapsulate the first compressible contribution, may be isolated and written as

$$u_1 = \frac{\partial \psi_1}{\partial y} - \rho_1 \frac{\partial \psi_0}{\partial y} \quad v_1 = \rho_1 \frac{\partial \psi_0}{\partial x} - \frac{\partial \psi_1}{\partial x} \quad (7-198)$$

$$\frac{\partial^2 \psi_1}{\partial x^2} + \frac{\partial^2 \psi_1}{\partial y^2} = \nabla \rho_1 \cdot \nabla \psi_0 - \omega_0 \rho_1 - \omega_1 \quad (7-199)$$

Page 446

$$\nabla \times (\mathbf{v}_0 \times \boldsymbol{\omega}_1) + \nabla \times (\mathbf{v}_1 \times \boldsymbol{\omega}_0) = -\nabla \rho_1 \times \nabla p_1 \quad (7-200)$$

$$-\nabla p_2 / \gamma = \nabla [(\nabla \psi_0 \cdot \nabla \psi_1) - \rho_1 (\nabla \psi_0 \cdot \nabla \psi_0)] + \rho_1 \nabla \left(\frac{1}{2} \nabla \psi_0 \cdot \nabla \psi_0 \right) + \omega_0 \nabla \psi_1 + \omega_1 \nabla \psi_0 \quad (7-201)$$

$$\rho_2 = \frac{p_2}{\gamma} + \frac{1-\gamma}{2\gamma^2} p_1^2 \quad \text{and} \quad T_2 = \frac{\gamma-1}{\gamma} p_2 + \frac{1-\gamma}{2\gamma^2} p_1^2 \quad (7-202)$$

As for the boundary conditions embodied in [Eq. \(7-191\)](#), they can be conveniently recast in terms of the stream function. One gets,

$$\text{Leading order:} \quad \frac{\partial \psi_0(x, 1)}{\partial y} = 0, \quad \frac{\partial \psi_0(0, y)}{\partial y} = 0, \quad \frac{\partial \psi_0(x, 1)}{\partial x} = 1, \quad \frac{\partial \psi_0(x, 0)}{\partial x} = 0 \quad (7-203)$$

$$\psi_0 = x \sin\left(\frac{1}{2}\pi y\right) \quad (7-204)$$

In order to write [Eq. \(7-194\)](#) purely in terms of the stream function, it is necessary to eliminate the vorticity that appears on its right-hand side. To this end, the compressible stream function defined in [Eq. \(7-186\)](#) is substituted into the leading-order vorticity transport [Eq. \(7-195\)](#). This enables us to realize that the resulting expression is secured if, and only if, $\omega_0 = C^2 \psi_0$. Upon substitution of this relation back into [Eq. \(7-194\)](#), one may use separation of variables and apply the boundary conditions specified in [Eq. \(7-203\)](#). As expected, one recovers the incompressible Taylor profile:

$$\psi_0 = x \sin\left(\frac{1}{2}\pi y\right) \quad (7-205)$$

The p_1 term can be determined by integrating the momentum [Eq. \(7-196\)](#) after eliminating the vorticity term, ω_0 , and inserting the solution from [Eq. \(7-205\)](#). The remaining thermodynamic variables can be determined through backward substitution into the isentropic relations given by [Eq. \(7-197\)](#). The remaining thermodynamic properties are found to be

$$p_1 = -\frac{1}{2}\gamma \left[\frac{1}{4}\pi^2 x^2 + \sin^2\left(\frac{1}{2}\pi y\right) \right], \quad \rho_1 = -\frac{1}{2} \left[\frac{1}{4}\pi^2 x^2 + \sin^2\left(\frac{1}{2}\pi y\right) \right] \quad \text{and} \quad T_1 = \frac{1}{2}(1-\gamma) \left[\frac{1}{4}\pi^2 x^2 + \sin^2\left(\frac{1}{2}\pi y\right) \right] \quad (7-206)$$

The procedure for obtaining the first-order compressible correction mirrors that of its leading order, albeit with non-homogenous terms. As usual, the vorticity transport [Eq. \(7-200\)](#) can be used to determine a relation between ω_1 and ψ_1 . After some effort, Maicke and Majdalani (2008) find a possible solution of the form

$$\omega_1 = \frac{1}{4}\pi^2\psi_1 \pm \frac{1}{32}\pi^2x\left[\pi^2x^2\sin\left(\frac{1}{2}\pi y\right) + 4\sin^2\left(\frac{1}{2}\pi y\right)\right] + F(\psi_0) \quad (7-207)$$

The terms arising after the \pm sign represent additional corrections that are needed to fulfill [Eq. \(7-200\)](#). Here $F(\psi_0)$ refers to an arbitrary function of the incompressible stream function, ψ_0 , which can be determined in a manner to secure the principal equations and their boundary conditions.

Next, the vorticity in [Eq. \(7-199\)](#) can be solved after incorporating all leading-order solutions. The resulting non-homogeneous terms suggest a first-order stream function of the type

$$\psi_1(x, \eta) = xg(\eta) + x^3h(\eta) \quad (7-208)$$

where $\eta \equiv \frac{1}{2}\pi y$ is taken to simplify bookkeeping. This form may be substituted back into [Eq. \(7-199\)](#), thereby giving rise to two ordinary differential equations that can be solved separately. When these are augmented by the boundary conditions specified in [Eq. \(7-204\)](#), the first-order correction can be retrieved very neatly and rearranged into

$$\psi_1 = -\frac{1}{48}x \sin \eta \left\{ \pi^2 x^2 [3 + \cos(2\eta)] + 3[7 - \cos(2\eta)] \right\} \quad (7-209)$$

Solving for the pressure requires separating [Eq. \(7-201\)](#) into its scalar components and then solving through partial integration. The resulting compressible pressure correction can be readily extracted into

$$p_2 = -\frac{1}{16}\gamma \left\{ [\cos(2\eta) + \cos^2(2\eta)] - \frac{1}{4}\pi^2 x^2 [7 - \cos^2(2\eta)] + \frac{1}{24}\pi^4 x^4 \right\} \quad (7-210)$$

Page 447

The remaining thermodynamic variables are determined through straightforward substitution into [Eq. \(7-202\)](#). One gets

$$\begin{cases} \rho_2 = \frac{1}{32}[1 - \gamma + 2(\gamma - 2)\cos(2\eta) - (\gamma + 1)\cos^2(2\eta)] + \frac{1}{64}\pi^2 x^2 [9 - 2\gamma + 2(\gamma - 1)\cos(2\eta) - \cos^2(2\eta)] + \frac{1}{384}(2 - 3\gamma)\pi^4 x^4 \\ T_2 = \frac{1}{192}(1 - \gamma) \left\{ 6[1 + 3\cos^2(2\eta)] - 3\pi^2 x^2 [5 + 2\cos(2\eta) - \cos^2(2\eta)] + 2\pi^4 x^4 \right\} \end{cases} \quad (7-211)$$

At this stage, all corrective terms can be substituted back into the Rayleigh–Janzen series expansions contained in [Eq. \(7-192\)](#), thus leading to the following two-term approximations:

$$\begin{cases} \rho_2 = \frac{1}{32}[1 - \gamma + 2(\gamma - 2)\cos(2\eta) - (\gamma + 1)\cos^2(2\eta)] + \frac{1}{64}\pi^2 x^2[9 - 2\gamma + 2(\gamma - 1)\cos(2\eta) - \cos^2(2\eta)] + \frac{1}{384}(2 - 3\gamma)\pi^4 x^4 \\ T_2 = \frac{1}{192}(1 - \gamma)\{6[1 + 3\cos^2(2\eta)] - 3\pi^2 x^2[5 + 2\cos(2\eta) - \cos^2(2\eta)] + 2\pi^4 x^4\} \end{cases} \quad (7-211)$$

$$u = \frac{1}{2}x \cos \pi \eta \left(1 - \frac{1}{48}\{\pi^2 x^2[\cos(2\eta) - 5] + 3[5 + \cos(2\eta)]\}Ma_w^2\right) \quad (7-212)$$

$$v = -\sin \eta \left[1 - \frac{1}{8}(\pi^2 x^2 + 3)\cos^2 \eta Ma_w^2\right] \quad (7-214)$$

$$p = 1 - \frac{1}{2}\gamma\left(\frac{1}{4}\pi^2 x^2 + \sin^2 \eta\right)Ma_w^2 - \frac{1}{16}\gamma\left\{[\cos(2\eta) + \cos^2(2\eta)] - \frac{1}{4}\pi^2 x^2[7 - \cos^2(2\eta)] + \frac{1}{24}\pi^4 x^4\right\}Ma_w^4 \quad (7-215)$$

$$\begin{aligned} \rho = 1 - \frac{1}{2}\left(\frac{1}{4}\pi^2 x^2 + \sin^2 \eta\right)Ma_w^2 + \frac{1}{32}\left\{[1 - \gamma + 2(\gamma - 2)\cos(2\eta) - (\gamma + 1)\cos^2(2\eta)] \right. \\ \left. + \frac{1}{2}\pi^2 x^2[9 - 2\gamma + 2(\gamma - 1)\cos(2\eta) - \cos^2(2\eta)] + \frac{1}{12}(2 - 3\gamma)\pi^4 x^4\right\}Ma_w^4 \end{aligned} \quad (7-216)$$

and

$$\begin{aligned} T = 1 + \frac{1}{2}(1 - \gamma)\left(\frac{1}{4}\pi^2 x^2 + \sin^2 \eta\right)Ma_w^2 \\ + \frac{1}{192}(1 - \gamma)\left\{6[1 + 3\cos^2(2\eta)] - 3\pi^2 x^2[5 + 2\cos(2\eta) - \cos^2(2\eta)] + 2\pi^4 x^4\right\}Ma_w^4 \end{aligned} \quad (7-217)$$

Naturally, the procedure can be repeated to improve its accuracy by retaining higher-order terms. In the meantime, the approximation presented here remains accurate to $O(Ma_w^4)$ in the velocity and $O(Ma_w^6)$ in the pressure, density, and temperature.

7-10.2 The Compressible Taylor–Culick Flow in a Porous Tube

The multi-dimensional procedure described above was first applied by Majdalani (2007) in the context of a right-cylindrical porous tube with sidewall injection, where the incompressible rotational motion is often referred to as the Taylor–Culick profile [Saad and Majdalani (2007)]. The physical configuration, which corresponds to a tube of length L_0 and radius a , has been ubiquitously used to model the bulk gaseous motion in solid rocket motors with circular grain perforations [Chedevergne et al. (2006) and Bouyges et al. (2017)]. As usual, the flow enters the tube isentropically along the sidewall at a uniform injection speed V_w . As before, the tilde can be used to denote dimensional variables with \tilde{x} and \tilde{r} alluding to the axial and radial coordinates, respectively. Our assortment of variables and operators is specified according to

$$x = \frac{\tilde{x}}{a}, \quad r = \frac{\tilde{r}}{a}, \quad u = \frac{\tilde{u}}{V_w}, \quad v = \frac{\tilde{v}}{V_w}, \quad p = \frac{\tilde{p}}{p_0}, \quad T = \frac{\tilde{T}}{T_0}, \quad \rho = \frac{\tilde{\rho}}{\rho_0}, \quad \psi = \frac{\tilde{\psi}}{\rho_0 a^2 V_w}, \quad \omega = \frac{\tilde{\omega} a}{V_w}, \quad \nabla = a \tilde{\nabla}, \quad L = \frac{L_0}{a} \quad (7-218)$$

where ψ stands for the compressible Stokes stream function, L refers to the porous tube's aspect ratio, and the subscript “0” denotes a reference condition at the headwall. Taking advantage of axisymmetry, our solution domain can be limited to $0 \leq x \leq L$ and $0 \leq r \leq 1$, as illustrated in [Fig. 7-30](#). To avoid the use of multiple subscripts, we resort to a variant (x, r, θ) coordinate system and designate our velocity and vorticity companions as $\mathbf{v} = (u, v,$

0) and $\boldsymbol{\omega} = \nabla \times \mathbf{v} = (0, 0, \omega)$. In this framework, the velocity components can be related to Stokes' compressible stream function via

$$x = \frac{\tilde{x}}{a}, \quad r = \frac{\tilde{r}}{a}, \quad u = \frac{\tilde{u}}{V_w}, \quad v = \frac{\tilde{v}}{V_w}, \quad p = \frac{\tilde{p}}{p_0}, \quad T = \frac{\tilde{T}}{T_0}, \quad \rho = \frac{\tilde{\rho}}{\rho_0}, \quad \psi = \frac{\tilde{\psi}}{\rho_0 a^2 V_w}, \quad \boldsymbol{\omega} = \frac{\tilde{\boldsymbol{\omega}} a}{V_w}, \quad \nabla = a \tilde{\nabla}, \quad L = \frac{L_0}{a} \quad (7-219)$$

Page 448

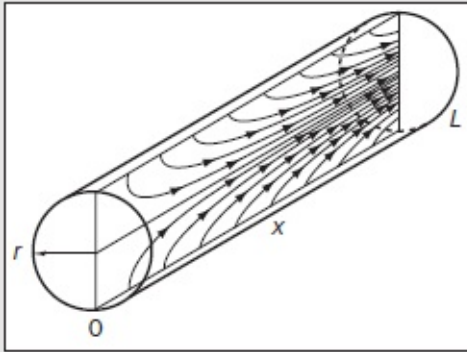


FIGURE 7-30

Schematic of a porous tube with wall-normal injection.

When [Eq. \(7-219\)](#) is inserted into the vorticity definition, one obtains a key relation between ω and ψ , specifically

$$\frac{\partial^2 \psi}{\partial x^2} + \frac{\partial^2 \psi}{\partial r^2} - \frac{1}{r} \frac{\partial \psi}{\partial r} = \frac{1}{\rho} (\nabla \rho \cdot \nabla \psi) - \omega r \rho \quad (\text{vorticity}) \quad (7-220)$$

In conformance with the vorticity-stream function approach, a second relation between ω and ψ may be arrived at through the vorticity transport equation. To this end, the curl of the momentum equation is taken such that

$$\nabla \times (\mathbf{v} \times \boldsymbol{\omega}) = -\frac{1}{\gamma Ma_w^2 \rho^2} \nabla \rho \times \nabla p \quad (\text{vorticity transport}) \quad (7-221)$$

As for the pressure, it may be retrieved from the normalized momentum equation,

$$-\frac{\nabla p}{\gamma Ma_w^2} = \rho \nabla \left[\frac{1}{2 \rho^2 r^2} (\nabla \psi \cdot \nabla \psi) \right] + \frac{1}{r} \omega \nabla \psi \quad (\text{momentum}) \quad (7-222)$$

Our last stop takes us to the isentropic flow relations, which enable us to extract the density and temperature directly from

$$\rho = p^{1/\gamma} \quad \text{and} \quad T = p^{(\gamma-1)/\gamma} \quad (\text{isentropic relations}) \quad (7-223)$$

The physical boundary conditions associated with the Taylor–Culick profile prohibit any radial flow across the centerline and any axial motion at either the headwall or the sidewall. They also require a constant radial velocity at the sidewall. In essence, we have

$$u(0, r) = 0, \quad u(x, 1) = 0, \quad v(x, 0) = 0, \quad v(x, 1) = -1 \quad (7-224)$$

At this juncture, having defined the governing equations and their boundary conditions, a Rayleigh–Janzen expansion can be employed to linearize [Eqs. \(7-220\)–\(7-223\)](#). This effort begins by writing each of the principal variables as a series of the Mach number squared:

$$\begin{cases} u(r, z) = u_0 + Ma_w^2 u_1 + O(Ma_w^4) & \rho(x, y) = 1 + Ma_w^2 \rho_1 + Ma_w^4 \rho_2 + O(Ma_w^6) \\ v(r, z) = v_0 + Ma_w^2 v_1 + O(Ma_w^4) & p(x, y) = 1 + Ma_w^2 p_1 + Ma_w^4 p_2 + O(Ma_w^6) \\ \psi(r, z) = \psi_0 + Ma_w^2 \psi_1 + O(Ma_w^4) & T(x, y) = 1 + Ma_w^2 T_1 + Ma_w^4 T_2 + O(Ma_w^6) \\ \omega(r, z) = \omega_0 + Ma_w^2 \omega_1 + O(Ma_w^4) \end{cases} \quad (7-225)$$

By inserting the decomposed variables into [Eqs. \(7-220\)–\(7-223\)](#), one may expand, rearrange, and collect terms that appear at the same order in the Mach number. Forthwith, the segregation of terms that do not contain the Mach number leads to the incompressible Taylor–Culick relations:

$$u_0 = \frac{1}{r} \frac{\partial \psi_0}{\partial r} \quad v_0 = -\frac{1}{r} \frac{\partial \psi_0}{\partial x} \quad (7-226)$$

$$\frac{\partial^2 \psi_0}{\partial x^2} + \frac{\partial^2 \psi_0}{\partial r^2} - \frac{1}{r} \frac{\partial \psi_0}{\partial r} + r \omega_0 = 0 \quad (7-227)$$

$$\nabla \times (\mathbf{v}_0 \times \boldsymbol{\omega}_0) = 0 \quad (7-228)$$

Page 449

$$-\frac{\nabla p_1}{\gamma} = \nabla \left[\frac{1}{2} \left(\frac{\nabla \psi_0 \cdot \nabla \psi_0}{r^2} \right) \right] + \frac{\omega_0}{r} \nabla \psi_0 \quad (7-229)$$

$$\rho_1 = \frac{p_1}{\gamma} \quad \text{and} \quad T_1 = \frac{\gamma-1}{\gamma} p_1 \quad (7-230)$$

In like manner, the equations that capture the first compressible correction may be identified as

$$u_1 = \frac{1}{r} \frac{\partial \psi_1}{\partial r} - \rho_1 \frac{1}{r} \frac{\partial \psi_0}{\partial r} \quad v_1 = \rho_1 \frac{1}{r} \frac{\partial \psi_0}{\partial x} - \frac{1}{r} \frac{\partial \psi_1}{\partial x} \quad (7-231)$$

$$\frac{\partial^2 \psi_1}{\partial x^2} + \frac{\partial^2 \psi_1}{\partial r^2} - \frac{1}{r} \frac{\partial \psi_1}{\partial r} + r \omega_1 = \nabla \rho_1 \cdot \nabla \psi_0 - r \omega_0 \rho_1 \quad (7-232)$$

$$\nabla \times (\mathbf{v}_0 \times \boldsymbol{\omega}_1) + \nabla \times (\mathbf{v}_1 \times \boldsymbol{\omega}_0) = -\frac{\nabla \rho_1 \times \nabla p_1}{\gamma} \quad (7-233)$$

$$-\frac{\nabla p_2}{\gamma} = \nabla \left[\frac{(\nabla \psi_0 \cdot \nabla \psi_1) - \rho_1 (\nabla \psi_0 \cdot \nabla \psi_0)}{r^2} \right] + \rho_1 \nabla \left(\frac{\nabla \psi_0 \cdot \nabla \psi_0}{2r^2} \right) + \frac{\omega_0 \nabla \psi_1 + \omega_1 \nabla \psi_0}{r} \quad (7-234)$$

$$\rho_2 = \frac{p_2}{\gamma} + \frac{1-\gamma}{2\gamma^2} p_1^2 \quad \text{and} \quad T_2 = \frac{\gamma-1}{\gamma} p_2 + \frac{1-\gamma}{2\gamma^2} p_1^2 \quad (7-235)$$

To complete this system, the problem's boundary conditions, specified by [Eq. \(7-224\)](#), can be conveniently written in terms of the stream function:

$$\text{Leading order:} \quad \frac{\partial \psi_0(0, r)}{\partial r} = 0, \quad \frac{\partial \psi_0(x, 1)}{\partial r} = 0, \quad \frac{\partial \psi_0(x, 1)}{\partial x} = 1, \quad \frac{\partial \psi_0(x, 0)}{\partial x} = 0 \quad (7-236)$$

$$\text{First order:} \quad \frac{\partial \psi_1(0, r)}{\partial r} = 0, \quad \frac{\partial \psi_1(x, 1)}{\partial r} = 0, \quad \frac{\partial \psi_1(x, 1)}{\partial x} = \rho_1, \quad \frac{\partial \psi_1(x, 0)}{\partial x} = 0 \quad (7-237)$$

To make further headway, [Eq. \(7-227\)](#) must be reduced to a function of a single dependent variable, ψ_0 , which, in turn, requires eliminating ω_0 . This can be accomplished by substituting the compressible stream function definition, given by [Eq. \(7-226\)](#), into the leading-order vorticity transport [Eq. \(7-228\)](#). It can then be shown that any relation of the form $\omega_0 = C^2 r \psi_0$ will satisfy the vorticity transport equation identically. When this particular relation is returned to [Eq. \(7-227\)](#), a linear differential equation is realized, namely,

$$\frac{\partial^2 \psi_0}{\partial x^2} + \frac{\partial^2 \psi_0}{\partial r^2} - \frac{1}{r} \frac{\partial \psi_0}{\partial r} + C^2 r^2 \psi_0 = 0 \quad (7-238)$$

One may then proceed to use the product solution method of the form $\psi_0(x, r) = X(x) R(r)$ in conjunction with [Eq. \(7-236\)](#) to recover the classical Taylor–Culick stream function,

$$\psi_0 = x \sin\left(\frac{1}{2} \pi r^2\right) \quad (7-239)$$

As for the pressure, p_1 can be deduced from the momentum [Eq. \(7-229\)](#) fairly straightforwardly. The density and temperature follow equally easily from [Eq. \(7-235\)](#). We get

$$p_1 = -\frac{1}{2} \gamma \left[\pi^2 x^2 + r^{-2} \sin^2\left(\frac{1}{2} \pi r^2\right) \right], \quad \rho_1 = -\frac{1}{2} \left[\pi^2 x^2 + r^{-2} \sin^2\left(\frac{1}{2} \pi r^2\right) \right] \quad \text{and} \quad T_1 = \frac{1}{2} (1 - \gamma) \left[\pi^2 x^2 + r^{-2} \sin^2\left(\frac{1}{2} \pi r^2\right) \right] \quad (7-240)$$

The first-order compressible correction entails nearly identical steps. First, [Eq. \(7-233\)](#) can be used to determine a relation between ω_1 and ψ_1 . After some effort [Majdalani (2007)], one finds

$$\omega_1 = \pi^2 r \psi_1 - \frac{1}{2} \pi^2 \left[\pi^2 r^2 x^2 + \sin^2\left(\frac{1}{2} \pi r^2\right) \right] \psi_0 / r + r F(\psi_0) \quad (7-241)$$

Here $F(\psi_0)$ represents an arbitrary function of ψ_0 that must be determined in a manner to satisfy all equations and boundary conditions. Next, [Eq. \(7-232\)](#) can be solved after expressing it solely as a function of the first-order stream function, ψ_1 . Majdalani (2007)

suggests a solution of the form

$$\psi_1(x, \eta) = \sin(\eta)[xf(\eta) + x^3 g(\eta)] \quad (7-242)$$

Page 450

where $\eta \equiv \pi r^2/2$ is used. It can then be shown that the substitution of [Eq. \(7-242\)](#) and other known quantities into [Eq. \(7-232\)](#) leads to two ordinary differential equations that can be solved separately. After some effort, one finds,

$$\begin{aligned} \psi_1 &= \frac{1}{4}\pi\psi_0\left\{-\pi x^2\left[1 + \frac{1}{3}\cos(2\eta)\right] + \frac{1}{4}\left\{\text{Si}(4\eta) + 2\text{Si}(2\eta) - \alpha + [\beta r^2 - 3\mathcal{E} + \text{Ci}(4\eta) + 2\text{Ci}(2\eta) - \ln(2\pi^3 r^6)]\cot(\eta)\right\}\right\} \\ &\approx -\frac{1}{4}\psi_0\left\{\pi^2 x^2\left[1 + \frac{1}{3}\cos(2\eta)\right] + 2\right\} \end{aligned} \quad (7-243)$$

where

$\alpha = 8/\pi + \text{Si}(2\pi) + 2\text{Si}(\pi) \simeq 7.6685048$, $\beta = \ln(2\pi^3) + 3\mathcal{E} - \text{Ci}(2\pi) - 2\text{Ci}(\pi) \simeq 5.7342087$, and $\mathcal{E} \simeq 0.577216$ stands for Euler's Gamma constant. Moreover, the sine and cosine integral functions are given by

$$\text{Si}(x) = \int_0^x t^{-1} \sin t \, dt = x - \frac{1}{18}x^3 + \frac{1}{600}x^5 + O(x^7) \quad \text{and} \quad \text{Ci}(x) = \int_0^x t^{-1} \cos t \, dt = \mathcal{E} + \ln x - \frac{1}{4}x^2 + \frac{1}{96}x^4 + O(x^6) \quad (7-244)$$

It should be noted that the last compact approximation provided by Majdalani (2007) in [Eq. \(7-243\)](#) can be used to bypass the need to use integral functions. As for the pressure, it may be extracted from the momentum [Eq. \(7-234\)](#) using partial integration. We get

$$p_2 = -\frac{1}{8}\pi^2\gamma\left[\frac{1}{3}\pi^2 x^4 + \frac{1}{2}x^2(2\pi\eta - \varsigma) + \frac{1}{4}\eta(5\eta - \varsigma/\pi)\right] \approx -\frac{1}{8}\pi^2\gamma\left[\frac{1}{3}\pi^2 x^4 + x^2(\pi\eta - 4) + \frac{1}{4}\eta(3\eta - 8/\pi)\right] \quad (7-245)$$

where $\varsigma = \pi\alpha - 2\beta \simeq 12.6229$. The remaining thermodynamic variables are determined through straightforward substitution into [Eq. \(7-235\)](#). One gets

$$\begin{cases} \rho_2 = -\frac{1}{8}\pi^2\left[\frac{1}{3}\pi^2 x^4(3\gamma - 2) + \frac{1}{2}x^2(2\pi\eta - \varsigma) + \pi x^2\eta^{-1}(\gamma - 1)\sin^2\eta + \frac{1}{4}\eta(5\eta - \varsigma/\pi) + \frac{1}{4}\eta^{-2}(\gamma - 1)\sin^4\eta\right] \\ \quad \approx -\frac{1}{8}\pi^2\left\{\frac{1}{3}\pi^2 x^4(3\gamma - 2) + \pi x^2\left[\eta + \eta^{-1}(\gamma - 1)\sin^2\eta - 4/\pi\right] - 2\eta/\pi + \frac{3}{4}\eta^2 + \frac{1}{4}\eta^{-2}(\gamma - 1)\sin^4\eta\right\} \\ T_2 = -\frac{1}{8}\pi^2(\gamma - 1)\left[\frac{4}{3}\pi^2 x^4 + \frac{1}{2}x^2(2\pi\eta - \varsigma) + \pi x^2\eta^{-1}\sin^2\eta + \frac{1}{4}\eta(5\eta - \varsigma/\pi) + \frac{1}{4}\eta^{-2}\sin^4\eta\right] \\ \quad \approx -\frac{1}{8}\pi^2(\gamma - 1)\left[\frac{4}{3}\pi^2 x^4 + \pi x^2(\eta + \eta^{-1}\sin^2\eta - 4/\pi) - 2\eta/\pi + \frac{3}{4}\eta^2 + \frac{1}{4}\eta^{-2}\sin^4\eta\right] \end{cases} \quad (7-246)$$

In the interest of simplicity, a solution that consolidates the leading and compressible contributions may be written as

$$\psi(x, r) \approx x\sin(\eta)\left(1 - \frac{1}{4}\left\{\pi^2 x^2\left[1 + \frac{1}{3}\cos(2\eta)\right] + 2\right\}Ma_w^2\right) \quad (7-247)$$

and so, for the basic flow velocity components, we have

$$u \approx \pi x \cos(\eta)\left(1 + \frac{1}{4}\left\{\pi^2 x^2\left[\frac{5}{3} - \cos(2\eta)\right] + r^{-2}[1 - \cos(2\eta)] - 2\right\}Ma_w^2\right) \quad (7-248)$$

$$v \approx -r^{-1} \sin(\eta) \left(1 - \frac{1}{4} \{ \pi^2 x^2 [1 + \cos(2\eta)] - r^{-2} [1 - \cos(2\eta)] + 2 \} Ma_w^2 \right) \quad (7-249)$$

The corresponding pressure, density, and temperature become

$$p \approx 1 - \frac{1}{2} \pi \gamma (\pi x^2 + \frac{1}{2} \eta^{-1} \sin^2 \eta) Ma_w^2 - \frac{1}{8} \pi^2 \gamma \left[\frac{1}{3} \pi^2 x^4 + x^2 (\pi \eta - 4) + \frac{1}{4} \eta (3\eta - 8/\pi) \right] Ma_w^4 \quad (7-250)$$

$$\rho \approx 1 - \frac{1}{2} \pi (\pi x^2 + \frac{1}{2} \eta^{-1} \sin^2 \eta) Ma_w^2 - \frac{1}{8} \pi^2 \left\{ \frac{1}{3} \pi^2 x^4 (3\gamma - 2) + \pi x^2 [\eta + \eta^{-1} (\gamma - 1) \sin^2 \eta - 4/\pi] \right. \\ \left. - 2\eta/\pi + \frac{3}{4} \eta^2 + \frac{1}{4} \eta^{-2} (\gamma - 1) \sin^4 \eta \right\} Ma_w^4 \quad (7-251)$$

and

$$T \approx 1 - \frac{1}{2} \pi (\gamma - 1) (\pi x^2 + \frac{1}{2} \eta^{-1} \sin^2 \eta) Ma_w^2 - \frac{1}{8} \pi^2 (\gamma - 1) \left[\frac{4}{3} \pi^2 x^4 + \pi x^2 (\eta + \eta^{-1} \sin^2 \eta - 4/\pi) \right. \\ \left. - 2\eta/\pi + \frac{3}{4} \eta^2 + \frac{1}{4} \eta^{-2} (\gamma - 1) \sin^4 \eta \right] Ma_w^4 \quad (7-252)$$

This concludes our compressible expansion analysis of rotational profiles, which follows the procedure described in [Fig. 7-31](#), where the stream function and pressure equations are solved sequentially. The procedure requires first identifying a relation between the vorticity and stream function that satisfies the vorticity transport equation and then inserting such a relation into the definition of the vorticity—which now becomes expressible as a sole function of the stream function. The resulting linear differential equation in the stream function is then carefully solved using separation of variables in a manner to secure the problem's boundary conditions. After extracting a solution for the stream function at a given order, the corresponding pressure is deduced through partial integration of the momentum equation; this is followed by the density and temperature, which can be determined from the isentropic flow relations quite straightforwardly. This procedure can be repeated at higher orders of the Mach number as needed to achieve a desired degree of precision. Unsurprisingly, solving for the compressible counterpart of irrotational flows proves to be a lot simpler, as shown by Maicke et al. (2012). The interested reader is referred in this regard to the last two exercise problems that illustrate the procedure for the treatment of irrotational flows.

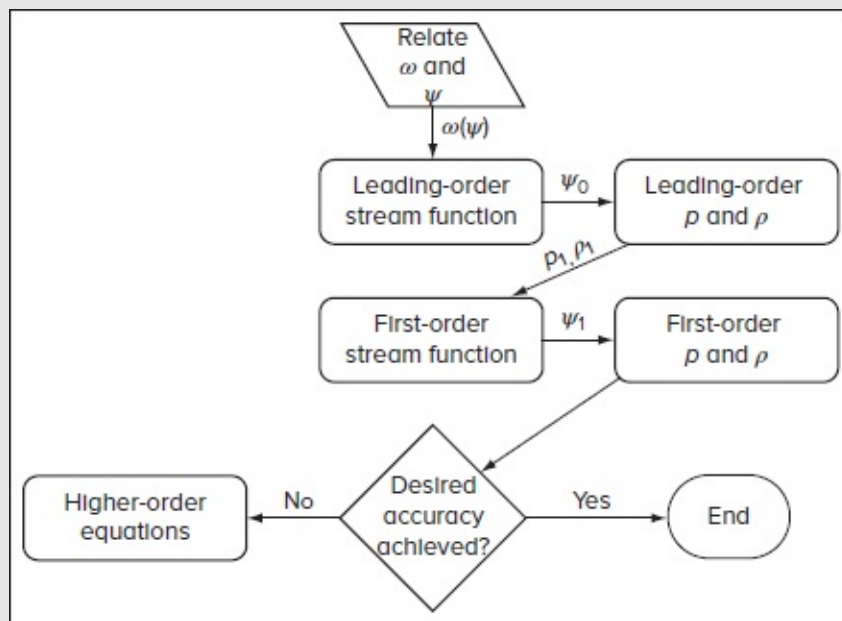


FIGURE 7-31

Flowchart of the Rayleigh–Janzen compressible-flow expansion procedure.

SUMMARY

This chapter introduces the analysis of steady compressible boundary layers for both laminar and turbulent flows. Such flows can be handled either by approximate (integral or correlative) techniques or by “exact” (finite-difference) computations, and some of the most popular methods are discussed. While the main emphasis is placed on flat-plate and stagnation-point flows, the effects of pressure gradient, heat transfer, and shock-wave interaction are briefly discussed. In this process, a presentation is made of analytically inverted forms of several isentropic flow relations that yield the Mach number, pressure, density, and temperature directly as a function of the expansion area ratio. Such relations provide a simple alternative to the use of compressible-flow tables in the treatment of isentropic expansions through convergent–divergent nozzles. Our coverage ends with a description of the powerful Rayleigh–Janzen expansion method for the treatment of compressible flows. In principle, this approach can be used to obtain a compressible analytical approximation to any mean flow profile for which an incompressible solution exists.

Naturally, it is not possible in one short chapter to treat many of the viscous-flow phenomena that have been studied under high-speed flow conditions. Some topics omitted involve mass transfer at the wall, species diffusion due to dissociation or foreign-gas injection, chemical reactions, three-dimensional flows, shock-wave impingement and leading-edge bluntness effects, wall roughness, and supersonic jets and wakes. The reader is

referred to the extensive aerospace literature on such flows including the monographs by Dorrance (1962), Schreier (1982), Schetz (1984), Smits and Dussauge (1996), Anderson (2000), Settles (2004), Schetz and Bowersox (2011), and others. It is hoped that the present chapter whets the reader's appetite to further explore this rich and ever-expanding field of compressible viscous flow.

PROBLEMS

- 7-1. Consider compressible-laminar-boundary-layer flow past a flat plate with a cold wall. If $Pr \approx 1$, find the value of T_w , in terms of (T_e, c_p, U_e) for which the maximum temperature in the boundary layer occurs at the point where $u = 0.5 U_e$. Sketch the profile $T(y)$.
- 7-2. Consider the flow of an ideal gas, $\gamma = 1.4$, past a flat plate ($\beta = 0$) at $Ma_e = 3.0$. Solve the similarity relations, Eqs. (7-47a) and (7-47b), numerically. Plot the resulting velocity and temperature profiles and compare them to (a) the finite-differencePage 452 results in [Fig. 7-13](#) and (b) the Crocco–Busemann approximation in [Eq. \(7-29\)](#). Solve for either an adiabatic wall or a cold wall, $T_w = T_e$.
- 7-3. Air at 0°C and 13 kPa is in laminar flow past a flat plate at 800 m/s. Estimate (a) the adiabatic-wall temperature in $^\circ\text{C}$ and (b) the heat-transfer rate in W/m^2 at $x = 15$ cm if the wall temperature is 20°C .
- 7-4. Evaluate the flat-plate recovery factor numerically from [Eq. \(7-50\)](#) for a value of Pr not listed in Table 7-1. Compare your results with the approximations associated with Eqs. (7-52a) and (7-52b).
- 7-5. Air at 20°C and 20 kPa flows at 1200 m/s past an insulated flat plate. At $x = 10$ cm, assuming laminar flow with no shock-wave interactions, estimate (a) the wall shear stress (in Pa) and (b) the wall heat-transfer rate (in W/m^2).
- 7-6. Helium at 20°C and 14 kPa flows axially at 1600 m/s toward a 25 cm diameter cylinder with a hemispherical nose. Using normal-shock, perfect-gas theory, estimate the velocity gradient K in s^{-1} at the nose of the hemisphere.
- 7-7. Air at 20°C and 40 kPa flows at $Ma = 3.5$ toward a sphere of diameter 10 cm whose surface is at 400°C . Assuming an ideal gas, estimate the heat-transfer rate (in W/m^2) at the stagnation point.
- 7-8. In hypersonic flow past an insulated surface, the density is small near the wall and causes the shape factor $H = \delta^*/\theta$ from [Eqs. \(7-75\)](#) to be quite large. For laminar flow,

assuming a linear velocity profile $u/U_e \approx y/\delta$ (see [Fig. 7-3a](#)) and the Crocco–Busemann temperature correlation [Eq. \(7-28\)](#), show that

$$\frac{\delta^*}{\delta} \approx 1 - \frac{1}{2a} \ln(1 + a) \quad a = \frac{\gamma - 1}{2} Ma_e^2$$

Compute the value of the shape factor if $\gamma = 1.4$ and $Ma_e = 8.0$.

- 7-9.** Consider laminar flow at constant U_e and Ma_e past an adiabatic flat plate. Use the method of Gruschwitz from Sec. 7-4.3 to solve for the variation of momentum thickness and skin-friction coefficient along the wall. Compare with other flat-plate formulas. Hint: Closed form integration is possible.
- 7-10.** Program the finite-difference method of Sec. 7-4.4, with either an explicit or implicit model, for laminar flat-plate flow with $Ma_e = 7.0$ and $\gamma = 1.4$. Assume an adiabatic wall. Compute enough downstream sections to establish the validity of the similarity variable $(y/x)Re_x^{1/2}$. Compare the computed velocities, temperatures, and skin-friction coefficients with the van Driest results in [Figs. 7-2](#) to [7-4](#).
- 7-11.** Modify Prob. 7-10 for a cold wall with $T_w = T_e/4$.
- 7-12.** Air at 20°C and 8000 Pa is in laminar flow past a flat plate at 4200 m/s. Using [Fig. 7-17](#), estimate the shock-induced pressure p_e , in pascals, at the position $x = 8$ cm along the plate.
- 7-13.** As shown in [Fig. P7-13](#), air at 20°C and 30 kPa flows at $Ma = 3.5$ toward a symmetric two-dimensional wedge of half-angle 15°. If the wedge surface is insulated, estimate its temperature (in °C) for an assumed laminar-flow condition.

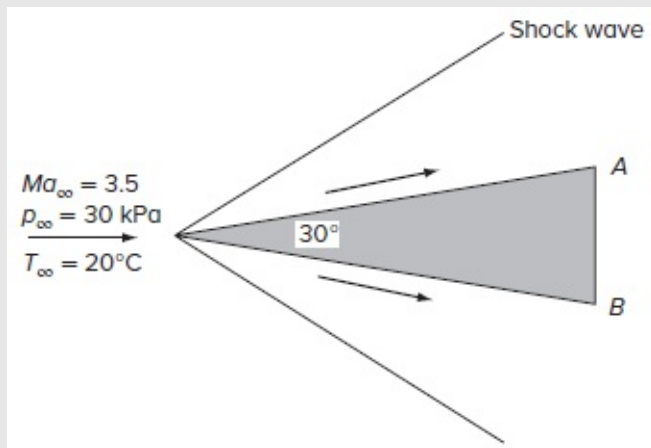


FIGURE P7.13

- 7-14. Modify Prob. 7-13 to find the total heat transfer per unit width on the upper surface of the wedge if the base AB has a length of 10 cm. Let $T_w = 300$ K.
- 7-15. Modify Prob. 7-13 for an assumed turbulent-flow condition.

Page 453

- 7-16. Modify Prob. 7-14 for an assumed turbulent-flow condition.
- 7-17. Figure P7-17 is a shadowgraph of airflow at $Ma = 2.85$ striking a 20° ramp, from Settles et al. (1979). The white line at left shows the thickness of the approaching turbulent boundary layer. (a) Determine if the shock-wave angle (the thick black line) is in agreement with oblique-shock theory. (b) Discuss how the details of the shadowgraph can be explained by boundary-layer concepts.

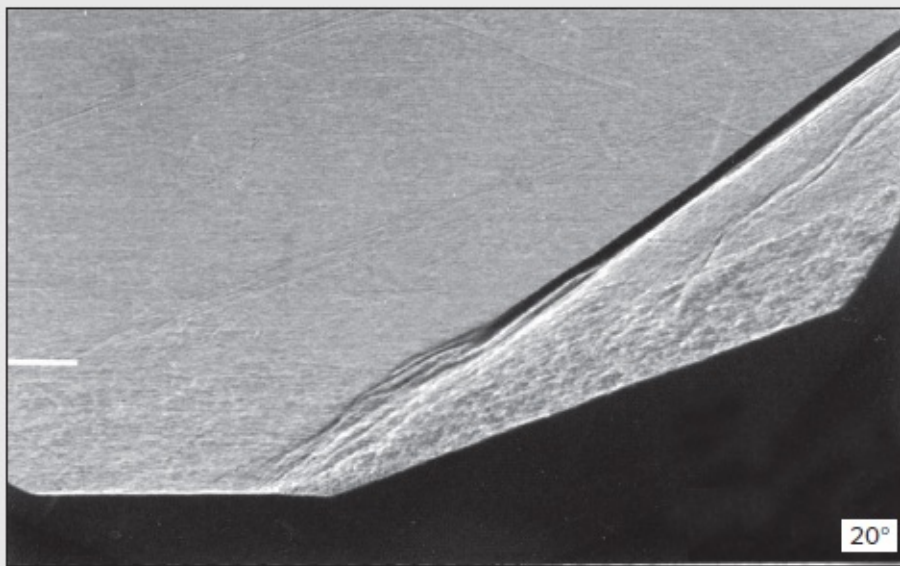


FIGURE P7.17

- 7-18. Solve the hypersonic-interaction [Eqs. \(7-104\)](#) and [\(7-106\)](#) numerically for $\gamma = 1.4$ and $T_w = T_{aw}$ in the range $0 < \chi < 10$. Compare your results with [Fig. 7-17](#) and with the simple linear approximation given by [Eq. \(7-108\)](#).
- 7-19. Air at 20°C and 25 kPa flows at 2200 m/s past an insulated flat plate. At the point $x = 2$ cm, use hypersonic-interaction theory to estimate the actual surface pressure (in Pa).
- 7-20. Consider the turbulent-boundary-layer energy Eq. (7-125d) with negligible viscous

shear, heat transfer, and pressure gradient. Near the wall, we have $\tau \approx \tau_w$ and negligible convection. Integrate the energy equation to obtain $q = q_w + \bar{u}\tau_w$. Then, introducing the eddy viscosity and turbulent Prandtl number, integrate to find the temperature in the form of [Eq. \(7-164\)](#), as found by Huang et al. (1993).

- 7-21.** At a certain position in a turbulent flat-plate boundary layer, the air freestream conditions are $U_e = 900$ m/s and $T_e = 20^\circ\text{C}$. The wall temperature is 300°C and the wall heat transfer is 30 kW/m² into the wall. The boundary-layer thickness is 6 mm. Using the compressible law of the wall, estimate the local wall shear stress (in Pa). Compare your estimate with other flat-plate formulas. Let $p_e = 1$ atm.
- 7-22.** Modify Prob. 7-5 to study the position $x = 1$ m, where the boundary-layer motion is turbulent.
- 7-23.** In the experiment of Coles (1954), for smooth adiabatic-wall flat-plate airflow at three Mach numbers and three x stations, some of the reported data may be listed as follows:

Ma_e	$U_e x / \nu_e$	C_f
2.6	4.84×10^6	0.00181
2.6	8.32×10^6	0.00166
3.7	3.98×10^6	0.00162
3.7	7.25×10^6	0.00138
4.5	3.37×10^6	0.00155
4.5	3.52×10^6	0.00148
4.5	6.91×10^6	0.00123

Compare these data with predictions by the turbulent flat-plate methods of van Driest and White and Christoph in Sec. 7-8. Also show comparative predictions for $Ma_e = 0$.

- 7-24.** The data from the experiment of Zwarts (1970), used in preparing [Fig. 7-28](#), may be listed as follows:

x [in]	U_e [ft/s]	Ma_e	C_f (exp)
0.75	2204	4.016	0.000850
2.25	2174	3.727	0.000767
3.75	2132	3.464	0.000778
5.25	2082	3.266	0.000810
6.75	2037	2.987	0.000774
8.25	2023	2.958	0.000950
9.75	2025	2.974	0.001145
11.75	2024	2.950	0.001175
13.75	2047	3.083	0.001295
15.75	2020	2.947	0.001151
17.75	1967	2.751	0.000998

The freestream kinematic viscosity was $1.06 \times 10^{-4} \text{ ft}^2/\text{s}$. Make your own curve fit to the velocity and Mach number data and, starting at the first position, compute a theoretical skin-friction distribution for comparison, using the method of Walz [Eqs. (7-174) and (7-175)]. Numerical integration is required.

- 7-25. Repeat Prob. 7-24 using the White–Christoph inner variable method given by Eqs. (7-181a) and (7-181b).
- 7-26. The answer to Prob. 7-13 is $T_{aw} \approx 919 \text{ K}$. (a) Assuming laminar flow, find the wedge half-angle for which $T_{aw} \approx 950 \text{ K}$. (b) Find the adiabatic-wall temperature of a flat plate (wedge angle = 0) with a stream Mach number of 3.5. (c) One of your answers (a, b) will be less than the other. Give a thermodynamic explanation for this result.
- 7-27. In a wind tunnel experiment, air at 20°C and 8000 Pa flows past an adiabatic flat plate at $Ma \approx 4.5$. Turbulent-boundary-layer velocities are measured as follows:

y [mm]	5.4	8.6	14.0	21.6
\bar{u} [m/s]	1100	1160	1240	1310

Using the van Driest transformation, estimate the wall shear stress in pascals.

- 7-28. Show that in the water hammer problem, although the radial velocity is far smaller than the axial component, it should not be neglected in the governing equation. Hint: Solve the equation by ignoring the radial velocity and then check the validity of the solution you obtain.
- 7-29. Solve the first member of Eq. (7-112) in Sec. 7-5.3 assuming $u_1(x, r, t) = J_0(\lambda_1 r)$, where $J_0(r)$ denotes the zeroth-order Bessel function, and λ_1 reproduces its first root. Hint: $u_1(x, r, t)$ can be solved using separation of variables.

Answer: $u_1(x, r, t) = J_0(\lambda_1 r) e^{-\lambda_1^2 t}$

7-30. Solve [Eq. \(7-119\)](#) in Sec. 7-5.3 using the Laplace transform method. Note that

$$F_\varepsilon(t) = 4 \sum_{n=1}^{\infty} \lambda_n^{-2} e^{-\varepsilon \lambda_n^2 t}.$$

7-31. In seeking a compressible solution for the irrotational mean-flow profile in a porous channel (see Fig. P7-31), one may use a steady, two-dimensional, compressible potential flow equation that incorporates the effects of the porous wall Mach number Ma_w , specifically,

$$\nabla^2 \phi = Ma_w^2 \left\{ \left(\frac{\partial \phi}{\partial x} \right)^2 \frac{\partial^2 \phi}{\partial x^2} + \left(\frac{\partial \phi}{\partial y} \right)^2 \frac{\partial^2 \phi}{\partial y^2} + 2 \frac{\partial \phi}{\partial x} \frac{\partial \phi}{\partial y} \frac{\partial^2 \phi}{\partial x \partial y} + \frac{\gamma - 1}{2} \left[\left(\frac{\partial \phi}{\partial x} \right)^2 + \left(\frac{\partial \phi}{\partial y} \right)^2 \right] \nabla^2 \phi \right\}$$

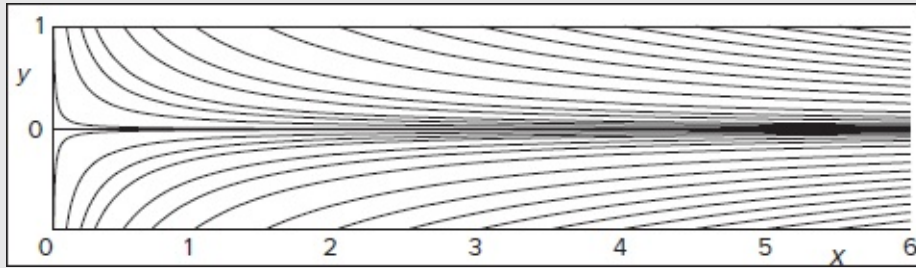


FIGURE P7.31

where all spatial coordinates are normalized by the channel half height, velocity components by the wall injection speed, and other variables by their reference values.

Page 455

(a) By substituting into the compressible potential flow equation given here a Rayleigh–Janzen expansion of the type

$$\phi(x, y) = \phi_0(x, y) + Ma_w^2 \phi_1(x, y) + O(Ma_w^4)$$

show that the leading- and first-order equations for the compressible potential function are:

$$\begin{aligned} \frac{\partial^2 \phi_0}{\partial x^2} + \frac{\partial^2 \phi_0}{\partial y^2} &= 0 \\ \frac{\partial^2 \phi_1}{\partial x^2} + \frac{\partial^2 \phi_1}{\partial y^2} &= \left(\frac{\partial \phi_0}{\partial x} \right)^2 \frac{\partial^2 \phi_0}{\partial x^2} + \left(\frac{\partial \phi_0}{\partial y} \right)^2 \frac{\partial^2 \phi_0}{\partial y^2} + 2 \frac{\partial \phi_0}{\partial x} \frac{\partial \phi_0}{\partial y} \frac{\partial^2 \phi_0}{\partial x \partial y} + \frac{\gamma - 1}{2} \left[\left(\frac{\partial \phi_0}{\partial x} \right)^2 + \left(\frac{\partial \phi_0}{\partial y} \right)^2 \right] \nabla^2 \phi_0 \end{aligned}$$

(b) Using additive separation of variables of the form $\phi_0 = f_0(x) + g_0(y)$, determine the general solution to the leading-order potential function equation. Show that

$$f_0(x) = \frac{1}{2} C_0 x^2 + C_1 x + C_2 \quad \text{and} \quad g_0(y) = -\frac{1}{2} C_0 y^2 + C_3 y + C_4$$

(c) For a porous tube, the potential flow boundary conditions may be written as

$$\frac{\partial \phi_0(0, y)}{\partial x} = 0; \quad \frac{\partial \phi_0(x, 0)}{\partial y} = 0; \quad \frac{\partial \phi_0(x, 1)}{\partial y} = -1; \quad \phi_0(0, 0) = 0$$

Show that $\phi_0 = \frac{1}{2}(x^2 - y^2)$ is the particular solution for the leading-order potential function equation.

(d) Determine the general solution to the first-order potential function equation. Assume the same separation of variables form and set all of the boundary conditions in Part (c) equal to zero. Show that the particular solution is

$$\phi_1(x, y) = \frac{1}{12}(x^4 - y^4) - \frac{1}{6}(x^2 - y^2)$$

(e) Recalling that $\mathbf{v} = u\hat{\mathbf{e}}_x + v\hat{\mathbf{e}}_y = \nabla\phi$, show that the compressible velocity profile may be expressed as

$$\begin{cases} u = x + \frac{1}{3}x(x^2 - 1)Ma_w^2 + O(Ma_w^4) \\ v = -y + \frac{1}{3}y(1 - y^2)Ma_w^2 + O(Ma_w^4) \end{cases}$$

(f) The differential form of the pressure may be written as

$$dp = -\frac{\gamma\rho Ma_w^2}{2} d\left[\left(\frac{\partial\phi}{\partial x}\right)^2 + \left(\frac{\partial\phi}{\partial y}\right)^2\right]$$

Using a Rayleigh–Janzen expansion for the pressure and density of the form

$$\begin{cases} p(x, y) = 1 + Ma_w^2 p_1(x, y) + Ma_w^4 p_2(x, y) + O(Ma_w^6) \\ \rho(x, y) = 1 + Ma_w^2 \rho_1(x, y) + Ma_w^4 \rho_2(x, y) + O(Ma_w^6) \end{cases}$$

expand and show that the successive equations for the pressure lead to

$$dp_1 = -\frac{1}{2}\gamma d\left[\left(\frac{\partial\phi_0}{\partial x}\right)^2 + \left(\frac{\partial\phi_0}{\partial y}\right)^2\right] \quad \text{and} \quad \begin{cases} \frac{\partial p_2}{\partial x} = -\gamma \left[\rho_1 \left(\frac{\partial\phi_0}{\partial x} \frac{\partial^2\phi_0}{\partial x^2} \right) + \frac{\partial\phi_0}{\partial x} \frac{\partial^2\phi_1}{\partial x^2} + \frac{\partial\phi_1}{\partial x} \frac{\partial^2\phi_0}{\partial x^2} \right] \\ \frac{\partial p_2}{\partial y} = -\gamma \left[\rho_1 \left(\frac{\partial\phi_0}{\partial y} \frac{\partial^2\phi_0}{\partial y^2} \right) + \frac{\partial\phi_0}{\partial y} \frac{\partial^2\phi_1}{\partial y^2} + \frac{\partial\phi_1}{\partial y} \frac{\partial^2\phi_0}{\partial y^2} \right] \end{cases}$$

(g) Integrate the pressure corrective equations. When integrating a partial differential equation, remember to include a function of the other variable in lieu of a pure constant. Show that

$$p_1 = -\frac{1}{2}\gamma(x^2 + y^2) \quad \text{and} \quad p_2 = -\gamma\left[\frac{1}{3}(x^2 + y^2) + \frac{1}{4}x^2y^2 - \frac{5}{24}(x^4 + y^4)\right]$$

7-32. In seeking a compressible solution for the irrotational Hart–McClure profile in a porous tube with a circular cross section (see [Fig. P7-32](#)), Maicke et al. (2012) use a steady, axisymmetric, compressible potential flow equation that incorporates the

effects of the porous wall Mach number Ma_w , specifically,

$$\nabla^2 \phi = Ma_w^2 \left\{ \left(\frac{\partial \phi}{\partial r} \right)^2 \frac{\partial^2 \phi}{\partial r^2} + \left(\frac{\partial \phi}{\partial z} \right)^2 \frac{\partial^2 \phi}{\partial z^2} + 2 \frac{\partial \phi}{\partial r} \frac{\partial \phi}{\partial z} \frac{\partial^2 \phi}{\partial r \partial z} + \frac{\gamma - 1}{2} \left[\left(\frac{\partial \phi}{\partial r} \right)^2 + \left(\frac{\partial \phi}{\partial z} \right)^2 \right] \nabla^2 \phi \right\}$$

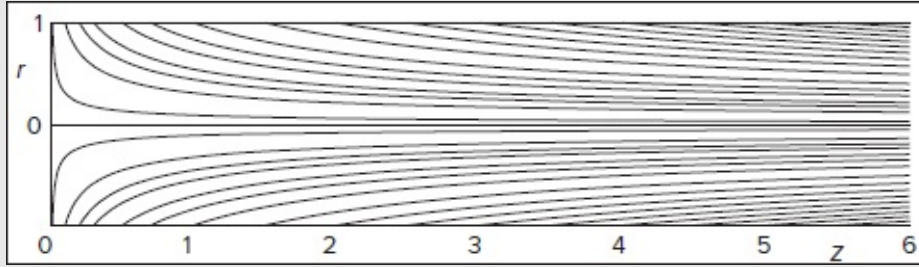


FIGURE P7.32

where all spatial coordinates are normalized by the tube radius, velocity components by the wall injection speed, and other variables by their reference values.

Page 456

(a) By substituting into the compressible potential flow equation given here a Rayleigh–Janzen expansion of the type

$$\phi(r, z) = \phi_0(r, z) + Ma_w^2 \phi_1(r, z) + O(Ma_w^4)$$

show that the leading- and first-order equations for the compressible potential function are

$$\begin{aligned} \frac{\partial^2 \phi_0}{\partial r^2} + \frac{1}{r} \frac{\partial \phi_0}{\partial r} + \frac{\partial^2 \phi_0}{\partial z^2} &= 0 \\ \frac{\partial^2 \phi_1}{\partial r^2} + \frac{1}{r} \frac{\partial \phi_1}{\partial r} + \frac{\partial^2 \phi_1}{\partial z^2} &= \left(\frac{\partial \phi_0}{\partial r} \right)^2 \frac{\partial^2 \phi_0}{\partial r^2} + \left(\frac{\partial \phi_0}{\partial z} \right)^2 \frac{\partial^2 \phi_0}{\partial z^2} + 2 \frac{\partial \phi_0}{\partial r} \frac{\partial \phi_0}{\partial z} \frac{\partial^2 \phi_0}{\partial r \partial z} + \frac{\gamma - 1}{2} \left[\left(\frac{\partial \phi_0}{\partial r} \right)^2 + \left(\frac{\partial \phi_0}{\partial z} \right)^2 \right] \nabla^2 \phi_0 \end{aligned}$$

(b) Using additive separation of variables of the form $\phi_0 = f_0(r) + g_0(z)$, determine the general solution to the leading-order potential function equation. Show that

$$f_0(r) = \frac{1}{4} C_0 r^2 + C_1 \ln r + C_2 \quad \text{and} \quad g_0(z) = -\frac{1}{2} C_0 z^2 + C_3 z + C_4$$

(c) For a porous tube, the potential flow boundary conditions may be written as

$$\frac{\partial \phi_0(r, 0)}{\partial z} = 0; \quad \frac{\partial \phi_0(0, z)}{\partial r} = 0; \quad \frac{\partial \phi_0(1, z)}{\partial r} = -1; \quad \phi_0(0, 0) = 0$$

Show that $\phi_0 = -\frac{1}{2} r^2 + z^2$ is the particular solution for the leading-order potential function equation.

(d) Determine the general solution to the first-order potential function equation. Assume the same separation of variables form and set all of the boundary conditions in Part (c) equal to zero. Show that the particular solution is:

$$\phi_1(r, z) = \frac{1}{8}r^2 - \frac{1}{16}r^4 + \frac{2}{3}z^4 - \frac{1}{4}z^2$$

(e) Recalling that $\mathbf{v} = v_r \hat{\mathbf{e}}_r + v_z \hat{\mathbf{e}}_z = \nabla \phi$, show that the compressible Hart–McClure velocity profile may be expressed as

$$\begin{cases} v_r = -r + \frac{1}{4}(1 - r^2)rMa_w^2 + O(Ma_w^4) \\ v_z = 2z + \frac{1}{6}(16z^2 - 3)zMa_w^2 + O(Ma_w^4) \end{cases}$$

(f) The differential form of the pressure may be written as

$$dp = -\frac{\gamma \rho Ma_w^2}{2} d \left[\left(\frac{\partial \phi}{\partial r} \right)^2 + \left(\frac{\partial \phi}{\partial z} \right)^2 \right]$$

Using a Rayleigh–Janzen expansion for the pressure and density of the form

$$\begin{cases} p(r, z) = 1 + Ma_w^2 p_1(r, z) + Ma_w^4 p_2(r, z) + O(Ma_w^6) \\ \rho(r, z) = 1 + Ma_w^2 \rho_1(r, z) + Ma_w^4 \rho_2(r, z) + O(Ma_w^6) \end{cases}$$

expand and show that the successive equations for the pressure lead to

$$dp_1 = -\frac{1}{2}\gamma d \left[\left(\frac{\partial \phi_0}{\partial r} \right)^2 + \left(\frac{\partial \phi_0}{\partial z} \right)^2 \right] \quad \text{and} \quad \begin{cases} \frac{\partial p_2}{\partial r} = -\gamma \left[\rho_1 \left(\frac{\partial \phi_0}{\partial r} \frac{\partial^2 \phi_0}{\partial r^2} \right) + \frac{\partial \phi_0}{\partial r} \frac{\partial^2 \phi_1}{\partial r^2} + \frac{\partial \phi_1}{\partial r} \frac{\partial^2 \phi_0}{\partial r^2} \right] \\ \frac{\partial p_2}{\partial z} = -\gamma \left[\rho_1 \left(\frac{\partial \phi_0}{\partial z} \frac{\partial^2 \phi_0}{\partial z^2} \right) + \frac{\partial \phi_0}{\partial z} \frac{\partial^2 \phi_1}{\partial z^2} + \frac{\partial \phi_1}{\partial z} \frac{\partial^2 \phi_0}{\partial z^2} \right] \end{cases}$$

(g) Integrate the pressure corrective equations. When integrating a partial differential equation, remember to include a function of the other variable in lieu of a pure constant. Show that

$$p_1 = -\frac{1}{2}\gamma(r^2 + 4z^2) \quad \text{and} \quad p_2 = -\gamma \left[\frac{1}{8}(r^4 - 2r^2) - r^2 z^2 + \frac{10}{3}z^4 - z^2 \right]$$

APPENDIX

A

VECTOR IDENTITIES

$$(\mathbf{V} \cdot \nabla) \mathbf{V} = \frac{1}{2} \nabla (\mathbf{V} \cdot \mathbf{V}) + (\nabla \times \mathbf{V}) \times \mathbf{V} \text{ (Lamb's identity)} \quad (\text{A-1})$$

$$\nabla^2 \mathbf{V} = \nabla (\nabla \cdot \mathbf{V}) - \nabla \times (\nabla \times \mathbf{V}) \text{ (vector Laplacian equivalence to the divergence and curl)} \quad (\text{A-2})$$

$$\nabla \times (\nabla^2 \mathbf{V}) = \nabla^2 (\nabla \times \mathbf{V}) \text{ (curl of the Laplacian equivalence to the Laplacian of the curl)} \quad (\text{A-3})$$

$$\nabla \cdot (\mathbf{U} \times \mathbf{V}) = \mathbf{V} \cdot (\nabla \times \mathbf{U}) - \mathbf{U} \cdot (\nabla \times \mathbf{V}) \text{ (divergence of a cross product)} \quad (\text{A-4})$$

$$\mathbf{U} \cdot (\mathbf{V} \times \mathbf{W}) = (\mathbf{U} \times \mathbf{V}) \cdot \mathbf{W} = \mathbf{V} \cdot (\mathbf{W} \times \mathbf{U}) = (\mathbf{V} \times \mathbf{W}) \cdot \mathbf{U} \text{ (mixed vector scalar products)} \quad (\text{A-5})$$

$$\mathbf{U} \times (\mathbf{V} \times \mathbf{W}) = (\mathbf{U} \cdot \mathbf{W}) \mathbf{V} - (\mathbf{U} \cdot \mathbf{V}) \mathbf{W} \text{ (vector triple product)} \quad (\text{A-6})$$

$$(\mathbf{U} \times \mathbf{V}) \cdot (\mathbf{U} \times \mathbf{V}) = (\mathbf{U} \cdot \mathbf{U})(\mathbf{V} \cdot \mathbf{V}) - (\mathbf{U} \cdot \mathbf{V})(\mathbf{U} \cdot \mathbf{V}) \text{ (Lagrange's identity)} \quad (\text{A-7})$$

$$(\mathbf{U} \times \mathbf{V}) \cdot (\mathbf{W} \times \mathbf{X}) = (\mathbf{U} \cdot \mathbf{W})(\mathbf{V} \cdot \mathbf{X}) - (\mathbf{U} \cdot \mathbf{X})(\mathbf{V} \cdot \mathbf{W}) \text{ (mixed outer-inner products)} \quad (\text{A-8})$$

$$(\mathbf{U} \times \mathbf{V}) \times (\mathbf{W} \times \mathbf{X}) = (\mathbf{U} \times \mathbf{V} \cdot \mathbf{X}) \mathbf{W} - (\mathbf{U} \times \mathbf{V} \cdot \mathbf{W}) \mathbf{X} \text{ (mixed outer cross products)} \quad (\text{A-9})$$

$$\mathbf{U} \times (\nabla \times \mathbf{V}) = (\nabla \mathbf{V}) \cdot \mathbf{U} - (\mathbf{U} \cdot \nabla) \mathbf{V} \text{ (vector curl cross product)} \quad (\text{A-10})$$

$$\mathbf{U} \times (\mathbf{V} \times \mathbf{W}) + \mathbf{W} \times (\mathbf{U} \times \mathbf{V}) + \mathbf{V} \times (\mathbf{W} \times \mathbf{U}) = 0 \text{ (Jacobi's identity)} \quad (\text{A-11})$$

$$\nabla^2 (\mathbf{U} \cdot \mathbf{V}) = \mathbf{U} \cdot \nabla^2 \mathbf{V} - \mathbf{V} \cdot \nabla^2 \mathbf{U} + 2 \nabla \cdot [(\mathbf{V} \cdot \nabla) \mathbf{U} + \mathbf{V} \times (\nabla \times \mathbf{U})] \text{ (Green's vector identity)} \quad (\text{A-12})$$

$$(\nabla \times \mathbf{V}) \times \mathbf{U} = (\mathbf{U} \cdot \nabla) \mathbf{V} - (\nabla \mathbf{V}) \cdot \mathbf{U} \text{ (vector curl cross product)} \quad (\text{A-13})$$

$$\nabla (\mathbf{U} \cdot \mathbf{V}) = (\mathbf{U} \cdot \nabla) \mathbf{V} + (\mathbf{V} \cdot \nabla) \mathbf{U} + \mathbf{U} \times (\nabla \times \mathbf{V}) + \mathbf{V} \times (\nabla \times \mathbf{U}) \text{ (dot product gradient)} \quad (\text{A-14})$$

$$\nabla \cdot (\mathbf{U} \mathbf{V}) = (\nabla \cdot \mathbf{U}) \mathbf{V} + \mathbf{U} \cdot (\nabla \mathbf{V}) \text{ (divergence of a vector tensor)} \quad (\text{A-15})$$

$$\nabla \times (\mathbf{U} \times \mathbf{V}) = (\mathbf{V} \cdot \nabla) \mathbf{U} + (\nabla \cdot \mathbf{V}) \mathbf{U} - (\nabla \cdot \mathbf{U}) \mathbf{V} - (\mathbf{U} \cdot \nabla) \mathbf{V} \text{ (curl of a cross product)} \quad (\text{A-16})$$

$$\nabla \cdot (\nabla \times \mathbf{V}) = 0 \text{ (solenoidal proof of vector curls, e.g., vorticity)} \quad (\text{A-17})$$

$$\nabla \times (\nabla \phi) = 0 \text{ (irrotational proof of scalar gradients, e.g., potential velocity)} \quad (\text{A-18})$$

$$\nabla \cdot (\nabla \phi) = \nabla^2 \phi \text{ (divergence of a scalar gradient equivalence to the Laplacian of a scalar)} \quad (\text{A-19})$$

$$\nabla \cdot (\phi \mathbf{V}) = \phi \nabla \cdot \mathbf{V} + \mathbf{V} \cdot \nabla \phi \text{ (mixed vector scalar divergence, e.g., mass flux)} \quad (\text{A-20})$$

$$\nabla \times (\phi \mathbf{V}) = \phi \nabla \times \mathbf{V} + (\nabla \phi) \times \mathbf{V} \text{ (mixed vector scalar curl, e.g., momentum)} \quad (\text{A-21})$$

$$\nabla(\phi\psi) = \phi \nabla \psi + \psi \nabla \phi \text{ (scalar product gradient)} \quad (\text{A-22})$$

$$\nabla \cdot \left(\frac{\mathbf{V}}{\phi} \right) = \frac{\phi \nabla \cdot \mathbf{V} - \mathbf{V} \cdot \nabla \phi}{\phi^2} \text{ (quotient rule for vector-scalar divergence)} \quad (\text{A-23})$$

$$\nabla \times \left(\frac{\mathbf{V}}{\phi} \right) = \frac{\phi \nabla \times \mathbf{V} + \mathbf{V} \times \nabla \phi}{\phi^2} \text{ (quotient rule for vector-scalar curl)} \quad (\text{A-24})$$

APPENDIX

B1

3D KINEMATIC EXPRESSIONS IN CARTESIAN COORDINATES

Velocity: $\mathbf{V} = u\mathbf{i} + v\mathbf{j} + w\mathbf{k}$ **Gravity:** $\mathbf{g} = g_x\mathbf{i} + g_y\mathbf{j} + g_z\mathbf{k}$ **Differential Operator:** $\nabla = \frac{\partial}{\partial x}\mathbf{i} + \frac{\partial}{\partial y}\mathbf{j} + \frac{\partial}{\partial z}\mathbf{k}$

Gradient: $\nabla p = \frac{\partial p}{\partial x}\mathbf{i} + \frac{\partial p}{\partial y}\mathbf{j} + \frac{\partial p}{\partial z}\mathbf{k}$ **Laplacian of a Vector:** $\nabla^2 \mathbf{V} = \left(\frac{\partial^2}{\partial x^2} + \frac{\partial^2}{\partial y^2} + \frac{\partial^2}{\partial z^2} \right) (u\mathbf{i} + v\mathbf{j} + w\mathbf{k})$

Divergence: $\nabla \cdot \mathbf{V} = \frac{\partial u}{\partial x} + \frac{\partial v}{\partial y} + \frac{\partial w}{\partial z}$ **Curl:** $\nabla \times \mathbf{V} = \left(\frac{\partial w}{\partial y} - \frac{\partial v}{\partial z} \right)\mathbf{i} + \left(\frac{\partial u}{\partial z} - \frac{\partial w}{\partial x} \right)\mathbf{j} + \left(\frac{\partial v}{\partial x} - \frac{\partial u}{\partial y} \right)\mathbf{k}$

Continuity: $\nabla \cdot \mathbf{V} = \frac{\partial u}{\partial x} + \frac{\partial v}{\partial y} + \frac{\partial w}{\partial z} = 0$

Incompressible Navier-Stokes Equation: $\rho \frac{D\mathbf{V}}{Dt} = \rho \frac{\partial \mathbf{V}}{\partial t} + (\mathbf{V} \cdot \nabla)\mathbf{V} = -\nabla p + \mathbf{g} + \mu \nabla^2 \mathbf{V}; \nu = \mu / \rho$

Navier-Stokes x-momentum: $\rho \frac{Du}{Dt} = -\frac{\partial p}{\partial x} + \mu \nabla^2 u + \rho g_x$

Navier-Stokes y-momentum: $\rho \frac{Dv}{Dt} = -\frac{\partial p}{\partial y} + \mu \nabla^2 v + \rho g_y$

Navier-Stokes z-momentum: $\rho \frac{Dw}{Dt} = -\frac{\partial p}{\partial z} + \mu \nabla^2 w + \rho g_z$

Substantial Derivative: $\frac{DA}{Dt} = \frac{\partial A}{\partial t} + u \frac{\partial A}{\partial x} + v \frac{\partial A}{\partial y} + w \frac{\partial A}{\partial z}$ **Laplacian:** $\nabla^2 = \frac{\partial^2}{\partial x^2} + \frac{\partial^2}{\partial y^2} + \frac{\partial^2}{\partial z^2}$

Stream Function Definition: $u = \frac{\partial \psi}{\partial y}$ $v = -\frac{\partial \psi}{\partial x}$ (in 2D only)

Stream Function Equation: $\nabla^2 \psi = \frac{\partial^2 \psi}{\partial x^2} + \frac{\partial^2 \psi}{\partial y^2}$ from $\nabla \times \mathbf{V} = \mathbf{0}$

Potential Function Definition: $u = \frac{\partial \phi}{\partial x}$ $v = \frac{\partial \phi}{\partial y}$ $w = \frac{\partial \phi}{\partial z}$ from $\mathbf{V} = \nabla \phi$

Potential Function Equation: $\nabla^2 \phi = \frac{\partial^2 \phi}{\partial x^2} + \frac{\partial^2 \phi}{\partial y^2} + \frac{\partial^2 \phi}{\partial z^2}$ from $\nabla \cdot \mathbf{V} = 0$

Viscous Shear Stresses: $\tau_{xx} = 2\mu \frac{\partial u}{\partial x}$ $\tau_{yy} = 2\mu \frac{\partial v}{\partial y}$ $\tau_{zz} = 2\mu \frac{\partial w}{\partial z}$

Off-Diagonal: $\tau_{xy} = \mu \left(\frac{\partial v}{\partial x} + \frac{\partial u}{\partial y} \right)$ $\tau_{xz} = \mu \left(\frac{\partial w}{\partial x} + \frac{\partial u}{\partial z} \right)$ $\tau_{yz} = \mu \left(\frac{\partial w}{\partial y} + \frac{\partial v}{\partial z} \right)$

Extensional Strain Rates: $e_{xx} = \frac{\partial u}{\partial x}$ $e_{yy} = \frac{\partial v}{\partial y}$ $e_{zz} = \frac{\partial w}{\partial z}$

Off-Diagonal: $e_{xy} = \frac{1}{2} \left(\frac{\partial v}{\partial x} + \frac{\partial u}{\partial y} \right)$ $e_{xz} = \frac{1}{2} \left(\frac{\partial w}{\partial x} + \frac{\partial u}{\partial z} \right)$ $e_{yz} = \frac{1}{2} \left(\frac{\partial w}{\partial y} + \frac{\partial v}{\partial z} \right)$

APPENDIX

B2

REDUCED KINEMATIC EXPRESSIONS IN STEADY 2D CARTESIAN COORDINATES

Steady Flow: $\frac{\partial A}{\partial t} = 0, \forall A$ 2D Motion in xy Plane: $w = 0$ 2D Motion in xy Plane: $\frac{\partial A}{\partial z} = 0, \forall A$

Continuity: $\nabla \cdot \mathbf{V} = \frac{\partial u}{\partial x} + \frac{\partial v}{\partial y} = 0$

Navier-Stokes x-momentum: $\rho \left(u \frac{\partial u}{\partial x} + v \frac{\partial u}{\partial y} \right) = -\frac{\partial p}{\partial x} + \mu \left(\frac{\partial^2 u}{\partial x^2} + \frac{\partial^2 u}{\partial y^2} \right) + \rho g_x$

Navier-Stokes y-momentum: $\rho \left(u \frac{\partial v}{\partial x} + v \frac{\partial v}{\partial y} \right) = -\frac{\partial p}{\partial y} + \mu \left(\frac{\partial^2 v}{\partial x^2} + \frac{\partial^2 v}{\partial y^2} \right) + \rho g_y$

Navier-Stokes z-momentum: $0 = 0$

Velocity: $\mathbf{V} = u\mathbf{i} + v\mathbf{j}$ Gravity: $\mathbf{g} = g_x\mathbf{i} + g_y\mathbf{j}$ Differential Operator: $\nabla = \frac{\partial}{\partial x}\mathbf{i} + \frac{\partial}{\partial y}\mathbf{j}$

Gradient of a Scalar: $\nabla p = \frac{\partial p}{\partial x}\mathbf{i} + \frac{\partial p}{\partial y}\mathbf{j}$ Laplacian of a Vector: $\nabla^2 \mathbf{V} = \left(\frac{\partial^2}{\partial x^2} + \frac{\partial^2}{\partial y^2} \right) (u\mathbf{i} + v\mathbf{j})$

Divergence of a Vector: $\nabla \cdot \mathbf{V} = \frac{\partial u}{\partial x} + \frac{\partial v}{\partial y}$

Curl of a Vector: $\nabla \times \mathbf{V} = \left(\frac{\partial v}{\partial x} - \frac{\partial u}{\partial y} \right) \mathbf{k}$

Stream Function Definition: $u = \frac{\partial \psi}{\partial y}$ $v = -\frac{\partial \psi}{\partial x}$

Stream Function Equation: $\nabla^2 \psi = \frac{\partial^2 \psi}{\partial x^2} + \frac{\partial^2 \psi}{\partial y^2}$ from $\nabla \times \mathbf{V} = 0$

Potential Function Definition: $u = \frac{\partial \phi}{\partial x}$ $v = \frac{\partial \phi}{\partial y}$ from $\mathbf{V} = \nabla \phi$

Potential Function Equation: $\nabla^2 \phi = \frac{\partial^2 \phi}{\partial x^2} + \frac{\partial^2 \phi}{\partial y^2}$ from $\nabla \cdot \mathbf{V} = 0$

Viscous Shear Stresses: $\tau_{xx} = 2\mu \frac{\partial u}{\partial x}$ $\tau_{yy} = 2\mu \frac{\partial v}{\partial y}$ $\tau_{xz} = 0$

Off-Diagonal: $\tau_{xy} = \mu \left(\frac{\partial v}{\partial x} + \frac{\partial u}{\partial y} \right)$ $\tau_{xz} = 0$ $\tau_{yz} = 0$

Extensional Strain Rates: $\epsilon_{xx} = \frac{\partial u}{\partial x}$ $\epsilon_{yy} = \frac{\partial v}{\partial y}$ $\epsilon_{zz} = 0$

Off-Diagonal: $\epsilon_{xy} = \frac{1}{2} \left(\frac{\partial v}{\partial x} + \frac{\partial u}{\partial y} \right)$ $\epsilon_{xz} = 0$ $\epsilon_{yz} = 0$

APPENDIX

B3

3D KINEMATIC EXPRESSIONS IN CYLINDRICAL COORDINATES

Velocity: $\mathbf{V} = v_r \mathbf{e}_r + v_\theta \mathbf{e}_\theta + v_z \mathbf{e}_z$

Gravity: $\mathbf{g} = g_r \mathbf{e}_r + g_\theta \mathbf{e}_\theta + g_z \mathbf{e}_z$

Differential Operator: $\nabla = \mathbf{e}_r \frac{\partial}{\partial r} + \mathbf{e}_\theta \frac{1}{r} \frac{\partial}{\partial \theta} + \mathbf{e}_z \frac{\partial}{\partial z}$

Gradient: $\nabla p = \frac{\partial p}{\partial r} \mathbf{e}_r + \frac{1}{r} \frac{\partial p}{\partial \theta} \mathbf{e}_\theta + \frac{\partial p}{\partial z} \mathbf{e}_z$

Laplacian of a Vector: $\nabla^2 \mathbf{V} = \left(\frac{\partial^2}{\partial r^2} + \frac{1}{r} \frac{\partial}{\partial r} + \frac{1}{r^2} \frac{\partial^2}{\partial \theta^2} + \frac{\partial^2}{\partial z^2} \right) (v_r \mathbf{e}_r + v_\theta \mathbf{e}_\theta + v_z \mathbf{e}_z)$

Divergence: $\nabla \cdot \mathbf{V} = \frac{1}{r} \frac{\partial}{\partial r} (r v_r) + \frac{1}{r} \frac{\partial v_\theta}{\partial \theta} + \frac{\partial v_z}{\partial z} \equiv \frac{\partial v_r}{\partial r} + \frac{v_r}{r} + \frac{1}{r} \frac{\partial v_\theta}{\partial \theta} + \frac{\partial v_z}{\partial z}$

Curl: $\nabla \times \mathbf{V} = \left(\frac{1}{r} \frac{\partial v_z}{\partial \theta} - \frac{\partial v_\theta}{\partial z} \right) \mathbf{e}_r + \left(\frac{\partial v_r}{\partial z} - \frac{\partial v_z}{\partial r} \right) \mathbf{e}_\theta + \frac{1}{r} \left[\frac{\partial}{\partial r} (r v_\theta) - \frac{\partial v_r}{\partial \theta} \right] \mathbf{e}_z$

Continuity: $\nabla \cdot \mathbf{V} = \frac{1}{r} \frac{\partial}{\partial r} (r v_r) + \frac{1}{r} \frac{\partial v_\theta}{\partial \theta} + \frac{\partial v_z}{\partial z} \equiv \frac{\partial v_r}{\partial r} + \frac{v_r}{r} + \frac{1}{r} \frac{\partial v_\theta}{\partial \theta} + \frac{\partial v_z}{\partial z} = 0$

Incompressible NS: $\frac{\partial \mathbf{V}}{\partial t} + (\mathbf{V} \cdot \nabla) \mathbf{V} \equiv \frac{\partial \mathbf{V}}{\partial t} + \nabla \left(\frac{\mathbf{V}^2}{2} \right) - \mathbf{V} \times (\nabla \times \mathbf{V}) = -\frac{\nabla p}{\rho} + \mathbf{g} + \nu \nabla^2 \mathbf{V}$

Using Vector Identity: $(\mathbf{V} \cdot \nabla) \mathbf{V} = \frac{1}{2} \nabla (\mathbf{V} \cdot \mathbf{V}) - \mathbf{V} \times (\nabla \times \mathbf{V})$ and $\nu = \mu / \rho$

NS r -momentum: $\rho \left(\frac{Dv_r}{Dt} - \frac{v_\theta^2}{r} \right) = -\frac{\partial p}{\partial r} + \mu \left(\nabla^2 v_r - \frac{v_r}{r^2} - \frac{2}{r^2} \frac{\partial v_\theta}{\partial \theta} \right) + \rho g_r$

NS θ -momentum: $\rho \left(\frac{Dv_\theta}{Dt} + \frac{v_r v_\theta}{r} \right) = -\frac{1}{r} \frac{\partial p}{\partial \theta} + \mu \left(\nabla^2 v_\theta - \frac{v_\theta}{r^2} + \frac{2}{r^2} \frac{\partial v_r}{\partial \theta} \right) + \rho g_\theta$

NS z -momentum: $\rho \frac{Dv_z}{Dt} = -\frac{\partial p}{\partial z} + \mu \nabla^2 v_z + \rho g_z$

Substantial Derivative: $\frac{DA}{Dt} = \frac{\partial A}{\partial t} + v_r \frac{\partial A}{\partial r} + \frac{v_\theta}{r} \frac{\partial A}{\partial \theta} + v_z \frac{\partial A}{\partial z}$

Laplacian: $\nabla^2 = \frac{1}{r} \frac{\partial}{\partial r} \left(r \frac{\partial}{\partial r} \right) + \frac{1}{r^2} \frac{\partial^2}{\partial \theta^2} + \frac{\partial^2}{\partial z^2} \equiv \frac{\partial^2}{\partial r^2} + \frac{1}{r} \frac{\partial}{\partial r} + \frac{1}{r^2} \frac{\partial^2}{\partial \theta^2} + \frac{\partial^2}{\partial z^2}$

Stream Function Definition: $v_r = \frac{1}{r} \frac{\partial \psi}{\partial \theta} \quad v_\theta = -\frac{\partial \psi}{\partial r}$ (in 2D only)

Stream Function Equation: $\nabla^2 \psi = \frac{1}{r} \frac{\partial}{\partial r} \left(r \frac{\partial \psi}{\partial r} \right) + \frac{1}{r^2} \frac{\partial^2 \psi}{\partial \theta^2} = 0$ from $\nabla \times \mathbf{V} = 0$

Potential Function Definition: $v_r = \frac{\partial \phi}{\partial r} \quad v_\theta = \frac{1}{r} \frac{\partial \phi}{\partial \theta} \quad v_z = \frac{\partial \phi}{\partial z}$ from $\mathbf{V} = \nabla \phi$

Potential Function Equation: $\nabla^2 \phi = \frac{1}{r} \frac{\partial}{\partial r} \left(r \frac{\partial \phi}{\partial r} \right) + \frac{1}{r^2} \frac{\partial^2 \phi}{\partial \theta^2} + \frac{\partial^2 \phi}{\partial z^2} = 0$ from $\nabla \cdot \mathbf{V} = 0$

Viscous Shear Stresses: $\tau_{rr} = 2\mu \frac{\partial v_r}{\partial r}$ $\tau_{\theta\theta} = 2\mu \left(\frac{1}{r} \frac{\partial v_\theta}{\partial \theta} + \frac{v_r}{r} \right)$ $\tau_{zz} = 2\mu \frac{\partial v_z}{\partial z}$

Off-Diagonal: $\tau_{r\theta} = \mu \left[\frac{1}{r} \frac{\partial v_r}{\partial \theta} + r \frac{\partial}{\partial r} \left(\frac{v_\theta}{r} \right) \right]$ $\tau_{\theta z} = \mu \left(\frac{1}{r} \frac{\partial v_z}{\partial \theta} + \frac{\partial v_\theta}{\partial z} \right)$ $\tau_{rz} = \mu \left(\frac{\partial v_z}{\partial r} + \frac{\partial v_r}{\partial z} \right)$

Extensional Strain Rates: $\varepsilon_{rr} = \frac{\partial v_r}{\partial r}$ $\varepsilon_{\theta\theta} = \frac{1}{r} \frac{\partial v_\theta}{\partial \theta} + \frac{v_r}{r}$ $\varepsilon_{zz} = \frac{\partial v_z}{\partial z}$

Off-Diagonal: $\varepsilon_{r\theta} = \frac{1}{2} \left[\frac{1}{r} \frac{\partial v_r}{\partial \theta} + r \frac{\partial}{\partial r} \left(\frac{v_\theta}{r} \right) \right]$ $\varepsilon_{\theta z} = \frac{1}{2} \left(\frac{1}{r} \frac{\partial v_z}{\partial \theta} + \frac{\partial v_\theta}{\partial z} \right)$ $\varepsilon_{rz} = \frac{1}{2} \left(\frac{\partial v_z}{\partial r} + \frac{\partial v_r}{\partial z} \right)$

APPENDIX

B4

REDUCED KINEMATIC EXPRESSIONS IN STEADY 2D CYLINDRICAL COORDINATES

Steady Flow: $\frac{\partial A}{\partial t} = 0, \quad \forall A$ **2D Motion in r - θ Plane:** $v_z = 0$ **2D Motion in r - θ Plane:** $\frac{\partial A}{\partial z} = 0, \quad \forall A$

Continuity: $\nabla \cdot \mathbf{V} = \frac{1}{r} \frac{\partial}{\partial r}(r v_r) + \frac{1}{r} \frac{\partial v_\theta}{\partial \theta} \equiv \frac{\partial v_r}{\partial r} + \frac{v_r}{r} + \frac{1}{r} \frac{\partial v_\theta}{\partial \theta} = 0$

NS r -momentum: $\rho \left(v_r \frac{\partial v_r}{\partial r} + \frac{v_\theta}{r} \frac{\partial v_r}{\partial \theta} - \frac{v_\theta^2}{r} \right) = -\frac{\partial p}{\partial r} + \mu \left(\frac{\partial^2 v_r}{\partial r^2} + \frac{1}{r} \frac{\partial v_r}{\partial r} + \frac{1}{r^2} \frac{\partial^2 v_r}{\partial \theta^2} - \frac{v_r}{r^2} - \frac{2}{r^2} \frac{\partial v_\theta}{\partial \theta} \right) + \rho g_r$

NS θ -mom.: $\rho \left(v_r \frac{\partial v_\theta}{\partial r} + \frac{v_\theta}{r} \frac{\partial v_\theta}{\partial \theta} + \frac{v_r v_\theta}{r} \right) = -\frac{1}{r} \frac{\partial p}{\partial \theta} + \mu \left(\frac{\partial^2 v_\theta}{\partial r^2} + \frac{1}{r} \frac{\partial v_\theta}{\partial r} + \frac{1}{r^2} \frac{\partial^2 v_\theta}{\partial \theta^2} - \frac{v_\theta}{r^2} + \frac{2}{r^2} \frac{\partial v_r}{\partial \theta} \right) + \rho g_\theta$

NS z -momentum: $0 = 0$

Velocity: $\mathbf{V} = v_r \mathbf{e}_r + v_\theta \mathbf{e}_\theta$ **Gravity:** $\mathbf{g} = g_r \mathbf{e}_r + g_\theta \mathbf{e}_\theta$ **Differential Operator:** $\nabla = \mathbf{e}_r \frac{\partial}{\partial r} + \mathbf{e}_\theta \frac{1}{r} \frac{\partial}{\partial \theta}$

Gradient of a Scalar: $\nabla p = \frac{\partial p}{\partial r} \mathbf{e}_r + \frac{1}{r} \frac{\partial p}{\partial \theta} \mathbf{e}_\theta$ **Laplacian of a Vector:** $\nabla^2 \mathbf{V} = \left(\frac{\partial^2}{\partial r^2} + \frac{1}{r} \frac{\partial}{\partial r} + \frac{1}{r^2} \frac{\partial^2}{\partial \theta^2} \right) (v_r \mathbf{e}_r + v_\theta \mathbf{e}_\theta)$

Divergence of a Vector: $\nabla \cdot \mathbf{V} = \frac{1}{r} \frac{\partial}{\partial r}(r v_r) + \frac{1}{r} \frac{\partial v_\theta}{\partial \theta} \equiv \frac{\partial v_r}{\partial r} + \frac{v_r}{r} + \frac{1}{r} \frac{\partial v_\theta}{\partial \theta}$

Curl of a Vector: $\nabla \times \mathbf{V} = -\frac{\partial v_\theta}{\partial z} \mathbf{e}_z + \frac{1}{r} \left[\frac{\partial}{\partial r}(r v_\theta) - \frac{\partial v_r}{\partial \theta} \right] \mathbf{e}_z$ **Stream Function Definition:** $v_r = \frac{1}{r} \frac{\partial \psi}{\partial \theta}$ $v_\theta = -\frac{\partial \psi}{\partial r}$

Stream Function Equation: $\nabla^2 \psi = \frac{1}{r} \frac{\partial}{\partial r} \left(r \frac{\partial \psi}{\partial r} \right) + \frac{1}{r^2} \frac{\partial^2 \psi}{\partial \theta^2} = 0$ from $\nabla \times \mathbf{V} = 0$

Potential Function Definition: $v_r = \frac{\partial \phi}{\partial r}$ $v_\theta = \frac{1}{r} \frac{\partial \phi}{\partial \theta}$ from $\mathbf{V} = \nabla \phi$

Potential Function Equation: $\nabla^2 \phi = \frac{1}{r} \frac{\partial}{\partial r} \left(r \frac{\partial \phi}{\partial r} \right) + \frac{1}{r^2} \frac{\partial^2 \phi}{\partial \theta^2} = 0$ from $\nabla \cdot \mathbf{V} = 0$

Viscous Shear Stresses: $\tau_{rr} = 2\mu \frac{\partial v_r}{\partial r}$ $\tau_{\theta\theta} = 2\mu \left(\frac{1}{r} \frac{\partial v_\theta}{\partial \theta} + \frac{v_r}{r} \right)$ $\tau_{zz} = 0$

Off-Diagonal: $\tau_{r\theta} = \mu \left[\frac{1}{r} \frac{\partial v_r}{\partial \theta} + r \frac{\partial}{\partial r} \left(\frac{v_\theta}{r} \right) \right]$ $\tau_{\theta z} = \mu \frac{\partial v_\theta}{\partial z}$ $\tau_{rz} = 0$

Extensional Strain Rates: $\varepsilon_{rr} = \frac{\partial v_r}{\partial r}$ $\varepsilon_{\theta\theta} = \frac{1}{r} \frac{\partial v_\theta}{\partial \theta} + \frac{v_r}{r}$ $\varepsilon_{zz} = 0$

Off-Diagonal: $\varepsilon_{r\theta} = \frac{1}{2} \left[\frac{1}{r} \frac{\partial v_r}{\partial \theta} + r \frac{\partial}{\partial r} \left(\frac{v_\theta}{r} \right) \right]$ $\varepsilon_{\theta z} = \frac{1}{2} \frac{\partial v_\theta}{\partial z}$ $\varepsilon_{rz} = 0$

APPENDIX C

TRANSPORT PROPERTIES OF VARIOUS NEWTONIAN FLUIDS

THE VISCOSITY AND THERMAL CONDUCTIVITY OF WATER

Kestin and Wakeham (1988) recommend the following formula for the viscosity of water at atmospheric pressure:

$$\log_{10}\left(\frac{\mu}{1.002}\right) \approx \frac{20 - T}{T + 96} [1.2378 - 1.303 \times 10^{-3}(20 - T) + 3.06 \times 10^{-6}(20 - T)^2 + 2.55 \times 10^{-8}(20 - T)^3]$$

with μ in $[\text{mPa} \cdot \text{s}]$ and T in $[\text{°C}]$. Numerical values are tabulated below. They further state that $k(T)$ is not known very accurately for any liquid. Estimated values of $k(T)$ for water are given below.

Temperature $T[\text{°C}]$	Viscosity $\mu[\text{mPa} \cdot \text{s}]$	Thermal conductivity $k[\text{W}/(\text{m} \cdot \text{K})]$
0	1.792	0.564
5	1.519	0.574
10	1.307	0.584
15	1.138	0.593
20	1.002	0.602
25	0.890	0.610
30	0.797	0.617
35	0.719	0.624
40	0.653	0.631
45	0.596	0.637
50	0.547	0.643
55	0.504	0.648
60	0.467	0.653
65	0.434	0.657
70	0.405	0.662
75	0.379	0.665
80	0.355	0.669
85	0.334	0.673
90	0.315	0.676
95	0.298	0.678
100	0.282	0.681
Uncertainty	$\pm 0.4\%$	$\pm 2.5\%$

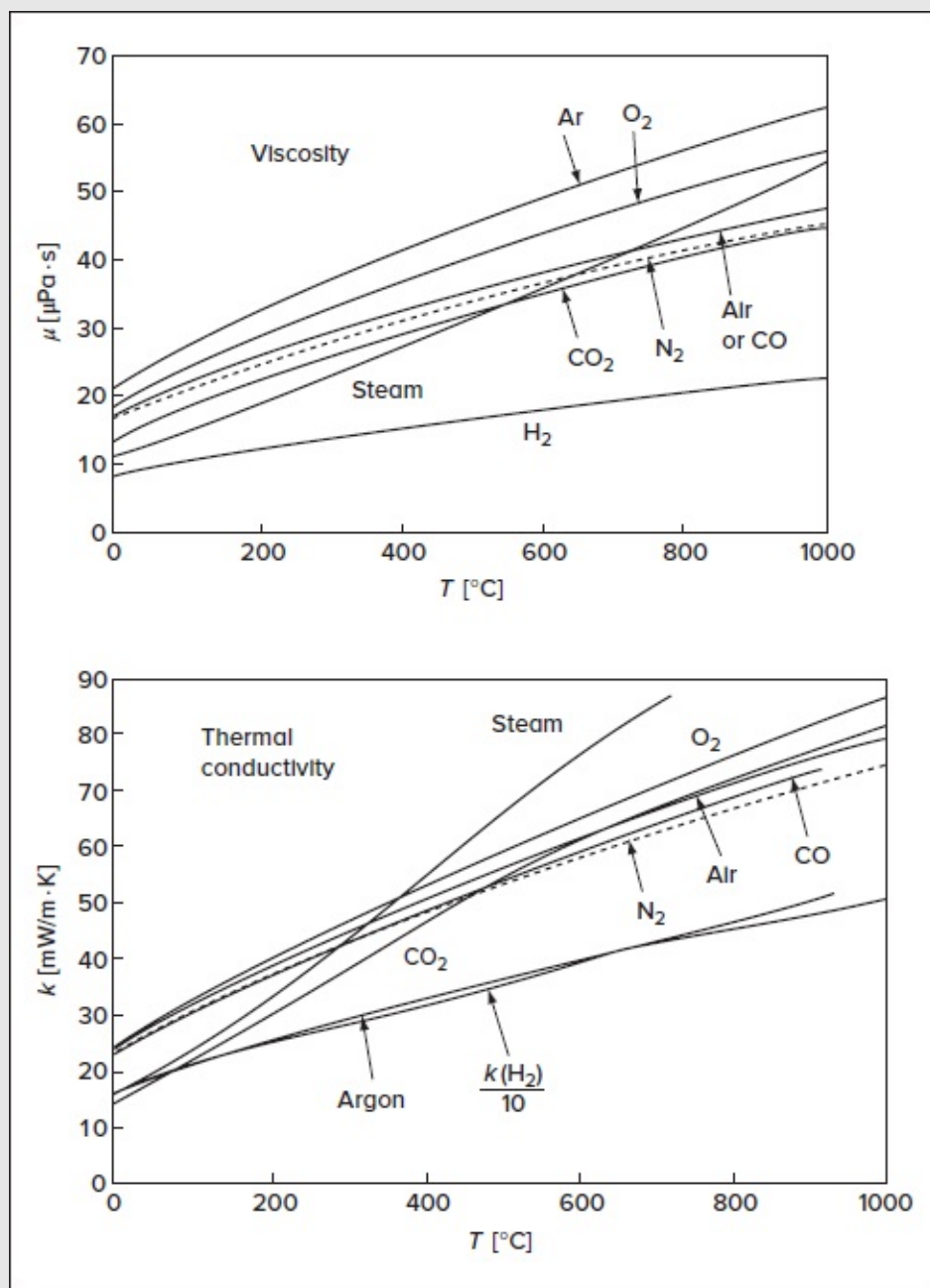


FIGURE C-1

Viscosity and thermal conductivity of common gases at low pressures.

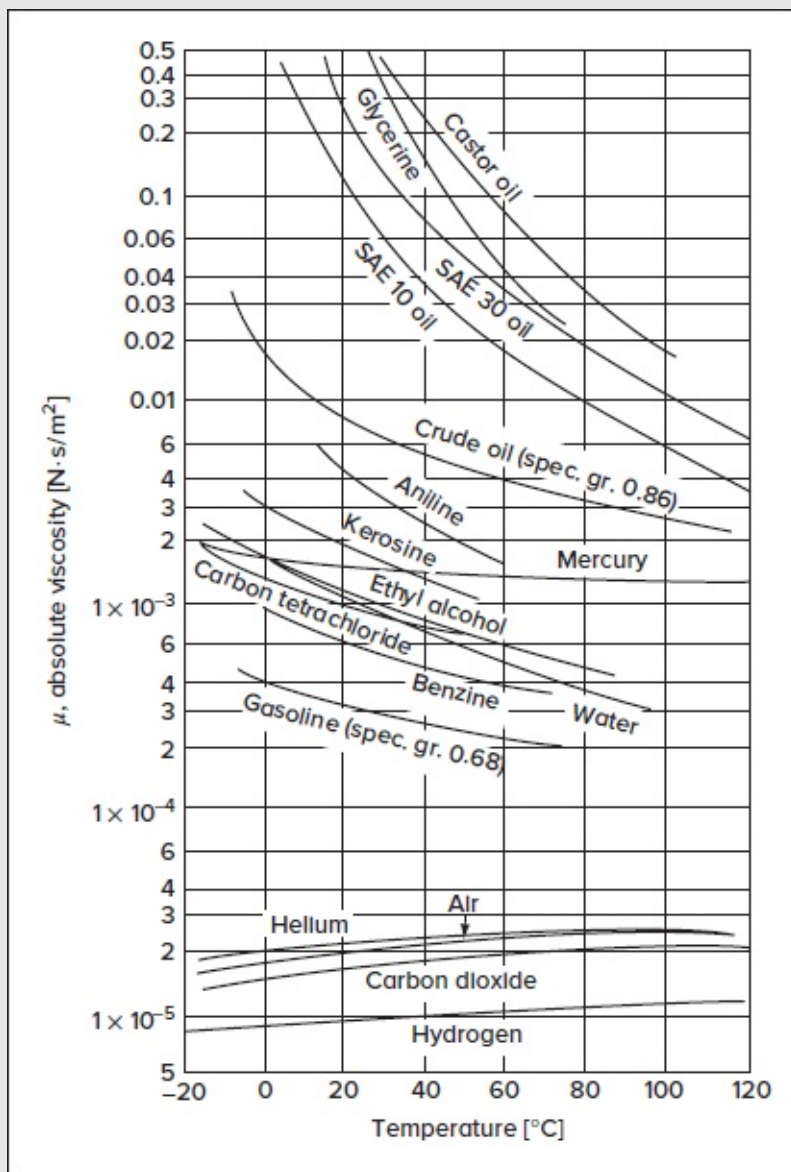


FIGURE C-2

Absolute viscosity of common fluids at atmospheric pressure.

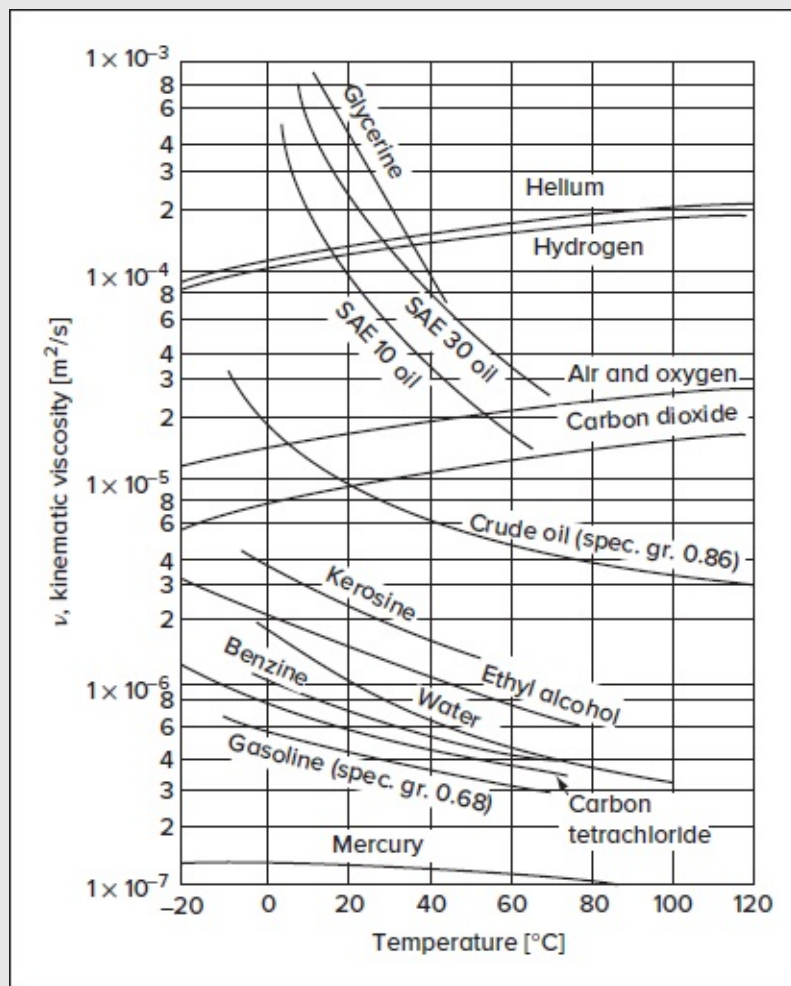


FIGURE C-3

Kinematic viscosity of common fluids at atmospheric pressure.

TABLE C-1

Properties of saturated water at atmospheric pressure

Temperature $T[^{\circ}\text{C}]$	Density $\rho[\text{kg}/\text{m}^3]$	Viscosity $\mu[\text{mPa}\cdot\text{s}]$	Surface tension [†] $\mathcal{T}[\text{N}/\text{M}]$	Vapor pressure $p_v[\text{kPa}]$	Bulk modulus $K[\text{MPa}]$
0	1000	1.792	0.0757	0.61	2062
20	998	1.002	0.0727	2.34	2230
40	992	0.653	0.0696	7.38	2304
60	983	0.467	0.0662	19.92	2301
80	972	0.355	0.0627	47.35	2235
100	958	0.282	0.0589	101.3	2120
150	915	0.182	0.0488	461	1692
200	863	0.136	0.0377	1580	1190
250	797	0.107	0.0261	3970	716
300	707	0.086	0.0144	8560	342
350	487	0.068	0.0038	16,500	82
374 [†]	315	0.019	0.0	22,100	0

[†]Critical point.

^{*}In contact with air.

Page 467

TABLE C-2

Properties of air at atmospheric pressure

$T[^{\circ}\text{C}]$	$\rho[\text{kg}/\text{m}^3]$	$\mu[\mu\text{Pa}\cdot\text{s}]$	$k[\text{mW}/(\text{m}\cdot\text{K})]$	$c_p[\text{J}/\text{kg}\cdot\text{K}]$	Pr
0	1.294	17.2	24.2	1003	0.71
50	1.093	19.5	27.6	1006	0.71
100	0.947	21.7	31.0	1010	0.71
150	0.835	23.8	34.4	1016	0.70
200	0.747	25.7	37.6	1024	0.70
250	0.675	27.6	40.8	1034	0.70
300	0.616	29.3	43.9	1045	0.70
400	0.525	32.5	49.7	1069	0.70
500	0.457	35.5	55.3	1093	0.70
600	0.405	38.3	60.9	1114	0.70
700	0.363	40.9	65.9	1135	0.70
800	0.329	43.4	70.3	1153	0.71
900	0.301	45.7	74.7	1170	0.72
1000	0.277	47.9	78.6	1184	0.72

Source: White (1988).

TABLE C-3

Properties of common liquids at 1 atm and 20°C (68°F)

Liquid	ρ [kg/m ³]	μ [kg/(m·s)]	\mathcal{S} [N/m]*	p_o [N/m ²]	Bulk modulus, K[N/m ²]
Ammonia	608	2.20E-4	2.13E-2	9.10E+5	—
Benzene	881	6.51E-4	2.88E-2	1.01E+4	1.4E+9
Carbon tetrachloride	1590	9.67E-4	2.70E-2	1.20E+4	9.65E+8
Ethanol	789	1.20E-3	2.28E-2	5.7E+3	9.0E+8
Ethylene glycol	1117	2.14E-2	4.84E-2	1.2E+1	—
Freon 12	1327	2.62E-4	—	—	—
Gasoline	680	2.92E-4	2.16E-2	5.51E+4	9.58E+8
Glycerin	1260	1.49	6.33E-2	1.4E-2	4.34E+9
Kerosene	804	1.92E-3	2.8E-2	3.11E+3	1.6E+9
Mercury	13,550	1.56E-3	4.84E-1	1.1E-3	2.55E+10
Methanol	791	5.98E-4	2.25E-2	1.34E+4	8.3E+8
SAE 10W oil	870	1.04E-1 [‡]	3.6E-2	—	1.31E+9
SAE 10W30 oil	876	1.7E-1 [‡]	—	—	—
SAE 30W oil	891	2.9E-1 [‡]	3.5E-2	—	1.38E+9
SAE 50W oil	902	8.6E-1 [‡]	—	—	—
Water	998	1.00E-3	7.28E-2	2.34E+3	2.19E+9
Seawater (30%)	1025	1.07E-3	7.28E-2	2.34E+3	2.33E+9

*In contact with air.

[‡]Representative values. The SAE oil classifications allow a viscosity variation of up to ± 50 percent.

TABLE C-4

Properties of common gases at 1 atm and 20°C (68°F)

Gas	Molecular weight	R [m ² /(s ² ·K)]	ρg [N/m ³]	μ [(N·s)/m ²]	Specific-heat ratio
H ₂	2.016	4124	0.822	9.05E-6	1.41
He	4.003	2077	1.63	1.97E-5	1.66
H ₂ O	18.02	461	7.35	1.02E-5	1.33
Ar	39.944	208	16.3	2.24E-5	1.67
Dry air	28.97	287	11.8	1.80E-5	1.40
CO ₂	44.01	189	17.9	1.48E-5	1.30
CO	28.01	297	11.4	1.82E-5	1.40
N ₂	28.02	297	11.4	1.76E-5	1.40
O ₂	32.00	260	13.1	2.00E-5	1.40
NO	30.01	277	12.1	1.90E-5	1.40
N ₂ O	44.02	189	17.9	1.45E-5	1.31
Cl ₂	70.91	117	28.9	1.03E-5	1.34
CH ₄	16.04	518	6.54	1.34E-5	1.32

TABLE C-5

Critical-point constants for common fluids

Substance	Molecular weight	T_c [°R]	p_c [atm]	μ_c [$\mu\text{Pa} \cdot \text{s}$]	k_c [mW/(m·K)]
H ₂	2.016	60.0	12.8	3.47	90.0
He	4.003	9.47	2.26	2.54	20.8
Ar	39.944	272	48.0	26.4	29.8
Air	28.97 [†]	238 [†]	36.4 [†]	19.3 [†]	38.1 [†]
CO ₂	44.01	548	72.9	34.3	51.1
CO	28.01	239	34.5	19.0	36.2
N ₂	28.02	227	33.5	18.0	36.3
O ₂	32.00	278	49.7	25.0	44.1
NO	30.01	324	64	25.8	49.5
N ₂ O	44.02	557	71.7	33.2	54.9
Cl ₂	70.91	751	76.1	42.0	40.7
CH ₄	16.04	343	45.8	15.9	66.1

[†]Values for air are pseudocritical properties computed for the average composition of sea-level dry air.

TABLE C-6

Sutherland and power-law constants for gas viscosity

Gas	T_0 [°R]	μ_0 [slugs/(ft·h)]	S [°R]	n
Ammonia	491.6	0.000722	679	0.981
Chlorine	491.6	0.000970	585	1.00
Deuterium	545.7	0.000974		0.699
Ethylene	491.6	0.000722	407	
Helium	491.6	0.001406	143	0.666
Hydrogen chloride	491.6	0.001030	643	1.03
Hydrogen sulfide	491.6	0.000880	596	
Krypton	491.6	0.001744	338	
Methane	491.6	0.000902	356	0.873
Methyl chloride	491.6	0.000743	817	
Neon	491.6	0.002233	110	0.657
Nitric oxide	491.6	0.001346	230	0.78
Nitrous oxide	491.6	0.001015	493	0.89
Sulfur dioxide	491.6	0.000880	749	
Xenon	491.6	0.001579	454	

Source: Chapman and Cowling (1970).

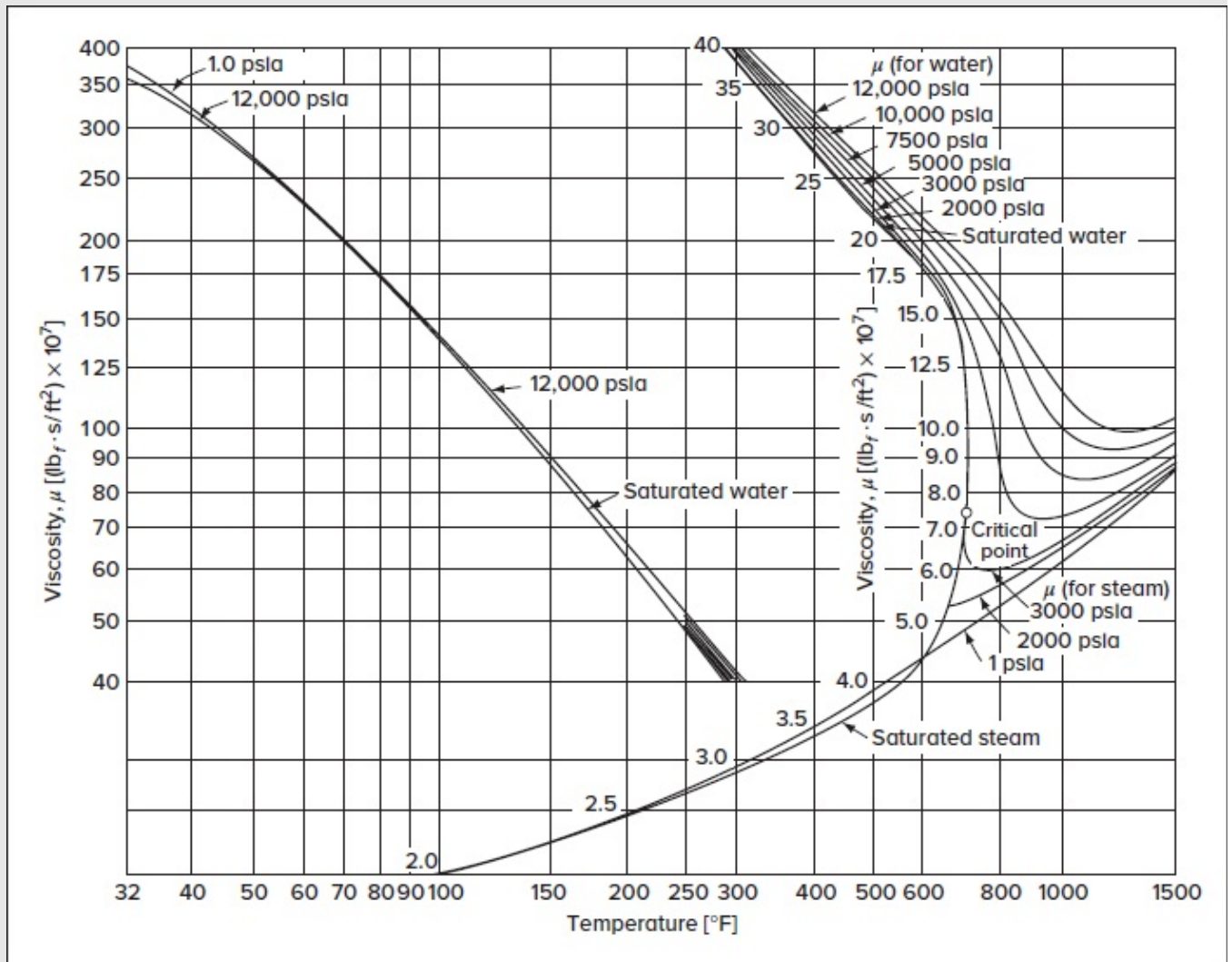


FIGURE C-4

Viscosity of steam and water. (*From the 1967 ASME Steam Tables.*)

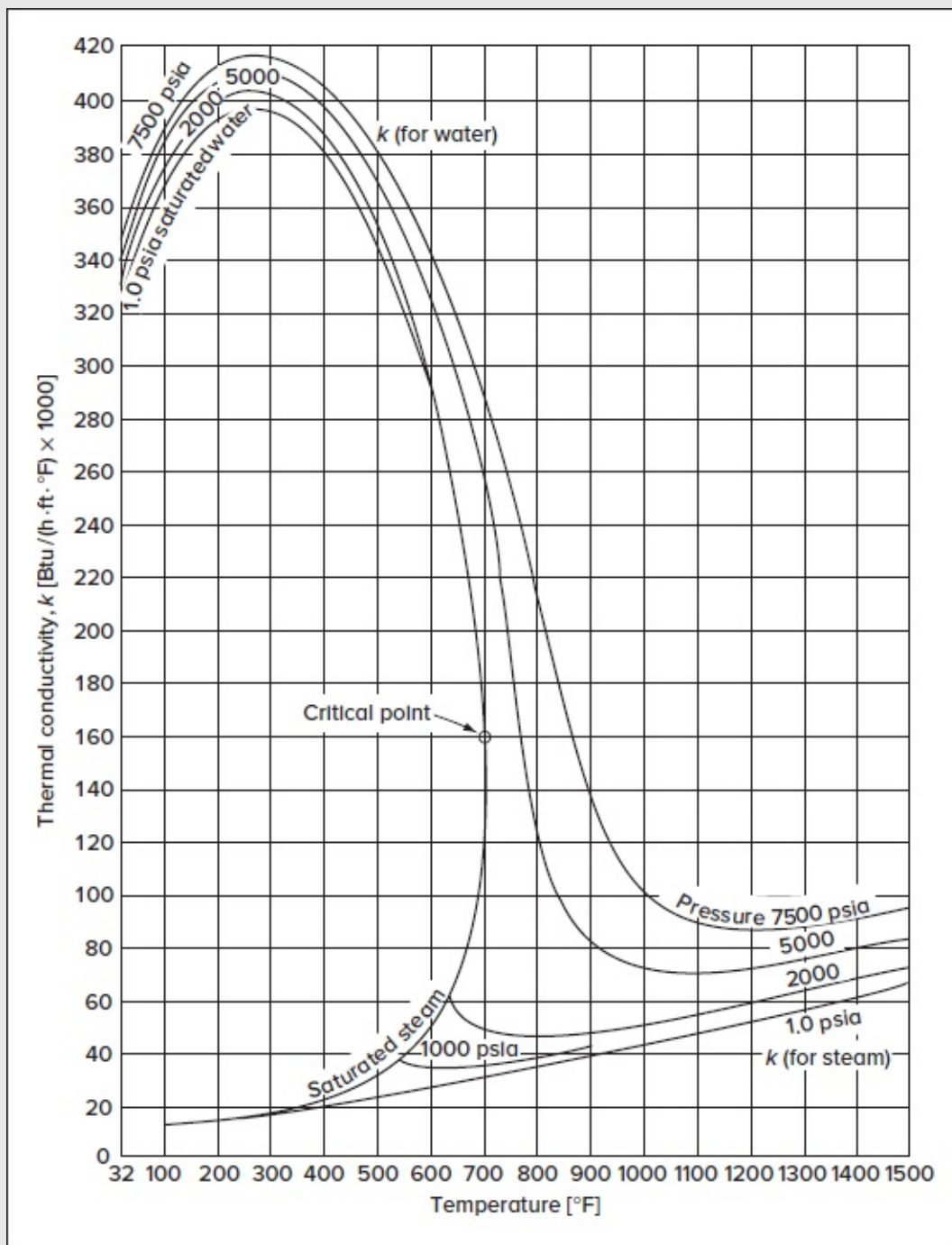


FIGURE C-5

Thermal conductivity of steam and water. (From the 1967 ASME Steam Tables.)

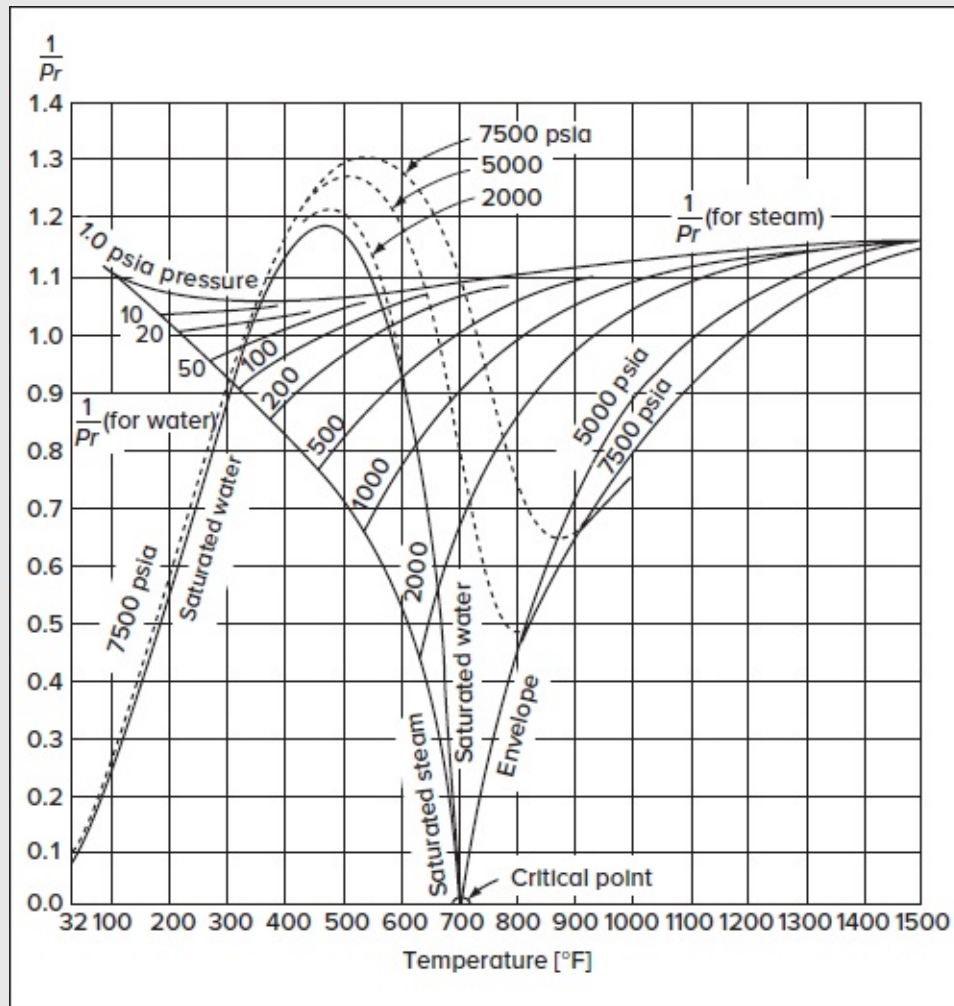


FIGURE C-6

Reciprocal Prandtl number $1/Pr$ for steam and water. (From the 1967 ASME Steam Tables.)

TABLE C-7

Molecular parameters for dilute-gas transport properties, [Eqs. \(1-33\)](#) and (1-41)

Gas	$\sigma[\text{\AA}]$	$T_c[\text{K}]$
H ₂	2.827	59.7
He	2.551	10.22
Ar	3.542	93.3
Air	3.711	78.6
CO ₂	3.941	195.2
CO	3.690	91.7
O ₂	3.467	106.7
N ₂	3.798	71.4
NO	3.492	116.7
N ₂ O	3.828	232.4
Cl ₂	4.217	316.0
CH ₄	3.758	148.6

Source: R.A. Svehla, *NASA Tech. Rep. R-132*, 1962.

APPENDIX D

EINSTEIN'S INDICIAL NOTATION

Range Convention:

The *range indices* are small subscripted Latin letters that are not repeated in a term. The range indices take on values of 1, 2, or 3, depending on the spatial dimension(s). For example, the subscript “ i ” in $A_i = (A_1, A_2, A_3)$; i denotes a range index.

Order of a Tensor:

The order of a tensor is determined by the number of range indices. For example:

A : represents a tensor of zeroth order, i.e., a scalar.

A_i : represents a first-order tensor, i.e., a vector.

A_{ij} : represents a second-order tensor, i.e., a matrix.

A_{ijk} : represents a third-order tensor, i.e., a Rubik's cube; an $i \times j \times k$ tensor is a k array of $i \times j$ matrices.

Summation Convention:

The *summation index* is a small subscripted Latin letter which is repeated twice, and twice only in a term, to imply summation over the range indices 1, 2, and 3.

For example, in specifying a vector transformation, one may use the standard range convention for spatial directions and write $A'_i = a_{i1}A_1 + a_{i2}A_2 + a_{i3}A_3$. When evaluated over the range indices, we get

$$\begin{cases} A'_1 = a_{11}A_1 + a_{12}A_2 + a_{13}A_3 \\ A'_2 = a_{21}A_1 + a_{22}A_2 + a_{23}A_3 \\ A'_3 = a_{31}A_1 + a_{32}A_2 + a_{33}A_3 \end{cases} \quad (\text{D-1})$$

Note that i is unrepeated whereas “1,” “2,” and “3” are repeated in the first, second, and third terms of each equation, respectively. The summation index can thus be used by writing, $A'_i = a_{ij}A_j$, to denote a summation on j .

Kronecker Delta:

By definition, the Kronecker Delta is equivalent to the identity matrix as it yields

$$\delta_{ij} \equiv \begin{cases} 1, & \text{if } i = j \\ 0, & \text{if } i \neq j \end{cases} \quad (\text{D-2})$$

In three-dimensional space, this practically means that

$$\delta = \{\delta_{ij}\} = \begin{bmatrix} \delta_{11} & \delta_{12} & \delta_{13} \\ \delta_{21} & \delta_{22} & \delta_{23} \\ \delta_{31} & \delta_{32} & \delta_{33} \end{bmatrix} = \begin{bmatrix} 1 & 0 & 0 \\ 0 & 1 & 0 \\ 0 & 0 & 1 \end{bmatrix} \quad (\text{D-3})$$

Page 473

Permutation Tensor:

$$\epsilon_{ijk} = \begin{cases} +1, & \text{cyclic permutation of } ijk \\ -1, & \text{non - cyclic permutation of } ijk \\ 0, & \text{repeated index} \end{cases} \quad (\text{D-4})$$

Gradient of a Scalar:

The gradient of a scalar ϕ may be prescribed using a subscripted comma of the form $\phi_{,i}$:

$$\nabla \phi = \left\{ \frac{\partial \phi}{\partial x_i} \right\} = \left(\frac{\partial \phi}{\partial x_1}, \frac{\partial \phi}{\partial x_2}, \frac{\partial \phi}{\partial x_3} \right) \equiv \{\phi_{,i}\} \quad (\text{D-5})$$

Divergence of a Vector:

The divergence of a vector A_i may be prescribed using a subscripted comma of the form $A_{i,i}$

$$\nabla \cdot \mathbf{A} = \frac{\partial A_1}{\partial x_1} + \frac{\partial A_2}{\partial x_2} + \frac{\partial A_3}{\partial x_3} = \frac{\partial A_i}{\partial x_i} \equiv A_{i,i} \quad (\text{D-6})$$

Curl of a Vector:

The curl of a vector A_i may be prescribed using $(\nabla \times \mathbf{A})_i = \epsilon_{ijk} \nabla_j A_k = \epsilon_{ijk} A_{k,j}$

Divergence of a Tensor:

$$\nabla_j \equiv \frac{\partial}{\partial x_j} \quad \text{and so} \quad (\nabla \cdot \boldsymbol{\tau})_i = \nabla_j \tau_{ji} = \frac{\partial \tau_{ji}}{\partial x_j} \equiv \tau_{ji,j} \quad (\text{D-7})$$

Multiplication of Cartesian Tensors:

The inner product of A_i and B_{ij} results in

$$(\mathbf{A} \cdot \mathbf{B})_i = A_j B_{ji} \text{ and } (\mathbf{B} \cdot \mathbf{A})_i = B_{ij} A_j. \quad (\text{D-8})$$

APPENDIX E1

ADVANCED ENERGY LOSS EVALUATION

Fundamental Energy Equation:

$$\frac{P_1}{\gamma} + \frac{V_1^2}{2g} + z_1 = \frac{P_2}{\gamma} + \frac{V_2^2}{2g} + z_2 + h_w + h_L \quad (\text{E1-1})$$

Energy equation applied to a steady incompressible flow between two points separated by a distance L . $h_w = \frac{\dot{W}}{\dot{m}g}$, where \dot{W} represents the rate at which work is removed from the fluid. It is positive and equal to the net input power to a turbine; it is negative and equal to the net output power from a pump.

Head-Loss Equation:

$$h_L = h_M + h_m = \left(f \frac{L}{D} + f \sum \frac{L_e}{D} + \sum K\right) \frac{V^2}{2g} = \left(f \frac{L}{D} + f \sum \frac{L_e}{D} + \sum K\right) \frac{8Q^2}{\pi^2 g D^4} \quad (\text{E1-2})$$

$$f = \begin{cases} \frac{64}{Re}; & Re \leq 2300; \text{ else} \\ 1.6364 / \ln^2 \left[\frac{6.9}{Re} + \frac{(\epsilon/D)^{1.11}}{3.7} \right] \end{cases} \quad (\text{E1-3})$$

Flow-Rate Problem:

When Q and V are unknown:

$$(1) \text{ Guess} \quad Q = \frac{\pi D^2}{4} V = -0.965 \sqrt{\frac{g D^5 h_L}{L}} \ln \left[\frac{\epsilon/D}{3.7} + \sqrt{\frac{3.17 \mu^2 L}{g \rho^2 D^3 h_L}} \right] \quad (\text{exact if } h_m = 0, \text{ no minor loss}) \quad (\text{E1-4})$$

$$(2) \text{ Evaluate} \quad Re = \frac{\rho V D}{\mu} = \frac{4 \rho Q}{\pi \mu D} = \frac{4 \dot{m}}{\pi \mu D} \quad (\text{E1-5})$$

(3) Find f from Eq. (E1-3).

(4) Find Q that satisfies Eq. (E1-2):
$$Q = \frac{\pi D^2}{4} V = \sqrt{\frac{\pi^2 g D^4 h_L}{8 \left(f \frac{L}{D} + f \sum \frac{L_e}{D} + \sum K \right)}} \quad (\text{E1-6})$$

Page 475

(5) Repeat steps (2)–(4) until satisfied.

Pipe-Sizing Problem:

When D is unknown:

(1) Guess
$$D = 0.66 \left[\epsilon^{1.25} \left(\frac{LQ^2}{gh_L} \right)^{4.75} + \frac{\mu}{\rho} Q^{9.4} \left(\frac{L}{gh_L} \right)^{5.2} \right]^{0.04} \quad (\text{exact if } h_m = 0) \quad (\text{E1-7})$$

(2) Evaluate
$$Re = \frac{\rho V D}{\mu} = \frac{4 \rho Q}{\pi \mu D} = \frac{4 \eta}{\pi \mu D} \quad \text{and } (\epsilon/D) \quad (\text{E1-8})$$

(3) Find f from Eq. (E1-3).

(4) Find an update for D that satisfies Eq. (E1-2):
$$D = \left[\frac{8 Q^2 \left(f \frac{L}{D} + f \sum \frac{L_e}{D} + \sum K \right)}{\pi^2 g h_L} \right]^{0.25} \quad (\text{E1-9})$$

(5) Repeat steps (2)–(4) until satisfied.

APPENDIX E2

TRADITIONAL/ITERATIVE ENERGY LOSS EVALUATION

Fundamental Energy Equation:

$$\frac{P_1}{\gamma} + \frac{V_1^2}{2g} + z_1 = \frac{P_2}{\gamma} + \frac{V_2^2}{2g} + z_2 + h_w + h_L \quad (\text{E2-1})$$

Energy equation applied for a steady incompressible flow between two points separated by a distance L . $h_w = \frac{\dot{W}}{\dot{m}g}$, where \dot{W} represents the rate at which work is removed from the fluid. It is positive and equal to the net input power to a turbine, and it is negative and equal to the net output power from a pump.

Head-Loss Equation:

$$h_L = h_M + h_m = \left(f \frac{L}{D} + f \sum \frac{L_e}{D} + \sum K \right) \frac{V^2}{2g} = \left(f \frac{L}{D} + f \sum \frac{L_e}{D} + \sum K \right) \frac{8Q^2}{\pi^2 g D^4} \quad (\text{E2-2})$$

$$f = \begin{cases} \frac{64}{Re}; & Re \leq 2300; \text{ else} \\ 1.6364 / \ln^2 \left[\frac{6.9}{Re} + \frac{(\epsilon/D)^{1.11}}{3.7} \right] \end{cases} \quad (\text{E2-3})$$

Flow-Rate Problem:

When Q and V are unknown:

(1) To start, set $Re = 10^8$ and find f from Eq. (E2-3) (fully rough zone).

$$(2) \text{ Find } Q \text{ that satisfies Eq. (E2-2): } Q = \frac{\pi D^2}{4} V = \sqrt{\frac{\pi^2 g D^4 h_L}{8 \left(f \frac{L}{D} + f \sum \frac{L_e}{D} + \sum K \right)}} \quad (\text{E2-4})$$

$$(3) \text{ Evaluate } Re = \frac{\rho V D}{\mu} = \frac{4 \rho Q}{\pi \mu D} = \frac{4 \dot{m}}{\pi \mu D} \quad (\text{E2-5})$$

(4) Find f from Eq. (E2-3).

(5) Repeat steps (2)–(4) until satisfied.

Page 477

Pipe-Sizing Problem:

When D is unknown:

(1) To start, guess $f = 0.03$ and a value for D .

(2) Find an update for D that satisfies Eq. (E2-2): $D = \left[\frac{8Q^2 \left(f \frac{L}{D} + f \sum \frac{L_e}{D} + \sum K \right)}{\pi^2 g h_L} \right]^{0.25}$ (E2-6)

(3) Evaluate $Re = \frac{\rho V D}{\mu} = \frac{4 \rho Q}{\pi \mu D} = \frac{4 \dot{m}}{\pi \mu D}$ and (ϵ/D) (E2-7)

(4) Find f from Eq. (E2-3).

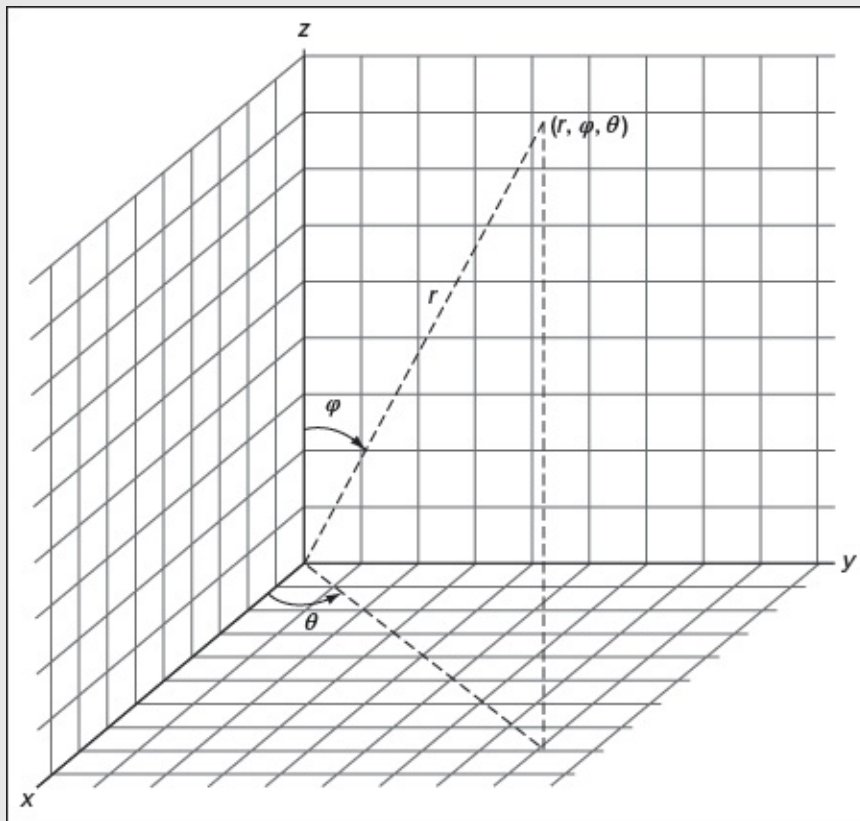
(5) Repeat steps (2)–(4) until satisfied.

APPENDIX

F

BRAGG–HAWTHORNE EQUATION FOR AXISYMMETRIC FLOW IN SPHERICAL COORDINATES

In modeling axisymmetric flow motion, Euler's steady momentum equation for incompressible fluids can be readily transformed into a single second-order partial differential equation of the stream function. In what follows, this relation, which is referred to as the Bragg–Hawthorne, Hicks, or Long–Squire equation, is derived using the spherical coordinates (r, φ, θ) specified in Fig. F-1.

**FIGURE F-1**

Spherical coordinate system with the same azimuthal angle θ as in cylindrical coordinates.

To begin, Euler's steady momentum equation may be written as $\nabla\left(\frac{1}{2}\mathbf{V}\cdot\mathbf{V}\right) - \mathbf{V}\times(\nabla\times\mathbf{V}) = -\nabla p/\rho$, where, for simplicity, gravity is ignored and Lamb's vector identity in App. A is substituted for the steady inertial force. Next, the pressure term is consolidated with the kinetic energy term such that $\nabla H - \mathbf{V}\times\boldsymbol{\omega} = 0$, where $H \equiv p/\rho + \frac{1}{2}V^2$. Page 479 Here $H(\psi)$ denotes the total head, which is conserved along a streamline. Then using spherical coordinates and a projection along the polar direction, we get $\nabla H \cdot d\boldsymbol{\varphi} = (\mathbf{V}\times\boldsymbol{\omega}) \cdot d\boldsymbol{\varphi}$, where $d\boldsymbol{\varphi} \equiv d\varphi\mathbf{e}_\varphi$. Realizing that $\mathbf{V}\times\boldsymbol{\omega} = (v_\theta\omega_r - v_r\omega_\theta)\mathbf{e}_\omega + \dots$ and the only polar gradient that survives the projection is $(r^{-1}\partial H/\partial\varphi)\mathbf{e}_\varphi$, the two members of the vorticity transport equation may be readily evaluated to give

$$\begin{cases} \nabla H \cdot d\boldsymbol{\varphi} = \frac{1}{r} \frac{\partial H}{\partial\varphi} d\varphi = \frac{1}{r} \frac{dH}{d\psi} \frac{\partial\psi}{\partial\varphi} d\varphi \\ (\mathbf{V}\times\boldsymbol{\omega}) \cdot d\boldsymbol{\varphi} = (v_\theta\omega_r - v_r\omega_\theta) d\varphi \end{cases} \quad \text{and so} \quad \frac{1}{r} \frac{dH}{d\psi} \frac{\partial\psi}{\partial\varphi} = v_\theta\omega_r - v_r\omega_\theta \quad (\text{F-1})$$

To make further headway, ω_r and ω_θ may be straightforwardly retrieved from the vorticity equation,

$$\boldsymbol{\omega} = \nabla\times\mathbf{V} = \frac{1}{r\sin\varphi} \left[\frac{\partial(\sin\varphi v_\theta)}{\partial\varphi} - \frac{\partial v_\varphi}{\partial\theta} \right] \mathbf{e}_r + \left[\frac{1}{r\sin\varphi} \frac{\partial v_r}{\partial\theta} - \frac{1}{r} \frac{\partial(rv_\theta)}{\partial r} \right] \mathbf{e}_\varphi + \frac{1}{r} \left[\frac{\partial(rv_\varphi)}{\partial r} - \frac{\partial v_r}{\partial\varphi} \right] \mathbf{e}_\theta \quad (\text{F-2})$$

Moreover, axisymmetry about the z-axis of rotation enables us to extract

$$\omega_r = \frac{1}{r\sin\varphi} \left[\frac{\partial(\sin\varphi v_\theta)}{\partial\varphi} \right] \quad \omega_\varphi = -\frac{1}{r} \frac{\partial(rv_\theta)}{\partial r} \quad \omega_\theta = \frac{1}{r} \left[\frac{\partial(rv_\varphi)}{\partial r} - \frac{\partial v_r}{\partial\varphi} \right] \quad (\text{F-3})$$

and so, backward substitution into the projected vorticity transport Eq. (F-1) yields

$$\frac{dH}{d\psi} \frac{\partial\psi}{\partial\varphi} = \frac{v_\theta}{\sin\varphi} \left[\frac{\partial(\sin\varphi v_\theta)}{\partial\varphi} \right] - v_r \left[\frac{\partial(rv_\varphi)}{\partial r} - \frac{\partial v_r}{\partial\varphi} \right] \quad (\text{F-4})$$

At this stage, v_r , v_φ , and v_θ must be related to ψ . In this vein, the incompressible stream function can be introduced to replace the radial and polar velocities, namely, by letting

$$v_r = \frac{1}{r^2\sin\varphi} \frac{\partial\psi}{\partial\varphi} \quad v_\varphi = -\frac{1}{r\sin\varphi} \frac{\partial\psi}{\partial r} \quad (\text{F-5})$$

As for the swirl velocity v_θ , it may be expressed in terms of the angular momentum by recognizing that the steady azimuthal momentum equation for this case becomes

$$v_r \frac{\partial v_\theta}{\partial r} + \frac{v_\varphi}{r} \frac{\partial v_\theta}{\partial\varphi} + \frac{v_\theta}{r\sin\varphi} \frac{\partial v_\theta}{\partial\theta} + \frac{v_r v_\theta}{r} + \frac{v_\varphi v_\theta \cot\varphi}{r} = -\frac{1}{r\sin\varphi} \frac{\partial p}{\partial\theta} \quad (\text{F-6})$$

Equation (F-6) may be multiplied by $r\sin\varphi$ and simplified, under axisymmetric conditions, to give

$$v_r \left(r \sin \varphi \frac{\partial v_\theta}{\partial r} + v_\theta \sin \varphi \right) + \frac{v_\varphi}{r} \left(r \sin \varphi \frac{\partial v_\theta}{\partial \varphi} + r v_\theta \cos \varphi \right) = 0 \quad (\text{F-7})$$

Further grouping of terms into derivatives of products yields

$$v_r \sin \varphi \left[r \frac{\partial v_\theta}{\partial r} + v_\theta \frac{\partial r}{\partial r} \right] + \frac{v_\varphi}{r} \left[r \left(\sin \varphi \frac{\partial v_\theta}{\partial \varphi} + v_\theta \frac{\partial \sin \varphi}{\partial \varphi} \right) \right] = 0 \quad \text{or} \quad v_r \frac{\partial}{\partial r} (r v_\theta \sin \varphi) + \frac{v_\varphi}{r} \frac{\partial (r v_\theta \sin \varphi)}{\partial \varphi} = 0 \quad (\text{F-8})$$

This expression proves that the material derivative of $r v_\theta \sin \varphi$ must vanish because

$$\frac{D}{Dt} = v_r \frac{\partial}{\partial r} + \frac{v_\varphi}{r} \frac{\partial}{\partial \varphi} \quad \text{and so} \quad \frac{D(r v_\theta \sin \varphi)}{Dt} = 0 \quad \text{or} \quad v_\theta = \frac{B(\psi)}{r \sin \varphi} \quad (\text{F-9})$$

Finally, backward substitution of Eqs. (F-9) and (F-5) into Eq. (F-4) leads to

$$\frac{dH}{d\psi} \frac{\partial \psi}{\partial \varphi} = \frac{B}{r \sin^2 \varphi} \left[\frac{\partial(r^{-1} B)}{\partial \varphi} \right] - \frac{1}{r^2 \sin \varphi} \frac{\partial \psi}{\partial \varphi} \left[\frac{\partial}{\partial r} \left(-\frac{1}{\sin \varphi} \frac{\partial \psi}{\partial r} \right) - \frac{\partial}{\partial \varphi} \left(\frac{1}{r^2 \sin \varphi} \frac{\partial \psi}{\partial \varphi} \right) \right] \quad (\text{F-10})$$

which may be readily rearranged and simplified into

$$\frac{dH}{d\psi} \frac{\partial \psi}{\partial \varphi} = \frac{B}{r^2 \sin^2 \varphi} \frac{dB}{d\psi} \frac{\partial \psi}{\partial \varphi} + \frac{1}{r^2 \sin \varphi} \frac{\partial \psi}{\partial \varphi} \left[\frac{1}{\sin \varphi} \frac{\partial^2 \psi}{\partial r^2} + \frac{1}{r^2} \frac{1}{\sin \varphi} \frac{\partial^2 \psi}{\partial \varphi^2} - \frac{\cos \varphi}{r^2 \sin^2 \varphi} \frac{\partial \psi}{\partial \varphi} \right] \quad (\text{F-11})$$

and so

$$\begin{cases} \frac{\partial^2 \psi}{\partial r^2} + \frac{1}{r^2} \frac{\partial^2 \psi}{\partial \varphi^2} - \frac{\cot \varphi}{r^2} \frac{\partial \psi}{\partial \varphi} = r^2 \sin^2 \varphi \frac{dH}{d\psi} - B \frac{dB}{d\psi} \\ \text{or} \\ \frac{\partial^2 \psi}{\partial r^2} + \frac{\sin \varphi}{r^2} \frac{\partial}{\partial \varphi} \left(\frac{1}{\sin \varphi} \frac{\partial \psi}{\partial \varphi} \right) = r^2 \sin^2 \varphi \frac{dH}{d\psi} - B \frac{dB}{d\psi} \end{cases} \quad (\text{F-12})$$

APPENDIX G

EQUATIONS OF MOTION OF INCOMPRESSIBLE NEWTONIAN FLUIDS IN CYLINDRICAL AND SPHERICAL POLAR COORDINATES

The general equations of motion for incompressible flow with constant transport properties are

Continuity: $\nabla \cdot \mathbf{V} = 0$ (G-1a)

Navier–Stokes: $\frac{D\mathbf{V}}{Dt} = \frac{1}{\rho} \nabla p + \mathbf{g} + \frac{1}{\rho} \nabla \cdot \boldsymbol{\tau}_{ij}$ (G-1b)

Energy: $\rho c_p \frac{DT}{Dt} = k \nabla^2 T + \Phi$ (G-1c)

where $\Phi = \mu \left(\frac{\partial u_i}{\partial x_j} + \frac{\partial u_j}{\partial x_i} \right) \frac{\partial u_i}{\partial x_j}$

CYLINDRICAL COORDINATES

These coordinates (r, θ, z) are related to the Cartesian (x, y, z) by

$$x = r \cos \theta \quad y = r \sin \theta \quad z = z \quad (\text{G-2})$$

The velocity components are (v_r, v_θ, v_z) . The equations of motion become Continuity:

$$\frac{1}{r} \frac{\partial}{\partial r}(r v_r) + \frac{1}{r} \frac{\partial}{\partial \theta}(v_\theta) + \frac{\partial}{\partial z}(v_z) = 0 \quad (\text{G-3})$$

Convective time derivative:

$$\mathbf{V} \cdot \nabla = v_r \frac{\partial}{\partial r} + \frac{1}{r} v_\theta \frac{\partial}{\partial \theta} + v_z \frac{\partial}{\partial z} \quad (\text{G-4})$$

Laplacian operator:

$$\nabla^2 = \frac{1}{r} \frac{\partial}{\partial r} \left(r \frac{\partial}{\partial r} \right) + \frac{1}{r^2} \frac{\partial^2}{\partial \theta^2} + \frac{\partial^2}{\partial z^2} \quad (\text{G-5})$$

r-momentum:

$$\frac{\partial v_r}{\partial t} + (\mathbf{V} \cdot \nabla) v_r - \frac{1}{r} v_\theta^2 = -\frac{1}{\rho} \frac{\partial p}{\partial r} + g_r + \nu \left(\nabla^2 v_r - \frac{v_r}{r^2} - \frac{2}{r^2} \frac{\partial v_\theta}{\partial \theta} \right) \quad (\text{G-6})$$

Page 481

θ -momentum:

$$\frac{\partial v_\theta}{\partial t} + (\mathbf{V} \cdot \nabla) v_\theta + \frac{v_r v_\theta}{r} = -\frac{1}{\rho r} \frac{\partial p}{\partial \theta} + g_\theta + \nu \left(\nabla^2 v_\theta + \frac{2}{r^2} \frac{\partial v_r}{\partial \theta} - \frac{v_\theta}{r^2} \right) \quad (\text{G-7})$$

z -momentum:

$$\frac{\partial v_z}{\partial t} + (\mathbf{V} \cdot \nabla) v_z = -\frac{1}{\rho} \frac{\partial p}{\partial z} + g_z + \nu \nabla^2 v_z \quad (\text{G-8})$$

Energy:

$$\rho c_p \left[\frac{\partial T}{\partial t} + (\mathbf{V} \cdot \nabla) T \right] = k \nabla^2 T + \mu \left[2(\epsilon_{rr}^2 + \epsilon_{\theta\theta}^2 + \epsilon_{zz}^2) + \epsilon_{\theta z}^2 + \epsilon_{rz}^2 + \epsilon_{r\theta}^2 \right] \quad (\text{G-9})$$

where

$$\begin{aligned} \epsilon_{rr} &= \frac{\partial v_r}{\partial r} & \epsilon_{\theta\theta} &= \frac{1}{r} \frac{\partial v_\theta}{\partial \theta} + \frac{v_r}{r} & \epsilon_{zz} &= \frac{\partial v_z}{\partial z} \\ \epsilon_{\theta z} &= \frac{1}{r} \frac{\partial v_z}{\partial \theta} + \frac{\partial v_\theta}{\partial z} & \epsilon_{rz} &= \frac{\partial v_r}{\partial z} + \frac{\partial v_z}{\partial r} & \epsilon_{r\theta} &= \frac{1}{r} \frac{\partial v_r}{\partial \theta} + \frac{\partial v_\theta}{\partial r} - \frac{v_\theta}{r} \end{aligned}$$

Vorticity components:

$$\omega_r = \frac{1}{r} \frac{\partial v_z}{\partial \theta} - \frac{\partial v_\theta}{\partial z} \quad \omega_\theta = \frac{\partial v_r}{\partial z} - \frac{\partial v_z}{\partial r} \quad \omega_z = \frac{1}{r} \frac{\partial}{\partial r} (r v_\theta) - \frac{1}{r} \frac{\partial v_r}{\partial \theta}$$

SPHERICAL POLAR COORDINATES

These coordinates (r, φ, θ) are related to (x, y, z) by the transformations

$$x = r \sin \varphi \cos \theta \quad y = r \sin \varphi \sin \theta \quad z = r \cos \varphi \quad (\text{G-10})$$

The equations of motion then become, for velocity components $(v_r, v_\varphi, v_\theta)$:

Continuity:

$$\frac{1}{r^2} \frac{\partial}{\partial r} (r^2 v_r) + \frac{1}{r \sin \varphi} \frac{\partial}{\partial \varphi} (v_\varphi \sin \varphi) + \frac{1}{r \sin \varphi} \frac{\partial}{\partial \theta} (v_\theta) = 0 \quad (\text{G-11})$$

Time derivative following the particle:

$$\frac{D}{Dt} = \frac{\partial}{\partial t} + v_r \frac{\partial}{\partial r} + \frac{v_\varphi}{r} \frac{\partial}{\partial \varphi} + \frac{v_\theta}{r \sin \varphi} \frac{\partial}{\partial \theta} \quad (\text{G-12})$$

Laplacian operator:

$$\nabla^2 = \frac{1}{r^2} \frac{\partial}{\partial r} \left(r^2 \frac{\partial}{\partial r} \right) + \frac{1}{r^2 \sin \varphi} \frac{\partial}{\partial \varphi} \left(\sin \varphi \frac{\partial}{\partial \varphi} \right) + \frac{1}{r^2 \sin^2 \varphi} \frac{\partial^2}{\partial \theta^2} \quad (\text{G-13})$$

r -momentum:

$$\frac{D v_r}{Dt} - \frac{1}{r} (v_\varphi^2 + v_\theta^2) = -\frac{1}{\rho} \frac{\partial p}{\partial r} + g_r + \nu \left(\nabla^2 v_r - \frac{2 v_r}{r^2} - \frac{2}{r^2} \frac{\partial v_\varphi}{\partial \varphi} - \frac{2 v_\varphi \cot \varphi}{r^2} - \frac{2}{r^2 \sin \varphi} \frac{\partial v_\theta}{\partial \theta} \right) \quad (\text{G-14})$$

θ -momentum:

$$\frac{D v_\varphi}{Dt} + \frac{1}{r} (v_r v_\varphi - v_\theta^2 \cot \varphi) = -\frac{1}{\rho r} \frac{\partial p}{\partial \varphi} + g_\varphi + \nu \left(\nabla^2 v_\varphi + \frac{2}{r^2} \frac{\partial v_r}{\partial \varphi} - \frac{v_\varphi}{r^2 \sin^2 \varphi} - \frac{2 \cos \varphi}{r^2 \sin^2 \varphi} \frac{\partial v_\theta}{\partial \theta} \right) \quad (\text{G-15})$$

ϕ -momentum:

$$\frac{D v_\theta}{Dt} + \frac{1}{r} (v_r v_\theta + v_\varphi v_\theta \cot \varphi) = -\frac{1}{\rho r \sin \varphi} \frac{\partial p}{\partial \theta} + g_\theta + \nu \left(\nabla^2 v_\theta - \frac{v_\theta}{r^2 \sin^2 \varphi} + \frac{2}{r^2 \sin^2 \varphi} \frac{\partial v_r}{\partial \theta} + \frac{2 \cos \varphi}{r^2 \sin^2 \varphi} \frac{\partial v_\varphi}{\partial \theta} \right) \quad (\text{G-16})$$

Page 482

Energy:

$$\rho c_p \frac{DT}{Dt} = k \nabla^2 T + \mu \left[2(\epsilon_{rr}^2 + \epsilon_{\varphi\varphi}^2 + \epsilon_{\theta\theta}^2) + \epsilon_{\varphi\theta}^2 + \epsilon_{\varphi r}^2 + \epsilon_{r\theta}^2 \right] \quad (\text{G-17})$$

where

$$\epsilon_{rr} = \frac{\partial v_r}{\partial r} \quad \epsilon_{\varphi\varphi} = \frac{1}{r} \frac{\partial v_\varphi}{\partial \varphi} + \frac{v_r}{r} \quad \epsilon_{\theta\theta} = \frac{1}{r \sin \varphi} \frac{\partial v_\theta}{\partial \theta} + \frac{v_r}{r} + \frac{v_\varphi \cot \varphi}{r}$$

$$\epsilon_{\varphi\theta} = \frac{\sin \varphi}{r} \frac{\partial}{\partial \varphi} \left(\frac{v_\theta}{\sin \varphi} \right) + \frac{1}{r \sin \varphi} \frac{\partial v_\varphi}{\partial \theta} \quad \epsilon_{\varphi r} = r \frac{\partial}{\partial r} \left(\frac{v_\varphi}{r} \right) + \frac{1}{r} \frac{\partial v_r}{\partial \varphi}$$

$$\epsilon_{r\theta} = \frac{1}{r \sin \varphi} \frac{\partial v_r}{\partial \theta} + r \frac{\partial}{\partial r} \left(\frac{v_\theta}{r} \right)$$

APPENDIX H1

DETERMINATION OF DIMENSIONLESS PARAMETERS

FORCE F : MLt^{-2}	μ : $ML^{-1}t^{-1}$	ρ : ML^{-3}	LENGTH SCALE L : L	SPEED U : Lt^{-1}
PRESSURE p : $ML^{-1}t^{-2}$	ν : L^2t^{-1}	g : Lt^{-2}	f or ω : t^{-1}	SUR. TENSION \mathfrak{S} : Mt^{-2}
TORQUE T : ML^2t^{-2}	WORK W : ML^2t^{-2}	AREA A : L^2	FLOW RATE Q : L^3t^{-1}	VOLUME \mathfrak{V} : L^3
MASS FLOW RATE : Mt^{-1}	POWER : ML^2t^{-3}	$\gamma = \rho g$: $ML^{-2}t^{-2}$	YOUNG'S MODULUS:	$E = Y$: $ML^{-1}t^{-2}$

Buckingham Pi Theorem Procedural Steps:

1. List the “ n ” parameters involved, starting with the dependent parameter.
2. Under each parameter, write the primary dimensions $MLtT$.
3. Find the rank “ r ” of the dimensional matrix. Typically r = number of primary dimensions.
4. Select r *repeating parameters* from the n available. Avoid the *dependent variable* along with μ , a (speed of sound), Δp or \mathfrak{S} unless they are intended to be used at the basis of several Π groups. The repeating parameters must have independent units that yet include in total all the primary dimensions. The best choice is that of parameters similar to ρ , U , L (or D for internal flows).
5. For each of the $(n - r)$ remaining parameters (called *nonrepeating*, form a nondimensional Pi parameter, Π , starting with the dependent variable.
6. Express the Pi parameter containing the dependent variable as a function of the remaining Pi parameters: $\Pi_1 = F(\Pi_2, \Pi_3, \dots)$. Identify well-known Pi parameters, especially those that are named after known scientists.

$$\frac{\rho UL}{\mu} = Re \quad \text{Reynolds number} \approx \frac{\text{Inertial Force}}{\text{Viscous Force}} \text{ near solid boundaries.}$$

$$\frac{U}{a} = \sqrt{\frac{\rho U^2}{p}} = \frac{U}{\sqrt{kRT}} = Ma \quad \text{Mach number} \approx \frac{\text{Inertial Force}}{\text{Compressibility Force}} \text{ in high-speed gaseous flows.}$$

$$\frac{\omega L}{U} \text{ or } \frac{fL}{U} = St \quad \text{Strouhal number} \approx \frac{\text{Unsteady Inertial Force}}{(\text{Steady}) \text{ Inertial Force}} \text{ unsteady/oscillatory flows.}$$

$$L\sqrt{\frac{\omega}{\nu}} = \alpha \quad \text{Womersley number} \approx \frac{\text{Unsteady Inertial Force}}{\text{Viscous Force}} \text{ unsteady flows near walls.}$$

$$\frac{U^2}{gL} \text{ or } \frac{U}{\sqrt{gL}} = Fr \quad \text{Froude number} \approx \frac{\text{Inertial Force}}{\text{Gravitational Force}} \text{ in free-surface flows.}$$

Page 484

$$\frac{\rho U^2 L}{\gamma} = We \quad \text{Weber number} \approx \frac{\text{Inertial Force}}{\text{Surface Tension Force}} \text{ in capillary flows, droplets, ripple waves.}$$

$$\frac{\mu U}{\gamma} = Ca \quad \text{Capillarity number} \approx \frac{\text{Viscous Force}}{\text{Surface Tension Force}} \text{ in capillary flows near solid boundaries.}$$

$$\frac{\Delta p}{\frac{1}{2}\rho U^2} = Eu \quad \text{Euler number} \approx \frac{\text{Pressure Force}}{\text{Inertial Force}} \text{ important when pressure gradients drive the flow.}$$

$$\frac{p - p_v}{\frac{1}{2}\rho U^2} = C \quad \text{Cavitation number} \approx \frac{\text{Pressure Force}}{\text{Inertial Force}} \text{ when pressure drops below vapor pressure.}$$

$$\frac{F_D}{\frac{1}{2}\rho U^2 A} = C_D \quad \text{Drag coefficient} \approx \frac{\text{Drag Force}}{\text{Inertial Force}} \text{ when drag is important.}$$

$$\frac{U^3}{\nu \omega^2 L} = Mj \quad \text{Penetration number} \approx \frac{\text{Unsteady Inertial Force}}{\text{Unsteady Viscous Force}} \text{ oscillatory motion over porous walls.}$$

APPENDIX

H2

LIST OF DIMENSIONLESS PARAMETERS

No	Dimensionless number	Definition	Interpretation
1.	Acoustic Reynolds number (Re_a)	$\frac{aL}{\nu} = \frac{Re}{Ma} = \frac{1}{\delta_a^2}$	Ratio of compressive and viscous forces, where a is the speed of sound; $\delta_a = \sqrt{\nu/(aL)} \ll 1$ gauges viscous diffusion relative to acoustic wave propagation
2.	Archimedes number (Ar)	$\frac{g\rho L^3}{\mu^2}$	Ratio of gravitational and viscous forces
3.	Arrhenius number (α)	$\frac{E_a}{RT}$	Ratio of activation and thermal energies
4.	Atwood number (A)	$\frac{\rho_1 - \rho_2}{\rho_1 + \rho_2}$	Relative ratio of the density difference between heavier and lighter fluids that controls the hydrodynamic instability of a density stratified flow
5.	Bejan number (Be)	$\frac{\Delta p L^2}{\mu \nu}$	Dimensionless pressure drop in a duct of length L ; relates the drag coefficient to Re_L and the ratio of the wet and frontal duct areas
6.	Bingham number (Bm)	$\frac{\tau_y L}{\mu U}$	Ratio of yield and viscous stresses
7.	Biot number (Bi)	$\frac{hL}{k}$	Ratio of the internal thermal resistance of a solid and the boundary layer thermal resistance
8.	Biot number (Bi_m) for mass transfer or mass transfer Biot number	$\frac{h_m L}{k}$	Ratio of internal species transfer and boundary layer species transfer resistance with a mass transfer coefficient h_m
9.	Blake number (Bl)	$\frac{\rho U D_h}{\mu(1-\phi)}$	Ratio of inertial to viscous forces in flow through beds of solids with a void fraction (or porosity) ϕ and hydraulic diameter D_h
10.	Bond number (Bo)	$\frac{g \Delta \rho L^2}{\mathfrak{S}}$	Ratio of gravitational and surface tension forces, where \mathfrak{S} denotes the surface tension; controls the shape of entrained bubbles or drops
11.	Brinkman number (Br)	$\frac{\mu U^2}{k(T_w - T_f)} = PrEc$	Ratio of viscous dissipation and thermal conduction effects
12.	Capillary number (N_c or Ca)	$\frac{\mu U}{\mathfrak{S}}$	Ratio of viscous and surface tension forces
13.	Cauchy number (C)	$\frac{\rho U^2}{K}$	Ratio of inertial to compressibility forces
14.	Chapman-Rubesin parameter (C)	$\frac{\rho}{\rho_e} \frac{\mu}{\mu_e}$	Ratio of the boundary layer density and viscosity to their freestream or edge values; controls skin friction and heat transfer in high-speed flow
15.	Clauser's equilibrium parameter (β)	$\frac{\delta^* dp_e}{\tau_w dx}$	Ratio of normalized pressure gradient and wall shear stress that controls the condition of equilibrium turbulent flow
16.	Cavitation number (Ca or σ_c)	$\frac{p - p_v}{\frac{1}{2}\rho U^2}$	Ratio of excess local static pressure and velocity heads

17.	Coefficient of friction (C_f) or friction coefficient	$\frac{\tau}{\frac{1}{2}\rho U^2}$	Dimensionless surface shear stress
18.	Colburn J factor (J_H)	$StPr^{2/3}$	Dimensionless heat transfer coefficient for fully developed turbulent motion with duct $Re > 10^4$, $0.7 < Pr < 160$, and $L/D > 60$
19.	Colburn J factor (J_M)	$St_m Sc^{2/3}$	Dimensionless mass transfer coefficient for fully developed turbulent motion with duct $Re > 10^4$, $0.7 < Pr < 160$, and $L/D > 60$
20.	Condensation number (Co)	$\frac{g\rho^2 \Delta H_{vap} L^3}{k\mu \Delta T}$	Dimensionless parameter used in condensation calculations
21.	Damköhler number (Da)	$k_T \tau$	Ratio of chemical kinetics reaction and convective mass transport timescales for a temperature-dependent reaction rate constant k_T and a mean residence time τ
22.	Darcy friction factor (f or Λ)	$\frac{\Delta p}{\frac{1}{2}(L/D)\rho U^2}$	Dimensionless pressure drop for internal flows; four times the Fanning friction factor
23.	Darcy number (Da)	$\frac{K}{L^2}$	Ratio of the permeability of the porous medium and the cross-sectional area
24.	Dean number (De or Dn)	$Re \sqrt{\frac{L}{2R_c}}$	Ratio of the by-product of inertial and centrifugal forces to viscous forces, thus leading to the Reynolds number times the ratio of centrifugal and inertial forces; here R_c is the radius of curvature
25.	Drag coefficient (C_D)	$\frac{F_D}{\frac{1}{2}\rho U^2 A}$	Ratio of drag and inertial forces used to measure the resistance to fluid motion
26.	Eckert number (Ec)	$\frac{U^2}{c_p(T_w - T_\infty)}$	Ratio of flow kinetic energy and the boundary layer enthalpy difference
27.	Ekman number (Ek)	$\frac{\nu}{\Omega L^2}$	Ratio of viscous and Coriolis forces for an angular rotational speed of Ω and a representative length L
28.	Elasticity number (El)	$\frac{\theta\mu}{\rho R^2}$	Ratio of elastic and inertial forces in viscoelastic fluids
29.	Eötvös number (Eu)	$\frac{g(\rho - \rho_f)L^2}{\mathfrak{S}}$	Ratio of gravitational and surface forces; equivalent to the Bond number Bo
30.	Euler number (Eu)	$\frac{\Delta p}{\rho U^2}$	Ratio of pressure and inertial forces
31.	Wall expansion ratio (α)	$\frac{R\dot{R}}{\nu}$	Reynolds number based on the radial (or normal) expansion (or contraction) speed, \dot{R} , in a duct of hydraulic radius R
32.	Fanning friction factor (f)	$\frac{\Delta p}{2(L/D)\rho U^2}$	Dimensionless pressure drop for internal flows; one-fourth the Darcy friction factor
33.	Fourier number (Fo)	$\frac{\alpha\tau}{L^2}$	Dimensionless time and ratio of the heat conduction rate and the rate of thermal energy storage in a solid
34.	Fourier number (Fo_m) for mass transfer or mass transfer Fourier number	$\frac{D\tau}{L^2}$	Dimensionless time and ratio of the species diffusion rate and the rate of species storage
35.	Froude number (Fr)	$\frac{U^2}{gL}$ or $\frac{U}{\sqrt{gL}}$	Ratio of inertial and gravitational forces
36.	Galileo or Galilei number (Ga)	$\frac{gL^3}{\nu^2} = Re^2 Ri$	Reynolds number times the gravitational force over the viscous force
37.	Görtler number (G)	$\frac{U\theta}{\nu} \sqrt{\frac{\theta}{R}}$	Ratio of centrifugal and viscous forces in a concave wall boundary layer for a radius of curvature R and momentum thickness θ
38.	Graetz number (L^* or Gz)	$\frac{mc_p}{kL} = \frac{D_H}{L} Re Sc$	Ratio of thermal capacity and convective heat transfer for laminar flow
39.	Grashof number (Gr)	$\frac{g\beta(T_w - T_\infty)L^3}{\nu^2}$	Ratio of buoyancy and viscous forces under natural convection

40.	Hagen number (Hg)	$-\frac{L^3}{\rho\nu^2}\frac{dp}{dx}$	Ratio of buoyancy and viscous forces under forced convection
41.	Hodgson number (H)	$\frac{fU\Delta p}{\rho Q}$	Time constant of the system over the period of pulsation for a frequency f and volume flowrate Q
42.	Hypersonic interaction parameter (χ)	$Ma_\infty^3 \left(\frac{C_w}{Re_{x_w}} \right)^{1/2}$	Measures the strength of leading-edge interactions in hypersonic flow; here $C_w = \rho_w \mu_w / (\rho_\infty \mu_\infty)$ denotes the near-wall Chapman–Rubesin parameter
43.	Iribarren number (Ir), breaker or surf similarity parameter	$T\sqrt{\frac{g}{2\pi H}}\tan\alpha$	Relative measure of breaking wave intensity on beaches and coastal structures depending on the seaward slope angle α , the wave height H , and the deep water period T
44.	Jakob number (Ja)	$\frac{c_p(T_s - T_{sat})}{\Delta H_{vap}}$	Ratio of sensible and latent energies absorbed during liquid-vapor phase change
45.	Karlovitz number (Ka)	$\frac{1}{k_T\tau} = \frac{1}{Da}$	Ratio of convective mass transport and chemical kinetics reaction timescales for a temperature-dependent reaction rate constant k_T and a mean residence time τ
46.	Kármán–Pohlhausen parameter (Λ)	$\frac{\delta^2}{\nu}\frac{dU}{dx} = -\frac{\delta^2}{\mu U}\frac{dp}{dx}$	Dimensionless freestream pressure gradient used in the Kármán–Pohlhausen integral momentum analysis
47.	Kinetic Reynolds number (Re_k , Re_ω or ω^* , similar to Roshko's)	$\frac{\omega L^2}{\nu} = StRe = St^3Mj$	Ratio of unsteady inertial and viscous forces; equivalent to α^2 , the Womersley number squared
48.	Keulegan–Carpenter number (K_C)	$\frac{U\tau}{L}$	Ratio of drag and inertial forces for an oscillatory motion over a bluff body with an unsteady wave amplitude U , period τ , and characteristic body length L
49.	Knudsen number (Kn)	$\frac{\lambda}{L}$	Ratio of the mean free path and the characteristic length scale
50.	Laplace (La) or Suratman number (Su)	$\frac{\rho L\mathfrak{S}}{\mu^2} = \frac{Re^2}{We}$	Ratio of surface tension and momentum transport
51.	Lewis number, (Le)	$\frac{\alpha}{D} = \frac{Sc}{Pr}$	Ratio of thermal and mass diffusivities
52.	Lift coefficient (C_L)	$\frac{F_L}{\frac{1}{2}\rho U^2 A_L}$	Ratio of the lifting pressure and the dynamic pressure
53.	Mach number (M or Ma)	$\frac{U}{a}$	Ma^2 represents the ratio of inertial to compressive forces
54.	Majdalani number (Mj) or Majdalani's penetration number (S_p)	$\frac{U^3}{\nu\omega^2 L} = \frac{U^3\tau^2}{\nu L}$ or $\frac{Re_w}{St} = \frac{Re}{St^2} = \frac{Re_k}{St^3}$	Controls the depth of penetration of rotational waves over porous walls; it also controls the depth of viscous and rotational effects in the cross-stream-wise direction
55.	Nusselt number (Nu)	$\frac{hL}{k}$	Ratio of convective and conductive heat transfer
56.	Off-swirl parameter (κ)	$\frac{A_i}{2\pi RL} = \frac{R}{2\pi\sigma L}$	Ratio of axial to tangential (swirl) velocities in a rotating flow in a chamber of radius R and tangential injection area A_i ; inversely proportional to the product of the modified swirl number and the chamber aspect ratio L/R ; the swirl intensity increases with $1/\kappa$
57.	Ohnesorge number (Oh)	$\frac{\mu}{\sqrt{\rho L\mathfrak{S}}} = \frac{\sqrt{We}}{Re}$	Ratio of viscous forces to the square root of the product of inertial and surface forces
58.	Péclet number (Pe)	$\frac{UL}{\alpha} = RePr$	Ratio of convective and thermal diffusive transport rates
59.	Poiseuille number (Po)	$\frac{2h\tau}{\mu U} = C_f Re_k$	Product of the friction factor and the Reynolds number in duct flow
60.	Mass transfer Péclet number (Pe_m)	$\frac{UL}{D}$	Ratio of convective and molecular diffusive transport rates
61.	Pipeline parameter (ρ^*)	$\frac{aU}{2gh}$	Maximum water hammer pressure rise over twice the static pressure head h when a and U denote the speeds of the wave and initial flow
62.	Power number (N_p)	$\frac{P}{N^3\rho L^5}$	Ratio of drag and inertial forces for power consumption calculations where N and P denote the rate of rotation and the power, respectively

63.	Prandtl number (Pr)	$\frac{\nu}{\alpha}$	Ratio of momentum and thermal diffusivities
64.	Pressure coefficient (C_p)	$\frac{p - p_\infty}{\frac{1}{2} \rho U^2}$	Ratio of the freestream pressure differential and the dynamic pressure
65.	Rayleigh number (Ra)	$GrPr$	Ratio of buoyancy and viscous forces in free convection
66.	Reynolds number (Re)	$\frac{\rho UL}{\mu} = St^2 Mj$	Ratio of inertial and viscous forces
67.	Richardson number (Ri)	$\frac{g\beta(T_w - T_\infty)L}{U^2} = \frac{Gr}{Re^2}$	Ratio of buoyancy and shear forces
68.	Roshko number (Ro)	$\frac{fL^2}{\nu} = ReSt$	Ratio of viscous dissipation and unsteady inertial timescales for oscillatory motion; similar to the kinetic Reynolds number
69.	Rossby (Ro) or Kibel number	$\frac{U}{L\Omega}$	Ratio of inertial and Coriolis forces
70.	Schmidt number (Sc)	$\frac{\nu}{D}$	Ratio of momentum and mass diffusivities
71.	Shape factor (H)	$\frac{\delta^*}{\theta} = \frac{\eta^*}{\theta^*}$	Ratio of displacement and momentum thicknesses in boundary layer flow
72.	Normalized displacement thickness (η^*)	$\frac{\delta^*}{\delta}$	Ratio of displacement and disturbance thicknesses in boundary layer flow
73.	Normalized momentum thickness (θ^*)	$\frac{\theta^*}{\delta}$	Ratio of momentum and disturbance thicknesses in boundary layer flow
74.	Sherwood (Sh) or mass transfer Nusselt number	$\frac{h_m L}{D}$	Ratio of convective mass transfer and mass diffusion rates
75.	Stanton number (C_h or St)	$\frac{h}{\rho U c_p} = \frac{Nu}{RePr}$	Ratio of convective heat transfer and fluid thermal capacity; modified Nusselt number
76.	Stanton number (St_m) for mass transfer	$\frac{h_m}{\rho_m U} = \frac{Sh}{ReSc}$	Ratio of convective mass transfer and mass capacity; modified Sherwood number
77.	Stokes number (Stk)	$\frac{\tau_p U}{L} = \frac{1}{18} \frac{\rho_p U d_p}{\mu} \left(\frac{d_p}{L} \right)$	Ratio of a particle's dynamic relaxation time and the convective time for a particle to cross a distance L at a speed U ; measures particle inertia and resistance to entrainment; a low Stk enables the particle to faithfully follow the flow streamlines
78.	Stokes parameter (λ_s)	$L \sqrt{\frac{\omega}{2\nu}} = \frac{1}{\sqrt{2}} Re_k^{1/2}$	λ_s^2 represents the ratio of unsteady inertial and viscous forces; similar to the Womersley number
79.	Swirl number (S)	$\frac{\pi ab}{A_i}$	Ratio of the axial flux of the tangential velocity momentum and the axial flux of the axial velocity momentum with A_i , a , and b denoting the inlet injection area, the outer radius, and the outlet radius, respectively
80.	Swirl number (S), modified or modified swirl number	$\frac{a^2}{A_i}$	Reciprocal of the normalized tangential injection area with A_i and a denoting the injection area and the chamber radius
81.	Strouhal number (St , S or Sr)	$\frac{\omega L}{U}$ or $\frac{L}{U\tau}$	Dimensionless frequency and ratio of unsteady and steady inertial forces; inversely proportional to the vortex spacing
82.	Taylor number (Ta)	$\frac{4\Omega^2 R^4}{\nu^2}$	Ratio of centrifugal (inertial) and viscous forces for a fluid rotating at an angular speed Ω about an axis with a characteristic radius R
83.	Thwaites (or Holstein-Bohlen) parameter (λ)	$\frac{\theta^2}{\nu} \frac{dU}{dx}$	Dimensionless pressure gradient parameter used by Thwaites' method; different from Pohlhausen's pressure gradient parameter
84.	Vadasz number (Va)	$\frac{\phi \nu L^2}{\alpha K} = \frac{\phi Pr}{Da}$	Relevant to porous thermal convection where K is the permeability and ϕ is the void fraction or porosity

85.	Vortex Reynolds number (Vo , V or Re_V)	$\frac{UA_i}{\nu L} = \frac{m_i}{\mu L} = \frac{Re R}{\sigma L}$	Ratio of the inlet Reynolds number and the product of the modified swirl number and cyclonic chamber aspect ratio; controls the thickness of the wall and core shear layers in wall-bounded cyclonic flows
86.	Wave Reynolds number (Re_w)	$\frac{U^2}{\omega \bar{w}} = StMj$	$\sqrt{Re_w}$ is the ratio of a wave's propagation speed due to mean flow convection and its speed due to viscous diffusion; controls the phase lead of the oscillatory pressure with respect to the velocity near a wall with blowing speed U
87.	Weber number (We)	$\frac{\rho U^2 L}{\mathfrak{F}}$	Ratio of inertial and surface tension forces
88.	Womersley number (α or Wo)	$L \sqrt{\frac{\omega}{\nu}} = \sqrt{Re_k}$	Ratio of the unsteady inertial and viscous forces for unsteady motion near solid boundaries

APPENDIX

I

TRIGONOMETRIC IDENTITIES

ADDITION AND SUBTRACTION FORMULAS

$$\sin(a \pm b) = \sin a \cos b \pm \cos a \sin b; \quad \cos(a \pm b) = \cos a \cos b \mp \sin a \sin b \quad (\text{I-1})$$

$$\sin\left(\frac{1}{2}\pi \pm b\right) = \cos b; \quad \cos\left(\frac{1}{2}\pi \pm b\right) = \mp \sin b \quad (\text{I-2})$$

$$\tan(a \pm b) = \frac{\tan a \pm \tan b}{1 \mp \tan a \tan b}; \quad \cot(a \pm b) = \frac{\cot a \cot b \mp 1}{\cot b \pm \cot a}; \quad \tan\left(\frac{1}{4}\pi \pm b\right) = \frac{1 \pm \tan b}{1 \mp \tan b} = \frac{\cos b \pm \sin b}{\cos b \mp \sin b} \quad (\text{I-3})$$

WERNER'S FORMULAS

$$\sin a \sin b = \frac{1}{2}[\cos(a - b) - \cos(a + b)]; \quad \sin a \cos b = \frac{1}{2}[\sin(a + b) + \sin(a - b)] \quad (\text{I-4})$$

$$\cos a \cos b = \frac{1}{2}[\cos(a + b) + \cos(a - b)] \quad (\text{I-5})$$

INVERSE OF WERNER'S FORMULAS

$$\sin a + \sin b = 2 \sin\left(\frac{a+b}{2}\right)\cos\left(\frac{a-b}{2}\right); \quad \sin a - \sin b = 2 \cos\left(\frac{a+b}{2}\right)\sin\left(\frac{a-b}{2}\right) \quad (\text{I-6})$$

$$\cos a + \cos b = 2 \cos\left(\frac{a+b}{2}\right)\cos\left(\frac{a-b}{2}\right); \quad \cos a - \cos b = -2 \sin\left(\frac{a+b}{2}\right)\sin\left(\frac{a-b}{2}\right) \quad (\text{I-7})$$

TRANSFORMATION OF SUMS INTO PRODUCTS OF FUNCTIONS

$$\tan a + \tan b = \sin(a + b)/(\cos a \cos b); \quad \tan a - \tan b = \sin(a - b)/(\cos a \cos b) \quad (\text{I-8})$$

$$\cot a + \cot b = \sin(a + b)/(\sin a \sin b); \quad \cot a - \cot b = -\sin(a - b)/(\sin a \sin b) \quad (\text{I-9})$$

DUPLICATION FORMULAS

$$\sin 2a = 2 \sin a \cos a; \quad \cos 2a = 2 \cos^2 a - 1 = 1 - 2 \sin^2 a = \cos^2 a - \sin^2 a \quad (\text{I-10})$$

$$\tan 2a = 2 \tan a / (1 - \tan^2 a); \quad \cot 2a = (\cot^2 a - 1) / (2 \cot a) \quad (\text{I-11})$$

TRIPLICATION FORMULAS

$$\sin 3a = 3 \sin a - 4 \sin^3 a; \quad \cos 3a = 4 \cos^3 a - 3 \cos a \quad (\text{I-12})$$

$$\tan 3a = (3 \tan a - \tan^3 a)/(1 - 3 \tan^2 a); \quad \cot 3a = (\cot^3 a - 3 \cot a)/(3 \cot^2 a - 1) \quad (\text{I-13})$$

Page 491

BISECTION FORMULAS

$$\sin \frac{a}{2} = \pm \sqrt{\frac{1}{2}(1 - \cos a)}; \quad \cos \frac{a}{2} = \pm \sqrt{\frac{1}{2}(1 + \cos a)} \quad (\text{I-14})$$

$$\tan \frac{a}{2} = \pm \sqrt{\frac{1 - \cos a}{1 + \cos a}}; \quad \cot \frac{a}{2} = \pm \sqrt{\frac{1 + \cos a}{1 - \cos a}} \quad (\text{I-15})$$

CONVERSION OF POWERS INTO MULTIPLE ANGLES

$$\sin^2 a = \frac{1}{2}(1 - \cos 2a); \quad \cos^2 a = \frac{1}{2}(1 + \cos 2a) \quad (\text{I-16})$$

$$\sin^3 a = \frac{1}{4}(3 \sin a - \sin 3a); \quad \cos^3 a = \frac{1}{4}(3 \cos a + \cos 3a) \quad (\text{I-17})$$

$$\sin^4 a = \frac{1}{8}(\cos 4a - 4 \cos 2a + 3); \quad \cos^4 a = \frac{1}{8}(\cos 4a + 4 \cos 2a + 3) \quad (\text{I-18})$$

$$\sin^5 a = \frac{1}{16}(10 \sin a - 5 \sin 3a + \sin 5a); \quad \cos^5 a = \frac{1}{16}(10 \cos a + 5 \cos 3a + \cos 5a) \quad (\text{I-19})$$

$$\sin^6 a = \frac{1}{32}(10 - 15 \cos 2a + 6 \cos 4a - \cos 6a); \quad \cos^6 a = \frac{1}{32}(10 + 15 \cos 2a + 6 \cos 4a + \cos 6a) \quad (\text{I-20})$$

BIBLIOGRAPHY

- Abbasbandy, S. (2007), “A Numerical Solution of Blasius Equation by Adomian’s Decomposition Method and Comparison with Homotopy Perturbation Method,” *Chaos, Solitons & Fractals*, vol. 31, no. 1, pp. 257–260. doi: <https://doi.org/10.1016/j.chaos.2005.10.071>
- Abbasbandy, S., and Bervillier, C. (2011), “Analytic Continuation of Taylor Series and the Boundary Value Problems of Some Nonlinear Ordinary Differential Equations,” *Applied Mathematics and Computation*, vol. 218, no. 5, pp. 2178–2199. doi: <https://doi.org/10.1016/j.amc.2011.07.035>
- Abramovich, G. N. (1963), *The Theory of Turbulent Jets*, M.I.T. Press, Cambridge, MA.
- Adams, N. A., and Kleiser, L. (1993), “Numerical Simulation of Transition in a Compressible Flat Plate Boundary Layer,” in Kral, L. D., and Zang, T. A. (Eds.), *Transitional and Turbulent Compressible Flows—1993*, ASME Fluids Engineering Division, vol. 151, pp. 101–110.
- Agarwal, R. (1999), “Computational Fluid Dynamics of Whole-Body Aircraft,” *Annual Review of Fluid Mechanics*, vol. 31, pp. 125–169. <https://doi.org/10.1146/annurev.fluid.31.1.125>
- Aghakhani, M., Suhatri, M., Mohammadhassani, M., Daie, M., and Toghrol, A. (2015), “A Simple Modification of Homotopy Perturbation Method for the Solution of Blasius Equation in Semi-Infinite Domains,” *Mathematical Problems in Engineering*, vol. 2015, p. 7. doi: <https://doi.org/10.1155/2015/671527>
- Agullo, O., and Verga, A. D. (1997), “Exact Two Vortices Solution of Navier–Stokes Equations,” *Physical Review Letters*, vol. 78, no. 12, p. 2361. doi: <https://doi.org/10.1103/PhysRevLett.78.2361>
- Ahmad, F., and Al-Barakati, W. H. (2009), “An Approximate Analytic Solution of the Blasius Problem,” *Communications in Nonlinear Science and Numerical Simulation*, vol. 14, no. 4, pp. 1021–1024. doi: <https://doi.org/10.1016/j.cnsns.2007.12.010>
- Akiki, M. H., “Multidimensional Compressible Framework for Modeling Biglobal Stability in Rocket Motors,” Ph.D. Dissertation, University of Tennessee, Department of Mechanical, Aerospace, and Biomedical Engineering, August 2013.
- Alizadeh-Pahlavan, A., and Borjani-Boroujeni, S. (2008), “On the Analytical Solution of Viscous Fluid Flow Past a Flat Plate,” *Physics Letters A*, vol. 372, no. 20, pp. 3678–3682. doi: <https://doi.org/10.1016/j.physleta.2008.02.050>

- Allan, F. M., and Syam, M. I. (2005), "On the Analytic Solutions of the Nonhomogeneous Blasius Problem," *Journal of Computational and Applied Mathematics*, vol. 182, no. 2, pp. 362–371. doi: <https://doi.org/10.1016/j.cam.2004.12.017>
- Ambrok, G. S. (1957), "Approximate Solutions of Equations for the Thermal Boundary Layer with Variations in the Boundary Layer Structure," *Soviet Physics. Technical Physics*, vol. 2, no. 9, pp. 1979–1986.
- Ames, W. F. (1965), *Nonlinear Partial Differential Equations in Engineering*, Academic, New York.
- Ames, W. F., and Adams, E. (1947), "A Family of Exact Solutions for Laminar Boundary Layer Equations," *Journal of Applied Mathematics and Mechanics (ZAMM)*, vol. 54, no. 12, pp. 180–181. doi: <https://doi.org/10.1002/zamm.19740541297>
- Andereck, C. D., Liu, S., and Swinney, H. (1986), "Flow Regimes in a Circular Couette System with Independently Rotating Cylinders," *Journal of Fluid Mechanics*, vol. 164, pp. 155–183. doi: <https://doi.org/10.1017/S0022112086002513>
- Anderson, J. D., Jr. (1995), *Computational Fluid Dynamics: The Basics with Applications*, McGraw-Hill, New York.
- (2000), *Hypersonic and High Temperature Gas Dynamics*, American Institute of Aeronautics and Astronautics, Reston, VA.
- (2001), *Fundamentals of Aerodynamics*, 3rd ed., McGraw-Hill, New York.
- (2003), *Modern Compressible Flow with Historical Perspective*, 3rd ed., McGraw-Hill, New York.
- Anil Lal, S., and Neeraj Paul, M. (2014), "An Accurate Taylors Series Solution with High Radius of Convergence for the Blasius Function and Parameters of Asymptotic Variation," *Journal of Applied Fluid Mechanics*, vol. 7, no. 4, pp. 557–564. doi: <https://doi.org/10.36884/jafm.7.04.21339>
- Antonia, R. A., and Bilger, R. W. (1973), "An Experimental Investigation of an Axisymmetric Jet in a Co-Flowing Air Stream," *Journal of Fluid Mechanics*, vol. 61, pp. 805–822. doi: <https://doi.org/10.1017/S0022112073000959>
- Apelt, C. J. (1961), "The Steady Flow of a Viscous Fluid Past a Circular Cylinder at Reynolds Numbers 40 and 44," *Aeronautical Research Council*, R & M 3175. <http://naca.central.cranfield.ac.uk/reports/arc/rm/3175.pdf>
- Aref, H. (2004), *Introduction to Computational Fluid Dynamics*, Cambridge University Press, New York.
- Aris, R. (1990), *Vectors, Tensors, and the Basic Equations of Fluid Mechanics*, Dover, New York.
- Arnal, D. (1984), "Description and Prediction of Transition in Two-Dimensional Incompressible Flow," pp. 2–1–2–71 of AGARD.

- Arpaci, V. S. (1984), *Convection Heat Transfer*, Prentice-Hall, Upper Saddle River, NJ.
- Asaithambi, A. (2016), “Numerical Solution of the Blasius Equation with Crocco–Wang Transformation,” *Journal of Applied Fluid Mechanics*, vol. 9, no. 5, pp. 2595–2603. doi: <https://doi.org/10.18869/acadpub.jafm.68.236.25583>
- Asaithambi, A. (2005), “Solution of the Falkner–Skan Equation by Recursive Evaluation of Taylor Coefficients,” *Journal of Computational and Applied Mathematics*, vol. 176, no. 1, pp. 203–214. doi: <https://doi.org/10.1016/j.cam.2004.07.013>
- Au-Yang, M. K. (2001), *Flow-Induced Vibration of Power and Process Plant Components: A Practical Workbook*, ASME Press, New York.
- Avalon, G., and Lambert, D. (2001), “Campagne D’essais Valdo, Période 2000–2001,” ONERA, Etablissement de Palaiseau, Technical Report RT 2/05424 DEFA Rept., October.
- Avalon, G., Casalis, G., and Griffond, J., “Flow Instabilities and Acoustic Resonance of Channels with Wall Injection,” 34th AIAA/ASME/SAE/ASEE Joint Propulsion Conference and Exhibit, AIAA Paper 1998-3218, July 1998. doi: <https://doi.org/10.2514/6.1998-3218>
- Bae, Y. Y., and Emanuel, G. (1989), “Boundary-Layer Tables for Similar Compressible Flow,” *AIAA Journal*, vol. 27, no. 9, pp. 1163–1164. doi: <https://doi.org/10.2514/3.10240>

Page 493

- Bairstow, L. (1925), “Skin Friction,” *The Journal of the Royal Aeronautical Society*, vol. 29, no. 169, pp. 3–23. doi: <https://doi.org/10.1017/S0368393100139380>
- Bake, S. D., Meyer, G. W., and Rist, U. (2002), “Turbulence Mechanism in Klebanoff Transition: A Quantitative Comparison of Experiment and Direct Numerical Simulation,” *Journal of Fluid Mechanics*, vol. 459, pp. 217–243. doi: <https://doi.org/10.1017/S0022112002007954>
- Baker, A. J. (1983), *Finite Element Computational Fluid Mechanics*, Hemisphere, New York.
- Baker, C. J. (1979), “The Laminar Horseshoe Vortex,” *Journal of Fluid Mechanics*, vol. 95, pt. 2, pp. 347–367. doi: <https://doi.org/10.1017/S0022112079001506>
- Baker, R. C. (2003), *Introductory Guide to Flow Measurement*, ASME Press, New York.
- Baldwin, B. S., and Lomax, H. (1978), “Thin Layer Approximation and Algebraic Model for Separated Turbulent Flows,” AIAA Paper 78-257. doi: <https://doi.org/10.2514/6.1978-257>
- Barber, T. A., and Majdalani, J. (2017), “On the Beltramian Motion of the Bidirectional Vortex in a Conical Cyclone,” *Journal of Fluid Mechanics*, vol. 828, pp. 708–732. doi: <https://doi.org/10.1017/jfm.2017.494>

- Barenblatt, G. I., Chorin, A. J., and Prostokishin, V. M. (1997), "Scaling Laws for Fully Developed Turbulent Flow in Pipes," *Applied Mechanics Reviews* vol. 50, no. 7, pp. 413–429. doi: <http://doi.org/10.1115/1.3101726>
- Baritaud, T. (1996), *Direct Numerical Simulation for Turbulent Reacting Flows*, Editions Technip, Paris.
- Barnwell, R. W., and Wahls, R. A. (1991), "Skin Friction Law for Compressible Turbulent Flow," *AIAA Journal*, vol. 29, no. 3, pp. 380–386. doi: <https://doi.org/10.2514/3.10589>
- Barrett, M. J., and Hollingsworth, D. K. (2003), "Heat Transfer in Turbulent Boundary Layers Subjected to Freestream Turbulence: Part I, Experimental Results, Part II, Analysis and Correlation," *Journal of Turbomachinery* vol. 125, no. 2, April, pp. 232–241. doi: <https://doi.org/10.1115/1.1538622>
- Bear, J. (1988), *Dynamics of Fluids in Porous Media*, Dover Publications, New York.
- Becker, A. A. (2004), *Introductory Guide to Finite Element Analysis*, ASME Press, New York.
- Beer, G. (2001), *Programming the Boundary Element Method: An Introduction for Engineers*, Wiley, New York.
- Bejan, A. (1994), *Convection Heat Transfer*, 2nd ed., Wiley, New York.
- Bender, C. M., Milton, K. A., Pinsky, S. S., and Simmons, L. M., Jr. (1989), "A New Perturbative Approach to Nonlinear Problems," *Journal of Mathematical Physics (New York)*, vol. 30, no. 7, pp. 1447–1455. doi: <https://doi.org/10.1063/1.528326>
- Benjamin, T. B. (1960), "Effects of a Flexible Boundary on Hydrodynamic Stability," *Journal of Fluid Mechanics*, vol. 9, pt. 4, pp. 513–532. doi: <https://doi.org/10.1017/S0022112060001286>
- Berger, S. A. (1971). *Laminar Wakes*, Elsevier, New York.
- Bergstrom, D. J., Kotey, N. A., and Tachie, M. F. (2002), "The Effects of Surface Roughness on the Mean Velocity Profile in a Turbulent Boundary Layer," *Journal of Fluids Engineering*, vol. 124, no. 3, September, pp. 664–670. doi: <https://doi.org/10.1115/1.1493810>
- Berker, A. R. (1963), "Intégration des équations du mouvement d'un fluide visqueux incompressible," in S. Flügge (ed.), *Encyclopedia of Physics*, vol. 8, pt. 2, pp. 1–384, Springer, Berlin.
- Berman, A. S. (1958), "Effects of Porous Boundaries on the Flow of Fluids in Systems with Various Geometries," *Proceedings of the Second United Nations International Conference on the Peaceful Uses of Atomic Energy*, vol. 4, pp. 351–358.
- Bernard, P. S., and Wallace, J. M. (2002), *Turbulent Flow: Analysis, Measurement, and Prediction*, Wiley, New York.

- Bertram, M. H. (1958), "Boundary Layer Displacement Effects in Air at Mach Numbers of 6.8 at 9.6," NACA Technical Note 4133, February.
- Bertram, M. H., and Blackstock, T. A. (1961), "Some Simple Solutions to the Problem of Predicting Boundary Layer Self-Induced Pressures," National Aeronautics and Space Administration Technical Note D-798, April.
- Betchov, R., and Szewczyk, A. B. (1963), "Stability of a Shear Layer Between Parallel Streams," *Physics of Fluids*, vol. 6, pp. 1391–1396. doi: <https://doi.org/10.1063/1.1710959>
- Betchov, R., and Criminale, W. O. (1967), *Stability of Parallel Flows*, Academic, New York.
- Bird, G. A. (1994), *Molecular Gas Dynamics and the Direct Simulation of Gas Flows*, 2nd ed., Clarendon Press, Oxford.
- Bird, R. B., Armstrong, R. C., and Hassager, O. (1977), *Dynamics of Polymeric Liquids Volume 1: Fluid Mechanics*, 2nd ed., Wiley, New York.
- Bird, R. B., Curtiss, C. F., Armstrong, R. C., and Hassager, O. (1977), *Dynamics of Polymeric Liquids Volume 2: Kinetic Theory*, 2nd ed. Wiley, New York.
- Bird, R. B., Stewart, W. E., and Lightfoot, E. N. (2007), *Transport Phenomena*, 2nd ed., Wiley, New York.
- Blackwell, B. F. (1973), "The Turbulent Boundary Layer on a Porous Plate: An Experimental Study of the Heat Transfer Behavior with Adverse Pressure Gradients," Ph.D. Dissertation, Stanford University, Stanford, CA.
- Blasius, H. (1908), "Grenzschichten in Flüssigkeiten mit kleiner Reibung," *Journal of Applied Mathematics and Physics (ZAMP)*, vol. 56, pp. 1–37 [English translation in NACA Technical Memo. 1256].
- (1913), "Das Ähnlichkeitsgesetz bei Reibungsvorgängen in Flüssigkeiten," *Forschung Arbeitsgemeinschaft Ingenieurwesen*, no. 134, Berlin.
- Blazek, J. (2001), *Computational Fluid Dynamics: Principles and Applications*, Elsevier, New York.
- Blevins, R. D. (1977), *Flow-Induced Vibrations*, Van Nostrand, New York.
- Bloor, M. I. G., and Ingham, D. B. (1987), "The Flow in Industrial Cyclones," *Journal of Fluid Mechanics*, vol. 178, no. 1, pp. 507–519. doi: <https://doi.org/10.1017/S0022112087001344>
- Bluman, G. W., and Cole, J. D. (1974), *Similarity Methods for Differential Equations*, Springer, New York.
- Blyth, M. G., Hall, P., and Papageorgiou, D. T. (2003), "Chaotic Flows in Pulsating Cylindrical Tubes: A Class of Exact Navier–Stokes Solutions," *Journal of Fluid Mechanics*, vol. 481, pp. 187–213. doi: <https://doi.org/10.1017/S0022112003003835>

- Bödewadt, U. T. (1940), “Die Drehströmung über festem Grund,” *Journal of Applied Mathematics and Mechanics (ZAMM)*, vol. 20, pp. 241–253. doi: <https://doi.org/10.1002/zamm.19400200502>
- Boris, J. P. (1989), “New Directions in Computational Fluid Dynamics,” *Annual Review of Fluid Mechanics*, vol. 21, no. 1, pp. 345–385. doi: <https://doi.org/10.1146/annurev.fl.21.010189.002021>
- Bourchtein, A. (2002), “Exact Solutions of the Generalized Navier–Stokes Equations for Benchmarking,” *International Journal for Numerical Methods in Fluids*, vol. 39, no. 11, pp. 1053–1071. doi: <https://doi.org/10.1002/fld.361>
- Bouyges, M., Chedeveigne, F., Casalis, G., and Majdalani, J. (2017), “Asymptotically Based Self-Similarity Solution of the Navier–Stokes Equations for a Porous Tube with a Non-Circular Cross-Section,” *Journal of Fluid Mechanics*, vol. 826, pp. 396–420. doi: <https://doi.org/10.1017/jfm.2017.430>Page 494
- Boyd, J. P. (1997), “Padé Approximant Algorithm for Solving Nonlinear Ordinary Differential Equation Boundary Value Problems on an Unbounded Domain,” *Computers in Physics*, vol. 11, no. 3, pp. 299–303. doi: <https://doi.org/10.1063/1.168606>
- Boyd, J. P. (1987), “Spectral Methods Using Rational Basis Functions on an Infinite Interval,” *Journal of Computational Physics*, vol. 69, no. 1, pp. 112–142. doi: [https://doi.org/10.1016/0021-9991\(87\)90158-6](https://doi.org/10.1016/0021-9991(87)90158-6)
- Boyd, J. P. (1999), “The Blasius Function in the Complex Plane,” *Experimental Mathematics*, vol. 8, no. 4, pp. 381–394. doi: <https://doi.org/10.1080/10586458.1999.10504626>
- Boyd, J. P. (2008), “The Blasius Function: Computations before Computers, the Value of Tricks, Undergraduate Projects, and Open Research Problems,” *SIAM Review*, vol. 50, no. 4, pp. 791–804. doi: <https://doi.org/10.1137/070681594>
- Boyd, J. P. (1982), “The Optimization of Convergence for Chebyshev Polynomial Methods in an Unbounded Domain,” *Journal of Computational Physics*, vol. 45, no. 1, pp. 43–79. doi: [https://doi.org/10.1016/0021-9991\(82\)90102-4](https://doi.org/10.1016/0021-9991(82)90102-4)
- Boyd, J. P. (2001), *Chebyshev and Fourier Spectral Methods*, 2nd ed., Dover Publications, New York.
- Boyd, J. P., Rangan, C., and Bucksbaum, P. H. (2003), “Pseudospectral Methods on a Semi-Infinite Interval with Application to the Hydrogen Atom: A Comparison of the Mapped Fourier-Sine Method with Laguerre Series and Rational Chebyshev Expansions,” *Journal of Computational Physics*, vol. 188, no. 1, pp. 56–74. doi: [https://doi.org/10.1016/S0021-9991\(03\)00127-X](https://doi.org/10.1016/S0021-9991(03)00127-X)
- Boyer, G., Casalis, G., and Estivalèzes, J. L. (2013), “Stability and Sensitivity Analysis in a Simplified Solid Rocket Motor Flow,” *Journal of Fluid Mechanics*, vol. 722, pp. 618–644. doi: <https://doi.org/10.1017/jfm.2013.90>

- Bradshaw, P. (1977), "Compressible Turbulent Shear Layers," *Annual Review of Fluid Mechanics*, vol. 9, pp. 33–52. doi: <https://doi.org/10.1146/annurev.fl.09.010177.000341>
- (1987), "Turbulent Secondary Flows," *Annual Review of Fluid Mechanics*, vol. 19, pp. 53–74. doi: <https://doi.org/10.1146/annurev.fl.19.010187.000413>
- Bradshaw, P., and Ferriss, D. H. (1971), "Calculation of Boundary-Layer Development Using the Turbulent Energy Equation: Compressible Flow on Adiabatic Walls," *Journal of Fluid Mechanics*, vol. 46, no. 1, pp. 83–110. doi: <https://doi.org/10.1017/S0022112071000417>
- Bragg, S. L., and Hawthorne, W. R. (1950), "Some Exact Solutions of the Flow through Annular Cascade Actuator Discs," *Journal of the Aeronautical Sciences (Institute of the Aeronautical Sciences)*, vol. 17, no. 4, pp. 243–249. doi: <https://doi.org/10.2514/8.1597>
- Bramley, J. S., and Sloan, D. M. (1987), "Numerical Solution for Two-Dimensional Flow in a Branching Channel Using Boundary-Fitted Coordinates," *Computers & Fluids*, vol. 15, no. 3, pp. 297–311. doi: [https://doi.org/10.1016/0045-7930\(87\)90012-0](https://doi.org/10.1016/0045-7930(87)90012-0)
- Branover, H., Moiseyev, S., Golbraikh, E., and Eidelman, A. (Eds.) (1999), *Turbulence and Structures: Chaos, Fluctuations, and Helical Self-Organization in Nature and the Laboratory*, Academic, New York.
- Brauer, H., and Sucker, D. (1976), "Umströmung von Platten, Zylinder und Kugeln," *Chemie Ingenieur Technik*, vol. 48, pp. 665–671 [English translation in *Int. Chem. Eng.*, vol. 18, no. 8, pp. 367–374]. doi: <https://doi.org/10.1002/cite.330480803>
- Brennen, C. E. (1995), *Cavitation and Bubble Dynamics*, Oxford University Press, New York.
- Breuer, M. (1998), "Large Eddy Simulation of the Subcritical Flow Past a Circular Cylinder: Numerical and Modeling," *International Journal for Numerical Methods in Fluids*, vol. 28, no. 9, pp. 1281–1302. doi: [https://doi.org/10.1002/\(SICI\)1097-0363\(19981215\)28:9<1281::AID-FLD759>3.0.CO;2-%23](https://doi.org/10.1002/(SICI)1097-0363(19981215)28:9<1281::AID-FLD759>3.0.CO;2-%23)
- Brinich, P. F. (1954), "Boundary Layer Transition at Mach 3.12 with and Without Single Roughness Element," NACA Technical Note 3267.
- Brown, G. L., and Roshko, A. (1974), "On Density Effects and Large Structure in Turbulent Mixing Layers," *Journal of Fluid Mechanics*, vol. 64, pt. 4, pp. 775–816. doi: <https://doi.org/10.1017/S002211207400190X>
- Brown, W. B. (1962), "Exact Numerical Solutions of the Complete Linearized Equations for the Stability of Compressible Boundary Layers," Norair Report NOR-62-15, Northrop Aircraft Inc., Hawthorne, Calif.
- Brush, S. G. (1965), *Kinetic Theory Vol. 1*, Pergamon Press, New York.
- Brush, S. G. (1966), *Kinetic Theory Vol. 2 Irreversible Processes*, Pergamon Press, New York.

- Brush, S. G. (1972), *Kinetic Theory Vol. 3 The Chapman—Enskog Solution of the Transport Equation for Moderately Dense Gases*, Pergamon Press, New York.
- Brutin, D., and Tadrist, L. (2003), “Experimental Friction Factor of a Liquid Flow in Microtubes,” *Physics of Fluids*, vol. 15, no. 3, pp. 653–661. doi: <https://doi.org/10.1063/1.1538612>
- Bruun, H. H. (1995), *Hot-Wire Anemometry: Principles and Signal Analysis*, Oxford University Press, New York.
- Buddenberg, J. W., and Wilke, C. R. (1949), “Calculation of Gas-Mixture Viscosities,” *Industrial & Engineering Chemistry*, vol. 41, no. 7, pp. 1345–1347. doi: <https://doi.org/10.1021/ie50475a011>
- Burgers, J. M. (1924), “The Motion of a Fluid in the Boundary Layer along a Plane Smooth Surface,” *Proceedings of the First International Congress for Applied Mechanics*, p. 113–128, Delft.
- Burmeister, L. C. (1993), *Convective Heat Transfer*, 2nd ed., Wiley, New York.
- Buschmann, M. H., and Gad-el-Hak, M. (2003), “Debate Concerning the Mean Velocity Profile of a Turbulent Boundary Layer,” *AIAA Journal*, vol. 41, no. 4, pp. 565–572. <https://doi.org/10.2514/2.1994>
- Busemann, A. (1931), *Handbuch der Physik*, vol. 4, pt. 1, p. 366, Geest and Portig, Leipzig.
- Cantwell, B., Coles, D., and Dimotakis, P. (1978), “Structure and Entrainment in the Plane of Symmetry of a Turbulent Spot,” *Journal of Fluid Mechanics*, vol. 87, no. 4, pp. 641–672. doi: <https://doi.org/10.1017/S0022112078001809>
- Callegari, A. J., and Friedman, M. B. (1968), “An Analytical Solution of a Nonlinear, Singular Boundary Value Problem in the Theory of Viscous Fluids,” *Journal of Mathematical Analysis and Applications*, vol. 21, no. 3, pp. 510–529. doi: [https://doi.org/10.1016/0022-247X\(68\)90260-6](https://doi.org/10.1016/0022-247X(68)90260-6)
- Callegari, A., and Nachman, A. (1978), “Some Singular, Nonlinear Differential Equations Arising in Boundary Layer Theory,” *Journal of Mathematical Analysis and Applications*, vol. 64, no. 1, pp. 96–105. doi: [https://doi.org/10.1016/0022-247X\(78\)90022-7](https://doi.org/10.1016/0022-247X(78)90022-7)
- Campos, L. M. B. C. (2007), “On 36 Forms of the Acoustic Wave Equation in Potential Flows and Inhomogeneous Media,” *Applied Mechanics Reviews*, vol. 60, no. 4, pp. 149–171. doi: <https://doi.org/10.1115/1.2750670>
- Carey, G. F. (1997), *Computational Grids: Generations, Adaptation, and Solution Strategies*, Taylor & Francis, Washington, DC.
- Carlson, D. R., Widnall, S. E., and Peeters, M. F. (1982), “A Flow-Visualization Study of Transition in Plane Poiseuille Flow,” *Journal of Fluid Mechanics*, vol. 121, pp. 487–505. doi: <https://doi.org/10.1017/S0022112082002006>

- Carr, B., and Young, V. E. (1996), "Videotapes and Movies on Fluid Dynamics and Fluid Machines," in *Handbook of Fluid Dynamics and Fluid Machinery*, vol. II, J. A. Schetz and A. E. Fuhs (Eds.), Wiley, New York. doi: <https://doi.org/10.1002/9780470172643.ch17>Page 495
- Carslaw, H. S., and Jaeger, J. C. (1959), *Conduction of Heat in Solids*, 2nd ed., Clarendon, Oxford.
- Casalis, G., Avalon, G., and Pineau, J. P. (1998), "Spatial Instability of Planar Channel Flow with Fluid Injection through Porous Walls," *Physics of Fluids*, vol. 10, no. 10, pp. 2558–2568. doi: <https://doi.org/10.1063/1.869770>
- Cassel, K. W., Rubin, A. I., and Walker, J. D. A. (1996), "Influence of Wall Cooling on Hypersonic Boundary-Layer Separation and Stability," *Journal of Fluid Mechanics*, vol. 321, pp. 189–216. doi: <https://doi.org/10.1017/S0022112096007690>
- Caughey, D. A., and Hafez, M. M. (Eds.) (2004), *Frontiers of CFD 2002*, World Scientific, River Edge, NJ. doi: <https://doi.org/10.1142/4887>
- Cebeci, T. (1984), "Problems and Opportunities with Three-Dimensional Boundary Layers," AGARD Report 719, Paper 6.
- (1988), *Physical and Computational Aspects of Convective Heat Transfer*, Springer, New York.
- (2003), *Modeling and Computation of Turbulent Flows*, Elsevier, New York.
- Cebeci, T. (Ed.) (1982), *Numerical and Physical Aspects of Aerodynamic Flows*, Springer-Verlag, New York.
- Cebeci, T., and Cousteix, J. (1998), *Modeling and Computation of Boundary-Layer Flows*, Horizons, Long Beach, CA.
- Cebeci, T., and Smith, A. M. O. (1974), *Analysis of Turbulent Boundary Layers*, Academic, New York.
- CECAM (2004), "Dynamics of Fluids at Interfaces," European Centre for Atomic and Molecular Computations, CECAM, Lyon, France, July 26–29.
- Cecil, O. M., and Majdalani, J., "Convergence of Two Internal Mean Flow Solutions for Spinning Rocket Motors," *AIAA Journal*, vol. 57, no. 12, December 2019, pp. 5339–5350. doi: <https://doi.org/10.2514/1.J058620>
- Cecil, O., and Majdalani, J. (2017), "The Taylor-Culick Profile for Spinning Rocket Motors," 53rd AIAA/SAE/ASEE Joint Propulsion Conference, AIAA Paper 2017-4779, July 10–12. doi: <https://doi.org/10.2514/6.2017-4779>
- Cercignani, C. (2000), *Rarefied Gas Dynamics*, Cambridge University Press, New York.
- Chandrasekhar, S. (1961), *Hydrodynamic and Hydromagnetic Stability*, Oxford University Press, London.

- Chang, M. W., and Findlayson, B. A. (1987), "Heat Transfer in Flow Past Cylinders at $Re < 150$: Part 1, Calculations for Constant Fluid Properties," *Numerical Heat Transfer*, vol. 12, no. 2, pp. 179–195. doi: <https://doi.org/10.1080/10407788708913580>
- Chapman, D. R., and Rubesin, M. W. (1949), "Temperature and Velocity Profiles in the Compressible Laminar Boundary Layer with Arbitrary Distribution of Surface Temperature," *Journal of the Aeronautical Sciences*, vol. 16, no. 9, pp. 547–565. doi: https://doi.org/10.1007/978-3-319-14373-6_7
- Chapman, D. R., and Kester, R. H. (1953), "Measurements of Turbulent Skin Friction on Cylinders in Axial Flow at Subsonic and Supersonic Velocities," *Journal of the Aeronautical Sciences*, vol. 20, no. 7, pp. 441–448. doi: <https://doi.org/10.2514/8.2685>
- Chapman, S., and Cowling, T. G. (1970), *The Mathematical Theory of Nonuniform Gases*, 3rd ed., Cambridge University Press, London.
- Charbeneau, R. J. (1999), *Groundwater Hydraulics and Pollutant Transport*, Prentice-Hall, Upper Saddle River, NJ.
- Chattot, J. J. (2002), *Computational Aerodynamics and Fluid Dynamics*, Springer, New York.
- Chedevergne, F., Casalis, G., and Féraïlle, T. (2006), "Biglobal Linear Stability Analysis of the Flow Induced by Wall Injection," *Physics of Fluids*, vol. 18, no. 1, pp. 014103-1 - 014103-14. doi: <https://doi.org/10.1063/1.2160524>
- Chedevergne, F., Casalis, G., and Majdalani, J. (2012), "Direct Numerical Simulation and Biglobal Stability Investigations of the Gaseous Motion in Solid Rocket Motors," *Journal of Fluid Mechanics*, vol. 706, pp. 190–218. doi: <https://doi.org/10.1017/jfm.2012.245>
- Chen, C.-J., and Jaw, S.-Y. (1997), *Fundamentals of Turbulence Modeling*, Taylor & Francis, Washington, DC.
- Chesnakas, C. J., and Simpson, R. L. (1997), "Detailed Investigation of the Three-Dimensional Separation about a 6:1 Prolate Spheroid," *AIAA Journal*, vol. 35, no. 6, pp. 990–999. doi: <https://doi.org/10.2514/2.208>
- Chevray, R. (1989), "Chaos and the Onset of Turbulence," in W. K. George and R. Arndt (Eds.), *Advances in Turbulence*, pp. 127–158, Hemisphere, New York.
- Choi, C-H., Westin, K. J. A., and Breuer, K. S. (2003), "Apparent Slip Flows in Hydrophilic and Hydrophobic Microchannels," *Physics of Fluids*, vol. 15, no. 10, pp. 2897–2902. doi: <https://doi.org/10.1063/1.1605425>
- Chomaz, J.-M. (2005), "Global Instabilities in Spatially Developing Flows: Non-Normality and Nonlinearity," *Annual Review of Fluid Mechanics*, vol. 37, no. 1, pp. 357–392. doi: <https://doi.org/10.1146/annurev.fluid.37.061903.175810>
- Chung, T. J. (2002), *Computational Fluid Dynamics*, Cambridge University Press, New York.

- Churchill, S. W. (1988), *Viscous Flows—The Practical Use of Theory*, Butterworth, Stoneham, MA.
- Churchill, S. W., and Ozoe, H. (1973), "A Correlation for Laminar Free Convection from a Vertical Plate," *Journal of Heat Transfer*, vol. 95, no. 4, pp. 540–541. doi: <https://doi.org/10.1115/1.3450105>
- Churchill, S. W., and Chu, H. S. (1975), "Correlating Equations for Laminar and Turbulent Free Convection from a Vertical Plate," *International Journal of Heat and Mass Transfer*, vol. 18, no. 11, pp. 1323–1329. doi: [https://doi.org/10.1016/0017-9310\(75\)90243-4](https://doi.org/10.1016/0017-9310(75)90243-4)
- Churchill, S. W., and Usagi, R. (1972), "A General Expression for the Correlation of Rates of Transfer and Other Phenomena," *AIChE Journal*, vol. 18, no. 6, pp. 1121–1128. doi: <https://doi.org/10.1002/aic.690180606>
- Clauser, F. H. (1954), "Turbulent Boundary Layers in Adverse Pressure Gradients," *Journal of the Aeronautical Sciences*, vol. 21, no. 2, pp. 91–108. doi: <https://doi.org/10.2514/8.2938>
- (1956), "The Turbulent Boundary Layer," *Advances in Applied Mechanics*, vol. 4, pp. 1–15, Academic, New York.
- Clift, R., Grace, J. R., and Weber, M. E. (1978), *Bubbles, Drops, and Particles*, Academic, New York.
- Cochran, W. G. (1934), "The Flow Due to a Rotating Disk," *Proceedings of the Cambridge Philosophical Society*, vol. 30, no. 3, pp. 365–375. doi: <https://doi.org/10.1017/S0305004100012561>
- Cohen, C. B., and Reshotko, E. (1956), "Similarity Solutions for the Compressible Laminar Boundary Layer with Heat Transfer and Arbitrary Pressure Gradient," NACA Report 1293 [see also NACA Report 1294].
- Cole, J. D., and Aroesty, J. (1968), "The Blowhard Problem-Inviscid Flows with Surface Injection," *International Journal of Heat and Mass Transfer*, vol. 11, no. 7, pp. 1167–1183. doi: [https://doi.org/10.1016/0017-9310\(68\)90033-1](https://doi.org/10.1016/0017-9310(68)90033-1)
- Coles, D. E. (1954), "Measurements of Turbulent Friction on a Smooth Flat Plate in Supersonic Flow," *Journal of the Aeronautical Sciences*, vol. 21, no. 7, pp. 433–448. doi: <https://doi.org/10.2514/8.3083>
- (1956), "The Law of the Wake in the Turbulent Boundary Layer," *Journal of Fluid Mechanics*, vol. 1, no. 2, pp. 191–226.
- (1965), "Transition in Circular Couette Flow," *Journal of Fluid Mechanics*, vol. 21, no. 3, pp. 385–425. doi: <https://doi.org/10.1017/S0022112065000241>
- Coles, D. E., and Hirst, E. A. (1968), "Computation of Turbulent Boundary Layers—1968 AFOSR-IFP Stanford Conference," vol. 2, Stanford University, Stanford, CA. Page 496

- Comini, G., and Sunder, B. (Eds.) (2000), *Computational Analysis of Convective Heat Transfer*, WIT Press/Computational Mechanics, Bosto, MA.
- Constantin, P., and Foias, C. (1988), *Navier–Stokes Equations*, The University of Chicago Press, Chicago.
- Constantinescu, G. S., et al. (2002), “Numerical Investigation of Flow Past a Prolate Spheroid,” *Journal of Fluids Engineering*, vol. 124, no. 4, pp. 904–910. doi: <https://doi.org/10.1115/1.1518700>
- Constantinescu, V. N. (1995), *Laminar Viscous Flow*, Spring-Verlag, New York. doi: <https://doi.org/10.1007/978-1-4612-4244-4>
- Corrsin, S., and Kistler, A. L. (1955), “Freestream Boundaries of Turbulent Flows,” NACA Report 1244.
- Cortell, R. (2005), “Numerical Solutions of the Classical Blasius Flat-Plate Problem,” *Applied Mathematics and Computation*, vol. 170, no. 1, pp. 706–710. doi: <https://doi.org/10.1016/j.amc.2004.12.037>
- Cottet, G.-H., and Koumoutsakos, P. D. (1999), *Vortex Methods: Theory and Practice*, Cambridge University Press, New York. doi: <https://doi.org/10.1017/CBO9780511526442>
- Couette, M. (1890), “Etudes sur le frottement des liquides,” *Ann. Chim. Phys.*, ser. 6, vol. 21, pp. 433–510.
- Cousteix, J. (1986), “Three-Dimensional and Unsteady Boundary-Layer Computations,” *Annual Review of Fluid Mechanics*, vol. 18, pp. 173–196. doi: <https://doi.org/10.1146/annurev.fl.18.010186.001133>
- Craft, T. J., Gerasimov, A. V., Iacovides, H., and Launder, B. E. (2002), “Progress in the Generalization of Wall-Function Treatments,” *International Journal of Heat and Fluid Flow*, vol. 23, no. 2, pp. 148–160. doi: [https://doi.org/10.1016/S0142-727X\(01\)00143-6](https://doi.org/10.1016/S0142-727X(01)00143-6)
- Cox, S. M. (1991), “Two-Dimensional Flow of a Viscous Fluid in a Channel with Porous Walls,” *Journal of Fluid Mechanics*, vol. 227, no. 1, pp. 1–33. doi: <https://doi.org/10.1017/S0022112091000010>
- Cox, S. M., and King, A. C. (1997), “On the Asymptotic Solution of a High-Order Nonlinear Ordinary Differential Equation,” *Proceedings of the Royal Society of London, Series A: Mathematical, Physical and Engineering Sciences*, vol. 453, no. 1959, pp. 711–728. doi: <https://doi.org/10.1098/rspa.1997.0040>
- Cox, S. M., and King, J. R. (2004), “Large-Reynolds-Number Asymptotics of the Berman Problem,” *Studies in Applied Mathematics*, vol. 113, no. 3, pp. 217–243. doi: <https://doi.org/10.1111/j.0022-2526.2004.01512.x>
- Craik, A. D. D. (1971), “Non-linear Resonant Instability in Boundary Layers,” *Journal of Fluid Mechanics*, vol. 50, pp. 393–413. doi:

<https://doi.org/10.1017/S0022112071002635>

- Crank, J., and Nicolson, P. (1947), “A Practical Method for Numerical Evaluation of Solutions of Partial Differential Equations of the Heat-Conduction Type,” *Proceedings of the Cambridge Philosophical Society*, vol. 43, no. 1, pp. 50–67. doi: <https://doi.org/10.1017/S0305004100023197>
- Crocco, L. (1932), “Sulla trasmissione del calore da una lamina piana a un fluido scorrente ad alta velocita,” *L’Aerotecnica*, vol. 12, pp. 181–197 [translated as NACA Technical Memo. 690].
- Crolet, J. M. (Ed.) (2000), *Computational Methods for Flow and Transport in Porous Media*, Springer Netherlands. doi: <https://doi.org/10.1007/978-94-017-1114-2>
- Cruz, D. O. A., and Silva-Freire, A. P. (2002), “Note on a Thermal Law of the Wall for Separating and Recirculating Flows,” *International Journal of Heat and Mass Transfer*, vol. 45, no. 7, pp. 1459–1465. doi: [https://doi.org/10.1016/S0017-9310\(01\)00232-0](https://doi.org/10.1016/S0017-9310(01)00232-0)
- Culick, F. E. C. (1966), “Rotational Axisymmetric Mean Flow and Damping of Acoustic Waves in a Solid Propellant Rocket,” *AIAA Journal*, vol. 4, no. 8, pp. 1462–1464. doi: <https://doi.org/10.2514/3.3709>
- Cunningham, W. J. (1963), “The Concept of Stability,” *American Scientist*, vol. 51, no. 4, pp. 425–436. <https://www.jstor.org/stable/27838846>
- Curle, N. (1958), “Accurate Solutions of the Laminar Boundary Layer Equations, for Flows Having a Stagnation Point and Separation,” *Aeronautical Research Council, R & M* 3164.
- Currie, I. G. (1993), *Fundamental Mechanics of Fluids*, 2nd ed., McGraw-Hill, New York.
- Darcy, H. P. G. (1856), *Les fontaines publiques de la ville de Dijon*, Victor Dalmont, Paris.
- Das, D. K. (1987), “A Numerical Study of Turbulent Separated Flows,” *American Society of Mechanical Engineers Forum on Turbulent Flows*, FED vol. 51, pp. 85–90.
- (1988), “A Simple Theory for Calculating Turbulent Boundary Layers under Arbitrary Pressure Gradients,” *International Journal of Fluids Engineering*, vol. 1, no. 1, pp. 83–99.
- Das, D. K., and White, F. M. (1986), “Integral Skin Friction Prediction for Turbulent Separated Flows,” *Journal of Fluids Engineering*, vol. 108, no. 4, pp. 476–482. doi: <https://doi.org/10.1115/1.3242606>
- Dauenhauer, E. C., and Majdalani, J. (2003), “Exact Self-Similarity Solution of the Navier–Stokes Equations for a Porous Channel with Orthogonally Moving Walls,” *Physics of Fluids*, vol. 15, no. 6, pp. 1485–1495. doi: <https://doi.org/10.1063/1.1567719>
- Davis, S. H. (1976), “The Stability of Time-Periodic Flows,” *Annual Review of Fluid Mechanics*, vol. 8, pp. 57–74. doi: <https://doi.org/10.1146/annurev.fl.08.010176.000421>

- (1987), “Thermocapillary Instabilities,” *Annual Review of Fluid Mechanics*, vol. 19, pp. 403–435. doi: <https://doi.org/10.1146/annurev.fl.19.010187.002155>
- Debnath, L., and Riahi, D. N. (Eds.) (2000), *Nonlinear Instability, Chaos, and Turbulence*, vol. 2 of *Advances in Fluid Mechanics*, WIT Press/Computational Mechanics, Boston.
- Defant, A. (1961), *Physical Oceanography*, vols. 1–2, Pergamon, New York.
- Delery, J. M., and Marvin, J. G., and Reshotko, E. (1986), “Shock-Wave Boundary Layer Interaction,” AGARD-AG-280.
- Denn, M. M. (2001), “Extrusion Instabilities and Wall Slip,” *Annual Review of Fluid Mechanics*, vol. 33, pp. 265–287. doi: <https://doi.org/10.1146/annurev.fluid.33.1.265>
- Dennis, S. R. C., and Dunwoody, J. (1966), “The Steady Flow of a Viscous Fluid Past a Flat Plate,” *Journal of Fluid Mechanics*, vol. 24, pp. 577–595. doi: <https://doi.org/10.1017/S0022112066000831>
- Devenport, W. J., and Schetz, J. A. (2002), Boundary Layer Applets, URL: <http://www.engapplets.vt.edu/fluids/>
- Dhawan, S., and Narasimha, R. (1958), “Some Properties of Boundary Layer Flow During Transition from Laminar to Turbulent Motion,” *Journal of Fluid Mechanics*, vol. 3, no. 4, pp. 418–436. doi: <https://doi.org/10.1017/S0022112058000094>
- Dimas, A. A., Collins, J. P., and Bernard, P. S. (1998), “Fast Parallel Vortex Method for Turbulent Flow Simulation”, Paper FEDSM98–5000, ASME 1998 Fluids Eng. Conf., Washington, D.C.
- Donaldson, C. (1956), “Solutions of the Navier–Stokes Equations for Two and Three-dimensional Vortices,” Ph.D. dissertation, Princeton University.
- Dorrance, W. H. (1962), *Viscous Hypersonic Flow: Theory of Reacting and Hypersonic Boundary Layers*, McGraw-Hill, New York. Page 497
- Drazin, P. G. (2002), *Introduction to Hydrodynamic Stability*, Cambridge University Press, New York. doi: <https://doi.org/10.1017/CBO9780511809064>
- Drazin, P. G., and Reid, W. H. (2004), *Hydrodynamic Stability*, 2nd ed., Cambridge University Press, New York, NY. doi: <https://doi.org/10.1017/CBO9780511616938>
- Drazin, P. G., and Riley, N. (2006), *The Navier–Stokes Equations: A Classification of Flows and Exact Solutions*, *London Mathematical Society Lecture Note Series*, Cambridge University Press, Cambridge. doi: <https://doi.org/10.1017/CBO9780511526459>
- Drazin, P. G., and Reid, W. H. (1981), *Hydrodynamic Stability*, Cambridge University Press, London.
- Dresner, L. (1983), *Similarity Solutions of Nonlinear Partial Differential Equations*, Pitman Advanced Pub. Program, Boston, MA.
- Dryden, H. L. (1934), “Boundary Layer Flow Near Flat Plates,” *Proceedings of the Fourth*

International Congress of Applied Mechanics, p. 175, Cambridge University Press, London.

- (1953), “Review of Published Data on the Effect of Roughness on Transition from Laminar to Turbulent Flow,” *Journal of the Aeronautical Sciences*, vol. 20, pp. 477–482. doi: <https://doi.org/10.2514/8.2693>
- Dunham, J. (1972), “Prediction of Boundary Layer Transition on Turbomachinery Blades,” AGARD Meeting on Boundary Layers in Turbomachines.
- Dunn, D. W., and Lin, C. C. (1955), “On the Stability of the Laminar Boundary Layer in a Compressible Fluid,” *Journal of the Aeronautical Sciences*, vol. 22, pp. 455–477. doi: <https://doi.org/10.2514/8.3374>
- Durbin, O. A., and Pettersson, R. B. A. (2001), *Statistical Theory and Modeling for Turbulent Flows*, Wiley, New York.
- Durbin, P. A. (1995), “Separated Flow Computations with the k - ϵ -v2 Model,” *AIAA Journal*, vol. 33, pp. 659–664. doi: <https://doi.org/10.2514/3.12628>
- Durst, F. (1992), *Principles and Practice of Laser-Doppler Anemometry*, 2nd ed., Academic, New York.
- Dwoyer, D. L., and Hussaini, M. Y. (Eds.) (1987), *Stability of Time Dependent and Spatially Varying Flows*, Springer, New York.
- Dwyer, H. A. (1981), “Some Aspects of Three-Dimensional Laminar Boundary Layers,” *Annual Review of Fluid Mechanics*, vol. 13, pp. 217–229. doi: <https://doi.org/10.1146/annurev.fl.13.010181.001245>
- Dyck, N. J., and Straatman, A. G. (2019), “Exact Solutions to the Three-Dimensional Navier–Stokes Equations Using the Extended Beltrami Method,” *Journal of Applied Mechanics*, vol. 87, no. 1. doi: <https://doi.org/10.1115/1.4044927>
- Ebaid, A., and Al-Armani, N. (2013), “A New Approach for a Class of the Blasius Problem Via a Transformation and Adomian’s Method,” *Abstract and Applied Analysis*, vol. 2013, p. 8. doi: <https://doi.org/10.1155/2013/753049>
- Eckert, E. R. G. (1942), “Die Berechnung des Wärmeübergangs in der laminaren Grenzschicht,” *Forsch. Ver. Deutsch. Ing.*, vol. 416, pp. 1–23.
- (1955), “Engineering Relations for Friction and Heat Transfer to Surfaces in High Velocity Flow,” *Journal of the Aeronautical Sciences*, vol. 22, pp. 585–587.
- Eckert, E. R. G., and Drake, Jr., R. M. (1972), *Analysis of Heat and Mass Transfer*, McGraw-Hill, New York.
- Eckert, E. R. G., and Irvine, Jr., T. F. (1957), “Incompressible Friction Factor, Transition and Hydrodynamic Entrance Length Studies of Ducts with Triangular and Rectangular Cross Sections,” *Proceedings of the Fifth Midwestern Conference on Fluid Mechanics*, pp. 122–145, University of Michigan Press, Ann Arbor, MI.

- Eckert, E. R. G., Donoughe, P. L., and Moore, B. J. (1957), "Velocity and Friction Characteristics of Laminar Viscous Boundary Layer and Channel Flow over Surfaces with Ejection and Suction," NACA Technical Note 4102.
- Ehlers, W., and Bluhm, J. (Eds.) (2002), *Porous Media*, Springer-Verlag, New York.
- Eichelbrenner, E. A. (1973), "Three-Dimensional Boundary Layers," *Annual Review of Fluid Mechanics*, vol. 5, pp. 339–360. doi: <https://doi.org/10.1146/annurev.fl.05.010173.002011>
- Elghobashi, S. (2019), "Direct Numerical Simulation of Turbulent Flows Laden with Droplets or Bubbles," *Annual Review of Fluid Mechanics*, vol. 51, no. 1, pp. 217–244. doi: <https://doi.org/10.1146/annurev-fluid-010518-040401>
- Elliott, T. S., and Gibson, W. A., "Stability Analysis of the Swirling Majdalani-Fist Mean Flowfield in Solid Rocket Motors," *AIAA Journal*, vol. 57, no. 12, December 2019, pp. 5331–5338. doi: <https://doi.org/10.2514/1.J058568>
- Ekman, V. W. (1905), "On the Influence of the Earth Rotation on Ocean Currents," *Arkiv for Matematik, Astronomi, och Fysik*, bd. 2, no. 11, pp. 1–53.
- Emmons, H. W. (1951), "The Laminar-Turbulent Transition in a Boundary Layer: Part I," *Journal of the Aeronautical Sciences*, vol. 18, pp. 490–498. doi: <https://doi.org/10.2514/8.2010>
- (1970), "Critique of Numerical Modeling of Fluid-Mechanics Phenomena," *Annual Review of Fluid Mechanics*, vol. 2, pp. 15–36. doi: <https://doi.org/10.1146/annurev.fl.02.010170.000311>
- Engquist, B., and Rizzi, A. (2004), *Computational Fluid Dynamics*, Cambridge University Press, New York.
- Esmaeilpour, M., and Ganji, D. D. (2007), "Application of He's Homotopy Perturbation Method to Boundary Layer Flow and Convection Heat Transfer over a Flat Plate," *Physics Letters A*, vol. 372, no. 1, pp. 33–38. doi: <https://doi.org/10.1016/j.physleta.2007.07.002>
- Eucken, A. (1913), "Über das Wärmeleitvermögen, die spezifische Wärme und die innere Reibung der Gase (Concerning the Thermal Conductivity, Specific Heat, and Viscosity of Gases)," *Physikalische Zeitschrift*, vol. 14, no. 3, pp. 324–332.
- Evans, H. (1968), *Laminar Boundary Layers*, Addison-Wesley, Reading, Mass.
- Fabignon, Y., Dupays, J., Avalon, G., Vuillot, F., Lupoglazoff, N., Casalis, G., and Prévost, M. (2003), "Instabilities and Pressure Oscillations in Solid Rocket Motors," *Journal of Aerospace Science and Technology*, vol. 7, no. 3, pp. 191–200. doi: [https://doi.org/10.1016/S1270-9638\(02\)01194-X](https://doi.org/10.1016/S1270-9638(02)01194-X)
- Fage, A. (1936), "Experiments on a Sphere at Critical Reynolds Numbers," *Aeronautical Research Council*, R & M 1766.

- Falkner, V. M., and Skan, S. W. (1931), “Some Approximate Solutions of the Boundary Layer Equations,” *Philosophical Magazine*, vol. 12, no. 7, pp. 865–896 [see also *Aeronautical Research Council*, R & M 1314, 1930]. doi: <https://doi.org/10.1080/14786443109461870>
- Falkner, V. M. (1936), “A Method of Numerical Solution of Differential Equations,” *Philosophical Magazine*, vol. 21, no. 141, pp. 624–640. doi: <https://doi.org/10.1080/14786443608561611>
- Fang, T., Liang, W., and Lee, C. F. (2008), “A New Solution Branch for the Blasius Equation —A Shrinking Sheet Problem,” *Computers & Mathematics with Applications*, vol. 56, no. 12, pp. 3088–3095. doi: <https://doi.org/10.1016/j.camwa.2008.07.027>
- Faraco-Medeiros, M.A., and Silva-Freire, A. P. (1992), “Transfer of Heat in Turbulent Boundary Layers with Injection or Suction: Universal Laws and Stanton Number Equations,” *International Journal of Heat and Mass Transfer*, vol. 35, no. 4, pp. 991–995. doi: [https://doi.org/10.1016/0017-9310\(92\)90264-S](https://doi.org/10.1016/0017-9310(92)90264-S)
- Favre, A. (1965), “Equations des Gaz Turbulents Compressibles,” *Journal de Mecanique*, vol. 4, pp. 361–421.
- (1995), *Chaos and Determinism: Turbulence as a Paradigm for Complex Systems Converging Toward Final States*, Johns Hopkins University Press, Baltimore, MD. Page 498
- Fay, J. A., and Riddell, F. R. (1958), “Theory of Stagnation Point Heat Transfer in Dissociated Air,” *Journal of the Aeronautical Sciences*, vol. 25, pp. 73–85. doi: <https://doi.org/10.2514/8.7517>
- Fazio, R. (1992), “The Blasius Problem Formulated as a Free-Boundary Value-Problem,” *Acta Mechanica*, vol. 95, pp. 1–7. doi: <https://doi.org/10.1007/BF01170800>
- Fazio, R. (2019), “The Non-Iterative Transformation Method,” *International Journal of Non-Linear Mechanics*, vol. 114, pp. 41–48. doi: <https://doi.org/10.1016/j.ijnonlinmec.2019.04.008>
- Fedorov, A. (2011), “Transition and Stability of High-Speed Boundary Layers,” *Annual Review of Fluid Mechanics*, vol. 43, no. 1, pp. 79–95. doi: <https://doi.org/10.1146/annurev-fluid-122109-160750>
- Felcman, J., Straskraba, I., and Feistauer, M. (2003), *Mathematical and Computational Methods for Compressible Flow*, Oxford University Press, New York.
- Feng, Z-G., and Michaelides, E. E. (2001), “Drag Coefficients of Viscous Spheres at Intermediate and High Reynolds Numbers,” *Journal of Fluids Engineering*, vol. 123, pp. 841–849. doi: <https://doi.org/10.1115/1.1412458>
- Fernholz, H. H., and Krause, E. (Eds.) (1982), *Three-Dimensional Turbulent Boundary Layers*, Springer, Berlin.

- Fernholz, H. H., and Finley, P. J. (1980), "A Critical Commentary on Mean Flow Data for Two-Dimensional Compressible Turbulent Boundary Layers," AGARDograph 253 [see also AGARDographs 223 and 263].
- (1996), "Incompressible Zero-Pressure-Gradient Turbulent Boundary Layer: An Assessment of the Data," *Prog. Aerosp. Sci.*, vol. 32, no. 4, pp. 245–311. doi: [https://doi.org/10.1016/0376-0421\(95\)00007-0](https://doi.org/10.1016/0376-0421(95)00007-0)
- Ferziger, J. H. (1998), *Numerical Methods for Engineering Application*, 2nd ed., Wiley, New York.
- Ferziger, J. H., Lyrio, A. A., and Bardina, J. C. (1982), "New Skin Friction and Entrainment Correlations for Turbulent Boundary Layers," *Journal of Fluids Engineering*, vol. 104, pp. 537–540. doi: <https://doi.org/10.1115/1.3241902>
- Ferziger, J. H., and Peric, M. (2001), *Computational Methods for Fluid Dynamics*, Springer, New York.
- Fist, A., and Majdalani, J. (2017), "On the Swirling Trkalian Mean Flow Field in Solid Rocket Motors," *Journal of Fluid Mechanics*, vol. 824, pp. 265–285. doi: <https://doi.org/10.1017/jfm.2017.342>
- Fjørtoft, R. (1950), "Application of Integral Theorems in Deriving Criteria of Stability for Laminar Flows and for the Baroclinic Circular Vortex," *Geofysiske Publikasjoner Oslo*, vol. 17, no. 6, pp. 1–52.
- Flachsbart, O. (1932), "Winddruck auf Gasbehälter," AVA Reports, Göttingen, series IV, pp. 134–138.
- Frankl, F. I. (1934), "The Theory of the Laminar Boundary Layer in Compressible Gases," *Transactions from Central Aero-Hydrodynamical Institute, Moscow*, no. 176.
- Freitas, C. J. (1995), "Perspective: Selected Benchmarks from Commercial CFD Codes," *Journal of Fluids Engineering*, vol. 117, June, pp. 208–218. doi: <https://doi.org/10.1115/1.2817132>
- Friedrichs, K. O. (1942), "Theory of Viscous Fluid," in *Fluid Dynamics*, ch. 4, Brown University Press, Providence, RI.
- Fulford, G. D. (1964), "The Flow of Liquids in Thin Films," *Advances in Chemical Engineering*, vol. 5, pp. 151–236. doi: [https://doi.org/10.1016/S0065-2377\(08\)60008-3](https://doi.org/10.1016/S0065-2377(08)60008-3)
- Gad-el-Hak, M. (1996), "Modern Developments in Flow Control," *Applied Mechanics Reviews*, vol. 49, July, pp. 365–380. doi: <https://doi.org/10.1115/1.3101931>
- Gad-el-Hak, M. (Ed.) (2001), *The MEMS Handbook (Mechanical Engineering)*, CRC Press, Boca Raton, Fl.
- Galbraith, R. A. McD., Sjolander, S. A., and Head, M. R. (1977), "Mixing Length in the Wall Region of Turbulent Boundary Layers," *Aeronautical Quarterly*, vol. 27, pt. 2, pp. 97–110. doi: <https://doi.org/10.1017/S0001925900008003>

- Garg, S., and Settles, G. S. (1998), "Measurements of a Supersonic Turbulent Boundary Layer by Focusing Schlieren Deflectometry," *Experiments in Fluids*, vol. 25, no. 3, pp. 254–264. doi: <https://doi.org/10.1007/s003480050228>
- Garg, V. K. (Ed.) (1998), *Applied Computational Fluid Dynamics*, Marcel Dekker, New York.
- Gaster, M. (1962), "A Note on the Relation Between Temporally-Increasing and Spatially-Increasing Disturbances in Hydrodynamics Stability," *Journal of Fluid Mechanics*, vol. 14, pp. 222–224. doi: <https://doi.org/10.1017/S0022112062001184>
- Gazanion, B., Chedevergne, F., and Casalis, G. (2014), "On the Laminar-Turbulent Transition in Injection-Driven Porous Chambers," *Experiments in Fluids*, vol. 55, no. 1. doi: <https://doi.org/10.1007/s00348-013-1643-y>
- Gazley, C., Jr., and Wazzan, A. R. (1984), "Control of Water Boundary Layer Stability and Transition by Surface Temperature Distributions," in V. V. Kozlov (Ed.), *Laminar-Turbulent Transition*, Springer, New York.
- Gebhart, B. (1969), "External Natural Convection Flow," *Applied Mechanics Reviews*, vol. 22, pp. 691–701.
- Gebhart, B., and Majahan, R. L. (1982), "Instability and Transition in Buoyancy-Induced Flows," *Advances in Applied Mechanics*, vol. 22, pp. 231–315. doi: [https://doi.org/10.1016/S0065-2156\(08\)70067-X](https://doi.org/10.1016/S0065-2156(08)70067-X)
- Gebhart, B., Jaluria, Y., Mahajan, R. L., and Sammakia, B. (1988), *Buoyancy-Induced Flows and Transport*, Hemisphere, New York.
- George, W. K. (1989), "The Self-Preservation of Turbulent Flows and Its Relation to Initial Conditions and Coherent Structures," in W. K. George and R. Arndt (Eds.), *Advances in Turbulence*, pp. 39–73, Hemisphere, New York.
- George, W. K., and Castillo, L. (1997), "Zero Pressure Gradient Turbulent Boundary Layer," *Applied Mechanics Reviews*, vol. 50, no. 12, pp. 689–729. doi: <https://doi.org/10.1115/1.3101858>
- Gersten, K. (1959), "Corner Interference Effects," AGARD Report 299.
- Geurts, B. (2003), *Elements of Direct and Large Eddy Simulation*, R. T. Edwards, Flourtown, Penn.
- Gibbings, J. C. (1959), "On Boundary Layer Transition Wires," Aeronautical Research Council, CP-462.
- Giedt, W. H. (1949), "Investigation of Variation of Point Unit Heat Transfer Coefficient around a Cylinder Normal to an Air Stream," *ASME Transactions*, vol. 71, pp. 375–381.
- Glauert, M. B. (1956), "The Wall Jet," *Journal of Fluid Mechanics*, vol. 1, pp. 625–643. doi: <https://doi.org/10.1017/S002211205600041X>

- Glauert, M. B., and Lighthill, M. J. (1955), "The Axisymmetric Boundary Layer on a Long Thin Cylinder," *Proceedings of the Royal Society of London, Series A*, vol. 230, pp. 188–203. doi: <https://doi.org/10.1098/rspa.1955.0121>
- Godrèche, C., and Manneville, P. (Eds.) (1998), *Hydrodynamics and Nonlinear Instabilities*, Oxford University Press, New York.
- Goldberg, P. (1958), "A Digital Computer Solution for Laminar Flow Heat Transfer in Circular Tubes," M.S. thesis, Mech. Engineering Dept., M.I.T., Cambridge, MA.
- Goldstein, R. J. (Ed.) (1996), *Fluid Mechanics Measurements*, 2nd ed., Taylor & Francis, Washington, DC. Page 499
- Goldstein, S. (1930), "Concerning Some Solutions of the Boundary Layer Equations in Hydrodynamics," *Proceedings of the Cambridge Philosophical Society*, vol. 26, pp. 1–30. doi: <https://doi.org/10.1017/S0305004100014997>
- (1938), *Modern Developments in Fluid Dynamics*, vols. 1–2, Oxford University Press, London.
- (1948), "On Laminar Boundary Layer Flow Near a Position of Separation," *Quarterly Journal of Mechanics and Applied Mathematics*, vol. 1, pp. 43–69. doi: <https://doi.org/10.1093/qjmam/1.1.43>.
- Görtler, H. (1942), "Berechnung von Aufgaben der freien Turbulenz auf Grund eines neuen Näherungsansatzes," *Journal of Applied Mathematics and Mechanics (ZAMM)*, vol. 22, pp. 244–254. doi: <https://doi.org/10.1002/zamm.19420220503>
- (1955), "Dreidimensionales zur Stabilitätstheorie Laminarer Grenzschichten," *Journal of Applied Mathematics and Mechanics (ZAMM)*, vol. 35, pp. 362–363.
- (1957), "A New Series for the Calculation of Steady Laminar Boundary Layer Flows," *Journal of Mathematics and Mechanics*, vol. 6, pp. 1–66. <https://www.jstor.org/stable/24900611>
- Graetz, L. (1883), "Über die Wärmeleitungsfähigkeit von Flüssigkeiten," *Annalen der Physik*, pt. 1, vol. 18, pp. 79–94; pt. 2, vol. 25, pp. 337–357.
- Granville, P. S. (1953), "The Calculation of the Viscous Drag of Bodies of Revolution," David Taylor Model Basin Report 849.
- (1987), "Baldwin–Lomax Factors for Turbulent Boundary Layers in Pressure Gradients," *AIAA Journal*, vol. 25, no. 12, pp. 1624–1627. doi: <https://doi.org/10.2514/3.9834>
- (1989), "A Modified Van Driest Formula for the Mixing Length of Turbulent Boundary Layers in Pressure Gradients," *Journal of Fluids Engineering*, vol. 111, pp. 94–97. doi: <https://doi.org/10.1115/1.3243606>
- Greenwood, D. T. (1988), *Principles of Dynamics*, 2nd ed., Prentice-Hall, Englewood Cliffs, NJ.

- Grégoire, G., Favre-Marinet, M., and Julien Saint Amand, F. (2003), "Modeling of Turbulent Fluid Flow over a Rough Wall with or without Suction," *Journal of Fluids Engineering*, vol. 125, pp. 636–642. doi: <https://doi.org/10.1115/1.1593705>
- Gregory, N., J. T. Stuart, and Walker, W. S. (1955), "On the Stability of Three-Dimensional Boundary Layers with Application to the Flow Due to a Rotating Disc," *Philosophical Transactions of the Royal Society of London, Series A*, vol. 248, pp. 155–199. doi: <https://doi.org/10.1098/rsta.1955.0013>
- Griffond, J., and Casalis, G. (2001), "On the Nonparallel Stability of the Injection Induced Two-Dimensional Taylor Flow," *Physics of Fluids*, vol. 13, no. 6, pp. 1635–1644. doi: <https://doi.org/10.1063/1.1367869>
- Griffond, J., Casalis, G., and Pineau, J. P. (2000), "Spatial Instability of Flow in a Semiinfinite Cylinder with Fluid Injection through Its Porous Walls," *European Journal of Mechanics – B/Fluids*, vol. 19, no. 1, pp. 69–87. doi: [https://doi.org/10.1016/S0997-7546\(00\)00105-9](https://doi.org/10.1016/S0997-7546(00)00105-9)
- Gross, A., and Burchard, H. (2002), *Applied Turbulence in Marine Waters*, Springer-Verlag, New York.
- Grove, A. S., Shair, F. H., Petersen, E. E., and Acrivos, A. (1964), "An Experimental Investigation of the Steady Separated Flow Past a Circular Cylinder," *Journal of Fluid Mechanics*, vol. 19, pp. 60–80. doi: <https://doi.org/10.1017/S0022112064000544>
- Gruschwitz, E. (1950), "Calcul approché de la couche limite laminaire en écoulement compressible sur une paroi nonconductrice de la chaleur," ONERA Pub. 47, Paris.
- Guo, B-Y, and Kuo, P.-Y. (1998), *Spectral Methods and Their Applications*, World Scientific, River Edge, NJ.
- Haaland, S. E. (1983), "Simple and Explicit Formulas for the Friction Factor in Turbulent Pipe Flow," *Journal of Fluids Engineering*, vol. 105, pp. 89–90. doi: <https://doi.org/10.1115/1.3240975>
- Hadamard, J. (1911), "Mouvement permanent lent d'une sphere liquide visqueuse dans un liquid visqueux," *C. R. Acad. Sci. Paris Sér. A–B*, vol. 152, pp. 1735–1739.
- Haddad, C. T., and Majdalani, J. (2013), "Transverse Waves in Simulated Liquid Rocket Engines," *AIAA Journal*, vol. 5, no. 3, pp. 591–605. doi: <https://doi.org/10.2514/1.J051912>
- Hadjiconstantinou, N. G. (2003), "Comment on Cercignani's Second-Order Slip Coefficient," *Physics of Fluids*, vol. 15, no. 8, pp. 2352–2354. doi: <https://doi.org/10.1063/1.1587155>
- Hagen, G. (1839), "Über die Bewegung des Wassers in engen zylinderschen Rohren," *Poggendorff's Ann. Phys. Chem.*, vol. 46, pp. 423–442.
- Haller, G. (2004), "Exact Theory of Unsteady Separation for Two-Dimensional Flows,"

Journal of Fluid Mechanics, vol. 512, pp. 257–311. doi: <https://doi.org/10.1017/S0022112004009929>

- Hamdan, M. H. (1998), “Alternative Approach to Exact Solutions of a Special Class of Navier–Stokes Flows,” *Applied Mathematics and Computation (New York)*, vol. 93, no. 1, pp. 83–90. doi: [https://doi.org/10.1016/S0096-3003\(97\)10047-9](https://doi.org/10.1016/S0096-3003(97)10047-9)
- Hamel, G. (1917), “Spiralförmige Bewegung zäher Flüssigkeiten,” *Jahresber. Deutsch. Math. Ver.*, vol. 25, pp. 34–60.
- Hanjalic, K. (1994), “Advanced Turbulence Closure Models: A View of Current Status and Future Prospects,” *International Journal of Heat and Fluid Flow*, vol. 15, pp. 178–203. doi: [https://doi.org/10.1016/0142-727X\(94\)90038-8](https://doi.org/10.1016/0142-727X(94)90038-8)
- Hanjalic, K., and Launder, B. E. (1972), “A Reynolds Stress Model of Turbulence and Its Application to Thin Shear Flows,” *Journal of Fluid Mechanics*, vol. 52, pp. 609–638. doi: <https://doi.org/10.1017/S002211207200268X>
- (1976), “Contribution Towards a Reynolds-Stress Closure for Low-Reynolds-Number Turbulence,” *Journal of Fluid Mechanics*, vol. 74, pt. 4, pp. 593–610. doi: <https://doi.org/10.1017/S0022112076001961>
- Hansen, A. G. (1964), *Similarity Analyses of Boundary Value Problems in Engineering*, Prentice-Hall, Englewood Cliffs, NJ.
- (1967), *Fluid Mechanics*, Wiley, New York.
- Hansen, C. F. (1958), “Approximations for Thermodynamic and Transport Properties of High Temperature Air,” NACA Technical Note 4150.
- Happel, J., and Brenner, H. (1983), *Low Reynolds Number Hydrodynamics*, 2nd ed., Prentice-Hall, Englewood Cliffs, NJ.
- (1983), *Low Reynolds Number Hydrodynamics: With Special Applications to Particulate Media*, Martinus Nijhoff, Boston.
- Harlow, F. H., and Welch, J. E. (1965), “Numerical Calculation of Time-Dependent Viscous Incompressible Flow of Fluid with Free Surface,” *Physics of Fluids*, vol. 8, pp. 2182–2189. doi: <https://doi.org/10.1063/1.1761178>
- Hartnett, J. P., and Eckert, E. R. G. (1957), “Mass Transfer Cooling in a Laminar Boundary Layer with Constant Properties,” *ASME Transactions*, vol. 79, pp. 247–254.
- Hartree, D. R. (1937), “On an Equation Occurring in Falkner and Skan’s Approximate Treatment of the Equations of the Boundary Layer,” *Proceedings of the Cambridge Philosophical Society*, vol. 33, pp. 223–239. doi: <https://doi.org/10.1017/S0305004100019575>
- (1939), “The Solution of the Equations of the Laminar Boundary Layer for Schubauer’s Observed Pressure Distribution for an Elliptic Cylinder,” *Aeronautical Research Council*, R & M 2427.

- Harvey, H. et al. (2014), *ASME International Steam Tables for Industrial Use*, 3d ed., ASME Press, New York. Page 500
- Hashim, I. (2006), “Comments on “a New Algorithm for Solving Classical Blasius Equation” by L. Wang,” *Applied Mathematics and Computation*, vol. 176, no. 2, pp. 700–703. doi: <https://doi.org/10.1016/j.amc.2005.10.016>
- Haskell, R. E. (2015), *Vectors and Tensors by Example*, CreateSpace.
- Hastings, S. P. (1972), “Reversed Flow Solutions of the Falkner–Skan Equation,” *SIAM Journal on Applied Mathematics*, vol. 22, no. 2, pp. 329–334. doi: <https://doi.org/10.1137/0122031>
- Hastings, S. P., Lu, C., and MacGillivray, A. D. (1992), “A Boundary Value Problem with Multiple Solutions from the Theory of Laminar Flow,” *SIAM Journal on Mathematical Analysis*, vol. 23, no. 1, pp. 201–208. doi: <https://doi.org/10.1137/0523010>
- Hausen, H. (1943), “Darstellung des Wärmeüberganges in Rohren durch verallgemeinerte Potenzbeziehungen,” *Z. VDI Beih. Verfahrenstech*, no. 4, p. 91.
- Hayes, W. D., and Probstein, R. F. (1959), *Hypersonic Flow Theory*, Academic, New York.
- He, J.-H. (1999c), “Variational Iteration Method – A Kind of Non-Linear Analytical Technique: Some Examples,” *International Journal of Non-Linear Mechanics*, vol. 34, no. 4, pp. 699–708. doi: [https://doi.org/10.1016/S0020-7462\(98\)00048-1](https://doi.org/10.1016/S0020-7462(98)00048-1)
- He, J.-H. (1998), “Approximate Analytical Solution of Blasius’ Equation,” *Communications in Nonlinear Science and Numerical Simulation*, vol. 3, no. 4, pp. 260–263. doi: [https://doi.org/10.1016/S1007-5704\(98\)90046-6](https://doi.org/10.1016/S1007-5704(98)90046-6)
- He, J.-H. (1999b), “Approximate Analytical Solution of Blasius’ Equation,” *Communications in Nonlinear Science and Numerical Simulation*, vol. 4, no. 1, pp. 75–78. doi: [https://doi.org/10.1016/S1007-5704\(99\)90063-1](https://doi.org/10.1016/S1007-5704(99)90063-1)
- He, J.-H. (2000), “A Review on Some New Recently Developed Nonlinear Analytical Techniques,” *International Journal of Nonlinear Sciences and Numerical Simulation*, vol. 1, no. 1, p. 51. doi: <https://doi.org/10.1515/IJNSNS.2000.1.1.51>
- He, J.-H. (2003), “A Simple Perturbation Approach to Blasius Equation,” *Applied Mathematics and Computation*, vol. 140, no. 2, pp. 217–222. doi: [https://doi.org/10.1016/S0096-3003\(02\)00189-3](https://doi.org/10.1016/S0096-3003(02)00189-3)
- He, J.-H. (1999a), “Homotopy Perturbation Technique,” *Computer Methods in Applied Mechanics and Engineering*, vol. 178, no. 3, pp. 257–262. doi: [https://doi.org/10.1016/S0045-7825\(99\)00018-3](https://doi.org/10.1016/S0045-7825(99)00018-3)
- He, J.-H., and Wu, X.-H., “Variational Iteration Method: New Development and Applications,” *Computers & Mathematics with Applications*, vol. 54, no. 7, pp. 881–894. doi: <https://doi.org/10.1016/j.camwa.2006.12.083>
- Head, M. R. (1958), “Entrainment in the Turbulent Boundary Layer,” *Aeronautical Research*

Council, R & M 3152.

- Heinz, S. (2003), *Statistical Mechanics of Turbulent Flows*, Springer-Verlag, New York.
- Hele-Shaw, H. S. (1898), “Investigation of the Nature of Surface Resistance of Water and of Stream Motion under Certain Experimental Conditions,” *Transactions of the Society of Naval Architects*, vol. 11, p. 25.
- Herbert, T. (1983), “Secondary Instability of Plane Channel Flow to Subharmonic Three-Dimensional Disturbances,” *Physics of Fluids*, vol. 26, pp. 871–874. doi: <https://doi.org/10.1063/1.864226>
- Herbert, T. (1997), “Parabolized Stability Equations,” *Annual Review of Fluid Mechanics*, vol. 29, no. 1, pp. 245–283. doi: <https://doi.org/10.1146/annurev.fluid.29.1.245>
- Hermann, R. (1936), “Wärmeübertragung bei freier Strömung am waagerechten Zylinder in zwei-atomigen Gasen,” VDI Forschungsheft 379 [see also NACA Technical Memo. 1366, 1954].
- Herring, H. J., and Mellor, G. L. (1968), “A Method of Calculating Compressible Turbulent Boundary Layers,” National Aeronautics and Space Administration CR-1144, September [see also NASA SP-216, pp. 27–132].
- Herring, H. J., and Norbury, J. F. (1967), “Some Experiments on Equilibrium Turbulent Boundary Layers in Favorable Pressure Gradients,” *Journal of Fluid Mechanics*, vol. 27, pp. 541–549. doi: <https://doi.org/10.1017/S0022112067000527>
- Hicks, W. M. (1898), “Researches in Vortex Motion. Part III. On Spiral or Gyrostatic Vortex Aggregates,” *Proceedings of the Royal Society of London, Series A*, vol. 62, no. 379–387, pp. 332–338. doi: <https://doi.org/10.1098/rspl.1897.0119>
- Hiemenz, K. (1911), “Die Grenzschicht an einem in den gleichförmigen Flüssigkeitsstrom eingetauchten geraden Kreiszylinder,” *Dinglers Polytechnisches Journal*, vol. 326, p. 321.
- Hill, R., and Power, G. (1956), “Extremum Principles for Slow Viscous Flow and the Approximate Calculation of Drag,” *Quarterly Journal of Mechanics and Applied Mathematics*, vol. 9, pp. 313–319. doi: <https://doi.org/10.1093/qjmam/9.3.313>
- Hilpert, R. (1933), “Wärmeabgabe von geheizten Drähten und Rohren im Luftstrom,” *Forschungsergebnisse auf dem Gebiete des Ingenieurwesens*, vol. 4, pp. 215–224.
- Hilsenrath, J., et al. (1955), *Tables of Thermodynamic and Transport Properties*, National Bureau of Standards Circular 564; reprinted (1960) by Pergamon.
- Hinze, J. O. (1975), *Turbulence*, 2nd ed., McGraw-Hill, New York.
- Hirata, M., and Kasagi, N. (Eds.) (1988), *Transport Phenomena in Turbulent Flows*, Hemisphere, New York.
- Hirsch, C. (1988), *Numerical Computation of Internal and External Flows*, Wiley, New York.

- Hirschfelder, J. O., Curtiss, C. F., and Bird, R. B. (1954), *Molecular Theory of Gases and Liquids*. Wiley, New York.
- Ho, C.-M., and Huerre, P. (1984), "Perturbed Free Shear Layers," *Annual Review of Fluid Mechanics*, vol. 16, pp. 365–424. doi: <https://doi.org/10.1146/annurev.fl.16.010184.002053>
- Hoffmann, K. A., and Chiang, S. T. (1998), *Computational Fluid Dynamics*, 2 vols., Engineering Education Systems, Austin, TX.
- Hollingsworth, D. K., Moffat, R. J., and Kays, W. M. (1992), "Effect of Concave Surface Curvature on the Turbulent Prandtl Number and the Thermal Law of the Wall," *Experimental Thermal and Fluid Science*, vol. 5, no. 3, pp. 299–306. doi: [https://doi.org/10.1016/0894-1777\(92\)90074-F](https://doi.org/10.1016/0894-1777(92)90074-F)
- Holmes, P., et al. (1998), *Turbulence, Coherent Structures, Dynamical Systems, and Symmetry*, Cambridge University Press, New York.
- Holstein, H., and Bohlen, T. (1940), "Ein einfaches Verfahren zur Berechnung laminarer Reibungsschichten, die dem Näherungsverfahren von K. Pohlhausen genügen," *Lilienthal-Gesellschaft für Luftfahrtforsch*, S-10, pp. 5–16.
- Homann, F. (1936), "Der Einfluss grosser Zähigkeit bei der Strömung um den Zylinder und um die Kugel," *Journal of Applied Mathematics and Mechanics (ZAMM)*, vol. 16, pp. 153–164. doi: <https://doi.org/10.1002/zamm.19360160304>
- Howarth, L. (1938), "On the Solution of the Laminar Boundary Layer Equations," *Proceedings of the Royal Society of London, Series A*, vol. 164, pp. 547–579. doi: <https://doi.org/10.1098/rspa.1938.0037>
- Howarth, L. (1939), "On the Solution of the Laminar Boundary Layer Equations," *Proceedings of the Royal Society of London, Series A*, vol. 164, no. 919, pp. 547–579. doi: <https://doi.org/10.1098/rspa.1938.0037>
- Huang, P. G., and Bradshaw, P. (1995), "Law of the Wall for Turbulent Flows in Pressure Gradients," *AIAA Journal*, vol. 33, no. 4, pp. 624–632. <https://doi.org/10.2514/3.12624>Page 501
- Huang, P. G., Bradshaw, P., and Coakley, T. J. (1993), "Skin Friction and Velocity Profile Family for Compressible Turbulent Boundary Layers," *AIAA Journal*, vol. 31, no. 9, pp. 1600–1604. doi: <https://doi.org/10.2514/3.11820>
- Huebner, K. H., et al. (2001), *The Finite Element Method for Engineers*, 3rd ed., Wiley, New York.
- Hughes, T. H., and Reid, W. H. (1965), "On the Stability of the Asymptotic Suction Boundary Layer Profile," *Journal of Fluid Mechanics*, vol. 23, pp. 715–735. doi: <https://doi.org/10.1017/S0022112065001647>
- Hussain, A. K. M. F. (1986), "Coherent Structures and Turbulence," *Journal of Fluid*

- Mechanics*, vol. 173, pp. 303–356. doi: <https://doi.org/10.1017/S0022112086001192>
- Hutton, J. F., et al. (1989), *An Introduction to Rheology*, Elsevier Health Sciences, Philadelphia.
- Hytopoulos, E., Schetz, J. A., and Gunzburger, M. (1993), “Numerical Solution of the Compressible Boundary Layer Equations Using the Finite Element Method,” *AIAA Journal*, vol. 31, no. 1, pp. 6–7. doi: <https://doi.org/10.2514/3.48999>
- Iaccarino, G. (2001), “Predictions of a Turbulent Separated Flow Using Commercial CFD Codes,” *Journal of Fluids Engineering*, vol. 123, Dec., pp. 819–828. doi: <https://doi.org/10.1115/1.1400749>
- Iacono, R., and Boyd, J. P. (2015), “Simple Analytic Approximations for the Blasius Problem,” *Physica D: Nonlinear Phenomena*, vol. 310, pp. 72–78. doi: <https://doi.org/10.1016/j.physd.2015.08.003>
- Iglisch, R. (1944), “Exakte Berechnung der laminaren Reibungsschicht an der längsangeströmten ebenen Platte mit homogener Absaugung,” *Schr. Deutsch. Akad. Luftfahrtforschung*, Series B, vol. 8, pp. 1–51 (translated as NACA Technical Memo. 1205).
- Iida, O., and Nagano, Y. (1998), “Relaminarization Mechanisms of Turbulent Channel Flow at Low Reynolds Numbers,” *Turbulence and Combustion*, vol. 60, no. 2, pp. 193–213. doi: <https://doi.org/10.1023/A:1009999606355>
- Illingworth, C. R. (1950), “Some Solutions of the Equations of Flow of a Viscous Compressible Fluid,” *Proceedings of the Cambridge Philosophical Society*, vol. 46, pp. 469–478. doi: <https://doi.org/10.1017/S0305004100025986>
- Imai, I. (1957), “Second Approximation to the Laminar Boundary Layer Flow over a Flat Plate,” *Journal of the Aeronautical Sciences*, vol. 24, pp. 155–156.
- Ingham, D. B., and Pop, I. (2002), *Transport Phenomena in Porous Media*, 2 vols., Pergamon, New York.
- Irgens, Fridtjov (2013), *Rheology and Non-Newtonian Fluids*, Springer.
- Jacobson, S. A., and Reynolds, W. C. (1998), “Active Control of Streamwise Vortices and Streaks in Boundary Layers,” *Journal of Fluid Mechanics* vol. 360, pp. 179–211. doi: <https://doi.org/10.1017/S0022112097008562>
- Jaffe, N. A., Okamura, T. T., and Smith, A. M. O. (1970), “Determination of Spatial Amplification Factors and Their Application to Predicting Transition,” *AIAA Journal*, vol. 8, no. 2, pp. 301–308. doi: <https://doi.org/10.2514/3.5660>
- Jaluria, Y. (1980), *Natural Convection: Heat and Mass Transfer*, Pergamon, New York.
- Jaluria, Y., and Torrance, K. E. (1986), *Computational Heat Transfer*, Hemisphere, New York.

- Jankowski, T. A., and Majdalani, J., “Axially Traveling Waves in Porous Tubes with Arbitrary Crossflow Velocity,” 46th AIAA/ASME/SAE/ASEE Joint Propulsion Conference and Exhibit, AIAA Paper 2010–6801, July 2010. doi: <https://doi.org/10.2514/6.2010-6801>
- Jankowski, T. A., and Majdalani, J., “General Asymptotic Solutions for the Oscillatory Channel Flow with Arbitrary Suction,” 31st AIAA Fluid Dynamics Conference AIAA Paper 2001-2789, June 2001. doi: <https://doi.org/10.2514/6.2001-2789>
- Jankowski, T. A., and Majdalani, J. (2002), “Laminar Flow in a Porous Channel with Large Wall Suction and a Weakly Oscillatory Pressure,” *Physics of Fluids*, vol. 14, no. 3, pp. 1101–1110. doi: <https://doi.org/10.1063/1.1445419>
- Jankowski, T. A., and Majdalani, J. (2006), “Symmetric Solutions for the Oscillatory Channel Flow with Arbitrary Suction,” *Journal of Sound and Vibration*, vol. 294, nos. 4–5, pp. 880–893. doi: <https://doi.org/10.1016/j.jsv.2005.12.035>
- Jankowski, T. A., and Majdalani, J. (2005), “Vortical and Acoustical Mode Coupling inside a Porous Tube with Uniform Wall Suction,” *Journal of the Acoustical Society of America*, vol. 117, no. 6, pp. 3448–3458. doi: <https://doi.org/10.1121/1.1905639>
- Jeffery, G. B. (1915), “The Two-Dimensional Steady Motion of a Viscous Fluid,” *Philosophical Magazine*, vol. 29, pp. 455–465. doi: <https://doi.org/10.1080/14786440408635327>
- Johnston, J. P. (1960), “On Three-Dimensional Turbulent Boundary Layers Generated by Secondary Flow,” *Journal of Basic Engineering*, vol. 82, pp. 233–248. doi: <https://doi.org/10.1115/1.3662539>
- (1998), “Review: Diffuser Design and Performance Analysis by a Unified Integral Method,” *Journal of Fluids Engineering*, vol. 120, no. 1, pp. 6–18. doi: <https://doi.org/10.1115/1.2819663>
- Jones, O. C. (1976), “An Improvement in the Calculation of Turbulent Friction in Rectangular Ducts,” *Journal of Fluids Engineering*, vol. 98, pp. 173–181. doi: <https://doi.org/10.1115/1.3448250>
- Jones, O. C., and Leung, J. C. M. (1981), “An Improvement in the Calculation of Turbulent Friction in Smooth Concentric Annuli,” *Journal of Fluids Engineering*, vol. 103, pp. 615–623. doi: <https://doi.org/10.1115/1.3241781>
- Jones, W. P., and Launder, B. E. (1972), “The Prediction of Laminarization with a Two-Equation Model of Turbulence,” *International Journal of Heat and Mass Transfer*, vol. 15, pp. 301–314. doi: [https://doi.org/10.1016/0017-9310\(72\)90076-2](https://doi.org/10.1016/0017-9310(72)90076-2)
- (1973), “The Calculation of Low Reynolds Number Phenomena with a Two-Equation Model of Turbulence,” *International Journal of Heat and Mass Transfer*, vol. 16, pp. 1119–1130. doi: [https://doi.org/10.1016/0017-9310\(73\)90125-7](https://doi.org/10.1016/0017-9310(73)90125-7)
- Jordinson, R. (1970), “The Flat Plate Boundary Layer, Part 1, Numerical Integration of the

Orr–Sommerfeld Equation,” *Journal of Fluid Mechanics*, vol. 43, pp. 801–811. doi: <https://doi.org/10.1017/S0022112070002756>

Joseph, D. D. (1976), *Stability of Fluid Motions*, Springer-Verlag, Berlin.

Joslin, R. D., Erlebacher, G., and Hussaini, M. Y. (1996), “Active Control of Instabilities in Laminar Boundary Layers: Overview and Concept Validation,” *Journal of Fluids Engineering*, vol. 118, pp. 494–497. doi: <https://doi.org/10.1115/1.2817785>

Joukowski, N., (1898), “Über den hydraulischen Stoss in Wasserleitungsröhren (on the hydraulic hammer in water supply pipes)”, *Mémoires de l'Académie Impériale des Sciences de St.-Petersbourg*, Series 8, vol. 9, no. 5 (in German, English translation, partly, by Simin, 1904).

Kader, B. A. (1981), “Temperature and Concentration Profiles in Fully Turbulent Boundary Layers,” *International Journal of Heat and Mass Transfer*, vol. 24, no. 9, pp. 1541–1544. doi: [https://doi.org/10.1016/0017-9310\(81\)90220-9](https://doi.org/10.1016/0017-9310(81)90220-9)

Kakaç, S., and Yener, Y. (1994), *Convective Heat Transfer*, 2nd ed., CRC Press, Boca Raton, FL.

Kakaç, S., Aung, W., and Viskanta, R. (1985), *Natural Convection: Fundamentals and Applications*, Taylor & Francis, Washington, DC. Page 502

Kamemoto, K., and Tsutahara, M. (Eds.) (2000), *Vortex Methods*, World Scientific, River Edge, NJ.

Kaplan, R. E. (1964), “The Stability of Laminar Incompressible Boundary Layers in the Presence of Compliant Boundaries,” Aeroelastic and Structures Research Lab. Report. ASRL-TR 166–1, M.I.T., Cambridge, MA.

Karim, S. M., and Rosenhead, L. (1952), “The Second Coefficient of Viscosity of Liquids and Gases,” *Reviews of Modern Physics*, vol. 24, pp. 108–116. doi: <https://doi.org/10.1103/RevModPhys.24.108>

Kármán, T. von (1911), “Über den Mechanismus des Widerstandes, den ein bewegter Körper in einer Flüssigkeit erzeugt,” *Wissenschaften zu Go'ttingen, Mathematisch-physikalische Klasse II*, pp. 509–517, 547–556.

——(1921) “Über laminare und turbulente Reibung,” *Journal of Applied Mathematics and Mechanics (ZAMM)*, vol. 1, pp. 233–252 (English translation in NACA Technical Memo. 1092). doi: <https://doi.org/10.1002/zamm.19210010401>

——(1939), “The Analogy between Fluid Friction and Heat Transfer,” *ASME Transactions*, vol. 61, pp. 705–710.

——(1964), *The Wind and Beyond*, Little Brown, Boston, MA.

Karniadakis, G. E., and Bestok, A. (2001), *Micro Flows*, Springer-Verlag, New York.

Karniadakis, G. E., and Sherwin, S. J. (1999), *Spectral/HP Element Methods for CFD*,

Oxford University Press, New York.

Kauzmann, W. (2012), *Kinetic Theory of Gases*, Dover, New York.

Kaviany, M. (2001), *Principles of Convective Heat Transfer*, 2nd ed., Springer-Verlag, New York.

Kays, W. M., and Crawford, M. E. (1993), *Convective Heat and Mass Transfer*, 3rd ed., McGraw-Hill, New York.

Kee, R. J., Elliott, M. C., and Glarborg, P. (2003), *Chemically Reacting Flow: Theory and Practice*, Wiley, New York.

Keenan, J. H. (1941), *Thermodynamics*, Wiley, New York.

Kegelman, J. T., and Mueller, T. J. (1986), "Experimental Studies of Spontaneous and Forced Transition on an Axisymmetric Body," *AIAA Journal*, vol. 24, no. 3, pp. 397–403. doi: <https://doi.org/10.2514/3.9280>

Keh, H. J., and Chen, P. Y. (2001), "Slow Motion of a Droplet between Two Parallel Plane Walls," *Chemical Engineering Science*, vol. 56, no. 24, pp. 6863–6871. doi: [https://doi.org/10.1016/S0009-2509\(01\)00323-2](https://doi.org/10.1016/S0009-2509(01)00323-2)

Keller, H. B., and Takami, H. (1966), "Steady Two-Dimensional Viscous Flow of an Incompressible Fluid Past a Circular Cylinder," in *Proc. Symp. Numerical Solutions of Nonlinear Differential Equations*, pp. 115–140 [see also *Physics of Fluids Supplement*, vol. 12, pp. II-51–II-56 (1969)]. doi: <https://doi.org/10.1063/1.1692469>

Kemp, N. H., R. H. Rose, and Detra, R. W. (1959), "Laminar Heat Transfer Around Blunt Bodies in Dissociated Air," *Journal of the Aerospace Sciences*, vol. 26, pp. 421–430. doi: <https://doi.org/10.2514/8.8128>

Kennard, E. H. (1938), *Kinetic Theory of Gases*, McGraw-Hill, New York.

Kestin, J., and Persen, L. N. (1962), "The Transfer of Heat Across a Turbulent Boundary Layer at Very High Prandtl Numbers," *International Journal of Heat and Mass Transfer*, vol. 5, pp. 355–371. doi: [https://doi.org/10.1016/0017-9310\(62\)90026-1](https://doi.org/10.1016/0017-9310(62)90026-1)

Kestin, J., and Wakeham, W. A. (1988), *Transport Properties of Fluids: Thermal Conductivity, Viscosity, and Diffusion Coefficient*, Center for Information and Numerical Data Analysis and Synthesis, Data Series, vol. I-1, Hemisphere, New York.

Kestin, J., Maeder, P. F., and Sogin, H. H. (1961), "The Influence of Turbulence on the Transfer of Heat to Cylinders Near the Stagnation Point," *Journal of Applied Mathematics and Physics (ZAMP)*, vol. 12, pp. 115–132. doi: <https://doi.org/10.1007/BF01601012>

Khabibrakhmanov, I. K., and Summers, D. (1998), "The Use of Generalized Laguerre Polynomials in Spectral Methods for Nonlinear Differential Equations," *Computers & Mathematics with Applications*, vol. 36, no. 2, pp. 65–70. doi: [https://doi.org/10.1016/S0898-1221\(98\)00117-5](https://doi.org/10.1016/S0898-1221(98)00117-5)

- Khonsari, M. M., and Booser, E. R. (2001), *Applied Tribology: Bearing Design and Lubrication*, Interscience, New York.
- Kim, K., Sung, H. J., and Chung, M. K. (2002), "Assessment of Local Blowing and Suction in a Turbulent Boundary Layer," *AIAA Journal*, vol. 40, no. 1, pp. 175–177. doi: <https://doi.org/10.2514/2.1629>
- King, J. R., and Cox, S. M. (2001), "Asymptotic Analysis of the Steady-State and Time-Dependent Berman Problem," *Journal of Engineering Mathematics*, vol. 39, no. 1, pp. 87–130. doi: <https://doi.org/10.1023/A:1004824527547>
- Klebanoff, P. S. (1955), "Characteristics of Turbulence in a Boundary Layer with Zero Pressure Gradient," NACA Report 1247.
- Klebanoff, P. S., and Tidstrom, K. D. (1972), "Mechanism by Which a Two-Dimensional Roughness Element Induces Boundary-Layer Transition," *Physics of Fluids*, vol. 15, no. 7, pp. 1173–1188. doi: <https://doi.org/10.1063/1.1694065>
- Klebanoff, P. S., Tidstrom, K. D., and Sargent, L. M. (1962), "The Three-Dimensional Nature of Boundary Layer Instability," *Journal of Fluid Mechanics*, vol. 12, pp. 1–34. doi: <https://doi.org/10.1017/S0022112062000014>
- Kleiser, L., and Zang, T. A. (1991), "Numerical Simulation of Transition in Wall-Bounded Shear Flows," *Annual Review of Fluid Mechanics*, vol. 23, pp. 495–537. doi: <https://doi.org/10.1146/annurev.fl.23.010191.002431>
- Kline, S. J., Cantwell, B. J., and Lilley, G. M. (1982), "The 1980–81 AFOSR-HTTM Stanford Conference on Complex Turbulent Flows: Comparison of Computation and Experiment," vols. 1–3, Department of Mechanical Engineering, Stanford University, Stanford, CA. doi: <https://doi.org/10.1017/S0022112085211367>
- Kline, S. J., Abbott, D. E. and Fox, R. W. (1959), "Optimum Design of Straight-Walled Diffusers," *Journal of Basic Engineering*, Ser. D, vol. 81, pp. 305–320. doi: <https://doi.org/10.1115/1.4008462>
- Kline, S. J., Morkovin, M. V., Sovran, G., and Cockrell, D. J. (1968), "Computation of Turbulent Boundary Layers—1968 AFOSR-IFP Stanford Conference," vol. 1, Stanford University, Stanford, CA.
- Knauss, J. A. (1978), *Introduction to Physical Oceanography*, Prentice-Hall, Englewood Cliffs, NJ.
- Knowles, C. P., and Gebhart, B. (1968), "Stability of the Laminar Natural Convection Boundary Layer," *Journal of Fluid Mechanics*, vol. 34, pp. 657–686. doi: <https://doi.org/10.1017/S0022112068002156>
- Kobayashi, R., Kohama, Y. and Takamade, Ch. (1980), "Spiral Vortices in Boundary Layer Transition Regime on a Rotating Disk," *Acta Mechanica*, vol. 35, pp. 71–82. doi: <https://doi.org/10.1007/BF01190058>

- Kohr, M., and Pop, I. (Eds.) (2004), *Viscous Incompressible Flow: For Low Reynolds Numbers*, WIT Press/Computational Mechanics, Boston, MA.
- Korkegi, R. H. (1956), "Transition Studies and Skin Friction Measurements on an Insulated Flat Plate at a Mach Number of 5.8," *Journal of the Aerospace Sciences*, vol. 23, pp. 97–102. doi: <https://doi.org/10.2514/8.3515>
- Korobkin, I. (1954), Naval Ordnance Lab., Report no. 3841.
- Koschmieder, E. L. (1993), *Bénard Cells and Taylor Vortices*, Cambridge University Press, New York.
- Koumoutsakos, P., and Leonard, A. (1995), "High-Resolution Simulations of the Flow Around an Impulsively Started Cylinder Using Vortex Methods," *Journal of Fluid Mechanics*, vol. 296, pp. 1–38. doi: <https://doi.org/10.1017/S0022112095002059>Page 503
- Kovaznay, L. S. G., Kibens, V., and Blackwelder, R. F. (1970), "Large Scale Motion in the Intermittent Region of a Turbulent Boundary Layer," *Journal of Fluid Mechanics*, vol. 41, pp. 283–325. doi: <https://doi.org/10.1017/S0022112070000629>
- Kral, L. D., and Zang, T. A. (Eds.) (1993), *Transitional and Turbulent Compressible Flows—1993*, ASME Fluids Engineering Division, vol. 151, New York.
- Kramer, M. O. (1957), "Boundary Layer Stabilization by Distributed Damping," *Journal of the Aeronautical Sciences*, vol. 24, pp. 459–460.
- Kramers, H. (1946), "Heat Transfer from Spheres to Flowing Media," *Physica*, vol. 12, pp. 61–80. doi: [https://doi.org/10.1016/S0031-8914\(46\)80024-7](https://doi.org/10.1016/S0031-8914(46)80024-7)
- Kreiss, H.-O., and Lorenz, J. (1989), *Initial-Boundary Value Problems and the Navier–Stokes Equations*, Academic, New York.
- Kreyszig, E. (1999), *Advanced Engineering Mathematics*, 8th ed., Wiley, New York.
- Kreyszig, E. (2011), *Advanced Engineering Mathematics*, 10th ed., Wiley, New York.
- Kuehn, T. H., and Goldstein, R. J. (1980), "Numerical Solution to the Navier–Stokes Equations for Laminar Natural Convection about a Horizontal Isothermal Circular Cylinder," *International Journal of Heat and Mass Transfer*, vol. 23, pp. 971–980. doi: [https://doi.org/10.1016/0017-9310\(80\)90071-X](https://doi.org/10.1016/0017-9310(80)90071-X)
- Kuo, B. L. (2003), "Application of the Differential Transformation Method to the Solutions of Falkner-Skan Wedge Flow," *Acta Mechanica*, vol. 164, no. 3, pp. 161–174. doi: <https://doi.org/10.1007/s00707-003-0019-4>
- Kuo, B. L. (2005), "Heat Transfer Analysis for the Falkner–Skan Wedge Flow by the Differential Transformation Method," *International Journal of Heat and Mass Transfer*, vol. 48, no. 23, pp. 5036–5046. doi: <https://doi.org/10.1016/j.ijheatmasstransfer.2003.10.046>

- Kuo, B. L. (2004), "Thermal Boundary-Layer Problems in a Semi-Infinite Flat Plate by the Differential Transformation Method," *Applied Mathematics and Computation*, vol. 150, no. 2, pp. 303–320. doi: [https://doi.org/10.1016/S0096-3003\(03\)00233-9](https://doi.org/10.1016/S0096-3003(03)00233-9)
- Lachmann, G. V. (1961), *Boundary Layers and Flow Control*, vols. 1–2, Pergamon, London.
- Lachowicz, J. T., Chokani, N., and Wilson, S. P. (1996), "Boundary-Layer Stability Measurements in a Hypersonic Quiet Tunnel," *AIAA Journal*, vol. 34, pp. 2496–2500. doi: <https://doi.org/10.2514/3.13430>
- Ladyzhenskaya, O. A. (1969), *The Mathematical Theory of Viscous Incompressible Flow*, 2nd ed., Gordon and Breach, New York.
- Lai, W. M., Krempl, E., and Rubin, D. (1995), *Introduction to Continuum Mechanics*, 3rd ed., Butterworth-Heinemann, Woburn, MA.
- Lamb, H. (1932), *Hydrodynamics*, 6th ed., Cambridge University Press, London (reprinted by Dover in 1945).
- Lamb, P. (Ed.) (1987), *Proceedings of the Tenth U.S. National Congress of Applied Mechanics*, American Society of Mechanical Engineers, New York.
- Landahl, M. T., and Mollo-Christensen, E. (1992), *Turbulence and Random Processes in Fluid Mechanics*, 2nd ed., Cambridge University Press, New York.
- Landau, L. D., and Lifschitz, E. M. (1959), *Fluid Mechanics*, Pergamon, London.
- Laney, C. B. (1998), *Computational Gasdynamics*, Cambridge University Press, New York.
- Langlois, W. E. (1964), *Slow Viscous Flow*, Macmillan, New York.
- Lapidus, L., and Pinder, G. F. (1999), *Numerical Solution of Partial Differential Equations in Science and Engineering*, Wiley Interscience, New York.
- Lauchle, G. C., and Gurney, G. B. (1984), "Laminar Boundary-Layer Transition on a Heated Underwater Body," *Journal of Fluid Mechanics*, vol. 144, pp. 79–101. doi: <https://doi.org/10.1017/S0022112084001518>
- Launder, B. E., Reece, B. J. and Rodi, W. (1975), "Progress in the Development of a Reynolds-Stress Turbulence Closure," *Journal of Fluid Mechanics*, vol. 68, pp. 537–566. doi: <https://doi.org/10.1017/S0022112075001814>
- Launder, B., and Sandham, N. (Eds.) (2001), *Closure Strategies for Turbulent and Transitional Flows*, Cambridge University Press, New York.
- Lee, C. (2002), "Large Eddy Simulation of Rough-Wall Turbulent Boundary Layers," *AIAA Journal*, vol. 40, no. 10, pp. 2127–2130. doi: <https://doi.org/10.2514/2.1548>
- Lee, J. H. W., and Chu, V. (2003), *Turbulent Jets and Plumes: A Lagrangian Approach*, Kluwer Academic, New York.
- Lees, L. (1956), "Laminar Heat Transfer over Blunt-Nosed Bodies at Hypersonic Flight Speeds," *Jet Propulsion*, vol. 26, pp. 259–269, 274. doi: <https://doi.org/10.2514/8.6977>

- Lees, L., and Lin, C. C. (1946), "Investigation of the Stability of the Laminar Boundary Layer in a Compressible Fluid," NACA Technical Note 1115.
- Lefebvre, P. J., and White, F. M. (1989), "Experiments on Transition to Turbulence in a Constant-Acceleration Pipe Flow," *Journal of Fluids Engineering*, vol. 111, pp. 428–432. doi: <https://doi.org/10.1115/1.3243663>
- Lefebvre, P. J., and White, F. M. (1991), "Further Experiments on Transition to Turbulence in Constant-Acceleration Pipe Flow," *Journal of Fluids Engineering*, vol. 113, pp. 223–227. doi: <https://doi.org/10.1115/1.2909484>
- Legendre, R. (1965), "Lignes de courant d'un écoulement continu," *Rech. Aéropat.*, vol. 105, pp. 3–9.
- Leibenson, L. S. (1935), "The Energy Form of the Integral Condition in the Theory of the Boundary Layer," *Dokl. Akad. Nauk SSSR*, vol. 2, pp. 22–24.
- Lesieur, M. and Métais, O. (1996), "New Trends in Large-Eddy Simulations of Turbulence," *Annual Review of Fluid Mechanics*, vol. 28, pp. 45–82. doi: <https://doi.org/10.1146/annurev.fl.28.010196.000401>
- Lewis, J. A., and Carrier, G. F. (1949), "Some Remarks on the Flat Plate Boundary Layer," *Quarterly of Applied Mathematics*, vol. 8, pp. 228–234. doi: <https://doi.org/10.1090/qam/34160>
- Liao, S. J. (1997), "A Kind of Approximate Solution Technique Which Does Not Depend Upon Small Parameters — II. An Application in Fluid Mechanics," *International Journal of Non-Linear Mechanics*, vol. 32, no. 5, pp. 815–822. doi: [https://doi.org/10.1016/S0020-7462\(96\)00101-1](https://doi.org/10.1016/S0020-7462(96)00101-1)
- Liao, S. J. (1999a), "A Uniformly Valid Analytic Solution of Two-Dimensional Viscous Flow over a Semi-Infinite Flat Plate," *Journal of Fluid Mechanics*, vol. 385, pp. 101–128. doi: <https://doi.org/10.1017/S0022112099004292>
- Liao, S. J. (1999b), "An Explicit, Totally Analytic Approximate Solution for Blasius' Viscous Flow Problems," *International Journal of Non-Linear Mechanics*, vol. 34, no. 4, pp. 759–778. doi: [https://doi.org/10.1016/S0020-7462\(98\)00056-0](https://doi.org/10.1016/S0020-7462(98)00056-0)
- Liao, S. J. (2010), "An Optimal Homotopy-Analysis Approach for Strongly Nonlinear Differential Equations," *Communications in Nonlinear Science and Numerical Simulation*, vol. 15, no. 8, pp. 2003–2016. doi: <https://doi.org/10.1016/j.cnsns.2009.09.002>
- Libby, P. A. (1996), *An Introduction to Turbulence*, Taylor & Francis, New York.
- Libby, P. A., and Liu, T. M. (1967), "Further Solutions of the Falkner–Skan Equation," *AIAA Journal*, vol. 5, pp. 1040–1042. doi: <https://doi.org/10.2514/3.4130>Page 504
- Liepmann, H. W. (1943), "Investigations on Laminar Boundary-Layer Stability and Transition on Curved Boundaries," NACA Wartime Report W107 (ACR3H30) [see also

NACA Technical Memo. 1196 (1947) and NACA Report 890 (1947)].

- Lim, F. J., and Schowalter, W. R. (1989), "Wall Slip of Narrow Molecular Weight Distribution Polybutadienes," *Journal of Rheology*, vol. 33, no. 8, pp. 1359–1382. doi: <https://doi.org/10.1122/1.550073>
- Lin, C. C. (1955), *The Theory of Hydrodynamic Stability*, Cambridge University Press, London.
- Lin, C.-S., and Han, Q.-S. (1991), "Boundary Element Analysis of Low Reynolds Number Viscous Fluid Flow," in *Computational Mechanics*, A. A. Balkema, Hong Kong, pp. 1481–1486.
- Lin, J. (1999), "A New Approximate Iteration Solution of Blasius Equation," *Communications in Nonlinear Science and Numerical Simulation*, vol. 4, no. 2, pp. 91–94. doi: [https://doi.org/10.1016/S1007-5704\(99\)90017-5](https://doi.org/10.1016/S1007-5704(99)90017-5)
- Lindgren, E. R. (1965), "Experimental Study on Turbulent Pipe Flows of Distilled Water," Oklahoma State University, Civil Engineering Dept., Report 1AD621071.
- Lingwood, R. J. (1995), "Absolute Instability of the Boundary Layer on a Rotating Disk," *Journal of Fluid Mechanics*, vol. 299, pp. 17–33. doi: <https://doi.org/10.1017/S0022112095003405>
- (1996), "An Experimental Study of Absolute Instability of a Rotating-Disk Boundary-Layer Flow," *Journal of Fluid Mechanics*, vol. 314, pp. 373–405. doi: <https://doi.org/10.1017/S0022112096000365>
- List, E. J. (1982), "Turbulent Jets and Plumes," *Annual Review of Fluid Mechanics*, vol. 14, pp. 189–212. doi: <https://doi.org/10.1146/annurev.fl.14.010182.001201>
- Little, W. J. (1963), *Arnold Engineering Development Complex*, Report AEDC-TDR-63–190, Tullahoma, TN.
- Lock, R. C. (1951), "The Velocity Distribution in the Laminar Boundary Layer Between Parallel Streams," *Quarterly Journal of Mechanics and Applied Mathematics*, vol. 4, pp. 42–63. doi: <https://doi.org/10.1093/qjmam/4.1.42>
- Löhner, R. (2001), *Applied CFD Techniques: An Introduction Based on Finite Element Methods*, Wiley, New York.
- Lomax, H., Pulliam, T. H., and Zingg, D. (2001), *Fundamentals of Computational Fluid Dynamics*, Springer-Verlag, New York.
- Long, R. R. (1953), "Steady Motion around a Symmetrical Obstacle Moving Along the Axis of a Rotating Liquid," *Journal of Meteorology*, vol. 10, no. 3, pp. 197–203. doi: [https://doi.org/10.1175/1520-0469\(1953\)010<0197:SMAASO>2.0.CO;2](https://doi.org/10.1175/1520-0469(1953)010<0197:SMAASO>2.0.CO;2)
- Loos, H. G. (1955), "A Simple Laminar Boundary Layer with Secondary Flow," *Journal of the Aeronautical Sciences*, vol. 22, pp. 35–40.

- Lucquin, B., and Pironneau, O. (1998), *Introduction to Scientific Computing*, Wiley, New York.
- Ludwig, H., and Tillmann, W. (1949), “Untersuchungen über die Wandschubspannung in Turbulenten Reibungsschichten,” *Inženýr architekt*, vol. 17, pp. 288–299 (translated as NACA Technical Memo. 1285).
- Lu, C. (1997), “On the Asymptotic Solution of Laminar Channel Flow with Large Suction,” *SIAM Journal on Mathematical Analysis*, vol. 28, no. 5, pp. 1113–1134. doi: <https://doi.org/10.1137/S0036141096297704>
- Lu, C., MacGillivray, A. D., and Hastings, S. P. (1992), “Asymptotic Behaviour of Solutions of a Similarity Equation for Laminar Flows in Channels with Porous Walls,” *IMA Journal of Applied Mathematics*, vol. 49, no. 2, pp. 139–162. doi: <https://doi.org/10.1093/imamat/49.2.139>
- Luchini, P., and Bottaro, A. (2014), “Adjoint Equations in Stability Analysis,” *Annual Review of Fluid Mechanics*, vol. 46, no. 1, pp. 493–517. doi: <https://doi.org/10.1146/annurev-fluid-010313-141253>
- Lumley, J. L. (1989), “The State of Turbulence Research,” in W. K. George and R. Arndt (Eds.), *Advances in Turbulence*, pp. 1–10, Hemisphere, New York.
- M. Spiegel, Lipshutz, S. and Spellman, D. *Vector Analysis* (2009), 2nd ed, Schaum’s Outline.
- MacGillivray, A. D., and Lu, C. (1994), “Asymptotic Solution of a Laminar Flow in a Porous Channel with Large Suction: A Nonlinear Turning Point Problem,” *Methods and Applications of Analysis*, vol. 1, no. 2, pp. 229–248. doi: <https://dx.doi.org/10.4310/MAA.1994.v1.n2.a5>
- Mack, L. M. (1954), “An Experimental Investigation of the Temperature Recovery Factor,” California Institute of Technology Report 20–80, Pasadena, CA.
- (1969), “Boundary Layer Stability Theory,” Document 900–277, Rev. A, Jet Propulsion Lab., Pasadena, CA.
- (1977), “Transition Prediction and Linear Stability Theory,” pp. 1-1–1-22 of AGARD.
- (1977a), “Transition and Laminar Instability,” Publication 77–15, Jet Propulsion Lab., Pasadena, CA.
- (1984), “Boundary Layer Stability Theory,” pp. 3-1–3-81 of AGARD.
- (1987), “Review of Linear Compressible Stability Theory,” in D. L. Dwoyer and M. Y. Hussaini (Eds.), *Stability of Time Dependent and Spatially Varying Flows*, pp. 164–187, Springer, New York. doi: https://doi.org/10.1007/978-1-4612-4724-1_9
- Maicke, B. A., and Majdalani, J., “A Constant Shear Stress Core Flow Model of the Bidirectional Vortex,” *Proceedings of the Royal Society, London, Series A*, vol. 465, no. 2103, March 2009, pp. 915–935. doi: <https://doi.org/10.1098/rspa.2008.0342>

- Maicke, B. A., and Majdalani, J. (2008), "On the Rotational Compressible Taylor Flow in Injection-Driven Porous Chambers," *Journal of Fluid Mechanics*, vol. 603, no. 1, pp. 391-411. doi: <https://doi.org/10.1017/S0022112008001122>
- Maicke, B. A., Cecil, O. M., and Majdalani, J. (2017), "On the Compressible Bidirectional Vortex in a Cyclonically Driven Trkalian Flow Field," *Journal of Fluid Mechanics*, vol. 823, pp. 755–786. doi: <https://doi.org/10.1017/jfm.2017.310>
- Maicke, B. A., Majdalani, J., and Geisler, R. L. (2013), "Characterization of the Startup and Pressure Blowdown Processes in Rocket Nozzles," *Aerospace Science and Technology*, vol. 25, no. 1, pp. 273-282. doi: <https://doi.org/10.1016/j.ast.2012.02.003>
- Maicke, B. A., Saad, T., and Majdalani, J. (2012), "On the Compressible Hart-McClure and Sellars Mean Flow Motions," *Physics of Fluids*, vol. 24, no. 9, pp. 096101-20. doi: <https://doi.org/10.1063/1.4748349>
- Majdalani, J. (2008), "Exact Navier–Stokes Solution for the Pulsatory Viscous Channel Flow with Arbitrary Pressure Gradient," *Journal of Propulsion and Power*, vol. 24, no. 6, pp. 1412–1423. doi: <https://doi.org/10.2514/1.37815>
- Majdalani, J. (2012), "Helical Solutions of the Bidirectional Vortex in a Cylindrical Cyclone: Beltramian and Trkalian Motions," *Fluid Dynamics Research*, vol. 44, no. 6, pp. 065506-38. doi: <https://doi.org/10.1088/0169-5983/44/6/065506>
- Majdalani, J. (1995), "Improved Flowfield Models in Rocket Motors and the Stokes Layer with Sidewall Injection," Ph.D. Dissertation, University of Utah.
- Majdalani, J. (2009), "Multiple Asymptotic Solutions for Axially Travelling Waves in Porous Channels," *Journal of Fluid Mechanics*, vol. 636, no. 1, pp. 59–89. doi: <https://doi.org/10.1017/S0022112009007939>
- Majdalani, J. (2007), "On Steady Rotational High Speed Flows: The Compressible Taylor-Culick Profile," *Proceedings of the Royal Society of London, Series A*, vol. 463, no. 2077, pp. 131–162. doi: <https://doi.org/10.1098/rspa.2006.1755>
- Majdalani, J. (1999), "Boundary Layer Structure in Cylindrical Rocket Motors," *AIAA Journal*, vol. 37, no. 4, pp. 505–508. doi: <https://doi.org/10.2514/2.742>Page 505
- Majdalani, J., and Maicke, B. A. (2013), "Direct Calculation of the Average Local Mach Number in Converging-Diverging Nozzles," *Aerospace Science and Technology*, vol. 24, no. 1, pp. 111–115. doi: <https://doi.org/10.1016/j.ast.2011.10.009>
- Majdalani, J., and Maicke, B. A. (2011), "Explicit Inversion of Stodola's Area-Mach Number Equation," *Journal of Heat Transfer*, vol. 133, no. 7, pp. 071702-7. doi: <https://doi.org/10.1115/1.4002596>
- Majdalani, J., and Maicke, B. A. (2012), "Inversion of the Fundamental Thermodynamic Equations for Isentropic Nozzle Flow Analysis," *Journal of Engineering for Gas Turbines and Power*, vol. 134, no. 3, pp. 031201-9. doi: <https://doi.org/10.1115/1.4003963>

- Majdalani, J., and Rienstra, S. W. (2007), "On the Bidirectional Vortex and Other Similarity Solutions in Spherical Coordinates," *Journal of Applied Mathematics and Physics (ZAMP)*, vol. 58, no. 2, pp. 289-308. doi: <https://doi.org/10.1007/s00033-006-5058-y>
- Majdalani, J., and Roh, T. S. (2000), "The Oscillatory Channel Flow with Large Wall Injection," *Proceedings of the Royal Society of London, Series A*, vol. 456, no. 1999, pp. 1625–1657. doi: <https://doi.org/10.1098/rspa.2000.0579>
- Majdalani, J., and Saad, T. (2012), "Internal Flows Driven by Wall-Normal Injection," *Advanced Fluid Dynamics*, edited by H. W. Oh, InTech, Rijeka, Croatia, pp. 95–134. doi: <https://doi.org/10.5772/25839>
- Majdalani, J., and Saad, T. (2007), "The Taylor–Culick Profile with Arbitrary Headwall Injection," *Physics of Fluids*, vol. 19, no. 9, pp. 093601-10. doi: <https://doi.org/10.1063/1.2746003>
- Majdalani, J., and Van Moorhem, W. K. (1998), "Improved Time-Dependent Flowfield Solution for Solid Rocket Motors," *AIAA Journal*, vol. 36, no. 2, pp. 241–248. doi: <https://doi.org/10.2514/2.7507>
- Majdalani, J., and Van Moorhem, W. K. (1997), "Multiple-Scales Solution to the Acoustic Boundary Layer in Solid Rocket Motors," *Journal of Propulsion and Power*, vol. 13, no. 2, pp. 186–193. doi: <https://doi.org/10.2514/2.5168>
- Majdalani, J., and Xuan, L. -J. (2020), "On the Kármán Momentum-Integral Approach and the Pohlhausen Paradox," *Physics of Fluids*, Vol. 32, No. 12, p. 123605. doi: <https://doi.org/10.1063/5.0036786>
- Majdalani, J., Barron, J. T., and Van Moorhem, W. K. (2002), "Inception of Turbulence in the Stokes Boundary Layer over a Transpiring Wall," *ASME Journal of Fluids Engineering*, vol. 124, no. 9, pp. 678–684. doi: <https://doi.org/10.1115/1.1490375>
- Majdalani, J., Ramesh-Kumar, T., and Akiki, M., "Biglobal Instability of the Compressible Taylor–Culick Solution in Cylindrical Rockets," 52nd AIAA/SAE/ASEE Joint Propulsion Conference and Exhibit AIAA Paper 2016-4792, July 2016. doi: <https://doi.org/10.2514/6.2016-4792>
- Majdalani, J. (2014), Unified Framework for Modeling Swirl Dominated Helical Motions, AIAA-2014-3677, 50th AIAA/ASME/SAE/ASEE Joint Propulsion Conference, Cleveland, OH, July 28–30. doi: <https://doi.org/10.2514/6.2014-3677>
- Malik, M. R. (1986), "The Neutral Curve for Stationary Disturbances in Rotating Disk Flow," *Journal of Fluid Mechanics*, vol. 164, pp. 275–287. doi: <https://doi.org/10.1017/S0022112086002550>
- Malvern, L. E. (1997), *Introduction to Mechanics of a Continuous Medium*, Prentice-Hall, Upper Saddle River, NJ.
- Mangler, W. (1945), "Boundary Layers on Bodies of Revolution in Symmetrical Flow," *Ber. Aerodyn. Versuchsanst. Goett.*, Report 45/A/17.

- (1948), “Zusammenhang zwischen ebenen und rotationsymmetrischen Grenzschichten in kompressiblen Flüssigkeiten,” *Journal of Applied Mathematics and Mechanics (ZAMM)*, vol. 28, p. 97–103. doi: <https://doi.org/10.1002/zamm.19480280401>
- Mathieu, J., and Scott, J. (2000), *An Introduction to Turbulent Flow*, Cambridge University Press, New York.
- Mattingly, G. E., and Criminale, W. O. (1972), “The Stability of an Incompressible Two-Dimensional Wake,” *Journal of Fluid Mechanics*, vol. 51, pp. 233–272. doi: <https://doi.org/10.1017/S0022112072001193>
- Maxwell, C. (1860), *Scientific Papers of Clerk Maxwell*, vol. 2, p. 1, Dover, New York.
- Mayle, R. E. (1991), “The Role of Laminar-Turbulent Transition in Gas Turbine Engines: A Discussion,” *Journal of Turbomachinery*, vol. 113, October, pp. 509–536. doi: <https://doi.org/10.1115/1.2929110>
- Meier, H. U., and Bradshaw, P. (Eds.) (1987), *Perspectives in Turbulence Studies*, Springer, Berlin.
- Meksyn, D. (1961), *New Methods in Laminar Boundary Layer Theory*, Pergamon, London.
- Mellor, G. L., and Gibson, D. M. (1966), “Equilibrium Turbulent Boundary Layers,” *Journal of Fluid Mechanics*, vol. 24, pp. 225–253. doi: <https://doi.org/10.1017/S0022112066000612>
- Menna, J. D., and Pierce, F. J. (1988), “The Mean Flow Structure around and within a Turbulent Junction or Horseshoe Vortex—Part I,” *Journal of Fluids Engineering*, vol. 110, pp. 406–414 [see also Part II, pp. 415–423]. doi: <https://doi.org/10.1115/1.3243571>
- Merzkirch, W. (1974), *Flow Visualization*, Academic, New York.
- (1987), *Flow Visualization*, 2nd ed., Elsevier, New York.
- Meseguer, A. (2003), “Streak Breakdown Instability in Pipe Poiseuille Flow,” *Physics of Fluids*, vol. 15, no. 5, pp. 1203–1213. doi: <https://doi.org/10.1063/1.1564093>
- Meskin, D. (1961), *New Methods in Laminar Boundary-Layer Theory*, Pergamon Press, London.
- Messiter, A. F. (1970), “Boundary-Layer Flow near the Trailing Edge of a Flat Plate,” *SIAM Journal on Applied Mathematics*, vol. 18, pp. 241–257. doi: <https://doi.org/10.1137/0118020>
- Michaelides, E. E. (2003), “Hydrodynamic Force and Heat/Mass Transfer from Particles, Bubbles, and Drops—The Freeman Scholar Lecture,” *Journal of Fluids Engineering*, vol. 125, March, pp. 209–238. doi: <https://doi.org/10.1115/1.1537258>
- Michel, R. (1952), “Etude de la transition sur les profils d’aile—établissement d’un point de transition et calcul de la traînée de profil en incompressible,” ONERA Report no. 1/1578A.

- Middleman, S. (1995), *Modeling Axisymmetric Flows: Dynamics of Films, Jets, and Drops*, Elsevier Science & Technology, New York.
- Miles, J. P., and Farrashkhalvat, M. (2003), *Basic Structural Grid Generation*, Butterworth-Heinemann, Woburn, MA.
- Mills, R. D. (1968), "Numerical Solutions of Viscous Flow through a Pipe Orifice at Low Reynolds Numbers," *Journal of Mechanical Engineering Science*, vol. 10, no. 2, pp. 133–140. doi: https://doi.org/10.1243/JMES_JOUR_1968_010_020_02
- Millsaps, K., and Pohlhausen, K. (1953), "Thermal Distribution in Jeffery–Hamel Flows between Nonparallel Plane Walls," *Journal of the Aeronautical Sciences*, vol. 20, pp. 187–196. doi: <https://doi.org/10.2514/8.2587>
- Milne, W. E. (1953), *Numerical Solution of Differential Equations*, Wiley, New York.
- Milne-Thomson, L. M. (1968), *Theoretical Hydrodynamics*, 5th ed., Macmillan, New York.
- Minkowycz, W. J., Sparrow, E. M., Schneider, G. E., and Pletcher, R. H. (1988), *Handbook of Numerical Heat Transfer*, Wiley, New York.
- Miyake, Y., Tsujimoto, K., and Nakaji, M. (2001), "Direct Numerical Simulation of Rough-Wall Heat Transfer in a Turbulent Channel Flow," *International Journal of Heat and Fluid Flow*, vol. 22, no. 3, pp. 237–244. doi: [https://doi.org/10.1016/S0142-727X\(01\)00085-6](https://doi.org/10.1016/S0142-727X(01)00085-6)
- Moeini, M., and Chamani, M. R. (2017), "New Perspectives on the Laminar Boundary Layer Physics in a Polarized Pressure Field with Temperature Gradient: An Analytical Approximation to Blasius Equation," *Journal of Applied Fluid Mechanics*, vol. 10, no. 4, pp. 1071–1077. doi: <https://doi.org/10.18869/acadpub.jafm.73.241.27544>Page 506
- Moffat, R. J., and Kays, W. M. (1984), "A Review of Turbulent Boundary Layer Heat Transfer Research at Stanford, 1958–1983," *Advances in Heat Transfer*, vol. 16, pp. 241–365. doi: [https://doi.org/10.1016/S0065-2717\(08\)70206-5](https://doi.org/10.1016/S0065-2717(08)70206-5)
- Moin, P. (2001), *Fundamentals of Engineering Numerical Analysis*, Cambridge University Press, New York.
- Moin, P., and Mahesh, K. (1998), "Direct Numerical Simulations: A Tool in Turbulence," *Annual Review of Fluid Mechanics*, vol. 30, pp. 539–578. doi: <https://doi.org/10.1146/annurev.fluid.30.1.539>
- Monin, A. S., and Yaglom, A. M. (1972), *Statistical Fluid Mechanics*, 2 vols., M.I.T. Press, Cambridge, MA.
- Monnoyer, F. (1997), "Hypersonic Boundary Layer Flows," Chap. 12 of *Flows at Large Reynolds Numbers*, H. Schmitt (Ed.), WIT Press, Computational Mechanics, Boston, MA.
- Moody, L. F. (1944), "Friction Factors for Pipe Flow," *ASME Transactions*, vol. 66, pp. 671–684.

- Moore, F. K. (1958), "On the Separation of the Unsteady Laminar Boundary Layer," in *Boundary Layer Research*, H. G. Görtler (Ed.), Springer, Berlin. doi: https://doi.org/10.1007/978-3-642-45885-9_23
- Moretti, P. M., and Kays, W. M. (1965), "Heat Transfer to a Turbulent Boundary Layer with Varying Free-stream Velocity and Varying Surface Temperature—An Experimental Study," *International Journal of Heat and Mass Transfer*, vol. 8, pp. 1187–1202. doi: [https://doi.org/10.1016/0017-9310\(65\)90062-1](https://doi.org/10.1016/0017-9310(65)90062-1)
- Morgan, K. (2004), *Introduction to Computational Fluid Dynamics*, Cambridge University Press, New York.
- Morkovin, M. V. (1962), "Effects of Compressibility on Turbulent Flows," in A. Favre (Ed.), *Mécanique de la Turbulence*, CNRS, Paris, pp. 367–380.
- (1969), "Critical Evaluation of Transition from Laminar to Turbulent Shear Layers with Emphasis on Hypersonically Traveling Bodies," AFFDL-TR-68-149, Wright-Patterson AFB, Ohio [see also C. S. Wells (1969), pp. 1–31].
- (1969a), "On The Many Faces of Transition," in *Viscous Drag*, C. S. Wells (Ed.), Plenum Press, New York. doi: https://doi.org/10.1007/978-1-4899-5579-1_1
- Morris, P. J., Raman, G., and McLaughlin, D. (Eds.) (2002), *High Speed Jet Flows: Fundamentals and Applications*, Taylor & Francis, New York.
- Morrison, G. L. (2003), "Euler Number Based Orifice Discharge Coefficient Relationship," *Journal of Fluids Engineering*, vol. 125, January, pp. 189–191. doi: <https://doi.org/10.1115/1.1521955>
- Moses, H. L., Jones, R. R. III, and Sparks, J. F. (1979), "An Integral Method for the Turbulent Boundary Layer with Separated Flows," in *Turbulent Boundary Layers*, ASME FED vol. G00145, pp. 69–73.
- Mueller, T. (Ed.) (2004), *Flow Visualization XI: Proceedings 11th Int. Symp.*, CD-ROM, University of Notre Dame, South Bend, IN.
- Muggli, F. A. (1997), "Flow Analysis in a Pump Diffuser—Part 2: Validation and Limitations of CFD for Diffuser Flows," *Journal of Fluids Engineering*, vol. 119, no. 4, pp. 978–984. doi: <https://doi.org/10.1115/1.2819526>
- Nachtsheim, P. R. (1963), "Stability of Free Convection Boundary Layer Flow Investigation by Integration of Disturbance Differential Equations," National Aeronautics and Space Administration Technical Note D-2089.
- (1964), "An Initial Value Method for the Numerical Treatment of the Orr–Sommerfeld Equation for the Case of Plane Poiseuille Flow," National Aeronautics and Space Administration Technical Note D-2414.
- Nakayama, A. (1995), *PC-Aided Numerical Heat Transfer and Convective Flow*, CRC Press, Boca Raton, FL.

- Nakayama, A., and Rahai, H. R. (1984), "Measurement of Turbulent Flow Behind a Flat Plate Mounted Normal to the Wall," *AIAA Journal*, vol. 22, pp. 1817–1819. doi: <https://doi.org/10.2514/3.8857>
- Nakayama, Y. (ed.) (1988), *Visualized Flow*, Pergamon, Oxford.
- Nakayama, Y., and Tanida, Y. (Eds.) (1996), *Atlas of Flow Visualization, vol. II*, CRC Press, Boca Raton, FL.
- Nansen, F. (1902), "The Oceanography of the North Polar Basin: The Norwegian North Polar Expedition," *Scientific Research (Christianiana)*, vol. 3, p. 357.
- Narasimha, R., and Sreenivasan, K. R. (1979), "Relaminarization of Fluid Flows," *Advances in Applied Mechanics*, vol. 19, pp. 221–309. doi: [https://doi.org/10.1016/S0065-2156\(08\)70311-9](https://doi.org/10.1016/S0065-2156(08)70311-9)
- Navier, C. L. M. H. (1823), "Mémoire sur les lois du mouvement des fluides," *Mem. Acad. R. Sci. Paris*, vol. 6, pp. 389–416.
- Nayfeh, A. H. (2000), *Perturbation Methods*, Wiley, New York.
- Newman, B. G. (1951), "Some Contributions to the Study of the Turbulent Boundary Layer Near Separation," Aust. Dept. Supply, Report ACA-53.
- Nikuradse, J. (1933), "Strömungsgesetze in rauhen Röhren," *Forsch. Arb. Ing.-Wes.*, no. 361.
- Obi, S., Aoki, K., and Masuda, S. (1993), "Experimental and Computational Study of Turbulent Separating Flow in an Asymmetric Plane Diffuser," *Proceedings of the 9th Symposium on Turbulent Shear Flows*, pp. 305–312, Kyoto, Japan.
- Obot, N. T. (1988), "Determination of Incompressible Flow Friction in Smooth Circular and Noncircular Passages: A Generalized Approach Including Validation of the Nearly Century-Old Hydraulic Diameter Concept," *Journal of Fluids Engineering*, vol. 110, pp. 431–440. doi: <https://doi.org/10.1115/1.3243574>
- Obremski, H. J., and Fejer, A. A. (1967), "Transition in Oscillating Boundary Layer Flow," *Journal of Fluid Mechanics*, vol. 29, pp. 93–111. doi: <https://doi.org/10.1017/S0022112067000655>
- Obremski, H. J., and Morkovin, M. V. (1969), "Application of a Quasi-Steady Stability Model to Periodic Boundary-Layer Flows," *AIAA Journal*, vol. 7, no. 7, pp. 1298–1301. doi: <https://doi.org/10.2514/3.5337>
- Obremski, H. J., et al. (1969), "A Portfolio of Stability Characteristics of Incompressible Boundary Layers," AGARDograph no. 134, NATO, Paris.
- Ockendon, H., and Ockendon, J. R. (1995), *Viscous Flow*, Cambridge University Press, New York.
- (2004), *Waves and Compressible Flow*, Springer-Verlag, New York.
- Oleinik, O. A., and Samokhin, V. N. (1999), *Mathematical Models in Boundary Layer*

Theory, CRC Press, Boca Raton, FL.

- Oliveira, A. C., and Almeida, A. C. L. (2019), “Numerical Solution of Boundary Layer Equations Based on Optimization: The Ostrach and Blasius Models,” *International Journal of Non-Linear Mechanics*, vol. 113, pp. 103–111. doi: <https://doi.org/10.1016/j.ijnonlinmec.2019.03.017>
- Oljaca, M., and Sucec, J. (1997), “Prediction of Transpired Turbulent Boundary Layers with Arbitrary Pressure Gradients,” *Journal of Fluids Engineering*, vol. 119, Sept., pp. 526–532. doi: <https://doi.org/10.1115/1.2819276>
- Oosthuizen, P. H. (1999), *Introduction to Convective Heat Transfer*, McGraw-Hill, New York.
- Oosthuizen, P. H., and Carscallen, W. E. (1997), *Compressible Fluid Flow*, McGraw-Hill, New York.
- Oran, E. S., Oh, C. K., and Cybyk, B. Z. (1998), “Direct Simulation Monte Carlo: Recent Advances and Applications,” *Annual Review of Fluid Mechanics*, vol. 30, pp. 403–441. doi: <https://doi.org/10.1146/annurev.fluid.30.1.403>Page 507
- Orr, W. M’F. (1907), “The Stability or Instability of the Steady Motions of a Perfect Liquid and of a Viscous Liquid,” *Proceedings of the Royal Irish Academy A*, vol. 27, pp. 9–68; 69–138.
- Orszag, S. A., Glowinski, R., and Fletcher, C. A. J. (1991), *Computational Techniques for Fluid Dynamics: Fundamental and General Techniques*, Springer-Verlag, New York.
- Oseen, C. W. (1910), “Über die Stokes’sche Formel und über eine verwandte Aufgabe in der Hydrodynamik,” *Arkiv för matematik, astronomi och fysik*, vol. 6, no. 29.
- (1927), “Neure Methoden und Ergebnisse in der Hydrodynamik,” Akademische Verlag, Geest & Portig, Leipzig.
- Osterlund, J. M. (1999), “Experimental Studies of Zero-Pressure-Gradient Turbulent Boundary Layer Flow,” Ph.D. Dissertation, Dept. of Mechanics, Royal Institute of Technology, Stockholm, Sweden.
- Osterlund, J. M., Johansson, A. V., and Nagib, H. M. (2000), “Comment on ‘A Note on the Intermediate Region in Turbulent Boundary Layers,’” *Physics of Fluids*, vol. 12, no. 9, pp. 2360–2363. doi: <https://doi.org/10.1063/1.1287660>
- Ostrach, S. (1953), “An Analysis of Laminar Free-Convection Flow and Heat Transfer about a Flat Plate Parallel to the Direction of the Generating Body Force,” NACA Report 1111.
- (1982), “Low Gravity Fluid Flows,” *Annual Review of Fluid Mechanics*, vol. 14, pp. 313–345. doi: <https://doi.org/10.1146/annurev.fl.14.010182.001525>
- Owens, E. J., and Thodos, G. (1957), “Thermal Conductivity Reduced-State Correlation for the Inert Gases,” *AIChE Journal*, vol. 3, pp. 454–461.

- Owens, R. G., and Phillips, T. N. (2002), *Computational Rheology*, Imperial College Press, London.
- Pai, S. I. (1954), *Fluid Dynamics of Jets*, Van Nostrand, New York.
- Paneras, A. G. (1997), “On the Calculation of Turbulent Incompressible Flow about a 6:1 Prolate Spheroid at High Incidence,” in *Advances in Fluid Mechanics*, vol. 11, pp. 323–360, Computational Mechanics, Boston.
- Panton, R. L. (1996), *Incompressible Flow*, 2nd ed., Wiley, New York.
- Papanastasiou, T., A. N. Alexandrou, and Georgiou, G. (1999), *Viscous Fluid Flow*, CRC Press, Boca Raton, FL.
- Parand, K., and Taghavi, A. (2009), “Rational Scaled Generalized Laguerre Function Collocation Method for Solving the Blasius Equation,” *Journal of Computational and Applied Mathematics*, vol. 233, no. 4, pp. 980–989. doi: <https://doi.org/10.1016/j.cam.2009.08.106>
- Parand, K., Dehghan, M., and Baharifard, F. (2013), “Solving a Laminar Boundary Layer Equation with the Rational Gegenbauer Functions,” *Applied Mathematical Modelling*, vol. 37, no. 3, pp. 851–863. doi: <https://doi.org/10.1016/j.apm.2012.02.041>
- Parand, K., Dehghan, M., and Pirkhedri, A. (2009), “Sinc-Collocation Method for Solving the Blasius Equation,” *Physics Letters A*, vol. 373, no. 44, pp. 4060–4065. doi: <https://doi.org/10.1016/j.physleta.2009.09.005>
- Parand, K., Dehghan, M., and Taghavi, A. (2010), “Modified Generalized Laguerre Function Tau Method for Solving Laminar Viscous Flow: The Blasius Equation,” *International Journal of Numerical Methods for Heat and Fluid Flow*, vol. 20, no. 7, pp. 728–743. doi: <https://doi.org/10.1108/09615531011065539>
- Park, C. (1990), *Nonequilibrium Hypersonic Aerothermodynamics*, Wiley, New York.
- Parlange, J. Y., Braddock, R. D., and Sander, G. (1981), “Analytical Approximations to the Solution of the Blasius Equation,” *Acta Mechanica*, vol. 38, no. 1, pp. 119–125. doi: <https://doi.org/10.1007/BF01351467>
- Parry, W. T., Bellows, J. C., Gallagher, J. S., and Harvey, A. H. (2000), *ASME International Steam Tables for Industrial Use*, ASME Press, New York (software also available).
- Patankar, S. V. (1980), *Numerical Heat Transfer and Fluid Flow*, Hemisphere, New York.
- Patel, V. C. (1998), “Perspective: Flow at High Reynolds Numbers and Over Rough Surfaces—Achilles Heel of CFD,” *Journal of Fluids Engineering*, vol. 120, pp. 434–444. doi: <https://doi.org/10.1115/1.2820682>
- Patel, V. C., Rodi, W., and Scheuerer, G. (1985), “Turbulence Models for Near-Wall and Low Reynolds Number Flows: A Review,” *AIAA Journal*, vol. 23, no. 9, pp. 1308–1319. doi: <https://doi.org/10.2514/3.9086>

- Peaceman, D. W., and Rachford, H. H. (1955), "The Numerical Solution of Parabolic and Elliptic Differential Equations," *Journal of the Society for Industrial and Applied Mathematics*, vol. 3, pp. 28–41. doi: <https://doi.org/10.1137/0103003>
- Peker, H. A., Karaoğlu, O., and Oturanç, G. (2011), "The Differential Transformation Method and Pade Approximant for a Form of Blasius Equation," *Mathematical and Computational Applications*, vol. 16, no. 2, pp. 507–513. doi: <https://doi.org/10.3390/mca16020507>
- Petukhov, B. S. (1970), "Heat Transfer and Friction in Turbulent Pipe Flow with Variable Physical Properties," *Advances in Heat Transfer*, vol. 6, pp. 503–564. doi: [https://doi.org/10.1016/S0065-2717\(08\)70153-9](https://doi.org/10.1016/S0065-2717(08)70153-9)
- Peyret, R. (2002), *Spectral Methods for Incompressible Viscous Flow*, Springer-Verlag, New York.
- Peyret, R., and Taylor, T. D. (1983), *Computational Methods for Fluid Flow*, Springer, New York.
- Pfenninger, W., and Reed, V. D. (1966), "Laminar Flow Research and Experiments," *Astronautics and Aeronautics*, vol. 4, no. 7, pp. 44–50.
- Phillips, O. M. (1978), *Dynamics of the Upper Ocean*, 2nd ed., Cambridge University Press, New York.
- Piercy, N. A. V., and Preston, J. H. (1936), "A Simple Solution of the Flat Plate Problem of Skin Friction and Heat Transfer," *Philosophical Magazine*, vol. 21, no. 143, pp. 995–1005. doi: <https://doi.org/10.1080/14786443608561644>
- Piercy, N. A. V., Hooper, M. S., and Winny, H. F. (1933), "Viscous Flow through Pipes with Cores," *Philosophical Magazine*, vol. 15, no. 7, pp. 647–676. doi: <https://doi.org/10.1080/14786443309462212>
- Pipes, L. A. (1958), *Applied Mathematics for Engineers and Physicists*, McGraw-Hill, New York.
- Piquet, J., Richards, J. A., and Jia, X. (2001), *Turbulent Flows: Models and Physics*, Springer-Verlag, New York.
- Pironneau, O. (1989), *Finite Element Methods for Fluids*, Masson, Paris.
- Pirozzoli, S. (2011), "Numerical Methods for High-Speed Flows," *Annual Review of Fluid Mechanics*, vol. 43, no. 1, pp. 163–194. doi: <https://doi.org/10.1146/annurev-fluid-122109-160718>
- Pirro, D. M., Wills, J. G., and Wessol, A. (2001), *Lubrication Fundamentals*, Marcel Dekker, New York.
- Plapp, J. E. (1957), "The Analytic Study of Laminar Boundary Layer Stability in Free Convection," *Journal of the Aeronautical Sciences*, vol. 24, pp. 318–319.

- Plesniak, M. W., and Johnston, J. P. (1988), "The Effects of Stabilizing and Destabilizing Curvature on a Plane Mixing Layer," in M. Hirata, and N. Kasagi (Eds.), *Transport Phenomena in Turbulent Flows*, pp. 377–390, Hemisphere, New York.
- Pletcher, R. H. (1978), "Prediction of Incompressible Turbulent Separating Flows," *Journal of Fluids Engineering*, vol. 100, pp. 427–433. doi: <https://doi.org/10.1115/1.3448702>
- (1988), "Progress in Turbulent Forced Convection," *Journal of Heat Transfer*, 50th Anniv. Issue, pp. 1129–1144. Page 508
- Pohlhausen, E. (1921), "Der Wärmeaustausch zwischen festen Körpern und Flüssigkeiten mit kleiner Reibung und kleiner Wärmeleitung," *Journal of Applied Mathematics and Mechanics (ZAMM)*, vol. 1, pp. 115–121. doi: <https://doi.org/10.1002/zamm.19210010205>
- Pohlhausen, K. (1921), "Zur Näherungsweise Integration Der Differentialgleichung Der laminaren Grenzschicht," *Journal of Applied Mathematics and Mechanics (ZAMM)*, vol. 1, no. 4, pp. 252–290. doi: <https://doi.org/10.1002/zamm.19210010402>
- Poiseuille, J. L. M. (1840), "Recherches expérimentales sur le mouvement des liquides dans les tubes de très-petits diamètres," *Comptes Rendus*, vol. 11, pp. 961–967; 1041–1048.
- Polderman, H. G., Velraeds, G., and Knol, W. (1986), "Turbulent Lubrication Flow in an Annular Channel," *Journal of Fluids Engineering*, vol. 108, pp. 185–192. doi: <https://doi.org/10.1115/1.3242561>
- Polymeropoulos, C. E., and Gebhart, B. (1967), "Incipient Instability in Free Convection Boundary Layers," *Journal of Fluid Mechanics*, vol. 30, pp. 225–239 [see also *AIAA Journal*, vol. 4, p. 2066–2068 (1966)]. doi: <https://doi.org/10.1017/S0022112067001405>
- Pope, S. B. (2000), *Turbulent Flows*, Cambridge University Press, New York.
- Prandtl, L. (1904), "Über Flüssigkeitsbewegung bei sehr kleiner Reibung," *Proceedings of the Third International Mathematical Congress Heidelberg* [English translation in NACA Technical Memo. 452].
- (1921), "Bemerkung über die Entstehung der Turbulenz," *Journal of Applied Mathematics and Mechanics (ZAMM)*, vol. 1, pp. 431–436. doi: <https://doi.org/10.1002/zamm.19210010602>
- (1925), "Über die ausgebildete Turbulenz," *Journal of Applied Mathematics and Mechanics (ZAMM)*, vol. 5, pp. 136–139. doi: <https://doi.org/10.1002/zamm.19250050212>
- (1945a), "Über ein neues Formelsystem für die ausgebildete Turbulenz," *Nachrichten der Akademie der Wissenschaften zu Göttingen, Mathematisch-physikalische Klasse. II*, p. 6.
- (1945b), "Über Reibungsschicht bei dreidimensionalen Strömungen," *Betz-Festschrift 1945*, pp. 134–141.

- (1961), *Collected Works*, vols. 1–3, Springer, Berlin.
- Present, R. D. (1958), *Kinetic Theory of Gases*, McGraw-Hill, New York.
- Profilo, G., Soliani, G., and Tebaldi, C. (1998), “Some Exact Solutions of the Two-Dimensional Navier–Stokes Equations,” *International Journal of Engineering Science*, vol. 36, no. 4, pp. 459–471. doi: [https://doi.org/10.1016/S0020-7225\(97\)00065-7](https://doi.org/10.1016/S0020-7225(97)00065-7)
- Proudman, I., and Pearson, J. R. A. (1957), “Expansions at Small Reynolds Numbers for the Flow Past a Sphere and a Circular Cylinder,” *Journal of Fluid Mechanics*, vol. 2, pp. 237–262. doi: <https://doi.org/10.1017/S0022112057000105>
- Punnis, B. (1956a), “Zur Differentialgleichung Der Plattengrenzschicht Von Blasius,” *Journal of Applied Mathematics and Mechanics (ZAMM)*, vol. 36, no. S1, pp. S26–S26. doi: <https://doi.org/10.1002/zamm.19560361310>
- Punnis, B. (1956b), “Zur Differentialgleichung Der Plattengrenzschicht Von Blasius,” *Archiv der Mathematik*, vol. 7, no. 3, pp. 165–171. doi: <https://doi.org/10.1007/BF01899833>
- Raffel, M., Willert, C. E., and Kompenhaus, J. (1998), *Particle Image Velocimetry: A Practical Guide*, Springer-Verlag, New York.
- Ragab, S. A., and Nayfeh, A. H. (1982), “A Comparison of the Second Order Triple-Deck Theory with Interacting Boundary Layers,” in T. Cebeci (Ed.), *Numerical and Physical Aspects of Aerodynamic Flows*, p. 237, Springer, New York [see also AIAA Paper 80-0072, 1980]. doi: https://doi.org/10.1007/978-3-662-12610-3_14
- Raithby, G. (1971), “Laminar Heat Transfer in the Thermal Entrance Region of Circular Tubes and Two-Dimensional Rectangular Ducts with Wall Suction and Injection,” *International Journal of Heat and Mass Transfer*, vol. 14, no. 2, pp. 223–243. doi: [https://doi.org/10.1016/0017-9310\(71\)90091-3](https://doi.org/10.1016/0017-9310(71)90091-3)
- Rasmussen, M. (1994), *Hypersonic Flow*, Interscience, New York.
- Raupach, M. R., Antonia, R. A., and Rajagopalan, S. (1997), “Rough Wall Turbulent Boundary Layers,” *Applied Mechanics Reviews*, vol. 44, pp. 1–25. doi: <https://doi.org/10.1115/1.3119492>
- Rayleigh, Lord (1880), *Scientific Papers*, vol. 1, pp. 474–487, Dover, New York.
- (1916), “On the Dynamics of Revolving Fluids,” *Proceedings of the Royal Society of London, Series A*, vol. 93, pp. 148–154. <https://doi.org/10.1098/rspa.1917.0010>
- Reed, H. L., Saric, W. S., and Arnal, D. (1996), “Linear Stability Theory Applied to Boundary Layers,” *Annual Review of Fluid Mechanics*, vol. 28, no. 1, pp. 389–428. doi: <https://doi.org/10.1146/annurev.fl.28.010196.002133>
- Reichardt, H. (1956), “Über die Geschwindigkeitsverteilung in einer geradlinigen turbulenten Couette-Strömung,” *Journal of Applied Mathematics and Mechanics (ZAMM)*, Sonderheft, vol. 36, pp. 26–29. doi: <https://doi.org/10.1002/zamm.19560361311>

- Reid, R. C., Pravsnitz, J. M., and Sherwood, T. K. (1987), *The Properties of Gases and Liquids*, 4th ed., McGraw-Hill, New York.
- Reiner, M. (1969), *Deformation, Strain and Flow: An Elementary Introduction to Rheology*, 3rd ed., H. K. Lewis, London.
- Remove: Kreyszig, E. (1999), *Advanced Engineering Mathematics*, 8th ed., Wiley, New York.
- Reshotko, E. (1976), "Boundary Layer Stability and Transition," *Annual Review of Fluid Mechanics*, vol. 8, pp. 311–349. doi: <https://doi.org/10.1146/annurev.fl.08.010176.001523>
- (1979), "Drag Reduction by Cooling in Hydrogen-Fueled Aircraft," *Journal of Aircraft*, vol. 16, no. 9, pp. 584–590. doi: <https://doi.org/10.2514/3.58571>
- (1985), "Control of Boundary Layer Transition," AIAA Paper 85-0562, March 12–14, Boulder, CO.
- (1987), "Stability and Transition, How Much Do We Know?," in Lamb (Ed.), *Proceedings of the Tenth U.S. National Congress of Applied Mechanics*, pp. 421–434, Amer. Soc. Mech. Engineers, New York.
- (1988), "Stability and Transition of Boundary Layers," in H. Branover, M. Mond, and Y. Unger (Eds.), *Progress in Astronautics and Aeronautics*, vol. 112, pp. 278–311, AIAA, Washington, DC.
- Reynolds, O. (1874), "On the Extent and Action of the Heating Surface for Steam Boilers," *Manchester Literary and Philosophical Society*, vol. 14, pp. 7–12. doi: [https://doi.org/10.1016/0017-9310\(61\)90087-4](https://doi.org/10.1016/0017-9310(61)90087-4)
- (1883), "An Experimental Investigation of the Circumstances Which Determine Whether the Motion of Water Shall be Direct or Sinuous, and the Law of Resistance in Parallel Channels," *Philosophical Transactions of the Royal Society of London, Series A*, vol. 174, pp. 935–982. doi: <https://doi.org/10.1098/rstl.1883.0029>
- (1886), "On the Theory of Lubrication and Its Application to Mr. Beauchamp Tower's Experiments Including an Experimental Determination of the Viscosity of Olive Oil," *Philosophical Transactions of the Royal Society of London, Series A*, vol. 177, pp. 157–234. doi: <https://doi.org/10.1098/rstl.1886.0005>
- (1895), "On the Dynamical Theory of Incompressible Viscous Fluids and the Determination of the Criterion," *Philosophical Transactions of the Royal Society of London, Series A*, vol. 186, pp. 123–164. doi: <https://doi.org/10.1098/rsta.1895.0004>Page 509
- Reynolds, W. C., Kays, W. M., and Kline, S. J. (1958), "Heat Transfer in the Turbulent Incompressible Boundary Layer: Part 1, Constant Wall Temperature; Part 2, Step-Wall Temperature Distribution; Part 3, Arbitrary Wall Temperature and Heat Flux; Part 4, Effect of Location of Transition and Prediction of Heat Transfer in a Known Transition

Region,” NACA Memos. no. 12–1-58W–12–4-58W.

- Riahi, D. N. (2000), *Flow Instability*, WIT Press/Computational Mechanics, Boston, MA.
- Richardson, E. G., and Tyler, E. (1929), “The Transverse Velocity Gradients near the Mouth of a Pipe in Which an Alternating or Continuous Flow of Air Is Established,” *Proceedings of the Physical Society London*, vol. 42, pp. 1–15. doi: <https://doi.org/10.1088/0959-5309/42/1/302>
- Richardson, J., and Power, H. (1996), “A Boundary Element Analysis of Creeping Flow Past Two Porous Bodies of Arbitrary Shape,” *Engineering Analysis with Boundary Elements*, vol. 17, no. 3, pp. 193–204. doi: [https://doi.org/10.1016/S0955-7997\(96\)00003-3](https://doi.org/10.1016/S0955-7997(96)00003-3)
- Richardson, S. (1973), “On Blasius’s Equation Governing Flow in the Boundary Layer on a Flat Plate,” *Mathematical Proceedings of the Cambridge Philosophical Society*, vol. 74, no. 1, pp. 179–184. doi: <https://doi.org/10.1017/S0305004100047939>
- Rist, U., and Fasel, H. (1995), “Direct Numerical Simulation of Controlled Transition in a Flat-Plate Boundary Layer,” *Journal of Fluid Mechanics*, vol. 298, pp. 211–248. doi: <https://doi.org/10.1017/S0022112095003284>
- Rivkin, S. L. (1988), *Thermodynamic Properties of Gases*, 4th ed., Hemisphere, New York.
- Roache, P. J. (1976), *Computational Fluid Dynamics*, revised ed., Hermosa Press, Albuquerque.
- Robertson, J. M. (1965), *Hydrodynamics in Theory and Application*, Prentice-Hall, Englewood Cliffs, NJ.
- Robinson, W. A. (1976), “The Existence of Multiple Solutions for the Laminar Flow in a Uniformly Porous Channel with Suction at Both Walls,” *Journal of Engineering Mathematics*, vol. 10, no. 1, pp. 23–40. doi: <https://doi.org/10.1007/BF01535424>
- Rodi, W. (1976), “A New Algebraic Relation for Calculating Reynolds Stress,” *Journal of Applied Mathematics and Mechanics (ZAMM)*, vol. 56, pp. 331–340. doi: <https://doi.org/10.1002/zamm.19765613093>
- (1984), *Turbulence Models and Their Application in Hydraulics*, Brookfield, Brookfield, VT.
- Rogers, D. F. (1992), *Laminar Flow Analysis*, Cambridge University Press, New York.
- Rogers, M. G., and Lance, G. N. (1960), “The Rotationally Symmetric Flow of a Viscous Fluid in the Presence of an Infinite Rotating Disk,” *Journal of Fluid Mechanics*, vol. 7, pp. 617–631. doi: <https://doi.org/10.1017/S0022112060000335>
- Roll, H. U. (1965), *Physics of the Marine Atmosphere*, International Geophysics Series, vol. 7, Academic, New York.
- Roman-Miller, L., and Broadbridge, P. (2000), “Exact Integration of Reduced Fisher’s Equation, Reduced Blasius Equation, and the Lorenz Model,” *Journal of Mathematical*

- Analysis and Applications*, vol. 251, no. 1, pp. 65–83. doi: <https://doi.org/10.1006/jmaa.2000.7020>
- Rose, P. H., and Stark, W. I. (1958), “Stagnation Point Heat Transfer Measurements in Dissociated Air,” *Journal of the Aeronautical Sciences*, vol. 25, pp. 86–97. doi: <https://doi.org/10.2514/8.7519>
- Rosenhead, L. (1940), “The Steady Two-Dimensional Radial Flow of Viscous Fluid between Two Inclined Plane Walls,” *Proceedings of the Royal Society of London, Series A*, vol. 175, pp. 436–467. <https://doi.org/10.1098/rspa.1940.0068>
- Rosenhead, L. (Ed.) (1963), *Laminar Boundary Layers*, Oxford University Press, London.
- Ross, J. A., and Barnes, F. H. (1970), “The Flat Plate Boundary Layer, Part 3, Comparison of Theory with Experiment,” *Journal of Fluid Mechanics*, vol. 43, pp. 819–832. doi: <https://doi.org/10.1017/S002211207000277X>
- Rott, N. (1964), “Theory of Time-Dependent Laminar Flows,” in F. K. Moore (Ed.), *High Speed Aerodynamics and Jet Propulsion—Theory of Laminar Flows*, Section D, vol. IV, pp. 395–438, Princeton University Press, Princeton, NJ. doi: <https://doi.org/10.1515/9781400875375>
- Rott, N., and Crabtree, L. F. (1952), “Simplified Laminar Boundary Layer Calculation for Bodies of Revolution and Yawed Wings,” *Journal of the Aeronautical Sciences*, vol. 19, pp. 553–565. doi: <https://doi.org/10.2514/8.2381>
- Rotta, J. C. (1956), “Experimenteller Beitrag zur Entstehung turbulenter Strömung im Rohr,” *Inženýr architekt*, vol. 24, pp. 258–281. doi: <https://doi.org/10.1007/BF00536526>
- (1986), “Experience of Second Order Turbulent Closure Models,” *Zeitschrift für Flugwissenschaften und Weltraumforschung* vol. 10, pp. 401–407.
- Roumeliotis, J., and Fulford, G. R. (2000), “Droplet Interactions in Creeping Flow,” *Computers & Fluids*, vol. 29, no. 4, pp. 435–450. doi: [https://doi.org/10.1016/S0045-7930\(99\)00032-8](https://doi.org/10.1016/S0045-7930(99)00032-8)
- Rouse, H., and Ince, S. (1957), *History of Hydraulics*, State University of Iowa, Institute of Hydraulic Research, Iowa City, Ia.
- Runge, C. (1901), “Über empirische Funktionen und die Interpolation zwischen äquidistanten Ordinaten,” *Zeitschrift für Mathematik und Physik*, vol. 46, pp. 224–243.
- Rybczynski, W. (1911), “Über die fortschreitende Bewegung einer flüssigen Kugel in einem zähen Medium,” *Bulletin International de l’Academie des Sciences de Cracovie*, vol. 1911A, pp. 40–46.
- Sachdev, P. L. (2000), *Self-Similarity and Beyond: Exact Solutions of Nonlinear Problems*, CRC Press, Boca Raton, Fl.
- Sagaut, P., and Germano, M. (2002), *Large Eddy Simulation for Incompressible Flows: An Introduction*, Springer-Verlag, New York.

- Saad, T., and Majdalani, J. (2010), "On the Lagrangian Optimization of Wall-Injected Flows: From the Hart–McClure Potential to the Taylor–Culick Rotational Motion," *Proceedings of the Royal Society of London, Series A*, vol. 466, no. 2114, pp. 331–362. doi: <https://doi.org/10.1098/rspa.2009.0326>
- Saad, T., and Majdalani, J. (2009), "Rotational Flowfields in Porous Channels with Arbitrary Headwall Injection," *Journal of Propulsion and Power*, vol. 25, no. 4, pp. 921–929. doi: <https://doi.org/10.2514/1.41926>
- Saad, T., and Majdalani, J. (2012), "Some Thoughts on the Pressure Integration Requirements of the Navier-Stokes Equations," *Fluid Dynamics Research*, vol. 44, no. 7, pp. 065508-11. doi: <https://doi.org/10.1088/0169-5983/44/6/065508>
- Saad, T., and Majdalani, J. (2017), "Viscous Mean-Flow Approximations for Porous Tubes with Radially Regressing Walls," *AIAA Journal*, vol. 55, no. 11, pp. 3868–3880. doi: <https://doi.org/10.2514/1.J055949>
- Sandham, N. D., and Reynolds, W. C. (1987), "Some Inlet Plane Effects on the Numerically Simulated Spatially Developing Two-Dimensional Mixing Layer," *Proceedings of the Sixth Symposium on Turbulent Shear Flows*, pp. 22–4-1–22–4-6, Toulouse, France. doi: https://doi.org/10.1007/978-3-642-73948-4_33
- Saric, W. S., and Nayfeh, A. S. (1975), "Nonparallel Stability of Boundary Layer Flows," *Physics of Fluids*, vol. 18, pp. 945–950. doi: <https://doi.org/10.1063/1.861266>
- Saric, W. S., and Thomas, A. S. W. (1984), "Experiments on the Subharmonic Route to Turbulence in Boundary Layers," in T. Tatsumi (Ed.), *Turbulence and Chaotic Phenomena in Fluids*, pp. 117–122, Elsevier, New York.
- Saric, W. S., and Reed, H. L. (1987), "Three-Dimensional Stability of Boundary Layers," in Meier, H. U., and Bradshaw, P. (Eds.), *Perspectives in Turbulence Studies*, pp. 71–92, Springer, Berlin.
- Saric, W. S., Reed, H. L., and Kershen, E. J. (2002), "Boundary-Layer Receptivity to Freestream Disturbances," *Annual Review of Fluid Mechanics*, vol. 34, pp. 291–319. doi: <https://doi.org/10.1146/annurev.fluid.34.082701.161921Page510>
- Saric, W. S., Reed, H. L., and White, E. B. (2003), "Stability and Transition of Three-Dimensional Boundary Layers," *Annual Review of Fluid Mechanics*, vol. 35, no. 1, pp. 413–440. doi: <https://doi.org/10.1146/annurev.fluid.35.101101.161045>
- Sasmal, G. P., and Hochstein, J. I. (1994), "Marangoni Convection with a Curved and Deforming Surface in a Cavity," *Journal of Fluids Engineering*, vol. 116, Sept., pp. 577–582. doi: <https://doi.org/10.1115/1.2910316>
- Savaş, Ö. (2012), "An Approximate Compact Analytical Expression for the Blasius Velocity Profile," *Communications in Nonlinear Science and Numerical Simulation*, vol. 17, no. 10, pp. 3772–3775. doi: <https://doi.org/10.1016/j.cnsns.2012.02.002>
- Schetz, J. A. (1980), *Injection and Mixing in Turbulent Flow*, AIAA, vol. 69, New York.

- (1984), *Foundations of Boundary Layer Theory for Momentum, Heat, and Mass Transfer*, Prentice-Hall, Englewood Cliffs, NJ.
- (1992), *Boundary Layer Analysis*, Prentice-Hall, Upper Saddle River, NJ.
- Schetz, J. A. (1984), *Foundations of Boundary Layer Theory for Momentum, Heat, and Mass Transfer*, 1st ed., Prentice Hall.
- Schetz, J. A., and Bowersox, R. D. W. (2011), *Boundary Layer Analysis, AIAA Education Series*, 2nd ed., American Institute of Aeronautics and Astronautics, Reston, United States. doi: <https://doi.org/10.2514/4.868245>
- Schlichting, H. (1932), “Berechnung ebener periodischer Grenzschichtströmungen,” *Phys. Z.*, vol. 33, pp. 327–335.
- (1933a), “Laminare Strahlenausbreitung,” *Journal of Applied Mathematics and Mechanics (ZAMM)*, vol. 13, pp. 260–263. doi: <https://doi.org/10.1002/zamm.19330130403>
- (1933b), “Zur Entstehung der Turbulenz bei der Plattenströmung,” *Nachrichten von der Gesellschaft der Wissenschaften zu Göttingen, Mathematisch-physikalische Klasse*, pp. 182–208.
- (1979), *Boundary Layer Theory*, 7th ed., McGraw-Hill, New York.
- Schlichting, H., and Bussmann, K. (1943), “Exakte Lösungen für die laminare Grenzschicht mit Absaugung und Ausblasen,” *Schr. Deutsch. Akad. Luftfahrtforschung*, ser. B, vol. 7, no. 2.
- Schlichting, H., and Gersten, K. (2000), *Boundary Layer Theory*, 8th ed., Springer, New York.
- Schlichting, H., and Gersten, K. (2017), *Boundary-Layer Theory*, 9th ed., Springer-Verlag, Berlin.
- Schmid, P. J., and Henningson, D. S. (2001), *Stability and Transition in Shear Flows*, Springer, New York.
- Schmidt, E., and Wenner, K. (1941), “Wärmeabgabe über den Umfang eines angeblasenen geheizten Zylinders,” *Forsch. Arb. Ing.-Wes.*, vol. 12, pp. 65–73. doi: <https://doi.org/10.1007/BF02584944>
- Schmidt, E., Beckmann, W., and Pohlhausen, E. (1930), “Das Temperatur- und Geschwindigkeitsfeld vor einer Wärme abgebenden senkrechten Platte bei natürlicher Konvektion,” *Forsch. Arb. Ing.-Wes.*, vol. 1, pp. 391–404. doi: <https://doi.org/10.1007/BF02660553>
- Schmidt, F. W., and Zeldin, B. (1969), “Laminar Flow in the Inlet Section of Tubes and Ducts,” *AIChE Journal*, vol. 15, pp. 612–614. doi: <https://doi.org/10.1002/aic.690150425>

- Schmitt, H. (Ed.) (1997), *Flow at Large Reynolds Numbers, Advances in Fluid Mechanics*, vol. 11, Computational Mechanics, Boston, MA.
- Schoenherr, K. E. (1932). "Resistance of Plates," *Transactions of the Society of Naval Architects and Marine Engineers*, vol. 40, p. 285.
- Schreier, S. (1982), *Compressible Flow*, Willey, New York.
- Schubauer, G. B. (1935), "Airflow in a Separating Laminar Boundary Layer," NACA Report 527.
- Schubauer, G. B., and Skramstad, H. (1947), "Laminar Boundary Layer Oscillations and Transition on a Flat Plate," *Journal of Research of the National Bureau of Standards*, vol. 38, pp. 251–292 [see also NACA Report 909 (1948)].
- Schubauer, G. B., and Klebanoff, P. S. (1955), "Contributions on the Mechanics of Boundary Layer Transition," NACA Technical Note 3489 [see also NACA Report 1289].
- Scott, J. L., Brennan, J. A., and Blakeslee, D. M. (1994), "GRI/NIST Orifice Meter Discharge Coefficient Database, vol. 1," NIST Standard Reference Database 45, U.S. Dept. of Commerce, National Institute of Standards, Gaithersburg, Md.
- Sears, W. R. (1948), "Boundary Layer of Yawed Cylinders," *Journal of the Aeronautical Sciences*, vol. 15, pp. 49–52 [see also *Applied Mechanics Reviews*, vol. 7, pp. 281–285 (1954)]. doi: <https://doi.org/10.2514/8.11499>
- Sedov, L. I. (1959), *Similarity and Dimensional Methods in Mechanics*, Academic, New York.
- Sellars, J. R. (1955), "Laminar Flow in Channels with Porous Walls at High Suction Reynolds Numbers," *Journal of Applied Physics*, vol. 26, no. 4, pp. 489–490. doi: <https://doi.org/10.1063/1.1722024>
- Sellars, J. R., Tribus, M., and Klein, J. S. (1956), "Heat Transfer to Laminar Flow in a Round Tube or Flat Conduit: The Graetz Problem Extended," *ASME Transactions*, vol. 78, pp. 441–448. doi: <https://doi.org/10.21236/ada280848>
- Senecal, V. E., and Rothfus, R. R. (1953), "Transition Flow of Fluids in Smooth Tubes," *Chemical Engineering Progress*, vol. 49, pp. 533–538.
- Settles, G. S. (2004), *Schlieren and Shadowgraph Techniques; Visualizing Phenomena in Transparent Media*, Springer-Verlag, New York.
- Settles, G. S., Fitzpatrick, T. J., and Bogdonoff, S. M. (1979), "Detailed Study of Attached and Separated Compression Corner Flowfields in High Reynolds Number Supersonic Flow," *AIAA Journal*, vol. 17, no. 6, pp. 579–585. doi: <https://doi.org/10.2514/3.61180>
- Sexl, T. (1930), "Über Den Von E.G. Richardson Entdeckten 'Annulareffekt'," *Zeitschrift für Physik*, vol. 61, no. 5-6, pp. 349–362. doi: <https://doi.org/10.1007/BF01340631>
- Shah, R. K. (1978), "A Correlation for Laminar-Hydrodynamic Entry Length Solutions for

- Circular and Noncircular Ducts,” *Journal of Fluids Engineering*, vol. 100, pp. 177–179. doi: <https://doi.org/10.1115/1.3448626>
- Shah, R. K., and London, A. L. (1978), *Laminar Flow Forced Convection in Ducts*, Academic, New York.
- Shank, M. E. (1954), “Brittle Failure of Nonship Steel-plate Structures,” *Mechanical Engineering*, vol. 76, pp. 23–28.
- Shapiro, A. H. (1953, 1954), *The Dynamics and Thermodynamics of Compressible Fluid Flow*, vols. 1 and 2, Ronald Press, New York.
- Sharatchandra, M. C., Sen, M., and Gad-el-Hak, M. (1997), “Navier–Stokes Simulations of a Novel Viscous Pump,” *Journal of Fluids Engineering*, vol. 119, June, pp. 372–382. doi: <https://doi.org/10.1115/1.2819144>
- Sharipov, F., and Kalempa, D. (2003) “Velocity Slip and Temperature Jump Coefficients for Gaseous Mixtures. 1. Viscous Slip Coefficient,” *Physics of Fluids*, vol. 15, no. 6, pp. 1800–1806. doi: <https://doi.org/10.1063/1.1574815>
- Sharipov, F., and Seleznev, V. (1998), “Data on Internal Rarefied Gas Flows,” *Journal of Physical and Chemical Reference Data*, vol. 27, p. 657. doi: <https://doi.org/10.1063/1.556019>
- Shen, S. F. (1954), “Calculated Amplified Oscillations in Plane Poiseuille and Blasius Flows,” *Journal of the Aeronautical Sciences*, vol. 21, pp. 62–64. doi: <https://doi.org/10.2514/8.2920>Page 511
- Sherman, F. S. (1990), *Viscous Flow*, McGraw-Hill, New York.
- Shima, N. (1993), “Prediction of Turbulent Boundary Layers with a Second Moment Closure: Part 1. Effects of Periodic Pressure Gradient, Wall Transpiration, and Freestream Turbulence,” *Journal of Fluids Engineering*, vol. 115, no. 1, pp. 56–63. doi: <https://doi.org/10.1115/1.2910113>
- Sibulkin, M. (1952), “Heat Transfer near the Forward Stagnation Point of a Body of Revolution,” *Journal of the Aeronautical Sciences*, vol. 19, pp. 570–571.
- Shih, K. (1987), “On the Existence of Solutions of an Equation Arising in the Theory of Laminar Flow in a Uniformly Porous Channel with Injection,” *SIAM Journal on Applied Mathematics*, vol. 47, no. 3, pp. 526–533. doi: <https://doi.org/10.1137/0147035>
- Sidebottom, W., Ooi, A., and Jones, D. (2015), “A Parametric Study of Turbulent Flow Past a Circular Cylinder Using Large Eddy Simulation”, *Journal of Fluids Engineering*, 137(9):091202-091202-13. doi: <https://doi.org/10.1115/1.4030380>
- Simpson, R. L. (1968), “The Turbulent Boundary Layer on a Porous Wall,” Ph.D. Dissertation, Stanford University, Stanford, CA.
- (1989), “Turbulent Boundary Layer Separation,” *Annual Review of Fluid Mechanics*, vol. 21, pp. 205–234. doi: <https://doi.org/10.1146/annurev.fl.21.010189.001225>

- Simpson, R. L., Whitten, D. C., and Moffat, R. J. (1970), "An Experimental Study of the Turbulent Prandtl Number of Air with Injection and Suction," *International Journal of Heat and Mass Transfer*, vol. 13, pp. 125–143. doi: [https://doi.org/10.1016/0017-9310\(70\)90030-X](https://doi.org/10.1016/0017-9310(70)90030-X)
- Sirignano, W. A. (1999), *Fluid Dynamics and Transport of Droplets and Sprays*, Butterworth-Heinemann, Woburn, MA.
- Skalak, F. M., and Wang, C. Y. (1978), "On the Nonunique Solutions of Laminar Flow through a Porous Tube or Channel," *SIAM Journal on Applied Mathematics*, vol. 34, no. 3, pp. 535–544. doi: <https://doi.org/10.1137/0134042>
- Slattery, J. C., and Bird, R. B. (1958), "Calculation of the Diffusion Coefficient of Dilute Gases and of the Self-Diffusion Coefficient of Dense Gases," *AIChE Journal*, vol. 4, pp. 137–142. doi: <https://doi.org/10.1002/aic.690040205>
- Sleicher, C. A., and Rouse, M. W. (1975), "A Convenient Correlation for Heat Transfer to Constant and Variable-Property Fluids in Turbulent Pipe Flow," *International Journal of Heat and Mass Transfer*, vol. 18, pp. 677–683. [https://doi.org/10.1016/0017-9310\(75\)90279-3](https://doi.org/10.1016/0017-9310(75)90279-3)
- Smith, A. G., and Spalding, D. B. (1958), "Heat Transfer in a Laminar Boundary Layer with Constant Fluid Properties and Constant Wall Temperature," *Journal of Royal Aeronautical Society*, vol. 62, pp. 60–64. doi: <https://doi.org/10.1017/S0368393100067948>
- Smith, A. M. O., and Clutter, D. W. (1963), "Solution of the Incompressible Boundary Layer Equations," *AIAA Journal*, vol. 1, pp. 2062–2071. doi: <https://doi.org/10.2514/3.1994>
- (1965), "Machine Calculations of Compressible Laminar Boundary Layers," *AIAA Journal*, vol. 3, pp. 639–647. <https://doi.org/10.2514/3.12032>
- Smith, A. M. O., and Gamberoni, N. (1956), "Transition, Pressure Gradient, and Stability Theory," Douglas Aircraft Report ES-26388 [see also *Proceedings of the Ninth International Congress of Applied Mechanics*, vol. 4, pp. 234–244 (1957)].
- Smith, F. T. (1977), "The Laminar Separation of an Incompressible Fluid Streaming Past a Smooth Surface," *Proceedings of the Royal Society of London, Series A*, vol. 356, pp. 443–463. <https://doi.org/10.1098/rspa.1977.0144>
- Smith, S. H. (1994), "An Exact Solution of the Unsteady Navier–Stokes Equations Resulting from a Stretching Surface," *Journal of Applied Mechanics*, vol. 61, no. 3, pp. 629–633. doi: <https://doi.org/10.1115/1.2901506>
- Smits, A. J., and Dussauge, J.-P. (1996), *Turbulent Shear Layers in Supersonic Flow*, Springer-Verlag, New York.
- Smits, A. J., and Lim, T. T. (Eds.) (2000), *Flow Visualization: Techniques and Examples*, Imperial College Press, London.

- Smoluchowski, M. von (1898), *Sitzungsber. Akad. Wiss. Wien*, vol. 107, Abt. 2a, pp. 304–329; vol. 108, Abt. 2a, pp. 5–23.
- So, R. M. C., et al. (1994), “Logarithmic Laws for Compressible Turbulent Boundary Layers,” *AIAA Journal*, vol. 32, no. 11, pp. 2162–2168. doi: <https://doi.org/10.2514/3.12273>.
- Sod, G. A. (1985), *Numerical Methods in Fluid Dynamics*, Cambridge University Press, New York.
- Sofialidis, D., and Primos, P. (1996), “Wall Suction Effects on the Structure of Fully Developed Pipe Flow,” *Journal of Fluids Engineering*, vol. 118, no. 1, pp. 33–39. doi: <https://doi.org/10.1115/1.2817507>
- (1997), “Fluid Flow and Heat Transfer in a Pipe with Wall Suction,” *International Journal of Heat and Mass Transfer*, vol. 40, no. 15, pp. 3627–3640. doi: [https://doi.org/10.1016/S0017-9310\(96\)00386-9](https://doi.org/10.1016/S0017-9310(96)00386-9)
- Sokolnikoff, I. S. (1946), *Mathematical Theory of Elasticity*, McGraw-Hill, New York.
- Sommerfeld, A. (1908), “Ein Beitrag zur hydrodynamischen Erkl  rung der turbulenten Flussigkeitsbewegungen,” *Proc. Fourth Int. Cong. Math., Rome*, vol. III, pp. 116–124.
- Sowerby, L. (1954), “Secondary Flow in a Boundary Layer,” *Aeronautical Research Council*, Report 16832.
- Spain, B. (2003), *Tensor Calculus: A Concise Approach*, Dover, Mineola, NY.
- Spalart, P. R. (1988), “Direct Simulation of a Turbulent Boundary Layer up to $Re_{\tau} = 1400$,” *Journal of Fluid Mechanics*, vol. 187, pp. 61–98. doi: <https://doi.org/10.1017/S0022112088000345>
- Spalding, D. B. (1961), “A Single Formula for the Law of the Wall,” *Journal of Applied Mechanics*, vol. 28, no. 3, pp. 455–458. doi: <https://doi.org/10.1115/1.3641728>
- Spalding, D. B., and Chi, S. W. (1964), “The Drag of a Compressible Turbulent Boundary Layer on a Smooth Flat Plate with and without Heat Transfer,” *Journal of Fluid Mechanics*, vol. 18, no. 1, pp. 117–143. doi: <https://doi.org/10.1017/S0022112064000088>
- Spalding, D. B., and Pun, W. M. (1962), “A Review of Methods for Predicting Heat-Transfer Coefficients for Laminar Uniform-Property Boundary Layer Flows,” *International Journal of Heat and Mass Transfer*, vol. 5, no. 3-4, pp. 239–250. doi: [https://doi.org/10.1016/0017-9310\(62\)90014-5](https://doi.org/10.1016/0017-9310(62)90014-5)
- Spangler, I. G., and Wells, C. S. Jr. (1968), “Effect of Freestream Disturbances on Boundary Layer Transition,” *AIAA Journal*, vol. 6, no. 3, pp. 534–545. doi: <https://doi.org/10.2514/3.4533>
- Sparrow, E. M. (1955), “Analysis of Laminar Flow Convection Heat Transfer in the Entrance Region of Flat Rectangular Ducts,” NACA Technical Note 3331.

- Sparrow, E. M., and Gregg, J. L. (1956), "Laminar Free-Convection Heat Transfer from the Outer Surface of a Vertical Circular Cylinder," *ASME Transactions*, vol. 78, pp. 1823–1829 [see also vol. 96, pp. 178–183].
- Spells, K. E. (1952), "A Study of Circulation Patterns within Liquid Drops Moving Through a Liquid," *Proceedings of the Physical Society Series B*, vol. 65, pp. 541–546. doi: <https://doi.org/10.1088/0370-1301/65/7/310>
- Speziale, C. G. (1991b), "Analytical Methods for the Development of Reynolds-Stress Closures in Turbulence," *Annual Review of Fluid Mechanics*, vol. 23, pp. 107–157. doi: <https://doi.org/10.1146/annurev.fl.23.010191.000543>
- Speziale, C. G., Sarkar, S., and Gatski, T. B. (1991a), "Modeling the Pressure-Strain Correlation of Turbulence: An Invariant Dynamical Systems Approach," *Journal of Fluid Mechanics*, vol. 227, pp. 245–272. doi: <https://doi.org/10.1017/S0022112091000101>Page 512
- Spina, E. F., Smits, A. J., and Robinson, S. K. (1994), "The Physics of Supersonic Turbulent Boundary Layers," *Annual Review of Fluid Mechanics*, vol. 26, pp. 287–319. doi: <https://doi.org/10.1146/annurev.fl.26.010194.001443>
- Squire, H. B. (1933), "On the Stability of Three-Dimensional Distribution of Viscous Fluid between Parallel Walls," *Proceedings of the Royal Society, Series A*, vol. 142, no. 847, pp. 621–628. doi: <https://doi.org/10.1098/rspa.1933.0193>
- (1951), "The Round Laminar Jet," *Quarterly Journal of Mechanics and Applied Mathematics*, vol. 4, no. 3, pp. 321–329. doi: <https://doi.org/10.1093/qjmam/4.3.321>.
- Squire, H. B. (1956), "Rotating Fluids," *Surveys in Mechanics. A Collection of Surveys of the Present Position of Research in Some Branches of Mechanics, Written in Commemoration of the 70th Birthday of Geoffrey Ingram Taylor*, vol. 37, edited by G. K. Batchelor and R. M. Davies, WILEY-VCH Verlag GmbH & Co. KGaA, Weinheim, pp. 139–169.
- Squire, W. (1959), "Application of Generalized Gauss-Laguerre Quadrature to Boundary-Layer Problems," *Journal of the Aerospace Sciences*, vol. 26, no. 8, pp. 540–541. doi: <https://doi.org/10.2514/8.8188>
- Sreenivasan, K. R. (1982), "Laminar, Relaminarizing, and Retransitional Flows," *Acta Mechanica*, vol. 44, pp. 1–48. doi: <https://doi.org/10.1007/BF01190916>
- Sreenivasan, K. R., and Narasimha, R. (1982), "Equilibrium Parameters for Two-Dimensional Turbulent Wakes," *Journal of Fluids Engineering*, vol. 104, no. 2, pp. 167–169. doi: <https://doi.org/10.1115/1.3241801>
- Steinheuer, J. (1968), "Similar Solutions for the Laminar Wall Jet in a Decelerating Outer Flow," *AIAA Journal*, vol. 6, no. 11, pp. 2198–2200. doi: <https://doi.org/10.2514/3.4962>
- Stetson, K. F. (1988), "On Nonlinear Aspects of Hypersonic Boundary Layer Stability," *AIAA Journal*, vol. 26, no. 7, pp. 883–885. doi: <https://doi.org/10.2514/3.9983>

- Stevenson, T. N. (1963), "A Law of the Wall for Turbulent Boundary Layers with Suction or Injection," Cranfield College, Aero. Report 166.
- Stewartson, K. (1954), "Further Solutions of the Falkner–Skan Equation," *Proceedings of the Cambridge Philosophical Society*, vol. 50, no. 3, pp. 454–465. doi: <https://doi.org/10.1017/S030500410002956X>
- (1964), *The Theory of Laminar Boundary Layers in Compressible Fluids*, Oxford University Press. London.
- (1969), "On the Flow near the Trailing Edge of a Flat Plate II," *Mathematika*, vol. 16, no. 1, pp. 106–121. doi: <https://doi.org/10.1112/S0025579300004678>
- (1974), "Multistructured Boundary Layers on Flat Plates and Related Bodies," *Advances in Applied Mechanics*, vol. 14, pp. 145–239. doi: [https://doi.org/10.1016/S0065-2156\(08\)70032-2](https://doi.org/10.1016/S0065-2156(08)70032-2)
- Stokes, G. G. (1845), "On the Theories of Internal Friction of Fluids in Motion," *Transactions of the Cambridge Philosophical Society*, vol. 8, pp. 287–305. doi: <https://doi.org/10.1017/CBO9780511702242.005>
- (1851), "On the Effect of the Internal Friction of Fluids on the Motion of Pendulums," *Transactions of the Cambridge Philosophical Society*, vol. 9, pp. 8–106. doi: <https://doi.org/10.1017/CBO9780511702266.002>
- Stratford, B. S. (1954), "Flow in the Laminar Boundary Layer Near Separation," *Aeronautical Research Council*, R & M 3002.
- (1959), "Prediction of Separation of the Turbulent Boundary Layer," *Journal of Fluid Mechanics*, vol. 5, no. 1, pp. 1–16. doi: <https://doi.org/10.1017/S0022112059000015> [see also pp. 17–35].
- Strawn, R. C., and Kline, S. J. (1983), "A Stall Margin Design Method for Planar and Axisymmetric Diffusers," *Journal of Fluids Engineering*, vol. 105, no. 1, pp. 28–33. doi: <https://doi.org/10.1115/1.3240936>
- Stuart, J. T. (1987), "Instability, Three-Dimensional Effects, and Transition in Shear Flows," in H. U. Meier and P. Bradshaw (Eds.), *Perspectives in Turbulence Studies*, pp. 1–25, Springer, Berlin. doi: https://doi.org/10.1007/978-3-642-82994-9_1
- Sucec, J. (1999), "Prediction of Heat Transfer in Turbulent Transpired Boundary Layers," *Journal of Heat Transfer*, vol. 121, no. 1, February, pp. 186–190. doi: <https://doi.org/10.1115/1.2825940>
- Sucker, D., and Brauer, H. (1975), "Fluiddynamik bei der angeströmten Zylindern," *Wärme und Stoffübertragung*, vol. 8, pp. 149–158. doi: <https://doi.org/10.1007/BF01681556>
- Sumitani, Y., and Kasagi, N. (1995), "Direct Numerical Simulation of Turbulent Transport with Uniform Wall Injection and Suction," *AIAA Journal*, vol. 33, no. 7, pp. 1220–1228. doi: <https://doi.org/10.2514/3.12363>

- Sutherland, W. (1893), "The Viscosity of Gases and Molecular Force," *Philosophical Magazine*, vol. 5, pp. 507–531. doi: <https://doi.org/10.1080/14786449308620508>
- Swinney, H. L., and Gollub, J. P. (1981), *Hydrodynamic Instabilities and the Transition to Turbulence*, Springer, New York.
- Sychev, V. V. (1972), "Laminar Separation," *Fluid Dynamics*, vol. 7, pp. 407–417. doi: <https://doi.org/10.1007/BF01209044>
- Szeri, A. Z. (1998), *Fluid Film Lubrication: Theory and Design*, Cambridge University Press, New York.
- Szymanski, F. (1932), "Quelques solutions exactes des équations de l'hydrodynamique de fluide visqueux dans le cas d'un tube cylindrique," *Journal de Mathématiques Pures et Appliquées*, (9), vol. 11, pp. 67–107.
- Tajvidi, T., Razzaghi, M., and Dehghan, M. (2008), "Modified Rational Legendre Approach to Laminar Viscous Flow over a Semi-Infinite Flat Plate," *Chaos, Solitons & Fractals*, vol. 35, no. 1, pp. 59–66. doi: <https://doi.org/10.1016/j.chaos.2006.05.031>
- Talpaert, Y. R. (2003), *Tensor Analysis and Continuum Mechanics*, Dover, Mineola, NY.
- Taneda, S. (1956), "Experimental Investigation of the Wakes Behind Cylinders and Plates at Low Reynolds Numbers," *Journal of the Physical Society of Japan*, vol. 11, pp. 302–307. doi: <https://doi.org/10.1143/JPSJ.11.302>
- (1979), "Visualization of Separating Stokes Flows," *Journal of the Physical Society of Japan*, vol. 46, pp. 1935–1942. <https://doi.org/10.1143/JPSJ.46.1935>
- Tani, I. (1949), "On the Solution of the Laminar Boundary Layer Equations," *Journal of the Physical Society of Japan*, vol. 4, pp. 149–154. doi: <https://doi.org/10.1143/JPSJ.10.149>
- (1969), "Boundary Layer Transition," *Annual Review of Fluid Mechanics*, vol. 1, pp. 169–196. doi: <https://doi.org/10.1146/annurev.fl.01.010169.001125>
- Tannehill, J. C., Anderson, D. A. and Pletcher, R. H. (1997), *Computational Fluid Mechanics and Heat Transfer*, Taylor & Francis, Washington, DC.
- Tanner, R. I. (1993), "Stokes Paradox for Power-Law Flow Around a Cylinder," *Journal of Non-Newtonian Fluid Mechanics*, vol. 50, no. 2–3, pp. 217–224. doi: [https://doi.org/10.1016/0377-0257\(93\)80032-7](https://doi.org/10.1016/0377-0257(93)80032-7)
- Tatsumi, T. (1952), "Stability of the Laminar Inlet-Flow Prior to the Formation of Poiseuille Regime," *Journal of the Physical Society of Japan*, vol. 7, pp. 489–495. doi: <https://doi.org/10.1143/JPSJ.7.489>Page 513
- Tatsumi, T. (Ed.) (1984), *Turbulence and Chaotic Phenomena in Fluids*, Elsevier, New York.
- Taulbee, D. B. (1989), "Engineering Turbulence Models," in W. K. George and R. Arndt (Eds.), *Advances in Turbulence*, pp. 75–125, Hemisphere, New York.
- Taylor, G. I. (1923), "Stability of a Viscous Liquid Contained Between Two Rotating

- Cylinders,” *Philosophical Transactions of the Royal Society of London, Series A*, vol. 223, no. 605-615, pp. 289–343. doi: <https://doi.org/10.1098/rsta.1923.0008>
- Taylor, G. I. (1956), “Fluid Flow in Regions Bounded by Porous Surfaces,” *Proceedings of the Royal Society of London, Series A*, vol. 234, no. 1199, pp. 456–475. doi: <https://doi.org/10.1098/rspa.1956.0050>
- Taylor, R. P., Coleman, H. W., and Hodge, B. K. (1985), “Prediction of Turbulent Rough-Wall Skin Friction Using a Discrete Element Approach,” *Journal of Fluids Engineering*, vol. 107, no. 2, pp. 251–257. doi: <https://doi.org/10.1115/1.3242469>
- Taylor, R. P., Scaggs, W. F., and Coleman, H. W. (1988), “Measurement and Prediction of the Effects of Nonuniform Surface Roughness on Turbulent Flow Friction Coefficients,” *Journal of Fluids Engineering*, vol. 110, no. 4, pp. 380–384. doi: <https://doi.org/10.1115/1.3243567>
- Telionis, D. P. (1981), *Unsteady Viscous Flows*, Springer-Verlag, New York.
- Tennekes, H., and Lumley, J. L. (1972), *A First Course in Turbulence*, MIT Press, Cambridge, MA.
- Terrill, R. M. (1960), “Laminar Boundary Layer Flow with Separation with and Without Suction,” *Philosophical Transactions of the Royal Society, Series A*, vol. 253, pp. 55–100. doi: <https://doi.org/10.1098/rsta.1960.0018>
- Terrill, R. M. (1964), “Laminar Flow in a Uniformly Porous Channel (Laminar Flow in Two-Dimensional Channel with Porous Walls Assuming Uniformly Injected Fluid),” *The Aeronautical Quarterly*, vol. 15, no. 3, pp. 299–310. doi: <https://doi.org/10.1017/S0001925900010908>
- Terrill, R. M. (1965), “Laminar Flow in a Uniformly Porous Channel with Large Injection,” *The Aeronautical Quarterly*, vol. 16, no. 4, pp. 323–332. doi: <https://doi.org/10.1017/S0001925900003565>
- Terrill, R. M., and Thomas, P. W. (1969), “On Laminar Flow through a Uniformly Porous Pipe,” *Applied Scientific Research*, vol. 21, no. 1, pp. 37–67. doi: <https://doi.org/10.1007/BF00411596>
- Theodorsen, T., and Regier, A. (1944), “Experiments on Drag of Revolving Discs, Cylinders, and Streamline Rods at High Speeds,” NACA Report 793.
- Theofilis, V. (2011), “Global Linear Instability,” *Annual Review of Fluid Mechanics*, vol. 43, no. 1, pp. 319–352. doi: <https://doi.org/10.1146/annurev-fluid-122109-160705>
- Theofilis, V., Duck, P. W., and Owen, J. (2004), “Viscous Linear Stability Analysis of Rectangular Duct and Cavity Flows,” *Journal of Fluid Mechanics*, vol. 505, pp. 249–286. doi: <https://doi.org/10.1017/S002211200400850X>
- Thilmany, J. (2003), “How Does Your Fluid Flow?,” *Mechanical Engineering*, vol. 125, no. 12, pp. 35–37. doi: <https://doi.org/10.1115/1.2003-DEC-3>

- Thom, A. (1933), “Flow Past Circular Cylinders at Low Speeds,” *Proceedings of the Royal Society of London, Series A*, vol. 141, no. 845, pp. 651–669. doi: <https://doi.org/10.1098/rspa.1933.0146>
- Thomas G. Mezger (2014), *The Rheology Handbook*, 4th ed, Vincentz Network.
- Thomas, L. C., and Kadry, H. M. (1990), “A One Parameter Integral Method for Turbulent Boundary Layer Flow,” *Journal of Fluids Engineering*, vol. 112, no. 4, pp. 433–436. doi: <https://doi.org/10.1115/1.2909421>
- Thomas, L. C., and Hasani, S. M. F. (1989), “Supplementary Boundary-Layer Approximations for Turbulent Flow,” *Journal of Fluids Engineering*, vol. 111, no. 4, pp. 420–427. doi: <https://doi.org/10.1115/1.3243662>
- Thompson, J. F., et al. (Eds.) (1998), *Handbook of Grid Generation*, CRC Press, Boca Raton, FL.
- Thwaites, B. (1949), “Approximate Calculation of the Laminar Boundary Layer,” *Aeronautical Quarterly*, vol. 1, no. 3, pp. 245–280. doi: <https://doi.org/10.1017/S0001925900000184>
- Timoshenko, S., and Goodier, J. N. (1970), *Theory of Elasticity*, 3rd ed., McGraw-Hill, New York.
- Tobak, M., and Peake, D. J. (1982), “Topology of Three-Dimensional Separated Flows,” *Annual Review of Fluid Mechanics*, vol. 14, pp. 61–85. doi: <https://doi.org/10.1146/annurev.fl.14.010182.000425>
- Tollmien, W. (1929), “Über die Entstehung der Turbulenz,” *Wissenschaften zu Göttingen, Mathematisch-physikalische Klasse II*, pp. 21–44 [translated in NACA Technical Memo. 609].
- (1931), “Grenzschichttheorie,” *Handbuch der experimentalischen Physik*, vol. IV, pt. 1, pp. 241–287, Leipzig.
- Töpfer, K. (1912), “Bemerkung Zu Dem Aufsatz Von H. Blasius: Grenzschichten in Flüssigkeiten Mit Kleiner Reibung,” *Journal of Applied Mathematics and Physics (ZAMP)*, vol. 60, pp. 397–398.
- Tomotika, S., and Aoi, T. (1951), “An Expansion Formula for the Drag on a Circular Cylinder Moving through a Viscous Fluid at Small Reynolds Numbers,” *Quarterly Journal of Mechanics and Applied Mathematics*, vol. 4, pp. 401–406. doi: <https://doi.org/10.1093/qjmam/4.4.401>
- Tomotika, S., Aoi, T., and Yosinabu, H. (1953), “On the Forces Acting on a Circular Cylinder Set Obliquely in a Uniform Stream at Lower Values of Reynolds Number,” *Proceedings of the Royal Society of London, Series A*, vol. 219, pp. 233–244. doi: <https://doi.org/10.1098/rspa.1953.0142>
- Townsend, A. A. (1984), “Axisymmetric Couette Flow at Large Taylor Numbers,” *Journal of*

Fluid Mechanics, vol. 144, pp. 329–362. doi:
<https://doi.org/10.1017/S0022112084001634>

- Trefethen, A. E., Trefethen, L. N., and Schmid, P. J. (1999), “Spectra and Pseudospectra for Pipe Poiseuille Flow,” *Computer Methods in Applied Mechanics and Engineering*, vol. 175, pp. 413–420. [https://doi.org/10.1016/S0045-7825\(98\)00364-8](https://doi.org/10.1016/S0045-7825(98)00364-8)
- Trefethen, L. N. (2001), *Spectral Methods in MATLAB*, Society for Industrial & Appl. Math., Philadelphia.
- Trefethen, L. N., Trefethen A. E., Reddy, S. C., and Driscoll, T. A. (1993), “Hydrodynamic Stability Without Eigenvalues,” *Science*, vol. 261, pp. 578–584. doi: <https://doi.org/10.1126/science.261.5121.578>
- Trefethen, L. N., and Embree, M. (2005), *Spectra and Pseudospectra: The Behavior of Nonnormal Matrices and Operators*, Princeton University Press.
- Tretheway, D. C., and Meinhart, C. D. (2002), “Apparent Fluid Slip at Hydrophobic Microchannel Walls,” *Physics of Fluids*, vol 14, no. 3, pp. L9–L12. doi: <https://doi.org/10.1063/1.1432696>.
- Trimmer, L. L. (1968), Arnold Engineering Development Center, Tenn., Report AEDC-TR-68–99.
- Tritton, D. J. (1959), “Experiments on the Flow Past a Circular Cylinder at Low Reynolds Numbers,” *Journal of Fluid Mechanics*, vol. 6, pp. 547–567. doi: <https://doi.org/10.1017/S0022112059000829>
- Trogon, S. A., and Farmer, M. T. (1991), “Unsteady Axisymmetric Creeping Flow from an Orifice,” *Acta Mechanica*, vol. 88, nos. 1–2, pp. 61–75. doi: <https://doi.org/10.1007/BF01170593>
- Truesdell, C. (1954), “The Present Status of the Controversy Regarding the Bulk Viscosity of Liquids,” *Proceedings of the Royal Society of London, Series A*, vol. 226, pp. 1–69. doi: <https://doi.org/10.1098/rspa.1954.0237>Page 514
- Truitt, R. W. (1960), *Aerodynamic Heating*, Ronald Press, New York.
- Tsai, P. Y., and Chen, C. K. (2011), “A New Algorithm on the Solutions of Forced Convective Heat Transfer in a Semi-Infinite Flat Plate,” *Journal of Mechanics*, vol. 27, no. 1, pp. 63–69. doi: <https://doi.org/10.1017/jmech.2011.8>
- Tsangaris, S., and Vlachakis, N. W. (2003), “Exact Solution of the Navier–Stokes Equations for the Fully Developed, Pulsating Flow in a Rectangular Duct with a Constant Cross-Sectional Velocity,” *Journal of Fluids Engineering*, vol. 125, March, pp. 382–385. doi: <https://doi.org/10.1115/1.1537250>.
- Tsou, F. K., and Sparrow, E. M. (1970), “Hydrodynamic Stability of Boundary Layers with Surface Mass Transfer,” *Applied Scientific Research*, vol. 22, pp. 273–286. doi: <https://doi.org/10.1007/BF00400533>

- Tzabiras, G. (Ed.) (2003), *Calculation for Complex Turbulent Flows*, WIT Press/Computational Mechanics, Boston, MA.
- Uchida, S. (1956), “The Pulsating Viscous Flow Superposed on the Steady Laminar Motion of Incompressible Fluid in a Circular Pipe,” *Journal of Applied Mathematics and Physics (ZAMP)*, vol. 7, pp. 403–422. doi: <https://doi.org/10.1007/BF01606327>
- Uyehara, O. A., and Watson, K. M. (1944), “High Pressure Vapor-Liquid Equilibria,” *Natl. Pet. News*, vol. 36, pp. R623-R635 [see also Hougen, O. A., and Watson, K. M. (1960), *Chemical Process Principles Charts*, Wiley, New York].
- Vainshtein, P., Shapiro, P., and Gutfinger, C. (2002), “Creeping Flow Past and Within a Permeable Spheroid,” *International Journal of Multiphase Flow*, vol. 28, no. 12, pp. 1945–1963. doi: [https://doi.org/10.1016/S0301-9322\(02\)00106-4](https://doi.org/10.1016/S0301-9322(02)00106-4)
- Van Dommelen, L. L., and Shen, S. F. (1981), “The Spontaneous Generation of the Singularity in a Separating Laminar Boundary Layer,” *Journal of Computational Physics*, vol. 38, pp. 125–140. [https://doi.org/10.1016/0021-9991\(80\)90049-2](https://doi.org/10.1016/0021-9991(80)90049-2)
- (1982), “The Genesis of Separation,” Chap. 17 of Cebeci (1982). doi: https://doi.org/10.1007/978-3-662-12610-3_17
- Van Driest, E. R. (1951), “Turbulent Boundary Layer in Compressible Fluids,” *Journal of the Aeronautical Sciences*, vol. 18, pp. 145–160. doi: <https://doi.org/10.2514/8.1895>
- (1952a), “Investigation of Laminar Boundary Layer Compressible Fluids Using the Crocco Method,” NACA Technical Note 2597.
- (1952b), “Turbulent Boundary Layer on a Cone in a Supersonic Flow at Zero Angle of Attack,” *Journal of the Aeronautical Sciences*, vol. 19, pp. 55–57, 72. doi: <https://doi.org/10.2514/8.2149>
- (1956), “The Problem of Aerodynamic Heating,” *Aerospace Engineering Review*, vol. 15, no. 10, pp. 26–41 [see also *Journal of the Aeronautical Sciences*, vol. 23, pp. 1007–1011, 1036, 1956].
- (1956a), “On Turbulent Flow Near a Wall,” *Journal of the Aeronautical Sciences*, vol. 23, pp. 1007–1011. doi: <https://doi.org/10.2514/8.3713>
- (1959), C. C. Lin (Ed.), *Turbulent Flows and Heat Transfer*, pp. 339–427, Princeton University Press, Princeton, NJ.
- Van Driest, E. R., and Blumer, C. B. (1963), “Boundary Layer Transition, Freestream Turbulence, and Pressure Gradient Effects,” *AIAA Journal*, vol. 1, pp. 1303–1306. <https://doi.org/10.2514/3.1784>
- Van Dyke, M. (1964), *Perturbation Methods in Fluid Mechanics*, Academic, New York [reprinted in 1975 by Parabolic Press, Stanford, CA.].
- (1969), “Higher Order Boundary Layer Theory,” *Annual Review of Fluid Mechanics*, vol. 1, pp. 265–292. doi: <https://doi.org/10.1146/annurev.fl.01.010169.001405>

- (1982), *An Album of Fluid Motion*, Parabolic Press, Stanford, CA.
- Van Ingen, J. L. (1956), “A Suggested Semi-Empirical Method for the Calculation of the Boundary Layer Transition Region,” Institute of Technology, Department of Aeronautics and Engineering, Report VTH-74, Delft, Holland.
- Van Oudheusden, B. W. (1997), “Complete Crocco Integral for Two-Dimensional Laminar Boundary Layer Flow over an Adiabatic Wall for Prandtl Numbers Near Unity,” *Journal of Fluid Mechanics*, vol. 353, Dec. 25, pp. 313–330. doi: <https://doi.org/10.1017/S0022112097007507>
- Van Oudheusden, B. W. (1997), “A Complete Crocco Integral for Two-Dimensional Laminar Boundary Layer Flow over an Adiabatic Wall for Prandtl Numbers near Unity,” *Journal of Fluid Mechanics*, vol. 353, pp. 313–330. doi: <https://doi.org/10.1017/S0022112097007507>
- (2004), “Compressibility Effects on the Extended Crocco Relation and the Thermal Recovery Factor in Laminar Boundary Layer Flow,” *Journal of Fluids Engineering*, vol. 126, January, pp. 32–41. <https://doi.org/10.1115/1.1637626>
- Varapaev, V. N., and Yagodkin, V. I. (1969), “Flow Stability in a Channel with Porous Walls,” *Fluid Dynamics (Izvestiya Akademii Nauk SSSR, Mechanika Zhidkosti i Gaza)*, vol. 4, no. 5, pp. 91–95. doi: <https://doi.org/10.1007/BF01015958>
- Varin, V. P. (2014), “A Solution of the Blasius Problem,” *Computational Mathematics and Mathematical Physics*, vol. 54, no. 6, pp. 1025–1036. doi: <https://doi.org/10.1134/S096554251406013X>
- Varin, V. P. (2018), “Asymptotic Expansion of Crocco Solution and the Blasius Constant,” *Computational Mathematics and Mathematical Physics*, vol. 58, no. 4, pp. 517–528. doi: <https://doi.org/10.1134/S0965542518040164>
- Varley, E., and Seymour, B. R. (1994), “Applications of Exact Solutions to the Navier–Stokes Equations: Free Shear Layers,” *Journal of Fluid Mechanics*, vol. 274, pp. 267–291. doi: <https://doi.org/10.1017/S0022112094002120>
- Versteeg, H. K., and Malalasekera, W. (1996), *An Introduction to Computational Fluid Dynamics: The Finite Volume Method*, Addison-Wesley, Reading, MA.
- Voigt, R., Gottlieb, D., and Hussaini, M. (1984), *Spectral Methods for Partial Differential Equations*, Society for Industrial and Applied Mathematics, Philadelphia.
- Volino, R. J., and Simon, T. W. (1997), “Velocity and Temperature Profiles in Turbulent Boundary Layer Flows Experiencing Streamwise Pressure Gradients,” *Journal of Heat Transfer*, vol. 119, no. 3, pp. 433–439. doi: <https://doi.org/10.1115/1.2824116>
- Volker, J. (2003), *Large Eddy Simulation of Turbulent Incompressible Flows*, Springer-Verlag, New York.
- von Kries, J. (1883), “Ueber die Beziehungen zwischen Druck und Geschwindigkeit, welche

bei der Wellenbewegung in elastischen Schläuchen bestehen (On the relationships between pressure and velocity, which exist in connection with wave motion in elastic tubing),” Festschrift der 56. Versammlung Deutscher Naturforscher und Ärzte (Festschrift of the 56th Convention of German Scientists and Physicians) (in German), Tübingen, Germany: Akademische Verlagsbuchhandlung: 67–88, archived from the original on 2017-03-28

- Vyas, A. B., and Majdalani, J., “Exact Solution of the Bidirectional Vortex,” *AIAA Journal*, vol. 44, no. 10, October 2006, pp. 2208–2216. doi: <https://doi.org/10.2514/1.14872>
- Wagner, R. D., and Fischer, M. C. (1984), “Fresh Attack on Laminar Flow,” *Aerospace America*, vol. 22, no. 3, pp. 72–76.
- Walker, J. E., G. A. Whan, and Rothfus, R. R. (1957), “Fluid Friction in Noncircular Ducts,” *AIChE Journal*, vol. 3, pp. 484–489. doi: <https://doi.org/10.1002/aic.690030412>
- Walz, A. (1969), *Boundary Layers of Flow and Temperature*, MIT Press, Cambridge, MA. Page 515
- Wang, C. Y. (1990), “Exact Solutions of the Navier–Stokes Equations: The Generalized Beltrami Flows, Review and Extension,” *Acta Mechanica*, vol. 81, nos. 1–2, pp. 69–74. doi: <https://doi.org/10.1007/BF01174556>
- Wang, C. Y. (1991), “Exact Solutions of the Steady-State Navier-Stokes Equations,” *Annual Review of Fluid Mechanics*, vol. 23, no. 1, pp. 159–177. doi: <https://doi.org/10.1146/annurev.fl.23.010191.001111>
- Wang, K. C. (1997), “Features of Three-Dimensional Separation and Separated Flow Structure,” Chap. 1 of *Flows at Large Reynolds Numbers*, H. Schmitt (Ed.), WIT Press/Computational Mechanics, Boston, MA.
- Wang, L. (2004), “A New Algorithm for Solving Classical Blasius Equation,” *Applied Mathematics and Computation*, vol. 157, no. 1, pp. 1–9. doi: <https://doi.org/10.1016/j.amc.2003.06.011>
- Warnack, D., and Fernholz, H. H. (1998), “Effects of a Favorable Pressure Gradient and of the Reynolds Number on an Incompressible Axisymmetric Turbulent Boundary Layer. Part 2. The Boundary Layer with Relaminarization,” *Journal of Fluid Mechanics*, vol. 359, March 25, pp. 357–381. doi: <https://doi.org/10.1017/S0022112097008501>
- Watson, J. (1958), “A Solution of the Navier–Stokes Equations, Illustrating the Response of a Laminar Boundary Layer to a Given Change in the External Stream Velocity,” *Quarterly Journal of Mechanics*, vol. 11, pp. 302–325. doi: <https://doi.org/10.1093/qjmam/11.3.302>
- Wazwaz, A. M. (2001), “A Reliable Algorithm for Solving Boundary Value Problems for Higher-Order Integro-Differential Equations,” *Applied Mathematics and Computation*, vol. 118, no. 2, pp. 327–342. doi: [https://doi.org/10.1016/S0096-3003\(99\)00225-8](https://doi.org/10.1016/S0096-3003(99)00225-8)
- Wazwaz, A. M. (2007), “The Variational Iteration Method for Solving Two Forms of Blasius

- Equation on a Half-Infinite Domain,” *Applied Mathematics and Computation*, vol. 188, no. 1, pp. 485–491. doi: <https://doi.org/10.1016/j.amc.2006.10.009>
- Wazwaz, A.-M. (2006), “The Modified Decomposition Method and Padé Approximants for a Boundary Layer Equation in Unbounded Domain,” *Applied Mathematics and Computation*, vol. 177, no. 2, pp. 737–744. doi: <https://doi.org/10.1016/j.amc.2005.09.102>
- Wazzan, A. R. (1975), “Spatial Stability of Tollmien–Schlichting Waves,” *Progress in Aerospace Sciences*, vol. 16, no. 2, pp. 99–127. doi: [https://doi.org/10.1016/0376-0421\(75\)90012-3](https://doi.org/10.1016/0376-0421(75)90012-3)
- Wazzan, A.R., Gazley, C. Jr., and Smith, A.M.O. (1979), “Tollmien–Schlichting Waves and Transition,” *Progress in Aerospace Sciences*, vol. 18, no. 2, pp. 351–392. doi: [https://doi.org/10.1016/0376-0421\(77\)90012-4](https://doi.org/10.1016/0376-0421(77)90012-4)
- (1981), “H-Rx Method for Predicting Transition,” *AIAA Journal*, vol. 19, no. 6, pp. 810–812. <https://doi.org/10.2514/3.7819>
- Wazzan, A. R., Taghavi, H., and Keltner, G. (1984), The Effect of Mach Number on the Spatial Stability of Adiabatic Flat Plate Flow to Oblique Disturbances,” *Physics of Fluids*, vol. 27, no. 2, pp. 331–341. doi: <https://doi.org/10.1063/1.864630>
- Wazzan, A. R., Okamura, T. T., and Smith, A. M. O. (1968a), “The Stability of Water Flow over Heated and Cooled Flat Plates,” *Journal of Heat Transfer*, vol. 90, pp. 109–114. doi: <https://doi.org/10.1115/1.3597439>
- (1968b), “Spatial and Temporal Stability Charts for the Falkner–Skan Boundary Layer Profiles,” Douglas Aircraft Co. Report DAC-67086.
- Weber, H. C. (1939), *Thermodynamics for Chemical Engineers*, Wiley, New York.
- Weideman, J., and Reddy, S., “A Matlab Differentiation Matrix Suite,” *ACM Transactions on Mathematical Software*, vol. 26, no. 4 doi: <https://doi.org/10.1145/365723.365727>
- Weissberg, H. L. (1959), “Laminar Flow in the Entrance Region of a Porous Pipe,” *Physics of Fluids*, vol. 2, pp. 510–516. doi: <https://doi.org/10.1063/1.1705941>
- Wells, C. S. (1967), “Effects of Freestream Turbulence on Boundary Layer Transition,” *AIAA Journal*, vol. 5, no. 1, pp. 172–174. doi: <https://doi.org/10.2514/3.3931>
- Wells, C. S. (Ed.) (1969), *Viscous Drag Reduction*, Plenum Press, New York.
- Wesseling, P. (2001), *Principles of Computational Fluid Dynamics*, Springer, New York.
- Weyl, H. (1941), “Concerning the Differential Equations of Some Boundary Layer Problems,” *Proceedings of the National Academy of Sciences*, vol. 27, no. 12, p. 578. doi: <https://doi.org/10.1073/pnas.27.12.578>
- Weyl, H. (1942a), “Concerning the Differential Equations of Some Boundary Layer Problems. II,” *Proceedings of the National Academy of Sciences*, vol. 28, no. 3, p. 100.

doi: <https://doi.org/10.1073/pnas.28.3.100>

- Weyl, H. (1942b), “On the Differential Equations of the Simplest Boundary-Layer Problems,” *Annals of Mathematics*, vol. 43, no. 2, pp. 381–407. doi: <https://doi.org/10.2307/1968875>
- White, F. M. (1959), “Laminar Flow in Porous Ducts,” Ph.D. Dissertation, Georgia Institute of Technology.
- (1962a), “Laminar Flow in a Uniformly Porous Tube,” *Journal of Applied Mechanics*, vol. 29, pp. 201–204. doi: <https://doi.org/10.1115/1.3636459>
- (1962b), “Hypersonic Laminar Viscous Interactions on Inclined Flat Plates,” *Journal of the American Rocket Society*, vol. 32, pp. 780–781.
- (1969), “A New Integral Method for Analyzing the Turbulent Boundary Layer with Arbitrary Pressure Gradient,” *Journal of Basic Engineering*, vol. 91, pp. 371–378. doi: <https://doi.org/10.1115/1.3571122>
- (1988), *Heat and Mass Transfer*, Addison-Wesley, Reading, MA.
- (2003), *Fluid Mechanics*, 5th ed., McGraw-Hill, New York.
- White, F. M., Barfield, B. F., and Goglia, M. J. (1958), “Laminar Flow in a Uniformly Porous Channel,” *Journal of Applied Mechanics*, vol. 25, pp. 613–617.
- White, F. M., and Christoph, G. H. (1972), “A Simple Theory for the Two-Dimensional Compressible Turbulent Boundary Layer,” *Journal of Basic Engineering*, vol. 94, pp. 636–642. doi: <https://doi.org/10.1115/1.3425519>
- White, F. M., Lessmann, R. C., and Christoph, G. H. (1973), “Calculations of Turbulent Heat Transfer and Skin Friction,” *AIAA Journal*, vol. 11, pp. 1046–1048. doi: <https://doi.org/10.2514/3.6872>
- White, F. M., and Xue, H. (2021), *Fluid Mechanics*, 9th ed., McGraw-Hill Education, New York, NY.
- Whitfield, J. D., and Iannuzzi, F. A. (1969), “Experiments on Roughness Effects on Cone Boundary Layer Transition up to Mach 16,” *AIAA Journal*, vol. 7, pp. 465–470. doi: <https://doi.org/10.2514/3.5130>.
- Wieghardt, K., and Tillmann, W. (1951), “On the Turbulent Friction Layer for Rising Pressure,” NACA Technical Memo. 1314.
- Wieselberger, C. (1914), “Der Luftwiderstand von Kugeln,” *Zeitschrift für Flugtechnik und Motorluftschiffahrt*, vol. 5, pp. 140–144 [see also *Zeitschrift für Physik*, vol. 22, pp. 321–328; vol. 23, pp. 219–224 (1921)].
- Wilcox, D. C. (1998), *Turbulence Modeling for CFD*, 2nd ed., DCW Industries, La Cañada, CA.
- Wilcox, D. C., and Rubesin, M. W. (1980), “Progress in Turbulence Modeling for Complex

Flow Fields Including Effects of Compressibility,” NASA TP–1517.

- Wild, J. M. (1949), “The Boundary Layer of Yawed Infinite Wings,” *Journal of the Aeronautical Sciences*, vol. 16, pp. 41–45. doi: <https://doi.org/10.2514/8.11722>Page 516
- Wilke, C. R. (1950), “A Viscosity Equation for Gas Mixtures,” *Journal of Chemical Physics*, vol. 18, pp. 517–519 [see also *Industrial & Engineering Chemistry*, vol. 41, pp. 1345–1347 (1949)]. doi: <https://doi.org/10.1063/1.1747673>
- Wrobel, L. C. (2002), *The Boundary Element Method*, vol. 1, Wiley, New York.
- Wu, J. C. (1961), “On the Finite Difference Solution of Laminar Boundary Layer Problems,” *Proceedings of the 1961 Heat Transfer and Fluid Mechanics Institute*, pp. 55–69, Stanford University Press, Stanford, CA.
- Wynanski, I., Champagne, F., and Marasli, B. (1986), “On the Large Scale Structures in Two-Dimensional, Small-Deficit Turbulent Wakes,” *Journal of Fluid Mechanics*, vol. 168, pp. 31–71. doi: <https://doi.org/10.1017/S0022112086000289>
- Wynanski, I., and Fiedler, H. (1969), “Some Measurements in the Self-Preserving Jet,” *Journal of Fluid Mechanics*, vol. 38, pt. 3, pp. 577–612. doi: <https://doi.org/10.1017/S0022112069000358>
- Wynanski, I., Sokolov, M., and Friedman, D. (1976), “On a Turbulent ‘Spot’ in a Laminar Boundary Layer,” *Journal of Fluid Mechanics*, vol. 78, pt. 4, pp. 785–819. doi: <https://doi.org/10.1017/S0022112076002747>
- Xu, D., and Guo, X. (2013), “Application of Fixed Point Method to Obtain Semi-Analytical Solution to Blasius Flow and Its Variation,” *Applied Mathematics and Computation*, vol. 224, pp. 791–802. doi: <https://doi.org/10.1016/j.amc.2013.08.066>
- Xu, D., Xu, J., and Xie, G. (2014), “Revisiting Blasius Flow by Fixed Point Method,” *Abstract and Applied Analysis*, vol. 2014, p. 9. doi: <https://doi.org/10.1155/2014/953151>
- Xuan, L.J. (2011), “An Investigation of Multi-Process Interaction in Complex Flow and High-Order Finite Integral Method,” Ph.D. dissertation, Peking University.
- Xuan, L.J., Mao, F., and Wu, J.Z. (2012), “Water Hammer Prediction and Control: the Green’s Function Method,” *Acta Mechanica Sinica*, vol. 28, no. 2, pp. 266–273. doi: [10.1007/s10409-012-0051-5](https://doi.org/10.1007/s10409-012-0051-5)
- Yakhot, V., and Smith, L. M. (1992), “The Renormalization Group, the ε -Expansion, and Derivation of Turbulence Models,” *Journal of Scientific Computing*, no. 7, pp. 35–61. doi: <https://doi.org/10.1007/BF01060210>
- Yang, W.-J. (1989), *Handbook of Flow Visualization*, Hemisphere, New York.
- (1994), *Computer-Assisted Flow Visualization*, Begell House, New York.
- Yoon, K. T., and Chung, T. J. (1996), “Three-Dimensional Mixed Explicit-Implicit Generalized Galerkin Spectral Element Methods for High-Speed Turbulent

- Compressible Flows,” *Computer Methods in Applied Mechanics and Engineering*, vol. 135, Sept, 1, pp. 343–367. doi: [https://doi.org/10.1016/0045-7825\(96\)01066-3](https://doi.org/10.1016/0045-7825(96)01066-3)
- Yu, L. T., and Chen, C. K. (1998), “The Solution of the Blasius Equation by the Differential Transformation Method,” *Mathematical and Computer Modelling*, vol. 28, no. 1, pp. 101–111. doi: [https://doi.org/10.1016/S0895-7177\(98\)00085-5](https://doi.org/10.1016/S0895-7177(98)00085-5)
- Yuan, S. W. (1956), “Further Investigation of Laminar Flow in Channels with Porous Walls,” *Journal of Applied Physics*, vol. 27, no. 3, pp. 267–269. doi: <https://doi.org/10.1063/1.1722355>
- Yuan, S. W., and Finkelstein, A. B. (1956), “Laminar Pipe Flow with Injection and Suction through a Porous Wall,” *ASME Transactions*, vol. 78, pp. 719–724. doi: <https://doi.org/10.21236/ad0058831>
- Yun, B. I. (2014), “Algebraic Type Approximation to the Blasius Velocity Profile,” *Journal of Applied Mathematics*, vol. 2014, 5 pages. doi: <https://doi.org/10.1155/2014/754910>
- Yun, B. I. (2011), “An Iteration Method Generating Analytical Solutions for Blasius Problem,” *Journal of Applied Mathematics*, vol. 2011, 8 pages. doi: <https://doi.org/10.1155/2011/925649>
- Yun, B. I. (2012), “Approximate Analytical Solutions Using Hyperbolic Functions for the Generalized Blasius Problem,” *Abstract and Applied Analysis*, vol. 2012, 10 pages. doi: <https://doi.org/10.1155/2012/581453>
- Yun, B. I. (2014), “Constructing Uniform Approximate Analytical Solutions for the Blasius Problem,” *Abstract and Applied Analysis*, vol. 2014, 6 pages. doi: <https://doi.org/10.1155/2014/495734>
- Yun, B. I. (2010), “Intuitive Approach to the Approximate Analytical Solution for the Blasius Problem,” *Applied Mathematics and Computation*, vol. 215, no. 10, pp. 3489–3494. doi: <https://doi.org/10.1016/j.amc.2009.09.050>
- Zagarola, M. V., and Smits, A. J. (1998), “Mean Flow Scaling in Turbulent Pipe Flow,” *Journal of Fluid Mechanics*, vol. 373, pp. 33–79. doi: <https://doi.org/10.1017/S0022112098002419>
- Zukauskas, A., and Ziukzda, J. (1985), *Heat Transfer on a Cylinder in Crossflow*, Hemisphere, New York.
- Zaturka, M. B., Drazin, P. G., and Banks, W. H. H. (1988), “On the Flow of a Viscous Fluid Driven Along a Channel by Suction at Porous Walls,” *Fluid Dynamics Research*, vol. 4, no. 3, pp. 151–178. doi: [https://doi.org/10.1016/0169-5983\(88\)90021-4](https://doi.org/10.1016/0169-5983(88)90021-4)
- Zhang, J., and Chen, B. (2009), “An Iterative Method for Solving the Falkner–Skan Equation,” *Applied Mathematics and Computation*, vol. 210, no. 1, pp. 215–222. doi: <https://doi.org/10.1016/j.amc.2008.12.079>
- Zhao, Y., Lin, Z., and Liao, S. J. (2013), “An Iterative HAM Approach for Nonlinear

Boundary Value Problems in a Semi-Infinite Domain,” *Computer Physics Communications*, vol. 184, no. 9, pp. 2136–2144. doi: <https://doi.org/10.1016/j.cpc.2013.04.009>

Zheng, J., Han, X., Wang, Z., Li, C., and Zhang, J. (2017), “A Globally Convergent and Closed Analytical Solution of the Blasius Equation with Beneficial Applications,” *AIP Advances*, vol. 7, no. 6, p. 065311. doi: <https://doi.org/10.1063/1.4985741>

Zhong, X., and Wang, X. (2011), “Direct Numerical Simulation on the Receptivity, Instability, and Transition of Hypersonic Boundary Layers,” *Annual Review of Fluid Mechanics*, vol. 44, no. 1, pp. 527–561. doi: <https://doi.org/10.1146/annurev-fluid-120710-101208>

Zwarts, F. J. (1970), “The Compressible Turbulent Boundary Layer in a Pressure Gradient,” Ph.D. Dissertation, McGill University, Montreal.

INDEX

A

- Absolute instability, 271
- Acceleration, of fluid, 9–10
 - relaminarization, 374–375
- Acoustic Reynolds number, 307
- Acoustic streaming, 226–227
- Active control, of boundary layers, 286
- Adiabatic wall temperature, 408, 421
- Adverse pressure gradient, 166, 178, 261, 369–370
 - in equilibrium flow, 338
 - prediction of, 369–370, 441–443
- Airfoil, flow past, 3–4
- Air-water interface, 30, 186–187
- Algebraic stress models, 362
- Amplification, 255
- Angle of attack, 4
- Angular velocity, 11
- Annulus flow, 87–88
- Applets for boundary layers, 199–200, 423, 441
- Asymptotic uniform heat-flux approximation, 90–91
- Atmospheric pressure
 - properties of air at, 467
 - properties of saturated water at, 466
- Axisymmetric boundary layers, 45–46, 62, 212–218
 - along cylinder, 215–216
 - cone flow, 213–214, 424–425, 440–441
 - round jet, 217
 - round wake, 217–218
 - sphere flow, 214–215
 - spherical coordinates, Bragg–Hawthorne equation for, 478–479
 - Thwaites-type method, 214

B

Backflow, 85

Baldwin–Lomax model, 357–358

Bernoulli numbers, 101

Bernoulli's equation, 45, 60, 165, 332, 400

Bessel function, 428–429

- roots, 95

Biharmonic equation, 61, 133

Bingham plastic, 14

Blasius equation, 406

- compressible laminar flow, 406

- flat-plate formulas, 157, 170

- similarity solution, 167–176

- stability of, 258–259

Blasius pipe friction, 85, 342

Blasius velocity function, 174

Blowing. *See* Suction flows

Blowing parameter, 183, 389

Body forces, 40

Boltzmann's constant, 24

Boundary conditions, 27–31, 49–50, 445–446

- biglobal stability problems, 293–295

- in boundary-layer theory, 165, 212, 332, 401, 431

- at deformable fluid–solid interface, 30–31, 49

- for finite-difference methods, 421

- in free convection, 229

- at free liquid surface, 29–30, 49

- at inlet or exit, 50

- at liquid–vapor interface, 49–50

- for Orr–Sommerfeld equation, 255

- at solid surface, 28, 49

Boundary-element methods, 140

Boundary layer

- approximations, 160

- concept, 2, 121, 153, 160, 164–165

- on curved wall, 166

- equations of motion

 - laminar, 164–166

 - turbulent, 332–334, 430–432

- finite-difference analysis of, 367–368

- predictions, 158

- stability, 253–261

- thickness, 154–155
 - on flat plate, 155–157, 347, 411
 - on oscillating plate, 106
 - on rotating disk, 127, 129
 - in stagnation flow, 121–122, 124
 - on suddenly moved plate, 105
- transition processes, classification of, 275–276
 - with turbulent pressure gradients, 362–375, 441–443
- Boundary-layer flows, 44
- Boundary-layer receptivity, 276, 285
- Boussinesq viscosity model, 354, 383
- Bragg–Hawthorne equation, 45–46
 - for axisymmetric flow in spherical coordinates, 478–479
- Brinkman number, 79, 81
- Buckingham Pi theorem, 483–484
- Buffer layer, 337
- Bulk modulus, 26–27
 - of various liquids, 467
 - of water, 27
- Bulk viscosity coefficient, 43
- Buoyancy of various fluids, 228
- Bypass transition, 275, 282–283

C

- Canonical equation of state, 22
- Cartesian coordinates, 51
 - steady 2D, reduced kinematic expressions in, 459
 - 3D kinematic expressions in, 458
- Cavitation number, 57, 58
- Centrifugal instability, 270–271
- Chaos and turbulence, 286–287
- Chapman–Rubesin parameter, 409, 417
- Chebyshev spectral collocation scheme, 291–292
- Chemical reactions, 8
- Circular pipe flow
 - laminar, 7, 84–85
 - roughness values, 346
 - turbulent, 341–342
- Classification, of equations, 38–39
 - of solutions to Navier–Stokes, 76–77
- Clauser eddy viscosity model, 355, 378

- Clauser parameter, 337, 363–365
- Clauser's experiments, 339, 370
- Coefficient of bulk viscosity, 43
- Coefficient of mass diffusivity, 19–20
- Coherent structures, 324–325
- Colebrook interpolation formula, 346
- Coles' law. *See* Law of wake
- Complementary error function, 104–105
- Complex turbulent flows, 372–375
- Compliant boundaries, 268–269
- Compressibility factor, 24–25, 434
- Compressibility transformation
 - for laminar flow, 405–407
 - for turbulent flow, 432–433, 437–438
- Compressible viscous flow
 - approximations for quasi-viscous flows, 444–451
 - basic equations, 401
 - biglobal stability of, 295–310
 - laminar boundary layers, 400–401
 - Morkovin's hypothesis, 430–432
 - in porous channel, 444–447
 - stability, 266–268
 - turbulent boundary layers, 436–451
- Computational fluid dynamics
 - of laminar boundary layers, 199–204
 - in axisymmetric flow, 214
 - for compressible flow, 419–424
 - for temperatures, 206–207
 - of Navier–Stokes equations
 - illustrative examples, 423
 - for turbulent boundary layers, 419–423
- Concentration gradient, 19
- Conditioned sampling, 327
- Conduction thickness, 204–205
- Cone rule, supersonic
 - laminar, 424–425
 - turbulent, 440–441
- Connection parameter, 168
- Conservation laws, 38
 - of energy, 46–48, 65
 - integral forms, 333–334, 417–418
 - of mass, 39–40, 64

- of momentum, 40–46, 64
- Continuity equation, 39
 - for turbulent flow, 329
- Control of transition, 285–286
- Control-volume formulations, 63–65
 - flat-plate boundary-layer analysis, 154–163
 - wall-temperature change, 160–161
- Convective acceleration, 10
- Convective heat transfer
 - laminar, 204–209
 - turbulent, 383–392
- Coordinate transformation, 292–293
- Coriolis acceleration, 63
- Coriolis effects, 118–119
- Corner flow, 223

Page 518

- Corresponding states, principle of, 15
- Couette flows, 77–82
 - between axially moving concentric cylinders, 79–80
 - combined with Poiseuille flow, 85–86
 - between parallel plates, 77–79, 107–108
 - between rotating concentric cylinders, 80–83
 - stability of, 82, 262–263, 270–271
 - unsteady, 103–108
- Creeping motion, 61, 133–144
 - about cylinder, 139–140
 - about disk, 136
 - about droplet/bubble, 140
 - about flat plate, 139
 - about immersed bodies, 134–136
 - about sphere, 134–136 140
 - about spheroid, 136–137
 - in duct entrance, 211
 - heat transfer in, 141–142
 - lubrication theory, 142–144
 - Oseen, improvement of, 138–140
- Critical point correlations
 - for thermal conductivity, 17
 - for viscosity, 15
- Critical point data for various fluids, 468
- Critical Reynolds number, 249

- Crocco–Busemann relation
 - laminar flow, 220, 404–405
 - turbulent flow, 431–432
- Crossflow Reynolds number, 110, 114
- Cup-mixing temperature, 91, 386
- Curved-wall boundary layers, 166
- Curvilinear coordinates, 50–52, 166, 219
 - for rotationally symmetric flow, 212
- Cylinder flow
 - equations of motion for incompressible, 480–481
 - normal to freestream, 4–6, 198–199
 - drag, 139–140
 - finite-difference solution, 203
 - heat transfer, 142, 207–208
 - integral solution, 198–199
 - parallel to freestream, 215–216
 - rotating, 80–82
- Cylindrical polar coordinates, 51
 - steady 2D, reduced kinematic expressions in, 462
 - 3D kinematic expressions in, 460–461

D

- d'Alembert paradox, 4
- Damping factor, 355, 356, 357, 391
- Darcy friction factor, 84, 342
- Defect thickness, 338
 - velocity profiles, 335–338
- Deformation, of fluid element, 42–43
 - types of, 10
- Density
 - air, 467
 - of common liquids, 467
 - water, 466
- Diffuse reflection, 28
- Diffuser flow, 7
- Diffusion, 19–20
 - low-speed, 54–55
- Diffusion velocity, 19
- Diffusivity, 19–20, 54
- Dilatant fluids, 14
- Dilatation, 12, 39

- Dimensional analysis, 2
- Dimensionless parameters, 56–59
 - in boundary conditions, 57–59
 - determination of, 483–484
 - in equations of motion, 56–57
 - in free convection, 57
 - list of, 485–489
 - in turbulent boundary layer, 335–336

Page 519

- variables, 56
- Direct numerical simulation (DNS), 250
 - of transition, 279–280
 - of turbulence, 325, 354, 361, 369, 381
- Discrete-element model, 352
- Discriminant function, 53
- Displacement thickness, 154–155
 - compressible, 418
 - defined, 122, 154
 - in Falkner–Skan flows, 180
 - in flat-plate flow, 156–157, 170
 - in laminar hypersonic flow, 426
 - in stagnation flow, 122
 - in turbulent flow, 333
 - viscous interaction parameter, 426
- Dissipation, 78, 330–331, 404
 - integral, 194, 334
 - thickness, 194
 - turbulent, 331, 333
- Dissipation function, 48
- Dissociation, of gases, 25
- Disturbance equation, 250–251, 253
- Double contraction, 47
- Double-dot product, 47
- Drag coefficient, 136, 156, 171, 351
- Drag crisis, 6
- Drag force
 - in axial cylinder flow, 215–216
 - on cylinder in crossflow, 6, 139
 - of disk, 136
 - of droplet/bubble, 140
 - of flat-plate

- laminar, 155, 171, 411
- turbulent, 350–351, 437
- of sphere, 136, 139
- Duct flows
 - laminar, steady, 82–95
 - inlet effects, 210–211
 - noncircular, 86–88
 - porous, 110–117
 - temperature distribution, 89–90
 - thermal entrance problem, 91–93
 - turbulent, 341–347
 - noncircular, 344
 - unsteady, 95–103
 - oscillatory, 96–97
 - oscillatory pressure gradient, 99–103
 - pulsatory pressure gradient, 97–99
 - starting flow, 95–96
 - weakly compressible, 427–429
- Dynamic pressure, 84

E

- Eccentric annulus, 87–88
- Eckert number, 56–57, 164
- Eckert reference temperature, 409
- Eddy coefficients
 - of conductivity, 383–384, 431
 - of viscosity, 354–358, 431
- Eigenvalues
 - compressible problem formulation, 297–302
 - in Graetz problem, 92–93
 - incompressible problem formulation, 289–291
 - in stability theory, 252, 255
- Einstein's indicial notation, 472–473
- Einstein summation notation, 331
- Ekman spiral flow, 118–119
- Elliptic
 - cylinder flow, 191, 223–224
 - differential equation, 53–54
 - duct flow, 86
 - integral, 131
- Emmons spots, 271–275

Energy

- defined, 21
- equation of, 46–49, 65, 164–165, 400, 474
 - dimensionless form, 56
 - integral analysis of, 160–161
 - for turbulence, 330, 383, 400, 431
- integral relation, 160–161, 194, 204, 333
- loss evaluation
 - advanced, 474–475

Energy loss evaluation

- advanced, 474–475
- traditional/iterative, 476–477

Enthalpy, of fluid, 22, 48

Enthalpy thickness, 161

Entrainment, integral, 334, 364–365

- in jet flow, 188
- shape factor, 364

Entropy, 20

Entry flow in ducts, 82, 210–211

- circular pipe, 7
- friction factor, 210
- thermal-entrance length, 94

Equation of state, 20–21, 401

- canonical, 22
- of perfect gas, 24, 401, 431

Equations of motion, 49

- in general orthogonal coordinates, 50–52, 166
- for turbulent flow, 328–331, 431

Equilibrium turbulent flow, 339, 369–370

- Clauser parameter, 363–365

Equilibrium turbulent flows, 337–338

- Clauser parameter, 337

Error function, 104–105, 174

Eulerian formulation, 9

Euler's equation, 45, 54, 220

Euler–Tricomi equation, 53

Explicit finite-difference method

- for laminar boundary layers, 200–201, 206–207, 419–421

F

Falkner–Skan equation, 178, 407

- application to heat transfer, 205
- for compressible flow, 406, 415–417
- nonuniqueness, 180
- Nusselt numbers, 181–182
- relation to cone flows, 213
- solutions, 180
- stability of, 258–260
- transition, 280
- wedge flow application, 177–181

Fanning friction factor, 84

Favorable pressure gradient, 121, 166, 178, 336, 434

- effect on law of wall, 434
- in Jeffrey–Hamel flow, 131
- in stagnation flow, 122, 126

Favre-averaging, 430

Fick's law of diffusion, 19–20

Finite-difference methods. *See* Computational fluid dynamics

First law of thermodynamics, 21, 46–49, 65, 330

Flat-plate flow

- Blasius solution, 167–176, 406
- compressible, laminar, 407–414, 421
 - turbulent, 436–441
- laminar flow, integral analysis, 154–163
- with suction/blowing, 183–184
 - developing, 191–192
- three-dimensional, 221–223
- in turbulent boundary layer, 347
- turbulent flow, 347–353, 436–441
 - fluctuations, 323
 - roughness effects, 351–352
 - visualization, 323

Flat-plate theory, of van Driest, 436–437

Focus/spiral node, 224

Fourier series, 98

Fourier's law, 17, 46, 177

Fractals in turbulence, 286, 327

Free convection, 57, 227–231

- basic equations, 228–229
- on horizontal cylinder, 231
- on inclined plates, 231
- stability of, 269–270
- on vertical cylinder, 231

- on vertical plate, 229–231
- Free-shear flows
 - laminar, 185–190
 - mixing, 186–187
 - plane jet, 187–189
 - plane wake, 189–190
 - round jet, 217
 - round wake, 217–218
 - stability of, 263–264
 - turbulent, 375–383
 - mixing layer, 325, 379–381
 - plane jet, 378
 - round jet, 378–379
 - wake, 381–383
- Freestream disturbances, 281
- Freestream turbulence, 208
 - effect on transition, 280–283
- Free surface, 29–30
- Free turbulence. *See* Free-shear flows
- Friction factor, 78, 156, 342
 - applications. *See* Skin friction coefficient
- Froude number, 56, 164
- Fully developed duct flow, 7, 83
- Fully rough flow, 345–346, 352

G

- Gamma functions, 208, 390
- Gas constant, 24, 401
 - of various fluids, 468
- Gaussian velocity distribution, 189, 217, 381–382
 - intermittency profiles, 327–328
- Geophysical flows, 63, 117–119
- Goldstein singularity, 191
- Görtler vortices, 271
- Gradient of scalar, 473
- Graetz duct-temperature problem, 91–93
- Graetz number, 94
- Grashof number, 57, 227–228
 - modified for heat flux, 230–231
- Grid conditioning, 292–293
- Gruschwitz, method of, 418–419

H

Hagen–Poiseuille flow, 84–85

Hard blowing, 352

Heat, defined, 21, 46

Heat-conduction equation, 53–54, 189

Heat flux, turbulent inertia term, 330

Heat-flux approximation, asymptotic uniform, 90–91

Heat transfer, 17

- on circular cylinder, 142, 207–208

- compressible flow parameter, 434

- evaluation for laminar flow, 161–163

- in Falkner–Skan wedge flow, 415, 416

- on flat plate, 176–177, 409, 410–411

- in incompressible turbulent flow, 383–392

- in stagnation flow, 124–125, 412

- with suction and blowing, 183–184, 387–389

- with variable wall temperature, 208–209, 389–390

Heat-transfer coefficient, 79, 208

- applications. *See* Stanton number

Helmholtz’ theorem, 60

Hicks equation, 46

Historical outline, 1–2

Hodograph

- laminar flow, 220–221

Homotopy analysis method (HAM), 168, 169

Horseshoe vortex, 225

Hot-wire anemometer, 141

Howarth, linearly retarded flow of, 190–191, 201

- compressible form, 421–423

- by method of Thwaites, 197

Hydraulically smooth wall, 345

Hydraulic diameter concept, 89

- laminar, 88–89

- turbulent, 343

Hydraulic radius, 86

Hydrostatics, 42

Hyperbolic differential equation, 53–54

Hypersonic flow

- inviscid theory, 414, 426

- leading-edge interaction, 425–427

I

Ideal gas. *See* Perfect-gas law

Illingworth transformation, 405–407

modified form of, 417

Implicit finite-difference method

for laminar boundary layers, 201–204, 206–207, 421

Incompressible flow, 44–45

approximation, 48–49

equations of motion of, 480–482

vorticity considerations in, 59–60

Incompressible viscous flow

biglobal stability of, 287–295

Independence principle for swept wings, 222–223

Inner layer, turbulent, 336–337

Inner-variable analysis, 365–367

for compressible turbulent flow, 437–439, 442

for flat-plate turbulent flow, 349–351, 437–439

for pressure gradient flow, 365–367, 442

Integral methods

compressible flow, 417–418, 441–442

inner-variable type, 365–367

laminar, momentum, 418

temperature, 204–206

turbulent, compressible, 441–442

Integral relations for boundary layers

boundary-layer, 192–193

energy, 161, 194, 333

entrainment, 364–365

laminar, compressible, 417–418

mechanical-energy, 194, 333

momentum, 155, 193, 333, 418

thermal-energy, 194

turbulent

compressible, 432, 441

incompressible, 192–199, 333–334, 362–367

Intermittency factor, 272, 325, 327, 355, 378

Invariants of tensor, 12

Inverse integral method, 371–372

Inviscid flow. *See* Potential flow analysis

Inviscid theory, 256, 270, 305

Irrotational flow, 11, 60

Isentropic compressible flow, 401–403, 417

Isentropic flow, 305
Isotropic fluid, 17, 42
Isotropic turbulence, 328

J

Jeffery–Hamel flow, 130–132
 separation criterion, 132
Jet flow
 laminar, two-dimensional, 187–189
 axisymmetric, 217
 stability of, 263–264
 turbulent, 376–379
Junction vortex, 225

K

Kármán integral relation. *See* Momentum integral relation
Kármán–Pohlhausen technique, 418
Kármán–Schoenherr incompressible drag formula, 437
Kármán vortex streets, 5
Kelvin–Helmholtz instability, 251–253, 324
 breaking waves, 253
Kelvin’s theorem, 60
K— ϵ model, 359–360
Kinematic properties, 8–13
Kinematic viscosity, 20, 54
 of various fluids, 466
Kinetic energy, 46, 48
 thickness, 441
 turbulent mean-flow equation, 331
Kinetic Reynolds number, 96, 129
Kinetic theory of gases
 for perfect gases, 24
 for slip velocity, 28–29
 for thermal conductivity, 18
 for viscosity, 16
 for wall-temperature jump, 29
King’s law, 141
Knudsen number, 28, 57, 85
Kolmogorov length scale, 323

Kronecker Delta, 472
Kronecker delta function, 40

L

Lag, in boundary layers, 366–367
Lagrange's theorem, 60
Lagrangian description, 8
Laminar boundary-layer equations, 164–167
 compressible flow, 401
 in free convection, 229
 three-dimensional, 219–220
Laminar boundary layers, 153–231
 displacement thickness, 154–155
Laminar flow theory
 for compressible boundary layers, 400–429
 exact solutions, 76–77
 for incompressible boundary layers, 153–231
Laplace's equation, 53, 133
Large-eddy simulation (LES), 354
Law of wake, 338–340, 362
 application to skin friction, 340
 for compressible flow, 433–435
 integral theory application, 362–363, 365
Law of wall, 336–337
 for compressible flow, 432–433
 with suction/blowing, 352–353, 387–389
 temperature, 384–386
 van Driest transformation, 432–433
Leibniz rule, 177
Lewis number, 20, 54
Lift coefficient, of airfoil, 3
Local derivative, 9

Page 520

Logarithmic law, turbulent, 335, 435
 applications, 341–347
 roughness effect, 344–345
 with suction/blowing, 352–353, 387–389
Logarithmic mean-temperature difference, 94
Logistic equation, 286–287

Long-cylinder parameter, 216
Long–Squire equation, 46
Low-density limit for transport properties, 16, 17
Lubrication theory, 142–144
Ludwig–Tillmann shear stress correlation, 362

M

Mach number, 29, 57, 267, 401–444
Macroflows, 28
Magnetohydrodynamics, 39
Mangler transformation, 214, 424
Marching methods, 165, 199–200
Mass-averaged velocity, 430
Mass diffusion, 19–20
Mass diffusivity, 54
Material derivative, 9
Mean free path, 16, 28
Mean Nusselt number, 93–95
Mechanical energy integral relation, 194
 turbulent flow, 333
Mechanical pressure, 43–44
Metric stretching factors, 50, 219
Microflows, 85
Mixing layer. *See* Free-shear flows
Mixing-length, turbulent, 354–355, 390
Models of turbulence. *See* Turbulence modeling
Modulus of rigidity, 13
Molecular parameters for dilute-gas transport properties, 471
Molecular weight, 24
 of mixtures of gases, 24
 of various gases, 468
Mollier chart, 22
Moment coefficient for rotating disk, 129
Momentum equation for turbulence, 330
Momentum integral relation
 for laminar flows, 155, 193, 418
 for turbulent flows, 362, 439–442
Momentum thickness
 compressible, 418
 defined, 155

- in Falkner-Skan flows, 180
- on flat-plate flow, 155–157, 170, 347
- transition correlation, 277
- in turbulent boundary layer, 333

Moody chart, 346

Morkovin's hypothesis, 430–431, 432

Moving-boundary flows, 103–108

- oscillating plate, 105–107
- suddenly accelerated plate, 104–105
- between two plates, 107–108

MRS separation criterion, 226

N

Natural convection, 26. *See* Free convection

Natural transition, 275

Navier–Stokes equations, 2, 54, 60

- for axisymmetric flow, 428
- compressible, linearized disturbance relations based on, 295–297
- dimensionless form, 56
- incompressible, linearized disturbance relations based on, 287–289
- solution for flat-plate flow, 172–173

Neutral curves, 258–259

Newman's experiment, 370–371

Newtonian fluids, 2, 14, 48

- deformation law for, 42–43
- incompressible, equations of motion of, 480–482
- transport properties of, 463–471

Newtonian hypersonic impact theory, 413–414

Newton's second law, 40

Nodal point, 224

Noncircular ducts, 86–88, 344

Nonfluids (solids), 8

Noninertial coordinates, 63

Non-Newtonian fluid, 14

Non-uniqueness problems, 131, 180

Normal modes, 252

Normal pressure gradient effect, 166–167

No-slip condition, 4, 13, 28–29, 49, 60, 79, 102

- for turbulent flow, 332

No-temperature-jump condition, 28–29, 49, 78, 332

Nuclear reactions, 8

Numerical stability, 201, 206, 421
Nusselt number, 57, 79
 in creeping motion, 141
 for duct flows, 90–91
 in Falkner–Skan flow, 181–182
 on flat plate, 162, 177
 in free convection, 230–231
 in general laminar boundary layers, 206
 mean, 93–95
 in stagnation flow, 125

O

One-dimensional flow approximation, 65
One-equation model, 354, 358–359
One-seventh power-law, 347
Order, of tensor, 472
Orr–Sommerfeld equation, 253–255
 numerical solution, 257
 parametric effects, 261–271
Orthogonal coordinate systems, 50–52, 166, 219
 Cartesian coordinates, 51
 cylindrical polar coordinates, 51
 spherical polar coordinates, 51–52
Oscillatory channel flow, 98
Oscillatory motion, 96–97, 99–103, 105–107
 transition in, 284
Oseen, theory of, 138–140
Outer layer, turbulent, 336–338
Overlap layer, turbulent, 335
 power-law approximation, 340
 roughness effect, 344–345

P

Parabolic differential equation, 53–54, 165, 199, 431
Parabolic flow on flat plate, 221–223
Parallel stream interaction, 186–187
Particle derivative, 9
Peclet number, 57, 92
Penetration depth, 101, 118
Penetration number, 58

Perfect-gas law, 23–25, 401–403, 431
 applications, 431
Perfect fluid theory. *See* Potential flow analysis
Permutation tensor, 473
Perturbation methods, 169, 444
Pipe flow. *See* Circular pipe flow
Pohlhausen–Gruschwitz polynomials, 419
Pohlhausen paradox, 158
Pohlhausen parameter, 195
Point sink flow, 185
Poiseuille flow, in pipe, 84–85
 between parallel plates, 85–86
 stability analysis, 262–263
 with wall slip, 85
Poiseuille number, 78, 89
 for various duct, 90
Poiseuille paraboloid, 84
Poisson equation, 53, 83, 255
Porous ducts. *See* Suction flows
Potential energy, 46, 48
Potential flow analysis, 3, 178–179
 for cylinder in crossflow, 4, 198
 for Falkner–Skan wedge flow, 178–179
 and reversibility, 137
 for sphere, 135
Potential vortex, 81
Power-law approximation
 for cone flow, 213, 440–441
 for equilibrium flow, 338, 370
 for free-shear flows, 383
 for non-Newtonian fluids, 14–15
 for overlap velocity profiles, 340–341
 for thermal conductivity, 18, 19
 for turbulent flat-plate flow, 347
 for viscosity, 16, 407, 421, 468
 for wedge flows, 178
Prandtl number, 18, 54–57, 404
 on flat plate, 176–177
 of gases, 26
 reciprocal, 471
 turbulent, 432
 of various fluids, 55

- Pressure drop in ducts, laminar, 210–211
 - turbulent, 341–347
- Pressure gradient parameter, 335–337, 357
- Pressure-gradient parameter, 434
- Pressure waveform, modulus of, 306
- Principal axes for strains and stresses, 12, 43
- Principia* (Newton), 1
- Principle of corresponding states, 15
- Prolate spheroid flow, 136
- Properties, of fluid, 8–27
 - kinematic properties, 8–13
 - surface tension, 30
 - thermodynamic properties, 8, 20–25
 - transport properties, 8, 13–20
- Pseudoplastic fluid, 14
- Pseudoresonance, 263
- Pulsatory channel flow, 98
- Pulsatory pressure gradient, duct flow due to, 97–99

Q

- Quasi-viscous flow, 61–62
- Quasi-viscous flows
 - compressible-flow approximations for, 444–451

R

- Radial frequencies, 307, 309
- Radius of curvature, 30, 166
- Range indices, 472
- Rayleigh–Janzen expansions, 444–447, 451
- Rayleigh number, 230
- Rayleigh stability theorems, 256
- Real fluids, 2
- Reattachment, 373
- Receptivity of boundary layers, 276
- Recovery factor
 - laminar, 405, 407–408, 410, 412, 422
 - turbulent, 432, 439–440
- Recovery temperature, 405
- Reduced properties, 15–16, 17

Reference temperature concept, 409
Reflection, 28
Relaminarization, 374–375
Relaxing flows, 366
Repeating parameters, 168

Page 521

Reverse flow, 85
Reversibility of creeping flows, 137
Reynolds analogy, 126, 183, 384, 412, 425, 437
 compressible flow, 405, 437
 effect of pressure gradient, 183
 laminar flat-plate flow, 183
 turbulent flat-plate flow, 386, 437
Reynolds dye experiment, 272
Reynolds equations of turbulence, 328–331
Reynolds lubrication equation, 144
Reynolds number, 2, 3, 56, 59, 78, 164, 172, 267
 acoustic, 307
 high, 61–62
Reynolds rules of averaging, 329
Reynolds stresses, 330–331
 basic equation, 331
 modeling, 361–362, 368
Reynolds transport theorem, 63
Rheology, 8
Rheopectic fluid, 14
Richardson's annular effect, 97, 102
Rossby number, 63
Rotating cylinders, 80–83, 270–271
 disk, 126–130
Rotationally symmetric flow, 212–218
Roughness effects
 of commercial pipes, 346
 at high Mach numbers, 284
 on transition, 283–284
 in turbulent flow, 344–347, 351–352
Round jet, laminar, 217
 turbulent, 378–379
Rules of time averaging, 325–326, 329
Runge–Kutta integration, 121

S

- Saddle point, 224
- Sand-grain roughness, 345
- Schmidt number, 20, 54
- Secondary flow, 129, 220–221
- Second coefficient of viscosity, 14, 43
- Second law of thermodynamics, 21
- Second-moment closure model, 354, 361
- Self-preserving free-shear flows, 376
- Self-similar flow, 110
- Self-sustaining motion, 324
- Separated-flow transition, 275
- Separation, concept of, 3, 5, 166–167
 - in corner flow, 138
 - in Couette–Poiseuille flow, 85–86
 - in creeping flow, 138
 - on cylinder in crossflow, 5
 - in diffuser, 7
 - in Falkner–Skan flow, 179–180
 - in Jeffery–Hamel flow, 132
 - in linearly retarded flow, 190–191, 198, 201
 - prediction criteria
 - laminar flow, 132, 196–197, 214, 419
 - turbulent flow, 363, 365, 442
 - reattachment, 373
 - singular behavior of, 191
 - on sphere, 215
 - three-dimensional, 4, 224–225
- Series solution for laminar boundary layers, 190–191
- Shape factor, 155, 180, 195, 263, 363
 - of Clauser, 338
 - effect on stability, 263, 278
 - effect on transition, 278
 - Thwaites' correlation, 196–197
 - in turbulent flow, 333, 363–364, 441
- Shear layer. *See* Free-shear flows
- Shear modulus, 13
- Shear stress in boundary layer, 167, 220
 - Thwaites' correlation, 197
 - turbulent, 356–357
- Shedding, 6
- Shock-wave boundary-layer interaction, 425–427

Similarity solutions

- basic concept, 10, 167
- for compressible laminar flow, 405–407, 415–417
- defined, 119
- for Falkner–Skan flows, 177–182
- for free convection, 229
- for laminar boundary layers, 167, 178, 185, 222
- of Navier–Stokes equations, 120–132
 - Jeffery–Hamel flow, 130–132
 - rotating disk, 126–130
 - stagnation flow, 120–126
- point sink flow, 185
- for Stokes’ moving-wall problems, 104
- for turbulent jets, 378

Similarity transformation, 405–407

Skewed boundary layers, 220–221

Skin friction coefficient, 156

- in duct flow, laminar, 84
- turbulent, 342
- on flat plate, laminar, 409
- turbulent, 347, 351, 437–438
- on long cylinder, 216
- in supersonic flow, 409
- in turbulent boundary layer, 340, 363

Slip flow in tubes, 85

Slip velocity, 28–29

Small-disturbance stability concept, 250

Solenoidal vorticity vector, 11

Spanwise vorticity, 272–273

Specific heats, 22, 25

- ratio of, 23, 25, 57
- of various gases, 468

Specular reflection, 28

Speed of sound, 23, 25–26, 401

Sphere flow, 134–136, 140

- equations of motion for incompressible, 481–482
- for laminar boundary layer, 214–215
- stagnation point velocity gradient, 413–414

Spherical polar coordinates, 51–52

Squire’s theorem, 255, 267

Stability of laminar flows, 249–310

- basic concept, 249–250

- of Couette flows, 82, 262–263, 270–271
- inviscid theory, 256, 270
- of numerical methods, 201, 206, 421
- of parallel flows, 253–261
- of Poiseuille flows, 262–263
- of rotating-disk flow, 129, 271
- temporal *versus* spatial, 255
- of viscous flows
 - basic equations, 256–257
 - centrifugal effects, 270–271
 - compliant boundaries, 268–269
 - compressibility effects, 266–268
 - experiment, 260–261
 - of Falkner–Skan flow, 258–260
 - of free-convection flows, 269–270
 - of free-shear flows, 263–264
 - heating and cooling effects, 265–266
 - incompressible, 287–295
 - Orr–Sommerfeld equation, 256
 - parametric effects, 261–271
- Stagnation enthalpy, 160, 194, 333, 401
- Stagnation-point flow, 120–126, 412–414
 - axisymmetric, 123, 412–413
 - compressible form, 412–414
 - freestream velocity gradient, 413
 - plane, 120–121, 412–414
 - Reynolds analogy, 126
 - temperature distributions, 123–126
- Stagnation temperature, 401
- Stall, of airfoil, 3–4
- Stanford Conference, 355, 358, 363, 443
- Stanton number, 126, 161, 183, 386, 388
 - for compressible flow, 411, 437
 - with suction and blowing, 388
- Start-up, of pipe flow, 95–96
 - of cylinder flow, 226
 - transition in, 284
- Stationary turbulence, 326
- Steady-flow energy equation, 65
- Stodola’s relation, 401–403
- Stokes’ first and second problems, 104–107
- Stokes flow. *See* Creeping motion

- Stokes' hypothesis, 43–44, 48
- Stokes operator, 62
- Stokes paradox, 134, 138–139
- Stokes stream function, 134, 447
- Strain-rate tensor, 12
- Streaklines, 5
- Stream function, 39–40, 110, 121
 - for Blasius flow, 168
 - compressible form, 39, 437
 - Stokes, 134
 - two-dimensional considerations, 60–62
 - vorticity to, 444
- Stream-function vorticity, 61
- Streamlines, 4, 5, 40, 113
- Stress tensor, 40
 - turbulent inertia form, 330
- Strouhal number, 6, 56
 - for circular cylinder, 6
- Sublayer, viscous, 336, 432
- Substantial derivative, 9
- Suction flows
 - on flat plate, 108–109, 183–184, 352–353
 - developing, 191–192
 - between parallel plates, 109–114
 - in porous pipe, 112
 - rotating, flow in, 114–117
 - stability of, 263
 - in turbulent flow, 352–353
- Summation index, 472
- Superlayer, 327, 328
- Surface forces, 40
- Surface tension, 30
 - of various fluids in air, 467
 - of water in air, 466
- Sutherland constant, 16
- Sutherland law approximation
 - for thermal conductivity, 18, 19
 - for viscosity, 16, 468
- Swept wings, 4, 223–224
- Swirl velocity, 212

T

Taylor–Culick flow, 303–310, 447–451
Taylor number, 82, 270
Taylor series method, 169–170
Taylor vortices, 270
TDMA, 202–204, 206, 421
Temperature gradient, 17
 law of wall, 384–386
Temperature jump, 29
Tensor invariants, 12
Thermal-accommodation coefficient, 29

Page 522

Thermal boundary layer
 defined, 124
 laminar flows, 176–177, 204–209
 thickness, 124
 turbulent flows, 386
Thermal conductivity, 17–19
 of gases, 17–19, 464
 of steam and water, 470
 of water, 463–471
Thermal decoupling, 44–45, 331
Thermal diffusivity, 20, 54
Thermal-energy integral relation, 194
 compressible form, 432
 for turbulent flow, 333
Thermal entrance in duct, 91–93
Thermal-entrance length, 94
Thermal expansion coefficient, 26–27, 57, 228
 of steam and water, 27
Thermodynamic equilibrium, 8
Thermodynamic pressure, 43–44
Thermodynamic properties, 8, 20–25
Thixotropic fluid, 14
Three-dimensional boundary layers, 4
 laminar, 219–225
 basic equations, 219–220
 corner flow, 223
 flat-plate flow, 221–223
 separation concepts, 224–225

- yawed infinite cylinder, 223–224
- turbulent, 372
- Three-dimensional singular point, 224
- Thumb curves, 258
- Thwaites, integral method of, 195–197
 - application to transition, 277–279
 - for axisymmetric flow, 214
- Time averaging, 325–326, 328–330
- Timelines, 5
- Tollmien–Schlichting waves, 254, 258, 271, 324
- Tornado-like vortex, 225
- Total derivative, 9
- Total enthalpy. *See* Stagnation enthalpy
- Transition to turbulence, 82, 84–85, 271–276
 - boundary-layer transition processes, classification of, 275–276
 - control of, 285–286
 - on flat plate/cone, 275, 278–279, 440
 - freestream turbulence effects, 280–283
 - prediction methods, 276–287
 - pressure-gradient effects, 277–280, 282
 - Reynolds dye experiment, 272
 - roughness effects, 283–284
 - shape factor effects, 278
 - spanwise vorticity, 272–273
 - turbulent spots, 271–275
 - unsteady flow, 284–285
- Transpiration, 352
- Transport properties, 8, 13–20, 38
 - viscosity, 13–16
- Transverse-curvature effect, 215
- Traveling wave disturbance, 252, 254
- Tridiagonal matrix algorithm (TDMA), 202–204, 206, 421
- Trigonometric identities, 490–491
- Trip wire, 283
- Turbulence kinetic energy, 331
 - basic equation, 331, 333
 - modeling, 358–361
- Turbulence modeling, 353–362
 - for boundary layers, 355
 - direct numerical simulation, 325, 354, 369
 - eddy conductivity, 383–384, 431
 - eddy viscosity, 354–358, 359

- higher order models, 358–362
- K- ϵ model, 359–360
 - at low Reynolds numbers, 360–361
 - mixing layer, 379–381
 - mixing-length, 354–355, 391
- Turbulent boundary layers, 347–353
 - with pressure gradient, 362–375
- Turbulent dissipation, 330–333, 359
- Turbulent-energy methods, 358–361
- Turbulent flows
 - basic equations, 329–331
 - boundary layer, 347, 430
 - channel flow, 342–344
 - complex, 372–375
 - compressible, 430–432, 436–451
 - convective heat transfer, 383–392
 - on flat plate, 436–441
 - on flat-plate, 323, 327, 347–353, 356
 - integral relations, 333–334, 347
 - jets and wakes, 375–383
 - pipe flow, 341–342
 - roughness effects, 344–347, 351–352
 - in rough pipes, 344–347
 - temperature jump in, 29
 - three-dimensional, 372
 - unsteady, 329
- Turbulent fluctuations, 323, 325–327, 379, 380, 382
 - compressible, 430
 - frequency spectra, 328
 - hot-wire measurements, 326
 - statistical theory, 326
 - time averaging, 325–326, 328–330
- Turbulent flux, 330
- Turbulent heat flux, 330
- Turbulent inertia. *See* Reynolds stresses
- Turbulent Prandtl number, 359, 383–384, 432
 - for kinetic energy and dissipation, 359
- Turbulent shear stress, 326, 330, 332
- Two-equation models, 354, 359–360, 367

U

- Uncoupling of temperature, 331
- Unfavorable gradient. *See* Adverse pressure gradient
- Unheated starting length, 162
- Uniform heat-flux approximation, asymptotic, 90–91
- Unit Reynolds number effect, 272
- Unsteady boundary layers, 226–227
 - transition of, 284–285
 - water hammer problem, 427–429
- Unsteady Couette flows, 103–108
- U-shaped junction, 225

V

- van Driest
 - damping factor, 355–356, 391
 - effective velocity, 433
 - flat-plate theory of, 436–437
 - transformation, 432–433
- Vapor pressure
 - of various fluids, 467
 - of water, 466
- Variable-wall-temperature solutions, 208–209, 389–390
- Vector identities, 457
- Velocity defect, 335–336, 338
- Velocity potential, 60
- Velocity profile
 - defined, 78
 - for turbulent flow, 334
- Velocity vector, 9
- Viscometry, 82, 87
- Viscosity, 13–16
 - coefficient, defined, 14
 - critical point correlations for, 15
 - as function of temperature and pressure, 15–16
 - gas, 16, 465, 468
 - of liquids, 20, 466–467
 - second coefficient, 14, 43
 - of steam and water, 469
 - of water, 463–471
- Viscous diffusivity, 54
- Viscous length scale, 336
- Viscous sublayer, 336, 432

- Visualization of flow, 323–325
- von Kármán's viscous pump, 127
- Vortex, decay
 - methods, 50
 - shedding, 6
 - stretching, 60
- Vortex breakdown, 274
- Vortex Reynolds number, 59
- Vortex sheet, 251
- Vortex street, 5
- Vortex-stretching term, 60
- Vorticity, 11
 - equation, 54
 - in incompressible viscous flow, 59–60
 - spanwise, 272–273
 - to stream function, 444
- Vorticity transport equation, 60

W

- Wake flow
 - Coles parameter, 339, 363
 - laminar, two-dimensional, 189–190
 - axisymmetric, 217–218
 - stability of, 263–264
 - turbulent, 381–383
- Wake function, 339
- Wall-conduction temperature, 385
- Wall-friction velocity, 335, 349
- Wall functions, 360–361
- Wall jet, laminar, 181
- Wall Reynolds number, 110, 115
- Wall transpiration, 352
- Wall-wake law, 339–340, 348, 365, 432–435
- Walz, method of, 441–442
- Water hammer problem, 427–429
- Wave cancellation control, 286
- Wave equation, 53
- Weber number, 57–58
- Wedge flows, 177–181
- Wentzel–Kramers–Brillouin (WKB) method, 100
- Wind-driven flows, 117–119

Ekman spiral flow, 118–119
penetration depth, 118
starting flow, 117–118
Wind stress, over water surface, 118
Work, defined, 21, 46

Y

Yawed cylinder flow, 223–224
Yielding fluids, 14

Z

Zero-equation model, 354–358, 367
Zwarts, supersonic experiment of, 443



501111